

AFGL-TR-77-0051

AIR FORCE SURVEYS IN GEOPHYSICS, NO. 364

NASA TMX-73537

# Proceedings of the Spacecraft Charging Technology Conference

C.P. PIKE  
R.R. LOVELL  
Editors

24 February 1977

Approved for public release; distribution unlimited.

This report is the result of a joint U.S. Air Force and NASA sponsored conference held 27-29 October 1976 at the United States Air Force Academy, Colorado. Portions of the AFGL papers were supported by the Air Force In-House Laboratory Independent Research Fund.



SPACE PHYSICS DIVISION PROJECT ILIR, 7661  
AIR FORCE GEOPHYSICS LABORATORY  
HANSCOM AFB, MASSACHUSETTS 01731

AIR FORCE SYSTEMS COMMAND, USAF

NATIONAL AERONAUTICS AND SPACE ADMINISTRATION

LEWIS RESEARCH CENTER  
CLEVELAND, OHIO 44135

(NASA-TM-X-73537) PROCEEDINGS OF THE  
SPACECRAFT CHARGING TECHNOLOGY CONFERENCE  
Interim Report (NASA) 985 P HC A99/MF A01

CSCI 22B

G3/12

50749

Unclass

N78-10182

THRU

N78-10129





12  
PRECEDING PAGE BLANK NOT FILMED

## Preface

The Spacecraft Charging Technology Conference was held at the USAF Academy from 27-29 October 1976. The Conference provided the initial opportunity for an exchange of results from the AF/NASA Spacecraft Charging Technology Program. This program is coordinated by the AFSC(DL)/NASA(OAST) Space Research and Technology Review Group. The Review Group coordinates interdependent technology programs between the two agencies. At the Conference, USAF, NASA, industry and university groups working in the spacecraft charging technology area were able to present their results. Spacecraft charging technology encompasses a broad based technology effort, composed of expertise spanning the spectrum from geophysics to spacecraft design engineering. The Conference provided a medium for a comprehensive presentation of results from programs in these diverse disciplines. The technology base formed at the Conference, and contained in this document, has immediate and direct application to design and test requirements for on-going and planned USAF, NASA, and industry space systems.

We would like to thank Col. John E. Brooke, Assistant Director of Science and Technology, USAF Systems Command, and Dr. Robert E. Smylie, Acting Associate Administrator for Aeronautics and Space Technology, National Aeronautics and Space Administration, for their approval and endorsement of the Conference. C. Pike would like to thank Col. Bernard S. Morgan, Jr., Commander of the USAF Geophysics Laboratory, USAF Systems Command, for his encouragement and for his support of the Conference. We would also like to thank Lt. Gen. James R. Allen, Superintendent, USAF Academy, for supporting the Conference, including arrangements for accommodations, transportation, meals and facilities,

and Brig. Gen. William T. Woodyard, Dean of Faculty, USAF Academy, for his welcoming address. In particular, thanks are extended to Capt. Mark Torreano, Directorate of Conferences, USAF Academy, for his outstanding support at the Conference. Members of the Conference Program Committee are Capt. M. H. Bunn, Dr. M. L. Minges, Dr. A. Rosen, Dr. R. W. Rostron, and Dr. E. C. Whipple.

C. P. PIKE  
R. R. LOVELL  
Co-Chairmen, USAF/NASA Spacecraft  
Charging Technology Conference

## Contents

EXECUTIVE SUMMARY	9
KEYNOTE ADDRESS by Robert E. Smylie	21
SPACECRAFT CHARGING TECHNOLOGY CONFERENCE, P78-2 by Douglas F. Shane, Lt/Col USAF	25
SESSION I - Environment	35
1. The Plasma Environment at Geosynchronous Orbit by Sherman E. DeForest	37
2. Composition of the Hot Plasma Near Geosynchronous Altitude by R. G. Johnson, R. D. Sharp, and E. G. Shelley	53
3. INJUN 5 Observations of Vehicle Potential Fluctuations at 2500 km by R. C. Sagalyn	67
4. Preliminary Report on the CTS Transient Event Counter Performance Through the 1976 Spring Eclipse Season by N. John Stevens, Robert R. Lovell, and Vernon W. Klinect	81
5. Active Control of Spacecraft Charging on ATS-5 and ATS-6 by Carolyn K. Purvis, Robert O. Bartlett, and Sherman E. DeForest	107
6. Active Control of Potential of the Geosynchronous Satellites ATS-5 and ATS-6 by Raymond Goldstein	121
7. Plasma Distribution and Spacecraft Charging Modeling Near Jupiter by Raymond Goldstein and Neil Divine	131
8. Active Spacecraft Potential Control System Selection for the Jupiter Orbiter With Probe Mission by John R. Beattie and Raymond Goldstein	143
9. Nuclear Burst Plasma Injection into the Magnetosphere and Resulting Spacecraft Charging by A. L. Pavel, J. A. Cipolla, M. B. Silevitch, and K. I. Golden	167

## Contents

10. Electrification of the Proof Mass of a Drag-Free or Accelerometric Satellite by Rémy Juillerat and Jean-Pierre Philippon	175
11. Analysis of Penumbral Eclipse Data by H. B. Garrett, 1/Lt USAF	191
12. The Multiple Applications of Electron/Emitters in Space by Réjean J. L. Grard	203
SESSION II -- Modeling	223
1. Modeling of Spacecraft Charging by Elden C. Whipple, Jr.	225
2. A Charging Model for Three-Axis Stabilized Spacecraft by M. J. Massaro, T. Green, and D. Ling	237
3. Induced Charging of Shuttle Orbiter by High Electron-Beam Currents by H. B. Liemohn	271
4. An Altitude-Dependent Spacecraft Charging Model by J. W. Haffner	287
5. Pioneer Venus Spacecraft Charging Model by P. A. Robinson, Jr. and A. B. Holman	297
6. Numerical Simulation of Spacecraft Charging Phenomena by J. G. Laframboise and S. M. L. Prokopenko	309
7. Dynamic Modeling of Spacecraft in a Collisionless Plasma by Ira Katz, Donald E. Parks, Sang Wang, and Andrew Wilson	319
8. Calculation of Sheath and Wake Structure About a Pillbox-Shaped Spacecraft in a Flowing Plasma by Lee W. Parker	331
9. Experimental Modeling of Plasma Flow Interactions by W. A. Oran and N. H. Stone	367
10. Prediction of Large Negative Shaded-Side Spacecraft Potentials by S. M. L. Prokopenko and J. G. Laframboise	369
11. A Simulation Model of Time-Dependent Plasma-Spacecraft Interactions by P. L. Rothwell, A. G. Rubin, and G. K. Yates	389
12. Photoelectric Charging of Partially Sunlit Dielectric Surfaces in Space by Bibhas P. De and David R. Criswell	413
SESSION III -- Materials Characterization	421
1. The Lewis Research Center Geomagnetic Substorm Simulation/Facility by Frank D. Berkopec, N. John Stevens, and John C. Sturman	423
2. Testing of Typical Spacecraft Materials in a Simulated Substorm Environment by N. John Stevens, Frank D. Berkopec, John V. Staskus, Richard A. Blech, and Steven J. Narciso	431
3. Charging Characteristics of Materials: Comparison of Experimental Results With Simple Analytical Models by Carolyn K. Purvis, N. John Stevens, and Jon C. Oglebay	459
4. Investigation of a CTS Solar Cell Test Patch Under Simulated Geomagnetic Substorm Charging Conditions by K. P. Bogus	487
5. Charge Distributions Near Metal-Dielectric Interfaces Before and After Dielectric Surface Flashover by James W. Robinson	503
6. Electrical Equilibration of Dielectrics When Exposed to Energetic Electron Beams by William Saylor	517

## Contents

7. Surface Micro-discharges on Spacecraft Dielectrics by K. G. Balmain, M. Cuchanski, and P. C. Kremer	519
8. Surge Current and Electron Swarm Tunnel Tests of Thermal Blanket and Ground Strap Materials by D. K. Hoffmaster, G. T. Inouye, and J. M. Sellen, Jr.	527
9. A Rugged Electron/Ion Source for Spacecraft Charging Experiments by J. E. Nanevicz and R. C. Adamo	549
<b>SESSION IV -- Materials Development</b>	<b>557</b>
1. Conductive Spacecraft Materials Development Program by W. L. Lehn	559
2. Results of Literature Search on Dielectric Properties and Electron Interaction Phenomena Related to Spacecraft Charging by J. A. Wall, E. A. Burke, and A. R. Frederickson	569
3. Electrically Conductive Paints for Satellites by J. E. Gilligan, R. E. Wolf, and C. Ray	593
4. Formulation of Electrically Conductive, Thermal-Control Coatings by M. C. Shai	613
5. Materials and Techniques for Spacecraft Static Charge Control by L. J. Amore and A. E. Eagles	621
6. Secondary Emission Conductivity of High Purity Silica Fabric by V. J. Belanger and A. E. Eagles	635
7. Conductivity Effects in High-Voltage Spacecraft Insulating Materials by R. C. Adamo, J. E. Nanevicz, and N. Grier	669
8. Investigation of Conductive Thermal Control Coatings by a Contactless Method in Vacuo by W. Viehmann, C. M. Shai, and E. L. Sanford.	687
9. Spacecraft Charging/Contamination Experiment on SCATHA by D. F. Hall	699
10. The Effects of the Geosynchronous Energetic Particle Radiation Environment on Spacecraft Charging Phenomena by J. B. Reagan, W. L. Imhof, and E. E. Gaines	701
11. Oscillations in Insulator Leakage Current Under Steady Conditions of Synchronous Orbit Plasma and Photoillumination by R. C. Adamo and J. E. Nanevicz	715
<b>SESSION V -- Design and Test</b>	<b>717</b>
1. System Aspects of Spacecraft Charging by S. P. Bower	719
2. Transient Response Measurements on a Satellite System by J. E. Nanevicz	723
3. Provisional Specification for Satellite Time in a Geomagnetic Substorm Environment by N. John Stevens, Robert R. Lovell, and Carolyn K. Purvis.	735
4. Development of Environmental Charging Effect Monitors for Operational Satellites by N. John Stevens, John C. Sturman, and Frank D. Berkopec	745

## Contents

5. Viking and STP P78-2 Electrostatic Charging Designs and Testing by R. O. Lewis, Jr.	753
6. Design, Construction, and Testing of the Communications Technology Satellite-Protection Against Spacecraft Charging by J. Victor Gore	773
7. Common Approach to Solving SGEMP, DEMP, and ESD Survivability by D. Ling	789
8. Plasma Charging Testing of Communication Satellites by F. Rosen	805
9. Qualification Model Spacecraft Tests for DEMP, SGEMP, and ESD Effects by E. Paul Chivington, Peter J. Madle, and Peter H. Stadler	815
10. Spacecraft Charging Anomalies on the DSCS II, Launch 2 Satellites by George T. Inouye	829
11. Space Environmental Effects on the SKYNET 2B Spacecraft by A. Robbins and C.D. Short	853
12. RCA Satcom 3 - Axis Spacecraft Experience at Geosynchronous Altitude by Joseph Napoli and Joseph Seliga	865
PANEL DISCUSSION	873

**PROCEEDINGS OF THE SPACECRAFT  
CHARGING TECHNOLOGY CONFERENCE**

**Executive Summary**

- Session I. .... C. P. Pike  
Air Force Geophysics Laboratory  
Hanscom AFB, MA 01731
- Session II. .... E. C. Whipple, Jr.  
University of California, San Diego  
LaJolla, CA 92093
- Session III. .... N. J. Stevens  
NASA Lewis Research Center  
Cleveland, OH 44135
- Session IV. .... M. L. Minges and W. L. Lehn  
Air Force Materials Laboratory  
Wright-Patterson AFB, OH 45433
- Session V. .... M. H. Bunn, Captain, USAF  
Space and Missile Systems Organization  
Los Angeles, CA 90009

**SESSION I. ENVIRONMENT**

DeForest reviewed the geosynchronous plasma environment including the high energy tail, the thermal background plasma, the low temperature "warm plasma," locally produced secondaries, substorm injection events, field aligned currents

---

(Received for publication 24 February 1977)

and magnetopause crossings. A synchronous environment plasma model was presented that includes omnidirectional and unidirectional electron fluxes. Charging in cavities located at the ends of a spacecraft can be dominated by the intense field aligned fluxes. Johnson et al reported observations of field aligned fluxes of  $O^+$  and  $H^+$  ions. Fluxes of  $10^8$  ions/cm sec or and with keV energies are seen. Sagalyn and Burke reported on vehicle potential and plasma density and temperature measurements. At 2500 km altitude in polar orbit, vehicle potentials of up to -40 V are observed during impulsive auroral electron precipitation events. Stevens et al examined data from the Transient Event Counter on the CTS satellite. When discharges occurred, they were often recorded at the rate of a few per second, but no spacecraft anomalies appear directly related to the discharges. Purvis et al reported on active control of spacecraft charging using ATS-5 and ATS-6. Data from the ion engine neutralizer and an unbiased electron emitter were used. With the neutralizer on, the potential was -10 volts in eclipse and, when the neutralizer was turned off, the potential went to -1200 volts. The plasma bridge neutralizer is more effective than the emitter in maintaining vehicle potential near ground. Goldstein examined ATS-6 ion engine neutralizer data in conjunction with the UCSD particle detector. When the spacecraft potential was clamped to -10 volts, positive cesium ions flowed back to the spacecraft. He recommends mounting discharge devices away from the spacecraft on a boom in order to minimize contamination. Goldstein and Divine calculated spacecraft potential levels for Jupiter. Potentials of  $10^3$  to  $10^4$  volts are expected. Beattie and Goldstein described the selection process, including various trade-offs, for the active control system for the Jupiter Orbiter with Probe (JOP) spacecraft. Calculations by Pavel et al indicated that high altitude nuclear bursts can lead to processes which result in high charging levels on synchronous satellites. Juillerat and Philippon showed that proton fluxes in the South Atlantic Anomaly lead to currents which charge the proof mass of a low altitude "drag-free" satellite. Garrett combined measurements of ATS-6 eclipse data on particle fluxes and AE-C satellite data on UV radiation. He presented a nearly linear relationship between solar illumination/photoelectron flux and the logarithm of spacecraft potential. Grand described the many applications that an electron source such as a simple cathode may have to scientific and engineering satellite payloads.

## SESSION II. MODELING

This summary will attempt to indicate the trends of research in the area of modeling with an emphasis on what is still needed. A detailed summary of the

talks that were given will not be given. Some of the points to be discussed were brought out in the panel discussion which followed the main sessions of the conference.

The ultimate aim of the modeling efforts is to provide a theoretical scheme which can be used to describe the structure of the sheath around the spacecraft and to calculate the charging currents to the spacecraft. In order for the model to be useful, it should be readily applicable to real spacecraft, and the results should be capable of verification by comparison with data.

A full three-dimensional, self-consistent, time-dependent model for spacecraft charging is likely to be so complicated and time-consuming on a computer that its application to real problems would be quite limited. An important aspect of modeling research is finding out what approximations can be made. Any approximation which does not compromise the essential physics and which reduces the complexity of the computations should be very useful. A number of such approximations were discussed at the conference.

One obvious approximation is the neglect of time-dependence and the assumption of quasistatic conditions. There are probably many situations where this is a realistic assumption since the time constant for the plasma response is usually short compared to the time scale for changes in conditions. Occasions where this assumption is not valid may occur during discharge events and possibly during the charging of dielectrics which have large capacitances and hence long time constants for charging.

Another approximation is the utilization of a more restricted geometry than the full three-dimensions. Such models can give insight into the basic physical mechanisms and their relative importance with less cost. However, their application to realistic spacecraft configurations is probably restricted.

Neglect of space charge may be a valid approximation under some circumstances. In particular, it is probably quite realistic to neglect the contribution to the space charge from the ambient plasma in environments where the electron density in the magnetospheric plasma is small compared to the photoelectron density. Including only the space charge due to the photoelectrons is probably adequate in such circumstances.

An aim that all modelers should keep in mind is the possibility of representing their numerical results with analytic formulas. As insight is gained into the relative importance of the various physical processes, it is probable that many of these processes can be individually modeled with some sort of an analytic representation. Any such representation could be extremely useful in reducing computing time and costs.

Another important aspect of modeling is that of verification. This involves at least two things. First, a model must be built for an actual spacecraft which will be obtaining data. Second, data must be obtained with experiments on that spacecraft which can be used to compare with the predictions of the model.

Thought should be given now to the problem of developing a charging model for specific spacecraft. Two spacecraft which are obvious candidates are ATS-6 which is at present providing most of the currently available data on spacecraft charging in synchronous orbit, and the SCATHA spacecraft which will be launched in early 1979. Differential charging has been detected on ATS-6 but a full interpretation of the data requires a modeling effort. A charging model for SCATHA will be essential for the interpretation of data from that spacecraft.

One final comment on verification: the experiments on the ATS satellites and on SCATHA were developed without the insights that a charging model would provide. It is highly likely that as a charging model is developed and compared with spacecraft data, new experiments and better configurations of existing instruments will be devised for verification of charging processes. In this respect, the present modeling work must be regarded as an interim effort until there has been at least one iteration of the modeling - verification cycle.

### SESSION III. MATERIALS CHARACTERIZATION

The materials characterization session of this conference was devoted to presentations on the experimental determination of the behavior of typical spacecraft materials when exposed to simulated geomagnetic substorm conditions. In addition, there were papers on facility related topics.

Papers by Stevens et al and Saylor presented results of survey tests on the response of various materials to electron bombardment. Results given by Stevens et al were based on measurements of leakage current and surface voltage, while those given by Saylor were based on measurements of leakage current. Surface voltages given by Saylor were calculated from the leakage current and sample capacity. The most striking difference in results was in the surface voltages reported. Saylor reports large positive surface voltages (2-3 kV) for teflon and kapton samples under bombardment by electron beams with beam energies up to 7 keV. In contrast, Stevens et al report only negative surface voltages for these materials under bombardment by electron beams with beam energies from 2 to 20 keV.

The test results for flexible solar array segments were given by Stevens et al and Bogus. The results were similar. The tests reported by Bogus were more

complete and concluded that temperature can have an influence on discharging characteristics.

Edge voltage gradients were discussed by Robinson. This work complimented that presented by Stevens et al. However, in this work, discharges in the silver teflon samples were hard to obtain until the sample was cut. Discharges were obtained in the tests described by Balmain. Here the characteristics of surface micro-discharges in dielectric samples in a scanning electron microscope facility were described.

Sellen discussed the problems of sample hysteresis and its effect on the interpretation of the results. Facilities and possible electron sources were discussed by Berkopec et al and Nanevicz and Adamo.

In general, the papers given in this session presented more information than was available one year ago. However, there are sufficient differences noted in these results to warrant a critical evaluation of test methods and sample preparation.

#### SESSION IV. MATERIALS DEVELOPMENT

##### 1. Overview

In principle, an attractive technique for controlling and minimizing spacecraft charging or at least for distributing the charge in an equipotential manner is through the use of electrically conductive surfaces for the materials exposed to the space environment. As discussed elsewhere during this symposium, the level of electrical conductivity required is relatively modest in most cases. Some promising advances have been made in this direction as summarized in some of the papers in this session. In other cases, further advances present a real challenge. Spacecraft surface materials are varied (for example, insulating blankets, solar cells, structural members, and optical components) and the task of developing electrically conductive analogues of all these materials while maintaining their primary functional features presents difficult technical issues. An example here would be electrically conductive thermal control coatings. Coatings, black in color (both visually and in the IR), can be produced readily based on the carbon black pigmented materials used widely in the aircraft industry. However, such coatings will clearly produce significant thermal loads in the substrates beneath them. While they will emit satisfactorily in the IR, they will have very high solar absorptance and thus not really perform the thermal control function at all. Obtaining acceptable thermal control features along with electrical conductivity in a practical coating is proving to be very difficult.

Even with conductive surfaces, practical methods of electrically interconnecting different surface regions may not be straightforward. An example here would be the interconnection of optical solar reflector mirrors which have been coated with electrically conductive surface material. The OSRs are, of course, quite small, thus the interconnections have to be numerous. The mirrors are also fragile and their coatings are delicate, thus introduction of conduction paths through the adhesion materials around and under the mirrors is a difficult design problem. An additional design requirement especially important for Department of Defense satellites is dependable long term performance. Assuring long lifetime, on the order of 5 to 10 years, for materials which must perform under a multiplicity of environmental stresses can be difficult. For example, one of the central issues at present is the interdependency of contamination and spacecraft charging. Questions such as the following arise: (1) does contamination change the electrical characteristics of conductive surfaces? (2) does significant contamination arise when electrical discharging occurs especially when the latter is low level, but chronic, over long periods of time? Several papers at this symposium address these questions.

As discussed at some length during the symposium, there are design alternatives to conductive materials for control of charging effects. Electromagnetic shielding of critical components would be one example, simply halting operation of the satellite during periods of high level solar activity would be another. Some methods of control, especially the so-called "active" techniques of dissipating charge, actually depend on the presence of interconnected electrically conductive surfaces to "funnel" the charge to the point of dissipation.

Once conductive materials become available, issues of spacecraft system design using these materials arise. From the material developer's view, this generally means that a substantial design information package must be developed including the response of the material in a number of combined-environment exposure situations. Again, as discussed frequently during this symposium, there are a number of unresolved questions as to exactly what tests are necessary and sufficient to produce the design package. Since the required materials characterizations seem to be complex and the effects in the materials subtle, questions arise as to intercomparisons of test results among different investigators and how standardization of the test methodology can be affected.

Even though the development of conductive materials represents high risk, probably long range technology, the effort should be undertaken because of the high payoff in spacecraft design flexibility and reliability. Without improved materials, alternative design fixes or change in modes of system operation present penalties in higher system weight, shorter lifetime, and lessened reliability.

The papers in this session can conveniently be divided into two categories. First is a group dealing specifically with new electrically conductive materials development: paper numbers IV-1, 3, 4, 5 and 6. Second is a group dealing with effects on materials of an electrically energetic environment and with the methods of materials characterization: paper numbers IV-2, 7, 8, 9, 10 and 11. As mentioned above, the effects/characterization issues are central to the effective use of these new materials in spacecraft design and for high confidence predictions of performance especially in long lifetime missions.

## 2. Materials Development Papers

The first paper in this group by W. L. Lehn (IV-1) presents an overview of the on-going and planned materials development efforts under a cooperative USAF/NASA program. A jointly planned USAF-NASA interagency cooperative research and technology program has been established and implemented to investigate spacecraft charging phenomena. The majority of the materials development task under this joint program is the responsibility of and is being directed by the USAF Materials Laboratory (AFML). This paper gives an overview of the materials development work, much of it just recently initiated, in four fundamentally different functional areas: (1) thermal control materials, (2) insulative materials, (3) transparent materials for OSR application and conductive materials for solar cell application, and (4) conductive low outgassing adhesives.

The current situation in the development of electrically conductive thermal control coatings (paints) is summarized by J. E. Gilligan (paper IV-3) of IIT Research Institute working under Air Force sponsorship and by C. M. Shai (paper IV-4) who discusses the in-house work at NASA Goddard.

A wide variety of approaches for the development of conductive paint type thermal control coatings have been investigated under the IITRI program. Materials which have been investigated and evaluated include both standard as well as electrically conductive organic and inorganic binders pigmented with conductive metallic and inorganic doped oxides. The paint systems formulated using commercially available conductive organic quaternary-ammonium salt-polyvinyl-carbazole polymers are interesting but will require a substantial, long term development before space stable materials will be realized. A major concern is poor vacuum and radiation stability of the polymeric binders. Several promising coatings based on a conductive antimony-doped tin oxide pigment in silicone and silicate binders with resistivities in the desired range of  $1 \times 10^9$  ohm-cm or lower were prepared but further development is required. From an overall point of view, the inorganic silicate coatings offer the greatest near term potential. The standard state-of-the-art Z-93 specification inorganic thermal control coating exhibits good

electrical properties and is a very space stable system. This material does develop a low level surface charge but does not arc/discharge. Development of an inorganic coating with improved electrical conductivity properties could be completed in 1-2 years. The materials developed were evaluated based on electrical conductivity, goal of  $1 \times 10^9$  ohm-cm or lower, physical properties and stability of the spectral reflectance under simulated space vacuum ultraviolet exposure.

The NASA coatings development program is in direct support of the International Sun Earth Explorer (ISEE) spacecraft. Materials which have been developed and evaluated include both organic and inorganic binders pigmented with standard dielectric as well as semiconductor pigments. The formulation, evaluation, and testing of these materials are presented. Conductive paints ranging in color from white and light yellow to green exhibiting solar absorptance values from 0.22 to 0.65 have been formulated from doped inorganic oxide pigments in inorganic mixed alkali silicate binders. Emittance values range from 0.87 to 0.90 and resistivities from  $1 \times 10^3$  to  $1 \times 10^5$  ohm-m<sup>2</sup>. The green paint has been selected for application on the ISEE satellite. Results of the materials characterization studies have shown that conventional thermal control paints charge to a certain degree under simulated synchronous orbit radiation exposure, but they do not arc or discharge, the excess charge being lead/conducted to the conductive substrate or ground. The conductive paints do not charge but conduct the charge to ground.

An entirely different approach to thermal control is discussed by V.J. Belanger and A.E. Eagles (paper IV-6). Their concept, developed at General Electric under USAF sponsorship, involves the use of high purity silica fabric as an extremely space stable, low solar absorptance to emittance ratio (white paint type) coating. The application of these high purity silica fabrics and conductive fiber/silica fiber interweaves to control the effects of spacecraft charging is being investigated. Further, a number of satellite systems contractors are considering use of the material because of its extreme space stability, contamination resistance, long life characteristics, and its resistance to heat pulse loading. The materials prepared have been studied as part of the NASA responsibility for the engineering characterization of the materials developed under the broad USAF/NASA joint program. It has been found that under simulated synchronous orbit charging conditions the silica fabric coating material, either by itself or when used as the outer layer of multilayer insulation (MLI) blankets, does become charged but does not arc or discharge. All of the other typical MLI configurations using outer layers of dielectric polymeric materials charge and arc/discharge to an excessive degree. The basic fabric material is commercially available. Secondary emission conductivity, proposed as the mechanism for the observed behavior, is discussed in the paper. A program to develop a silica fabric with optimized thermal optical, weight, and other physical and engineering properties has been initiated.

The final paper in the materials development category (paper IV-5) by L. Amore, A. E. Eagles and E. Okress of General Electric describes the design, fabrication and testing of conductive coating materials in the form of low cost conductive transparent coatings for optical solar reflectors, solar cell cover glasses and conductive polymeric films for a variety of uses such as thermal insulation blankets.

Examples of the approaches discussed in the paper include the deposition of transparent metal oxide coatings (indium tin oxide) on Kapton and Teflon metallized polymeric films. Thus far, good adhesion has been obtained and there has been little degradation of the thermal control features of the films. Conductive grids, photoetched on polymeric film substrates, also perform well as described in the paper. OSR and solar cell cover glass modifications have shown to hold promise. Glass frits modified or doped with zinc, lead, lithium, and cerium are effective in producing conductive surfaces in these materials.

### 3. Materials Effects and Characterization Papers

The first paper in this group by J. A. Wall, E. A. Burke, A. R. Frederickson and J. C. Garth (paper IV-2) deals with electrical properties of insulating materials. A knowledge of the dielectric properties and electron interaction phenomena of the materials applied to the exterior surfaces of a spacecraft is required in order to determine the susceptibility of the spacecraft to the ambient as well as the disturbed synchronous environment. A comprehensive literature search was performed by Wall and coworkers at Rome Air Development Center on spacecraft insulating materials in the areas of electrical conductivity, basic mechanisms of energetic electron interactions, (for example, secondary emission, backscatter, range, etc.) charge storage and electrical breakdown. The search concentrated primarily on polymeric dielectrics. Although work has continued in these areas for a number of years, much of the information has been generated only in the past 5 to 10 years and new data and theoretical approaches are appearing more and more frequently. With the exception of dielectric breakdown, much of the data and theory needed to help solve the spacecraft charging problem except for certain specific materials should therefore be available soon in the open literature.

In the next paper (IV-7), R. C. Adamo and J. E. Naneticz of Stanford Research Institute discuss photoconductivity effects in high voltage space insulating materials. The dark and photoconductivity of various external satellite dielectric materials is an important factor in any synchronous orbit charging/discharging situation. Recent investigations of several typical and potential spacecraft insulating materials have shown that the conductivity under simulated synchronous orbit conditions as well as the conditions required for electrical breakdown are a function of temperature, illumination intensity and wavelength, and electron beam energy and current.

These authors indicate that many of their samples showed an increase in conductivity of several orders of magnitude, particularly at higher temperatures while Kapton showed a change of five orders of magnitude under illumination. Adamo and Nanevich conclude that further materials investigations in this area are warranted to help provide guidance and direction for future development efforts.

A technique for determining the conductance of thermal control coatings by a contactless method in vacuo is outlined by W. Viehmann, C. M. Shai and E. L. Sanford of NASA Goddard (paper IV-8). In order to simulate orbital conditions more closely, current-density-voltage (j-v) curves were obtained with the contactless method in which the paint on an aluminum substrate was the anode of a vacuum diode configuration with a tungsten filament cathode. Conductances per unit area which satisfy the ISEE requirement were observed on black paints containing carbon and in "white" and green paints filled with zinc oxide which had been "fired" in order to induce defect conductivity. Because of surface effects and the nonhomogeneous nature of paints, large discrepancies were found between measurements with the contactless method and measurements employing metallic contacts, particularly at low current densities. Therefore, measurements with metallic contacts were considered to be of questionable value in deciding the suitability of coatings for electrostatic charge control.

D. F. Hall of Aerospace Corporation describes the charging/contamination experiment on the SCATHA spacecraft (paper IV-9). The ML-12 experiment, a joint project of the AF Materials Laboratory and Aerospace Corp. is designed to determine if spacecraft charging contributes significantly to the rate of contamination arriving at exterior spacecraft surfaces, and some of the characteristics and effects of the contamination collected. The contamination transport mode under investigation involves the ionization of molecules outgassed or released by the vehicle within the vehicle plasma sheath and their subsequent electrostatic reattraction to the vehicle.

Two sensor types will be flown. One type is a combination retarding potential analyzer (RPA) and temperature controlled quartz crystal microbalance (TQCM). With it, distinction can be made between charged and uncharged arriving molecules, and information concerning the temperature dependence of contamination absorption and desorption rates obtained. The other sensor type exposes samples of different spacecraft surface materials to arriving contamination and continuously measures the solar absorptance ( $\alpha_s$ ) of these materials. Changes in  $\alpha_s$  of space-stable samples will be entirely ascribed to contamination effects whereas changes in other samples will result from a combination of contamination, photochemical, and radiation effects. Upon ground command, some samples will go through a heating sequence designed to roughly determine the temperature at which contamination is desorbed.

In addition to describing the goals and techniques of ML-12 in more detail, the expected performance of the sensors and the need for coordination with other experiments on SCATHA are discussed in the paper.

Paper IV-10 by J. B. Reagan, W. L. Imhof and E. E. Gaines at Lockheed Palo Alto Research Laboratory deals with the effects of energetic particle radiation on spacecraft charging at geosynchronous orbit. In addition to the low energy, 5 to 50 keV electron environment at geosynchronous orbit which affects the external dielectric surfaces of the spacecraft there is also a very intense, dynamic and penetrating radiation environment, particularly at penetrating energies  $>1.5$  MeV, which is responsible for a variety of adverse charging effects on spacecraft components. The most serious of these is the degradation and failure of the widely used complimentary-metal-oxide-semiconductor (CMOS) electronic components as a result of internal charge-buildup induced by the energetic electrons. The dose received by a CMOS device from energetic electrons and associated bremsstrahlung was predicted with two computational codes. The two models were found to be different by as much as a factor of six. Resolving these discrepancies with the High Energy Particle Spectrometer experiment (SC-3) on SCATHA is discussed by these authors along with a review of the present discrepancies in the radiation models and the corresponding influences on spacecraft materials and component lifetimes.

Finally, a paper entitled "Electrical Discharges Caused by Satellite Charging at Synchronous Orbit Altitudes" by Nanevich, Adamo and Shaw of Stanford Research Institute was substituted for the paper originally scheduled (paper IV-11). This paper which complements the earlier CTS Transient Event paper by Stevens et al in Session I reports on some of the earlier, on-orbit measurements of satellite discharge events.

#### SESSION V. DESIGN AND TEST

The papers in this section cover several subjects pertinent to the satellite design engineer: environmental specifications, charge effect monitor devices and several approaches in vehicle design to limit, control or prevent spacecraft charging.

The paper by Bower provided an overview of the spacecraft charging problems encountered by satellite systems and what must be done to circumvent these problems. The charging phenomenon is very geometry-dependent and therefore varies immensely from satellite to satellite, but there are certain fundamentals which can be considered. The surfaces of current on-orbit systems are almost entirely dielectric, whether that dielectric is the 12 mils of cover glass over the solar

cells, the 2 mils of kapton surface on multiple layer thermal blankets, or the 2 mils of cover glass backed by aluminum or silver used as second surface reflectors. These surfaces become capacitors when electrons are deposited on them, and in the environment described preliminarily by Stevens/Lovell/Purvis in the third paper, they charge to the breakdown voltage. The subsequent discharge and punch-through induces spurious signals in the cables between electronic boxes with the possibility of upsetting the electronics or burning them out. This burn-out must be a concern, but can be coped with by eliminating the charging and subsequent discharging, by preventing coupling into the cables through shielding, or by designing immunity into the electronics.

Conductive fabrics are currently being defined and conductive polymeric coatings for cover glasses are in the development stages, but they are expensive and they may attenuate x-ray hardening in the case of military satellites. Considering the weight penalty of increased shielding, current preference is to design immunity into the electronics. The lack of a data base around which to design, however, leads to some over-design; in fact, most systems being designed today utilize all three approaches to controlling charging and discharging. Fortunately, but again only in the case of military systems, the design approach to solve SGEMP and EMP problems may solve ESD problems, and this is discussed extensively in the papers by Smith and Holman and Ling. Lewis described the design approaches used on two experimental satellite systems. One, requiring survival upon entry into the Martian atmosphere, allowed operation with corona but prevented arcing, while the other will be subjected to energetic particle charging and subsequent arcing.

An approach to solving the problem after-the-fact (subsequent to design) is presented by Gore. The extensive grounding, shielding and strict adherence to EMI requirements proved successful on this Canadian/US venture.

The original problem of convincing satellite designers and operators that some anomalous occurrences were indeed caused by arc discharge-triggered transients was aggravated by the fact that no on-orbit record existed. In fact, charge effect monitor devices are not included on the majority of satellites scheduled for launch in the near future. Nanevich and Stevens et al discussed the importance of establishing a one-to-one correlation between system electronic perturbations and the local environment, as well as how it can be done.

Rosen presented an approach to radiation susceptibility tests through pulse injection on an engineering model of the satellite electrical system, and concludes that the radiative part of the problem is controllable by means of reasonable EMC controls.

An entire spectrum of possibilities for limiting or preventing charging is thus presented, but the measures are expensive and much work remains in order to fully understand the problem.

## Keynote Address

Robert E. Smylie  
Nasa Headquarters  
Washington, D.C.

### INTRODUCTORY REMARKS

The purpose of this meeting is to provide both a focus for technologists and a current assessment to management of a relatively new phenomenon that has come to be known as spacecraft charging. This Conference which was sponsored jointly by USAF and NASA is intended to become the regular forum for disseminating the information gained in the investigation of this phenomenon. Before proceeding to technical presentations, I would like to discuss the USAF/NASA interdependency program and give a brief overview of the spacecraft charging program.

### USAF/NASA INTERDEPENDENCY

By 1973 both USAF and NASA were becoming increasingly aware that they had many common technology problems in both aeronautics and space. The natural consequence of this realization and continually tightening budgetary constraints was the interdependency program. Existing technology programs of mutual interest were identified. Where one agency had more expertise in a specific area, it was assigned the responsibility of providing the technology for both agencies. In some

cases, an agency has cancelled its program and transferred funds to the responsible agency. Where both agencies have desired to maintain programs, the programs have been jointly managed and the technical responsibility has been clearly established. Although it has taken some time for programs to merge into an interdependent mode, the concept is now being successfully exploited and benefits are beginning to accrue. The obvious benefits of the interdependency program have been to stretch the limited dollars available to both agencies, to reduce or eliminate duplication, and to provide both agencies enhanced capabilities.

#### THE SPACECRAFT CHARGING INTERDEPENDENCY PROGRAM

The spacecraft charging USAF/NASA program is an excellent specific example of interdependency. Since spacecraft charging has influenced the performance of military, commercial and NASA satellites, it became a logical candidate for a joint program. A program plan for USAF/NASA spacecraft charging investigation was approved by Colonel Brooke and myself in November of 1975. It was planned from the beginning to reflect true interdependency. Each element of the program was assigned to either NASA or USAF with well defined accountability. The success of the total program requires that both organizations execute their portion successfully.

The objective of the spacecraft charging investigation is to provide the design criteria, materials, techniques, and test methods to insure control of the absolute and differential charging of spacecraft surfaces. This objective is being met by conducting a combined flight test and ground technology program. It is estimated that the investigation will require another 4 years to complete.

The information generated in this interdependency program will be incorporated into a design criteria handbook and test specifications which will be available to the aerospace community. The handbook will catalog the materials behavior and develop the criteria for minimizing the charge buildup. The specifications will detail the procedures for testing satellites to guarantee that they will withstand the environment without anomalies. It is planned that preliminary documents will be available by late next spring.

#### SPACECRAFT CHARGING PHENOMENON

Spacecraft charging has come to be defined as the condition that arises when the geomagnetic substorm environment changes the potential of satellite surfaces relative to the space plasma potential. The charging phenomenon is usually

thought of in association with geosynchronous satellites, but it can also influence satellites in other orbits.

During the early 1970's, several synchronous satellites experienced spurious switching activity. Somewhat later, experimental measurements on-board ATS-5 suggested that the satellite could become charged to large negative voltages by a geomagnetic substorm. Through a detailed study of these anomalies and ground observatory data, a link was established showing that the substorm condition and the anomalies were occurring simultaneously. Laboratory tests were conducted to demonstrate that the electromagnetic pulse from an electrical discharge of an insulator could be coupled into the telemetry harness as a pseudocommand or as noise. Continued studies of the phenomenon have resulted in the concept of differential charging of satellite surfaces, in the demonstration of thermal control coating degradation, and in the possibility of enhanced contamination due to electrostatic forces. In addition, the uncontrolled and unwanted electric fields hinder scientific missions to measure low energy phenomena. The results of these studies will be presented in the following sessions of this Conference.

#### THE CONFERENCE

In the next 3 days, you will hear discussions of what is being done to define the geomagnetic substorm environment, of the analytical tools that are being developed as guides to future spacecraft design, of the work that is underway to characterize material responses, of the material modifications that are necessary to minimize charging, and of the flight experiment aspect of the investigation, as a part of that flight program, the USAF SCATHA satellite will be launched in 1979 to investigate the charging phenomenon in the actual space environment. You will hear in some depth a discussion of the SCATHA satellite in the following talk.

By the completion of this Conference, I believe that you will have a general understanding of spacecraft charging and what is being done to handle this phenomenon. You will see that the spacecraft charging investigation is a cooperative effort between NASA and USAF to attain a goal of nationwide interest to designers, experimenters and users of future spacecraft. Successful completion of this joint program will provide us with the capability to control the adverse effects of spacecraft charging on satellite operations and scientific investigations. Such a capability is essential to the development of the sophisticated long-life satellites which will serve us all in the future.

## Contents

1. Overview	25
2. Objectives	27
3. Management	28
4. Sponsors	29
5. Payloads	30
6. Orbital Parameters	32
7. Schedule	32

## Spacecraft Charging Technology Conference, P78-2

Douglas F. Shane, Lt/Col USAF  
LA Air Force Station  
Los Angeles, California

### I. OVERVIEW

The SAMSO Space Test Program (P78-2 Space Flight) is a vital portion of the NASA/USAF Charging Investigation. As shown in Figure 1, various tasks are the responsibility of a diversified collection of government and civilian agencies. The materials portion of this program is to be accomplished by the USAF Materials Laboratory and the testing of space vehicle models and experiment packages is a venture of NASA Lewis and the experiment Principal Investigators. Environmental work is being done by both the USAF Geophysics Laboratory and NASA. Other agencies such as the USAF Weapons Lab are assisting in the evaluation of suitable components to survive the natural radiation environment. There are some dozen experiments which will be flying on the P78-2 space vehicle attempting to characterize the natural environment and measure the buildup and breakdown of charge on the various components of the space vehicle.

The Space and Missile Systems Organization itself is primarily concerned with this phenomenon as a measure of the survivability of satellites. Although military sponsored satellites are our main concern, the problem is common to all satellites, especially those in the near-synchronous region. The P78-2 SCATHA

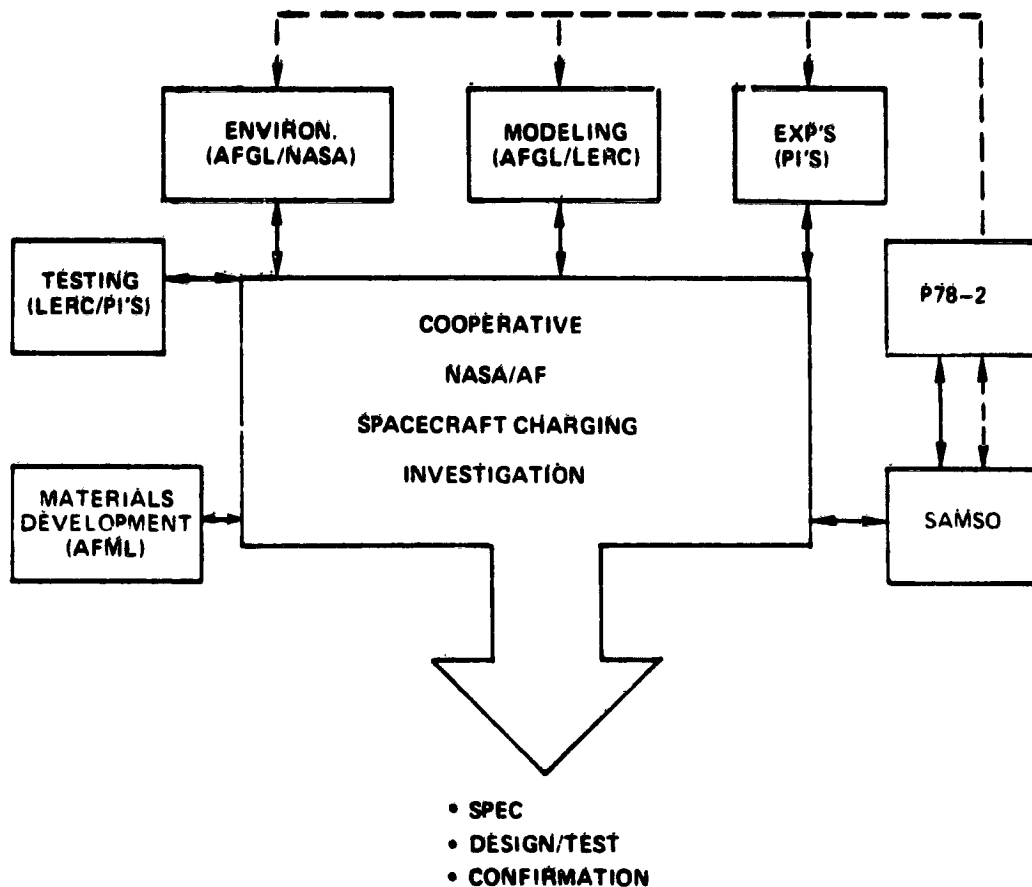


Figure 1. Program Plan

spaceflight itself is a validation of the modeling activities and a source of new on-orbit data. The final product is a specification to be followed when designing spacecraft so as to negate or minimize the effects of spacecraft charging, that is, a way to design and test satellites, and a confirmation that a spacecraft is built such that it does not experience charge-induced anomalies.

Numerous approaches to the charging problem have been investigated already. One method is to fabricate the spacecraft entirely from conductive material. However, this method has been shown to be enormously expensive for materials that are (and remain) conducting. It is being successfully used for "one-shot" application, but in view of the numbers of satellites of various types flown — both military and commercial — there must be a better way.

## 2. OBJECTIVES

The objective (Figure 2) of this mission, in the most general sense is to provide data to program offices (military and civilian) to insure that survivable space systems are designed, tested, and flown. The STP P78-2 mission is much more confined than that. The P78-2 objectives are to fly two types of packages, one set associated with charging and one set concerned with materials effects, by providing a space vehicle which supports the payload objectives, and by operating that spacecraft for a minimum of 1 year retrieving and distributing data as requested by the experimenters.

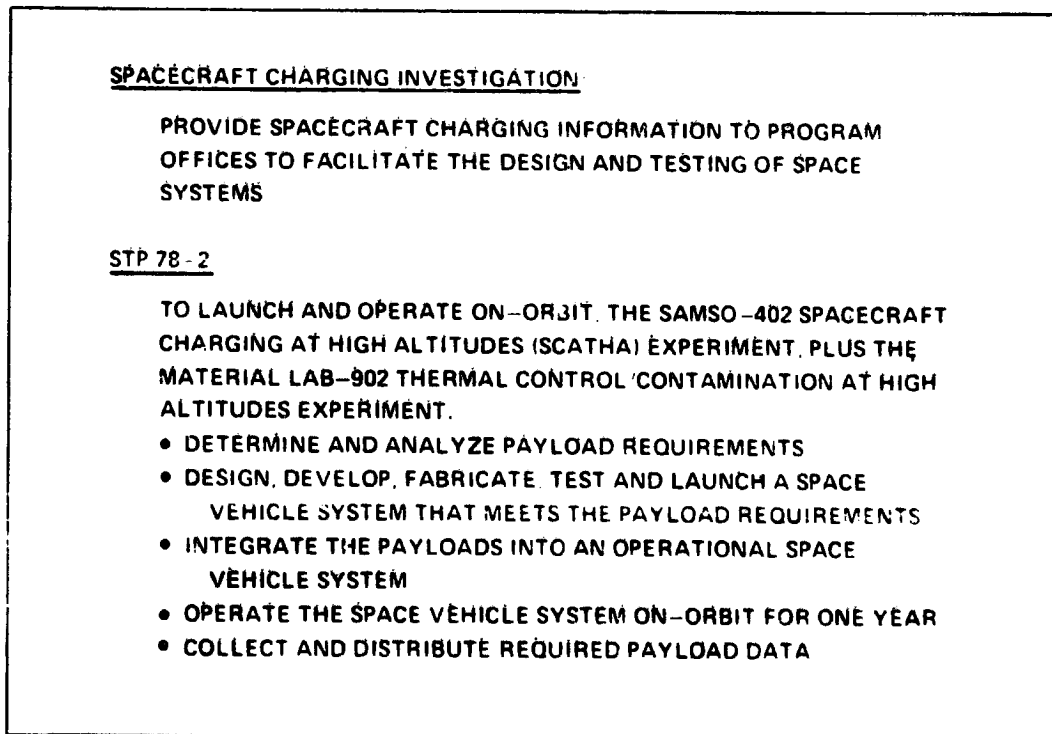


Figure 2. Mission Objectives

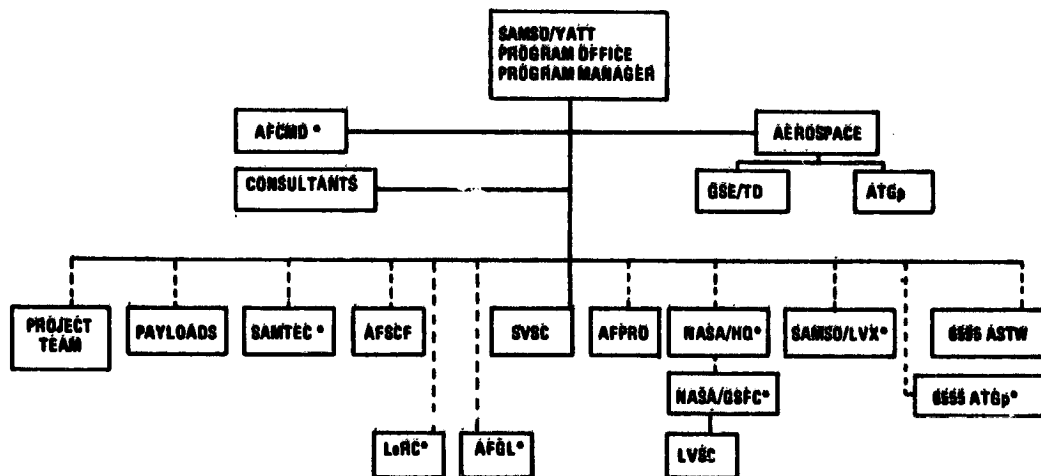
In order to properly accomplish these objectives, it was first necessary to determine the experimenter requirements, no easy task with the dozen different experiments on this mission. Next came the problem of designing and building a space vehicle which supports those diversified requirements. As an aid to the accomplishment of this task, 6 months was spent in a definition phase attempting

to optimize the mission. It is also necessary that the payloads and space vehicle operate in harmony and continue to do so for 1 year on orbit. STP will operate the vehicle during that year and collect the required data which will be processed and analyzed according to an integrated plan currently being developed. Eventually, each experimenter will profit from having the benefit of the combined data rather than just his own.

### 3. MANAGEMENT. ....

From a management viewpoint (see Figure 3), the SCATHA mission is quite different from previous STP missions. Although the program is currently assigned to the Space Test Program during the flight Demonstration Phase, it originated within the Survivability Directorate and after the Launch and Orbital Operations Phase will return to Survivability. To assure continuity, Survivability personnel are currently assigned to the program full time within STP and those personnel will revert to Survivability with the end of the space mission. The overall Mission Manager function is filled by STP personnel.

Consulting agencies and the Aerospace Corporation provide support for the overall mission. The General System Engineering and Technical Direction role is performed by the Aerospace Corporation for the Space Vehicle fabrication and



NOTE: \* MDA

Figure 3. Organizational Chart

testing. An Application Task Group composed of representatives from Aerospace and consultants provide similar support for the scientific aspects of the mission. A Project Team has also been formed to coordinate the requirements of the individual experimenters. The composition of these various teams fluctuate according to the particular mission phase. The Project Team has proven absolutely invaluable during the spacecraft definition phase. Requirements have been modified in a spirit of cooperation to optimize the mission from an overall scientific approach. Data is the real output of any space mission and the P78-2 Integrated Data Analysis Plan will mesh the efforts of SAMTEC, AFGL, and the individual experiment Principal Investigators to furnish the maximum of data with a minimum of processing and analysis expense. Control of the vehicle on orbit is through the USAF Satellite Control Facility.

NASA Lewis Research Center and the USAF Geophysics Laboratory support the mission in terms of the overall modeling effort.

The Space Vehicle System Contractor is the Martin Marietta Corporation in Denver, Colorado. Technical support at the contractor facility is the responsibility of the AFPRO.

The launch vehicle is a NASA Delta 2914 under the responsibility of NASA Goddard Space Flight Center.

The mission will be supported by SAMSO/Launch Vehicles and the 6595th Aerospace Test Wing and SAMTEC at Vandenberg AFB, CA. The 6555th Aerospace Test Group is the USAF organization which will oversee the preparation for launch at the Eastern Test Range at Cape Canaveral.

#### 4. SPONSORS

See Figure 4. The USAF Systems Command is sponsoring 6 experiments. SC 1 and 2 are being built by the Aerospace Corporation at SAMSO. AFML 12 is also being built by Aerospace. The USAF Geophysics Laboratory is providing SC 4, 5 and 6. Three experiments are being sponsored by Office of Naval Research. SC 9 is being supplied by the University of San Diego. Lockheed Palo Alto Research Laboratory is providing SC 3 and 8. NASA Goddard is sponsoring SC 10 and 11. NASA Marshall Space Flight Center is sponsoring SC 7.

The development of the Space Vehicle Transient Pulse Monitor will be managed from our program office.

- AIR FORCE SYSTEMS COMMAND**
- **AEROSPACE CORPORATION**
    - SC1 - ENGINEERING EXPERIMENTS
    - SC2 - SPACECRAFT SHEATH ELECTRIC FIELDS
  - **AIR FORCE GEOPHYSICS LABORATORY**
    - SC4 - PARTICLE BEAM SYSTEMS
    - SC5 - RAPID SCAN PARTICLE DETECTOR
    - SC6 - THERMAL ELECTRON MEASUREMENTS
  - **AIR FORCE MATERIALS LABORATORY**
    - ML12 - THERMAL CONTROL AND CONTAMINATION
- OFFICE OF NAVAL RESEARCH**
- **UNIVERSITY OF CALIFORNIA AT SAN DIEGO**
    - SC9 - SAN DIEGO PARTICLES DETECTORS
  - **LOCKHEED PALO ALTO RESEARCH LABORATORY**
    - SC3 - HIGH ENERGY PARTICLE SPECTROMETER
    - SC8 - LOCKHEED ENERGETIC ION SPECTROMETER
- NATIONAL AERONAUTIC AND SPACE ADMINISTRATION**
- **GODDARD SPACE FLIGHT CENTER**
    - SC10 - ELECTRIC FIELD DETECTOR
    - SC11 - MAGNETIC FIELD MONITOR
  - **MARSHALL SPACE FLIGHT CENTER**
    - SC7 - LIGHT ION MASS SPECTROMETER

Figure 4. Sponsoring Agencies

## 5. PAYLOADS

Figures 5 and 6 portray the engineering payloads and the energy range of the various particle detectors along with the Principal Investigators. It should be evident that a complimentary group of experiments has been selected which cover the energy spectrum. The mission should provide a means of complete investigation of the environment.

● SURFACE POTENTIAL OF SELECTED MATERIALS TRANSIENT SHAPE IDENTIFIER & COUNTER PULSE SHAPE LOW FREQUENCY ELECTROMAGNETIC SIGNALS	SCI	H. KOONS
● TRANSIENT PULSE MONITOR	SPACE VEHICLE	SRI
● POTENTIAL NEAR SPACECRAFT	SC2	J. FENNELL
● THERMAL PROPERTY CHANGES OF MATERIALS	ML12	D. PRINCE D. HALL
CONTAMINATION RATE MEASUREMENTS		
● ELECTRIC FIELDS	SC10	T. AGGSON
● MAGNETIC FIELDS	SC11	B. LEDLEY

Figure 5. Engineering Payloads

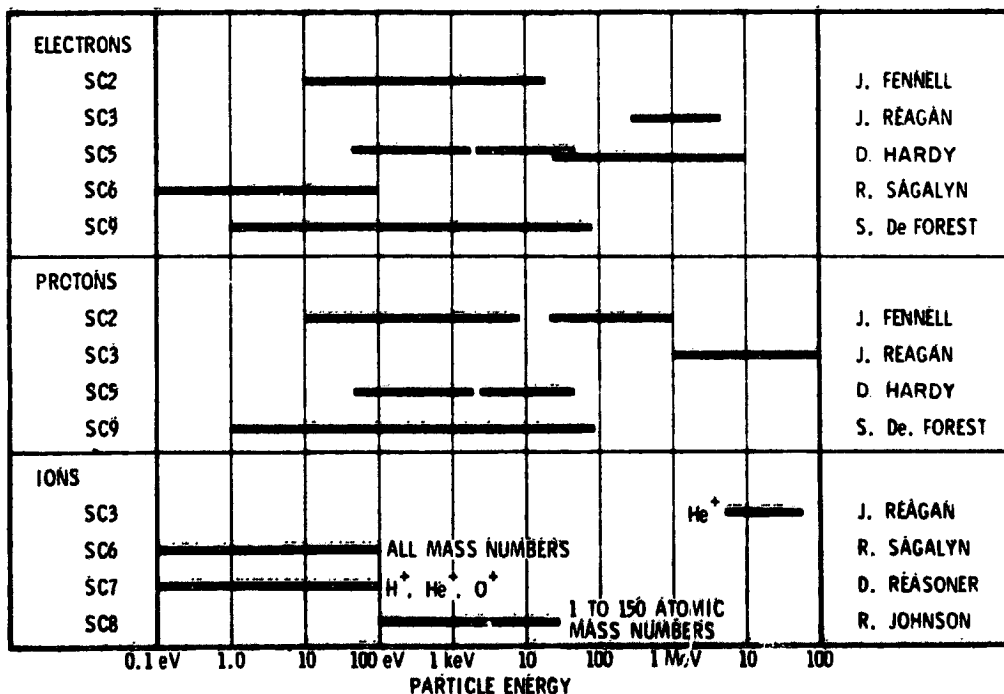


Figure 6. Energy Range of Particle Detectors

## 6. ORBITAL PARAMETERS

The final orbit parameters are currently as follows:

Apogee	23,100 nm
Perigee	15,030
Inclination	2.5°
Ascending Mode	0°
Drift	6°/day nominal

Figure 7 depicts the orbital parameters graphically but fails to portray the desire to have apogee at local midnight during the eclipse season. The period is 23.54 hr and approximately 12.62 hr of each revolution are spent above synchronous altitude.

An Orbital Requirements Document and Operations Plan will be available in January of 1978 which will provide the detailed mission timeline.

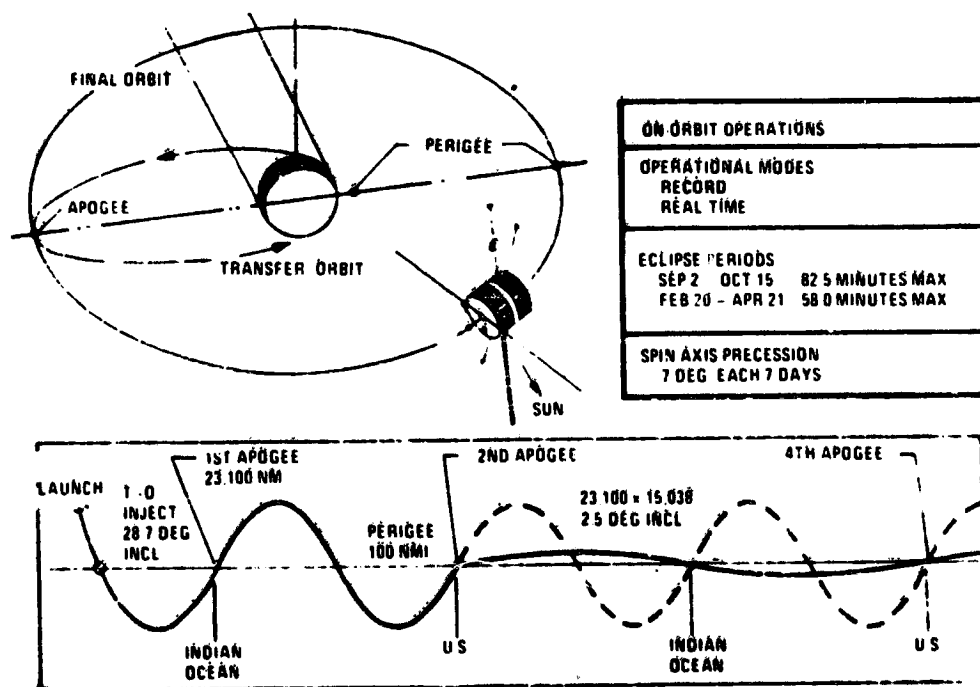
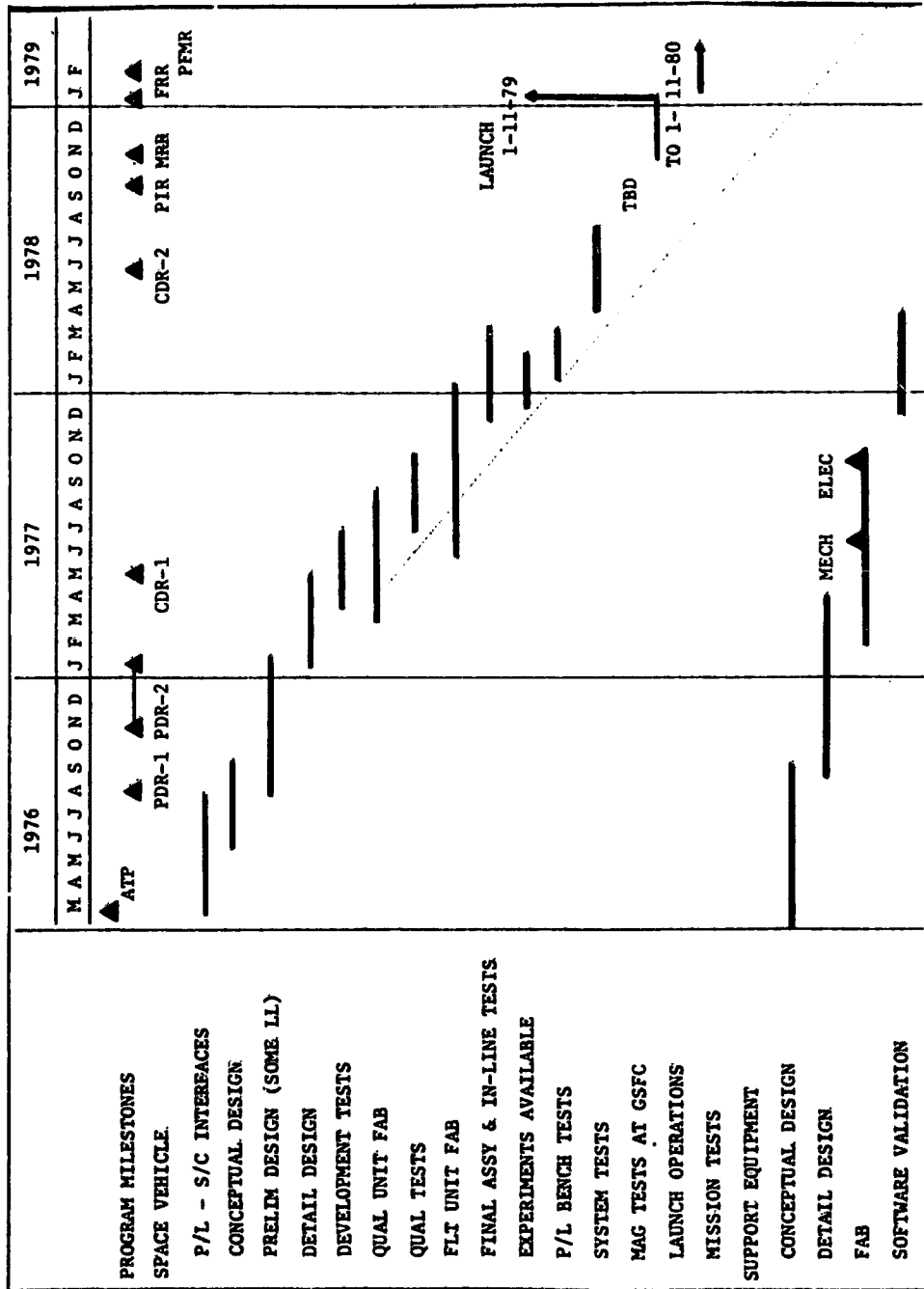


Figure 7. Orbital Parameters

## 7. SCHEDULE

Figure 8 portrays the program master schedule.



NOTE: THIS SCHEDULE HAS BEEN REVISED AS OF DEC 76 AND REFLECTS A PROGRAM LAUNCH CHANGE OF SIX MONTHS DUE TO DIRECTED FUNDING LIMITATIONS.

Figure 8. P78-2 Milestone Schedule

SESSION I  
ENVIRONMENT

35

34  
PAGE INTENTIONALLY  
PRECEDING PAGE BLANK NOT FILMED

## Contents

1. Introduction	37
2. General Morphology and Dynamics	39
3. Detailed Observations and Events	42
4. Model	47
Acknowledgement	49
References	49
Appendix	51

## 1. The Plasma Environment at Geosynchronous Orbit

Sherman E. DeForest  
University of California, San Diego  
La Jolla, California

### 1. INTRODUCTION

The scope of this paper is two-fold:

(1) To present a picture of the magnetosphere about geosynchronous orbit (GSO) to the nonspecialist, and

(2) To introduce a preliminary model which should be of use to spacecraft designers as well as certain others.

The emphasis of both the environmental discussion and the model presentation is to give information to investigators who are not necessarily engaged in magnetospheric research.

In designing this type of presentation, one must first ask, "why is it important?", and "who is the audience?". For purposes of this presentation, we assume that the importance of the plasma environment is due to the fact that it interacts with spacecraft surfaces to produce electrostatic charging. We will give only nodding recognition to the important and exciting geophysical implications of the plasma dynamics at GSO. Similarly, we will assume that a large fraction of the intended audience will not be intimately familiar with the specialized jargon of the magnetospheric physicist.

Finally, we acknowledge that this paper presents work in progress and that the many gaps in our understanding of the conditions of GSO will not be closed until after the GEOS and SCATHA missions are successfully completed.

The magnetosphere is a very complicated place, and GSO is located at the boundary of several distinct plasma regions. As can be seen from Figure 1 - which is a new version of a much used figure by W. Heikkila - the low altitude plasma is a low-temperature relatively high-density region, called the plasmasphere (a temperature of a few electron volts and densities of 10-1000 particles/cm<sup>3</sup>, see Chappell<sup>1</sup>). Higher altitude plasma in general is much hotter and less dense (1000's of electron volts and 1 particle/cm<sup>-3</sup>, see DeForest and McIlwain<sup>2</sup>). This is generally called the plasmasheet. Much of the physics governing spacecraft charging at GSO is determined by the interplay of these two regions as they move in and out past a space vehicle.

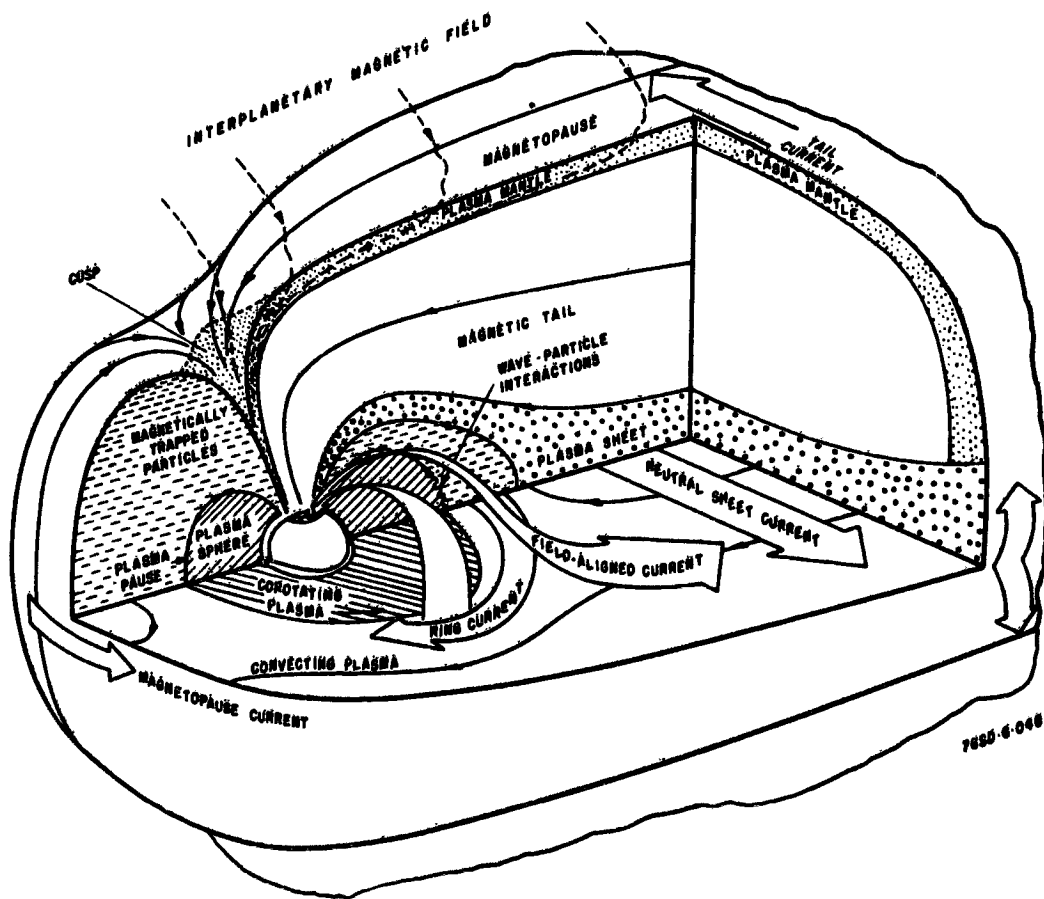


Figure 1. Magnetosphere (after Heikkila)

During geomagnetically active times, all the boundaries shown in Figure 1 tend to move inwards. This means that the magnetopause can occasionally pass inside at GSO and expose a vehicle there to the magnetosheath particles.<sup>3, 4</sup> Russell (private conversation) has estimated that approximately 3 percent of the time a vehicle at GSO will be in the magnetosheath. At least one, ATS-5 was actually exposed to the unshocked solar wind.<sup>5</sup> No operating anomalies are known to be associated with these transitions. And since the characteristic energies of the magnetosheath particles are much lower than those of the plasmasheet, no further discussion of these regions will be presented here. However, a complete model must take these regions into account.

## 2. GENERAL MORPHOLOGY AND DYNAMICS

### 2.1 Global Variations

Although the theory of plasma dynamics in the magnetosphere is still being developed, rather simple considerations can be used to predict that the plasmasphere should not be spherically symmetrical at all, but should bulge on the dusk side. This has been shown repeatedly by both ground-based and in situ measurements.<sup>1, 6, 7</sup> Furthermore the boundary, called the plasmapause, moves inward with increasing activity. As a general rule, features of the plasmasphere co-rotate or nearly co-rotate with the earth until they dissipate and can no longer be observed. Also as a general rule, the density decreases strongly with increasing equatorial altitude. These rules are very approximate since we are really discussing a type of weather.

Since the plasmaspheric particles are not very energetic, their motions will be predominantly determined by local electric fields. This is contrasted with the more energetic plasmasheet particles which tend to be dominated by magnetic effects.

This difference in the dynamics of the two populations also determines certain differences in the nature of their spectra. Plasmasheet particles appear suddenly in injection events<sup>2</sup> which have a one-to-one correlation with ground based substorms.<sup>8, 9</sup> After injection, electrons gradient drift to the East and the ions gradient drift to the West. The speed of the drift is proportional to the energy of the particle. At lower energies, these motions get modified by electric field effects. The net result is that even though the plasma is Maxwellian at the injection, the nature of the particles that will strike a vehicle surface depends strongly on where that vehicle is with respect to the location of the injection. In general, a vehicle will encounter high fluxes of electrons between midnight and dawn. This is simply because they move that way shortly after injection. Contrariwise, excess energetic

ions can be encountered in the premidnight sector. This latter situation has not proven to be as hazardous to spacecraft operation as the former. Therefore, we will tend to emphasize the electron dynamics in what follows.

The electric fields present at GSO have not been measured directly, but they are of the order of mV/m. From this and the condition stated above, one can conclude that gross charge neutrality always holds for the plasma. That is, after an injection, a polarization field is set up as the particles try to gradient drift apart. This field then affects the sea of low-energy particles in such a way as to reduce it.

The magnetic field has been measured at GSO by a variety of space vehicles and is therefore reasonably well-known.

Using plasma data from ATS, McIlwain<sup>10</sup> derived a best fit static electric field for the magnetosphere after an injection\* as shown in Figure 2. Note the closed field lines which bulge on the dark side. This delimits the approximate plasmopause.

With both electric and magnetic fields in hand, Mauk and McIlwain<sup>11</sup> could go one step further and show that injections occur with a sharp well-defined spiral boundary. This is shown in Figure 3. This boundary moves in and out with geomagnetic activity in a quantitative way. Confirmation of the existence of this boundary has been provided by Konradi et al<sup>12</sup> in their studies of EX 45 data.

This boundary can be used to predict approximately where a space vehicle will first encounter hot electrons and thus might become a useful tool for operational spacecraft. However, the calculations needed to make predictions cannot now be made on-line. Perhaps this will be a fruitful area for future research.

## 2.2 Time Variations

Substorms (or plasma injections) tend to occur approximately every three hours. Only rarely will a period as long as a day go by without any significant activity.<sup>13</sup> The giant storms which attract popular attention by creating bright aurorae at latitudes which are heavily populated and by affecting radio transmissions are composed by several substorms occurring in so rapid a succession that the magnetosphere does not have time to recover between them. Then each successive injection delivers particles deeper in. Both periods of extreme quiet and extreme activity can be predicted with some accuracy by solar observations. The same is not true of substorms. Whipple (this conference) has stated that he believes that a suitable precursor can be found for substorms, and Rostaker<sup>14</sup> has

---

\* Actual fields during injection are undefined and during very quiet times the field at GSO is much smaller than shown here. Therefore, this field is at best a useful approximation.

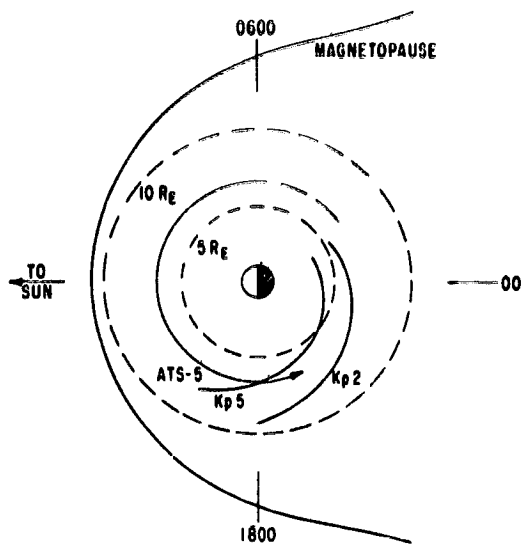


Figure 2. Electric Fields by McIlwain

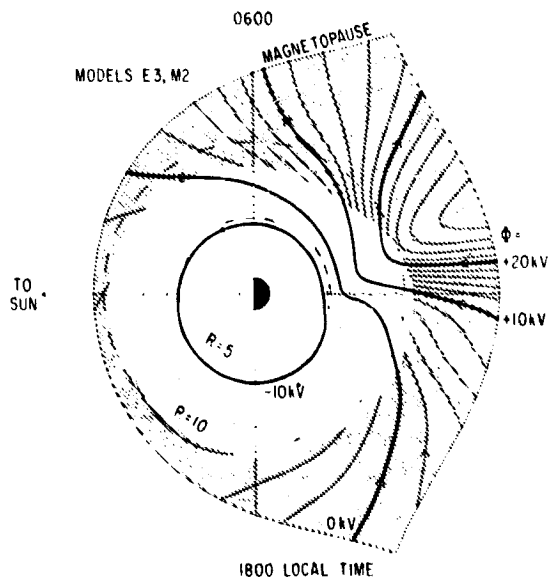


Figure 3. Injection Boundary (Mauk and McIlwain)

postulated a certain type of wave activity before a substorm based on observations from standard ground-based magnetometers.

On the longer time scale, the frequency of all kinds of geomagnetic activity is determined by the solar cycle and we are approaching a solar maximum so we can expect more activity in the next couple of years.

Recent work<sup>15</sup> has shown that there might be periods when the sun is very quiet and no sun spots or auroral activity is seen for tens of years. This is current research, but we are unlikely to enter such a quiet condition in time to affect design of present day spacecraft.

Time variations with periods much shorter than associated with substorms are probably not global in nature, but localized events as discussed in the next section.

### 3. DETAILED OBSERVATIONS AND EVENTS

#### 3.1 Observations

The direct measurements of the plasma distribution function at GSO are very limited. In spite of the great popularity of this orbit for operational spacecraft, only three semiresearch oriented space vehicles have flown there (ATS-1, 5 and 6). Many spacecraft have made cuts through this region, but since these cuts come at large intervals (for example, 2 days) and last for only minutes, they do not allow detailed studies. Low altitude-high inclination vehicles can detect particles that will traverse the GSO equatorial region, but uncertainties about the proper mapping make inferences difficult (and a fruitful area for further research).

Although a low-energy instrument was carried on ATS-1,<sup>16</sup> it did not have the energy resolution necessary to measure the spectra. This means that most of our information comes from the UCSD instruments on ATS-5 and 6. We eagerly await the observations of GEOS (launch in Spring 1977) and SCATHA (launch in Fall 1978) to augment the data base. Of particular interest will be the mass spectrometer results and the various field measurements.

#### 3.2 Waves

Many classes of waves exist in the magnetosphere with periods of many seconds to VLF waves. Some theorists would even consider substorms a wave phenomena.

It is far beyond the scope of this paper to review the types of waves that have been observed. Therefore, we will present a single example of a type of wave which might be able to affect spacecraft operations. This is a Pc4 wave of the type which has been seen on geosynchronous spacecraft equipped with magnetometers

for quite some years.<sup>17</sup> However the work shown here - which is taken from a paper being prepared by DeForest, Cummings, and McPherson for submission to the Journal of Geophysical Research - is the first observation when both particle and field measurements were available. The spectrogram in Figure 4 shows the modulation produced in a detector parked looking West during the wave event (readers unfamiliar with spectrograms should refer to the description in DeForest and McIlwain<sup>2</sup>). Fortunately, this detector was parked while another detector faced East and a third looked radially outward. This allowed us to calculate the flow velocity implicit in the modulations. From that information and the known magnetic field, the complete wave can be described. (Strictly speaking, only the component of flow in the plane of the detectors is measured.)

The part of this type of wave which really concerns the spacecraft designer is that the modulations in Figure 4 represent flows of 150-200 km/sec with a period of 150 sec. By comparison, a 50 eV proton has only a speed of 100 km/sec. This means that first one side of the space vehicle than the other will experience a depletion of the lowest energy particles. We do not know yet what effects this might have.

We expect with the launch of SCATHA to detect waves interactions all the way up to VLF frequencies. Such waves might be able to couple directly into spacecraft harness and change logic states.

### 3.3 Field Aligned Fluxes

One of the outstanding discoveries of ATS-6 is the occasional presence of intense field-aligned fluxes of electrons.<sup>18</sup> Detailed studies of the general anisotropy are still in progress, but the situation at present is that a well-developed loss cone can exist for high-energy particles at the same time that a "source cone" or field-aligned flux exists for lower energy particles. Similarly, the electrons can show excess field-aligned fluxes at the same time that the ions show a loss cone. Examples of these situations are shown in Figures 5 to 8. These were taken from a talk given by Mauk.<sup>19</sup>

We do not yet know how these anisotropies fit into magnetospheric dynamics. Even worse, we are unable to quote good statistics on their occurrence since whether they are observed or not is in great part an artifact of the orbit and orientation of the detector.

However, we do know<sup>20</sup> that the fluxes of field-aligned electrons can at times completely dominate the charging in cavities at the ends of spacecraft. This is true even though the total anisotropic component is small compared to the isotropic component.

ORIGINAL PAGE IS  
OF POOR QUALITY

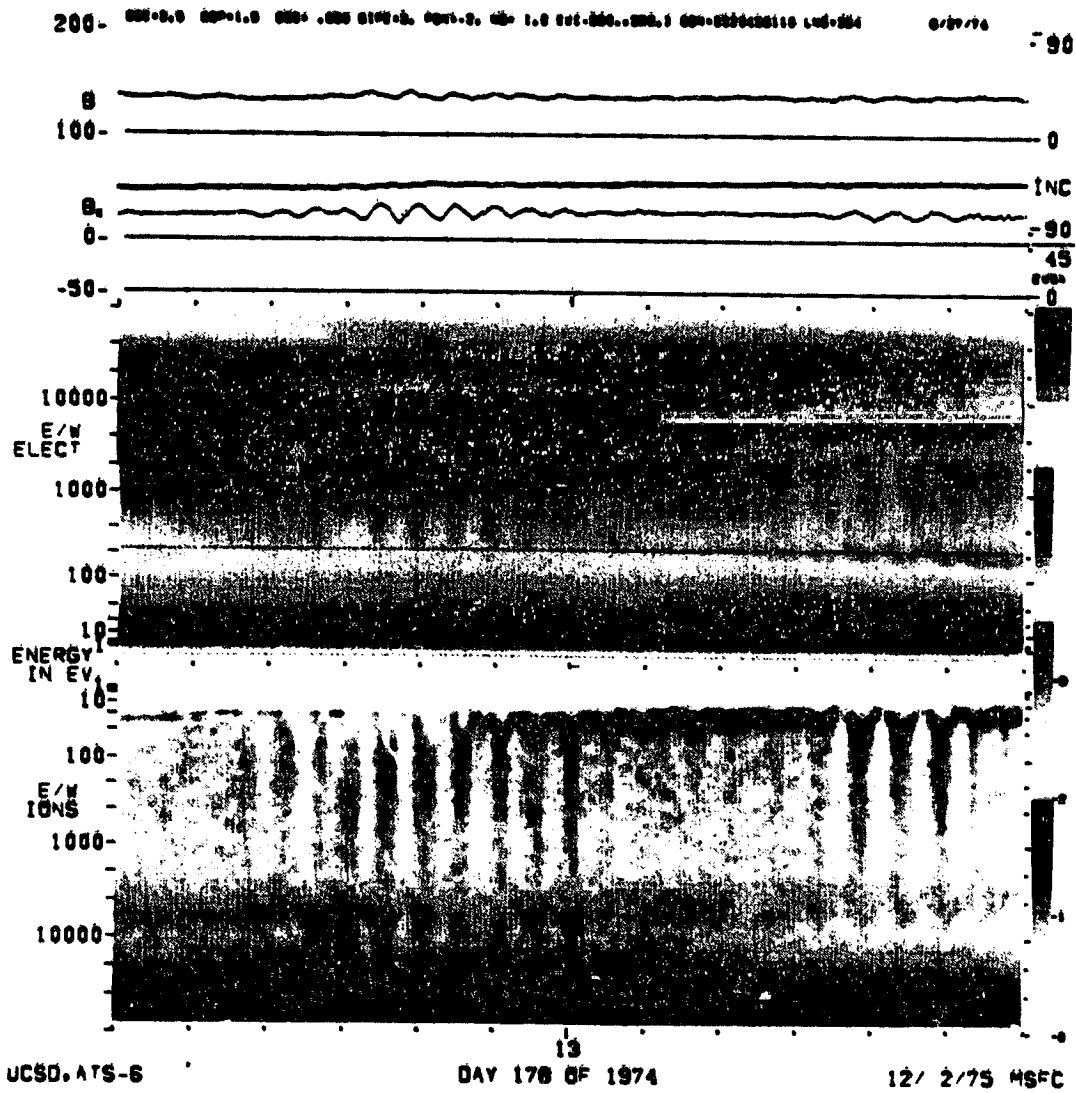


Figure 4. Spectrogram of Pc4 Event

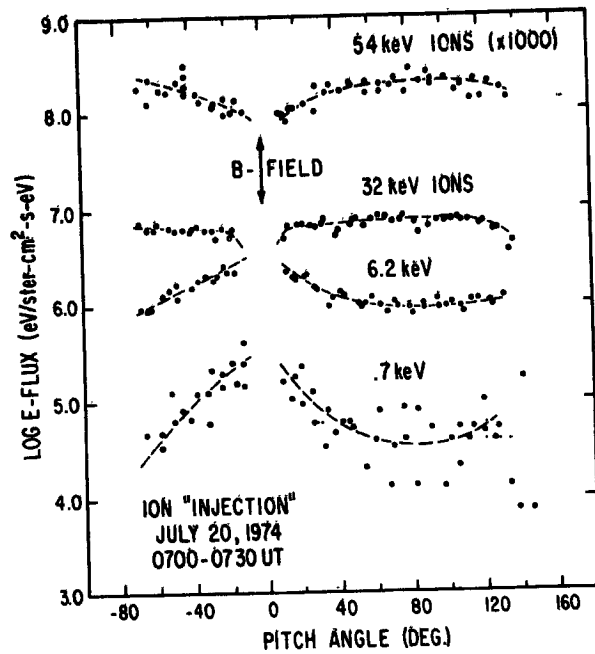


Figure 5. Particle Anisotropies From ATS-6

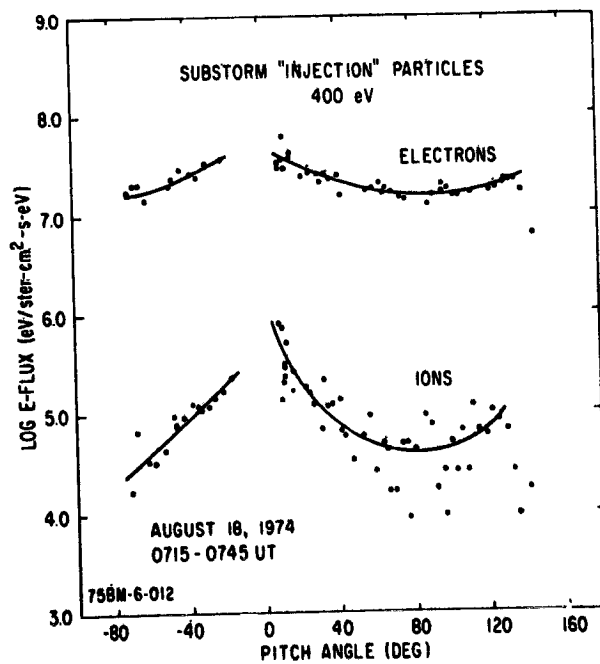


Figure 6. Particle Anisotropies from ATS-6

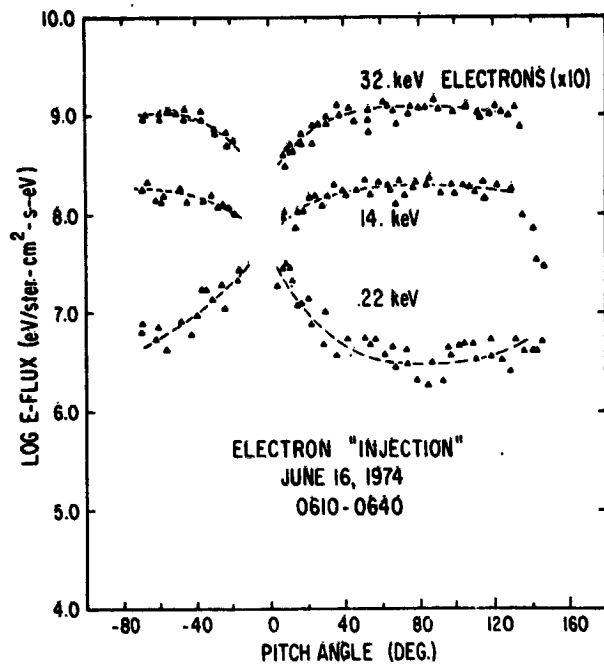


Figure 7. Particle Anisotropies from ATS-6

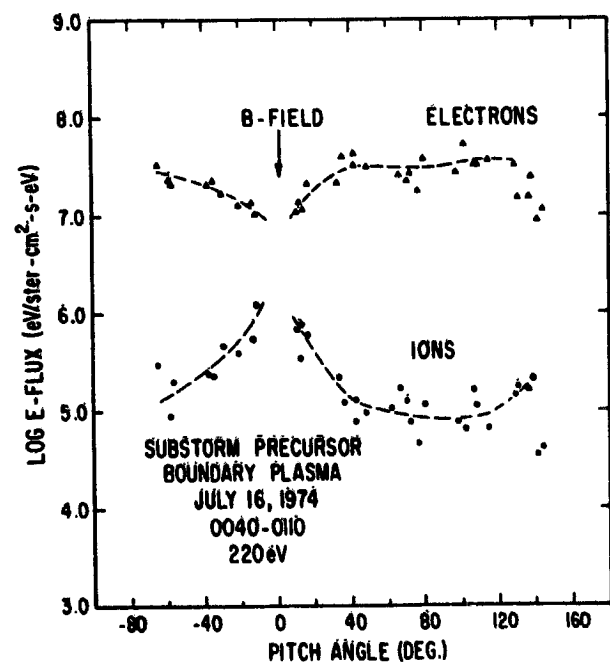


Figure 8. Particle Anisotropies from ATS-6

### 3.5 Comments

We are still finding new plasma phenomena at GSO. We understand the overall patterns fairly well and are making progress on understanding such things as waves. But one must always remember that this is a very complex environment.

When certain classes of operating anomalies fail to correlate with substorm injections or other indications of activity, the reason might simply be that the spacecraft was inadvertently oriented in a manner that protected it. Next time around the spacecraft might slew in orbit or the magnetic field might tip. The new type of anomaly might be recorded. Since operational spacecraft do not normally carry either environmental monitors or even local noise counters, the real cause of the event can only be guessed, and that guessing can be very expensive.

A convenient comparison is to say that substorms are like the earthly thunderstorms that we can predict and understand reasonably well. Many of these unusual events are like tornados. We understand a little about them. We know they are associated with larger events, and they are potentially dangerous.

### 4. MODEL

The general problem of modeling this environment is quite difficult because of the inherent complexity of plasma interactions. One can easily name 21 different independent parameters that would have to be specified as a function of time to represent the environment. And that would be possible only by assuming a Maxwellian distribution for the various constituents.

The particular problem of providing a simple model to the spacecraft designer is also difficult since blindly specifying the worst case for all parameters could result in severe overdesign and waste.

The initial model proposed in this study was to select representative days from the five years of available ATS-5 data and add to this a model of field-aligned fluxes and low-energy plasmas that had been derived from the more recent ATS-6 data. This approach has the benefit of providing users with real data suitable for computer modeling in a relatively quick and low cost way.

Six days have been picked which have examples of many different types of activity.

However, the potential users at this conference have expressed a desire for an even simpler environmental specification even though they realize it would not be as definitive. Therefore, we are currently reassembling the available data to assemble such a simplified model in a timely fashion.

One observation that can be of use is shown in Figure 9. Data for a whole year were scanned to find those substorms which occurred in the immediate

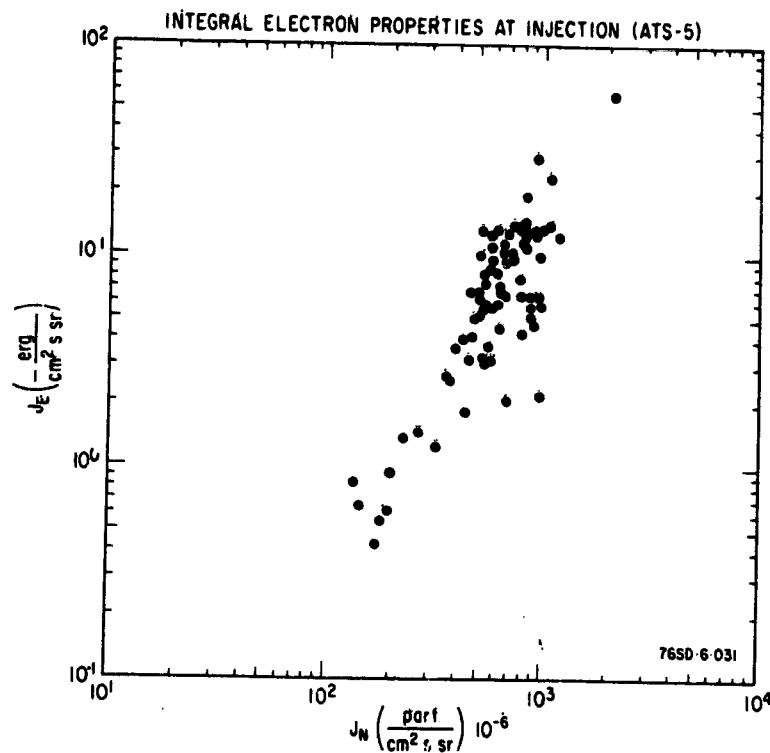


Figure 9. Energy Flux Versus Number Flux of Electrons at GSO.

vicinity of ATS-5. Then the measured energy flux was plotted against the number flux. Far from being random, the points are well-ordered, if somewhat confusing. A slope of 1 on the figure would indicate a constant temperature. That is definitely not the case, but no suitable explanation for the shape has yet been proposed. Still we can fit a curve to these points and eliminate at least one variable in the model.

We will use such simplifications and assumptions to derive a probability of encountering fluxes above a given level. Then the designer can determine an appropriate design specification based on his particular mission. The exact form of this simplified specification has not been determined at the time of this writing, but we hope to complete it before the end of the year. Work will continue of the more complete model, but only after the simplified version has been distributed.

## Acknowledgment

This work was supported by Air Force Contract F19628-76-C-0214.

## References

1. Chappell, C. R. (1970) A study of the influence of magnetic activity on the location of the plasmapause as measured by OGO 5, J. Geophys. Res. 75:50.
2. DeForest, S. E., and McIlwain, C. E. (1971) Plasma clouds in the magnetosphere, J. Geophys. Res. 76:3587.
3. Skillman, T. L., and Sugiura, M. (1971) Magnetopause crossing of the geostationary satellite ATS-5 at 6.6  $R_E$ , J. Geophys. Res. 76:44.
4. Bogott, F. H., and Mozer, F. S. (1971) Magnetopause electric field inferred from energetic partial measurements on ATS-5, J. Geophys. Res. 76:892.
5. DeForest, S. E. (1973) Detection of solar wind at synchronous orbit, J. Geophys. Res. 78:1195.
6. Carpenter, D. L. (1970) Whistler evidence of the dynamic behavior of the duskside bulge in the plasmasphere, J. Geophys. Res. 75:3825.
7. Reasoner, D. L., Lennartson, W., and Chappell, C. R. (1976) The relationship between ATS-6 spacecraft charging occurrence and warm plasma encounters, Spacecraft Charging by Magnetospheric Plasmas, Edited by A. Rosen, MIT Press.
8. Akasofu, S. I., DeForest, S. E., and McIlwain, C. E. (1974) Auroral displays near the foot of the field line of the ATS-5 satellite, Planet. Space Sci. 22:25.
9. Eather, R. A., Mende, S. B., and Judge, R. J. R. (1976) Plasma injection at synchronous orbit and spatial and temporal auroral morphology, J. Geophys. Res. 81:2805.
10. McIlwain, C. E. (1971) Plasma convection in the vicinity of the geosynchronous orbit, Earth Magnetospheric Processes, Edited by B. M. McCormac, R. Reidel, Dordrecht-Holland.
11. Mauk, B., and McIlwain, C. (1974) Correlation of  $K_p$  with the substorm-injected plasma boundary, J. Geophys. Res. 79:3193.
12. Konradi, A., Semer, C., and Fritz, T. (1975) Substorm-injected protons and electrons and the injection boundary model, J. Geophys. Res. 80:543.
13. Akasofu, S. I. (1968) Polar and Magnetospheric Substorms, Springer, New York.
14. Rostoker, G. (1968) Macrostructure of geomagnetic bays, J. Geophys. Res. 73:4217.
15. Eddy, J. A. (1976) The maunder minimum, Science 192:1189.
16. Freeman, J. W. J., Maguire, J. J. (1968) On the variety of partial phenomena discernible at the geostationary orbit via the ATS-1 satellite, Am. Geophys. 24 (No. 1).

17. Cummings, W. D., Mason, F., and Coleman Jr., P. J. (1972) Some Characteristics of the low-frequency oscillations observed at ATS-1, J. Geophys. Res. 77:748.
18. McIlwain, C. E. (1976) Auroral electron beams near the magnetic equator, Physics of the Hot Plasma in the Magnetosphere, Edited by B. Hulquist and L. Stenflo, Plenum Publishing Co., New York.
19. Mauk, B. (1975) Magnetospheric substorm pitch angle distribution, EOS 56:423.
20. Vogl, J. L., Sanders, M. L., and DeForest, S. E. (1976) Substorm-induced spacecraft-charging current from field-aligned and omnidirectional particles, Spacecraft Charging by Magnetospheric Plasmas, Edited by A. Rosen, MIT Press.

## Appendix A

### Preliminary Environmental Specification for Geosynchronous Orbit

#### 1. OMNIDIRECTIONAL ELECTRON FLUXES

Data for a complete year (1970) were scanned using ATS-5. The relative occurrence of number fluxes greater than any amount was computed and is shown in Figure A1. The data included in the figure are not all injections, but only those that occurred in the immediate vicinity of the spacecraft and hence did not have time to disperse by gradient drifting before the measurement was made. The last measured point is at  $1.5 \times 10^{-4}$  part/cm<sup>2</sup> sr sec. The curve has been arbitrarily extended to 100 percent at  $10^{-6}$ . From this curve, we can define two relevant fluxes:

- (1)  $10^{-3}$  part/cm<sup>2</sup> sr sec for typical exposure.
- (2)  $10^{-2}$  part/cm<sup>2</sup> sr sec for extreme exposure.

The second limit is somewhat arbitrary, but should be a safe design limit. The probability of exceeding  $10^{-2}$  in a year is probably less than 1 part in  $10^4$ .

Using the electron correlation data of the main text, we can now estimate the corresponding energy fluxes as:

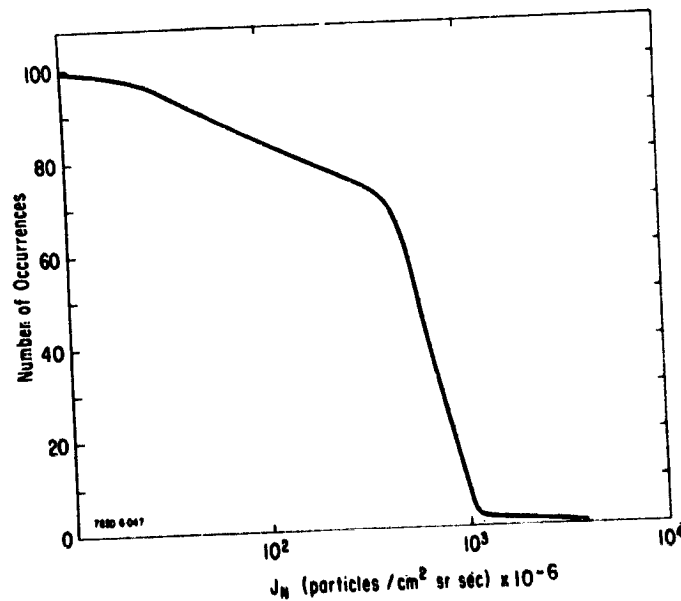


Figure A-1. Relative Occurrence of Number Fluxes Greater than any Amount.

- (1)  $16 \text{ erg/cm}^2 \text{ sec eV}$  (average energy = 16,000 ev).
- (2)  $770 \text{ erg/cm}^2 \text{ sec eV}$  (average energy = 77,000 ev).

The worse case from the spacecraft charging view probably comes when this electron flux is neutralized not by the corresponding injected ion flux, but by lower energy ions. If we assume that the sunlit side of the vehicle is held at ground while the dark side is bombarded by these fluxes, then the maximum electrostatic stress is placed on the surface.

## 2. UNIDIRECTIONAL ELECTRON FLUXES

To simulate electrostatic fluxes that might be placed on surfaces lining cavities on space vehicles, one should assume that the whole surface is held to ground while the cavity is exposed to a  $3.5^\circ$  wide electron beam. Since as was also shown in the text, the ions can be deficient in the classical "loss" cone, we take as a limit, no ions at all. Then we can use the work cited earlier (reference 20) for typical and worse cases.

### (1) Typical

$$\begin{aligned}\text{Flux} &= 2 \times 10^9 \text{ electrons/cm}^2 \text{ sec} \\ E &= 220 \text{ eV} .\end{aligned}$$

### (2) Worst Case

$$\begin{aligned}\text{Flux} &= 3.5 \times 10^8 \text{ electrons/cm}^2 \text{ sec} \\ E &= 2200 \text{ eV} .\end{aligned}$$

The user is warned that the statistics on the occurrence of these field-aligned fluxes is still poor. The numbers above are based on 20 events. The second event was named as worse case because of the higher energies. A more conservative approach might be to assume both the higher flux and higher energy occur simultaneously even though this has not been observed.

## 3. USE OF THIS MODEL

The numbers presented in this appendix are not meant to represent an environmental specification in any final sense. They are meant to give typical and maximum fluxes that might reasonably be expected so that designers can at least make a start without utilizing a full computer simulation. Special events such as rapid flows, waves, or fluxes of heavy ions will be considered in the more developed models to follow.

## Contents

1. Introduction	53
2. Observations at Low Altitudes	55
3. Observations at Intermediate Altitudes	59
4. Observations at Synchronous Altitude	62
5. Summary	64
Acknowledgment	64
References	64

## 2. Composition of the Hot Plasma Near Geosynchronous Altitude

R. G. Johnson, R. D. Sharp, and E. G. Shelley  
 Lockheed Palo Alto Research Laboratory  
 Palo Alto, California

### Abstract

Although there have been no direct measurements of the composition of the hot (keV) plasma at geosynchronous altitudes, the combination of other observations lead to the conclusion that, at least during geomagnetically disturbed periods, there are significant fluxes of ions heavier than protons in this region. Ion composition measurements below 8000 km altitude show upward streaming fluxes of both  $O^+$  and  $H^+$  ions in the L-region of the geosynchronous orbit. These observations are consistent with the conclusion that at least a portion of the total ion fluxes observed at geosynchronous altitude to be highly peaked near the magnetic field lines are heavier than protons and originate in the ionosphere.

### 1. INTRODUCTION

Quantitative measurements on the ion composition of the hot (keV) plasma near geosynchronous altitude have not yet been performed. Thus, the plasma composition in this region of the magnetosphere must be inferred primarily from composition information obtained at other locations in the magnetosphere. Prior to the work of Shelley et al<sup>1</sup> it was generally believed (or assumed) that the dominant ion

species in the hot magnetospheric plasma was always hydrogen ( $H^+$ ) and that the source of the ions was the solar wind. There is increasing evidence that energetic oxygen ( $O^+$ ) and helium ( $He^+$ ) ions of ionospheric origin are frequently significant components in the hot plasma and that during geomagnetically disturbed conditions  $O^+$  ions may be the dominant hot plasma ions in some regions of the magnetosphere. Satellite measurements at low altitudes (near 800 km) during magnetic storms have shown that large fluxes of  $O^+$  ions in the energy range 0.7-12 keV are precipitated along with  $H^+$  ions from the magnetosphere at magnetic L-shells corresponding to the region of geosynchronous altitude.<sup>2, 3, 4</sup> Satellite measurements at intermediate altitudes (near 8000 km) have shown that large fluxes of  $O^+$  and  $H^+$  ions in the keV range are being accelerated out of the ionosphere and injected into the magnetosphere over a wide range of magnetic L-shells.<sup>5, 6, 7</sup> Under certain impulsive magnetospheric conditions which produce velocity dispersion of the trapped ions, measurements at geosynchronous altitude indicate that ions heavier than protons are present in the kilovolt energy range.<sup>8</sup> Thus, it appears likely that significant fluxes of ions other than protons are present near geosynchronous altitude at least for some magnetospheric conditions. In this paper, discussion of the composition of the hot plasma is limited to particle energies less than 50 keV since the dominant plasma density and energy near geosynchronous altitude is produced by particles in this energy range. Composition measurements at higher energies and their importance to magnetospheric processes have recently been reviewed.<sup>9</sup>

The importance of knowing the ion composition of the plasma and the detailed energy and angular distributions of the ion species for modeling the secondary emission effects, current balance, sheath characteristics, etc., during spacecraft charging events is discussed in several other papers in this proceeding and will not be reviewed in this paper. However, for highly anisotropic ion fluxes and certain spacecraft configurations it is possible to have limited regions of a spacecraft acquire a large positive potential with respect to the plasma, in contrast to the large negative potential generally observed and discussed. This possibility of large positive potentials will be discussed in conjunction with the observations of intense ion fluxes aligned nearly parallel with the geomagnetic field direction.

For the purpose of the present discussion, the information presented on the composition of the hot plasma in the magnetosphere will be divided into the three general categories of low, intermediate, and high altitude satellite measurements. The reported observations and plasma composition results in these altitude regions are briefly reviewed and their significance to the geosynchronous altitude environment is discussed.

## 2. OBSERVATIONS AT LOW ALTITUDES

The most extensive measurements on the composition of the hot magnetospheric plasma have been obtained with an ion mass spectrometer aboard the polar orbiting 1971-089A satellite near 800 km. The satellite was three-axis stabilized with one axis always aligned near the earth's radius vector. The ion mass spectrometer was oriented at  $55^\circ$  to the zenith and thus nearly always sampled ions precipitating from the magnetosphere into the atmosphere. The spectrometer covered the energy range from 0.7 to 12 keV and the mass range from 1 to 32 AMU and the data were acquired primarily during the period from October 1971 to December 1972.

The most prominent ion observed other than  $H^+$  was  $O^+$ . The  $O^+$  intensities were largest during principal magnetic storms<sup>4</sup> but significant fluxes were also observed during magnetic substorms.<sup>10</sup> A detailed study of the morphology of the  $O^+$  ions during the rather classic 17-18 December 1971 magnetic storm has been made and reported in the literature.<sup>2,3</sup> Figure 1 from Shelley et al<sup>1</sup> shows  $H^+$  and  $O^+$  data from 6 consecutive satellite traversals of the nightside (0300 LT) high latitude regions during the main phase of the storm. The ordinate is approximately proportional to the integral number flux in the instrument energy range from 0.7 to 12 keV. The principal features of note are: (1) the  $O^+$  fluxes at L-shells (near  $L = 6.6$ ,  $\lambda_L = 67^\circ$ ) corresponding to geosynchronous altitude can be comparable in intensity to the  $H^+$  fluxes, (2) the latitudinal distributions of both species have significant structure and vary from pass to pass, and (3) at a given location the relative composition of the flux changes from pass to pass.

The locations in magnetic latitude of the  $O^+$  and  $H^+$  precipitation regions throughout the time period of the magnetic storm are shown in Figure 2.<sup>10</sup> The integral energy flux of the  $O^+$  and  $H^+$  ions was computed over the latitudinal range  $40^\circ < \lambda_L < 80^\circ$  and the circle for the  $H^+$  ions and the square for the  $O^+$  ions in Figure 2 represents the 50 percent point in the zone integral with the bars representing the 10 percent and 90 percent points in the same integral. From this figure it is seen that significant  $O^+$  precipitation is frequently occurring during the storm at magnetic latitudes (near  $\lambda_L = 67^\circ$ ) corresponding to the geosynchronous altitude.

The latitudinal dependence of the average precipitation intensity during the entire period of the storm (0532 UT on 17 December to 1146 UT on 18 December) is shown in Figure 3. It is seen that at magnetic latitudes near 67 degrees the  $O^+$  and  $H^+$  fluxes are comparable when averaged over the storm and that the  $O^+$  ion intensities exceed the proton intensities below  $65^\circ$  magnetic latitude.

The energy distributions of the precipitating  $O^+$  and  $H^+$  ions were found to be highly variable at all magnetic latitudes.<sup>1</sup> The average energy for the  $O^+$  ions in the measured energy range during the storm-time period is shown in Figure 4 and

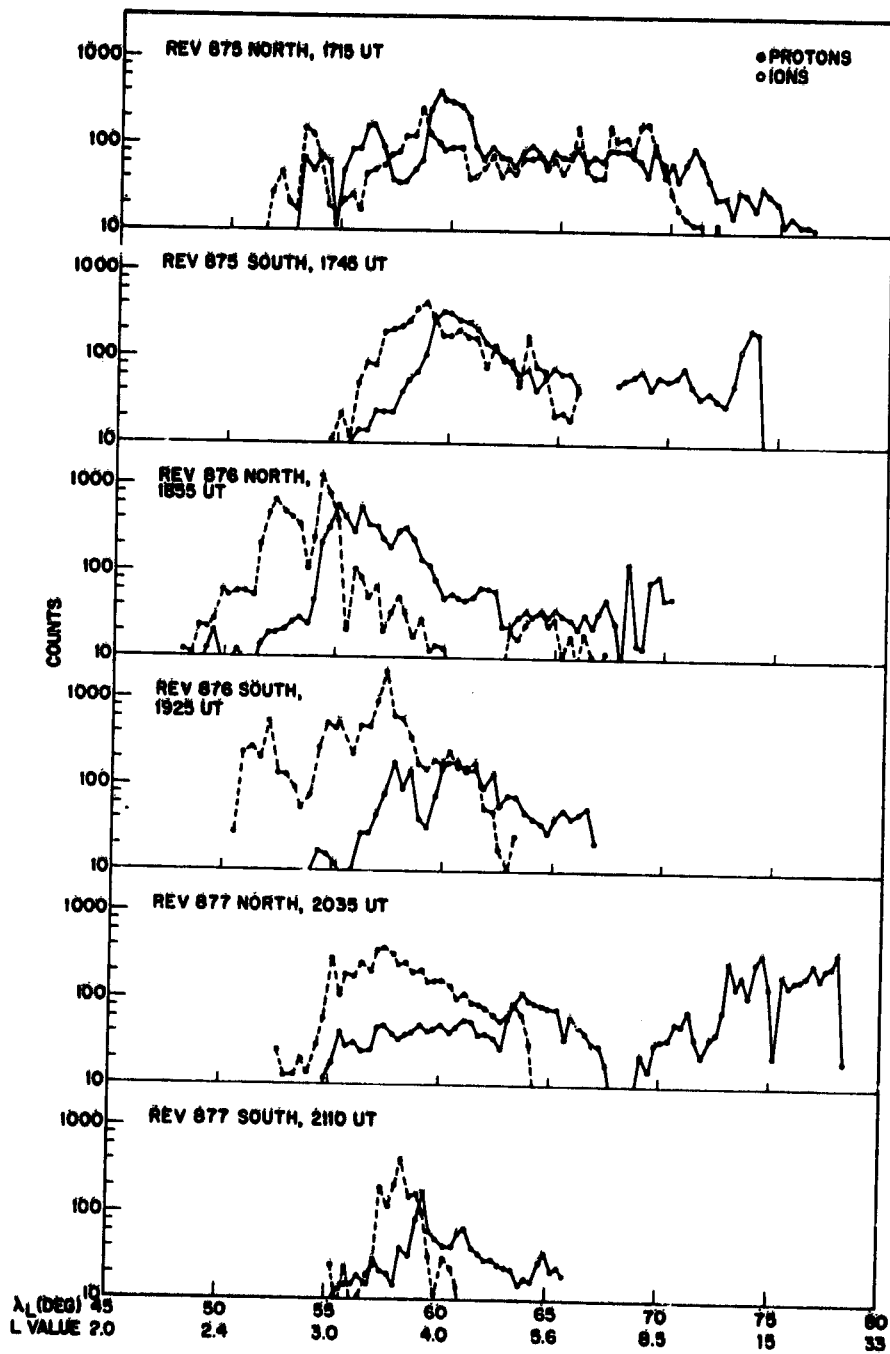


Figure 1. Ion Fluxes During the 17 December 1971 Magnetic Storm (From Shelley et al<sup>1</sup>)

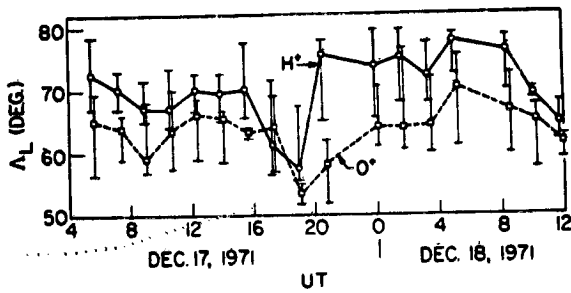


Figure 2. Locations of the Precipitation Zones of  $O^+$  and  $H^+$  Ions During the 17-18 December Magnetic Storm (From Johnson et al<sup>10</sup>)

Figure 3. Latitudinal Variation of the Energy Flux of  $O^+$  and  $H^+$  Ions During the Time Period 0532 UT on 17 December to 1146 UT on 18 December 1971 (From Johnson et al<sup>10</sup>)

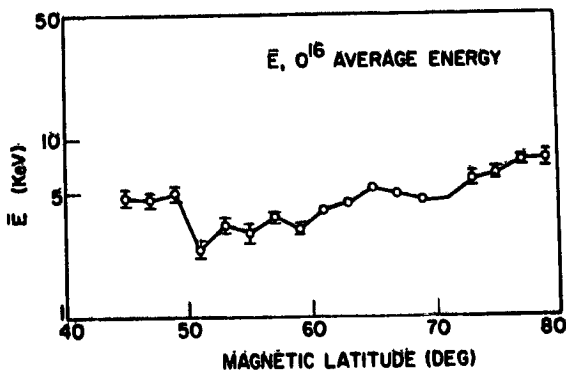
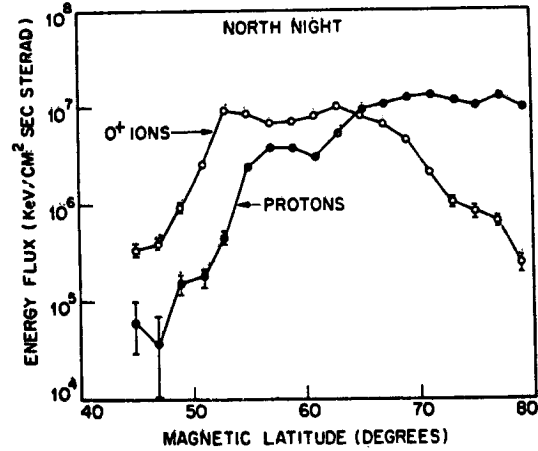


Figure 4. Latitudinal Variation of the Average Energy of  $O^+$  Ions During the Time Period Shown in Figure 2 (From Johnson et al<sup>10</sup>)

is seen to be about 5 keV near the magnetic latitudes appropriate to the geosynchronous location.

To assess the local time dependence of the  $O^+$  precipitation during magnetic storms, a synoptic study was made of data from one year's operation of the energetic ion mass spectrometer aboard the 1971-089A satellite.<sup>4</sup> Data were utilized from three orbits in each of eleven principal magnetic storms during the period from December 1971 to November 1972.  $O^+$  ion precipitation was observed during each of the storms. The latitudinal extent and local magnetic time distribution of the  $O^+$  regions are shown in Figure 5 from Shelley et al.<sup>4</sup> The dot indicates the

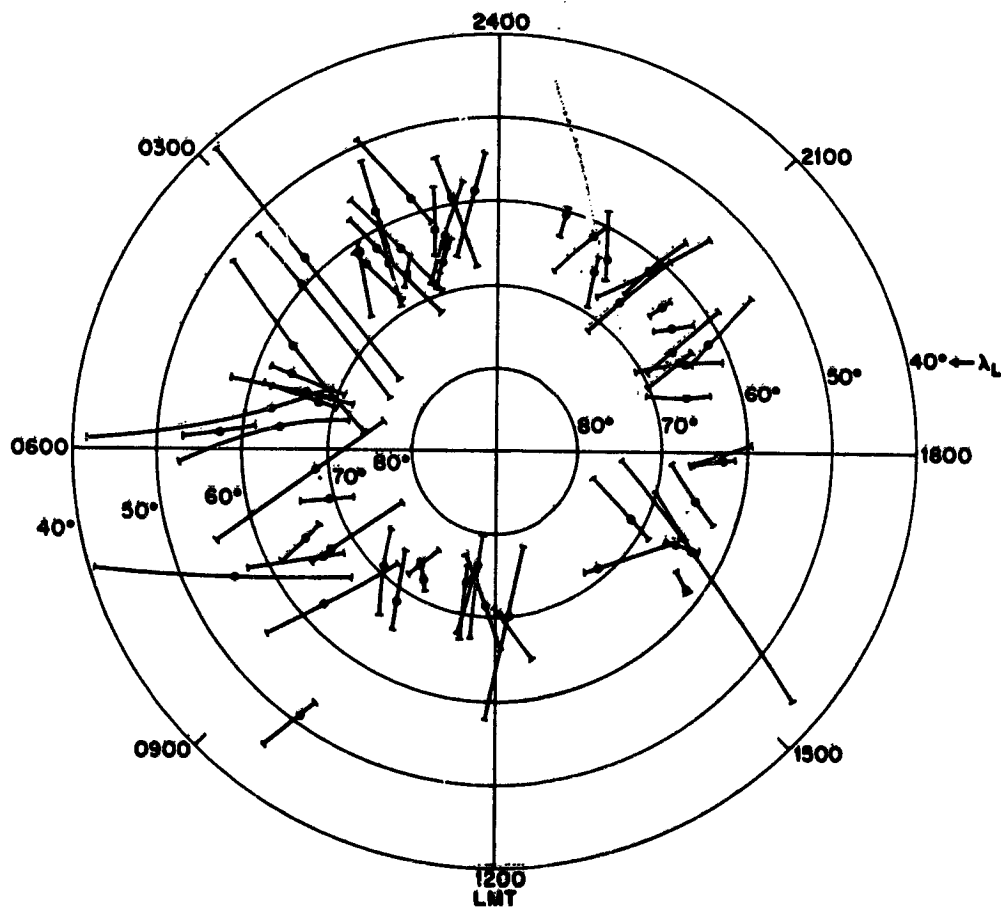


Figure 5. Polar Plot in Invariant Latitude and Magnetic Local Time of the Regions of Observed  $O^+$  Precipitation During 11 Major Storms (From Shelley et al<sup>4</sup>)

position of the maximum flux intensity during each pass and the lines indicate the position of the pass during which the flux was above the spectrometer sensitivity threshold of about  $2 \times 10^5$  ions/cm<sup>2</sup>-sec-sr. From these data, it is seen that O<sup>+</sup> fluxes were frequently observed at the geosynchronous L-shells at essentially all local times, except for possibly a few hours near 1200 local magnetic time. The peak fluxes were typically in the range  $5 \times 10^5$  to  $4 \times 10^7$ /cm<sup>2</sup>-sec-sr. The O<sup>+</sup> peak intensities near noon were found to be, on the average, about a factor of ten lower than near the midnight sector.<sup>4</sup>

Precipitating O<sup>+</sup> fluxes have been observed with the same spectrometer in association with magnetic substorms.<sup>10</sup> The peak intensities were in the range of  $3 \times 10^5$  to  $3 \times 10^6$  ions/cm<sup>2</sup>-sec-sr and were observed at L-shells corresponding to the geosynchronous altitude.

Precipitating fluxes of He<sup>+</sup> and He<sup>++</sup> were also observed with the 1971-089A satellite on L-shells corresponding to geosynchronous altitude.<sup>11, 12</sup> The He<sup>+</sup> and He<sup>++</sup> fluxes were observed much less frequently than the O<sup>+</sup> fluxes and their intensities were much less than those typically observed for the O<sup>+</sup> ions during magnetic storms. However, based on ion lifetime considerations Tinsley<sup>13</sup> and Lyons and Evans<sup>14</sup> conclude that He<sup>+</sup> is most likely the dominant ion in the late-time ring current.

Rocket measurements with ion mass spectrometers at altitudes below 1000 km have also shown the presence of energetic He<sup>++</sup> and O<sup>+</sup> ions in the magnetosphere.<sup>15, 16</sup> These measurements have been made near Ft. Churchill, Canada and thus have been limited to the high magnetic latitudes near L = 9.

### 3. OBSERVATIONS AT INTERMEDIATE ALTITUDES

Preliminary results are now available from an energetic ion mass spectrometer experiment aboard the spacecraft 1976-65B which is in an elliptical polar orbit with apogee near 8000 km.<sup>5</sup> The spacecraft is spinning and provides for the first time detailed pitch angle distribution measurements with identifiable mass-per-unit-charge. The experiment covers the energy-per-unit-charge range from 0.5 to 16 keV and the mass range from 1 to 150 AMU.

O<sup>+</sup> and H<sup>+</sup> ions are frequently observed streaming upward along magnetic field lines with intensities of both O<sup>+</sup> and H<sup>+</sup> often found to be near  $10^8$  ions/cm<sup>2</sup>-sec-sr. The upward streaming ions have been observed over all the local magnetic time range thus far examined from 0900 to 2200 hours. The latitude distributions of these ions have not been determined in detail but during magnetic storms upward streaming fluxes in the evening sector are frequently observed in the range of 65°

to  $70^\circ$  magnetic latitude, thus spanning the L-shell regions at geosynchronous altitude. During the 24 August 1976 magnetic storm, upward streaming  $H^+$  and  $O^+$  fluxes were observed continuously over a latitudinal extent of several hundred kilometers. The energy distributions of the ions extended to at least 8.5 keV and the  $O^+$  energy spectrums were frequently harder than the  $H^+$  spectrums.<sup>6</sup> The upward streaming ion fluxes are observed during quiet as well as disturbed magnetic periods.

The angular distributions of the upstreaming ions are often sharply peaked along the magnetic field lines. A typical example of this<sup>5</sup> is shown in Figure 6 for a segment of data acquired in the northern auroral region at a local time of about 21 hours on 13 July 1976. The relative flux intensities of the  $O^+$  and  $H^+$  ions are plotted versus time and can be compared with the look direction of the instrument relative to the magnetic field direction (upper panel) as determined from the on-board magnetometer. The energy-per-unit-charge of the measured ions is also indicated above the  $O^+$  panel. One can readily see the sharply peaked angular distributions of both the  $O^+$  and  $H^+$  ions. The peak upstreaming  $O^+$  flux observed corresponds to about  $10^8$  ions/cm<sup>2</sup>-sec-sr-keV. The lowest panel shows the response of the electron detector which sampled the energy range  $0.35 \leq E \leq 1.13$  keV. The deep minima in the electron flux at pitch angles corresponding to the atmospheric loss cones are clearly evident at the same locations as the ion peaks.

The foregoing type of angular distributions for the ions and electrons could lead to a net positive upward streaming flux at angles near the magnetic field direction. If an anisotropic flux of this type is incident on a spacecraft with a hole in the outer skin, then a nonconducting surface on a component inside the skin and on the same magnetic field line as the hole, will become positively charged providing the hole subtends an angle from the component surface equal to or less than the pitch angle range over which the positive ion flux is larger than the electron flux. Assuming that the electron flux is higher than the ion flux at the larger pitch angles (which is typical), then a large negative potential could be formed on the component surface adjacent to a large positive potential. This configuration is illustrated schematically in Figure 7, and to simplify this example, the secondary electron emission from the surface is assumed to be negligible. The surface position L on the component lies along the magnetic field line through the hole in the spacecraft skin. Angles  $\theta_1$  and  $\theta_2$  are taken to be less than the pitch angle range over which the ion flux is greater than the electron flux so that a positive potential will occur at position L. Position N illustrates a surface region at angles between  $\theta_1$  and  $\theta_2$  to the magnetic field direction where the electron flux is larger

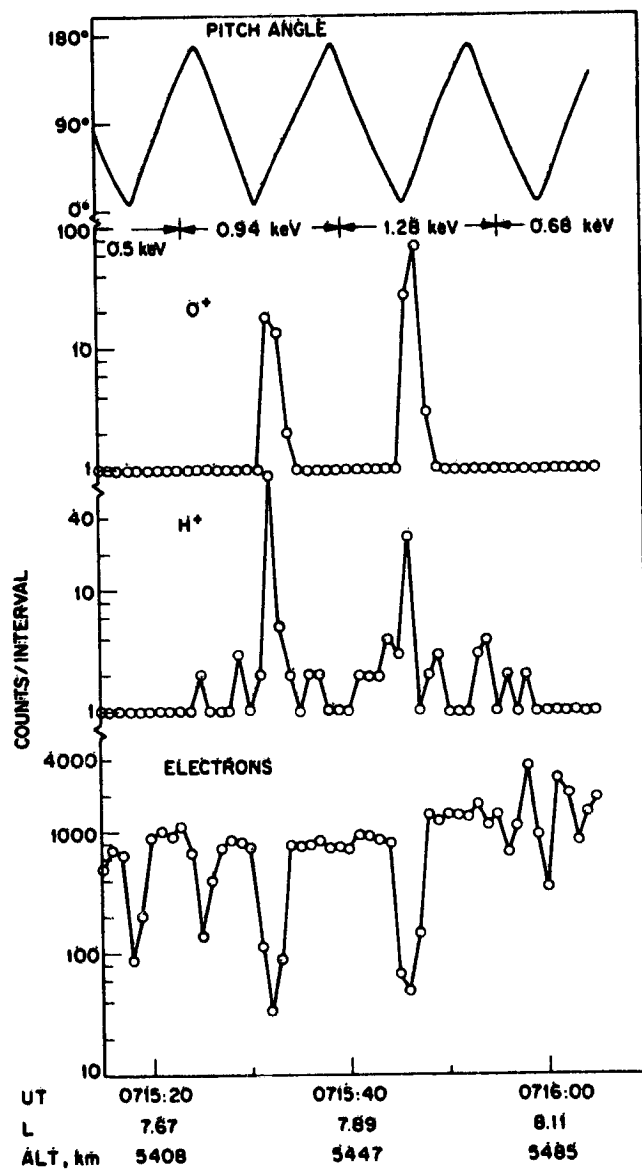


Figure 6. Data From Revolution 35 on July 13, 1976. The upper panel shows the pitch angle of the center of the instrument field of view. The two center panels show data from the mass spectrometer at the indicated energies, and the lower panel shows electron fluxes in the energy range from 0.35 to 1.13 keV. The relative temporal precision of the plots is about one second (from Shelley et al<sup>9</sup>)

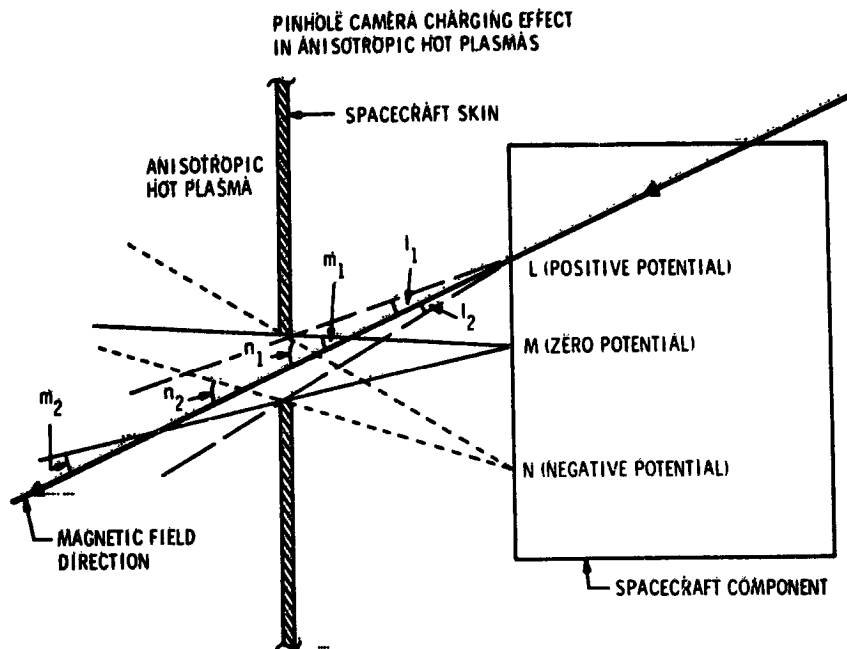


Figure 7. Schematic Drawing Illustrating the Geometry for the Pinhole Camera Charging Effect in Anisotropic Hot Plasmas

than the ion flux. At this position a negative potential will occur. At some position, M, between N and L the electron and ion fluxes will be equal and a zero potential will occur. It can be seen that the surface charging at each position on the surface is related to the pitch angles subtended at the hole in the skin and thus, in analogy to pinhole cameras for electromagnetic radiations, this will be referred to as the "pinhole camera charging effect." Although it has been illustrated for a net positive flux along the field line, an anisotropic electron flux will also produce a potential gradient across the surface in essentially the same way. Another case to consider in relation to the pinhole camera charging effect is the one in which the spacecraft skin is charged highly negative. In this case, the anisotropic ion flux could be produced by the acceleration of the ions along the field line by the spacecraft surface potential, while the electron flux reaching the spacecraft surface at angles near the magnetic field direction is reduced by the negative potential of the surface.

#### 4. OBSERVATIONS AT SYNCHRONOUS ALTITUDE

Extensive measurements on the electron and total ion characteristics of the hot plasma at geosynchronous altitude have been made with instruments aboard the

ATS-5 and ATS-6 satellites.<sup>17, 18</sup> Although the instrumentation could not distinguish the ion species, analysis of bouncing clusters of ions during some types of transient events can provide information on the ion masses. In two cases, McIlwain<sup>8</sup> reports that the data are best fit if  $\text{He}^+$  or  $\text{O}^+$  ions are assumed for the cluster ions, but quantitative values for the fluxes are not reported.

Angular distribution measurements on the ATS-6 satellite show that the ion fluxes below 10 keV are often enhanced at small pitch angles.<sup>18, 19</sup> An example of this enhancement is shown in Figure 8 from the paper by Mauk and McIlwain.<sup>19</sup> It is seen that the enhancement extends to 6.2 keV and to pitch angles well outside the region of the atmospheric loss cone of about  $5^\circ$ . Enhancement of the ions at small pitch angles at synchronous altitude is consistent with the continued upward flow of the upward streaming ionospheric ions observed at lower altitudes and discussed in the preceding section. Thus, it is reasonable to expect similar ion composition in the peaked ion fluxes at synchronous altitude as is found in the upward flowing ions on the same L-shells at the lower altitudes.

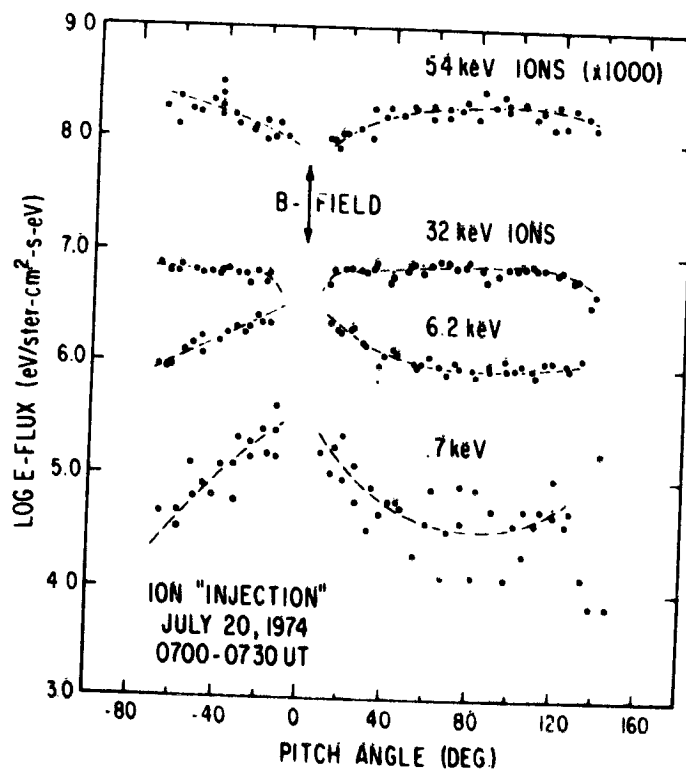


Figure 8. Ion Pitch Angle Distributions as Measured on the ATS-6 Synchronous Satellite During an Ion Injection Event on 20 July 1974 (From Mauk and McIlwain<sup>19</sup>)

McIlwain<sup>8</sup> also notes that simultaneous ion and electron field-aligned beams at the higher energies do not seem to occur. Thus, the pinhole camera charging effect discussed in the previous section may be particularly applicable near geosynchronous altitudes.

## 5. SUMMARY

Plasma composition measurements at low altitudes show that relatively large fluxes of  $O^+$  ions as well as  $H^+$  ions are precipitated from the magnetosphere at magnetic L-shells corresponding to geosynchronous altitude. Upward streaming  $O^+$  and  $H^+$  ions from the ionosphere are also observed on field lines threading the geosynchronous location. Observations at synchronous altitude of ion fluxes highly peaked at small pitch angles are consistent with the ionosphere as the source of the ions. Thus, although there are no definitive measurements of the composition of the hot plasma near geosynchronous altitude, other observations strongly support the conclusion that at least during magnetic storms significant fluxes of ions heavier than protons are also present there.

## Acknowledgments

This work was supported in part by the Atmospheric Sciences Section of the National Science Foundation under Grant DES 74-21834.

## References

1. Shelley, E. G., Johnson, R. G., and Sharp, R. D. (1972) Satellite observations of energetic heavy ions during a geomagnetic storm, J. Geophys. Res. 77:6104.
2. Sharp, R. D., Johnson, R. G., and Shelley, E. G. (1976) The morphology of energetic  $O^+$  ions during two magnetic storms: Latitudinal variations, J. Geophys. Res. 81:3292.
3. Sharp, R. D., Johnson, R. G., and Shelley, E. G. (1976) The morphology of energetic  $O^+$  ions during two magnetic storms: Temporal variations, J. Geophys. Res. 81:3283.
4. Shelley, E. G., Johnson, R. G., and Sharp, R. D. (1974) Morphology of energetic  $O^+$  in the magnetosphere, in Magnetospheric Physics, B. M. McCormac, Ed., D. Reidel, Dordrecht, Netherlands, pp. 135-139.

5. Shelley, E.G., Sharp, R.D., and Johnson, R.G. (1976) Satellite observations of an ionospheric acceleration mechanism, Geophys. Res. Letters 3:654.
6. Johnson, R.G., Sharp, R.D., and Shelley, E.G. (1976) Characteristics of upward-flowing, energetic (keV) ions during a geomagnetically disturbed period, EOS 57:992.
7. Sharp, R.D., Shelley, E.G., and Johnson, R.G. (1976) Observation of an ionospheric acceleration mechanism producing energetic (keV) ions primarily normal to the geomagnetic field direction, submitted to the J. Geophys. Res.
8. McIlwain, C.E. (1976) Bouncing clusters of ions at seven earth radii, EOS 57:307.
9. Fritz, T.A. (1976) Ion composition, Proceedings of the International Symposium on Solar-Terrestrial Physics, Vol. II, D.J. Williams, Editor, published by American Geophysical Union, pp. 716-729.
10. Johnson, R.G., Sharp, R.D., and Shelley, E.G. (1975) Composition of the hot plasmas in the magnetosphere, in Physics of the Hot Plasma in the Magnetosphere, B. Hultqvist and L. Stenflo, Editor, Plenum Publishing Corp., New York, pp. 45-68.
11. Johnson, E.G., Sharp, R.D., and Shelley, E.G. (1974) The discovery of energetic He<sup>+</sup> ions in the magnetosphere, J. Geophys. Res. 79:3135.
12. Sharp, R.D., Johnson, R.G., and Shelley, E.G. (1974) Satellite measurements of auroral alpha particles, J. Geophys. Res. 79:5167.
13. Tinsely, B.A. (1976) Evidence that the recovery phase ring current consists of helium ions, J. Geophys. Res. 81:6193.
14. Lyons, L.R., and Evans, D.S. (1976) The inconsistency between proton charge exchange and the observed ring current decay, J. Geophys. Res. 81:6197.
15. Whalen, B.A., and McDiarmid, I.B. (1972) Further low-energy auroral ion composition measurements, J. Geophys. Res. 77:1306.
16. Lynch, J., Pulliam, D., Leach, R., and Scherb, F. (1976) The charge spectrum of positive ions in a hydrogen aurora, J. Geophys. Res. 81:1264.
17. DeForest, S.E. (1977) The plasma environment at geosynchronous altitude, This Proceedings.
18. McIlwain, C.E. (1975) Auroral electron beams near the magnetic equator, Physics of the Hot Plasma in the Magnetosphere, B. Hultqvist and L. Stenflo, Editor, Plenum Publ. Corp., New York.
19. Mauk, B.H., and McIlwain, C.E. (1975) ATS-6 UCSD auroral particles experiment, IEEE Trans. on Aerospace and Electronic Systems AES-11: 1125.

**Contents**

1. Introduction	68
2. Observations	69
3. Summary and Conclusions	78
References	78

### 3. INJUN 5 Observations of Vehicle Potential Fluctuations at 2500 km

R. C. Sagalyn  
Air Force Geophysics Laboratory  
Hanscom AFB, Massachusetts

William J. Burke  
Regis College Research Center  
Weston, MA 92193

**Abstract**

The AFGL spherical electrostatic analyzers aboard the polar orbiting Injun 5 satellite were designed to measure the temperature and density of the plasma as well as the vehicle potential. Significant vehicle potential fluctuations have been observed at altitudes near 2500 km in the nighttime, topside ionosphere. At auroral latitudes, precipitating magnetospheric electrons frequently drive the satellite to such strongly negative potentials that the ambient electrons are shielded from our instruments. In such cases, simultaneous measurements by the Iowa State University LEPEDA experiment can be used to calculate the vehicle potential. Potentials of up to -40 volts are observed during impulsive precipitation events. Within the plasma trough vehicle potentials vary between -1.5 and -4 volts, as compared with the -0.5 to -1 volt observed in the polar cap. The source of this vehicle potential enhancement is ascribed to fluxes of photoelectrons that have escaped from the sunlit conjugate ionosphere.

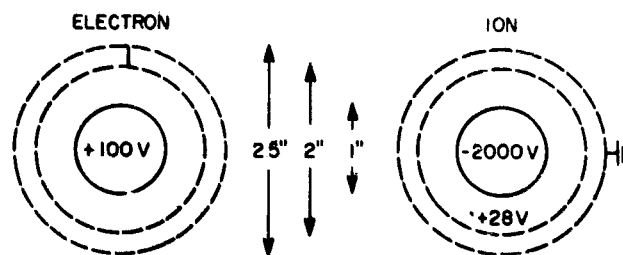
## 1. INTRODUCTION

The potential of a satellite in the topside ionosphere varies in response to changing plasma parameters.<sup>1-4</sup> In this report, we discuss spacecraft charging mechanisms in the topside ionosphere utilizing data obtained by the two AFGL spherical electrostatic analyzers (SEA) aboard the polar-orbiting Injun 5 satellite.

The AFGL experiments on board Injun 5 are discussed elsewhere.<sup>5</sup> Briefly, Injun 5 was launched into polar orbit with an inclination of  $81^\circ$ , an apogee of 2543 km, and a perigee of 677 km. The two AFGL sensors are placed on 5 foot booms and, due to the satellite's magnetic alignment, are well outside the vehicle wake. A schematic of the probes given in Figure 1 shows that both the ion and electron SEA's consist of 1-inch diameter solid collectors surrounded by two wire mesh grids. The potentials of the collectors are set at -2000 and +100 volts. The outer grid of the ion SEA is grounded and the inner grid is held at +28 volts with respect to satellite ground, thus filtering ions with energies less than 28 volts. The electron sensor grids are electrically connected and are operated sequentially in two modes, each of 15.9 sec duration. In Mode 1, the grids are set at +6 volts. This positive resting bias is intended to counteract expected negative satellite potentials. In Mode 2, the grids are swept from -10 to +3 volts. Operating in these modes, we are normally able to measure the ambient electron temperature and density, the satellite potential, and the omnidirectional flux of ions with energies greater than 28 eV.

### INJUN 5 LOW ENERGY PLASMA DETECTORS

#### CONFIGURATION A



ELECTRON SENSOR { MODE 1 GRIDS AT RESTING BIAS OF 15 V  
MODE 2 GRIDS SWEEPED FROM -10V TO +3V

Figure 1. Schematic of the AFGL Electron and Ion Spherical Electrostatic Analyzers Aboard Injun 5

## 2. OBSERVATIONS

Results of vehicle potential measurements are discussed in terms of four typical cases. All data were taken while the satellite was in darkness and near apogee over the northern hemisphere during December 1968. In the first (polar cap) and second (plasma trough) cases, the satellite potential was directly measured from Mode 2 current - voltage curves. The third and fourth cases were during soft and hard inverted-V precipitation events. Here the University of Iowa LEPEDEA measurements are used in conjunction with those of the SEA to place bounds on the satellite potential.

Figure 2 gives a Mode 2 log I vs. V plot taken from the quiet time orbit No. 1463 while the satellite was in the polar cap region. For strongly retarding potentials, we note a steady background current which corresponds to a hyperthermal electron flux of  $2 \times 10^7/\text{cm}^2 \text{ sec}$ . This flux is due to polar rain precipitation.<sup>6</sup> Near zero applied volts the current rises sharply, then approaches a saturation level in the electron acceleration region. We note that the applied voltage is relative to satellite ground. The applied voltage with respect to the plasma is found by algebraically adding the satellite potential.

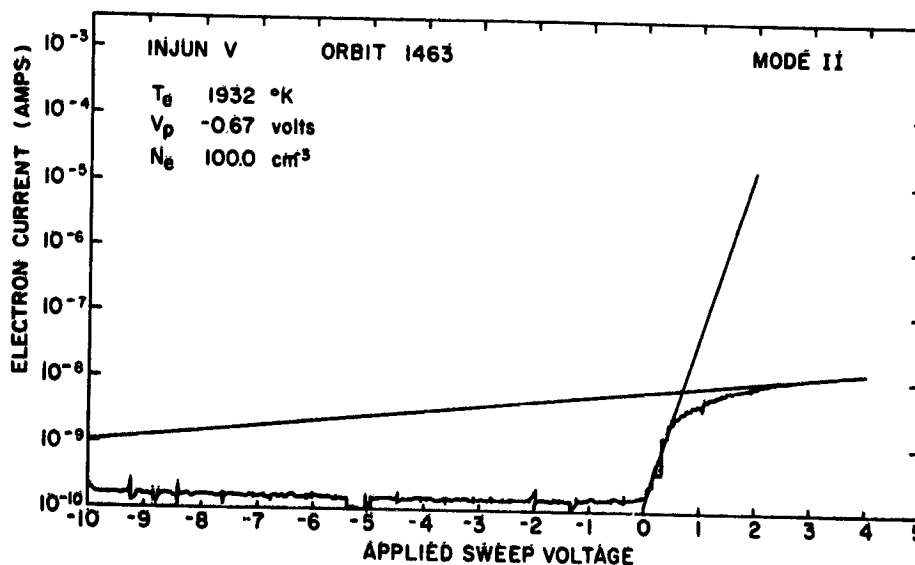


Figure 2. A Mode 2 Plot of log I versus V Taken while the Satellite was at ~2500 km Over the Northern Winter Polar Cap

Electron temperatures  $T_e$  are calculated by assuming that the ambient plasma is Maxwellian and applying the equations of Mott-Smith and Langmuir<sup>7</sup>

$$T_e = \frac{q}{2.3k} \left[ \frac{d \log_{10} I}{d V} \right]^{-1} \quad (1)$$

where  $q$  is the electron charge and  $k$  the Boltzmann constant. A 50 point running linear regression is performed on the data to determine the steepest slope in the retarding portion of the curve and is used in Eq. (1). To calculate the vehicle potential, a linear regression is performed on the final 30 points of the Mode 2  $\log I$  vs  $V$  data. The potential at the intercept of the retarding and accelerating regression lines is the negative of the satellite potential with respect to the plasma  $V_s$

$$V_s = -V_{\text{intercept}} \quad (2)$$

For the case presented in Figure 2,  $n_e = 100 \text{ cm}^{-3}$ ,  $T_e = 1932^\circ\text{K}$ , and  $V_s = -0.67$  volt, where  $n_e$  is the ambient electron density.

The second example is taken from another quiet time orbit No. 1380 as the satellite passed through the midlatitude plasma trough (Figure 3). Using the methods described above, we calculate that  $n_e = 100 \text{ cm}^{-3}$  and  $T_e = 7600^\circ\text{K}$ . Though the density is the same as in the first case, the temperature is a factor of four higher. Where  $\log I(V)$ , in the extreme retarding portion of the sweep, was constant in the polar cap, here it rises linearly with increasing applied voltage. By calculating the solar zenith angle in the production region of the conjugate ionosphere, it can be shown that the hyperthermal electrons are photoelectrons from the sunlit southern hemisphere.<sup>8</sup> To the SEA, the conjugate photoelectrons appear as a nearly Maxwellian population with a temperature of  $\sim 10 \text{ eV}$  and a density of  $\sim 4 \text{ cm}^{-3}$ . Because the conjugate photoelectrons are efficient heaters of trough electrons,<sup>9</sup> they affect the satellite potential in two ways: (1) directly as a current away from the satellite, and (2) indirectly through enhanced thermal electron currents. Thus in the trough the satellite potential was  $-1.65$  volts as opposed to  $-0.67$  volt in the polar cap.

It is to be expected that the most dramatic examples of ionospheric spacecraft charging are found in the nighttime auroral oval. We now consider the vehicle potential response to a low energy and a high energy inverted  $V$  precipitation event.

The University of Iowa LEPEDA<sup>10</sup> electron observations for the quiet orbit No. 1463 are given in Figure 4. Note that the more poleward inverted- $V$  is marked by a sharp onset at 02:27:30 UT, a double peak in intensity, and maximum differential fluxes near a few hundred electron volts. SEA data for the same event are

ORIGINAL PAGE IS  
OF POOR QUALITY

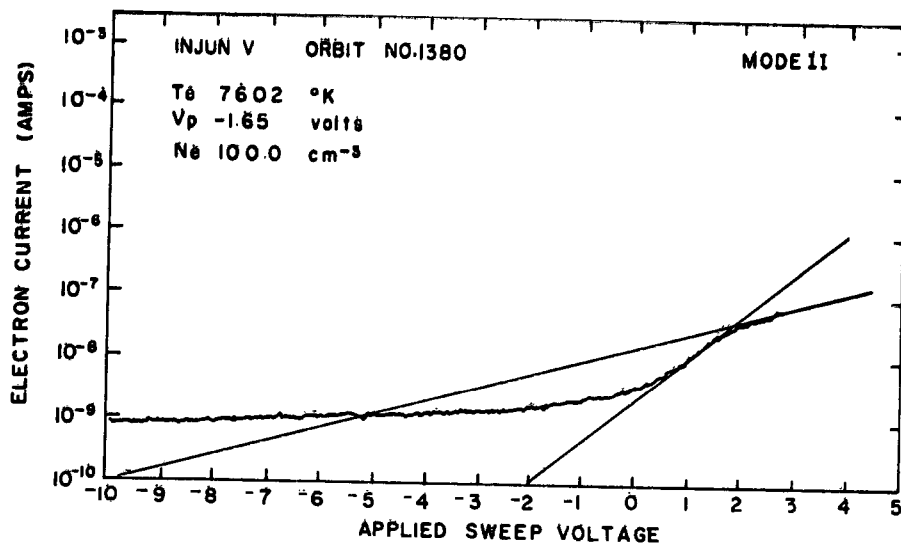


Figure 3. A Mode 2 Plot of  $\log I$  versus  $V$  Taken while the Satellite was at  $\sim 2500$  km Over the Winter Midlatitude Trough

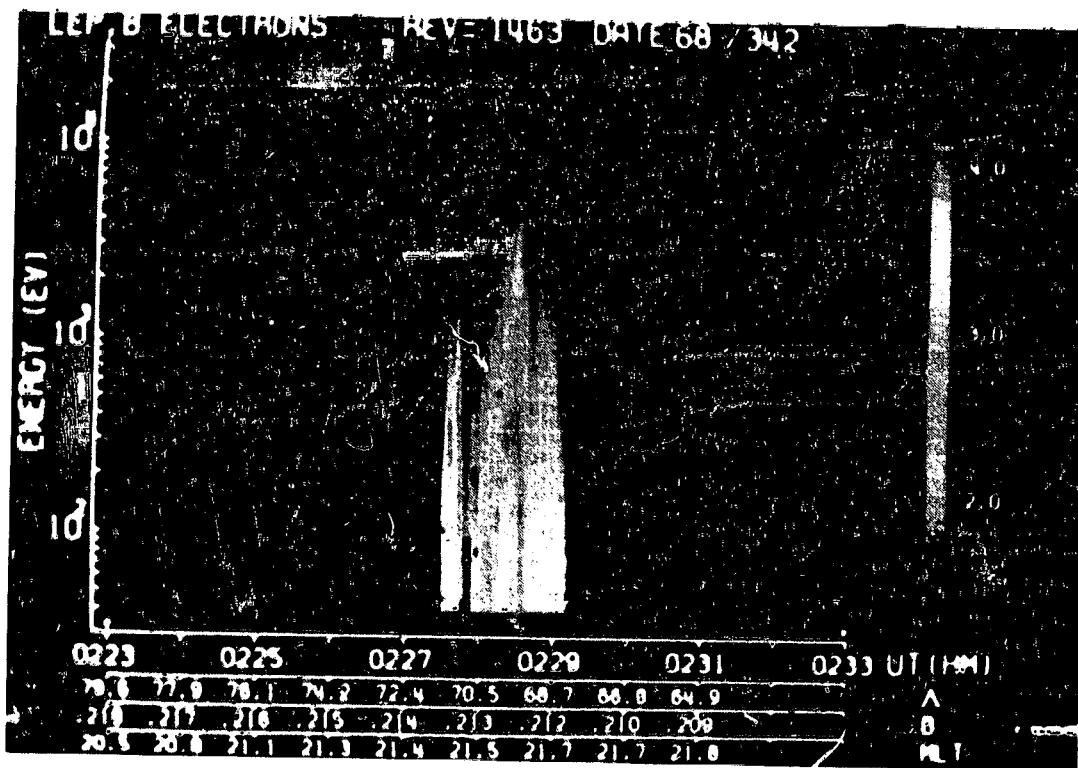


Figure 4. LEPEDA Electron Spectrogram From Injun 5 Orbit No. 1463 (Frank and Ackerson)

shown in Figure 5. Omnidirectional fluxes of positive ions with  $E > 28$  eV are given in the upper trace, and alternating Mode 1/Mode 2 electron fluxes are shown below. In the ion data, the inverted  $V_1$  at 02:27:30 UT appears as a flux enhancement with the same double peaked structure observed in the LEPDEEA electrons. The electron sensor was in Mode 1 with a grid resting bias of +6 volts at the start of this event. The total measured electron flux decreased as the precipitating flux increased and increased at the time of the valley between the two peaks. During the second half of the inverted  $V_1$  event, the electron sensor switched to Mode 2. The anticorrelation between measured and precipitating fluxes during the Mode 1 portion of the event indicates that the vehicle was being negatively charged. The flux measured in the extreme retarding portion of the subsequent Mode 2 sweep is a direct measurement of the omnidirectional flux of precipitating electrons.

The degree of charging during this low energy precipitation event can be estimated if we assume that the ambient plasma remained fairly constant through the

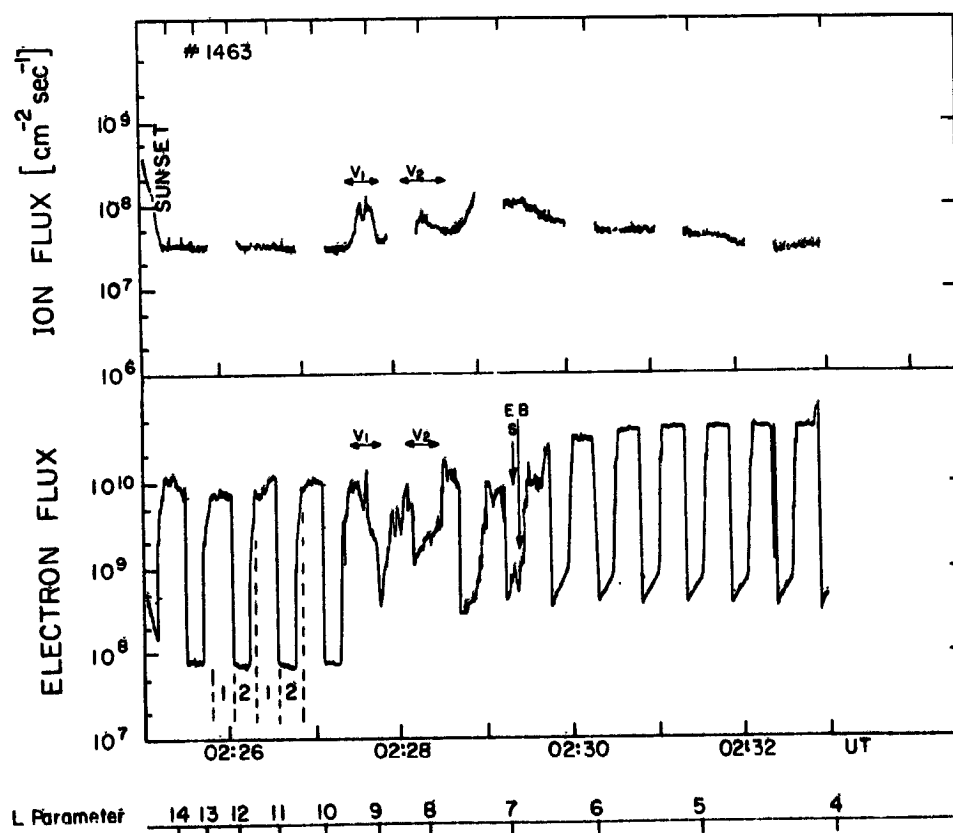


Figure 5. The Ion (Top Trace) and Electron (Bottom Trace) Flux Measurements During Orbit No. 1463

event. Since the resting bias of the grids was +6 volts, the flux measured during the Mode 1 portion was the sum of the thermal and hyperthermal flux that would be measured if the grids were biased at  $V = 6 + V_g$ . At 02:27:36 UT, the time of the first precipitation peak, the measured electron flux was  $5.5 \times 10^9 \text{ cm}^{-2} \text{ sec}^{-1}$  (Figure 6). The measured flux at 02:27:42 UT, the time of the second precipitation

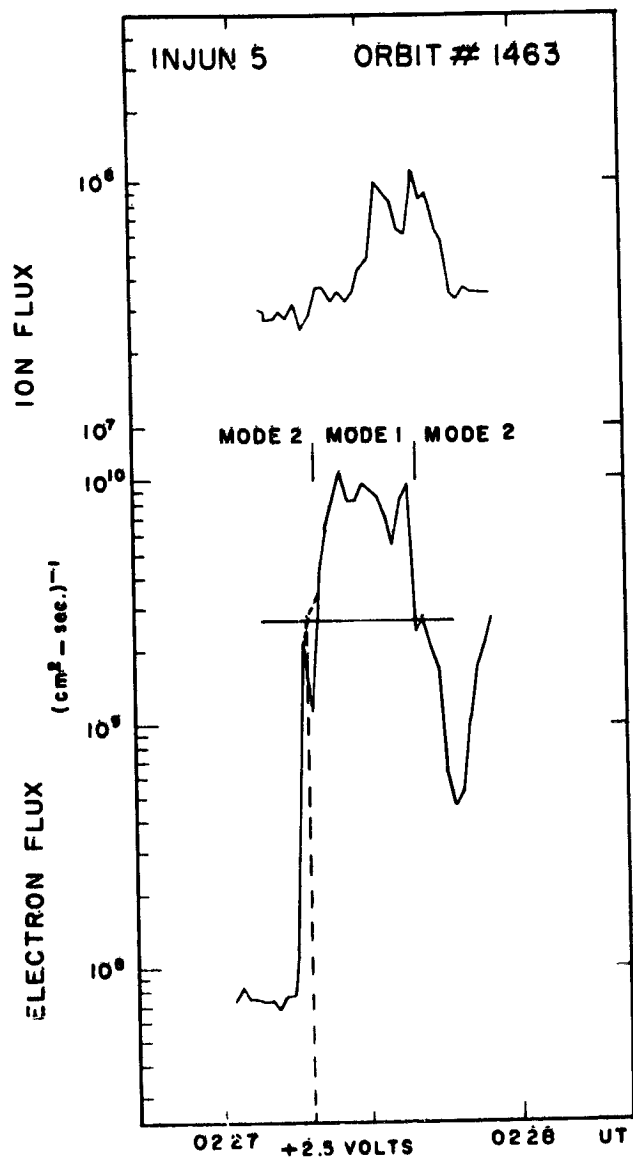


Figure 6. Same as Figure 5 for the Time Period 02:27:00 to 02:28:00 UT, Orbit No. 1463

peak, was  $2.8 \times 10^9 \text{ cm}^{-2} \text{ sec}^{-1}$ . Since the precipitating flux in the first and second peaks were about equal, the thermal electron flux contribution at 02:27:36 was  $\sim 2.7 \times 10^9 \text{ cm}^{-2} \text{ sec}^{-1}$ . We next compare this with the flux measured during the previous sweep. At 02:27:18 UT, a flux of  $2.7 \times 10^9 \text{ cm}^{-2} \text{ sec}^{-1}$  was measured with the sweep voltage was at +2.5 volts. This means that the satellite potential was approximately -3.5 volts (-2.5 - 6.0).

Satellite potential variations typical of more intense precipitation events were observed during orbit No. 1487. The LEPEDA<sup>11</sup> electron observations for this orbit show adjacent inverted V's at 01:48:00 and 01:48:45 UT (Figure 7). Counting rates peak near 5 keV in the first, and at greater than 10 keV during the second inverted V event. The flux of electrons<sup>11</sup> with  $50 \text{ eV} \leq E \leq 15 \text{ keV}$  and pitch angles of  $0^\circ$  and  $90^\circ$  are shown in Figure 8. The directional fluxes at these pitch angles were  $\sim 10^9 \text{ cm}^{-2} \text{ sec}^{-1} \text{ sr}^{-1}$ , and generally within a factor of two of one another. The LEPEDA<sup>12</sup> was unable to measure a field aligned proton flux in the energy

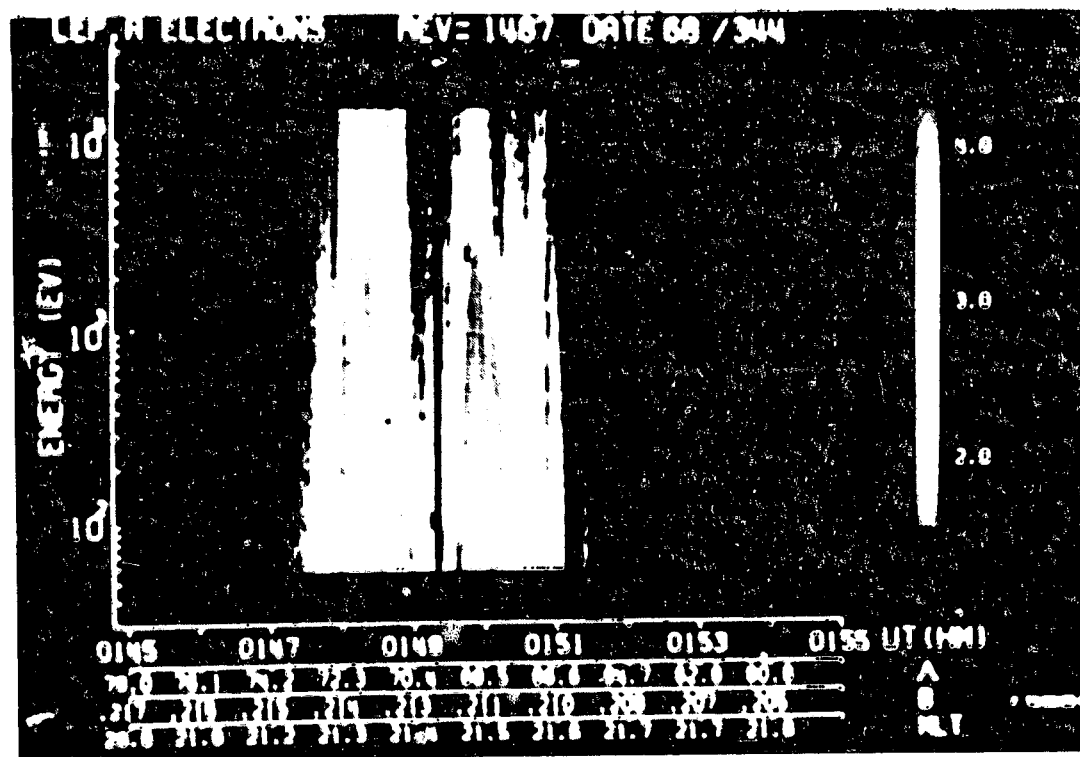


Figure 7. LEPEDA Electron Spectrogram From Injun 5 Orbit No. 1487 (Frank 1975).

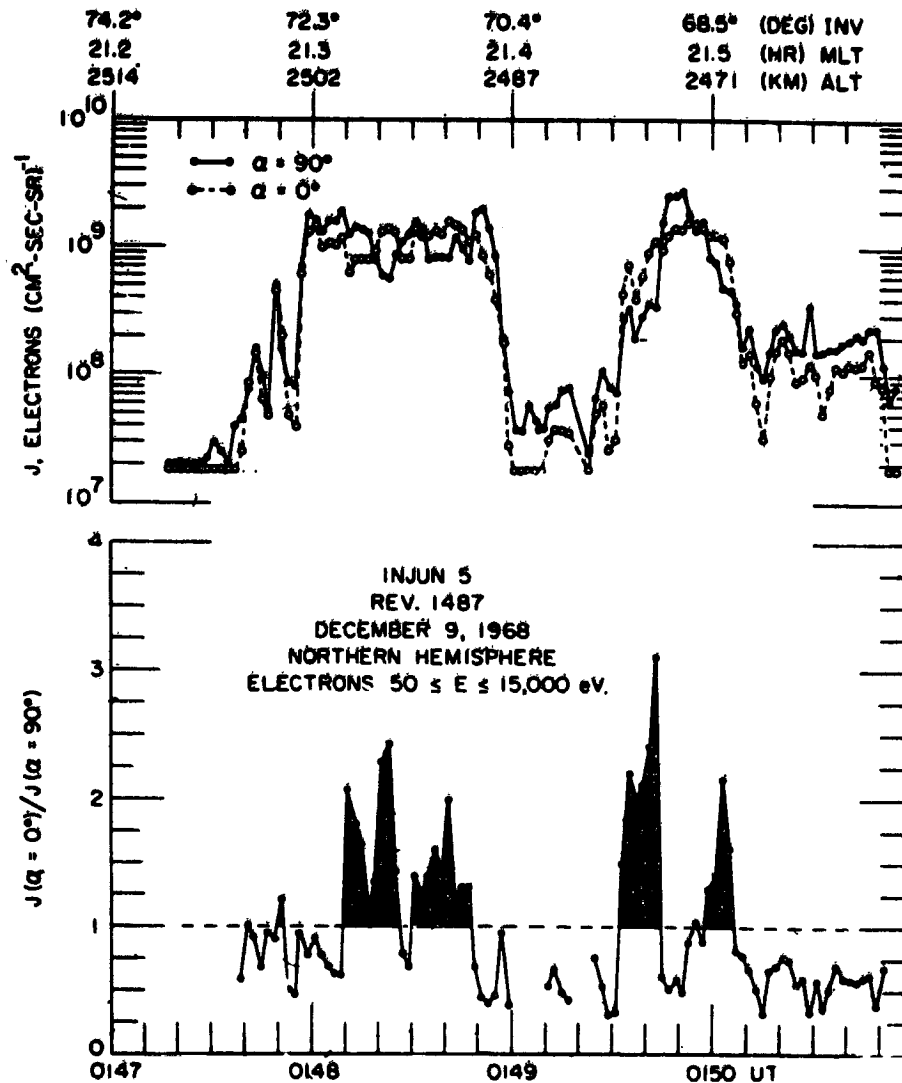


Figure 8. LEPEDEA Electron Fluxes at Pitch Angles of  $0^\circ$  and  $90^\circ$  in the Energy Range  $eV \leq E \leq keV$  During Inverted V Events of Orbit No. 1487 (Frank, 1975)

range  $40 eV \leq E \leq 15 keV$  during these events (Figure 9). The SEA observations are given in Figure 10. It is impossible to distinguish between Mode 1 and Mode 2 fluxes during the second inverted V event. This is because ambient electron collection is completely suppressed by a satellite potential whose upper bound can be set at -6 volts (because of the +6 Mode 1 grid bias). During this period the ion flux, the upper trace of Figure 10, varied rapidly between  $4 \times 10^6$  and  $8 \times 10^8$   $cm^{-2} - sec^{-1}$ . The lower value is a default level indicating that the current to the

ORIGINAL PAGE IS  
OF POOR QUALITY

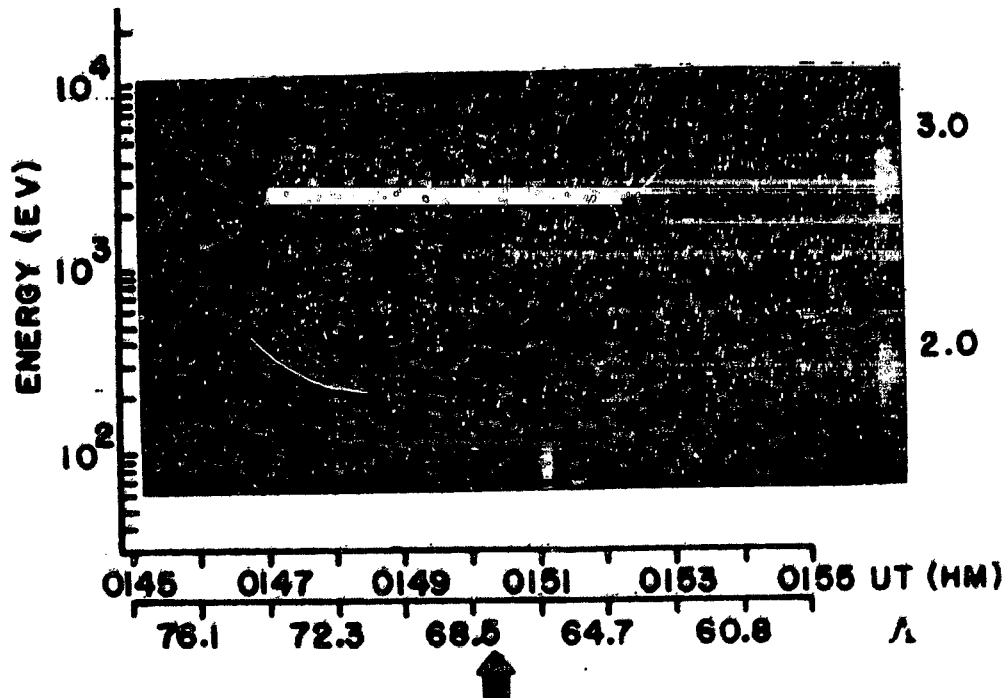


Figure 9. LEPEDEA Proton Spectrogram From Injun 5 Orbit No. 1487 (Frank and Ackerson, 1972)

ion sensor was negative. That is, the flux of electrons with  $E > 2$  keV, the ion collector bias, exceeded the total ion flux.

The peak ion flux observed during the second inverted V of  $8 \times 10^8 \text{ cm}^{-2} \text{ sec}^{-1}$  could be due either to precipitating protons or to a combination of precipitating protons and ambient ions accelerated to the sensor by a negative satellite potential  $< -28$  volts.

To test the first hypothesis, we first calculate the density of the parent electron population. If we assume that the precipitating flux is isotropic over the down coming hemisphere, then the total electron flux is

$$\phi_e = \frac{1}{2} n_e v_{th,e} \quad (3)$$

where  $n_e$  and  $v_{th,e}$  are the precipitating electron's density and mean thermal velocity in their magnetospheric source region. Their temperature is estimated from the LEPEDEA observations to be  $\sim 10$  keV and their omnidirectional flux as

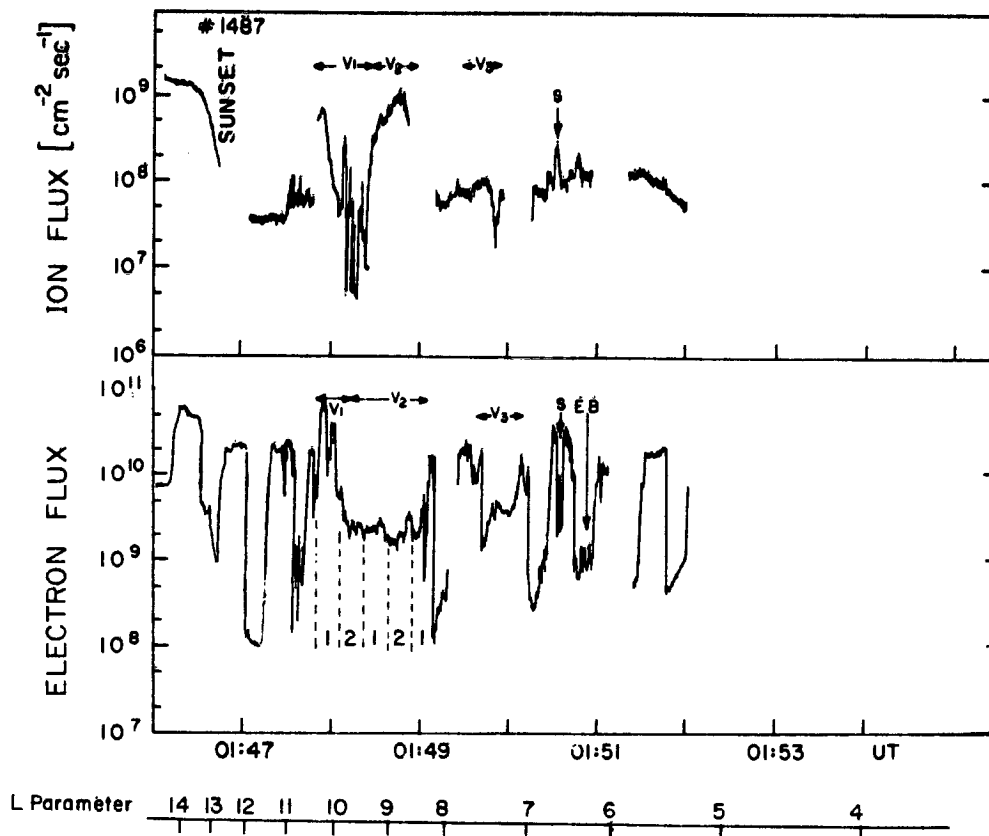


Figure 10. The Ion (Top Trace) and Electron (Bottom Trace) Fluxes Measured by the AFGL SEA During Injun 5 Orbit No. 1487

measured by the SEA is  $\sim 2.5 \times 10^9 \text{ cm}^{-2} \text{ sec}^{-1}$ . Substitution of these values into Eq. (3) gives a parent density of  $0.83 \text{ cm}^{-3}$ , a value typical of the plasma sheet. Assuming that the proton flux is isotropic and that  $n_e \approx n_i$  in the source region, a flux of  $8 \times 10^8 \text{ cm}^{-2} \text{ sec}^{-1}$  implies a magnetospheric proton temperature of 480 keV. This is considerably higher than any measured proton temperature. Mozer and Bruston<sup>13</sup> have measured fluxes of precipitating protons with similar energies over an auroral form but with fluxes decreased by two orders of magnitude. We conclude that the ion flux cannot be due primarily to precipitating protons.

If we accept the second hypothesis that accelerated ambient ions are contributing to the measured flux, then an upper bound of -28 volts can be set on the vehicle potential. A lower bound of -40 volts can be set on the vehicle potential. There are 117 energy channels measured by LEPEDA in the range  $40 \text{ eV} \leq E \leq 15 \text{ keV}$ . It is highly unlikely that an ion flux of  $8 \times 10^8$  could pass undetected.

The satellite potential adjusts itself so that the total current is zero. The precipitating electron flux is  $\sim 2.5 \times 10^9 \text{ cm}^{-2} \text{ sec}^{-1}$ . In the absence of an electron flux to the ion sensor, the measured ion flux would be equal to the electron flux. The electron flux to the negatively biased ion sensor collector (-2 kV) is

$$\phi_{e,i} = 2.5 \times 10^9 e^{-qV/kT_e} \quad (4)$$

where  $\phi_{e,i}$  is the hyperthermal electron flux to the ion sensor,  $V = 2000$  volts, and  $kT_e \approx 10$  keV. Thus  $\phi_{e,i} \approx 2 \times 10^9 \text{ cm}^{-2} \text{ sec}^{-1}$ . Thus the measured ion flux should be  $\phi_{\text{net}} = 2.5 \times 10^9 - \phi_{e,i} = 5 \times 10^8 \text{ cm}^{-2} \text{ sec}^{-1}$ . Given the uncertainty in the precipitating electron temperature in Eq. (4), this number compares favorably with the measured ion flux of  $8 \times 10^8 \text{ cm}^{-2} \text{ sec}^{-1}$ .

The vehicle charging hypothesis also helps to explain the rapid variations in the ion flux between high values and the default level near 01:48 UT of orbit No. 1487. Relatively small modulations of the vehicle potential above and below -28 volts allow the ion sensor grid to act as a gate determining whether ambient ions or energetic electrons reach the collector.

### 3. SUMMARY AND CONCLUSIONS

In this report, we have presented ion and electron fluxes observed by the AFGL sensors aboard Injun 5. All data were taken while the satellite was in darkness. They can be used to establish typical values of spacecraft charging in the topside ionosphere. The vehicle potential was found to range from -0.67 volt in the cold tenuous plasma of the polar cap to  $\sim -40$  volts as the satellite passed through an intense auroral precipitation event. To a first approximation, the results are consistent with a simple flux balance calculation of the vehicle potential.

### References

1. Beard, D. B., and Johnson, F. S. (1961) Ionospheric limitations on attainable satellite potential, J. Geophys. Res. 66:4113-4122.
2. Whipple, E. C. Jr. (1965) The equilibrium electric potential of a body in the upper atmosphere and in interplanetary space, NASA Rpt. X615-65-296, Goddard Space Flight Center, Greenbelt, MD.
3. Samir, U., and Willmore, A. P. (1966) The equilibrium potential of a spacecraft in the ionosphere, Planet. Sp. Sci. 14:1131-1137.

4. Kasha, M. A. (1969) The Ionosphere and Its Interaction with Satellites, Gordon and Breach, New York.
5. Burke, W. J., Dulong, F. D., and Sagalyn, R. C. (1976) Injun 5 observations of low energy plasma in the high latitude topside ionosphere, (submitted to J. Geophys. Res.).
6. Winningham, J. D., and Heikkila, W. J. (1974) Polar cap auroral electron fluxes observed with ISIS I, J. Geophys. Res. 79:949.
7. Mott-Smith, H. M., and Langmuir, I. (1926) The theory of collectors in gaseous discharges, Phys. Rev. 28:727.
8. Maier, E. J., and Rao, B. C. N. (1968) Observations of the superthermal electron flux and electron temperatures at high latitudes, J. Geophys. Res. 75:7168.
9. Hanson, W. B. (1963) Electron temperatures in the upper atmosphere, Space Research 3:282.
10. Frank, L. A., and Ackerson, K. L. (1971) Observation of charged particle precipitation into the auroral zone, J. Geophys. Res. 76:3612-3641.
11. Frank, L. A. (1975) Magnetospheric and auroral plasmas: a short survey of progress, Rev. Geophys. and Sp. Phys. 13:974.
12. Frank, L. A., and Ackerson, K. L. (1972) Local time survey of plasma at low altitudes over the auroral zone, J. Geophys. Res. 77:4116.
13. Mozer, F. S., and Bruston, P. (1968) Auroral zone proton-electron anticorrelations, proton angular distributions, and electric fields, J. Geophys. Res. 71:4461-4468.

## Contents

1. Introduction	82
2. Transient Event Counter (TEC) Description	84
3. Discussion of TEC Flight Data	88
4. Concluding Remarks	104
References	105

#### 4. Preliminary Report on the CTS Transient Event Counter Performance Through the 1976 Spring Eclipse Season

N. John Stevens, Robert R. Lovell, and Vernon W. Klinec  
Lewis Research

#### Abstract

The first known harness transient detector flown on a synchronous satellite has been operating on the joint Canadian-American Communications Technology Satellite (CTS) since 31 January 1976. This detector, called the transient event counter (TEC), senses and counts transients having a voltage rise of greater than 5 volts in three separate wire harnesses: the attitude control harness, the solar array instrumentation harness, and the solar array power harness.

This report describes the TEC, defines its operational characteristics, and presents the preliminary results obtained through the first 90 days of operation including the Spring 1976 eclipse season. The results show that the CTS has been charged to the point where discharges have occurred. The discharge induced transients have not caused any anomalous events in spacecraft operation. The data indicates that discharges can occur at any time during the day without preference to any local time quadrant. The number of discharges occurring in the 1 sec sample interval are greater than anticipated. The compilation and review of the data is continuing.

81  
PRELIMINARY  
PAGE BLANK NOT FILM

## I. INTRODUCTION

The joint Canadian-American Communications Technology Satellite (CTS) is the first of a new generation of high power, high frequency communications satellites utilizing a 12 GHz, 200 W rf transmitting system.<sup>1</sup> This satellite was launched 17 January 1976, and placed in a synchronous equatorial orbit at 116° West Longitude.

Since the early 1970's satellites in synchronous orbits have been experiencing anomalous electronic switch events.<sup>2</sup> This anomalous behavior is believed to be caused by the coupling of environmentally induced discharge pulses into the low level logic circuits used on these satellites. The data from an experiment on the ATS-5 and -6 satellites has shown that clouds of kilovolt electrons can occur at synchronous altitudes.<sup>3</sup> It has been shown that these clouds can charge the satellite ground to potentials that range from a few hundred volts to several kilovolts negative.<sup>4, 5</sup> The range to which the spacecraft grounds can be charged in a given particle environment is determined by the areas of the satellite grounded metal surfaces that are in the sunlight. The photo-emitted electron current from these sunlit surfaces can partially balance the incoming electron flux and maintain the spacecraft potential within a few hundred volts relative to the space plasma potential. If the spacecraft ground can be charged in this manner, then it must be assumed that the insulators can also be charged. Furthermore, the insulator surfaces that are shaded can be charged to the kilovolt level even when the spacecraft grounds are maintained at the few hundred volt level. When the satellite insulator surfaces are charged to the kilovolt level, a discharge can be triggered and the resulting pulse of electromagnetic energy can cause anomalous behavior in sensitive electronic circuits.

The Communications Technology Satellite (CTS) was designed in the 1970-1971 time period when the spacecraft charging phenomenon was barely recognized by project personnel. As a result the satellite incorporated design techniques which were normally used at that time for lightweight satellites. Thermal blankets were used to close the top and bottom spacecraft body openings and solar cells, optical solar reflectors, and silvered Teflon were used on the satellite exterior (see Figure 1).

The unique feature of the satellite is the size and construction of the deployable solar arrays, each 1.2 x 7.6 m long which have the solar cells mounted on a 0.5-mil Kapton fiberglass composite substrate. The satellite is three axis stabilized and the solar arrays track the Sun. Therefore, this satellite has large areas of exposed insulator surfaces that are shaded when the satellite is in orbit. These surfaces can be charged by the electron clouds at synchronous altitudes.

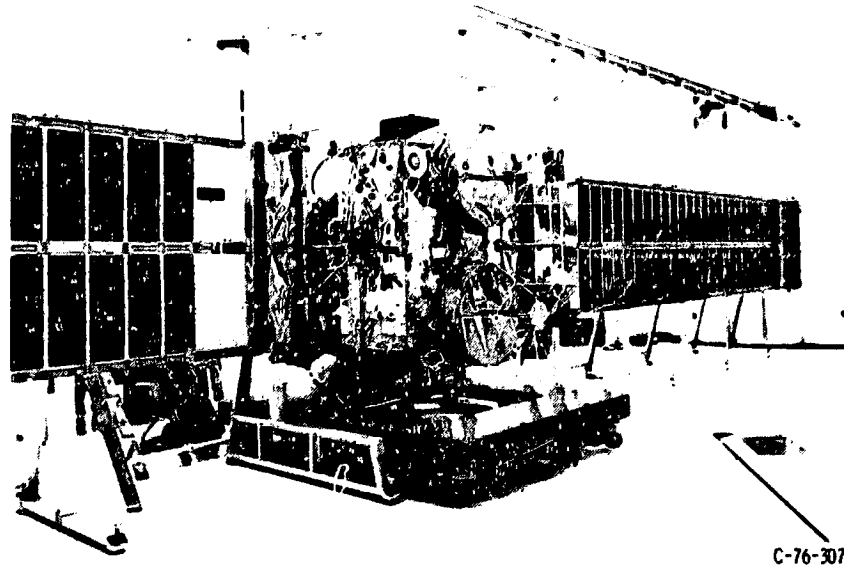


Figure 1. CTS Spacecraft (Prelaunch Checkout)

The concern for possible spacecraft charging effects on the CTS led to the establishment of an investigation to determine the response of the spacecraft surfaces to the substorm particle fluxes.<sup>6</sup> Late in the CTS program, a recommendation was made to incorporate a charging diagnostic device. This recommendation was accepted by the CTS Project provided that the weight and power consumption were minimized. A decision was made that a harness transient detector would be an acceptable minimum device. It was assumed that the data on the environment that could charge the surfaces could be obtained from other sources. Thus, the harness transient detector, called the Transient Event Counter (TEC) was built, qualified, and integrated into the flight spacecraft 6 months prior to launch. This is the first such detector known to be on a satellite in geosynchronous orbit.

This report will describe the TEC, define its operational characteristics, and present the preliminary results obtained through the 1976 Spring eclipse season. The data on charging environment is still being collected. However, the preliminary data of an indication of the state of the environment, the K index, from the ground station at Anchorage, Alaska, is given as a gross indicator. This K index measures the geomagnetic effects of solar particle flux at a specific station at 3 hr intervals.<sup>7</sup> Hence, it can be used as an indication of the state of the environment. The K index values are given on a scale of 0 to 9. The higher numbers indicate a disturbed or charging environment, while the lower numbers indicate a quiet environment.

## 2. TRANSIENT EVENT COUNTER (TEC) DESCRIPTION

The Transient Event Counter (TEC) is a small electronic device capable of sensing and counting transient pulses having an amplitude greater than 5 volts that are transmitted along the spacecraft internal wiring harnesses. The objectives of this device are:

- (1) to obtain flight data on arc discharge events related to spacecraft charging which would aid in the design of future spacecraft,
- (2) to count the number of discharges as a function of satellite time,
- (3) to locate approximately the sources of the discharge, and
- (4) to provide diagnostic information relating anomalous performance to charging events.

Due to the limited time available to design, build, qualify, and integrate the TEC, a decision was made to count the transients only at three specific locations on the satellite. It was desirable to record the amplitude of the transients, but it was felt that the additional development time might jeopardize the incorporation of the TEC on the satellite.

The elements of the TEC are shown in the block diagram of Figure 2. The three detectors sense the transient pulses in the harnesses. These pulses are counted for a 1 sec interval and stored in a register. The stored counts are transmitted to ground through the satellite telemetry system. The general specifications for the TEC are given in Table 1.

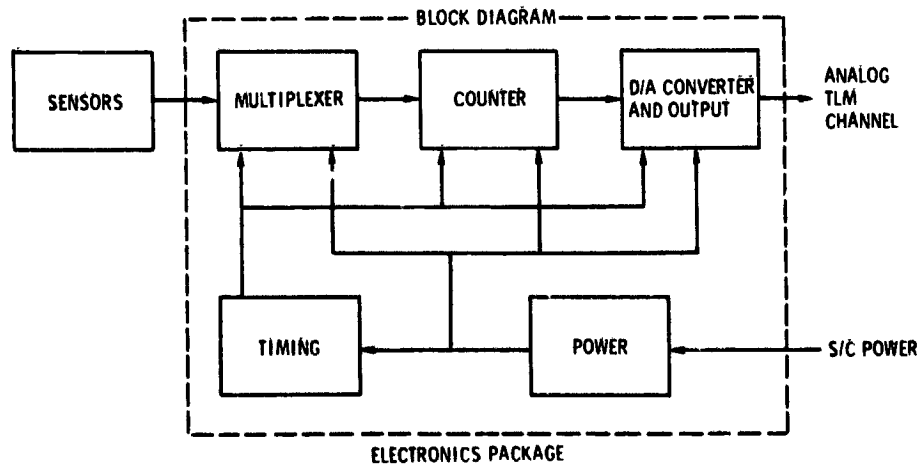


Figure 2. Transient Event Counter

Table 1. TEC Specifications

Power	330 mW
Size	7.62 × 10.16 × 5.5 cm (3 × 4 × 2.16 in.)
Weight	326.6 grams (11.5 oz)
Input Voltage	+15 VDC ± 15 percent
Output Voltage	0-5V DC
Output Impedance	< 3 ohms
Telemetry	one analog channel
Commands	none
Outgassing	venting holes provided
Measurements	3 channels, subcommutated with calibrated and ID signal
Counting Capacity	64 transients/sec

## 2.1 Sensors

The sensors are coaxial cables with 60 cm of the shield removed at one end. These unshielded portions of the cables are laced to the spacecraft wire harnesses at three separate locations within the spacecraft. Each sensor acts as an antenna coupling to the transient pulse within the harness. The location of the sensors are as follows (see Figure 3):

(1) Channel 1: Attached to the attitude control instrumentation wire harness between the nonspinning Earth sensor assembly and the attitude control electronics assembly. It is assumed that this sensor would pick up discharges from the forward platform thermal blankets, the antenna system, the silver Teflon on the variable conductance heat pipe radiator, and the Earth sensor assemblies. The shielded length of this cable is about 1.5 m.

(2) Channel 2: Attached to the south solar array instrument harness within the spacecraft body at the slip rings. The instrument lines on the solar array are unshielded and are routed down the center of the wing. This sensor will detect arc discharges occurring in the center area of the solar array wing. The shielded length of this cable is about 0.5 m.

(3) Channel 3: Attached to the south solar array power harness within the spacecraft body at the slip rings. The power lines on the solar array are also unshielded and run along both the outside edges of the wing. This sensor, then, will detect discharges occurring at the edges of the wing and at the solar cells. The shielded length of this cable is also about 0.5 m.

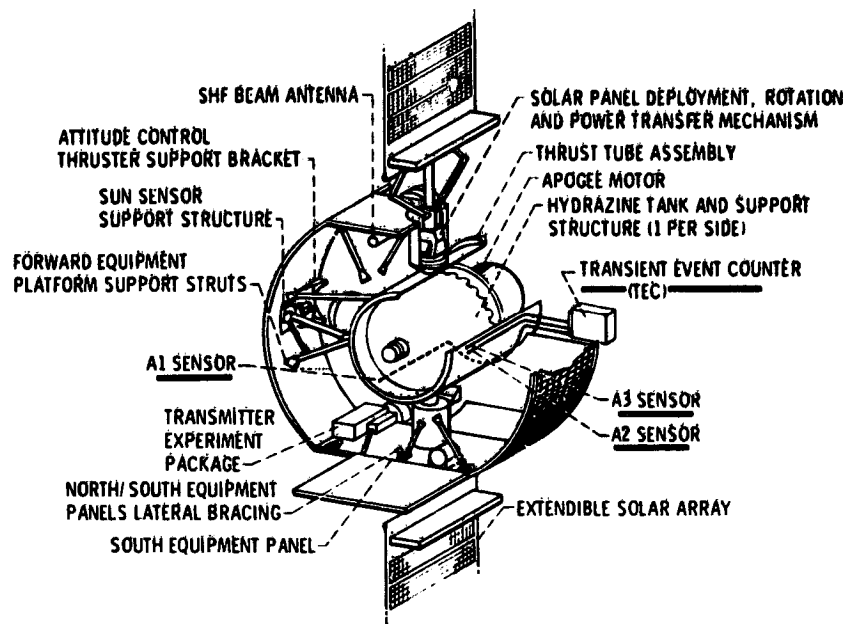


Figure 3. TEC and Sensor Locations

These locations were chosen so that the sensors would monitor those parts of the spacecraft where discharge activity was anticipated.

The unshielded sensors were attached to the outside of these wire harnesses instead of within the harness because the wire harnesses were completed and installed in the flight spacecraft before the decision to fly the TEC was made. Mounting the sensor in this manner decreased the sensitivity and increased the possibility of pickup from sources outside the harness. However, testing of the TEC on the satellite using a portable spark source indicated that the desired threshold of 5 volt sensitivity could be achieved.

## 2.2 Electronics Package

The electronics package houses the counting and storage circuits in a box,  $7.6 \times 10 \times 5.5$  cm, that weighs 327 grams (see Figure 4). This package is mounted on the exterior CTS aft platform under the thermal blanket (see Figure 3).

The allocation of only one telemetry channel to the TEC necessitated the inclusion of a multiplexer and timer to control this experiment. The multiplexer switches in the first sensor channel for about 1 sec. During this interval the counter will count the transients in the harness with an amplitude greater than 5 volts and store the total count in the register. A maximum of 63 transients can

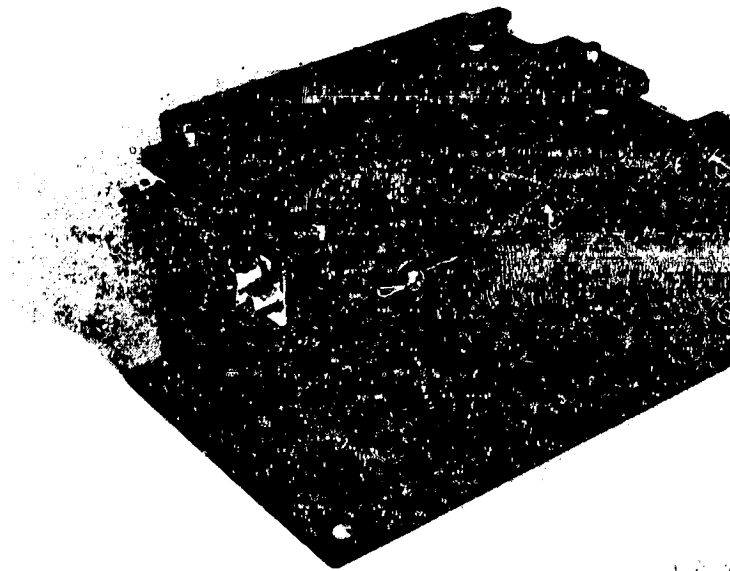


Figure 4. TEC Electronics Package

be counted in the sampling period. An overflow indicator (the sixty-fourth transient count) is used when greater than 63 transients are counted. There is a built in  $5 \mu\text{sec}$  delay after a discharge pulse is counted. This delay is to prevent the counting of line ringing as separate discharge pulses. The delay was selected as a result of the ground tests on materials' characteristics conducted at the LeRC.

At the end of the 1 sec interval the total count is stored in the register, the timer resets the counter to zero, and the multiplexer switches to the next channel. Discharge transients on this line are then counted for a second after which this total count is stored in the register. The cycle is then repeated for the third sensor. The multiplexer has a fourth position at which time a calibrate signal is fed into the register. After the calibrate signal, the cycle repeats. The telemetry format is shown in Figure 5.

The telemetry system samples the storage register at about once per second. Hence, the transient pulses on each sensor are counted for about 1 sec every 4 sec. Since the telemetry rate and the TEC counter are not synchronized, the channel being sampled is determined from the calibrate signals: every other cycle has a maximum count calibrate signal with a zero count calibrate in between. The TEC timer was allowed to be free running to minimize the ties to the CTS telemetry system.

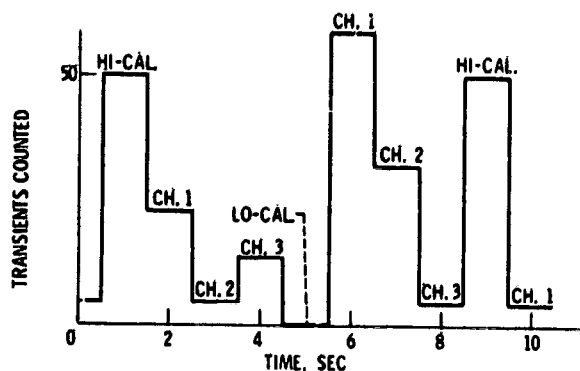


Figure 5. Typical Telemetry Output

### 3. DISCUSSION OF TEC FLIGHT DATA

The CTS was launched on 17 January 1976, and placed in a synchronous, equatorial orbit at  $116^{\circ}$  West Longitude. The TEC has been operating continuously since the main solar array deployment on 31 January 1976.

A complete summary of the TEC flight data for the period from 31 January 1976, through the Spring eclipse period until 30 April 1976, is given in Table 2 as a function of satellite local time. The data given in this table are the total number of transients counted in the 1 sec sampling of that channel. The satellite local time is defined such that local noon occurs when the satellite is on the Sun-Earth line. This time scale is of more interest for spacecraft charging investigations since it allows for a better visualization of surface shadowing and correlation of substorm data. The satellite local time can be converted to Universal Time (UT) by adding 7 hr and 44 min.

The number of transients counted on each channel by TEC for this 90 day period is summarized in Figure 6. This same data is shown in more detail on the 15 day graphs of Figures 7 to 12. Preliminary values of the K index from the Anchorage, Alaska station have been plotted on the 15 day transient data plots as a gross indicator of the state of the environment. The K index value is given on a scale of 0 to 9; the higher the number, the more severe the substorm. It must be realized that the data from the Anchorage station may not be indicative of the state of the environment at the CTS location since the environment can be highly localized; a short, intense substorm at the CTS position may not be indicated in the station data averaged over the 3 hr period.

Table 2. TEC Flight Data

Date	S/C time	No. of Transients			Eclipse	
		CH 1	CH 2	CH 3	Start	Stop
1/31/76	23:16 23:18 23:20		3 2	3		
2/1/76	18:53	8				
2/2/76	11:08 11:24 15:19		6	4 3		
2/18/76	05:19 09:15 09:30 09:32 09:32 09:33 09:34 09:40 09:42 09:45 09:47 18:05		3 12 2 49	1 3 33 6 3		
		12 33				
2/19/76	11:24 14:11		33 12			
2/20/76	03:04 03:06 15:25 16:19 18:13 21:15	1 1	1 12 24	1		
2/21/76	01:17 02:32 06:34 09:05 23:20		33 1	3 3 6		
2/22/76	01:24 11:01	1	1			
2/23/76	02:03 02:49 04:52	1	1	3		
2/24/76	08:01 09:38 13:31		6 49 46			
2/25/76	14:33			33		

Table 2. TEC Flight Data (Cont.)

Date	S/C time	No. of Transients			Eclipse	
		CH 1	CH 2	CH 3	Start	Stop
2/26/76	07:51 13:38 19:59	24 6 6				
2/27/76	08:41 10:17 18:14 18:14	1	1 12	12		
2/28/76	10:49 18:35 18:53	62 33	24			
2/29/76	00:26 20:36	12		1		
3/1/76	01:57 08:28	12	3		00:02:53	00:22:14
3/2/76	04:48 05:04 05:26 05:32 05:34 05:38 05:53 06:07 06:13 17:33 21:06	6 1 14	26 41 3 6 19 3 1	6	23:58:32	00:26:07
3/3/76	12:28 12:28 12:29		3 3 33		23:55:19	00:26:07
3/4/76	16:16 16:31 16:40 18:19		24 1 24	6	23:51:25	00:28:53
3/5/76	02:42		1		23:49:11	00:33:54
3/6/76	04:56 10:45 16:10	2	1 31		23:47:14	00:35:23
3/7/76	22:14		1		23:45:26	00:36:36
3/8/76	23:01			1	23:43:49	00:37:37

Table 2. TEC Flight Data (Cont.)

Date	S/C time	No. of Transients			Eclipse	
		CH 1	CH 2	CH 3	Start	Stop
3/9/76	04:34 05:10 17:09	1	11	1	23:42:19	00:38:30
3/10/76	02:17 16:00	1	1		23:40:57	00:39:14
3/11/76	03:31 23:15		1 33		23:40:31	00:39:03
3/12/76	00:52 03:56 04:01	3	1 33		23:39:21	00:39:35
3/15/76	09:28 22:46 22:51	33	12	12	23:36:33	00:40:42
3/16/76	10:19	4			23:35:47	00:40:53
3/17/76	02:36 07:29	5 2			23:35:06	00:40:59
3/20/76	15:17 15:31 15:32 15:58 17:40	2 1	2 5	2	23:33:28	00:40:45
3/23/76	08:27 11:02 12:35 17:23 21:06		4 4	1 2 24	23:32:28	00:39:47
3/24/76	00:40 02:24 04:27 17:14	10	36 6	1	23:32:16	00:39:19
3/25/76	17:15	3			23:32:09	00:38:45
3/26/76	21:34 21:59 22:07 23:18	1 3	1	25	23:32:07	00:38:07
3/27/76	10:45 21:57		24 12		23:32:11	00:37:27

Table 2. TEC Flight Data (Cont.)

Date	S/C time	No. of Transients			Eclipse	
		CH 1	CH 2	CH 3	Start	Stop
3/28/76	02:04		16		23:32:18	00:36:39
	02:08			41		
	09:47	33				
	09:48		3			
	09:57	10				
	10:35		1			
	12:29		1			
	12:49		6			
	14:29			1		
	15:45		2			
	15:51			12		
	15:54			6		
	17:25		24			
	19:29	25				
3/29/76	19:36	1			23:32:31	00:35:47
3/30/76	02:28	6			23:32:48	00:34:50
	06:00	1				
	07:07	8				
	09:59			1		
	12:27		1			
3/31/76	06:21		33		23:33:11	00:33:47
	06:21	1				
4/1/76	21:19			1	23:33:39	00:32:39
4/6/76	08:13			1	23:38:12	00:23:26
	12:46			33		
4/7/76	06:01			49	23:39:37	00:23:26
	12:24		1			
	14:31	6				
4/8/76	18:40	49			23:41:18	00:21:15
	19:16	51				
	20:52		49			
	23:42		1			
4/9/76	00:11	6			23:43:19	00:18:44
	00:11		49			
	00:12		33			
	00:13			24		
	00:13			12		
	00:14	6				
	00:15		1			
	00:15			3		
	00:17			1		
	00:17	33				
	00:18	12				

Table 2. TEC Flight Data (Cont.)

Date	S/C time	No. of Transients			Eclipse	
		CH 1	CH 2	CH 3	Start	Stop
4/9/76	00:20		6			
	09:34	49				
	09:37			3		
	09:38	1				
	09:41	1				
	12:15			33		
	16:09			42		
4/10/76	22:39			1		
	07:53	49	6		23:45:48	00:15:46
	15:19		31			
4/11/76	20:52					
	15:28	1	24		23:49:02	00:12:01
4/12/76	19:14					
	09:58		1		23:54:20	00:06:13
4/13/76	00:02		1			
	02:01			1		
	02:10		1			
	02:12			1		
	02:15			1		
	02:28			1		
	02:37		1			
	02:41		1			
	02:42	1				
	02:47	1				
	02:52			1		
	03:12		1			
	03:21		1			
	10:44	33				
11:37				6		
4/15/76	06:10		1			
	06:20		6			
	06:26			1		
4/17/76	18:13		33			
4/18/76	01:02			6		
	17:12	1				
4/19/76	03:12		1			
4/20/76	14:37			1		

Table 2. TEC Flight Data (Cont.)

Date	S/C time	No. of Transients			Eclipse	
		CH 1	CH 2	CH 3	Start	Stop
4/21/76	07:30		33			
	17:01			33		
	17:01	49				
	17:13			24		
	17:14		1			
	17:15		6			
	17:16		24			
	17:27	6				
	17:28	33				
	18:25		49			
	19:33		12			
	22:04	33				
	22:27	24				
	22:50			1		
	22:54			24		
23:04				49		
23:55			12			
4/22/76	00:31	24				
	01:01		3			
	05:02	3				
	05:39		1			
	06:08			33		
	06:26		12			
	06:35		1			
	07:12			6		
	07:37		12			
	09:08		12			
	09:15	6				
	09:59	12				
	10:07			6		
	11:10	24				
	12:59			33		
	13:08			6		
15:10			1			
13:27				3		
21:03	6					
4/23/76	03:32	3				
	07:29	1				
	15:06	1				
4/24/76	04:29		24			
	04:29					
	11:49	24				
4/25/76	12:44	2				
4/26/76	12:13		12			
	12:13		49			

Table 2. TEC Flight Data (Cont.)

Date	S/C time	No. of Transients			Eclipse	
		CH 1	CH 2	CH 3	Start	Stop
4/27/76	02:53	1				
4/28/76	08:57	33				
	23:39	3				
4/29/76	07:57	49				
	08:00		1			
	08:07	1				
	19:30	10				
	20:34		12			
4/30/76	00:37	33				
	01:32	25				
	04:06			1		
	04:17	3				
	06:58			33		
	08:17		3			
	09:57		12			

The TEC data shows that transients exist in the wire harnesses. All satellite data have been reviewed to verify that no commands were being executed and that there were no power fluctuations at the times of the TEC counted transients. Therefore, it is assumed that these transients are caused by discharges resulting from the environmental charging of the satellite surfaces.

The number of transients being sensed by the TEC in the 1 sec sampling time is, at times, higher than one would anticipate based on the ground test data. The TEC does have a built-in 5- $\mu$ sec delay after it counts a transient pulse and this should prevent the counting of line ringing as transients. These high TEC counts may be due to sequential discharging of the large insulator surfaces on the satellite. The ground data does indicate that this sequential discharging may be possible. The evaluation of the high number of TEC transients is continuing.

The correspondence between the transients and the state of the environment as shown in Figures 7 to 12 is rather poor. At times that the environment appeared to be very active (for example, February 7, 8, and 27, March 25 and 26, and April 1), no transients were counted. At other times when the environment is reasonably quiet, there are transients. Transients are also counted when the environment is active. This apparent inconsistency could be due to the uncertainty of the actual substorm conditions at the satellite position in space. Environmental monitors on

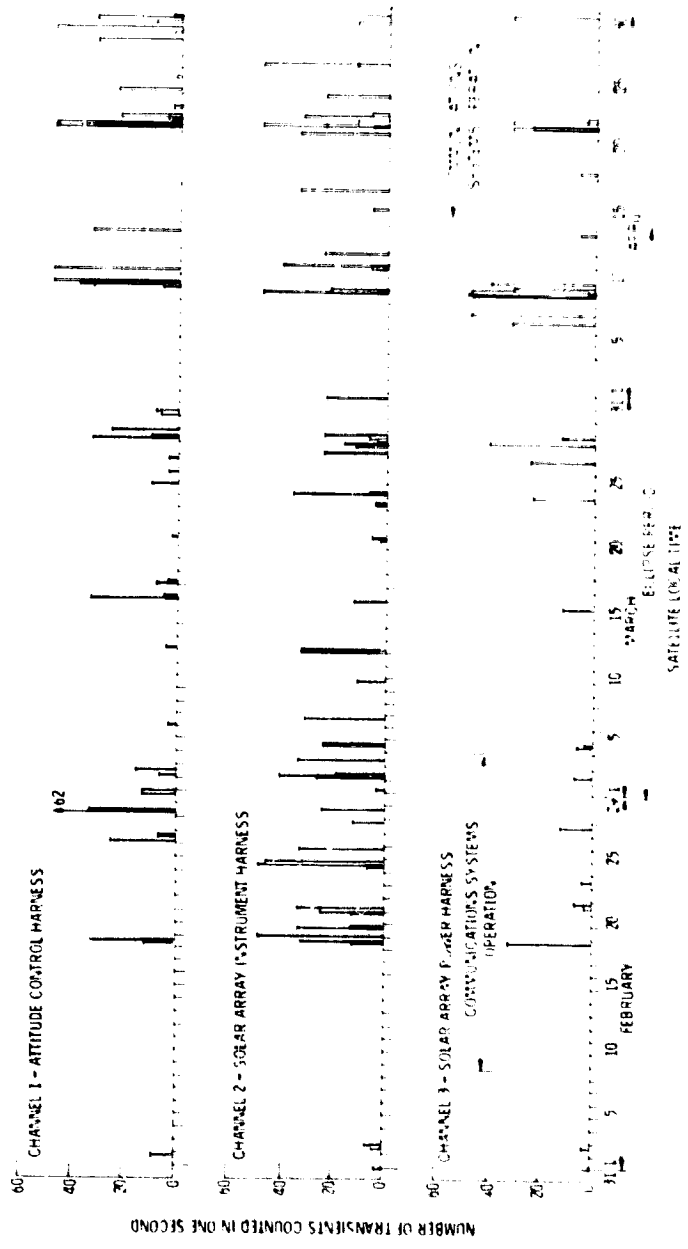


Figure 6. Preliminary Data - CTS Transient Event Counter January 31-April 15, 1973

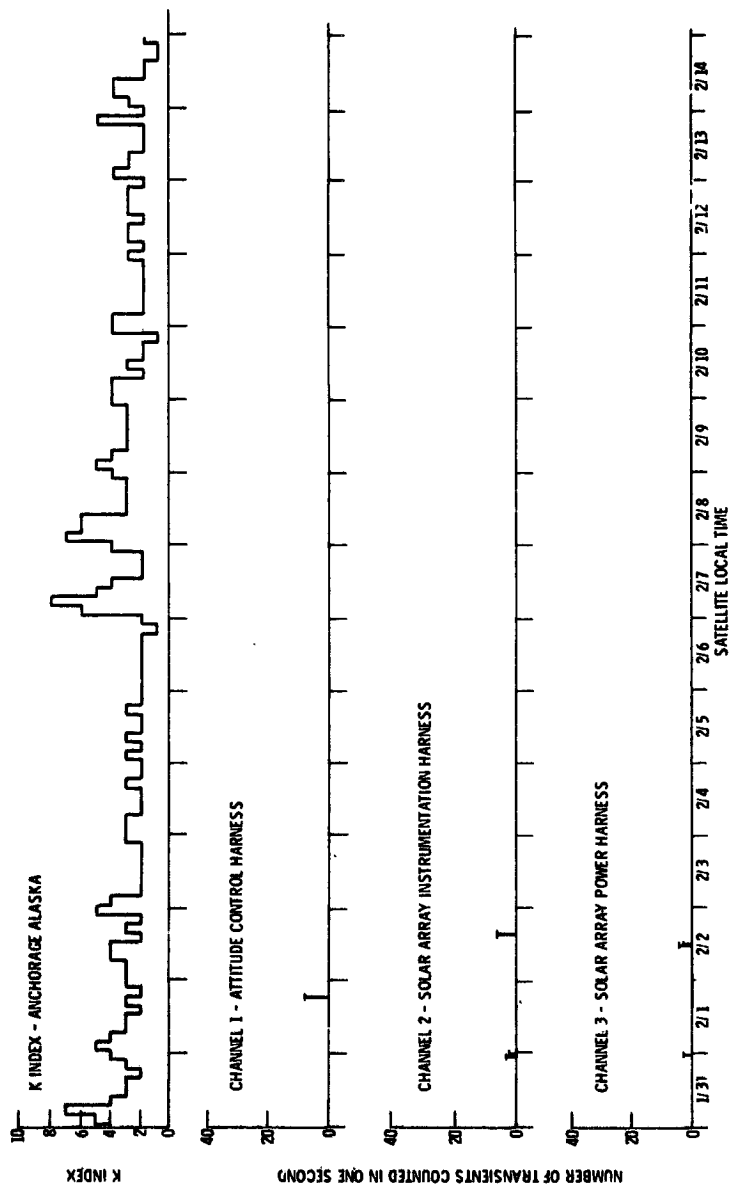


Figure 7. TEC Preliminary Data January 31-February 14

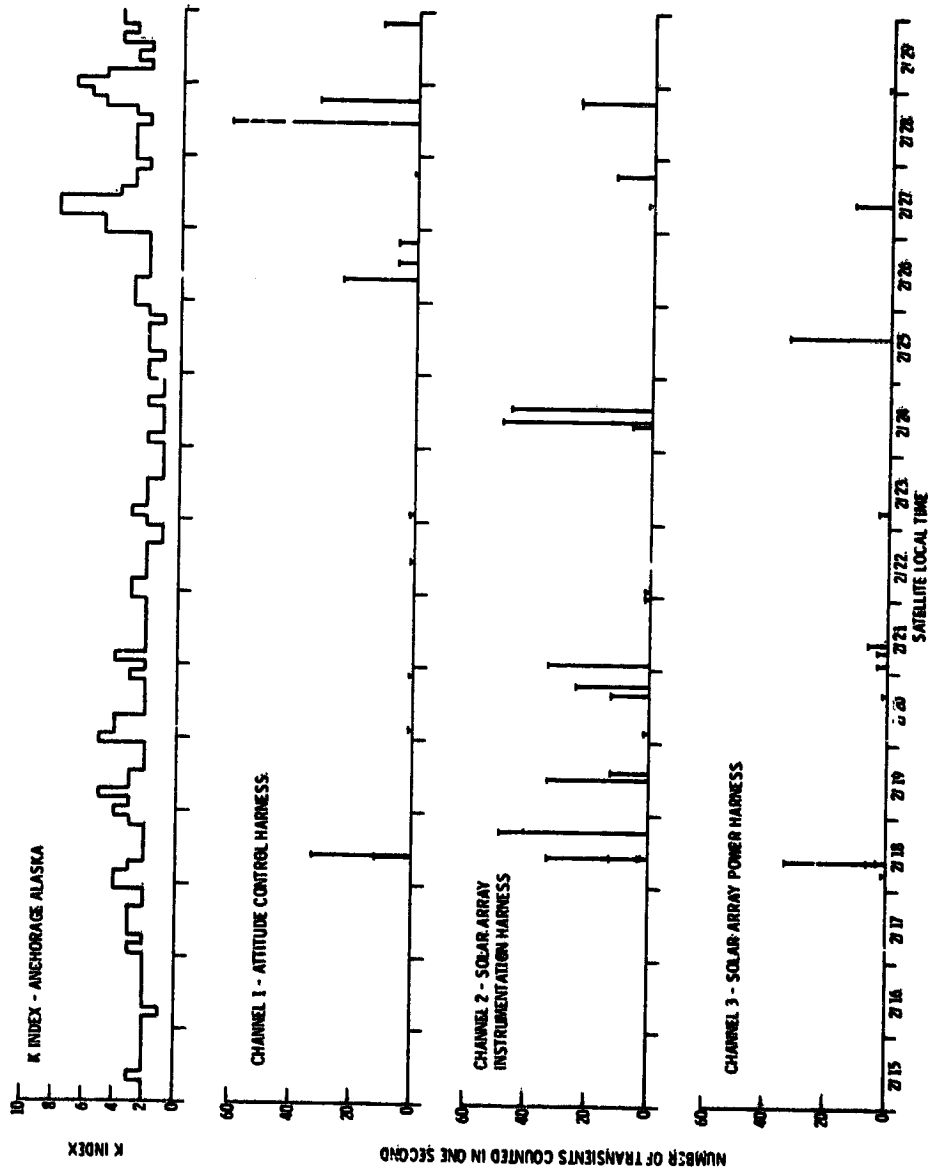


Figure 8. TEC Preliminary Data February 15-February 29

ORIGINAL PAGE IS  
OF POOR QUALITY

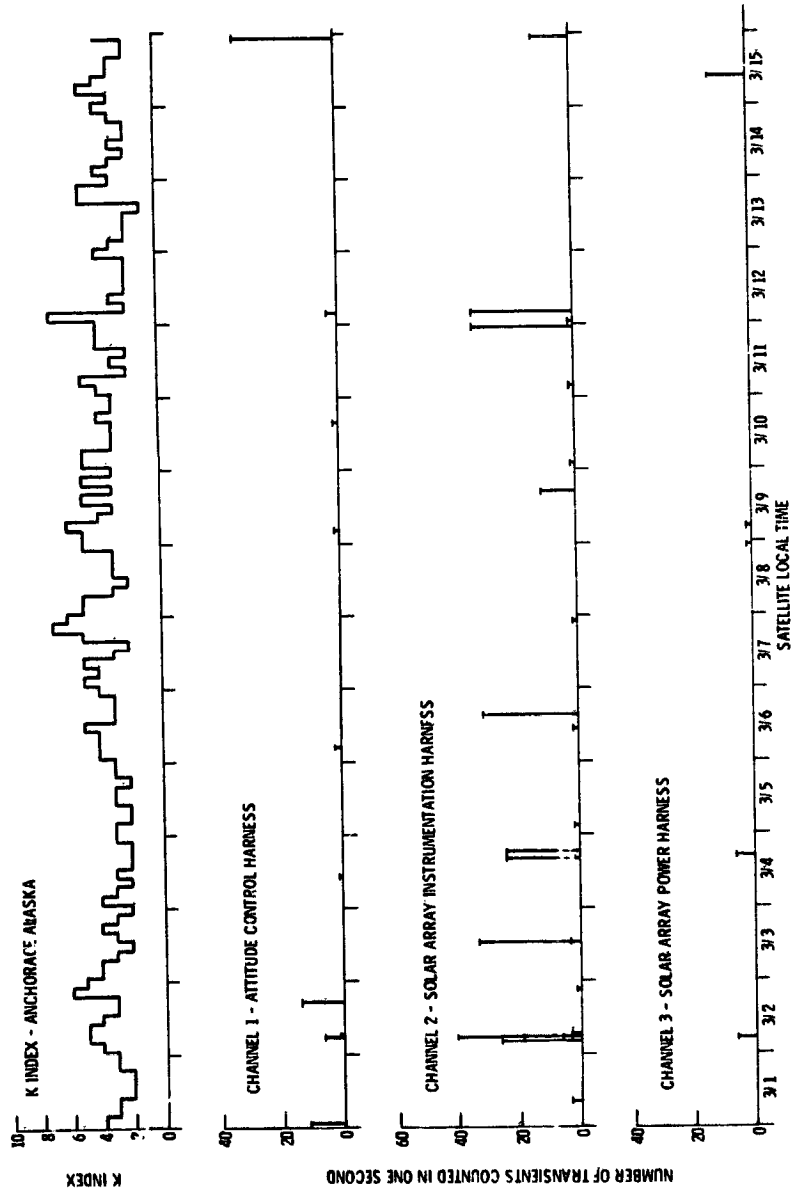


Figure 9. TEC Preliminary Data March 1-March 15

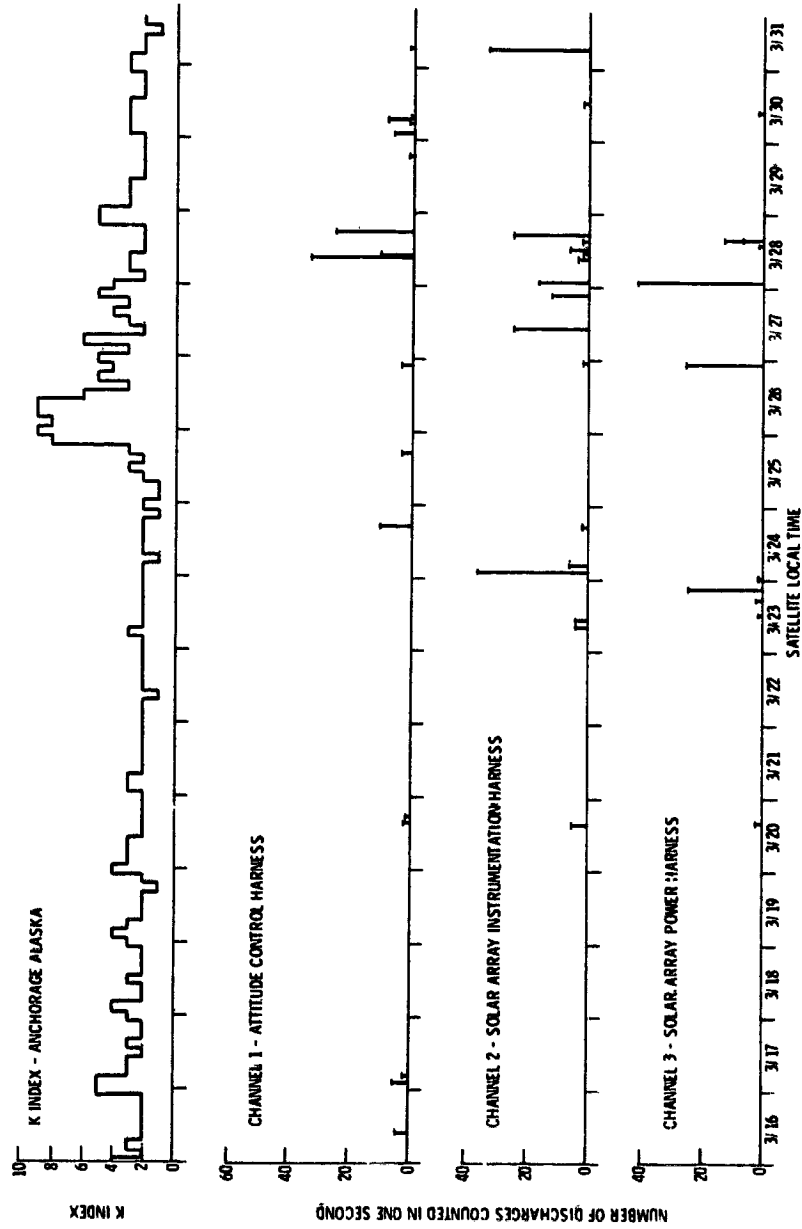


Figure 10. TEC Preliminary Data March 16-March 31

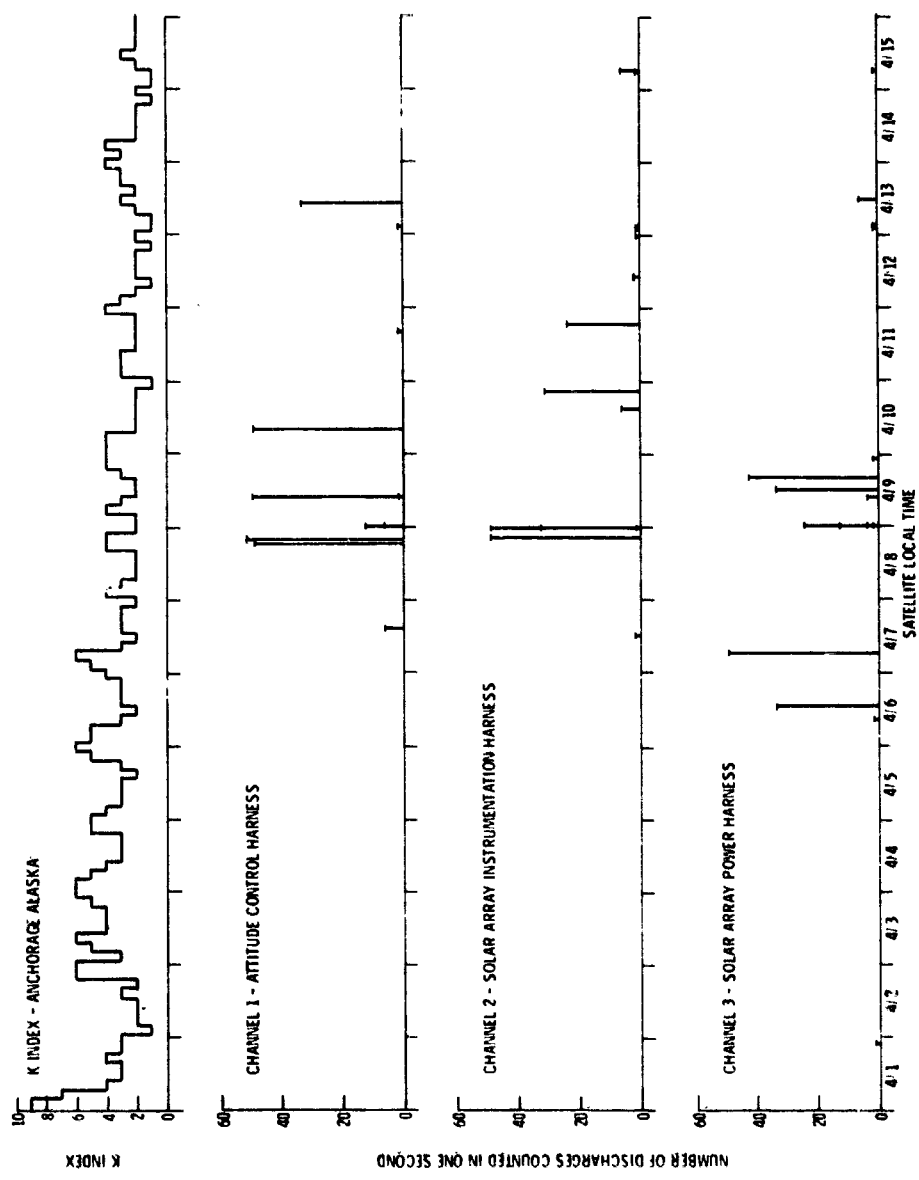


Figure 11. TEC Preliminary Data April 1-April 15

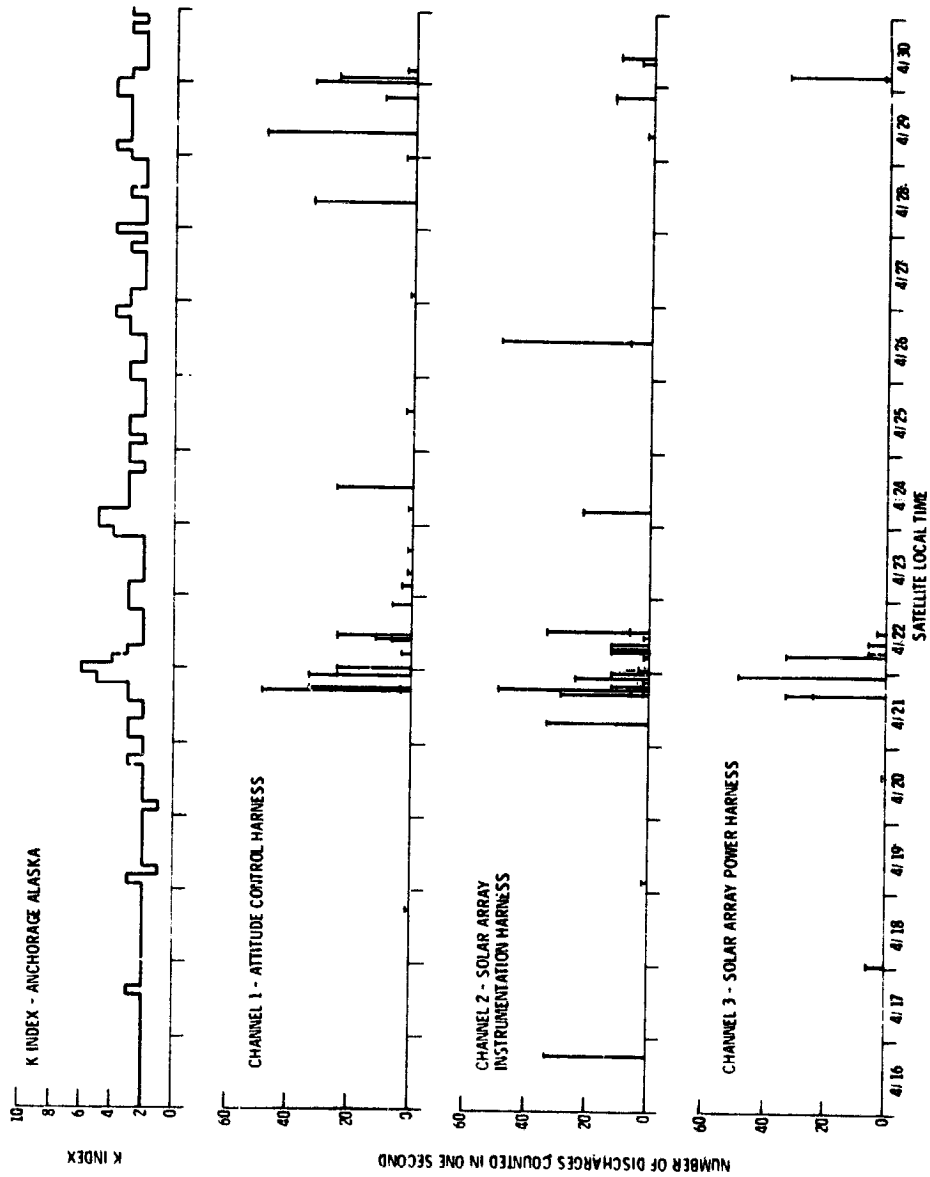


Figure 12. TEC Preliminary Data April 15-April 30

the satellite are necessary to determine if the transient occurred as an immediate result of a substorm or as a delayed discharge due to a differential voltage condition.

The distribution of discharge events is plotted in Figure 13. This is a polar view of the Earth with a 24 hr local time scale superimposed. The TEC transients for each channel are plotted at the spacecraft local time of occurrence without concern for the number of transients. The radial distance on these plots is proportional to the K index. From this figure it is apparent that the pattern of the occurrence of transients is random. This behavior is believed to be due to the fact that the CTS has large insulator surfaces that can be alternately sunlit and shaded so that differential charging is possible. Once charged, the insulators can maintain this charge for long periods of time. These surfaces can discharge, then, at any time in its orbit by responding to an, as yet unknown, trigger mechanism. The evaluation of this behavior is also continuing.

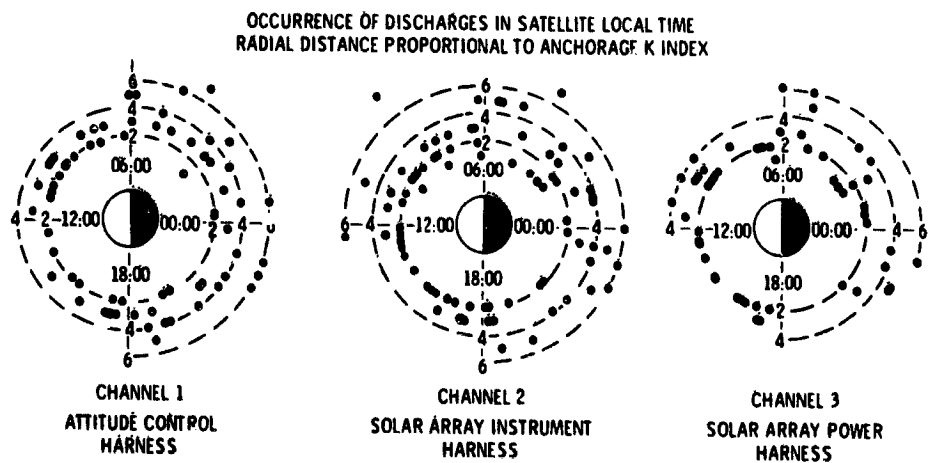


Figure 13. TEC Transient Data January 31-April 30, 1976

The data plotted in Figure 13 also shows that channels No. 1 and 2 are more active than channel No. 3. This behavior was expected since the solar array power bus line is filtered which should limit transients.

These transient pulses detected by the TEC have yet to cause an anomaly in the satellite operation. The CTS was built to conduct high voltage, high power, and high frequency communication experiments. Therefore, considerable care was taken to make the components insensitive to any transients that may result from breakdowns within the high voltage components. This care seems to have

made the satellite immune to the anomalous electronic switching behavior of other synchronous satellites.

#### 4. CONCLUDING REMARKS

The Transient Event Counter (TEC) has been monitoring transient pulses in three separate wire harnesses within the CTS spacecraft since 31 January 1976. This detector counts all transients within the harness that have a voltage rise greater than 5 volts. The three harnesses that are monitored are:

- (1) Attitude Control Harness
- (2) Solar Array Instrumentation Harness
- (3) Solar Array Power Harness

The results to date show that the CTS surfaces seem to be charged to the point where discharges occur and these discharge pulses are being transmitted in the spacecraft harnesses. These pulses have not yet caused any anomalous behavior in the spacecraft.

The discharges can occur at any time during the satellite day with no special preference for any local time quadrant. This effect may be due to shadowing of the insulators which can cause differential charging which can result in discharges.

The number of transients being counted is larger than anticipated. This large number may be due to the sequential discharging of large insulator surfaces on the satellite producing a pulse train in the harnesses.

The correlation of the TEC data to the occurrence of substorms has been hindered by the lack of real time environmental data at the CTS position at synchronous altitudes. The preliminary ground station data for the K index from Anchorage, Alaska has been used as an indicator of activity. However, the correlation is poor. It is strongly recommended that any future satellite using a TEC-type detector also include a simple environment monitor as well. This would remove all uncertainty on the state of the environment when transients are counted.

The preliminary review of the TEC operation on the Communications Technology Satellite for the first 90 days has been completed. There are indications of discharge events but no anomalous behavior has been detected. The compilation and review of the data is continuing.

## References

1. Franklin, C. A., and Davison, E. H. (1972) A high-power communications technology satellite for the 12 and 14 GHz bands. AIAA Paper 72-580.
2. McPherson, D. A., Cauffman, D. P., and Schober, W. (1975) Spacecraft charging at high altitudes, the SCA THA satellite program. AIAA Paper 75-92.
3. DeForest, S. E., and McIlwain, C. E. (1971) Plasma clouds in the magnetosphere, J. Geophys. Res. 76:(No. 16):3587-3611.
4. DeForest, Sherman E. (1972) Spacecraft charging at synchronous orbits, J. Geophys. Res. 77(No. 4):651-659.
5. Bartlett, R. O., DeForest, S. E., and Goldstein, R. (1975) Spacecraft charging control demonstration at geosynchronous altitude, AIAA Paper 75-359.
6. Stevens, N. John, Lovell, Robert R., and Gore, Victor (1975) Spacecraft charging investigation for the CTS Project, NASA TM X-71795.
7. Rosen, A. (1975) Spacecraft charging-environment induced anomalies, AIAA Paper 75-91.

## Contents

1. Introduction	108
2. ATS-5 Spacecraft and Ion Engine Experiment	108
3. ATS-6 Spacecraft and Ion Engine Experiment	110
4. ATS-5 and ATS-6 Plasma Detectors	112
5. Charging Response of ATS-5 and ATS-6	113
6. Response to Active Control	115
7. Summary and Conclusions	119
References	120

## 5. Active Control of Spacecraft Charging on ATS-5 and ATS-6

Carolyn K. Purvis  
NASA Lewis Research Center  
Cleveland, Ohio

Robert O. Barlett  
NASA Goddard Space Flight Center  
Greenbelt, MD

Sherman E. DeForest  
University of California at San Diego  
La Jolla, California

### Abstract

Effects on spacecraft ground potential of active emission of charged particles are being investigated through experiments using the ATS-5 and ATS-6 spacecraft. Each of these spacecraft is equipped with ion engine neutralizers which emit low energy charged particles, and with the University of California at San Diego (UCSD) Auroral Particles experiments which are capable of determining the spacecraft potentials. Despite great differences in design between the two spacecraft, they attain similar potentials in similar environments. Therefore, effects on spacecraft potential of neutralizer operations can be used to compare the effects of operating the two different neutralizers (hot wire filament and plasma bridge). The neutralizers on both spacecraft have now been operated in eclipse. Results of these operations are presented and spacecraft responses compared.

## 1. INTRODUCTION

One of the objectives of the joint NASA/AF Charging Investigation is to determine the feasibility of active control of spacecraft charging. An investigation is currently underway to study the possibility of active control by charged particle emission using the ATS-5 and ATS-6 spacecraft. This effort is an extension of studies previously reported by Bartlett et al<sup>1</sup> and by Goldstein and DeForest.<sup>2</sup> The present paper reports results of operating the ion engine neutralizers on the two spacecraft during eclipses. The intent is to compare the effectiveness of the two neutralizers in maintaining the spacecraft potentials near ground during eclipse and substorm conditions.

Experiments have been conducted using the ATS-5 hot wire filament electron emitter, the ATS-6 plasma bridge neutralizer, and the UCSD plasma detectors. The particle data were then studied to determine the charge state of the spacecraft before, during, and after neutralizer operations, in order to compare the effects of neutralizer operations. Such experiments have been performed with the ATS-5 spacecraft during several eclipse seasons, so that a relatively large data base exists, and some general trends in spacecraft response can be identified. Due to mission constraints, operation of the ATS-6 neutralizer during eclipse was not possible until the fall 1976 eclipse period. Thus, the data points for ATS-6 neutralizer operations in eclipse are few; however, the available results do provide a basis for some preliminary comparisons.

## 2. ATS-5 SPACECRAFT AND ION ENGINE EXPERIMENT

The ATS-5 spacecraft was launched in August 1969. It is in a geosynchronous orbit stationed at 105°W longitude. The spacecraft has a cylindrical geometry, 1.3 m in diameter and 2 m in length. It is divided into three cylindrical sections of approximately equal length. Most experiments and spacecraft systems are contained in the center section, while the two outer most sections are open-ended shells to which solar cells have been mounted. These latter two sections have an outer surface primarily of quartz glass covering the solar cells. The center section is covered with a fiberglass skin to which a nonconductive thermal control paint has been applied. Therefore, the outermost surface of ATS-5 is generally an electrical insulator.

Two contact ion engine systems are aboard ATS-5. All engine operations described here involve the No. 2 system. Its location relative to the ATS-5 UCSD Auroral Particles experiment is shown in Figure 1. Due to a design fault in the ATS-5, the spacecraft could not be despun and hence was never gravity gradient

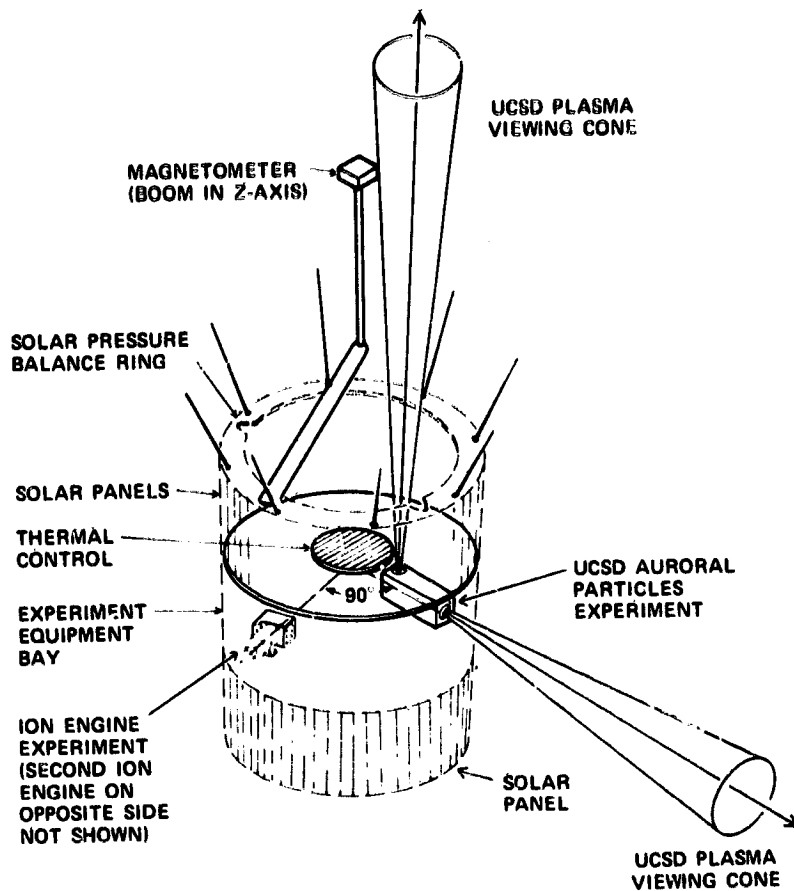


Figure 1

stabilized as planned. As a result of the 76 RPM spin about the spacecraft z-axis, each ion engine is subjected to centripetal force producing an effective gravitational field of 4 G's.

The force on the cesium feed system is sufficient to drive liquid cesium down the vapor feed tube to the ionizer and thus preclude normal thruster operation. The cesium reservoir is sealed by a thermally actuated valve. The ion engine system is designed such that the "Ionizer On" command turns on the ionizer and neutralizer heaters. It has been determined that the heat transferred to the reservoir valve from the ionizer heater when operated continuously is sufficient to open the valve. However, if the ionizer heater is operated for a maximum of 40 min with a 20 percent duty cycle, the valve will remain closed. Therefore, the 20 percent duty cycle was selected for the spacecraft neutralization tests. No ion beam is produced during this type of operation.

The ATS-5 ion engine system has been described in detail by Worlock et al.<sup>3</sup> Its contact ion source was designed to deliver 1 mA of singly charged cesium ions which are neutralized by a hot filament electron source. In studying the control of spacecraft charging, this electron source has been utilized. The ion engine exhaust aperture in the spacecraft skin is 5 cm in diameter. The neutralizing filament is recessed 2.5 cm within the spacecraft and operates at spacecraft potential. The resistively heated filament is powered by a 2 Vac power supply. Thus, the energy of emitted electrons is  $\leq 2$  volts. The filament of yttrium doped tantalum is 0.18 mm in diameter and operates at a temperature of 1700°C. At this temperature, the neutralizer is emission limited at about 3 mA. The minimum resolvable neutralizer emission current telemetry signal represents 6  $\mu$ a. No discernible neutralizer emission current has been observed during any of the experimentation described here.

### 3. ATS-6 SPACECRAFT AND ION ENGINE EXPERIMENT

The ATS-6 spacecraft was launched in May 1974, and is in a geosynchronous orbit. The first year's operational station was at a longitude of 94°W. For its second year of service, ATS-6 was moved to a longitude of 35°E. The spacecraft has now been relocated to its permanent station at 140°W. The configuration of the ATS-6 spacecraft is shown in Figure 2. The end-to-end dimension between the two solar arrays is 16.5 m. The near cubical module at the focus of the 9.1 m parabolic reflector is about 1.6 m on a side. The outer surface of most of the structure is covered with kapton thermal insulation. However, all conductive elements of the structure and the vapor deposited aluminum surfaces of the thermal blankets are bonded to the common spacecraft ground. The parabolic reflector is formed utilizing a dacron mesh with a copper coating. The copper is covered with a noncontinuous coating of silicon rubber. While the copper mesh of the reflector is grounded to the structure, the reflector's outer surface characteristic is dominated by the silicon rubber insulator. The solar cells are covered by quartz glass. Thus, the majority of the outer surface of ATS-6 is nonconducting.

There are two cesium bombardment ion engine systems on ATS-6. They are located on the north and south faces of the earth viewing module as shown in Figure 2. The thrust axis of each engine is in the Y-Z plane and exhausts outward from the spacecraft at an angle of 38° to the +Z axis. The orbital operations of the ion engine experiment have been reported by Worlock et al.<sup>4</sup> Each of the two ion engine systems has been operated. The initial operation of each thruster was nominal. However, subsequent attempts to restart either system have not been successful. It is believed that the restart problem is due to a design error in the

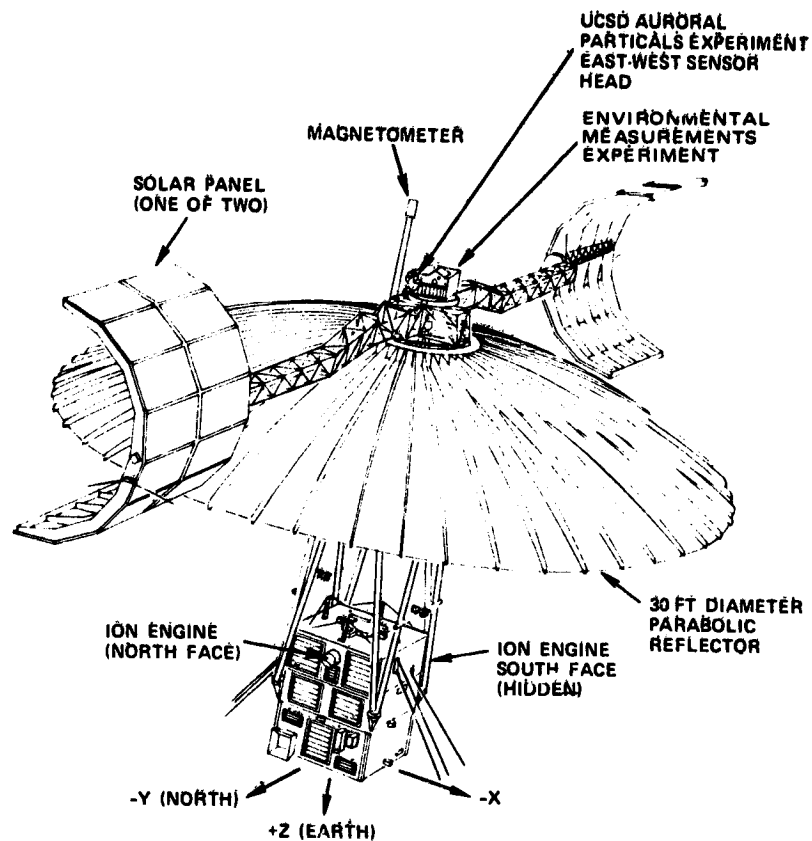


Figure 2. ATS -6 Spacecraft Configuration

main propellant feed system. This design problem has not precluded the operation of the ion engine's neutralizer and its cesium feed system. Operation of the neutralizer of each ion engine has been demonstrated subsequent to its initial operation.

The ATS-6 ion engine system has been described in detail by James et al.<sup>5</sup> Basically, each system produces a 115 mA beam of singly charged cesium ions which are extracted from a primary plasma. This beam is then neutralized by electrons which are extracted from a second cesium plasma. This electron source, or neutralizer, is of interest when studying the control of the interaction of a geosynchronous spacecraft with its ambient plasma since it can serve as a source of both electrons and ions.

The neutralizer consists of a feed system which supplies cesium vapor to a hollow cathode electron source. The hollow cathode consists of a heated tantalum emitter which is placed at the end of the cesium vapor feed tube. The feed tube is then capped with a plug containing a 0.15 mm diameter orifice. An electrode, or

plasma probe, is mounted 3.2 mm outboard from the cathode aperture. To initiate operation, this electrode is biased 150 Vdc positive with respect to the tantalum emitter and serves as an anode. The emitter operates at spacecraft ground potential. Cesium vapor is introduced into the hollow cathode and a plasma discharge occurs. This process requires about 35 min from initiation of the operations. After the neutralizer discharge starts, the probe is operated from a high impedance +15 Vdc power supply. In this mode, 50 mA of electrons are extracted from the neutralizer's plasma by the probe. The probe also serves as a plasma potential sensing element for control purposes. For normal ion engine operations, the ion beam would become the hollow cathode's anode with the neutralizer's plasma providing a low impedance bridge to the beam. However, when the ion beam is not present, the plasma probe will continue to function as an anode. During operation, the power supply is typically loaded down to 6 or 7 volts. Thus the energy of emitted electrons is <15 volts, typically 6 or 7 volts. The aperture for the ion engine's exhaust beam is approximately 12 cm outboard from the spacecraft's skin with the neutralizer located an additional 5 cm outboard.

The emission characteristics of the neutralizer vary with its cesium flow and the temperature of the tantalum emitter. Neutralizer control is accomplished by presetting the emitter temperature and regulating the pressure of the cesium vapor in the hollow cathode in response to the potential of the plasma probe. For normal operations, the neutralizer is emission limited at about 3A of electrons and a few milliamperes of ions. Since the experiment's telemetry scale was sized for operations as an ion thruster, the minimum resolvable neutralizer emission current is 1 mA of electrons only. No measurable neutralizer emission current has been observed during any of the experiments described here.

#### 4. ATS-5 AND ATS-6 PLASMA DETECTORS

The UCSD Auroral Particles experiment on ATS-5 consists of two pairs of plasma detectors. These are mounted to the body of the spacecraft (see Figure 1) so that one pair looks parallel to the spacecraft spin axis and the other pair looks perpendicular to it. Each pair of detectors is comprised of an electron detector and an ion detector which cover the energy range from 50 eV to 50 keV. These detectors have been described in more detail by DeForest and McIlwain.<sup>6</sup>

The ATS-6 instrument is an outgrowth of the ATS-5 detector. The main detectors are arranged in two electron-ion pairs. These are mounted on the Environmental Monitor Experiment (see Figure 2), one pair in the north-south plane and one pair in the east-west plane. They can be mechanically swept in their respective planes to obtain angular information. The energy range covered

by these detectors is 1 eV to 80 keV. The ATS-6 detectors are described in more detail by Bartlett et al<sup>1</sup> and by McIlwain.<sup>7</sup>

The voltages to which the spacecraft grounds are charged can be estimated by observing shifts in the particle flux-energy distributions measured by the plasma detectors. Such shifts are most evident in the ion spectra. Examples of spectrograms showing this type of spectral shift are given by Goldstein and DeForest.<sup>2</sup>

#### 5. CHARGING RESPONSE OF ATS-5 AND ATS-6

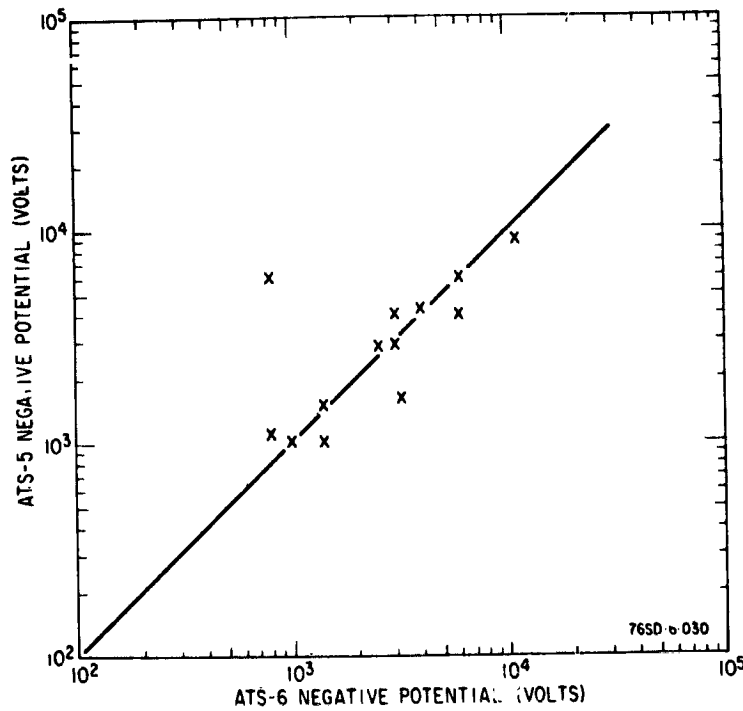
In order to make meaningful predictions about the possibility of active control of spacecraft potentials, it is necessary to be able to predict the potential that a spacecraft will assume when immersed in a natural plasma. In particular, this task is made much more difficult if there are first-order differences due to the details of a given configuration. Table 1 gives the comparison of spacecraft and systems for ATS-5 and 6. Clearly, these two spacecraft are very different in size, construction, orientation, and outer surface composition. Therefore, if these two space vehicles change to approximately the same potential when exposed to the same environment, then perhaps a detailed study of either one will have some general validity. During two eclipse seasons (fall 1974 and spring 1975) when ATS-5 and 6 were separated by only 1.2 earth radii, and when the on-board plasma

Table 1. Comparison of Spacecraft and Systems

	ATS-5	ATS-6
Characteristic Size	2 m	10 m
Stabilization	Spin (Axis Parallel to Earth's)	3-Axis
Outer Surface	Mostly Quartz (Good Insulator)	Quartz, Kapton, Paint, Aluminum (Mixed Insulator and Conductor)
Ion Engine Neutralizer	Thermal Emission (Electrons Only)	Discharge Plasma
Neutralizer Placement	Recessed: 2.5 cm	Outboard: 17 cm
UCSD Detectors	Body Mounted (50 eV - 50 keV)	Rotating (1 eV - 80 keV)

instruments on both indicated similar plasmas, the simultaneous potentials were calculated and are plotted in Figure 3. The line in this figure is the line of equal potentials and was drawn before the points were added. Considering the differences shown in the table and the fact that there is variability in the plasma, the agreement is remarkable. (Note: The earth's umbra at this distance is approximately 2 earth radii across, allowing ample opportunity for the two spacecraft to be simultaneously eclipsed.)

Since the two vehicles behave similarly in the natural plasma, it is possible to compare their responses to active control using the assumption that differences in response are due to differences in the characteristics of the neutralizers rather than to differences in spacecraft charging response.



## 6. RESPONSE TO ACTIVE CONTROL

As was previously noted in Section 1, the data on ATS-5 response to neutralizer operations are far more extensive than those for ATS-6. In addition, because of differences inherent in the two neutralizers and operational constraints, the operations themselves are somewhat different.

The ATS-5 hot wire filament can be turned on and off in very short times, that is, it requires no "warm up" period. The experiment sequence used for the tests reported here was to allow the spacecraft to enter eclipse with the neutralizer off, to command the neutralizer on 10 min later, and to command the neutralizer off again 5 min later. Particle data were taken for at least 15 min before and after the neutralizer operations. Some experiments are also being run using a 10 min "neutralizer on" period. Results of these will be reported as data become available.

In contrast to the fast response time of the hot filament, the ATS-6 plasma bridge neutralizer requires about 35 min after the "on" command is given to come into full on operation (see Section 3). Because of concern for the spacecraft's power system, the neutralizer was brought into full operation before entry into eclipse during the fall 1976 eclipse period. The neutralizer remained on for 10 min after entry into eclipse and was then commanded off. Particle data were taken 24 hr per day during these neutralizer operations. Additional experiments are being conducted using these ATS-6 instruments, and results will be reported as the data become available.

The operating conditions for the experiments reported here are summarized in Table 2.

Table 2. Comparison of Test Operations

	ATS-5	ATS-6
Turn-On Time	<1 min	35 min
Turn-Off Time	<1 min	~ 2 min
Full-On Operation Time in Eclipse	5 min	10 min
Emission Current	<6 $\mu$ A	<1 mA
Energy of Emitted Particles	~ 2 V	~ 7 V

Figure 4 shows the response of the ATS-5 spacecraft to activation of the neutralizer. The potential with and without the electron emitter energized is shown here. The potential determinations were made within minutes of each other and under conditions where the potential was not changing rapidly. The dashed line here is the line along which the two potentials are equal; the solid line is fit to the data.

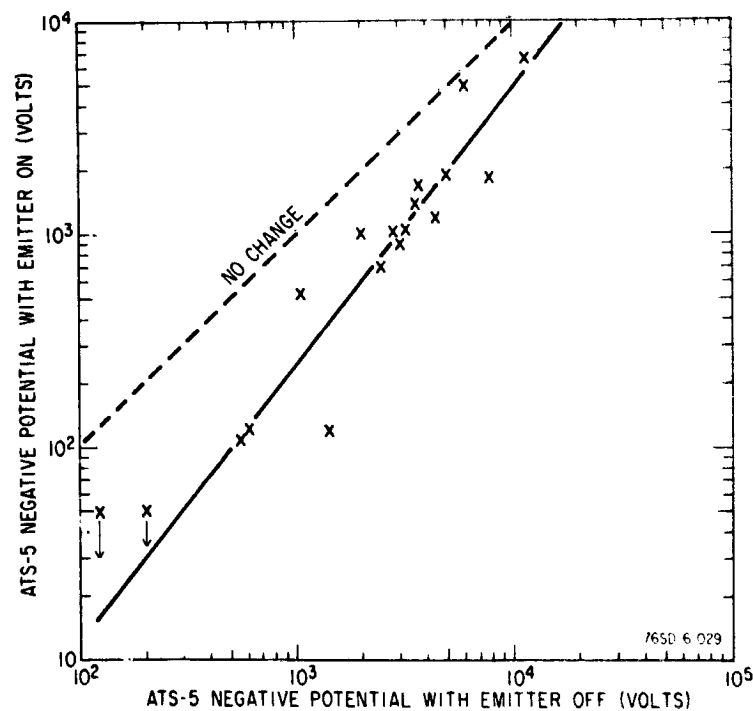


Figure 4. Effect of A TS-5 Electron Emitter on Spacecraft Potentials

The first conclusion that one reaches from Figure 4 is that the electron emitter does lower the potential, but it has the unfortunate characteristic of being less effective in maintaining the spacecraft potential near ground at larger magnitude initial potentials and very effective in doing this at potentials which are already sufficiently low in magnitude that they do not pose much of a problem. This result is supported by laboratory simulations reported elsewhere in this conference by Goldstein.<sup>8</sup> Since the emitter filament on ATS-5 is located within a cavity, perhaps its effectiveness is decreased by the shielding action of the spacecraft body. In addition,

there is evidence that a potential barrier may exist around spacecraft.<sup>9</sup> Thus, it is possible that the electrons leaving the filament cannot escape from the spacecraft because they lack sufficient energy to penetrate such a barrier. An emitter that was both exposed and biased with respect to spacecraft ground might be more effective in coupling to the plasma.

There are insufficient data to make a similar plot for ATS-6. Figure 5 shows the spacecraft response to the neutralizer activation. This figure shows the spacecraft response on the most "active" day for which data are available. ("Active" here refers to magnetospheric substorm activity.) The plasma environment remained relatively constant from about 2350 until after 0130 on this day so that the changes in the spacecraft's potential can be attributed to the neutralizer's operation and to entry into and exit from eclipse. The figure shows that the spacecraft potential was maintained within 10 volts of ground during the entire neutralizer

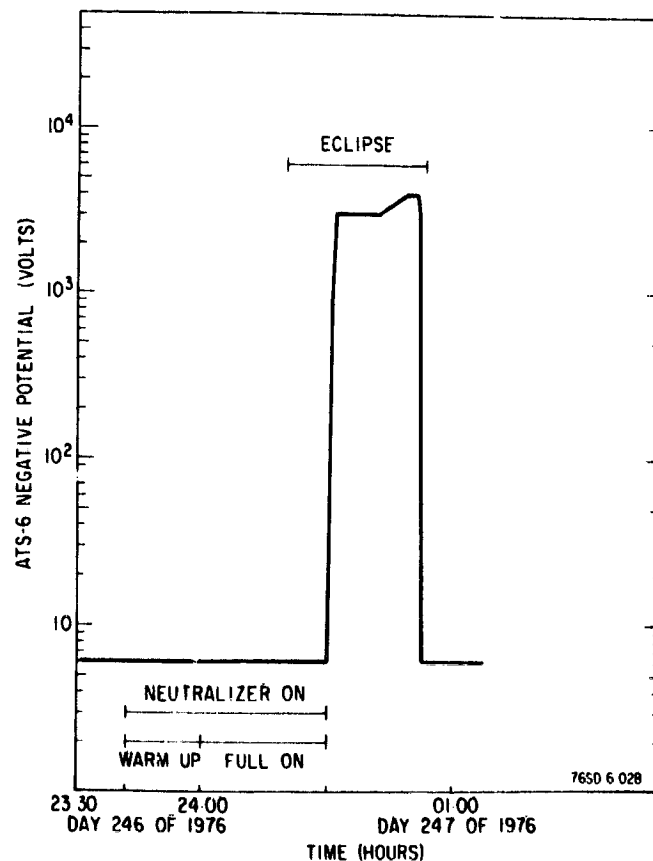


Figure 5. Effect of ATS-6 Neutralizer on Spacecraft Potential

operation, both in sunlight and in eclipse. The fact that the spacecraft potential changes rapidly to several thousand volts negative when the neutralizer is turned off implies that very large potentials can be discharged by this neutralizer.

The low energy electron spectrum is also affected by neutralizer operation. While this has not been studied in detail, such effects have been interpreted as representing changes in the potential barrier surrounding the ATS-6 spacecraft caused in this case by neutralizer operation.<sup>2</sup>

Comparison of this event with the ATS-5 results leads one to believe that the plasma discharge may be the more effective method of control.

One other difference between the two systems can be noticed. ATS-6 seems to have been held to a steady potential during neutralizer operation, but this is not always the case for operation of the electron emitter on ATS-5. Figure 6 gives the time history of discharge for three events on ATS-5. The changes in potential

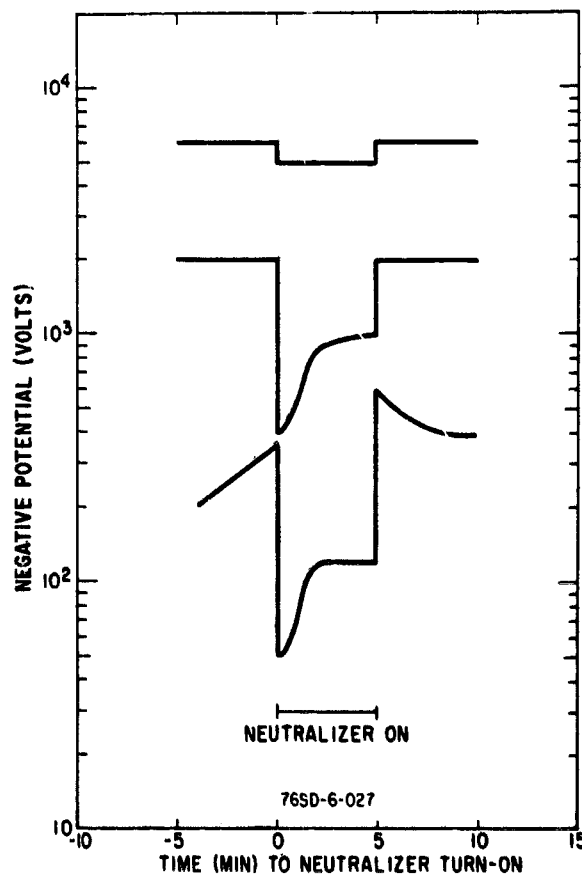


Figure 6. Effect of Electron Emitter on ATS-5 Ground Potentials

during neutralizer operation shown in this figure do not seem to have been produced by changing environmental conditions. The reason for this strange behavior is not known.

## 7. SUMMARY AND CONCLUSIONS

Active control of spacecraft potential has been demonstrated using both an unbiased electron emitter and a plasma discharge. Activation of either of these devices resulted in reductions in the magnitude of the spacecraft potential. Of the two devices studied here, the plasma bridge neutralizer was more successful in maintaining the spacecraft potential near ground. Its operation held the spacecraft potential steady and less than 10 volts from ground. In contrast to this behavior, the ATS-5 potential during electron emitter operation is more variable. Also, although operating this neutralizer results in reduction of the magnitude of the spacecraft potential, it does not, in general, hold the potential near ground. In fact, while the absolute magnitude of the change in potential increases with increasing magnitude of the "neutralizer off" potential, the percent change decreases with increasing magnitude of the "off" potential. Thus, this device is considered less effective than the ATS-6 plasma device.

This result does not imply that no electron emitter could hold the spacecraft ground potential near plasma ground. The particular device being used is both unbiased and recessed into the spacecraft body. As noted earlier, this recessed location may result in suppression of the emission, particularly since the spacecraft surface near the emitter is an insulator and thus would remain charged negatively even when the frame is discharged. The fact that the filament is unbiased further means that the electrons leaving it will have energies determined by the 2 Vac filament power supply, that is, 2 volts. These may not have sufficient energy to overcome a potential barrier surrounding the spacecraft. It appears that a biased emitter extended some distance from the spacecraft surface would be preferable for active control purposes.

The plasma device on ATS-6 has the inherent advantage that ions from the discharge can be attracted to nearby negative surfaces, so that this device has a mechanism for discharging insulator surfaces as well as the spacecraft frame. An electron emitter has no such mechanism available to it. In addition, the location of the ATS-6 device, about 17 cm outboard of the spacecraft body, and the fact that the emitted electrons have energies on the order of 7 volts seem advantageous compared to the location and electron energies characteristic of the ATS-5 device. The fact that the spacecraft is maintained within 10 volts of plasma ground throughout neutralizer operation implies that electrons are escaping from the

spacecraft. This could be because the electrons are emitted with sufficient energy to overcome the potential barrier or because neutralizer operation alters the barrier in some advantageous way.

The ATS-6 device, then, looks promising as an active control device. However, additional experiments using this device under a variety of natural environmental conditions are needed. Such experiments, as well as experiments utilizing both ATS-5 and ATS-6 in conjunction with one another, are being conducted as a part of the Spacecraft Charging Investigation.

## References

1. Bartlett, R.O., DeForest, S.E., and Goldstein, R. (1975) Spacecraft charging control demonstration at geosynchronous altitude, AIAA Paper 75-359, AIAA 11th Electric Propulsion Conference, New Orleans, La.
2. Goldstein, R., and DeForest, S.E. (1976) Active control of spacecraft potentials at geosynchronous orbit in Progress in Astronautics and Aeronautics 47:169, A. Rosen, Editor, MIT Press, Cambridge, Mass.
3. Worlock, R., Davis, J.J., James, E.L., Ramirez, P. and Wood, O. (1968) An advanced contact ion microthruster system, AIAA Paper 68-552, AIAA 4th Propulsion Joint Specialist Conference, Cleveland, Ohio.
4. Worlock, R.M., James, E.L., Hunter, R.E., and Bartlett, R.O. (1975) The cesium bombardment engine north-south station-keeping experiment on ATS-6, AIAA Paper 76-363, AIAA 11th Electric Propulsion Conference, New Orleans, La.
5. James, E.L., Worlock, R.M., Dillon, T., Gant, G., Jan, L., and Trump, G. (1970) A one millipound cesium ion thruster system, AIAA Paper 70-1149, AIAA 8th Electric Propulsion Conference, Stanford, Calif.
6. DeForest, S.E., and McIlwain, C.E. (1971) Plasma clouds in the magnetosphere, J. Geophys. Res. 76:3587.
7. McIlwain, C.E. (1975) Auroral electron beams near the magnetic equator in Physics of the Hot Plasma in the Magnetosphere, B. Hultquist and L. Stenflo, Editors, Plenum Publishing Co., New York.
8. Goldstein, R. (1976) Active control of potential of the geosynchronous satellite ATS-6, Paper I-6, Spacecraft Charging Technology Conference, Colorado Springs, Colo.
9. Whipple, E.C., Jr. (1976) Observation of photoelectrons and secondary electrons reflected from a potential barrier in the vicinity of ATS-6, J. Geophys. Res. 81:715.

**Contents**

1. Introduction	122
2. ATS-6 Plasma Emitter Flight Tests	122
3. ATS-5 Neutralizer Emitter Laboratory Simulation Tests	126
4. Summary and Conclusions	128
Acknowledgment	129
References	129

**6. Active Control of Potential of the  
Geosynchronous Satellites ATS-5 and ATS-6**

Raymond Goldstein  
Jet Propulsion Laboratory  
Pasadena, California

**Abstract**

The ATS-6 geosynchronous satellite carries two cesium ion thrusters as part of the technology experiment package. Their effectiveness in controlling the spacecraft potential has been shown during normal operation of the thrusters. The University of California at San Diego auroral particles detectors were used to estimate spacecraft potential, amount of cesium propellant backflow to the spacecraft, and "electron signature" of the thruster. Operation of the thruster clamps the spacecraft to about -10 v in the presence of a wide range of ambient particle flux. Some positive ions from the thruster are returned to the spacecraft during this period. The plasma bridge neutralizer of the thruster is also effective in controlling the spacecraft potential. Laboratory simulation tests of the ATS-5 ion thruster thermionic emitter neutralizer showed that negative differential charging on the spacecraft surface probably prevents the emitter from completely discharging the spacecraft in flight.

---

This paper presents the results of one phase of research carried out at the Jet Propulsion Laboratory, California Institute of Technology, under Contract NAS7-100, sponsored by the National Aeronautics and Space Administration.

## 1. INTRODUCTION

The effectiveness of the cesium ion thrusters and their neutralizers carried on the geosynchronous satellites ATS-5 and ATS-6 to control the spacecraft potential under a wide range of environmental conditions has recently been reported.<sup>1, 2, 3</sup> Some variation of these devices is a likely candidate to be used on a spacecraft explicitly for active potential control. It is therefore important to understand details of the operation of these devices and their effects on the spacecraft. For spacecraft conducting scientific measurements, for example, of particles and fields, the question arises as to the direct effect of the discharge device on the measurements. That is, it is desirable to know in what way, if any, the device will contaminate the measurement with spurious contributions. In the following, an analysis of some of the data from the University of California at San Diego auroral particles detectors on ATS-6, taken during operation of a thruster, is described and discussed. It is shown that operation of the discharge device has a marked effect on the character of the measured data.

While the plasma devices on ATS-6 appear capable of clamping the spacecraft potential even during severe environmental conditions, the ATS-5 thermionic emitter has not been entirely successful. The spacecraft usually can only be partially discharged, and even then, the potential generally does not remain constant. In order to understand the cause of these effects, some laboratory simulation studies were performed using a flight spare ATS-5 thruster. The tests and results are described below.

## 2. ATS-6 PLASMA EMITTER FLIGHT TESTS

### 2.1 Ion Measurements

The configuration of ATS-6 is shown in Figure 1. The features of interest here include the two ion thrusters, one of which is located on the north and the other on the south facing surfaces on the Earth Viewing Module (EVM). The UCSD detectors are located on the Environmental Measuring Experiment (EME) at the top of the spacecraft. The detector of concern in the investigation discussed here is capable of rotating so as to accept electrons or ions in a N-S almost vertically oriented plane. A 10-m diameter mesh antenna lies between the EVM and EME (approximately 13 m apart). Each of the solar array booms is approximately 17-m long.

During the flight operation of the north-facing thruster in 1974, it was observed that higher than normal count rates were observed in the low energy ion detector channels.<sup>2</sup> Furthermore, during the period of time in which the detector was

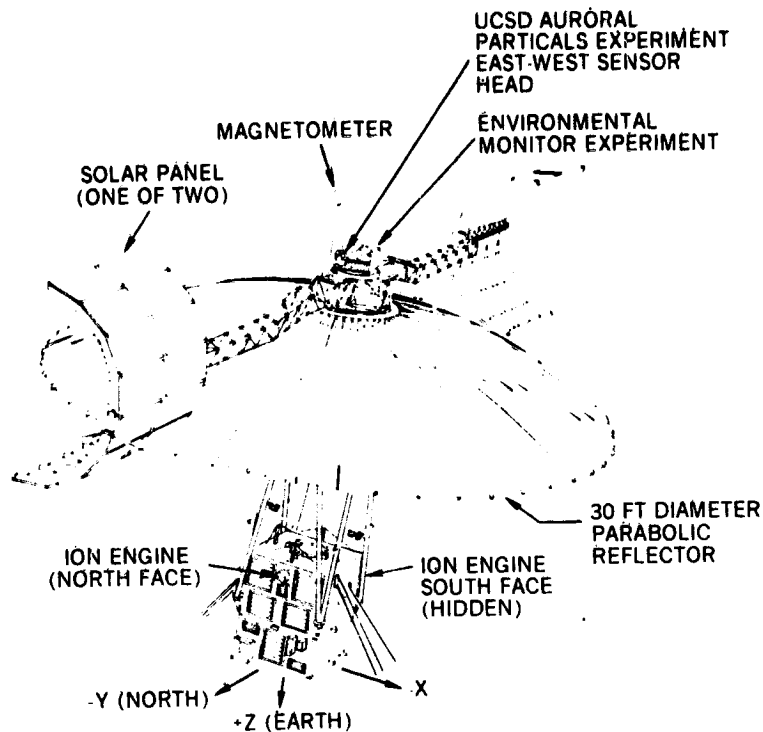


Figure 1. ATS-6 Spacecraft Configuration

rotated, a strong angular dependence of the counts was also observed. In Figure 2, this angular dependence is shown for ions in the 11.8 eV channel, corresponding to the peak in the low energy counts. A strong maximum is seen near the due north ( $0^\circ$ ) direction, with a weaker maximum near the "straight up" ( $90^\circ$ ) direction.

The thruster beam was directed downward at an angle of  $60^\circ$  with an energy of 550 eV. Hence, the primary beam ions would not likely travel to the detector, particularly since the local magnetic field was roughly along the beam direction. A more likely source of the ions detected is the cloud of thermal energy charge exchange ions formed near the beam boundary, especially near the thruster exit. These low energy ions are greatly influenced by the electric fields resulting from differential charging on spacecraft surfaces. Whipple<sup>4</sup> has shown in fact, that the solar array surfaces of ATS-6 can often be the order of one or two hundred volts negative with respect to the rest of the spacecraft. In addition, the differential charging also appears to produce a negative potential "well" in the vicinity of the solar panels. Such potentials would be sufficient to attract ions to the upper portion of the spacecraft. In fact, the  $0^\circ$  angle of Figure 2 corresponds to the detector looking approximately at the north solar panel. The data of Figure 2 therefore

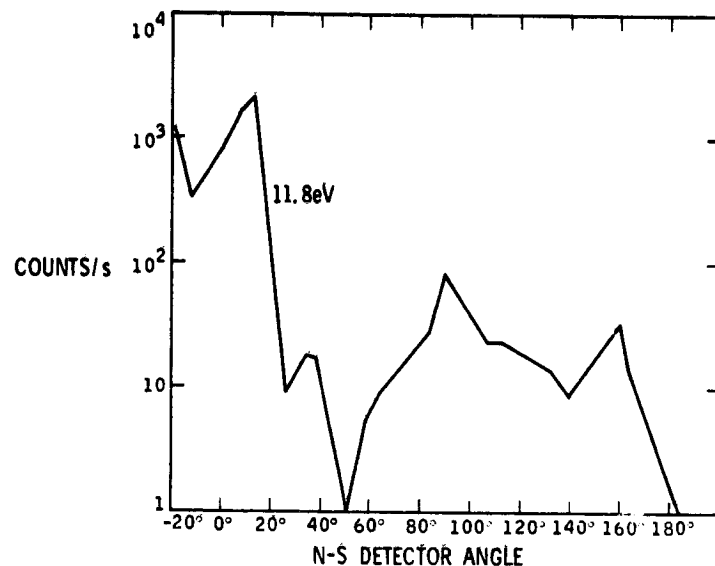


Figure 2. Angular Dependence of 11.8 eV Ion Count Rate During N Ion Thruster Operation on ATS

probably corresponds to low energy ions produced in the thrust beam and then bent around the EME by the negative differential charging and potential well in the vicinity of the solar panels.

Analysis of the energy distribution shows that the low energy ions observed during thruster operation have a peak around 10 eV but have a very nonMaxwellian distribution. Such characteristics are normally not seen in the environmental plasma. This is further evidence that these ions are introduced by the thruster and are not truly environmental in origin. Since the thruster couples the spacecraft to about -10 V with respect to plasma potential, thermal thruster ions reach the spacecraft with energy of 10 eV, explaining the peak measured at that energy. Of course, any low energy environmental ions present would also appear at that potential. However, no low energy environmental ions were seen prior to thruster operation.

Operation of the plasma bridge neutralizer alone is sometimes but not always accompanied by a similar low energy ion peak. These data have not been analyzed in great detail, and it is not understood why this variability exists.

## 2.2 Electron Measurements

The electron detector normally shows a group of low energy electrons to be present under almost all conditions. These electrons, which peak around 10 eV, correspond to secondaries and photoelectrons produced at the spacecraft and trapped by the negative potential well surrounding it. These low energy electrons persist even during daylight charging events of a few hundred volts negative.<sup>4</sup> During operation of the ion thruster the count rate for these electrons drastically decreases, indicating their ability to escape from the spacecraft vicinity.<sup>2</sup> The character of the remaining low energy electrons is quite different, however, from those without thruster operation.

This difference is shown in Figure 3, where the phase space density (effectively the count rate divided by the square of the energy) is plotted for the low

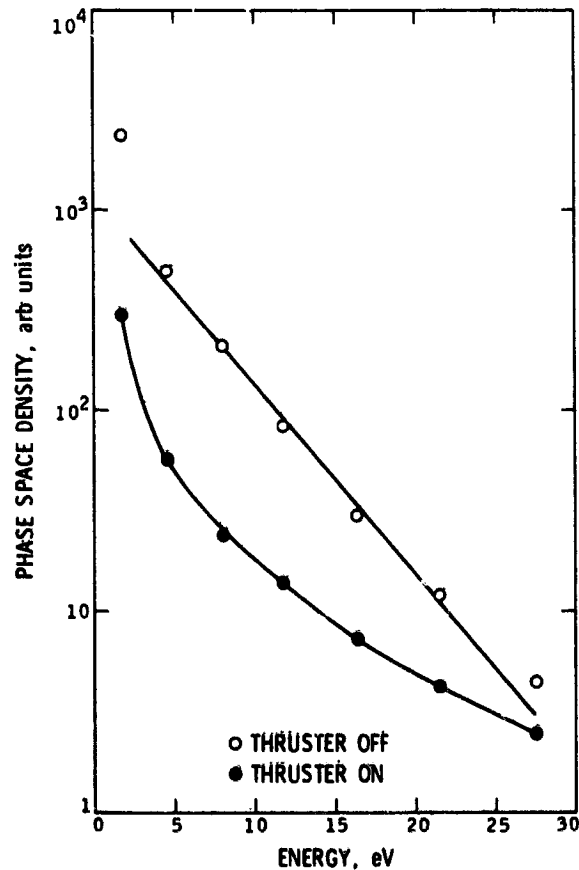


Figure 3. Phase Space Density of Low Energy Electrons Before and During Ion Thruster Operation on ATS-6

energy electrons before and during thruster operation. Note that a Maxwellian distribution should give a straight line, the effective temperature determining the slope. The thruster-off electrons follow a straight line quite closely, indicating a near Maxwellian distribution (temperature  $\approx 5$  eV). It should be noted that the lowest energy point is subject to relatively large error because of energy scale calibration difficulties. The thruster-on electrons, aside from being fewer in number, show a distinctly different distribution. They are no longer Maxwellian.

It is not likely that electrons from the thruster plasma have arrived at the detector, because of the adverse potential gradients. A more probable explanation is that modification of the potential barrier by the thruster plasma has allowed low energy environmental electrons to reach the detector. Normally these electrons are repelled by the negative potential barrier and do not reach the spacecraft. The electrons detected with the thruster on are thus probably a mixture of spacecraft generated secondaries and true environmental electrons. Since the spacecraft was clamped at  $-10$  V by the thruster, the environmental electrons were retarded in energy by that amount.

Operation of the neutralizer alone has a similar but less drastic effect on measured electrons as does full thruster operation. The neutralizer does not have as significant an effect on the potential barrier.

The thruster operation does not have a clear effect on the angular dependence of the low energy electron counts. Since most of these electrons originate at the spacecraft, this is not surprising.

### 3. ATS-5 NEUTRALIZER EMITTER LABORATORY SIMULATION TESTS

A series of tests were performed in the Xerox-Electro Optics Systems 2 ft  $\times$  5 ft long vacuum chamber to study the characteristics of the ATS-5 thermionic emitter under conditions simulating differential charging on the spacecraft. A schematic diagram of the test setup is shown in Figure 4. A flight spare ATS-5 ion thruster was mounted along the centerline near one end of the vacuum chamber. The end of the thruster protruded through a hole in an electrically isolated metal plate simulating the spacecraft surface. This arrangement resembled closely the actual mounting of the thruster on the (cylindrical) spacecraft. A second metal plate, 2 ft from the first, was used to simulate a plasma sheath or potential barrier. Power supplies were provided to bias the two metal plates as shown. Currents were measured as indicated in the figure.

Power was applied to the thermionic emitter neutralizer appropriate to give  $1760^{\circ}\text{C}$ , the flight nominal temperature of the emitter. With no biasing about  $4.25 \mu\text{a}$  emission was obtained. It was then noted that up to 200 v negative on the

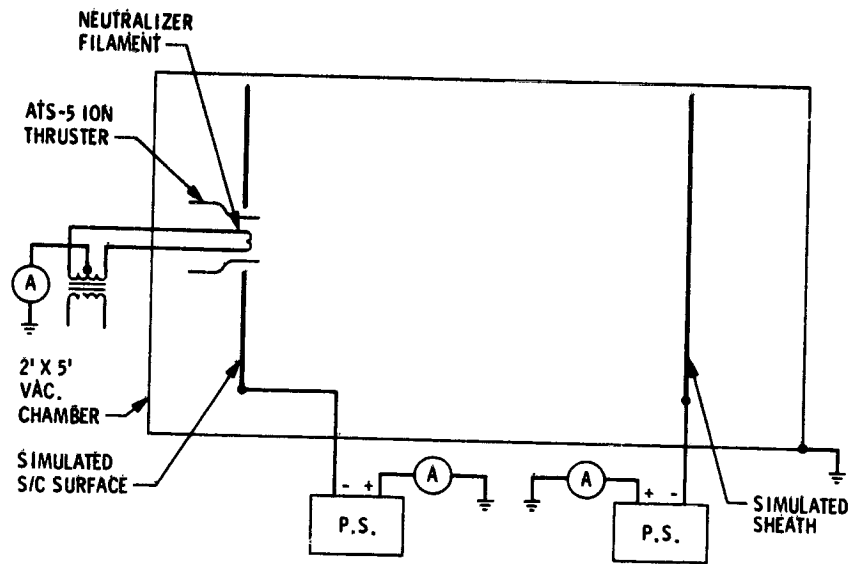


Figure 4. Schematic Diagram of ATS-5 Emitter Laboratory Test

simulated sheath had little (< a few percent) effect on the emission current. However, even a small negative bias on the spacecraft surface produced a marked reduction in the emission current. This effect is shown in Figure 5, which is taken from an X-Y plotter output. The total emission is the total current leaving the filament. For comparison, the current intercepted by the thruster shell (identified as ATS-5 Ion Thruster in Figure 4) is also shown. Note that almost all of the current escapes the thruster and little is returned directly to the thruster body even though the filament is recessed a few inches from the opening.

Differential charging on the spacecraft surface is thus very effective in suppressing emission from the filament. In the case of the flight tests described in References 1 and 2, the spacecraft was charged to a high negative potential in eclipse. Both the surface of the spacecraft (largely covered with solar cells and hence is dielectric) and the frame should be at about the same potential. However, if the filament is turned on the spacecraft frame becomes less negative while the surface remains at the original potential. The filament then experiences a negative differential potential which suppresses the emission, as in Figure 5. The filament is not able to reduce the potential further and the potential may remain approximately constant or increase in magnitude. The details of the environment particle fluxes and energy distribution, as well as the geometry of the spacecraft determine the actual voltage history of the spacecraft during this process.

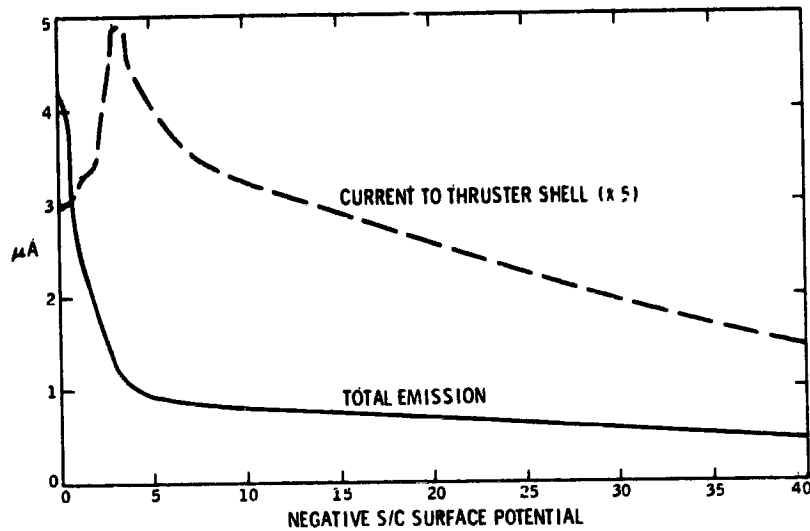


Figure 5. Emission Suppression by Negative Surface Potential

#### 4. SUMMARY AND CONCLUSIONS

The change in character of low energy electrons and ions detected at the spacecraft during ion thruster operation has been examined. The result indicates that use of a plasma device for spacecraft potential control produces a signature at on-board particle detectors. In order to minimize or understand contamination effects a careful calibration, in the laboratory or in flight, would be necessary. In addition, mounting of the discharge device on a boom well away from the spacecraft is probably desirable. Dielectric surfaces, which can cause differential charging, aggravate the contamination problem and should be avoided on the spacecraft.

Laboratory simulation studies have shown that differential charging on spacecraft surfaces is very effective in inhibiting electron emission from the ATS-5 neutralizer filament. This effect prevents the emitter from completely discharging the spacecraft under those conditions, and explains poor results of attempts to control the spacecraft potential in flight. Dielectric surfaces should be avoided for electron emitters to be effective potential controllers. Mounting on a boom away from the spacecraft would also minimize interactive effects.

## Acknowledgment

The author is grateful to E. L. James of Xerox-Electro Optics Systems and J. R. Beattie and L. C. Pless for assistance and suggestions in carrying out the measurements on the ATS-5 emitter characteristics.

## References

1. Bartlett, R. O., DeForest, S. E., and Goldstein, R. (1975) Spacecraft charging control demonstration at geosynchronous altitude, AIAA Paper 75-359.
2. Goldstein, R., and DeForest, S. E. (1976) Active control of spacecraft potentials at geosynchronous orbits, in Spacecraft Charging by Magnetospheric Plasmas, Rosen, Editor, AIAA, New York in cooperation with MIT Press, Cambridge, Mass. and London, England, pp. 169-181.
3. Purvis, C. K., Bartlett, R. O., and DeForest, S. E. (1976) Active control of spacecraft charging on ATS-5 and ATS-6. Presented at USAF/NASA Spacecraft Charging Technology Conference, U. S. Air Force Academy. Also this volume.
4. Whipple, E. C., Jr. (1976) Observation of photoelectrons and secondary electrons reflected from a potential barrier in the vicinity of ATS-6, J. Geophys. Res. 81:(No. 4):715-719.

## Contents

1. Introduction	132
2. Plasma Model Development	132
3. Plasma Model Specification	133
4. Energetic Particle Model	136
5. Spacecraft Charging Calculation	137
6. Results and Discussion	138
7. Summary and Conclusion	140
References	140

## 7. Plasma Distribution and Spacecraft Charging Modeling Near Jupiter

Raymond Goldstein and Neil Divine  
Jet Propulsion Laboratory  
Pasadena, California

### Abstract

To assess the role of spacecraft charging near Jupiter, the plasma distribution in Jupiter's magnetosphere has been modeled using data from the plasma analyzer experiments on Pioneer 10 (published results) and on Pioneer 11 (preliminary results). In the model, electron temperatures are  $kT = 4$  eV throughout, whereas proton temperatures range over  $100 \leq kT \leq 400$  eV. The model fluxes and concentrations vary over three orders of magnitude among several co-rotating regions, including, in order of increasing distance from Jupiter, a plasma void, plasma sphere, sporadic zone, ring current, current sheet, high latitude plasma and magnetosheath. Intermediate and high energy electrons and protons (to 100 MeV) are modeled as well. The models supply the information for calculating particle fluxes to a spacecraft in the Jovian environment. The particle balance equations (including effects of secondary and photoemission) then determine the spacecraft potential. Negative potentials the order of  $10^3$  volts are calculated in the near region (magnetic shell parameter  $\leq 6.5$  Jovian radii). In the outer region, severe differential charging ( $\sim 10^4$  volts) can occur for shadowed, electrically isolated portions of the spacecraft.

This paper presents the results of one phase of research carried out at the Jet Propulsion Laboratory, California Institute of Technology, under Contract No. NAS7-100, sponsored by the National Aeronautics and Space Administration.

130  
READING PAGE BLANK NOT FILMED

## 1. INTRODUCTION

Several facts suggest that spacecraft operating in Jupiter's magnetosphere can charge to significant potentials. These include the existence of a highly structured magnetosphere, with novel features compared to the earth's, and known to contain both stable and dynamic populations of thermal and energetic (MeV) electrons and ions. Experience with spacecraft in earth environment, especially at synchronous altitudes, shows that spacecraft charging occurs in such environments, and some anomalies in the operation of the Pioneer 10 and 11 spacecraft near Jupiter have been attributed to such charging. The survival and satisfactory operation of a spacecraft orbiting in the Jovian environment is thus of concern, because of the long period of time spend in the severe environment. To assess this problem, environmental models developed from Pioneer data are described below and are applied to preliminary computations of likely spacecraft equilibrium potentials in several magnetosphere regions, in both sunlight and shadow.

## 2. PLASMA MODEL DEVELOPMENT

The major features of Jupiter's thermal plasma distributions are derived from Frank et al,<sup>1</sup> who present a thorough discussion of the proton component data from the plasma analyzer experiment on Pioneer 10. These data range over values of L (magnetic shell parameter, in Jovian radii  $R_J$ ) between 2.85 and 25 (within the centrifugally dominated region) and are summarized in their Figure 8.<sup>1</sup> Comparable results from Pioneer 11 are not yet complete but the major additional results are: a plasma void for  $L \leq 1.8$  to 2.0 (within the gravitationally dominated region), and plasma properties nearly independent of latitude for  $L \leq 12$ . For high latitudes at  $L > 12$ , the density is assumed about an order of magnitude smaller than in the current sheet.

For the electron component more limited results, from Pioneer 10, are discussed by Intriligator and Wolfe,<sup>2</sup> the main conclusion being an electron peak in energy near 4 eV throughout the magnetosphere. Assuming charge neutrality (that is, electron concentrations equal to proton ones) an electron model can be inferred from the above proton distribution.

Ancillary information has been used in the models as follows, in order of increasing distance from Jupiter. Fjeldbo et al,<sup>3</sup> who reports results of Pioneer 10 radio occultations, provide information which has been used for a very crude specification of the ionosphere; for details of this multilayered environment in Jupiter's upper atmosphere the original reference should be consulted. Near the Galilean satellite Io, the configuration of the atomic hydrogen torus suggests a

local proton concentration which ionizes H by charge exchange<sup>4, 5, 6</sup> and the atomic sodium distribution suggests the importance of ionization by local electrons.<sup>7</sup> These results have been used to confirm or modify the description of the plasma-sphere. Magnetic field data from Pioneer 10 confirm the reality of the ring current (the source of external field terms for magnetic field modeling,<sup>8</sup> and the proton concentration in the current sheet.<sup>9</sup> Elsewhere various indirect observations and theoretical considerations are generally consistent with the foregoing interferences; they include discussions of Faraday rotation for HF bursts,<sup>10</sup> waveparticle interactions (diffusion, whistlers, etc.),<sup>11, 12, 13, 14</sup> and numerous, primarily qualitative, analyses.<sup>15, 16, 17, 18, 19, 20</sup> A description of the magnetosheath plasma is taken from considerations of Figure 5 of Wolfe et al.<sup>21</sup>

The present preliminary plasma model should be improved to include aspects of the extended distribution of neutral sodium atoms<sup>7</sup> which is possibly in equilibrium with a sodium ion population. In addition, there are observations of neutral hydrogen,<sup>6</sup> suggesting protons, and of an ionized sulfur nebula.<sup>22</sup> Other considerations for modification of the model include the character of the 4 eV electron peak seen at large L. This is not clearly thermal in origin and could have been the result of differential charging on Pioneer 10.<sup>23</sup> The low energy data from the San Diego scintillators on Pioneer 11<sup>24</sup> should also be included.

### 3. PLASMA MODEL SPECIFICATION

The plasma distribution derived from the above considerations is specified in Table 1, and the several regions and their boundaries are illustrated in Figure 1.

Values and uncertainties for boundaries and concentrations (equal for electrons and protons) have been estimated. The thermal energy values are quoted without uncertainty because the uncertainties in the distributions which result from the concentration column are already large. In the co-rotating frame [see note (2), Table 1], the thermal distributions are isotropic and may be derived from the entries in Table 1 using the following formulae:

$$J_o = 2N_o \left( \frac{2kT}{\pi m} \right)^{1/2} \quad (1)$$

$$= (1.56 \times 10^6 \text{ cm}^{-2} \text{ s}^{-1}) N_o (kT)^{1/2} \text{ for protons}$$

or

$$= (6.69 \times 10^7 \text{ cm}^{-2} \text{ s}^{-1}) N_o (kT)^{1/2} \text{ for electrons .}$$

ORIGINAL PAGE IS  
OF POOR QUALITY

Table 1. Plasma Characteristics for Regions Near Jupiter

Region	Protons			Electrons		
	Approximate outer boundary	Characteristic energy, kT, eV	Flux, $J_0$ , $\text{cm}^{-2}\text{s}^{-1}$	Concentration, $N_0$ , $\text{cm}^{-3}$	Flux, $J_0$ , $\text{cm}^{-2}\text{s}^{-1}$	Characteristic Energy, kT, eV
Ionosphere	$R_J + (\sim 4000 \text{ km})$	0.07	$\leq 10^{11}$	$\leq 3 \times 10^5$	$\leq 5 \times 10^{12}$	0.07
Plasma void	$L = (1.9 \pm 0.1) R_J$	100	$\leq 10^8$	$\leq 10$	$\leq 10^9$	
Plasmasphere	$L = (6 \pm 0.5) R_J$ (Plasmapause and $I_0$ flux tubes)	100	$(1.6 \times 10^{\pm 1}) \times 10^9$	$100 \times 2^{\pm 1}$	$(1.3 \times 2^{\pm 1}) \times 10^{10}$	
Sporadic zone	$L = (7.8 \pm 0.5) R_J$	400	$10^8 \times 3^{\pm 1}$	$3 \times 3^{\pm 1}$	$(4 \times 3^{\pm 1}) \times 10^6$	
Ring current (Europa flux tubes)	$L = (9.6 \pm 0.5) R_J$	400	$(4 \pm 2) \times 10^8$	12 $\pm 5$	$(1.6 \pm 0.7) \times 10^9$	
Current sheet	$L = (12 \pm 1) R_J$ $Z = \pm (1 \pm 0.5) R_J$	400 (2)	$(3 \times 3^{\pm 1}) \times 10^7$ (2)	$1 \times 3^{\pm 1}$	$(1.3 \times 3^{\pm 1}) \times 10^8$	
High latitude plasma	$R_1 = R_M \pm 40 R_J$ (Magnetopause)	400 (2)	$3 \times 10^{6 \pm 1}$ (2)	$0.1 \times 10^{\pm 1}$	$1.3 \times 10^{7 \pm 1}$	
Magnetosheath (and tail)	$R_1 \pm 15 R_J$	34 (4)	$(2 \times 3^{\pm 1}) \times 10^7$ (4)	$0.6 \times 2^{\pm 1}$	$(2 \times 3^{\pm 1}) \times 10^8$	34
Interplanetary (solar wind)	Several AU beyond Jupiter's orbit					

SEF NASA SP-8118

- Notes: (1) A location is outside the current sheet only if both conditions pertain:  $L > (12 \pm 1) R_J$  and  $|Z| > (1 \pm 0.5) R_J$
- (2) If the speed  $v$  relative to the co-rotating plasma exceeds the proton thermal speed, the appropriate entries must be replaced by  $mv^2/2$  and  $Nv$  for a stationary observer  $v = (1.3 \times 10^6 \text{ km/s}) (R/R_J)$  and  $E = mv^2/2 = (0.83 \text{ eV}) (R/R_J)^2$  dominate for  $R \geq 22 R_J$
- (3) These boundary locations vary strongly with direction from Jupiter [cf. Eq. (6) for  $R_M$ ] and with time in response to changes in the external solar wind
- (4) In the magnetosheath, the variable bulk plasma flow ( $v \sim 300 \text{ km/s}$ ) dominates the proton thermal speed, so the corresponding flux entry is  $Nv$

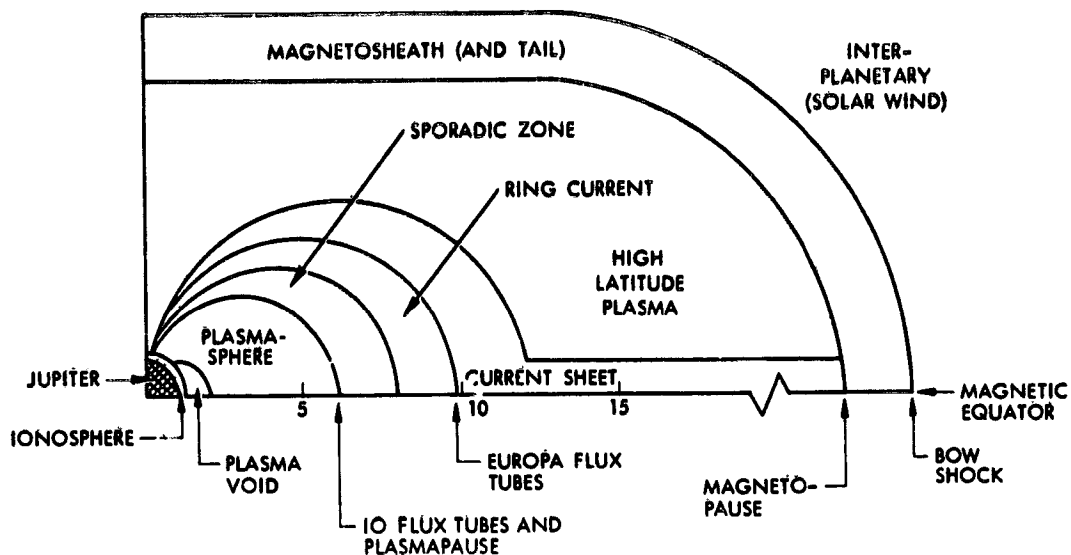


Figure 1. Schematic of Plasma Regions at Jupiter for One Quadrant of a Magnetic Meridional Plane. Drawing is not to scale, although three distances (in  $R_J$ ) from Jupiter are indicated along the magnetic equator

integral flux (energy  $> E$ )       $J = J_0 (1 + E/kT) \exp(-E/kT) + J_2 + j_2 (E_2 - E) .$       (2)

differential flux       $j = J_0 E(kT)^{-2} \exp(-E/kT) + j_2 .$       (3)

In these expressions, values of  $N_0$ ,  $J_0$ , and  $kT$  are to be taken from Table 1; in that table,  $Z$  represents the vertical distance from the magnetic equatorial plane, and the notes are important. Equations (1) through (3) apply for all thermal and intermediate energies  $0 \leq E \leq E_2$  and specify fluxes  $J$  and  $j$  which are continuous with those in the radiation belt models (see below) when  $J_2$  and  $j_2$  are evaluated at energy  $E_2$ , where  $E_2 = 40,000$  eV for electrons and  $E_2 = 610,000$  eV for protons. Care should be taken that energy unit conversions (between MeV and eV) are included when  $J$  and  $j$  are evaluated in  $\text{cm}^{-2} \text{s}^{-1}$  and  $\text{cm}^{-2} \text{s}^{-1} \text{eV}^{-1}$  respectively.

For completeness, in Table 1 reference is made to NASA SP-8118<sup>25</sup> for a description of parameters in the solar wind.

## 1. ENERGETIC PARTICLE MODEL

For energies exceeding  $E_2$  (see above), there exists a large body of data from four energetic charged particle experiments on each of the Pioneer 10 and 11 spacecraft. Because the literature sources and the model specification for this environment are so detailed they will not be described here. The former are exemplified by several articles in Journal of Geophysical Research, Vol. 79, No. 25 (1974, Sept. 1) and in Science, Vol. 188, No. 4187 (1975, May 2). The model has been developed for the Jupiter-Orbiter-Probe Study, and has been published for limited distribution.<sup>26</sup> As an example, inner magnetosphere electron flux profiles are shown in Figure 2. The complete radiation belt model includes both integral and differential fluxes as functions of position L and  $\lambda$  (magnetic latitude) and particle energy, for both electrons and protons.

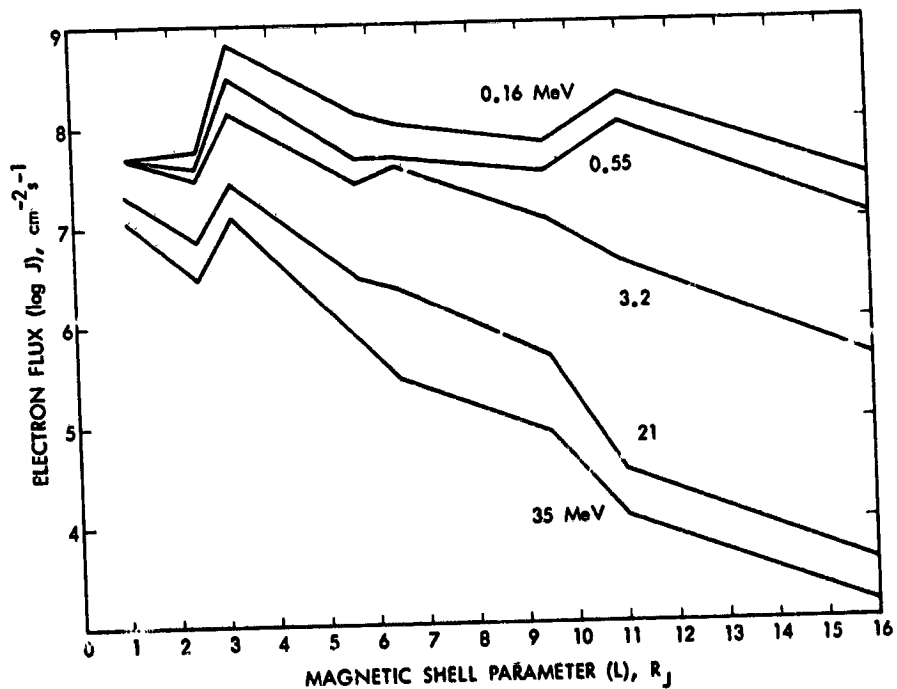


Figure 2. Distance Variation of Equatorial Flux of Electrons Having Energy Greater than the Indicated Threshold Values

### 5. SPACECRAFT CHARGING CALCULATION

The net current to the spacecraft  $I_{\text{net}}$  is given by

$$I_{\text{net}} = I_p - I_e + I_s + I_{\text{PE}} \quad (4)$$

where  $I_p$  is the total proton current intercepted by the spacecraft,  $I_e$  is the incident electron current,  $I_s$  is the total secondary electron emission from the spacecraft (including backscattered electrons), and  $I_{\text{PE}}$  is the photoelectron emission current from the spacecraft. Each term is a function of the spacecraft potential  $V_{s/c}$  because of the energy dependence of each term. At steady state the net current must be zero, establishing the condition for determining  $V_{s/c}$ . If Equation (4) is divided by the appropriate area, this condition can be expressed in terms of particle fluxes. It is assumed that essentially all of the spacecraft is covered with electrically conductive material, and that on the average, only 25 percent of the surface is exposed to sunlight. Then the condition for zero net current becomes

$$J_p(V_{s/c}) - J_e(V_{s/c}) + J_s(V_{s/c}) + J_{\text{PE}}(V_{s/c}) = 0 \quad (5)$$

The  $J$ 's represent the particle fluxes of the corresponding terms of Eq. (4); and the dependence on  $V_{s/c}$  is explicitly shown for emphasis. To normalize the photoelectric term properly, a factor 0.25 is implicitly included in  $J_{\text{PE}}$ .

Equation (5) was used to calculate  $V_{s/c}$  at various locations in the Jovian magnetosphere using values of  $J_p$  and  $J_e$  provided by the model described in the previous sections. The results of Sternglass for aluminum, as reported by Whipple,<sup>27</sup> were used to calculate  $J_s$ . Whipple's value of photoelectron yield for aluminum at 1 AU ( $3 \times 10^{-9}$  A cm<sup>-2</sup>) reduced for 5.2 AU, was used to determine  $J_{\text{PE}}$ . Although most spacecraft are not likely to be covered with aluminum, the yields were taken to be typical of conductive materials.

The calculations were performed by assuming a  $V_{s/c}$  and then iterating until a self-consistent value could be obtained. Usually a rapid convergence of the calculation was obtained with very few iterations. This is largely due to the dependence of the secondary emission yield on incident proton energy. Below about  $10^3$  eV the yield is much less than unity, but above  $10^3$  eV the yield rises very rapidly with energy exceeding unity at about  $2 \times 10^3$  eV. This rapid increase in yield with energy produces a high sensitivity of the calculation to  $V_{s/c}$  since all low energy protons are accelerated by a negative spacecraft potential. The high secondary yield thus tends to limit negative spacecraft potentials to a few keV in regions of the magnetosphere where photoemission is unimportant.

## 6. RESULTS AND DISCUSSION

The contribution of each term of Eq. (5) at the steady state spacecraft potential for several locations in the Jovian equatorial plane is shown in Figure 3. The calculated spacecraft potentials are also given. The lower part shows the incident electron current density. In the upper part of the figure, the proton as well as secondary and photoemission contributions are shown. Note that for  $L \leq 6.5 R_J$  photoemission is not very important. For higher  $L$ , however, photoemission begins to dominate and the spacecraft charges to a slight positive potential. In those cases the actual secondary and photoemission contributions depend on details of their energy distributions, and for simplicity were not calculated in detail. Their sum is thus shown in Figure 3 for  $L \geq 9.5 R_J$ .

The incident electron current density corresponding to the  $V_{s/c}$  calculated at steady state is indicated by the light horizontal line shown in the electron contributions separating two differently shaded regions. The full column represents the total  $J_e(0)$  that would occur if the potential were zero, and hence the doubly cross-hatched region corresponds to that portion of the electron spectrum repelled by the spacecraft to produce the current balance.

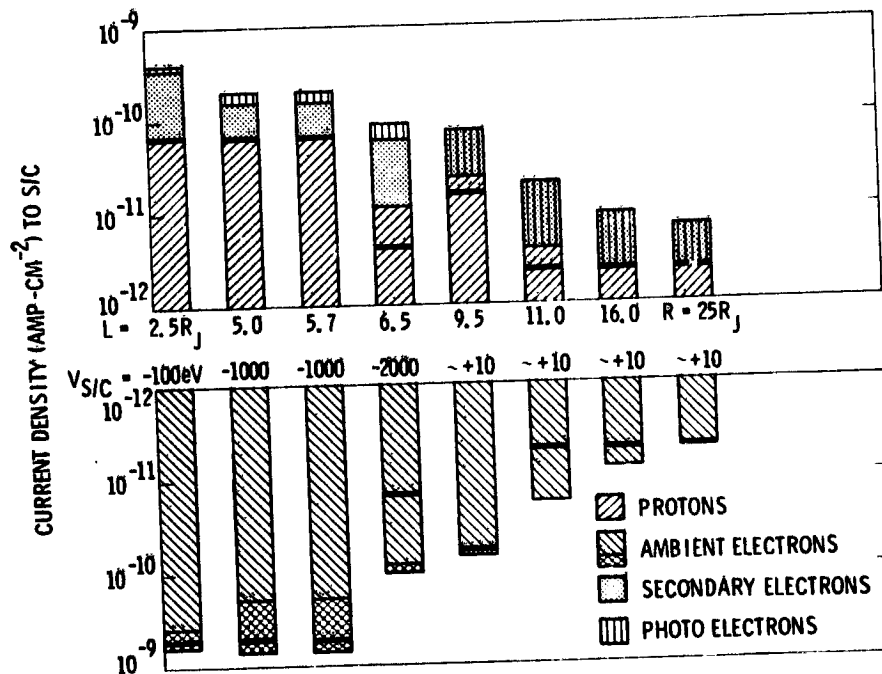


Figure 3. Distribution of Particle Fluxes to and From Spacecraft in Jovian Equatorial Plane

The heavy horizontal line appearing in each column shows the relative contribution to the total incident flux due to low energy plasma particles and high energy particles. In each case the plasma contribution is the portion closest to the center of the figure.

Calculations were also carried out neglecting the photoemission term, that is, for a spacecraft in eclipse. In the inner region, where photoemission is unimportant (cf. Figure 3), potentials for the dark case are not very different from the sunlit case. However, in the outer regions where photoemission is important, relatively high potentials are calculated for a spacecraft in darkness. The potentials for both the sunlit as well as eclipse cases are summarized in Table 2. Also shown there are the potentials calculated for one point in the high latitude region ( $L = 16.0 R_J$ ,  $\lambda = 45^\circ$ ). In the outer regions total eclipse of the spacecraft is unlikely, but the eclipse potentials indicate the level to which electrically isolated portions in darkness are likely to charge.

Some calculations were also performed to determine the sensitivity of the results to the fraction of the spacecraft assumed to be in sunlight. In the inner region this is not too important, but in the outer region a 10 percent sunlit spacecraft would have a negative ( $10^2 - 10^3$ ) potential.

Table 2. Calculated Spacecraft Potentials in the Jovian Environment

Location	$V_{sc}$ Sun (volts)	$V_{sc}$ ECL (volts)
$L = 2.5 R_J$	-100	-200
5.0	-1000	-1500
5.7	-1000	-1500
6.5	-2000	-3500
9.5	~+10	~+10
11.0	~+10	$-10^4$
16.0	~+10	-1500
$16.0, \lambda = 45^\circ$	~+10	$-10^4$
$R = 25 R_J$	~+10	$-10^4$

## 7. SUMMARY AND CONCLUSIONS

A model of the Jovian charged particle environment has been constructed from results of Pioneer 10 and 11 measurements. This model was used to calculate the potential to which a spacecraft would charge in the Jovian environment. In the inner region ( $L \leq 6.5 R_J$ ), the potentials calculated ( $\sim 10^3$  volts negative) indicate severe disturbances to fields and particles measurements from the spacecraft. "Clean" measurements would therefore require active control of the spacecraft potential. In the outer regions, electrically isolated portions of the spacecraft are likely to charge differentially  $\sim 10^3$ - $10^4$  volts with respect to sunlit portions. High differential charging seriously distorts fields and particles measurements, and represents sources for arcing severe enough to damage the spacecraft or cause malfunction.

## References

1. Frank, L.A. et al (1976) Observations of plasmas in the Jovian magnetosphere, J. Geophys. Res. 81(No. 4):457-468.
2. Intriligator, D.S., and Wolfe, J.H. (1974) Initial observations of plasma electrons from the Pioneer 10 flyby of Jupiter, Geophys. Res. Letters 1(No. 7):281-284.
3. Fjeldbo, G. et al (1975) The Pioneer 10 radio occultation measurements of the ionosphere of Jupiter, Astronomy and Astrophysics 39(No. 1):91-96.
4. McDonough, T.R. (1975) A theory of the Jovian hydrogen torus, Icarus 24(No. 4):400-406.
5. Carlson, R.W., and Judge, D.L. (1974) Pioneer 10 ultraviolet photometer observations at Jupiter encounter. J. Geophys. Res. 79(No. 25):3623-3633.
6. Carlson, R.W., and Judge, D.L. (1975) Pioneer 10 ultraviolet photometer observations of the Jovian hydrogen torus: the angular distribution, Icarus 24(No. 4):395-399.
7. Carlson, R.W. et al (1975) Electron impact ionization of Io's sodium emission cloud, Geophys. Res. Letters 2(No. 10):469-472.
8. Smith, E.J. et al (1976) Jupiter's magnetic field and magnetosphere, in Jupiter, University of Arizona Press, Tucson, pp. 788-829.
9. Smith, E.J. et al (1974) The planetary magnetic field and magnetosphere of Jupiter: Pioneer 10, J. Geophys. Res. 79(No. 25):3501-3513.
10. Goertz, C.K. (1974) Polarization of Jovian decametric radiation, Planetary and Space Sci. 22(No. 11):1491-1500.
11. Scarf, F.L., and Sanders, N.L. (1976) Some comments on the whistler mode instability at Jupiter, J. Geophys. Res. 81(No. 10):1787-1790.
12. Barbosa, D.D., and Coroniti, F.V. (1975) Whistler stability analysis in Jupiter's inner radiation belt, AGU Trans. EOS 56(No. 12):1041.

13. Sentman, D.D. et al (1976) Plasma densities in the inner Jovian magnetosphere, AGU Trans. EOS 57(No. 4):316.
14. Eviatar, A., and Ershkovich, A.I. (1976) Plasma density in the outer Jovian magnetosphere, J. Geophys. Res. 81(No. 22):4027-4028.
15. Hill, T.W. et al (1974) Configuration of the Jovian magnetosphere, Geophys. Res. Letters 1(No. 1):3-6.
16. Barish, F.D., and Smith, R.A. (1975) An analytical model of the Jovian magnetosphere, Geophys. Res. Letters 2(No. 7):269-272.
17. Prakash, A., and Brice, N. (1975) Magnetospheres of Earth and Jupiter after Pioneer 10, Space Sci. Reviews 17(No. 6):823-835.
18. Roederer, J.G. (1976) Planetary plasmas and fields, AGU Trans. EOS 57(No. 2):53-62.
19. Goertz, C.K. (1976) The current sheet in Jupiter's magnetosphere, AGU Trans. EOS 57(No. 3):155.
20. Goertz, C.K. (1976) Plasma in the Jovian Magnetosphere, J. Geophys. Res. 81(No. 13):2007-2014.
21. Wolfe, J.H. et al (1974) Pioneer 10 observations of the solar wind interaction with Jupiter, J. Geophys. Res. 79(No. 25):3489-3500.
22. Brown, R.A. (1976) A model of Jupiter's sulfur nebula, Astrophys. J. 206(No. 3):L179-L183.
23. Grard, R.J.L., DeForest, S.E., and Whipple, Jr., E.C. A reinterpretation of low energy electron measurements in the Jovian magnetosphere, J. Geophys. Res. in press.
24. Fillius, R.W., McIlwain, C.E., and Mogro-Campero, A. (1975) Radiation belts of Jupiter: a second look, Science 188(No. 4187):465-467.
25. Divine, N. (1975) Interplanetary Charged Particle Models (1974), NASA SP-8118.
26. Divine, N. (1976) Jupiter Charged-Particle Environment for Jupiter Orbiter Probe 1981/1982 Mission, Document 660-24, Jet Propulsion Laboratory, Revised August 1976.
27. Whipple, E.C., Jr. (1965) The Equilibrium Electric Potential of a Body in the Upper Atmosphere and in the Interplanetary Space, NASA Technical Note X-615-65-296.

**Contents**

1. Introduction	144
2. Spacecraft Charging in the Jovian Environment	145
3. Active Spacecraft Potential Control System	147
4. Charged Particle Release Devices	148
5. Power and Mass Estimates	162
6. Summary and Conclusions	164
References	165

## 8. Active Spacecraft Potential Control System Selection for the Jupiter Orbiter With Probe Mission

John R. Beattie and Raymond Goldstein  
Jet Propulsion Laboratory  
Pasadena, California

### Abstract

The Jupiter orbiter with probe (JOP) spacecraft is briefly described. It is shown that the high flux of energetic plasma electrons and the reduced photoemission rate in the Jovian environment can result in the spacecraft developing a large negative potential. The effects of the electric fields produced by this charging phenomenon are discussed in terms of spacecraft integrity as well as charged particle and fields measurements. The primary area of concern is shown to be the interaction of the electric fields with the measuring devices on the spacecraft. The need for controlling the potential of the spacecraft is identified, and a system capable of active control of the spacecraft potential in the Jupiter environment is proposed. The desirability of using this system to vary the spacecraft potential relative to the ambient plasma potential is also discussed. Various charged particle release devices are identified as potential candidates for use with the spacecraft potential control system. These devices are evaluated and compared on the basis of system mass, power consumption, and system complexity and reliability. The results of this comparison are then used to identify the optimum particle release devices which are capable of actively controlling the spacecraft potential.

---

This paper presents the results of one phase of research carried out at the Jet Propulsion Laboratory, California Institute of Technology, under Contract NAS7-100, sponsored by the National Aeronautics and Space Administration.

143  
 PREVIOUS PAGE INTENTIONALLY BLANK  
 PRECEDING PAGE BLANK NOT FILMED

## 1. INTRODUCTION

The scientific objective of the proposed Jupiter orbiter with probe mission is to conduct intensive investigations of Jupiter's atmosphere, satellites, and magnetosphere. If the mission is approved, the spacecraft will be launched by the Space Shuttle/Interim Upper Stage in early 1982 and will arrive at Jupiter some 3 years later. The nominal mission length is 12 months, which provides for multiple encounters with Jupiter and its satellite Ganymede as well as a possible encounter with the satellite Io.

The proposed spacecraft is a dual spin configuration consisting of an orbiter and an atmospheric entry probe. The probe will pass through the Jovian atmosphere on the sunlit side of the planet, and during its 30 min lifetime will transmit atmospheric data to the orbiter which will relay this information back to Earth. The orbiter will continue along its trajectory collecting scientific data in the Jovian magnetosphere and the vicinity of the Jovian satellites.

One of the primary science objectives of the orbiter is to obtain the charged particle distribution functions in the planetary magnetosphere and satellite ionospheres. In order to obtain distribution functions which are representative of the undisturbed plasma, the perturbation in electric potential caused by the presence of the spacecraft must be minimized. Potential variations in the region near the charged particle detectors could result in erroneous information regarding the distribution functions of the charged species. The principal source of error caused by the presence of an electric field in the vicinity of these detectors is a perturbation in the energy and direction of the low-energy particles and a perturbation in the direction of the high-energy particles. Even if the spacecraft potential is close to that of the undisturbed plasma, local potential depressions or barriers<sup>1</sup> may lead to erroneous interpretation of low-energy particles data. For example, the existence of a potential well of magnitude  $\phi$  near these detectors invalidates any electron flux measurements in the energy range from zero to  $\phi$ . The reason for this is, of course, that ambient electrons in this energy range cannot reach the spacecraft, while photoemitted electrons having energies in this range cannot escape the spacecraft. Therefore, in order to obtain accurate information regarding the distribution functions of the charged species, spacecraft design practices should be enforced to (1) maintain the spacecraft at or near the ambient plasma potential and (2) eliminate the presence of differentially charged areas of the spacecraft, thereby eliminating localized electric fields and minimizing potential barriers produced by the release of low-energy secondary and photoemission electrons. The former requirement can be met by providing a return current to space equal to the difference between the incoming electron current and the sum of the incoming ion

current plus secondary and photoemission currents. The latter requirement can be satisfied by the use of conductive coatings and surfaces on the spacecraft.

Some of the quantitative results to be presented reflect the emission current requirements of the Jupiter orbiter with probe mission. However, the particle release devices and active potential control systems described herein have wide application and their use is not restricted to a specific mission.

## 2. SPACECRAFT CHARGING IN THE JOVIAN ENVIRONMENT

The equilibrium potential of a passive spacecraft subjected to Jupiter's charged particle flux has been calculated by Goldstein and Divine<sup>2</sup> using a plasma environmental model derived from Pioneer 10 and 11 measurements. The results of their calculations indicate the JOP spacecraft (modeled as a passive conducting sphere) will attain negative floating potentials as high as 10 kV when in eclipse. Spacecraft potentials of this magnitude will surely invalidate proton measurements in the energy range up to 10 kV and will not allow electron measurements in the energy range less than 10 kV. Goldstein and Divine's analysis also indicated that sunlit portions of the spacecraft will discharge, and they may lead to differential charging of adjacent eclipsed and sunlit areas of the spacecraft. These large potentials clearly indicate the need for an active potential control system on the spacecraft as well as the requirement for a conductive spacecraft coating.

A conservative estimate of the net spacecraft collection current during eclipse conditions can be made using the Jupiter environmental model of Goldstein and Divine and neglecting the current contribution due to secondary electron emission. A stationary collector maintained at the same potential as the surrounding plasma produces no disturbing sheath effects and its collection current is the product of the net plasma current density and the collector surface area. The estimated collection area of the JOP spacecraft is about  $49 \text{ m}^2$ . Using this area and the Jupiter environmental model, the net current collected by the spacecraft when maintained at the same potential as the surrounding plasma can be calculated. The results of these calculations are presented in Figure 1 which indicates the net spacecraft current, as well as the high-energy and Maxwellian electron contributions, as a function of Jupiter's magnetic shell parameter. The net current is the sum of the two electron currents shown in the figure minus the proton current. These results indicate a spacecraft collection current on the order of 0.3 mA in the region near  $2-6 R_J$  (Jupiter radii), and this value drops nearly two orders of magnitude at the nominal mission periJove of  $15 R_J$ . The initial mission periJove for delivery of the atmospheric entry probe is  $6 R_J$ , and according to Figure 1 this corresponds to the region of highest electron collection. These results also indicate the dominant term in the current collection at this location is the Maxwellian electron current.

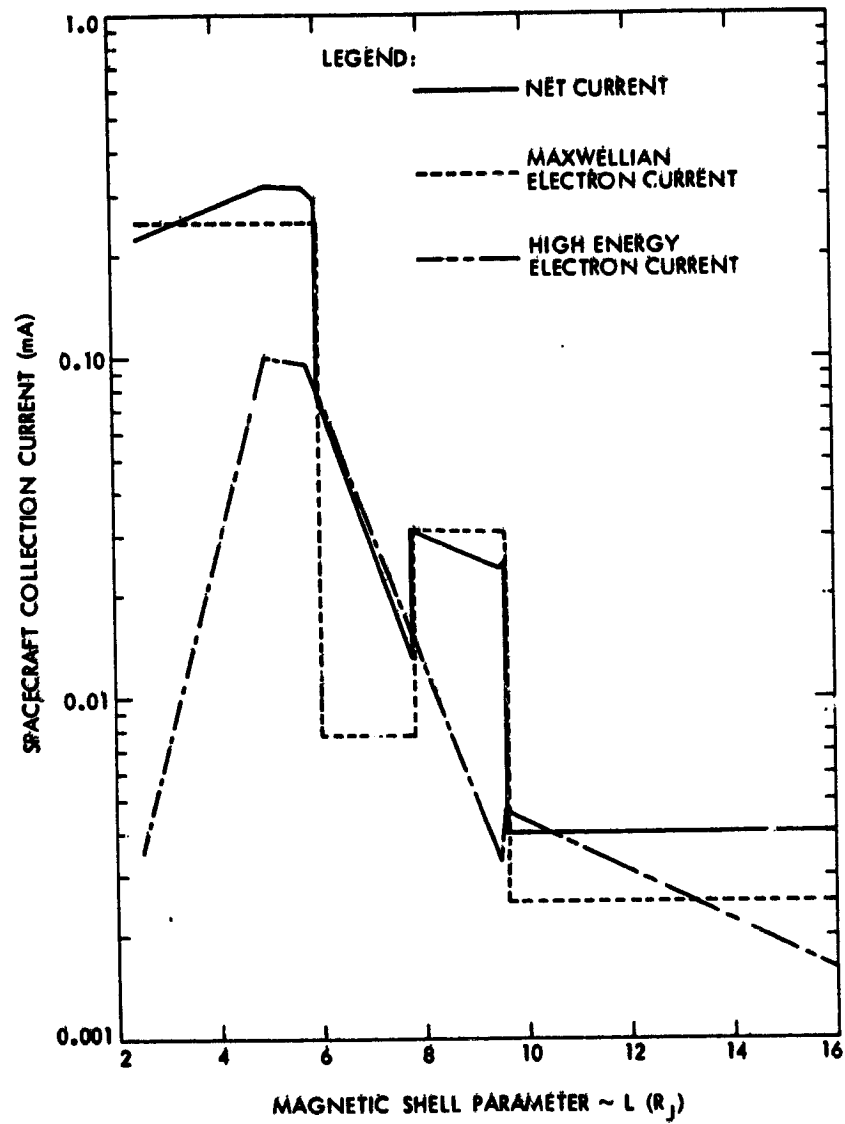


Figure 1. Calculated Spacecraft Collection Current as a Function of Jupiter's Magnetic Shell Parameter

Figure 1 can be used to estimate the release current requirements of a charged particle release device since the spacecraft collection current at the plasma potential must be returned to space by the particle release device. This is a conservative estimate since the contribution due to secondary and photoelectron emission has been neglected.

### 3. ACTIVE SPACECRAFT POTENTIAL CONTROL SYSTEM

The two basic functions of an active spacecraft potential control system are (1) sensing the potential difference between the spacecraft and the surrounding plasma and (2) releasing a current of the proper sign and magnitude to maintain a desired spacecraft potential. In addition, there are two possible control schemes which could be used to couple these functions: (1) closed loop and (2) open loop. The closed loop control system would employ a potential sensing device such as an electric field meter or floating emissive probe to measure the potential difference between the spacecraft and its surroundings. This potential difference can then be maintained at a preselected value by proper biasing of the charged particle release device. The control circuitry which couples the output of the voltage sensor with the biasing power supply serves as the link to form a closed loop control system. An open loop system, on the other hand, would employ a current sensing device to monitor the current through the biasing power supply and, hence, the current-voltage characteristics of the spacecraft. Periodic analysis of this characteristic allows one to determine the bias potential which corresponds to a spacecraft potential equal to the local plasma potential, and one can then adjust the bias potential to give the desired spacecraft potential relative to the ambient plasma. In order to operate in this open loop mode the bias potential must be known relative to a stable reference, and this identifies a general requirement of the charged particle release device: The current-voltage relationship of the ideal charged particle emitter should have infinite slope so that the emission current of the device is essentially independent of its voltage. Two additional requirements of an active potential control system are (1) the particle release device should be mounted so as to minimize any interaction between the released particles and sensitive spacecraft surfaces or science instruments and (2) the thrust produced by the ejected charged particles should not result in any disturbing forces or moments on the spacecraft.

In either, the closed or open loop control scheme one can employ the charged particle release device not only to discharge the spacecraft, but to act as a science instrument as well. As a plasma diagnostic tool<sup>3</sup> the spacecraft potential control system should enable the local Maxwellian electron density and temperature to be determined by analysis of the current-voltage characteristics of the spacecraft.

#### 4. CHARGED PARTICLE RELEASE DEVICES

The charged particle release devices which are considered suitable for use in an active spacecraft potential control system fall into two categories: (1) electron devices and (2) plasma devices. These categories may be further divided according to the energy of the released or ejected particles. The primary reason for identifying the two major categories is related to the direction in which the devices can drive the spacecraft potential. For instance, a negatively charged spacecraft can be discharged to zero or even a positive potential by the release of negative charge from either an electron emitter or a plasma device. A positively charged spacecraft, on the other hand, can be discharged to zero or negative potentials only by the release of positive charge from a plasma device.

Another reason for identifying the two major categories is that unless the spacecraft is an equipotential surface, the successful control of the spacecraft potential may dictate the release of both negative and positive charge; even though the net release current requirement is almost always negative. This is based on the results of attempts to control actively the potential of the ATS-5 and ATS-6 spacecraft in Earth's geosynchronous orbit.<sup>4</sup> In these tests it was found that electron release alone was sometimes unsuccessful in maintaining the spacecraft at near-zero potential. Operation of the ion thruster, on the other hand, proved successful in clamping the spacecraft potential to approximately 4 V negative with respect to the ambient plasma potential. The reasons for the failure of the electron device and the success of the plasma device in controlling the spacecraft potential in these tests are not fully understood. One explanation is that the release of electrons alone may result in space charge effects which limit the release of negative charge and thus limits the ability to maintain the spacecraft at zero potential. The use of the ion thruster, on the other hand, may eliminate the space charge limitation by providing charge carriers of both signs. Another explanation is closely related to the classification of charged particle release devices into the low-energy and high-energy groups: Potential barriers may form in the vicinity of the spacecraft and limit the release of low-energy electrons. However, by accelerating the electrons to energies in excess of the potential well value, it may be possible to attain a near-zero spacecraft potential by release of electrons alone. Discharging the spacecraft, however, does not necessarily eliminate the potential barrier; this phenomenon is generally thought to be caused by differential charging of adjacent spacecraft surfaces.

## 4.1 Electron Devices-Low Energy

### 4.1.1 FIELD EMISSION

Electron field emission from tungsten surfaces is appreciable for electric field strengths on the order of  $10^9$  V/m. Thus a sharp tungsten rod (radius of curvature of  $10^{-6}$  m or less) will emit appreciable current at potentials on the order of 1 kV. A spherical cluster or brush composed of 100 of these needles can yield emission currents on the order of milliamperes when biased\* to a potential of a few hundred volts.

Grard<sup>5, 6</sup> has proposed the use of an electron field emitter for actively controlling the spacecraft potential. His device consists of a cluster of small diameter tungsten wire bristles which is attached to the spacecraft by means of a boom. A separation between the spacecraft and probe on the order of twice the characteristic dimension of the spacecraft is sufficient to yield field strengths at the tips of the wires which are within 25 percent of the values obtained for infinite separation. Emission currents as high as 6 mA can be drawn from the device, with the current limitation imposed by the thermal properties of tungsten, rather than a space charge limit. A schematic diagram of Grard's arrangement is presented in Figure 2 which indicates the spacecraft collection current  $I$  and illustrates the return of this current to space by means of the electron field emission probe and biasing power supply.

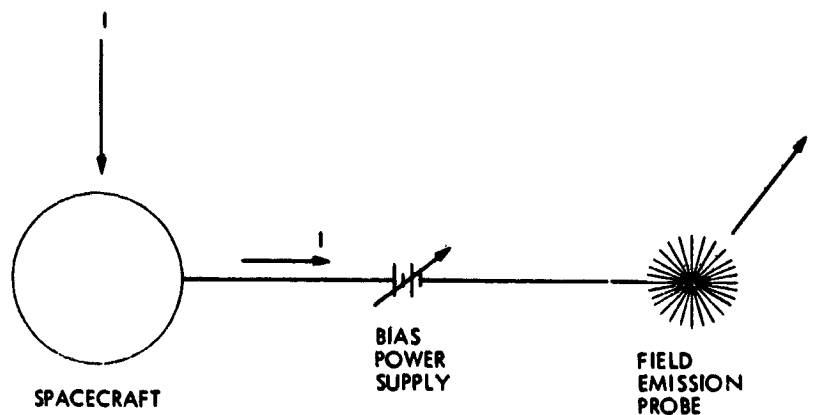


Figure 2. Schematic Diagram of an Active Spacecraft Potential Control System which Utilizes an Electron Field Emission Probe

\* Unless stated otherwise, the bias and filament potentials mentioned throughout the paper are negative with respect to the surrounding plasma.

The electron field emission current is governed by the Fowler-Nordheim equation, and the current-voltage characteristics calculated using this relationship are presented in Figure 3 for a probe consisting of one hundred 0.1- $\mu\text{m}$  diameter tungsten needles. The general trend illustrated by this figure is a voltage threshold of about 400 V beyond which the current increases rapidly with voltage. This feature of the current-voltage characteristic enables the field emission probe to be used as a stable voltage reference for biasing the entire spacecraft. At the initial mission perijove the release current required to maintain the JOP spacecraft at the ambient plasma potential is about 0.3 mA, and from Figure 3 a biasing potential of 625 V is required to achieve this emission level. Thus the power requirement to maintain the spacecraft at the ambient plasma potential is a relatively modest 200 mW. This is a conservative estimate since the actual current required to maintain this potential would be somewhat less than 0.3 mA due to secondary and photoemission currents.

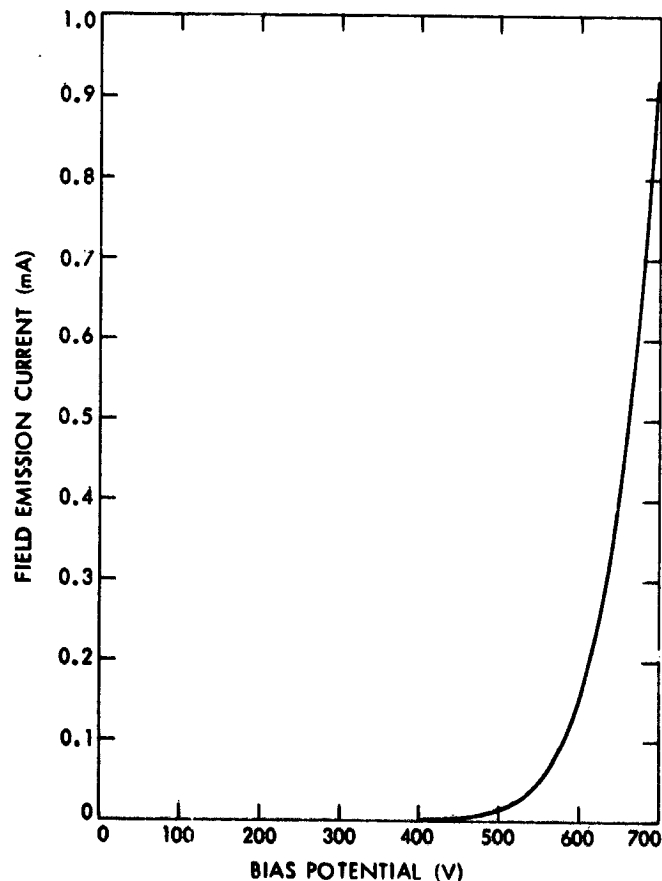


Figure 3. Calculated Electron Field Emission Current From a Probe Consisting of One Hundred 0.1- $\mu\text{m}$  Diameter Tungsten Needles

The electron field emission probe is an attractive system for use in active spacecraft potential control since it requires no expellant, is lightweight (Grard<sup>6</sup> estimates 150 g for the emitter and boom), relatively simple, and requires only a biasing power supply. However, there is a drawback associated with the device: Tungsten needles having dimensions on the order of 0.1  $\mu\text{m}$  are fragile and not visible to the naked eye. Thus the use of an electron field emitter for active potential control on a spacecraft may not be practical due to problems associated with handling and launching the device.

#### 4.1.2 THERMIONIC EMISSION

The refractory metal cathode has been used for the active control of spacecraft potential since the first ion thruster flight test was conducted in 1964.<sup>7</sup> In-flight thrust measurements conducted during this test verified the effectiveness of the heated tantalum filament neutralizer in producing a neutral exhaust beam and preventing spacecraft charging. More recent tests using the filament neutralizer on the ATS-5 spacecraft have shown that operation of the neutralizer filament alone can (at least in some instances) restore the potential of the spacecraft to a value near zero, even after having been initially charged to negative potentials on the order of a few thousand volts.<sup>4</sup>

Grard et al<sup>8</sup> have proposed a spacecraft potential control and plasma diagnostic system which employs a thermionic electron emitter. The system consists of a heated filament and biasing power supply as illustrated schematically in Figure 4. The current-voltage characteristics of the device can be calculated by assuming space charge limited flow conditions between two concentric spheres. The inner sphere represents the boom-mounted emitter, and the outer sphere represents the plasma sheath boundary. The space charge limited flow solutions obtained for the spherical geometry are presented in Figure 5 for a concentric sphere diameter ratio of 30. This ratio is representative of the plasma sheath thickness and emitter dimensions, although (as will be shown later) the results are not too sensitive to this parameter. The rapid rise in emission current with voltage, as illustrated in Figure 5, suggests the thermionic emitter can be used as a stable voltage reference for biasing the entire spacecraft. Figure 5 indicates a biasing potential of about 10 V is sufficient to maintain the spacecraft at the ambient plasma potential by supplying an emission current of 0.3 mA. This results in a bias power requirement of about 3 mW, which is significantly less than the 200 mW requirement of the field emission probe. However, this difference is more than offset by the filament power requirement of about 500 mW for a tantalum filament operated at 2100°K.

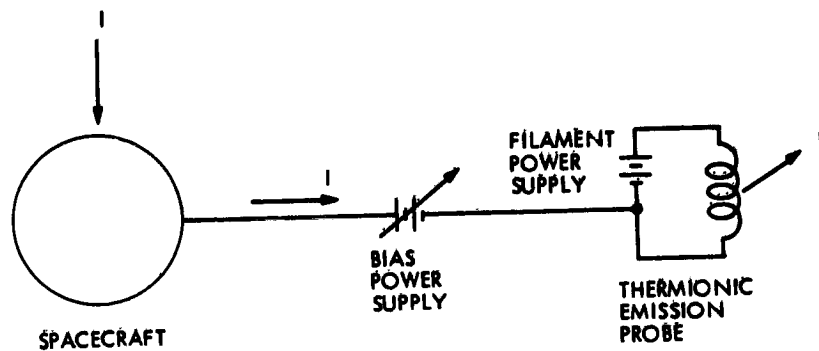


Figure 4. Schematic Diagram of an Active Spacecraft Potential Control System which Utilizes an Electron Thermionic Emission Probe

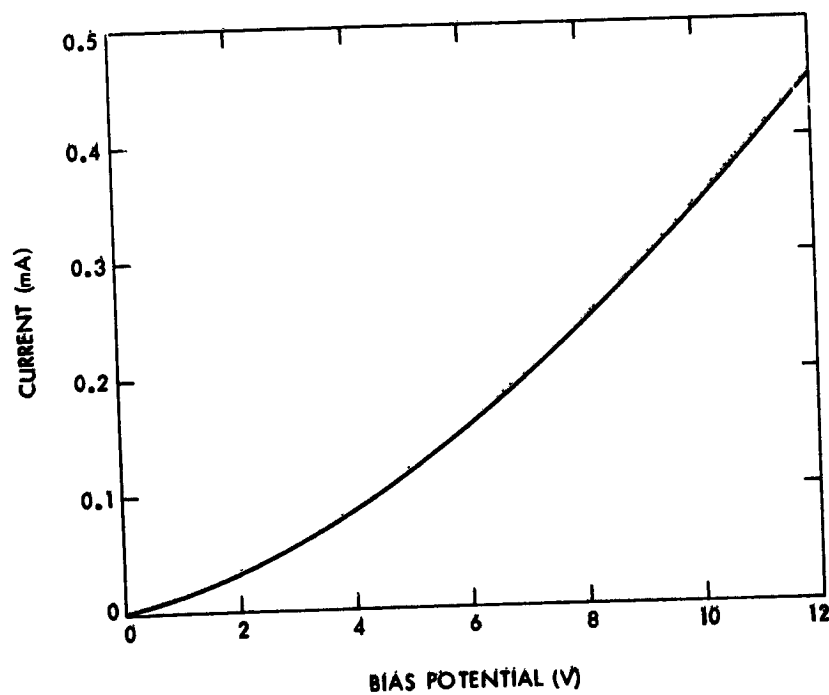


Figure 5. Calculated Space Charge Limited Electron Current Between Concentric Spheres Having a Diameter Ratio of 30

The refractory metal cathode is a viable candidate for a low-energy electron release device and has several outstanding features. The system requires no expellant, has a power consumption of less than 1 W, and is lightweight (Grard et al<sup>8</sup> estimate 150 g for the emitter and boom). In addition, the device is relatively simple and thermionic electron emitters have been used successfully in space for many years. The results of the ATS-5 spacecraft potential control demonstration have shown that the thermionic emitter can reduce the potential of a spacecraft (initially charged negatively) to a value near zero. However, in some instances the ATS-5 neutralizer filament was ineffective in maintaining the spacecraft potential near zero... There are at least two plausible explanations for these failures: (1) A potential well may exist near the surface of the spacecraft which suppresses the emission of low-energy electrons from the heated filament and (2) the ATS-5 neutralizer filament is recessed about 2.5 cm within a 5-cm diameter aperture located on the surface of the spacecraft, and under some conditions local space charge effects may reduce the filament emission current obtained with this geometry. However, the problems discussed above may well be eliminated by use of the system illustrated in Figure 4, since the filament is mounted on a long boom and can be biased relative to the ambient plasma.

#### 4.1.3 EMISSIVE CLAMP

An electron emissive clamp for use in actively controlling the spacecraft potential has been proposed by Roy et al<sup>9</sup> and is discussed by Sellen and Fitzgerald.<sup>10</sup> The device is illustrated schematically in Figure 6 and consists of a heated filament nested within two concentric spherical grids. The filament is maintained at the spacecraft potential and the grids are biased positive with respect to the filament. Electrons emitted by the filament are accelerated radially outward by the electric fields existing between the filament and grids. These electrons form a cloud or virtual cathode near the outer grid radius. Some of the electrons in the cloud are collected by the grids, and the remainder escape to space. The difference between the escaping electron current and the net plasma collection current represents the emission current of the device.

The basis for the emissive probe design can be understood by considering the expression for space charge limited flow between two electrodes of arbitrary geometry

$$I = kV^{3/2} \quad (1)$$

where  $I$  is the space charge limited current, and  $V$  is the potential difference between the electrodes. In general the perveance  $k$  is a constant for a given electrode pair and is determined by the geometry and size of the electrodes. For the case of spherical geometries, the value of  $k$  is determined by the ratio

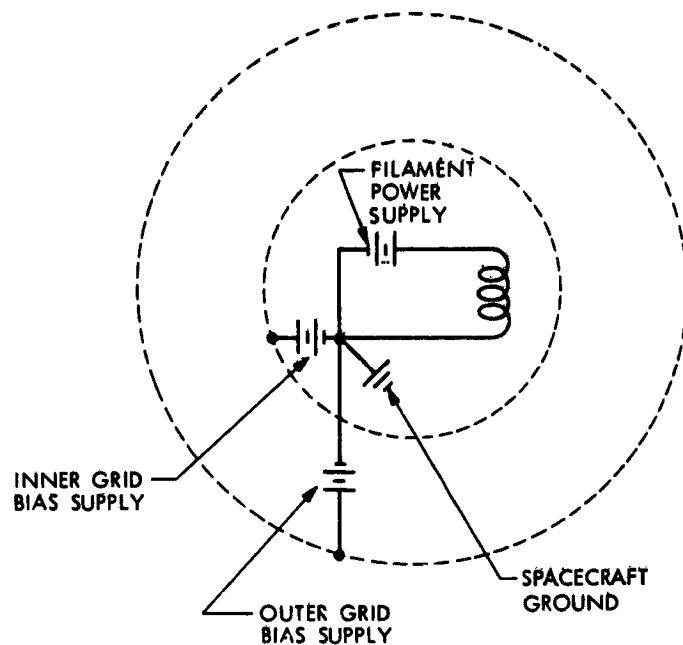


Figure 6. Schematic Diagram of the Emissive Clamp Device of Roy et al<sup>9</sup>

of the diameter of the outer and inner concentric spheres. In this case the outer spherical diameter is determined by the plasma Debye length  $\lambda_D$ , and the inner diameter is determined by the radius of the virtual cathode  $R_0$ . The variation of  $k$  with the diameter ratio is presented in Figure 7, where it is seen that for diameter ratios greater than about 20 the value of  $k$  remains fairly constant. However, for diameter ratios less than about 10 the value of  $k$  increases rapidly with decreasing diameter ratio. For an outer spherical collector diameter determined by the plasma Debye length  $\lambda_D$ , a reduction in the diameter ratio corresponds to an increase in the diameter of the inner spherical emitter. Thus, in order to achieve significant emission current levels at low spacecraft potentials, it is desirable to emit the electrons from a relatively large spherical cathode. The emissive clamp geometry accomplishes this by use of a set of nested spherical grids which surround a thermionic emitter. This arrangement produces a virtual cathode some 30 cm in diameter<sup>10</sup> and allows substantial emission currents to be drawn at relatively low spacecraft potentials.

Laboratory data obtained with the emissive clamp are presented in Figure 8 which shows the emission current as a function of negative spacecraft (filament) potential for various values of the voltage applied to the outer spherical grid. The data presented in Figure 8 indicate release currents on the order of tens of

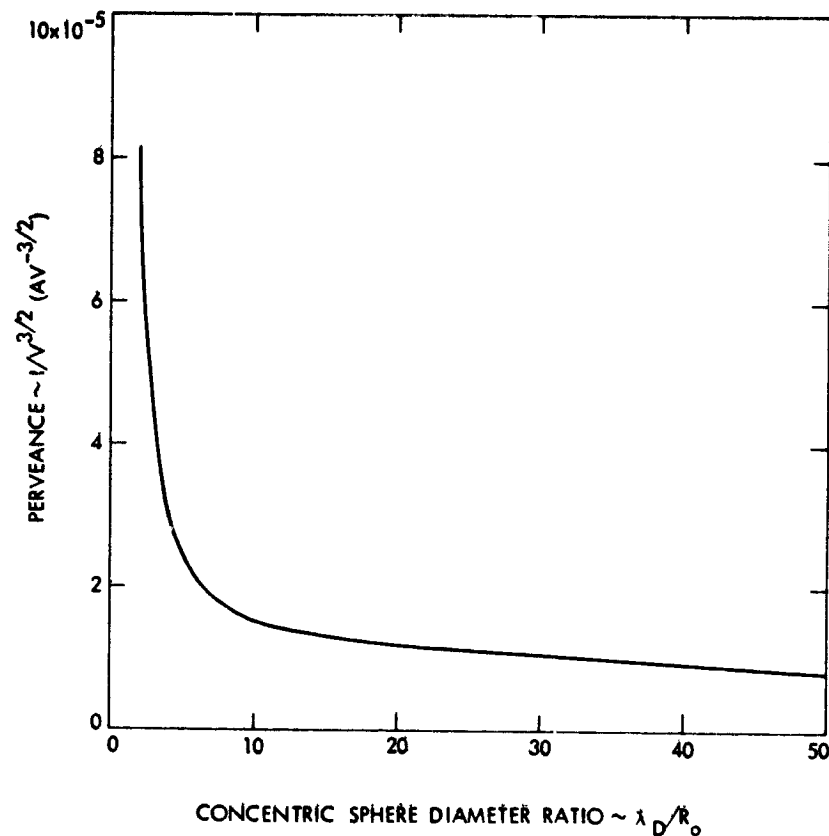


Figure 7. Variation of the Perveance  $k$  with Diameter Ratio for Space Charge Limited Electron Flow between Concentric Spherical Electrodes

microamperes can be achieved at spacecraft potentials on the order of 1 V. The spacecraft potential required for a given release current is dependent on the potential applied to the outer spherical grid, and this permits the spacecraft to be biased by varying the outer grid potential.

In order to obtain the emission current required for the JOP application while maintaining the spacecraft at the ambient plasma potential, the emissive clamp must be biased negative with respect to the spacecraft. An estimate of the biasing potential required to achieve the desired emission current was made by extrapolating the experimental data of Figure 8. These results are presented in Figure 9 which indicates the required biasing potential as a function of the outer grid potential. The extremes of Figure 9 correspond to a biasing power requirement in the 3.0 to 7.5 mW range. The total power requirement of the emissive clamp and

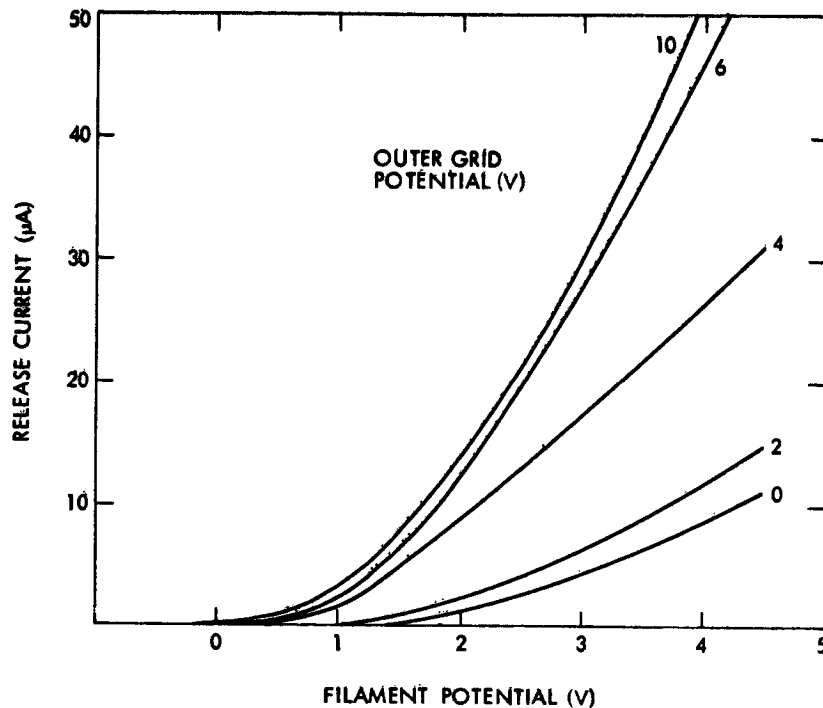


Figure 8. Release Current From Electron Emissive Clamp as a Function of Filament Potential. (From Reference 10.)

biasing supply is estimated at about 1.4 W, with most of the power consumed by the heated filament. The estimated system mass is 0.9 kg.

The electron emissive clamp is capable of providing relatively large emission current levels at low spacecraft potential. However, in order to maintain the spacecraft at the ambient plasma potential a biasing power supply must be used. In this sense the emissive clamp is less efficient than a biased thermionic emitter, since it requires power supplies for both the inner and outer grids as well as the filament and biasing supplies. However, in perhaps a more important application the emissive clamp may be used as a sensitive indicator of the sign of the spacecraft potential relative to the surrounding plasma. The current-voltage characteristics of the emissive clamp indicate that a relatively small potential difference between the spacecraft and its surroundings produces a measurable release current, and this feature allows the clamp to act as a sensitive switch for use in an active control system. In this application, the absence of any release current from the emissive clamp would indicate a positively charged spacecraft and could be used to signal positive ion release from a plasma device. Likewise, the

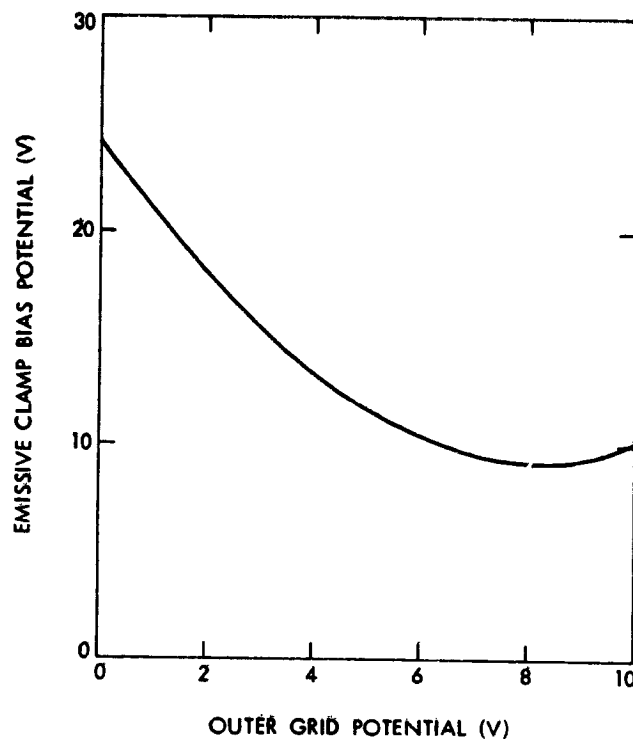


Figure 9. Emissive Clamp Bias Potential as a Function of Outer Grid Potential for a Release Current of 0.3 mA

presence of a release current from the clamp would indicate a negatively charged spacecraft and could be used to signal electron release from either an electron emitter or plasma device.

## 4.2 Electron Devices-High Energy

### 4.2.1 ELECTRON GUN

Electron guns have been used for many years on spacecraft and rockets designed to obtain scientific data such as magnetic field line length and shape, particle drift rates, and various other magnetospheric phenomena. In planning these experiments the problem of spacecraft charging caused by the electron gun operation was recognized, and steps were taken to minimize the potential excursions experienced by the spacecraft. For example, Hess et al<sup>11</sup> describe the use of an inflatable conducting collector which was deployed around the rocket to increase its collection area. The large collector area minimized the positive potential the rocket must attain in order to compensate for the current released by the electron gun.

More recently, Polychronopoulos and Goodall<sup>12</sup> have used an electron gun to control actively the potential of a rocket flown in Earth's ionosphere. In this particular application, the electron gun was used to maintain the rocket body at constant potential while making Langmuir probe measurements. The electron gun arrangement employed by these investigators is illustrated in Figure 10 and consists of the electron emitter, accelerating grid, and spacecraft potential sensing device. The electron accelerator grid is electrically attached to the spacecraft structure, and the heated filament can be biased with respect to the spacecraft. A floating probe or collector is used as a voltage reference, and the potential difference between the probe and spacecraft is sensed by a voltage follower. When a potential difference is sensed, the voltage follower develops a voltage at its output and this signal is inverted and amplified. When the potential difference is negative, indicating a negatively charged spacecraft, the amplified and inverted output of the voltage follower biases the filament negative and increases the release current. A positively charged spacecraft, on the other hand, results in a positive

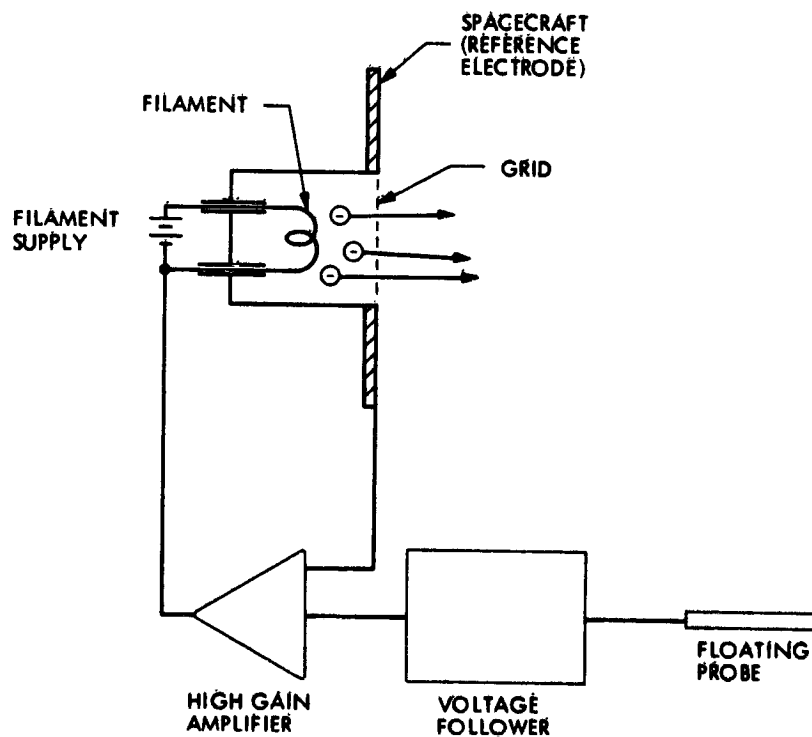


Figure 10. Schematic Diagram of the Electron Gun Configuration of Polychronopoulos and Goodall<sup>12</sup>

filament bias which suppresses the release current. The emitting filament used in their electron gun experiment was a commercially available light bulb with the glass cover removed. The filament power requirement is about 3 W, and laboratory tests indicated the electron gun could provide a release current of 0.2 mA with a filament bias of 10 V. The estimated mass of the electron gun configuration is about 0.5 kg.

Both laboratory tests and rocket flight tests demonstrated the ability of this system to maintain the spacecraft potential to within  $\pm 10$  mV of the floating probe potential. However, two potential problem areas were identified as a result of the rocket flight tests: (1) the floating probe must be deployed far enough away from the spacecraft to insure that it senses the undisturbed plasma and (2) the contact potential difference between the spacecraft and floating probe must be minimized.

The electron gun is a viable candidate for increasing\* the potential of a negatively charged spacecraft. The power and mass requirements of the device are fairly modest, and the system has been successfully employed to increase the potential of a negatively charged rocket in tests conducted in Earth's ionosphere. There are, however, two problems which are recognized and would require some modification of the control system used by Polychronopoulos and Goodall: (1) the system uses the undisturbed plasma floating potential as a reference voltage. In the Jovian environment the floating potential is variable and may be several kilovolts negative with respect to the plasma potential. Thus, this reference is unacceptable; and (2) the system suppresses electron release when the spacecraft potential exceeds the reference value, and this prevents biasing the spacecraft positive relative to the reference potential. The former problem can be overcome by use of an emissive floating probe or some other device for measuring the plasma potential. A solution to the latter problem would involve some additional control circuit logic. For example, if a positive spacecraft potential were desirable, the inverting function of the amplifier could be eliminated and the amplifier gain varied until the desired spacecraft potential was reached.

### 4.3 Plasma Devices-Low Energy

#### 4.3.1 HOLLOW CATHODE

Hollow cathodes have replaced the filament neutralizers in many ion thruster designs and have been operated successfully during the SERT II and ATS-6 flight tests. The low-density plasma produced by the hollow cathode discharge is a conducting medium which allows efficient coupling between the cathode and positive ion beam. This coupling permits an electron current equal in magnitude to the ion

\*An increase in potential is, in this context, an algebraic increase.

beam current to be extracted from the neutralizer plasma with a relatively low bias potential. Current neutralization of an ion beam in this manner prevents the spacecraft from charging to large negative potentials. In a different application, the hollow cathode plasma has been used to couple effectively a spacecraft to the ambient space plasma. In these recent tests, the cesium hollow cathode neutralizer on the ATS-6 satellite was used to prevent this spacecraft from charging to large negative potentials during eclipse periods. The fact that the cathode discharge plasma is quasineutral suggests the device might also be used for lowering the potential of a positively charged spacecraft. However, in this application one would expect larger coupling voltages (and hence higher power requirements) due to the low mobility of the heavier ions.

A sketch of the hollow cathode is presented in Figure 11. The device consists of a cylindrical cavity with an orifice located at the downstream end. The upstream end is attached to a valve or vaporizer which controls the flow of a gas such as mercury, cesium, argon, or xenon.\* An anode or keeper electrode is located downstream of the cathode orifice, and an electrical discharge between these electrodes produces the low-density plasma. The plasma acts as a good conductor and electron emission currents on the order of amperes can be achieved at a coupling or biasing potential on the order of a few volts. The steady-state power requirements of ion thruster hollow cathodes are typically 2-10 W for the keeper power supply and 3 W for the bias supply. In addition, a heater power requirement of about 30 W is generally required for startup. The mass of the ATS-6 neutralizer assembly is about 45 g, and the estimated xenon gas required for 1000 hr of hollow cathode operation is 25 g. Hollow cathodes using mercury gas have been operated in laboratory tests for as long as 20,000 hr,<sup>13</sup> and cesium and mercury cathodes have accumulated many operational hours in space. The mercury hollow cathodes on the SERT II spacecraft have been restarted several hundred times and remain fully operational after some 6 years in space.<sup>14</sup>

There remains another aspect of operating a plasma device, such as a hollow cathode or an ion thruster, which may ultimately dictate their use for obtaining meaningful spacecraft potential control. Spacecraft charging tests conducted with the filament neutralizer on the ATS-5 spacecraft indicated that although this device could reduce the potential to a near-zero value, a potential barrier surrounded the spacecraft.<sup>15</sup> The effect of this barrier was to prevent the low-energy plasma electrons from reaching the particle detectors on the spacecraft. The use of the ATS-6 ion thruster, on the other hand, successfully discharged the spacecraft and reduced substantially the potential barrier effect. These results suggest the

---

\*For spacecraft charging applications an inert, noncondensable gas such as argon or xenon is desirable in order to prevent contamination of the cold spacecraft surfaces.

beam plasma produces a space charge neutralization effect which affects a reduction in the potential barrier height. Operation of the hollow cathode may well produce the same result.

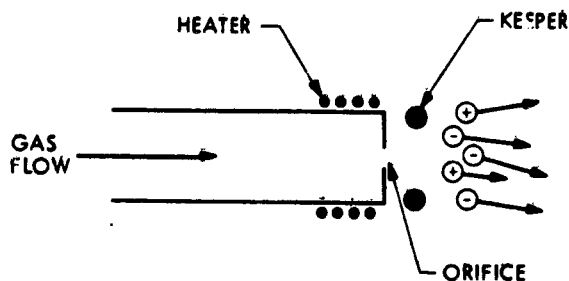


Figure 11. Schematic Diagram of a Hollow Cathode

#### 4.4 Plasma Devices-High Energy

##### 4.4.1 PLASMA GUN

Among the various types of plasma guns, the electron bombardment ion thruster is probably best suited for use as a high-energy plasma source for active spacecraft potential control. This type of source has been operated successfully in space and has been fabricated and tested in a variety of sizes ranging from less than a centimeter to 1.5 m in diameter. The SCATHA satellite<sup>16</sup> will employ a 2-cm diameter xenon ion source for use in spacecraft charging control experiments.

A schematic diagram of an electron bombardment ion source is presented in Figure 12. The device consists of a hollow cathode, anode, and accelerating electrodes. Electrons produced in the hollow cathode discharge are used to ionize the gas atoms as a result of collisions, and the collision probability is increased by use of a magnetic field arranged parallel to the thruster axis. Some of the ions produced in the discharge chamber drift toward the accelerating electrodes and are drawn out to produce the high-energy ion beam. To prevent excessive charging of the spacecraft on which the ion source is mounted, an electron source is located downstream of the accelerator system. The source of the neutralizing electrons can be either a heated filament or hollow cathode neutralizer. The quasineutral beam acts as a good conductor and assumes a potential near that of the environment. This allows the spacecraft to be biased by controlling the emission current of the neutralizer. A reduction in neutralizer emission current causes the spacecraft to charge negatively, while an increase in emission current

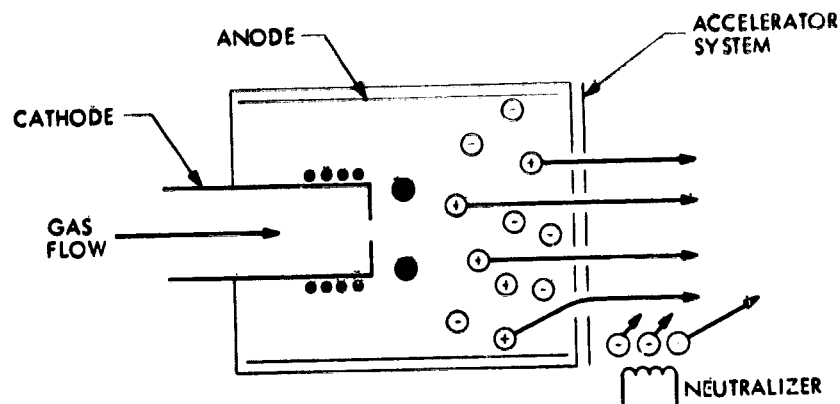


Figure 12. Schematic Diagram of an Electron-Bombardment Ion Source

causes the spacecraft to charge positively. The ability of the ion thruster to increase the potential of a negatively charged spacecraft has been demonstrated in the ATS-6 flight tests.<sup>15</sup> However, attempts to bias a spacecraft positive with respect to the surrounding plasma have not been successful in either laboratory or flight tests.<sup>17</sup> The reason for these failures is thought to be due to the interaction between the ion beam and spacecraft caused by the presence of the charge exchange plasma produced downstream of the accelerator system. Mounting the plasma source on a boom should substantially reduce this interaction, however, since the plasma density is inversely proportional to the square of the distance from a point source.

The steady-state power and mass requirements of the plasma sources are substantially higher than those for an electron emitter. The large power requirements reflect the additional energy required to ionize the neutral gas atoms as well as energy loss mechanisms, such as recombination and radiation, which occur within the ionization chamber. The higher mass requirement is, of course, due to the increased power supply requirements, in addition to the mass of the expellant and its storage and control system.

##### 5. POWER AND MASS ESTIMATES

The estimated power and mass requirements of the charged particle release devices are presented in Table 1. The devices are arranged in the table according to increasing complexity which generally corresponds to increasing power and mass penalties as well as attractiveness as a release device. The majority of the

Table 1. Estimated Power and Mass Requirements

Device	Power	Mass	Comments
Electron Field Emitter	0.2 W	0.2 kg	Possible Handling and Launch Problems
Electron Thermionic Emitter	0.5 W	0.3 kg	Flight Experience. Demonstrated Limited Potential Control Capability on ATS-5.
Electron Emissive Clamp	1.4 W	0.9 kg	Laboratory Tested.
Electron Gun	3.5 W	0.5 kg	Flight Experience Both as a Control Device and Diagnostic Tool.
Plasma Hollow Cathode	13 W	1.6 kg	Flight Experience. Demonstrated Potential Control Capability on ATS-6.
Plasma Gun	25 W	7.3 kg	Flight Experience, Used as a Potential Control Device on SERT II and ATS Spacecraft.

data presented in Table 1 were taken from hardware and design information available in the literature. In those instances where no data were available, the power and mass requirements were calculated based on either the experimental or theoretical emission current characteristics of the device. The power estimates for the hollow cathode were based on experience with ion thruster hollow cathode designs, and these estimates may therefore be overly conservative since ion thruster cathode emission currents are on the order of amperes, while the present application requires an emission current on the order of a milliampere. The requirements shown for the plasma gun were taken from the SCATHA ion source design goals, and it is interesting to note that a significant fraction of the power requirement of this device is consumed by the hollow cathode. Hence the development of an efficient, low-power hollow cathode would greatly enhance the competitive positions of both the hollow cathode and plasma gun devices.

The mass estimates presented in Table 1 include the release device and associated power supplies, and in the case of the electron devices the mass of a support boom is included. The mass estimates for the plasma devices also include a quantity of xenon gas sufficient to provide 1000 hr of continuous operation, as well as the gas storage and flow control equipment.

## 6. SUMMARY AND CONCLUSIONS

Accurate determination of the charged particle distribution functions in Jupiter's magnetosphere will require an active potential control system on the Jupiter Orbiter spacecraft. A spacecraft in Jupiter's magnetosphere will generally tend to charge negatively with respect to the surrounding plasma, and this dictates a net electron release current in order to increase the spacecraft potential. This current requirement can be met by use of a thermionic electron source or a plasma device.

As a result of this preliminary investigation, the following general conclusions can be drawn concerning the selection of a charged particle release device for use in an active spacecraft potential control system:

(1) Electron release devices have the lowest power and mass requirements and are simpler, but flight experience suggests they may not be as effective as plasma devices in controlling spacecraft potential. Their capability of discharging the spacecraft is apparently degraded by the presence of differentially charged areas of the spacecraft, and this dictates the following design considerations:  
(a) Eliminate differential charging by designing an equipotential spacecraft, and  
(b) mount the emitter sufficiently far from the spacecraft to minimize the interaction between the two.

(2) Plasma devices have higher power and mass penalties associated with them, but they are more flexible than electron emitters since they provide the capability of releasing charge carriers of either sign.

(3) The selection of a charged particle release device for use with an active potential control system will ultimately reflect a compromise between the mission science objectives, spacecraft conductivity, and the power and mass requirements of the devices.

(4) Either type device may be considered as a potential science instrument for performing plasma diagnostic studies, since they are capable of varying the potential of the entire spacecraft.

## References

1. Whipple, E.C., Jr. (1976) Observation of photoelectrons and secondary electrons reflected from a potential barrier in the vicinity of ATS-6, J. Geophys. Res. 81(No. 4):715-719.
2. Goldstein, R., and Divine, N. (1976) Plasma distribution and spacecraft charging modeling near Jupiter. Paper presented at the USAF/NASA Spacecraft Charging Technology Conference, Colorado Springs, Colo.
3. Grard, R.J.L. (1976) The multiple applications of electron emitters in space. Paper presented at the USAF/NASA Spacecraft Charging Technology Conference, Colorado Springs, Colo.
4. Bartlett, R.D., DeForest, S.E., and Goldstein, R. (1975) Spacecraft charging control demonstration at geosynchronous altitude. Paper presented at the AIAA 11th Electric Propulsion Conference, New Orleans, La.
5. Grard, R.J.L. (1976) Spacecraft charging control by field emission, J. Geophys. Res. 81(No. 10):1805-1806.
6. Grard, R.J.L. (1975) Spacecraft potential control and plasma diagnostic using electron field emission probes, Space Science Instrumentation 1:363-376.
7. Cybulski, R.J., et al (1965) Results from SERT I Ion Rocket Flight Test, NASA Tech. Note D-2718.
8. Grard, R., et al (1975) Spacecraft potential control and plasma diagnostics in the magnetosphere. Experiment proposed for the second Ariane development flight, Space Plasma Physics Division, European Space Agency.
9. Roy, N.L., Komatsu, G.K., and Ogawa, H.S. (1972) An emissive potential "clamp" for spacecraft equilibration, TRW Document No. 22322-6001-R0-00.
10. Sellen, J.M., Jr., and Fitzgerald, D.J. (1975) Design considerations in the creation and maintenance of electrostatic cleanliness for solar electrically propelled spacecraft. Paper presented at the AIAA 11th Electric Propulsion Conference, New Orleans, La.
11. Hess, W.N., et al (1971) Artificial auroral experiment: Experiment and principal results, J. Geophys. Res. 76(No. 25):6067-6081.
12. Polychronopoulos, B., and Goodall, C.V. (1973) A system for measuring and controlling the surface potential of rockets flown in the ionosphere, in Photon and Particle Interactions with Surfaces in Space, R.J.L. Grard, Ed., D. Reidel Publ. Co., Dordrecht-Holland.
13. Hudson, W.R., and Banks, B.A. (1973) An 8-cm electron bombardment thruster for auxiliary propulsion. Paper presented at the AIAA 10th Electric Propulsion Conference, Lake Tahoe, Nev.
14. Kerlake, W.R. (1976) Status of SERT II ion thrusters and spacecraft-1976. Paper presented at the AIAA International Electric Propulsion Conference, Key Biscayne, Fla.
15. Goldstein, R., and DeForest, S.E. (1976) Active control of spacecraft potentials at geosynchronous orbit, in Progress in Astronautics and Aeronautics 47, A. Rosen, Editor, American Institute of Aeronautics and Astronautics, New York.

16. McPherson, D. A., Cauffman, D. P., and Schober, W. R. (1975) Spacecraft charging at high altitudes: SCATHA satellite program, J. Spacecr. Rockets 12(No. 10):621-626.
17. Worlock, R., et al (1973) Measurement of ion thruster exhaust characteristics and interaction with simulated ATS-F spacecraft. Paper presented at the AIAA 10th Electric Propulsion Conference, Lake Tahoe, Nev.

**Contents**

1. Introduction	168
2. Instability Excitation	169
3. Comparison of Burst Fluxes With Magneto- spheric Substorm Fluxes	171
4. Conclusions	173
References	173

## 9. Nuclear Burst Plasma Injection into the Magnetosphere and Resulting Spacecraft Charging

A. L. Pável  
Air Force Geophysics Laboratory  
Bedford, Mass.

J. A. Cipolla, M. B. Silevitch, and K. I. Golden  
Northeastern University  
Boston, Mass.

### Abstract

The passage of debris from a high altitude (>400 km) nuclear burst over the ionospheric plasma is found to be capable of exciting large amplitude whistler waves which can act to structure a collisionless shock. This instability will occur in the loss cone exits of the nuclear debris bubble, and the accelerated ambient ions will free-stream along the magnetic field lines into the magnetosphere. Using Starfish-like parameters and accounting for plasma diffusion and thermalization of the propagating plasma mass, it is found that synchronous orbit plasma fluxes of high temperature electrons (near 10 keV) will be significantly greater than those encountered during magnetospheric substorms. These fluxes will last for sufficiently long periods of time so as to charge immersed bodies to high potentials and arc discharges to take place. Synchronous orbit satellites expecting to operate in a high latitude, high altitude nuclear burst environment should be designed against this effect as well as the radiation encountered.

## 1. INTRODUCTION

Turbulent coupling between the ejected debris plasma and background air plasma of a high-altitude nuclear burst appears capable of bringing about electron streaming to high altitudes. In the presence of the compressed magnetic field which can penetrate the debris bubble, plasma turbulence takes the form of large amplitude whistler waves. These waves can couple the background air plasma with the expanding debris plasma. Hot electrons are acquired and some have sufficiently large velocities to escape along the distended field lines. The nonlinear wave-resonant particle interactions produce anomalous resistivity whose scale length determines the extent of magnetic field penetration into the bubble which, in turn, determines the rate of escape of  $\beta$  and plasma electrons.

Superalfvénic debris plasma can escape directly through loss cone exits in the debris bubble since, in general, the cylindrical axis of the bomb casing is not initially aligned with the direction of the geomagnetic field. The more perpendicular the cylindrical axis is to the field lines, the greater the number of such escape particles. Their superalfvénic velocities suggest the formation of parallel collisionless shock waves ( $V_{\text{shock}} \parallel B$  - geomagnetic field). Studies<sup>1, 2</sup> reveal that such shock fronts are structured by turbulent whistler modes which couple the incoming background air plasma to the shocked debris plasma. Air plasma can therefore be picked up by the loss cone debris and accelerated to high altitudes.

The presence of a magnetic field has a significant effect on shock wave structure. Gradients in the magnetic field give rise to electron currents that can drive ion acoustic waves unstable and increase the effective collision frequency<sup>(3, 4)</sup> (this dictates the penetration depth of the compressed magnetic field into the debris bubble, so that the rate of escape of debris and air electrons is profoundly affected). When propagation is perpendicular to the magnetic field, the magnetic field can inhibit the electrons from shorting out ion plasma oscillations for wavelengths long compared with the electron gyroradius<sup>5, 6, 7, 8, 9, 10</sup> and wavelengths short compared with the electron gyroradius.<sup>11, 12</sup> Interactions between the ion beam mode and the electron Bernstein modes generate instabilities which are stabilized by electron heating, resonance broadening, or ion trapping. For oblique or parallel propagation, interactions of whistler waves with ion acoustic beam modes<sup>13</sup> or ion-cyclotron beam modes<sup>1, 2</sup> are likely to be important, and the existence of whistlers depends upon the presence of a magnetic field.

An instability found to be especially attractive as a collisionless mechanism for pickup and heating of air electrons is the ion cyclotron beam mode-whistler mode (current-free) instability that Golden<sup>1, 2</sup> found to be operative along the field lines and particle trajectories issuing directly from the loss cone exits.

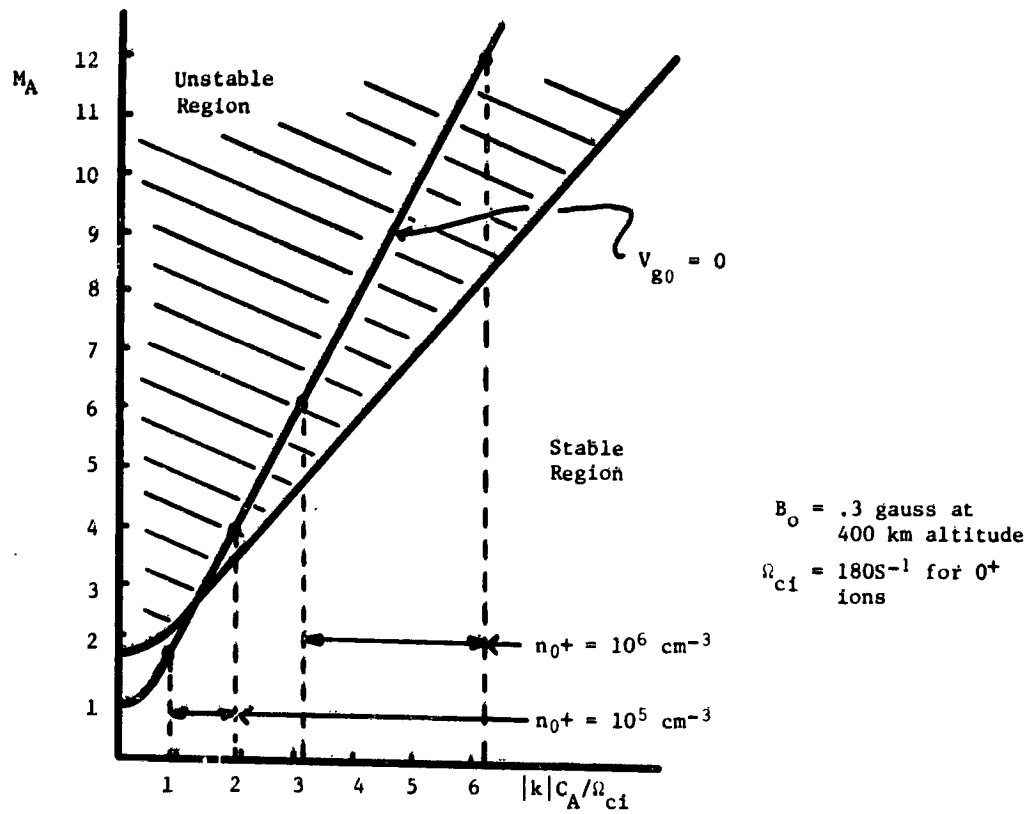
The collisionless shock waves can be modeled as Mott-Smith layers of interpenetrating unshocked (background air) and shocked (thermalized debris-air piston) flows, so that these layers are natural environments for streaming instabilities.

Recent linear dispersion investigations of parallel shock layers<sup>2</sup> which form ahead of the debris plasma issuing from the loss cone exits reveal that, for a given Mach number  $M_A > M^* = 2.77$  ( $M_A = V_u/C_A$ ,  $V_u$  = shock velocity,  $C_A$  = Alfvén speed in unshocked plasma), the shocked hot ion cyclotron beam mode can always drive unstable a particular whistler mode which, in the rest frame of the shock front, is stationary near the leading edge. An analysis of the shock interior reveals that the shock Mach number determines the portion of the shock thickness in which unstable whistlers are stationary in the shock rest frame. For  $M_A = 2.77$ , such modes may stand only at the leading edge, whereas for stronger shocks ( $M_A > 2.77$ ), they may stand at all points between the leading edge and some interior point which is dependent on shock strength. For very strong shocks ( $M_A \gg 1$ ), fully one-third of the shock thickness is filled with these modes, which can therefore grow to large amplitude and couple the quiescent background air plasma to the expanding debris-air piston.

## 2. INSTABILITY EXCITATION

The number of such debris particles which enter a loss cone exit depends critically on the mass and orientation of the bomb casing just prior to the burst. In the loss cone corridor, the debris plasma drives a shock wave. This shock is structured by unstable whistler waves which stand at its leading edge. To verify that these whistler modes can grow to sufficiently large amplitude to scatter incoming air ions (as viewed in the reference frame of the shock front) the following analysis is performed: During daylight burst conditions the density of oxygen ions is  $n_o \sim 10^5 - 10^6$ , the larger value reflecting maximum sunspot activity. For an ambient field strength  $B \sim 0.3$  gauss, this corresponds to an Alfvén speed  $C_A \sim 163 - 516$  km/sec in the ambient air plasma.

For typical initial casing velocities of from 500 km/sec to 2000 km/sec, the initial Alfvén Mach numbers are from 1.96 to 12.22. A summary of the spectrum of stationary unstable leading edge whistlers, based on the whistler dispersion relation,<sup>14</sup> is given in Figure 1. It is seen there that a broad range of wave numbers can grow to large amplitude during daytime ( $n \sim 10^6 \text{ cm}^{-3}$ ) bursts. To investigate whether these modes can achieve these large amplitudes in the loss cone exit, we must calculate the growth rate of these unstable waves. For simplicity we choose  $|k|C_A/\Omega_{ci} = 2$  for which  $M_A = 4.12$ , indicating a realistic initial debris velocity of  $u = 674$  km/sec. In this case the calculated linear growth rate



	1,000 km/sec	2,000 km/sec
$n_{O^+} = 10^6 \text{ cm}^{-3}$ $C_A = 164 \text{ km/sec}$	$M_A = 6.1$ $\frac{k C_A}{\Omega_{ci}} = 3.05$	$M_A = 12.2$ $\frac{k C_A}{\Omega_{ci}} = 6.1$
$n_{O^+} = 10^5 \text{ cm}^{-3}$ $C_A = 516 \text{ km/sec}$	$M_A = 1.94$ $\frac{k C_A}{\Omega_{ci}} = .9$	$M_A = 3.88$ $\frac{k C_A}{\Omega_{ci}} = 1.94$

Figure 1. Summary of Unstable Leading Edge Whistlers

for leading edge modes, from the whistler dispersion relation,<sup>14</sup> is  $\gamma = 167\eta$  where  $\eta$  is shock strength expressed as the ratio of shocked to unshocked densities. For  $l = 500$  km and  $\eta = .2$  at the shock leading edge, we find  $\gamma l/u \approx 10$ , indicating 10 e-folding times pass as the shock traverses 500 km of the loss cone corridor. This  $|k| = 2\Omega_{ci}/C_A$  unstable whistler mode can grow to sufficiently large amplitude after traveling 500 km along the loss cone corridor to pick up background air plasma. The air electrons are rapidly accelerated by ensuing ion-electron electrostatic instabilities. Since the calculation is based on the lower bound of  $M_A$ , it is clear that 10 e-folding times in 500 km is a conservative estimate since stronger shocks will have larger growth rates.

### 3. COMPARISON OF BURST FLUXES WITH MAGNETOSPHERIC SUBSTORM FLUXES

In the past few years there has been considerable concern over the phenomena of synchronous orbit satellites charging to high potentials as a result of magnetospheric substorms.<sup>15</sup> These substorms consist of the injection of high energy plasma from the earth's magnetotail into the region of synchronous orbit. Those portions of a satellite subject to the high energy plasma will charge to a potential several times the electron energy, while other portions of the satellite will remain at ground potential. Potentials near ground are maintained by photoelectron emission from illuminated surfaces on the spacecraft or by contact with the ambient low energy plasma.

During eclipse photoelectron emission disappears, and during a substorm the ambient low energy plasma flux is strongly dominated by the injected high energy plasma. The most damaging discharges probably occur between shadowed spacecraft components influenced by substorm plasma and illuminated components at ground potential. When the discharge passes through electrical circuitry between the components, damage can result. Electromagnetic interference can also result from surface discharges and considerable surface deterioration can be caused by arcing.

The following discussion will be an assessment of the possible spacecraft charging effects which can result from the large scale transport of ionospheric plasma to synchronous orbit by a nuclear burst. The plasma instability just discussed demonstrates a mechanism for structuring a collisionless shock wave. This mechanism will operate during a high altitude nuclear burst as the expanding nuclear debris passes over the stationary ionospheric plasma. Through the interaction of large amplitude whistler mode waves, plasma will be picked up by the collisionless shock and accelerated into the magnetosphere.

Using nuclear burst parameters for a Starfish-like (nominally 1.5 megaton) burst, <sup>16</sup> calculations <sup>14</sup> have conservatively estimated that near  $10^{27}$   $0^+$  ions would be carried by the shock when 1 percent of the total debris exits the loss cone. Depending on orientation, mass, and shape of the bomb casing, this number could be considerably higher. This number is reasonably estimated by the mass of debris which exits the loss cone, for ion pickup slows the debris piston and eventually shuts off the pickup instability.

The total propagation time for the plasma mass from the burst point just above the earth's surface to synchronous orbit is tens of seconds and more than sufficient to have thermalization of the complete plasma mass at near the ion temperature as the mass slows and diffuses. <sup>17</sup>

The estimated pickup of  $10^{27}$   $0^+$  ions by the nuclear burst shock wave would have an energy of approximately 10 keV at reasonable shock velocities. The demands of plasma neutrality would quickly accelerate an equal number of electrons which would thermalize with energies equal to or greater than the ion energy. <sup>17</sup> At the loss cone exits these  $10^{27}$  electrons with energies of 10 keV would be in a cylindrical volume of approximately  $2 \times 10^{21}$   $\text{cm}^3$ , assuming 1 percent of the nuclear burst bubble as comprising the loss cone exit and the plasma pickup region being several hundred kilometers in extent. These numbers and energies translate to an omnidirectional flux at the loss cones of  $J_o \approx 3 \times 10^{15}$  electrons/ $\text{cm}^2$ -sec.

The calculation of fluxes at higher altitudes than the burst altitude follows directly from the Liouville Theorem that a differential intensity along particle trajectory is constant ( $j_o = j_f$ ). Conservation of magnetic flux ( $B_o dA_o = B_f dA_f$ ) and solid angle area ( $dA_o d\Omega_o = dA_f d\Omega_f$ ) yields the following relation between initial omnidirectional flux ( $J_o$ ) and final omnidirectional flux ( $J_f$ ); from  $\left( J = \int_{4\pi} j d\Omega \right)$  and

$$\left( J_f = \int_{4\pi} j_f d\Omega_f = \int_{4\pi} j_o \frac{dA_o}{dA_f} d\Omega_o = \frac{B_f}{B_o} \int_{4\pi} j_o d\Omega_o \right)$$

the relationship  $\left( J_f = \frac{B_f}{B_o} J_o \right)$  is obtained.

During a magnetospheric substorm, many of the plasma injections observed are characterized by omnidirectional electron fluxes near  $10^9$  electrons/ $\text{cm}^2$ -sec. <sup>18, 19</sup> The previous calculations would yield omnidirectional electron fluxes from high altitude nuclear bursts of approximately  $J_f \approx 10^{13}$  electrons/ $\text{cm}^2$ -sec at synchronous orbit. It is clear that these fluxes are significantly greater than those encountered during a magnetospheric substorm and would pose a strong spacecraft charging environment.

While the duration of the nuclear burst and resulting injection will be on the order of seconds and therefore much shorter than a typical substorm, studies<sup>20</sup> indicate the charging process takes only fractions of a second.

## 1. CONCLUSIONS

The atmospheric nuclear burst environment appears to present the potential for spacecraft charging effects at synchronous orbits. The calculated fluxes, and energies of the injected electrons are greater than those encountered during substorms, and which have been observed to cause spacecraft charging.

These calculations contain many approximations, but preliminary results indicate that it may be expected that synchronous orbit satellites under certain nuclear burst conditions would find themselves subject to a short, but intense, period of spacecraft charging. Potentials in the tens of kilovolts are suggested. The resulting transient charging and arc discharging should be a part of the design criteria of any spacecraft expected to survive a situation where high altitude nuclear bursts are involved.

## References

1. Golden, K. I., Linson, L. M., and Mani, S. A. (1973) Ion streaming instabilities with application of collisionless shock wave structure, Phys. Fluid 16:2319.
2. Cipolla, J. W., and Golden, K. I. (1975) Role of streaming plasma instabilities in parallel shock wave structures, Phys. Lett. 51A:251.
3. Jackson, J. D. (1960) Longitudinal plasma oscillations, Plasma Phys. (J. Nuclear Energy, Part C) 1:171.
4. Stringer, T. E. (1964) Electrostatic instabilities in current-carrying and counterstreaming plasmas, J. Nuclear Energy, Part C 6:267.
5. Papadopoulos, K., Davidson, R. C., Dawson, J. M., Haber, I., Hammer, D. A., Krall, N. A., and Shanny, R. (1971) Heating of counterstreaming ion beams in an external magnetic field, Phys. Fluids 14:849.
6. Landau, R. W. (1972) Counterstreaming ion instability for arbitrary angles, Phys. Fluids 15:1991.
7. McBride, J. B., and Ott, E. (1972) Electromagnetic and finite  $\beta_e$  effects on the modified two stream instability, Phys. Lett. 39A:363.
8. Ott, E., McBride, J. B., Orens, J. H., and Boris, J. P. (1972) Turbulent heating in computer simulations of the modified plasma two stream instability, Phys. Rev. Lett. 28 48.

9. McBride, J. B., Ott, E., Boris, J. P., and Orens, J. H. (1972) Theory and simulation of turbulent heating by the modified two stream instability, Phys. Fluids 15:2367.
10. Cipolla, J. W., and Golden, K. I. (1975) Crossfield magnetosonic two stream instability, Can. J. Phys. 53:1022.
11. Lampe, M., Mannheimer, W. M., McBride, J. B., Papadopoulos, K., Orens, J. H., Shanny, R., and Sudan, R. N. (1972) Theory and simulation of the beam cyclotron instability, Phys. Fluids 15:662.
12. Forslund, D., Morse, R., Nielson, C., and Fu, J. (1972) Electron cyclotron drift instability and turbulence, Phys. Fluids 15:1303.
13. Lindman, E. L., and Drummond, W. E. (1971) Studies of Oblique Shock Structure, Report ARA-28, Austin Research Associates, Inc., Austin, Texas.
14. Cipolla, J. W., Golden, K. I., Pavel, A. L., and Silevitch, M. B. (1976) Nuclear Burst Induced Shock Wave Modeling of Energetic Electron Injection into the Magnetosphere, AFGL-TR-76-0186, AF Geophysics Laboratory, Bedford, Mass.
15. Rosen, A. (1975) Spacecraft Charging: Environment induced anomalies, AIAA Paper 75-91.
16. Zinn, T., Hoerlin, H., and P. tachek, A. (1966) Motion of bomb debris following the Starfish test, Radiation Trapped in the Earth's Magnetic Field, Edited by Billy McCormac (Gordon and Breach, New York).
17. Biskamp, D. (1973) Collisionless shock waves in plasmas, Nuclear Fusion, 13:719.
18. Sharp, R. D., and Johnson, R. G. (1972) The behavior of low-energy particles during substorms, Planet. and Space Sci. 20(No. 9):1433.
19. DeForest, S. F., and McIlwain, C. E. (1971) Plasma clouds in the magnetosphere, J. Geophys. Res. 76(No. 16):3587.
20. Rothwell, P. L., Rubin, A. G., Pavel, A. L., and Katz, I. (1976) Simulation of the plasma sheath surrounding a charged spacecraft, Proc. of Conference on Spacecraft Charging by Magnetospheric Plasmas, AIAA.

## Contents

1. Introduction
  2. Principle of the Drag-Free and Accelerometric Satellites
  3. Perturbation Due to the Electrification of the Proof Mass
  4. The Cactus/D5B Experiment
  5. Detailed Calculation of the Proof Mass Charging Current
  6. Conclusion
- References

## 10. Electrification of the Proof Mass of a Drag-Free or Accelerometric Satellite

Rémy Juillerat and Jean-Pierre Philippon\*  
 Office National d'Etudes et de Recherches  
 Aérospatiales (ONERA)  
 92320 Chatillon, France  
 \*Centre d'Etudes et de Recherches de Toulouse

### Abstract

The exploitation of the data provided by the Cactus accelerometer, developed at ONERA, which makes up the payload of the D5B Castor Satellite of CNES (the French Space Agency) confirmed the existence of an electric current charging the proof mass under the influence of the magnetospheric protons, and revealed a periodic variation of this current, due to the passage of the apogee through the South Atlantic magnetic anomaly.

The paper presents the results of in-orbit measurements of this charging current, and those of calculations made for determining this current and its variations from data on proton flux at the satellite altitudes. The comparison of measured and calculated values shows that the calculation method is valid and precise enough to be used for drag-free or accelerometric satellites.

### 1. INTRODUCTION

A "drag-free" satellite<sup>1</sup> is essentially made of a proof mass protected from the surface forces acting on it and which are due to the slowing down created by the residual atmosphere as well as the various radiation pressures. The piloting system of the satellite controls the thrusters in such a way that the cage containing

the proof mass never comes into contact with it. The satellite trajectory is then in principle purely gravitational. In practice, the compensation by the thrusters of the surface forces is not perfect, the residue of compensation being due to internal perturbing forces acting on the proof mass and thus modifying the reference trajectory.

The structure of an accelerometric satellite<sup>2</sup> is similar, but the servo-control function takes place by the action of a force on the proof mass so that the latter is maintained in the vicinity of the cage center. The measurement of the internal forces developed by the servo-control then constitutes a measure of the sum of the surface forces acting on the satellite. The internal perturbing forces are also at the origin of the physical limitations pertaining to this type of instrument.

Electrification of the proof mass by proton and electron fluxes from the radiation belts makes up one of the main perturbations, all the more so as this electrification may increase with time and reach high levels.

So, during the definition of a drag-free or accelerometric satellite, it is important to be able to determine a priori the value that will take the current charging the proof mass in orbit so as to decide on the procedure to implement to compensate this effect.

The present paper gives the results of a comparison which has been made between this charging current as calculated for a particular orbital configuration, and the results of measurements obtained in orbit on a three-axis accelerometer (Cactus) making up the payload of the French satellite D5B-Castor.

## 2. PRINCIPLE OF THE DRAG-FREE AND ACCELEROMETRIC SATELLITES

Let us consider (Figure 1) a material sphere of mass  $m$  placed inside a cage fixed within a satellite. The mass of this satellite - including that of the proof mass - is  $M$ . The position of the proof mass center  $O_B$  is defined by the vector  $\vec{\xi}$  in a reference frame  $O_SXYZ$  linked to the satellite and such that  $O_S$  be at the center of mass of the satellite.

Let it be:

$\vec{F}_L$  the resultant of the internal forces of attraction of the proof mass by the satellite,

$\vec{F}_E$  the resultant of the surface forces acting on the satellite (atmospheric drag, radiation pressure),

$\vec{F}_P$  the thrust due to the thrusters, and

$\vec{G}_B$  and  $\vec{G}_S$  the local gravitational acceleration in  $O_B$  and  $O_S$ .

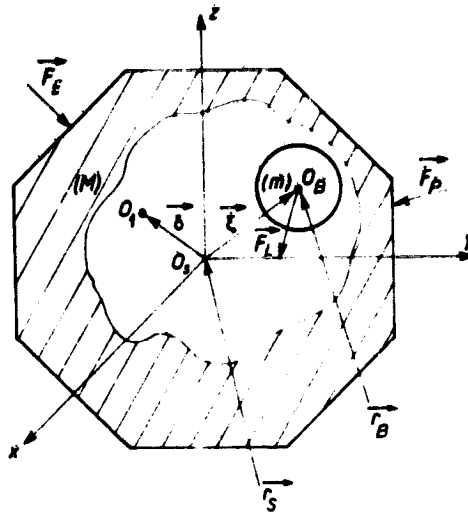


Figure 1. Drag-Free or Accelerometric Satellite Definitions

If  $\vec{r}_B$  and  $\vec{r}_S$  represent respectively the coordinates of  $O_B$  and  $O_S$  in an absolute frame of reference, the movements of the proof mass ( $m$ ) and the satellite alone ( $M - m$ ) are given by the equation of dynamics:

$$\frac{d^2 \vec{r}_B}{dt^2} = \vec{G}_B + \frac{\vec{F}_L}{m} \quad (1)$$

$$\frac{d^2 \vec{r}_S}{dt^2} = \vec{G}_S - \frac{\vec{F}_L}{M - m} + \frac{\vec{F}_E + \vec{F}_P}{M - m} \quad (2)$$

### 2.1 Drag-Free Satellite

If we suppress any link between proof mass and cage ( $\vec{F}_L = 0$ ), the trajectory of the proof mass is purely gravitational.

By piloting the satellite in such a way that, under the action of the thrusters, the amplitude of  $\vec{\xi}$  remains at any moment lower than a value  $\xi_M$  previously chosen, we have a satellite whose trajectory can also be characterized as purely gravitational, as it only differs from that of the proof mass by a distance almost equal to  $\xi_M$ , a distance always small as compared to the satellite dimensions.

But if a perturbing force  $\vec{f}$  remains between the two bodies, the true trajectory of the satellite departs from a purely gravitational trajectory and the metric

difference appearing after a time  $t$  between these two trajectories becomes equal to:

$$\Delta = \left| \int_0^t \frac{\vec{f}}{m} dt' dt'' \right| . \quad (3)$$

## 2. Accelerometric Satellite

Such a satellite is devoid of any propulsion means ( $\vec{F}_p = 0$ ), but a servo-control mechanism acts on the proof mass to maintain the points  $O_B$  and  $O_S$  in a single position (within the error of the servo-control). In general, considering the smallness of the forces, no material contact should exist between proof mass and cage and the liaison force  $\vec{F}_L$  is – for example – of electrostatic nature.

In these conditions  $\vec{r}_B - \vec{r}_S = 0$  and  $\vec{G}_B = \vec{G}_S$ .

Relations (1) and (2) then give:

$$\frac{\vec{F}_L}{m} = \frac{\vec{F}_E}{M} \quad (4)$$

The acceleration imposed on the satellite by the external forces – apart from gravity – is equal to the force of proof mass-cage liaison divided by the mass of the proof mass. Thus, the measurement of this liaison force  $\vec{F}_L$  makes it possible to know the resultant of external forces  $\vec{F}_E$ .

If an internal perturbing force  $\vec{f}$  is added to the force  $\vec{F}_L$  developed by the servo-control, the measure of the acceleration due to the external forces is then made false by a systematic error equal to  $\vec{f}/m$ .

## 3. PERTURBATION DUE TO THE ELECTRIFICATION OF THE PROOF MASS

In both systems that have been just described, the perturbation (of the trajectory or of the force measurement) is directly given by the acceleration  $\vec{f}/m$  that the perturbing force would communicate to this proof mass alone.

These perturbing forces are of various natures and have already been the object of detailed studies<sup>3</sup> as well as of measurements in flight.<sup>4, 5, 6</sup> Among them the force provided by the defect of electric neutrality of the proof mass constitutes a perturbation that may become very important. In this case, the proof mass is subjected to an attracting force by the cage walls on which are induced electric charges whose sum is equal and of contrary sign to the charge carried by the proof

mass. Due to the spherical symmetry of the cage, this attraction is a central force around a point  $O_1$  (Figure 1), geometric center of the cage which we try to make as near as possible of center  $O_S$ . This perturbing force  $\vec{f}_E$  can be expressed by:<sup>3, 6</sup>

$$\vec{f}_E = m\beta Q^2(\vec{E} - \vec{\delta}) \quad (5)$$

where  $\vec{\delta} = \overrightarrow{O_S O_1}$  and  $\beta$  is a coefficient defined by the geometry of the instrument.

This force is thus proportional to the square of the electric charge carried by the proof mass.

This may have two very different origins.

(1) Electrification of internal origin which appears when the proof mass leaves its contact with the cage, a contact obtained either in the presence of gravity (on the ground) or under the action of a force obtained by remote control (in orbit). This electrification is due to the charges developed either by instantaneous potentials of the various electrodes of the cage or by the differences of the work functions of the materials making up the proof mass and the cage walls.

(2) Electrification of external origin due to the accumulation of charges penetrating into the satellite, originated by the high energy particles of the radiation belts.

The first kind of electrification may be minimized by appropriate technological means. The second appears as a current charging the proof mass whose order of magnitude is hardly predictable without a detailed study. Indeed, it is very difficult to know a priori if the proof mass charge will reach a prohibitive value within a few days or few years.

Though it is necessary, during the project of a drag-free satellite or an accelerometric satellite, to foresee the adequate means for discharging the proof mass, it is highly desirable that their optimization might take into account the maximum and minimum values of the electric current that will charge the proof mass in orbit.

## 1. THE CACTUS D5B EXPERIMENT

The Cactus accelerometer (in French: Capteur accélérométrique capacitif triaxial ultra sensible) has been designed and built by ONERA, and made up the payload of the French satellite Castor (D5B) placed in orbit on 17 May 1975. This satellite has been built and launched by CNES (The French Space Agency) who ensured the further exploitation of the instrumentation.

#### 1.1-Description of the Experiment

The Cactus accelerometer has a measuring range of  $\pm 10^{-5}$  g on each of its three axes. The sum of internal perturbations has been evaluated before launching at  $10^{-9}$  g. These values, as well as all the other characteristics, have been confirmed by the results obtained in orbit.<sup>5, 7</sup>

The core of the accelerometer is made by a proof mass in rhodium-plated platinum – whose mass is 550 g – placed in a cage forming with it a gap of 85  $\mu$ m (Figure 2). The force linking proof mass in cage is of electrostatic nature and is obtained by means of continuous voltages applied on three systems of electrodes distributed over three orthogonal axis. These voltages are made proportional to the relative displacement of the proof mass in the cage thanks to another set of electrodes realizing, on each axis, a capacitive measurement of position. The system functions by position servo-control of the proof mass and the measure of the voltages applied on the acting electrodes on each axis makes it possible, after preliminary calibration, to know the liaison force  $\vec{F}_L$  and thus to determine the sum of the external forces  $\vec{F}_E$  (Eq. (4)).

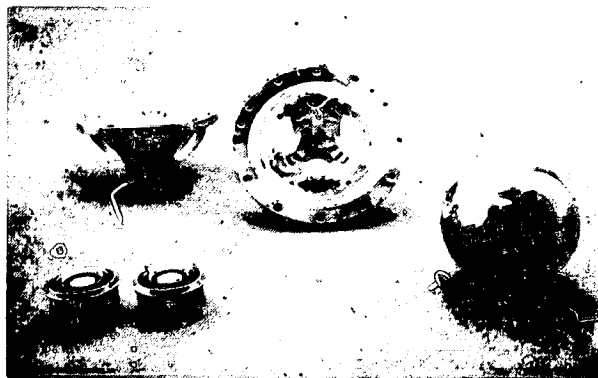


Figure 2. Cage, Proof Mass and Electrodes of the Cactus Accelerometer

The D5B/Cactus experiment aimed at:

- (1) ensuring qualification in orbital flight of the accelerometer,<sup>7</sup> and
- (2) providing scientific data on aeronomy.<sup>8</sup>

The orbit chosen was slightly excentric, with an inclination of  $30^\circ$ . The altitudes of apogee and perigee of the first orbit were respectively 1275 km and 277 km.

## 4.2 First Calculations of the Proof Mass Charging Current

At the same time as the studies for defining this experiment, theoretical and experimental studies<sup>9, 10, 11</sup> were performed with a view to attempt to determine the mean value of the proof mass charging current.

These works showed that:

- (1) the evolution of the proof mass charge is essentially due to the bombardment of the satellite by the magnetosphere electrons and protons; and
- (2) the interactions of these two types of particles with the satellite structure have widely different characteristics.

### 4.2.1 ELECTRONS

While crossing the materials of the satellite and the accelerometer cage, the primary electrons give rise to secondary electrons and to photons, part of which reach the proof mass and interact with it. The results are that electrons and photons circulate in both directions between proof mass and cage. The opposite fluxes of electrons are not equal, hence the existence of a charging current whose value and sign can be determined only by a detailed study.

### 4.2.2 PROTONS

Contrary to electrons, the protons crossing the matter do not generate secondary effects of any importance, and propagate practically in straight lines. The protons stopped within the proof mass are at the origin of a charge increase.

The work carried out at ONERA showed that:

- (1) the charging current is essentially due to the primary effect of the protons stopped by the proof mass; the presumed mean value of this current has been evaluated at  $(2 \pm 1) 10^{-11}$  Coulomb per day; and
- (2) only the electrons whose energy is about 4 MeV can give a perceptible charging current; by extrapolation above 4 MeV of the known values of the flux, the presumed electronic charging current has been evaluated at  $-1.7 10^{-12}$  Coulomb per day, as a mean value.

At the end of this study, the expected mean value of the charging current was thus near  $+2.10^{-11}$  Coulomb per day, or  $2.3.10^{-16}$  ampere.

The methods used to calculate this current, as well as the assumption adopted, are described in Section 5.

## 4.3 Determination in Orbital Flight of the Proof Mass Charging Current

The acceleration measured by the accelerometer when the satellite is near its apogee - where the atmospheric drag is negligible - and in the shadow of the earth - where the acceleration due to the sun radiation pressure disappears - constitutes a good measure of all the internal perturbations of the instrument, as the only error

of this measurement comes from the earth radiation pressure, which provides the satellite with an acceleration of the order of  $4 \cdot 10^{-10}$  g.

The existence of a proof mass charging current is well revealed by an increase with time of this acceleration and by the returns of the latter to its bottom level during each contact between proof mass and cage, obtained by remote control. But, moreover, systematic readings of these data have also revealed time periods of about 10 days, renewed every 38 days, and during which the charging current becomes weaker.

As an illustration, Figure 3 represents the values of the modulus of the acceleration measured by the accelerometer when the satellite is at a high altitude between the 10th of May and the 20th of August 1976. We can see on this figure the periods when this current weakens: they are the periods from 18th to 31st of May, from 25th of June to 8th of July and from 28th of July to 10th of August. Outside these, the charging current takes again a higher value characterized by the increase of the measured acceleration.

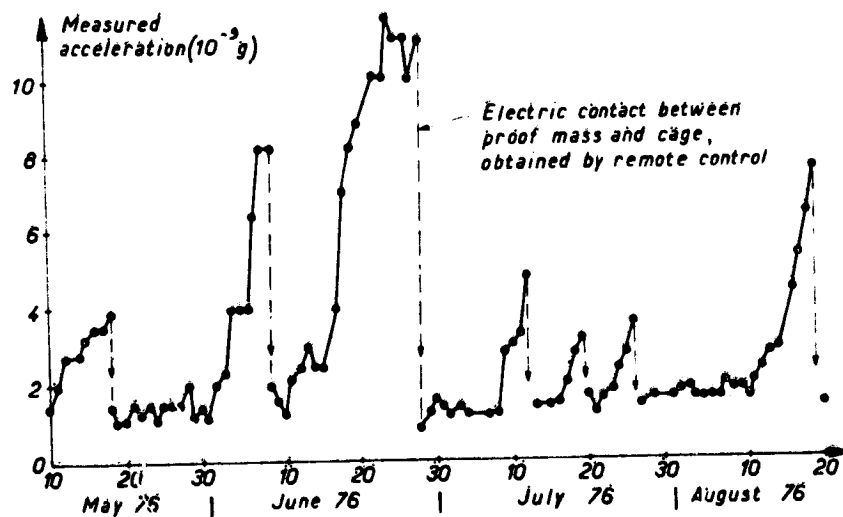


Figure 3. Acceleration Measured by Cactus at High Altitude

Various methods have been used to determine the charging current from the data transmitted by the satellite.<sup>6, 8</sup> These methods consist in identifying the various internal perturbations and the accelerations due to the external forces from a realistic modeling of these accelerations and by using the attitude data of the satellite. When the electric charge level becomes high enough, we consider

that the perturbation due to the charge constitutes the main term of the acceleration measured when the satellite is at a high altitude. Using Eq. (5) on the smoothed data then permits a simple but sufficiently precise calculation of  $Q$  and its time variation. For the application of Eq. (5), the knowledge of the values of  $\beta$  and  $\bar{\delta}$  is necessary. Coefficient  $\beta$  had been determined on the ground before launch and has a value of  $6.9 \cdot 10^{17} \text{ A}^{-2} \text{ s}^{-4}$ . The components of the  $\bar{\delta}$  vector have been measured in flight by a particular manoeuvre<sup>6</sup>; its modulus has the value  $2.16 \mu\text{m}$ .

These various methods gave coherent results which are as follows; expressed as a mean value of the charging current during the considered period of time:

-For periods with strong charging current:

- . From 28th of June to 8th of July 1975:  $2.1 \cdot 10^{-11}$  Coulomb per day ( $2.4 \cdot 10^{-16} \text{ A}$ )
- . From 3rd to 6th of November 1975:  $1.3 \cdot 10^{-11}$  Coulomb per day ( $1.5 \cdot 10^{-16} \text{ A}$ )
- . From 10th to 20th of June 1976:  $1.3 \cdot 10^{-11}$  Coulomb per day ( $1.5 \cdot 10^{-16} \text{ A}$ )
- . From 25 August to 5 September 1976:  $1.02 \cdot 10^{-11}$  Coulomb per day ( $1.2 \cdot 10^{-16} \text{ A}$ ).

-For periods with weak charging current:

- . From 23rd to 28th of June 1976: current lower than  $5 \cdot 10^{-13}$  Coulomb per day ( $5.8 \cdot 10^{-18} \text{ A}$ )
- . From 6th to 15th of September 1976:  $1.2 \cdot 10^{-12}$  Coulomb per day ( $1.4 \cdot 10^{-17} \text{ A}$ ).

## 5. DETAILED CALCULATION OF THE PROBE MASS CHARGING CURRENT

### 5.1 Interpretation of the Variations Observed on the Charging Current

We can see that the periods during which the charging current is strongly attenuated are centered on the dates when the apogee latitude is North and at its maximum value, that is  $30^\circ$ , a value corresponding to the orbit inclination. This important variation of the charging current may be explained by the following fact:

(1) the proton and electron fluxes decreasing rapidly with altitude, the charging current reaches a significant value only when the satellite is around its apogee; and

(2) due to the fact that the magnetic anomaly of South Atlantic which is characterized, at the altitudes where flies the satellite, by more intense particle fluxes centered over a point situated at about  $25^\circ$  latitude south and  $40^\circ$  longitude west (Figure 4), the charging current takes a high value each time the satellite flight crosses this zone.

Thus we can see that when the apogee latitude is around  $30^\circ$  south the satellite crosses this zone every day, while when the apogee is about  $30^\circ$  north this zone is avoided by the satellite.

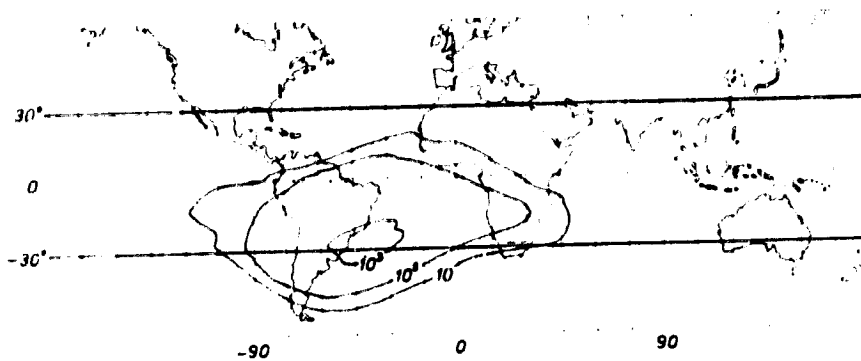


Figure 4. Proton Flux Contours  $-E > 100 \text{ MeV}$

This effect, which is a combination of the orbital movement with a geographic anomaly, is all the more marked as the orbit inclination is close to  $25^\circ$ , which is the case of the Castor satellite.

With a view to provide a quantitative support to this interpretation, studies previously carried out on the determination of the charging current have been repeated in order to evaluate the daily charge acquired by the proof mass during a complete-cycle of 38 days.

#### 4.2 Calculation of the Fluxes Received by the Satellite

Since 1972, when the first calculations of the charging current have been made, the description of the radiation belt has been refined and the extrapolation of the values of electron fluxes at energies higher than 4 MeV (see Section 4.2) appeared as having no meaning. This statement confirms that only the protons in period of normal activity are at the origin of the charging current.

Two methods are usually used for evaluating a flux received by a satellite during its useful life.<sup>12, 13</sup> If the mission duration is long enough, the experimenter may be interested only in the mean flux and the calculation consists in determining the probability for the satellite to pass within each volume element, tabulated in energy. Here the calculation requires more precision. Indeed, a satellite in low orbit, as D5B, is subjected to an intense particle bombardment only during rather short periods which correspond to the passage through the South Atlantic anomaly.

To calculate the proof mass charging current, we must be able in each point of the orbit to estimate the flux of incident protons. Account being taken of the drift of orbital parameters, ascending node and perigee argument, a calculation of the number of protons received every 24 hr seems sufficient and remains significant. To this end, each orbit is described step by step and every minute the

geographic coordinates (altitude, latitude, longitude) are transformed into geomagnetic coordinates ( $B, L$ ) that permit the consultation of the files of protons whose energies are higher 100 MeV (see Section 5.3).

Figure 5 gives as a function of time, from 3rd of June to 3rd of July, the omnidirectional mean fluxes of protons of an energy higher than 100 MeV, per square centimeter and per day, as well as the apogee latitude. The first curve illustrates well the north-south asymmetry of the radiation belt due to the South Atlantic anomaly at the altitude considered. The periodicity of this phenomenon makes it possible to extrapolate this flux curve before 3rd of June and after 3rd of July, as represented by a broken line on the figure,

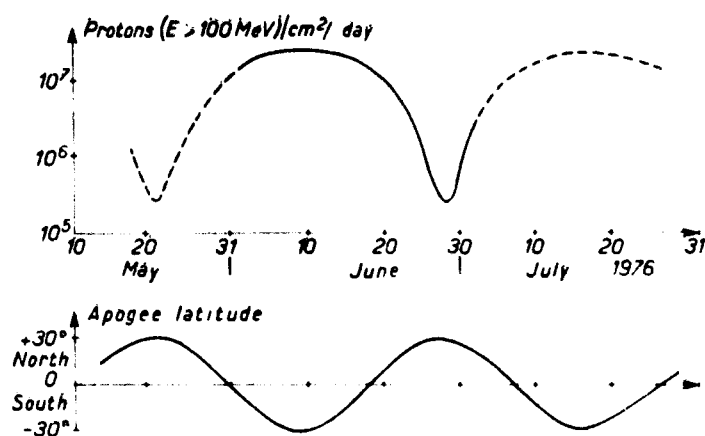


Figure 5. Isotropic Proton Flux Density Received by the Castor Satellite and Apogee Latitude at the Same Periods

### 5.3 Absorption of Protons by the Satellite Structure

The satellite shape is a regular polyhedron with 26 faces whose geometric center is at the center of mass and also at the center of the proof mass. A simple model of proton absorption by the satellite structure has thus been established by decomposing it into 26 equal solid angles. For each of these, the nature and the thickness of the various materials encountered by a particle moving on a straight line and reaching the center have been surveyed. Using the density of each material as a weighting parameter, these various thicknesses have then been converted in equivalent thicknesses of aluminum. These equivalent thicknesses vary from 270 mm (in a solid angle of  $4\pi/13$ ) to 42 mm (in a solid angle of  $4\pi/26$ ).

Moreover, the accelerometer proof mass being in platinum and having a diameter of 38 mm, the equivalent aluminum thickness corresponding to a diametral crossing of the proof mass is 316 mm.

Consequently, the proof mass charge will be due to protons whose energy is high enough to cross 42 mm of aluminum but whose energy remains lower than that necessary to cross 586 mm of the same metal.

Figure 6, taken from,<sup>11</sup> makes it possible to give a simple analytic formulation of the path  $x$  of protons of energy  $E$  in aluminum:

$$x = \alpha E^{-\gamma} \quad (6)$$

With  $x$  in mm and  $E$  in MeV, we obtain the following empirical values:  
 $\alpha = 0.01$  and  $\gamma = 1.73$ .

Expression (6) thus permits for each solid angle of the satellite the determination of energy band of the protons which will participate in the proof mass charge. For the satellite as a whole, there are the protons whose energy is between 100 and 500 MeV which are to be considered.

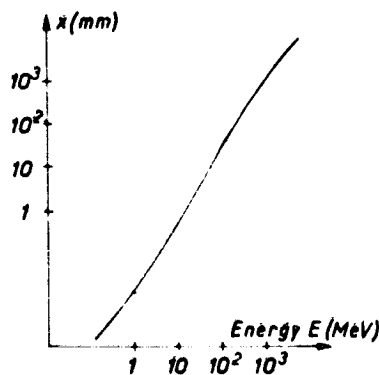


Figure 6. Proton Path in Aluminum

#### 5.4 Calculation of the Daily Charging of the Proof Mass

The argument is that used by J. Tiffon,<sup>11</sup> recalled hereafter.

The flux density of protons of an energy higher than  $E$ ,  $\phi(>E)$ , is represented by the following analytic expression:

$$\phi(>E) = k E^{-\eta} \quad (7)$$

Parameters  $k$  and  $\eta$  are determined empirically from the straight line which makes up a good approximation of the law representing the variation of the logarithm of the integrated flux as a function of the logarithm of energy.

As an illustration, Figure 7 represents the values of the integrated flux of protons received by the satellite during the day of 8th of June 1976, as well as the straight line giving its approximate expression.

Inside a solid angle  $\Omega_i$  (Figure 8) corresponding to the previously defined dividing and for which the aluminum thickness to be crossed is  $x_i$ , the number of protons issued from a solid angle  $d\omega$  and reaching the proof mass within a day is defined from Eq. (6) and (7) by:

$$d\dot{N}_{i1} = k \left( \frac{x_i}{\sigma} \right)^{-\eta/\gamma} R \Omega_i \cos \theta \frac{d\omega}{4\pi} \quad (8)$$

where  $R$  is the mean radius of the screen of thickness  $x_i$ . Among these, a certain quantity  $d\dot{N}_{i2}$  comes out of the proof mass:

$$d\dot{N}_{i2} = k \left[ \frac{x_i}{\sigma} + \frac{2x_r}{\sigma} \left( 1 - \frac{R^2}{r^2} \sin^2 \theta \right)^{1/2} \right]^{-\eta/\gamma} R \Omega_i \cos \theta \frac{d\omega}{4\pi} \quad (9)$$

In this expression,  $r$  is the proof mass radius - in platinum - and  $x_r$  its equivalent aluminum thickness.

A number of protons stopped daily by the proof mass and penetrating into the solid angle  $\Omega_i$  is thus:

$$\dot{n}_i = \int_{\theta=0}^{\theta=\theta_0} (d\dot{N}_{i1} - d\dot{N}_{i2})$$

or, after calculation:

$$\dot{n}_i = \frac{r^2 \Omega_i k \sigma^{\eta/\gamma}}{4} \left\{ x_i^{-\eta/\gamma} - \frac{1}{2x_r^2} \left[ \frac{x_i^{2-\frac{\eta}{\gamma}}}{\left(2 - \frac{\eta}{\gamma}\right) \left(1 - \frac{\eta}{\gamma}\right)} + \frac{(x_i + 2x_r)^{2-\frac{\eta}{\gamma}}}{2 - \frac{\eta}{\gamma}} - \frac{x_i(x_i + 2x_r)^{1-\frac{\eta}{\gamma}}}{1 - \frac{\eta}{\gamma}} \right] \right\} \quad (10)$$

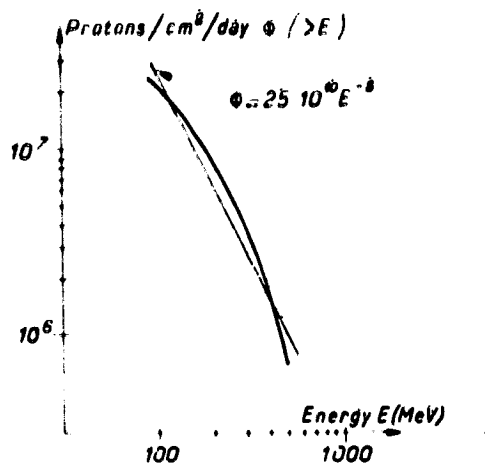


Figure 7. Proton Flux Received on June 8, 1976

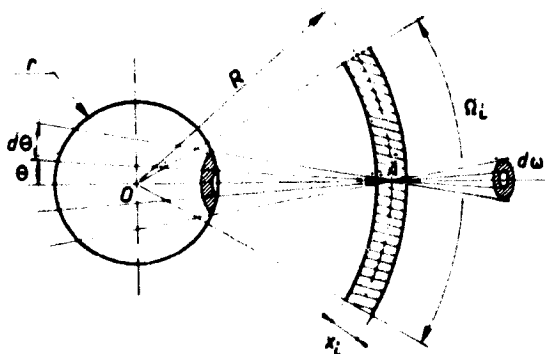


Figure 8. Method for Calculating the Proof Mass Charge

The application of Eq. (10) to each of the solid angles defined in Section 5.3 and for each day during which the radiation doses received by the satellite are characterized by the parameters  $k$  and  $\eta$ , permits, after summation, the calculation of the electric charge acquired daily by the proof mass.

These results are presented on Figure 9, which represents the daily charge acquired as a function of time. The abscissa corresponds to the 30 days of the month of June 1976 for which the calculation has been performed. The dates where the apogee latitude is at  $30^\circ$  north and  $30^\circ$  south have also been shown. This makes it possible to generalize the result obtained at any date of the satellite life in as much as the orbit decay is not too important.

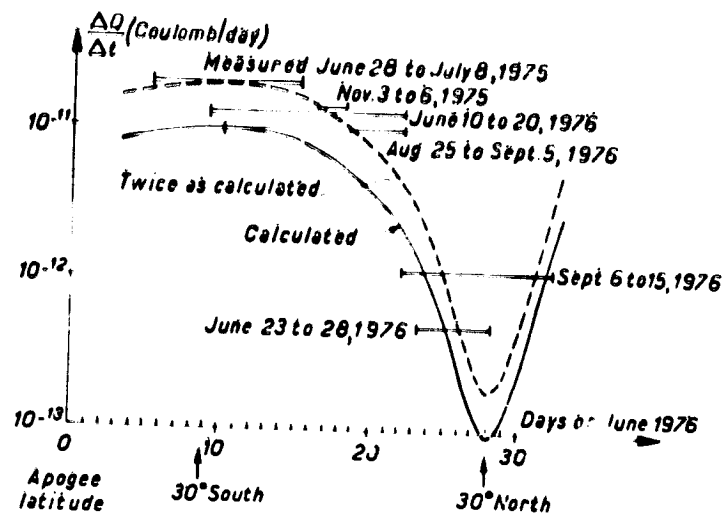


Figure 9. Calculated and Measured Values of the Charge Acquired Daily by the Proof Mass

This result obtained emphasizes well the very important variation of the charging current due to the primary effect of protons, a variation that appears as a decrease by a factor 100 when the apogee latitude is at 30° north.

#### 6. CONCLUSION

The values of the charging currents determined from the data provided by the accelerometer are also shown on Figure 9 as horizontal lines. These lines give the mean value of this current over a period corresponding to the line length. The results corresponding to July 1975, November 1975, and September 1976 are placed with the same scale but are shifted relative to the apogee latitude.

We can see that the currents, measured by this way, follow correctly the law defined by the calculated current.

On a quantitative point of view, there appears a ratio of about 2 between the measured and calculated currents. This ratio is emphasized by the broken line curve which is traced by doubling the values of the calculated currents. This coefficient 2 is not very high and may be attributed to the model of proton absorption.

Thus the results obtained confirm that it is possible, while designing the project of a drag-free satellite – or an accelerometric satellite – to determine with a sufficient precision the various values that will take the proof mass charging current as a function of orbital situations.

This evaluation should permit a better definition of the means to implement and the procedure to use to maintain the proof mass electrification to a tolerable level.

## References

1. Lange, B.O. (1964) The drag free satellite, in AIAA Journal 2(No. 9):1590-1606.
2. Bernard, A., and Gay, M. (1976) Description de l'accéléromètre Cactus, in Les essais en orbite de l'accéléromètre Cactus, Publication ONERA No. 1976-5.
3. Juillerat, R. (1972) Analyse des limitations physiques des accéléromètres pour sonde spatiale et de détecteurs de sonde à traînée compensée, in International School of Physics, Varenne, Juillet 1972, Academic Press.
4. Staff of the Space Department (Johns Hopkins University, Md) and staff of the Guidance and Control Laboratory (Stanford University, Calif.) A satellite freed of all but gravitational forces: "TRIAD 1".
5. Beaussier, J., Mainguy, A.M., Olivero, A. and Rolland, R. (1976) In orbit Performance of the Cactus Accelerometer. Paper presented at the XXVII International Astronautical Congress, Anaheim, Cal. Oct. 10-16, 1976.
6. Beaussier, J., and Juillerat, R. Caractérisation du seuil de l'accéléromètre Cactus, in Les essais en orbite de l'accéléromètre Cactus, Publication ONERA No. 1976-5.
7. Bouttes, J., Delattre, M., and Juillerat, R. (1976) Qualification in orbital flight of the Cactus high sensitivity accelerometer. Paper presented at the 19th COSPAR Meeting, Philadelphia, June 9-16, 1976.
8. Barlier, F., Boudon, Y., Falin, J.L., Futaully, R., Villain, J.P., Walch, J.J., Mainguy, A.M., Boudon, J.P. (1976) Preliminary results obtained from the microaccelerometer Cactus. Paper presented at the 19th COSPAR Meeting, Philadelphia, June 9-16, 1976.
9. Bourriau, J., and Schuttler, R. (1970) Programme Eldose pour le calcul des répartitions de doses absorbées dans les écrans minces, ONERA/CERT/DERTS, NT 02/20.
10. Bourriau, J., and Schuttler, R. (1972) Transmission des électrons par les écrans plans épais, ONERA/CERT/DERTS, NT 02/24.
11. Tiffon, J. (1972) Influence des rayonnements de haute énergie sur la charge électrique de la masse d'épreuve de l'accéléromètre Cactus, ONERA Technical Note No. 200.
12. Philippon, J.P. (1970) Evaluation théorique et calcul des flux de particules dans la zone stable de la magnétosphère, Thèse d'Université, Toulouse.
13. Pellat, R., and Philippon, J.P. (1976) Calcul de flux à long terme, Unpublished.

Contents

1. Introduction	191
2. Observations	192
3. Theoretical Analysis	197
4. Conclusions	199
Acknowledgments	201
References	201

## 11. Analysis of Penumbral Eclipse Data

H. B. Garrett, 1/Lt. USAF  
 Air Force Geophysics Laboratory  
 Hanscom AFB  
 Bedford, Mass.

### Abstract

Two days of data from the ATS-6 1976 eclipse season were analyzed to determine the effects of varying photoelectron flux on spacecraft potential. Particular emphasis was placed on the variation in potential as the satellite entered the earth's penumbra. Measurements from the AE-C satellite of the solar UV radiation were used to construct a model of atmospheric attenuation. This model was found to be consistent with direct measurements of the variations in photoelectron flux as INJUN V passed into eclipse. Applying the model to the ATS-6 data gave the time-dependency of the solar illumination/photoelectron flux as the satellite was eclipsed. This relationship, when combined with the ATS-6 measurements of satellite potential, revealed a nearly linear relation between the solar illumination/photoelectron flux and the logarithm of the satellite potential.

### 1. INTRODUCTION

The charging of spacecraft at geosynchronous orbit has become a primary concern for engineers and satellite designers. A major goal of scientists concerned with the problem is to provide to the engineers and designers adequate models of this phenomenon. Although several models of the sheath surrounding the spacecraft,

0-3

of the way in which this sheath alters the ambient particle fluxes, and of the subsequent interaction with the spacecraft surface exist in varying degrees of sophistication, few means exist for verifying these models.<sup>1</sup> The purpose of this report will be to present observations of the variation in the ATS-6 spacecraft potential as one parameter, the photoelectron flux, was varied in a known manner. This will be accomplished by detailed analysis of data from periods when the sun, as observed by a satellite, is eclipsed by the earth.

## 2. OBSERVATIONS

The highest potentials yet observed on spacecraft have been by the ATS-5 and ATS-6 satellites as they passed into the earth's shadow. These potentials are only observed when the satellites are immersed in the hot plasma associated with geomagnetic storms and plasma injection events. Briefly, as a satellite passes into eclipse, the incident solar photon flux is decreased resulting in a decrease in the photoelectron current emitted from the satellite surface. It is the elimination of this current source that results in a current imbalance which leads to a large negative potential.

Figures 1 and 2 are spectrograms for 28 February (Day 59) and 6 March (Day 66) of the particle populations observed by the ATS-6 satellite during the spring 1976 eclipse season (see<sup>2</sup> for an explanation of these spectrograms). The intense bands observed in each positive ion spectrogram are the cold background ion population which has been accelerated by electric fields on the spacecraft. These data can be interpreted as voltage changes on ATS-6 amounting to over -10,000 volts and are coincident with the passage of the satellite into eclipse. In Figure 3, the voltage changes as the spacecraft passes into eclipse (exits eclipse) are plotted as continuous (dashed) lines for Days 59 and 66. Entry and exit (reversed in time) have been superimposed on each other to show their agreement for each eclipse. This agreement is a consequence of the eclipse symmetry and the apparent stability of ambient conditions during each eclipse.

Figures 4 and 5 show the plasma distribution functions for the electrons and ions associated respectively with the eclipses on Day 59 and Day 66. Figure 4, for Day 59, shows the plasma conditions before and after eclipse (dashed lines) and during eclipse (solid lines). The spectra immediately before and after eclipse are nearly identical; whereas the spectra measured while the satellite was in eclipse show the effects of charging. Normally these effects result in a constant, positive

ORIGINAL PAGE IS  
OF POOR QUALITY

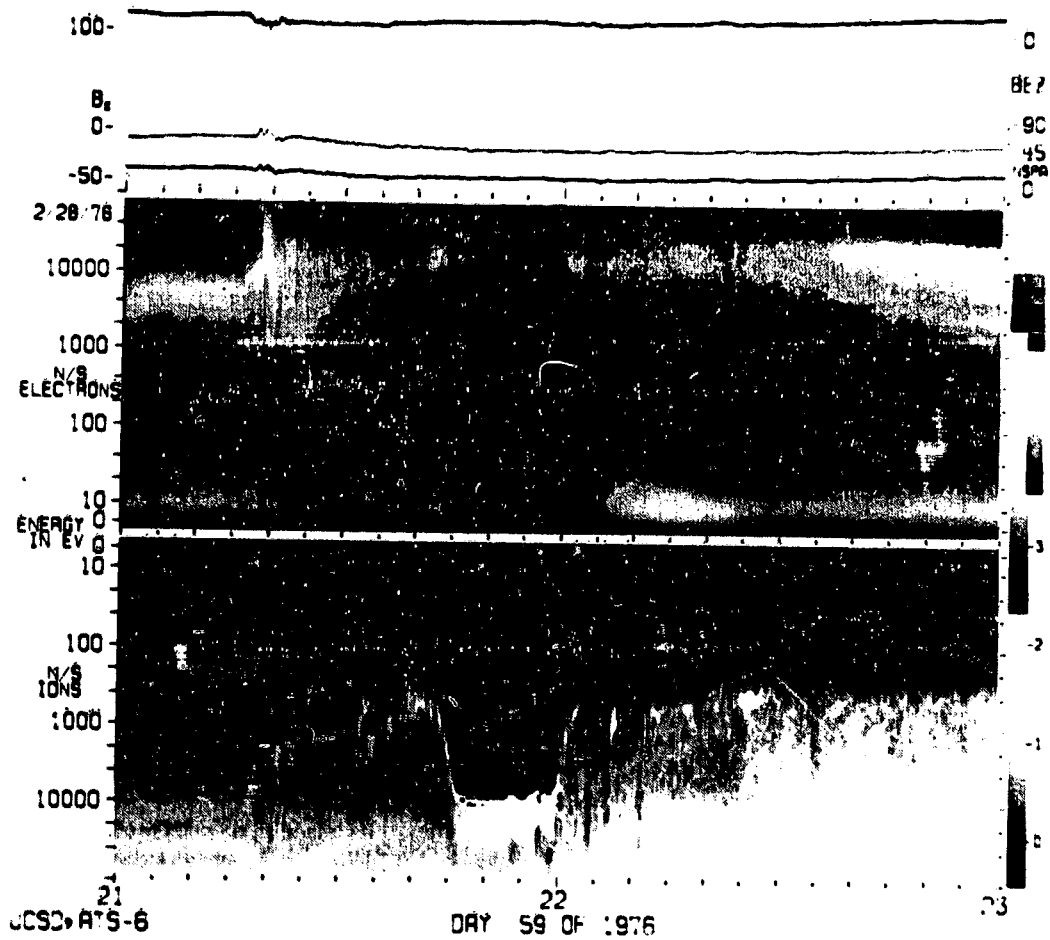


Figure 1. Spectrogram of ATS-6 Count Rates as a Function of Time and Energy for Day 59 of 1976. The spacecraft develops a potential of -10,000 V as reflected by the ion data when it is eclipsed near 2200 UT

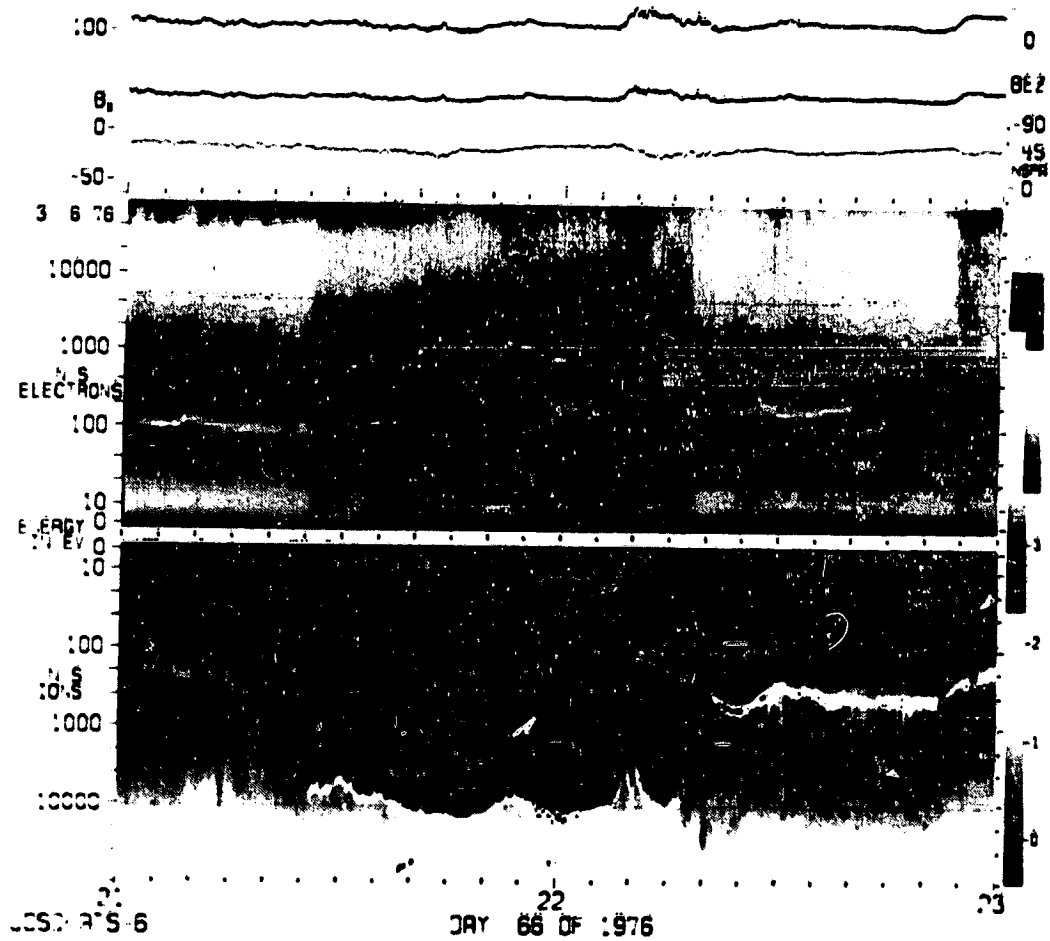


Figure 2. Spectrogram of ATS-6 Count Rates as a Function of Time and Energy for Day 66 of 1976. The spacecraft is eclipsed by the Earth between 2100 and 2300 UT

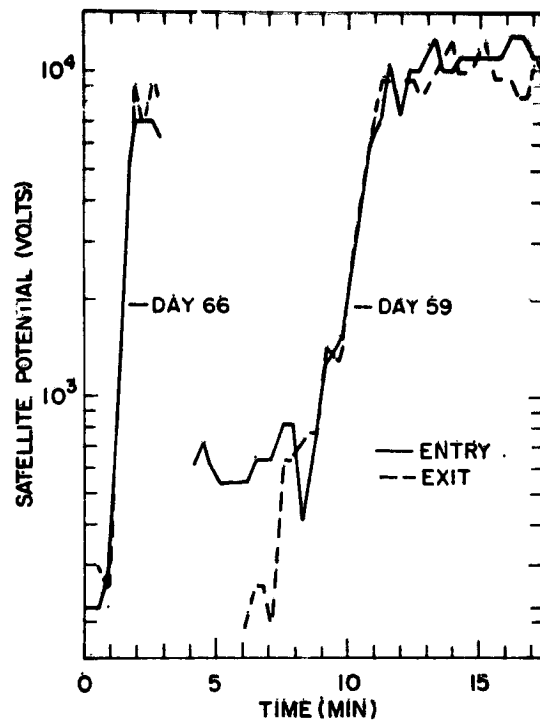


Figure 3. ATS-6 Potential as a Function of Time for Day 59 and Day 66. For reference, as the time axis is not absolute, ATS-6 had voltages in excess of  $-10,000$  V for 1060 sec on Day 59 and 3126 sec on Day 66

displacement in energy of the ion distribution function that is equal to the potential on the satellite and a corresponding negative displacement in the electron distribution function. The spectra for Day 66 in Figure 6 show this effect, but, for energies above 30 keV, the spectra for Day 59 are not consistent with this behavior. The exact cause of the departure is not known but it may result from effects on the spacecraft due to the eclipse rather than to changes in the ambient plasma.

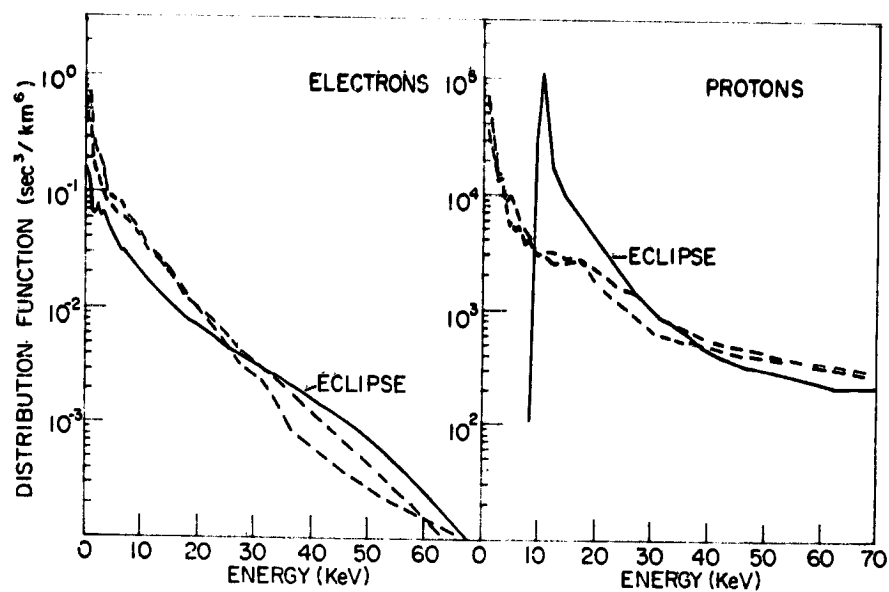


Figure 4. Electron and Ion Distribution Functions as Functions of Energy for Day 59. Dashed lines represent the spectra before and after eclipse. Solid lines represent eclipse spectra

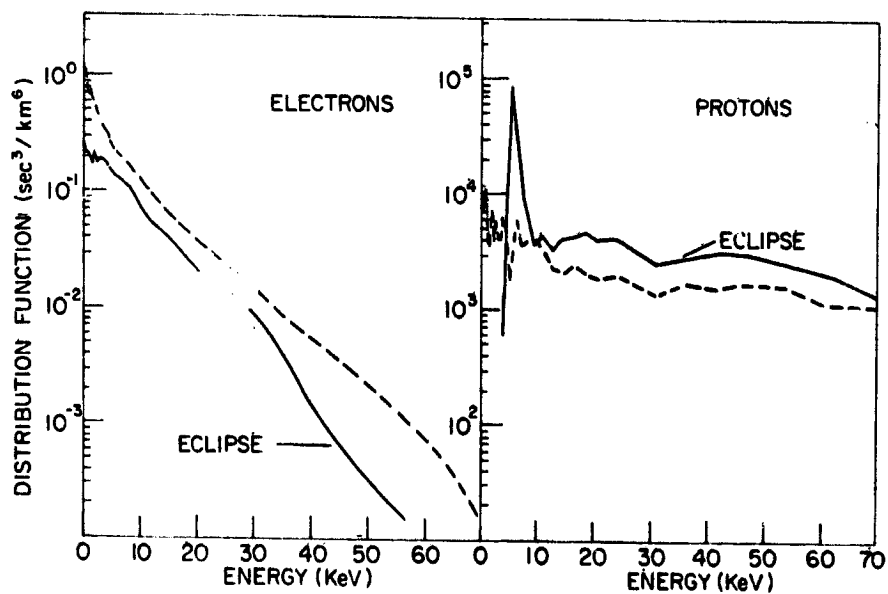


Figure 5. Electron and Ion Distribution Functions versus Energy for Day 66. Dashed lines represent spectra before eclipse. Solid lines represent eclipse spectra

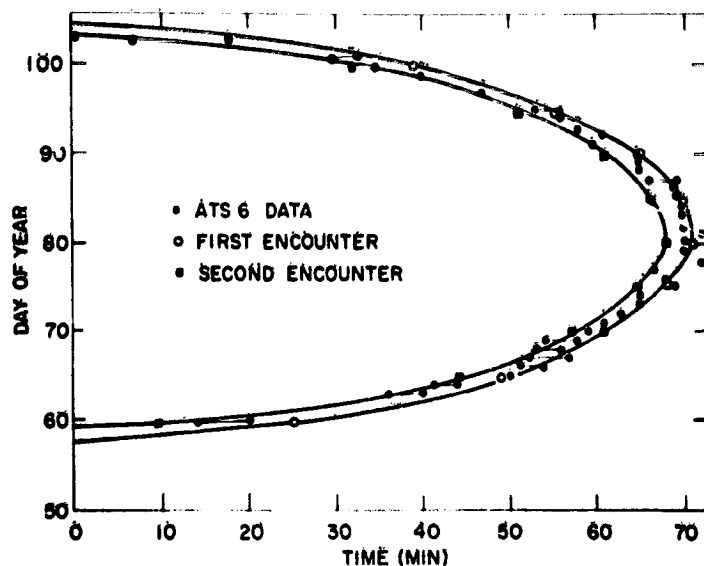


Figure 6. Duration of Penumbral and Umbral Eclipse Periods as a Function of Day of the Year for the ATS-6 1976 Spring Eclipse Season. Observed and predicted results are plotted

### 3. THEORETICAL ANALYSIS

In the preceding section, the experimental data were presented along with a brief description of the plasma conditions. Based on these data, I feel that the ambient plasma distribution during eclipse Days 59 and 66 did not change significantly except for a displacement in the distribution function due to charging effects. As previously discussed, it is the loss of the photoemission current as the sun is eclipsed which is the apparent source of the charging. To analyze the charging in more detail, it is necessary to accurately model the time variation of the solar illumination. To accomplish this, data from several sources will be used to compute and test a model of the penumbral variation.

A simple model of the penumbral region can be derived by assuming the earth and sun to be well defined discs. Geometry then gives a relation between the percentage of solar illumination and time. In Figure 6, the duration of eclipse versus day of year for the ATS-6 1976 spring eclipse season has been plotted. Where it was possible to estimate both, entry into the penumbral and umbral regions are shown connected by a line. The two curves represent the theoretical prediction of partial and total eclipse. The data indicate that even this simple theory gives an adequate prediction of the duration of partial and total eclipse at synchronous orbit. Note that Day 59 is an example of grazing incidence while Day 66 illustrates direct entry into eclipse.

The major objection to such a simple theory is the exclusion of atmospheric effects. For low altitudes (less than 2 earth radii), such effects are clearly important. This is demonstrated in Figure 7 where the variation of photoelectron flux (dots) versus time as the INJUN V satellite passed into eclipse is plotted. At the time of these data, the INJUN V satellite was at 1.5 earth radii. The solid line is a theoretical curve of the percentage of solar illumination versus time when atmospheric effects are included in the eclipse model. Ignoring atmospheric effects gives the dashed curve in Figure 7 (note: the earth's eclipse boundary was placed at 6378 km + 145 km for this calculation).

Using data from the AE-C satellite,<sup>3</sup> the attenuation,  $\tau$  (such that  $\phi = \phi_0 e^{-\tau}$ , where  $\phi$  is the observed photon flux), as a function of minimum ray height above sea level, was calculated. At a given wavelength, it was readily found that:

$$\tau = e \frac{-(X - X_0)}{\delta} \quad (1)$$

where

$X$  = height above sea level,

$X_0$  = constant, dependent on frequency of light, and

$\delta$  = scale height, dependent on frequency of light.

As the detailed variation of the photoelectron flux is dependent on the materials of which the spacecraft is constructed and as the atmosphere itself varies in time, it is difficult to construct a more exact model. Careful consideration of the photoelectron emission versus frequency and the attenuation versus frequency from the AE-C satellite gave average values of:

$$X_0 = 145 \text{ km} \quad (2)$$

$$\delta = 23.5 \text{ km} \quad (3)$$

The INJUN V data of Figure 7 are fit with a value of 60 km for  $\delta$ , whereas ATS-6 is better fit by  $\delta = 23.5$  km. The difference is likely due to the materials of which the satellites are constructed as the INJUN V detector is made of tungsten which is responsive to longer wavelengths than aluminum, the primary ATS-6 material.

To first order, the effect of the atmosphere is to make the earth appear larger (approximately 145 km larger) in radius. Although  $\delta$  is not accurately known, the AE-C data implies values of less than 100 km. This uncertainty generates timing errors in our estimation of the eclipse duration on the order of 30 sec or less but does not greatly alter the results to be presented. By comparison, ephemeris

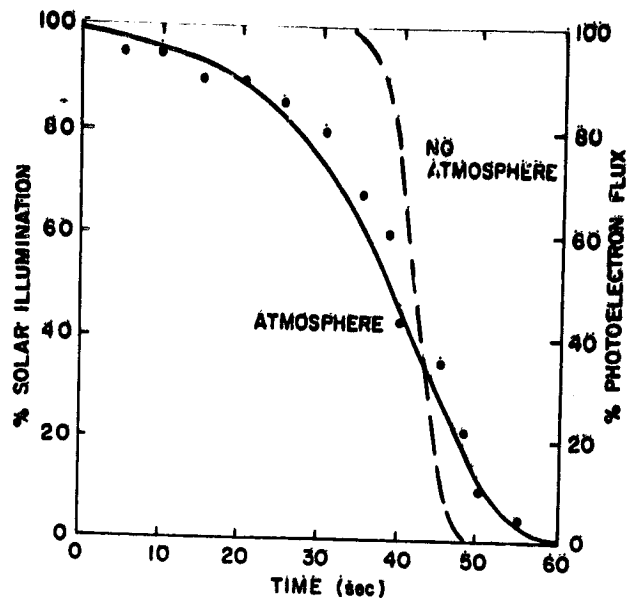


Figure 7. INJUN V Measurements of the Photoelectron Flux as a Function of Time in the Penumbra Region (Dots). Also shown are two theoretical curves of the solar illumination for the case of no atmosphere (dashed line) and with an atmosphere (solid line)

errors are of the same order indicating that the atmospheric model is consistent with the accuracy inherent in the problem.

#### 4. CONCLUSIONS

The voltage data in Figure 3 can be fit as a function of time between roughly -2000 and -10,000 volts by:

$$\text{Day 59: } V \approx -10^3 e^{0.016(T+530)} \quad (4)$$

$$\text{Day 66: } V \approx -10^3 e^{0.05(T+1563)} \quad (5)$$

where V = voltage (volts)

T = time (seconds).

Assuming  $\delta = 23.5$  km and  $X_O = 145$  km in the atmospheric model, the solar illumination versus voltage for Days 59 and 66 are plotted in Figure 8. The error bars are for the results arrived at by assuming no atmosphere (upper) or by assuming  $\delta = 60$  km (lower).

As the percentage of solar illumination is directly related to the photoelectron flux (Figure 7), Figure 8 can be interpreted as illustrating the effect of varying the photoelectron flux on the satellite potential. Timing errors in the ephemeris and the atmospheric model may alter the quantitative results of Figure 8 within roughly the error bars shown, but will not alter the qualitative result inherent in the figure - namely that the voltage is proportional to the exponential of the photoelectron flux. This result is of real value as it can be used as a test of the predictions of various theoretical models. In particular, it can be used to check the modeling of photoelectron variations. As it is almost impossible to distinguish secondary and back-scattered electrons from photoelectrons, the results have broader implications since they can be applied to testing any model which includes the effects of variable electron emission. This latter observation is particularly important when one recalls that standard sheath models imply a logarithmic, not exponential, relation between electron emission and voltage.

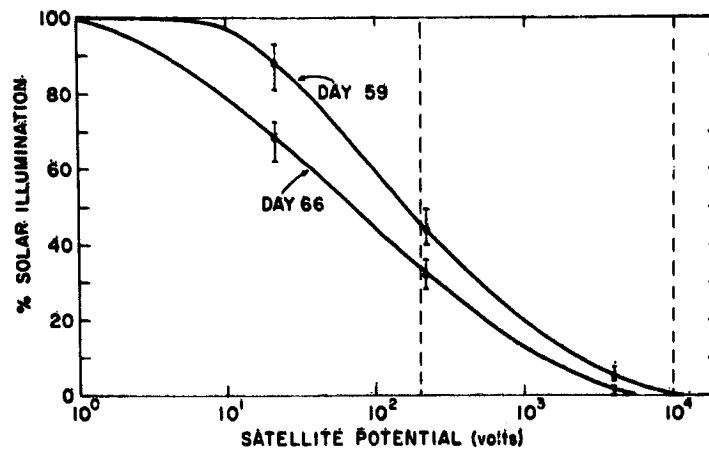


Figure 8. Composite Plot of the Solar Illumination (or Photoelectron Flux) as a Function of Satellite Potential for Day 59 and Day 66

## Acknowledgments

I would like to thank Drs. DeForest and Whipple for providing the ATS-6 data and taking the time to explain data formats. Useful discussions were held with Drs. Burke (INJUN V data), Hinteregger (AE-C data), Rubin, Rothwell, and Pike.

## References

1. DeForest, S. E. (1972) Spacecraft charging at synchronous orbit, J. Geophys. Res. 77:651-659.
2. DeForest, S. E., and McIlwain, C. E. (1971) Plasma clouds in the magnetosphere, J. Geophys. Res. 76:3587-3611.
3. Hinteregger, H. E., Bedo, D. E., and Manson, J. E. (1973) The EUV spectrophotometer on Atmosphere Explorer, Rad. Sci. 8(No. 4):349-359.

## Contents

1. Introduction	204
2. Interaction Between a Spacecraft and its Environment	205
3. Possible Uses of Electron Emitters	208
4. Experimental Arrangement	212
5. Conclusion	218
Acknowledgments	219
References	219

## 12. The Multiple Applications of Electrons in Space

Réjean J. L. Grad  
Space Science Department  
European Space Agency  
Noordwijk, The Netherlands

### Abstract

An electron source such as a simple cathode is a cheap and light device which can serve several technological and scientific purposes in space:

(i) Electrostatic charging of a spacecraft can be limited by releasing electrons accumulated on the conductive elements of their surface. Clamping the reference potential of scientific instruments, such as particle detectors, can significantly improve their performance in a magnetospheric environment.

(ii) The erosion of conductive coatings and the ability of conductive paints to withstand the space environment can be evaluated by monitoring the flow of charged particles impinging on their surface, that is, by simply measuring the rate at which electrons are emitted from the cathode.

(iii) Measuring the current collected by the spacecraft surface as a function of its potential with respect to an emitter is a very sensitive diagnostic technique which can yield a number of plasma parameters, such as density and temperature.

(iv) It is possible to convert the thermal motion of space plasmas into electrical energy by collecting energetic electrons and returning them to the medium as cold particles. This concept may find applications in the magnetosphere of distant planets where solar cells are inefficient.

(v) A wave in a plasma is characterized by a conduction current density which gives rise to fluctuations of the current flowing to the surface. An investigation of the frequency spectrum of the cathode current will therefore disclose the existence of electromagnetic and electrostatic waves without using any antenna.

## 1. INTRODUCTION

The potential of a body in space is defined by the current balance of the charged particles emitted and collected by its surface. In equilibrium the difference between the flows of plasma electrons and ions equals the rate at which electrons extracted from the surface by photo- and secondary emissions are escaping into the surrounding plasma.

When the random flux of the plasma electrons is relatively large, the surface develops a potential sufficiently negative to limit the incoming flow of these particles and to make it equal to the combined contribution of the other species. The magnitude of this potential is then in direct proportion to the temperature of the ambient electrons. Such conditions are often met in dense or hot plasmas when surface emission cannot match the net flow of ambient particles. In planetary outer magnetospheres, the electron mean kinetic energy is so high that surface potentials of the order of several kilovolts are frequently encountered. This phenomenon, commonly referred to as spacecraft charging, disturbs the particle population in the surrounding plasma and is therefore a source of interferences for scientific measurements.<sup>1</sup>

It has also been observed that different materials insulated from each other do not reach the same floating potential. This differential charging gives rise to large electric fields between adjacent elements and can cause discharges which are responsible for the degradation of spacecraft materials and anomalies in the behaviour of electronic subsystems.<sup>2, 3</sup>

This situation has led up scientists and engineers to compound their effort in an attempt to understand and control these phenomena.<sup>4</sup> The basic remedies are simple. The entire surface of the spacecraft must be made conductive in order to be equipotential and the negative charge accumulated on this body must be released into space through an electron emitter.

A number of materials, conductive coatings, and paints have been developed and qualified, and new testing procedures have been set up to check the ability of the spacecraft to withstand the magnetospheric environment.

This paper recapitulates the principles which govern the interaction of a spacecraft with its environment,<sup>5, 6</sup> and reviews the various techniques which are available for controlling the electrostatic potential of a spacecraft. It is demonstrated that electron emitters are requisite to any scientific mission in a magnetospheric environment, in the vicinity of Jupiter in particular. It is also emphasized that electron sources can be simultaneously used for a number of additional tasks such as monitoring the degradation of spacecraft material surfaces, converting the thermal motion of plasmas into electrical energy, measuring the density and temperature of the ambient electrons, and receiving waves without aerials.

## 2. INTERACTION BETWEEN A SPACECRAFT AND ITS ENVIRONMENT

### 2.1 Spacecraft Without Emitter

The variations of the different current components collected by a planar probe in space as function of its potential are schematically represented in Figure 1, where  $i_e$  and  $i_i$  are the ambient electron and ion contributions, and  $i_{ph}$  is the current due to photoelectron emission. Secondary emission is neglected in first approximation and the potential  $\phi$  is referred to that of infinity.

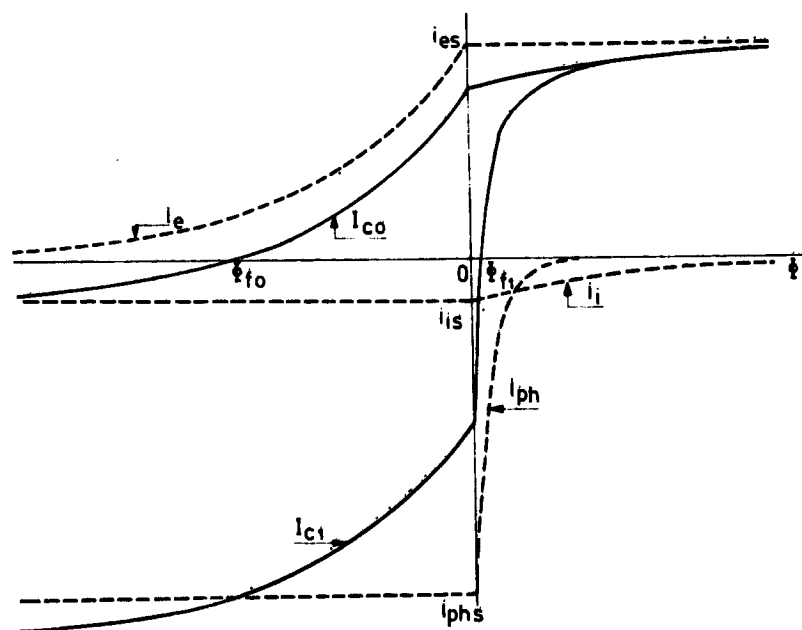


Figure 1. Current-Voltage Characteristics of a Probe in a Plasma

It is assumed that the various species have Maxwellian distributions, and that the magnitude of the saturation current of the plasma electrons  $i_{es}$  is much larger than that of the ions  $i_{is}$ ; the photoelectron saturation current is noted  $i_{phs}$ .

The current balance is defined by

$$i_e + i_i + i_{ph} = 0 \quad (1)$$

and the floating potential is given by

$$\phi_f = -\phi_e \ln \left| \frac{i_{es}}{i_{phs} + i_{is}} \right| \quad (2)$$

when  $|i_{es}| > |i_{phs} + i_{is}|$ , and by

$$\phi_f \approx \phi_{ph} \ln \left| \frac{i_{phs} + i_{is}}{i_{es}} \right| \quad (3)$$

when  $|i_{es}| < |i_{phs} + i_{is}|$ . The quantities  $\phi_e$  and  $\phi_{ph}$  are the mean kinetic potentials of the plasma electrons and photoelectrons, respectively.\*

The current-voltage characteristic of a body in shadow ( $i_{ph} = 0$ ) is illustrated by the curve labelled  $I_{C0}$  in Figure 1. The floating potential  $\phi_{f0}$  is negative and approximately equal to  $-3.8\phi_e$  in the case of an hydrogen plasma in thermal equilibrium.<sup>7</sup> In a magnetospheric environment,  $\phi_e$  can be of the order of 1-10 kV, which explains why a geostationary spacecraft develops large negative potentials during eclipses.<sup>8, 9, 10</sup> The same situation also occurs in sunlight when photoemission cannot balance the flow of ambient particles. This condition is occasionally fulfilled in the Earth environment, but it must always be met in the magnetosphere of Jupiter where the photoemission rate is 27 times less than at the Earth's orbit.

In a relatively cold and rarefied plasma, such as the solar wind, the photoemission saturation current is generally predominant; this situation is illustrated by the curve labelled  $I_{C1}$  in Figure 1. The corresponding floating potential  $\phi_{f1}$  is given by Eq. (3) and is of the order of the photoelectron mean kinetic potential, which is typically equal to 1.5V.<sup>11</sup>

## 2.2 Spacecraft With Electron Emitter

A spacecraft fitted with an electron source is schematically represented in Figure 2a. The electron source and the conductive elements of the spacecraft surface are referred to as the emitter (E) and the collector (C), respectively. It is assumed that the emitter and collector are sufficiently decoupled, so that their

\*The kinetic potential of a charged particle is given by the magnitude of the accelerating voltage associated with its kinetic energy. The kinetic potential, in V, therefore, is measured by the same number as the kinetic energy, in eV.

current voltage characteristics are, in first approximation, independent of their separation.

The voltage-current characteristic of the emitter is schematically represented in Figure 2b and c by the curves labelled  $I_E$ ; the voltage reference is that of the surrounding plasma, not that of the spacecraft. The area of the emitter is relatively small and its current is, therefore, insensitive to the fluxes of photons and ambient particles. When electron emission is space charge limited,  $I_E$  is proportional to  $(-\phi)^{3/2}$ . The shape of the characteristic is otherwise defined by the temperature of the emitter, as well as by the magnitude of the electric field at its surface.<sup>12</sup> It is assumed that the saturation current of the emitter is larger than that of the ambient electrons, which can always be easily fulfilled.

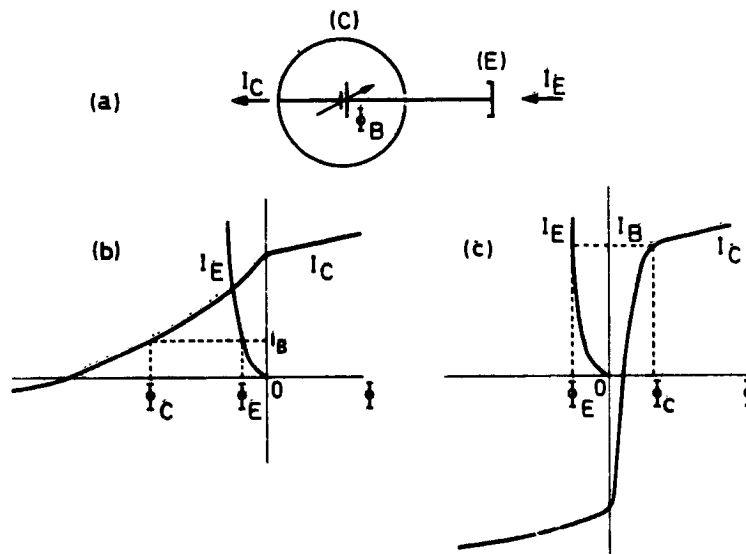


Figure 2. Current Balance and Potentials of Emitter and Collector

When collector and emitter are connected through a voltage source  $\phi_B$ , their respective potential  $\phi_C$  and  $\phi_E$  are linked by the relation

$$\phi_C - \phi_E = \phi_B \quad (4)$$

and the emitted and collected currents are of course equal,

$$I_E = I_C = I_B \quad (5)$$

as illustrated in Figure 2.

### 3. POSSIBLE USES OF ELECTRON EMITTERS

#### 3.1 Spacecraft Potential Clamping

When the bias voltage  $\Phi_B$  is zero, the equilibrium potential of the collector-emitter combination is defined by the intersection of the curves  $I_C$  and  $I_E$ . In a magnetospheric environment the floating potential can then be maintained at a few volts, rather than several kV negative, as illustrated in Figure 2b.<sup>13, 14, 15</sup> The potential of the collector can even be adjusted to zero exactly by biasing its potential positively with respect to that of the emitter until a break in the slope of the characteristic is observed.<sup>16</sup> The ability to control the spacecraft potential allows one to minimize the perturbation to the environment and provides a stable voltage reference for scientific instruments.

An electron emitter cannot indeed reduce the floating potential when photoemission is predominant (Figure 2c), but this is a relatively unimportant point since this positive potential is typically of the order of 3V.<sup>17</sup>

#### 3.2 Plasma Diagnostics

It will be seen in the following that the potential of the emitter is practically independent of its current; this system operates like a potential reference with respect to which the collector may be biased. The emitted current may be measured as function of the bias potential. The spacecraft then behaves like a Langmuir probe<sup>18</sup> with a collecting area equal to that of the conductive parts of its surface.<sup>19, 20</sup> This technique for measuring electron density and temperature is extremely sensitive, and irregularities in plasma densities can be detected by investigating the low frequency fluctuations of the collected current.

The electron saturation current can be monitored under all circumstances, and this measurement is absolutely not impaired by photoemission (see Figure 2c). A variable resistor  $R$  can replace the voltage source, as shown in Figure 3, but the bias voltage  $-R I_B$  can only take negative values. This possibility is nevertheless extremely

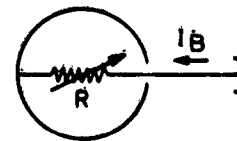


Figure 3. Negative Bias of the Collector Using a Resistor

advantageous in energetic plasmas where voltages of several kV would be required to describe the characteristic down to the floating potential.

### 3.3 Monitoring of Material Surface Degradation

Spacecraft are partly covered with materials and paints, generally insulators, in order to maintain the temperature within specified limits. Conductive paints and coatings have consequently been developed to cope with the problem of differential charging. Solar cell covers and second surface mirrors can similarly be covered with 100Å thick layers of Indium oxide which also insures electric potential uniformity, but are optically transparent.<sup>21</sup>

The ability of these conductive materials to keep their properties in space under the bombardment of energetic particles can be easily tested in situ, as illustrated in Figure 4. The current collected by the test material,  $I_t$ , is simply compared to that impinging on a metallic surface,  $I_r$ , taken as a reference. This measurement is instantaneous and independent of the properties of the cathode.

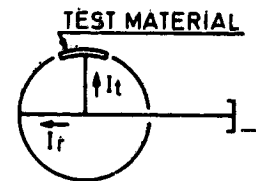


Figure 4. Test on Material Surface Degradation

### 3.4 Energy Conversion

It has been shown previously that energy can be dissipated in a resistor when the floating potential is negative (Figure 3). It is therefore possible to convert the thermal motion of electrons into electrical power.<sup>22</sup> This concept may find applications in space environments where energetic plasmas are likely to be found, but sufficiently distant from the sun to render the use of photovoltaic conversion unpractical. Such conditions are met in the magnetospheres of distant planets such as Jupiter and Saturn.<sup>23, 24</sup>

The efficiency of this system, that is, the ratio of the plasma energy input to the available electric energy equals 0.37 for a Maxwellian energy distribution. The corresponding maximum power output per  $m^2$  of collecting surface is given as function of the ambient plasma density,  $N_e$ , and mean kinetic potential,  $\phi_e$ , in Figure 5. If the collecting area of the spacecraft is insufficient, the power output can be increased by the adjunction of a large sail made of metallic foil, for example.

It may be possible to reach specific power equivalent to that of the radio-isotope thermal generators presently used for the outer planetary missions,<sup>25, 26</sup> that is, a few  $Wkg^{-1}$ , provided the plasma power density input lies in the range  $10^{-2}-10^{-1} Wm^{-2}$ . This figure may be met in the environment of Jupiter, but is has to be established by proper in situ measurements.

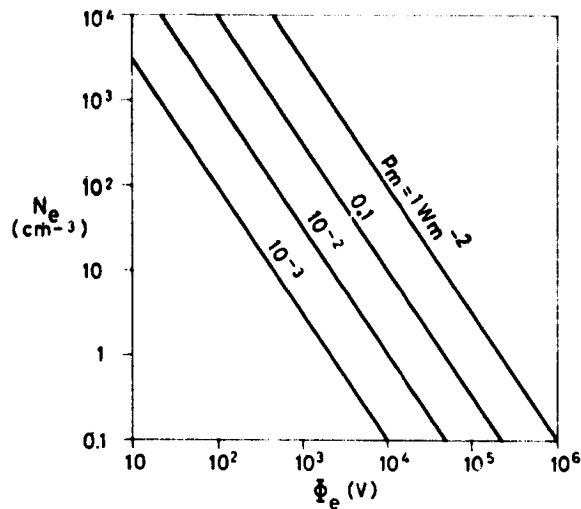


Figure 5. Maximum Power Density Output as a Function of the Electron Density and Mean Kinetic Potential

### 3.5 Detection of Electromagnetic and Electrostatic Waves

A wave propagated in a plasma is characterized by an electric field  $\vec{E}$ , a magnetic field  $\vec{H}$ , and a conduction current density  $\vec{J}$ . These three quantities are related by Maxwell's equations:

$$\nabla \times \vec{E} = -\mu_0 \partial \vec{H} / \partial t \quad , \quad (6)$$

$$\nabla \times \vec{H} = \vec{J} + \epsilon_0 \partial \vec{E} / \partial t \quad , \quad (7)$$

where  $\mu_0$  and  $\epsilon_0$  are the vacuum permeability and permittivity. Time and space variations are assumed to be of the form  $\exp i(\vec{k}\vec{r} - \omega t)$ , where  $\vec{k}$  and  $\omega = 2\pi f$  are the wave vector and angular frequency,  $\vec{r}$  and  $t$  are space and time variables.

After Fourier transformation of Eq. (6) and (7), and elimination of  $\vec{H}$ , the projection of  $\vec{J}$  parallel and perpendicular to the wave vector are respectively

$$\vec{J}_{\parallel} = i\epsilon_0 \omega \vec{E}_{\parallel} \quad (8)$$

and

$$\vec{J}_{\perp} = i\epsilon_0 \omega (1 - \mu^2) \vec{E}_{\perp} \quad , \quad (9)$$

where  $E_{\parallel}$  and  $E_{\perp}$  are the projections of  $\vec{E}$  along directions respectively parallel and perpendicular to  $\vec{k}$ , and  $\mu$  is the refractive index of the medium.

The wave conduction current which can be intercepted is

$$I = A_c J \quad (10)$$

where  $J$  is the modulus of  $\vec{J}$  and  $A_c$  is the cross section area of the collector in a plane perpendicular to  $\vec{J}$ . This current is superimposed on the random plasma ion and electron currents. The information carried by the ambient charged particles is consequently best detected when the spacecraft is collecting the saturation current of these species.<sup>27, 28</sup> The collector potential must therefore be maintained at a value near to zero, or possibly be biased at a few volts positive if photoemission is preponderant (Figure 2b and c). Neglecting the ion contribution this dc current is then approximately given by

$$i_{es} = A J_e \quad (11)$$

where  $A$  is the entire collecting area, and

$$J_e = N_e e \left( \frac{e \phi_e}{2 \pi m} \right)^{1/2} \quad (12)$$

is the electron random current density, in the case of a Maxwellian energy distribution. The quantities  $e$  and  $m$  are the electron charge and mass respectively.

The level of the smallest detectable signal is, of course, limited by the shot noise resulting from the random arrival of plasma particles to the spacecraft surface and the random emission of electrons from the cathode into the environment. The root mean square deviation of  $i_{es}$  in a frequency bandwidth  $B$  therefore defines the lowest measurable wave conduction current<sup>29, 30, 31</sup>

$$I = (2e i_{es} B)^{1/2} \quad (13)$$

The capability of this technique can be assessed by comparing its performance to that of an electric aerial in a given bandwidth. This is simply achieved by equating Eq. (10) and (13), and expressing the sensitivity in terms of electric field  $E$ , rather than conduction current  $J$ .

Consider a wave with a transverse electric field ( $E = E_{\perp}$ ), for example, an electromagnetic wave in an isotropic plasma or a longitudinal wave in a magneto-plasma. Combining Eq. (9)-(13) yields

$$\frac{E}{B^{1/2}} = \frac{4}{(2\pi)^{3/4}} \frac{(me)^{1/4}}{\epsilon_0^{1/2}} \frac{\Phi_c^{1/4}}{\rho} \frac{f_p}{f} \frac{1}{|1 - \mu^2|} \quad (14)$$

where the electron plasma frequency is defined

$$f_p = \left( \frac{N_e e^2}{2\pi \epsilon_0 m} \right)^{1/2} \quad (15)$$

and the collector is taken to be a sphere of radius  $\rho$ , that is,  $A = 4 A_c$ .

Using the MKSA system of units and replacing various quantities by their numerical values yields

$$\frac{E}{B^{1/2}} = 2 \times 10^{-7} \frac{\Phi_e^{1/4}}{\rho} \frac{f_p}{f} \frac{1}{|1 - \mu^2|} \quad (16)$$

The sensitivity to longitudinal electric fields and to electrostatic waves in general ( $E = E_{||}$ ) can be evaluated if Eq. (8) is used, the equivalent sensitivity then becomes

$$\frac{E}{B^{1/2}} = 2 \times 10^{-7} \frac{\Phi_e^{1/4}}{\rho} \frac{f_p}{f} \quad (17)$$

Under most conditions and provided the sensitivity and frequency response of the current measuring device permits, this concept allows the detection of waves with electric field spectral density of the order of  $10^{-6}$ - $10^{-8}$   $V m^{-1} Hz^{-1/2}$  up to frequencies equal to a few times that of the local plasma resonance. In this frequency range, these performances are certainly comparable to those of other types of antenna used in space.

#### 4. EXPERIMENTAL ARRANGEMENT

##### 4.1 Location of the Emitter

It is desirable to optimize the plasma diagnostic measurements by mounting the electron source at some distance from the collector. Coupling and mutual interactions are indeed the result of the direct interception by the spacecraft of a

fraction of the emitted current. Trajectories of electrons emitted with zero velocity are illustrated in Figure 6. It can be seen that the role of the spacecraft is minimal even when its potential is more positive than that of the emitter.

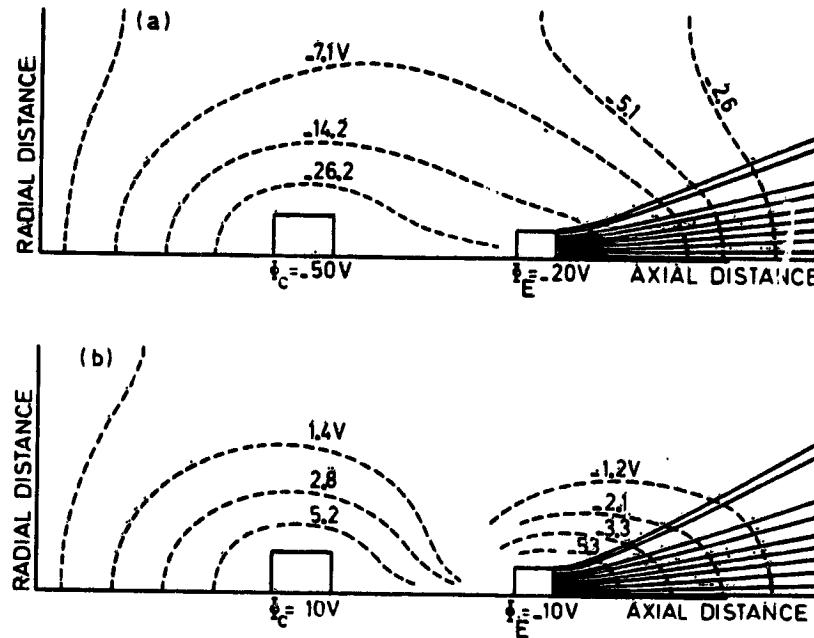


Figure 6. Electron Trajectories in an Axial Symmetrical Field

Potential clamping is more efficient if the electric properties of the electron source environment are as little as possible influenced by the proximity of the spacecraft. The potential developed by the collector in the vicinity of the emitter has so far been taken equal to zero, but this assumption is only valid at large distances from its surface. Approximating the collector by a sphere of radius  $\rho$ , the potential at a distance  $r$  from its center is given by

$$\phi_r = \phi_C \frac{\rho}{r} \quad (18)$$

The effect of probe separation is graphically demonstrated in Figure 7. When the potential reference for the emitter characteristic is shifted by the amount given by Eq. (18), the collector potential becomes

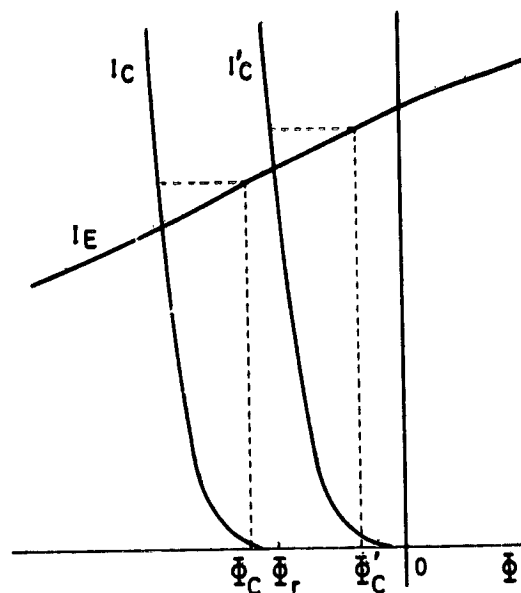


Figure 7. Effect of Collector-Emitter Separation

$$\phi_C = \phi_C' \frac{1 - dI_C/dI_E}{1 - dI_C/dI_E - \rho/r} \approx \frac{\phi_C'}{1 - \rho/r} \quad (19)$$

where  $\phi_C'$  is the spacecraft potential for infinite separation. The quantity  $dI_C/dI_E$  which represents the ratio of the collector and emitter current variations for a given voltage increment is close to zero in energetic plasmas. The result given by Eq. (19) is indeed approximate since it does not account for direct electron flow between emitter and collector, but it shows the tendency for the spacecraft potential to increase with decreasing separation.

Potential clamping can be achieved without bias voltage. It can be anticipated, however, that limitations caused by space charge near the emitter and potential barriers resulting from differential charging, as observed on ATS 6<sup>32</sup> and possibly Pioneer 10,<sup>33</sup> are more important when the electron source is mounted too close to the surface (Figure 8a). Nevertheless, it has been demonstrated that spacecraft potentials could be controlled with an emitter mounted in an open cavity under the surface, but only for limited periods of time (Figure 8b). In fact, if electrons are emitted with zero velocity, their injection into the plasma is impossible unless the emitter is biased negatively with respect to the collector. This type of consideration naturally leads to the concept of electron guns with grid system (Figure 8c), such as those mounted on the ISEE-A spacecraft.<sup>34, 35</sup>

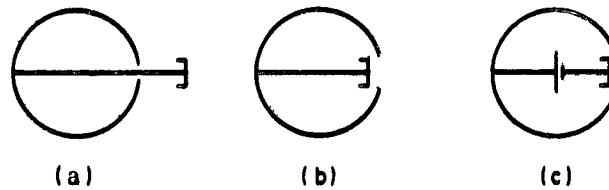


Figure 8. Three Emitter-Collector Configurations

## 4.2 Types of Emitter

### 4.2.1 ACTIVE EMITTERS

Electron emission from a metal in vacuum is a function of its temperature and of the electric field existing at its surface.

Thermoionic emission describes the situation where temperature is the most important parameter. A directly heated tungsten filament is the simplest type of emitter but it dissipates a power of several W. An indirectly heated cathode impregnated with a barium compound requires less than 1W of heating power and offers in addition a uniform surface potential (Figure 9a and b).

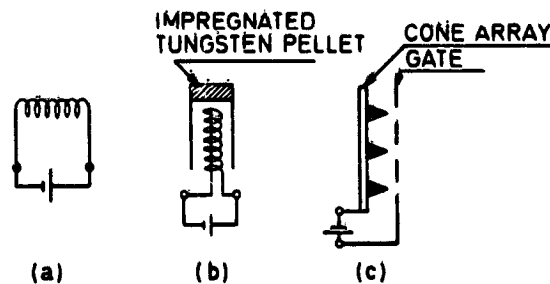


Figure 9. Three Types of Active Electron Emitter

Electron field emission occurs when an electric field of the order of  $10^9 \text{ Vm}^{-1}$  exists at the surface of a metal. Cathodes working on this principle, that is, without any heater, have recently been developed using thin film technology.<sup>36</sup> Electrons are extracted from an array of sharply pointed cones and a voltage of the order of 100 V is applied on a perforated electrode called gate, located at about  $1 \mu\text{m}$  (Figure 9c). Controlling the energy of the emitted electrons, and thus the

potential of the spacecraft, requires the existence of an additional grid placed in front of the gate and electrically biased with respect to the collector. The structure of this emitter then resembles very much that of a miniature electron gun with typical dimensions of 1 mm; energy is only required for accelerating the electrons.

The saturation current of these cathodes, of the order of several mA, is always larger than the plasma electron saturation current collected by the spacecraft. The saturation current density in a plasma characterized by  $N_e = 1 \text{ cm}^{-3}$  and  $\phi_e = 1 \text{ kV}$ , for example, is less than  $1 \mu\text{A m}^{-2}$ . Electron emission is therefore space charge limited like in a diode and the current is of the form

$$I_E = K \phi_E^{3/2} / 2 \quad . \quad (29)$$

If  $I_E$  is measured in A and  $\phi_E$  in V,  $K = 3 \times 10^{-5}$  for spherical symmetry and  $\alpha$  is function of the ratio  $r_a/r_c$  of the anode-to-cathode ratio.<sup>37</sup>

In first approximation, infinite collector-emitter separation and spherical symmetry are assumed;  $r_c$  is given by the physical dimension of the cathode and  $r_a$  is the distance over which space-charge neutrality is restored in the plasma, that is, a distance of the order of the Debye length.

The cathode current is represented by straight lines in Figure 10 for values of  $r_a/r_c$  ranging from 10 to  $10^6$ . Also shown is the electron current collected by a conductive sphere of radius 2 m, in various plasma environments, photoelectron and ion currents are neglected. The clamping potential in absence of any biasing voltage is defined by the intersection of two of these curves; it is seen that this potential is not much influenced by the ratio  $r_a/r_c$ , and is of the order of 0.1-10V negative for electrons emitted with zero energy.

#### 4.4.2 PASSIVE EMITTER

An entirely passive emitter can be simply made of sharp-pointed filaments, electrically connected to the spacecraft but positioned at a distance equal to a few times the typical dimension of the vehicle, as shown in the insert of Figure 11.<sup>19</sup> The separation is requisite since it ensures that the strength of the electric field at the tips is not reduced by the charge induced in the surface of the main body.<sup>38</sup>

It is assumed that the collector is a sphere, 1 m in radius, immersed in a Maxwellian plasma with  $N_e = 1 \text{ cm}^{-3}$  and  $\phi_e = 1 \text{ kV}$ . The separation between the emitter and the surface is considered to be much larger than the sphere radius. In fact, for a distance of 3 radii, the clamping potential is within 25 percent of the value obtained for infinite separation. The emitter is made of 100 tips with a curvature radius  $a = 0.1 \mu\text{m}$ ; the emissive area is taken to be  $2\pi a^2$  and the strength of the electric field at the tips is of the order of  $|\phi_E/a|$ .

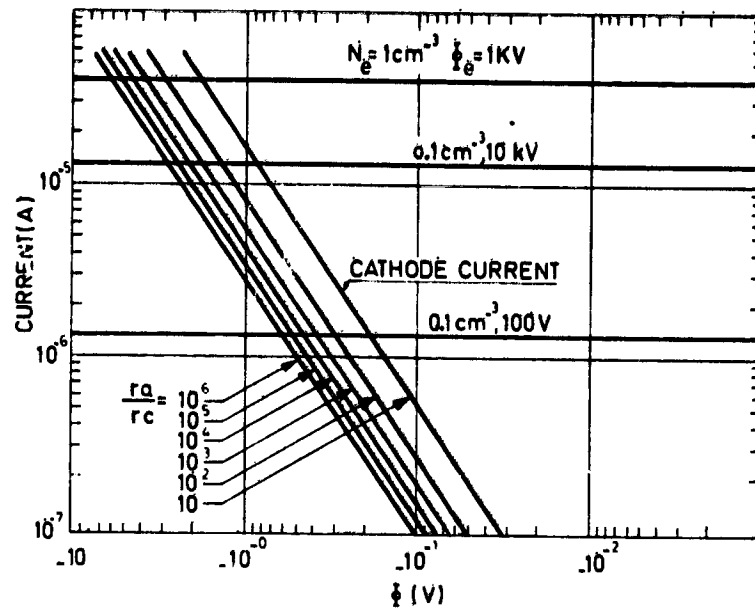


Figure 10. Determination of the Clamping Potential with an Active Electron Emitter

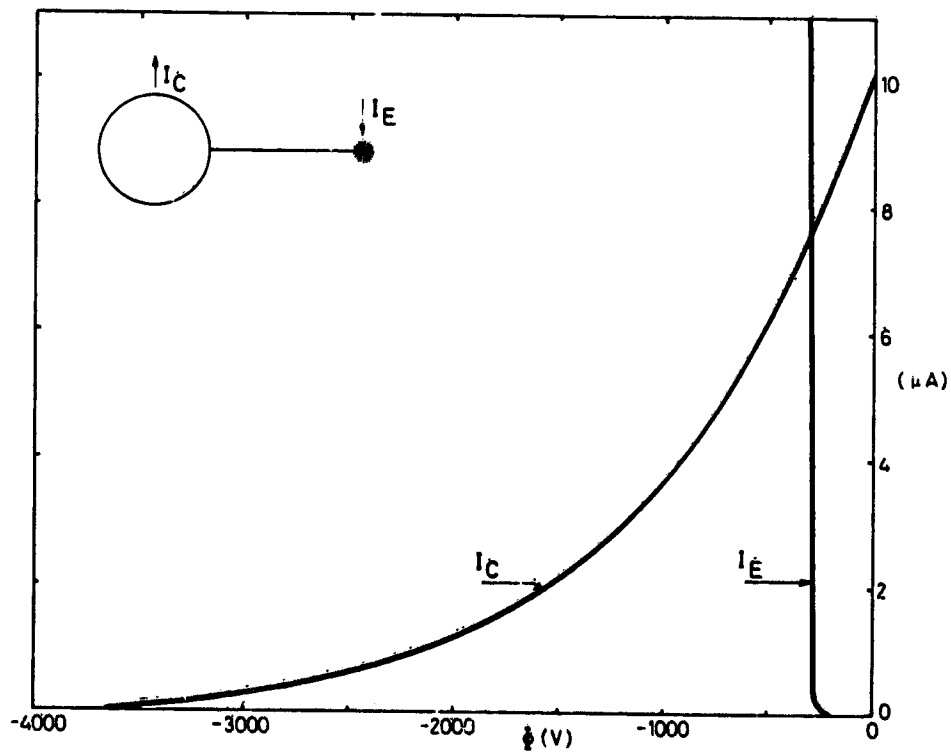


Figure 11. Determination of the Clamping Potential With Passive Electron Field Emitter

The current characteristic of the emitter is given by the Fowler-Nordheim equation,<sup>39</sup> and the potential of the sphere equal to  $-3800$  V without emitter ( $-3.8\Phi_e$ ) is increased to  $-316$  V when connected to the emitter; potential closer to zero are certainly possible with sharper points. The current that can be emitted from such a probe is limited by thermal dissipation and is of the order of 3 mA.

## 5. CONCLUSION

Electron emitters can prevent a spacecraft from accumulating negative charges and clamp its potential close to zero, provided its surface is conductive. As such, they should be part of any scientific magnetospheric payload because they significantly increase the value of field and particle measurements, in particular.

Information on the ambient medium can be obtained at a very little extra cost; such a diagnostic technique is very sensitive in rarefied plasma and can disclose small scale irregularities in the electron density. The existence of electromagnetic and electrostatic waves can also be detected, without any antenna, by investigating the frequency spectrum of the emitted current, that is, observing the current fluctuations associated with the alternative motion of the ambient particles.

Electron emitters also have interesting technological applications; they can monitor the degradation of conductive paints and coating in space and transform the thermal agitation of a plasma into electrical energy.

The choice of a system for space applications is motivated by considerations on reliability, weight, and power consumption. A thin-film field emission needs no heating but requires a grid system for electron extraction and energy control. A passive electron emitter is very simple but must be mounted on a boom with a length larger than the typical dimension of the collector. Presently, indirectly heated dispenser cathodes seem to offer the best compromise between these various requirements. They have been extensively tested in the laboratory and have lifetimes longer than one year. Provided they are mounted on an appendage of moderate length, say 0.5 m, they can clamp a spacecraft at a potential between  $-10$  and  $-1$  V and perform most of their functions without any grid or polarization system.

## Acknowledgments

The author wishes to thank the European Office of Aerospace Research and Development for arranging and supporting his participation at the Conference.

## References

1. Grard, R. J. L., Knott, K., and Pedersen, A. (1973) The influence of photoelectron and secondary electron emission on electric field measurements in the magnetosphere and solar wind, in Photon and Particle Interactions with Surfaces in Space, R. Grard, Editor, p. 163, Reidel, Dordrecht, Holland.
2. Fredricks, R. W., and Scarf, F. L. (1973) Observations of spacecraft charging effects in energetic plasma regions, in Photon and Particle Interactions with Surfaces in Space, R. Grard, Editor, p. 277, Reidel, Dordrecht, Holland.
3. Nanevicz, J. E., Adamo, R. C., and Shaw, R. R. (1975) Electronic discharges caused by satellite charging at synchronous orbit altitudes, in the Proceedings of the 1975 Conference on Lightning and Static Electricity, Paper V2, The Royal Aeronautical Society, London.
4. McPherson, D. A., Cauffman, D. D., and Schober, W. (1975) Spacecraft charging at high altitude - the SCATHA satellite program, AIAA Paper 75-92, AIAA 13th Aerospace Sciences Meeting, Pasadena, Ca.
5. Grard, R. J. L. (1975) Effect of the ambient medium upon the electric properties of the spacecraft surface and environment, in the Proceedings of the 1975 Conference on Lightning and Static Electricity, Paper VI, The Royal Aeronautical Society, London.
6. Rosen, A. (1975) Spacecraft charging: environment induced anomalies, AIAA Paper 75-91, AIAA 13th Aerospace Sciences Meeting, Pasadena, Ca.
7. Self, S. A. (1963) Exact solution of the collisionless plasma sheath equation, Physics of Fluids 6:1762.
8. Knott, K. (1972) The equilibrium potential of a magnetospheric satellite in an eclipse situation, Planet Space Sci. 20:1137.
9. DeForest, S. E. (1972) Spacecraft charging at synchronous orbit, J. Geophys. Res. 77:651.
10. DeForest, S. E. (1973) Electrostatic potentials developed by ATS. 5, in Photon and Particle Interactions with Surfaces in Space, R. Grard, Editor, p. 263, Reidel, Dordrecht, Holland.
11. Grard, R. J. L. (1973) Properties of the satellite photoelectron sheath derived from photoemission laboratory measurements, J. Geophys. Res. 78:2885.
12. Murphy, E. L., and Good Jr., R. H. (1956) Thermionic emission, field emission and the transition region, Phys. Rev. 102:1464.
13. Bartlett, R. O., DeForest, S. E., and Goldstein, R. (1975) Spacecraft charging control demonstration at geosynchronous altitude, AIAA Paper 75-359, New Orleans, La.

14. Goldstein, R., and DeForest, S. E. (1976) Active control of spacecraft potentials at geosynchronous orbit, in Spacecraft Charging by Magnetospheric Plasmas, A. Rosen, Editor, AIAA Progress in Astronautics and Aeronautics Series, Vol. 47, p. 169.
15. Grard, R. J. L., Gonfalone, A., and Pedersen, A. (1976) Spacecraft potential control with electron emitters, in Spacecraft Charging by Magnetospheric Plasmas, A. Rosen, Editor, AIAA Progress in Astronautics and Aeronautics Series, Vol. 47, p. 159.
16. Polychronopoulos, B., and Goodall, C. V. (1973) A system for measuring and controlling the surface potential of rockets flown in the ionosphere, in Photon and Particle Interactions with Surfaces in Space, R. Grard, Editor, p. 309, Reidel, Dordrecht, Holland.
17. Grard, R. J. L., and Tunaley, J. K. E. (1971) Photoelectron sheath near a plasma probe in interplanetary space, J. Geophys. Res. 76:2498.
18. Chen, F. F. (1965) Electric probe, in Plasma Diagnostic Techniques, R. H. Huddlestone and S. L. Leonard, Editor, Academic Press, New York.
19. Grard, R. J. L. (1975) Spacecraft potential control and plasma diagnostic using electron field emission probes, Space Science Instrumentation, 1:363.
20. Grard, R. J. L. (1976) Spacecraft charging control by field emission, J. Geophys. Res. 81:1805.
21. Köstlin, H., and Atzei, A. (1973) Present state of the art in conductive coating technology, in Photon and Particle Interaction with Surfaces in Space, R. Grard, Editor, p. 333, Reidel, Dordrecht, Holland.
22. Grard, R. J. L. (1977) The magnetospheric plasma as a source of energy for space instrumentation, Planet. Space Sci., in press.
23. Scarf, F. L. (1975) The magnetospheres of Jupiter and Saturn, in The Magnetosphere of the Earth and Jupiter, V. Formisano, Editor, p. 433, Reidel, Dordrecht, Holland.
24. Baker, D. N., and Van Allen, J. A. (1976) Energetic electrons in the Jovian magnetosphere, J. Geophys. Res. 81:617.
25. Brittain, W. M., and Christenbury, S. T. (1974) SNAP 19 Viking RTG flight configuration and integration testing, in 9th Intersociety Energy Conversion Engineering Conference Proceedings, p. 185, The American Society of Mechanical Engineers, New York.
26. Russo, F. A. (1974) Operational testing of the high performance thermoelectric generator (HPG-02), in 9th Intersociety Energy Conference Proceedings, p. 193, The American Society of Mechanical Engineers, New York.
27. Grard, R. J. L. (1976) Plasma diagnostic and wave detection with electron emitters, in the Proceedings of the Symposium on European Programmes on Sounding Rocket and Balloon Research in the Auroral Zone, SP 115, p. 221, European Space Agency, Noordwijk, Holland.
28. Grard, R. J. L. (1976) A new concept for detecting electromagnetic and electrostatic waves in space plasmas, Planet. Space Sci. 24:1097.
29. Bell, D. A. (1960) Electrical Noise, Van Nostrand, London.
30. Tunaley, J. K. E. (1970) The effect of noise on probe measurements in the magnetosphere, Ann. Geophys. 26:853.
31. Petit, M. (1975) Bruit radioélectrique dû aux photoélectrons, A.Télec. 30:351.

32. Whipple Jr., E.C. (1976) Observation of photoelectrons and secondary electrons reflected from a potential barrier in the vicinity of ATS 6, J. Geophys. Res. 81:715.
33. Intriligator, D. S. (1975) Pioneer 10 observations of the Jovian magnetosphere: plasma electron results, in The Magnetosphere of the Earth and Jupiter, V. Formisano, Editor, p. 313, Reidel, Dordrecht, Holland.
34. Mozer, F. S., Fahleson, U. V., Fälthammar, C. G., Kelley, M. C., Knott, K., and Pedersen, A. (1972) A Proposal to Measure Quasistatic Electric Fields on the Mother/Daughter Satellites, UCBSL 454, University of California, Berkeley.
35. Gonfalone, A. (1976) An Electron Gun for Spacecraft Potential Control, EWP 1016, European Space Agency, Noordwijk, Holland.
36. Spindt, C. A., Brodie, I., Humphrey, L., and Westerberg, E. R. (1976) Physical properties of thin-film emission cathodes, J. Appl. Phys. 47:5248
37. Spangenberg, K. (1948) Vacuum Tubes, McGraw-Hill, New York.
38. Jeans, Sir James (1963) The Mathematical Theory of Electricity and Magnetism, p. 196, Cambridge University Press, New York.
39. Gomer, R. (1961) Field Emission and Field Ionisation, Harvard University Press.

SESSION II  
MODELING

223

222  
PRECEDING PAGE BLANK NOT FILMED

## Contents

1. The Concept of Modeling	225
2. Modeling Spacecraft Charging	227
3. Model Verification	232
Acknowledgments	233
References	233

## 1. Modeling of Spacecraft Charging

Elden C. Whipple, Jr.  
University of California  
La Jolla, Ca.

## 1. THE CONCEPT OF MODELING

Webster's New Collegiate Dictionary<sup>1</sup> has the following definition for the word "model," in the sense in which we will be using it: "Model ... a system of postulates, data, and inferences presented as a mathematical description of an entity or a state of affairs." The reason that we are interested in modeling is that we would like to be able to predict an effect; namely, spacecraft charging. A model may be regarded as a mathematical representation of the link between cause and effect. If we can identify the cause, then the model provides a method for calculating (that is, predicting) the effects about which we are concerned.

There are different kinds of models, which can be conveniently arranged into three categories: (1) statistical models; (2) parametric models; and (3) physical models. A statistical model is usually the first kind of model that is arrived at in describing a phenomenon. For example, if it is cloudy, the probability of rain is increased, because we know that clouds and rain correlate. Statistical models using correlation can be useful because they can provide clues as to what is the cause for a phenomenon. But they can also be misleading because the correlation may be between two effects, or, the correlation may be coincidental. An example

of a correlation related to spacecraft charging is shown in Figures 1 and 2. Spacecraft anomalies occur more frequently between 0000 and 0600 hours in local time. Spacecraft charging events also show the same pattern. These figures are taken from papers by McPherson, Cauffman and Schober,<sup>2</sup> and from Reasoner et al.<sup>3</sup> The correlation between the two patterns provides evidence that the two phenomena - spacecraft anomalies and spacecraft charging - may be related.

The most useful kind of model is one that is based on understanding the physics of the actual processes that are involved in the phenomenon. Frequently, the processes are complicated or are only imperfectly understood. In such a case, a parametric model may be useful. Here, one or more physical parameters are selected which characterize the physical processes, and an approximate model is constructed based on these parameters. An example of such a model is shown in Figure 3 where the electron current to a sphere in a plasma has been calculated with the assumption of a spherically symmetric Debye potential distribution.<sup>4</sup> The current depends upon the Debye length parameter, as well as upon the plasma density and temperature and the sphere radius. This calculation is not exact but it gives the correct qualitative behavior and is much easier to calculate than the exact current.

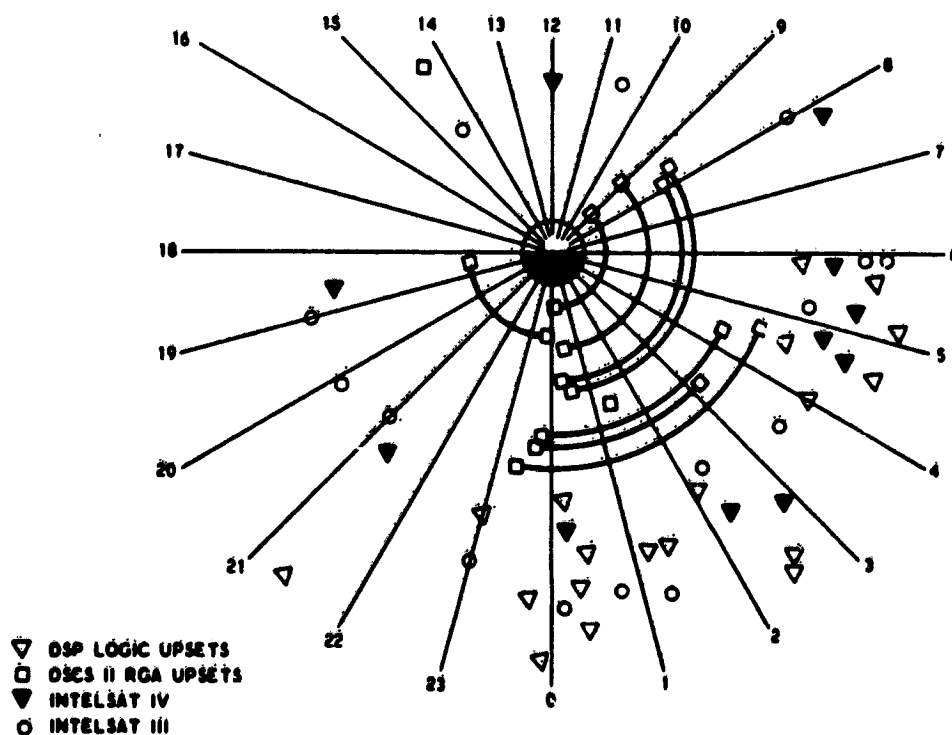


Figure 1. Local Time Dependence of Circuit Upset for Several DoD and Commercial Satellites

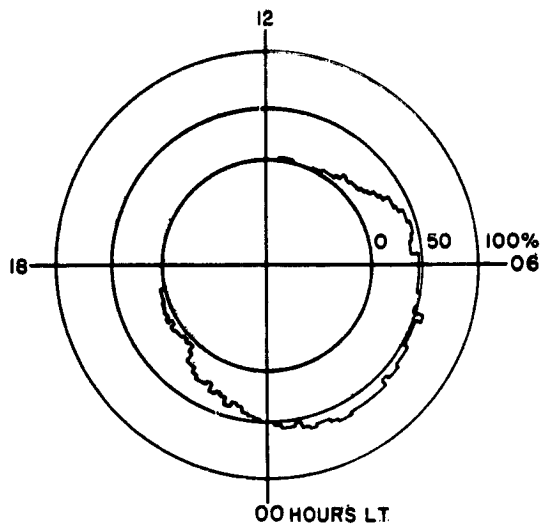
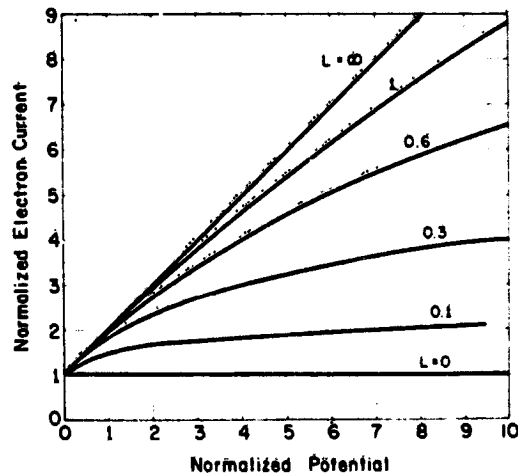


Figure 2. Local Time Distribution of ATS-6 Spacecraft Charging Events

Figure 3. Electron Current to a Sphere with an Assumed Debye Potential Distribution. The parameter  $L$  is the ratio of the Debye length to the sphere radius



## 2. MODELING SPACECRAFT CHARGING

There are four categories of models for spacecraft charging, and McPherson<sup>5</sup> has identified these four categories with four regions in the spacecraft-environment configuration, as shown in Figure 4. Region 1 is the undisturbed plasma far away from the spacecraft. This region may be assumed to be free from fields due to sheath effects. It is the source region for the plasma particles which make up part of the spacecraft charging currents.

Region 2 is the plasma sheath region where there are quasistatic electric fields. These electric fields are caused by the local charge distributions (space charge and surface charges) and in turn affect the trajectories of the charged

## FOUR REGIONS FOR MODELING

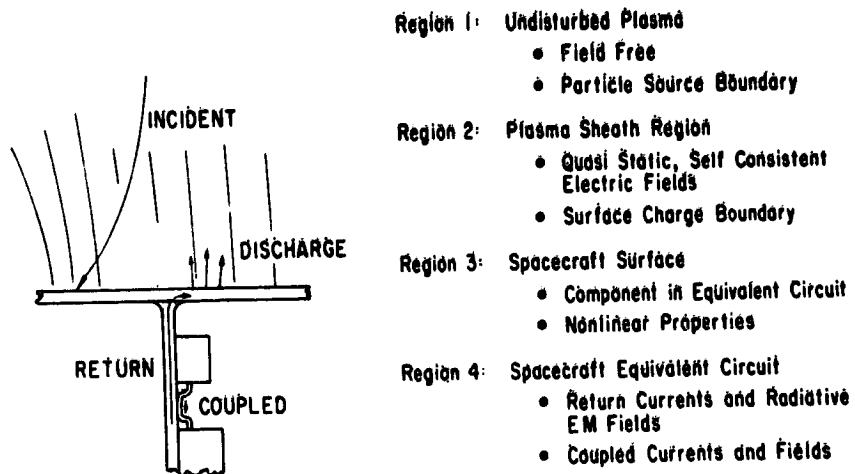


Figure 4. Regions Involved in Modeling Spacecraft Charging

particles going through this region. Hence, a self-consistent solution must be obtained for the particle and field distributions.

Region 3 is the spacecraft surface which is characterized by different materials and hence different properties for absorbing, emitting, and conducting charged particles. These properties may be very nonlinear. The spacecraft surface with its charge and potential distributions is a boundary for region 2, and it is also a part of the spacecraft electric circuit.

Region 4 is the spacecraft equivalent circuit describing the paths for currents and coupling for electromagnetic fields between the spacecraft components. One of the ultimate objectives for the overall modeling is to understand and predict the response of spacecraft components to the charging phenomena.

The first session of the conference has discussed region 1, the geosynchronous environment. Later sessions will discuss regions 3 and 4; that is, characterization of spacecraft materials and response to charging events. In the remainder of this discussion, a review will be made of some of the approaches to modeling region 2, the sheath about the spacecraft, and the related charge and potential distributions on the spacecraft surfaces.

The objective of modeling the spacecraft sheath is to obtain accurate values for the various charging currents which traverse the sheath and help to determine

the spacecraft surface potential and charge distributions. In this case the cause is the undisturbed environment, the effect is the surface potentials and charges, and the link is the charging currents. There are a number of different kinds of charging currents, as shown in Figure 5. Electrons and ions from the plasma travel to the spacecraft. Photoelectrons, secondary electrons, and reflected and backscattered electrons can travel from the spacecraft to the plasma or to other parts of the spacecraft surface. All of the particle trajectories which are external to the spacecraft are both influenced by the sheath electric fields and contribute to their configuration.

### KINDS OF CHARGING CURRENTS

(in rough order of importance)

- ① Electrons from plasma
- ② Photoelectrons from spacecraft surfaces
- ③ Ions from plasma
- ④ Secondary electrons from surface --- from electron impact
- ⑤ Secondary electrons from surface --- from ion impact

### TRANSFER OF CHARGE CAN OCCUR:

- ① From environment to spacecraft
- ② From spacecraft to environment
- ③ Between different spacecraft surfaces
  - { via external trajectories }
  - { via internal paths }

Figure 5. Different Charging Currents which Affect Spacecraft Charging

The condition for equilibrium -- that is, a steady-state or quasistatic situation -- is that the net current density vanishes at every point on the surface of insulating materials, or that the net current to every conducting element vanishes. In some situations -- for example, when discharges occur -- it is important to look at the time-dependent behavior of the charging currents, but for the most part the time

constants for charging are so short that the gross features of the sheath may be considered to be in quasistatic equilibrium.

Mathematically, the sheath problem may be described in terms of: (1) the Poisson equation, which tells one how to find the potential distribution for given space charge densities and boundary conditions; and (2) the Vlasov equation which tells one how to find the space charge densities for a given potential distribution. The solution of each of these equations depends upon knowing the solution to the other, so that a self-consistent procedure must be found for a solution. Usually, the procedure involves an initial guess and then successive improvements by iteration.

The various approaches that have been used in attempting to solve this problem have differed mainly in how the Vlasov equation has been solved. The Vlasov equation essentially states that the velocity distribution function (strictly speaking, the phase space density) for a given kind of particle is constant along the particle's trajectory. Consequently, a solution involves either a calculation (or approximation) of the particle trajectory, or else it must make use of some other physical relationship that provides equivalent information.

In table 2 of Parker,<sup>6</sup> the various approaches to the Vlasov equation are arranged into three categories. This classification is taken from a review by Parker<sup>6</sup> of theoretical work done on satellite sheaths and wakes. The following summary of the various treatments is also largely taken from Parker's report.

The inside-out method follows particle trajectories backwards in time from a point in the sheath at which the density is desired to the point of origin of the particles. At the origin of the trajectory the distribution function may be evaluated since the origin is either in the undisturbed plasma or at the spacecraft surface, where the distribution functions may be assumed to be known. The inside-out method is flexible since the points at which the density is to be evaluated may be chosen arbitrarily. Also, the method applies equally well to ions or electrons. The disadvantage of this method is that the information obtained about a trajectory is lost when one moves to the next point for obtaining density, and hence the computation can be time-consuming.

The inside-out method was developed by Parker,<sup>7</sup> and has been used by Fournier<sup>8</sup> to calculate the wake of a moving cylinder, and by Parker<sup>6</sup> for calculating the steady-state plasma flow about an arbitrarily thick disk. The method was used by Grabowski and Fischer<sup>9</sup> in conjunction with the assumption of quasineutrality, so that their treatment was not general. It was also used by Taylor<sup>10</sup> for the wake of an infinitely long cylinder of rectangular cross-section, but the calculation was not carried beyond the first iteration, and is therefore not self-consistent. Parker and Whipple<sup>11, 12</sup> used the method for two-electrode probes on a satellite but did not self-consistently solve for the sheath potential distribution. Liu and

Hung<sup>13</sup> used this method for the far-wake zone of a satellite to predict wave-like behavior. Parker<sup>14, 15</sup> has also used the method for two-electrode rocket-borne and laboratory probe systems, and for the problem of a small probe in the sheath of a large electrode.

The outside-in method follows particle trajectories in the same direction as the actual particle motion. The main disadvantage of this method is that it is difficult to choose the trajectories in such a way that an accurate density can be obtained at an arbitrary point. In the special case where trajectories do not cross or reverse direction, the flux tube method of choosing trajectories may be used. This technique was used by Davis and Harris<sup>16</sup> for a wake calculation assuming cold ions, by Call<sup>17</sup> for the cold-ion wakes of both cylinders and spheres, by Martin<sup>18</sup> for the cold-ion wakes of a strip and disk, and by McDonald and Smetana<sup>19</sup> for the wake of an infinitely long cylinder in a drifting monoenergetic plasma. Another approach using the outside-in method is to divide the space into cells and to evaluate the density in each cell according to the time that the particle spends in it. This method is closely related to "particle-pushing" or simulation calculations, and can be readily adapted to time-dependent problems. Again, accurate calculations can be time-consuming since many trajectories are required to obtain good statistics within cells. This method was studied by Parker<sup>7</sup> for mono-energetic-ion distribution with drift, and was used by Maslennikov and Sigov<sup>20</sup> for the cold-ion wake of a sphere.

"Other" methods are defined as treatment which avoid explicit trajectory calculations and make use of other physical relationships. For example, configurations with inherent symmetry such as spheres or cylinders in an isotropic plasma may be treated by working with constants of the motion (that is, energy, angular momentum, etc.) which characterize the particle trajectories. These simple configurations are useful because solutions can serve as benchmarks for the numerical methods developed for more realistic problems. Also, they serve to illustrate the basic physical processes that may be involved in the charging phenomenon. Bernstein and Rabinowitz<sup>21</sup> used this approach to treat the problem of a sphere in a plasma containing mono-energetic ions. Laframboise<sup>22</sup> treated exactly the problems of both spheres and cylinders in Maxwellian plasmas. Chang and Blenkowski<sup>23</sup> used this approach to treat the problem of a thin sheath when there is emission of electrons at the surface of a spherical probe in a plasma. Schroder<sup>24</sup> and Whipple<sup>25</sup> extended this to treat the case of a thick sheath. Parker<sup>26</sup> has formulated a computer program which treats arbitrary sheath thicknesses for electron emitting spherical probes in an isotropic plasma with arbitrary velocity distributions.

Other approaches which avoid trajectory calculations have used various assumptions or approximations such as expressing the ion or electron density in

terms of the local potential by means of the Boltzmann factor, neglecting ion thermal velocities, assuming quasineutrality, etc. Liu<sup>27</sup> and Jew<sup>28</sup> assumed that the ion axial component of velocity is constant. They then determined limiting trajectories for the density integral by further approximations, namely, an additional assumed approximate constant of the motion, evaluated using the local field in the vicinity of the point in question. Kiel, Gey, and Gustafson<sup>29</sup> treated the wake of a sphere, assuming straight-line paths for the ion trajectories, and also assuming approximate formulas for the electron densities. Gurevich et al<sup>30</sup> assumed quasineutrality, using the Boltzmann factor for both ions and electrons, and assumed in addition that the ion axial component of velocity was constant and that the ion thermal velocity was small.

### 3. MODEL VERIFICATION

A model cannot be considered to be reliable until it has been verified. Verification means comparing the prediction of the model with experimental results and finding agreement. As can be seen from the number of theoretical treatments of the spacecraft sheath problem, models are fairly easy to generate. It is much more difficult, in general, to perform the kind of experiment which will provide data for verification or nonverification of the model. This seems to be especially true in space physics, where there is such a long process involved in performing experiments on spacecraft. The process begins with a proposal, and then continues through the experiment design and construction, a great deal of testing, finally a launch which may or may not be completely successful, and then data acquisition, transmission through telemetry links and ground stations back to the experimenter, and finally reduction and analysis of the data by the experimenter. This cycle from the conception of the experiment until its analysis typically involves several years, and it is no wonder that in space physics the connection between a theoretical model and its experimental verification is frequently somewhat remote.

An example of how models can be rendered academic by the acquisition of data is provided by work that has been done on the photoelectron sheath about a spacecraft. A number of workers, beginning with Singer and Walker<sup>31</sup> in 1962 have discussed the effect of photoelectrons on the plasma sheath surrounding a spacecraft. Various velocity distribution functions for the photoelectrons were treated in various geometries, but almost all of the treatments were for a conducting body. Guernsey and Fu<sup>32</sup> and Fu<sup>33</sup> showed that if the photoelectrons dominate the space charge near the satellite surface, it would be possible for a potential minimum to develop in the sheath so that the potential distribution would be nonmonotonic.

(See Whipple<sup>25</sup> for a review of these treatments.) Such a potential minimum was found by analysis of the electron data obtained from the UCSD particle detectors on the ATS-6 satellite.<sup>34</sup> However, it was shown that none of the models could adequately explain the data.<sup>25</sup> The potential minimum which was inferred from the data was much too large to be explained in terms of the ordinary space charge limited effect. It is probable that the minimum must be explained in terms of differential charging of the spacecraft surfaces. Electrons are emitted from these differentially charged portions of the spacecraft surface providing the required negative space charge for the formation of the potential minimum. However, a quantitative model for this phenomenon has not yet been formulated.

Another way of verifying sheath models that has not been adequately exploited is through laboratory experiments. Although it is not possible to completely simulate the geosynchronous environment in a laboratory, it should be possible to study many of the individual processes. It is certainly possible to generate fluxes of particles in the appropriate energy ranges in the laboratory, and there should be no problem in simulating solar photoemission. It should be possible to learn a great deal about the charging process and especially about the interaction between various spacecraft elements by using realistic models of a spacecraft in such a laboratory environment.

## Acknowledgments

I would like to thank Dr. Lee W. Parker for permission to use material from his reviews.<sup>5, 35</sup> This work was supported by NASA Grant NGL 05-005-007 and Air Force Contract F19628-76-C-0214.

## References

1. Webster (1975) New Collegiate Dictionary, G. and C. Merriam Co., Springfield, Mass.
2. McPherson, D. A., Cauffman, D. P., and Schober, W. (1975) Spacecraft charging at high altitudes: SCATHA satellite program, J. Spacecraft and Rockets 12:621.
3. Reasoner, D. L., Lennartsson, W., and Chappell, C. R. (1975) The relationship between ATS-6 spacecraft charging occurrences and warm plasma encounters, presented at AIAA/AGU Joint Session on Spacecraft Charging, Washington, D. C.

4. Whipple, E. C., Warnock, J. M., and Winkler, R. H. (1974) Effect of satellite potential on direct ion density measurements through the plasmopause, J. Geophys. Res. 79:179.
5. McPherson, D. A. (1976) Spacecraft charging modeling status SAI Report, Science Applications, Inc., El Segundo, Ca.
6. Parker, L. W. (1976) Computation of collisionless steady-state plasma flow past a charged disk, NASA CR-144159, Lee W. Parker, Inc., Concord, Mass.
7. Parker, L. W. (1964) Numerical methods for computing the density of a rarefied gas about a moving object, AFGL-64-193, Allied Res. Assoc., Inc., Concord, Mass.
8. Fournier, G. (1971) Collisionless plasma flow around a cylinder considering applications to ionospheric probes, Pub. No. 137, Office Nat. d'Etudes et de Recherches Aérospatiales, Paris.
9. Grabowski, R., and Fischer, T. (1975) Theoretical density distribution of plasma streaming around a cylinder, Planet. Space Sci. 23:287.
10. Taylor, J. C. (1967) Disturbance of a rarefied plasma by a supersonic body on the basis of the Poisson-Vlasov equations - I, Planet. Space Sci. 15:155.
11. Parker, L. W., and Whipple, E. C. (1967) Theory of a satellite electrostatic probe, Ann. Phys. 44:126.
12. Parker, L. W., and Whipple, E. C. (1970) Theory of spacecraft sheath structure, potential, and velocity effects on ion measurements by traps and mass spectrometers, J. Geophys. Res. 75:4720.
13. Liu, V. C., and Hung, R. J. (1968) Double scattering of the plasma streams in a bi-thermal ionosphere, Planet. Space Sci. 19:845.
14. Parker, L. W. (1968) Theory of the external sheath structure and ion collection characteristics of a rocket-borne mass spectrometer, AFGL-71-0105, Mt. Auburn Res. Assoc., Cambridge, Mass.
15. Parker, L. W. (1973) Computer solutions in electrostatic probe theory, AFAL-TR-72-222, Mt. Auburn Res. Assoc., Newton, Mass.
16. Davis, A. H. and Harris, I. (1961) Interaction of a charged satellite with the ionosphere, in Rarefied Gas Dynamics, L. Talbot, Editor, Academic, New York.
17. Call, S. M. (1969) The interaction of a satellite with the ionosphere, Report 68, Columbia University, New York.
18. Martin, A. R. (1974) Numerical solutions to the problem of charged particle flow around an ionospheric spacecraft, Planet. Space Sci. 22:121.
19. McDonald, P. W., and Smetana, F. O. (1969) Results of a numerical experiment to determine the current collected by a charged cylinder in a collisionless plasma stream, in Rarefied Gas Dynamics, L. Trilling and H. Y. Wachman, Editors, p. 1627, Academic, New York.
20. Maslennikov, M. V., and Sigov, Y. S. (1965) A discrete model for the study of the flow of a rarefied plasma about a body, Soviet Phys. Doklady 9:1063.
21. Bernstein, I. B., and Rabinowitz, I. N. (1959) Theory of electrostatic probes in a low-density plasma, Phys. Fluids 2:112.
22. Laframboise, J. G. (1966) Theory of spherical and cylindrical langmuir probes in a collisionless Maxwellian plasma at rest, UTIAS Report 100, Univ. of Toronto, Ontario.
23. Chang, K. W., and Blenkowski, G. K. (1970) Effects of electron emission on electrostatic probes at arbitrary pressures, Phys. Fluids 13:902.

24. Schroder, H. (1973) Spherically symmetric model of the photoelectron sheath for moderately large plasma Debye lengths, in Photon and Particle Interactions with Surfaces in Space, R.J.L. Grard, Editor, p. 51, D. Reidel, Dordrecht.
25. Whipple, E.C. (1976) Theory of the spherically symmetric photoelectron sheath: a thick sheath approximation and comparison with the ATS 6 observation of a potential barrier, J. Geophys. Res. 81:601.
26. Parker, L.W. (1975) Computer methods for satellite plasma sheath in steady-state spherical symmetry, AFGL-TR-75-0410, Lee W. Parker, Inc., Concord, Mass.
27. Liu, V.C. (1969) Ionospheric gas dynamics of satellite and diagnostic probes, Space Sci. Rev. 9:423.
28. Jew, H. (1968) Numerical studies of the rarefied plasma interaction at mesothermal speeds, Ph.D. Thesis, University of Michigan.
29. Kiel, R.E., Gey, G.C., and Gustafson, W.A. (1968) Electrostatic fields of an ionospheric satellite, AIAA Jour. 6:690.
30. Gurevich, A.V., Pitaevskii, L.P., and Smirnova, V.V. (1969) Ionospheric aerodynamics, Space Sci. Rev. 9:805.
31. Singer, S.F., and Walker, E.H. (1962) Photoelectric screening of bodies in interplanetary space, Icarus 1:7.
32. Guernsey, R.L., and Fu, J.H.M. (1970) Potential distribution surrounding a photo-emitting diode in a dilute plasma, J. Geophys. Res.
33. Fu, J.H.M. (1971) Surface potential of a photo-emitting diode, J. Geophys. Res. 76:2506.
34. Whipple, E.C. (1976) Observation of photoelectrons and secondary electrons reflected from a potential barrier in the vicinity of ATS 6, J. Geophys. Res. 81:715.
35. Parker, L.W. (March 1974) Present status of in-situ wake and sheath measurements, in Report of the Plasma Physics and Environmental Perturbation Laboratory (PPEPL) Working Groups; Vol. I Plasma Probes, Wakes, and Sheaths Working Group, Appendix A, NASA TM X-64856.

## Contents

1. Introduction	238
2. Spacecraft Charging Model Development	240
3. Spacecraft Charging Simulation Results	255
4. Conclusions and Discussion	264
References	266
Appendix A	268

## 2. A Charging Model for Three-Axis Stabilized Spacecraft

M. J. Massaro, T. Green, and D. Ling  
 General Electric Company  
 Space Division  
 Philadelphia, Pa.

### Abstract

A charging model is developed for geosynchronous, three-axis stabilized spacecraft when under the influence of a geomagnetic substorm. The differential charging potentials between the thermally coated or blanketed outer surfaces and metallic structure of a spacecraft are determined when the spacecraft is immersed in a dense plasma cloud of energetic particles. The spacecraft-to-environment interaction is determined by representing the charged particle environment by equivalent current source forcing functions and by representing the spacecraft by its electrically equivalent circuit with respect to the plasma charging phenomenon. The charging model includes a sun/earth/spacecraft orbit model that simulates the sun illumination conditions of the spacecraft outer surfaces throughout the orbital flight on a diurnal as well as a seasonal basis. Transient and steady-state numerical results for a three-axis stabilized spacecraft are presented.

\*This work was performed under a General Electric Space Division 1976 Internal Research and Development Program, No. 76SDS4161.

## 1. INTRODUCTION

Recent data from the geosynchronous orbiting NASA satellites ATS-5 and ATS-6<sup>1, 2, 3</sup> has indicated that the surface of these satellites can charge to hundreds of volts when in sunlight and thousands of volts (up to -10 kV) when in eclipse. Data transmitted from these satellites during these charging events has indicated the existence of transient fluxes of energetic particles. It has been suggested<sup>4</sup> that these clouds of energetic particles are injected into the local-midnight-to-dawn region of the geosynchronous altitude during geomagnetic substorm activity. Consequently, during a geomagnetic substorm, spacecraft at altitudes greater than three Earth radii, in the local time sector from just before midnight to past dawn, occasionally will encounter and be immersed in a dense plasma cloud of energetic particles. It has been further postulated that this charged particle environment is the major cause of spacecraft charging. That is, in the steady-state, every isolated part of a spacecraft immersed in the space environmental plasma will come into electrical equilibrium by developing surface charges of the proper sign and magnitude such that the net current - represented by the deposition and release of charged particles from the surface of the spacecraft - is zero. The equilibrium potential of the surface of the spacecraft is the potential difference between the surface and ambient plasma sheath. The most important contributors to the equilibration currents are the primary plasma electron and proton arrivals at the surface and the photoelectrons released when sunlight illuminates the surface. In addition, the contributions of secondary electrons released from the surface under primary proton or electron impact and possible electron reattraction to the surface, are also significant and must be considered in a complete analysis of the problem.

In the coincidence with the geomagnetic substorm activity in this local time quadrant, is the occurrence of anomalous events on-board satellites in geosynchronous orbit when immersed in the substorm plasma. Specifically, anomalous behavior experienced by several satellites has included<sup>5</sup> control circuit switching, power system failure, sensor data noise, thermal control degradation, and telemetry logic switching. There is a growing body of evidence which demonstrates the dependence of satellite anomalous behavior on geophysical parameters such as local time and geomagnetic activity.

Consequently, it has been postulated<sup>1, 4</sup> that the anomalous behavior of synchronous spacecraft is due to electrostatic charging of the various spacecraft surfaces to large negative potentials and their subsequent discharging. The electromagnetic pulses produced by the discharges contain enough energy to interact with electronic logic circuits at distances of tens of centimeters, and cause voltage spikes large enough to change logic states. Other data from spacecraft indicate that repeated discharging also results in the degradation of thermal control surfaces.

Thus, it is the differential charging of the various thermally blanketed or coated outer surface materials with respect to each other and with respect to the spacecraft metallic structure and the subsequent discharging, when the dielectric strength of the surface materials is exceeded, that is one of the major causes of satellite anomalous behavior.

The purpose of this paper is to develop a spacecraft charging simulation model which adequately represents the spacecraft-to-environment interaction when the spacecraft is immersed in the charged particle environment that is encountered at geosynchronous orbit during a geomagnetic substorm. Further, the principal results of the simulation analysis model developed will be the differential charging potentials between the thermally blanketed or coated outer surfaces and the metallic structure of the spacecraft. To determine the spacecraft-to-environment interaction, the equivalent electrical model of the spacecraft with respect to the charging phenomenon is developed and the plasma environment is represented by equivalent current forcing functions. The equivalent current sources of the charged particle environment simulate the ambient plasma as a charging current source and the surface photoelectron and secondary electron emissions as discharging current sources. The spacecraft outer surface configuration is represented by constituent dielectric and metallic surfaces which collect charge from the environment. In addition, a S/C geometrical model and a solar/earth orbital model are also developed to determine the sun-illumination condition of the outer surfaces as a function of spacecraft orbital position. That is, the geometrical and orbital models are used to determine whether a surface is sun-illuminated, self-shadowed, or earth-shadowed. In addition, when a surface is sun-illuminated, the intensity of the illumination, which is a function of the sun/spacecraft surface aspect angle, is also determined by the models.

Charging models have appeared recently in the literature.<sup>2, 6, 7</sup> However, the models are based primarily on the analysis of spin-stabilized spacecraft. For the particular types of spacecraft analyzed, there was considerable seasonal and diurnal variation of the exposed metallic area illuminated by the sun. However, due to the restricted location of thermal blanket materials and the external structural form of spin-stabilized spacecraft, there were small diurnal variations in both the amount and location of the thermal blanket material areas illuminated by the sun during the midnight-to-dawn local time quadrant. Consequently, no attempt was made to determine the sun-illumination condition of exposed dielectric surfaces during the daily orbital flight. However, for three-axis stabilized spacecraft the diurnal as well as the seasonal variations of the amount and location of both the dielectric and exposed metallic areas illuminated by the sun are considerable. The model discussed in this paper determines the variations of sun-illumination condition of all of the exposed surfaces throughout the daily orbital path in addition

to considering the seasonal changes. Also, the previous models have not considered the intrinsic capacitance of the spacecraft structure with respect to the plasma sheath. In this paper, the structural capacitance has been included in the simulation model, and it will be shown that the structural capacitance has a significant influence on the transient response.

In the following sections, the development of the spacecraft charging model is discussed in general terms and includes a discussion of the plasma model, the electrical model, the geometrical model, a solar/earth orbital model, the material properties and configuration definition, and the numerical integration approach. Spacecraft charging results are given for a geosynchronous satellite during the midnight-to-dawn local time quadrant for the fall-equinox and winter-solstice seasonal periods.

## 2. SPACECRAFT CHARGING MODEL DEVELOPMENT

The spacecraft charging model development can best be described in terms of the flow chart shown in Figure 1. The S/C charging model consists of four separate models: a plasma model, an electrical model, a S/C geometrical model; and a solar/earth orbital model. The plasma model represents the charging and discharging mechanism of the ambient plasma with respect to the spacecraft by equivalent current sources. The current sources, which are dependent on the particle energy distribution functions, constitute the forcing functions of the charging model equations. The electrical model defines the lumped element equivalent circuit representation of the spacecraft surfaces with respect to the electrostatic charging phenomenon. The plasma model and electrical model are combined to form the nonlinear spacecraft charging equations. The spacecraft geometrical model defines the spacecraft outer surfaces in terms of approximate planar surfaces and curved surface projections and defines the vertices of all planar and curved surfaces in terms of a spacecraft reference coordinate system. The solar/earth orbital model determines the location of the spacecraft with respect to the sun and the earth. The geometrical model and the solar/earth orbital model are combined to determine the variation of the sun-illumination conditions of the outer surfaces with respect to orbital position.

To complete the modeling, the surface material properties and configuration are defined. The surface material properties that are most important in a spacecraft charging analysis are: the relative dielectric constant, the variation of the surface resistivity with respect to electrical stress level, and the variation of the bulk resistivity with respect to electrical stress level. The material configuration definition describes the location of the various thermal blanket and surface coating materials.

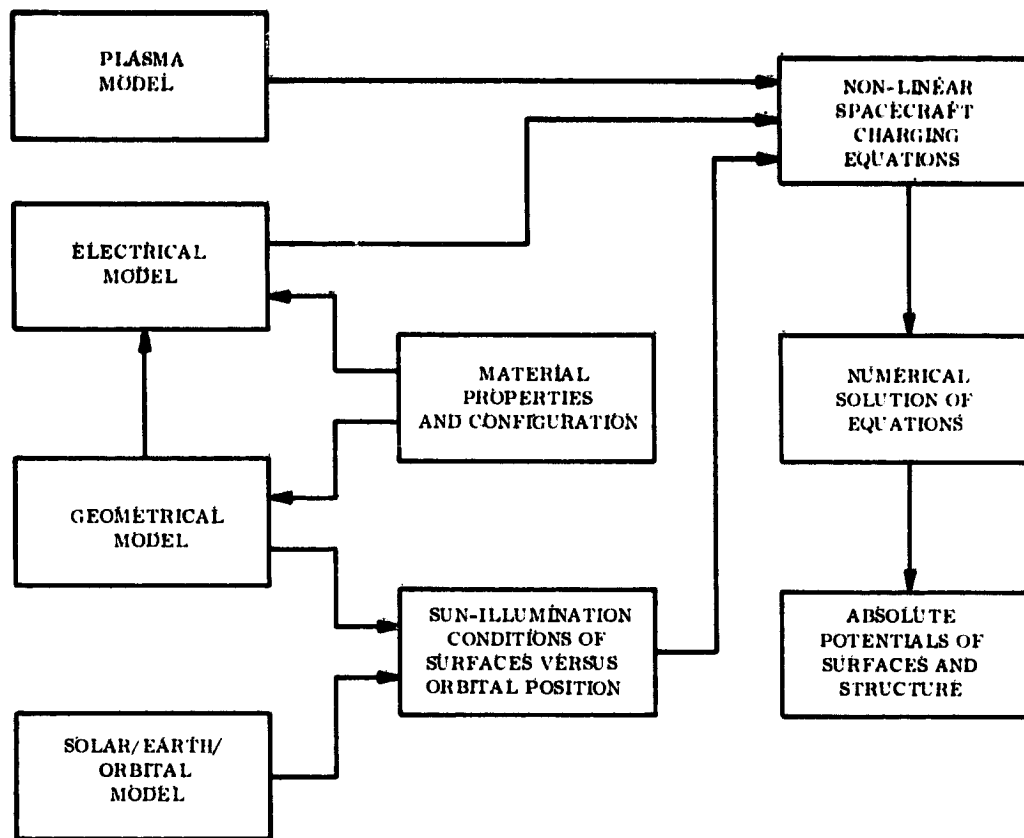


Figure 1. Spacecraft Charging Model Flow Chart

The elements of the flow chart will now be discussed in greater detail.

### 2.1 Plasma Model

As discussed previously, spacecraft at geosynchronous orbit will occasionally encounter energetic charged particle fluxes and these fluxes will cause the various outer surfaces to charge to large potentials. The charging and discharging mechanism of the ambient plasma with respect to the spacecraft can be represented or simulated by equivalent current sources that become the forcing functions of the charging model equations. The constituent particle fluxes that affect the charging of a surface are protons, electrons, photoelectrons, and secondary electrons.

Several investigators<sup>6, 8, 9</sup> have approximated the energy distribution of the particle fluxes as measured on ATS-5 by a Maxwell-Boltzmann (M-B) energy distribution and, further, have assumed the particle fluxes to have an omnidirectional energy distribution; that is, the energy distribution of the particles is identical in

each direction. Thus, it is possible to characterize the particle energy distributions by a thermal energy ( $K\tau$ ) expressed in electron volts. This approximation is used in this paper to simplify the analysis and to provide an insight into the problem that might otherwise be obscured by a more complex approach.

The total current flowing into the outer surface of a spacecraft is

$$I = J_T \cdot A \quad (1)$$

where  $A$  is the surface area and  $J_T$  is the total positive current density into the surface and is given by

$$J_T = J_p + J_{sp} - J_e + J_{se} + J_{ph} \quad (2)$$

where  $J_p$  is the incident proton current density,  $J_{sp}$  is the secondary electron current density produced by incident protons,  $J_e$  is the incident electron current density,  $J_{se}$  is the secondary electron current density produced by incident electrons, and  $J_{ph}$  is the photoelectron current density.

A charged surface at a given potential in a charged particle environment will accelerate particles of the opposite polarity and repel particles of the same polarity. Thus, assuming an omnidirectional Maxwellian energy distribution, the fraction of ambient plasma electrons reaching a large surface at a potential  $V$  is<sup>10</sup>

$$N_e = N_{e_0} \exp\left(\frac{eV}{K\tau_e}\right), \quad V \leq 0 \quad (3)$$

where  $N_e$  is the incident electron density,  $N_{e_0}$  is the ambient electron density,  $V$  is the potential of the surface under consideration,  $K$  is Boltzmann's constant,  $e$  is the charge of an electron, and  $\tau_e$  is the absolute temperature of the M-B electron energy distribution.

The average ambient electron current density incident to a neutral surface is given by

$$J_{e_0} = N_{e_0} e \bar{v}_e \quad (4)$$

where  $J_{e_0}$  is the average ambient electron current density and  $\bar{v}_e$  is the mean ambient thermal velocity.

Thus, from Eqs. (3) and (4), the average electron current density incident to a large surface at potential  $V$  is

$$J_e = N_e e \bar{v}_e = J_{e_0} \left( \frac{eV}{K\tau_e} \right), \quad V \leq 0 \quad (5)$$

or

$$J_e = J_{e_0} e^{(V/T_e)}, \quad V \leq 0 \quad (6)$$

where

$$T_e = \frac{K\tau_e}{e} \quad (7)$$

is the equivalent temperature, expressed in volts, of the M-B distribution approximating the plasma electron energy distribution, and  $J_e$  is the electron current density incident to a large surface at potential  $V$ . For a positive surface

$$J_e = J_{e_0}, \quad V \geq 0 \quad (8)$$

That is, a surface at a positive potential will attract oppositely charged particles but cannot extract more particles from the plasma environment than the ambient particle density  $N_{e_0}$ . Similarly, the proton current density incident to a large surface at potential  $V$  is

$$J_p = J_{p_0} e^{-V/T_p}, \quad V \geq 0 \quad (9)$$

and

$$J_p = J_{p_0}, \quad V \leq 0 \quad (10)$$

where  $J_{p_0}$  is the average ambient proton current density incident to a neutral surface, and  $T_p$  is the equivalent temperature of the M-B distribution approximating the plasma proton energy distribution and is expressed in volts.

In addition to the above charged particle fluxes, there will be secondary emission electrons as well as photoelectron emissions. Both types of charged particles will be repelled by a surface at a negative potential and attracted by a surface at a positive potential. Consequently, based on the previous discussion, the secondary electrons leaving a surface of potential  $V$  is given by

$$J_{se} = J_{se_0} e^{-V/T_s}, \quad V \geq 0 \quad (11)$$

$$J_{se} = J_{se_0}, \quad V \leq 0 \quad (12)$$

$$J_{sp} = J_{sp_0} e^{-V/T_s}, \quad V \geq 0 \quad (13)$$

$$J_{sp} = J_{sp_0}, \quad V \leq 0 \quad (14)$$

where  $J_{se_0}$  and  $J_{sp_0}$  are the average secondary electron current densities emitted from a neutral surface produced by incident electrons and protons, respectively,  $J_{se}$  and  $J_{sp}$  are the secondary electron current densities emitted by the incident electrons and protons, respectively, and  $T_s$  is the equivalent temperature of the M-B distribution representing the energy distribution of the secondary emission electrons and is expressed in volts. The secondary emission electron current densities are directly related to the incident particle current densities. It is assumed that the secondary electrons emitted from a neutral surface are related to the incident particles by a fixed constant and can be expressed as

$$J_{se_0} = J_e f_e \quad (15)$$

$$J_{sp_0} = J_p f_p \quad (16)$$

where  $f_e$  is the ratio of secondary electrons to incident electrons and  $f_p$  is the ratio of secondary electrons to incident protons. In general, the secondary emission constants,  $f_e$  and  $f_p$ , will have different values for dielectric and metallic surfaces.

A similar development holds for the photoelectron emissions produced by sun illumination. The photoelectron current is directly proportional to the intensity of sunlight which is related to the angle of incidence. Consequently, the photoelectron current density emitted from a surface at potential  $V$  can be expressed as

$$J_{ph} = J_{ph_0} e^{-V/T_{ph}} \cos \alpha, \quad V \geq 0 \quad (17)$$

$$J_{ph} = J_{ph_0} \cos \alpha, \quad V \leq 0 \quad (18)$$

where  $J_{ph}$  is the photoelectron current density emitted from an illuminated surface at potential  $V$ ,  $J_{ph_0}$  is the average photoelectron current density emitted from an illuminated neutral surface,  $T_{ph}$  is the equivalent temperature of the M-B distribution representing the energy distribution of the photoelectrons expressed in volts,  $\alpha$  is the angle between the sun-line and the surface normal vector (sun/spacecraft surface aspect angle) and

$$\cos \alpha = \begin{cases} \cos \alpha & \text{for } |\alpha| < \pi/2 \\ 0 & \text{for } |\alpha| \geq \pi/2 \text{ (self-shadowing conditions)} \end{cases} \quad (19)$$

The total positive current density into a surface can take one of four possible forms depending on the polarity, positive or negative, of the surface potential and the presence or absence of sun illumination. Thus, for a large dielectric surface, the current forcing function will have the general form

$$I_D(V) = \left[ J_{p_0} e^{-V/T_p} \left( 1 + f_{p_D} e^{-V/T_s} \right) + J_{ph_0} (\cos \alpha) e^{-V/T_{ph}} + J_{e_0} e^{V/T_e} \left( f_{e_D} e^{-V/T_s} - 1 \right) \right] \cdot A \quad (20)$$

where  $I_D$  is the total positive current into a large dielectric surface,  $A$  is the area of the surface, and all other terms have been defined previously. The above equation must satisfy the following condition

$$e^{sV/X} = \begin{cases} 1 & \text{if } s = +1 \text{ and } V > 0; \text{ otherwise leave unchanged} \\ 1 & \text{if } s = -1 \text{ and } V \leq 0; \text{ otherwise leave unchanged} \end{cases} \quad (21)$$

Exposed metallic parts of the structure can be located on many different outer surfaces of the spacecraft; consequently, the various exposed metallic surfaces, which are electrically connected, can have different sun-illumination conditions and the current forcing function will have a more complex form. In addition, the exposed metallic surfaces are generally small in area. Fewer charged particles will be deflected from a small surface at a given potential than a large surface at

the same potential; consequently, a correction factor must be applied to small surface areas. Thus, the positive current flowing into the exposed metallic structure is

$$\begin{aligned}
 I_M(V) = & A_{M_T} J_{p_0} (1 + V/T_p) e^{-V/T_p} \left( 1 + f_{p_M} e^{-V/T_s} \right) \\
 & + A_{M_T} J_{e_0} e^{V/T_e} \left( f_{e_M} e^{-V/T_s} - 1 \right) (1 + |V/T_e|) \\
 & + \sum_{i=1}^m A_{M_i} J_{ph_0} (\cos \alpha_i) e^{-V/T_{ph}} \quad (22)
 \end{aligned}$$

where Eq. (21) holds for the above equation,  $A_{M_T}$  is the total exposed metallic area,  $A_{M_i}$  is the exposed area of the  $i^{\text{th}}$  metallic surface,  $m$  is the total number of exposed metallic surfaces,  $\alpha_i$  is the sun aspect angle for the  $i^{\text{th}}$  metallic surface, and the following holds for the small area correction terms<sup>7</sup>

$$(1 + V/T_p) = \begin{cases} (1 + V/T_p) & \text{for } V \geq 0 \\ 1 & \text{for } V < 0 \end{cases} \quad (23)$$

$$(1 + |V/T_e|) = \begin{cases} (1 + |V/T_e|) & \text{for } V \leq 0 \\ 1 & \text{for } V > 0 \end{cases} \quad (24)$$

Equations (20) and (22) are the plasma and photoemission generated current sources and constitute the forcing functions of the spacecraft charging equations.

## 2.2 Material Properties and Configuration

The spacecraft outer surface material: properties and configuration definition are needed to complete both the geometrical and electrical models. Essentially, the material properties and configuration definition consist of describing the location of the various outer surface thermal blankets and coatings and their electrical properties. The location of the materials is needed in the geometrical model to establish the number of constituent planar and curved surfaces of the spacecraft. The electrical properties of the materials are needed in the electrical model to determine the equivalent circuit element values of the outer surfaces of the spacecraft.

The electrical properties of the outer surface thermal materials that are most important in a spacecraft charging analysis are:

- (1) The relative dielectric constant.
- (2) The variation of the surface resistivity with respect to electrical stress level.
- (3) The variation of bulk resistivity with respect to electrical stress level.
- (4) Ratio of surface to bulk leakage currents.

All of the above properties can be determined experimentally. In fact, for meaningful results, the last three parameters should be measured under conditions similar to those experienced in the charged particle environment at synchronous orbit during a substorm. That is, the measurement results will be somewhat dependent on the energy levels and current densities of the charged particles bombarding the dielectric surface of the thermal blanket materials. In practice, however, these properties are measured by bombarding the materials with a monoenergetic electron beam.

### 2.3 Geometrical Model.

The purpose of the geometrical model is to define the spacecraft outer surface areas in terms of approximate planar and curved surface projections, establish a reference coordinate system in the spacecraft, and define the vertices of all of the planar and curved surfaces in terms of the reference coordinate system. Furthermore, the results of the geometrical model are needed to complete the electrical model. That is, the approximate geometrical surfaces of the spacecraft outer configuration are used in the computation of the equivalent capacitor and resistor element values of the electrical model (each value is related to the surface area). The reference coordinate system can be selected anywhere inside the vehicle structure and should be chosen such that one or more coordinate axes are parallel to the axes of symmetry, or parallel to the major planar outer surfaces.

The reference coordinate system is useful in determining the relative locations and orientations of the constituent outer surfaces. In addition, the reference coordinate system is needed to determine the location of the spacecraft with respect to the earth and sun. The surface vertices are used in the computation of the surface normal vectors, and the surface normal vectors together with the location of the spacecraft with respect to the sun are used to determine the sun illumination condition of the surface; that is, whether the surface is illuminated by the sun, self-shadowed, or earth-shadowed. It should be noted that there can exist outer surfaces that are never illuminated by the sun; these areas are designated as "permanently" shadowed areas.

In order to determine the sun-illumination condition of the constituent surfaces, all outer surface areas must be expressed in terms of the six major planes parallel to the coordinate axes. Hence, the areas of the constituent planar surfaces parallel to a coordinate axis can be easily expressed in terms of the six major planes. However, for planar surfaces not parallel to a coordinate axis, the effective surface areas projected into the six major planes must be determined. The projected areas in the six major planes are then assumed to have the same normal vectors associated with the six major planes when determining their sun-illumination condition; however, the true, unprojected area is used when determining the area that is subject to the charged particle environment. The same procedure is followed for all curved surfaces, that is, cones, spheres, cylinders, etc.

The exposed metallic parts of the spacecraft structure require special attention. Since the exposed structural parts can exist on almost any constituent planar surface of the spacecraft, the exposed metallic parts will have different sun-illumination conditions depending on the particular location of the exposed part. The effective projected area of each exposed metallic part is computed in each of the six major reference planes as outlined above. The effective projected area in conjunction with the particular sun/spacecraft surface aspect angle is used in the computation of the photoemission current; this is represented by the last term of Eq. (22). However, the actual exposed area of a metallic part is subject to the plasma environment; thus, the total exposed metallic area is used in the computation of the incident particle currents. This is represented by the first two terms of Eq. (22).

## 2.1 Electrical Model

The electrical model defines the lumped element, equivalent circuit representation of the spacecraft outer surfaces with respect to the electrostatic charging phenomenon. The equivalent electrostatic circuit is a network consisting of capacitors and resistors whose values are either computed or measured. It will be assumed that a dielectric surface can be represented as a simple lumped capacitor and a parallel leakage resistance; however, this is an approximate representation when considering the complex processes that occur when a dielectric surface is bombarded by high energy particles. The capacitor components represent the capacitance of the various dielectric surfaces with respect to the spacecraft structure. The resistor components represent the leakage current from the dielectric surfaces to the spacecraft structure. Additional capacitors and resistors are needed to represent the surface capacitance and leakage current between adjacent surfaces and between illuminated and nonilluminated sections of a surface. However, these surface interaction processes are second-order coupling effects and will not be considered in the model. This is a conservative assumption and does

not affect the ability of the model to predict the potential differences between a surface and the structure or the potential differences between adjacent surfaces. Consequently, the equivalent circuit of the spacecraft with respect to the charging phenomenon has the simplified form shown in Figure 2.

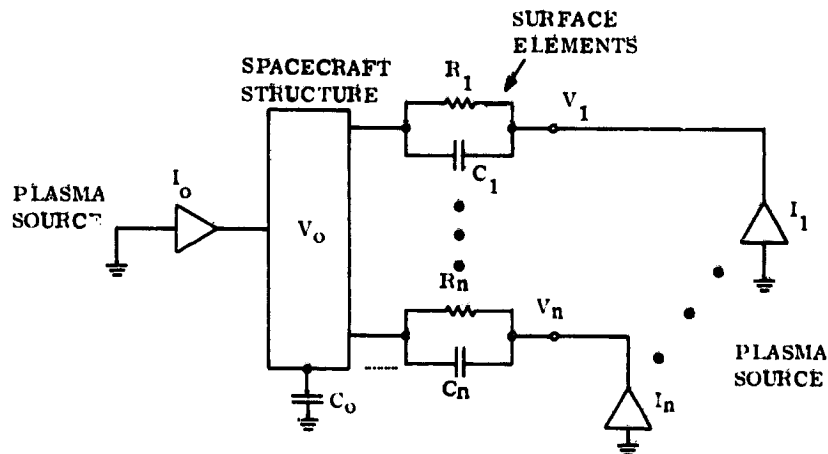


Figure 2. Spacecraft Equivalent Circuit

It has been assumed that there are  $n$  outer surfaces. The  $i$ -th surface has an absolute potential of  $V_i$  volts and each surface, or node, has a corresponding plasma and photoemission generated current source having the general form of Eq. (20). The spacecraft structure has an absolute potential of  $V_o$  volts and  $I_o$  is the plasma and photoemission generated current source into the exposed metallic surfaces and is given by Eq. (22). The capacitance,  $C_o$ , is the intrinsic capacitance of the spacecraft structure with respect to the plasma. This structural capacitance can be approximated by the isolated capacitance of the structure. This is a reasonable approximation since the plasma sheath outer boundary, which represents the terminus of the strong satellite fields due to spacecraft charging, has a depth on the order of tens of meters.

The following set of simultaneous spacecraft charging equations can be written for the simplified circuit of Figure 2:

$$\frac{C_1 d(V_1 - V_0)}{dt} + \frac{(V_1 - V_0)}{R_1(V_1 - V_0)} = I_1(V_1)$$

$$\vdots \quad \quad \quad \vdots \quad \quad \quad \vdots$$

$$\frac{C_n d(V_n - V_0)}{dt} + \frac{(V_n - V_0)}{R_n(V_n - V_0)} = I_n(V_n)$$

$$C_0 \frac{dV_0}{dt} = \sum_{i=0}^n I_i \quad (25)$$

Equation (25) in general will be nonlinear since the leakage resistances are nonlinear functions of stress level ( $V_i - V_0$ ) and the plasma and photoemission generated currents are nonlinear functions of absolute potential. The number of equations,  $n$ , is a function of both the number of surfaces with different dielectric materials and the number of surfaces with different sun-illumination conditions.

### 2.5 Solar/Earth/Spacecraft Orbit Model

The purpose of the solar/earth/spacecraft orbit model is to determine the sun-illumination condition of a spacecraft surface including both earth-shadowing and self-shadowing conditions. The sun-illumination condition of a surface is determined by first defining the planar surface and its vertices with respect to the spacecraft reference coordinate system. This is essentially accomplished in the geometrical model. Next, the normal vector of this surface is computed and the relative location of the normal vector with respect to the spacecraft reference coordinate system is determined. The relative position of the sun with respect to the earth is computed as well as the relative position of the spacecraft with respect to the earth. Using coordinate transformations, the relative position of the spacecraft coordinate system with respect to the sun is then determined. Finally, the angle between the surface normal and the sun vector, the aspect angle, is computed. The intensity of sun-illumination is proportional to the cosine of the aspect angle with full illumination occurring for an aspect angle of  $0^\circ$ . The surface is self-shadowed when the absolute value of the aspect angle exceeds  $90^\circ$ . Also, the earth-shadowing condition, which occurs when the spacecraft is in the umbra of the earth, can be similarly determined. The solar/earth/spacecraft orbit

model consists of four separate parts: the spacecraft ephemeris model, the solar model, the coordinate transformations, and the solar/vehicle/earth geometrical model.

The relative geometry between the earth, the sun, the spacecraft, and a constituent surface is shown in Figure 3. As indicated in Figure 3, the surface is defined by the vertices A, B, and C. To determine the solar/spacecraft surface aspect angle, the surface normal vector and the surface-sun vector must be computed. The vertex vectors of the surface expressed in vehicle coordinates are

$$\left. \begin{array}{l} \overline{FA} \\ \overline{FB} \\ \overline{FC} \end{array} \right\} \quad (26)$$

and the sun vector in inertial coordinates at the center of the earth is

$$\overline{OS} \quad (27)$$

and is computed by the solar model program. The spacecraft vector expressed in inertial coordinates is

$$\overline{OF} \quad (28)$$

and is computed by the vehicle ephemeris program.

From Figure 3, it can be seen that the surface normal vector is given by

$$\overline{N} = (\overline{FA} - \overline{FB}) \times (\overline{FC} - \overline{FB}) \quad (29)$$

the solar/spacecraft surface aspect angle is then given by

$$\cos \alpha = (\overline{N} \cdot \overline{BS}) / (|\overline{N}| |\overline{BS}|) \quad (30)$$

and the earth aspect angle is

$$\cos \beta = (\overline{BS} \cdot \overline{BO}) / (|\overline{BS}| |\overline{BO}|) \quad (31)$$

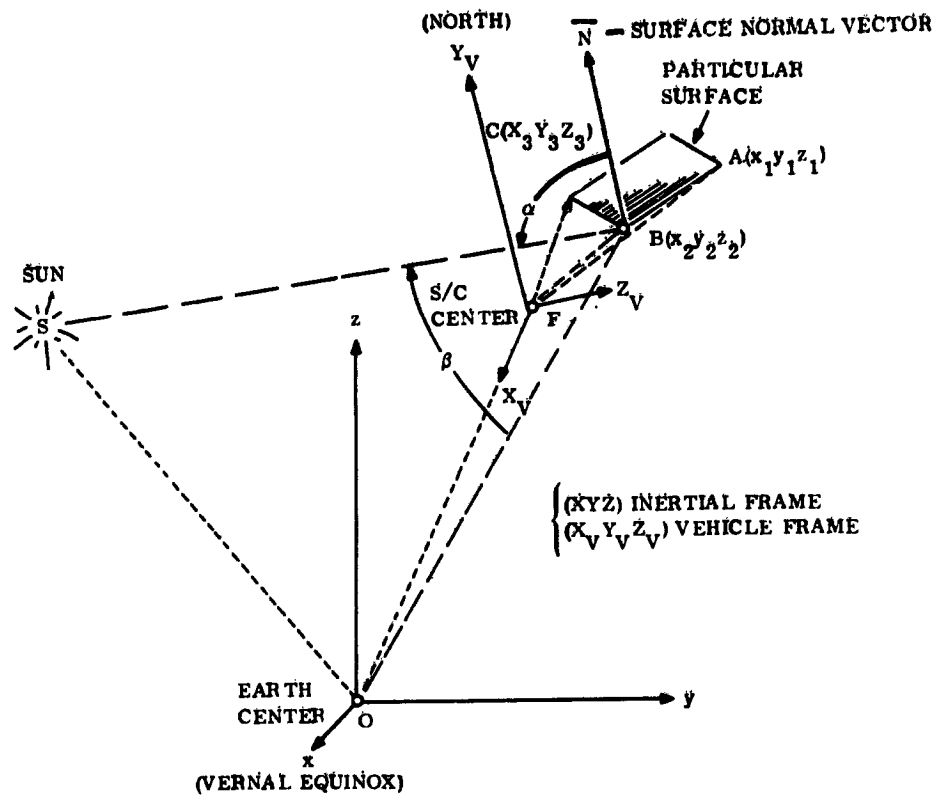


Figure 3. Sun-Earth-Spacecraft Orbital Geometry

Earth-eclipsing (shadowing) of a surface is given by the following condition

$$\beta < \beta_T \quad \text{eclipse condition} \quad (32)$$

$$\beta \geq \beta_T \quad \text{non-eclipse condition}$$

where

$$\begin{aligned} \beta_T &= \sin^{-1} (R_e/r) \\ R_e &= \text{radius of earth} \\ r &= |\overline{OF}| \end{aligned} \quad (33)$$

and  $\beta_T$  is the earth disc aspect angle subtended at the spacecraft. Thus, an earth-eclipsing condition occurs when the spacecraft is in the umbra of the earth. Self-shadowing or self-eclipsing of a surface by the spacecraft itself is given by the following condition:

$$\left. \begin{array}{l} |\alpha| \geq \pi/2 \quad \text{eclipse condition} \\ |\alpha| < \pi/2 \quad \text{non-eclipse condition} \end{array} \right\} \quad (34)$$

where  $\alpha$  is the solar/spacecraft surface aspect angle determined from the solar projection upon the surface normals.

In the simplified spacecraft ephemeris model, the location of the spacecraft with respect to the inertial coordinate system of the earth is determined. There is no need for a precise spacecraft orbit so an abbreviated model is used. The orbit is assumed to be circular with a constant radius and a nominal period of 1440 min. The spacecraft is flown in the equatorial plane (inclination =  $0^\circ$ ). In the solar model, the position of the sun with respect to the earth is derived from the American Ephemeris and Nautical Almanac which provides mean position in terms of a series expansion of elapsed centuries from a base epoch. Conventional coordinate transformations are employed to determine the position of the sun with respect to the spacecraft (vehicle) reference coordinate system.

#### 2.6 Numerical Integration Approach

The first order, simultaneous, nonlinear spacecraft charging differential Eqs. (25) with forcing functions represented by Eqs. (20) and (22) are of such a form that standard closed-form methods of solution do not apply. Consequently, several "initial value" numerical integration techniques were utilized to compute the time response of the absolute potentials,  $V_1, \dots, V_n$ . The greatest success was achieved with the Runge-Kutta<sup>11</sup> integration process. After some preliminary experimentation, it was found that a step size of 0.001 sec produced satisfactory results in the time response computation. The step size is the incremental value of the independent variable, time, at which the dependent variable value, absolute potential, is computed.

From initial computations of the time response of the set of Eqs. (25) using actual circuit values of capacitance and nonlinear resistance and actual plasma substorm parameters, it became apparent that the transient and steady-state results could not be obtained in a single numerical integration execution. First, it was found that the steady-state values of potential are reached after several hours. Second, the computer execution time-to-solution time was enormous (typical run times were on the order of 20 to 30 min to obtain 1 to 3 min of simulated time). Consequently, it was decided to characterize the transient behavior by computing the transient response up to that point in time at which the transient response was well-behaved, that is, either monotonically decreasing or increasing (usually on the order of 1 to 3 min). The steady-state solution was computed

separately in a rapidly executed program. This overall approach was not rigorously accurate since plasma conditions can change within minutes and illumination conditions can change within tens of minutes. However, if worst case plasma and illumination conditions are employed, the solutions, both transient and steady-state, will represent worst case values and more accurate solutions should not be necessary.

To obtain the steady-state solution, a more direct method was employed. The steady-state condition is characterized by the condition  $dV_i/dt = 0$ . From Eq. (25), this results in the steady-state system of equations

$$\frac{dV_i}{dt} = 0 = \frac{1}{C_i} \left[ I_i - \frac{(V_i - V_0)}{R_i(V_i - V_0)} \right], \quad 1 \leq i \leq n \quad (35)$$

and

$$\frac{dV_0}{dt} = 0 = \sum_{i=0}^n I_i \quad (36)$$

The solution to this system of equations can be viewed as an optimization problem where Eq. (36), which represents the current balance condition, must be minimized while simultaneously satisfying the set of  $n$  nonlinear equations, Eqs. (35), which can be considered as constraint equations on the current balance condition. For simplicity, it was decided to use a simple direct enumeration scheme to iteratively search the region

$$V_L \leq V_i \leq V_U, \quad 0 \leq i \leq n \quad (37)$$

where

$$V_i = V_L + n\Delta V, \quad 0 \leq i \leq n \quad (38)$$

such that Eq. (36) was minimized while satisfying the  $n$  constraint Eqs. (35). The terms  $V_L$  and  $V_U$  are the lower and upper bounds, respectively, of the absolute potentials of the surfaces and structure. Positive potential values were incremented by  $\Delta V = 0.1$  volts and negative potential values by  $\Delta V = 50$  volts.

### 3. SPACECRAFT CHARGING SIMULATION RESULTS

Spacecraft charging simulation results for a three-axis stabilized spacecraft are presented in this section. The spacecraft analyzed, with thermal blankets in place, could be adequately modeled geometrically as a "box-like" structure with large "flat panel" type solar cell arrays which are located above and below the north and south panels, respectively, of the main spacecraft structure. The antenna structures, with thermal blankets, could be modeled as conical structures that protrude from the front side of the spacecraft main structure and point towards the earth's surface. The dielectric properties of the thermal blankets and surface-coating materials were measured and the equivalent capacitances and leakage resistances of the constituent surfaces were computed. The results are listed in Table 1. There were 13 surfaces with either different materials or different orientations (with respect to the spacecraft reference coordinate system) that had to be considered in the spacecraft charging analysis. The front side had three different materials and the north and south panels had two different materials. The resistor values listed in Table 1 are based on the bulk resistivity characteristic and represent the values computed at low stress level. The last element in the table is the structural capacitance and was computed by using some of the formulas listed in Appendix A.

Table 1. Element Value Summary of Three-Axis Stabilized Spacecraft Analyzed

Element Location	Resistor Value (ohms)	Capacitor Value ( $\mu f$ )
1. Backside	$R_1 = 8.9 \times 10^7$	$C_1 = 0.37$
2. West Panel	$R_2 = 1.2 \times 10^8$	$C_2 = 0.29$
3. North Panel	$R_3 = 2.1 \times 10^8$	$C_3 = 0.16$
4. North Panel	$R_4 = 1.8 \times 10^9$	$C_4 = 0.16$
5. South Panel	$R_5 = 1.4 \times 10^8$	$C_5 = 0.24$
6. South Panel	$R_6 = 4.0 \times 10^{10}$	$C_6 = 0.08$
7. East Panel	$R_7 = 1.2 \times 10^8$	$C_7 = 0.28$
8. Front Panel	$R_8 = 2.5 \times 10^8$	$C_8 = 0.13$
9. Front Side	$R_9 = 9.5 \times 10^{10}$	$C_9 = 0.069$
10. Front Side	$R_{10} = 2.8 \times 10^{11}$	$C_{10} = 0.024$
11. Solar Array Sun-Side	$R_{11} = 3.0 \times 10^{10}$	$C_{11} = 0.65$
12. Solar Array Dark-Side	$R_{12} = 1.4 \times 10^8$	$C_{12} = 4.4$
13. Permanently Shadowed Sides	$R_{13} = 3.8 \times 10^8$	$C_{13} = 0.087$
14. Spacecraft Structure	-----	$C_{14} = 0.000356$

In general, the bulk resistivity is a function of stress level. The bulk resistivities of all the dielectric materials were measured by bombarding samples of the materials by high energy electrons and measuring the through conduction leakage current as a function of electron accelerating beam voltage. It was conservatively assumed that the surface stress level was approximately equal to the beam voltage and a piecewise approximation to the bulk resistivity versus beam voltage characteristic was computed. All of the piecewise approximations of the dielectric materials had a form similar to the piecewise approximation of Chemglaze paint shown in Figure 4. To simplify the simulation and to decrease the execution time, the piecewise approximation of all of the materials were employed in the analysis.

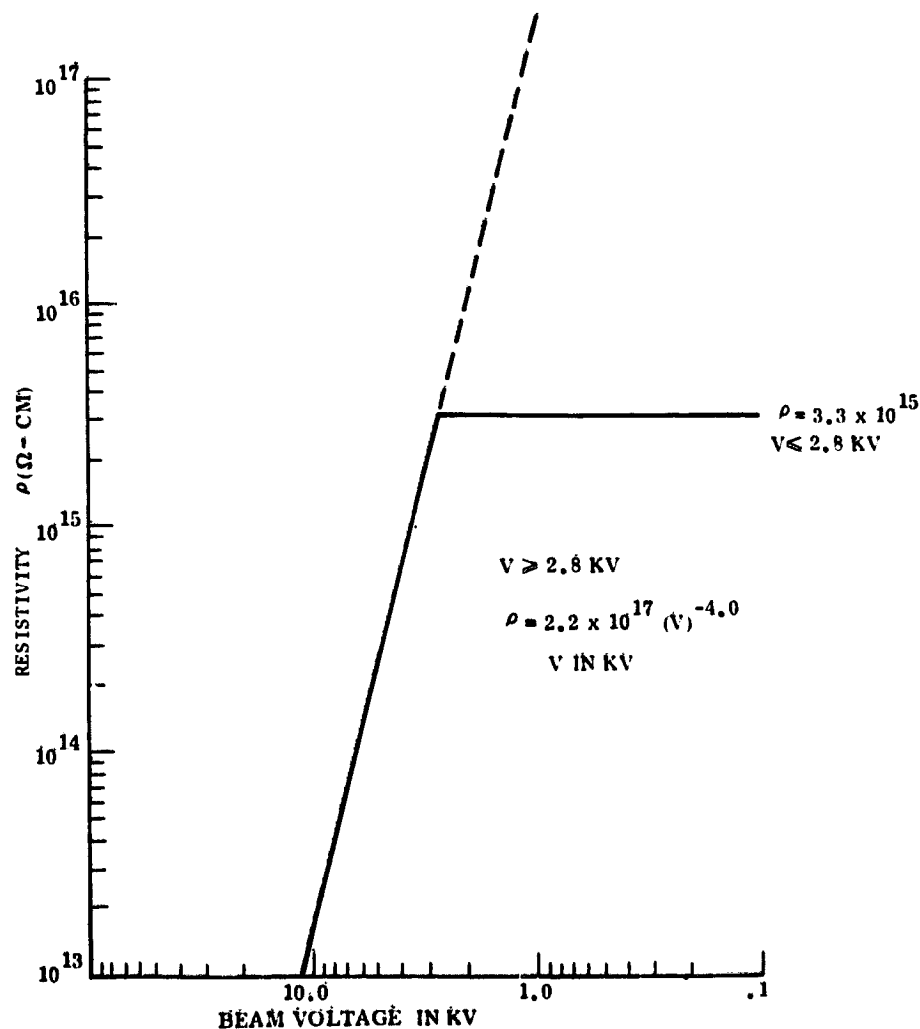


Figure 4. Piece-Wise Approximation of Chemglaze Paint Bulk Resistivity

Spacecraft charging simulation results were obtained for the three-axis stabilized spacecraft during the peaks of the fall-equinox and winter-solstice periods. These two periods of the earth-sun orbit represent the extremes of sun-illumination condition experienced by a geosynchronous satellite. For example, during the equinox period the satellite is totally shadowed because of earth-eclipsing and the spacecraft structural potential will achieve its highest-negative value. The earth eclipse period can last as long as 72 min roughly from 23:30 to 0:45 local time. During the peak of the winter-solstice period the south panel of the spacecraft as well as the solar array, east panel, and backside are sun-illuminated. The maximum amount of exposed metal that is illuminated by the sun occurs during this period because the south panel has more exposed metal than the north panel; if the reverse had been true, the maximum amount of exposed metal that is illuminated by the sun would occur during the summer-solstice period. Thus, during the winter-solstice period the spacecraft structure will achieve its lowest negative value.

Using the average plasma substorm parameters of the 2 January 1970 substorm, which was the worst substorm measured by ATS-5 during the first 50 days of 1970, and assuming a time-invariant, omnidirectional charged particle substorm, the absolute potentials of the spacecraft structure and outer surfaces were computed. That is, it was assumed in the analysis that the substorm can be adequately represented as a "step" function in electron and proton temperatures and particle current densities over their values that normally occur during the "quite-time," that is, their quiescent conditions.

The average substorm parameters as well as other parameters used in the analysis are listed in Table 2. The complete substorm profiles for the 2 January substorm as well as the average values have been given in a previous paper.<sup>6</sup> Based on ATS-5 data of the 2 January substorm, a "step" function of 9 hr duration was employed in the simulation model, existing roughly from 23:00 to 8:00 local time. Starting with initial values of zero absolute potential at 23:00 hours, the Runge-Kutta numerical integration procedure was employed to determine the variation of the surface and structural potentials with time. Since the numerical integration technique produced roughly 60 sec of simulation results for every 1000 sec of execution time, the continuous substorm response could not be computed for the full 9 hr duration. Instead, the transient solution was computed using the Runge-Kutta procedure until the surface and structural potential time responses were well-behaved and approaching their steady-state values.

Since the magnitude of the transient response is approximately proportional to the magnitude of the change in forcing function conditions, the more significant transient responses will occur when there is a significant change in the particle

Table 2. Photoemission, Secondary Emission, and Omnidirectional Plasma Parameters

Parameter	Typical Range	Value Selected
$T_{ph}$	$1 \text{ V} \leq T_{ph} \leq 3 \text{ V}$	2 V
$T_s$	$2 \text{ V} \leq T_s \leq 4 \text{ V}$	2 V
$f_{eM}$	$0 \leq f_{eM} \leq 1$	0.5
$f_{eD}$	$0 \leq f_{eD} \leq 1$	0.75
$f_{pM}$	$0 \leq f_{pM} \leq 1$	0.5
$f_{pD}$	$0 \leq f_{pD} \leq 1$	0.75
$T_e$	----	{ 6.0 kV (substorm) 3.0 kV (quiet) 20.0 kV (severe substorm)
$T_p$	----	{ 12.0 kV (substorm) 6.0 kV (quiet) 40.0 kV (severe substorm)
$J_{ph_0}$	$0.82 \text{ na/cm}^2 \leq J_{ph_0} \leq 4 \text{ na/cm}^2$	2.0 na/cm <sup>2</sup>
$J_{e_0}$	$0.02 \text{ na/cm}^2 \leq J_{e_0} \leq 2 \text{ na/cm}^2$	0.6 na/cm <sup>2</sup> (substorm) 0.02 na/cm <sup>2</sup> (quiet)
$J_{p_0}$	$2 \text{ pa/cm}^2 \leq J_{p_0} \leq 32 \text{ pa/cm}^2$	0.02 na/cm <sup>2</sup> (substorm) 2.0 pa/cm <sup>2</sup> (quiet)

current densities or energies. Consequently, transient solutions were obtained at the onset of the plasma substorm, where particle temperatures (energies) and current densities change suddenly from their quiescent values to their substorm values; at the beginning of earth-eclipse, where the photoelectron current forcing function is zero; and at the end of earth-eclipse, where the photoelectron current forcing function becomes nonzero. The transient response of the structure, the solar array, and the surface that exhibited the greatest steady-state potential difference is shown in Figure 5 for the onset of the 6 kV substorm. In this figure, as well as the others to be presented, the transient response is shown for a period of 70 sec and the steady-state solutions are shown on the right side of the figure. The transition period from the transient to the steady-state solutions is indicated by the dashed lines. (As expected, the surface that consistently exhibited the

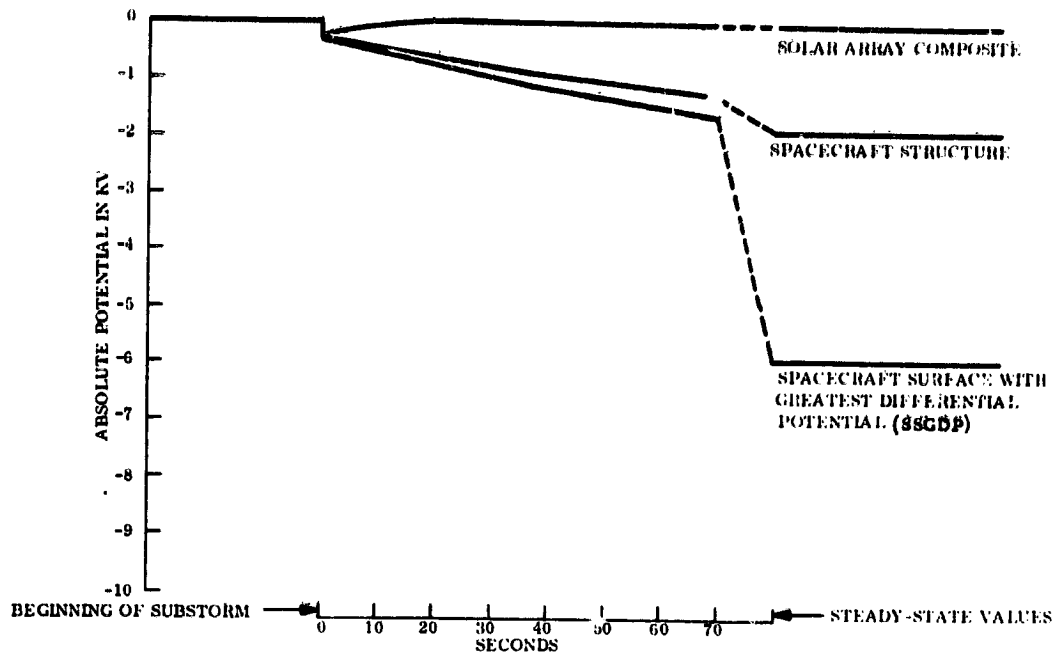


Figure 5. Transient Response at Onset of a 6 kV Substorm. Fall-Equinox 23:00 LT

greatest steady-state potential difference between the structure and the surface itself, was covered with dielectric material that experimentally had the highest value of bulk resistivity.) It was assumed that all potentials were initially at zero volts. It can be seen that the surfaces "fall" instantaneously to a few hundred volts with small potential differences between the two outer surfaces and the underlying structure. This behavior was typical of all of the surfaces of the spacecraft. The absolute potentials then "fall" monotonically negative until, after a long period of time, the final steady-state values are achieved. The transient response at the onset of earth-eclipse is shown in Figure 6. It was assumed, as a worst case, that the steady-state values of the previous period had been achieved at the start of the earth-eclipse and are the initial values used in the numerical integration program. It can be seen that the structure instantaneously "falls" to a negative value of about 9 kV, however, the initial potential differences are maintained but decrease monotonically in the steady-state to small values on the order of a few hundred volts. The transient response at the end of the earth-eclipse period is shown in Figure 7. Again it was assumed, as a worst case, that the steady-state values of the previous period had been achieved at the end of the earth-eclipse period and these values then became the initial values in the numerical integration program. The structural potential instantaneously decreases to a negative value of

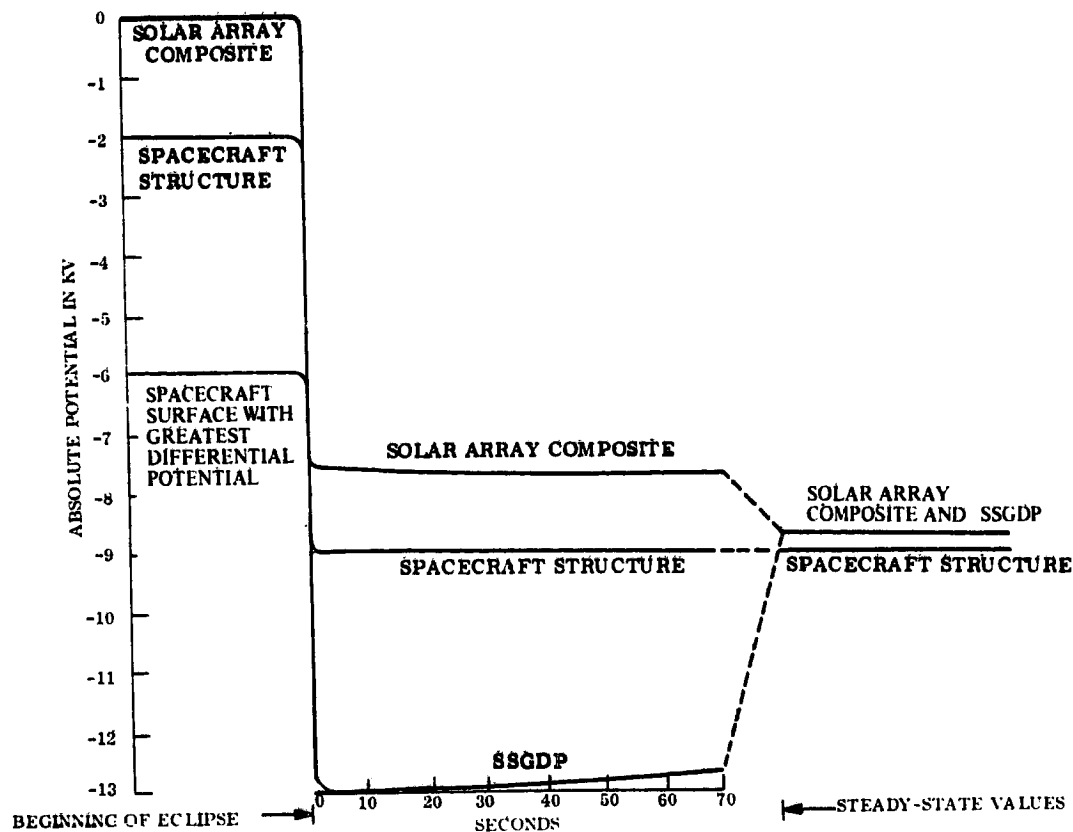


Figure 6. Transient Response into Eclipse for a 6 kV Substorm. Fall-Equinox 23:30 LT

a few hundred volts; however, the potential differences are maintained initially and then increase monotonically to somewhat larger values. The solar array is "clamped" to zero volts (actually less than one volt positive) by photoemission. This condition occurs for most surfaces with full sun-illumination intensity.

Upon comparing the steady-state with the transient solution values, it becomes apparent that the final steady-state values, that is, those values achieved if the sun-illumination conditions did not change, represent the worst-case differential values. Also, the differential potentials can change instantaneously by no more than a few hundred volts. But, the absolute potential of the spacecraft structure

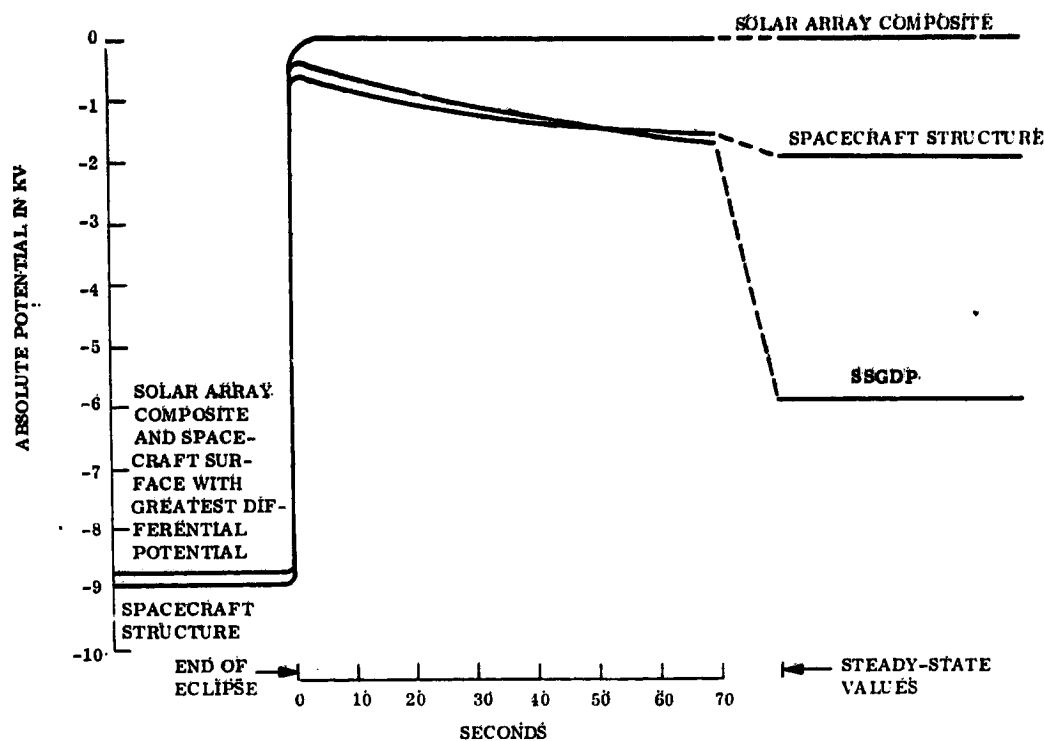


Figure 7. Transient Response Out of Eclipse for a 6 kV Substorm. Fall-Equinox 00:45 LT

can change almost instantaneously since it has small capacitance. In all cases, the transient response times are controlled by either the potential constants of the forcing functions or the time constants of the circuit elements or both. The differential potentials of the outer surfaces do not change instantaneously by large amounts since the circuit element time constants, which are large in value (the product of resistance and capacitance), are dominant. However, the absolute potential of the surfaces, which is the sum of the absolute potential of the structure and the differential potential between the surface and the structure, can change instantaneously in conjunction with the structure. This is demonstrated in all of the transient responses and in particular in Figures 6 and 7. At the beginning and at the end of earth-eclipse, the absolute potential of the structure changes by a large amount and the absolute potentials of the surfaces change by a similar amount; thus the potential differences do not change in value initially.

At the onset of the substorm, the structure "falls" slowly negatively since there are photoelectron emissions which tend to cancel the influx of electrons from the plasma current source. At the onset of earth-eclipse there are no photoelectron currents and the plasma electron current sources dominant and rapidly charge-up the small structural capacitance. At the end of earth-eclipse, the large photoelectron-current sources again reoccur. The large outflux of electrons from the exposed metallic parts produced by the photoemission currents is instantaneously supplied by the structural capacitance and consequently, there is a rapid decrease in the negative absolute potential of the structure.

As discussed previously, for three-axis stabilized spacecraft there is considerable diurnal as well as seasonal variations in the amount and location of the outer surface areas of the spacecraft that are exposed to the sun. Thus, the sun illumination condition of the 13 dielectric surfaces of the spacecraft are computed throughout the orbital path. From the solar/earth/spacecraft orbit model it was found that the sun-illumination condition did not change significantly in local time increments less than 30 min. Consequently, steady-state solutions were computed at 30 min increments throughout the duration of the substorm. In general, the final steady-state solution will never be achieved at the end of the 30 min period since some of the source potential and network time constants involved are on the order of thousands of seconds and the initial sun-illumination conditions, on which the final steady-state solution is based, will change significantly every 30 min. A summary of the spacecraft steady-state values using the average plasma parameter values of the 2 January substorm, is listed in Table 3 for 1 hr increments throughout the duration of the substorm for the fall-equinox period. The hourly incremental values are representative of the worst-case potential differences obtained when compared against the values computed in the smaller half-hour increments. The widely varying values of the absolute potential of the spacecraft structure are shown as well as the maximum surface differential potentials. It can be seen that during eclipse (lasting roughly from 23:30 to 0:45) the spacecraft, in steady-state, achieves a negative potential of about 9 kV and a maximum surface potential difference of -4.5 kV was reached towards dawn.

A similar analysis was conducted for the peak of the winter-solstice period for the 6 kV test substorm. As expected, the lowest negative spacecraft structural potential was achieved during this period. A summary of steady-state values is presented in Table 4. A maximum potential difference of -4.6 kV was achieved.

As can be seen from the summary tables, the spacecraft structural potential varies widely reaching a maximum negative value of about 9 kV at eclipse and a minimum negative value of 450 kV during the winter-solstice period. In this particular design, the structural exposed metal was kept to a minimum and this

Table 3. Summary of Steady-State Results for 6 kV Substorm During Fall-Equinox

Local Time	Material with the Maximum Potential Difference for Assumed Plasma Conditions		Absolute Potential of S/C Structure (volts)
	Absolute Potential (volts)	$\Delta V$ Between Surface and S/C Structure	
23:00	-5950	-4000	-1950
24:00 (eclipse)	-8750	200	-8950
1:00	-5950	-4000	-1950
2:00	-5500	-4250	-1250
3:00	-5500	-4250	-1250
4:00	-5500	-4250	-1250
5:00	-5700	-4200	-1500
6:00	-5850	-4050	-1800
7:00	-5350	-4350	-1000
8:00	-5200	-4500	-700

Table 4. Summary of Steady-State Results for 6 kV Substorm During Winter-Solstice

Local Time	Material with the Maximum Potential Difference for Assumed Plasma Conditions		Absolute Potential of S/C Structure (volts)
	Absolute Potential (volts)	$\Delta V$ Between Surface and S/C Structure	
23:00	-5250	-4400	-850
24:00	-5700	-4100	-1600
1:00	-5250	-4400	-850
2:00	-5200	-4500	-700
3:00	-5200	-4500	-700
4:00	-5200	-4500	-700
5:00	-5200	-4500	-700
6:00	-5350	-4350	-1000
7:00	-5050	-4600	-450
8:00	-5050	-4600	-450

helps to explain the fact that the structure never achieved zero potential when various exposed parts were illuminated by the sun. Examination of the steady-state values of all of the surfaces indicates that during eclipse all of the surfaces achieve almost the same absolute potential. This results from the fact that all surfaces have the same shadow and plasma current source conditions.

#### 4. CONCLUSIONS AND DISCUSSION

This paper has been concerned with the development and application of a charging model for three-axis stabilized spacecraft. The objective of the model is to determine the differential potentials between the outer surfaces and the structure of a spacecraft throughout its geosynchronous orbit when under the influence of a geomagnetic substorm. It was assumed that the interaction between the plasma and the spacecraft can be adequately represented by an equilibrium theory approach. That is, the energy distribution of the constituent plasma particles can be expressed in terms of an omnidirectional Maxwell-Boltzmann distribution. The plasma is then represented by equivalent voltage dependent current sources and the outer surfaces by simple lumped elements. The resulting first order differential equations are integrated and potential distributions determined. Sun-illumination conditions were determined by a solar/earth/spacecraft orbit model and the intrinsic capacitance of the spacecraft with respect to the plasma sheath is approximated by its isolated capacitance. Spacecraft charging simulation results, including both the transient and steady-state solutions, have been presented.

A knowledge of the potential distribution of the outer surfaces and structure of the spacecraft throughout its orbital path is important from a systems design and analysis viewpoint. In general, spacecraft materials that maintain stress levels below their dielectric strength level should be selected. If, from the analysis, it appears that the dielectric strength of various spacecraft surface materials will be exceeded, then, depending on the magnitude and repetition rate of the discharge and location of the material, corrective action such as modification or replacement of the material may be necessary. Thus, the spacecraft charging simulation results can be useful in determining the selection and location of the type of outer surface thermal blanket or coating materials to be employed in the design of spacecraft.

The spacecraft charging simulation results can be useful in establishing the relationship between the amount and location of the exposed structural metallic parts and the absolute potential of the spacecraft structure. For example, from the spacecraft charging simulation results, it was found that when a maximum amount of exposed metal was illuminated by the sun, the structural potential achieved its lowest negative value (because of photoemission). At the same time, the surface differential potential attained its maximum value. Conversely, when a minimum amount of exposed metal was illuminated, the spacecraft structure achieved its highest negative value and the surface differential potential attained its minimum value. The above results demonstrate that it is desirable to employ design approaches that allow the structural potential to attain values between the surfaces "clamped" at zero potential and those with the highest negative potential since the differential potentials are then minimized. The exact design approaches taken will depend on the spacecraft configuration, orbit, and outer surface materials.

In the simulation analysis employing a step function, that is, time-independent, representation for the plasma substorm, the worst case differential potentials occurred at steady-state and not during the transient response. This representation is not realistic since the particle energies and current densities are slowly but widely varying functions of time. Because of the large time constants of the equivalent spacecraft circuit, a steady-state response using the actual time-dependent plasma forcing functions would never be reached. However, the transient response obtained with a step forcing function is indicative of the type of response that can be expected when using the time-dependent forcing functions. In addition, the steady-state response to a step forcing function can be used as an upper bound of the worst-case differential potentials when the step function is used with worst-case plasma values. This is supported by simulation results which indicate that the magnitude of the differential potentials as well as the absolute potentials are directly related to the magnitude of the substorm particle energies (temperatures) and current densities.

Upon examining the spacecraft charging results, it becomes apparent that the absolute potentials of the surfaces are controlled by the absolute potential of the structure. The structural potential can change instantaneously because of its small intrinsic capacitance. However, the time response of the differential potentials is controlled by the large time constants of the equivalent spacecraft electrostatic circuit and the large potential constants of the forcing functions.

The model presented in this paper is based on an equilibrium theory approach. Other, more accurate, but complex approaches take into consideration particle trajectories, their actual energy distributions, and determine the surface

potentials by solving Poisson's potential distribution equation in three dimensions. Although the model is based on simplistic assumptions, the simulation results obtained for the structural potential are in relative agreement with the structural potentials measured on-board ATS-6, a three-axis stabilized spacecraft. The charging model predicts that upon entering eclipse, the spacecraft structure falls almost instantaneously to a value of about -9 kV and leaving eclipse the spacecraft structure rises almost instantaneously to a few hundred volts negative. Similar transient results into and out of eclipse have been observed on ATS-6. In addition, the structural potential variations during the post-eclipse period, as predicted by the model, correspond, relatively, to measured results on ATS-6. For example, examining the steady-state stress levels in the post-eclipse period, it can be seen that the structural potential rises to a low negative value after eclipse but falls negatively towards dawn and then rises to a low negative value at dawn. These results are in relative agreement with data measured on board ATS-6.

## References

1. DeForest, S. E. (1973) Electrostatic potentials developed by ATS-5, Photon and Particle Interaction with Surfaces in Space, R. J. L. Garrd, Editor, D. Reidel Publishing Co., Dordrecht-Holland.
2. Inoye, G. T. et al (1975) Final Report, Spacecraft charging analysis: studies and analysis of the modified DSCS-II Flights 5 and 6 configuration, TRW Report.
3. Rosen, A. (1975) Spacecraft charging: Environment induced anomalies, AIAA 13th Aerospace Sciences Meeting, Pasadena, Calif., paper no. 75-91.
4. DeForest, S. E. (1972) Spacecraft charging at synchronous orbit, J. Geophys. Res. 77:651-659.
5. McPherson, D. A., Cauffman, D. P., and Schober, W. (1975) Spacecraft charging at high altitudes - The Scatha satellite program, AIAA 13th Aerospace Sciences Meeting, Pasadena, Calif. paper no. 75-92.
6. Inoye, G. T. (1975) Spacecraft charging model, AIAA 13th Aerospace Sciences Meeting, Pasadena, Calif. 1975, paper no. 75-255.
7. Inoye, G. T. et al (1974) Final Report, Spacecraft charging analysis: A study and analysis of the DSCS-II spacecraft orbital charging phenomena, TRW Report.
8. Fredricks, R. W., and Scarf, F. L. (1973) Observations of spacecraft charging effects in energetic plasma regions, Photon and Particle Interactions with Surfaces in Space, R. J. L. Garrd, Editor, D. Reidel Publishing Co., Dordrecht-Holland.
9. DeForest, S. E., and McIlwain, C. E. (1971) Plasma clouds in the magnetosphere, J. Geophys. Res. 76(No. 3587).

10. Reitz, J. R., and Milford, F. J. (1960) Foundations of Electromagnetic Theory, Addison-Wesley Co., Reading, Mass.
11. Hamming, R. W. (1962) Numerical Methods for Scientists and Engineers, McGraw-Hill Co., New York, N. Y.

## Appendix A

### Electrostatic Capacitance of Several Isolated, Three-Dimensional, Geometrical Structures

#### 1. INTRODUCTION

In this appendix, equations for the isolated electrostatic capacitance of several types of geometrical structures are given.

##### 1.1 Sphere

The isolated capacitance of a sphere is<sup>1</sup>

$$C_{\text{ISO}} = 4\pi\epsilon_0 R \quad (\text{A1})$$

where  $C_{\text{ISO}}$  is expressed in farads,  $R$  is the radius of the sphere in meters, and  $\epsilon_0$  is the permittivity of a vacuum ( $8.85 \times 10^{-12}$  farads/meter).

##### 1.2 Cube

The capacitance of an isolated cube has been found to be<sup>2,3</sup>

$$C_{\text{ISO}} = 4\pi\epsilon_0 (0.656) l \quad (\text{A2})$$

where  $l$  is the length of the sides of the cube in meters and  $C_{\text{ISO}}$  is expressed in farads.

##### 1.3 Cylinder

The capacitance of an isolated cylinder is given by\*

$$C_{\text{ISO}} = \frac{4\pi\epsilon_0 a}{\ln \left[ \frac{a + (a^2 + R^2)^{1/2}}{R} \right]} \quad (\text{A3})$$

where  $C_{\text{ISO}}$  is expressed in farads,  $a$  is one-half the length of the cylinder in meters, and  $R$  is the radius of the cylinder in meters.

---

\*This formula was derived by the authors.

#### 1.4 Truncated Cone

The capacitance of a truncated cone will be approximated by the capacitance of a cylinder with a length equal to that of the cone, but the radius of the equivalent cylinder is the average of the radii of the truncated cone. Using Eq. (A3), the results are

$$C_{\text{ISO}} \cong \frac{4\pi\epsilon_0 a}{\ln \left[ \frac{a + (a^2 + \hat{R}^2)^{1/2}}{\hat{R}} \right]} \quad (\text{A4})$$

where  $\hat{R} = (R_1 + R_2)/2$  and  $C_{\text{ISO}}$  is expressed in farads and the radii expressed in meters.

#### 1.5 Thin Rectangular and Elliptical Plates

The capacitance of thin rectangular and elliptical plates have been derived in a previous paper<sup>5</sup> and the results are given in graphical form for various values of length and width, and semimajor and semiminor axes, respectively.

#### 1.6 Thin Circular Plate

The capacitance of a thin circular plate is given by<sup>4</sup>

$$C_{\text{ISO}} = \frac{2R}{\pi} \quad (11.1) \quad (\text{A5})$$

where  $R$  is the radius of the circular disk in meters and  $C_{\text{ISO}}$  is in picofarads.

## References

1. Kraus, J. D. (1953) Electromagnetics, McGraw-Hill Co., New York.
2. Van Bladel, J. (1964) Electromagnetics Fields, McGraw-Hill Co., New York.
3. Reitan, D. K., and Higgins, T. J. (1951) Calculation of the electrical capacitance of a cube, J. Appl. Phys. 22:223-226.
4. Reitan, D. K., and Higgins, T. J. (1956) Accurate determination of the capacitance of a thin rectangular plate, Trans. Am. Inst. of Electrical Engineers 75:pt. 1.

## Contents

1. Introduction	272
2. Environmental Characteristics	273
3. Potential Induced by Electron Gun	277
4. Conclusions	285
References	286

### 3. Induced Charging of Shuttle Orbiter by High Electron-Beam Currents

H. B. Lienoh  
Battelle Pacific Northwest Laboratories  
Richland, Washington

#### Abstract

Emission of high-current electron beams that has been proposed for some Spacelab payloads requires substantial return currents to the Orbiter skin in order to neutralize the beam charge. Since the outer skin of the vehicle is covered with  $\sim 1300 \text{ m}^2$  of thermal insulation which has the dielectric quality of air and an electrical conductivity that has been estimated by NASA at  $10^{-9}$ - $10^{-10}$  mhos/m, considerable transient charging and local potential differences are anticipated across the insulation. The theory for induced charging of spacecraft due to operation of electron guns has only been developed for spherical metal vehicles and constant emission currents, which are not directly applicable to the Orbiter situation. Field-aligned collection of electron return current from the ambient ionosphere at Orbiter altitudes provides up to  $\sim 150 \text{ mA}$  on the conducting surfaces and  $\sim 2.4 \text{ A}$  on the dielectric thermal insulation. Local ionization of the neutral atmosphere by energetic electron bombardment or electrical breakdown may provide somewhat more return current. During electron gun operation, differential charging between the outer surface of the dielectric insulator and the internal metal conductors creates large potentials and electric fields across the insulation. Estimates of the transient behavior and potential magnitude are obtained by solving electric circuit analogies. For an electron beam charge of 1 coulomb (10 A for 100 msec), the potential across the insulator rises to  $10^5$ - $10^6$  volts depending on the induced external ionization. Since electrical breakdown across the insulation occurs at 50,000 volts, high gun currents may cause arcing through the insulation.

This research work was sponsored by NASA/GSFC under contract NAS8-31415.

## 1. INTRODUCTION

Electrical charging of spacecraft in the ionosphere and magnetosphere is a consequence of different fluxes of thermal electrons and ions striking the surface of the vehicle. Normally, a very small equilibrium potential is established over the skin of the vehicle which does not affect the operation of sensors and electronic instrumentation. However, the Space Shuttle Orbiter may acquire appreciable charge differentials and local electric fields due to its large airplane shape and its nonconducting outer skin. As the vehicle assumes different attitudes in the course of its mission, various outer surfaces will be shadowed from particle and/or photon bombardment. Owing to alignment of charged-particle trajectories along the geomagnetic field and the relatively large difference in electron and ion speeds, there are many more regions of the spacecraft surface that are accessible to electrons than to ions. In addition, the photoemission of electrons from the surface by solar ultraviolet will depend on spacecraft attitude. Thus, the local current flow to the skin of the vehicle will vary widely from point to point. The dielectric skin of the vehicle prevents rapid flow of surface current to neutralize the differential charging and as a consequence, potential differences and attendant electric fields may be anticipated. During normal passive operations of the vehicle, potential differences of several volts are expected between adjacent areas of the vehicle where the surface contour changes abruptly (edges of wings, payload bay door edges, and around corners).

Active experiments planned for the Orbiter Spacelab include ejection of large amounts of electrical charge in the form of electron beams that must be compensated by a return current to the vehicle. Relatively slow collection of return electron current from the ambient ionosphere prevents rapid neutralization of the electron-beam charge. Proposed gun currents of up to 10 A for 100 msec are predicted to cause transient excursions of the vehicle potential that exceed many thousands of volts, unless appropriate compensating return current is available. Since operation of an electron gun at keV energies from the AMPS Spacelab is a vital part of the overall mission objective, it is important to determine the magnitude of the transient potentials and their dynamic characteristics.

The published literature on ambient charging of spacecraft in the ionosphere and magnetosphere is quite thorough for vehicles with conducting outer skin. Only a few papers have treated the problem of large-electron current ejection from spacecraft, and their applicability to a realistic pulsed mode of operation is open to question. The Shuttle Orbiter presents additional complications due to its nonconducting outer skin which can only be discharged by the ambient plasma medium. For example, an electron gun pulse will drive the skin potential positive until enough return current is collected to neutralize the overall potential of the vehicle;

but by that time the skin will have built up a negative charge which must be neutralized by ion bombardment, photoemission, and conduction leakage to the interior structure.

The results presented here are based on a preliminary analysis of the Shuttle-Orbiter charging problem that is published elsewhere.<sup>1</sup> This earlier work includes summaries of the ambient ionospheric environment at Shuttle-Orbiter altitudes, the electrical characteristics of the vehicle skin, the disturbed atmospheric environment due to gas leakage from the vehicle, the local potential differences that are anticipated during passive operations, and the dynamic potentials that are expected during electron-gun operation. Only this latter topic is considered in detail here.

## 2. ENVIRONMENTAL CHARACTERISTICS

### 2.1 Ambient Ionosphere

The Shuttle Orbiter that carries the Spacelab payloads is scheduled to operate in a nominal altitude range between 250 and 400 km. The natural environment is described in great detail in many aeronomy textbooks.<sup>2-6</sup> At these F-region altitudes, the charged constituents consist principally of oxygen ions and electrons and the primary neutral constituent is atomic oxygen. Large variations in both density and temperature for these constituents are attributed to source and transport mechanisms that vary diurnally as well as with season and solar cycle.

As a consequence of the plasma temperature, the spacecraft speed is considerably greater than the mean thermal speed of the ions but significantly less than the mean thermal speed of electrons, which has important consequences for current collection by particle flux at the vehicle skin. The gyroradius for ions is a few meters, whereas for electrons it is a few centimeters so that plasma motion is field-aligned. Due to the geometrical configuration of the vehicle and the variety of attitudes it may assume during a mission and its cross-field orbits, many areas will be routinely shadowed from ion and electron bombardment as well as photon flux.

The mean free path of the ions, electrons and atoms is orders of magnitude greater than the Shuttle-Orbiter dimensions so that collisional effects may be ignored. However, collective plasma properties significantly influence the flow of charge to the vehicle. Electrical conductivity of the plasma is highly anisotropic due to the presence of the geomagnetic field. Along the field direction the conductivity is about 20 mhos/m, but normal to the magnetic field the conductivity is several orders of magnitude less, virtually prohibiting current flow unless the

electric field is very large. Thus, for most vehicle attitudes, there is very little electrical connection through the plasma between different parts of the vehicle.

## 2.2 Vehicle Surface

Less than 5 percent of the outer surface of the Shuttle Orbiter and Spacelab consists of good metallic conductor. More than 95 percent of the surface is good thermal insulating material consisting of fibrous silicon dioxide tiles, coated felt, and adhesives. The composite material has extremely high electrical resistivity, between  $10^{-10}$  and  $10^{-13}$  mhos/m. The dielectric constant of these thermal insulators is comparable to that of air, and breakdown potential of the tiles has been measured at 50,000 volts by NASA/JSC. Since the thickness of the sample is presumably a few centimeters, the corresponding limiting electric field at breakdown is taken as  $10^6$  volts/m. Such fields and potentials would not occur for ambient conditions; however, vehicle charging during electron gun operation may exceed these limits by substantial amounts as will be shown.

There are some metallic exterior surfaces that provide "shorted" electrical contact between the interior metal superstructure of the Orbiter and the external plasma. The largest area is provided by the metal rocket motor nozzles. Other substantial surface areas are provided by the antenna boom, pallet instruments, and the manipulator arm. Since the pallet is graphite epoxy which is a poor conductor, there is some question about the electrical contact between these latter instrument-related conductors and the interior superstructure. However, for purposes of the present analysis, all of the external metal surfaces are assumed to be in contact with each other and the internal superstructure.

The electrical properties of the primary external surfaces of the Orbiter and Spacelab are tabulated in Table 1. The insulation data was provided by Mr. John Lobb, NASA/JSC, Houston, in private communications. Of special interest for scientific researchers is the lack of an effective external ground plane; the Spacelab pallet and control room have graphite epoxy exterior surfaces which are not conductors. Overall, the metal surfaces amount to about  $60 \text{ m}^2$  whereas nonconductor surfaces cover  $1300 \text{ m}^2$ .

The electrical conductivity of the thermal insulation materials is a vital parameter for the conclusions in this study and, unfortunately, its value is in doubt at this time. The value  $10^{-9}$ - $10^{-10}$  mhos/m quoted in Table 1 is the current best NASA/JSC estimate, but no official experimental measurements have been made to date. An independent measurement of HRSI tiles has been made by Mr. Paul W. Edwards at Rockwell International who found a bulk conductivity of  $10^{-13}$  mhos/m. Such discrepancies are well within the range of conductivity values for different types of silica ( $10^{-7}$ - $10^{-14}$  mhos/m) as the manufacturing process,

Table 1. Orbiter/AMPS-Spacelab Outer Skin Materials

Location	Material	Area (m <sup>2</sup> )	Thickness (m)	Electrical Conductivity (mhos/m)	Dielectric Constant (κ)
Topside (low temp.)	FRSI	300	0.011	10 <sup>-10</sup>	~1
Topside (high temp.)	LRSI	280	0.010-0.030	10 <sup>-9</sup> -10 <sup>-10</sup>	~1
Underside (reentry shield)	HRSI	475	0.024-0.107	10 <sup>-9</sup> -10 <sup>-10</sup>	~1
Nose and Wing Edge	RRC	37.5	0.006	10 <sup>-6</sup>	~1
Rocket Exhaust Nozzles	Inconel 718	~30	--	6 × 10 <sup>6</sup>	--
Interior Bay Door Radiators	Teflon	~100	--	10 <sup>-10</sup>	~1
Spacelab Pallet	Graphite Epoxy	~90	--	10 <sup>-10</sup>	~1
Spacelab Control Room	Graphite Epoxy	~25	--	10 <sup>-10</sup>	~1
Spacelab Pallet Instruments	Aluminum	~10	--	3 × 10 <sup>7</sup>	--
Antenna Boom	Beryllium Copper	~15	--	1 × 10 <sup>7</sup>	--
Manipulator Arm	Aluminum	~5	--	3 × 10 <sup>7</sup>	--

purity of the material, and environmental conditions (handling and aerosols) all affect electrical insulation quality. However, there is a clear need for more accurate estimates of the electrical conductivity for the thermal insulation. For the present, the NASA values will be used, but effects of different values will be noted where appropriate.

Some external conditions or modes of experimental operation require conduction through the insulation to establish equilibrium. Under most situations, however, the thermal blanket acts as a dielectric capacitor which efficiently stores

charge on its external surfaces. The capacitance and resistance of the blanket per unit area are  $\kappa\epsilon_0/\Delta h$  and  $\Delta h/\sigma$ , respectively, where  $\kappa$  is the relative dielectric constant,  $\epsilon_0$  is the permittivity of free space ( $8.85 \mu\text{f/m}$ ),  $\sigma$  is the electrical conductivity, and  $\Delta h$  is the blanket thickness. The e-folding time constant for discharging such an electrical circuit is  $\tau_{RC} = \kappa\epsilon_0/\sigma$ . According to Table 1, this discharge constant is 0.01 - 0.1 sec for the thermal blanket. The total area of the thermal blanket gives an overall capacitance of 0.5  $\mu\text{f}$  and an overall resistance of  $2 \times 10^4$  to  $2 \times 10^5$  ohms using an average blanket thickness of 2.5 cm. This time constant is a critical parameter for estimating discharge rates, particularly during electron gun firings. According to the previous discussion, the thermal insulation may conceivably yield time constants from  $10^{-4}$  sec to  $10^3$  sec. The low end would provide welcome relief from charge buildup and its attendant hazards whereas the high end raises grave concerns about arcing, and its side effects.

### 2.3 Vehicle Gas Releases

There is considerable neutral gas released by the Shuttle Orbiter that may contaminate its natural environment. A comprehensive study of contamination control has recently been completed for NASA.<sup>7</sup> Results reported here are based on the conclusions in this report. Both passive releases from the outer skin materials and cabin atmosphere leakage, and active exhausting from vernier rockets and fuel-cells cause localized enhancements of the neutral gas around the vehicle. Outgassing is the steady release of heavy molecules ( $M \sim 100$ ) from the nonmetallic skin materials exposed to the vacuum environment of space. Offgassing is the prompt release of adsorbed volatile species primarily from the nonmetallic materials ( $M \sim 18$ ). Cabin atmosphere leaks from various seals around doors, windows, and skin joints. There are two flash evaporator vents near the rear of the fuselage that periodically expell large amounts of water vapor from the fuel cells. There are six 25 lb (nominal) thrust vernier control rocket engines that are used for vehicle attitude control. Outgassing of the main rocket engine following orbit insertion is not treated in the study because the exhaust product is water vapor that promptly dissipates.

Comparison of the ambient oxygen density at Orbiter altitudes with predicted offgassing and cabin leakage densities, shows that the Shuttle Orbiter is generating its own atmosphere. The principal source is cabin leakage which is one or two orders of magnitude greater than the natural oxygen density. In the first few hours offgassing of volatiles is comparable, but after the first day it is a minor contributor. The evaporators and vernier engines produce narrow rayed plumes that are several orders of magnitude denser than ambient, but these exhaust plumes move radially away from the vehicle and do not contribute appreciably to the total density adjacent to the skin.

### 3. POTENTIAL INDUCED BY ELECTRON GUN

#### 3.1 General Problem

Firing large current pulses of high-energy electrons away from the Spacelab produces a net positive charge on the Shuttle Orbiter that must be neutralized by return electron current from the plasma surrounding the vehicle. Several factors affect this neutralization process. If natural return currents are inadequate, large positive vehicle potentials would result, and local electric fields might ionize the neutral atoms increasing the available return current. The rapid motion of the Orbiter relative to the ions produces a positive charge in the spacecraft wake that alters the distribution of return current collection. Finally, the dielectric nature of the thermal insulation means that the neutralization current does not efficiently return to the electrical ground of the electron gun; instead, it causes differential charging between insulator outer surfaces and the inner metallic superstructure. Evidently, the temporal behavior of these processes is critical for determination of the magnitude of local charging and electric fields. Clearly, it is important to avoid generating potentials that do not allow the beam to escape or that cause electrical breakdown and significant arcing in the thermal insulation.

#### 3.2 Metal Satellites

The magnitude of the problem is illustrated by proposed theories for satellite potentials induced by large currents of high-energy electrons that have been developed for spherical metal vehicles.<sup>8-10</sup> Unfortunately, the theories are not directly applicable to the Shuttle-Orbiter configuration, and the results have not been adequately tested with rocket experiments. Furthermore, they represent steady-state solutions that describe continuous electron emission rather than current pulses.

The theories assume that the background plasma is entirely natural; there is no consideration of satellite sources of gas or additional plasma. Any additional ionization of the ambient ionosphere caused by the high electric fields radiating from the vehicle is also ignored. The return current is assumed to be derived from a Maxwellian distribution of electrons. Since the electrons move much faster than the vehicle, the spacecraft is assumed to be stationary and wake effects are ignored. The distinguishing difference between these theories is attributable to the way in which the geomagnetic field effects are handled.

In the initial analysis,<sup>8</sup> the magnetic forces were ignored. A subsequent analysis<sup>9</sup> rigorously included the magnetic field effects and obtained much larger potentials for a prescribed beam current due to inhibited collection of return current. Finally, in an effort to bridge the gap between these two results, a large turbulent region around the vehicle was postulated<sup>10</sup> to increase the collection

cross section while retaining the magnetic constraint. The interesting conclusion is that a 1 m sphere that emits 0.5 A continuously is predicted to have a potential of  $10^4$ - $10^6$  volts depending on the influence of the geomagnetic field. The magnitude of the induced potential is relatively independent of the size of the vehicle. If such large potentials occur, they would inhibit or destroy beams of 10-100 keV electrons.

### 3.3 Rocket Experiments

There have been several rocket experiments which fired electron beams, and the data from these experiments may provide some indication of the vehicle potential. However, because the experiments have successfully launched the beams, there has been little investigation or analysis of data pertaining to the ultimate induced potential of the vehicle. The electron echo experiments<sup>11</sup> fired beams upward along the field lines and observed the electromagnetic emissions and electrons after they had echoed back from the other hemisphere. Electron beams from rockets were also fired into the atmosphere to generate artificial auroras.<sup>12</sup> Other rocket experiments involving beam injections into the ionosphere to study excitation processes, have also been successfully performed by Air Force Cambridge Research Laboratories (H. Cohen, private communication). These electron guns had nominal power levels of a few kilowatts and used accelerator voltages of 1-40 kV. Currents of 5-500 mA were fired in short pulses (tens of milliseconds) at the rate of several times per second. Thus, these experiments are not accurate tests of the foregoing theory, although they do indicate a bound on the voltage excursion. Evidently, the electron beams were successfully fired away from the rockets, so their potentials must have been limited to something less than a kilovolt. The return current collection area was just the metal skin of the rocket in most cases (the auroral rocket partially deployed a large conducting "umbrella" to enhance its return current), which is about  $20 \text{ m}^2$ . Thus, the ambient return current of electrons is perhaps 100 mA maximum. This is sufficient to balance the gun current in most cases so that large potentials are not expected.

### 3.4 Numerical Estimates

The Shuttle Orbiter has its own peculiar characteristics that distinguish it from the foregoing rocket experiments or satellite theories. First, and foremost, is its enormous size which provides a return current collection area of  $1300 \text{ m}^2$  on dielectric and  $60 \text{ m}^2$  on metallic conductor (this metal surface area is significantly more than most rockets). The large dielectric area causes more serious discharging problems since the vehicle is no longer an equipotential as in the all-metal case.

Second, the shape of the Orbiter-Spacelab has many sharp corners and edges that produce very high electric fields with only modest potentials. Thus, local ionization enhancements and corona are to be anticipated. Third, the neutral atmosphere around the vehicle is well above ambient so that some cascading of electron return current is anticipated during electron gun firing.

When the electron gun is operated, the overall potential of the vehicle is driven positive. For "average" conditions at a nominal altitude of 400 km (near maximum electron density), it has been shown<sup>1, 4, 8</sup> that the ionosphere provides a field-aligned return current of up to 2.4 mA/m<sup>2</sup>. The cross section of surface area available to collect the current varies with vehicle orientation relative to the geomagnetic field. An effective collection area of 1000 m<sup>2</sup> is assumed here (500 m<sup>2</sup> each, above and below). Thus, the ambient return current can balance up to 2.4 A of gun current. Unfortunately, the return charge is mostly collected on the dielectric thermal insulation and does not directly neutralize the gun potential.

The electron gun is presumably grounded to the metallic superstructure of the vehicle which has an external surface area of only 60 m<sup>2</sup> or so. Thus, with proper orientation to take full advantage of the conductor cross section, the direct return current to the gun amounts of 150 mA. It is reasonable to conclude that this level of gun current can be accommodated without undue charging of the Orbiter dielectric insulation. For gun currents in excess of 150 mA, the electric potential is expected to increase significantly, large electric fields are generated, and the dielectric is charged up.

To illustrate some magnitudes, consider a 10 A gun current pulse for 100 msec, that is, 1 coulomb of charge. If the return current is limited to ambient ionospheric background levels, it requires 400 msec for the Orbiter skin to acquire a neutralizing charge. Most of this charge is collected on the dielectric insulation and subsequently leaks to the metallic inner structure. The time constant,  $\tau_{RC}$ , for such current leakage is about 50 msec for overall resistance of 10<sup>5</sup> ohms and capacitance of 0.5  $\mu$ f. However, over the range of conceivable insulator conductivities  $\tau_{RC}$  may vary from 250  $\mu$ sec to 250 sec. --

The effect of large vehicle potentials on the surrounding plasma distribution is uncertain. Some general properties can be surmised, however. If the potential exceeds +4 volts, the ion ram current is stopped. Since electrons are accelerated to the vehicle, there is a net positive charge in the vehicle wake. Its total charge is probably comparable to the charge in the gun current pulse. Again, consider a 10 A gun current for 100 msec. In 100 msec, the Orbiter has traveled 800 m and its wake diameter is at least comparable to its dimensions, say 50 m. Thus, the volume of the wake charge is at least  $1.5 \times 10^6$  m<sup>3</sup>, and the excess charge density is less than  $4 \times 10^{12}$  ions/m<sup>3</sup>. At this level the density is an order of magnitude above the ambient plasma density, but coulomb forces and plasma instabilities

rapidly dissipate the charge as electron return current enters the wake. During operation of the electron gun the increase in Orbiter potential is accompanied by large electric fields, but their local magnitude over the dielectric is difficult to estimate. Over sharply curved regions, however, potentials of 100 volts will generate fields of  $10^4$  volts/m around 1 cm radii. Protruding metal surfaces are apt to be even more sharply curved. These local areas of high electric fields can accelerate ambient electrons and these electrons cause ionization of the neutral atmosphere. Although the process is insignificant over much of the vehicle, there are locations where the neutral density is high and appreciable electron-ion pair production is feasible.

### 3.5 Electric Circuit Analogies

A comprehensive theoretical model for the overall vehicle-plasma interaction during the electron gun operation has not been developed. However, some quantitative limits can be deduced from electrical properties of the vehicle skin. Since the charge on the thermal insulator dielectric does not leak to the inner conductor immediately, negative charge builds up on the dielectric and reduces its potential relative to the conductor. As the overall vehicle potential returns to the ambient plasma level, the dielectric potential actually goes negative for a short while. During this interval, ion-ram current discharges forward areas on the dielectric but not the shielded areas. A qualitative illustration of the potential and charging scenario is displayed in Figure 1. Evidently, the vehicle is charge-neutral well before the conductor and dielectric are fully discharged by leakage current.

The equivalent electrical circuit for this process can be solved explicitly to get quantitative estimates for potentials and time constants. Initially, the return currents to the dielectric  $I_D$  and the conductor  $I_C$  are assumed constant. This is reasonable for modest potentials that do not ionize or otherwise enhance current collection. The gun current  $I_G$  is also constant during the time interval  $0 \leq t \leq t_G$ . The dielectric skin may be approximated as a high resistance in parallel with a capacitance. The simple electrical circuit and its current flows are shown in Figure 2. The effective charge on the capacitor is  $Q = Q_C - Q_D > 0$  where  $Q_C$  is the charge collected by the conductor and  $Q_D$  is the charge on the outer skin of the dielectric. The potential across the capacitance is

$$\phi = \phi_C - \phi_D = Q/C$$

The transient behavior of this circuit is described by Kirchoff's rules for electrical networks. The instantaneous leakage current  $I_L$  (positive) across the resistance  $R$  is determined by the voltage drop around the circuit

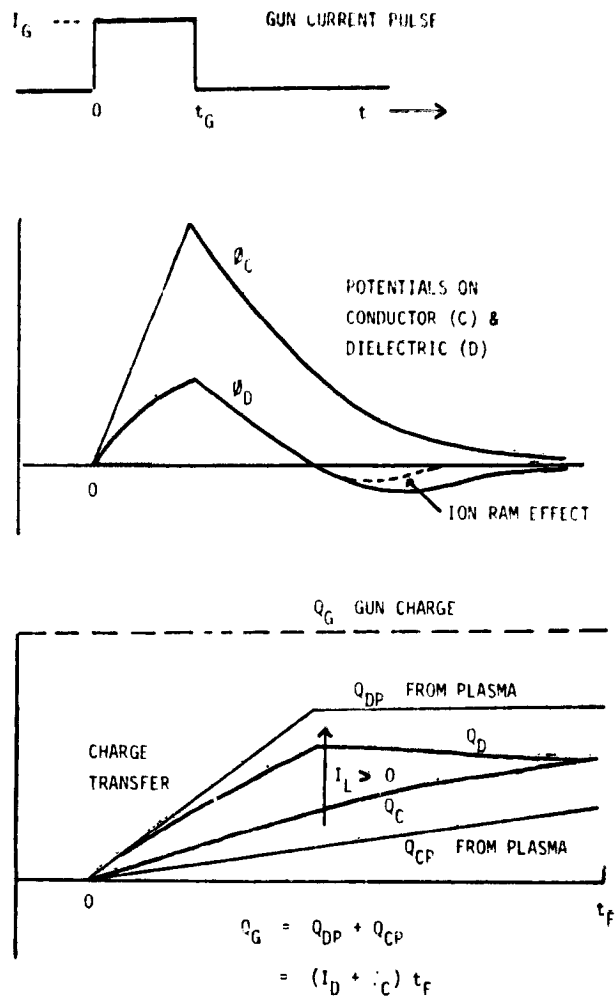


Figure 1. Qualitative Behavior of Potentials and Charges on Conductors and Dielectrics on Orbiter/Spacelab during Electron Gun Firing

$$-I_L R + Q/C = 0$$

The sum of the currents to the conductor is

$$-I_L - I_C + I_G = dQ_C/dt$$

and the corresponding sum to the dielectric is

$$-I_L - I_D = dQ_D/dt$$

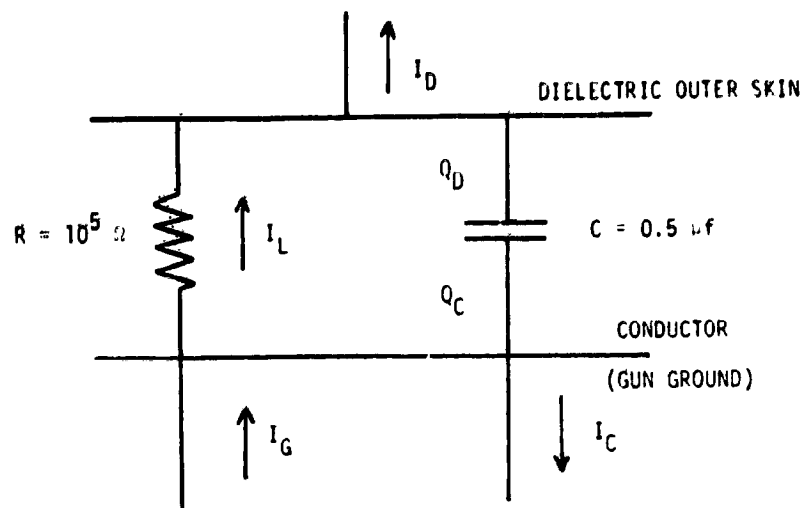


Figure 2. Equivalent Electrical Circuit for Orbiter Skin Neglecting Plasma Resistance

Together, these equations specify the temporal behavior of  $Q$  and  $\phi$  across the dielectric.

Subtracting the current equations gives

$$\frac{dQ}{dt} = I_D - I_C + I_G - 2I_L .$$

Eliminating  $I_L$  with the voltage equation leads to the elementary differential equation

$$\frac{dQ}{dt} + \frac{2Q}{\tau_{RC}} = I_D - I_C + I_G .$$

Its solution has the form

$$Q = \frac{1}{2} \tau_{RC} (I_D - I_C + I_G) [1 - \exp(-2t/\tau_{RC})] \quad \text{for } 0 \leq t < t_G$$

and

$$Q = \frac{1}{2} \tau_{RC} (I_D - I_C) [1 - \exp\{-2(t - t_G)/\tau_{RC}\}] + Q(t_G) \exp[-2(t - t_G)/\tau_{RC}]$$

for  $t \geq t_G$  .

where  $Q(t_G)$  is the maximum charge difference that occurs at  $t = t_G$  when the gun current terminates. During the time interval  $0 \leq t < t_G$ , the charge  $Q$  increases, and afterward it decreases. Discharging continues until the gun charge  $Q_G$  is balanced by the plasma return current,  $(I_D + I_C) t_P$ .

To test the original assumption that  $I_C$  and  $I_D$  are constant, consider the illustrative case  $I_G = 10$  A and  $t_G = 100$  msec. If  $I_D = 2.4$  A and  $I_C = 0.15$  A, the maximum charge is  $Q(t_G) \sim 0.3$  coulombs (assuming  $\tau_{RC} = 50$  msec). This gives a potential drop across the insulation of

$$\phi_C - \phi_D = Q(t_G)/C = 600,000 \text{ volts} .$$

This enormous potential would create electric fields of 24 MV/m across the insulation which is well above the electrical breakdown field for these materials.

With presently available materials, the original assumption of moderate potentials is not valid and the return current is not constant. Since the conductor is at the higher potential, it is expected to collect more current and  $\phi$  increases. Thus, as an initial estimate, assume  $I_C$  is proportional to  $\phi$  or

$$I_C = \phi/R'$$

where  $R'$  is a fictitious plasma resistance that simulates the effect of local ionization and enhanced return current. Its value is unknown, but in general  $R' < R$  if  $\phi$  is to be smaller. Hopefully, the dielectric insulator potential is not too high so that  $I_D$  may be assumed to remain constant for convenience. The new circuit is shown in Figure 3.

For these new assumptions, the differential equation for the charge becomes

$$\frac{dQ}{dt} + \frac{2Q}{\tau_{RC}} + \frac{Q}{\tau_{R'C}} = I_D + I_G .$$

Thus, the same type of solution is obtained with a new time constant

$$\frac{2}{\tau_{RC}} + \frac{1}{\tau_{R'C}} = \frac{1}{\tau_{R'C}} \left( 1 + \frac{2\tau_{R'C}}{\tau_{RC}} \right)$$

where it is assumed  $R' \ll R$ . For  $t_G \gg \tau_{R'C}$ , the maximum charge built up across the insulator is reduced to

$$Q(t_G) = \tau_{R'C} \left( 1 - \frac{2\tau_{R'C}}{\tau_{RC}} \right) (I_D + I_G)$$

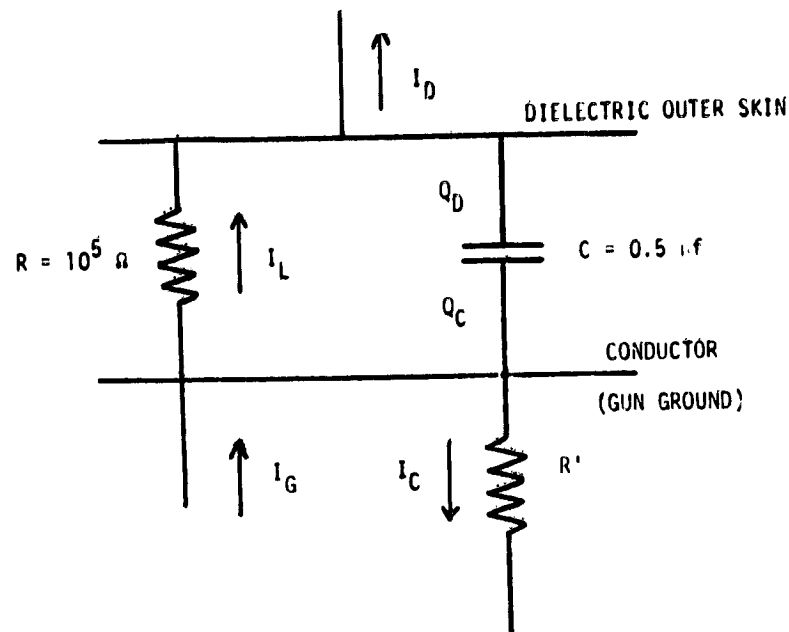


Figure 3. Equivalent Electrical Circuit for Orbiter Skin Including Plasma Resistance

and the corresponding maximum potential is

$$\phi_C - \phi_D = (I_D + I_G) R' (1 - 2R'/R) .$$

The value of  $R'$  seems to be the elusive critical parameter for the process. There is no simple plasma theory for it. A probable range of values may be deduced, however. In order to suppress the induced potential,  $I_C$  must grow to an appreciable fraction of  $I_G$ . It is limited by the condition that the total return current cannot exceed the gun current,

$$I_C + I_D \leq I_G .$$

In order for the conducting surfaces to collect most of the return current, their potential must be high enough to cause local ionization. This may be achieved with voltages of  $10^2$  to  $10^4$  volts to produce electron ionization or electric fields of  $10^6$  -  $10^7$  volts/m to produce breakdown in the local atmosphere. Such potentials and associated fields around the Orbiter are probably created by gun current pulses of less than 1 A, and, therefore,  $R'$  is in the range  $10^2$  -  $10^4$  ohms. For gun currents of 10 A, the conductor potential is probably  $10^3$  -  $10^5$  volts. The

corresponding plasma time constant  $RC$  for reaching quasi-steady state conditions is  $50 \mu\text{sec}$  to  $5 \text{ msec}$ . Thus, the rise time on the potential is extremely short compared to typical gun pulses of  $10 \text{ msec}$  or more.

#### 1. CONCLUSIONS

Generation of large spacecraft potentials externally and internally causes deleterious side effects. Perhaps the most obvious is that the electron beam fails to escape when the spacecraft potential exceeds the electron accelerator potential (around  $50 \text{ kV}$ ). Some experimental objectives require a series of bursts from the electron gun and the transient decay time becomes important. Although one pulse may not build up large potentials, a long series builds up charge if there is inadequate time for decay between gun pulses.

Another obvious problem is probable arcing through the insulation if voltages exceed  $50 \text{ kV}$  or more. In addition to minor physical damage along the discharge path, such occurrences generate broadband electromagnetic interference. Another important aspect is local geometry such as sharp edges or bends which have much higher local electric fields and are more prone to discharges. In some locations repeated (continuous?) discharges are conceivable.

In view of the foregoing difficulties, major charging of the Orbiter skin (above  $10 \text{ kV}$ ) should be avoided. Operation of high current electron guns from the payload bay, therefore, requires much better electrical conductivity through the thermal insulation or auxiliary sources of return current. Doping the insulation materials with impurities to improve electrical conductivity may be a feasible solution. A thin coating of conducting material on the exterior surface of the insulation would be desirable if it does not appreciably alter its overall thermal response.

An important criterion for any suppression technique is that the return current it provides should more than equal the electron gun current. Otherwise the dielectric thermal insulation is charged significantly, and the usefulness of the collection system is dubious. As an example, an electron return current of  $1 \text{ A}$  requires at least  $400 \text{ m}^2$  of collector surface in the nominal environment. At lower or higher altitudes, the return current density is sharply reduced to perhaps  $0.1 \text{ mA/m}^2$  which requires  $10,000 \text{ m}^2$  of collector to balance  $1 \text{ A}$ . At some point there is a physical limit to the size of the collector no matter what technique is deployed, and this places an upper limit on the gun current that can be used.

## References

1. Liemohn, H. B. (1976) Electrical Charging of Shuttle Orbiter, Battelle Final Report to NASA on Contract NAS8-31415; revised version published in IEEE Trans. on Plasma Science PS-4:228-239.
2. Johnson, F. S., Editor (1965) Satellite Environment Handbook, 2nd Edition, Stanford University Press, Stanford, pp. 3-20 and 23-49.
3. Rishbeth, H., and Garriott, O. K. (1969) Intro to Ionospheric Physics, Academic Press, New York.
4. Kasha, M. A. (1969) The Ionosphere and Its Interaction with Satellites, Gordon and Breach, New York.
5. Whitten, R. C., and Poppoff, I. G. (1971) Fundamentals of Aeronomy, Wiley, New York.
6. Banks, P. M., and Kockarts, G. (1973) Aeronomy Parts A and B, Academic Press, New York.
7. Rantanen, R. O., and Ress, E. B. (1975) Payload/Orbiter Contamination Control Assessment Support, Tech Rpt MCR 75-13 by Martin Marietta Aerospace, for NASA Johnson Space Center NAS 9-14212.
8. Beard, D. B., and Johnson, F. S. (1961) Ionospheric limitations on attainable satellite potential, J. Geophys. Res. 66:4113-4122; also Correction (1966) J. Geophys. Res. 71:4707.
9. Parker, L. W., and Murphy, B. L. (1967) Potential buildup on an electron-emitting ionospheric satellite, J. Geophys. Res. 72:1631-1636.
10. Linson, L. M. (1969) Current-voltage characteristics of an electron-emitting satellite in the ionosphere, J. Geophys. Res. 74:2368-2375.
11. Winckler, J. R. (1974) Investigation of electron dynamics in the magnetosphere with electron beams injected from sounding rockets, J. Geophys. 40:729-749.
12. Hess, W. N., Trickel, M. C., Davis, T. N., Beggs, W. C., Kraft, G. E., Stassinopoulos, E., and Maier, E. J. R. (1971) Artificial aurora experiment: experiment and principal results, J. Geophys. Res. 76:6067-6081.

## Contents

1. Introduction	287
2. Altitude Dependence	288
3. Modeling	291
4. Charging Parameters	293
References	296

#### 4. An Altitude-Dependent Spacecraft Charging Model

J. W. Haffner  
 Rockwell International Corporation  
 Space Division  
 Downey, California

#### Abstract

A model for the altitude dependence of the hot plasma parameters responsible for the electrostatic charging of spacecraft has been developed. Based upon plasma plasma orbit theory, the directed velocity is a function of the ambient magnetic field flux density. A consequence of this approach is that while the thermal velocity distributions (assumed to be Maxwellian) of the plasma particles are independent of the magnetic field strength (and hence altitude), the particle densities increase with magnetic field strength. Thus, according to this model, while the equilibrium voltage is independent of altitude, the charging current density increases with decreasing altitude. However, the probability of such spacecraft charging decreases with decreasing altitude.

#### 1. INTRODUCTION

Almost all of the published data and analyses of spacecraft charging<sup>1, 2</sup> have been concerned with spacecraft in geosynchronous orbit ( $r \approx 6.6 R_E$ ). It is theoretically expected that the charging phenomenon can occur at other altitudes

H-7

as well. For spacecraft in earth orbit at other altitudes, the characteristics of such charging becomes of practical concern. The purpose of this study was to develop an analytical model which yielded the significant parameters of the spacecraft charging phenomenon as functions of altitude above the earth.

## 2. ALTITUDE DEPENDENCE

The major environment which has a strong altitude dependence at geosynchronous orbit is the earth's magnetic field. If this field is taken as approximately that of a dipole, its magnetic flux density may be written

$$B = \frac{B_0 \sqrt{1 + 3 \sin^2 \lambda_M}}{\left(\frac{r}{R_E}\right)^3} \quad (1)$$

where.

$B_0$  = the magnetic flux density at the surface of the earth at the magnetic equator  $\approx 0.3$  gauss =  $3 \times 10^{-5}$  webers/m<sup>2</sup>;

$\lambda_M$  = the magnetic latitude (degrees);

$r$  = distance from the magnetic center of the earth;

$R_E$  = radius of the earth.

It is necessary for  $r$  and  $R_E$  to be in the same units, and that  $r \geq R_E$ .

It is well known that a plasma can exist in a magnetic field only if the plasma energy density exceeds the magnetic field energy density. The energy density (E. D.) of the quasistatic magnetic field is  $B^2/2\mu$ , where  $\mu$  is the permeability of the medium which contains the magnetic field. For free space  $\mu = \mu_0 = 4\pi \times 10^{-7}$  H/m (MKS units). Thus for the dipole-approximated geomagnetic field,

$$\begin{aligned} \text{E. D. } B &= \frac{B_0^2 (1 + 3 \sin^2 \lambda_M)}{2 \mu_0 \left(\frac{r}{R_E}\right)^6} \\ &= 3.58 \times 10^{-4} \left[ \frac{1 + 3 \sin^2 \lambda_M}{\left(\frac{r}{R_E}\right)^6} \right] \frac{\text{joules}}{\text{m}^3} \end{aligned} \quad (2)$$

Any plasma which is able to exist in such a magnetic field must possess an energy density at least this large.

The energy density of a two-component electrically neutral fully ionized non-relativistic plasma may be written

$$E. D. p = KE (\text{directed}) + KE (\text{thermal}) \quad (3)$$

where

$$\frac{KE (\text{directed})}{N} = 1/2 (m_+ + m_-) v (\text{dir})^2 ;$$

$$\frac{KE (\text{thermal})}{N} = 1/2 m_+ v_+ (\text{th})^2 + 1/2 m_- v_- (\text{th})^2 .$$

In these equations,  $m_+$  and  $m_-$  are the rest masses of the positively charged and negatively charged plasma particles, respectively, while  $v(\text{dir})$  and  $v(\text{th})$  are the directed and the thermal velocities of those particles.  $N$  is the spatial density of each type of particle. As long as the plasma moves as an entity, the + and - particles will have the same directed velocities. In addition, if the plasma is in thermal equilibrium, the + and - particles will have the same average thermal energies, leading to the relationship

$$\frac{v_- (\text{th})}{v_+ (\text{th})} \approx \sqrt{\frac{m_+}{m_-}} . \quad (4)$$

This last relationship is only an approximation, as measurements in the hot plasmas responsible for spacecraft charging seem to show that the temperatures of the + component (largely protons) are about twice the temperatures of the - component (electrons).

The characteristics of the hot (spacecraft charging) plasmas at geosynchronous orbit show that the directed velocity generally lies between the thermal velocities of the electrons and the protons. Thus, the directed velocity is supersonic for the protons but subsonic for the electrons. Since  $m_+ \approx 1836 m_-$ , the energy density for such plasma is essentially all due to the directed motion of the protons. To illustrate this, for a plasma with a 5 keV temperature  $v_+ (\text{th}) \approx 10^8$  cm/sec while  $v_- (\text{th}) \approx 4.3 \times 10^9$  cm/sec. Taking  $v(\text{dir})$  as  $6 \times 10^8$  cm/sec (an intermediate value) yields directed energies of  $E_+ \approx 180$  keV and  $E_- \approx 0.1$  keV. Only if  $v(\text{dir})$  is not greater than  $v_+ (\text{th})$  is the plasma energy density not largely due to the directed motion of the heavier (+) component.

With  $E. D. p \approx 1/2 m_+ v(\text{dir})^2$ , it is possible to estimate how low in altitude a hot plasma moving radially toward the earth can get before its energy density is

not sufficient to prevent the geomagnetic field from tearing it apart. Equating  $E \cdot D_B$  and  $E \cdot D_p$  yields

$$r \approx R_E \left[ \frac{B_0}{v(\text{dir})} \right]^{1/3} \left[ \frac{1 + 3 \sin^2 \lambda_M}{\mu_0 m_p N} \right]^{1/6} \quad (5)$$

The results of this calculation are shown graphically in Figure 1 for  $\lambda_M = 0^\circ$  (magnetic equator). These results are an approximation because of many factors, but due to the steep radial gradient of the energy density of the geomagnetic field,

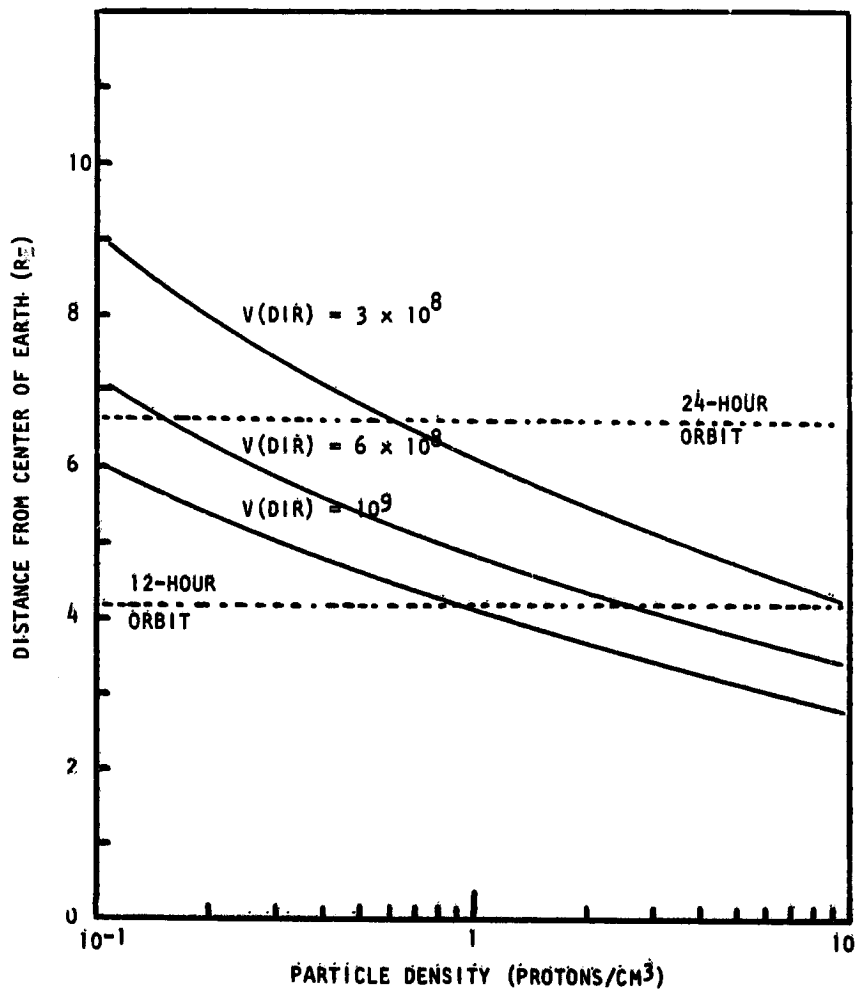


Figure 1. Calculated Hot Plasma Altitude Limit

the approximations produce only relatively small perturbations in the results. It is seen that a moderately dense ( $\gtrsim 10$  particles/cm<sup>3</sup>) plasma with a reasonably large directed velocity ( $\gtrsim 3 \times 10^8$  cm/sec) can reach the 12 hr circular orbit ( $r \approx 4.15 R_E$ ), while an increase in either particle density or directed velocity can result in spacecraft charging at even lower altitude earth orbits.

### 3. MODELING

There are various approximate ways of modeling a plasma to make plasma problems mathematically tractable. Each model deals with that portion of plasma properties which are most pertinent to the problem at hand while suppressing or ignoring less relevant properties. Plasma orbit theory is among those approximate models often used in situations in which the motions of individual plasma particles are important. (Hydrodynamic theory is often used for situations in which large-scale plasma oscillations are more important than individual particle motion.) The basis of orbit theory is the conservation of the angular momentum of individual particles about an axis (for example, the direction of the magnetic flux lines). Motion of the plasma particles parallel to the lines of magnetic flux is not affected (to a first approximation). Thus, it is possible to separate the thermal and the directed motions of the plasma particles by considering them to be parallel and perpendicular to the magnetic field, respectively. This simplified model results in a decrease in the directed velocity as the distance from the earth decreases (for example, as the magnetic field strength increases) while leaving the thermal velocity unchanged. It is obvious that this model neglects the compressional heating of the plasma, which certainly is a major factor in the production of the hot plasma in the first place. However, attempts to incorporate compressional heating resulted in a model in which the plasma energy density increases as rapidly as the geomagnetic field energy density, with the consequence that a plasma able to exist at any altitude could theoretically reach any other (lower) altitude. This is clearly at variance with observational data (spacecraft charging anomalies have not been reported for low-altitude earth orbits).

Based upon the simplified application of plasma orbit theory, it is possible to write

$$v(\text{dir}) = \bar{v}_{\text{th}} \cos \alpha \quad (6)$$

where  $\alpha$  is the pitch angle (angle between the velocity vector and the direction of the geomagnetic field). This is similar to the equation of motion for Van Allen belt particles. The second invariant for such particles leads to the relationship

$$\sin^2 \alpha = \frac{B}{B_{\max}} \quad (7)$$

By combining these last two equations, one can obtain

$$v_{\text{dir}} = \bar{v}_{\text{th}} \sqrt{1 - \frac{B}{B_{\max}}} \quad (8)$$

According to this model the average particle thermal velocity (plasma temperature) does not change with altitude while the directed velocity gradually decreases, reaching zero when  $B = B_{\max}$ . At that point, the plasma energy density has been reduced to the energy density of the geomagnetic field.

The negative voltage to which a body immersed in a plasma of a given temperature will charge is  $\sim 3.76$  times the average electron kinetic energy ( $E_0$ ) in electron volts. The negative voltage is due to the fact that the electrons have much higher thermal velocities than the protons, and therefore impact the spacecraft surface much more often.

The factor of 3.76 is due to the fact that the negative current to an unilluminated spacecraft surface varies exponentially with spacecraft voltage (to a first approximation) while the positive current varies linearly with voltage. This is a consequence of the fact that the electron motion is subsonic while the proton motion is supersonic. Mathematically,

$$J_+ = J_{\text{op}} \left( 1 + \frac{V}{V_{\text{op}}} \right) \quad (9)$$

$$J_- = J_{\text{oe}} e^{-V/V_{\text{oe}}} \quad (10)$$

where  $J_+$  and  $J_-$  are the surface current densities as a function of spacecraft voltage ( $V$ ), and  $J_{\text{oe}}$  and  $J_{\text{op}}$  are those current densities (including the effects of secondaries) when  $V = 0$ .  $V_{\text{op}}$  and  $V_{\text{oe}}$  are the average proton and electron kinetic energies in electron volts, respectively. Since  $m_+ \approx 1836 m_-$ ,  $J_{\text{oe}} \approx \sqrt{1836} J_{\text{op}} \approx 42.8 J_{\text{op}}$ . The value of  $V$  will increase until  $J_+ = J_-$ , assuming no electrical discharges take place. Equating  $J_+$  to  $J_-$  and solving for  $V$  yields

$$V = V_0 \left[ 3.76 + \ln \left( \frac{V_{\text{op}}}{V_{\text{op}} + V} \right) \right] \leq 3.76 V_{\text{oe}} \quad (11)$$

Since the secondary current components vary with spacecraft voltage differently than the primary currents do, this factor of 3.76 can be appreciably different in many situations. However, since the particles responsible for the charging have

an approximately Maxwellian energy distribution, it is understandable that a plasma with an average electron temperature of  $V_{oe}$  (volts) would charge a spacecraft to voltages  $V > V_{oe}$ .

#### 4. CHARGING PARAMETERS

Since, according to this model, the particle thermal velocities are unchanged by the directed motion of the plasma toward the earth, the equilibrium voltage which a spacecraft surface will reach in the plasma will not depend upon altitude. In the absence of electrical discharges, a spacecraft in a 12 hr circular orbit ( $r \approx 4.15 R_E$ ) will therefore theoretically charge to the same potential as one in a 24 hr geosynchronous orbit ( $r \approx 6.6 R_E$ ). However, the surface current densities (which determine how fast the spacecraft will charge) will be a function of altitude. The initial primary surface current density as a function of altitude may be estimated by calculating the limiting plasma particle density of the plasma just as its directed motion has ceased. Since the average particle energy (and the particle energy distribution) remains unchanged according to this model, the particle density must increase linearly with the energy density of the geomagnetic field.

The calculated numbers derived based upon this model are shown in Table 1. At each altitude  $r$  the average energy density of the geomagnetic field (dipole approximation) was taken as the average thermal energy density of a stationary plasma at that altitude. Assuming half of this thermal energy density was due to the electrons, the product  $\bar{E}_- \cdot N_-$  was obtained. For each value of limiting spacecraft potential  $V$ , the average electron energy was obtained by dividing by 3.76. The electron density ( $\text{cm}^{-3}$ ) was the quotient of  $\bar{E}_- \cdot N_-$  divided by  $E_e$  ( $E_- \equiv E_e$  here). The initial primary electron current density ( $J_-$ ) was obtained from the equation

$$J_- = N_- \cdot q \cdot \bar{v} \quad (12)$$

The results listed in Table 1 are also shown graphically in Figure 2. It is seen that the calculated initial current density increases rapidly as orbit altitude decreases. This altitude dependence decreases the importance of the photoelectric current density (which has an altitude-independent value  $< 1 \text{ nA/cm}^2$ ) at lower altitudes. Another consequence of this altitude dependence is that if the spacecraft surface cannot withstand the equilibrium potential to which the plasma can charge it, the rate at which electrical breakdowns (discharges) occur will be much greater at lower altitudes.

While the calculated surface current densities are larger at low altitudes than at geosynchronous altitude, the probability that a spacecraft will encounter the hot

$R_E$	$N_e$ (particles/cm <sup>3</sup> )	V = 9 keV $E_e = 1.33$ keV $\bar{v} = 4.3 \times 10^9$	V = 10 keV $E_e = 2.66$ keV $\bar{v} = 6.08 \times 10^9$	V = 15 keV $E_e = 3.99$ keV $\bar{v} = 7.45 \times 10^9$	V = 20 keV $E_e = 5.32$ keV $\bar{v} = 8.6 \times 10^9$	V = 25 keV $E_e = 6.65$ keV $\bar{v} = 9.62 \times 10^9$
6.6 (24 hr)	6.5	$N_e = 4.89$ $J_e = 3.36$	2.44 2.38	1.83 1.94	1.22 1.68	0.97 1.50
6	12.5	$N_e = 9.40$ $J_e = 6.47$	4.70 4.57	3.13 3.74	2.35 3.23	1.88 2.89
5.5	20	$N_e = 15.0$ $J_e = 10.35$	7.52 7.30	5.00 5.96	3.76 5.17	3.01 4.63
5	36	$N_e = 27.1$ $J_e = 18.6$	13.5 13.2	9.00 10.7	6.80 9.29	5.40 8.31
4.5	67.5	$N_e = 50.8$ $J_e = 34.9$	25.4 24.7	16.9 20.1	12.7 17.5	10.2 15.6
4.15 (12 hr)	110	$N_e = 82.7$ $J_e = 56.8$	41.4 40.2	27.6 32.8	20.7 28.5	16.6 25.5
3.5	313	$N_e = 235.0$ $J_e = 161.5$	117.5 114.3	78.3 93.3	58.8 80.8	47.0 72.3

v in cm/sec;  $N_e$  in particles/cm<sup>3</sup>;  $J_e$  in namps/cm<sup>2</sup>.

Table 1. Calculated Particle Densities and Initial Primary Current Densities as Functions of Altitude ( $\lambda_M = 0^\circ$ )

plasma at these lower altitudes is appreciably less. It would be theoretically possible to calculate an altitude-dependent probability if data were available concerning the probability of encountering a given plasma energy density at geosynchronous altitude. Such data are becoming available. However, the measured L-dependence of the probability of encountering > 15 volts on an antenna has been measured by IMP-6<sup>3</sup> (see Figure 3). This spacecraft was launched 31 March 1971 into a 28.7° elliptical orbit with an apogee of 32.4  $R_E$  and a perigee of 243 km. As the data shows, the probability of encountering hot (or at least warm) plasma at 4.15  $R_E$  is approximately an order of magnitude less than at 6.6  $R_E$ . While the inclination of the IMP-6 orbit makes analysis difficult, the data suggest that the spacecraft charging phenomenon may be more common near geosynchronous altitude than at any other.

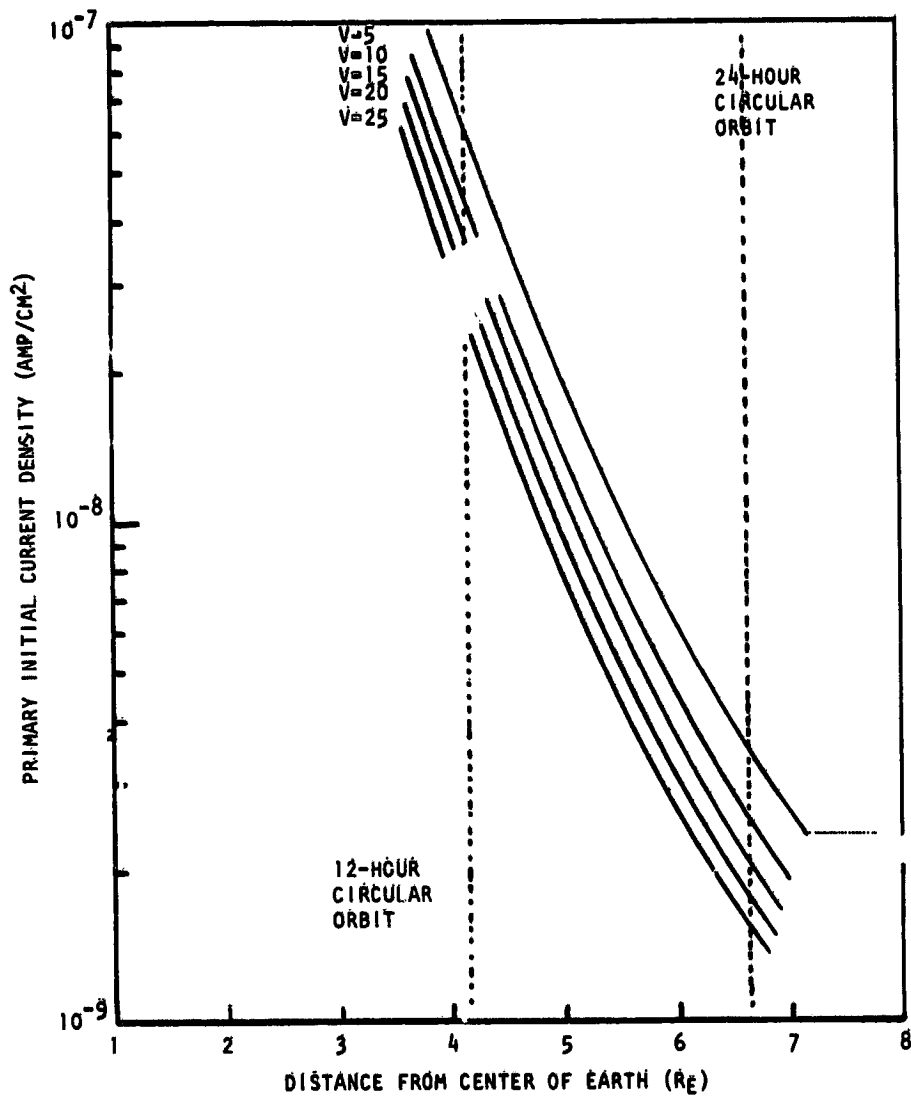


Figure 2. Calculated Primary Initial Current Density as a Function of Altitude ( $\lambda_M = 0^\circ$ )

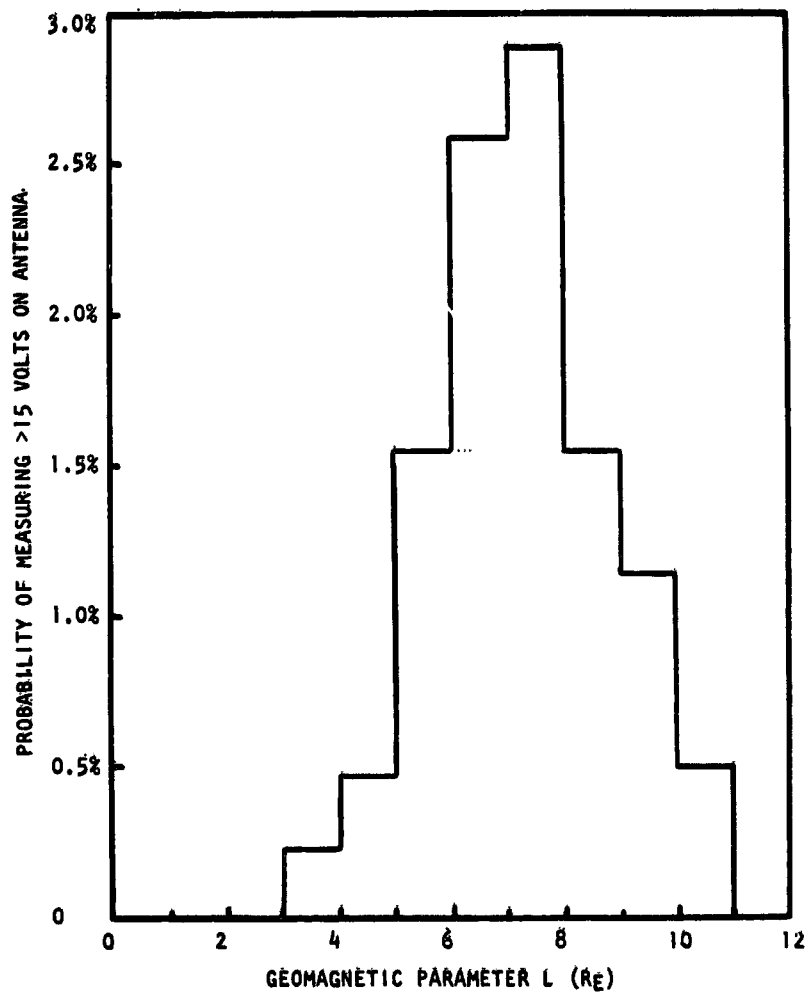


Figure 3. Probability of Measuring > 15 Volts on IMP-6 Antenna

### References .....

1. De Forest, S. E. (1972) Spacecraft charging at synchronous orbit J. Geophys. Res. 77:651-659.
2. Rosen, A. (1976) Spacecraft charging by magnetospheric plasmas, Progress in Aeronautics and Astronautics, 47, AIAA, New York.
3. Cauffman, D. P. (1974) A Study of IMP-6 Spacecraft Charging, ATR-74 (7451)-1, The Aerospace Corporation.

## Contents

1. Introduction	298
2. Charged Particle Environment	299
3. Spacecraft Electrical Model	303
4. ISPICE Calculation Results	306
References	308

## 5. Pioneer Venus Spacecraft Charging Model

P. A. Robinson, Jr. and A. B. Holman  
Hughes Aircraft Company  
Space and Communications Group  
El Segundo, California

### Abstract

Large potential differences between parts of the spacecrafts or between the spacecraft and the plasma will cause instruments to give misleading or meaningless data. Potentials and currents at various locations on the Pioneer Venus Orbiter are predicted by constructing an electrical model of the spacecraft and the environment, and calculating the response of the electrical model to the environment model.

Five environment models were constructed to represent the solar wind and the upper, middle, and lower ionosphere of Venus. The spacecraft structure was modeled with over 140 passive electrical elements representing structural elements of the spacecraft. Electron, ion, secondary electron, and photocurrents to the spacecraft from the plasma were calculated, ignoring sheath effects.

In all but one case, potentials of interest were less than 1 volt. Potential differences between widely separated points on the equipment shelf were less than 1 mV. The one area of concern is the solar panel potential when the orbiter is passing through the bowshock region. Here we assumed a high photocurrent and a low density, low temperature plasma, with solar panel potentials approaching 5 volts positive. Some experimenters indicated this would present a problem in interpreting results. Further study is needed to clarify this issue; otherwise, spacecraft potentials are well within design levels.

Work performed by Hughes for Ames Research Center under Contract NAS 28300.

ORIGINAL PAGE IS  
OF POOR QUALITY

## 1. INTRODUCTION

Spacecraft for two Pioneer Venus missions are being built by Hughes Aircraft Company for NASA Ames Research Center. In the multiprobe mission, a large entry probe will make detailed measurements of the Venusian atmosphere and clouds. Three small probes will simultaneously sample conditions at widely separated points. The probe bus will make upper atmospheric measurements prior to its entry and burnup. In the orbiter mission, a spacecraft will circle the planet for a Venusian year (225 days), examining long term and global effects. The orbiter will be placed in a highly inclined elliptical orbit with a low altitude, midlatitude periapsis location. Most of the measurements will be taken during the periapsis pass.

Figure 1 shows the Pioneer Venus Orbiter. There is a conducting mesh over the forward end of the spacecraft to ensure a uniform charge distribution. Table 1 lists the instruments on the orbiter that are concerned with the charge state of the spacecraft. None of the experimenters felt their instrument would influence the charge state of the spacecraft.

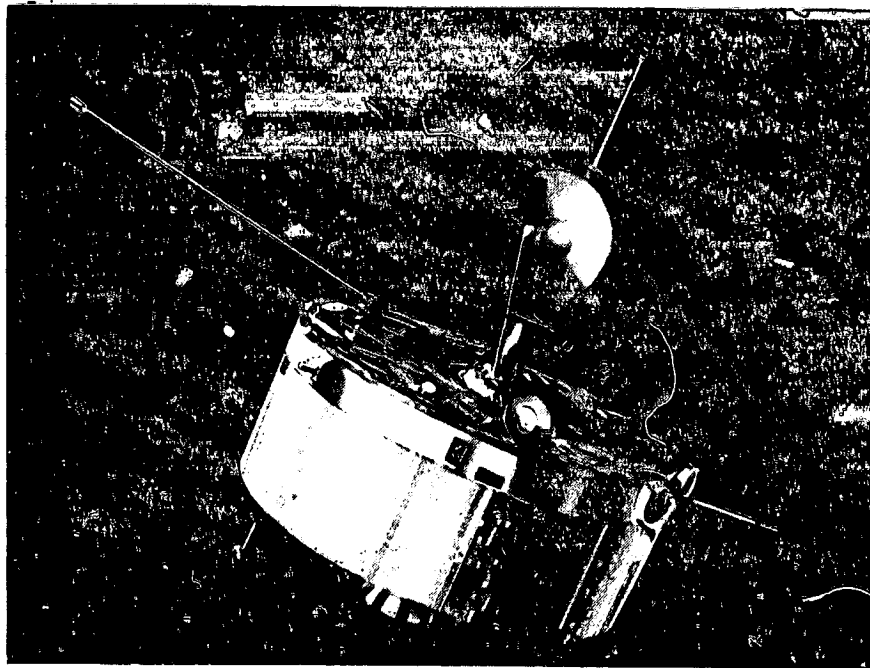


Figure 1. Pioneer Venus Orbiter

Table 1. Experiments Concerned with Charge State of Spacecraft

Instrument	Operating Altitude	Important Features
Ion. mass spectrometer Dr. Harry Taylor	<5000 km	No external potentials; current $\geq 5 \times 10^{-14}$ A. 2 in. dia aperture; would prefer negatively charged spacecraft
Electron temperature probe Dr. Larry Brace	$\geq 6000$ km	Exposed potentials vary from -5 to +7 V; total area $\sim 13$ cm <sup>2</sup> ; single probe area = 4 cm <sup>2</sup>
Retarding potential analyzer Dr. William Knudsen	All	Exposed potential +6 V current to instrument could be as high as $10^{-4}$ A; aperture diameter = 8 cm; would prefer spacecraft potential from -1 to -5 V.
Plasma analyzer Dr. John Wolfe	All	Potential $\pm 700$ V; maximum current $10^{-12}$ A; aperture area = 1 cm <sup>2</sup>
Electric field detector Dr. Fred Scarf	All	No exposed potentials; measures potential difference across instrument at frequencies above 100 Hz

## 2. CHARGED-PARTICLE ENVIRONMENT

The charged particle environment for the Pioneer Venus Orbiter mission is an upper bound on empirical information obtained from various sources.<sup>1-4</sup> The model covers the full range of altitudes where scientific packages on the orbiter vehicle are operational. The model is summarized in Table 2.

Table 2. Pioneer Venus Orbiter - Charged Particle Environment

Region Label	Environment Component	Altitude Range, km	Charged Particles	Maximum Density, per cm <sup>3</sup>	Energy Levels, eV
I	Solar wind	$\infty$ to 1000	Protons electrons	10 10	10 to 100 10 to 100
II	Upper ionosphere	1000 to 700	Ions (CO <sub>2</sub> <sup>+</sup> ) electrons	10 <sup>2</sup> 10 <sup>2</sup>	<0.1 <0.1
III	Middle ionosphere	700 to 350	Ions (CO <sub>2</sub> <sup>+</sup> ) electrons	10 <sup>3</sup> 10 <sup>3</sup>	<0.1 <0.1
IV	Lower ionosphere 1	350 to 200	Ions (CO <sub>2</sub> <sup>+</sup> ) electrons	$5 \times 10^4$ $5 \times 10^4$	<0.1 <0.1
V	Lower ionosphere 2	200 to 150	Ions (CO <sub>2</sub> <sup>+</sup> ) electrons	$5 \times 10^5$ $5 \times 10^5$	$\sim 0.06$ $\sim 0.06$

A cosmic ray background<sup>5</sup> will be present at all altitudes. Since the current densities are low and the particle energies high, there will be negligible contribution to a surface charge or potential buildup on the orbiter exterior surfaces from this source. The solar wind component of the environment dominates down to an altitude of approximately 1000 km, the bowshock region (actual altitude strongly dependent on vehicle trajectory). The ionosphere begins to develop at lower altitudes and particle and current densities peak at an altitude in the range of 150 to 200 km (~ 500°K thermosphere).

The ionosphere is extremely dynamic and the altitudes bounding the regions of interest should not be taken as rigid divisions. In addition, the solar radiation (~ 5750°K blackbody,  $2.7 \times 10^{-4}$  ergs/cm<sup>2</sup> sec) at Venus contributes strongly to the spacecraft charge for the orbiter because of the effect of photoemission from the spacecraft external surfaces.

Electron and ion currents, photoemission currents, and secondary electron currents are included as appropriate. Tables 3 and 4 list current density (amperes per square centimeter) used in calculations for each region. These current densities are one-half the expected maximum thermal currents. The secondary electron current is dependent on a parameter  $E_{max}$ , the energy at maximum secondary electron emission. Table 4 lists the secondary electron emission for two typical  $E_{max}$  and  $S_{max} = 1$ .  $S_{max}$  is the number of secondary electrons emitted at  $E_{max}$ . The resistivity of the plasma is calculated from kinetic theory.<sup>6</sup> In calculating the resistance to the plasma from each element, the Debye length<sup>6</sup> was used as the length through the plasma. Table 5 lists the terms included in a power series expansion of current versus potential.

#### KEY FOR TABLES 3 THROUGH 5

ALT	= altitude range	$\nu$	= collision frequency
$N_e$	= electron density, electron/cm <sup>3</sup>	$J_e$	= electron current density
$kT_e$	= electron temperature, eV	$J_i$	= ion current density
$\lambda_D$	= $\left(\frac{kT}{4\pi N_e e^2}\right)^{1/2}$ = Debye length, cm	$J_e/e$	= secondary electron current density
$\eta$	= $\frac{m_e c^2 \nu}{N_e e^2}$ = kinetic theory resistivity;	$J_{hu}$	= photoemission current density
		$J$	= total current density

Table 3. Plasma Parameters

Region	Altitude, km	$N_{e0}$ , $\text{cm}^{-3}$	$kT_e$ , eV	$\lambda_D$ , cm	$\eta$ , ohm-cm
I Solar wind	$\infty$ to 1000	10	100	$2.35 \times 10^3$	$3.194 \times 10^3$
II	1000 to 700	100	0.1	23.5	$2.8 \times 10^8$
III	700 to 350	$10^3$	0.1	7.43	$2.5 \times 10^7$
IV	350 to 200	$5 \times 10^4$	0.1	1.05	$5.0 \times 10^5$
V	200 to 150	$5.0 \times 10^5$	0.06	0.26	$5.0 \times 10^4$

Table 4. Plasma Currents Used in Calculations\*

Region	$J_{e0}$ , $\text{A/cm}^2$	$J_{i0}$ , $\text{A/cm}^2$	$J_{e/e0}$ , $E = 300$ , $\text{A/cm}^2$	$J_{e/e0}$ , $E = 400$	$J_{hu}$ , $\text{A/cm}^2$
I Solar wind	$1.34 \times 10^{-10}$	$3.13 \times 10^{-12}$	$1.35 \times 10^{-12}$	$1.12 \times 10^{-12}$	$6 \times 10^{-9}$
II	$4.24 \times 10^{-11}$	$9.89 \times 10^{-13}$	$1.01 \times 10^{-12}$	$7.6 \times 10^{-13}$	$3 \times 10^{-9}$
III	$4.24 \times 10^{-10}$	$9.89 \times 10^{-12}$	$1.01 \times 10^{-11}$	$7.6 \times 10^{-12}$	0
IV	$2.12 \times 10^{-8}$	$4.94 \times 10^{-10}$	$5.05 \times 10^{-10}$	$3.81 \times 10^{-10}$	0
V	$1.64 \times 10^{-7}$	$3.83 \times 10^{-9}$	$3.94 \times 10^{-9}$	$2.97 \times 10^{-9}$	0

Table 5. Power Series Expansion of Total Current Density in One Dimension

$$\begin{aligned}
 J_e &= \frac{n_0 e^2}{2} \left( \frac{-2kT}{\pi m c^2} \right)^{1/2} e^{-e\phi/kT} = J_{e0} e^{-e\phi/kT} \\
 J_i &= \frac{1}{40} J_e e^{e\phi/kT} = J_{i0} e^{e\phi/kT} \\
 J_{e/e0} &= J_{e0} (7.4) \frac{S_{\max}}{E_{\max}} \left\{ 1 - e^{kT/E_{\max}} \left( \frac{\pi kT}{E_{\max}} \right)^{1/2} \left[ 1 - \text{erf} \left( \left( \frac{kT}{E_{\max}} \right)^{1/2} \right) \right] \right\} \\
 J_{e/e} &= J_{e/e0} e^{+2e\phi/kT} \\
 J &= J_{hu} + J_i + J_{e/e} \cdot J_e \\
 J &= (J_{hu} + J_{i0} + J_{e/e0} \cdot J_{e0}) + (J_{i0} + 2 J_{e/e0} + J_{e0}) \left( \frac{e\phi}{kT} \right) \\
 &\quad + (J_{i0} + 4 J_{e/e0} \cdot J_{e0}) \frac{1}{2} \left( \frac{e\phi}{kT} \right)^2 + (J_{i0} + 8 J_{e/e0} \cdot J_{e0}) \frac{1}{6} \left( \frac{e\phi}{kT} \right)^3 \\
 &\quad + (J_{i0} + 16 J_{e/e0} \cdot J_{e0}) \frac{1}{24} \left( \frac{e\phi}{kT} \right)^4 + \dots
 \end{aligned}$$

\*One-half maximum values.

In addition to the thermal current, the spacecraft will see a current due to the relative velocity of the spacecraft and the plasma. This is called a ram current. Typical ram currents are shown in Table 6. Both the electron and ion currents will be increased by the ram current on surfaces facing into the velocity vector. Both currents will be reduced on surfaces hidden from the velocity vector. Table 7 compares ram and thermal currents for the Pioneer Venus Orbiter. In Region I, the relative velocity is that of the solar wind. In Regions II through V, the relative velocity is the velocity of the spacecraft in its orbit. In Regions I and II, the photocurrent dominates and ram currents will have little effect on the net spacecraft charge. In Regions III, IV and V, the ram current will tend to make the spacecraft potentials more positive.

Table 6. Ram Currents

Region, km	$\langle V \rangle$ , km/sec	$N$ , per $\text{cm}^3$	$J$ , $\text{A/cm}^2$
>1000	500.00	10	$8 \times 10^{-11}$
1000	9.16	100	$1.5 \times 10^{-11}$
700	9.38	1000	$1.5 \times 10^{-10}$
350	9.66	$5 \times 10^4$	$7.7 \times 10^{-9}$
200	9.78	$5 \times 10^5$	$7.8 \times 10^{-8}$

Table 7. Likely Effect of Ram Currents

Region, km	Thermal			Comment
	$J_{\text{rain}}$	$J_{e\text{max}}$	$J_{i\text{max}}$	
>1000	$8 \times 10^{-11}$	$3 \times 10^{-10}$	$6 \times 10^{-12}$	Photocurrent dominates; ram current will make no difference to charge state of spacecraft; may influence experiments.  Greatly increases $J_{i\text{g}}$ ; no effect when phase near zero; will tend to make spacecraft voltage more positive.
1000	$1.5 \times 10^{-11}$	$8 \times 10^{-11}$	$2 \times 10^{-12}$	
700	$1.5 \times 10^{-10}$	$8 \times 10^{-10}$	$2 \times 10^{-11}$	
350	$7.7 \times 10^{-9}$	$4 \times 10^{-8}$	$1 \times 10^{-9}$	
200	$7.8 \times 10^{-8}$	$3 \times 10^{-7}$	$8 \times 10^{-9}$	

### 3. SPACECRAFT ELECTRICAL MODEL

The electrical model for the orbiter includes more than 140 electrical elements and over 70 nodes, each representing an important spacecraft location (see Figure 2). This electrical model was constructed as described in<sup>7</sup> and the following discussion outlines the formulation of the models.

#### 3.1 Thrust Cone (Series 10)

The magnesium thrust cone was modeled as a series of linear inductors and resistors. A central node was used to provide a location for a capacitance to the surrounding solar panel substrate. The lower end of the cone was tied directly to the equipment shelf support struts and the upper end represented the interface with the BAPTA and equipment shelf.

#### 3.2 Equipment Shelf Support Struts (Series 20)

The 12 support struts were reduced to an equivalent configuration of four to fit the simplified quadrant model of the equipment shelves and surrounding solar panels and substrate. The four strut elements were then modeled as linear inductors and resistors. Estimated resistances of bonded joints were included where it was felt important.

#### 3.3 Equipment Shelf (Series 30)

The equipment shelf was modeled in quadrants with circumferential and radial inductances and resistances calculated for each. A capacitance to the forward aluminum mesh and thermal blanket was also included. (Where two capacitances appear in series with an unimportant intervening node and one is much larger in magnitude than the other, the larger capacitance is omitted from the model for simplification, or an equivalent calculated.)

#### 3.4 BAPTA and BAPTA Support Cone (Series 40)

The BAPTA and its support structure were modeled as an inductor and resistor tied at the ends to the equipment shelf and the main antenna supports.

#### 3.5 Main Antenna Support, Dish, and Forward Omni (Series 50)

The aluminum antenna support structures were modeled as linear inductors and resistors with a node at the main dish and at the omni. Capacitances were calculated for the dish and the omni to infinity. An estimate of mutual inductance coupling with the antenna feed structure was also included.

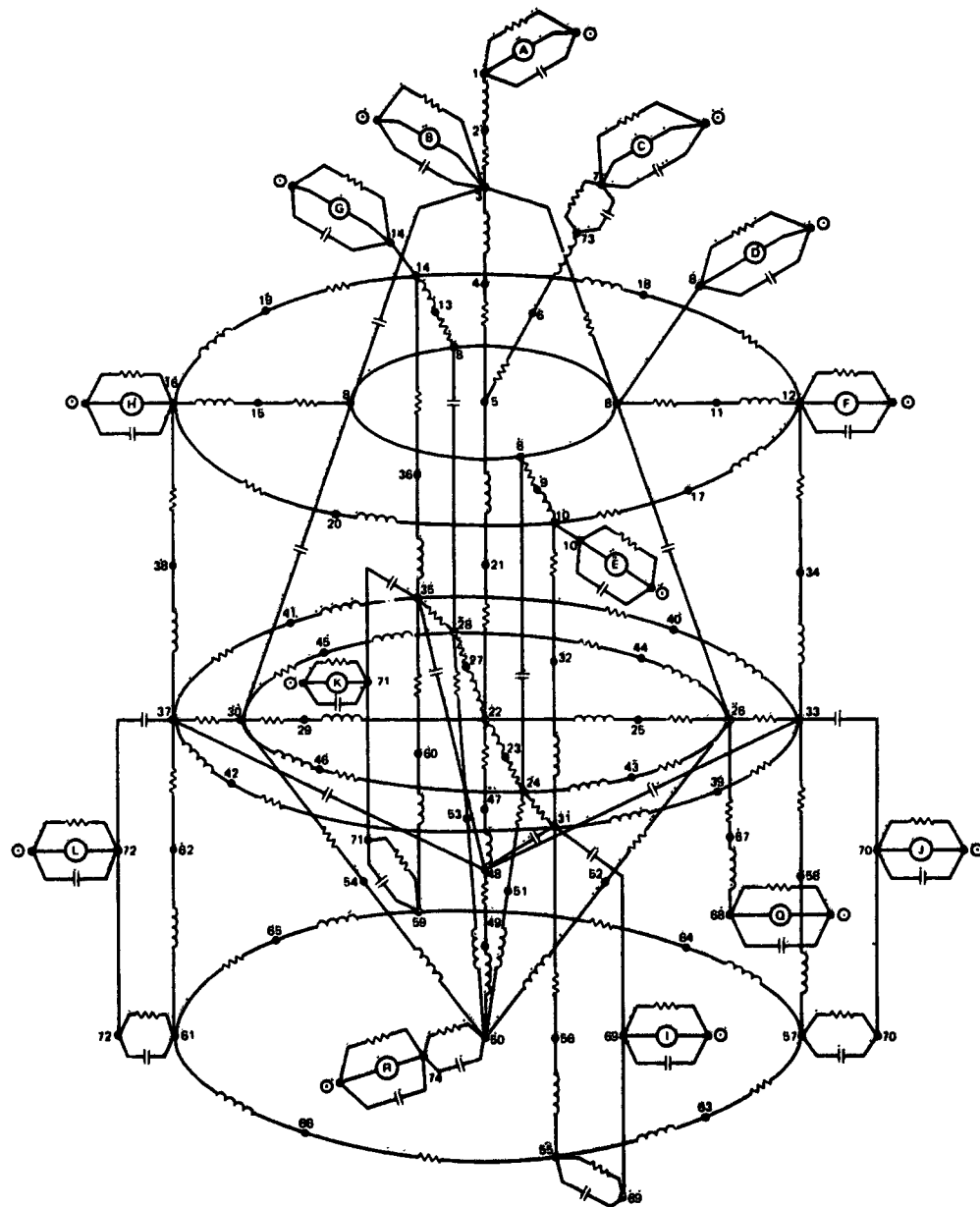


Figure 2. Pioneer Venus Electrical Model

ORIGINAL PAGE IS  
OF POOR QUALITY

KEY TO FIGURE 2

NODE	LOCATION	NODE	LOCATION
0 (ZERO)	GROUND		
1	FORWARD (OMNI) TOP OF MAST		
2	OMNI ANTENNA SUPPORT		
3	ANTENNA SUPPORT MAST		
4	SUPPORT MAST		
5	MAST/RAPTA INTERFACE		
6	ANTENNA FEED SUPPORT		
7	ANTENNA FEED		
8			
9, 11, 13, 15	FORWARD THERMAL BLANKET	31, 32, 33, 34	MESH/SUBSTRATE UPPER SECTION (LONGITUDINAL)
10, 12, 14, 16	FORWARD THERMAL BLANKET	35, 36, 37, 38	AND SOLAR ARRAY INTERFACE
17, 18, 19, 20	MESH/SUBSTRATE UPPER SECTION (RADIAL)	39, 40, 41, 42	SOLAR ARRAY TOP (CIRCUMFERENTIAL)
21	RAPTA	43, 44, 45, 46	EQUIPMENT SHELF (CIRCUMFERENTIAL)
22	RAPTA/EQUIPMENT SHELF/THRUST CONE INTERFACE	47, 48	THRUST CONE (UPPER)
23, 24, 25, 26	EQUIPMENT SHELF (RADIAL)	49, 50	THRUST CONE (LOWER)
27, 28, 29, 30		51, 52, 53, 54	EQUIPMENT SHELF SUPPORT STRUTS
		55, 56, 57, 58	SOLAR ARRAY (LONGITUDINAL)
		59, 60, 61, 62	
		63, 64, 65, 66	SOLAR ARRAY BOTTOM (CIRCUMFERENTIAL)
		67	AFT OMNI SUPPORT
		68	AFT OMNI
		69, 70, 71, 72	SOLAR ARRAY COVERGLASS
		73	ANTENNA FEED TOP
		74	AFT FACING SIDE

### 3.6 Antenna Feed Strut and Cap (Series 60)

The antenna feed structures were modeled as an inductor and resistor with a node at the feed. The capacitances to the feed cap and to infinity were included.

### 3.7 Solar Array and Substrate (Series 70)

The solar panel enclosure was modeled as an oblate spheroid in order to calculate a representative capacitance to infinity. It was then divided into quadrants and longitudinal and circumferential inductances calculated from the formulas for a lossless transmission line. Associated resistances were also apportioned. Capacitances were calculated between important elements within the solar array and to the thrust cone.

### 3.8 Substrate Extension and Mesh Wrap (Series 80)

Capacitances and inductances were calculated in the same manner as those for the solar array. Resistances were apportioned among the quadrant members.

### 3.9 Forward Mesh and Thermal Blanket (Series 90)

Radial inductances and resistances were calculated for the quadrants of the forward barrier in the same manner as for the equipment shelf. The capacitance of the antenna dish to the equipment shelf is also included.

### 3.10 Aft Structure and Aft Omni (Series 100)

The aft omni support and omni antenna were modeled similar to the forward omni.

#### 4. ISPICE CALCULATION RESULTS

The results of the Table 3 currents used on the electrical model are presented in Table 8. In Regions I and II, the photocurrent was modeled as an offset sine function with the phase angle depending on the quadrant. For example, Source I has a phase of  $0^\circ$ , J has a phase of  $90^\circ$ , etc. The offset is chosen to make the photocurrent maximum at  $90^\circ$  and zero at  $270^\circ$ . This overestimates the photocurrent per spin cycle. A rectified sine curve would better approximate the photocurrent. In these regions, the effect of this pulsating current is seen as an ac voltage on the perimeter of the shelf. The magnitude of this voltage is shown in Regions I and II at the four shelf locations and for the exterior of the solar panel. The frequency for this oscillation is the reciprocal of the spacecraft spin period.

The only voltage to exceed 1 volt in Table 8 is that of the solar panel in Region II. Here we assume a fairly high photocurrent and a very low plasma temperature and density. The electron current is predominately a thermal current, the only current available to neutralize the photocurrent. Therefore, positive potentials are possible.

Table 8. ISPICE Calculations - 85 Percent Porosity

Node	ISPICE Run	Altitude (max)				
		200	350	700	1000	>1000 km
		V	IV	III	II	I
1	Omni antenna	-3.4	-11	-37	<1	24
3	Dish antenna	-1.9	-9.8	-37	<1	24
7	Antenna feed	-1.9	-9.5	-42	<1	21
8	Mesh	-1.9	-9.2	-37	<1	24
16	Solar panel extension	-1.9	-9.2	-37	<1	24 ± 0.04
22	Center of shelf	-1.9	-9.2	-37	<1	24
24	Shelf $0^\circ$	-1.9	-9.2	-37	<1	24
26	Shelf $90^\circ$	-1.9	-9.2	-37	<1 ± 4 μ	24 ± 0.04 μ
28	Shelf $180^\circ$	-1.9	-9.2	-37	<1	24
30	Shelf $270^\circ$	-1.9	-9.2	-37	<1	24
72	Solar panel	-1.9	-9.2	-41	2344*	21 ± 20
74	Aft cavity	-37	-78	-91	-92	-54
R40N1	Current through BAPTA, μA	-2.3	-17	-1.1	13.6	-7.8

\* ±2333 mV.

NOTE: All voltages in millivolts unless otherwise noted.

Doubling the current densities in Table 2 will at most double the negative voltages for each region. In Regions I and II, the photocurrent still dominates and the voltages remain about the same.

Increasing the conductive mesh area does not significantly change the potentials on the spacecraft. Table 9 shows a series of calculations in which the area of the conductive mesh is calculated, assuming 0 percent porosity instead of 85 percent porosity. Modeling of the plasma and the spacecraft in this way is a new art and there are many areas of uncertainty. In extending these calculations, the ISPICE<sup>8</sup> representation of nonlinear voltage controlled current sources for low temperature plasmas needs improvement, as does the representation of photocurrents on a spinning body. The effect of ram currents as a function of orbit position and orientation, and the investigation of sheath formation, plasma resistivity, and geometrical effects are also of interest.

Table 9. ISPICE Calculations - 0 Percent Porosity

Node	Altitude (max)	200	350	700	1000	>1000 km
	Region	V	IV	III	II	I
	ISPICE Run	PV6	PV5	PV4	PV3	PV2
1	Omni antenna	-3.4	-1.1	-40	<1	11
3	Dish antenna	-1.9	-9.8	-40	<1	11
7	Antenna feed	-1.9	-9.5	-42	<1	21
8	Mesh	-1.0	-9.2	-40	<1	10
16	Solar panel extension	-1.9	-9.2	-40	<1	10
22	Center of shelf	-1.9	-9.2	-40	<1	10
24	Shelf edge 0°	-1.9	-9.2	-40	<1	10
26	Shelf edge 90°	-1.9	-9.2	-40	<1 ±4μ	10 ±13μ
28	Shelf edge 180°	-1.9	-9.2	-40	<1	10
30	Shelf edge 270°	-1.9	-9.2	-40	<1	10
72	Solar panel	-1.9	-9.3	-40	2344*	21
74	Aft cavity	-37	-78	-91	-92	-64
R40N1	Current through BAPTA, μA	-2.4	-18	-0.5	13.6	33

\*±2333 mV.

NOTE: All voltages in millivolts unless otherwise noted.

## References

1. Cloutier, P. A., et al (1974) Planetary Space Science, 22:967-990.
2. Kumar, S., and Hunten, D. (1974) J. Geophys. Res. 79(No. 16):2529-2532.
3. Stewart, R. W. (1971) J. Atmos. Sci. 28:1069-10...
4. Whitten, R. C., and Collin, L. (1974) Rev. of Geophys. and Space Physics 12(No. 2):155-192.
5. Binder, D., Smith, E. C., and Holman, A. B. (1975) IEEE Transactions on Nuclear Science NS-222(No. 6):2675-2680.
6. Spitzer, L. Jr. (1962) Physics of Fully Ionized Gases, Interscience.
7. DEMP Analysis of HS-3XX Spacecraft (1974) Intelcom: Rad Tech, INTEL-RT 6045-004.
8. ISPICE Reference Guide (1974) National CSS, Inc., (Proprietary to NCSS, Inc).

**Contents**

1. Introduction	309
2. Features of Numerical Spacecraft - Charging Model	310
3. Conclusions	317
Acknowledgments	317
References	317

## 6. Numerical Simulation of Spacecraft Charging Phenomena

J.G. Laframboise and S.M.L. Prokopenko  
Physics Department  
York University  
Toronto, Canada

**Abstract**

A numerical simulation program is being constructed having the following features: (1) infinite circular cylindrical geometry with angle-dependence, (2) inclusion of incident particles, photoelectrons, secondary electrons, backscattered electrons, any gun emissions, and any internal current pathways including surface conductive layers, (3) "quasistatic time-dependent iteration", in which sheath potential changes during particle transit times are ignored, (4) use of approximate, locally-dependent space charge density expressions in solving Poisson's equation for sheath potentials, with use of numerical orbit-following to determine surface currents, (5) incident particle velocity distributions isotropic or beam-like, or some superposition of these. Rationales for each of these features are discussed.

**1. INTRODUCTION**

The asymmetry between sunlit and shaded areas of a synchronous spacecraft is a key feature of the differential spacecraft charging problem at synchronous altitude. A realistic numerical model for the plasma sheath surrounding a

asynchronous spacecraft must therefore be at least two-dimensional. The only existing two-dimensional simulation which is completely self-consistent is that of Soop,<sup>1</sup> who did a time-dependent treatment for a sphere, in which several thousand photoelectrons were followed numerically. Such time-dependent treatments have until now provided relatively low accuracy for a given computational expense, although there now exist improved interpolation techniques for deducing space charge and flux from a limited amount of orbit information, which may change this situation in the future.

Two other more simplified treatments are noteworthy. Schröder<sup>2</sup> assumed that photoelectron emission was spherically symmetric, and thereby obtained a self-consistent solution for a unipotential sphere, which showed the presence of potential minima due to photoelectron space charge in some circumstances. Lafon<sup>3</sup> assumed spherical or cylindrical symmetry for space charge due to ambient particles, and negligible perturbation of this symmetry by photoelectrons. He thus obtained radially symmetric self-consistent sheath potentials, but angle-dependent photoelectron density profiles, again for unipotential spheres and cylinders.

Here we describe a two-dimensional self-consistent simulation which avoids a completely time-dependent treatment, but instead is based on a "quasistatic time-dependent" iteration described in Section 2.2. Although results from three-dimensional simulations are likely to become available in the near future,<sup>4</sup> it is generally true that the simplest realistic simulations are advantageous in elucidating basic physical effects, whereas more complicated ones are most useful for quantitatively predicting detailed interactions.

## 2. FEATURES OF NUMERICAL SPACECRAFT - CHARGING MODEL

### 2.1 Infinite Circular Cylindrical Geometry with Angle-Dependence

This geometry implies the use of a polar coordinate grid for computations. Several reasons for such a choice, in preference to the more obvious spherical geometry, are:

(1) Although a spherical geometry, with rotational (azimuthal) symmetry about the spacecraft-sun axis, is two-dimensional in position space, it is three-dimensional in velocity space because particles with different azimuthal angular momenta must be treated separately.

(2) Many spacecraft are finite circular cylinders.

(3) In spherical geometry with azimuthal symmetry, focusing of particles onto the spacecraft-sun axis occurs in some models, leading to singularities in fluxes and densities along this axis. Such effects must be regarded as spurious since real spacecraft are unlikely to have the high degree of symmetry necessary to produce them.

(4) An infinite cylinder, having a surface sector with distinct properties, can be rotated with respect to the sunward direction to study the effects of such rotation. In a spherical geometry with azimuthal symmetry, the corresponding surface feature would be an annulus about the spacecraft-sun axis, and no such rotation would be possible without destroying azimuthal symmetry.

(5) One major feature of spherical as opposed to cylindrical geometry, that is, the more rapid decrease of potential with increasing radius, can be modeled in an approximate way by simply adding the appropriate fictitious contribution to  $\nabla^2\phi$  in Poisson's equation.

## 2.2 Physical Processes

The model is to include velocity distributions of: incident particles, photoelectrons, secondary electrons, backscattered electrons, and any gun emissions. Internal current pathways including surface conductive layers are also being included.

## 2.3 Quasistatic Time-Dependent Iteration

In this procedure, sheath potential changes during particle transit times are ignored. This leads to the following iteration scheme: An angle-dependent surface potential is chosen. Poisson's equation is then solved to provide a radius- and angle-dependent static sheath potential (see Section 2.4 below). Particle orbits are then followed numerically in this potential, yielding surface charging rate as a function of angle (orbit-following is, however, not used to provide space charge densities for Poisson's equation; see Section 2.4 below). These rates are then averaged over any conducting sector, and any currents transferred internally (including those through any surface conductive layers) are subtracted. The resulting net charging rates are then used to carry forward one time step, yielding new surface potentials. This process is then repeated until a steady-state condition results, or, in a situation in which external conditions vary with time, is repeated to follow such time-dependence.

The use of this procedure, as opposed to a completely time-dependent simulation, should produce important computational economies. Clearly one will lose information about very rapid transient phenomena with this approach. However, steady-state or slowly time-varying situations are of major importance. These include changes in the incident particle distributions, which are likely to have time scales of seconds or minutes.

## 2.4 Use of Approximate Space-Charge Density Expressions

At synchronous altitude, the Debye length  $\lambda_D$  for ambient particles is usually  $\geq 10$  m, so for satellites of ordinary size, effects of ambient space charge on sheath potentials will be relatively small. Any reasonably realistic approximation of this space charge can therefore be expected to produce only negligible errors in solving Poisson's equation for sheath potentials. Furthermore, large savings in computer time can be expected to result if one can avoid exact density calculations involving numerical orbit-following. In the present work, it is intended that a relatively small amount of orbit-following be done to calculate surface currents (Section 2.3).

A more significant space-charge effect near the spacecraft may be caused by emitted photoelectrons or secondary electrons,<sup>1, 2</sup> because of their relatively low velocities compared to ambient values. However, effects of these are likely to also be small enough that any reasonably realistic approximations for their densities will yield good accuracy.<sup>3</sup> Such approximations must ultimately be validated by comparison with a few carefully chosen exact calculations. It is advantageous if such approximations depend on local potential only (rather than potentials at many locations), together with a relatively small number of other parameters, such as spacecraft potentials and potential barrier heights and locations. Here we propose three types of space-charge density approximation, as follows.

### 2.4.1 APPROXIMATIONS FOR POTENTIAL WELLS WITHOUT OBSTACLES

Exact density expressions have been developed for collisionless, Maxwellian particles in the presence of obstacle-free potential wells of arbitrary shape by Laframboise and Parker.<sup>5</sup> The appropriate expression for our purposes is the result given by their Eq. (2) for three-dimensional wells. This is true even for an "infinite", that is, very long cylindrical spacecraft geometry, because of particle entry at the ends of such a geometry. For definiteness, we consider a negative well given by  $\phi(x, y, z) \leq 0$ , with  $\phi \rightarrow 0$  as  $x^2 + y^2 + z^2 \rightarrow \infty$ , where  $\phi$  is electric potential. If only ambient particles are considered, Poisson's equation is:

$$\nabla^2 \phi = \frac{e}{\epsilon_0} (N_e - N_i) \quad (1)$$

where  $e$  is magnitude of unit electron charge,  $\epsilon_0$  is permittivity of space, and  $N_e$ ,  $N_i$  are electron and ion number densities, respectively. Since positive ions are the attracted species in this well, we use Eq. (2) of Laframboise and Parker<sup>5</sup> for ion density, and the usual Boltzmann factor for electron density. If  $\lambda_{De} = (\epsilon_0 kT_e / e^2 N_\infty)^{1/2}$ ,  $N_\infty$  is electron or ion density far from the spacecraft,

$L$  is a characteristic spacecraft length,  $\tilde{\nabla} = L\nabla$ ,  $\chi = e\phi/kT_e < 0$ ,  $k$  is Boltzmann's constant and  $T$  is temperature, Eq. (1) becomes:

$$\tilde{\nabla}^2 \chi = \left(\frac{L}{\lambda_{De}}\right)^2 \left\{ e^\chi - \frac{2}{\sqrt{\pi}} \left[ (-\chi T_e/T_i)^{1/2} + g(-\chi T_e/T_i)^{1/2} \right] \right\} \quad (2)$$

where  $g(s) = \frac{1}{2} \sqrt{\pi} \exp(s^2) \operatorname{erfc}(s) = \exp(s^2) \int_s^\infty \exp(-t^2) dt$ .

The important feature of Eq. (2) for our purposes is that its right-hand side is a function of  $\chi$  only. For small  $\chi$ , Eq. (2) reduces to:

$$\tilde{\nabla}^2 \chi = (1 + T_e/T_i) (L/\lambda_{De})^2 \chi \quad (3)$$

where terms of order  $\chi^{3/2}$  and higher have been ignored. The linear form of (3) permits the use of direct Poisson-solvers for finding  $\chi$ . Another simplified form can be obtained by rederiving Eq. (2) with monoenergetic instead of Maxwellian ions assumed. The appropriate monoenergetic velocity distribution (Chen;<sup>6</sup> Laframboise,<sup>7</sup> p. 14) is:

$$f \equiv \frac{d^3 N}{d^3 v} = \frac{m_i^2 N_\infty}{4\pi} \frac{\delta(E - E_1)}{(2m_i E_1)^{1/2}} \quad (4)$$

where  $E_1 = 4kT_i/\pi$  and  $m_i$  is ion mass; this distribution duplicates the ambient number density and flux values of a Maxwellian at temperature  $T_i$ . Rederivation of (2) using this distribution yields the computationally simpler form:

$$\tilde{\nabla}^2 \chi = \left(\frac{L}{\lambda_{De}}\right)^2 \left[ e^\chi - \left(1 - \frac{\pi}{4} \frac{T_e}{T_i} \chi\right)^{1/2} \right]. \quad (5)$$

If any regions exist where  $\chi > 0$ , the roles of ions and electrons are interchanged, and Eqs. (2)-(5) must be modified accordingly.

The essential approximation contained in Eqs. (2) - (5) is the neglect of orbit depletion due to intersection with the spacecraft. The densities of ambient ions and electrons will therefore both be overestimated near the spacecraft in these results. As long as the spacecraft is at least moderately smaller than  $\lambda_{De}$ , the effects of this overestimate will be small. The attracted-species density will be overestimated by the greater amount for reasons involving the curvatures of attracted and repelled particle orbits. The sheath profiles predicted by (2) or (5) will therefore be steeper than real profiles, if electron emission effects are ignored.

#### 2.4.2 APPROXIMATIONS BASED ON SYMMETRIC POTENTIALS

Laframboise,<sup>7</sup> and Laframboise and Godard,<sup>8</sup> Eqs. (7) and (8), have presented expressions for number densities of ambient attracted and repelled Maxwellian particles, respectively, which are exact for radially symmetric monotonic potentials near a perfectly absorbing spherical collector. These expressions contain terms identical to the ion and electron density expressions in (2), together with subtractive terms representing the effects of particle interception by the collector. Whipple<sup>9</sup> has used a thick-sheath approximation to develop density expressions for both ambient and emitted particles in the presence of a potential barrier, again for spherical symmetry. Lafon<sup>3</sup> has developed approximate density expressions for escaping photoelectrons, based on assumed spherical or cylindrical symmetry in the sheath potential, but not in the photoemission fluxes. Since all of these expressions depend only on local potential and a small number of other parameters, it is tempting to explore the possibility of using them even in the presence of sheath potentials which are known to be angle-dependent, and near spacecraft having non-spherical shapes. All of these expressions depend essentially on the solid angles subtended at any given radius, by orbits which have intersected the spacecraft, for all significantly populated particle energies, including<sup>7, 8, 9</sup> the effects of orbit curvature due to electric fields. It is likely that in many cases, such solid angles will not be greatly modified by angular asymmetries in sheath potentials (from symmetry, such modification must be of second order in angular variations). In using such approximations with irregular spacecraft shapes, it would be necessary to define some way of choosing "radius" for substitution into them. One way to do this would involve matching the solid angle subtended by the spacecraft at the location in question, with that subtended by a sphere as a function of radius. Similar procedures would be necessary for dealing with parameters describing potential barriers in these expressions. Lafon<sup>10, 11</sup> and Parker<sup>12</sup> have given useful general discussions of the formulation of density expressions for symmetric potentials.

#### 2.4.3 APPROXIMATIONS BASED ON EQUIVALENT POTENTIAL WELLS

We consider the idealized situation shown in Figure 1, in which a spacecraft is assumed to have shaded-side surface potentials which are very negative, and sunlit-side surface potentials which are close to space potential. The solid curves outside the spacecraft represent equipotentials. The dotted curve FGH represents a surface which passes through the saddle point G on the sunlit side, and is everywhere perpendicular to the equipotentials, so this surface represents the maximum extent of a sunlit-side potential barrier for electrons. Fahleson<sup>13</sup> has pointed out that such a barrier may exist even when space charge is negligible, because of the

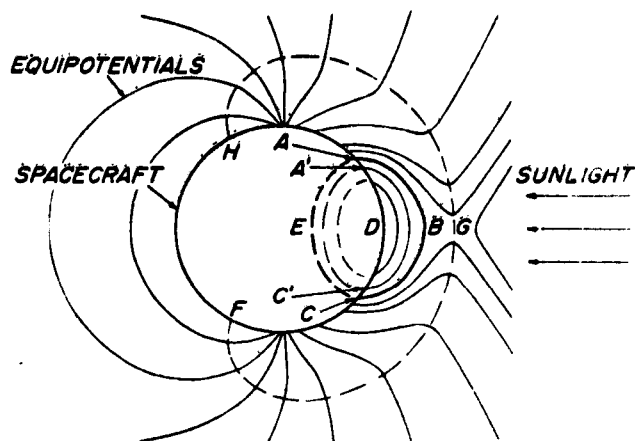


Figure 1. General Appearance of a Possible Sheath Potential Profile around a Spacecraft. Dotted curves inside the spacecraft surface are fictitious extensions of equipotential surfaces outside, as described following Eq. (6)

sunlit-shaded asymmetry in surface potentials. We consider as an example the process of approximately calculating photoelectron space charge density inside this barrier; calculation of secondary electron charge density is similar in most respects. We consider all those photoelectrons emitted with a total energy  $E_B$  equal (within some differential amount  $dE$ ) to the potential of the equipotential surface ABC. Such particles can never go outside ABC, but must reimpinge on the spacecraft surface ADC. If  $\xi_p(E)$  is the photoemission coefficient, that is, the energy-differential particle current density of photoemission from the spacecraft surface (this will depend on surface material and solar illumination angle), then the total photoemission particle current between energies  $E_B$  and  $E_B + dE$  is:

$$I_p = dE \iint d^2 S \xi_p [E_B + e\phi_S, S] \quad (6)$$

where  $E_B + e\phi_S \geq 0$ ,  $S$  represents surface position,  $\phi_S = \phi(r_S)$  is surface potential,  $E_B + e\phi_A = E_B + e\phi_C = 0$ , and the integration is over the surface ADC. Since  $\xi_p$  for most materials is largest for emission kinetic energies  $\frac{1}{2} m_e v^2 = E_B + e\phi_S \approx 1$  volt, most of the photoemission between energies  $E_B$  and  $E_B + dE$  will tend to come from regions such as, say, A' and C' in Figure 1, where  $\phi_S$  is about 1 volt more positive than at A and C. On the other hand, particle motions will tend to spread the reimpingement current more uniformly over ADC.

We now model this process approximately by mentally removing the spacecraft surface between A and C, and replacing it by an arbitrary extension AEC of the equipotential surface ABC. We also do the same for other equipotentials which lie inside this one, as also shown in Figure 1. We have now "constructed" an obstacle-free potential well, and we can use the Laframboise-Parker<sup>5</sup> theory to derive model density and flux profiles for such a well. We can then integrate the latter over ADC and match the result with Eq. (6). We rewrite the monoenergetic distribution (4) for electrons as follows:

$$f = \frac{m_e^2 N^*}{4\pi} \frac{\delta(E - E_B)}{(2m_e E_B)^{1/2}} \quad (7)$$

where  $N^*$  is now a reference number density to be evaluated. We obtain:

$$N \equiv N[\phi(\underline{r})] = \int f d^3 \underline{v} = N^* [1 + e\phi(\underline{r})/E_B]^{1/2} H[e\phi(\underline{r}) + E_B] \quad (8)$$

$$J \equiv J[\phi(\underline{r})] = \int f v_{\perp} d^3 \underline{v} = N^* (E_B/8m_e)^{1/2} [1 + e\phi(\underline{r})/E_B] H[e\phi(\underline{r}) + E_B] \quad (9)$$

where  $J$  is a number flux crossing an arbitrarily oriented surface element from either direction,  $v_{\perp}$  is velocity component perpendicular to such a surface element, and  $H(s) = \int_{-\infty}^s \delta(x) dx$  is the Heaviside step function. The total number flux crossing ADC from either direction is now given for our model well by:

$$I_w = \iint J(\phi_S) d^2 S \quad (10)$$

Our procedure for approximating the space charge density now involves performing the integrations over the surface ADC in both (6) and (10), then evaluating  $N^*$  by equating these two results. This is done for each of the discrete energies  $E_{Bj}$  which are chosen to represent the photoemission. The quantity  $dE$  in (6) must then be chosen equal to the separation between these energies. The resulting set of values  $N_j^*$  is then used together with (8) to construct the space-charge density expression:

$$N[\phi(\underline{r})] = \sum_j N_j^* [1 + e\phi(\underline{r})/E_{Bj}]^{1/2} H[e\phi(\underline{r}) + E_{Bj}] \quad (11)$$

This expression also has the advantage of dependence only on local potential, as do those derived in Sections 2.4.1 and 2.4.2. In using it, one would precalculate the coefficients  $N_j^*$  as described above, then use (11) as a contribution to

the space charge density in Poisson's equation. An important approximation contained in (11) involves neglect of the fact that photoemission fluxes given by (10) are in general distributed differently over ADC than those given by (6). For energies  $E_j > -e\phi_G > 0$ , where  $\phi_G$  is the saddle-point potential in Figure 1, some photoelectrons would escape, and the corresponding terms in (11) would be over-estimates.

### 2.5 Use of Isotropic or Beam-Like Incident Velocity Distributions

Important computational economies clearly result from assuming that incident velocity distributions are either isotropic or beam-like (monokinetic); the approximate density expressions described in Section 2.4 are examples of results for isotropic distributions. Any incident distribution may be modeled as closely as desired by a superposition of isotropic and beam-like distributions.

## 3. CONCLUSIONS

We have described the major features of a "quasistatic time-dependent" numerical simulation of differential spacecraft charging at synchronous altitude, incorporating an infinite cylindrical geometry with angle-dependence. The computer program involved is presently under construction.

## Acknowledgments

We are indebted to L. W. Parker for valuable discussions. This work was supported by the U. S. Air Force Office of Scientific Research under grant number AFOSR-76-2962.

## References

1. Soop, M. (1972) Report on photo-sheath calculation for the satellite GEOS, Planet. Space Sci. 20:859-870.
2. Schröder, H. (1973) Spherically symmetric model of the photoelectron sheath for moderately large plasma Debye lengths. In: Photon and Particle Interactions with Surfaces in Space, R. J. L. Gard, Editor, D. Riedel Pub. Co., Dordrecht, Holland.

3. Lafon, J.-P. J. (1976) On the sheath surrounding a conductor emitting photoelectrons in an isotropic collisionless plasma, Radio Science 11:483-493.
4. Katz, I., Parks, D. E., Wilson, A. (1976) Dynamic modeling of spacecraft in a collisionless plasma, Paper II-7, USAF-NASA Spacecraft Charging Technology Conference, Colorado Springs.
5. Laframboise, J. G., and Parker, L. W. (1973) Probe design for orbit-limited current collection, Phys. Fluids 16:629-636.
6. Chen, F. F. (1965) Numerical computations for ion probe characteristics in a collisionless plasma, Plasma Phys. (J. Nucl. Ener. Part C) 7:47-68.
7. Laframboise, J. G. (1966) Theory of spherical and cylindrical Langmuir probes in a collisionless, Maxwellian plasma at rest, Univ. of Toronto, Institute for Aerospace Studies, Rep. 100.
8. Laframboise, J. G., and Godard, R. (1974) Perturbation of an electrostatic probe by a spacecraft at small speed ratios, Planet. Space Sci. 22:1145-1155.
9. Whipple, E. C., Jr. (1976) Theory of the spherically symmetric photoelectron sheath: a thick sheath approximation and comparison with the ATS 6 observation of a potential barrier, J. Geophys. Res. 81:601-607.
10. Lafon, J. -P. J. (1973) On the perturbation of a plasma and particle collection by a cylinder in a magnetic field, J. Plasma Phys. 10:383-396.
11. Lafon, J. -P. J. (1975) On the behavior of a metallic body in an isotropic collisionless plasma I: General remarks, Plasma Phys. 17:731-740.
12. Parker, L. W. (1975) Computer Method for Satellite Plasma Sheath in Steady-State Spherical Symmetry, AFCRL-TR-75-0410, Final Report, Contract F19628-75-C-0182, Lee W. Parker, Inc.
13. Pahlson, U. (1973) Plasma-vehicle interactions in space: Some aspects of present knowledge and future development, In: Photon and Particle Interactions with Surfaces in Space, R.J.L. Grad, Editor, D. Riedel Pub. Co., Dordrecht, Holland.

Contents	
1. Introduction	319
2. Theory	319
3. Numerical Techniques	324
4. Sample Calculations	326
5. Conclusions	329
Acknowledgments	330
References	330

## 7. Dynamic Modeling of Spacecraft in a Collisionless Plasma

Ira Katz, Donald E. Parks, Sang Wang, and Andrew Wilson  
Plasma Physics Group  
Systems, Science and Software  
La Jolla, California

### 1. INTRODUCTION

Environmental charging of geosynchronous spacecraft to potentials of thousands of volts has been experimentally observed. Previous attempts to model spacecraft charging have employed techniques which are limited to simplified geometries and symmetry assumptions. In this paper, we describe a new computational model which can simulate the charging of complex geometrical objects in three dimensions. We present two sample calculations. In the first problem, the capacitance to infinity of a complex object similar to a satellite with solar array paddles is calculated. The second problem concerns the dynamical charging of a conducting cube partially covered with a thin dielectric film. In this calculation, the photoemission results in differential charging of the object.

### 2. THEORY

The interaction of a satellite and the magnetosphere can be separated into two parts. The first is the particle deposition, charge transport, and electrical

properties associated with charged particles impinging upon the satellite. The second part is the self-consistent ambient and photo-plasma interactions with the electric field. The field must satisfy boundary conditions on the satellite consistent with the charge deposited on the satellite. To solve both parts of this problem completely and self-consistently for general, ambient plasmas is a formidable task. Here, we shall be concerned only with a limited (albeit very important) range of plasma environments (a hot magnetosphere). As a result, certain approximations reduce the magnitude of the problem.

The timescales of phenomena which occur on a spacecraft in the magnetosphere range from nanoseconds to hours (Table 1). The lower end of this range is associated with effects such as the discharging of electrical circuit elements and electromagnetic wave phenomena. At the upper end of the range, slow variations in the magnetospheric environment are important. In this paper, we shall be concerned with the intermediate timescale range, from milliseconds to seconds. This range is determined by the charging time of the surface of a spacecraft by magnetospheric electron currents.

Table 1. Characteristic Times for Charged Spacecraft in the Magnetosphere

Phenomenon	Time
Breakdown in circuit elements	$\tau_B \sim 10^{-9} - 10^{-8}$ sec
Charging of bare conducting surface	$\tau_C \sim 10^{-3}$ sec
Differential charging of thin dielectric overlying conductor	$\tau_D \sim 1$ sec
Charge redistribution in a dielectric	$\tau_{RD} \gtrsim 100$ sec
Change in environmental conditions	$\tau_E \gtrsim 1$ to $\sim 10^3$ sec

Before entering upon the analysis of these phenomena, it is useful to set the scale of the various processes involved. These are listed in Table 2, and, in each case, the treatments which must be applied to describe the relevant field and particle phenomena are indicated. In the magnetosphere, the plasma sheath surrounding a spacecraft requires a particle description. This is necessary on account of the very long mean free paths and long Debye lengths  $\lambda_D$  which occur in these hot, diffuse plasmas. Electromagnetic treatments are needed only for describing effects such as transient surface current phenomena resulting from arcing excitations. Particle dynamics must be followed if sheath plasma

Table 2. Collisionless Satellite-Plasma Sheath Models. L is the Spacecraft Size,  $\omega_p$  is the Plasma Frequency and  $\lambda_D$  is the Debye Length

Model	Fields	Particle Treatment	Timescale
1. Electromagnetic	Maxwell's equations	Dynamic	$L/c$ $\sim 10^{-9}$ sec
2. Quasistatic	Poisson's equations ( $L \ll c\omega_p^{-1}$ )	Dynamic	$\omega_p^{-1}$ $\sim 10^{-5}$ sec
3. Equilibrium	(a) Poisson ( $\lambda_D \sim L$ ) (b) Laplace ( $\lambda_D \gg L$ )	Static	$\tau_c < t < \tau_D$ $> 10^{-3}$ sec

oscillatory behavior is important.<sup>1,2</sup> On a longer timescale, the plasma is characterized by an equilibrium-particle distribution.<sup>3,4</sup> This is the range which is considered here. Finally, at the longest timescale, the behavior is determined by changes in the environment or redistribution of charges within dielectrics.

We shall now describe the considerations underlying our analysis of the intermediate timescale phenomena. Let us consider a spacecraft with a spherical conducting surface. With a radius R (cm) and a charging current density j (A/cm<sup>2</sup>), the time taken to charge the spacecraft to a potential V is

$$\tau_c = \frac{C_\infty V}{4\pi R^2 j}$$

where  $C_\infty$  is the capacitance of the spacecraft with respect to infinity, and is given by

$$C_\infty = R \text{ esu} \\ \approx 10^{-12} R \text{ F}$$

With the following values

$$R = 100 \text{ cm} \\ V = 10^3 \text{ V} \\ j = 0.5 \times 10^{-9} \text{ A/cm}^2$$

the charging time is

$$\begin{aligned}\tau_c &\approx \frac{10^{-12} \text{ V}}{4\pi R j} \\ &\approx 2 \times 10^{-3} \text{ sec} .\end{aligned}$$

However, on most spacecraft, large areas are not bare conductors, but are covered by thin, insulating dielectrics overlying conducting substrates. In these cases, the capacitance of the dielectric,  $C_D$ , is important, rather than the capacitance with respect to infinity. The dielectric capacitance is

$$\begin{aligned}C_D &\approx \frac{1}{4\pi d} \text{ esu/cm}^2 \\ &\sim \frac{10^{-12}}{4\pi d} \text{ F/cm}^2 .\end{aligned}$$

With a thickness of 40 mil ( $d \sim 0.1 \text{ cm}$ ), the charging time  $\tau_D$  is now

$$\begin{aligned}\tau_D &\sim \frac{10^{-12} \text{ V}}{4\pi d j} \sim \frac{10^{-9}}{1.2 \times 0.5 \times 10^{-9}} \\ &\sim 1.6 \text{ sec} .\end{aligned}$$

The voltage buildup between a conductor and a dielectric insulator thus occurs very much more slowly than the buildup on a bare conductor. As a result, differential charging of a spacecraft takes place on a timescale longer than charging. Later, we shall describe the development of such a phenomenon over the time-scale range  $\tau_C < t \lesssim \tau_D$ .

Under the conditions found in magnetospheric substorms, essential simplifications can be made in the modeling of the charging. In particular, we demonstrate below for hot, low density plasmas where

$$\lambda_D \gg L,$$

$\lambda_D$  is the Debye length and  $L$  a characteristic object dimension, that if surface potentials on the satellite are of the order of the plasma temperature, one makes only a very small error by neglecting the ambient space charge density in Poisson's equation. This approximation, when justified, greatly reduces the amount of computation necessary to determine satellite potentials.

Let us examine the effect of a large ambient charge density fluctuation in a  $\theta = 10$  keV,  $n_e = 10 \text{ cm}^{-3}$  magnetospheric plasma. The Debye length of such a plasma is given by

$$\lambda_D \approx 743 \sqrt{\frac{\theta}{n_e}} \approx 2 \times 10^4 \text{ cm} \\ = 200 \text{ m.}$$

It has been shown<sup>5</sup> that in equilibrium plasmas, maximum charge variations are of order of the ambient charge density. It follows then that the magnitude of a potential associated with a spherical charge density fluctuation of 1 m in radius is at most

$$\phi \sim \frac{q}{4\pi\epsilon_0} = \frac{4}{3}\pi r^2 n_e e \text{ esu} \\ = \frac{4}{3}\pi \cdot 10^4 \times 10 \times 4.8 \times 10^{-10} \\ \sim 2 \times 10^{-4} \text{ statvolts} \\ \sim 6 \times 10^{-2} \text{ volts}$$

which is several orders of magnitude less than the satellite surface potentials.

Another useful quantity to examine is the relative amount of charge on a sphere of a meter radius charged up to the ambient temperature to the amount of space charge such a volume would contain. The surface charge on a sphere of radius  $r$  is

$$q_{\text{surface}} = r\phi \approx \frac{r\theta}{e} .$$

The space charge in such a plasma is

$$q_{\text{plasma}} = \frac{4}{3}\pi r^3 n_e e .$$

The ratio of these two charges is

$$\frac{q_{\text{plasma}}}{q_{\text{surface}}} = \frac{4}{3}\pi r^2 n_e \frac{e^2}{\theta} = \frac{1}{3} \left( \frac{r}{\lambda_D} \right)^2 \\ < 10^{-5} .$$

Thus, we have strong reasons to believe that the gross potential features surrounding an object whose dimensions are much smaller than a Debye length and whose surface potentials are comparable to the plasma temperature can be calculated ignoring ambient (as distinct from photosheath) space charge effects.

### 3. NUMERICAL TECHNIQUES

The dynamical model consists of two parts, namely: (1) the calculation of surface charge densities and net charging currents, given a potential distribution, and (2) the calculation of the potential subject to free space and appropriate satellite boundary conditions. Brief descriptions of the techniques used are given below. Further details will be presented at a later date.

#### 3.1 Surface Charging Calculation

We require the incident and outgoing currents  $\vec{j}_{in}$ ,  $\vec{j}_{out}$ , respectively at surface points  $\vec{r} = \vec{r}_0$ . The net charging current is then

$$\vec{j}_{net}(\vec{r}_0) = \vec{j}_{in}(\vec{r}_0) - \vec{j}_{out}(\vec{r}_0)$$

where

$$\vec{j}_{in}(\vec{r}_0) = \int d^3 v_0 \vec{v}_0 f_{in}(\vec{v}_0, \vec{r}_0)$$

$$\vec{j}_{out}(\vec{r}_0) = \int d^3 v_0 \vec{v}_0 f_{out}(\vec{v}_0, \vec{r}_0)$$

The distribution  $f_{out}$  is assumed known at the surface  $\vec{r} = \vec{r}_0$  and  $f_{in}$  is known at positions far away from the spacecraft. Since we are looking for equilibrium solutions of Vlasov's equation, the distribution functions satisfy

$$\frac{df}{dt} = 0$$

along particle trajectories. The object then is to calculate the trajectories of a selection of particles. Since we know the distribution function  $f$  far from the satellite, automatically we know the distribution, since  $f$  is constant along a given trajectory.

The Parker-Whipple<sup>6</sup> inside-out scheme makes use of this fact. Trajectories are initiated at the spacecraft surface and are traced backwards through the potential field to distant points where the distribution,  $f(\vec{v})$  is known. One advantage

of this scheme is that orbits which do not have an endpoint on the spacecraft surface are avoided. The neglect of such orbits is strictly valid only if the volume spacecharge has no influence on the particle trajectories.

It should be emphasized that the machinery is contained in our numerical technique for calculating ambient charge densities by constructing distribution functions,  $f$ , in each spatial zone and taking its zeroth moment (as opposed to  $j$ , which is a first moment)

$$\rho = \int f d\vec{v}$$

However, presently, we do not calculate this term, based upon the arguments presented in Section 2.

### 3.2 Potential Calculation

In calculating the potential in three dimensions around an arbitrary object, a gridded method must be employed since the specification of the surface is far too general for analytical or multipole techniques. Since satellites are the order of meters in length, we need at least 10 cm resolution as an upper bound in the vicinity of the spacecraft. However, for determining particle orbits, the fields hundreds of meters away must also be known. In order to keep storage down to a reasonable level, some type of variable gridding must be employed. This precludes the use of any straightforward Fourier transform technique. One technique for achieving high resolution in the region around the object and still being able to handle vast quantities of space is through local mesh refinement. Finite difference approaches, however, have difficulty in mesh transition regions, especially when grid lines are terminated, and generally lose an order of accuracy in such regions.

As a result of this, we decided upon a finite element approach using right parallelepiped elements and blended linear univariate edge interpolants. This permits the same degree of accuracy over the entire mesh, even though the mesh elements differ in size. It results in the standard trilinear interpolation scheme for each element.

The fundamental approach is to solve Poisson's equation

$$\nabla^2 \phi = -4\pi\rho \tag{1}$$

by solving the associated variational principle

$$0 = \frac{\delta}{\delta\phi} \left\{ \int dV [(\nabla\phi)^2 + 4\pi\rho\phi] + \int d\vec{S} \cdot (4\pi\vec{\sigma} + \nabla\phi)\phi \right\} \tag{2}$$

The first term in the integrand corresponds to the Laplacian operator. The second term is the volume spacecharge contribution. The remaining terms are surface contributions, referring to the surface charge and electric field, respectively.

In the variational calculation, we use locally defined basis sets, that is, trilinear interpolants within each cube-like element. Since the finite element equations are derived from Eq. (2), different mesh volumes automatically receive the correct variational weight. This ensures the maintenance of accuracy through mesh transition regions. The problem of local mesh refinement is approached by having grids within grids, that is, a chinese doll-like hierarchy of grids shown schematically in Figure 1. The theory of this technique is discussed in Birkhoff et al,<sup>7</sup> and Cavendish.<sup>8</sup> In order to have high computation speed, the linear equations resulting from the variational principle (Eq. (2)) in the interface region were coded up explicitly in a series of thirteen subroutines. These same routines are used for interfacing any pair of the meshes.

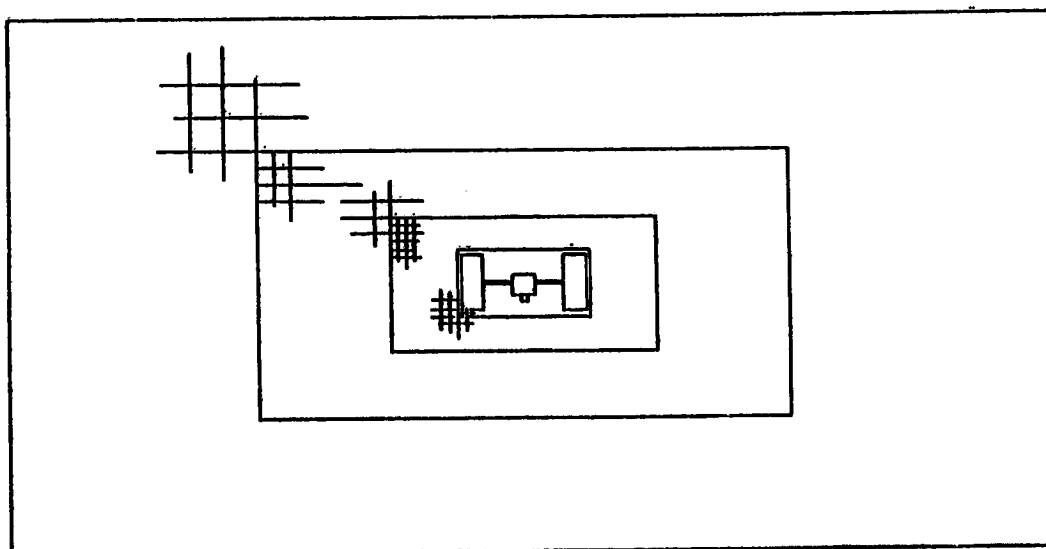


Figure 1. Cross-Section of Grid, Showing First Four Embedded Meshes

#### 4. SAMPLE CALCULATIONS

To demonstrate the capabilities of our 3D model, we have performed two sample calculations. First, we calculated the capacitance, surface charge distribution and electric fields around a geometrically complex, conducting satellite-like object. The object is shown in Figure 2, and the problem was gridded as

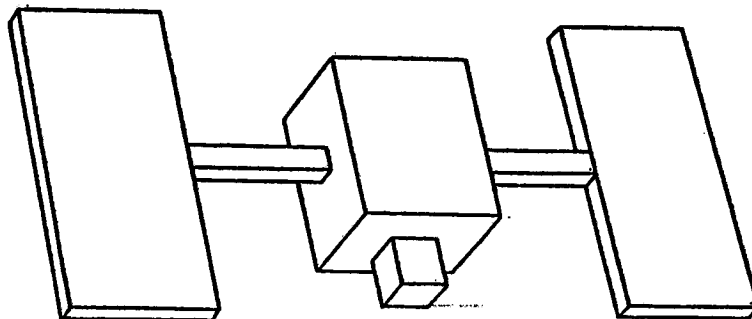


Figure 2. 3-D Model Spacecraft for Capacitance Calculation

shown in Figure 1. While it is electrically simple, being an equipotential surface, it has sufficient geometrical complexity to demonstrate some of the features of our TRILIN model. The overall length of the object is 6 m, with 20 cm resolution on the surface. The outermost grid is 51 m long, and there are about 30,000 variables in the problem. The outermost mesh had monopole ( $\phi = \frac{q}{r}$ ) boundary conditions imposed. Using an SOR routine, this problem took less than 4 min to solve on the CDC 7600 at Kirtland Air Force Base.

The capacitance calculated for this object is 83 pF. The surface area of the object is almost four times as great as that of a sphere of equivalent capacitance ( $r = 75$  cm). If placed in an environment with a charging current of  $10^{-9}$  A/cm<sup>2</sup>, this satellite-like object would charge to 10 keV in about 3 msec. The charge distribution is nonuniform, as expected, with most of the charge on the panels which have only 58 percent of the surface area. With the satellite charged to 10 kV, the total charge on the surface is approximately 2500 esu ( $\sim 0.9$   $\mu$ C). The average normal electric fields on each panel in such a problem is  $\sim 37.5$  V/cm while, on the body, it ranges from 20 V/cm to  $\sim 40$  V/cm.

The second sample calculation is of a simpler geometry, but has considerable physical complexity. The object consists of a conducting cube, 60 cm on an edge, partially covered with a 1 mm insulation skin of dielectric constant unity. Figure 3 shows a picture of the object. The object is placed in a 10 keV,  $n_e = 10$  cm<sup>-3</sup> electron plasma with an assumed neutralizing background. By the backward trajectory technique described above, incident electron currents on the object are determined. Charge impinging upon the dielectric skin is assumed to stick while charge landing on the exposed conducting surfaces is allowed to distribute itself in order to maintain the conductor as an equipotential surface. The potential on dielectric surfaces is related to that on the conductor by the line integral of the electric field through the surface. To add asymmetry and cause differential charging, we assume a light source at some large distance along the

positive x-axis. This light gives rise to a photocurrent of  $4 \text{ nA/cm}^2$  which acts to discharge that surface.

Initially the potential on the surface of the satellite rises very quickly. This corresponds to surface charging on a timescale determined by the net capacitance to infinity. However, after about 50 msec, the differential charging of the conductor and the front and back dielectric surfaces dominate the calculation. The potential at three locations as a function of time is plotted in Figure 4. We notice how the surface dielectric continues to charge, albeit at

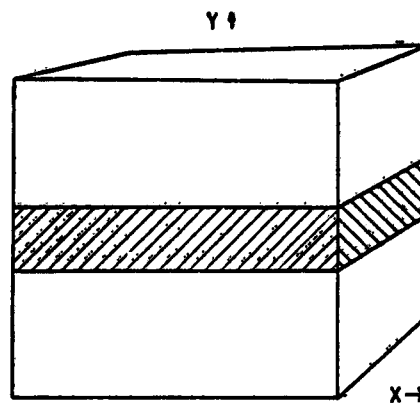


Figure 3. Spacecraft for Dynamical Calculation. Only dashed area is bare metal, the rest of the object is covered with a dielectric film

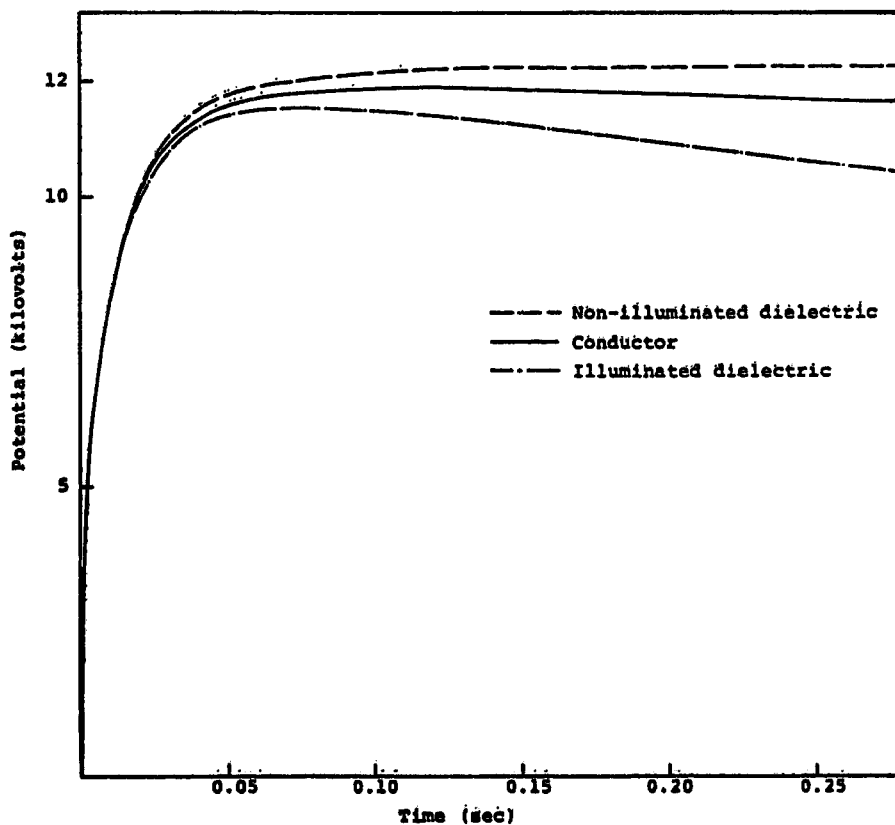


Figure 4. Comparison of Charge Buildup at Three Different Sections of Illuminated Spacecraft

a very slow rate, while the front surface dielectric discharges substantially. The conductor also discharged, but more slowly than the illuminated dielectric. Figure 5 shows a potential contour map through the x, y plane. We can see that the conductor is more than one thousand volts negative with respect to the front surface dielectric, while it is only a few hundred volts positive with respect to the rear surface dark dielectric. This implies that the conductor's surface charge under the illuminated dielectric is of negative sign while underneath the rear dielectric the conductor's surface charge is of positive sign. The potential difference between front and rear dielectrics is almost two kilovolts. Fields in the front dielectric are greater than  $10^4$  volts/cm.

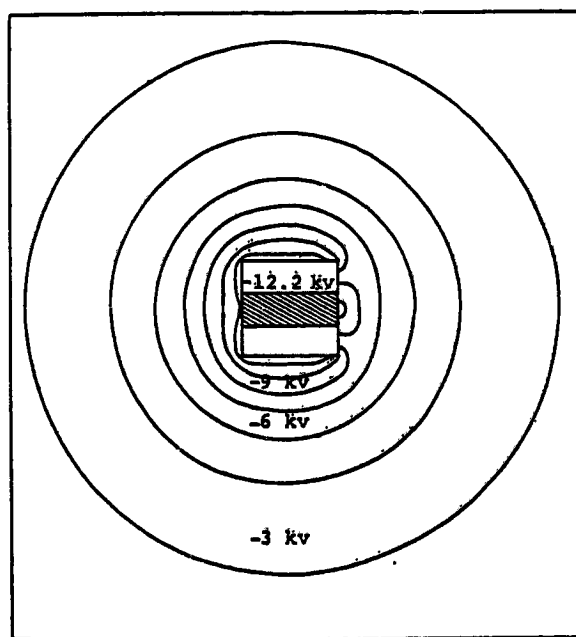


Figure 5. Potential Contour Plot Near the Spacecraft after 0.27 sec. Sunlight is incident from the right (x-direction)

## 5. CONCLUSIONS

The prediction of surface potentials on complex satellites is a formidable task. Material properties, geometrical effects, ambient plasma, and photosheath space charge all play roles in determining surface potential distributions.

However, for the range of plasma parameters frequently found in magnetospheric substorms, it is justifiable to neglect the self-consistent ambient plasma space charge. This assumption permits the calculation of potentials in asymmetric three-dimensional geometries. The resultant calculations demonstrate such effects as net object charging with respect to infinity, differential charging, and charge redistribution on conductors. These first calculations presented here employ large simplifications with respect to material properties, ion currents, etc. However, they show that the concept of three-dimensional spacecraft charging calculations is a practical one.

## Acknowledgments

This work was supported by the Defense Nuclear Agency under Contract DNA001-76-C-0121 and by the National Aeronautics and Space Administration under Contract NAS3-20119.

## References

1. Katz, I., Wilson, A., Parker, L. W., Rothwell, P. L., and Rubin, A. G. (1976) Static and dynamic behavior of spherical probe and satellite plasma sheaths, Conference on Nuclear and Space Radiation Effects, San Diego, July 1976 (to be published in IEEE Trans. on Nuclear Science, December, 1976).
2. Parks, D., Wilson, A., and Katz, I. (1976) Streaming instabilities in satellite plasma sheaths, Conference on Nuclear and Space Radiation Effects, San Diego, July 1976 (to be published in IEEE Trans. on Nuclear Science, December 1976).
3. Whipple, E. C., Jr. (1965) The Equilibrium Electric Potential of a Body in the Upper Atmosphere and in Interplanetary Space, NASA X-615-65-296, Goddard Space Flight Center, Greenbelt, Md.
4. Laframboise, J. G. (1966) UTIAS Report No. 100, University of Toronto, Canada.
5. Laframboise, J. G., and Parker, L. W. (1973) Phys. Fluids 16:629.
6. Parker, L. W. and Whipple, E. C., Jr. (1967) Ann. Phys. 44:126.
7. Birkhoff, G., Cavendish, J. C., and Gordon, W. J. (1974) Doc. Nat. Acad. Sci., USN 71:3423.
8. Cavendish, J. C. (1975) J. Comp. Phys. 19:211.

**Contents**

1. Introduction	332
2. The Inside-Out Method	341
3. The Poisson Problem: Poisson Difference Equations	348
4. Sample Results Applied to In-Situ Data	352
5. A Large-Body Problem	361
Acknowledgment	365
References	365

## 8. Calculation of Sheath and Wake Structure about a Pillbox-Shaped Spacecraft in a Flowing Plasma

Lee W. Parker  
Lee W. Parker, Inc.  
Concord, Mass.

### Abstract

This paper is concerned with a computer program used for studies of the disturbed zones around bodies in flowing plasmas, particularly spacecraft and their associated sheaths and wakes. The program solves a coupled Poisson-Vlasov system of nonlinear partial-differential-integral equations to obtain distributions of electric potential and ion and electron density about a finite-length cylinder in a plasma flow at arbitrary ion Mach numbers. Using the author's "inside-out method"<sup>6</sup> which follows ion and electron trajectories backward to their origin at the body surface or in the undisturbed plasma, together with a special iteration algorithm for self-consistency, the program takes into account the particle thermal motions with relatively few simplifying assumptions. The approach is applicable to a larger range of parameters than other available approaches. In sample calculations, bodies up to 100 Debye lengths in radius are treated, that is, larger than any previously treated realistically. Applications are made to in-situ satellite experiments.

## 1. INTRODUCTION

The problem of theoretically calculating the structure of the disturbed plasma (frequently referring to the wake and/or sheath) around a moving body in space involves the solution of a complicated system of coupled nonlinear partial differential/integral equations.<sup>1</sup> The equations consist of the Vlasov (collisionless Boltzmann) equations for the ions and electrons, and the Poisson equation relating the electric field to the distributions of ions and electrons. The difficulty is essentially a numerical one because analytic solutions are not possible (for cases of interest), and there is no unique approach. In cases of stationary bodies,<sup>2-5</sup> as well as moving bodies (theoretical references cited by Parker<sup>1</sup>), combinations of numerical techniques (finite differences, iteration, quadratures, etc.) are required for treating various parts of the problem. For either stationary or moving bodies, the choices of techniques and their use to achieve consistent solutions for any given set of physical parameters (defining body and plasma) have never been obvious. Innovations are frequently required. The purpose of this paper is to present a technique suitable for a pillbox-shaped body (with emphasis on the wake),<sup>1</sup> which appears to be reasonably successful over a large range of the physical parameters, and to present sample solutions including applications to in-situ spacecraft data. The pillbox problem is illustrated schematically in Figure 1.

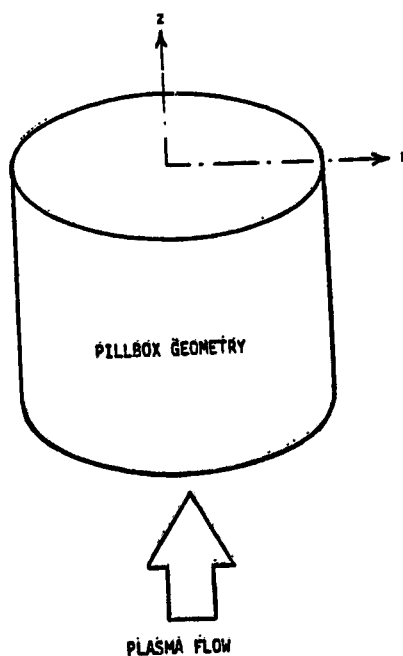


Figure 1. Spacecraft and Plasma-Flow Geometry

Various approaches which have been used for this type of problem are summarized by Parker.<sup>1</sup> In all such calculations, simplifying assumptions are made. The customary ones are:

- (1) Collisions negligible (but extensions of Parker's collisional theory<sup>4</sup> may be feasible for the wake problem).
- (2) Geomagnetic field negligible.
- (3) Simplified geometry (use of various types of symmetries).
- (4) Simplified surface reactions (usually, charged particles are neutralized).
- (5) Prescribed surface emission (usually none, but simplified photoelectron, backscattered-electron, and secondary-electron emission are includable).
- (6) Conducting body (usually perfectly conducting, but finite conductivities are includable).
- (7) Steady state.

These assumptions may be questioned (for example the neglect of time-dependent phenomena), but they may be at least partially relaxed by employing known techniques to generalize the calculations. In the interest of achieving reasonably economical calculations within the limits of available computers, the above assumptions in their usual form are adopted in the present work.

The techniques and computer program described by Parker<sup>1</sup> have been developed to solve the coupled Poisson-Vlasov system of equations to obtain distributions of ion and electron density, and potential, about three-dimensional bodies (with axial symmetry about the direction of plasma flow). The method involves the use of a numerical grid or mesh of discrete points in space, with the potential and density distributions defined at these points. The Poisson and Vlasov equations are represented in finite-difference form at the grid points. A sample of such a discretization in  $r$ - $z$  space is shown in Figure 2. Here the points represent circular rings about the  $z$ -axis. Associated with each point is a volume, in the form of a cylinder for points along the axis, and in the form of a torus of rectangular cross-section for all other points.

For the pillbox problem of Figure 1, the grid used has the form shown in Figure 3. The spacecraft surface is shown by a heavy outline in the interior of the grid. The surface of the pillbox coincides with certain rows and columns of grid points as shown. Here, the grid points are unequally spaced, so that a higher density of points can be used near the spacecraft surface and a lower density further away. This allows a given number of grid points to be used efficiently. The potentials at points on the surface can vary arbitrarily; the potential distribution shown corresponds to one part of the surface being at one potential (the "probe") while the remainder is at another potential. (The surface can consist of portions with arbitrarily assigned conductivity and emission characteristics. The actual number of grid points used was of the order of hundreds, rather than tens

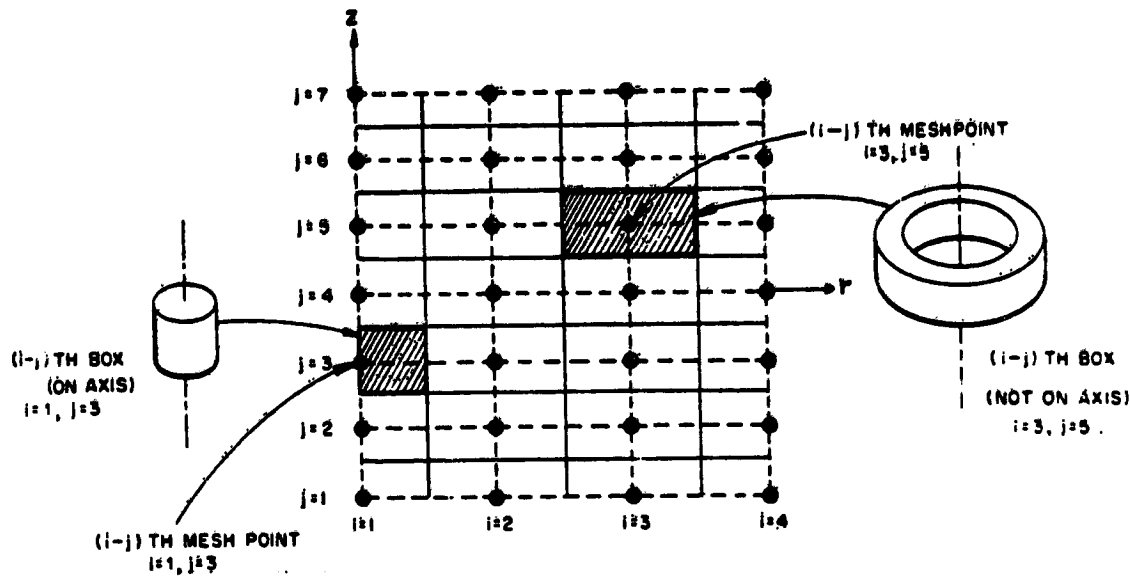


Figure 2. Discretization in r-z Space

as illustrated.) The shaded areas surrounding grid points are the cross-sections of toroidal volumes as in Figure 2. At the outer boundary of the grid, one must represent numerically the boundary condition at infinity, namely, such that the potential vanish and the velocity distribution be the unperturbed one. This boundary must be sufficiently far out to represent the outer condition accurately. It turns out to be more efficient to use a "floating" rather than a "fixed" condition on the potential (Section 3).

While the present problem is axially symmetric, it can be generalized to three dimensions as follows. The grid in Figure 3 consists of points in r-z space, and the associated volumes are tori. The generalization would consist of including the azimuthal variation by adding an azimuthal angle  $\theta$  to the coordinate system. The discretization in  $\theta$  would consist of having a number of azimuthal planes in r and z, each labeled by a given value of  $\theta$ . Thus, for example, the r-z plane of Figure 3 would be characterized by a given value of  $\theta$ . The volumes associated with the grid points would then be pie-shaped.

In the next section (Section 2) the "inside-out" method for evaluating particle fluxes and densities (solving the "Vlasov problem"), developed by the author<sup>6</sup> in 1964, will be discussed, with reference to the grid of Figure 3. In this method the ion and electron trajectories are followed backward in time, from the point in space at which it is desired to know the velocity distribution, to the source of the

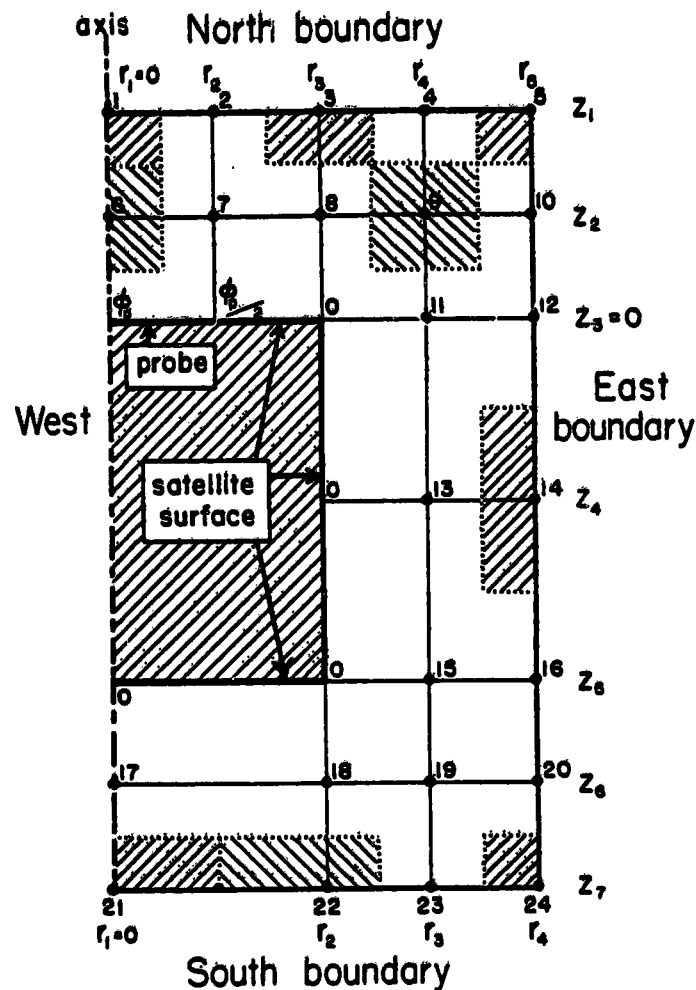
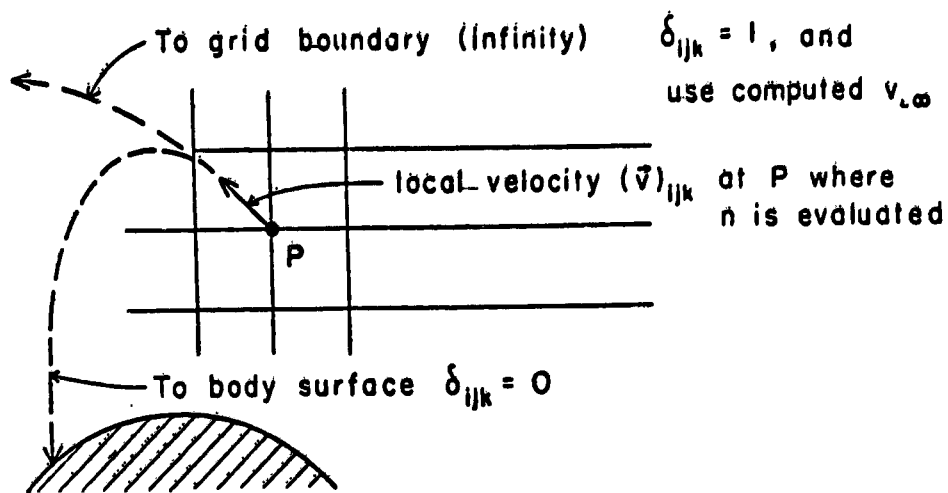


Figure 3. Difference Equation Grid

particles in the undisturbed plasma or at the surface, where the distributions are known. Figure 4, referred to again in the next section, illustrates schematically how a trajectory is traced backward from any point P and is found either to reach the body surface or "infinity" at the boundary of the grid. (The point P is usually but not necessarily one of the spatial grid points; it can also be a surface point.) The "delta-factor"  $\delta_{ijk}$  is a cutoff function, and i, j, and k are indices associated with one of the trajectories used to evaluate density or flux as discussed in the next section. The case illustrated is for contributions from the ambient plasma; for contributions from the surface, the values of  $\delta$  (zero and unity) are interchanged.



Evaluation of  $\delta_{ijk}$  for  $(i,j,k)$ -th trajectory by following (reversible) trajectories backward in time.

Figure 4. Basis of the Inside-Out Method

Figure 5 illustrates the four possible types of trajectories which can contribute to the particle density at a point. These are Types 1, 2, 3, and 4, so-named by Parker<sup>4</sup> and defined as follows:

Type 1

One-way trajectories, going from infinity to the surface, or from the surface to infinity.

Type 2

Two-way trajectories from infinity, which come in, pass through a position at minimum distance from the body surface, and go out again.

Type 3

Two-way trajectories from the body surface, which go out, pass through a position at maximum distance from the body surface, and come in again.

Type 4

Closed or nearly-closed trajectories which orbit about the body indefinitely. These can only be populated and depopulated by collisions, which are neglected in the present work. An analysis of the effects of collisions on Type-4 trajectories has been performed by Parker.<sup>4</sup>

It should be noted that contributions to surface fluxes can be comprised only of Type-1 and Type-3 trajectories, while all four types contribute to space charge.

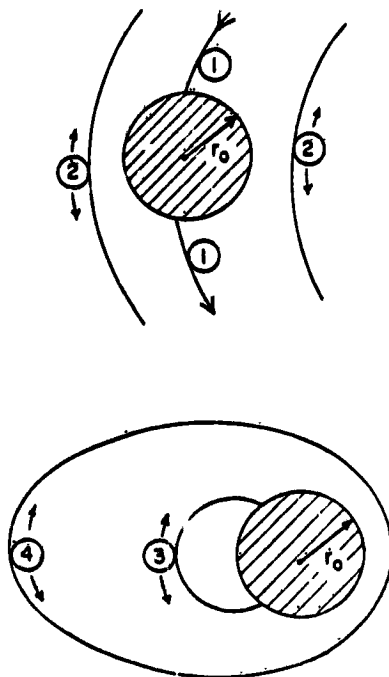


Figure 5. Types of Orbits

In Section 3 the "Poisson Problem" is discussed, where the electric field (potential distribution) is computed with the ion and electron densities considered known. On the other hand, the "Vlasov Problem" (Section 2) involves computation of the ion and electron densities with the field considered known. Hence, since neither the field nor the particle densities are known initially, the Poisson and Vlasov problems must be solved simultaneously.

An iteration method may be used for computing self-consistent charged-particle and potential distributions. This is herein referred to as the "Poisson-Vlasov iteration." Two principal options are employed for this procedure in the present program. In one of the options, the "charge-density" option, the space charge is initially and arbitrarily assumed to be zero. For this case, one obtains the Laplace (space-charge-less) electric field from the Poisson problem. This is the "zero-order" potential distribution, which becomes input to the Vlasov problem. The resulting solution of the Vlasov problem yields the ion and electron densities at the grid points, which are combined to make "zero-order" charge densities. These become input to the next Poisson problem, which then yields the "first-order" potentials, and so on. In this procedure one usually "mixes" successive charge-density iterates to improve stability; otherwise, the process can "blow up." One can also mix potential iterates rather than densities if desired. The dependence

of the stability and convergence of the above procedure on the mixing parameter have been studied analytically by Parker<sup>7</sup> and Parker and Sullivan.<sup>8</sup> (No other analysis of this type has been published to the author's knowledge.) This (charge-density) option is most effective when the spatial region of interest is not too many Debye lengths across. The analysis shows that one can (probably always) choose a mixing parameter sufficiently small to ensure convergence, but at the expense of additional iterations.

In the other option, the "ion-density option," the ion density distribution alone is assumed initially. Initial guesses which can be employed include (1) zero ion density everywhere, (2) unit ion density (the ambient value) everywhere, and (3) the neutral ion density which obtains when there are no forces. Whichever choice is made for the initial guess is designated the "zero-order" ion density. Now if one can assume the electron density to be given by the Boltzmann factor  $\exp(\phi)$ , thus avoiding trajectory calculations for the electrons and affording computer economy, the Poisson equation may be solved, holding the ion densities fixed, but regarding both the potentials and the electron densities at the grid points as unknowns. This is a nonlinear problem, which is solvable by a modification of the relaxation procedure used for the "charge-density" option. The new procedure is an important advance since the iteration is not as sensitive (tending to blow up) for small Debye numbers as in the charge density option. Thus, very large bodies (in multiples of the Debye length) can be treated. This has been the method used to obtain the large-body results shown below.<sup>1</sup> Similar ideas have been used by Call<sup>9</sup> and Fournier,<sup>10</sup> but these workers have not treated large bodies.

The assumption that the electron density is given by the Boltzmann factor becomes invalid when the body surface potential is near zero, or when there is a potential barrier or "well" in the wake such that the wake potentials are more negative than the surface potential (causing electrons to be attracted to the surface rather than repelled from it). In this case it is still possible to use the ion-density option, with its large-body capability, provided that, within each "major" iteration cycle a "minor" iteration is carried out with the ion densities held fixed such that the electron densities are computed realistically by trajectory calculations, at least for points near the surface.

This latter technique is as yet in an experimental stage, but it seems promising in that it may produce solutions with reasonable costs for large-body problems; in such problems, the conventional Poisson-Vlasov iteration based on the charge-density option becomes expensive.<sup>8</sup> A disadvantage of the ion-density option, however, is that its convergence properties are not understood; therefore, its costs are difficult to predict. This is in contrast to the case of the charge-density option where an analysis is available.<sup>8</sup>

Before considering further details, we make here some general remarks concerning the method. Following this, the principal results will be summarized.

Briefly, the present approach<sup>1</sup> differs from those of Call<sup>9</sup> and Martin<sup>11</sup> by including both the ion and the electron thermal motions, whereas Call and Martin represent the distribution of ions by a cold beam and use an "outside-in" method.<sup>1</sup> The approach differs from that of Taylor<sup>12</sup> in that (1) it is applied to three-dimensional bodies whereas Taylor treats an infinitely-long "thick strip" of rectangular cross-section, and (2) the Poisson and Vlasov calculations are cycled until self-consistency is achieved, whereas Taylor's calculation is not self-consistent because it is terminated after the first cycle. The approach differs from that of Grabowski and Fischer<sup>13</sup> because they (1) assume that quasineutrality holds everywhere (an invalid assumption in the very near wake - see below and Section 5), and (2) apply their method to an infinitely-long cylinder. Differences with other methods are outlined in Parker.<sup>1</sup> The most similar calculation previously done was for an infinitely-long cylinder by Fournier,<sup>10</sup> using the inside-out method. The present author has used the method for two-electrode rocket-borne<sup>7</sup> and laboratory probe systems,<sup>4</sup> for the problem of a small probe in the sheath of a large electrode,<sup>4</sup> and most recently for the problem of the pillbox-shaped spacecraft.<sup>1</sup> The inside-out method was also used by Parker and Whipple<sup>14</sup> for the theory of a satellite flush-mounted probe.

Two major advances are represented by the present program, as opposed to previous approaches, particularly with regard to wakes of three-dimensional bodies:

(1) Thermal motions of ions as well as of electrons are treated realistically by following their trajectories in the electric field. (The ion and electron temperatures can be different.)

(2) The technique for achieving self-consistency is promising for large bodies many orders-of-magnitude larger than the Debye length (the Shuttle-Orbiter or the moon, for example).

Solutions may be obtained with reasonable amounts of computer time by judicious choices of grid points and other numerical parameters. The method can be extended to include an arbitrarily-shaped body (presently a body of revolution), electron emission from the surface, and differential charging when the surface consists of sections with different conductivity.

In Sections 2 and 3 some details of the techniques for the flux and density calculation ("Vlasov problem"), and for the Poisson calculation, are treated.

Sample calculational results are presented in Sections 4 and 5.

### 1.1 Summary of Principal Results

The principal results are as follows. In-situ experiments associated with the Ariel 1 and Explorer 31 satellites are modeled by a pillbox geometry. The Ariel 1 experiment observes distinct wake structures associated with the main body and a small external ion probe. Transverse profiles of electron current are measured at 5 main-body radii downstream. The two wake structures are similar in that they both show a below-ambient central core or peak within a depleted region of the order of the width of the main body. The theoretical results for the assumed values of the parameters associated with the experiment show no well-defined central core. They further show that all structure dies away beyond 6 or 8 radii downstream. A pronounced electrical focusing of ions in the wake of the highly-negative ion probe is predicted by the calculation, but this disturbance is confined to the relatively near wake and does not persist downstream. The filling of the wake in both cases by the plasma suggests a fluid-like bulk motion of the plasma. As one moves downstream with the plasma, the motion is at first radially inward. This is followed by a pile-up and a single "bounce" after which the motion is outward. Simultaneously, the disturbance becomes weak and dies away.

Two Explorer 31 cases are computed for different values of the ion Mach number (the other parameters remaining roughly comparable), and in both cases the body is several  $kT$  negative. In the case of the larger Mach number (3.4), the ion density in the near wake is below the corresponding electron density, and both are significantly below ambient. This is consistent with the traditional picture of wake structures with ion Mach numbers significantly above unity. In the case of the lower Mach number (1.1) the ion density in the near wake is above the corresponding electron density, and moreover the ion density is roughly ambient. This latter may seem unexpected, but is understandable on the basis of Langmuir-probe sheath theory: In the sheath of a slowly-moving negative probe the ion density should predominate over the electron density. This latter result is new in wake theory, and arises because low-Mach-number wakes with space charge have not been previously rigorously computed.

For the wake of a large body (100 Debye lengths in radius) in the form of a disk, the results show that quasineutrality is valid outside of a cone-shaped region in the very near wake, and is invalid within this region. Other features of the large-body wake structure include (1) a potential well in the near wake, and (2) a central core of approximately ambient density of both ions and electrons. This latter feature seems similar to that observed in the Ariel 1 experiment.

## 2. THE INSIDE-OUT METHOD

There is more than one approach to the problem of calculating sheath and wake structures. These approaches have in common the following elements. The quantities to be computed include (1) the potential distribution, and (2) the ion and electron density distributions. One may also include the associated surface current densities. The equations to be solved simultaneously are (1) the Vlasov equation for ions, (2) the Vlasov equation for electrons, and (3) the Poisson equation. The solutions of the Vlasov equations (velocity-distribution functions) are used to compute number densities (and surface current densities). The number-density distributions become input to the (right-hand side of the) Poisson equation which yields the potential distribution. Finally, an iterative procedure is used for self-consistency, wherein the density and potential distributions are successively cycled until satisfactory convergence has been achieved.

The steady-state Vlasov equations for ions and electrons state that the velocity distribution functions remain constant along particle trajectories. With the electric field assumed given (numerically in terms of a spatial grid about the body), solving the Vlasov equations means formally that one determines, from the shapes of the trajectories, the ion and electron velocity distributions at the grid points. The trajectories relate local velocities at a given grid point to those at infinity or the surface. Through these relationships, the ion or electron number density at the point may be evaluated by a velocity-integral over the local velocity distribution. Similarly, the current density may be evaluated at desired locations (usually the body surface).

It is convenient to classify various theoretical approaches on the basis of how they treat the trajectory part of the Vlasov problem. An "inside-out" method follows the trajectories backward in time to their source, while an "outside-in" method follows the trajectories forward, in the direction of physical motion of the particles. (In an outside-in method, the velocity-distribution function is not calculated; rather, the density is evaluated directly.) There are in addition other (less realistic) methods involving approximations where trajectories are not followed at all. The three types of approaches are discussed in Parker.<sup>1</sup> There exists as yet no systematic comparison of the results of the various approaches with one another.

For the purposes of discussing the inside-out method, we define here the parameters of interest:

### Plasma Parameters

- $n_0$  = unperturbed number density at infinity
- $T_i, T_e$  = ion, electron temperatures (= T for equal ion and electron temperatures)
- $m_i$  = ion mass (electron mass not required)

$\lambda_D$  = electron Debye length

Body Parameters

$R_0$  = characteristic dimension

$v_0$  = relative velocity of body and plasma

$\phi_0$  = body potential

$\phi$  =  $e\phi_0/kT_e$  = dimensionless body potential

$M$  =  $v_0 \sqrt{m_i/2kT_i}$  = ion Mach number (electron Mach number assumed negligible)

$\lambda_D$  =  $\lambda_D/R_0$  = Debye number

Henceforth, all lengths are to be considered normalized by  $R_0$ . Thus,  $\lambda_D$  will denote the dimensionless Debye number. We also consider here the case of equal temperatures. Potentials are normalized by  $kT/e$ , so that  $\phi(\vec{r})$  denotes the dimensionless potential at the spatial point  $\vec{r}$ . Number densities are normalized by  $n_0$ , so that  $n(\vec{r})$  denotes the dimensionless density at  $\vec{r}$ . In the calculations involving integrations over velocities,  $\vec{v}$  will denote a velocity normalized by the value of  $\sqrt{2kT/m}$  associated with the particles of interest. Similarly,  $E$  will denote total energy normalized by  $kT$ . Velocity-distribution functions (denoted by  $f$ ) will be normalized by  $n_0$ . For a given body geometry, there are three dimensionless physical parameters of interest, namely,  $\lambda_D$ ,  $\phi_0$ , and  $M$ . (For unequal temperatures, the temperature ratio  $T_i/T_e$  represents an additional parameter.)

Consider a single species of (charged) particle, that is, ions or electrons. The electric field is assumed to be known. In order to compute the number density  $n(\vec{r})$  at the point  $\vec{r}$ , one must evaluate the triple integral over velocity space:

$$n(\vec{r}) = \iiint f(\vec{r}, \vec{v}) dv_x dv_y dv_z \quad (1)$$

where  $f(\vec{r}, \vec{v})$  is the distribution function which satisfies the Boltzmann equation for the given species of particle,  $\vec{r}$  is the radius vector of the space point of interest, and  $\vec{v}$  is the local velocity of a particle at  $\vec{r}$ . The velocity-volume element is written as if cartesian coordinates were being used, but the product  $dv_x dv_y dv_z$  is intended to symbolize an arbitrary coordinate system. Similarly, in order to compute the collected flux at points on the surface of a body, one must evaluate at each point a triple integral over velocity space of the form

$$j(\vec{r}) = \iiint f(\vec{r}, \vec{v}) v_n dv_x dv_y dv_z \quad (2)$$

where  $v_n$  is the component of the particle velocity normal to the surface at the point  $\vec{r}$ .

The problem is thus to evaluate  $f$ . Since the problems of interest are assumed to be collisionless and constant in time, the distribution function  $f$  satisfies the steady-state Vlasov (or collisionless Boltzmann) equation, namely,

$$\vec{v} \cdot \nabla f + \vec{a} \cdot \nabla_v f = 0 \quad (3)$$

where  $\vec{a}$  is the vector acceleration of a particle passing with velocity  $\vec{v}$  through the point  $\vec{r}$ . The gradient operators  $\nabla$  and  $\nabla_v$  operate on the components of  $\vec{r}$  and of  $\vec{v}$ , respectively. Equation (3) states that  $f$  is constant along a particle orbit, which is characterized by the constants of the motion. In a general electrostatic field (here assumed given) whose sources are volume and surface charges, the total energy  $E$  is conserved, where the dimensionless  $E$  is defined by

$$E = v^2 + \phi(\vec{r}) \quad (4)$$

and  $\phi(\vec{r})$  is the dimensionless potential energy of the particle at  $\vec{r}$ .

With  $\phi(\vec{r})$  a known function of  $\vec{r}$ , one may evaluate the integrals in Eqs. (1) and (2) by following orbits backward in time with trajectory calculations to a point where  $f$  is known. For example, in the case of a body immersed in a plasma,  $f$  is assumed to be known at infinity (where  $\phi$  vanishes), and is assumed to have at infinity a prescribed energy distribution, such as a Maxwellian with drift, or a more general distribution. Also,  $f$  is assumed to be known on the surfaces of the spacecraft. If a surface emits particles, its distribution function must be prescribed. If the surface absorbs without reemitting charged particles, the distribution function (of emitted particles) is prescribed to be zero. Thus,  $f$  is discontinuous in velocity space. That is, the physically-possible velocity space (at the point  $\vec{r}$ ) is divided into three domains, namely, the domain of orbits which have come to  $\vec{r}$  from infinity, the domain of orbits which have come to  $\vec{r}$  from the spacecraft surfaces, and the domain of trapped orbits (assumed to be unoccupied). The shapes of the boundaries between the domains depend, of course, on the geometry and the potential function  $\phi$ , and it is the heart of the problem (1) to determine the boundaries of the domains of orbits, and (2) to evaluate the integrals Eqs. (1) and (2) over those domains of velocity space.

In practice, one need not in general determine explicitly the boundary of a domain in velocity space. Rather, one may follow a large number of orbits backward in time (computationally), and evaluate the moment integrals, Eqs. (1) and (2), automatically from the results of the orbit-following. It may, however, under some circumstances be more accurate and efficient to determine this boundary. To do so would complicate the computer programming.

For a Maxwellian distribution flowing along the z-direction with Mach number M, the dimensionless velocity-distribution function at infinity may be written:

$$f_0 = \frac{1}{\pi^{3/2}} e^{-(v_\infty^2 + M^2 - 2Mv_{z\infty})} = \frac{1}{\pi^{3/2}} e^{-(\phi + v^2 + M^2 - 2Mv_{z\infty})} \quad (5)$$

(velocities in units of  $\sqrt{2kT/m}$ ,

$v_z$  = axial component of velocity)

where  $v_\infty^2 = v^2 + \phi$  may be identified with the total energy E, and  $v_{z\infty}$  with  $\sqrt{E}$  times the cosine of the angle between  $\vec{v}_\infty$  and the axis. A similar Maxwellian distribution may also be used to represent particles emitted from the surface. The moment integral (1) for number density may be approximated by a quadrature sum as follows:

$$n = \iiint \delta f_0 d^3\vec{v} \approx \sum_i \sum_j \sum_k A_{ijk} \delta_{ijk} (f_0)_{ijk} \quad (6)$$

where  $d^3\vec{v}$  is a short-hand notation for the element  $dv_x dv_y dv_z$ , and  $\delta$  is a cutoff (or step) function, equal to unity or zero, depending on (1) whether the trajectory is found to come from infinity or the body surface, and (2) whether n represents the density contributed by particles from infinity or from the surface. In the sum, the three indices refer to discrete values of three components of velocity, where the values are chosen in accord with a quadrature scheme (Gaussian), and the coefficients  $A_{ijk}$  are proportional to the associated weights and other factors. Each term in the sum represents an individual trajectory. A similar sum is obtained for the flux.

In order to evaluate Eq. (6) for the density, or the corresponding equation for the flux, we transform to energy (E) and angle ( $\alpha, \beta$ ) variables in velocity space. We define  $\alpha$  and  $\beta$  by:

$\alpha$  = polar angle with respect to z-axis

$\beta$  = azimuthal angle with respect to the plane containing the z-axis and the point  $\vec{r}$ .

The angles  $\alpha$  and  $\beta$  which define the orientation of the velocity-vector  $\vec{v}$  (while  $\sqrt{E}$  defines its magnitude) are illustrated in Figure 6.

It is shown by Parker<sup>1</sup> that the integrals for both the density and flux can be transformed to the following form suitable for Gaussian quadratures:

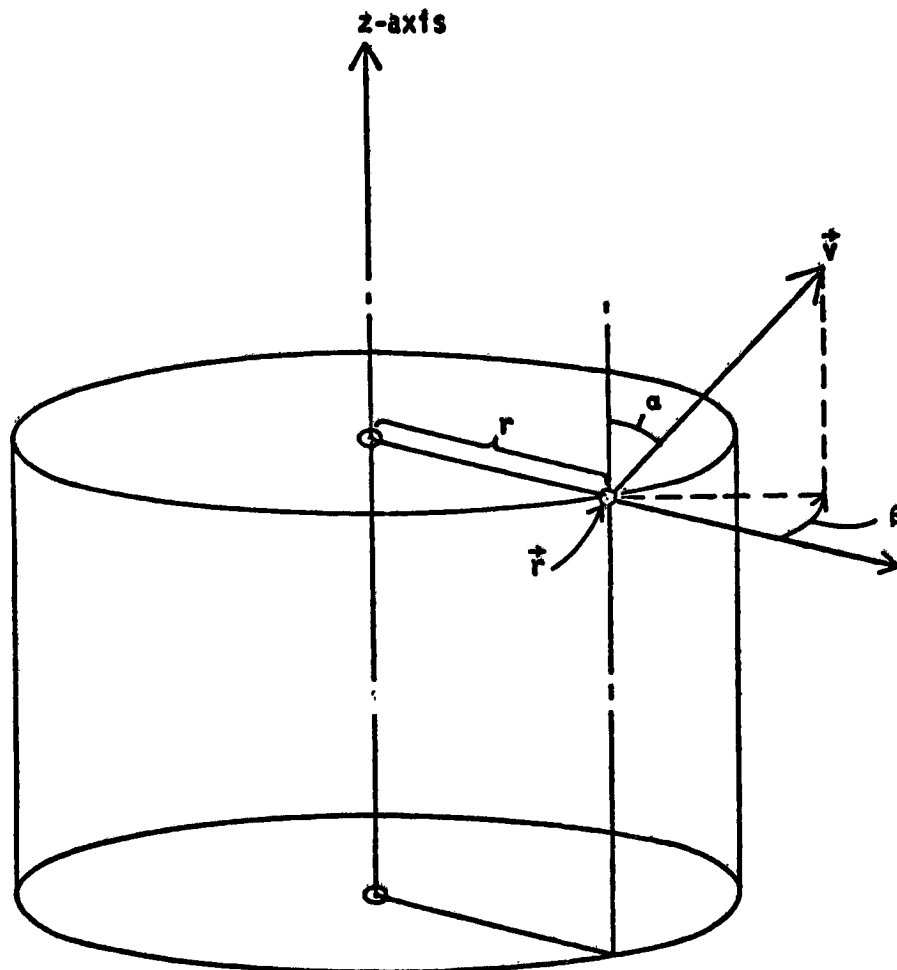


Figure 6. Angle Variables in Velocity Space

$$I = \int_{-1}^1 \int_{-1}^1 \int_{-1}^1 T(a, b, c) \cdot \delta(a, b, c) \cdot da db dc \quad (7)$$

Here, the ranges of  $\alpha$ ,  $\beta$ , and  $\bar{E}$  have been transformed to the interval  $(-1, 1)$  through the use of new variables  $a$ ,  $b$ , and  $c$ . In terms of these latter variables,  $\alpha$ ,  $\beta$ , and  $\bar{E}$  are given by

$$\left. \begin{aligned} \alpha(a) &= \cos^{-1} a \quad \text{for density} \\ \alpha(a) &= \sin^{-1} \sqrt{\frac{1+a}{2}} \quad \text{for flux} \end{aligned} \right\} \quad (8)$$

$$\beta(b) = \frac{\pi}{2} (1 + b) \quad (9)$$

$$E(c) = \frac{1+c}{1-c} + \phi_s \quad (10)$$

where the range of  $\alpha$  is from 0 to  $\pi$  for density and from 0 to  $\pi/2$  for flux; the range of  $\beta$  is from 0 to  $\pi$ ; and the range of  $E$  is from  $\phi_s$  to infinity, where  $\phi_s$  denotes the potential of the source (infinity or the surface).

The definition of  $T$  in the integrand of Eq. (7) is as follows:

$$T(a, b, c) \equiv \frac{e^{-U(a, b, c)}}{(1-c)^2} \cdot \begin{cases} \sqrt{\frac{E(c) - \phi}{\pi}} & \text{for density} \\ \frac{E(c) - \phi}{2} & \text{for flux} \end{cases} \quad (11)$$

where  $U(a, b, c)$  is given by

$$U(a, b, c) \equiv -\phi_s + E(c) + M^2 + 2M\sqrt{E(c)} \cdot \cos \alpha_\infty(a, b, c) \quad (12)$$

with  $\alpha_\infty$  denoting the value of the polar angle of the velocity-vector at infinity, which depends on the local values of  $\alpha$ ,  $\beta$ , and  $E$  (through  $a$ ,  $b$ , and  $c$ ). The product  $\sqrt{E} \cdot \cos \alpha_\infty$  in Eq. (12) is identical to the quantity  $v_{z\infty}$  in Eq. (5).

Now it is convenient for flexibility to divide the  $a$ -domain into  $M_a$  equal subintervals, the  $b$ -domain into  $M_b$  equal subintervals, and the  $c$ -domain into  $M_e$  equal subintervals, and then to use Gaussian quadratures of order 2 in each subinterval. This leads to a sum of the following form:<sup>1</sup>

$$I \rightarrow S \equiv \frac{1}{M_a M_b M_e} \sum_{K_a=1}^{M_a} \sum_{J_a=1}^2 \sum_{K_b=1}^{M_b} \sum_{J_b=1}^2 \sum_{K_e=1}^{M_e} \sum_{J_e=1}^2 T(a'; b'; c') \cdot \delta(a'; b'; c') \quad (13)$$

where

$$\begin{aligned} a' &= \frac{1}{M_a} \left( \frac{(-1)^{J_a}}{\sqrt{3}} + 2K_a - 1 - M_a \right) \\ b' &= \frac{1}{M_b} \left( \frac{(-1)^{J_b}}{\sqrt{3}} + 2K_b - 1 - M_b \right) \\ c' &= \frac{1}{M_e} \left( \frac{(-1)^{J_e}}{\sqrt{3}} + 2K_e - 1 - M_e \right) \end{aligned} \quad (14)$$

Finally, the form of Eq. (6) may be obtained from Eqs. (13) and (14) by writing

$$S = \frac{1}{M_a M_b M_e} \sum_i^I \sum_j^J \sum_k^K T(a_i, b_j, c_k) \cdot \delta(a_i, b_j, c_k) \quad (15)$$

where

$$\left. \begin{aligned} a_i &= a' & \text{with } i &= J_a + 2(K_a - 1) \\ b_j &= b' & \text{with } j &= J_b + 2(K_b - 1) \\ c_k &= c' & \text{with } k &= J_c + 2(K_c - 1) \\ I &= 2M_a & J &= 2M_b & K &= 2M_e \end{aligned} \right\} \quad (16)$$

The sum of Eq. (15) consists of  $8 M_a M_b M_e$  terms, each of which represents a trajectory, followed backward from the point of interest. The cutoff function  $\delta(a_i, b_j, c_k)$  is zero or unity, depending upon the trajectory defined by the indices  $i, j,$  and  $k$  characterizing the initial velocity components. The case illustrated in Figure 4 is for contributions from the ambient plasma; for contributions from the surface,  $\delta_{ijk}$  is zero or unity according as the trajectory reaches infinity or the body surface, respectively.

The computed results to be presented later are based on the assumption of no surface emission.

The method of computation of orbits involves integration of the equations of motion, with the forces given by the components of the gradients of potential. These components are obtained by interpolation between values of potential defined at the points of the grid, say of Figure 3, as described in Parker.<sup>1</sup> The criterion for "escape" or "absorption" of an orbit (that is, evaluation of  $\delta$ ) depends on the geometry of the problem and of the grid. The equations of motion are integrated step-by-step until the orbit either passes out of the outer boundary of the grid ("escapes") or returns to the spacecraft surface (is "absorbed"). The orbit computation time-step is not of physical importance in these time-independent problems where only the shape of the orbit matters. The time-step is kept as large as possible consistent with maintaining the energy loss or gain within desired limits. The method of integrating the equations of motion, the interpolation method to find the forces, and the control of step size, are discussed in Parker.<sup>1</sup>

An important consideration is the accuracy of the quadrature-sum. Naturally, the accuracy is related to the number of terms used, that is, the number of orbits where each term corresponds to a unique orbit. In a test of the energy quadrature alone, and with  $M = 0$ , the unperturbed value of density (unity) was computed for

values of  $M_e = 1, 2, 4, 8, 16,$  and  $32$ . The corresponding numerical errors were -6 percent, -7 percent, +1.5 percent, -0.05 percent, +0.013 percent, and +0.003 percent. This test was independent of geometry (the  $\alpha$  and  $\beta$  integrations were numerically exact). Thus,  $M_e = 4$  (8 values of  $E$ ) is taken to represent sufficient accuracy (within a few percent) for the purposes of computing density for a Maxwellian distribution without drift (or, for electrons). For large Mach number ( $M$ ) the accuracy of the above unmodified quadrature is diminished. Modification for improving the accuracy at large  $M$  by suitably weighting the integrand in the domains of importance are given in Parker.<sup>1</sup>

### 3. THE POISSON PROBLEM: POISSON DIFFERENCE EQUATIONS

In the present problem the electrostatic field is axially symmetric and is defined on a mesh of spatial grid points, such that at any point (including grid points) the potential and electric field can be obtained by interpolation.

Assume that the space charge density is known at the grid points. Consider a group of interior grid points, forming a portion of the overall grid as shown in Figure 7. In this figure, the vertical and horizontal directions are the  $z$  and  $r$  directions, respectively, where  $z$  and  $r$  denote the cylindrical axial and cylindrical radial coordinates, respectively. Three horizontal grid lines, of constant  $z$ -values  $z_{i-1}$ ,  $z_i$ , and  $z_{i+1}$ , and three vertical grid lines, of constant  $r$ -values  $r_{j-1}$ ,  $r_j$ , and  $r_{j+1}$ , are shown in the figure. (Note that the index ( $i$ ) of  $z$  increases as  $z$  decreases.) The set of grid lines intersect at 9 grid points, or nodes, as shown. Each point may be considered to be associated with a volume of space, and to have a group of four neighboring points which "interact" with it. Thus, consider the central point of the group, labeled  $C$  in the figure, which may be identified with one of the grid points in Figure 3. Associated with this point is a volume of revolution (a torus) whose cross-section is rectangular and is shown by the rectangular shaded area surrounding Point  $C$ . The shaded area is defined by connecting the midpoints of the surrounding mesh rectangles. Let  $\tau$  denote the volume of the torus, and let the neighboring points (above, below, to the right of, and to the left of  $C$ ) be labeled  $N$ ,  $S$ ,  $E$  and  $W$  (north, south, east and west, respectively).

Let the Poisson equation be written in dimensionless form as

$$\nabla^2 \phi = -\rho = (n_e - n_i) / \lambda_D^2 \quad (17)$$

where  $n_e$ ,  $n_i$ ,  $\lambda_D$ ,  $\phi$  and  $\rho$  denote the dimensionless electron density, ion density, Debye number, electrostatic potential and space-charge density, respectively, and all lengths are in units of the body radius.

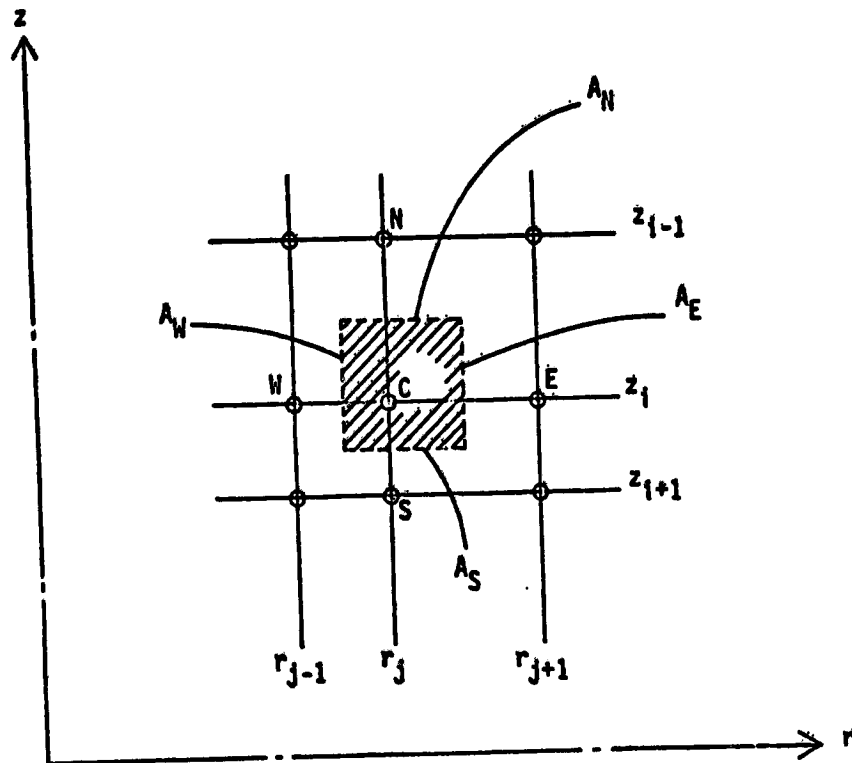


Figure 7. Group of Interior Grid Points in r-z Grid

The grid lines may be considered to be arbitrarily chosen so that the mesh intervals are nonuniform. In this case the Poisson difference equations may be obtained by integrating Eq. (17) over the volume  $\tau$  of the torus associated with Point C:

$$\iiint_{\tau} \nabla^2 \phi \, d\tau = - \iiint_{\tau} \rho \, d\tau \cong - \rho_C \tau \quad (18)$$

where  $\rho_C$  is known at the grid point C. The right-hand side has been approximated as shown since  $\tau$  is small in principle, and  $\rho_C$  is the value of  $\rho$  at Point C. By the divergence theorem, the left-hand side becomes

$$\iint_{\Sigma} \frac{\partial \phi}{\partial n} \, d\Sigma \cong A_N \left( \frac{\partial \phi}{\partial n} \right)_N + A_S \left( \frac{\partial \phi}{\partial n} \right)_S + A_E \left( \frac{\partial \phi}{\partial n} \right)_E + A_W \left( \frac{\partial \phi}{\partial n} \right)_W \quad (19)$$

where  $\Sigma$  denotes the surface of the torus;  $\partial\phi/\partial n$  is the component of  $\nabla\phi$  in the outward normal direction at the surface;  $A_N, A_S, A_E,$  and  $A_W$  denote the areas of the north, south, east, and west surfaces, respectively; and the quantities  $(\partial\phi/\partial n)_{N,S,E,W}$  denote values of  $\partial\phi/\partial n$  taken to be constant on the corresponding surfaces.

$(\partial\phi/\partial n)_{N,S,E,W}$  may be approximated by difference quotients, namely,

$$\begin{aligned} \left(\frac{\partial\phi}{\partial n}\right)_N &\cong \frac{(\phi_N - \phi)}{(z_{i-1} - z_i)} & \left(\frac{\partial\phi}{\partial n}\right)_S &\cong \frac{(\phi_S - \phi)}{(z_i - z_{i+1})} \\ \left(\frac{\partial\phi}{\partial n}\right)_E &\cong \frac{(\phi_E - \phi)}{(r_{j+1} - r_j)} & \left(\frac{\partial\phi}{\partial n}\right)_W &\cong \frac{(\phi_W - \phi)}{(r_j - r_{j-1})} \end{aligned} \quad (20)$$

where  $\phi$  denotes the potential at Point C and  $\phi_N, \phi_S, \phi_E, \phi_W$  denote the neighboring potentials. If Point C is an interior grid point, the areas  $A_N, A_S, A_E,$  and  $A_W$  are given by

$$\begin{aligned} A_N &= \frac{\pi}{4} \left[ (r_{j+1} + r_j)^2 - (r_j + r_{j-1})^2 \right] \\ A_S &= A_N \\ A_E &= \frac{\pi}{2} (r_{j+1} + r_j) (z_{i-1} - z_{i+1}) \\ A_W &= \frac{\pi}{2} (r_j + r_{j-1}) (z_{i-1} - z_{i+1}) \end{aligned} \quad (21)$$

and the volume  $\tau$  is given by

$$\tau = \frac{A_N}{2} (z_{i-1} - z_{i+1}) \quad (22)$$

Thus we obtain the difference equation in the form

$$C_N \phi_N + C_S \phi_S + C_E \phi_E + C_W \phi_W - C\phi = -\rho_C \tau \quad (23)$$

where

$$C = C_N + C_S + C_E + C_W \quad (24)$$

and

$$\begin{aligned}
C_N &= \frac{A_N}{(z_{i-1} - z_i)} & C_S &= \frac{A_S}{(z_i - z_{i+1})} \\
C_E &= \frac{A_E}{(r_{j+1} - r_j)} & C_W &= \frac{A_W}{(r_j - r_{j-1})}
\end{aligned}
\tag{25}$$

This shows how to form the difference equations used for the Poisson problems of this paper. Equation (24) holds only for an "interior" point of the grid, that is, a point surrounded by neighbors on all four sides. If Point C has a known neighboring potential (for example, if Point C is adjacent to the spacecraft surface), then the corresponding term on the left-hand side of Eq. (23) is transferred to the right-hand side as a known quantity.

The boundary conditions for the potentials in the Poisson problem are as follows. At points representing the body surface, the normalized potentials are fixed at the chosen values. At the external (boundary) points of the grid, where "infinity" is represented on the computer, a "floating" condition is optionally used, namely, a linear relation between  $\phi$  and  $\partial\phi/\partial n$ , the normal component of  $\nabla\phi$ . The exact relation of  $\phi$  to  $\partial\phi/\partial n$  is not important when the external boundary of the grid is sufficiently far away. (For the calculations to be reported, the assumed relation was the same as for a Coulomb potential.) In any case, either the fixed condition  $\phi = 0$  or the floating condition will give the same results, provided the grid boundary is moved sufficiently far out. The effect of various types of boundary conditions representing "infinity" have been studied by Taylor<sup>12</sup> and by Parker and Sullivan.<sup>8</sup> In general, the floating condition appears to be computationally more efficient than the fixed one. Of course, the floating condition becomes ideal when the true relation between  $\phi$  and  $\partial\phi/\partial n$  is used, but this requires that the asymptotic form of the solution be known in advance. For example, see Parker and Whipple.<sup>14</sup> The boundary conditions at the outer grid surfaces can be combinations of fixed and floating conditions.

Consider a Point C on the outer boundary of the grid where a floating boundary condition is chosen. If the potential is assumed to satisfy the linear law

$$\frac{\partial\phi}{\partial n} = \frac{\partial\phi}{\partial z} = -\alpha\phi
\tag{26}$$

on the z-boundary (North or South), and

$$\frac{\partial\phi}{\partial n} = \frac{\partial\phi}{\partial r} = -\beta\phi
\tag{27}$$

on the r-boundary (East only;  $\beta=0$  on the West), then the corresponding "neighbor term" on the left-hand side of Eq. (23) vanishes, and the corresponding "neighbor coefficient" on the right-hand side of Eq. (24) is replaced by  $\alpha A$  or  $\beta A$ , where  $A$  is the appropriate area. The quantities  $\alpha$  and  $\beta$  depend on the position and on the assumed model for the variation of the potential at large distances.

Once the coefficients of all of the equations (corresponding to the grid points where the potentials are unknown) are computed, the system of linear equations of the form of Eq. (23) may be solved by iteration. Point-successive over-relaxation is a well-known process and has been found to be effective in the present problem. For the relaxation process, one rearranges the equations, so that the "diagonal" term is alone on the left-hand side, while all the other terms are on the right-hand side with the known charge-density term. Thus, Eq. (23) becomes

$$C\phi = C_N\phi_N + C_S\phi_S + C_E\phi_E + C_W\phi_W + \rho_C \tau \quad (28)$$

First, an initial guess is made for the values of all the potentials. Then new values are obtained from the left-hand sides of all of the equations (28), using previous values on the right-hand sides. One "sweeps" through the equations successively, replacing the potentials on the right-hand sides with updated values as they become available from preceding equations. This procedure is usually stable and leads to convergence. "Over-relaxation" is the process of mixing successive potential iterates in such a way as to enhance the rate of convergence.<sup>1</sup>

When the potential distribution is such that the electron density  $n_e$  is approximated by the Boltzmann factor  $\exp(\phi)$ , the relaxation equations (28) can include the electron density as an unknown function on the left-hand side. The equations are then nonlinear; they may be solved for  $\phi$  by a Newtonian process, with the ion density  $n_i$  considered fixed. This procedure is promising for large-body problems.<sup>1</sup>

#### 4. SAMPLE RESULTS APPLIED IN IN-SITU DATA

The calculations reported here refer to two in-situ experiments, Ariel 1<sup>15</sup> and Explorer 31<sup>16</sup>, where data are available. These results are preliminary in that they are intended as an illustration of the capability of the program rather than as a systematic study. Geometrically, the body is assumed to be a pillbox, a cylinder of height equal to its diameter. The three dimensionless physical parameters defining the problem are  $\phi_0$ ,  $M$ , and  $\lambda_D$ , defined (earlier) by:

$$\phi_0 = e\Phi_0/kT$$

$$M = mv_0^2/2kT$$

$$\lambda_D = \lambda_D/R_0$$

where  $T$  is the plasma temperature (assumed to be the same for ions and electrons),  $\phi_0$  is the body potential (for a conducting nonemitting body),  $v_0$  is the velocity of the plasma flow relative to the body and parallel to its axis,  $m$  is the ion mass,  $R_0$  is the body radius, and  $\lambda_D$  is the dimensional Debye length.

The numerical parameters for the calculations to be described include of the order of 100 grid points, distributed mostly in the wake region, and of the order of 500 trajectories per grid point, distributed among the two angles and the energy.

#### 4.1 Ariel 1 Satellite—

Figure 8 is a schematic drawing of the Ariel 1 satellite, showing the location of electron and ion probes, after Henderson and Samir.<sup>15</sup> The boom-mounted

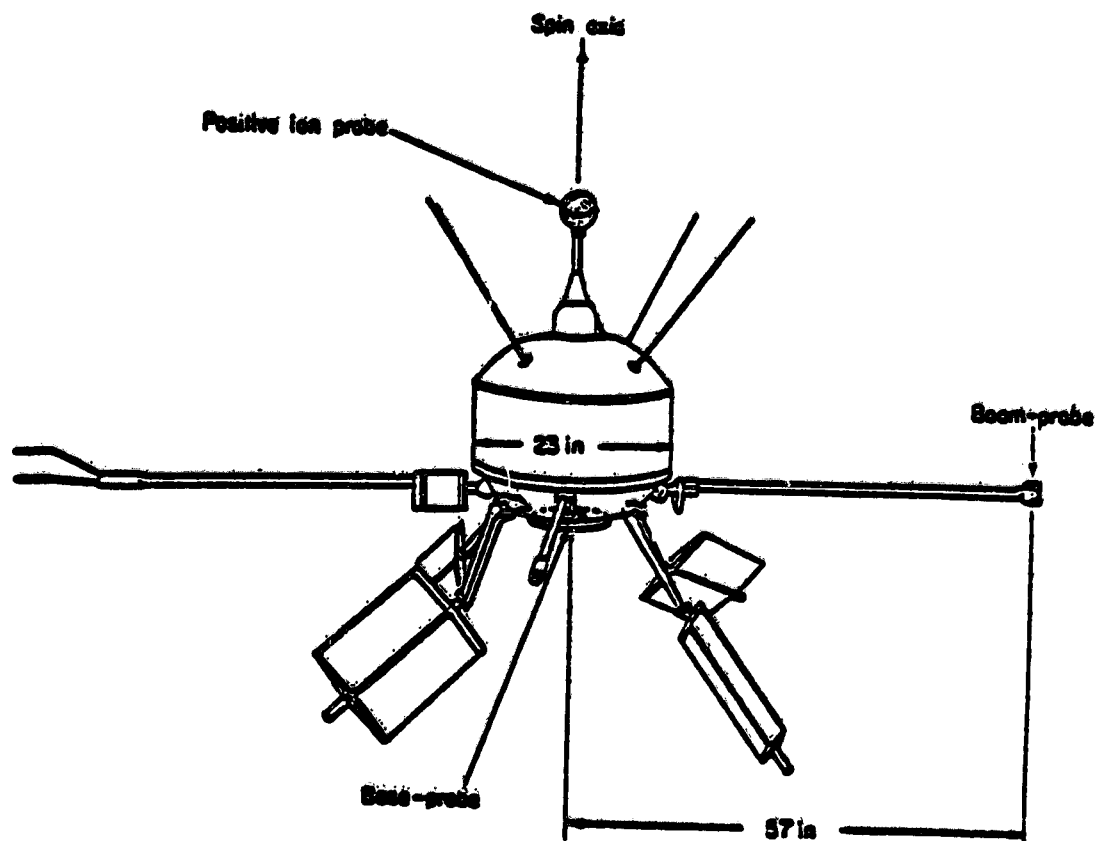


Figure 8. Ariel 1 Satellite Schematic. Shows main body, positive-ion probe, and electron boom-probe

probe measures electron currents at a distance  $5 R_0$  from the center of the satellite (main-body) which has a radius  $R_0 = 11.5$  in or 29 cm. The ion probe mounted near the surface and on the spin axis is a small sphere 6.6 times smaller than the main body. The satellite velocity is such that the ion Mach number is about 4. The satellite potential is about 4 kT (1 volt) negative with respect to space. The satellite radius is equal to about 10 Debye lengths. Due to the satellite motion, spin, and orientation, the boom probe sweeps through the wake during each spin revolution. In successive revolutions, it sweeps through at different angles and samples the structure of different parts of the wake.

Figure 9 shows normalized electron current data taken from the paper by Henderson and Samir (their figure 4).<sup>15</sup> In particular, the data at  $\theta = 84^\circ$  (labeled "MAIN") samples the wake structure associated with the main body, while the data at  $\theta = 60^\circ$  (labeled "I. P.") samples the wake structure of the ion probe. We will consider separately the main body and ion probe in the following comparisons between the data and theoretical calculations.

#### 4. 1. 1 ARIEL 1 MAIN BODY

Although the data in Figure 9 is "bumpy," the  $\theta = 84^\circ$  profile for the main body indicates a minor central peak or bump, of height about 80 percent of ambient, within the depleted wake region where the minimum is about 50 percent of ambient.

Figure 10 shows transverse profiles computed for the wake of the main body, of  $n_i$  (normalized ion density),  $n_e$  (normalized electron density), and  $\phi$  (dimensionless potential) in the wake region downstream. The parameter values in Figure 10 are  $\phi_0 = -4$ ,  $M = 4$ ,  $\lambda_D = 1/10$ . Thirteen major iterations (Poisson-Vlasov cycles) were computed. The profiles are in transverse planes at various distances downstream, and all lengths are normalized by the body radius. Thus,  $z$  denotes axial distance downstream, in radii, with  $z = 0$  defined as the rear surface of the pillbox (looking into the wake); and  $r$  denotes radial or transverse distance from the axis ( $r = 1$  is the body radius). The profiles of  $n_i$ ,  $n_e$ , and  $\phi$  are arranged vertically in order of increasing axial distance  $z$ . There are 8 values of  $z$ , namely,  $z = 0.2, 0.5, 1.0, 2.0, 3.0, 4.0, 5.0,$  and  $6.0$ . Each profile is constructed of 9 values of  $r$ , namely,  $r = 0, 0.1, 0.3, 0.6, 0.8, 1.0, 1.2, 1.5,$  and  $2.0$ . The outer-boundary conditions are applied at  $z = 6$  and  $r = 2$ ; for the main-body problem, the boundary condition at  $z = 6$  is the fixed one, while floating conditions are used elsewhere. The profiles consist of straight-line segments connecting the values of the functions ( $n_i$ ,  $n_e$ , or  $\phi$ ) computed at 72 grid points in the wake region.

The features of the wake structure are as follows. The near wake ( $z < 1$ ) is clearly depleted of both ions and electrons, with the ion density lower than the electron density. Further downstream the wake becomes increasingly filled in, between about  $z = 1$  and  $z = 4$ , where  $z = 4$  is the ion-Mach-number of radii

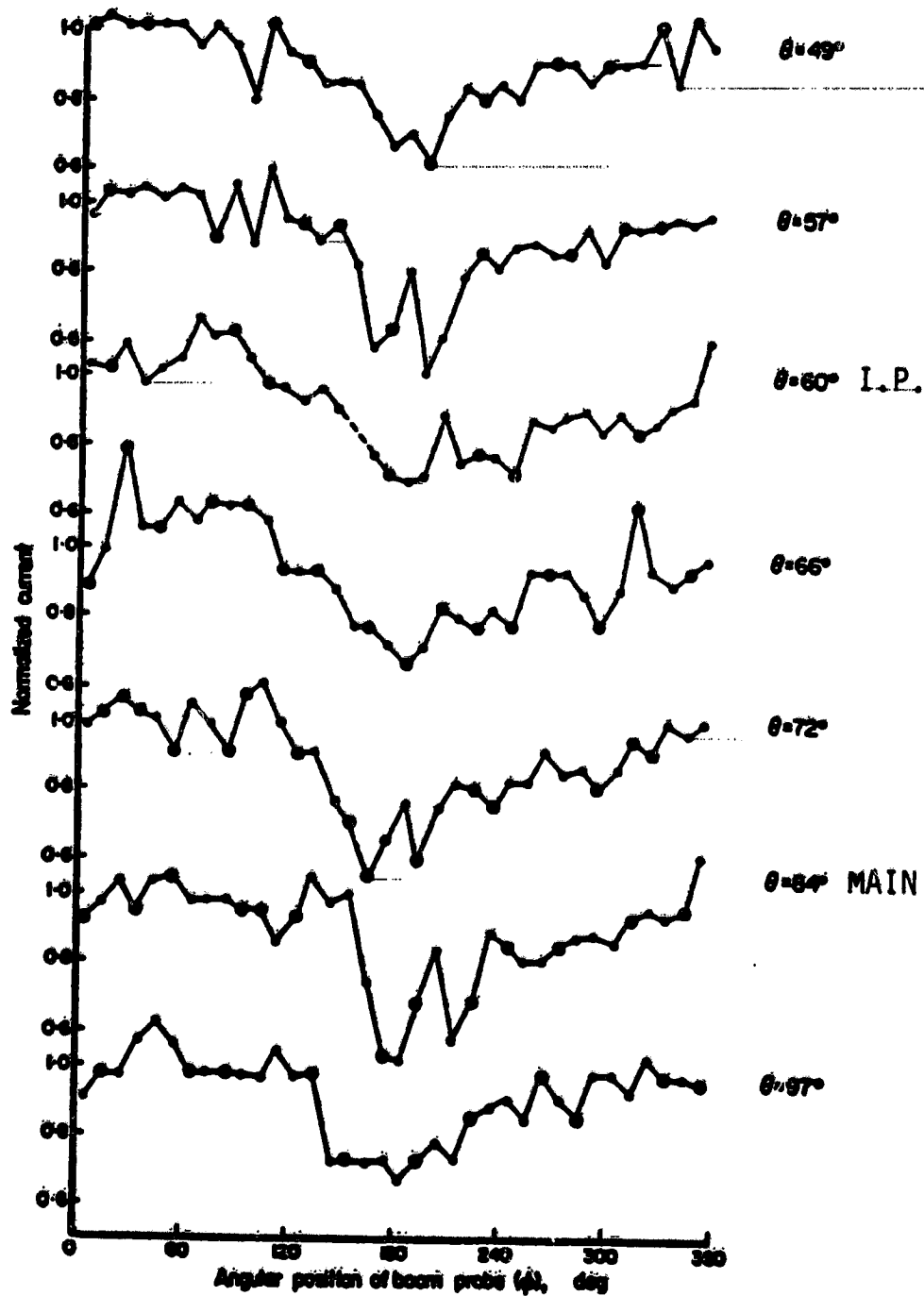


Figure 9. Normalized Electron Current versus Angular Position of the Boom Probe, for Various Spin-Orientation Angles

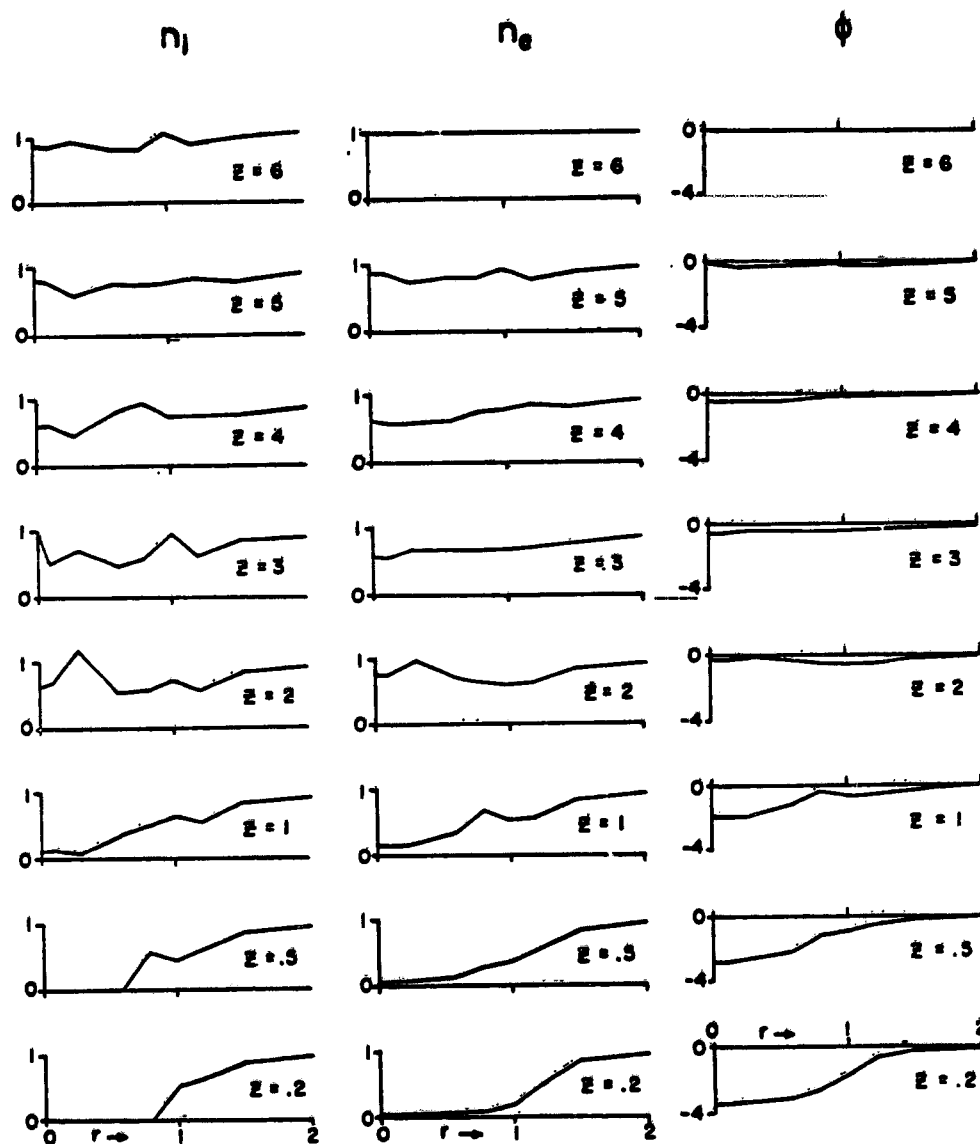


Figure 10. Ariel 1 Main Body Wake Profiles.  $\phi_0 = -4$ ,  $M = 4$ ,  
 $\lambda_D = (10)^{-1} = 0.1$

downstream. In this range of  $z$  the ion profiles tend to be relatively noisy, indicating sensitivity to numerical errors, which may in turn imply a tendency toward physical instability. The trend of the ion and electron profiles suggests a radially-inward bulk motion of the plasma within the wake as if it were a fluid wave propagating inward, piling up near the center, and bouncing out again as it moves downstream. The disturbance has essentially died away at  $z = 6$  radii downstream.

There is no well-defined central bump similar to that in the experimental data in Figure 9.

#### 4. 1. 2 ARIEL 1 ION PROBE

According to Henderson and Samir the profile in Figure 9 at  $\theta = 60^\circ$  samples the ion probe wake structure. This structure is similar to that of the main body, having a below-ambient central peak within a depleted region of about the same width as that associated with the main body. The ion probe is about 1.7 Debye lengths in radius and is biased at about 28 kT (7 volts) negative with respect to space. Hence it may be expected to produce at least a pronounced focusing effect, as is borne out by the following computed results.

Figure 11 shows transverse profiles computed for the wake of the ion probe. The notation is the same as that of Figure 10. The parameter values are  $\phi_0 = -28$ ,  $M = 4$ , and  $\lambda_D = 1/1.7$ . Ten major iterations were computed. The outer boundary at  $z = 10$  was placed sufficiently far downstream to ensure that the disturbances of interest are contained within the grid. Moreover, a floating condition is employed there as well as elsewhere. (The number of grid points was larger than in the main-body problem.)

The main features are as follows. The ion profiles at  $z = 1$  and  $z = 2$  show that a strong focusing effect occurs near the body. Further downstream, however, the disturbance dies out; there is essentially none at  $z = 8$  and beyond.

The radially-inward and outward bulk motion of the plasma as it fills the wake is again a fluid-like feature. Again, there is no persistent peak at the center of the wake as indicated by the data. If this were an isolated body, the Henderson-Samir data would imply that the peak persists far downstream to beyond a distance of 33 radii. The present theoretical calculation indicates no structure at  $z = 8$  and beyond.

#### 4. 1. 3 COMMENT ON COMPARISON OF THEORY WITH EXPERIMENT

A central bump may perhaps be generally expected on the basis of nonrigorous theoretical arguments invoking (1) electrostatic focusing effects or (2) convergence of ion streams during the filling of the wake principally at a Mach number of radii downstream, or (3) a combination of these.<sup>15</sup> However, previous theoretical calculations indicating such bumps have been deficient in some respect with regard to their rigorous applicability (for example, cold ions, infinitely-long cylinders, non-self-consistent). Similarly, there have been laboratory-simulation experiments which have indicated bumps.<sup>17</sup> However, it is presently still difficult to simulate ion transverse velocity distributions in the laboratory, and the effective ion temperature is generally too low. Hence, there does not exist thus far an unambiguous explanation of the Ariel 1 data. (Note:  $T_i$  was not measured, but was assumed here to be equal to  $T_e$ . Theoretically, bumps in the wake have been predicted for  $T_i$  less than  $T_e$ .<sup>11, 18</sup>)

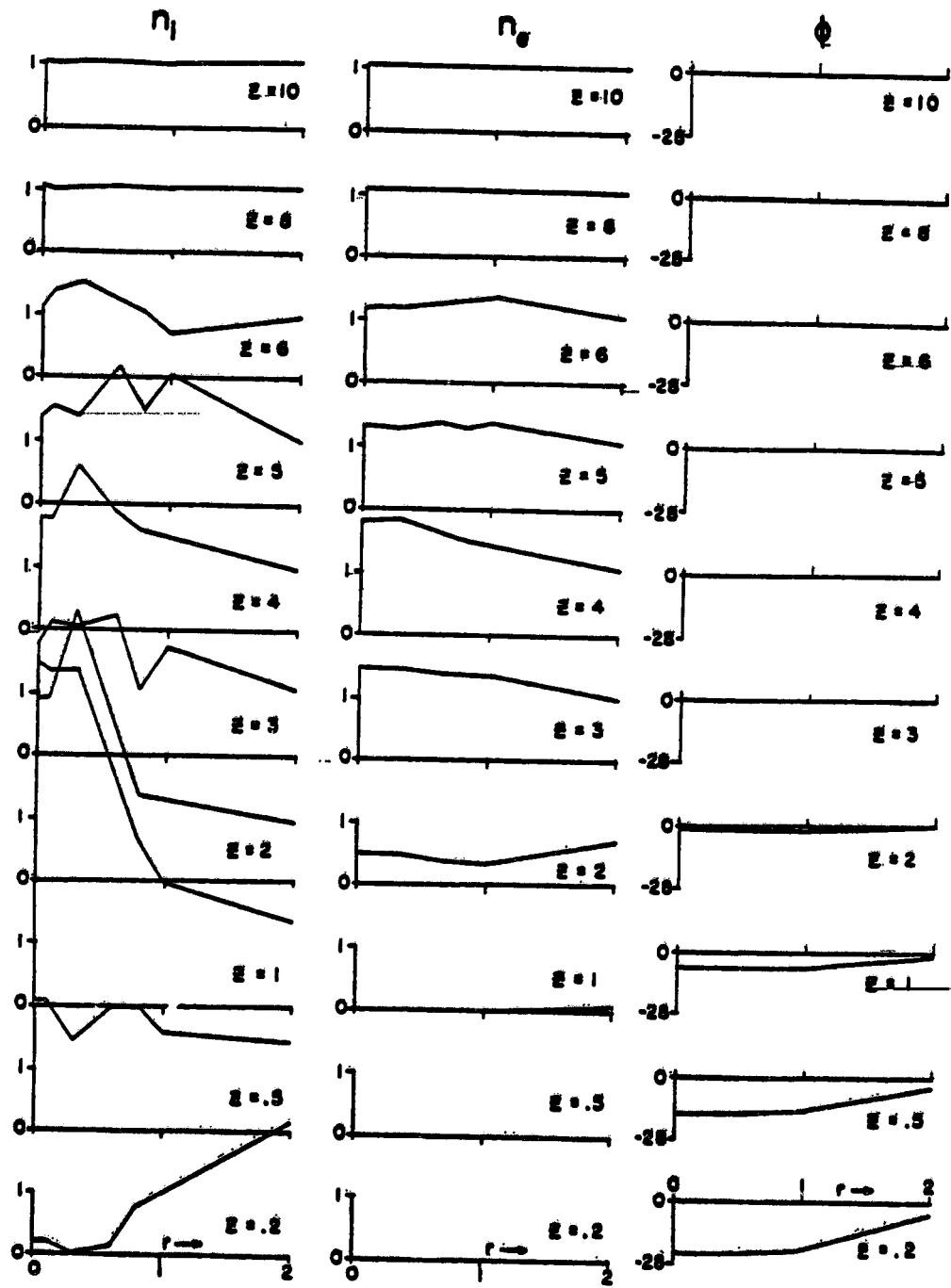


Figure 11. Ariel 1 Ion Probe Wake Profiles.  $\phi_0 = -28$ ,  $M = 4$ ,  
 $\lambda_D = (1.7)^{-1} = 0.6$

It is also of interest to note that a large body produces a central-core enhancement, as will be shown later.

#### 4.2 Explorer 31 Satellite

The results of this section were obtained in the process of computing a number of solutions to be compared with in-situ data obtained on the Explorer 31. The parameters adopted were suggested by Samir (private communication) based on 8 different passes of the Explorer 31 satellite, as listed in his paper with Jew.<sup>16</sup> A small portion of two of these cases will be discussed here, without a quantitative comparison with data, in order to illustrate a specific point.

Figure 12 shows computed electron and ion density transverse profiles in the very near wake of a body with the parameters

$$\begin{aligned}\phi_0 &= -4.3 \\ \lambda_D &= (6.9)^{-1} \\ M &= 3.4 .\end{aligned}$$

These are the parameters in the case of Curve No. 1 of Samir and Jew.<sup>16</sup> The computed profiles in Figure 12 are at  $z = 0.2$  radii downstream, that is, similar to the lowest profiles in Figure 10 where the parameters are of similar order. Here the vertical scale (normalized density) is logarithmic, as opposed to Figure 10, where it is linear. The ion densities are denoted by circles and the electron densities by squares. The principal features shown in Figure 12 are as follows. For  $r$  greater than about 0.8 radii, the ion density is higher than the electron density. Moreover, the ion density drops more abruptly in the vicinity of the "shoulder" ( $r \cong 1$ ) than the electron density. In the central wake both densities are far below normal, with the ion density about an order of magnitude below the electron density. This is the usually-expected picture of near-wake structure.

Figure 13, on the other hand, shows corresponding computational results for the case of Curve No. 4 of Samir and Jew,<sup>16</sup> where the parameters are:

$$\begin{aligned}\phi_0 &= -5.4 \\ \lambda_D &= (3.1)^{-1} \\ M &= 1.1 .\end{aligned}$$

Here, the most significant change is the lower Mach number (1.1). The curves in Figure 13 are qualitatively different from those in Figure 12. The new electron density profile is shifted downward slightly, but the new ion density profile is moved up to approximately a constant roughly equal to the normal value.

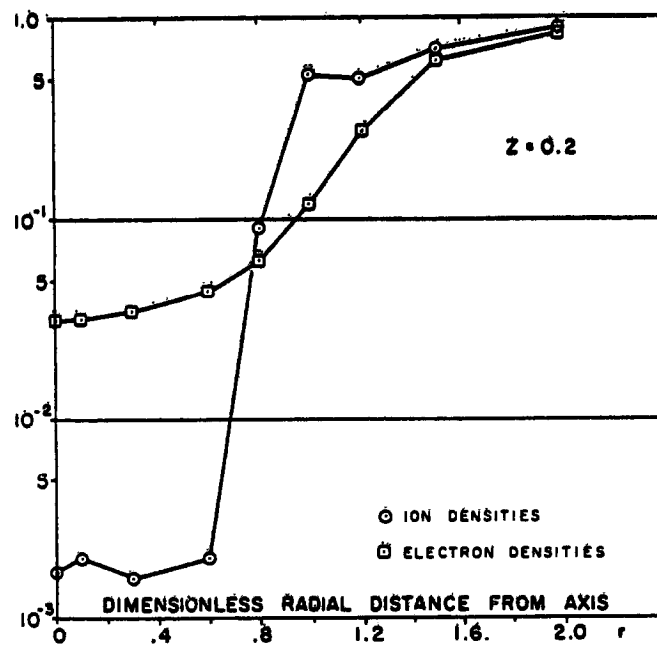


Figure 12. Explorer 31 Density Profiles, Case 1.  
 $\phi_0 = -4.3$ ,  $M = 3.4$ ,  $\lambda_D = (6.9)^{-1} = 0.145$

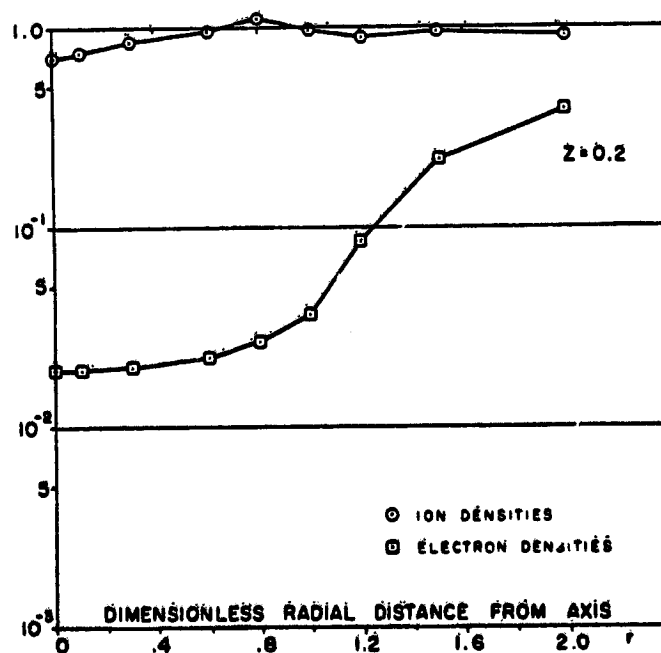


Figure 13. Explorer 31 Density Profiles, Case 4.  
 $\phi_0 = -5.4$ ,  $M = 1.1$ ,  $\lambda_D = (3.1)^{-1} = 0.32$

The fact that the ion wake density is above the electron density at all  $r$  may be unexpected from the point of view of "traditional" wake theory, but seems reasonable on the basis of Langmuir probe theory.<sup>2-5</sup> According to probe theory, a stationary negative electrostatic probe in a plasma will have adjacent to it a sheath in which the ion density exceeds the electron density. If the probe begins to move slowly relative to the plasma, one expects the sheath structure at first to be only slightly changed, with a continuation of the predominance of the ions over the electrons. At sufficiently large velocity, however, the traditional wake structure with electron domination over ions should appear as in Figure 12. The value of ion Mach number at which the transition should occur has not been predicted but can be established by additional computations of the present type.

## 5. A LARGE-BODY PROBLEM

In this section we consider the wake of a large body, 100 Debye lengths in radius.<sup>1</sup> The body is in the form of a disk oriented normal to the flow. For this case (Figures 14 and 15) the parameter values are

Figure 14

$$\phi_0 = -4$$

$$\lambda_D = (100)^{-1}$$

$$M = 4$$

Figure 15

$$\phi_0 = -4$$

$$\lambda_D = (100)^{-1}$$

$$M = 8$$

Here the parameter values differ qualitatively from those of the preceding problems in that  $\lambda_D$  is so small. This size of moving body is larger than has been previously treated by trajectory-following, that is, realistic, calculations. The results show what may be expected for the wake structure of large bodies in general. This case requires more effort (computer time and judicious selection of numerical parameters) than that of a smaller body. The solutions shown, therefore, are intended to be illustrative rather than accurate.

Six iterations, or Poisson-Vlasov cycles, were computed using the ion-density option, in which successive iterates were not mixed, starting with the neutral ion density as an initial guess. The nominal number of trajectories, 512, was used at all grid points.

The profiles of  $n_i$ ,  $n_e$ , and  $\phi$  in Figure 14 are constructed in the same way and at the same grid points as in Figure 10. Tabulated values are given in Parker.<sup>1</sup> The wake is essentially "empty" of both ions and electrons between  $z = 0$  and  $z = 1$ , and begins to fill up between  $z = 2$  and  $z = 3$ . In this way, the wake is qualitatively similar to that in Figure 10.

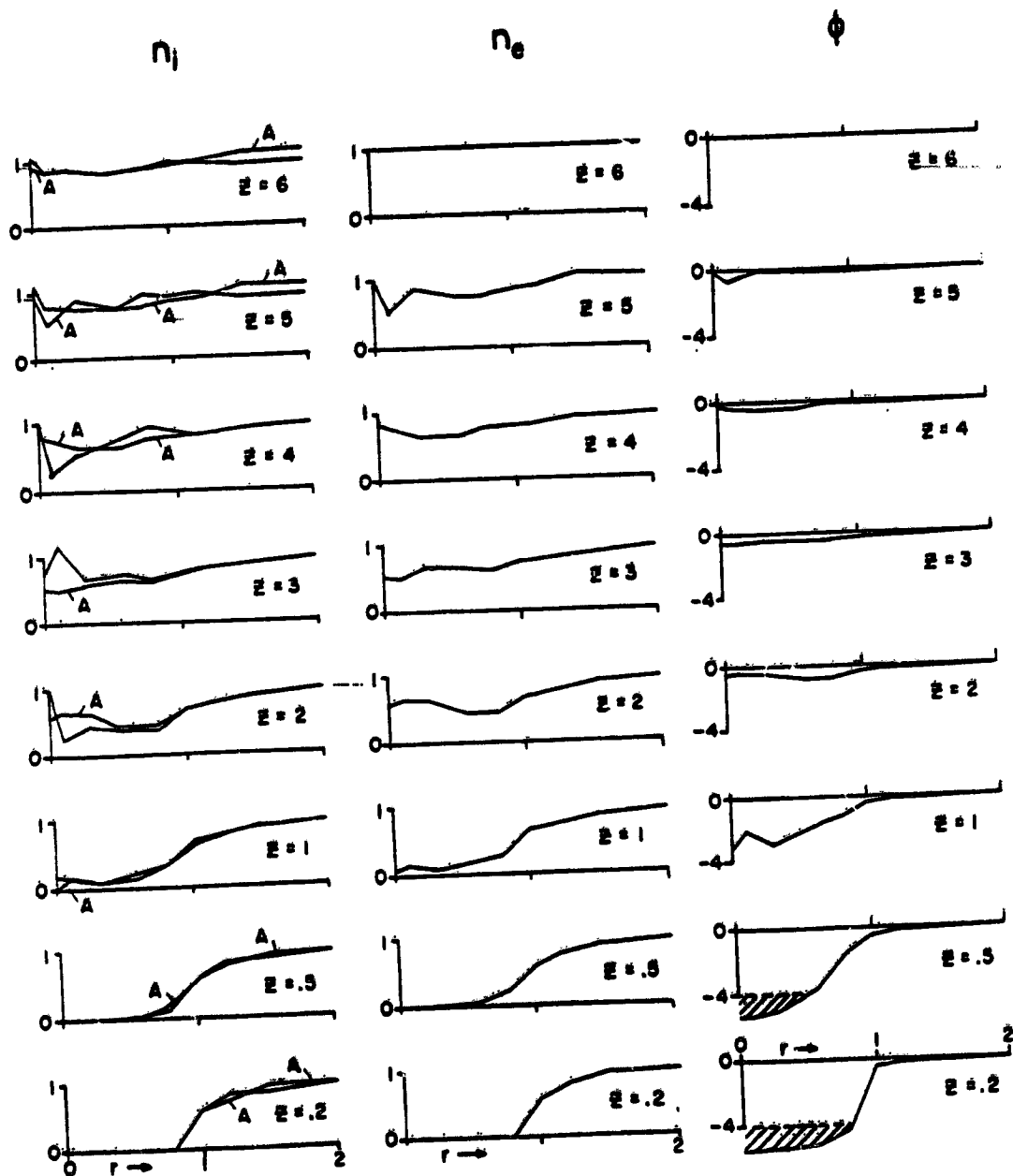


Figure 14. Large-Body Wake Profiles.  $\phi_0 = -4$ ,  $M = 4$ ,  
 $\lambda_D = (100)^{-1} = 0.01$

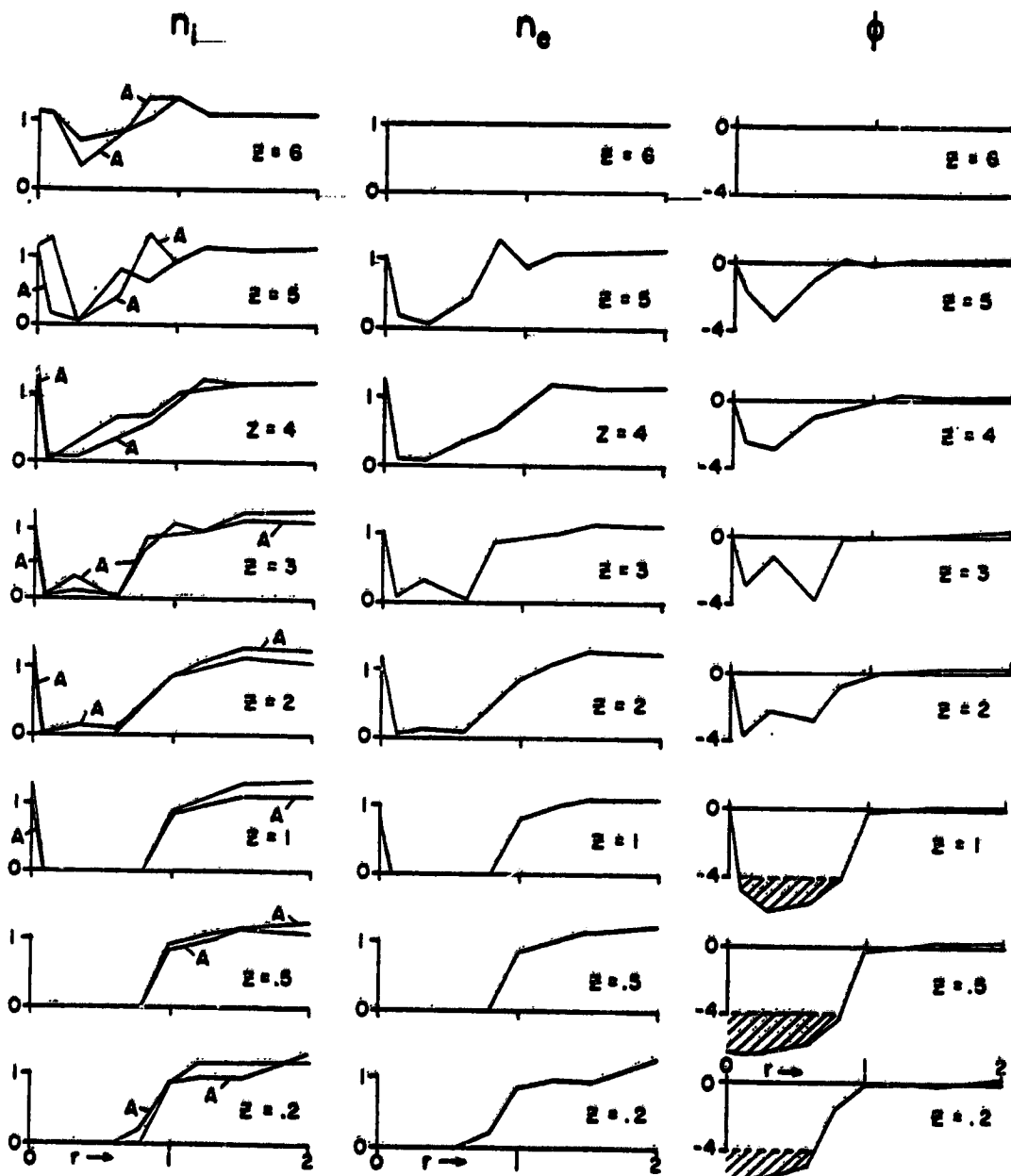


Figure 15. Large-Body Wake Profiles.  $\phi_0 = -4$ ,  $M = 8$ ,  
 $\lambda_D = (100)^{-1} = 0.01$

Two sets of ion-density profiles are shown on the left side of Figure 14, the unlabeled profiles for the 6th order (6th iteration), and the profiles labeled "A" for the 5th order. Comparison of the  $n_e$ -profiles with the 5th order  $n_i$ -profiles (labeled "A" to denote that the  $\phi$ -profiles and  $n_e$ -profiles in the figure are derived from these) indicates that the quasineutrality assumption is valid everywhere outside a cone-shaped region near the wake surface; the cone height along the axis is between 1 and 2 radii. This is in accord with expectation for a large body. Near the wake surface, however, quasineutrality is violated because the effective Debye length is large. The similarity of the  $n_i$ -profiles (labeled "A") and the  $n_e$  profiles in Figure 14 is a consequence of near-quasineutrality.

Comparison of the 5th and 6th order  $n_i$ -profiles (labeled "A" and unlabeled) in Figure 14 show that the solution is reasonably converged for  $z = 1$  and below, but that there is incomplete convergence at  $z = 2$  and beyond. The incomplete convergence and apparent structure at  $z = 2$  and beyond may be artifactual due to insufficient numerical accuracy. (No attempt was made to achieve high accuracy since this was regarded as a preliminary run.) The structure and lack of convergence are seen to extend past  $z = 5$ , so that the downstream boundary should be placed further than at  $z = 6$ .

Despite possible inaccuracies, one may infer additional physical conclusions indicated by Figure 14, namely, (1) the suggestion of a core of high (approximately ambient) density of ions and electrons on the axis, and (2) the occurrence of a potential well in the near wake, defined as a region with  $\phi$ -values below  $-4$ . The shading in the two lowest  $\phi$ -profiles denote cross-sections of this well. The wake-surface normalized fluxes are  $1.1 \times 10^{-8}$  (5th order) and  $2.4 \times 10^{-7}$  (6th order) for ions, and  $4.3 \times 10^{-3}$  for electrons. The electron current density is less than  $\exp(-4)$ , as would be expected in the presence of a potential well.

The region of wake disturbance probably extends more than 6 radii downstream, and between 2 and 3 radii in the transverse direction.

Another large-body case (Figure 15) is similar to the previous large-body case except that the Mach number is increased from  $M = 4$  to  $M = 8$ . Ten iterations were computed in which successive iterates were used without mixing, starting with uniform ambient ion density. (The latter starting condition was inadvertently different from that of the  $M = 4$  calculation which was started with the neutral ion density, but this difference should become unimportant after many iterations.) Similar statements may be made about the incompleteness of the convergence as in the  $M = 4$  case. The 9th and 10th order ion densities are labeled "A" and unlabeled, respectively. On comparing these, the convergence seems fairly good at  $z = 0.5$  and  $z = 1$ . Again, the disturbance extends beyond  $z = 5$ , so that the downstream boundary should be moved further than  $z = 6$ .

Despite inaccuracies, the consistency is such that physical conclusions may be drawn as follows. In this case, the wake is seen to remain empty further downstream than in the  $M = 4$  case. In addition, the suggestion is much stronger that there is a central core of ambient density for both ions and electrons along the axis. Moreover, the potential well is wider and longer than in the  $M = 4$  case, although the depth is about the same. The normalized wake-surface fluxes are  $7.4 \times 10^{-30}$  (9th order) and  $4.2 \times 10^{-30}$  (10th order) for ions, and  $3.7 \times 10^{-3}$  for electrons. The electron flux is slightly less than the  $M = 4$  value, and is again less than  $\exp(-4)$ .

The conical region behind the disk where quasineutrality breaks down is now longer than in the  $M = 4$  case, extending to between  $z = 4$  and  $z = 5$  along the axis.

The region of wake disturbance is probably longer than 6 radii downstream, as in the  $M = 4$  case, but may not extend beyond about 2 radii in the transverse direction.

## Acknowledgment

The author wishes to thank the National Aeronautics and Space Administration for its support of this work.

## References

1. Parker, L. W. (1976) Computation of Collisionless Steady-State Plasma Flow Past a Charged Disk, NASA CR-144159, Lee W. Parker, Inc.
2. Parker, L. W. (1976) Theory of Electron Emission Effects in Symmetric Probe and Spacecraft Sheaths, AFGL-TR-76-0294, Final Report, Lee W. Parker, Inc.
3. Parker, L. W. (1975) Computer Method for Satellite Plasma Sheath in Steady-State Spherical Symmetry, AFCRL-TR-75-0410, Final Report, Lee W. Parker, Inc.
4. Parker, L. W. (1973) Computer Solutions in Electrostatic Probe Theory, AFAL-TR-72-222, Final Report, Mt. Auburn Research Associates, Inc.
5. Laframboise, J. G. (1966) Theory of Spherical and Cylindrical Langmuir Probes in a Collisionless Maxwellian Plasma at Rest, UTIAS Report No. 100.
6. Parker, L. W. (1964) Numerical Methods for Computing the Density of a Rarefied Gas About a Moving Object, AFCRL-64-193, Allied Research Associates, Inc.

7. Parker, L. W. (1970) Theory of the External Sheath Structure and Ion Collection Characteristics of a Rocket-Borne Mass Spectrometer, AFCRL-71-0105, Mt. Auburn Research Associates, Inc.
8. Parker, L. W., and Sullivan, E. C. (1974) Iterative Methods for Plasma-Sheath Calculations, NASA TN D-7409.
9. Call, S. M. (1969) The Interaction of a Satellite with the Ionosphere, Columbia Univ. Report No. 46.
10. Fournier, G. (1971) Collisionless Plasma Flow Around a Cylinder Considering Applications to Ionospheric Probes (in French), O. N. E. R. A. Publication No. 137, Paris.
11. Martin, A. R. (1974) Numerical solutions to the problem of charged particle flow around an ionospheric spacecraft, Planet. Space Sci. 22:121-141.
12. Taylor, J. C. (1967) Disturbance of a rarefied plasma by a supersonic body on the basis of the Poisson-Vlasov equations, Planet. Space Sci. 15:155-187.
13. Grabowski, R., and Fischer, T. (1975) Theoretical density distribution of plasma streaming around a cylinder, Planet. Space Sci. 23:287-304.
14. Parker, L. W., and Whipple E. C., Jr. (1970) Theory of spacecraft sheath structure, potential, and velocity effects on ion measurements by traps and mass spectrometers, J. Geophys. Res. 75:4720-4733.
15. Henderson, C. L., and Samir, U. (1967) Observations of the disturbed region around an ionospheric spacecraft, Planet. Space Sci. 15:1499-1513.
16. Samir, U., and Jew, H. (1972) Comparison of theory with experiment for electron density distributions in the near wake of an ionospheric satellite, J. Geophys. Res. 77:6819-6827.
17. Oran, W. A., Stone, N. I., and Samir, U. (1975) The effects of body geometry on the structure in the near wake zone of bodies in a flowing plasma, J. Geophys. Res. 80:207-209.
18. Gurevich, A. V., and Dimant, Ya. S. (1975) Flow of a rarefied plasma around a disk, Geomagn. Aeron. (USSR, Engl. Transl.) 15:183-190.

## 9. Experimental Modeling of Plasma Flow Interactions

W. A. Oran and N. H. Stone  
NASA Marshall Space Flight Center  
Huntsville, Alabama

### Abstract

The rationale for conducting ground-based laboratory studies (simulating aspects of the interaction between spacecraft and the environmental space plasma) will be discussed. The discussion will be in the context of utilizing these ground-based facilities to complement both in-situ and theoretical studies of the disturbed zone around spacecraft in orbit. Data, which were taken in the "Plasma Wind Tunnel" facility at MSFC, will be presented showing some of the advantages and disadvantages of utilizing laboratory facilities. Finally, some discussion will be given on modifying presently available systems in order to better model aspects of the satellite environment in geosynchronous orbit.

Contents

1. Introduction	370
2. Theory	372
3. Results and Discussion	377
4. Conclusions	385
Acknowledgments	386
References	386

## 10. Prediction of Large Negative Shaded-Side Spacecraft Potentials

S. M. L. Prokopenko and J. G. Laframboise  
 Physics Department  
 York University  
 Toronto, Canada

### Abstract

A calculation by Knott, for the floating potential of a spherically symmetric synchronous-altitude satellite in eclipse, has been adapted to provide simple calculations of upper bounds on negative potentials which may be achieved by electrically isolated shaded surfaces on spacecraft in sunlight. To investigate geometrical effects, we have replaced Knott's use of the orbit-limited ion current expression for a sphere, by that for an infinite cylinder. Large (~60 percent) increases in predicted negative shaded-side potentials are obtained as a result. To investigate "effective-potential barrier" or "angular-momentum selection" effects due to the presence of less-negative sunlit-side or adjacent-surface potentials, we have also replaced these expressions by the ion random current, which is a lower bound for convex surfaces when such effects become very severe. Further large increases in predicted negative potentials are obtained, amounting to a doubling in some cases. Depending on surface properties and incident energy distributions, values exceeding -20 kV are now predicted, in good agreement with ATS-6 observations of potentials reaching -19 kV, as reported by Whipple. For isolated surfaces in shaded cavities, even more negative values may be reached. In some conditions, two distinct floating potentials exist, leading to the possibility of "bifurcation phenomena" in real situations.

368  
 PRECEDING PAGE BLANKS NOT FILMED

## I. INTRODUCTION

The performance of many satellites in synchronous orbit has been degraded by anomalous events which include frequent spurious spacecraft commands and in some cases permanent damage. These events invariably appear to involve electrical discharges caused by differential charging of spacecraft surfaces to large relative potentials. The latter condition in turn is known to result from the relatively large average energies (up to a few keV) of the charged particle environment at synchronous orbit altitude, particularly in disturbed magnetospheric conditions. Since photoelectron emission from sunlit surfaces tends to compensate for incident electron fluxes, thereby holding sunlit-side surface potentials close to space potential in most cases, an estimate of differential charging magnitudes can be obtained by simply calculating floating potentials of electrically isolated shaded surfaces, relative to space potential. In the present work, we have attempted to obtain upper bounds on such potentials, which in cases of interest are usually highly negative, because these bounds constitute "worst cases" for design purposes, and also because unlike more exact calculations, they can be obtained from simple current balance calculations. Furthermore, it is sufficient to consider local current balance only, because this corresponds to an electrically isolated surface element, which is also a "worst case" for differential charging. To calculate these bounds, we have extended a calculation by Knott,<sup>1</sup> of the floating potential of a spherically symmetric synchronous-altitude satellite in eclipse. To investigate geometrical effects, we have replaced Knott's use of the Mott-Smith and Langmuir<sup>2</sup> orbit-limited current expression for collection of Maxwellian ions by a unipotential sphere, by the corresponding expression for an infinite cylinder; both expressions have been shown<sup>3</sup> to be upper bounds for collisionless ion collection as a function of local surface potential, for three- and two-dimensional collectors, respectively, regardless of collector shape, sheath potential, or potential of other parts of the collector. This replacement causes a large decrease in ion collection and a correspondingly large increase in negative shaded-side floating potentials (Section 3). Another important ion-current restriction may be caused by "effective-potential barrier"<sup>3, 4, 5</sup> or "angular-momentum selection" effects, in which the presence of less-negative sunlit-side potentials produces dipole and higher moments in the sheath potential,<sup>6</sup> causing steepening and contraction of the potential well surrounding the shaded side (Figure 1). A similar steepening effect will also occur if an isolated shaded surface element is surrounded by adjacent shaded surfaces which for any reason have less negative potentials (Figure 2). The most extreme possibility would be a potential profile which was equal to space potential almost to the spacecraft surface, then fell discontinuously to surface potential. This limit would correspond to a "planar sheath" situation in which the ion collection

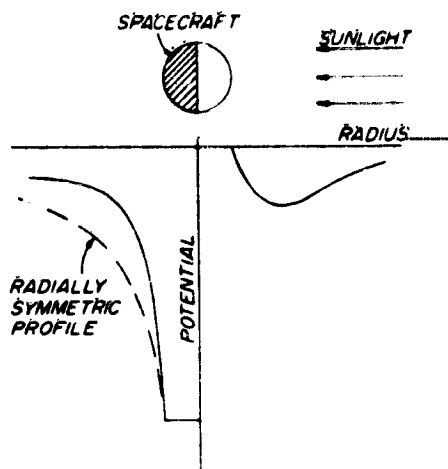


Figure 1. Steepling of Shaded Side Potential Profile for a Spacecraft with an Insulated Surface, after Föhleson<sup>6</sup>

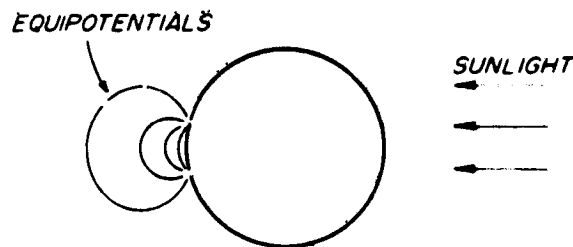


Figure 2. Conductive Spacecraft with Shaded Isolated Surface Patch

on any shaded convex surface would be given by just the ion random flux. This amounts to a further ion current restriction which produces even larger increases in negative shaded-side floating potentials (Section 3). This situation corresponds to a velocity-space cutoff boundary for incident ions which is "one-dimensional;" the cutoff boundaries corresponding to spherical and infinite cylindrical collectors are, respectively, "three-dimensional" and "two-dimensional"<sup>3</sup> (Section 2).

We also show (Section 3) that if shaded cavities containing isolated surfaces exist on a spacecraft, negative potentials on such surfaces may surpass even these predictions. In some cases, more than one possible floating potential results from the calculation; this implies the possibility of "bifurcation phenomena" in which adjacent isolated surfaces of the same material may arrive at different floating potentials as a result of differences in their charging histories (Section 3).

We have also modified Knott's calculation in another way, by including currents due to electron backscattering (Section 2). These currents will tend to decrease net electron collection, thereby making floating potentials less negative than otherwise (Section 3). A process not included by either Knott or ourselves is secondary electron emission due to ion impacts; this will also tend to make floating potentials less negative.

## 2. THEORY

The ambient electron energy distributions used in the present work are a model quiet-time spectrum (Knott,<sup>1</sup> Figure 1) and a model disturbed spectrum (Knott,<sup>1</sup> Figure 2b) based on measurements by Shield and Frank,<sup>7</sup> and DeForest and McIlwain,<sup>8</sup> respectively. Both of these distributions, and also the ambient ion distribution, are assumed isotropic. The disturbed spectrum was chosen from the three used by Knott because it has a higher average electron energy (~10 keV) than the others. In using it, we have changed it as follows: in the energy ranges  $0.5 \text{ keV} \leq E \leq 10 \text{ keV}$  and  $10 \text{ keV} \leq E \leq 40 \text{ keV}$ , we have replaced Knott's differential energy spectrum by  $\sqrt{2} \times 10^8 E^{-1/2}$  and  $\sqrt{2} \times 10^9 E^{-3/2}$  electrons/cm<sup>2</sup> sec sr keV, respectively, where E is energy. These relations are simpler than those indicated by Knott, and they also bring the model spectrum into closer agreement with the data on which it is based. We therefore believe that they may have been the ones actually used by Knott, and that the corresponding parts of Figure 2b in his paper may be incorrectly plotted. For any spacecraft surface having a negative potential  $\phi_s < 0$ , or for a three-dimensional (for example, spherical) surface having  $\phi_s > 0$ , the orbit-limited flux (particle current density)  $J_e$  of ambient electrons is given by:<sup>3</sup>

$$J_e = \int f v_n d^3 v = \int_{\max(0, -e\phi_s)}^{\infty} (1 + e\phi_s/E) (dJ_{e0}/dE) dE \quad (1)$$

where e is magnitude of unit electronic charge,  $\phi_s$  is local surface potential,  $dJ_{e0}/dE$  is the ambient energy-differential flux incident on one side of an arbitrarily oriented surface element, and  $v_n$  is the velocity component normal to the same surface element.  $dJ_{e0}/dE$  is  $\pi$  times the energy-differential flux per steradian used by Knott,<sup>1</sup> and is given in terms of the ambient electron velocity distribution  $f = d^3 N_{\infty} / d^3 v$  by the relation  $dJ_{e0}/dE = 2\pi f E / m_e^2$ , where  $m_e$  is electron mass and  $N_{\infty}$  is ambient ion or electron number density. Since f is isotropic,  $f \equiv f(E)$ . The factor  $(1 + e\phi_s/E)$  in Eq. (1) appears to have been neglected by Knott, and may account for some minor discrepancies between his results and ours (Section 3). The presence of this factor leads to a divergent integration in Eq. (1) if  $\phi_s > 0$ , unless  $dJ_{e0}/dE \rightarrow 0$  as  $E \rightarrow 0$ , that is,  $f(E)$  remains finite as  $E \rightarrow 0$ . This implies that the differential fluxes in Knott's Figures 1-3 must approach zero linearly with E at E values smaller than those shown in these figures. In the present work we have instead used a less-realistic sharp cutoff at 1 eV; this may slightly affect our results for positive floating potentials in Section 3. We have also introduced a sharp upper cutoff at 50 keV in the quiet-time spectrum, also in order to avoid a

divergent integration when calculating average energy for use in backscattering calculations (see below).

In order to obtain the orbit-limited electron flux expression for an arbitrary cylindrical collector, the lower integration limit in Eq. (1) must be replaced by the two-dimensional velocity-space cutoff boundary  $E_n = \max(0, -e\phi_s)$ , where  $E_n$  is the total energy of transverse motion  $\frac{1}{2} m_e (v_x^2 + v_y^2) - e\phi$ , and we have chosen a  $z$  coordinate perpendicular to the cylinder cross-section. If  $\phi_s > 0$ , this complicates the integration in Eq. (1), which may then be done in either of two ways. The first [Laframboise and Parker,<sup>3</sup> Eq. (6)] is to convert Eq. (1) into an integration using cylindrical coordinates in velocity space. This method has the disadvantage that the velocity distribution must be integrated over  $v_z$  in order to convert it into a distribution of transverse velocities. An alternate method<sup>2, 9</sup> is as follows. We choose rectangular coordinates  $(v_n, v_t, v_z)$  in velocity space, such that  $v_n$  is the velocity component in the inward normal direction at the collector surface. The  $v_t$  and  $v_z$  become tangential coordinates, with  $v_t$  in the plane of the cylinder cross-section. We then transform to spherical coordinates  $(v, \theta, \psi)$  with  $v_z$  as polar axis. Then:  $v_z = v \cos \theta$ ,  $v_n = v \sin \theta \cos \psi$ , and  $v_t = v \sin \theta \sin \psi$ . For  $\phi_s > 0$ , Eq. (1) is then replaced by:

$$\begin{aligned}
 J_e &= \int f v_n d^3 \underline{v} \\
 &= 2 \int_{E=0}^{E=e\phi_s} \int_{\psi=-\pi/2}^{\psi=\pi/2} \int_{\theta=\text{Arc sin}[e\phi_s/(E+e\phi_s)]}^{\theta=\pi/2} f(E)(v \sin \theta \cos \psi) \\
 &\quad \times (v^2 \sin \theta \, dv \, d\theta \, d\psi) \\
 &= \int_0^{\infty} \frac{2}{\pi} \left[ \text{Arc sin} \left( \frac{E}{E+e\phi_s} \right)^{1/2} + \frac{(Ee\phi_s)^{1/2}}{E+e\phi_s} \right] \left( 1 + \frac{e\phi_s}{E} \right) \frac{dJ_{eo}}{dE} \, dE \quad (2)
 \end{aligned}$$

In comparison with Eq. (1), we see that the integrand in Eq. (2) contains an extra, energy-dependent weighting factor, which arises from integration of  $v_n$  over the fractional solid angle over which ambient electrons can reach the collector at each energy.

A similar procedure is advantageous in obtaining the one-dimensional (Section 1) orbit-limited flux expression. In this case, the lower limit in Eq. (1) must be replaced by:  $E_n = \max(0, -e\phi_s)$ , where  $E_n = \frac{1}{2} m_e v_n^2 - e\phi$ . This time

we transform  $(v_x, v_y, v_z)$  to spherical coordinates  $(v, \theta, \psi)$  with  $v_x$  as polar axis. For  $\phi_s > 0$ , Eq. (1) is now replaced by:

$$J_e = \int_{E=0}^{\infty} \int_{\theta=0}^{\theta = \text{Arc cos}[e\phi_s/(E+e\phi_s)]^{1/2}} f(E)(v \cos \theta)(2\pi v^2 \sin \theta \, dv \, d\theta) \\ = \int_0^{\infty} \frac{dJ_{e0}}{dE} \, dE \quad (3)$$

independently of collector potential, as expected.

The corresponding expressions for ion flux  $J_i$  are simpler because the ions are assumed to be Maxwellian. Corresponding to the three-, two-, and one-dimensional velocity-space cutoffs described above, we obtain, respectively,<sup>2,3</sup> for ion-attracting surface potentials  $\chi_{is} > 0$ :

$$J_i = J_{i0} \begin{cases} (1 + \chi_{is}) & (4) \\ [2(\chi_{is}/\pi)^{1/2} + \exp(\chi_{is}) \text{erfc}(\chi_{is}^{1/2})] & (5) \\ (1) & (6) \end{cases}$$

where  $\chi_{is} = -e\phi_s/kT_i$ ,  $k$  is Boltzmann's constant,  $T_i$  is ion temperature and  $J_{i0}$  is the ion random flux  $N_{\infty}(kT_i/2\pi m_i)^{1/2}$ . For ion-retarding surface potentials  $\chi_{is} < 0$ , we obtain:

$$J_i = J_{i0} \exp(\chi_{is}) \quad (7)$$

We have assumed<sup>1</sup> that  $T_i = 1$  keV, and that the random ion to electron flux ratio  $J_{i0}/J_{e0} = 0.025$ .

For the secondary electron fractional yield  $\delta(E)$ , we have used, following Knott,<sup>1</sup> the relation of Sterngläss:<sup>10</sup>

$$\delta(E) = 7.4 \delta_{\max} (E/E_{\max}) \exp[-2(E/E_{\max})^{1/2}] \quad (8)$$

We have used the same selection of surface materials (Section 3) as that appearing in Table 1 of Knott,<sup>1</sup> for which the values of  $\delta_{\max}$  and  $E_{\max}$  were obtained from Gibbons<sup>11</sup> and Hächénberg and Brauer.<sup>12</sup>

The process of electron backscattering, which was not included in Knott's calculations, becomes important at incident electron kinetic energies larger than

those for which secondary emission is dominant. For the backscattered electron fractional yield  $\eta$ , we have fitted the results of Sternglass<sup>13</sup> with a relation of the form:

$$\eta(E) = AE + BE^{1/2} + C \quad (9)$$

where the coefficients A, B, and C are functions of the atomic number Z of the surface material. We have evaluated A, B, and C for each surface material considered (Section 3) by substituting Sternglass' values of  $\eta$  at 1, 3, and 5 keV, into Eq. (9). In all cases,  $\eta$  is a very slowly varying function of E. For compound surface materials, we have assumed that each atomic constituent contributes an independent backscattered flux proportional to its relative concentration. There exist more recent measurements of  $\eta$ <sup>14, 15</sup> which give generally larger values than those of Sternglass,<sup>13</sup> especially for electrons having near-tangential incidence. However, we have found these results to be too fragmentary for our purposes, and we have therefore used Sternglass' results throughout. Presumably we have therefore underestimated  $\eta$ , and our predicted floating potentials in Section 3 will therefore be slightly more negative than more realistic corresponding values.

When  $\phi_s > 0$ , not all secondary and backscattered electrons will escape. To calculate flux escaping, we assume<sup>13, 16</sup> for ease of calculation, that both secondary and backscattered electrons are emitted with Maxwellian velocity distributions having thermal energies

$$E_{\text{sec}} = kT_{\text{sec}} = 1 \text{ eV}, \text{ and } E_{\text{scat}} = kT_{\text{scat}} = (0.45 + 2 \times 10^{-3}Z)\bar{E} \text{ eV},$$

respectively, regardless of the form of the incident velocity distribution. Here,  $\bar{E}$  is the average incident electron energy. We further assume that escape of emitted electrons is orbit-limited, that is, that no barriers of effective potential<sup>3, 4, 5</sup> or negative barriers of electric potential exist on the shaded side. Fahleson<sup>6</sup> has pointed out that such barriers are likely to exist on the sunlit side independently of any space-charge effects, if substantial shaded-sunlit differences exist in  $\phi_s$ . The expressions for the escaping secondary and backscattered fluxes  $J_{\text{sec}}$  and  $J_{\text{scat}}$  therefore are:

$$J_{\text{sec}} = \int_{-e\phi_s}^{\infty} \delta(E + e\phi_s)(1 + e\phi_s/E)(dJ_{e_0}/dE) dE \quad (10)$$

$$J_{\text{scat}} = \int_{-e\phi_s}^{\phi} \eta(E + e\phi_s)(1 + e\phi_s/E)(dJ_{e0}/dE) dE \quad (11)$$

If  $\phi_s < 0$ . If  $\phi_s > 0$ , the three-, two-, and one-dimensional cases must be considered separately. We define  $\chi_{\text{sec}} = e\phi_s/kT_{\text{sec}}$  and  $\chi_{\text{scat}} = e\phi_s/kT_{\text{scat}}$ . For brevity, we consider only the secondary fluxes; the corresponding results for backscattered fluxes may be obtained by replacing  $\delta$  by  $\eta$  and  $\chi_{\text{sec}}$  by  $\chi_{\text{scat}}$  throughout. If  $J_s$  is the emitted flux of secondaries, then their velocity distribution at the surface is  $f_s = (J_s/2\pi)(m_e/kT_{\text{sec}})^2 \exp(-\frac{1}{2} m_e v^2/kT_{\text{sec}})$ . In the three-dimensional case, the cutoff condition for their escape is  $E = \frac{1}{2} m_e v^2 - e\phi_s > 0$ . We redefine  $v_n$  as velocity component in the outward normal direction, and we use spherical coordinates as defined in connection with Eq. (3). We obtain, for the escaping secondary flux:.....

$$\begin{aligned} J_{\text{sec}} &= \int f_s v_n d^3 \underline{v} \\ &= \frac{J_s}{2\pi} \left( \frac{m_e}{kT} \right)^2 \int_{E=0}^{\infty} \int_{\theta=0}^{\pi/2} \exp(-\frac{1}{2} m_e v^2/kT_{\text{sec}}) (v \cos \theta) (2\pi v^2 \sin \theta dv d\theta) \\ &= (1 + \chi_{\text{sec}}) \exp(-\chi_{\text{sec}}) \int_0^{\phi} \delta(E + e\phi_s)(1 + e\phi_s/E)(dJ_{e0}/dE) dE \quad (12) \end{aligned}$$

The factor  $(1 + \chi_{\text{sec}})$  is noteworthy, because it is specific to three-dimensional, as opposed to planar, sheath geometry. In the two-dimensional case, the cutoff condition for escape is  $\frac{1}{2} m_e (v_n^2 + v_t^2) - e\phi_s > 0$ , and the convolution integral for  $J_s$  contains the extra weighting factor which appears in Eq. (2). It is convenient to use spherical coordinates as defined in connection with Eq. (2). We obtain:

$$\begin{aligned}
J_{sec} &= \left[ 2(\chi_{sec}/\pi)^{1/2} + \exp(\chi_{sec}) \operatorname{erfc}(\chi_{sec}^{1/2}) \right] \exp(-\chi_{sec}) \\
&\times \int_0^{\infty} \frac{2}{\pi} \left[ \operatorname{Arc sin} \left( \frac{E}{E + e\phi_s} \right) + \frac{(Ee\phi_s)^{1/2}}{E + e\phi_s} \right] \left( 1 + \frac{e\phi_s}{E} \right) \delta(E + e\phi_s) \\
&\times \frac{dJ_{eo}}{dE} dE .
\end{aligned} \tag{13}$$

In the one-dimensional case, the escape condition is  $\frac{1}{2} m_e v_n^2 - e\phi_s > 0$ , and we again use spherical coordinates as defined in connection with Eq. (3). We obtain:

$$J_{sec} = \exp(-\chi_{sec}) \int_0^{\infty} \delta(E + e\phi_s) (dJ_{eo}/dE) dE . \tag{14}$$

The floating potential(s) of an isolated shaded surface element is (are) now given by the zero(s) of the function:

$$J_{net} = J_i - J_e + J_{sec} + J_{scat} . \tag{15}$$

### 3. RESULTS AND DISCUSSION

Table 1 shows floating potential values obtained by numerical solution of the equation  $J_{net} = 0$ , where  $J_{net}$  is given by Eq. (15) and we have assumed  $J_{scat} = 0$  in order to duplicate the physical situation of Knott,<sup>1</sup> whose results are shown in parentheses. We see that our results show qualitative but not quantitative agreement with his. Possible reasons for the disagreement are: (1) Knott appears to have solved the current balance equation graphically rather than numerically; (2) wherever his solution indicates a floating potential more negative than -3000 V, he has listed the result simply as "< -3000 V"; (3) wherever he has obtained a positive floating potential, he has listed it simply as "+5 V" whereas we have calculated it using the assumptions made in Section 2; (4) as mentioned following Eq. (1), his expression for incident electron flux may contain an error. The most important feature of Table 1 is the very large floating potentials which are evident in disturbed conditions in the presence of the two- and one-dimensional velocity-space cutoffs. The dramatic differences which exist among these results are

Table 1. Floating Potentials of Shaded Surfaces of Synchronous-Altitude Spacecraft, Using the Same Surface Properties and Incident Spectra as Assumed by Knott, with Three-, Two-, and One-Dimensional Velocity Space Cutoffs Corresponding to Orbit-Limited Ion Collection in Spherical, Infinite Cylindrical and Planar Symmetries, Respectively. Results in parentheses are from Table 1 of Knott. Backscattering is not included.

Material	Surface Data for Secondary Electron Emission		Spectrum 1 "Quiet"			Spectrum 2b "Disturbed"		
	$\delta_{max}$	$E_{max}$ (eV)	Floating Potential (volts)			Floating Potential (volts)		
			3-dimen.	2-dimen.	1-dimen.	3-dimen.	2-dimen.	1-dimen.
Gold	1.45	800	-890 (-800)	-1470	-4690	-6600 (<-3000)	-11,440	-21,490
Aluminum	0.97	300	-1690 (-2150)	-2610	-6390	-7410 (<-3000)	-12,510	-22,920
Aluminum with Oxide Coating	2.60	300	+0.49(+5) or -342 * or -1260	+0.50 or -326 * or -2100	+0.50 or -300 * or -5810	-7150 (<-3000)	-12,200	-22,560
Quartz	2.50	420	+0.37 (+5)	+0.37 or -494 * or -1570	+0.37 or -405 * or -5210	-6880 (<-3000)	-11,870	-22,130
Aquadag	0.75	350	-1700 (-2140)	-2620	-6400	-7410 (<-3000)	-12,510	-22,920
Beryllium Copper	2.20	300	+0.33(+5) or -228 * or -1390	+0.33 or -223 * or -2250	+0.33 or -211 * or -5960	-7220 (<-3000)	-12,280	-22,650
Beryllium Copper Activated	5.00	400	+1.1 (+5)	+1.1	+1.1	+0.04(+5) or -280 * or -6180	+0.17 or -278 * or -11,010	-0.17 or -275 or -21,200
No Secondary Electrons	-	-	-1870	-2840	-6690	-7550	-12,690	-23,130

\*Unstable

evidence that spacecraft geometry and sheath potential shape are important influences in determining floating potentials. It is important to note that as floating potential becomes more negative, it also becomes more sensitive to the presence of small amounts of high-energy electrons. This means that if a spacecraft should encounter conditions that are "more disturbed" than those given by Knott's spectrum 2b, the values in Table 1 most likely to be significantly exceeded are those for the one-dimensional cutoff. This implies that for design purposes in which worst-case information is desired, it is important to do calculations with the "most disturbed" electron spectra available.

In obtaining these results, we have made no attempt to calculate the time needed to approach the steady-state conditions which they represent. In general, the most negative potentials correspond to a balance between the smallest currents, and will therefore involve the longest charging times.

Also evident in Table 1 are situations in which the current-voltage characteristic of the surface has three roots. For these to occur, it is necessary that  $\delta_{\max}$  be substantially greater than one, and that the incident spectrum contain a sufficient proportion of electrons in the energy range where secondary emission is a maximum. The center root never represents a possible floating potential, because it is "unstable" in the sense that a small change in surface potential would cause a net current collection of a sign which would drive the surface potential away from this root to one on either side. A further consequence of such a situation is discussed below.

Table 2 includes the further addition of backscattered electron flux (Section 2) and therefore represents a more realistic physical situation. In most cases, the net effect of backscatter is a moderate reduction of negative floating potentials. In some cases, the reduction is large, as in the case of a gold surface exposed to the "quiet" spectrum. In several other cases, all associated with the quiet spectrum, backscattering changes a multiple-root to a single-root situation. As indicated in Section 2, we have probably underestimated backscattered fluxes, and we have also (Section 1) ignored secondary electron emission caused by ion impacts. Both of these effects would tend to further reduce negative potentials. However, such changes are likely to be small. The results in Table 2 should probably be regarded as consistent with observations of potentials reaching -19 kV on the ATS-6 spacecraft, as reported by Whipple.<sup>17</sup>

0-5

Table 2. Floating Potentials of Shaded Surfaces of Synchronous-Altitude Spacecraft, Using the Same Surface Properties and Incident Spectra as Assumed by Knott, 1 with Three-, Two-, and One-Dimensional Velocity Space Cutoffs Corresponding to Orbit-Limited Ion Collection in Spherical, Infinite Cylindrical and Planar Symmetries, Respectively. Electron backscattering is included

Surface Data for Backscattered Electron Emission		Spectrum 1 "Quiet"			Spectrum 2b "Disturbed"		
Material	Emission Coefficient $\eta$ (5000 eV) (Sternglass 14)	Floating Potential (volts)			Floating Potential (volts)		
		3-dimen.	2-dimen.	1-dimen.	3-dimen.	2-dimen.	1-dimen.
Gold	0.42	-28.0	-26.1	-28.6	-3570	-6520	-15,450
Aluminum	0.16	-1370	-2060	-5180	-6610	-11,250	-21,570
Aluminum with Oxide Coating	0.18	+0.68	+0.68 or -723 * or -1010	+0.68 or -490 * or -4210	-6200	-10,690	-20,920
Quartz	0.18	+0.55	+0.55	+0.55 or -922 * or -3190	-5860	-10,240	-20,380
Aquadag	0.08	-1560	-2390	-5900	-7090	-12,010	-22,350
Beryllium-Copper	0.31	+0.64	+0.64	+0.64 or -522 * or -3420	-5710	-9870	-19,830
Beryllium-Copper Activated	0.31	+1.4	+1.4	+1.4	+0.41 or -908 * or -3910	+0.54 or -843 * or -7520	+0.54 or -776 * or -17,580
No Secondary or Backscattered Electrons	-	-1870	-2040	-6690	-7550	-12,690	-23,130

\* Unstable

Figures 3-7 show current-voltage characteristics for some of the situations in Tables 1 and 2. Figure 3 shows a "typical" single-root situation in which secondary and backscatter contributions do not change the general shape of the net current curve. Figure 4 shows the above-mentioned case of gold exposed to the quiet spectrum, in which the backscatter contribution changes a large predicted negative floating potential to a much smaller value. Figure 5 shows a triple-root situation. Figure 6 shows the disappearance of a triple-root situation because of backscatter. In Figure 7, secondary electron current is sufficient by itself to prohibit a negative floating potential.

We now examine situations which may arise in the case of spacecraft which have shaded cavities containing electrically isolated interior surfaces. Figure 8 shows an idealization of such a spacecraft. We wish to show that the effects of surface concavity may cause ion collection to be reduced more than net electron collection at an interior point such as B, relative to an exterior point A; such a situation would result in floating potentials more negative than those of Table 2. To demonstrate this possibility, we first note that in the presence of an isotropic ambient plasma, incident fluxes to any surface depend only<sup>3</sup> on the locations, in velocity space, of the cutoff boundaries inside of which the orbits of ambient particles can connect "from infinity" to the surface. Figure 8 shows a set of the associated "cutoff orbits." We see from Figure 8 that the included angle between cutoff orbits has been reduced in going from A to B for ions but not for electrons, for which orbits tangential to the surface are shown as reaching both A and B. Accordingly, the incident ion current contribution for the energy shown will also be reduced, but the electron contribution will not. This picture is invalid for higher-energy electrons at B, whose orbits are straighter and will have a greater tendency to connect back to the interior surfaces of the cavity. Even though such higher-energy orbits will generally have lower populations than lower-energy orbits, it is not clear whether the relative current reduction at B will be greater for ions or for electrons. However, this argument is intended to demonstrate only the possibility that the bounds in Table 2 will be exceeded. On the other hand, this possibility will be enhanced by the effects of secondary and backscattered electrons, which will tend to be recollided inside any cavity, rather than escaping into space, thus tending to increase net electron collection and driving floating potentials more negative. This effect will be strongest for backscattered electrons because their higher emission energies will cause them to have straighter orbits. To draw firm conclusions will require detailed numerical simulation. An additional feature of cavities is their generally higher outgassing pressures, which will increase any tendencies for arcing to occur. More negative floating potentials may also result if the ambient electron distribution contains beam-like constituents<sup>18</sup> which happen

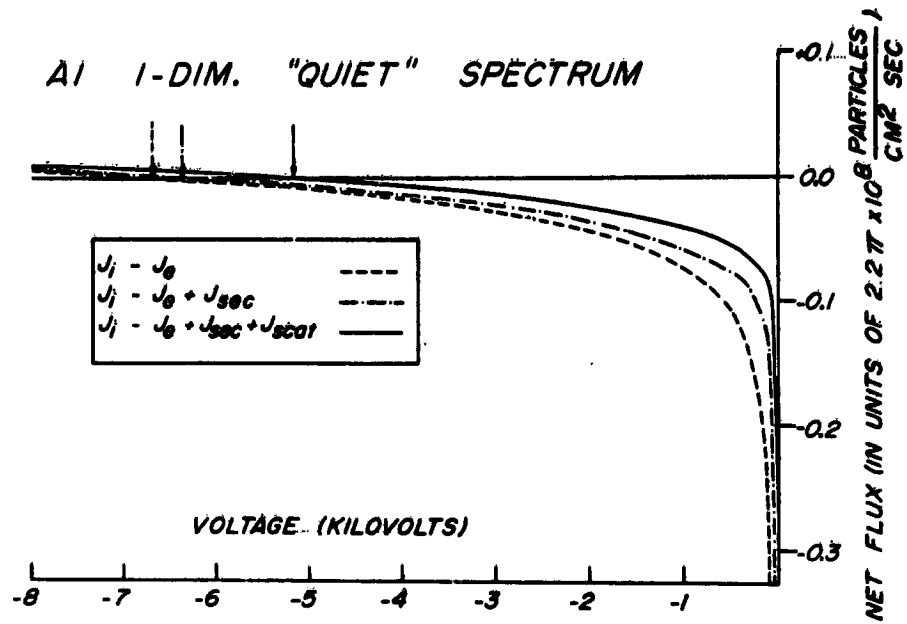


Figure 3. Current-Voltage Characteristic for Aluminum in "Quiet" Conditions, with a One-Dimensional Velocity-Space Cutoff. In Figures 3-7, the zeros of the characteristics are indicated by arrows

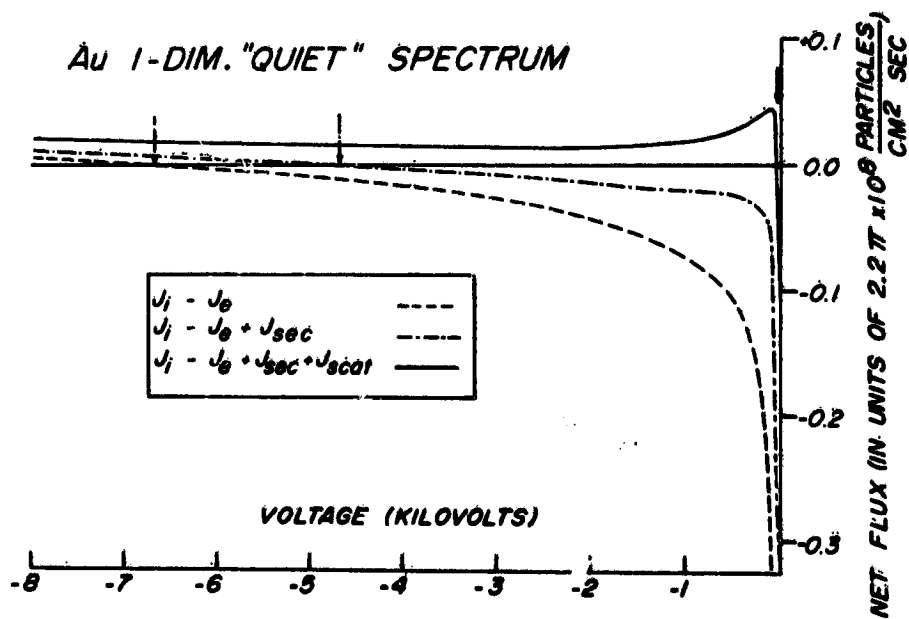


Figure 4. Current-Voltage Characteristic for Gold in "Quiet" Conditions, with a One-Dimensional Velocity-Space Cutoff

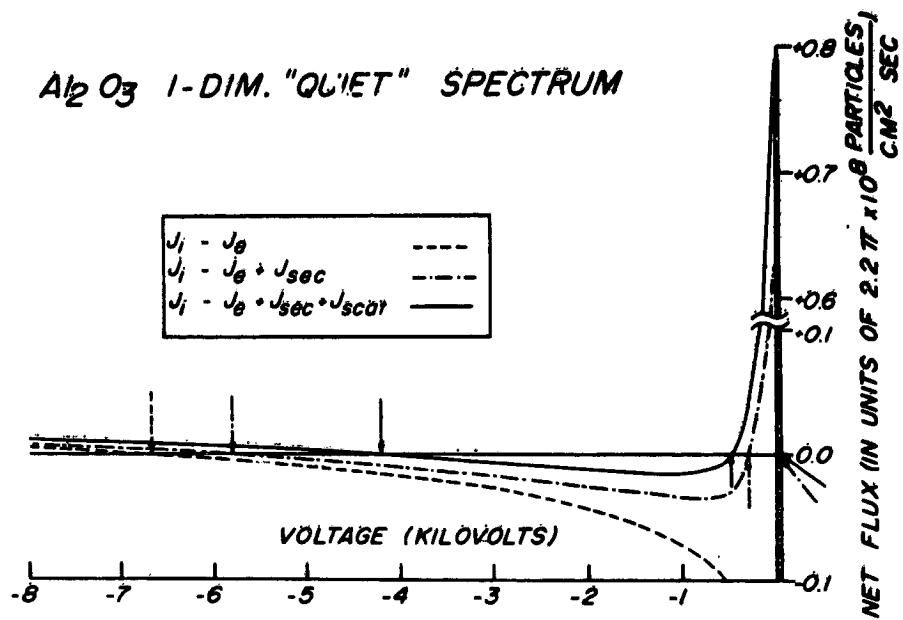


Figure 5. Current-Voltage Characteristic for Aluminum Oxide in "Quiet" Conditions, with a One-Dimensional Velocity-Space Cutoff

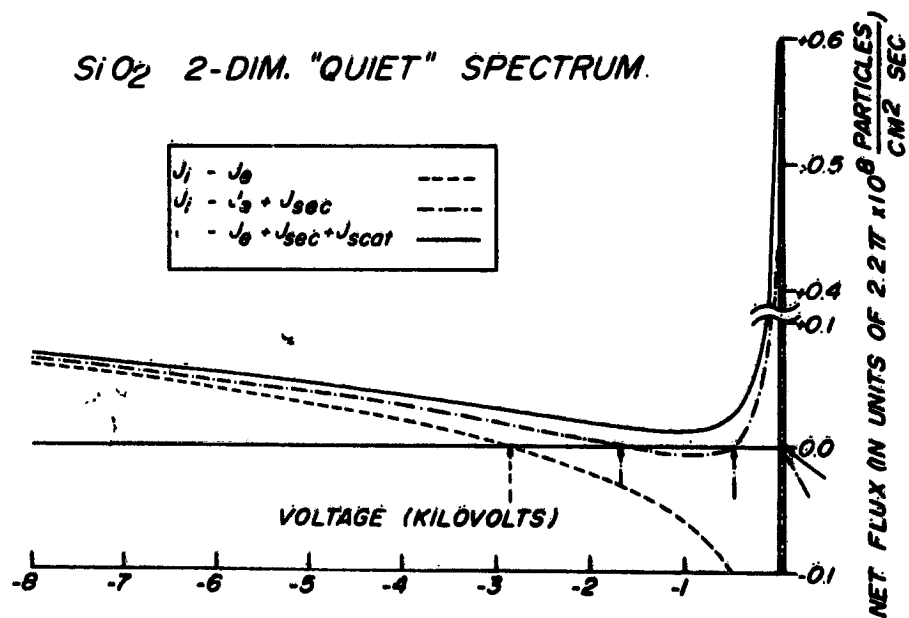


Figure 6. Current-Voltage Characteristic for Quartz in "Quiet" Conditions, with a Two-Dimensional Velocity-Space Cutoff

Beryllium Copper 1-DIM. "QUIET" SPECTRUM

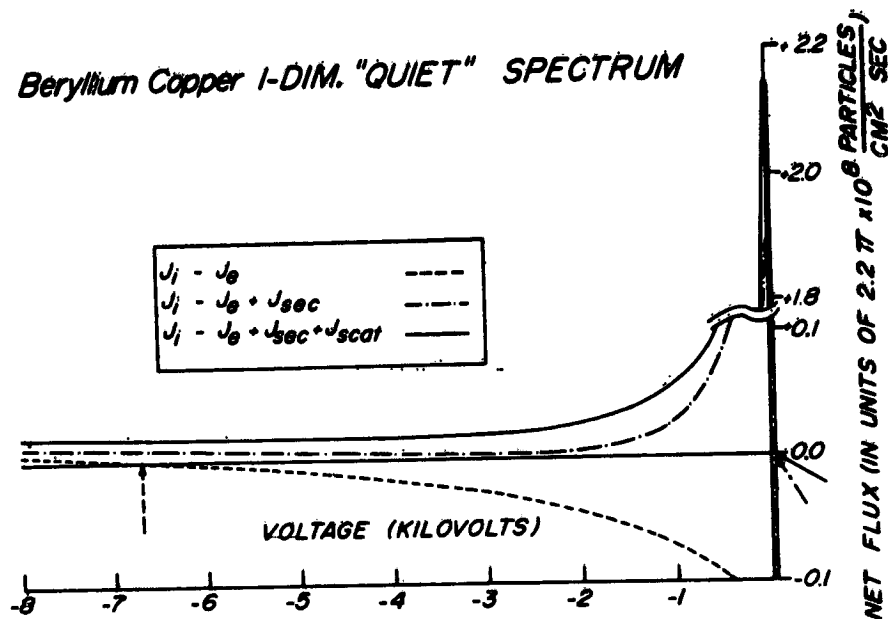


Figure 7. Current-Voltage Characteristic for Beryllium-Copper in "Quiet" Conditions, with a One-Dimensional Velocity-Space Cutoff

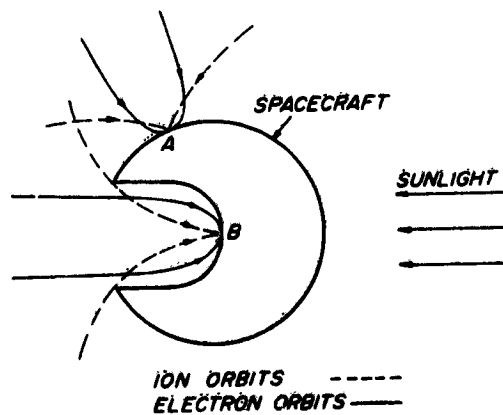


Figure 8. Spacecraft with Shaded Isolated Cavity, Showing Incident Ion and Electron Orbits with Energies Close to the Lowest for which Collection of Each Species is Possible. The orbits shown are cutoff orbits, defined as the most nearly tangential orbits for which incident particles of a given energy are able to reach a given point on the spacecraft surface, having tangential velocity component in a given direction

to be directed into a cavity. Especially severe arcing problems are known to have occurred between electronic components mounted inside a cavity at one end of the DSCS spacecraft.

Finally, we discuss some further implications of the multiple-root results shown in Tables 1 and 2 and Figure 5. Consider a situation involving two or more adjacent but isolated spacecraft surfaces which are made of the same material, and whose external conditions change with time, as in the case of time-varying ambient distributions, or a spacecraft rotation which carries these surfaces from sunlight into shadow. Such a situation might involve the continuous evolution of a single-root into a multiple-root situation, and the possibility would then arise of a "bifurcation" phenomenon in which different surface elements followed different potential histories, with a correspondingly large potential difference arising between them. Again, detailed numerical simulations are necessary in order to find out if such phenomena can actually occur.

#### 4. CONCLUSIONS

Upper bounds have been calculated for negative floating potentials which may be acquired by electrically isolated shaded surfaces on synchronous spacecraft. Effects of spacecraft shape and sheath potential profile have been shown to have large influences on such potentials. Inclusion of electron backscattering currents causes only a moderate reduction of these negative potentials in most cases. For isolated surfaces inside shaded cavities, negative floating potentials may exceed those on convex surfaces. In some conditions, two possible floating potentials exist, leading to the possibility of "bifurcation phenomena" in which adjacent isolated surfaces made of the same material may follow different charging histories.

## Acknowledgments

We are indebted to H. Cohen and Jen-Shih Chang for valuable comments. This work was supported by the U. S. Air Force Office of Scientific Research under grant number AFOSR-76-2962.

## References

1. Knott, K. (1972) The equilibrium potential of a magnetospheric satellite in an eclipse situation, Planet. Space Sci. 20:1137-1146.
2. Mott-Smith, H., Jr., and Langmuir, I. (1926) The theory of collectors in gaseous discharges, Phys. Rev. 28:727-760.
3. Laframboise, J.G., and Parker, L.W. (1973) Probe design for orbit-limited current collection, Phys. Fluids 16:629-636.
4. Bernstein, I.B., and Rabinowitz, I.N. (1959) Theory of electrostatic probes in a low-density plasma, Phys. Fluids 2:112-121.
5. Laframboise, J.G. (1966) Theory of spherical and cylindrical Langmuir probes in a collisionless, Maxwellian plasma at rest, Univ. of Toronto, Institute for Aerospace Studies, Rep. 100.
6. Fahlson, U. (1973) Plasma-vehicle interactions in space: Some aspects of present knowledge and future development. In: Photon and Particle Interactions with Surfaces in Space, R.J.L. Gard, Editor, D. Reidel Pub. Co., Dordrecht, Holland, pp. 563-569.
7. Shield, M.A., and Frank, L.A. (1970) Electron observations between the inner edge of the plasma sheet and the magnetosphere, J. Geophys. Res. 75:5401-5414.
8. DeForest, S.E., and McIlwain, C.E. (1971) Plasma clouds in the magnetosphere, J. Geophys. Res. 76:3587-3611.
9. Polychronopoulos, B. (1973) Effects of nonMaxwellian electron energy distributions on the orbital limited current-voltage characteristics of cylindrical and spherical Langmuir probes under collisionless conditions. Plasma Phys. 15:37-48.
10. Sternglass, E.J. (1950) Secondary electron emission and atomic shell structure, Phys. Rev. 80:925-926.
11. Gibbons, D.J. (1966) Secondary electron emission. In: Handbook of Vacuum Physics, A.H. Beck, Ed., Pergamon Press, Oxford, Vol. 2, pp. 301-395.
12. Hachenberg, O., and Brauer, W. (1959) Secondary electron emission from solids, Adv. Electronics Electron Phys. 11:413-499.
13. Sternglass, E.J. (1954) Backscattering of kilovolt electrons from solids, Phys. Rev. 95:345-358.
14. Thomas, S., and Pattinson, E.B. (1970) Range of electrons and contribution of back-scattered electrons in secondary production in aluminum, J. Phys. D: Appl. Phys. 3:349-357.

15. Darlington, E. H., and Cosslett, V. E. (1972) Backscattering of 0.5-10 keV electrons from solid targets, J. Phys. D: Appl. Phys. 5:1969-1981.
16. Chung, M. S., and Everhart, T. E. (1974) Simple calculation of energy distribution of low-energy secondary electrons emitted from metals under electron bombardment, J. Appl. Phys. 45:707-709.
17. Whipple, E. C., Jr. (1976) Modelling of spacecraft charging, Paper II-1, USAF-NASA Spacecraft Charging Technology Conference, Colorado Springs.
18. DeForest, S. E. (1976) The plasma environment at geosynchronous altitude, Paper I-1, USAF-NASA Spacecraft Charging Technology Conference, Colorado Springs.

## Contents

1. Introduction	389
2. Comparison with Analytic Approaches	390
3. The P. sheath	396
4. Plasma Oscillations	403
5. Summary and Conclusions	407
Acknowledgments	407
References	407
Appendix A	409

## 11. A Simulation Model of Time-Dependent Plasma-Spacecraft Interactions

P.L. Rothwell, A.G. Rubin, and G.K. Yates  
Air Force Geophysics Laboratory  
Hanscom AFB, Mass.

### Abstract

A plasma simulation code is presented that models the time-dependent plasma properties in the vicinity of a spherical, charged spacecraft. After showing agreement with analytic, steady-state theories and ATS-6 satellite data, the following three problems are treated: (1) transient pulses from photoemission at various emission temperatures and ambient plasma conditions, (2) spacecharge limited emission, <sup>1</sup> and (3) simulated plasma oscillations in the long-wavelength limit ( $k \lambda_D \ll 1$ ).

### 1. INTRODUCTION

#### 1.1 Model Objectives

The objective of this computer model is to realistically simulate plasma-spacecraft interactions. It presently treats time-dependent plasma phenomena in the limit of spherical symmetry. Although future plans anticipate the incorporation of a realistic three-dimensional spacecraft geometry, understanding of the spherically symmetric limit uniquely identifies plasma effects. In this manner, it is

hoped that the model will prove to be a useful tool in differentiating between plasma and geometric phenomena observed in the SCA THA satellite data.

## 1.2 Description of the Model

We use what is commonly called a "particle pusher" model. That is, one approximates the actual plasma by a number of "computer" particles whose charge, position, angular momentum, and velocity are tracked in time. By properly weighting these computer particles, reasonable statistics can be obtained near the spacecraft.<sup>2</sup>

Appropriate particle distributions are generated either by a Monte Carlo technique or by a systematic loading of the velocity and spatial intervals ("quiet start").<sup>3</sup>

For purposes of comparison, we have initially restricted ourselves to Maxwellian distributions. However, both methods (Monte Carlo and Quiet Start) can easily be extended to any distribution that can be numerically integrated. Once the neutral plasma is created, the computer tracks the particles and recalculates the potential at each time step. Particles that hit or are emitted from the spacecraft are taken into account as well as those that enter and exit the sheath boundary. Thus, the computerized sheath structure dynamically evolves in analogy with the physical situation. One may then store the results and restart the program with a new set of environmental parameters.

In Section 2 of this paper, we will show the agreement of the present work with that of other approaches and with the ATS-6 data. Section 3 deals with the photosheath. The minimum rise time of the spacecraft potential is determined for various emission temperatures and ambient plasma parameters. Space charge effects are also discussed as well as those due to secondary emission and back-scattering. Finally, in Section 4, we illustrate the possible presence of plasma oscillations by performing "computer experiments" with the code.

## 2. COMPARISON WITH ANALYTIC APPROACHES

### 2.1 Comparison with Langmuir Theory

As a first step we compared our steady-state results with those expected from Langmuir theory.<sup>4,5</sup> Figure 1 shows the comparison. In these results, the ambient plasma temperature and density were held fixed and the fixed potential on the probe (spacecraft) increased. The parameter  $I_p$  is the ambient current to the probe surface at zero voltage. If one makes the same assumption for the model as for the Langmuir theory (that is, no presheath acceleration), good agreement is

$$r_p = 1.0 \text{ m}$$

$$\lambda_D = 5.25 \text{ m}$$

———— MOTT-SMITH - LANGMUIR THEORY  
• - SIMULATION PROGRAM WITH PRESHEATH ACCELERATION  
x - SIMULATION PROGRAM WITHOUT PRESHEATH ACCELERATION

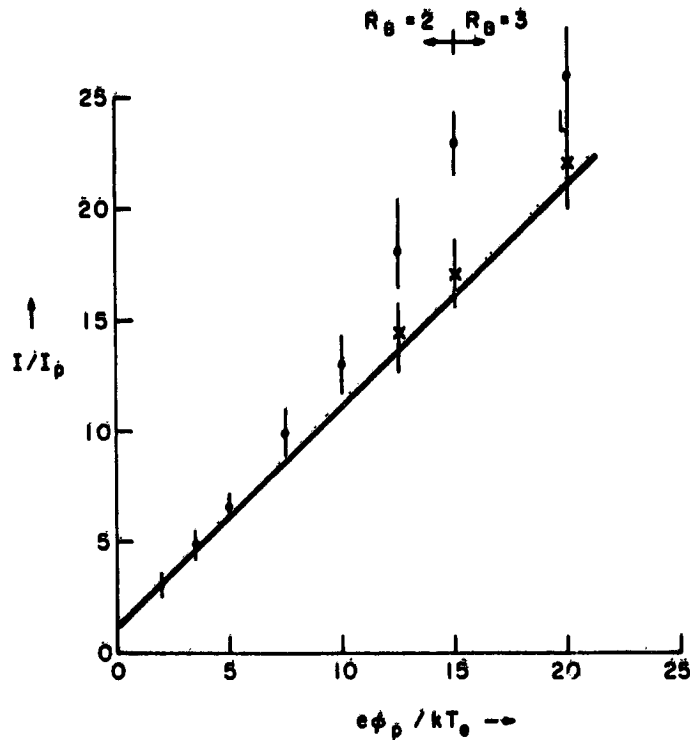


Figure 1. Comparison of the Simulation Code with the Mott-Smith-Langmuir Theory. This figure depicts a current-voltage curve in the thick-sheath approximation. The probe radius is 1 m and the outer sheath boundary has been set to  $R_B = 2$  and  $R_B = 3$  in units of  $\lambda_D$ . The dots represent the case where there is presheath acceleration. That is, when the potential at  $R_B$  is nonzero

obtained. (Presheath acceleration takes into account the dependence of the sheath size on the probe potential. In the code, this is represented by a Boltzmann factor at the sheath boundary.<sup>2)</sup>)

## 2.2 Comparison with Static Codes

We also compared our results in the steady-state limit to numerical solutions of the Vlasov and Poisson equations.<sup>6,7</sup> The steady-state limit is reached by allowing an initially neutral plasma to form a sheath around a voltage-biased probe. Figure 2 shows the code results after 0.17 msec. In this example, the probe has a bias voltage equal to minus ten times the average electron energy expressed in electron volts. From Figure 2 it is seen that both methods give the same voltage profile, but differ somewhat for the electron density at large  $r$ . This difference is probably due to the time-dependent code not having reached the true steady-state values.

Figure 3 shows a similar comparison for relatively intense monoenergetic electron emission from the probe surface.<sup>8</sup> The probe is positively biased at +2.0 volts. The emission energy is +1.0 electron volts so that all emitted electrons return to the probe surface. The resultant density and voltage profiles show good agreement. Scatter in the time-simulation results can be improved by using more computer particles. For example, in the present case we used approximately 4000 computer ions and electrons. This number can be significantly increased at the expense of longer computation time.

## 2.3 Comparison with ATS-6 Data

Two charging events in the eclipse region were analyzed from ATS-6 data supplied by DeForest.<sup>9</sup> The proton and electron temperature during these events as well as the simultaneous vehicle potential are shown in Table 1.<sup>10</sup> These two events represent a time when injection of hot plasma took place. Also shown in Table 1 are the vehicle potentials as predicted from a simple Boltzmann approximation and a thick-sheath approximation to the orbit-limited Langmuir theory.

The Boltzmann approximation assumes that the electron density is closely represented by  $N_e = N_{e0} e^{-e\phi_p/kT_e}$ . Protons are considered to be unaffected. Therefore, current balance is given by

$$\epsilon \left( \frac{kT_e}{m_e} \right)^{1/2} e^{-|e\phi_p|/kT_e} = \left( \frac{kT_p}{m_p} \right)^{1/2} \quad (1)$$

or

$$e\phi_p/kT_e = \ln \left[ \epsilon t_e m_p / t_p m_e \right]^{1/2}$$

where  $m_p$  = proton mass,  $m_e$  = electron mass,  $k$  = Boltzmann constant and  $\epsilon$  is defined below.

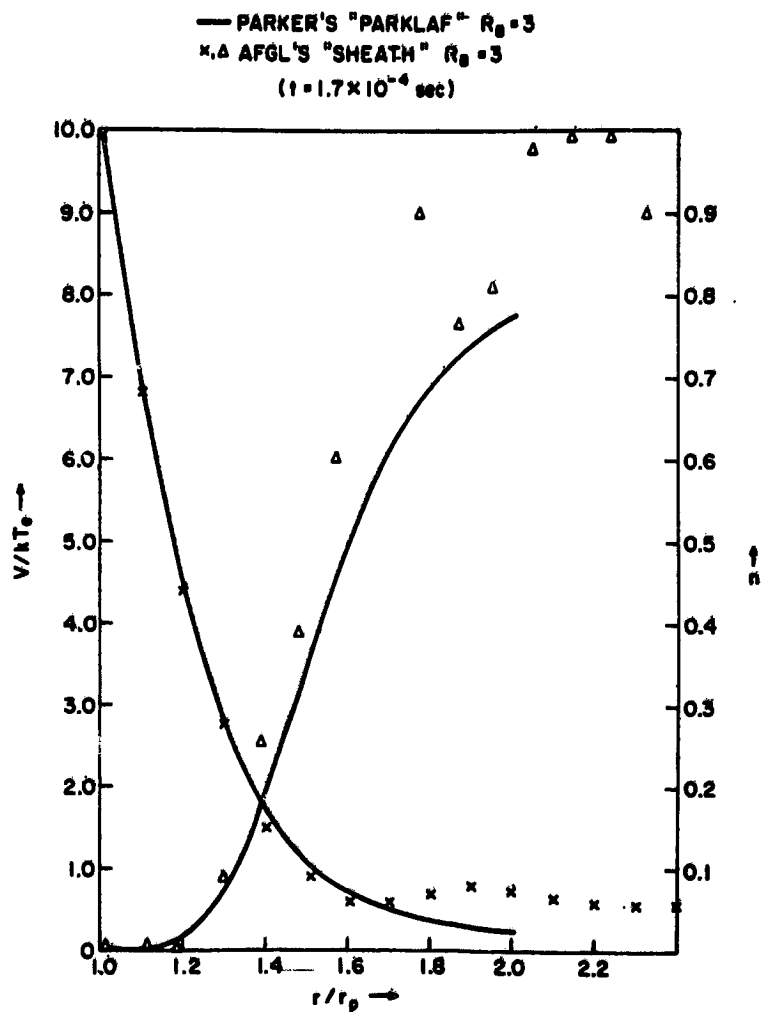


Figure 2. Potential and Density Profiles in the Sheath. Comparison of the time-dependent code with a steady-state numerical solution to the Vlasov-Poisson equations (L. W. Parker, private communication). The density,  $n$ , is normalized to its ambient value. The potential,  $V$ , is shown normalized to the electron temperature. The parameter,  $t$ , is the time at which the time-dependent results were taken. A negative bias of  $-10 kT_e$  volts is on the spacecraft surface.  $R_B$  is expressed in units of probe radii

$R_0 = 1m$   
 EMISSION CURRENT =  $10^{-6}$  amp/m<sup>2</sup>  
 EMISSION ENERGY = 1eV (monoenergetic electrons)  
 EMISSION DENSITY =  $211/cm^3$   
 AMBIENT TEMPERATURE = 5eV (Maxwellian)  
 AMBIENT DENSITY =  $1/cm^3$   
 $\Phi_0 = +2V$  = Sphere Potential (quasi-equilibrium)  
 vs. +1V equilibrium

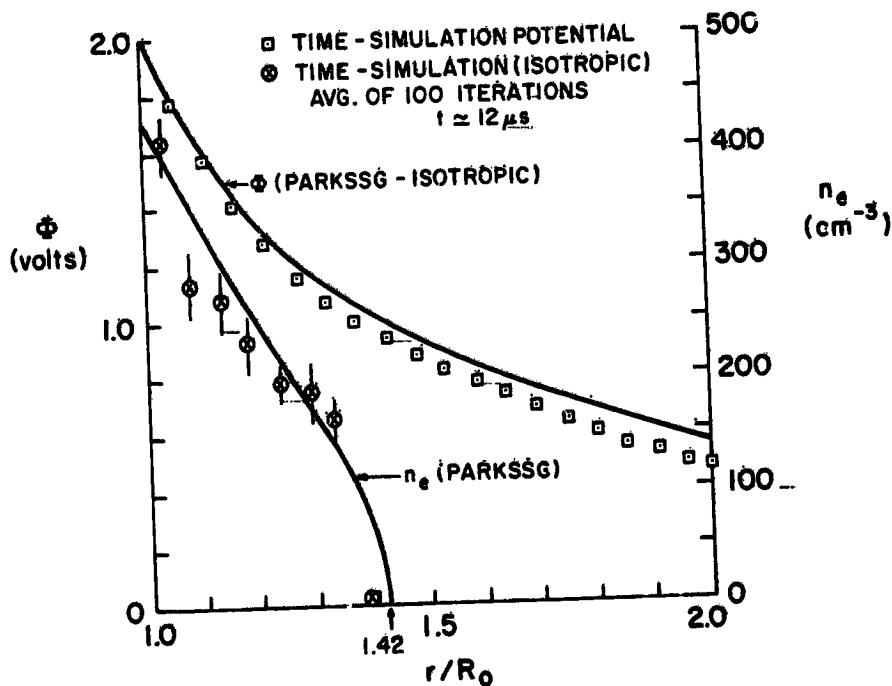


Figure 3. Comparison of the Time-Dependent Code with a Steady-State Numerical Solution with Monoenergetic Emission.  $R_0$  = satellite radius. PARKSSG is a code developed by L. W. Parker that includes electron surface emission. See reference 8

Table 1. Comparison of Boltzmann and Langmuir Theories with ATS-6 Data.  $\epsilon = 0.16$

Day of Event (1976)	$T_p$	$T_e$	$ e\phi /kT_e$		
			Meas.	Boltzmann	Langmuir Thick-Sheath
59	23.7	9.1	1.15	1.45	1.10
66	73.2	8.8	0.79	0.86	0.78

The Langmuir thick-sheath approximation is more realistic in that it also takes into account the effect of the spacecraft potential on the net proton current. It is given by

$$\epsilon \left( \frac{kT_e}{m_e} \right)^{1/2} e^{-|e\phi_p|/kT_e} = \left( \frac{kT_p}{m_p} \right)^{1/2} (1 + e\phi_p/kT_p) \quad (2)$$

a transcendental equation in the satellite potential,  $\phi_p$ , which can be reduced to a quadratic equation in  $(T_e/T_p)^{1/2}$ . The parameter,  $\epsilon$ , represents the net fractional electron current to the spacecraft and, thus, takes into account secondary emission, backscattering and photoemission. In Table 1 we have set  $\epsilon = 0.16$  (that is, 84 percent net backscatter, etc.) for both approximations. Examination of Eq. (2) shows that in the limit of large proton temperatures the thick-sheath approximation reduces to the Boltzmann case. This is also seen from Table 1. In both cases, the Langmuir thick-sheath approximation gives better agreement with measured results than the Boltzmann limit.

Insight into the expected sensitivity of spacecraft voltage to changes in the ambient current, can be seen from Figure 4 which contains a plot of Eq. (2). The top-half of this figure is a linear scale plot of normalized voltage to the net electron current incident on the spacecraft normalized to the ambient electron current (with the Boltzmann factor). The bottom half of the figure shows the same curve on a log-log scale plot. These curves will be modified by any voltage dependence in  $\epsilon$  such as space charge limiting effects.

In conclusion, for large negative spacecraft potentials, the thick-sheath approximation predicts the average spacecraft voltage, given the proper material characteristics and the ambient electron and proton temperatures. The code is consistent with the thick-sheath limit, and predicts sheath density and voltage profiles. The simulation code, however, is also valid where the thick-sheath approximation breaks down. That is, where space charge and time-dependent effects become important.

The importance of space charge is determined by comparing the spacecraft surface charge to the charge residing in the sheath. For large surface potentials and tenuous plasmas, spacecraft surface charge is dominant. In that case, Laplacian solutions with appropriate geometric boundary conditions should be adequate. At low vehicle potentials with surface emission, space charge effects become important.

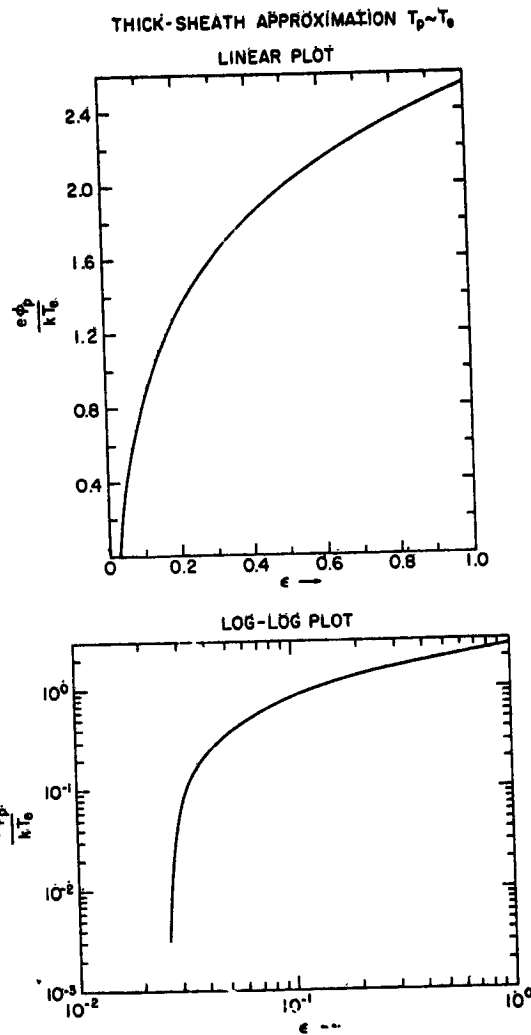


Figure 4. Spacecraft Voltage versus Net Electron Current as Normalized to the Ambient Current (Including the Boltzmann Factor)

### 3. THE PHOTOSHEATH

#### 3.1 Introduction

Incident sunlight causes the emission of low energy ( $\sim 2$  eV) electrons from the satellite surface. This emission, in a hot plasma environment, sometimes swings the satellite potential thousands of volts as the satellite enters and emerges

from the eclipse region. A second effect of photoemission is its background effect on ambient plasma density measurements. These measurements must be corrected for electrons originating on the satellite surface. A third effect of the photosheath is its possible interaction with onboard electron emitters either through space-charge limiting effects or by stimulation of plasma oscillations.

In the present code, we can simulate either monoenergetic or Maxwellian photoemission. The Maxwellian case is described in detail in Appendix A. The angular distribution of the emitted photoelectrons follow a cosine law relative to the surface normal.<sup>11</sup> In the following paragraphs, we consider photoemission to be switched "on" at  $t = 0$ . This is a worst case condition since satellites emerge from eclipse over a period of minutes.

### 3.2 Monoenergetic Emission

Figure 5 shows the simulation results for monoenergetic emission. The vertical axis represents the satellite (taken as a 1 m radius sphere) potential while the horizontal axis denotes time in microseconds. The satellite is taken to be at zero volts at  $t = 0$ . The bump in each of the curves occurs when the initially emitted electrons return to the satellite. The final surface is the result of two effects. First, emitted electrons do not return until the satellite reaches a voltage

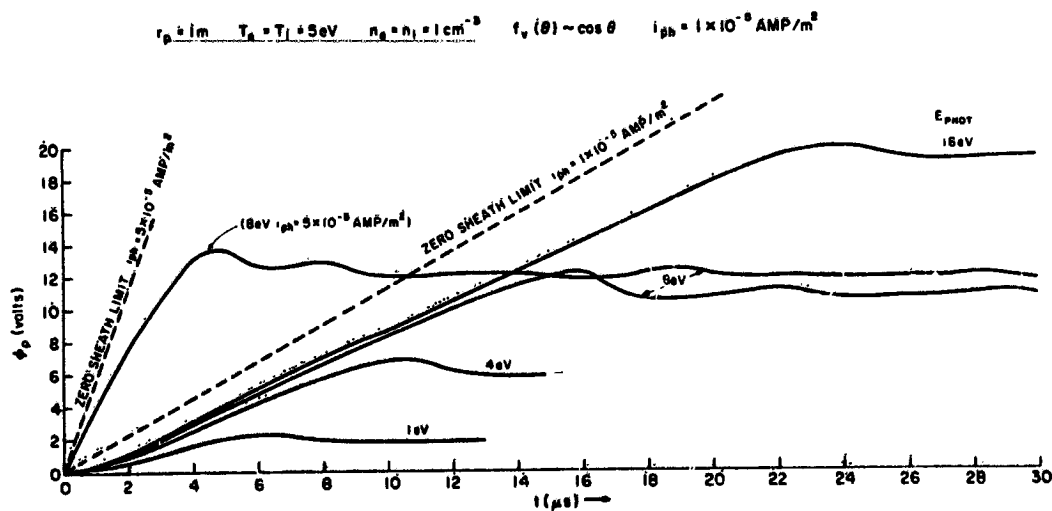


Figure 5. Monoenergetic Emission in a Tenuous Plasma. The emission is assumed to be switched "on" at  $t = 0$ . This represents a worst case condition. The abscissa is in microseconds

equal to the emission energy. Secondly, there is a finite transit time for the returning electrons. This means that the final voltage is higher than the emission energy expressed in electron volts. The dotted lines represent spacecraft voltage buildup in the limit where all emitted electrons escape. Further cases regarding monoenergetic photoemission can be found in Katz et al. <sup>12</sup>

### 3.3 Transient-Rise-Time

Figure 6 shows expected surface voltage rise-times at various ambient densities. In these runs the photoelectrons are emitted with a Maxwellian distribution with a temperature corresponding to 6 eV. <sup>13</sup> The ambient density is then varied to determine the rise-time sensitivity to the ratio of the photoelectron and ambient currents.

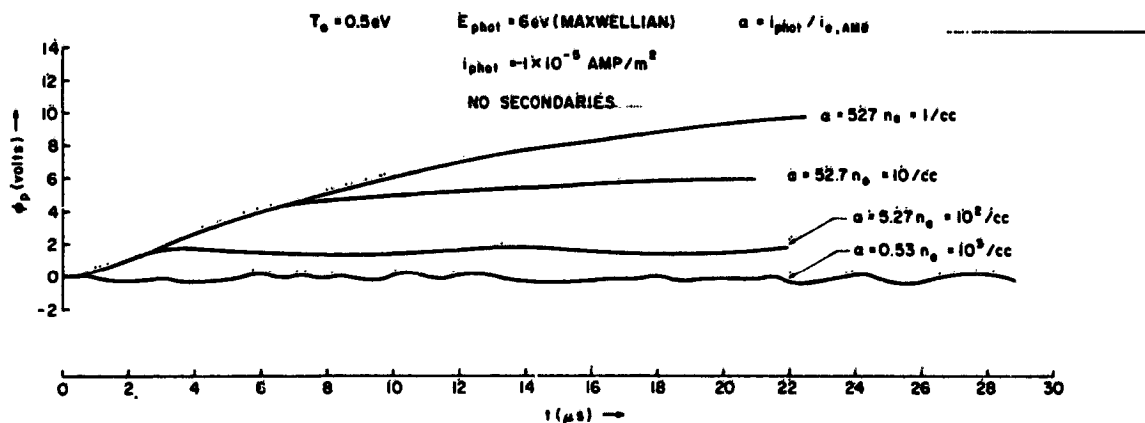


Figure 6. Spacecraft Voltage Transients for a Fixed Emission Temperature and Various Plasma Densities. No secondaries included

In Figure 7, we treat the alternative case. That is, the ambient plasma parameters are held constant and the photoemission temperature is varied. The dotted line represents 100 percent escape efficiency for the emitted electrons. The steady-state surface voltage, as expected is dependent on emission temperature.

The transients shown in Figures 6 and 7 could cause satellite malfunctions if they reached a critical logic circuit. Integrated circuits usually operate over 0-5 volts so that a  $\geq 2$  volt transient through the ground lines would give a false

$$I_{\text{PHOT}} = 1 \times 10^{-5} \text{ AMP/m}^2 \quad n_0 = 1/\text{cc} \quad T_0 = T_1 = 5 \text{ eV} \quad f_v(\theta) \sim \cos \theta$$

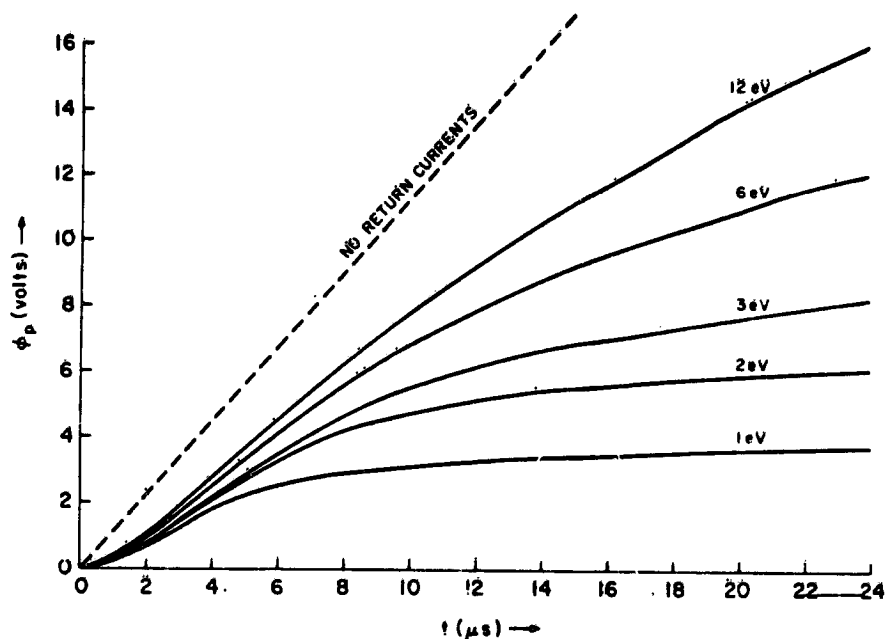


Figure 7. Transient Spacecraft Potentials for Strong Photoemission at Various Emission Temperatures. No secondaries included

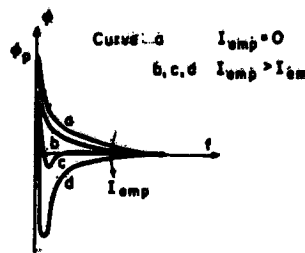
signal. The incident sunlight flux must change more rapidly than the characteristic time-constant of the surface materials. Otherwise, these rise times will not be significant. Further research into this area needs to be performed.

### 3.1 Space Charge Limited Emission

Chang and Bienkowski<sup>14</sup> showed that large current emission from a positively biased probe is inhibited by space-charge buildup in front of the surface. (See center Figure 8.) Whipple<sup>1</sup> used a similar approach to show that differential surface charging is necessary to explain the barrier potentials observed on ATS-6. In this section, we use the simulation code to produce space-charge effects. Application is then made to a floating spacecraft potential with and without active control experiments.

The versatility of the present code is illustrated in the lefthand side of Figure 8. The surface potential is held fixed at +6 volts while the electron emission current is increased. For a nominal  $5 \times 10^{-5} \text{ A/m}^2$  photoemission current density, no

CHANG AND BIENKOWSKI  
(PHYS. OF FLUID, VOL.13, 902, 1970)



TYPICAL POTENTIAL DISTRIBUTIONS OF A POSITIVELY BIASED PROBE IN THE PRESENCE OF ELECTRON EMISSION.

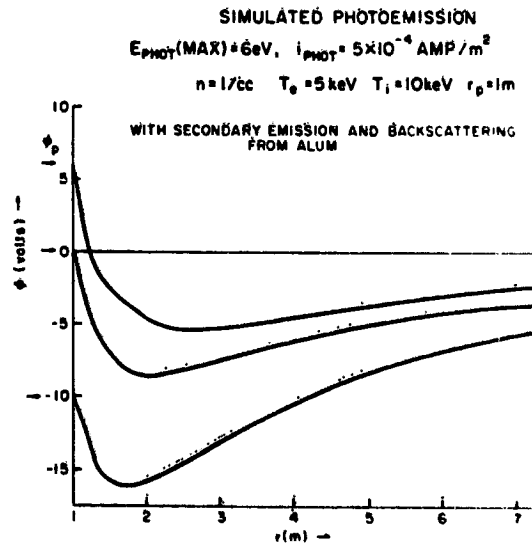
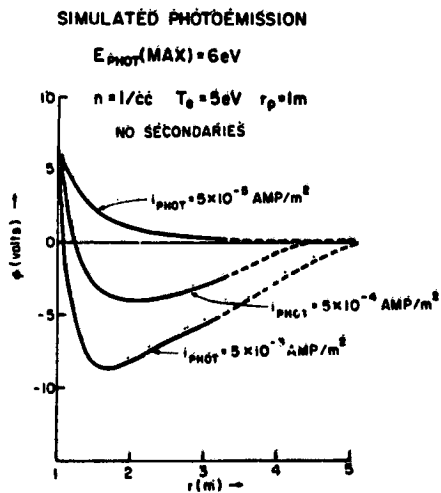


Figure 8. Simulated Maxwellian Emission Showing Potential Barriers. The lefthand figure shows the barrier depth as a function of emission intensity. (The higher values of  $i_{phot}$  are, of course, unrealistic and are used solely to illustrate the barrier). The righthand figure shows the barrier as a function of surface potential

potential barrier is observed. However, if the emission is artificially enhanced to 50 and  $500 \times 10^{-5} \text{ A/m}^2$  potential barriers are clearly evident and inhibit further emission. (In these runs, the sheath boundary was chosen at 3.32 m). The effect of the potential barrier is such that only 57.3 percent, 22.2 percent and 4.4 percent of the emitted flux reaches 3.32 m for the three respective cases. These results show that the simulation code can treat space-charge effects and predict emission efficiencies. The code can distinguish between emitted and ambient particles and, therefore, can be used to correct ambient plasma measurements.

The depth of the potential well is also dependent on the satellite voltage. On the righthand side of Figure 8 we show three curves for the same ambient and emission characteristics but at different surface potentials. For large negative values of the surface potential, the well is completely eliminated since emitted electrons are rapidly repelled. On the other hand, if the surface potential is too positive, the emitted electrons quickly return to the emitting surface and a significant spacecharge cannot form. Therefore, potential wells are expected for only a specific range of surface potentials.

The situation is more complex with a floating spacecraft potential. In this case, both the well depth and the surface voltage are strongly dependent on the net electron current. Figure 9 shows the expected voltage profile in the sheath at various emission currents and ambient densities. Runs were taken at three densities  $n = 1 \text{ cm}^{-3}$ ,  $5 \text{ cm}^{-3}$  and  $10 \text{ cm}^{-3}$  with a photoemission current of  $8.2 \mu \text{ A/m}^2$ .<sup>15</sup> The emitted current was then increased to  $40 \mu \text{ A/m}^2$  which is the limiting photoemission intensity for aluminum.<sup>16</sup> In addition to photoemission, 84 percent of the incident electrons were assumed to cause isotropic secondaries to be emitted with a Maxwellian energy distribution ( $kT = 2.5 \text{ eV}$ ). The 84 percent figure was estimated from ATS-6 eclipse data (Table 1). Figure 9 shows that the presence of a potential well is dependent on a "balance" between the ambient and emitted currents. Space charge also gives rise to the curious effect that a spacecraft may have a net positive charge but be at a negative potential relative to the ambient plasma.

The Figure 9 also shows the maximum barrier to be about -3 volts. These results are in agreement with those of Whipple<sup>1</sup> who showed that the barrier potentials inferred from ATS-6 data are too large to be explained in terms of a spherically symmetric photoelectron or secondary sheath surrounding a uniformly charged spacecraft. Differential charging between spacecraft surfaces is, therefore, mainly responsible for the potential barrier. The average satellite potential relative to the ambient plasma, however, is determined by the sheath.

Active control experiments in hot dense plasma could lead to more pronounced space-charge effects. As an extreme example, we took  $T_e = 9.1 \text{ k eV}$ ,  $T_i = 23.7 \text{ k eV}$  and  $n = 5 \times 10^4 \text{ cm}^{-3}$ . In that case in order to maintain neutrality, electron emission

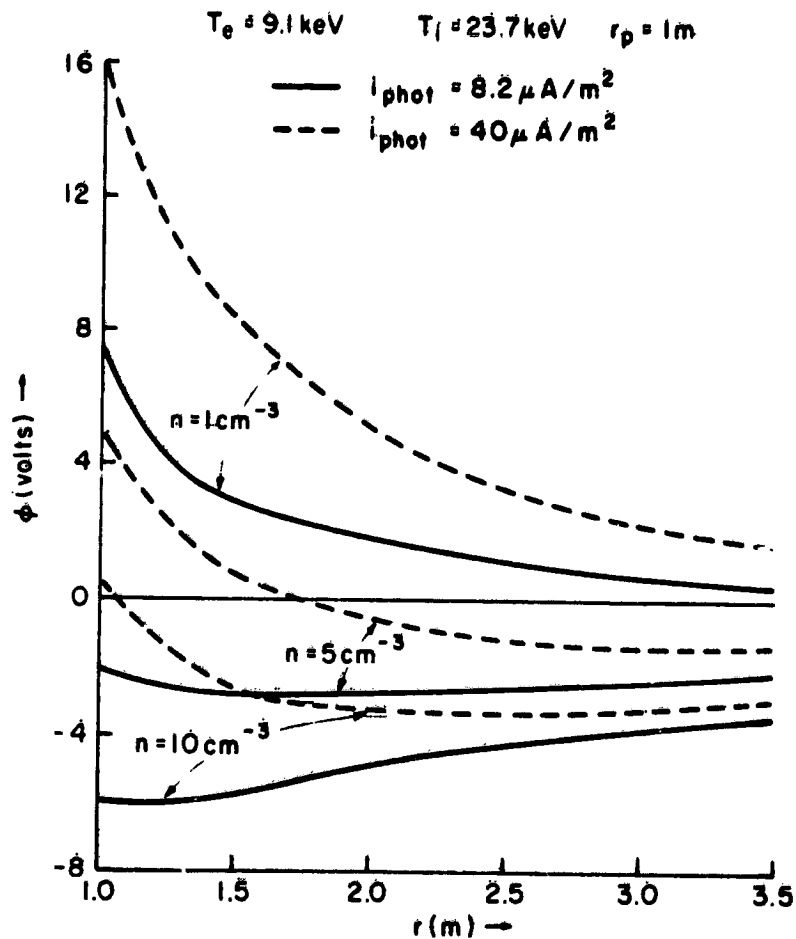


Figure 9. The Potential Profile in the Sheath at Various Emission Intensities and Ambient Densities. The surface potential is floating

of  $\sim 1.6 \text{ A}$  was required. A potential barrier on the order of hundreds of volts was obtained.

### 3.5 Future Plans

The Monte-Carlo approach is presently being applied to include realistic back-scattering and secondary emission from both electrons and incident ions. These processes are energy and material dependent. In this way, insight into the importance of material properties on spacecraft charging will be gained.

## 4. PLASMA OSCILLATIONS

### 4.1 Introduction.

Because of the dynamic nature of the plasma, the sheath potential may oscillate in time. Moving plasma particles "overshoot" their equilibrium positions and undergo simple harmonic motion. Collective oscillations are, therefore, closely connected with dynamic screening.<sup>17</sup> The natural frequency of these collective modes is the plasma frequency,

$$\omega_{P_e} = \left( \frac{4\pi e^2 n}{m_e} \right)^{1/2}$$

where  $n$  is the ambient plasma density. The sheath, therefore, is like a resonant cavity that oscillates under certain perturbations.

### 4.2 Observation of Plasma Oscillations

Initially, we looked for plasma oscillations in the thin-sheath limit. An ambient density of  $200 \text{ cm}^{-3}$  and an electron-ion temperature  $T_e = T_i = 0.2 \text{ eV}$  was chosen. This gives a Debye length of  $0.235 \text{ m}$  compared with a  $1 \text{ m}$  probe radius. The probe potential was biased at  $+1.0 \text{ volt}$ . The top three curves in Figure 10 show the sheath potential profile at  $10 \mu\text{sec}$  intervals. Some time-dependence is observed but its coherent property is not clear. The periodic nature of the time-dependence is enhanced by plotting the potential at a constant distance ( $r = 2.60 \text{ m}$ ) from the probe surface as shown in the bottom part of Figure 10. The local potential oscillates at a frequency comparable with the plasma frequency ( $\omega_{pe} = 7.99 \times 10^5 \text{ rad/sec}$ ). The nature of this oscillation is further delineated by performing a computer experiment.

### 4.3 A Computer Experiment

Figure 11 represents a computer experiment in which all the parameters except the ambient density remained constant. The ambient density in each curve is higher by a factor of 2 compared with the curve immediately above it. The points represent 10 iteration averages and the error bars the rms deviation from this average. The observation point was taken at approximately  $16 \lambda_D$  ( $\lambda_D = \text{Debye length}$ ) in each run. The average and standard deviation of the oscillation period, as estimated from these plots, is also given. In each instance the observed averaged period,  $T$ , is shorter than the plasma period  $\tau = 1.11 \times 10^{-4} / n \text{ sec}$ . In order to estimate the oscillation wavelength,  $\lambda$ , the one-dimensional plasma

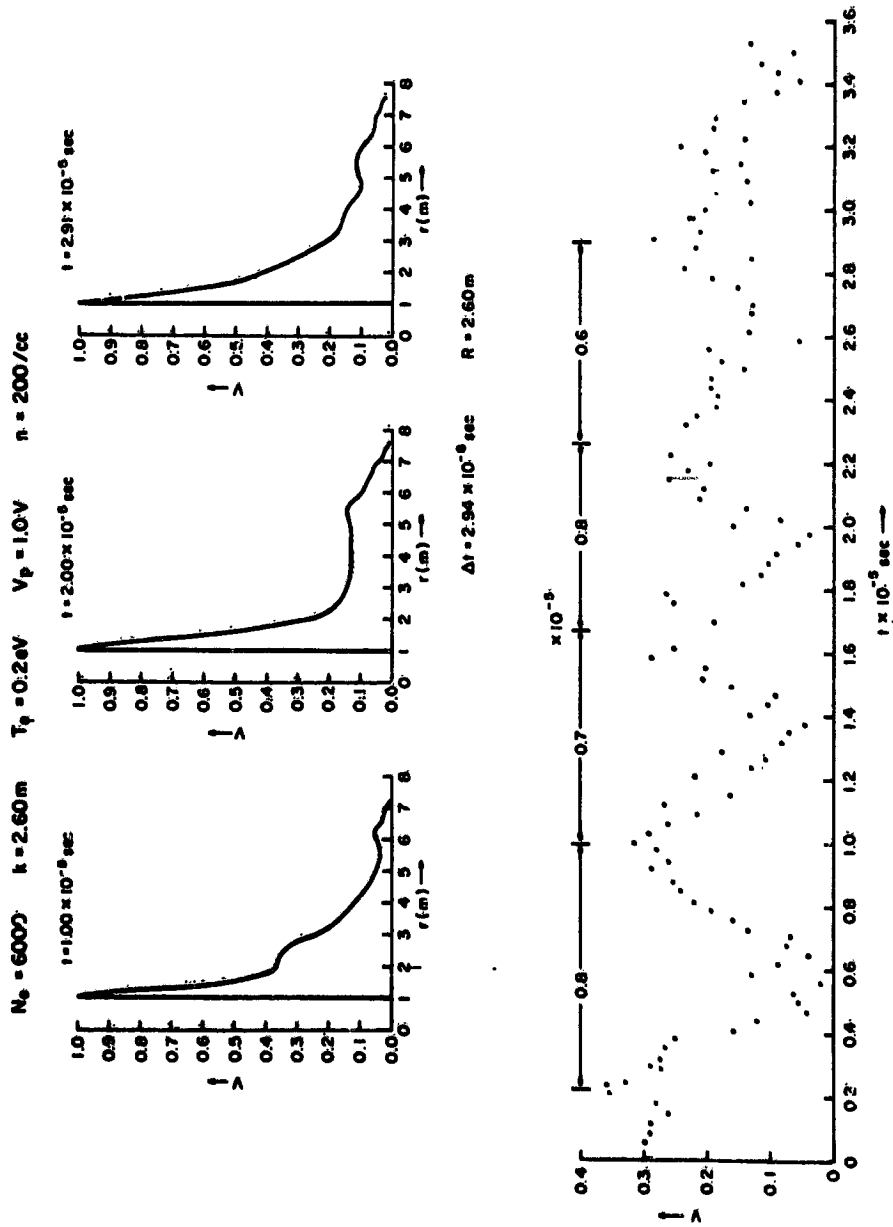


Figure 10. The Top Three Figures Denote the Sheath Potential Profile at  $10 \mu\text{sec}$  intervals. The time-step for each iteration was  $29.4 \text{ ns}$ . The bottom curve is a time-history of the voltage at a fixed position. Time is measured in units of  $10^{-5} \text{ sec}$

NE=NI=6000 T<sub>0</sub>=T<sub>i</sub>=0.2eV Δt=60ns R<sub>g</sub>=30λ<sub>0</sub> φ<sub>p</sub>=1.0V r<sub>p</sub>=1m

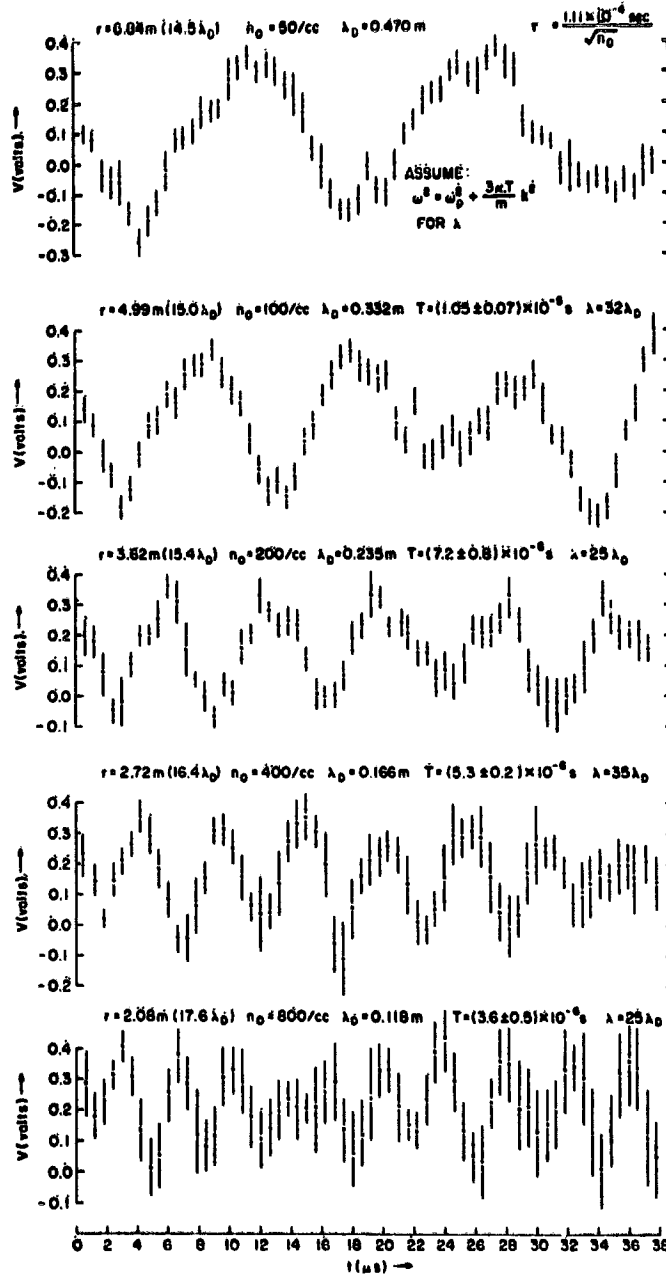


Figure 11. Simulated Plasma Oscillations. Each curve represents the voltage time-history for various densities. NE and NI are the number of computer electrons and ions respectively. Time is in microseconds.  $\lambda$  denotes wavelength which equals  $2\pi/k$

dispersion relation<sup>17</sup> is used. Although this is derived for a cartesian geometry, we assume it also holds for the spherical case in the thin sheath limit. The relation is

$$\omega^2 = \omega_{pe}^2 + 3 \langle kT \rangle k^2/m \quad (3)$$

where

$\lambda = 2\pi/k$ ,  $\omega =$  observed frequency,  $\omega_{pe} =$  plasma frequency

$\langle kT \rangle =$  mean electron energy

$m =$  electron mass

$k =$  wavenumber .

The respective wavelengths, as obtained from Eq. (3), are shown on the righthand side of Figure 11. The central values of T were used. Results imply a wavelength on the order of the sheath thickness ( $R_B - r_p$ ). Since the surface voltage is fixed at +1.0 volt and is close to zero at  $R_B$ , the analogy between the sheath and a resonant cavity is seen to be very close.

Plasma oscillations are Landau-damped by the transfer of wave energy to electrons traveling slightly below the wave phase velocity,  $V_p = \omega/k$ . To test the present code we artificially enhanced the high energy tail of the Maxwellian electron distribution but retained the condition  $\partial f/\partial V < 0$ . Under these conditions the wave amplitude shown in Figure 11 significantly decreased indicating, as expected, enhanced damping.

The oscillations shown in Figure 11 approach the long wavelength limit,  $k\lambda_D < 1$ . In that case, there is an analytic expression<sup>17</sup> for the rate of damping. It is

$$\gamma = \sqrt{\frac{\pi}{8}} \frac{\omega_{pe}}{(k\lambda_D)^3} \text{EXP} \left( -\frac{3}{2} - \frac{1}{2k^2\lambda_D^2} \right) \quad (4)$$

where  $\gamma =$  decay rate ( $\text{sec}^{-1}$ ),  $\omega_{pe} =$  electron plasma frequency. While there is substantial fluctuation in  $\gamma$  from its sensitivity to  $k$ , the shortest decay time is 190  $\mu\text{sec}$  for  $n = 800 \text{ cm}^{-3}$  run. This is sufficiently long so that no significant damping is expected to be seen in Figure 11.

At long wavelengths the wave phase velocity,  $V_p$ , is much greater than the thermal electron velocity so that there are few electrons in the resonant region. At shorter wavelengths ( $k\lambda_D \sim 1$ ) the wave phase velocity approaches the thermal particle velocity. The presence of many electrons in this velocity region rapidly damps the plasma wave. While the above results imply the usefulness of plasma simulation techniques in looking at collective behavior, some caution should be noted.

The basic problem is that the observed oscillations can be either physically stimulated or artificially driven by high frequency grid or computer "noise" that couples to the lower frequency plasma oscillation by aliasing.<sup>18</sup> The computer code should be sufficiently free from noise so that observed oscillations are consistent with analytic criteria.<sup>3</sup> The most common technique for reducing noise is to treat the computer particles as having a finite size<sup>19</sup> and to periodically smooth the distribution function in both velocity and spatial coordinates.<sup>20</sup> These sophistications should delineate the origin and nature of the oscillations.

### 5. SUMMARY AND CONCLUSIONS

Agreement has been shown between a time-dependent simulation code and steady-state solutions to the Vlasov-Poisson equations. Transient voltage rise-times due to photoemission were presented and space-charge limiting effects discussed. Finally, a computer "experiment" was presented that showed the presence of plasma waves. Caution is noted for possible aliasing effects.

It is concluded, based on the above results, that a simulation approach is a valuable and versatile method for dealing with complex, plasma-related space phenomena. In particular, additional features can be added as building blocks with little modification of the existing code. Care should be taken, however, in distinguishing between computer-related and physically-related effects.

### Acknowledgments

We would like to thank Lee W. Parker for many interesting conversations on the probe problem and C. P. Pike for his helpful comments. Finally, we would like to thank Mary Spanos and Louise Peterson for their assistance in preparing the manuscript.

### References

1. Whipple, E. C., Jr. (1976) Theory of the spherically symmetric photoelectron sheath: A thick sheath approximation and comparison with ATS-6 observation of a potential barrier, J. Geophys. Res. 81:601-607.

2. Rothwell, P. L., Rubin, A. G., Pavel, A. L., and Katz, L. (1976) Simulation of the plasma sheath surrounding a charged spacecraft in Spacecraft Charging by Magnetospheric Plasmas, A. Rosen, Editor, M. I. T. Press, Cambridge, MA and London, England.
3. Matsuda, Y., and Crawford, F. W. (1975) Computational study of nonlinear plasma waves: 1. Simulation model and monochromatic wave propagation, Phys. Fluids 18:1336-1353.
4. Chen, F. F. (1965) Electric probes, in Plasma Diagnostic Techniques by R. H. Huddlestone and S. L. Leonard, Editors, Academic Press, New York.
5. Laframboise, J. G. (1966) Theory of Spherical and Cylindrical Langmuir Probes in a Collisionless, Maxwellian Plasma at Rest, Univ. of Toronto Rpt. 100, Toronto, Canada.
6. Parker, L. W., and Whipple, E. C. Jr., (1970) Theory of spacecraft sheath structure, potential and velocity effects on ion measurements by traps and mass spectrometers, J. Geophys. Res. 75:4720-4733.
7. Parker, L. W., and Whipple, E. C. Jr., (1967) Theory of a satellite electrostatic probe, Ann. Phys. 44:126-161.
8. Parker, L. W. (1976) Theory of Electron Emission Effects in Symmetric Probe and Spacecraft Sheaths, AFGL-TR-76-0294.
9. DeForest, S. E. (1976) Private Communications.
10. Garrett, H. B. (1977) Analysis of Penumbral Eclipse Data, this volume.
11. Fadley, C. S. (1973) Theoretical aspects of x-ray photoelectron spectroscopy, Electron Emission Spectroscopy, Dekeyser, W., Fiermans, L., Valderkelen, G., and Vernik, J., D. Reidel Publishing Co., Dordrecht-Holland, pp. 151-224.
12. Katz, I., Wilson, A., Parker, L. W., Rothwell, P. L., and Rubin, A. G. (1976) Static and dynamic behavior of spherical probe and satellite plasma sheaths, IEEE Annual Conf. on Nuclear & Space Radiation Effects, San Diego, CA, July.
13. Wrenn, G. L., and Heikkila, W. J. (1973) Photoelectrons emitted from Isis spacecraft, Photon and Particle Interactions with Surfaces in Space, D. Reidel Publ. Co., Dordrecht-Holland, pp. 221-230.
14. Chang, K. W., and Bienkowski, G. K. (1970) Effects of electron emission on electrostatic probes at arbitrary pressures, Phys. of Fluids, 13:902-920.
15. DeForest, S. W. (1972) Spacecraft charging at synchronous orbit, J. Geophys. Res. 77:651-659.
16. Grand, R. J. L., Knott, K., and Pedersen, A. (1973) The influence of photoelectron and secondary electron emission on electric field measurements in the magnetosphere and solar wind, Photon and Particle Interaction with Surfaces in Space, D. Reidel Publ. Co., Dordrecht-Holland, pp. 163-189.
17. Akhiezer, A. I., and Akhiezer, I. A. (1975) Plasma Electrodynamics Volume 1: Linear Theory, Pergamon Press, Inc., New York.
18. Hamming, R. W. (1973) Numerical Methods for Scientists and Engineers, McGraw-Hill, New York pp. 505-515.
19. Langdon, A. B. (1970) Effects of the spatial grid in simulation plasmas, J. of Comp. Phys. 6:247-267.
20. Denavit, J. (1974) Discrete particle effects in whistler simulation, J. of Comp. Phys. 15:449-475.

## Appendix A

In this appendix the method used to simulate a Maxwellian photosheath is briefly discussed. The computation time is much shorter if the speed and direction of the emitted particles are determined rather than the individual velocity components. The probability,  $p$ , that the speed,  $U$ , is less than or equal  $U_0$  is given by

$$p (U \leq U_0) = \sqrt{\frac{2}{\pi}} \int_0^{U_0} U^2 e^{-U^2/2} dU \quad (A1)$$

where  $U$  and  $U_0$  are normalized to the thermal velocity,  $\sqrt{kT/m}$ .

One of us (GKY) has inverted Eq. A1 to give  $U_0$  as a function of  $p$  over the domain  $0 \leq p \leq 1$ . This domain was divided into six intervals and six empirical approximations determined. For  $p \rightarrow 1^-$ , the approach of Hastings<sup>1</sup> has been adopted.

The semiconvergent series for  $p$  as  $p \rightarrow 1^-$  is

$$p = 1 - e^{-U_0^2/2} U_0 \sqrt{\frac{2}{\pi}} \left( 1 + \frac{1}{U_0^2} - \frac{1}{U_0^4} + \frac{3}{U_0^6} - \frac{15}{U_0^8} + \dots \right) \quad (A2)$$

or

$$U_0^2 = -2 \ln(1-p) + \ln(U_0^2) + \ln \frac{2}{\pi} + \ln \left( 1 + \frac{1}{U_0^2} \dots \right)$$

substituting the lead term in the second term and ignoring terms of order  $U_0^{-2}$

$$U_0 \sim \sqrt{-2 \ln(1-p) + \ln[-2 \ln(1-p)] + \ln \frac{2}{\pi}} \quad (A3)$$

we have used

$$t = \sqrt{-2 \ln(1-p) + a_1 + a_2 \ln[-2 \ln(1-p)]} \quad (A4)$$

and

$$U_0 = t + \frac{a_3 + a_4 p + a_5 p^2 + a_6 p^3}{1 + a_7 p + a_8 p^2 + a_9 p^3} \quad (A5)$$

For  $p \rightarrow 0^+$ , the form can be derived formally

$$p = \sqrt{\frac{2}{\pi}} \left[ \frac{U_o^3}{3} - \frac{U_o^5}{10} + \frac{U_o^7}{56} \dots \right] \quad (A6)$$

Let

$$U_o = S + C_3 S^3 + C_5 S^5 \quad (A7)$$

Substituting Eq. (A7) in Eq. (A6) gives

$$p = \sqrt{\frac{2}{\pi}} \left[ \frac{S^2}{3} + (C_3 - \frac{1}{10}) S^5 + (C_5 + C_3^2 - \frac{C_3}{2} + \frac{1}{56}) S^7 + \dots \right]$$

The second and subsequent coefficients can be set to zero by appropriate choice of the  $C_n$  (that is,  $C_3 = 0.1$ ,  $C_5 = 0.0221428571$ , etc.)

$$\text{Thus } p = \sqrt{\frac{2}{\pi}} \frac{S^3}{3} \quad \text{or} \quad S = (4.5\pi)^{1/6} p^{1/3} \quad (A8)$$

For  $p \rightarrow 0^+$ , substitute Eq. (A8) in Eq. (A7). In some of the intermediate intervals of  $p$ , slightly modified analytic forms provided greater accuracy.

Experiments show that photoelectrons produced inside the material surface are emitted with a cosine distribution relative to the surface normal.<sup>2</sup> A second random number,  $q$ , generates the appropriate angle.

The numbers  $p$  and  $q$  are generated by the function, RANF, resident on the AFGL CDC 6600. This generates random numbers uniformly between 0 and 1, excluding the end points. This function is a multiplicative congruential generator. Our use of the random numbers is not affected by the limitations pointed out by Marsaglia.<sup>3</sup> The "seed" for RANF is the quasirandom bit string which is generated by the computer's real time clock.

## References

1. Hastings, C. Jr. (1955) Approximations for Digital Computers, Princeton University, Princeton, N. J.

2. Fadley, C.S. (1973) Theoretical aspects of x-ray photoelectron spectroscopy, Electron Emission Spectroscopy, Dekeyser, W., Fiermans, L., Vanderkelen, G., and Vernik, J., D. Reidel Publishing Co., Dordrecht-Holland, pp. 151-224.
3. Marsiglia, G. (1968) Random numbers fall mainly in the plains, Proceedings of the National Academy of Sciences 61:25-28.

## Contents

1. Introduction	413
2. Charge Separation Between Sunlit and Dark Areas	414
3. Conductor-Like Behavior of the Sunlit Area	415
4. Change in Potential of the Sunlit Area at Expansion or Contraction	418
5. General Conclusions	418
Acknowledgments	419
References	419

## 12. Photoelectric Charging of Partially Sunlit Dielectric Surfaces in Space

Bibhas R. De and David R. Criswell  
Lunar Science Institute\*  
Houston, Texas

### 1. INTRODUCTION

Spacecraft surfaces — or portions thereof — are often made of highly resistive dielectric material. During part of its orbit, a spacecraft assumes configurations where a section of the surface is sunlit and the rest is in darkness. Moreover, as the orbit progresses, this sunlight-shadow configuration changes, causing the sunlit area to expand or contract. These effects can give rise to special photoelectric charging circumstances.

In this paper, we outline some of these circumstances. Some applications of these circumstances to the problem of photoelectric charging of localized sunlit patches in the dark sunset terminator region of the Moon has been discussed elsewhere.<sup>1, 2</sup> In the following, we discuss charging due to the photoelectric effect alone. The presence of an ambient plasma modifies the situation, but the considerations discussed here still apply. However, the discussion of this paper is

\*The Lunar Science Institute is operated by the Universities Space Research Association under Contract No. NSR 09-051-001 with the National Aeronautics and Space Administration. This paper constitutes the Lunar Science Institute Contribution No. 263.

limited to cases where the spin period of the spacecrafts is of the order of or longer than the relevant time-scales that we define in Section 3.

## 2. CHARGE SEPARATION BETWEEN SUNLIT AND DARK AREAS

Figure 1 is a sketch of a partially sunlit dielectric surface. Photoelectrons emitted from the sunlit area can have three types of trajectories: Type A trajectory takes the electrons beyond a predefined limiting distance (such as a Debye-length) such that these electrons do not return to the sunlit area; Type B trajectory takes the electrons to the dark area to locations where the electrons are retained due to the high resistivity of the dielectric material. Type A and Type B electrons are lost to the sunlit area. Finally, Type C trajectory brings the electrons back to the sunlit area without changing the net charge of the area. A steady state is attained when all emitted electrons assume Type C trajectories.

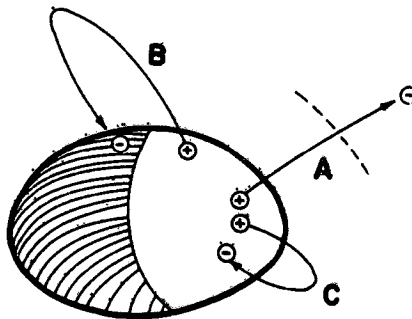


Figure 1. The Three Possible Types of Photoelectron Trajectories: Type A terminates beyond a predefined limiting distance, Type B on the dark area, and Type C on the sunlit area

A little consideration will show — as numerical computations do indeed show<sup>1</sup> — that the accreted electrons on the dark area tend to concentrate near the edge of the sunlight-shadow boundary (with the exception of the case where a dark area is not contiguous with the sunlit area). As we shall explain presently, the positive charges on the sunlit area also tend to concentrate near the sunlight-shadow boundary. This boundary thus represents a region of intense multipole electric fields.

### 3. CONDUCTOR-LIKE BEHAVIOR OF THE SUNLIT AREA

Since the photoemitting area is dielectric, one would commonly assume that the positive charges on the area are immobile. However, this assumption is likely to lead to erroneous results. The positive charges on a photoemitting dielectric surface possess an effective mobility - which causes them to tend to achieve a surface density distribution appropriate to a conducting surface. This is an effect which does not readily emerge from the conventional treatment of the charging problem by solving the Poisson-Vlasov equations. This effect thus represents a shortcoming of the Poisson-Vlasov treatment.

We present below a semiquantitative and heuristic argument to demonstrate the conductor-like behavior of a photoemitting dielectric surface. A full analysis of the problem cannot be undertaken without reference to a specific surface geometry with a specified photon and particle environment.

Consider for simplicity a flat sunlit dielectric surface of finite extent in space. For the moment we ignore the presence of any ambient plasma. Let  $N(\epsilon) d\epsilon$  represent the flux of the emitted electrons in the energy range  $\epsilon$  to  $\epsilon + d\epsilon$ , and let  $\epsilon_0$  be the highest effective energy of the emitted electrons. In the steady state, all emitted electrons return to the surface (that is, they execute Type C trajectories) and there is a steady charge density of  $n$  positive charges per unit area at any point on the surface. Under the assumption of charge immobility, this charge density has the same value over the entire surface.

The uniformity of the charge density over the entire surface gives rise to an electric field component  $E_{\parallel}$  parallel to the surface at any point on the surface. This field influences the Type C trajectories in such a way that the positive charges on the surface appear to be shifting in the direction of  $E_{\parallel}$  so as to annul this field. The positive surface charges thus have an effective mobility which tends to prevent the development of a parallel electric field component. The result is that the surface charge distribution tends to resemble that on a conducting surface and hence the dielectric surface tends to be equipotential. The present effect, however, is better not described in terms of a conductivity, since the surface charges are constrained to move in two-dimensions.

We need, however, to examine the rate at which the redistribution of surface charges takes place in order to determine if this effect is indeed important. The criterion for the effect to be important is that the time-scale for surface charge redistribution be smaller than or of the order of the time-scale over which the surface charge density  $n$  is established. The latter time-scale has a lower limit

$$\tau_n = n / \int_0^{\epsilon_D} N(\epsilon) d\epsilon \quad (1)$$

but is almost certainly larger than this value.

To illustrate the effective mobility, we make the following simplifying assumption: We assume that a typical value  $E_{\parallel}$  characterizing the entire surface has a constant value to a height  $h$  above the surface and vanishes above this height. An electron of energy  $\epsilon$  typically spends a time  $t \sim h \sqrt{m/\epsilon}$  in this field... During this time, the electron has its trajectory altered (from that in absence of a parallel electric field component) so that it is displaced through a distance  $\Delta r \sim h^2 e E_{\parallel} / \epsilon$  in the direction antiparallel to  $E_{\parallel}$  as shown in Figure 2 ( $e$  = electronic charge). This displacement is equivalent to that of a positive surface charge through a distance  $\Delta r$  in the opposite direction.

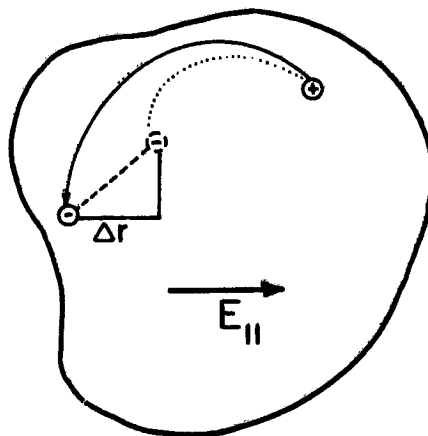


Figure 2. The Dotted Line Represents Trajectory of a Photoelectron Returning to the Sunlit Area in Absence of an Electric Field Component Parallel to the Surface. When such a field component  $E_{\parallel}$  is present, the trajectory is altered and is represented by the solid line. The result is a displacement of the electron through a distance  $\Delta r$  antiparallel to  $E_{\parallel}$ . This is equivalent to a displacement of a positive surface charge through a distance  $\Delta r$  parallel to  $E_{\parallel}$  - tending to counteract  $E_{\parallel}$ .

The value of  $\Delta r$  averaged over all electron energies may be found from

$$\langle \Delta r \rangle = h^2 e E_{\parallel} \frac{\int_0^{\epsilon_0} N(\epsilon) \epsilon^{-1} d\epsilon}{\int_0^{\epsilon_0} N(\epsilon) d\epsilon} . \quad (2)$$

However, regardless of how  $\langle \Delta r \rangle$  is calculated, the rate at which the surface charges move across a unit length perpendicular to  $E_{\parallel}$  is approximately

$$N_{\parallel} = \langle \Delta r \rangle \int_0^{\epsilon_0} N(\epsilon) d\epsilon \quad (3)$$

An upper limit to the charge distribution time-scale is now given by

$$\tau_{re} \approx n \langle \Delta r \rangle / N_{\parallel} = \tau_n . \quad (4)$$

Our approximate analysis thus shows that  $\tau_{re}$  and  $\tau_n$  (the lower limit) are of the same order, showing that the effect that we suggest is significant.

Once the surface has achieved a steady state with a conductor-like charge distribution, the surface charges remain in a steady state of flux and the photoelectrons return to such locations on the surface that the charge distribution remains unchanged subsequently.

If the sunlit portion of the surface is partly dielectric and partly conducting, then the above effect suggests that the conductor-dielectric boundary would not represent as sharp a conductivity discontinuity as one would normally assume. The Type C trajectories would cause the surface charges to migrate across the conductor-dielectric boundary at a nontrivial rate.

The conductor-like charge distribution on the sunlit area implies a concentration of positive charges near the sunlight-shadow boundary — as mentioned earlier.

#### 4. CHANGE IN POTENTIAL OF THE SUNLIT AREA AT EXPANSION OR CONTRACTION

When the sunlit area expands or contracts, the steady state established with a given sunlight-shadow geometry no longer holds. With the changing sunlight-shadow configuration, the surface tends to continually achieve new steady states. Whether or not such steady states are actually attained at each step depends on the rate at which the expansion or the contraction takes place.

Let  $\phi$ ,  $Q$ ,  $A$  and  $C$  be the instantaneous potential, net charge, total sunlit area and the capacitance of this area respectively. Let  $\sigma(\underline{r})$  be the surface charge density, which is a function of the position  $\underline{r}$  on the surface. Then the development of the potential with changing area may be expressed analytically as

$$\frac{d\phi}{dA} = -\frac{Q}{C^2} \frac{dC}{dA} + \frac{1}{C} \frac{d}{dA} \left[ \sum_i \sigma_i \Delta A_i \right] \quad (5)$$

where  $\Delta A_i$  represents an elemental surface area and where the summation extends over the entire sunlit area. The first term on the righthand side of this equation simply gives the change in potential due to the change in capacitance of the sunlit area. The second term gives the change in potential due to the change in the net charge of the sunlit area arising from two causes: (1) the loss or gain of area, and (2) the change in net charge by losing photoelectrons to newly shadowed positively charged portions of the surface, or by new photoemission from freshly annexed negatively charged dark portions of the surface. Using Eq. (5), the development of potential of a contracting or expanding sunlit area may be traced by using numerical simulation methods. We have presented elsewhere an example of such a method.<sup>2</sup>

Whether the potential of a contracting or expanding area increases or decreases with time depends on how the various terms in Eq. (5) compete. The major deciding factor is the rate of contraction or expansion - for this is what determines the attainment of steady states at the successive steps of contraction or expansion. In some cases, it is possible that the potential will increase with time, causing a "supercharging" of the sunlit area.

#### 5. GENERAL CONCLUSIONS

The following general conclusions may be drawn from our discussion:

- (1) Sunlight-shadow effects may substantially alter the charging situation for a dielectric surface. The sunlight-shadow boundary tends to be the site of intense multipole electric fields.

(2) Charges on a sunlit dielectric surface have a finite effective mobility. The charge distribution tends to resemble that on a conducting surface.

(3) A boundary between a conducting and a dielectric surface may not represent a conductivity discontinuity when this boundary is sunlit. Charges may migrate at a nontrivial rate across the boundary.

(4) A contracting or expanding sunlit area may experience a "supercharging." The presence of an ambient plasma will modify these conclusions to an extent depending on the parameters of the plasma medium and the strength of the radiation field.

## Acknowledgments

---

We thank Dr. Eldén C. Whipple for helpful discussions. This work was supported by the National Aeronautics and Space Administration under Contract No. NSG 7171.

## References

1. De, B. R., and Criswell, D. R. (1977) Intense localized photoelectric charging in the lunar sunset terminator region, Part I: Development of potentials and fields, to appear in J. Geophys. Res., 82, 999.
2. Criswell, D. R., and De, B. R. (1977) Intense localized photoelectric charging in the lunar sunset terminator region, Part II: Supercharging at the progression of sunset, to appear in J. Geophys. Res., 82, 1005.

**SESSION III**  
**MATERIALS CHARACTERIZATION**

421

**PRECEDING PAGE BLANK NOT FILMED**

N78-10155

**Contents**

1. Introduction	423
2. Facility Description	424
3. Test Procedure	428
4. Concluding Remarks	429
References	429

## 1. The Lewis Research Center Geomagnetic Substorm Simulation Facility

Frank D. Berkopec, N. John Stevens, and John C. Sturman  
National Aeronautics and Space Administration  
Lewis Research Center  
Cleveland, Ohio

### Abstract

A simulation facility has been established at the NASA-Lewis Research Center to determine the response of typical spacecraft materials to the geomagnetic substorm environment and to evaluate instrumentation that will be used to monitor spacecraft system response to this environment. Space environment conditions simulated include the thermal-vacuum conditions of space, solar simulation, geomagnetic substorm electron fluxes and energies, and the low energy plasma environment. Measurements for spacecraft material tests include sample currents, sample surface potentials, and the cumulative number of discharges. Discharge transients are measured by means of current probes and oscilloscopes and are verified by a photomultiplier. Details of this facility and typical operating procedures are presented.

### 1. INTRODUCTION

Geosynchronous spacecraft have experienced anomalous electronic switching in the midnight-to-dawn region of their orbits. <sup>1</sup> Environmental measurements

have shown that energies of transient particle fluxes are higher than expected in this region.<sup>2, 3, 4</sup> Spacecraft anomalous behavior correlates well with the occurrence of geomagnetic substorms.<sup>5, 6</sup> Differential charging of spacecraft surfaces can occur,<sup>7</sup> and breakdown of charged dielectric materials can follow. Breakdown can result in electromagnetic interference, degradation of thermal control surfaces, and surface contamination.<sup>8</sup>

A joint technology program has been implemented by NASA and the USAF to investigate the spacecraft charging phenomenon.<sup>9</sup> One objective of the joint program is to determine the charging behavior of spacecraft materials in a sub-storm environment and what effect configuration has on this behavior. This information will be used in future spacecraft design practice.

The approach to materials characterization is both experimental and analytical. The results of survey tests for a wide variety of spacecraft surface materials have been summarized and have been published.<sup>10-14</sup> An analytical program has been developed in parallel with the experimental effort.<sup>15</sup> The experimental work has been performed in a facility specifically developed to simulate the substorm environment. This substorm simulation facility is the subject of this paper.

## 2. FACILITY DESCRIPTION

The simulation facility was developed to characterize the behavior of spacecraft materials exposed to a simulation of the geomagnetic substorm environment. A schematic diagram of the spacecraft charging test facility is presented in Figure 1.

### 2.1 Test Chamber

The facility test chamber is a stainless steel vacuum chamber 1.8 m in diameter and 1.8 m in length. A 1.5-m diameter thermal control shroud lines the chamber interior. The shroud temperature is controlled by gaseous nitrogen which can be set to any temperature in the range from  $-185^{\circ}$  to  $+120^{\circ}\text{C}$ . The shroud is aluminum and is painted with a black electrically conductive paint providing a grounded boundary for all tests. The test chamber is pumped by a 0.9 m (36-in.) diameter oil diffusion pump and typically operates in the range from  $6 \times 10^{-8}$  to  $2 \times 10^{-7}$  torr. Pumpdown time is on the order of 90 to 120 minutes but generally testing is delayed until samples have sufficiently outgassed.

### 2.2 Simulation

The substorm environment is simulated in discrete increments. The aspect of the substorm environment that is of most interest is the electron environment.

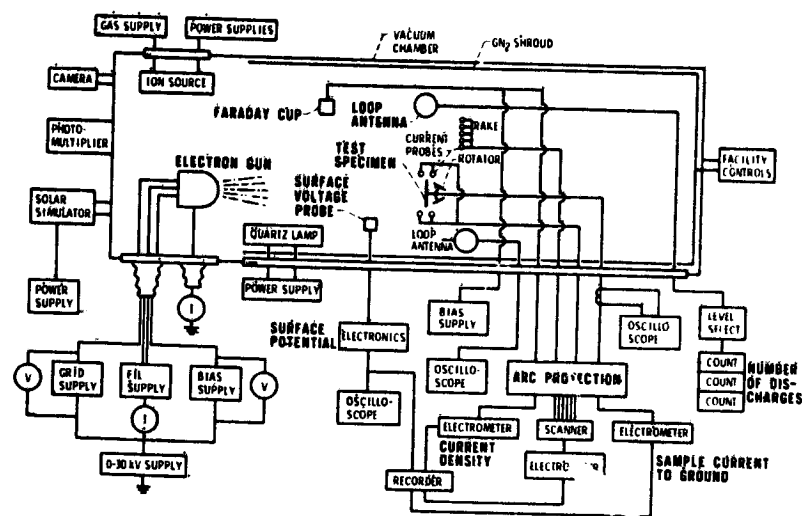


Figure 1. Schematic Diagram of the LeRC Substorm Simulation Facility

It is simulated with a monoenergetic electron beam operated at a voltage in the range from 0 to 30 kV and at a current density in the range from 0 to 5 nA/cm<sup>2</sup>. The divergent electron beam is generated from a hot wire filament by means of a spherical segment accelerating grid kept at ground potential. The cathode and the beam-forming grids are biased negatively relative to this accelerating grid. The electron beam current density is uniform to about 30 percent over a diameter of 0.5 m at the test plane. The test plane is approximately 1 m from the accelerating grid.

Solar simulation is used when photoeffects are to be determined. A 3/4-sun intensity xenon lamp is used; intensity is measured at the test plane. The solar simulator is located outside the chamber and the radiation is passed through a quartz window. The spectral distribution, with the quartz window of the chamber, is within 10 percent of that recently published<sup>16</sup> for solar radiation.

Low energy plasmas are simulated by means of a gaseous nitrogen electron bombardment plasma source. Nitrogen gas is admitted into a discharge chamber containing a hot wire filament cathode and a cylindrical shell anode. A magnetic field coil is spirally wound around the anode to increase the path length of the bombarding electrons from the cathode to the anode and thereby enhance the ionization efficiency. Plasma densities from about 10 particles per cm<sup>3</sup> up to 10<sup>6</sup> particles per cm<sup>3</sup> can be simulated. The plasma source is routinely used to discharge samples after testing.

### 2.3 Sample Accommodation

Figure 2 is a photograph of the test chamber interior. Samples to be tested are mounted on a three-position sample rotator. Up to three different samples can thus be tested during each pumpdown of the facility. Vacuum can be maintained for several weeks for survey tests of three samples. Samples up to 30 by 30 cm in size can be accommodated. The sample under test is located on the test chamber centerline as is the electron source. The electron source is mounted on the chamber door seen partially on the right in Figure 2.

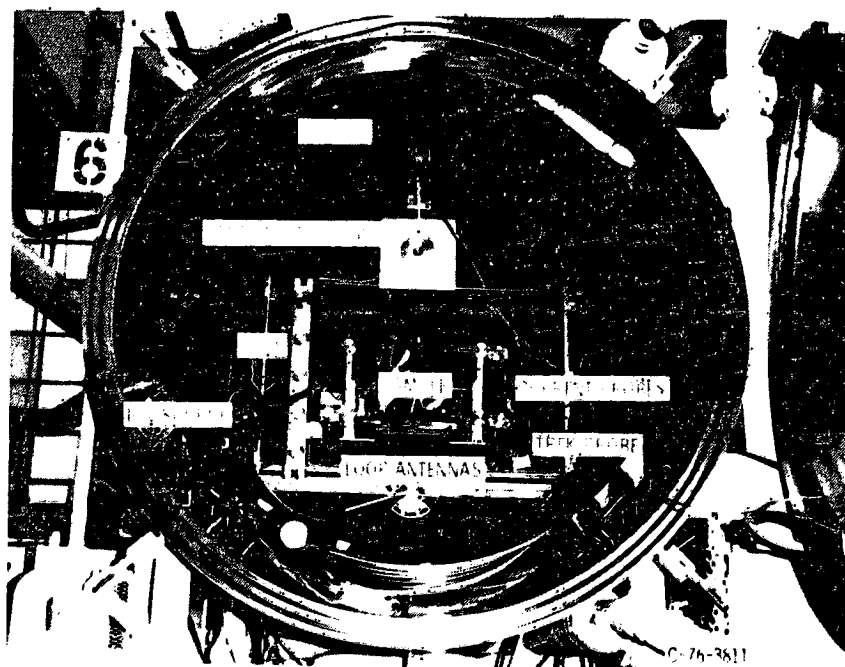


Figure 2. LeRC Substorm Simulation Facility Test Chamber Interior

### 2.4 Instrumentation

#### 2.4.1 ELECTRON ENVIRONMENT MEASUREMENTS

The electron current density at the test location is measured with a Faraday cup. The Faraday cup is mounted to a 30 by 30 cm metal plate which shields the test sample. The Faraday cup-sample shield assembly is positioned in front of the sample only while the current density is being set. The entrance area of the Faraday cup is 10 cm<sup>2</sup>. The suppression grid is operated at -40 volts. Stationary

current probes are mounted around the sample. These probes are plain metal disks, 5 cm<sup>2</sup> in area, that are used to monitor the current density at the test plane throughout testing. The current density profile of the test plane is obtained by sweeping a rake of 5 current probes across the test chamber. The Faraday cup, shield, stationary current probes, and rake can be seen in Figure 2.

#### 2.4.2 SAMPLE MEASUREMENTS

Two basic measurements are made when a sample is subjected to the simulated substorm environment. The first of these is the sample electron current-to-ground. Samples are generally mounted on a metal plate substrate with the dielectric surface facing the beam. During test the substrate is grounded through an electrometer. The current through the sample is then obtained as a function of time.

Sample surface potential is the second basic measurement made. Surface potential is measured by sweeping an electrostatic voltmeter probe across the sample surface. The electrostatic voltmeter is a noncontacting capacitance coupled device. The electrostatic voltmeter operates on a null balance principle whereby the surface potential probe is brought to the potential of the sample surface by a high voltage power supply. This design provides accurate measurement and minimizes voltage gradients in the measurement location. This measurement is made in the electron beam. Since the probe and the sample are nearly the same potential, the probability of arcing between the probe and the surface under measurement is minimal. The response time of the device is 20 msec to change 10 kV; this is faster than typical charging times being measured. The probe-to-sample surface spacing is generally maintained at 2.5 mm; resolution is within 5 percent at this spacing for spots larger than 9 mm in diameter or strips wider than 6.5 mm.

When arc discharges occur, some additional data is taken. Loop antennas are used to sense and quantify discharge activity. The loop antennas are 15 cm in diameter and the plane of the loop intersects the plane of the sample within the sample area. The antenna-to-sample spacing is about 0.7 m. The signals received by the antennas are amplitude discriminated such that all sensed pulses of greater than several specific magnitudes are counted. The cumulative number of discharges of amplitude greater than 1, 2.5, and 5 volts, for example, at the input to the discrimination circuitry then becomes the basic discharge data. When discharges occur, the sample current measuring electrometers are shorted out of the measurement circuitry and the sample current directly grounded. Inductively coupled current probes and fast oscilloscopes (100 and 250 MHz) are used to measure the arc-discharge currents. A photomultiplier tube is used to sense the visible emission portion of the discharges. The photomultiplier is also used to periodically verify the functioning of the discharge monitoring circuitry.

One of the most frequently used pieces of test chamber apparatus is a Polaroid camera which is used to photograph discharges. Discharge locations as well as some visual discharge characteristics are documented. Time exposures are made for varying periods, depending on the frequency of discharging.

### 3. TEST PROCEDURE

#### 3.1 Initial Condition

Prior to any testing, all instrumentation is calibrated. The test chamber is then evacuated to a pressure of less than  $5 \times 10^{-7}$  torr before any equipment is operated. Samples are generally maintained in vacuum for up to 16 hr before any high voltage testing is performed. Outgassing for this period has been found to be good practice. Before any testing is performed the sample surface potential is measured and discharged with the plasma source. The state of the sample surface is determined from measurements by the sample surface potential probe.

#### 3.2 Establish Electron-Substorm Conditions

The electron beam is established by bringing the Faraday cup-shield assembly to its position in front of the sample shielding the sample from the electron beam. The proper electron beam conditions are then set. These conditions are typically a beam voltage of 2, 5, 8, 10, 12, 14, 16, 18, or 20 kV negative at a current density of 0.5, 1, or 3 nA/cm<sup>2</sup>. Testing is performed by starting at the lowest beam voltage and current density and increasing these, in steps, as the test progresses.

#### 3.3 Testing

Testing is typically performed by setting the beam conditions and stepping through increasing beam voltages at a given current density, increasing the current density, and then again stepping through increasing beam voltages. The sample is discharged with the plasma source before the beam voltage is changed. In this manner, conditions from -2 kV at 0.5 nA/cm<sup>2</sup> to -20 kV at 3 nA/cm<sup>2</sup> are imposed upon the sample. If the test is a survey test, each condition is maintained for 20 minutes or until equilibrium is attained, whichever is longer. When long term effects are under investigation, the specific conditions of interest are imposed on the sample for periods of days or weeks as appropriate.

Testing is routinely done in the dark and at ambient temperature. When photoeffects are to be determined, testing is repeated with the solar simulator illuminating the sample. Simulation of solar eclipse conditions can be done by

testing with and without solar simulation for given periods of time. Eclipse testing might be performed, for example, with a -20 kV beam at 1 nA/cm<sup>2</sup> for 30 minute alternating periods of solar simulation and darkness.

#### 4. CONCLUDING REMARKS

The LeRC substorm facility is in continuous, reliable operation. Characterization of spacecraft materials is in progress and some results have been reported. The facility is modified to incorporate new techniques of measurement and simulation as they are required or as they are available. Independent development of instrumentation is continuously maintained and, when significant instrumentation advances are achieved, they are incorporated into the facility.

#### References

1. Fredricks, R. W. , and Scarf, F. L. (1973) Observations of spacecraft charging effects in energetic plasma regions in Photon and Particle Interactions with Surfaces in Space, R. J. L. Garrd, Editor, D. Reidel Publishing Co. , pp. 277-308.
2. DeForest, S. E. , and McIlwain, C. E. (1971) Plasma clouds in the magnetosphere, J. Geophys. Res. 76(No. 16):3587-3611.
3. DeForest, S. E. (1972) Spacecraft charging at synchronous orbit, J. Geophys. Res. 77(No. 4):651-659.
4. Bartlett, R. O. , DeForest, S. E. , and Goldstein, R. (1975) Spacecraft Charging Control Demonstration at Geosynchronous Altitude, AIAA Paper 75-359.
5. Pike, C. P. (1975) A correlation study relating spacecraft anomalies to environmental data, in Spacecraft Charging by Magnetospheric Plasmas, Progress in Astronautics and Astronautics, Vol. 47, A. Rosen, Editor. , Am. Inst. Aeronaut. Astronaut. /Mass. Inst. Tech. Press, pp. 45-60.
6. Shaw, R. R. , Nanevich, J. E. , and Adamo, R. C. (1975) Observations of electrical discharges caused by differential satellite charging, in Spacecraft Charging by Magnetospheric Plasma , Progress in Astronautics and Aeronautics, Vol. 47, A. Rosen, Editor, Am. Inst. Aeronaut. Astronaut. /Mass. Inst. Tech. Press, pp. 61-76.
7. Whipple, E. C. , Jr. (1975) Observation of Spacecraft Generated Electrostatic Fields in the Vicinity of the ATS-6 Satellite, AAS Paper 75-220.
8. Stevens, N. J. , Lovell, R. R. , and Gore, V. (1975) Spacecraft Charging Investigation for the CTS Project, NASA TM X-71795.
9. Lovell, R. R. , et al. (1975) Spacecraft charging investigation: A joint research and technology program, Paper presented at Spring Annual Meeting of the American Geophysical Union, Washington, D. C.

10. Stevens, N. J., Klinect, V. W., and Berkopec, F. D. (1976) Environmental Charging of Spacecraft Surfaces: Tests of Thermal Control Materials for Use on the Global Positioning System Flight Space Vehicle - Part 1: Specimens 1 to 5, NASA TM X-73467.
11. Stevens, N. J., Berkopec, F. D., and Blech, R. A. (1976) Environmental Charging of Spacecraft Surfaces: Tests of Thermal Control Materials for Use on the Global Positioning System Flight Space Vehicle - Part 2: Specimen 6 to 9, NASA TM X-73436.
12. Berkopec, F. D., et al. (1976) Environmental Charging Tests of Spacecraft Thermal Control Louvers, NASA TM X-73517.
13. Berkopec, F. D., and Stevens, N. J. (1976) Testing and evaluation of solar array segments in simulated geomagnetic substorm charging conditions, Presented at the IEEE 12th Photovoltaic Specialists Conference, Baton Rouge, La.
14. Stevens, N. John, et al. (1976) Testing of typical spacecraft materials in a simulated substorm environment, Paper presented at the USAF/NASA Spacecraft Charging Technology Conference, Colorado Springs, Colo.
15. Purvis, C. L., Stevens, N. J., and Oglebay, J. C. (1976) Charging characteristics of materials: Comparison of results with a simple analytical model, Paper presented at the USAF/NASA Spacecraft Charging Technology Conference, Colorado Springs, Colo.
16. (1971) Solar Electromagnetic Radiation, NASA SP 8005.

## Contents

1. Introduction	432
2. Procedure	433
3. Test Results	434
4. Concluding Remarks	455
References	456

## 2. Testing of Typical Spacecraft Materials in a Simulated Substorm Environment

N. John Stevens, Frank D. Berkopec, John V. Staskus,  
Richard A. Blech, and Steven J. Narciso  
National Aeronautics and Space Administration  
Lewis Research Center  
Cleveland, Ohio

### Abstract

A series of survey tests have been conducted in the Lewis Research Center — substorm simulation facility. The test specimens were spacecraft paints, silvered Teflon, thermal blankets and solar array segments. The samples, ranging in size from 300 to 1000 cm<sup>2</sup> were exposed to monoenergetic electron energies from 2 to 20 keV at a current density of 1 nA/cm<sup>2</sup>. The samples generally behaved as capacitors with strong voltage gradients at their edges. The charging characteristics of the silvered Teflon, Kapton, and solar cell covers were controlled by the secondary emission characteristics. Insulators that did not discharge were the spacecraft paints and the quartz fiber cloth thermal blanket sample. All other samples did experience discharges when the surface voltage reached -8 to -16 kV. The discharges were photographed. The breakdown voltage for each sample was determined and the average energy lost in the discharge was computed.

## 1. INTRODUCTION

Many satellites in geosynchronous orbits have experienced and are experiencing anomalous behavior in their electronic systems at various times in their operational life.<sup>1, 2</sup> This behavior is believed to be caused by the environment charging the insulator surfaces to the point that discharges can occur.<sup>3</sup> These discharges will produce an electromagnetic pulse which can couple into the spacecraft harness and cause an anomaly. Since parts of the satellite that are shaded can charge to a different value from a sunlit surface, the discharge can be between a shaded insulator and the spacecraft structure. Therefore, in order to understand this charging phenomenon, it is necessary to know how typical spacecraft materials respond to the charging environment and to determine what factors influence this charging.

An investigation to determine the materials characteristics under the charging conditions has been initiated at the NASA-Lewis Research Center under the joint USAF-NASA interdependency program.<sup>4</sup> This investigation is a continuation of the work initiated to support the Canadian-American Communications Technology Satellite program.<sup>5</sup>

The approach used in the materials characterization testing was to expose selected test specimens to simulated substorm conditions and determine their response to these conditions. The specimen surface potential and the specimen leakage current to ground were measured as a function of the simulation conditions. From this data the charge deposited and the energy stored in the sample were computed. For those tests where discharges occurred, the surface potential at breakdown, the charge lost and the energy dissipated in the discharge were determined. These tests were run on simple samples to investigate the material characteristics as a function of material geometry, thickness, surface temperature and test duration. Additional tests were run on more complex samples to determine the effects of assembly techniques, surroundings, and multiple surfaces on samples.

This paper will describe the results of survey-type testing conducted on the typical spacecraft external coatings listed in Table 1. The survey-type test is basically a short duration test of 20 minutes at each beam voltage. This period is sufficient to insure that the sample surface has come to its equilibrium potential. The tests were run in the Lewis geomagnetic substorm simulation facility.<sup>6</sup> The test results reported here are for  $1 \text{ nA/cm}^2$  beam current density tests. Unless otherwise specified all data is for dark conditions with the sample at room temperature. More detailed test reports on the samples can be found in the literature.<sup>7-9</sup>

Table 1. LeRC Materials Characterization Studies

Materials tested
Spacecraft paints
S-13G nonconductive paint
Conductive paints
Silvered Teflon samples
Thermal blanket samples
Kapton outer layer
Quartz cloth outer layer
Solar array segments
Standard cells on fiberglass substrate
Solar cells on flexible substrate
Solar cells with conductive film coverglass

## 2. PROCEDURE

The typical data set for the testing is shown in Figure 1. A capacitively coupled, noncontacting surface voltage probe is used to verify that the initial surface potential was zero and then swept across the test surface at fixed time intervals after the sample charging started. Since the probe functions with the beam operating, there is no need to interrupt the test to obtain the surface potential data. This procedure is followed for the test duration and results in transient charging curves for each test conditions. Each time the probe is swept across the sample, voltage profiles are automatically obtained. The typical steady-state profiles for insulating films are shown in the figure.

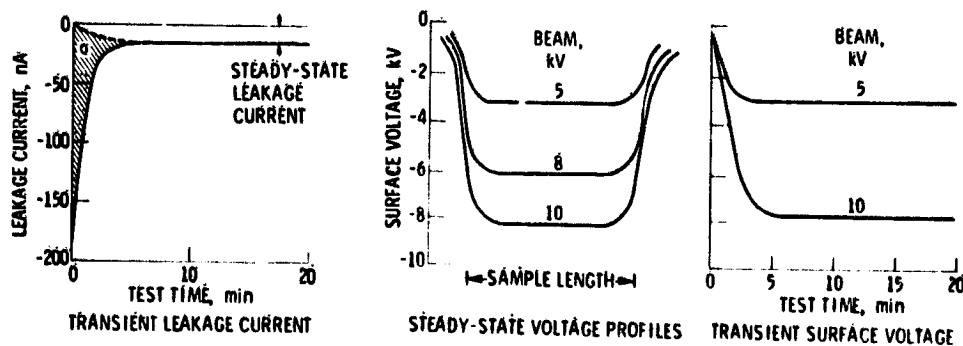


Figure 1. Typical Data Set of Materials Characterization Tests

The total leakage electron current to ground is measured as a function of time after the test start. A typical example of the electron current flow to ground is also shown in Figure 1. This current shows the characteristics of capacitor charging; an initial surge decaying with time to a steady-state value. The charge deposited on the surface can be obtained by integrating this transient current (as shown by the shaded area). Once the charge and surface potential are known, the capacitance and energy storage can be computed. The steady-state values of the surface potential and leakage current can be used to compute the effective resistance of the sample.

The same type of data can be used to obtain the discharge characteristics for the samples that experienced discharges. The voltage probe is used to follow the surface voltage through the discharge. In this manner the breakdown voltage and the potential of the surface after discharge can be determined. The transient leakage current is used to determine the charge deposited up to the breakdown and the charge remaining after the discharge. From this data the charge lost and the energy dissipated in the discharge can be computed.

### 3. TEST RESULTS

#### 3.1 Spacecraft Paints

##### 3.1.1 SAMPLE DESCRIPTION

Both conductive and nonconductive paint samples have been tested. The nonconductive paint chosen for evaluation was the S-13G low outgassing white paint. This paint uses zinc oxide as the pigment with an RTV silicone as the vehicle. The sample dimensions were 17 by 20 cm by 0.02 cm thick.

The conductive paints were black, white, and yellow conductive paints supplied by the Goddard Space Flight Center. These paints were formulated with conductive pigment to provide desired optical properties. The sample area was also 340 cm<sup>2</sup> but the thickness was 0.01 cm.

##### 3.1.2 TEST RESULTS

The results of the simulation test are shown in Figure 2. The conductive paints did not charge; the surface potential remained less than 1 V for all beam voltage conditions. There was no apparent physical damage to the samples as a result of these tests. It is planned to conduct long duration tests of these samples to determine if there will be any time dependent degradation due to the electron bombardment.

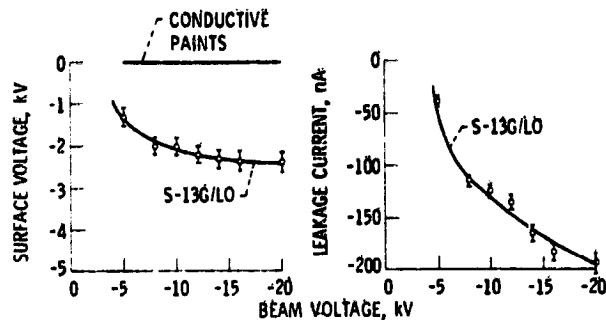


Figure 2. Spacecraft Paints Charging Survey Data

The nonconductive paint does charge but soon reaches a limiting value of about -2200 V. The behavior is typical of those insulators whose resistance decreases with voltage. The steady-state leakage current values verify this resistance decrease. There were no visible discharges during these tests nor was there any apparent damage to the samples as a result of the tests. It was noted, however, that the sample did "electrofluoresce" under electron bombardment - it glowed in the beam.

### 3.2 Silvered Teflon Samples

#### 3.2.1 SAMPLE DESCRIPTION

All of the tests described in this section were conducted with 15 by 20 cm silvered Teflon samples, 0.013 cm (5 mil) thick, with the Teflon surface exposed to the electron flux. The sample was usually made by covering a grounded metal substrate with 5 cm wide strips of silvered Teflon tape. A conductive adhesive was used so that the silver layer was electrically grounded within a few ohms.

#### 3.2.2 TEST RESULTS

##### 3.2.2.1 Charging Characteristics

The results of these tests are shown in Figure 3. The steady-state surface voltage profiles (a) show that the central portion of the insulator reaches a uniform potential dependent only on the beam voltage. Therefore, the central portion of the insulator seems to acquire the characteristics of a conductor - no transverse electric field. However, there is a very pronounced edge voltage gradient that appears to become more pronounced with increasing beam voltage. Apparently these edge voltage gradients can drive currents around the edges contributing significantly to the total leakage current measured in this experiment.

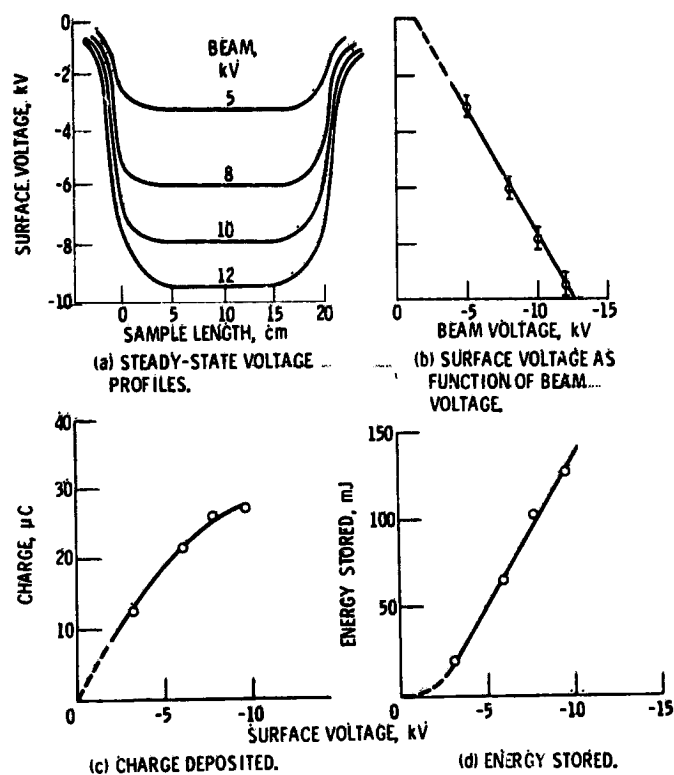


Figure 3. Silver Teflon Charging Data

If the steady-state surface potential for the central portion of the sample is plotted against the beam voltage, a linear relationship results as shown in Figure 3(b). The surface voltage is simply 1800 V less than the beam voltage for the range shown. Since 1800 V is approximately the value for the secondary emission yield to be unity, the surface voltage appears to be controlled by the secondary emission; the leakage currents are too small to influence the surface potential.

If the leakage current transients are integrated, the charge deposited on the sample can be computed. A plot of this charge versus the central surface potential for each test condition is shown in Figure 3(c). The slope of this curve is the effective capacitance of the sample. This curve indicates that the capacitance depends upon the surface voltage. This effect is believed to be due to the edge effect on the surface voltage and not due to a change in the material dielectric coefficient.

Once the charge and surface potential are available, the energy stored in the sample can be computed. This result is shown in Figure 3(d).

ORIGINAL PAGE IS  
OF POOR QUALITY

### 3.2.2.2 Discharge Characteristics

When the beam voltage is increased above -12 kV, visible discharges occur similar to those shown in Figure 4. Pictured is a single discharge event as a result of bombardment with 20 keV electrons. Pinholes were deliberately placed in the center of each 5 cm width of tape. The discharges originate at the edges of the tape and the pinholes which are the places where the largest voltage gradients would be expected.

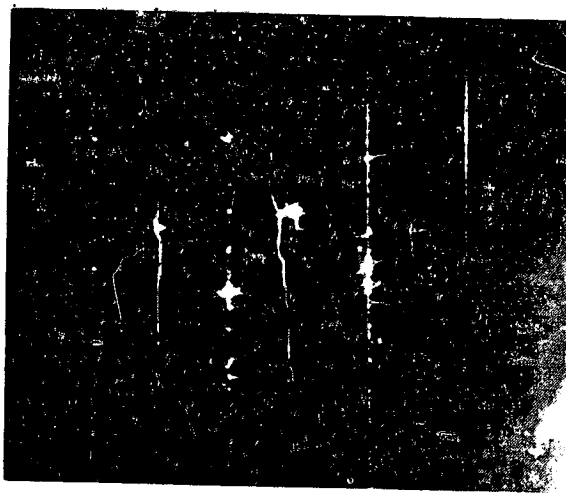


Figure 4. Discharges in Silver Teflon Sample.  
Tape sample, conductive adhesive

The surface voltage and leakage current data obtained during a discharge test are shown in Figure 5. The voltage probe was swept at discrete time intervals and the leakage current was recorded every minute. The actual time of the discharge was determined from the recorder trace of the leakage current. The charge deposited up to breakdown and the charge remaining on the sample after breakdown was computed by integrating the leakage current. The surface voltage was obtained from the probe readings. The energy lost was computed from the charge and voltage values. The effective value of the capacitance also computed from the charge and voltage values, was essentially a constant. The distinction between partial discharge and major discharge depends upon the charge and energy lost in the discharge; in a major discharge a large fraction of charge and stored energy is lost.

Typical characteristics for the discharges in silvered Teflon samples are summarized in Figure 6. One assumption made in these studies is that a single sweep across the sample provides a voltage profile representative of the entire

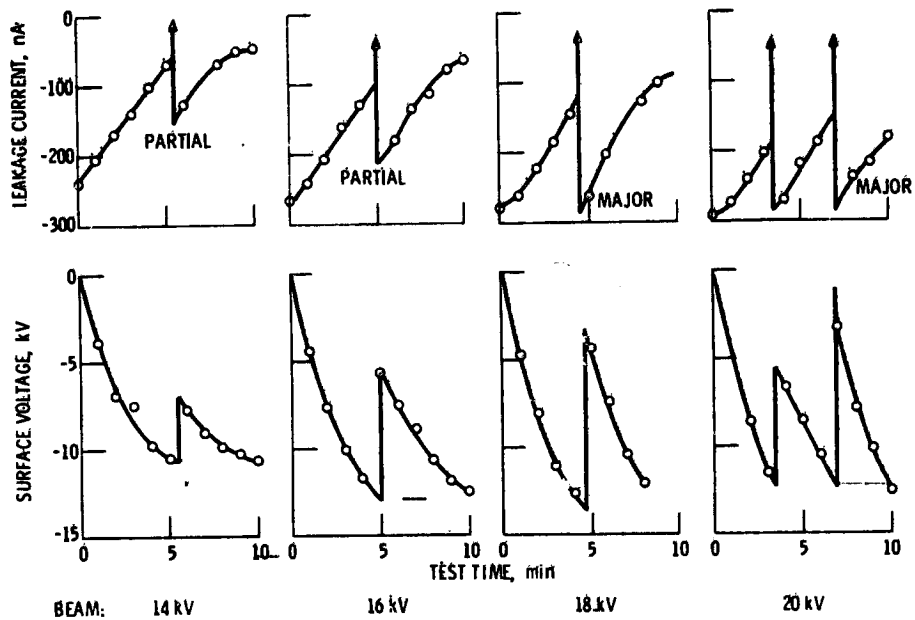


Figure 5. Discharge Characteristics of Silver Teflon Samples

AVERAGE DISCHARGE CHARACTERISTICS

VOLTAGE AT BREAKDOWN:  $-12 \text{ kV} \pm 1.5 \text{ kV}$   
 CHARGE DEPOSITED:  $50 \mu\text{C} \pm 10 \mu\text{C}$   
 CHARGE LOST IN DISCHARGE:  $20-60 \mu\text{C}$   
 ENERGY IN DISCHARGE:  $150-400 \text{ mJ}$

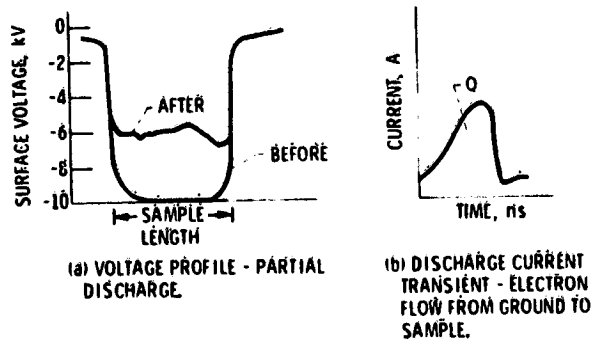


Figure 6. Discharge Characteristics of Silver Teflon Samples

sample. This assumption was verified by comparing sample surface potential profiles obtained just before and just after discharge with computed surface voltage values. These values were computed using a one-dimensional model for a silvered Teflon capacitor. These values are -10,700 V before discharge and -6500 V after discharge. These values are in good agreement with the actual probe readings of Figure 6(a). Hence, it appears that the voltage obtained from the probe sweep is representative of the whole sample.

The transient current pulses during a major discharge under 20 keV electron bombardment have also been obtained. A typical pulse is shown in Figure 6(b). The duration of this pulse is on the order of 500 nsec while the peak amplitude ranges between 20 and 100 A. The maximum values of charge represented by this pulse (from integration of the area under the curve) are on the order of 15  $\mu\text{C}$  instead of the 50 to 60  $\mu\text{C}$  of charge lost in discharge as computed from the surface voltage readings. The replacement current does not appear to compensate for all the charge that is lost in the discharge. A model of the discharge phenomenon is being developed.

As a result of the discharge tests there was some silver loss at the tape edges where the discharges originated. The loss was concentrated at the discharge location and did not appear to increase with time up to test times of several hours.

It was possible that the outgassing of the adhesive in the cracks between the tape might have influenced the discharging characteristics. To investigate this a test was conducted with a single sheet of silvered Teflon mounted on a wire frame with a minimal amount of adhesive on the sample back. Again the Teflon faced the electron beam. The silver layer was wired directly to the electrical ground. The test results were similar to those of the tape samples. The visible discharges observed under 20 keV electron bombardment are shown in Figure 7. This is a time exposure and represents about three major discharges. It appears that if there is any outgassing, it does not appreciably change the discharge characteristics.

### 3.3 Thermal Blanket Samples

#### 3.3.1 SAMPLE DESCRIPTION

Four different types of Kapton outer layer blankets were evaluated in this series of tests. These samples are shown in Figure 8. Sample A, B, and D have 0.013 cm (5 mil) thick Kapton as the outer layer. Sample C has a 0.005 cm (2 mil) thick Kapton outer layer. Sample D has a sewn edge construction while the others have open edges. The interior portions of the blankets are 15 or 20 layers of aluminized Mylar. All metallic layers of all blankets were grounded through the electrometer. In all cases the samples were tested with the Kapton layer facing the electron source.

ORIGINAL PAGE IS  
OF POOR QUALITY

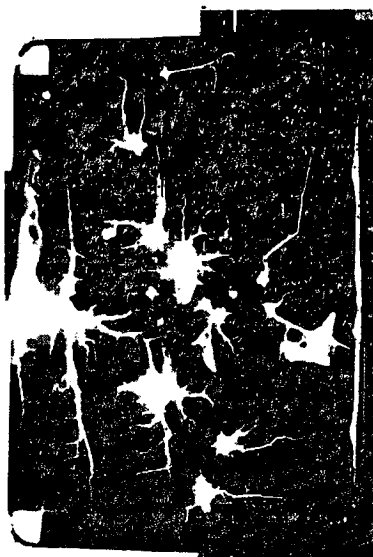


Figure 7. Discharges in Single Sheet Silver Teflon Sample

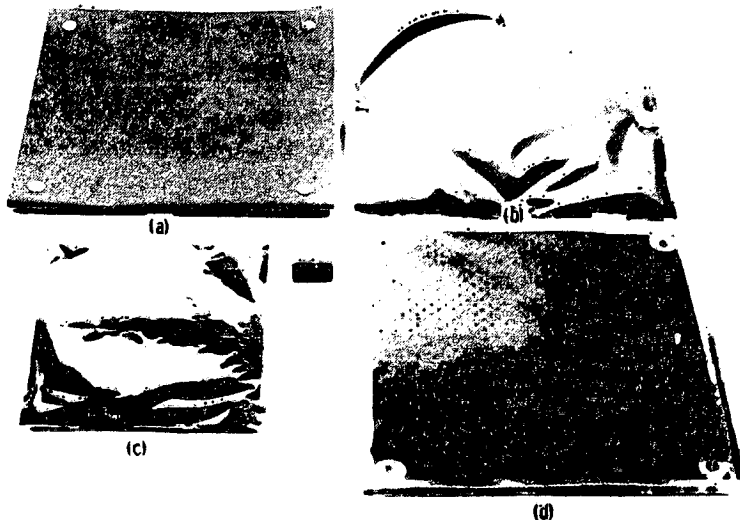


Figure 8. Kapton Thermal Blanket Samples

### 3.3.2 TEST RESULTS

#### 3.3.2.1 Charging Characteristics

The charging characteristics are shown in Figure 9. The steady-state voltage profiles (Figure 9(a)) show the same characteristics as the silvered Teflon film: uniform potential across the central portion of the Kapton with very strong gradients at the edges. The distortion in the voltage profile at the right hand edge (above 5 kV beam voltage) occurred when the probe passed close to a blanket grounding tab.

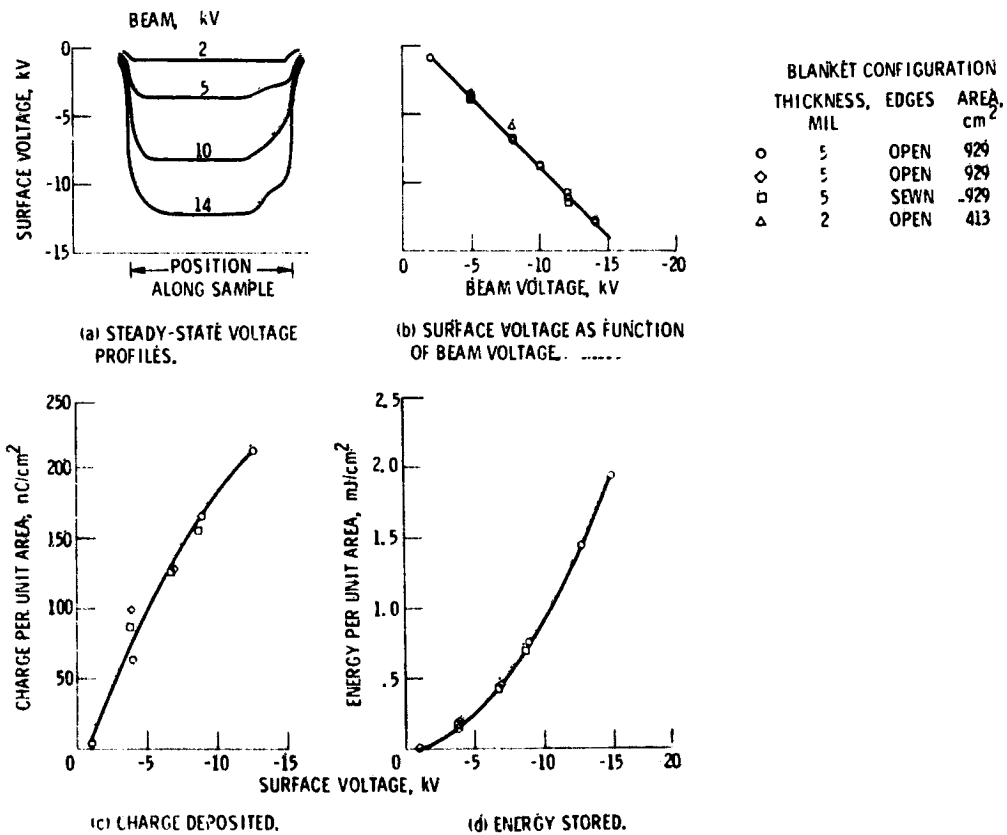


Figure 9

The plot of the steady-state voltage versus the beam voltage (Figure 9(b)) again shows a linear relationship for the 0.013 cm (5 mil) thick Kapton. The surface voltage for the Kapton is 1200 V less than the beam voltage, and again is controlled by the secondary emission characteristics of the surface. The 0.005 cm (2 mil) Kapton material begins with the surface voltage controlled by secondary emission. However, above -5 kV surface voltage, the effect of leakage current begins to slow the rise in surface voltage. This effect is expected based on the lower bulk resistance.

The charge deposited per unit surface area and the energy stored per unit surface area, are shown in Figure 9(c) and (d). The slope of the charge-surface voltage curve again changes with the voltage, showing that the capacitance varies with voltage. This variation is believed to be due to the voltage gradients at the material edges.

The conclusion from this work is that the charging characteristics of Kapton blankets do not appear to depend upon the method of edge treatment. The material thickness dependence is as anticipated. More pronounced effects of edge treatment will be discussed when discharge characteristics are reviewed.

#### 3.3.2.2 Discharge Characteristics

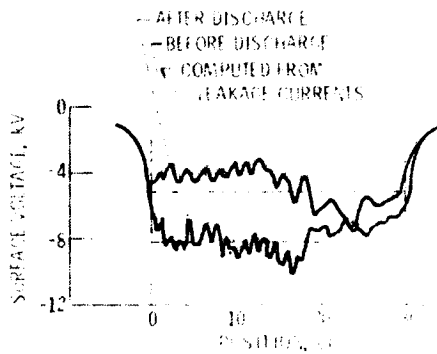
The discharge characteristic data are shown in Figures 10 and 11. Generally, the discharge characteristics of the two 0.013 cm Kapton open edge blankets (Figures 8(a) and (b)) were similar. The 0.005 cm Kapton blanket and the sewn edge blankets (Figures 8(c) and (d)) behaved in a similar manner. Therefore, the discharge characteristics will be discussed only in terms of sewn edge blankets and open edge blankets.

The discharge characteristics of the sewn edge blankets are shown in Figure 10(a). In this figure the surface voltage probe traces just before and after discharge are displayed. Using the transient leakage current data to obtain values for the charge, and the computed value of the capacitance, the surface voltage has been calculated and superimposed on the voltage probe traces. The agreement is very good. Applying these techniques to all of the test data results in the breakdown characteristics listed. It has been found that the initial breakdown for each beam voltage test above -10 kV occurred when the average surface voltage was about -10.4 kV. After this initial breakdown subsequent discharges occurred when the average surface potential reached -8.2 kV. The energy dissipated in these discharges is relatively low. The number of discharges per unit test time, however, is fairly high.

The visible discharges observed on the sewn edge blanket are shown in Figure 10(b). The characteristic of the discharge is that of a glow of light over the Kapton surface with definite discharge spots at the thread line of the blanket edges. It is believed that this sewing acts as the trigger for the discharge.

AVERAGE DISCHARGE CHARACTERISTICS  
MILITARY SPECIFICATION

VOLTAGE AT BREAKDOWN:	-4.5 kV	5.0 kV
CHARGE DEPOSITED:	100 $\mu$ C	100 $\mu$ C
CHARGE LOST IN DISCHARGE:	50 $\mu$ C	50 $\mu$ C
ENERGY IN DISCHARGE:	0.7 J	0.7 J



(a) Surface voltage profile.

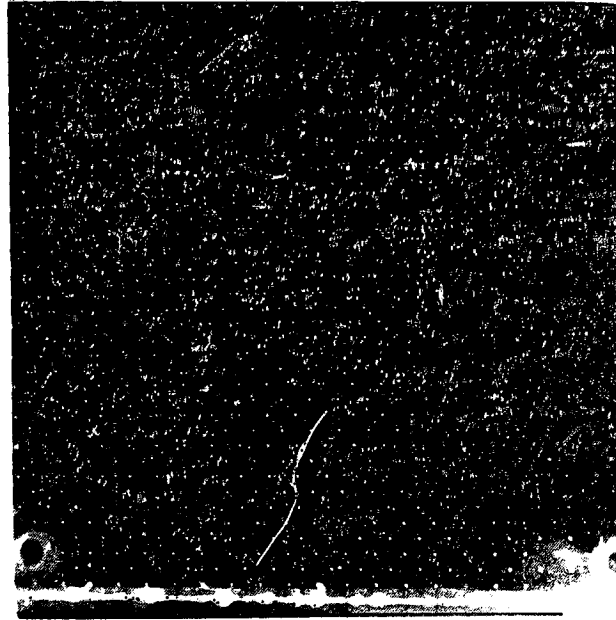
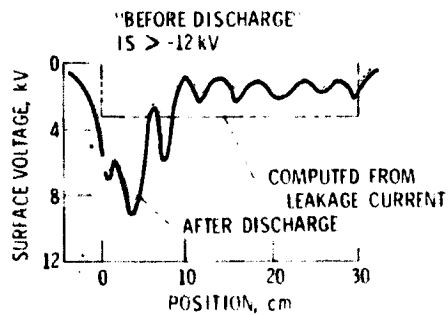


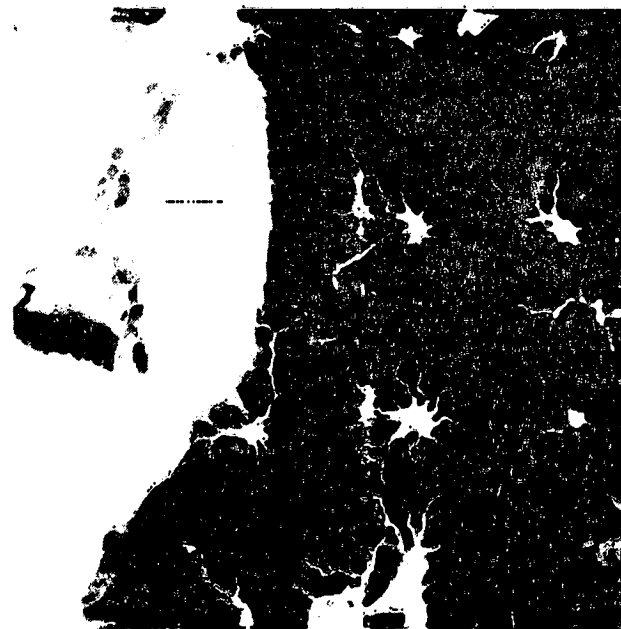
Figure 10. Discharge Characteristics of Sewn Edge Blanket

AVERAGE DISCHARGE CHARACTERISTICS

VOLTAGE AT BREAKDOWN:	-16.5 kV
CHARGE DEPOSITED:	250 $\mu$ C
CHARGE LOST IN DISCHARGE:	200 $\mu$ C
ENERGY IN DISCHARGE:	2.0 J



(a) Surface voltage profile.



(b) Visible damage.

Figure 11. Discharge Characteristics of Open Edge Blanket

The discharge characteristics of the open edge blankets are shown in Figure 11(a). Here, only the trace after the discharge has been obtained. The -12 kV limitation of the surface voltage probe prevented measuring the surface potential profile before discharges occurred. The agreement between the available voltage trace and computed average voltage is still good. As one can see from these characteristics, it requires a large voltage to cause the breakdown, but when it does discharge the energy dissipated is very large. Almost all of the stored energy in the blanket is lost. The visible discharges from this type of discharge are shown in Figure 11(b). The discharges appear as streaks originating at either vent holes or grounding points and extending across the blanket surface.

### 3.3.2.3 Effect of Sunlight on Kapton Blanket Characteristics

A sunlight-eclipse simulation test was conducted using an open edge, Kapton outer layer blanket (Figure 8(a)). The surface voltages measured during this test are shown in Figure 12. The conditions throughout this test were: -10 kV beam voltage with a  $1 \text{ nA/cm}^2$  beam current density. The test was started with the sample potential at zero volts and then exposed to the electron flux with the solar simulator off. The sample charged to about -9 kV as expected. The effective resistance of the sample under the dark steady-state conditions was  $3.6 \times 10^{11}$  ohms.

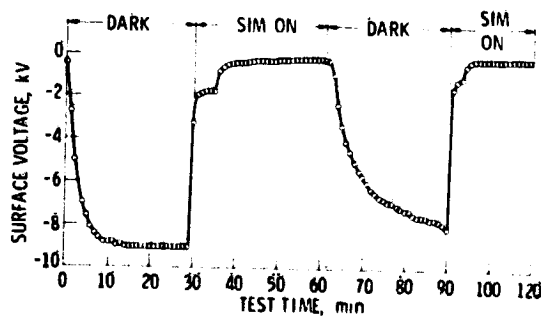


Figure 12. Effect of Sunlight on Kapton Thermal Blankets

The solar simulator was turned on 30 minutes after the test started and remained on for an additional 30 minutes. The surface voltage and the leakage current changed immediately (the step in the curve was caused by the two-stage turn on requirement of the solar simulator). After 30 minutes in the sunlight (at about 3/4 solar intensity), the surface voltage was decreased to about -200 V and the sample effective resistance reduced by 3 orders of magnitude (to  $3.6 \times 10^8$  ohms).

At this point the simulator was turned off and the sample allowed to charge up again. The charging rate for this eclipse cycle was slower than the first eclipse cycle. After the 30 minutes in the dark, the surface voltage reached only -7 kV corresponding to an effective resistance of  $4 \times 10^{10}$  ohms. Turning the solar simulator back on drove the the surface voltage back down to the -200 V level.

The test was repeated with the beam voltage set at 20 kV with a  $1 \text{ nA/cm}^2$  beam current density. The initial dark eclipse simulation resulted in a series of discharges. When the simulator was turned on, the surface potential dropped again to about -200 V and all discharge activity ceased. After 20 minutes into the second eclipse simulation the potential was only about -6 kV with no discharge activity.

The behavior appears to be related to the photoconductivity effect reported for Kapton.<sup>10</sup> The Kapton material has shown an immediate decrease in bulk resistance with illumination and appears to slowly return to the original properties when returned to dark conditions. The Kapton behavior exhibited in these tests is probably not the result of photoemission from the sample since no other material tested with the solar simulator exhibited such an immediate and pronounced drop. The reduction in bulk resistivity could be enhanced by an increase in the sample temperature. But this should take a finite time to cause the change.

### 3.3.3 QUARTZ CLOTH OUTER LAYER BLANKET SAMPLES

Two samples of thermal blankets with Astroquartz cloth substituted for the Kapton outer layer were tested. One sample had a sewn edge (provided by Rockwell International, Inc.) while the second had open edges.

The test results are shown in Figure 13(a) and (b). The steady-state surface voltage as a function of beam voltage (Figure 13(a)) shows that the surface charges only to slightly more than -4 kV under a 20 kV beam test condition. The characteristic corresponds to a sample in which the resistance increases with the surface voltage. The sample effective resistance is shown in Figure 13(b). The transient leakage current data indicate that there is little, if any, charge stored in these samples.

There were no discharges observed during these tests. However, as with the S-15G paint sample, the blanket did electrofluoresce in the beam. A picture of the sample glowing is shown in Figure 14.

## 3.4 Solar Array Segments

### 3.4.1 SAMPLE DESCRIPTION

Three different solar array segments were evaluated in this test series. The segments are shown in Figure 15. Segment A is called the standard solar array segment. It is an array of 24 2- by 2-cm cells in series. The cells are 10 mils (0.025 cm) thick, 10 ohm-cm resistivity, N on P type solar cells. The cover

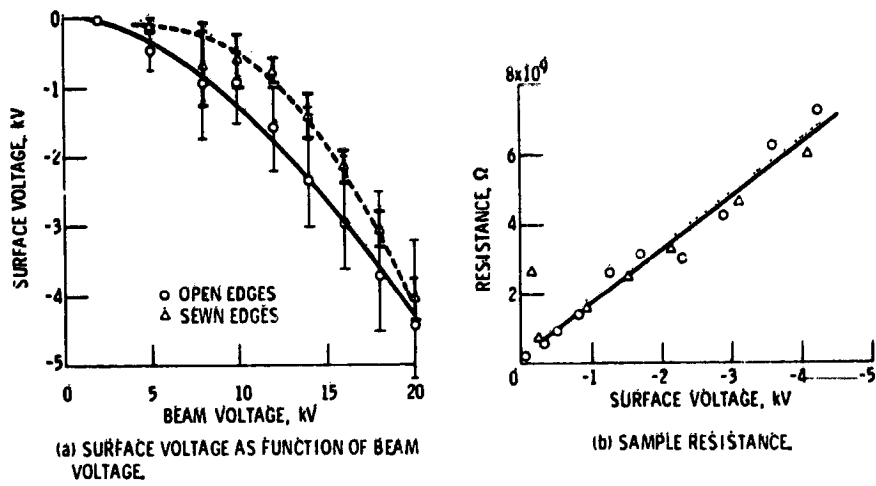
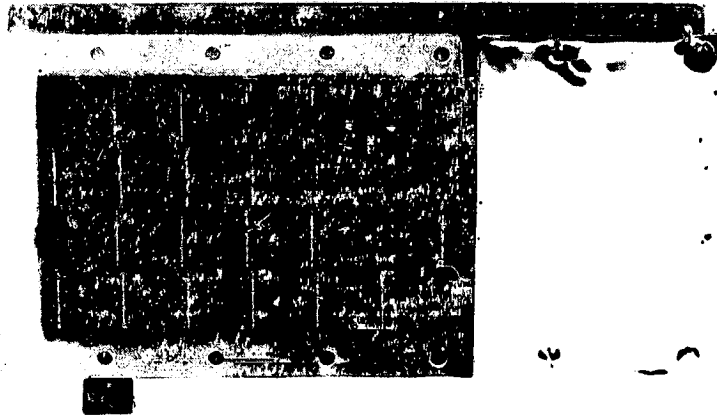


Figure 13. Quartz Cloth Thermal Blanket Charging Survey Data



Figure 14. Glow on Quartz Cloth Thermal Blanket

ORIGINAL PAGE IS  
OF POOR QUALITY



(a) Standard.

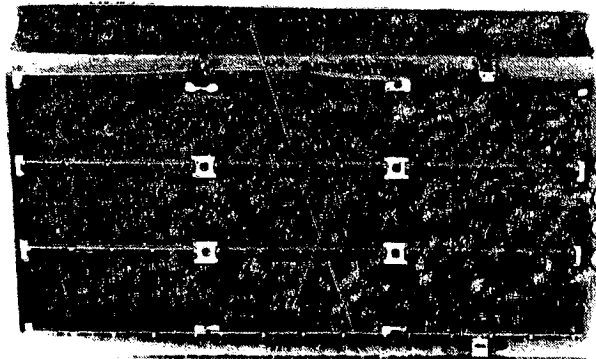
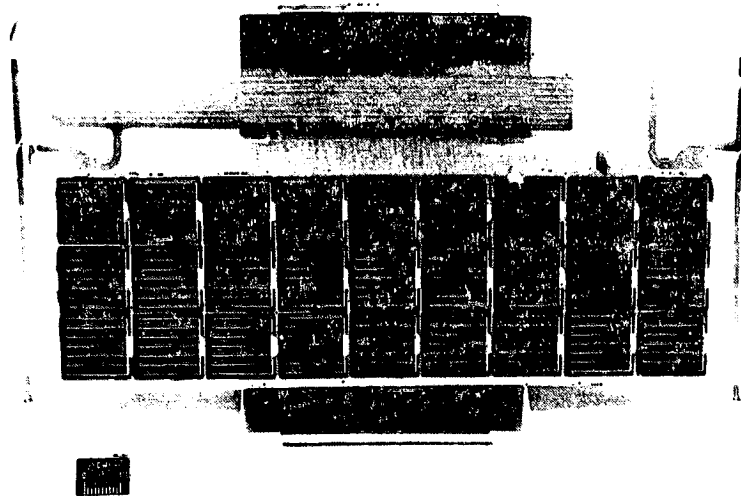


Figure 15

slides are 12 mils (0.03 cm) fused silica (Corning 7940). The cells are bonded to a Kapton sheet which is bonded to a fiberglass sheet. One end of the fiberglass board is covered with a grounded metal plate. The fiberglass on the other three edges of the segment is uncovered and exposed to the electron flux during the testing. The electrical circuit of the segment is grounded through the electrometer for the tests.

Segment B consists of 27 2- by 2-cm cells in a series/parallel configuration. These cells are mounted directly on a 3-mil (0.007-cm) Kapton-fiberglass flexible substrate. The cells are 8-mil (0.012-cm) thick, 1 ohm-cm solar cells. The cover slides are 4-mil (0.006-cm) thick cerium doped microsheet. This segment has been constructed using the same techniques employed in manufacturing the Canadian-American Communications Technology Satellite array.<sup>11</sup>

Segment C consists of nine 2- by 4-cm cells in a series/parallel configuration with a conductive coating on the coverslides. These cells are mounted on a fiberglass board with about a 0.6 cm fiberglass border exposed at all four edges. The cells are 11-mil (0.028-cm) thick, 15 to 45 ohm-cm solar cells. The cover slides are 12-mil (0.03-cm) fused silica (Corning 7940) with a thin, transparent conductive coating applied by the Optical Coatings Laboratory (OCLI). The conductive coatings on each cell have been connected together at the four corners and electrically grounded. During the tests of this segment, the current collected by the conductive covers is monitored separately from the current collected by the array circuit.

### 3.4.2 TEST RESULTS

#### 3.4.2.1 Charging Characteristics

The characteristics of the standard and flexible substrate segments (Figure 15(a) and (b)) are shown in Figures 16 and 17; the conductive coverslide segments will be discussed later. In Figure 16 the voltage profiles across the two segments are shown for various beam voltages. For both segments the effect of the edges is pronounced when the beam voltage exceeds -5 kV. The most severe voltage gradients are produced at the interface between the coverslides and the border. In fact, there is evidence that the border can control the charging of the coverslides (see Figure 16(a)). This effect suggests that material samples should be tested with the flight configuration boundaries in order to evaluate properly the behavior of any particular satellite exterior design.

The steady-state surface voltage reached by the coverslides and the substrates as a function of beam voltage, the charge deposited and energy stored in the segments are shown in Figure 17. The error bars on the voltage curves represent the range of values across the samples.

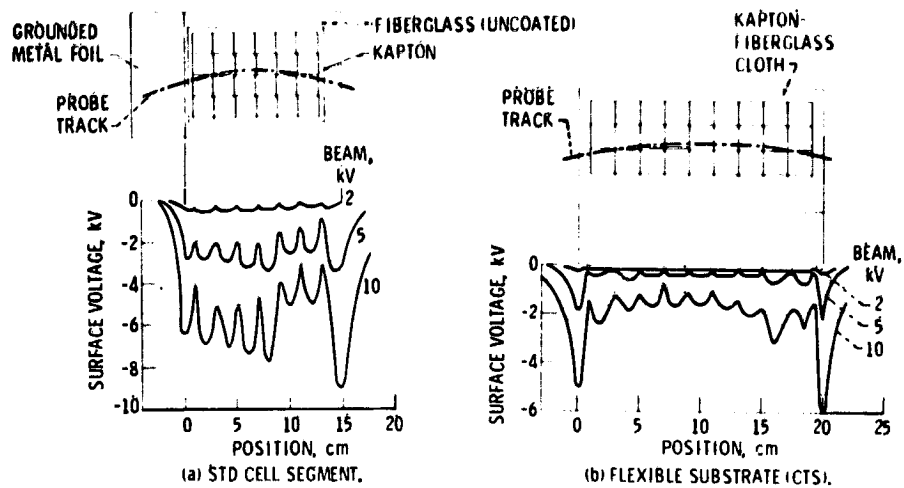
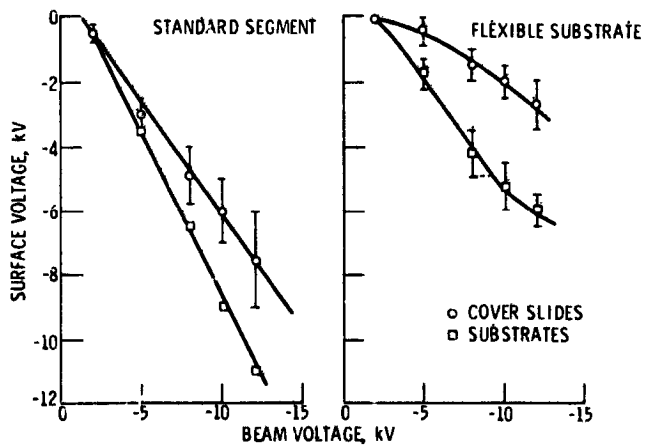
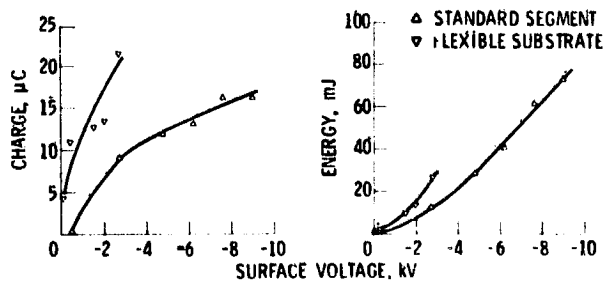


Figure 16



(a) SURFACE VOLTAGE AS FUNCTION OF BEAM VOLTAGE.



(b) CHARGE DEPOSITED ON COVERSLIDES.

(c) ENERGY STORED ON COVERSLIDES.

Figure 17

The surface voltage curve for the standard segment coverslide and the fiberglass are straight lines. This implies that the surface voltage for both is controlled by the secondary emission characteristics of each material with the fused silica being a slightly better emitter.

The surface voltage curve for the flexible substrate segment indicates that the cerium doped microsheet coverslides charge to a lesser value than the fused silica and behave as a material whose resistance increases with voltage. This behavior may be the result of the charging of the border and may not be real. This will be verified in future tests on the microsheet alone. The Kapton-fiberglass substrate behaves as expected. The surface voltage is controlled by secondary emission until the surface potential reaches about -9 kV at which point the leakage current influences the voltage and the curve starts to fall off.

The charge deposited on the coverslides of both segments, along with the energy stored, is shown in Figure 17(b) and (c) as a function of the coverslide average voltage. From these curves it is evident that, although the same charge is deposited on the flexible substrate segment as the standard segment, the energy stored in the flexible substrate segment is considerably less. This effect may be due to the charging of the substrate boundaries. In any case, the techniques used in constructing the flexible substrate segment appear to minimize the charging of the segment.

#### 3.4.2.2 Discharging Characteristics

The discharge characteristics of only the standard array segment have been obtained. For this segment, discharges are observed when the beam voltage is about -14 kV. A picture of a typical discharge is shown in Figure 18. The discharges seem to originate at the edges of the coverslides and culminate in a flash of light over most of the coverslides. There is no apparent physical damage to the coverslides due to these discharges. The voltage-current characteristics of the segment are the same after this test as before. Long time discharge tests are planned to determine if the discharges can eventually decrease the array performance.

The discharge characteristics for this segment have been obtained from the leakage current measurements as shown in Figure 19. The charge stored is computed by integrating this current. The breakdown voltage is computed from the value of the capacitance and the computed charge deposited up to the point of discharge. The energy lost in the discharge is obtained by computing the energy stored at the time of the discharge and the energy remaining after the discharge. The average results for the three partial discharges and the 15 major discharges are tabulated on Figure 19. As can be seen the discharges seem to occur between -8 and -9 kV. In a partial discharge only about 25 mJ are lost whereas the full

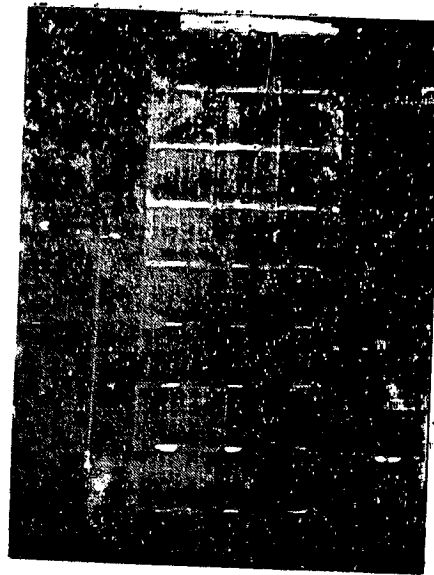


Figure 18. Discharges in Standard Solar Array Segment

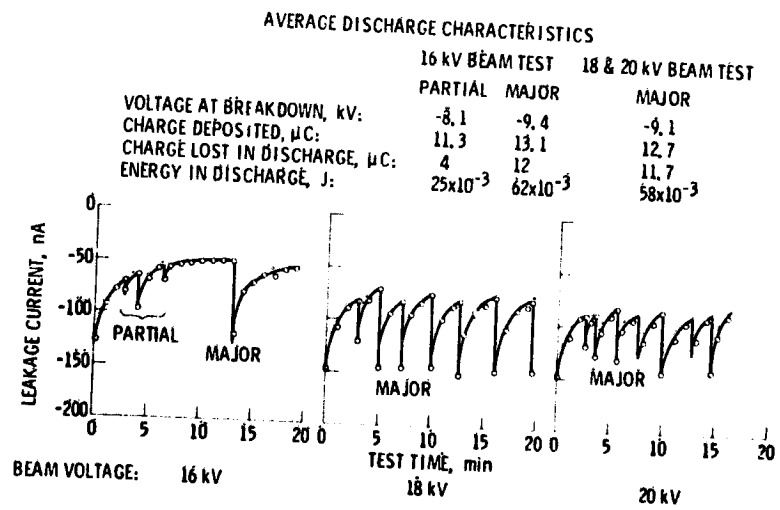


Figure 19. Discharge Characteristics of Standard Solar Array Segment

60 mJ stored in the segment are lost in a major discharge. The reasons for partial discharges in some tests and major discharges in other tests are still to be established.

#### 3.4.2.3 Effect of Solar Simulation on Flexible Substrate Segment

It is known that sunlight will increase the conduction in Kapton<sup>10</sup> exposed to the light. This increase would result in lowering the surface potential and possibly prevent discharging. However, there is a question of what would happen to the dark dielectric surfaces behind the solar cells if the array were exposed to a sub-storm condition while the cell side was illuminated. Would there be discharges? Or would the reduced resistivity of the illuminated Kapton affect the darkened areas? A test has been conducted at the LeRC to determine the response to these conditions. Additional testing of a similar array segment has been conducted in the ESTEC facility.<sup>12</sup>

The flexible substrate segment was mounted in the LeRC facility such that the dielectric side was exposed to the electron flux. A infrared, quartz arc lamp was mounted in the tank so that the light would illuminate the cell side of the segment at about 0.5 solar intensity. Test runs were made at several voltages at a beam current density of  $10 \text{ nA/cm}^2$  first with the lamp off for 30 minutes, then with the lamp on for 30 minutes, followed by 60 minutes again in the dark and finally, 30 minutes with the lamp on again. The total number of discharges detected by the loop antenna 50 cm from the segment was counted at each beam current voltage. The results for the -10, -12, and -14 kV beam voltage tests are shown in Figure 20. Similar trends were found in the -16, -18, and -20 kV tests.

As is apparent from Figure 20, the segment experienced numerous discharges when the segment was in the dark initially. When the light was turned on the discharges stopped immediately. When the lamp was again turned off, the discharges occurred again, but at a significantly lower rate. Even the lower rate was terminated when the lamp was again turned on. Therefore, the light on the cell side of the segment seems to stop the discharges that occur when the dielectric side is bombarded with kilovolt electrons while the cell electrical circuit is grounded. The reason for this behavior is either due to the photoconductivity effect in Kapton or thermal effects in the dielectric (there was no attempt to control or measure the segment temperature during these tests).

The discharges that were observed during this test are shown in Figure 21. This picture is a multiple discharge exposure of the segment in the dark while the dielectric is bombarded. The majority of the discharges occur at the cell interconnects. This implies that the Kapton-fiberglass cloth is charged to a point where there is a breakdown through the cloth to the grounded interconnect. Preliminary calculations indicate that the surface potential is about -8 to -9 kV at the discharge

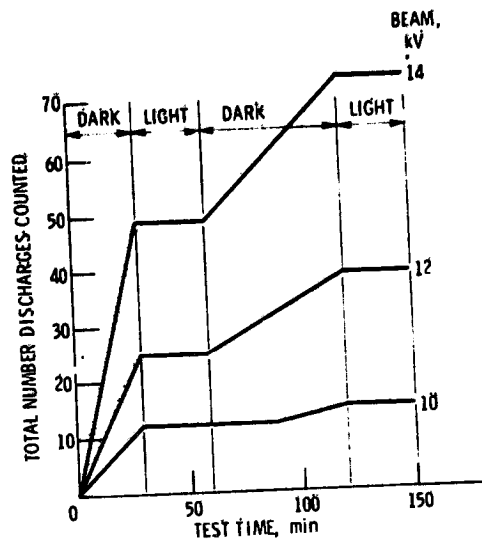


Figure 20. Discharge Characteristics. Eclipse simulation; flexible substrate segment, electron current density,  $10 \text{ nA/cm}^2$

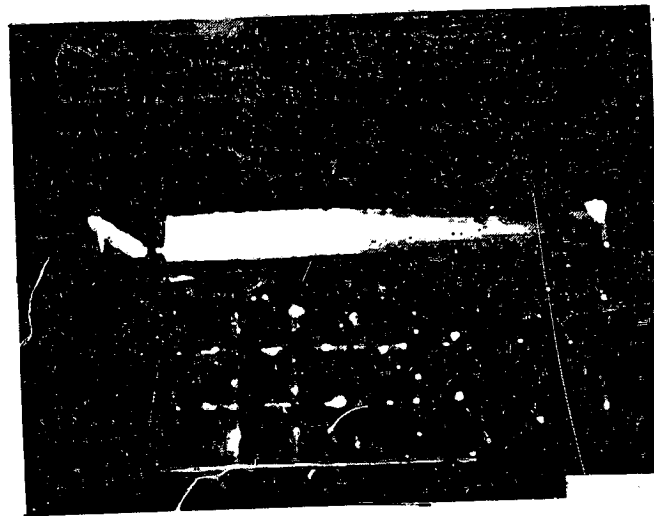


Figure 21. Discharges in Flexible Substrate Solar Array Segment

which is sufficient to break down the thin Kapton sheet between the fiberglass strands.

After running tests on the segment for about 40 hours, a marked decrease in the number of discharges was noted. The segment was removed from the facility and inspected. It was found that the cloth was punctured at every interconnect. This apparently reduced the number of discharges per unit time. There was no degradation of the cell characteristics as a result of these tests.

#### 3.4.2.4 Conductive Coverslide Test Results

This segment was exposed only to a limited test. The voltage profiles obtained are shown in Figure 22. These profiles show that the conductive coverslides remained at ground potential while the surrounding fiberglass boundary charged to rather high potentials. In fact, these reached a point where discharges between the fiberglass and the thin conductive covers were possible. Therefore, the test was stopped. The fiberglass will be covered and grounded and the test will be repeated.

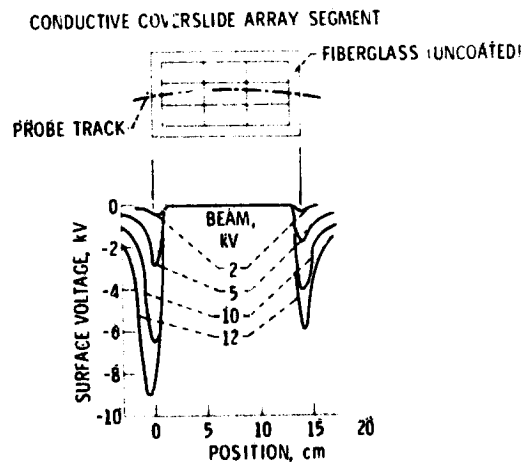


Figure 22. Steady-state Surface Voltage Profiles of Solar Array Segments

The conductive coverslides did collect currents proportional to the cell area and the beam current, as expected. There were no nonuniformities observed in the voltage profile over the conductive coverslides. The location of the gaps between the cells was barely discernible. The sample was very well behaved. The results again pointed out the need to test samples in flight configurations so that the effects of the surroundings can be evaluated.

#### 4. CONCLUDING REMARKS

A series of survey tests have been conducted in the Lewis Research Center geomagnetic substorm simulation facility on typical spacecraft materials. The samples, ranging in size from 300 to 1000 cm<sup>2</sup> were exposed to monoenergetic electron energies from 2 to 20 keV at a current density of 1 nA/cm<sup>2</sup>.

In general, all the insulator materials behave as if they were capacitors with one surface at ground potential while the surface facing the electron beam came to an equilibrium potential that depended upon the secondary emission, backscattering, and leakage currents. Strong voltage gradients were found at the edges of the samples and these must be considered in treating the sample as a simple capacitor. The effective capacitance of the sample appears to change with surface voltage as a result of this edge voltage gradient. Solar simulation changed the charging characteristics of the samples either because of photoemission, photoconduction, or thermal effects. Finally, it was found that the surroundings can influence the charging of the samples. Therefore, realistic evaluations of the behavior of materials for a specific design must include the effects of the surroundings in the flight configuration.

The samples in which discharges did not occur were the spacecraft paints (both conductive and nonconductive), quartz cloth samples and conductive cover-slide solar array segments. In the case of the S-13G paint and the quartz cloth the samples were charged to limited voltage values, but they did "electrofluoresce" in the electron beam.

All of the other samples tested did discharge. The discharges normally originate at the sample edges or at imperfections on the surface. These are the places where the voltage gradients are the most severe. The discharges were visible and have been photographed. The discharges occurred when the surface potential was in the range of -8 to -12 kV. The energy lost in the discharges was computed to be in the range of about 0.6 mJ/cm<sup>2</sup> for the solar array segments to about 2 mJ/cm<sup>2</sup> for Kapton blankets. Construction techniques and surroundings were found to influence the discharge characteristics of the samples so that the evaluation for a particular spacecraft design should involve testing in flight configurations.

There are two scaling factors that still must be resolved. The first is the geometric scaling, or how to determine the characteristics of very large spacecraft surfaces from tests on small area samples. In order to obtain this scaling factor, large area tests in very large facilities must be conducted. Such a test program is being considered for the near future.

The second scaling factor is the environmental scaling or the transition from monoenergetic electron fluxes to the distributed energy plasma of space. One attempt at this extrapolation is given in another paper of this session.<sup>13</sup> The final

answer will come only after space-flight data on the materials characteristics have been obtained from experiments such as those on SCATHA.<sup>2</sup>

The testing program that has been described here will continue until all of the significant parameters for the various spacecraft materials have been evaluated. The information gathered will be issued in reports and catalogued for incorporation in the Design Criteria Handbook that is to be the main output of the joint AF-NASA Spacecraft Charging Investigation.<sup>4</sup>

## References

1. Fredricks, R. W., and Scarf, F. L. (1973) Observation of spacecraft charging effects in energetic plasma regions, in Photon and Particle Interactions with Surfaces in Space, R.J.L. Grard, Editor, D. Reidel Publishing Co., pp. 277-308.
2. McPherson, D. A., Cauffman, D. P., and Schober, W. (1976) Spacecraft charging at high altitudes: The Scatha satellite program, in Spacecraft Charging by Magnetospheric Plasmas, Progress in Astronautics and Aeronautics, Vol. 47, A. Rosen, Editor, Am. Inst. Aeronaut. Astronaut. / Mass. Inst. Tech., 1976, pp. 15-30.
3. Rosen, A. (1975) Spacecraft Charging - Environment Induced Anomalies, AIAA Paper 75-91, Pasadena, Calif.
4. Lovell, R. R., et al (1976) Spacecraft charging investigation: A joint research and technology program, in Spacecraft Charging by Magnetospheric Plasmas, Progress in Astronautics & Aeronautics, Vol. 47, A. Rosen, Editor, Am. Inst. Aeronaut. Astronaut. / Mass. Inst. Tech., pp. 3-14.
5. Stevens, N. J., Lovell, R. R., and Gore, J. V. (1976) Spacecraft charging investigation for the CTS project, in Spacecraft Charging by Magnetospheric Plasmas, Progress in Astronautics & Aeronautics, Vol. 47, A. Rosen, Editor, Am. Inst. Aeronaut. Astronaut. / Mass. Inst. Tech., pp. 263-275.
6. Berkopéc, F. D., Stevens, N. J., and Sturman, J. C. (1976) The substorm simulation facility, Paper presented at the USAF/NASA Spacecraft Charging Technology Conference, Colorado Springs, Colo.
7. Stevens, N. J., Klinec, V. W., and Berkopéc, F. D. (1976) Environmental Charging of Spacecraft Surfaces: Tests of Thermal Control Materials for use on the Global Positioning System Flight Space Vehicle. Part 1: Specimens 1-5, NASA TM X-73467.
8. Stevens, N. J., Berkopéc, F. D., and Bléch, R. A. (1976) Environmental Charging of Spacecraft Surfaces: Tests of Thermal Control Materials for use on the Global Positioning System Flight Space Vehicle. Part 2: Specimens 6-9, NASA TM X-73436.
9. Berkopéc, F. D., and Stevens, N. J. (1976) Testing and evaluation of solar array segments in simulated geomagnetic substorm charging conditions, Paper presented at the 12th Photovoltaic Specialists Conference, Baton Rouge, La.

10. Coffey, H. T., Naniewicz, J. E., and Adamo, R. C. (1975) Photoconductivity of High-Voltage Space Insulating Materials, Stanford Research Inst., Menlo Park Calif.; also NASA CR-134995.
11. Buhs, R. (1974) Layout and technology of the CTS solar array blanket, in Conference Record on the 10th IEEE Photovoltaic Specialists Conference, Inst. Electric. Electron. Eng., New York, pp. 296-306.
12. Bogus, K. P. (1976) Investigation of a CTS solar cell test patch under simulated geomagnetic substorm charging conditions, Paper presented at the USAF/NASA Spacecraft Charging Technology Conference, Colorado Springs, Colo.
13. Purvis, C. K., Stevens, N. J., and Oglebay, J. C. (1976) Charging characteristics of materials: Comparison of experimental results with a simple analytical model, Paper presented at the USAF/NASA Spacecraft Charging Technology Conference, Colorado Springs, Colo.

**Contents**

1. Introduction	459
2. One-Dimensional (1-D) Ground Test Facility Model	460
3. Comparison with Experimental Data	462
4. One-Dimensional Space Charging Model	468
5. Concluding Remarks	472
References	474
Appendix A	475
Appendix B	479

**3. Charging Characteristics of Materials: Comparison of Experimental Results with Simple Analytical Models**

Carolyn K. Purvis, N. John Stevens, and Jon C. Oglebay  
Lewis Research Center  
Cleveland, Ohio

**Abstract**

An understanding of the behavior of materials, of dielectrics in particular, under charged particle bombardment is essential to the prediction and prevention of the adverse effects of spacecraft charging. This paper presents an effort to obtain such an understanding through a combined analytical and experimental approach.

A one-dimensional model for charging of samples in the LeRC test facility is used in conjunction with experimental data taken in this facility to develop "material charging characteristics" for silvered Teflon. These characteristics are then used in a one dimensional model for charging in space to examine expected response. Relative charging rates as well as relative charging levels for silvered Teflon and metal are discussed.

**1. INTRODUCTION**

Two previous papers<sup>1,2</sup> described the test facility, test methods and measurements, and the results of various materials characteristics test performed at the Lewis Research Center in support of the spacecraft charging investigation. The

present paper summarizes the analytical work which has been performed inter-actively with this experimental work. The goal of the analysis is twofold. First, is to model the charging of material samples in terms of the material's parameters. Second, since a goal of the entire study is to predict behavior of spacecraft surfaces, an attempt is made to "scale" the environment, that is, to relate results obtained using a monoenergetic beam in the ground test facility to expected results with distributed particle fluxes of the space environment. An approach to establish this environment scaling is to develop models of charging for both charged particle environments, and assume that the material properties are constant. Then differences between material charging behavior under ground test and in space are a result of the differences in the two environments. It is recognized that the vacuum levels in the ground test and space environments are also different. No attempt is made here to account for this factor.

This paper, then, represents a first attempt at attaining the two goals of characterizing material charging and scaling to the space environment. The models used are one-dimensional and describe charging of samples in terms of the charging of a capacitor. This type of model has been used by a number of workers<sup>3, 4, 5, 6</sup> to describe spacecraft charging.

The procedure used herein was to first develop a one-dimensional model to describe charging of samples in the LeRC vacuum test facility. This model contained a number of parameters which were varied to provide best fits to experimental data obtained in the facility. The values of these parameters which yielded the best fit were identified as the "material charging characteristics." These were then used in conjunction with a one-dimensional model for charging in the space substorm environment to make some predictions of the charging behavior of the materials in space. The insulator studied here is 5 mil silvered FEP Teflon. R

## 2. ONE-DIMENSIONAL (1-D) GROUND TEST FACILITY MODEL

In the LeRC test facility, a monoenergetic beam of electrons with energies of ~2 to 20 keV is directed at normal incidence to planar samples. A beam current density of 1 nA/cm<sup>2</sup> was used to obtain all test data discussed in this report.

The Ground Test Facility Model is a quasistatic current balance model. The current densities considered are those due to primary (beam) electrons, secondary electrons, backscattered electrons, and leakage current through the sample bulk. These are denoted by  $j_e$ ,  $j_s$ ,  $j_{BS}$ , and  $j_l$ , respectively. The sample is assumed to charge like a capacitor. Thus a time balance equation is of the form

$$C \frac{dV}{dt} + j_l = j_e - j_s - j_{BS} \quad (1)$$

where  $V_s$  is the magnitude of the surface voltage. All signs are explicit in this equation, and in all others used in the test facility model, that is, all symbols stand for positive numbers. The actual surface voltage is of course negative, and this is assumed throughout. Thus this model does not predict positive surface voltages correctly, since positive surface voltage would tend to reattract the emitted secondary electrons and this effect has not been included here.

The first term in Eq. (1) represents the net charge deposited on the surface (per  $\text{cm}^2$ ) in a time step, and so is termed the charging current density and denoted by  $j_c$ . The procedure used was to initialize at  $t = 0$  with  $V_s = 0$ . Then  $\Delta V_s$  was calculated from

$$\frac{\Delta V_s}{\Delta t} = \frac{1}{C} [j_e - j_s - j_{BS} - j_l] \quad (2)$$

The current densities are all functions of  $V_s$  and their functional forms are given in Figure 1. Equation (2) is solved by an iterative procedure. This equation can be expressed as

$$\Delta V_s = f(V_s) \Delta t \quad (3)$$

With the initial assumption  $V_s = 0$ , a suitable  $\Delta t$  is chosen, and  $\Delta V_s$  calculated.  $V_s$  is then incremented by  $\Delta V_s$  (set =  $\Delta V_s$  for the first iteration) and the procedure repeated until equilibrium is reached, that is, until

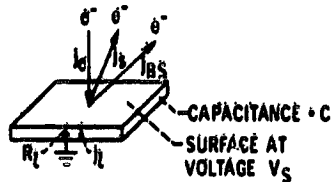
$$j_c = C \frac{dV_s}{dt} = 0$$

The several current densities in the preceding equations are functions of surface voltage. All but the leakage current density are functions of the primary electron beam voltage and current density. The parameters which can be varied are the secondary emission maximum yield,  $\delta_m$ , and energy for maximum yield,  $V_m$ , the backscatter coefficient,  $\xi$ , the resistivity,  $\rho$ , and the capacitance  $C$ . In practice, values for  $\delta_m$  and  $V_m$  were taken from the literature. Values for  $\rho$  were determined from the measured surface voltages and currents at equilibrium, and fits obtained by varying  $\xi$  and  $C$ . This is discussed more fully in Section 4.

It should be noted that this model does not account for beam spread in angle or energy, the presence of the vacuum tank walls, or residual gas in the chamber. Since it is one-dimensional, it can not, of course, explicitly describe edge effects, or effects due to surface variations.

Derivations of the current density equations are presented in Appendix A. A summary of the model and equations is given in Figure 1.

CURRENT DENSITIES TO SAMPLE



ASSUMPTIONS  
 MONOENERGETIC DIRECTED BEAM  
 NORMAL INCIDENCE ON PLANAR SAMPLES

CHARGING MODEL

$$j_b(V_S) - j_s(V_S) - j_{BS}(V_S) + j_l(V_S) + I_m$$

$$I_m = A j_m \cdot \text{CURRENT}$$

FUNCTIONAL FORMS  
 DARK CONDITION - NO PHOTOEMISSION

SYMBOL & FORMULA	CURRENT DENSITY DUE TO
$j_b = j_0 \left(1 - \frac{V_S}{V_B}\right)^{1/2}$	ELECTRON BEAM
$j_s = j_0 7.4 \delta_m \frac{V_B}{V_m} \left(1 - \frac{V_S}{V_B}\right)^{3/2} \exp\left(-2 \sqrt{\frac{V_B - V_S}{V_m}}\right)$	SECONDARY ELECTRONS
$j_{BS} = \epsilon j_0 \left(1 - \frac{V_S}{V_B}\right)^{1/2}$	BACKSCATTERED ELECTRONS
$j_l = \frac{V_S}{R_l A} = \frac{V_S}{\rho l} = \frac{V_S}{\rho \cdot l}$	LEAKAGE THROUGH INSULATOR
$j_c = C \frac{dV_S}{dt}$	SURFACE CHARGING

Figure 1. 1-D Model Ground Test Environment

3. COMPARISON WITH EXPERIMENTAL DATA

3.1 "Floating" Aluminum Plate

The first test data used in conjunction with the test facility charging model were those taken with a bare aluminum plate which is normally used for substrates. This plate was mounted in front of a second identical plate which was grounded to the chamber walls. These two plates were held apart and electrically isolated by a Teflon spacer plug 0.7 cm long. The plates are rectangular with dimensions 15 cm x 20 cm (~300 cm<sup>2</sup> area). Surface voltage of the floating plate was measured as a function of time using the surface voltage probe.<sup>1</sup>

Figure 2 shows these data and the best fit calculated curves. In obtaining these fits to the data, values of  $\delta_m = 3$  and  $V_{max} = 400$  were used. These are consistent with ranges of values for these parameters given by Gibbons<sup>7</sup> for a surface layer of Al<sub>2</sub>O<sub>3</sub>. It is reasonable to expect some oxide on the surface of the "bare aluminum" plate since it had in fact been exposed to air. This points up

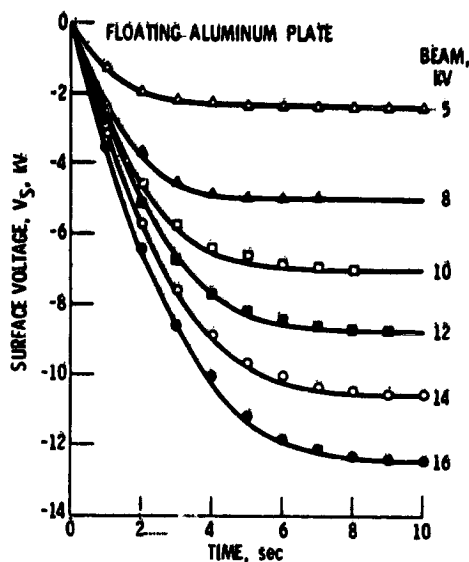


Figure 2. Comparison With Experimental Data

the strong dependence of charging phenomena on sample surface condition, and indicates that care must be taken in making predictions for charging to consider the state of the surface.

With these values in the expression for secondary emission, the values of  $C$  used to obtain the curves in Figure 2 varied from  $1.2 \times 10^{-10}$  farads at  $V_B = 5$  kV to  $5 \times 10^{-11}$  farads at  $V_B = 16$  kV, decreasing approximately linearly with increasing beam voltage. The values used for the "backscatter coefficient" varied from 0.15 at  $V_B = 5$  kV to 0.5 at  $V_B = 16$  kV, again in approximately linear fashion. The expression used to calculate secondary emission current density is derived from an expression for yield as a function of primary energy due to Sternglass.<sup>8</sup> It is plausible that the required variation of  $\xi$  to obtain fits to the data is accounted for, in part, by deviations of the actual secondary yield from that predicted by Sternglass formula. That is, the adjustments to  $\xi$  represent adjustments to the sum of the backscattered and secondary electrons.

The final point of concern here is the time scale for charging of the floating plate; it reaches its equilibrium floating voltage with a time constant of several seconds. This is not surprising, since the capacitance of the test plate to its surroundings is expected to be small. The timescale, is relevant, however, to the question of the behavior of composite samples. This is discussed more fully in Section 3.3.

### 3.2 Silvered Teflon Samples

The 1-D model was next used to fit current and surface voltage data from silvered Teflon samples. These consist of an aluminum substrate with three strips of 5 mil silvered Teflon mounted with conductive adhesive to the substrate. Each of these strips was 5 cm wide and 20 cm long. During test, the aluminum substrate (and consequently the silver) was grounded, while the Teflon surface was bombarded with electrons.

The data and calculated fits for beam voltages at which equilibrium is reached are shown in Figure 3. These data are a composite of four separate data sets, and indicate charging times on the order of minutes. The error bars reflect the scatter in the data as well as the  $\pm 5$  percent resolution uncertainty in the voltage measurements. Since for insulators there are strong voltage gradients near the edges of the samples, the surface voltage measurements are those read at the sample center which is uniform.

To obtain these curves, the effective resistance was calculated from the equilibrium values of surface voltage and leakage current. These values indicate an effective resistivity for the samples of about  $9 \times 10^{15} \Omega\text{-cm}$ , about an order of

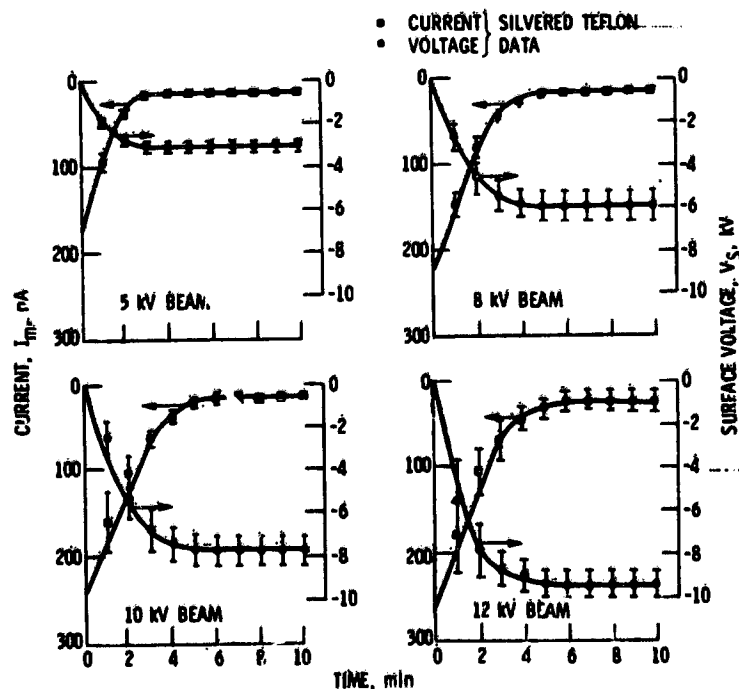


Figure 3. Comparison With Experimental Data. 5 Mil Silvered Teflon Samples; 300 cm<sup>2</sup> Area

magnitude below published values for Teflon. If one assumes that the published value of  $10^{17} \Omega\text{-cm}$  is accurate, then a parallel path having a resistance of about  $4 \times 10^{11} \Omega$  is indicated by the data. This could be a surface leakage, or an edge leakage, or leakage through the sheath.

Values of  $\delta_m = 3$  and  $V_{\max} = 300$  were used in the expression for secondary emission, in accordance with the data given by Willis and Skinner.<sup>9</sup> The values of  $C$  required ranged from  $14.6 \text{ pf/cm}^2$  at  $V_B = 5 \text{ kV}$  to  $10 \text{ pf/cm}^2$  at  $V_B = 12 \text{ kV}$  and decreased monotonically with increasing beam voltage. Extrapolation of the curve to  $V_B = 0$  indicates a dielectric constant for Teflon of  $\sim 2.1$ . This decrease in effective capacitance is believed to be associated with edge effects. Edge gradients are observed in the data. These become more pronounced at higher voltages reducing the effective area.<sup>2</sup> The value used for the backscatter coefficient varies about an order of magnitude for the Teflon samples. Not only does it change with beam voltage, but also appears to change during charging at a single beam voltage. For the initial portion of the charging curves,  $\xi$  varied from 0.25 at the lower beam voltages to 0.05 at high beam voltages. At equilibrium,  $\xi$  varied from 0.02 at low beam voltages to 0.25 at high ones. These variations were not linear; rather,  $\tau$  was relatively constant at low and high beam voltages, with a transition occurring between  $V_B = 8 \text{ kV}$  and  $V_B = 12 \text{ kV}$ . Again, part of these variations may be due to deviations of the actual secondary emission from that calculated by the analytical expression being used.

Some investigation was undertaken to study the behavior of the Teflon samples during arcing. Figure 4(a) shows a curve fit to a composite of two data sets for the initial charging transient with a beam voltage of 16 kV. Figure 4(b) shows the

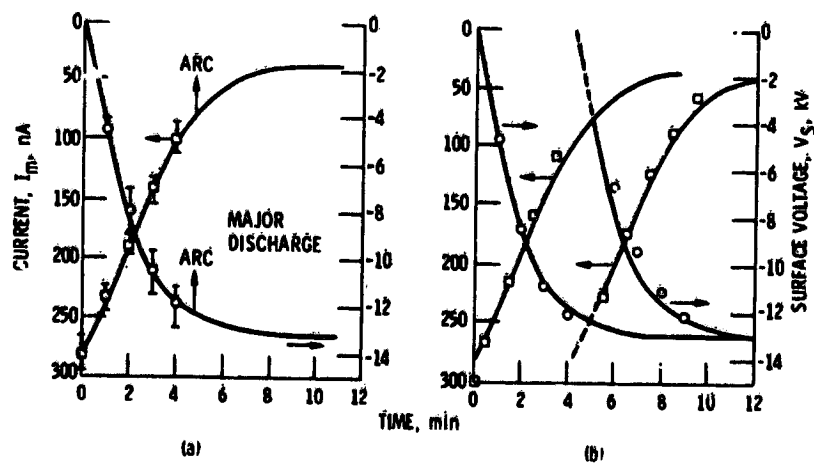


Figure 4. Comparison With Experimental Data. Discharge transients; silvered teflon samples; 16 kV beam

same calculated curves, this time with a single set of data. The left hand set of curves and points are the initial charging transient. An arc occurred on this sample between the time of the voltage reading at  $t = 4$  min and that of the current reading taken at  $t = 5-1/2$  min; the surface discharged, and charging was repeated. The curves shown for the post-arc charging transient are identical to those for the initial transient, but shifted in time. This indicates that the charging transient is quite repeatable, not only from test to test of Teflon samples, but also through arcing. That is, at least short term, the arcing does not affect the charging behavior of Teflon samples.

### 3.3 Composite Sample

One of the stated objectives of the present work was to investigate the "environment scaling" effects between the ground test and space environments. An obvious difference other than the environment between ground tests so far described and the space condition is that the studies of silvered Teflon discussed above were all conducted with the substrate grounded. In contrast, for the case of a spacecraft in orbit, the entire body, including the "grounds" must come into equilibrium with the charged particle environment. The question of the behavior of a composite system becomes particularly interesting because of the divergent time scales in which charging of "floating" metal plates and silvered Teflon above ground are observed to occur.

To investigate this question, a composite sample was built and tested. The sample consisted of an electrically floating standard aluminum substrate with two strips of the 5 cm silvered tape mounted on it. This allowed for a 5 cm strip of the aluminum between the two Teflon strips to be exposed to the electron beam. The aluminum substrate was mounted in the test chamber in the same manner as the floating aluminum plate described in Section 3.1. This configuration is depicted at the top of Figure 5(a). The bottom of this figure shows a voltage trace at equilibrium for this sample.

The expectation was that this composite sample would charge in two stages because of the different effective capacitances through which the aluminum and the Teflon must charge. The prediction, shown in Figure 5(b), is based on the idea that when the beam is turned on, the aluminum should charge to its equilibrium voltage with its time constant of seconds, carrying the Teflon voltage with it. When this has occurred, the Teflon should continue to charge from the equilibrium voltage of the aluminum to its own equilibrium voltage with its own time constant, that is, minutes. The curves in Figure 5(b) were thus obtained by superimposing the curves for aluminum above and for Teflon alone with the Teflon curve shifted so that it coincides with the aluminum curve at the point of equilibration for the aluminum. As can be seen from the data plotted in Figure 5(b), the expected behavior was found.

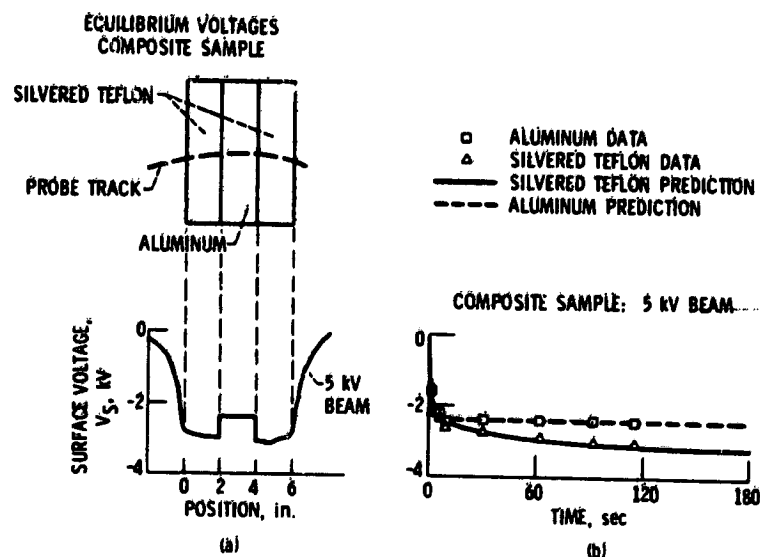


Figure 5. Silvered Teflon/Aluminum Composite Sample Floating

The expectation that the aluminum and Teflon comprising the composite sample should charge to the same surface voltages as had the floating plate; and the Teflon samples above grounded substrates was based on the observation that in both those cases the equilibration was dominated by secondary emission phenomena rather than by leakage currents to ground. This is evidenced in two ways. First, plots of surface voltage at equilibrium versus beam voltage are straight lines; such behavior is supposed to be associated with emission dominated equilibration. Second, examination of printouts of the model calculations reveals that, at equilibrium, the leakage current density term is several orders of magnitude smaller than the other currents in the model. The conclusion, then, is that for this type of composite sample, each part responds to the charging environment with its characteristic time constant, and comes into equilibrium at its characteristic surface voltage so long as leakage current does not play a dominant role in the equilibration.

It should be noted here that the tests run on this composite sample were not extensive. Further experimental investigation of this and other composite samples are planned.

## 1. ONE-DIMENSIONAL SPACE CHARGING MODEL

In order to predict charging behavior in space, a one-dimensional model for charging in space analogous to the one-dimensional ground test model was developed. The essential difference between the two models is that the space model assumes an isotropic Maxwellian particle distribution containing both electrons and ions and a spherical collection geometry. The current densities are derived from Langmuir probe calculations. This type of calculation has been used by several authors<sup>4, 5, 6, 10</sup> to treat the spacecraft charging problem. Derivation of the current density equations is given in Appendix B; a summary description is presented in Figure 6. As is indicated in this figure, the model as presented and used here assumes a geomagnetic substorm condition. That is, it assumes that  $V_S$  is negative, so that electrons are repelled and ions attracted. In these equations  $V_S$  is an algebraic quantity, that is, the sign is implicit.

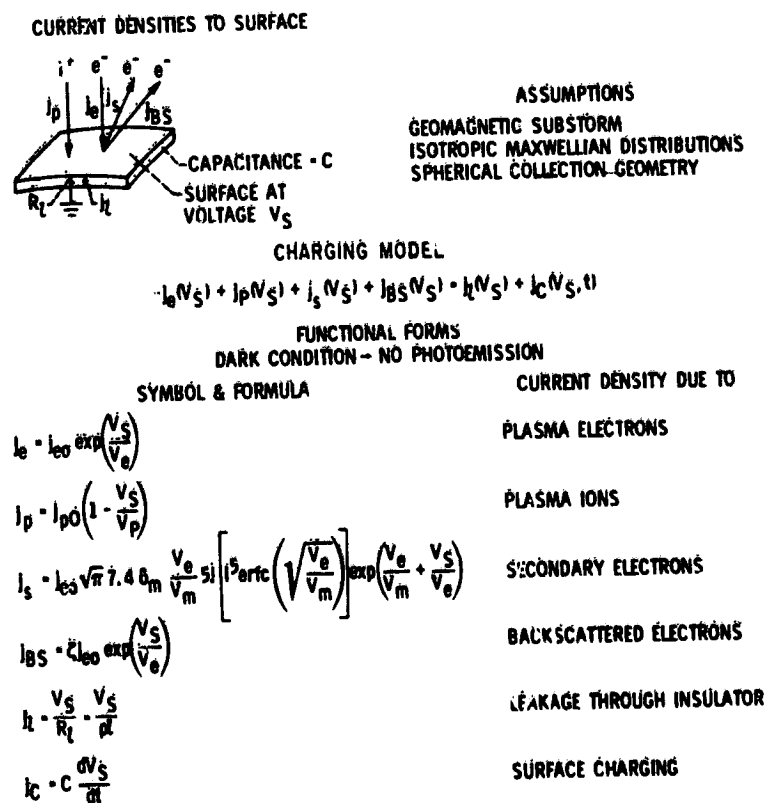


Figure 6. 1-D Model Space Substorm Environment

As is evident from the sketch in Figure 6, secondary electrons due to ion impact are not accounted for in this model. This is because the intent here is to use material charging characteristics found by fitting the ground test model to experimental data in conjunction with the space model to predict space charging. Since there were no ions used in the experiments, no coefficient for secondary electrons due to ion impact was determined. Therefore this current density source is not considered. The surface voltage values predicted by this model are therefore somewhat larger than if secondary electrons due to ion impact had been included. For example, a secondary coefficient of 1 would yield about a 10 percent reduction in the equilibrium voltage calculated for aluminum at  $V_e = 5$  kV.

The procedure used to calculate charging is identical to that described for the ground test model. Material characteristics used were those determined by fitting the ground test model to the data. The capacitance of the aluminum (considered to represent the spacecraft "ground") was taken to be  $15 \times 10^{-11}$  farads, which is the capacitance of a one meter diameter sphere (to represent a "typical" spacecraft dimension) to infinity. This capacitance was chosen because the relevant capacitance for charging floating metal objects is that of the object to its surroundings. Those parameters (notably  $C$  and  $\xi$  for Teflon, and  $\xi$  for aluminum) which varied as functions of beam (and therefore surface) voltage were associated with the equilibrium surface voltage for the appropriate test for purposes of making the space voltage calculations. The relationships between electron and ion temperatures and between temperatures and current densities were taken from the Provisional Specification for the Geomagnetic Substorm Environment.<sup>11</sup> This Specification is given as Figure 7. Thus, results of the space calculations, shown in Figure 8, are given as functions of electron temperature only.

In Figure 8(b) two curves are shown for the surface voltage of silvered Teflon as a function of electron temperature. The first curve calculated used the experimentally determined value of  $9 \times 10^{15}$   $\Omega$ -cm for the effective resistivity of Teflon. This curve bends sharply to the right as electron temperature increases. An inspection of the current densities driving the equilibrium indicated that leakage current played a large part in the equilibration of the Teflon. Thus, this curve yields a "good" value for the surface voltage of Teflon if the spacecraft "ground" is actually near plasma ground. This would be the case if, for example, photoemission were holding the spacecraft ground near plasma ground and the Teflon surface of concern were shaded. However, if the spacecraft is assumed to be in eclipse, the aluminum representing the spacecraft ground is predicted to acquire a large negative voltage (solid line). In this case it is clear that leakage current can not drive the equilibration of the Teflon surface according to the dashed line. Therefore a second curve was calculated for the Teflon, based on the assumption that there was no leakage. This is shown in the dash-dotted line.

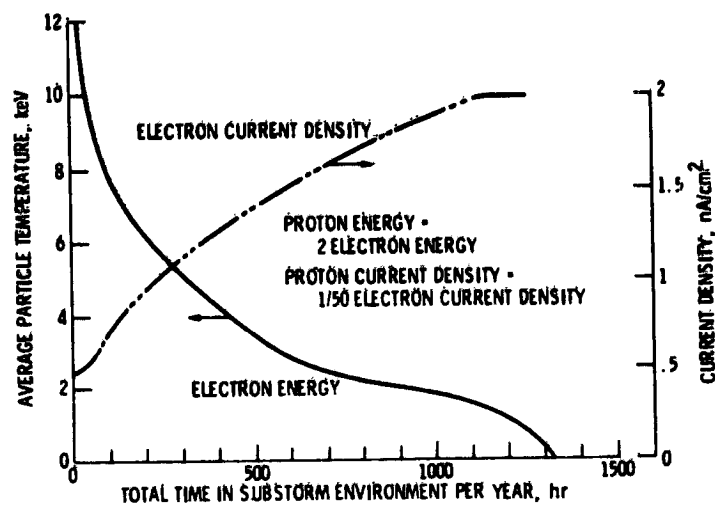


Figure 7. Provisional Specification for Satellite Time in a Geomagnetic Substorm Environment (Ref. 11)

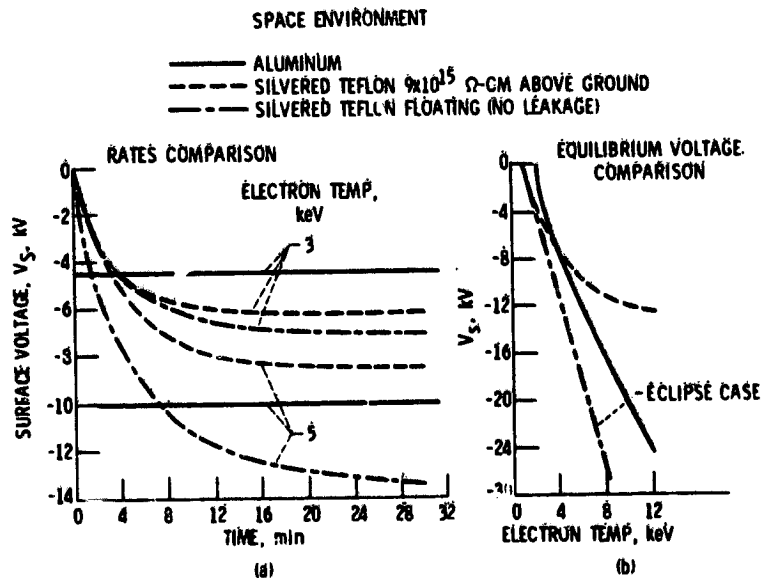


Figure 8. Predictions of Charging Silvered Teflon and Aluminum Samples

Figure 8(a) shows the rates of charging predicted for the space condition. The time to charge the aluminum is predicted to be seconds, comparable to the time required to charge the floating plate in the ground experiments. The time required to charge the Teflon is predicted to be several minutes at lower electron temperatures, ranging to tens of minutes as the electron temperature increases. Thus, equilibration of Teflon is predicted to require significantly longer time in space than it does in ground experiments.

Using the curves shown in Figure 8, it is possible to predict the response of a "spacecraft", composed of an aluminum structure partially covered with silvered Teflon, to substorm and eclipse conditions. Such a set of predictions is shown in Figure 9. For purposes of this figure, it is assumed that photoemission is sufficient to hold illuminated surfaces close to plasma ground.

Figure 9(a) assumes that the Teflon surface of interest is shaded when the spacecraft is in sunlight. A substorm injection with a 5 keV Maxwellian electron distribution is assumed to occur at  $t = 0$  and this environment is assumed to remain constant throughout the time shown. An eclipse is assumed to occur from  $t = 60$  min to  $t = 120$  min. When the substorm occurs, the dark Teflon charges according to the dashed curve of Figure 8(a), shown in Figure 9 as a solid curve; the aluminum at "ground" is assumed to be held near plasma ground by photoemission. The Teflon surface reaches its leakage dominated equilibrium voltage

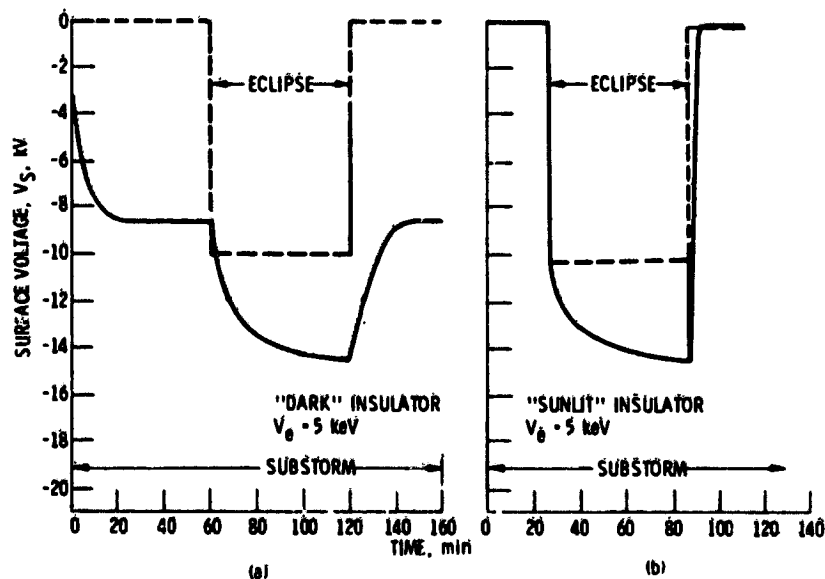


Figure 9. Response to Substorm and Eclipse. 1-D Model Predictions

of -8.5 kV with its time constant of about 20 min. When the spacecraft enters eclipse, the aluminum charges quickly (in seconds) to its equilibrium voltage of -10 kV. It is assumed that the charge on the Teflon surface is immobile on this time scale, so this surface remains at -8.5 kV. At this point, the leakage current, which was driven by the voltage differential of 8.5 kV disappears, so the Teflon finds itself to be no longer in equilibrium with its environment and proceeds to charge to its "floating" value of  $\sim -14.5$  kV in a characteristic 20-30 min period. Upon exit from eclipse, a similar pattern is followed. The aluminum falls quickly to near plasma ground. Because this discharging is driven by photoemission, it requires only about 0.02 sec for the aluminum to reach plasma ground (assuming  $\sim 10^{-9}$  A/cm<sup>2</sup> photocurrent). Now, the Teflon again finds itself out of equilibrium with its plasma environment, and proceeds to discharge slowly to its previous equilibrium potential of -8.5 kV.

Figure 9(b) shows a similar type of time history for an insulating surface which is exposed to sunlight. Again, the solid line represents the surface voltage of the Teflon and the dashed line the spacecraft ground. The entry into eclipse and subsequent charging up is analogous to the charging of the composite sample discussed in Section 4. The aluminum charges rapidly (in seconds) to its equilibrium value. Because the Teflon had no significant charge on its surface, its voltage follows that of the aluminum until the aluminum reaches equilibrium. The Teflon then continues to charge slowly to its equilibrium potential. Upon exit from eclipse, both the aluminum and the Teflon are discharged by photoemission. Thus, the aluminum reaches plasma ground in about 0.02 sec, as in the previous case. The Teflon also discharges more quickly than it charged; it requires about 4 min to reach plasma ground.

These results indicate a need for charging studies which take into account relative charging rates as well as different equilibrium charging levels of various spacecraft surfaces. A "typical" spacecraft has several different types of surfaces (solar cells, thermal blankets, etc.) each of which can be expected to charge with its own time constant. The importance of the effect of the different time constants should be assessed.

## 5. CONCLUDING REMARKS

The present study has resulted in the development of a set of "material charging characteristics" which describe the charging of small (300 cm<sup>2</sup>) samples of 5 mil silvered Teflon and oxidized aluminum. Based on these characteristics, predictions of charging in space have been made and used to estimate the behavior of a composite body under conditions of substorm and eclipse. Several interesting

differences between charging behavior under ground test conditions and predicted behavior in space have been noted for silvered Teflon. Under ground test conditions silvered Teflon acquires the same surface potential mounted on grounded and floating substrates because the equilibration is dominated by surface emission phenomena. However, in space, significant differences are predicted in surface voltage for these two mounting configurations. This is because leakage current dominates the equilibration of the Teflon when the aluminum is at ground, while surface emission dominates for the floating aluminum case. The time required for silvered Teflon to charge to equilibrium in tests is several minutes; this time is predicted to be several tens of minutes in space.

In contrast to the several minutes to several tens of minutes time scales for silvered Teflon, floating aluminum samples are observed in ground test and predicted in space to charge to equilibrium in seconds. Their capacitance is much lower than that of Teflon since it is determined by their surroundings. There are also orders of magnitude differences in time scales for discharging by photo-emission of aluminum and Teflon. This discrepancy in charging and discharging rates gives rise to sudden changes in the electric fields which the Teflon must sustain upon entry into and exit from eclipse. It is felt that these differential charging rates as well as differential charging levels may be important and should be investigated further. Thus, transient (quasistatic) as well as steady state models should be developed for charging.

The one-dimensional models described herein have been found useful in the interpretation of experimental results, and as guides to relating test results to expected space behavior. Models of ground test situations are needed since they can be used interactively with test data. This is especially true since it is impossible, or at least impractical, to simulate accurately the geosynchronous environment. Thus environment scaling must be done through use of models, at least for the present.

Finally, higher dimensional models are needed. One-dimensional models can not account for such things as edge effects or interactions between adjacent surfaces at different potentials as with different charging properties. Such effects are clearly important,<sup>2</sup> and may dominate the charging behavior of multisurface samples and spacecraft.

## References

1. Berkopec, F. D., Stevens, N. J., and Sturman, J. C. (1976) The LeRC substorm simulation facility, Paper III-1, Spacecraft Charging Technology Conference, Colorado Springs, Colo.
2. Stevens, N. J., Berkopec, F. D., Staskus, J. V., and Blech, R. A. (1976) Testing of typical spacecraft materials in a simulated substorm environment, Paper III-2, Spacecraft Charging Technology Conference, Colorado Springs, Colo.
3. DeForest, S. E. (1972) Spacecraft charging at synchronous orbit, J. Geophys. Res. 77:651.
4. Fredericks, R. W., and Scarf, F. L. (1973) Observations of spacecraft charging effects in energetic plasma regions, in Photon and Particle Interactions with Surfaces in Space, R. J. L. Grard, Editor, D. Reidel Publ. Co., Dordrecht, Holland.
5. Inouye, G. T. (1975) Spacecraft charging model, AIAA paper 75-255, AIAA 13th Aerospace Sciences Meeting, Pasadena, California.
6. Rosen, A. (1975) Spacecraft charging: Environment induced anomalies, AIAA Paper 75-91, AIAA 13th Aerospace Sciences Meeting, Pasadena, California.
7. Gibbons, D. J. (1966) Secondary electron emission, in Handbook of Vacuum Physics, Vol 2, A. H. Beck, Editor, Pergamon Press, Oxford, England.
8. Sternglass, E. J. (1950) J. Phys. Rev. 80:925
9. Willis, R. F., and Skinner, D. K. (1973) Secondary electron emission yield behavior of polymers, Solid State Communications 13:485.
10. Cauffman, D. P. (1975) Inclusion of secondary electrons in models of equilibrium potentials, Paper SA63 Presented at the Spring AGU Meeting, Washington, D. C.
11. Lovell, R. R., Stevens, N. J., and Purvis, C. K. (1976) Provisional specification for satellite time in a geomagnetic substorm environment, Paper V-2, Spacecraft Charging Technology Conference, Colorado Springs, Colo.
12. Langmuir, I., and Mott-Smith, H. M. (1926) The theory of collectors in gaseous discharges, Phys. Rev. 28 (No. 4):717.
13. Grard, R. J. L., Knott, K., and Pederson, A. (1973) The influence of photoelectron and secondary electron emission on electric field measurements in the magnetosphere and solar wind, in Photon and Particle Interaction with Surfaces in Space, R. J. L. Grard, Editor, D. Reidel, Dordrecht, Holland.
14. Abramowitz, M., and Stegun, I. A., Editors (1968) Handbook of Mathematical Functions, Dover Publications, Inc., New York.

## Appendix A

### One-Dimensional Ground Test Model

#### 1. INTRODUCTION

In this model, electrons from the electron gun are assumed to approach the planar sample normally. All motion is restricted to the x direction (see Figure A1). The electron beam is assumed monoenergetic, with energy

$$E_B \triangleq e V_B$$

where  $e$  is the electronic charge and  $V_B$  the beam voltage. The current density emitted from the gun is given by

$$j_0 = n_0 e \left( \frac{2E_B}{m_e} \right)^{1/2} \quad (A1)$$

where  $n_0$  = particle density. It is assumed here that  $n_0 e$  (the charge density) is constant, in order to account for the spreading of the beam in the real situation. Thus the continuity equation requires that some particles are "lost".

We wish to calculate current densities to the sample surface. Current densities to be considered are those due to primary electrons, secondary electrons, backscattered electrons, and leakage through the bulk of the insulator. The insulator is assumed to be mounted above a grounded substrate for purposes of calculating leakage.

Throughout this development the sample surface is assumed negative, and all secondary and backscattered electrons are assumed to escape. All signs are given explicitly so that symbols represent positive quantities.

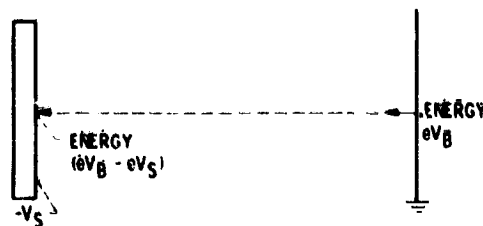


Figure A1.

## 2. CURRENT DENSITY DUE TO PRIMARY ELECTRONS

Consider electrons approaching the sample with energy  $E$ . It is assumed that the electrons do not collide with one another, and that motion is restricted to one-dimension. If the sample surface has a repulsive potential of magnitude  $V_S$ , energy conservation requires that they arrive at the surface with energy  $E - eV_S$ . Since all electrons leave the gun with energy  $eV_B$ , the current density to the sample surface is simply

$$j_e = n_0 e \left( \frac{2}{m_e} \right)^{1/2} (eV_B - eV_S)^{1/2} \quad (\text{A2})$$

Rearranging and using Eq. (A1), we find

$$j_e = j_0 \left( 1 - \frac{V_S}{V_B} \right)^{1/2} \quad (\text{A3})$$

since we are requiring that  $n_0 e$  remain constant.

## 3. CURRENT DENSITY DUE TO SECONDARY ELECTRONS

Sternglass<sup>1</sup> has given the following expression for secondary yield as a function of primary electron energy at impact:

$$\delta(E_i) = 7.4 \delta_m \frac{E_i}{eV_m} \exp \left[ -2 \left( \frac{E_i}{eV_m} \right)^{1/2} \right] \quad (\text{A4})$$

where  $\delta_m$  is the maximum yield,  $eV_m$  is the primary energy for which maximum yield is attained and  $E_i$  is primary energy at impact. From the discussion given in Eq. (A2) above, for this case

$$E_i = eV_B - eV_S \quad (\text{A5})$$

The secondary current density is then

$$j_s = j_e \delta(eV_B - eV_S) \quad (\text{A6})$$

which is

$$j_s = j_o \cdot 7.4 \delta_m \frac{V_B}{V_m} \left(1 - \frac{V_S}{V_B}\right)^{3/2} \exp \left[ -2 \left( \frac{V_B - V_S}{V_m} \right)^{1/2} \right] \quad (A7)$$

#### 4. CURRENT DENSITY DUE TO BACKSCATTERED ELECTRONS

No analytical expression was found for backscattered electron emission. For simplicity, it was therefore assumed that backscattered electron current density represents a fraction of the incident current density. Thus,

$$j_{BS} = \xi j_e = \xi j_o \left(1 - \frac{V_S}{V_B}\right)^{1/2} \quad (A8)$$

#### 5. LEAKAGE CURRENT DENSITY

Leakage current is generally represented by

$$i_1 = \frac{V_S}{R} \quad (A9)$$

In terms of bulk resistivity this is

$$i_1 = \frac{V_S A}{\rho l} \quad (A10)$$

where  $\rho$  is bulk resistivity,  $A$  is the area and the thickness of the sample. Then

$$j_1 = \frac{i_1}{A} = \frac{V_S}{\rho l} \quad (A11)$$

#### 6. THE 1-D MODEL

The primary electron current density represents a source of electrons arriving at the sample. The other three current densities represent loss of electrons from the surface. Thus the net current density to the surface is

5-6

$$j_c = j_e - j_s - j_{BS} - j_l \quad (A12)$$

This net current density plays the role of a charging current to the surface. Thus, if we represent the sample's charging as the charging of a capacitor, we have

$$j_c = C \frac{dV_S}{dt} = j_e - j_s - j_{BS} - j_l \quad (A13)$$

where  $C$  is capacitance, here expressed in farads per square centimeter to maintain consistency of units. Equation (A13) is solved in the manner described in the test on a computer to calculate the charging.

It remains to associate the experimentally measured parameters, surface voltage, and total current to ground, with calculated values. The surface voltage association is trivial; it is simply  $-V_S$ . The total current to ground is the charging current plus the leakage current for the sample as a whole. Thus

$$I_M = A(j_c + j_l) \quad (A14)$$

## References

1. Sternglass, E. J., (1950) J. Phys. Rev. 80:925.

## Appendix B

### One-Dimensional Space Substorm Model

#### I. INTRODUCTION

The one-dimensional space model assumes a two-dimensional isotropic Maxwellian velocity distribution for primary particles, and a spherical collection geometry. The calculations are essentially those for a spherical Langmuir probe. The present calculations are based on the work of Langmuir<sup>1</sup> and Grard et al,<sup>2</sup> and follow closely the derivation of Cauffman.<sup>3</sup> The latter work has not been published; therefore portions of it are reproduced here for clarity. Such portions are identified by superscript reference.

Geometry for the calculations is depicted in Figure B1.<sup>3</sup> The sheath is assumed to have radius  $a$ , and the collector radius  $R$ . The radial and tangential velocity components in the "undisturbed" region (sheath edge) are  $v_r$  and  $v_t$ , respectively, and those at the collector surface  $u_r$  and  $u_t$ . The surface potential of the collector is  $V_S$ . The potential in the sheath is assumed to be a function of radial distance from the collector and to be monotonic. The plasma is assumed collisionless, that is, orbit limited theory applies, and energy and angular momentum are assumed constant for each particle.

The integral requiring solution for current densities due to primary electrons<sup>3,2</sup> and ions, and backscattered electrons is

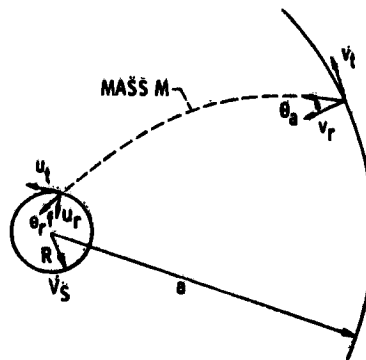


Figure B1.

$$j_i = \frac{i_i}{4\pi R^2} = \frac{4\pi a^2}{4\pi R^2} \int_0^{\pi/2} d\theta_R \int_0^\infty dE_R \frac{dj_i}{dE_R}(E_R, \theta_R) \quad (B1)$$

where the subscript  $i$  stands for either  $e$  (electrons) or  $p$  ( $H^+$  ions), and  $\theta_R$  and  $E_R$  are the angle and energy at impact on the collector (see Figure B1).

For secondary electron current, solution must be found for<sup>3,2</sup>

$$j_S = \frac{i_e}{4\pi R^2} = \frac{4\pi a^2}{4\pi R^2} \int_0^{\pi/2} d\theta_R \int_0^\infty dE_R \frac{dj_R}{dE_R}(E_R, \theta_R) s(E_R) \quad (B2)$$

where  $s(E_R)$  is the secondary electron yield as a function of electron impact energy.

These integrations cannot be performed directly because the distribution function for the particles at the collector is unknown, and therefore we can not determine  $dj_i/dE_R$ . However, we do know the distribution at the sheath edge, and can therefore determine  $dj_i/dE_a$ . If we assume the plasma to be collisionless, we can also convert the limits on  $E_R$  and  $\theta_R$  to limits on  $E_a$  and  $\theta_a$ , and perform the required integrations on these variables.

### 1.1 Conditions for Collection

In order to contribute to current collected at  $R$ , a particle must have energy  $E_R \geq 0$  and direction  $0_R \leq \theta \leq \pi/2$ . Since the plasma is assumed collisionless and  $V(r)$  is assumed monotonic, each particle's energy and angular momentum must be conserved. Assume the particles of interest have charge  $-e$ . Energy conservation demands

$$\frac{1}{2} m_i (u_r^2 + u_t^2) = \frac{1}{2} m_i (v_r^2 + v_t^2) + eV_S \Leftrightarrow E_R = E_a + eV_S \quad (B3)$$

Angular momentum conservation demands

$$R u_t = a v_t \Leftrightarrow R u \sin \theta_R = a v \sin \theta_a \quad (B4)$$

where

$$u = (u_r^2 + u_t^2)^{1/2} \quad \text{and} \quad v = (v_r^2 + v_t^2)^{1/2}$$

Solving for  $E_a$  and  $\theta_a$  in terms of  $E_R$  and  $\theta_R$  yields the conditions for collection<sup>3</sup>

$$0 \leq \theta_R \leq \frac{\pi}{2} \implies 0 \leq \theta_a \leq \sin^{-1} \left[ R \left( \frac{E_a + eV_S}{E_a} \right)^{1/2} \right] \triangleq \theta_0$$

$$\infty > E_R \geq 0 \implies \infty > E_a \geq E_0 \triangleq \begin{cases} 0 & \text{for } V_S > 0 \text{ (attraction)} \\ -eV_S & \text{for } V_S \leq 0 \text{ (repulsion)} \end{cases} \quad (\text{B5})$$

## 1.2 Energy Format

An isotropic Maxwellian velocity distribution in three-dimensions has a distribution given by

$$f(\vec{v}) = \left( \frac{m_i}{2\pi eV_i} \right)^{3/2} \exp \left[ \frac{-m_i \vec{v} \cdot \vec{v}}{2eV_i} \right] \quad (\text{B6})$$

We are interested in a two-dimensional distribution which can be found from

$$g(v_r, v_t) = \int_0^{2\pi} f(v_r, v_t \sin \chi, v_t \cos \chi) d\chi \quad (\text{B7})$$

Substituting for  $f(\vec{v})$  and integrating, we have

$$g(v_r, v_t) = \frac{1}{\sqrt{2\pi}} \left( \frac{m_i}{eV_i} \right)^{3/2} v_t \exp \left[ \frac{-m_i (v_r^2 + v_t^2)}{2eV_i} \right] \quad (\text{B8})$$

Langmuir<sup>1</sup> gives the incremental current across the sheath as

$$dj_i = 4\pi a^2 n e v_r g(v_r, v_t) dv_r dv_t \quad (\text{B9})$$

Then,

$$dj_i = \frac{di_i}{4\pi R^2} = \frac{a^2 n_i e}{R^2 \sqrt{2\pi}} \left( \frac{m_i}{eV_i} \right)^{3/2} v_r v_t \exp \left[ \frac{-m_i (v_r^2 + v_t^2)}{2eV_i} \right] dv_r dv_t \quad (\text{B10})$$

and, changing to  $E_a, \theta_a$  coordinates we have<sup>3</sup>

$$dj_i = \frac{a^2}{R^2} n_i e \left( \frac{eV_i}{2\pi m_i} \right)^{1/2} \frac{2}{(eV_i)^2} E_a \exp \left[ -\frac{E_a}{eV_i} \right] \sin \theta_a \cos \theta_a d\theta_a dE_a \quad (\text{B11})$$

as required.

## 2. PRIMARY AND BACKSCATTERED PARTICLE CURRENT DENSITIES

Since backscattered electron current density is considered to be simply a fraction of the incident electron current density, the same integration applies to both. The calculation for positive ion collection is the same as for electron collection with appropriate sign changes to account for the positive charge, and using the ion mass and temperature. In Eqs. (B9) to (B11), the sign on the leading charge has been suppressed. Appropriate signs will be supplied in Section B. 5.

The integration to be performed is

$$j_i = \frac{a^2}{R^2} n_i e \left( \frac{eV_i}{2\pi m_i} \right)^{1/2} \frac{2}{(eV_i)^2} \int_{E_0}^{\infty} \int_0^{\theta_0} \sin \theta_a \cos \theta_a E_a \exp \left( -\frac{E_a}{eV_i} \right) d\theta_a dE_a \quad (\text{B12})$$

Cauffman<sup>3</sup> evaluates this integral and finds, in agreement with Langmuir<sup>1</sup>

$$\begin{aligned} j_i &= j_{i0} \exp \left( \frac{V_S}{V_i} \right) & V_S \leq 0 \text{ (Repulsive)} \\ j_i &= j_{i0} \left( 1 + \frac{V_S}{V_i} \right) & V_S \geq 0 \text{ (Attractive)} \end{aligned} \quad (\text{B13})$$

where

$$j_{i0} = n_i e \left( \frac{eV_i}{2\pi m_i} \right)^{1/2}$$

Since the interest here is in modeling charging in substorms with no photoemission, we expect  $V_S$  negative. Thus, electrons are repelled and ions attracted. So we have for electrons

$$j_e = j_{e0} \exp \left( \frac{V_S}{V_e} \right) \quad (\text{B14})$$

for ions

$$j_p = j_{p0} \left( 1 - \frac{V_S}{V_p} \right) \quad (B15)$$

where the minus sign reflects the fact that ions are attracted by negative  $V_S$ . For backscattered electrons,

$$j_{BS} = \xi j_e = \xi j_{e0} \exp\left(\frac{V_S}{V_e}\right) \quad (B16)$$

where  $\xi$  is the backscatter coefficient.

### 3. SECONDARY ELECTRONS DUE TO ELECTRON IMPACT

Secondary yield as a function of electron impact energy has been given by Sternglass<sup>4</sup> as

$$\delta(E_R) = 7.4 \delta_m \frac{E_R}{eV_m} \exp\left[-2\left(\frac{E_R}{eV_m}\right)^{1/2}\right] \quad (A4)$$

where  $\delta_m$  is the maximum yield and  $eV_m$  the energy at which the maximum yield is obtained. To determine secondary electron current density, we must multiply the left hand side of equation (B11) by  $\delta(E_R)$  and integrate. Thus we need

$$j_s = \frac{a^2}{R} \cdot \frac{2}{(eV_e)^2} \frac{7.4 \delta_m}{eV_m} \int_{E_0}^{\infty} \int_0^{\theta_0} E_a (E_a + eV_S) \times \exp\left[\frac{-E_a}{eV_e} - 2\left(\frac{E_a + eV_S}{eV_m}\right)^{1/2}\right] \sin \theta_a \cos \theta_a d\theta_a dE_a \quad (B17)$$

which is Cauffman's<sup>3</sup> equation for secondary electrons, except that he uses a  $\sec \theta_r$  dependence of  $\xi$  on  $\theta_r$  which is not used here. The  $\theta_a$  integral is the same as before and yields

$$j_s = j_{e0} \frac{7.4 \delta_m}{(eV_e)^2 eV_m} \int_{E_0}^{\infty} (E_a + eV_S)^2 \exp\left[\frac{-E_a}{eV_e} - 2\left(\frac{E_a + eV_S}{eV_m}\right)^{1/2}\right] dE_a \quad (B18)$$

Now, sequentially setting  $\chi^2 = E_a + eV_S$  and  $\eta = (eV_e)^{-1/2} \chi + \left(\frac{V_e}{V_m}\right)^{1/2}$  and substituting, we find

$$j_S = 2j_{e0} 7.46 \frac{V_e}{m} \exp\left(\frac{V_S}{V_e} + \frac{V_e}{V_m}\right) \int_{\eta_0}^{\infty} \left[ z - \left(\frac{V_e}{V_m}\right)^{1/2} \right]^5 \exp(-\eta^2) d\eta \quad (\text{B19})$$

where

$$\eta_0 = \begin{cases} \left(\frac{V_S}{V_e}\right)^{1/2} + \left(\frac{V_e}{V_m}\right)^{1/2} & \text{for } V_S > 0 \\ \left(\frac{V_e}{V_m}\right)^{1/2} & \text{for } V_S \leq 0 \end{cases}$$

Since we are considering substorm cases only here, the condition  $V_S \leq 0$  is of interest. For this case the integral in Eq. (B19) is just

$$j = \int_{\left(\frac{V_e}{V_m}\right)^{1/2}}^{\infty} \left[ \eta - \left(\frac{V_S}{V_m}\right)^{1/2} \right]^5 \exp(-\eta^2) d\eta. \quad (\text{B20})$$

Recalling the expression for repeated integrals of the error function complement<sup>5</sup>

$$i^n \operatorname{erfc}(z) = \frac{2}{\sqrt{\pi}} \int_z^{\infty} \frac{(t-z)^n}{n!} \exp(-t^2) dt \quad (\text{B21})$$

where, by definition,

$$i^n \operatorname{erfc}(z) = \int_z^{\infty} i^{n-1} \operatorname{erfc}(t) dt$$

and

$$i^0 \operatorname{erfc}(z) = \frac{2}{\sqrt{\pi}} \int_z^{\infty} \exp(-t^2) dt = \operatorname{erfc}(z)$$

and identifying  $t$ ,  $z$  and  $n$  with the appropriate variables in (B20), we have

$$J = \frac{\sqrt{\pi}}{2} 5! i^5 \operatorname{erfc} \left( \sqrt{\frac{V_e}{V_m}} \right). \quad (\text{B22})$$

So, from Eqs. (B19) and (B22), we have

$$j_S = \sqrt{\pi} j_{e0} 7.46_m \frac{V_e}{V_m} 5! \left[ i^5 \operatorname{erfc} \left( \sqrt{\frac{V_e}{V_m}} \right) \right] \exp \left( \frac{V_S}{V_e} + \frac{V_e}{V_m} \right) \quad (\text{B23})$$

and we note that the dependence of  $j_S$  on  $V_S$  is the same as that of  $j_e$  and  $j_{BS}$ .

#### 4. LEAKAGE CURRENT DENSITY

Leakage current density is defined in the same manner for the space model as it was for the test facility model (see Section 5 of Appendix A). Thus, we have

$$j_l = \frac{V_S}{\rho l}$$

where  $\rho$  is bulk resistivity and  $l$  is the thickness of the insulating film.

#### 5. THE 1-D SPACE MODEL

Now, the net current density to the sample surface is

$$j_c = -j_e + j_p + j_s + j_{BS} - j_l \quad (\text{B24})$$

where the signs on the current densities are given explicitly here, and we recall that  $V_S$  in this model is algebraic (that is, can be positive or negative), although the derivations have assumed it negative.

The net current density plays the role of a charging current to the surface, so that

$$j_c = C \frac{dV_S}{dt} = -j_e + j_p + j_s + j_{BS} - j_l \quad (\text{B25})$$

where  $C$  is capacity expressed in farads per square centimeter and where we assume we are charging a capacitor. Equation (B26) is solved in the same way as Eq. (A13) on a computer to determine  $V_S$  versus time for charging.

## References

1. Langmuir, I., and Mott-Smith, H. M. (1926) The theory of collectors in gaseous discharges, Phys. Rev. 28(No. 4):717.
2. Grard, R. J. L., Knott, K., and Pederson, A. (1973) The influence of photoelectron and secondary electron emission on electric field measurements in the magnetosphere and solar wind, in Photon and Particle Interaction with Surfaces in Space, R. J. L. Grard, Editor, D. Reidel, Dordrecht, Holland.
3. Cauffman, D. P. (1975) Inclusion of secondary electrons in models of equilibrium potentials, Paper SA63 Presented at the Spring AGU Meeting, Washington, D. C.
4. Sternglass, E. J., (1950) J. Phys. Rev. 80:925.
5. Abramowitz, M., and Stegun, I. A., Editors (1968) Handbook of Mathematical Functions, Dover Publications, Inc., New York.

**Contents**

1. Introduction	487
2. Test Objectives	488
3. The Substorm Simulation Facility	489
4. Test Sample	490
5. Characteristics of Discharge Pulses	492
6. Influence of Ambient Temperature and Illumination on the Discharge Frequency	494
7. Conductivity Through the Substrate at High Electric Stress Levels	497
8. Impact of Electrostatic Discharge on the Array Experiment	498
9. Conclusions	501
References	501

#### 4. Investigation of a CTS Solar Cell Test Patch Under Simulated Geomagnetic Substorm Charging Conditions

K. P. Bogus  
European Space Technology Center of ESA  
Noordwijk, The Netherlands

**Abstract**

The CTS solar array technology experiment which consists of a solar cell test patch on the Kapton-substrate solar array and the appertaining electronics unit has been operating in geostationary orbit for nearly 1 year without any malfunction although it is expected to be strongly influenced by charging effects on the array surface.

The results of a post-launch test program show that the experiment would not survive a discharge due to electrostatic charging in the test patch area. In a simulated substorm, environment discharges were obtained only below a temperature threshold of about 30°C. With solar illumination, this threshold is reduced below 0°C.

**1. INTRODUCTION**

Spacecraft in geosynchronous orbit and under magnetic substorm conditions are known to be subject to differential charging of different material surfaces leading to high values of electric stress and arc discharges if the threshold for electrical breakdown is surpassed. The highest electric stress is expected on

insulating material surfaces which are not sun-illuminated and therefore cannot equilibrate at low potentials by photoemission of electrons.

The Communications Technology Satellite, CTS, which has been in orbit since January 1976 has a sun-oriented 2-wing solar array using a 75 micron thick kapton-glass fibre-compound flexible substrate. The insulating rearside of the array is shaded permanently and therefore constitutes a principal source of discharges.

The CTS flexible solar array is equipped with a solar cell test patch which forms part of the solar array technology experiment provided by ESTEC. The test patch and the appertaining electronics unit are expected to be strongly influenced by discharges on the solar array surface. Therefore, a post-launch test program was initiated in order to study the behaviour of the solar array electronics experiment under simulated substorm conditions. The tests described here were performed in the 2.5 m Space Simulation Chamber of DFVLR in Porzwaan, Germany, in the first quarter of 1976.

## 2. TEST OBJECTIVES

The data which are presently available on differential charging and arc discharges are not sufficient to predict the behaviour of the CTS solar array experiment in a geomagnetic substorm for two reasons:

(1) Most of the investigations have been done on materials level and the results cannot be applied to more complex structures because there is too little knowledge on structural and size effects.

(2) The investigations on representative samples<sup>1</sup> have not been performed in a representative environment, as far as solar simulation and temperature are concerned.

Therefore a principal goal of the investigation was to analyze the influence of simulated substorm electron plasmas on a representative solar cell test patch under representative environmental conditions.

In detail, the test objectives were as follows:

(1) Measurement of the electron beam induced leakage current through the substrate as a function of electron energy, ambient temperature and solar illumination.

(2) Analysis of the discharge pulse frequency and pulse shape at the output of the solar cell test patch as a function of temperature and solar illumination.

(3) Analysis of the AEE (array experiment electronics) performance in a simulated substorm.

The outcome of these measurements would allow for direct conclusions in conjunction with actual flight data:

(1) If characteristic anomalies occur at the AEE output during arc discharging, then the AEE could be used as a discharge indicator on CTS. Similarly, if arc discharges turn out to destroy the AEE, one could determine the time of the first substorm generated discharge pulse from the time of malfunction of the AEE.

(2) If the solar array experiment performance is not disturbed by discharge pulses, one can have more confidence in the reliability of the flight data.

### 3. THE SUBSTORM SIMULATION FACILITY

The large 2.5 m space simulation chamber at DFVLR, Porzahn, Germany, was selected because boundary effects from the wall chambers are kept to a minimum, and because it offers the possibility to mount much larger test samples in a future series of tests.

A cross section through the chamber is shown in Figure 1. The sample is mounted vertically by means of teflon wires. Illumination of the sample front side is provided by a sun simulator of 1 solar constant. The sample rear side can be irradiated homogeneously with electrons, the electron gun being mounted on the center flange of the chamber lid at the rear side. Visual control is possible through a window inclined  $15^\circ$  to the beam axis.

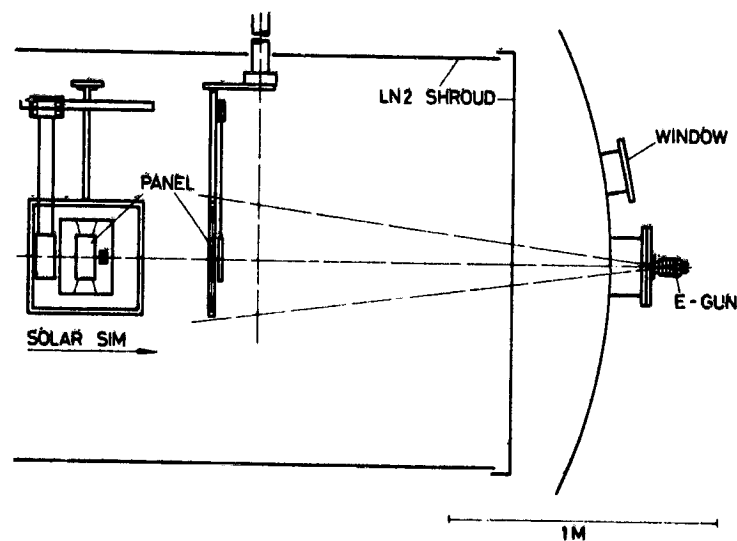


Figure 1. The Geomagnetic Substorm Simulation Facility

Using the liquid nitrogen cold shroud, the residual pressure is below  $10^{-6}$  torr. Without cold shroud, the pressure is between  $10^{-4}$  and  $10^{-5}$  torr.

The electron energy can be continuously varied between 0 and 60 kV. The current density at an electron beam diameter of  $1 \text{ m}^2$  in the test plane is between 1 and  $100 \text{ nA/cm}^2$ .

The uniformity of the electron beam intensity in the test plane can be checked using a detector with an array of six equally sized receiver plates. A beam uniformity of  $\pm 30$  percent is achieved without special adjustments.

#### 4. TEST SAMPLE

The test specimen consisted of two parts: the solar cell test patch on a flexible panel-substrate and the AEE engineering unit.

The layout of the test patch is shown in Figure 2. Three solar cells are arranged in parallel and 9 cells in series. On the right hand side is a representative part of the CTS solar array wiring. At the bottom two PT-temperature sensor are positioned beneath two dummy cells.

The substrate consists of a compound of:

25  $\mu\text{m}$  kapton H film.

35  $\mu\text{m}$  glass fibre cloth

5  $\mu\text{m}$  polyester adhesive (Dupont 46971)

The solar cells are mounted on the glass fiber side with RTV 560.

Typical I-V characteristics of the test patch under 1 solar constant illumination and at various temperatures are shown in Figure 3.

The AEE has the function to monitor the performance of the test patch in orbit.

The parameters to be monitored are:

- (1) the open circuit voltage  $V_{oc}$ ,
- (2) the short circuit current  $I_{sc}$ ,
- (3) current and voltage at four points of the I-V curve determined by resistors  $R_1 - R_4$  (see Figure 3), and
- (4) temperatures at the test patch and at four other positions of the panel.

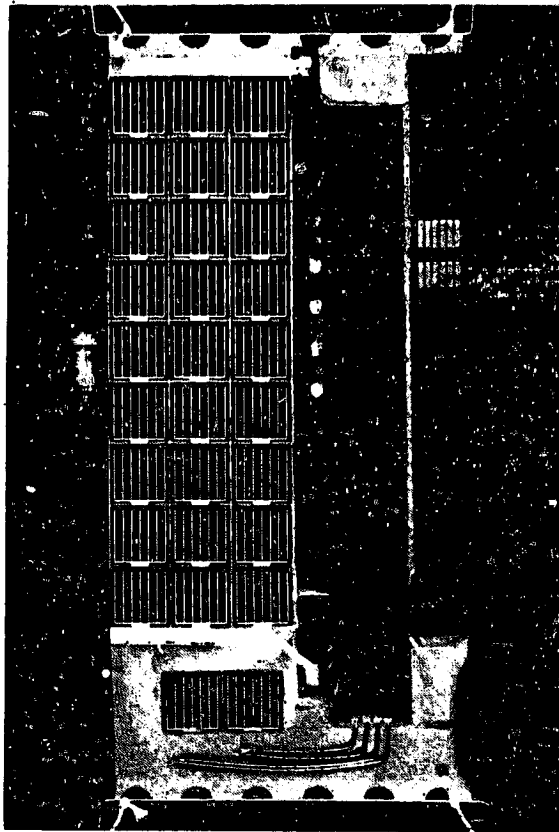


Figure 2. The CTS Solar Cell Test Patch

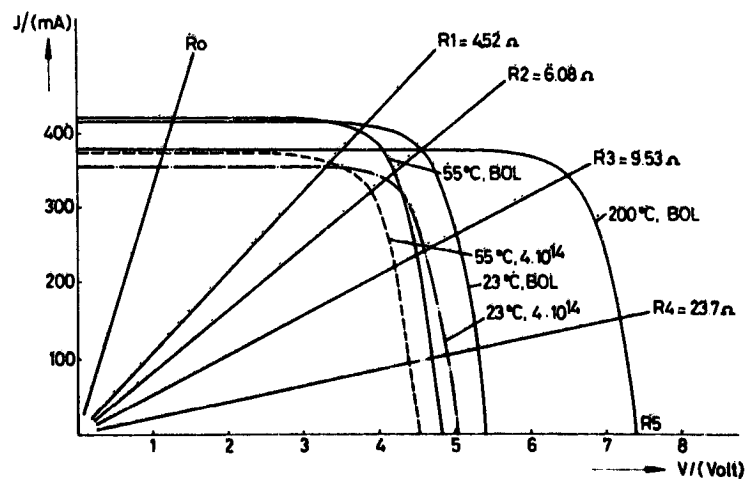


Figure 3. Test Patch I-V Curves

### 5. CHARACTERISTICS OF DISCHARGE PULSES

With the test patch at room temperature and no illumination, discharges were observed at electron energies above 15 kV.

The discharge frequency was found to be proportional to the electron beam current density. At a beam current of  $60 \text{ nA/cm}^2$  a discharge rate of 8 pulses/min was measured, the pulses occurring at rather regular intervals.

Visual observation of the test patch during discharges showed a localized spot of high intensity light emission surrounded by a lower intensity 'Lichtenberg-figure' covering the whole sample rearside. The position of the high intensity spot varied from discharge to discharge and no preferred position could be detected.

To analyze the electrical characteristics of discharges as seen at the test patch terminals, the test patch was connected to an external circuitry as shown in Figure 4. The length of the connecting leads corresponded approximately to the wiring on the spacecraft in order to simulate in-orbit conditions to a certain extent. Nevertheless, considerable deviations in the high frequency properties were anticipated due to different capacitive and inductive components.

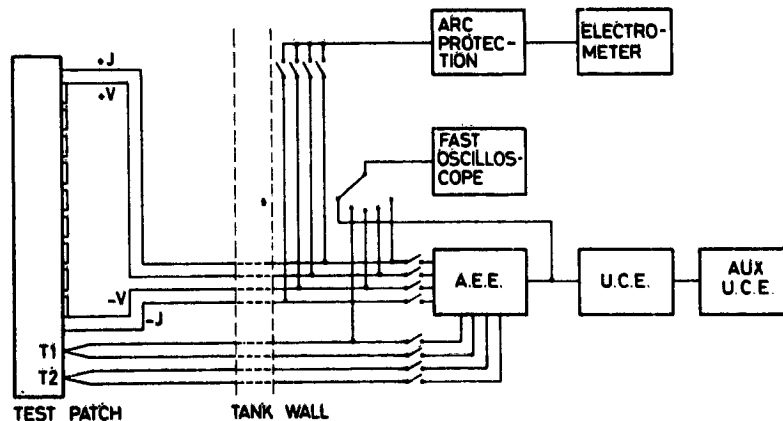


Figure 4. Wiring Diagram

A  $20 \text{ k}\Omega$  terminal resistor, consisting of  $20 \Omega + 180 \Omega + 1800 \Omega$  in series, was connected across the output of the  $3 \times 9$  solar cell module. This corresponds to the input impedance of the AEE when connected to the test patch. Transient signals during discharge were measured at the  $0 \Omega$ ,  $20 \Omega$ , and  $200 \Omega$  points of the terminal resistor using a Tektronix 7704-A oscilloscope with a 10:1 attenuator. The peak voltages obtained were:

2 V at 0  $\Omega$  (EMI)  
10 - 20 V at 20  $\Omega$   
100 - 200 V at 200  $\Omega$

From this, the extrapolated peak voltage at 2 K $\Omega$  would be 1 - 2 kV.

The transient pulses were recorded using a 2048 channel biotration transient recorder with a 50  $\Omega$  input impedance and a channel width of 10  $\mu$ sec. Typical recordings are shown in Figure 5. The initial portion of the signal is not displayed in full amplitude due to the voltage limitation of the recorder to  $\pm 5$  volts. As can be seen, the pulses consist of damped oscillations with a typical decay time of 3-5  $\mu$ sec for a terminal resistor of 50  $\Omega$ .

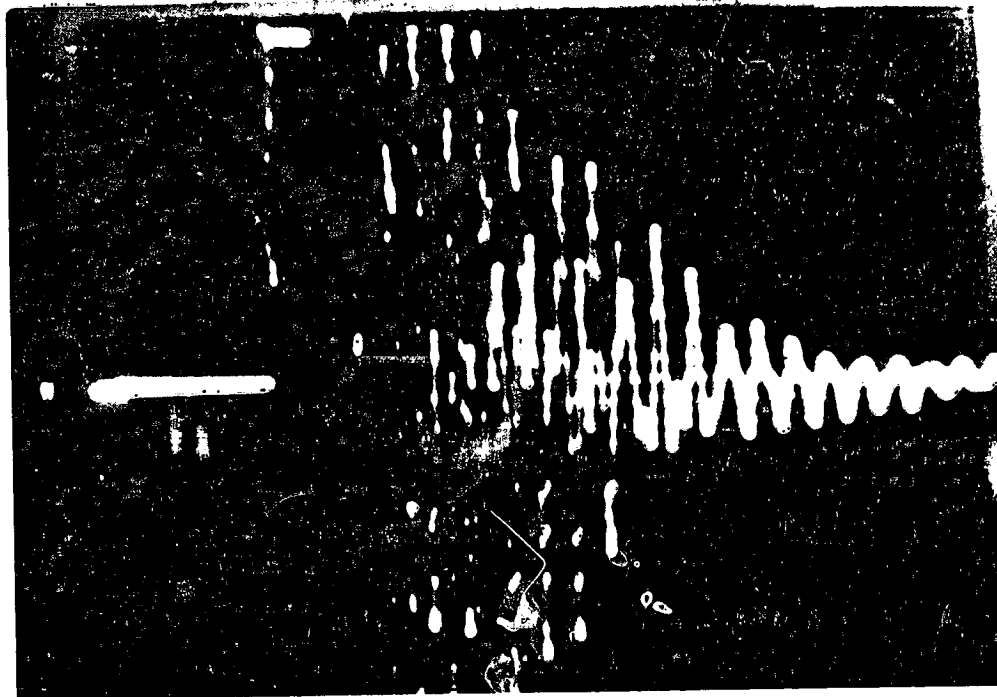


Figure 5. Discharge Transient Pulse (x-axis : 2  $\mu$ sec/div; y-axis : 1.25 V/div)

The high frequency ( 3 MHz) oscillations are considered to be strongly influenced by the external circuitry and no direct conclusions can be drawn which are applicable to in-orbit behaviour.

The pulse decay time, however, can be correlated with the RC time of the circuit consisting mainly of the solar cell capacitance of about 70 nF and the terminal resistor of 50  $\Omega$  and 2 k $\Omega$ , respectively. With the 2 k $\Omega$  terminal resistor, the peak voltage was 1000-2000 volt. From  $E_s = 1/2 CU^2$ , a pulse energy of about 100 mJoule is calculated.

It must be kept in mind that pulses of this energy occur at the solar cell test patch output due to pick-up from the energy of the discharge pulse at the rearside of the test patch. The maximum energy of the primary discharge pulse can be calculated on the assumption that the test patch represents a plate capacitor negatively charged over the whole rearside surface with respect to the solar cells on the front side which are on ground potential. The total capacitance of this plate capacitor is

$$C = \epsilon \epsilon_0 F/d \approx 4 \text{ nF} .$$

If the entire surface charge is discharged within one discharge pulse, then the total discharge energy would be at maximum

$$E_D = 450 \text{ mJoule} .$$

Comparing  $E_D$  with  $E_S$  and bearing in mind that  $E_S$  is only a fraction of  $E_D$  because only a fraction of the total energy is picked up by the solar cell module, the two energy figures indicate that, in fact, the charge accumulated over the whole rear surface is discharged in one pulse.

This is confirmed by the observed discharge rate of 8 pulses/min at the beam current density of 60 nA/cm<sup>2</sup>. From these figures it can be concluded that the maximum charge deposited on the whole rear surface of about 100 cm<sup>2</sup> area in between two pulses in about 40  $\mu$ A sec which at 15 kV represents a maximum stored energy

$$E_c = Q \cdot U \approx 600 \text{ mJoule} .$$

As part of the charge is lost by secondary emission and conduction,  $E_D$  has to be somewhat smaller than  $E_c$ .

#### 6. 1. FLUENCE OF AMBIENT TEMPERATURE AND ILLUMINATION OF THE DISCHARGE FREQUENCY

During these tests the discharges were monitored using the electron beam detector as receiver antenna. The beam current density was kept between 20 and

100 nA/cm<sup>2</sup>. Discharges on the test patch rearside caused a steep spike on the beam current recording sufficient for event counting purposes.

Regular discharges at normal rates (Section 5) were observed in the dark at room temperature. After opening the solar simulator shutter and exposing the front side of the test patch to one solar constant illumination the discharge activity ceased within less than a minute. No discharges were observed under illumination for time periods of more than 20 min and electron energies up to 20 keV. After turning off the illumination, it took about 3 min until the discharges occurred again.

Under illumination the temperature of the test patch as measured with the two temperature sensors rises to about 100°C with an initial slope of 40°C/min. Cool-down to ambient temperature after turn-off of the simulator takes about 5 min with an initial slope of 30°C/min.

The different behavior at turn-on and turn-off indicates that the temperature of the test patch has a strong influence on the discharge frequency. An additional influence of the illumination can, however, not be precluded.

A more detailed examination of the test patch showed that illumination of the front side causes also the rearside to be illuminated because light penetrates the gaps between solar cells into the substrate where it is scattered by the light-pipe action of the glass fiber over the whole rear surface. Photoemission from rearside could therefore prevent excessive charging of the rear surface. Another potential explanation would be photoconduction through the substrate.

To further investigate the influence of illumination, the tests were repeated with the cell gaps covered by a blackened Teflon mask inhibiting the penetration of light to the substrate. Figure 6 shows the discharge frequency before, during, and after solar illumination. The corresponding temperature profile is shown in the upper part. The same behavior as in the test without mask was found, that is, no discharge immediately after turn-on and delayed reoccurrence of discharges after turn-off of illumination.

These results indicate that the test patch temperature is mainly responsible for the ceasing of discharge under illumination.

To verify these results under representative conditions, the tests were repeated at liquid nitrogen ambient temperatures. The results are shown in Figure 7. In the dark the temperature is below -150°C. With 1 solar constant illumination the measured temperature rises to about 50°C. This measured temperature, however, is not identical to the solar cell test patch temperature because the sensors are located beneath two dummy solar cells at the edge of the test patch. Therefore, there is a tendency for measuring the temperature low due to the 'fin-effect' at the test patch edge. This could account for -5°C to -10°C. On the other hand, there

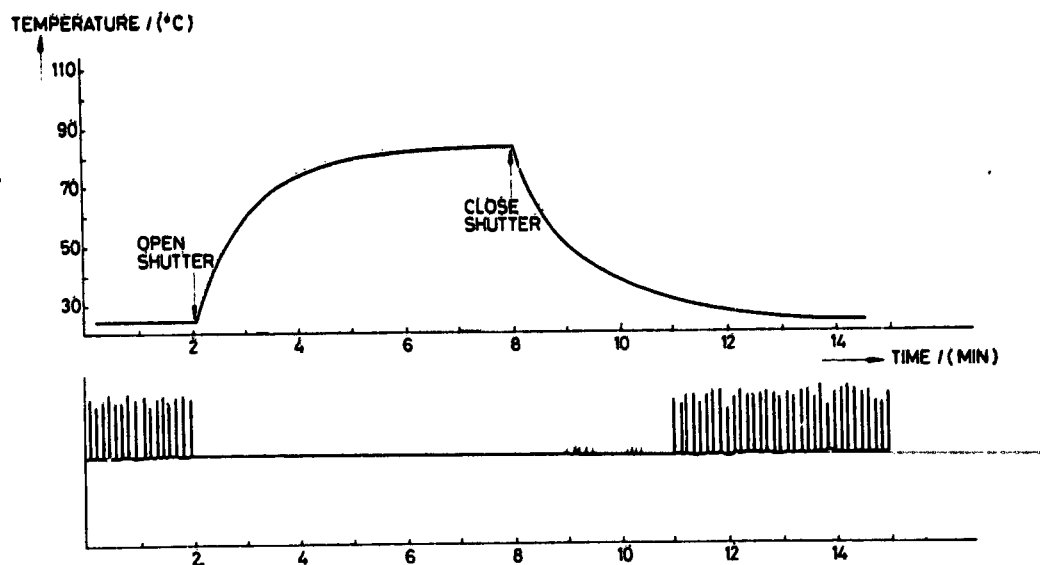


Figure 6. Discharge Rate During Illumination Transient (Without Cooling)

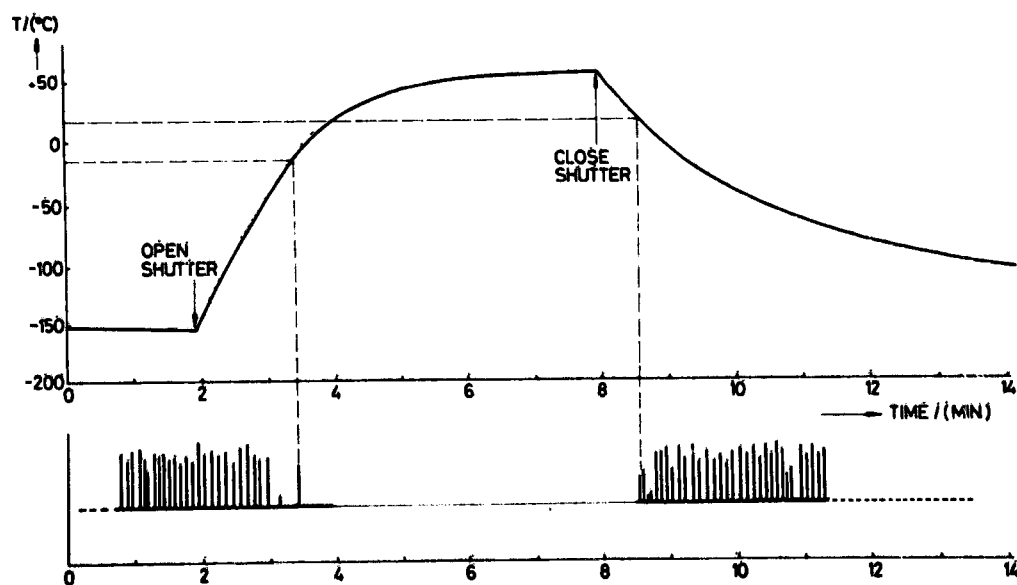


Figure 7. Discharge Rate During Illumination Transient (With LN<sub>2</sub> Cooling)

is a tendency to measure the temperature about  $10^{\circ}\text{C}$  too high because the solar cells of the module were loaded at maximum power in contrast to the cells on top of the sensors which were in open circuit.

At  $-150^{\circ}\text{C}$  the discharge frequency observed at 20 keV and a beam current density of  $40\text{ nA/cm}^2$  was  $15\text{ min}^{-1}$ . After turn-on of illumination the discharges continue for about 2.5 min. This corresponds to a critical temperature of about  $-30^{\circ}\text{C}$ . After turn-off of illumination the discharges reoccur at a sample temperature of about  $+15^{\circ}\text{C}$ .

This result, although qualitatively showing the expected delay for ceasing of discharge, is quantitatively in contradiction to the results obtained without cooling where the critical temperature for ceasing of discharge had been found to be between  $20^{\circ}\text{C}$  and about  $50^{\circ}\text{C}$ . It appears that in the presence of solar illumination the critical temperature is reduced by about  $60\text{-}70^{\circ}\text{C}$ .

This was confirmed by another test. With the chamber walls again cooled down to liquid nitrogen temperatures, the solar simulator intensity was reduced step-wise. At 0.5 solar constant still no discharges were observed although the sample temperature was down to  $-1^{\circ}\text{C}$ . At 0.25 solar constant regular discharges occurred again. The sample temperature then was about  $-45^{\circ}\text{C}$ .

## 7. CONDUCTIVITY THROUGH THE SUBSTRATE AT HIGH ELECTRIC STRESS LEVELS

The leakage current to the solar cell module through the substrate under electron irradiation of the rearside was measured by connecting the solar cell module terminal leads in parallel to the input of an electrometer. The measurements were made at room temperature at a beam current density of  $90\text{ mA/cm}^2$ . The beam energy was increased in 2 keV steps up to 16 keV. The results obtained in the dark are shown in Table 1, giving the equilibrium current after decay of the displacement current component. Between 1 and 5 keV positive current values were obtained indicating a secondary emission coefficient of more than 1. At higher voltages the leakage current increases supralinearly which shows that the conductivity increases with voltage.

Illumination has a considerable influence on the leakage current. At 16 keV the current increases from  $-2.25\text{ }\mu\text{A}$  to  $-5.6\text{ }\mu\text{A}$  after turn-on of the solar simulator. (The cell gaps were not covered by a mesh during these measurements but still the light intensity at the rearside is only a small fraction of 1. S.C.) These results are qualitatively in agreement with the results recently obtained at Stanford Research Institute, SRI<sup>2</sup> on pure kapton samples. At SRI a conductivity increase of  $10^5$  was observed when illuminating kapton-H-film with 2.3 suns of Xenon illumination.

Table 1. Current Through Sample versus Beam Voltage

U = 0 kV	j = 0 nA
2 kV	+40 ... +20 nA
(Maximum bei etwa 3 kV)	
4 kV	+25 ... +15 nA
6 kV	-30 nA
8 kV	-120 nA
10 kV	-260 nA
12 kV	-560 nA
14 kV	-1, 12 $\mu$ A
16 kV	-2, 25 $\mu$ A

#### 8. IMPACT OF ELECTROSTATIC DISCHARGES ON THE ARRAY EXPERIMENT ELECTRONICS UNIT

In normal operation the array experiment electronics unit (AEE) is used to monitor the I-V curve of the test patch at six points and the array temperature at five locations on the solar array. Details of the design, construction, and performance of the AEE can be found in Ansorge and Pischel.<sup>3</sup>

The AEE telemetry sample sequence is shown in Table 2.

For the purpose of the test, only the current and voltage sensing terminals of the AEE engineering unit and the wiring for two temperature sensors were connected to the test sample in the simulation chamber. The remaining input terminals were connected to the check-out unit which also provided the power supply and the clock signal.

A print-out of AEE/test patch data is shown in Figure 8 indicating an open circuit voltage of 4.75 volts and a short circuit current of 263 mA with the test patch under 1 S.C. illumination. With the AEE running continuously, the electron beam voltage was increased in steps of 1 kV starting at zero.

Up to 17 kV no discharges and no anomalies of the AEE performance were observed. Slightly above 17 kV still no discharges were observed, either visually or with the detecting antenna, but the AEE output showed loss of clock synchronization. The AEE switched to the next channel at random rate.

In order to obtain discharges, the solar simulation was turned off with the electron beam being kept at 17 kV. After 25 discharges, the solar simulation was turned on again and the electron beam was switched off. The AEE output at this stage is shown in Figure 9. The AEE samples only open circuit voltage values and zero current instead of the actual pairs of I/V values on the curve. This indicates

Table 2. AEF Sample Sequence

No.	Nomenclature	
	Channel A	Channel B
1	$V_{oc}^*$	T1
2	$I_{sc}^*$	T1
3	$V_3$	T1
4	$I_3$	T1
5	$V_2$	T1
6	$I_1$	T1
7	$V_1$	T1
8	$I_1$	T1
9	$V_4$	T1
10	$I_4$	T1
11	$V_{ref}$	<100 mV
12	$T_1$	<100 mV
13	$T_2$	<100 mV
14	$T_3$	<100 mV
15	$T_4$	<100 mV
16	$T_5$	<100 mV

\* $V_{oc}$  = open circuit voltage  
 $I_{sc}$  = short circuit current

that the input transistor(s) which load(s) the test patch according to the sample sequence has an open circuit failure.

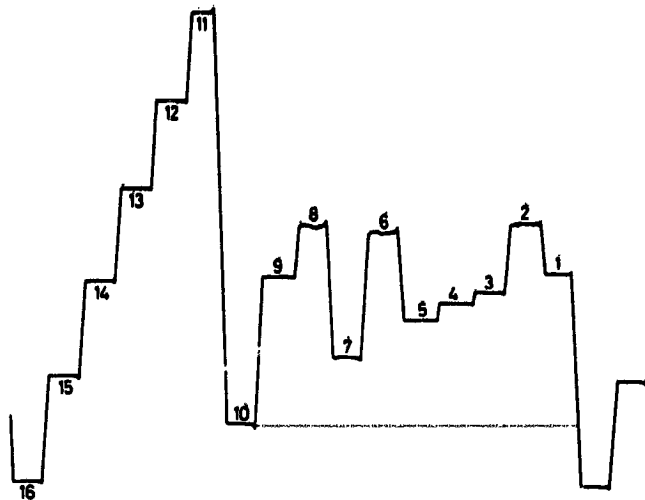


Figure 8. AEE Sample Sequence before Discharge

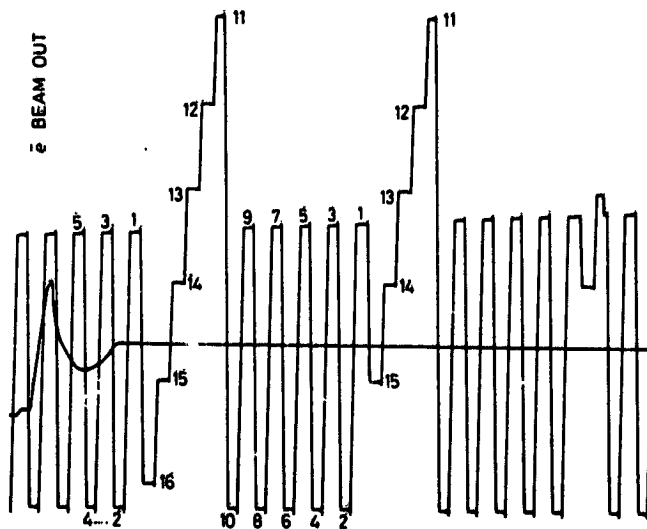


Figure 9. AEE Sample Sequence after Discharge

## 9. CONCLUSIONS

Several new phenomena have been observed in this series of substorm charging tests that may lead to a better understanding of the in-flight behavior of the CTS solar array experiment. Moreover, the test results may be of general importance for other solar arrays of similar design.

Discharges due to electrostatic charging of the solar cell test patch rear side occur at energies above 15 keV when the front side of the test patch is not sun-illuminated. After turn-on of solar simulation, the discharge frequency decreases to zero within a short time. It could be shown that the test patch temperature is an important parameter for the discharge frequency. Above 30<sup>o</sup>-40<sup>o</sup>C no discharges are obtained. Moreover, the illumination level on the front side was shown to have an influence on the temperature limit below which discharges are obtained.

Finally it was shown that the experiments electronics will not survive discharges in the test patch area. As the solar array experiment is still operating in space, it can be concluded that up to now no severe discharges have occurred in the test patch area. The conclusion is made plausible by the observed discharge frequency dependence on temperature and illumination.

The phenomenological nature of the tests does not allow more quantitative conclusions to be drawn. More detailed data, however, are needed for the design and the specification of future solar arrays. Therefore it is planned to continue the tests as soon as possible and to obtain quantitative results in the following areas:

- (1) Dependence of discharge energy, spectrum and frequency on the sample size.
- (2) Investigation of the temperature and illumination intensity dependence of charging/discharging phenomena.
- (3) Investigation of the behavior of new solar array substrate materials (for example, carbon-fiber-kapton compound) in a substorm environment.

## References

1. Stevens, N. Y., Lovell, R., and Gore, V. (1975) Spacecraft Charging Investigation for the CTS Project, NASA-TMX-71795.
2. Coffey, H. T., Nanewick, J. E., and Adams, R. C. (1975) Photoconductivity of High Voltage Space Insulating Materials, SRI Final Report for Contract NAS3-18912.
3. Anson, W., and Pischel, H. G. (1975) Final Report on the Array Experiment Electronics - AEE RFE Report.

**Contents**

1. Introduction	503
2. Experimental Procedures	504
3. Steady State Measurements	508
4. Flashover Measurements	512
5. Conclusions	515
Acknowledgments	515
References	515

**5. Charge Distributions Near Metal-Dielectric  
Interfaces Before and After  
Dielectric Surface Flashover**

James W. Robinson  
Electrical Engineering Department  
Pennsylvania State University  
University Park, Pa.

**Abstract.**

Flashovers on dielectric surfaces of spacecraft will produce currents to adjacent metallic surfaces and in many cases may be initiated by phenomena at the interface between metal and dielectric. A technique has been developed for measuring surface charge distribution near interfaces without placing any measuring apparatus near the face of the samples. This paper reports the results of measurements which have been made on FEP Teflon and Kapton dielectrics, before and after flashover, with various types of interfaces. Also given are data showing mean time between flashovers for various configurations exposed to a variety of environmental conditions. Several charge transfer mechanisms are considered as means by which stable charge distributions may be maintained near interfaces.

**1. INTRODUCTION**

Many of the flashovers which occur because of differential charging of a spacecraft surface will be initiated by phenomena near a metal-dielectric interface. This is especially true if the conductive frame of the spacecraft is maintained near local space potential by an active emitter while the dielectric becomes highly charged because of substorms. This report deals with phenomena at the interface

503  
**INTERNATIONALLY INDEXED**

so as to ascertain the conditions for flashover and to seek means of preventing flashover. Charge distribution measurements are the principal diagnostic tool.

The flashover is a process whereby negative charges adhering to a dielectric surface are abruptly released and transported tangentially to a nearby grounded conductor. Punchthrough is not considered. The charge distributions on the dielectric are formed by an impinging electron beam that is monoenergetic though unfocused. The breakdown process is suggestive of the failure of vacuum bushings except that the bushings fail because of cathode phenomena<sup>1</sup> whereas the system of interest has a remotely located cathode which plays no part in the flashover phenomena.

This report presents charge distribution data and flashover probabilities for different types of interface. From charge distributions, one can calculate electric fields and estimate limits where flashover becomes probable. An analysis of various charge transport mechanisms below the flashover threshold will lead to an eventual understanding of the phenomena controlling flashover.

## 2. EXPERIMENTAL PROCEDURES

### 2.1 Preparation of Specimens

Results described here are for 0.13 mm (5 mil) sheets of FEP Teflon having a silver-inconel coating. The coating is grounded with the specimen facing the electron beam such that charges on the surface of the sheet will induce comparable charges on the underlying metal film. When the metal film is segmented and each segment is grounded, then the surface charge distribution can be inferred by measuring the charges induced on each of the underlying segments. The schematic shown in Figure 1 illustrates the technique where it should be noted that the electrometer configured for charge measurement maintains the associated segment at virtual ground.

The charge data must be coupled with either segment areas or segment capacitances. Areas were determined by scaling from enlarged photographs and capacitances were measured directly by applying voltages of 500 and 1000 V to drops of aqueous salt solutions standing on the upper surface of the specimen. The two measurements were compatible with handbook data of 2.1 for a dielectric constant, though the capacitance measurements were the more precise and were used almost exclusively. A typical capacitance per segment was 1 pF.

The interface for many of the measurements was formed by placing a grounded metal aperture over the specimen. Variations of diameter, aperture thickness, and material were tried. In other measurements, the same type of aperture was used but a slit was cut through the dielectric sheet so as to expose the underlying

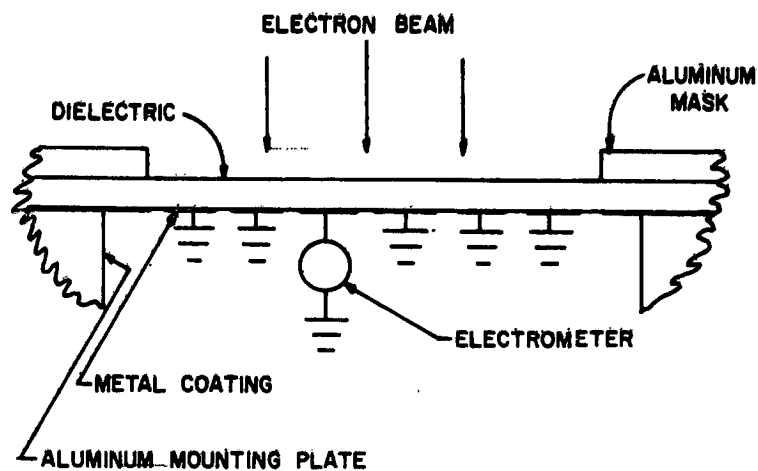


Figure 1. Mounting of the Dielectric Specimen (Film Thickness Exaggerated)

ground plane. In these latter cases, the ground plane was reinforced with a layer of conductive epoxy backed with stainless steel shimstock.

The segments were cut in the ground plane by means of an electrical discharge machining technique. A repetitive discharge from a 100 pF capacitor at 1 kV was used. With the use of guides the etching point could be moved so as to cut lines of about 0.2 mm in width though in practice wider lines were used. When the lines were too fine, flashovers would induce breakdown between the segments. The smallest segments used were approximately 1.5 mm wide and 4 mm long, this being the smallest size for which epoxy bonding of leads was convenient.

A line drawing from a photograph of an actual specimen is shown in Figure 2. The view is from the direction of the electron beam. The circular aperture exposes the transparent dielectric sheet and the underlying reflective ground plane. The etched lines are visible through the film and are easily photographed by the use of backlighting. The first segment in the illustration is partially hidden by the aperture.

## 2.2 Test Chamber

The specimen was inserted into a stainless steel vacuum chamber as illustrated in Figure 3. The various aspects of the system are described below.

The electron source was of simple construction having a heated tungsten filament and its aluminum enclosure maintained at a fixed negative voltage. Electrons from the recessed filament would emerge from the hole in the box and be accelerated toward the grounded supporting frame. They would pass through a

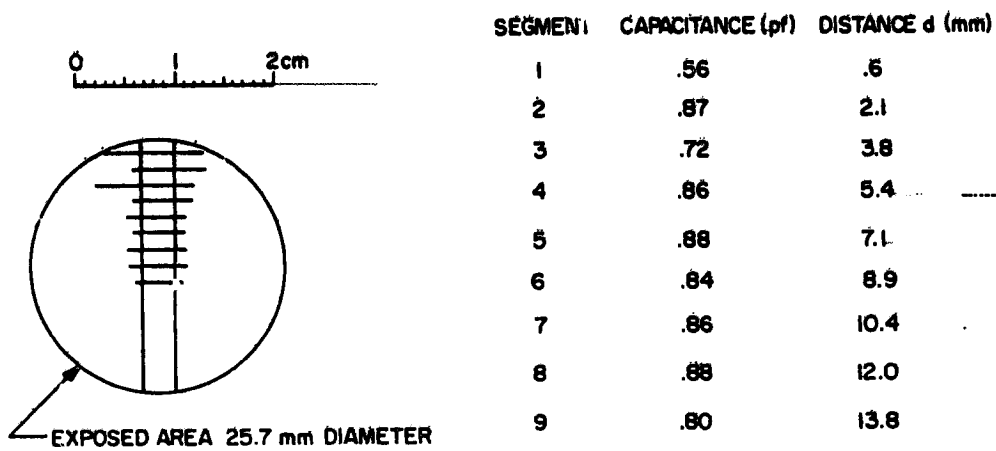


Figure 2. Typical Specimen Configuration

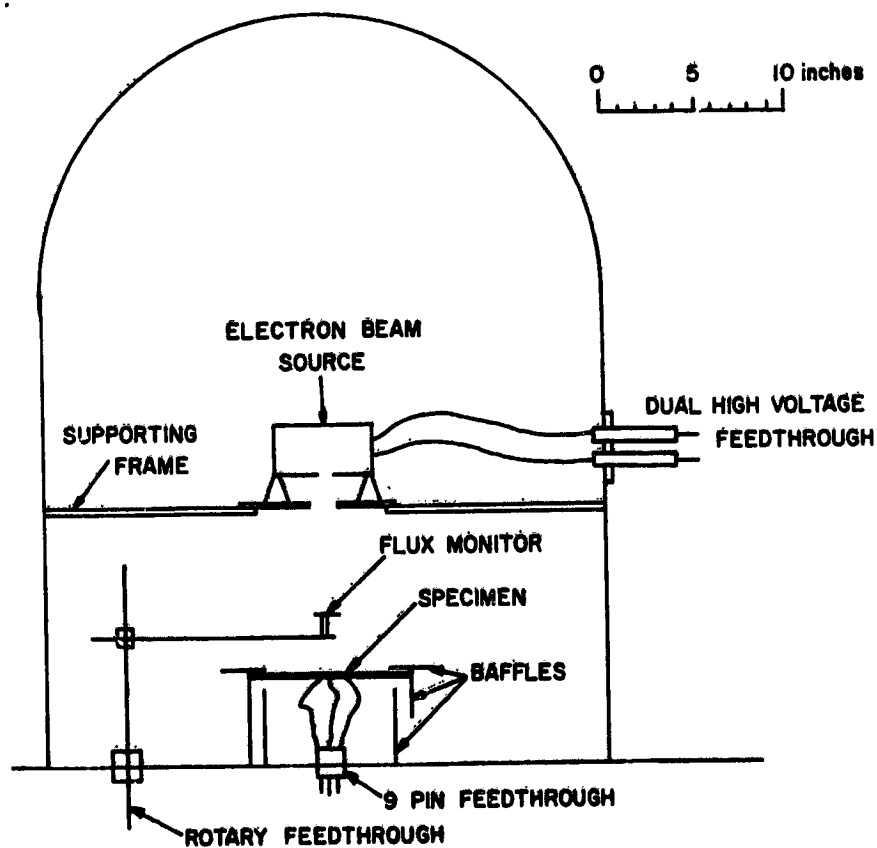


Figure 3. Placement of Apparatus in Vacuum Chamber

second hole in the frame and drift at constant velocity toward the specimen. The diameter of the beam at half-maximum intensity on the target was approximately 8 cm as determined by sensors on the specimen plane. Thus, specimen diameters were kept to less than 5 cm for all experiments. The beam source was fed by high-voltage feedthroughs remotely located from the other feedthroughs where sensitive measurements were being made.

The beam intensity was monitored by a small probe which could be swung into position above the specimen. Current to the probe was measured by an electrometer which held the probe near the ground potential. A geometrical factor was computed for converting the probe current to effective current density at the specimen face. Though the accuracy of this determination is not high, it is still adequate for comparing fluxes and providing reproducibility.

The specimen was mounted on a platform surrounded by baffles which were to keep scattered electrons from the sensitive leads. These leads were kept short and connected by a multipin, high-voltage feedthrough to an external terminal box where various electrical connections could be made.

The chamber was evacuated to a base pressure of  $10^{-6}$  torr with a turbomolecular pump. Pressure was monitored. A controlled leak was available but used little because varying the pressure had little effect upon the data.

### 2.3 Data Collection

Procedures were developed to reduce the impact of spurious events and systematic errors. In addition to the occurrence of occasional inconsistent data points, all data reflected the effects of electrometer drift and residual surface charges.

Drifting of the electrometers occurs because of charge leakage through the dielectric sheet but this was negligible and not measurable with FEP Teflon. Some tests with Kapton showed leakage but otherwise behavior similar to FEP Teflon. Of much greater significance was the scattering of electrons through the baffles to the back side of the specimen. This effect was controllable to a point where short term drifts of say a minute were negligible. Long term drifts were of little consequence and could have been due either to leakage or to scattering. Another source of drift was that due to humid air in the terminal box. This problem was controlled with dessicant.

The measurement of charge requires the ability to remove all charge from the specimen before and after a charging cycle. One simple way of removing charge, but a slow way, was to raise the pressure to  $10^{-3}$  torr and to wait for approximately 1 min. A quicker and equally effective way was to use secondary emission from the surface. With proper adjustment of the electron beam energy, the secondary emission coefficient would exceed unity and the surface would lose charge. With the proper sequence of beam voltage adjustments, the surface charge could then be brought to an adequately low value.

Two electrometers were used to monitor two segments simultaneously. Several sets of measurements then provided a basis for combining data from different runs with an assurance of consistency from one run to another.

Flashovers were easily observed by recording electrometer outputs on a strip chart recorder. The abrupt loss of charge on a segment was observable as a discontinuity on the trace. Partial and complete discharges have been observed through the great majority have been complete.

### 3. STEADY STATE MEASUREMENTS

#### 3.1 Charge Distributions

Detailed charge measurements were made for the FEP Teflon specimen illustrated in Figure 2. The diameter was 2.5 cm as determined by an aluminum aperture plate having a thickness of 1.3 mm. Measured segment capacitances were used to convert measured charges to surface potentials which are shown in Figure 4. Away from the boundaries, the potential is approximately the beam potential less the energy at which the secondary emission coefficient is unity. Incoming particles thus strike the surface so as to release an equal number of secondaries. The data of Willis and Skinner<sup>2</sup> indicate a unity crossover for PTFE Teflon of 1.8 kV which corresponds well with Figure 4. Near the boundaries, the potential is depressed such that a gradient of approximately 10 kV/mm is established. If one applies the data of Willis and Skinner to the depressed region, he concludes that the secondary emission coefficient in that region is less than unity such that some auxiliary charge release mechanism is acting in that region to maintain a steady state.

Charge measurements have been made for another specimen similar to that of Figure 2 except that it has a slit of 1 cm length through its center. Steady state conditions could not be achieved at such high voltages as for the first specimen, but charges were measured and potentials calculated as shown in Figure 5. Also shown in the figure is a curve at 10 kV taken from Figure 4 and positioned for comparison of the gradients with and without a slit.

It is evident that with the slit a high gradient will exist across the cut surface of the dielectric, this being as high possibly as 7 kV/0.13 mm or about 50 kV/mm.

Numerous other mappings have been made with results being essentially similar to those already shown. The edge effects are similar for a 5 cm diameter specimen, for a specimen with a copper aperture, and for a Kapton specimen.

Highly significant is the fact that steady state distributions do not depend upon electron flux density. From a steady state with a given flux, the electron source filament can be cooled until the flux is zero and no change in the charge is observed.

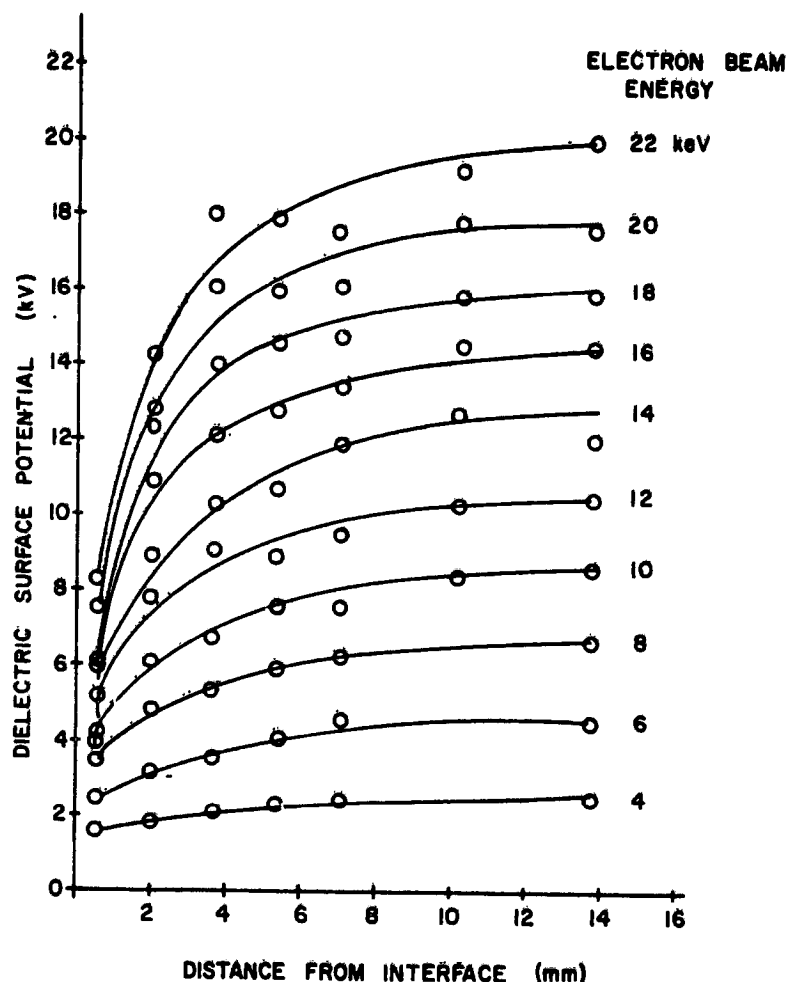


Figure 4. Steady State Surface Potentials for FEP Teflon

However, at very high fluxes exceeding  $1\text{-}\mu\text{A}/\text{cm}^2$  a drop of perhaps 5 percent of the surface charge is observed.

### 3.2 Equipotential Contours

Once charge distributions are known, Laplace's equation can be solved. The method used here was approximate, being most accurate near the surface and the interface. It involved approximating the problem with a two-dimensional model, doing a conformal transformation, and solving by use of separation of variables. The data points for the 20 kV case of Figure 4 were the basis of a calculation shown

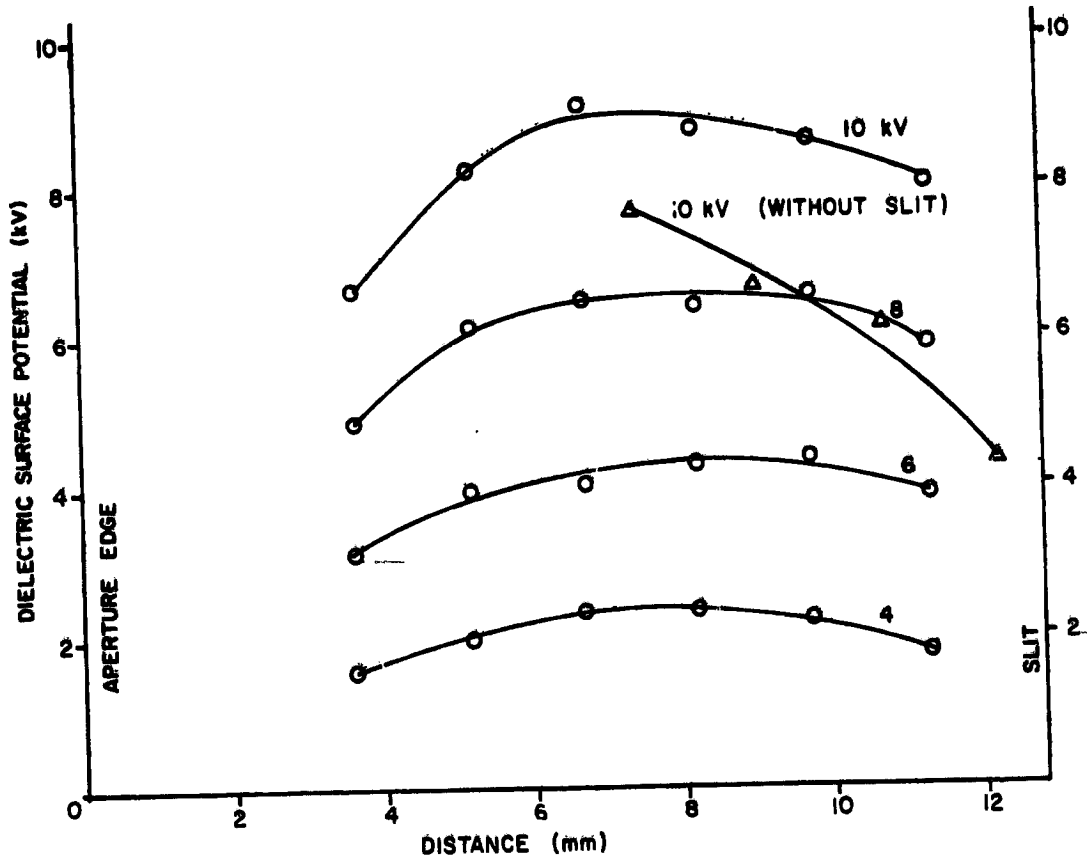


Figure 5. Steady State Potentials for Specimen With Slit

in Figure 6. The crucial point to be noted here is that the electric field has a normal component toward the surface.

### 3.3 Charge Release Mechanisms

The gradients near an interface are established through a balance of various charge transfer mechanisms. The fact that the balance is independent of primary flux density is an indication that all processes involved are proportional to primary flux. Various possibilities include field-enhanced secondary emission, x-ray production from the beam striking the aperture plate, ion neutralization, and bombardment-induced conductivity of the dielectric. The first of the suggestions is considered to be the most appropriate.

Measurements with a copper aperture were made to test for the possibility of x-ray effects. Copper was deliberately chosen because of its K-edge at 9 kV. If

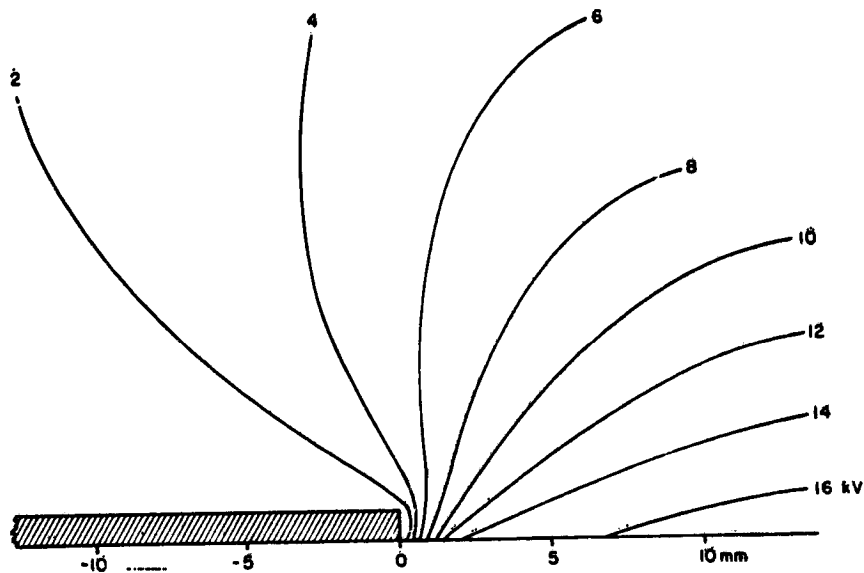


Figure 6. Equipotential Lines for Exposure to a 21 kV Beam

the charge distributions showed anomalies with 9-kV beam voltages, then x-rays would likely have a significant role in the charge balance. However, no differences could be found between measurements with copper and aluminum.

Ions might be attracted to the negative dielectric surface, yet they would go preferentially to the most negative center region and not to the edges where their contribution would be needed.

Though little information is at hand regarding conductivity of the dielectric under bombardment, it is felt that this phenomenon is not of sufficient magnitude, nor sufficiently linear, to account for the observed charge distributions.

Available data indicate that the secondary emission in the depressed regions near interfaces is inadequate to compensate for the incoming primary flux. Also, secondaries are accelerated away from the surface by the normal component of the field such that they cannot interact with the surface to cause an additional release of electrons. Note, however, that the data of Willis and Skinner<sup>2</sup> was recorded with techniques which minimized the buildup of charge on the dielectric surface and thus the field. It is possible that the secondary emission coefficient is increased in the presence of the field such that a steady state is maintained in the depressed regions.

#### 4. FLASHOVER MEASUREMENTS

##### 4.1 Specimen Without Slit

The probability of flashover has been found to be very low for Teflon specimens covered with the 1.3 mm aluminum aperture plate. Generally for all specimens without slits, but with aperture plates, the flashover rates have been low.

The flashover rate for the specimen of Figure 2 has been measured at various flux densities for a beam voltage of 21 kV. The rate is not constant but decreases with time, probably because of cleanup of the dielectric surface. The measurements shown in Figure 7 were made with a relatively dirty specimen which had not been long in vacuum. Even then a run-of 1 hr at  $0.16 \mu\text{A}/\text{cm}^2$  showed no flashovers. The flashovers which occurred showed a complete loss of charge from the surface of the specimen. After long exposure the surface of the specimen near the interface became frosted. For these tests the current levels were such that a steady state charge distribution was established in a few seconds. The system would reside in that condition for hundreds of seconds, exposed to an electron flux, before a flashover would occur.

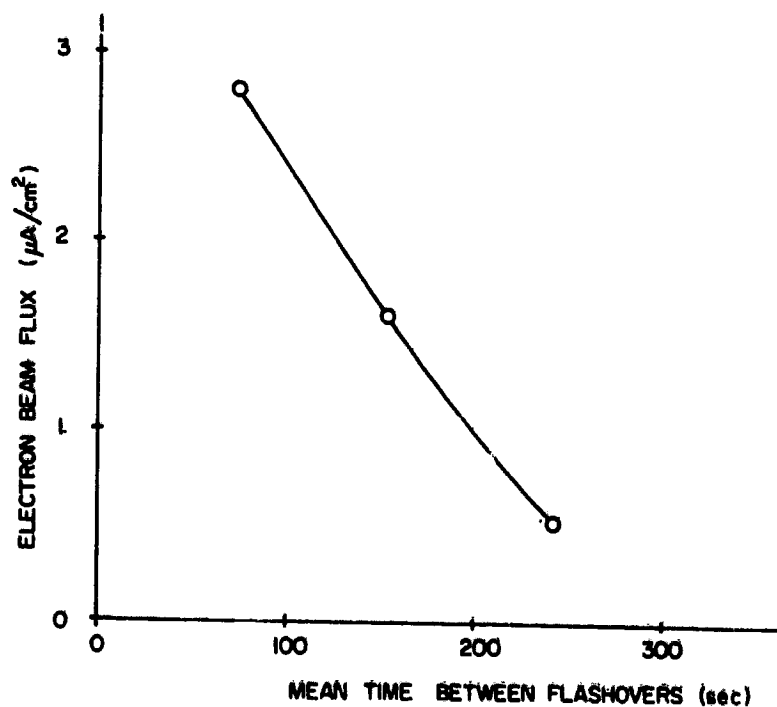


Figure 7. Flashovers in a 21 kV Beam

#### 4.2 Specimen With Slit

When a slit is cut in a specimen, the flashover rate increases drastically. Steady state is not attainable much above 10 kV. As before the flashovers cause a complete loss of surface charge. Visual observation shows light bursts concentrated on the slit when flashovers occur. Data points are shown in Figure 8 where the influence of both beam voltage and current density are shown.

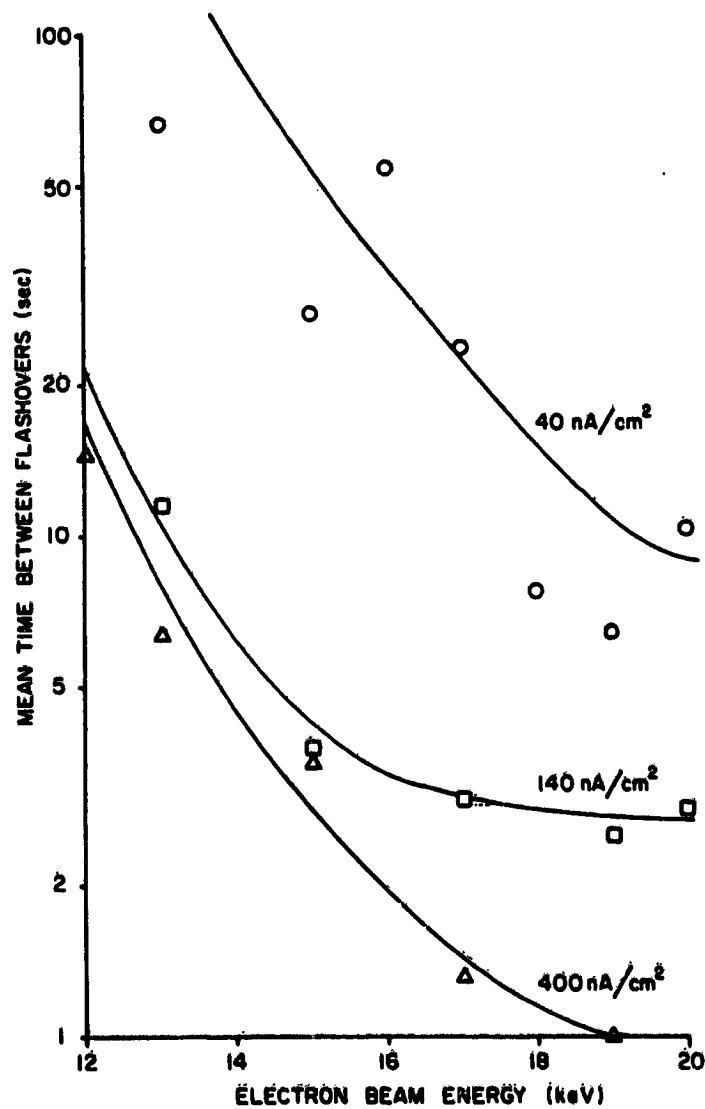


Figure 8. Flashovers for a Specimen with Slit

#### 4.3 Partial Flashovers

Partial flashovers have been noted, these being such as to leave some charge on the surface of the dielectric. Most of these observations were for FEP Teflon with a stainless steel aperture have a thickness of 0.08 mm. Furthermore, these partial flashovers occurred during the charging transient as shown in Figure 9. Two sequences are shown with the charges induced on two segments plotted against time. For this specimen, segment 5 was in the center, 3 near the edge, and 9 intermediately placed. The final steady state charges at 21 kV are consistent with expectations from Figure 4. No pattern of partial flashovers was distinguished except that in most cases only a single flashover occurred during the charging transient.

On rare occasions a single segment will lose a small fraction of its charge after having been in steady state for some time. Such events have not been counted in determining the mean time between flashovers shown in Figures 7 and 8.

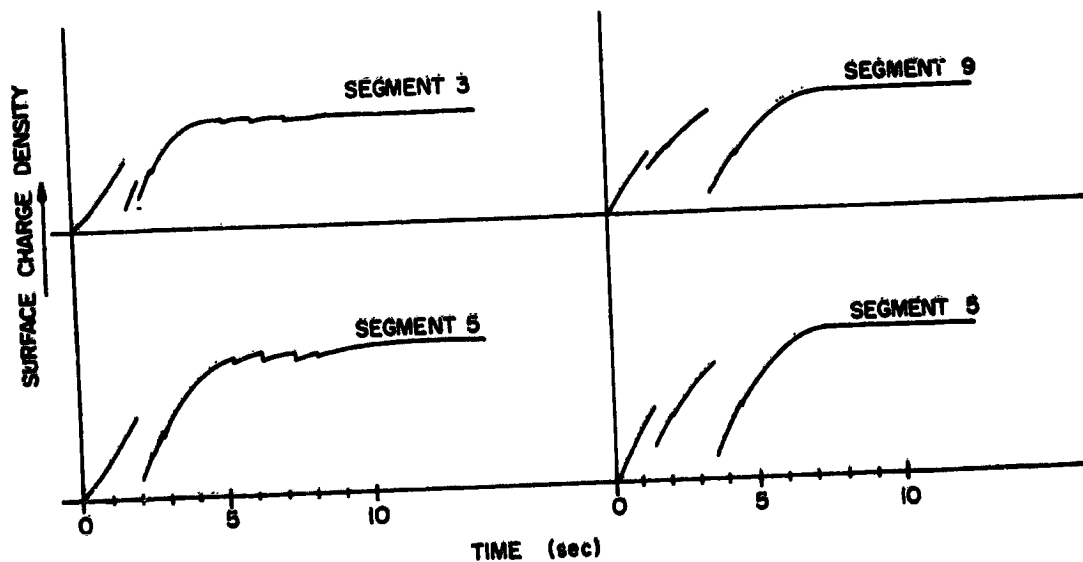


Figure 9. Partial Flashovers During Charging Transients

## 5. CONCLUSIONS

Measurements have demonstrated that gradients of 10 kV/mm can exist on the surface of dielectric materials with the probability of flashover being practically insignificant. The gradient is maintained by a balance among charge transfer processes which are thought to be dominated by secondary emission, although appropriate data to show this are unavailable.

The design of the metal dielectric interface has a marked effect upon the probability of flashover. An interface which exposes an edge of a dielectric sheet creates a strong field which initiates flashover at a relatively low level of charge on the dielectric surface. The threshold level for the onset of flashovers can be approximately doubled by covering the edge of the sheet with a ground plane.

The configurations investigated are not particularly useful for applications and, as a result, extensions of the work to multiple-aperture systems are anticipated. Breakdown probability and the propagation of flashover from one region to another are topics of interest. Also, the effects of punchthrough are to be investigated.

## Acknowledgments

S. G. Ehrenberg and N. Q. Nguyen have made significant contributions to the work described here. The support of the National Aeronautics and Space Administration under Grant NSG-3097 has been appreciated.

## References

1. Sudarshan, T. S., and Cross, J. D. (1973) DC Electric-field Modification Produced by Solid Insulators Bridging a Uniform-Field Vacuum Gap, IEEE Transactions on Electrical Insulation, EI-8 (No. 4):122-128.
2. Willis, R. F., and Skinner, D. K. (1973) Secondary electron emission behavior of polymers, Solid State Communications 13:685-688.

**PRECEDING PAGE BLANK NOT FILMED**

## **6. Electrical Equilibration of Dielectrics When Exposed to Energetic Electron Beams**

**William Saylor  
General Electric Company  
Philadelphia, Pa.**

### **Abstract**

In recent years, anomalous behavior has been noted for synchronous orbit spacecraft. These anomalies are now generally correlated with the occurrence of solar magnetic substorm activities when the spacecraft is in the plasma sheath environment. This can result in a nonuniform distribution of surface charge on the spacecraft dielectric thermal control surfaces. The resulting surface charge accumulation can leave large potential gradients for electrical discharges to occur which can pose a serious threat to the operational integrity of a spacecraft.

The purpose of this research experiment then was to gain an understanding of the complex nature of electrostatic charging. This experiment consisted of a series of measurements of electrical equilibration of selected dielectric materials when exposed to energetic electron charging beams. The electron beam simulates the environmental conditions in a magnetic substorm region of space, and the dielectric samples are representative of those found on the surface of a typical synchronous orbit spacecraft. The materials investigated were: Woven Silica Fabric, Thermal Control Paints, Solar Array Cover Glass, Teflon, Kapton and Mylar Films, and various composite combinations of the above. Also examined were polymeric films with special static charge control coatings applied. The Electrical Equilibration Measurement apparatus is shown and the results of the experiment are presented and discussed. The parameters that were determined include: The through conduction and surface leakage currents; the surface charge and equilibration potential; the bulk and surface resistivity; all as a function of the electron beam energy.

In general, the measurement results demonstrate that the magnitude of the surface charge potential is highly dependent upon (1) the bulk and surface resistivities of the dielectric materials, (2) the average energy of the bombarding electron beam, and (3) the secondary emission characteristics of the dielectric materials. The bulk and surface resistivities require threshold criteria for charge storage and/or leakage to take place, with the surface resistivity usually the dominant controlling factor. The criterion for charge storage versus charge leakage begins to show itself at a resistivity value of about  $10^{12}$  ohms. Significant charge leakage or storage can be obtained at values slightly less than or more than  $10^{12}$  ohms. The electron beam energy and the effective secondary emission "second cross-over potential" also play a large role in determining the magnitude and polarity of the surface charge potentials.

## Contents

1. Introduction	520
2. Recent Results	520
3. Conclusions	524
Acknowledgments	526
References	526

## 7. Surface Micro-Discharges on Spacecraft Dielectrics

K. G. Balmain, M. Cuchanski, and P. C. Kremer  
Department of Electrical Engineering  
University of Toronto  
Toronto, Canada

### Abstract

Extensive measurements on Teflon and Kapton in a scanning electron microscope indicate the existence of a well-defined family of surface micro-discharges characteristic of the dielectric material. The measurements are of the current flowing to a conducting pedestal supporting the dielectric, and carried out in both the time and frequency domains using a sampling oscilloscope and a spectrum analyzer. For a given small region exposed to the 16-20 kV electron beam, the strongest discharge pulses are similar in shape and amplitude. For Teflon, typical pulse durations are 2-3 ns, rise and fall times are sometimes as low as 0.2 ns, current amplitudes are approximately 100 mA flowing down to the pedestal (electrons flowing up), and the pulses are unidirectional with no ringing. The use of a rapid-scan electron microscope with a secondary-electron imaging system reveals complex charge distributions resembling Lichtenberg figures on a supposedly flat homogeneous dielectric surface. These patterns undergo extensive alteration at each micro-discharge pulse and indicate that both the charging and discharging processes are highly nonuniform over the dielectric surface. The use of a flood-beam (instead of the scanned spot-beam) causes the occurrence of larger-scale macro-discharges, in which a typical peak current is 40 A with a duration of 120 ns.

## 1. INTRODUCTION

The scanning electron microscope (SEM) has been used extensively to study charge accumulation on spacecraft dielectrics<sup>1</sup> and also to study the resultant discharges and their spectra.<sup>2</sup> These measurements have indicated that accumulated negative charge from the SEM electron beam spontaneously and very rapidly discharges from time to time, causing a downward current to flow in the conducting pedestal supporting the dielectric sheet, and resulting in a burst of electrons from the dielectric surface. A beam accelerating voltage of at least 16 kV was required to produce the above impulsive discharges, and measured spectra suggested discharge current rise and fall times of the order of a few nanoseconds.

The observed discharges had properties suggesting that they were initiated by the mechanism proposed by Meulenbergh whose unique and fundamental work<sup>3</sup> demonstrates that breakdown could occur between a submerged layer of electrons and a positive surface layer caused by secondary emission. Events subsequent to this initial breakdown remain a mystery although arc propagation through the submerged layer as described by Gross<sup>4</sup> is a possibility.

## 2. RECENT RESULTS

### 2.1 Interpretation of Previous Measurements

The discharge-current spectra reported earlier<sup>2</sup> were measured on a slowly-sweeping spectrum analyzer so that each discharge appeared as a dot on the oscilloscope display. The pattern of dots gave an indication of the discharge spectrum, but little attention was paid in the earlier publication to a significant property of the dot patterns, namely that most of the patterns taken had well-defined upper limits. This upper-limit property shows that the strongest discharge current pulses have the same spectra. Furthermore the spectra did not change appreciably as the highly focussed electron beam was moved from point to point on the specimen, nor did the spectra change more than a few dB as the spot beam was defocussed and enlarged to a cross-sectional area of  $1 \text{ mm}^2$  (and a current density of  $10 \text{ nA/cm}^2$ ).

### 2.2 Pulse Measurements With a Sampling Oscilloscope

A sampling oscilloscope can be used in a mode in which the time separation between triggering and sampling is increased by a small time interval after each pulse is sampled. This time interval is independent of the time between pulses, so that a regular pulse envelope will be displayed on the oscilloscope for randomly

occurring pulses, provided that all the pulses have the same shape. Such measurements were carried out mainly on Teflon specimens because of their high rate of discharge occurrence. When the triggering level was set to be reached only by the strongest pulses, regular pulse envelopes were measured as for example in Figure 1. Moving the electron beam from point to point on the specimen produced changes in the details of the pulse shape but had little effect on its peak amplitude of about 100 mA or on its duration of 2 to 3 ns. The fastest variation measured using a 4 GHz sampling oscilloscope was the 0.2 ns fall time in the pulse outline of Figure 2.

Similar measurements were carried out on Kapton H (Polyimide). Regular pulse leading edges were fairly easy to record, and the indicated rise times and pulse amplitudes were similar to those for Teflon. However, the Kapton pulse measurements exhibited a great deal of scatter for 5 to 10 ns following the initial rise. The most probable explanation for this is the occurrence of a succession of small discharges, each triggered by the one before.

Some sampling oscilloscope measurements were carried out on Teflon specimens given a prior heating to 38°C in air and transferred quickly on a heated base to the SEM chamber. These specimens produced discharges similar in shape to those already described at room temperature, but the pulse amplitudes for the heated specimens were smaller by factors of 3 to 4.

The fact that it is possible to get regular pulse outlines in most situations using the above techniques shows that the strongest pulses are virtually identical... in shape, at least for Teflon and to a more limited degree for Kapton. Because these pulses are so similar, it seems reasonable to think of them as members of a well-defined family of micro-discharges.

### 2.3 Macro-Discharges

Large-scale discharges on dielectric surfaces have been produced and studied by a number of researchers.<sup>3, 5, 6, 7, 8</sup> A proper understanding of the small-scale (micro) discharges requires their comparison with the large-scale (macro) discharges in a similar experimental environment. By the use of a large electron beam aperture and by the proper adjustment of the magnetic lenses, a scanning electron microscope can be made to produce a nonscanned relatively uniform flood beam of electrons more than 5 cm in diameter, with a current density of the order of 50 nA/cm<sup>2</sup>. Such a beam has been used to charge Mylar specimens measuring 48 × 26 × 0.12 mm. The resultant discharges are readily visible to the naked eye as "lightning" flashes which dart in irregular paths across the specimen, usually terminating at its edge. Figures 3 and 4 are photographs of such discharges which are visible as white lines in the central region of the specimen. The ray-like patterning around the edge of the specimen is luminescence due to electron impact

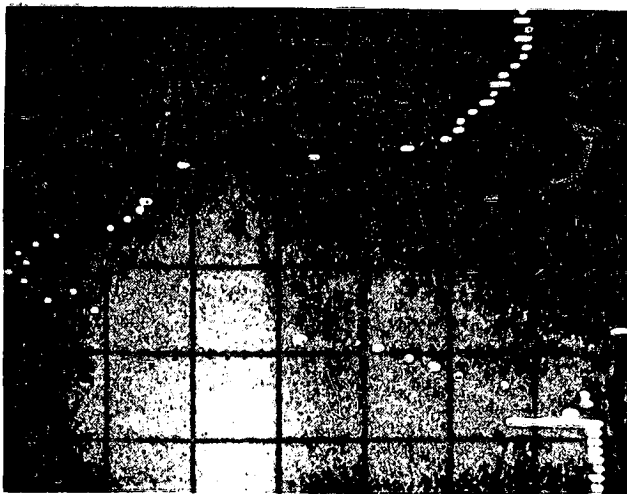


Figure 1. Micro-Discharge Current Pulse as Measured With a Sampling Oscilloscope. The upward direction corresponds to current flowing downward from the pedestal on which rests the Teflon specimen, measuring  $10 \times 10^{-6} \times 0.5$  mm. The 18 kV electron beam is highly focussed and only a small area of the Teflon is exposed to it. Horizontal scale 1 ns/div and vertical scale 100 mA/7 div

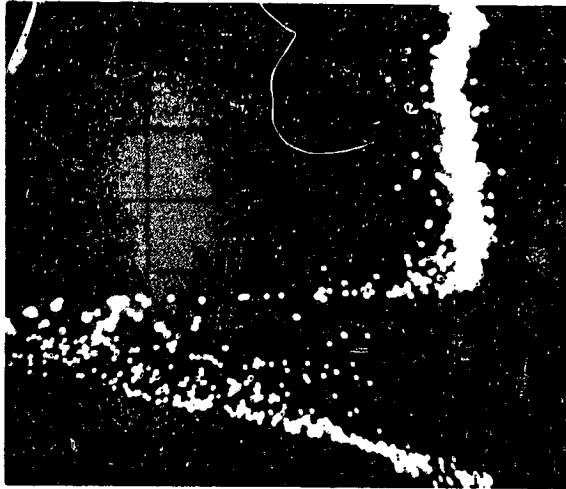


Figure 2. Micro-Discharge Current Pulse Measured Under Same Conditions as Figure 1, Except that the Spot Beam has been Moved to a Different Area on the Same Specimen

ORIGINAL PAGE IS  
OF POOR QUALITY



Figure 3. Macro-Discharge on Surface of Mylar Specimen  $26 \times 48 \times 0.12$  mm. The primary arc discharge goes from the central bright spot (due to filament illumination) to the lower edge of the specimen. The other bright areas are luminescence. The beam accelerating voltage is 20 kV



Figure 4. Macro-Discharge Under the Same Conditions as Figure 3. The arc can be seen crossing the central illuminated area

with the dielectric immediately following the discharge, when there is not enough negative surface charge left to repel the incident beam. The large bright spot in the centre of each photograph is due to light emitted by the SEM filament. Note in Figure 4 that this illuminated region is traversed by the discharge path indicating that the light intensity is not sufficient to discharge the specimen through photoemission.

The macro-discharge current to the conducting pedestal as measured in a 275 MHz bandwidth oscilloscope is shown in Figures 5 and 6. The peak current downward into the pedestal is consistently very close to 40A and the duration varies from 80 to 150 ns. The current flows into a 12.5 ohm load (three 50 ohm shunts plus 50 ohm attenuator) so that the peak instantaneous power is 20 kW and the total energy is of the order of 2 mJ. The total energy stored in the accumulated charge could be as high as 50 mJ (for a 20 kV beam); conceivably part of the energy difference could be dissipated in the discharge arc itself as it propagates across the specimen and over its edge to the pedestal.

#### 2.4 Observations With a TV-Type Scan

Rapid scanning with a television-type raster and secondary-electron detection produces real-time images of submerged charge distribution (because the negative submerged charge increases the probability that secondary electrons will escape from the dielectric surface). Observations of this type indicate complex charge distribution patterns which change slowly in response to changes in the region being viewed and very rapidly in response to impulsive discharges. These observations suggest that an apparently clean and smooth dielectric surface may be very nonuniform with respect to charge accumulation, on a scale as small as a fraction of a millimeter. Also noted during these experiments was a tendency for discharge initiation to occur along the borders between relatively charged and uncharged areas.

### 3. CONCLUSIONS

Surface micro-discharges on thin sheets of dielectric at room temperature are readily identifiable as producing 100 mA, 2-3 ns pulses into a grounded backing conductor. On the other hand, surface macro-discharges are both stronger and longer in duration, by about two orders of magnitude for both peak current and pulse duration in the experiments described. The area exposed to the electrons (and thus the area discharged) seems to be the factor that distinguishes the two types of discharge. There is also a possibility that a succession of micro-discharges could make up (or at least trigger) a macro-discharge. Certainly the

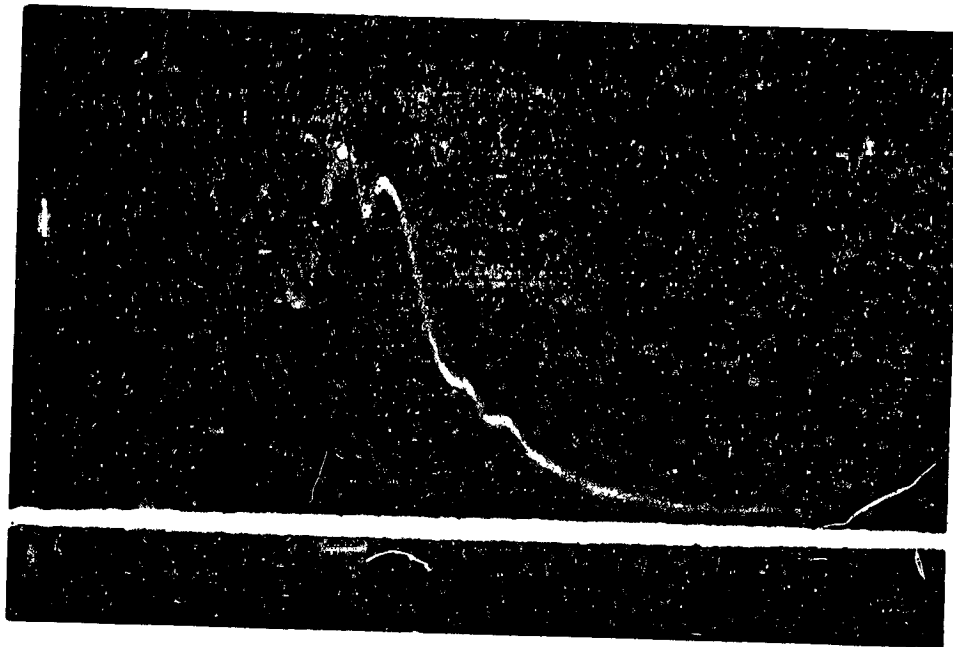


Figure 5. Macro-Discharge Current into the Conducting Pedestal Supporting the Mylar Specimen of Figures 3 and 4. Horizontal scale 50 ns/div and vertical scale 13A/div

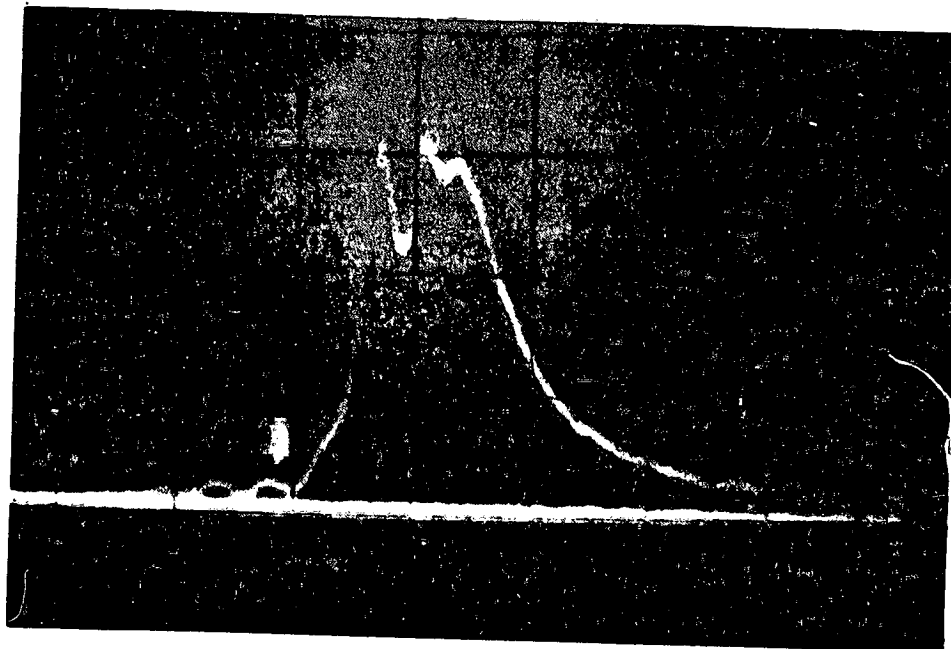


Figure 6. Macro-Discharge Current Under Same Conditions as Figure 5 (for Another Discharge)

nonuniformity of the observed charging patterns and the irregularity of the observed discharge paths indicate that the phenomena under study are very complex in terms of their detailed behaviour.

## Acknowledgments

The authors thank M. Palfreyman and J. V. Gore for many helpful discussions and for supplying the spacecraft materials used in the experiments. The research was supported by the Communications Research Centre, Department of Communications, Canada, under Department of Supply and Services Contract No. OSU 76-00064. Permission by the Department of Communications to publish the results of this study is acknowledged. Support was also provided by the National Research Council of Canada, under Grant No. A-4140. The assistance of W. C. Nixon is gratefully acknowledged.

## References

1. Balmain, K. G. (1973) Charging of spacecraft materials simulated in a scanning electron microscope, Electronics Letters, 9:544-546.
2. Balmain, K. G., Orszag, M., and Kremer, P. (1976) Surface discharges on spacecraft dielectrics in a scanning electron microscope, Progress in Astronautics and Aeronautics, 47:213-223.
3. Meulenbergh, A. (1976) Evidence for a new discharge mechanism for dielectrics in a plasma, Progress in Astronautics and Aeronautics, 47:237-246.
4. Gross, B. (1958) Irradiation effects in plexiglas, Journal of Polymer Science, 27:135-143.
5. Stevens, N. J., Lovell, R. R., and Gore, V. (1976) Spacecraft-charging investigation for the CTS project, Progress in Astronautics and Aeronautics, 47:263-275.
6. Hoffmaster, D. K., and Sellen, J. M. (1976) Spacecraft material response to geosynchronous substorm conditions, Progress in Astronautics and Aeronautics, 47:185-211.
7. Adamo, R. C., and Nanevicz, J. E. (1976) Spacecraft-charging studies of voltage breakdown process on spacecraft thermal control mirrors, Progress in Astronautics and Aeronautics, 47:225-235.
8. Walther, F. G. (1974) private communication.

Contents	
1. Introduction	527
2. Material Description	528
3. Ground Strap Surge Current Tests	528
4. Electron Swarm Tunnel Tests	540
5. Summary and Recommendations	546
References	547

## 8. Surge Current and Electron Swarm Tunnel Tests of Thermal Blanket and Ground Strap Materials

D.K. Hoffmaster, G.T. Inouye, and J.M. Sellen, Jr.  
TRW Defense and Space Systems Group  
Redondo Beach, Calif.

### 1. INTRODUCTION

This technical memorandum will describe the results of a series of current conduction tests with a thermal control blanket to which grounding straps have been attached. The material and the ground strap attachment procedure will be described more fully in Section 2. The current conduction tests consisted of a surge current examination of the ground strap and a dilute flow, energetic electron deposition and transport through the bulk of the insulating film of this thermal blanket material. Both of these test procedures have been used previously with thermal control blanket materials. The surge current test procedure (and accompanying test results) has been previously described in Hoffmaster et al.<sup>1</sup> The electron deposition procedure (and accompanying results) has been described in Hoffmaster and Sellen.<sup>2</sup> Because of the length of these previous memoranda, there will be no attempt to represent here the content of these papers, and it is recommended that these earlier test procedures and results be read as a portion of the total TRW in-house examination of thermal control blanket material response to particle injection and to surge currents.

Without presenting specific experimental details here, it will be noted that the behavior of the material to these test procedures is considered as a distinct

improvement over previously observed behavior. Since the ultimate selection of spacecraft surface materials will, undoubtedly, involve many different features of the materials, superior performance to surge currents and deposited currents may not be the final, and crucial, material aspects. In view, however, of acknowledged problems in charge up discharge in magnetic substorms at geosynchronous altitudes, the material performance to be described here under certain simulations of these space environmental conditions should be considered as a strong reason for their use.

## 2. MATERIAL DESCRIPTION

The thermal control blanket material used here (ORCON KN-10) is a 0.0005 in. ( $1.27 \times 10^{-3}$  cm) Kapton\* film with a rear face of Vacuum Deposited Aluminum (VDA) to a depth of  $\sim 1000 \text{ \AA}$ . At the rear (exterior) face of the VDA film, a grid of NOMEX ribbon thread (described as a Mylar-like insulator) is attached. The grid is  $\sim 6$  threads per inch in each of two directions. The thread dimensions are  $\sim 0.0025$  in.  $\times$  0.020 in.

The ground straps are aluminum foil of 0.75 in. width and 0.002 in. thickness, bonded to the VDA layer with a conducting epoxy. The joints are overlaid with a 1.00 in.  $\times$  1.25 in. aluminum tape as per the current DSCS fabrication technique. Each Kapton sample had an area of 3 in.  $\times$  4 in. and was equipped with two grounding straps.

## 3. GROUND STRAP SURGE CURRENT TESTS

### 3.1 General Considerations

In the surge current tests, the current is injected over a broad area at the midplane of the VDA film on the rear face of the Kapton and is conducted into a single ground strap. In principle, then, the current flow is in the VDA film and hence to the conducting epoxy and to the ground strap. In practice, it is apparent that, in addition to the conducting path above, current flow may also (if necessary) take place in the NOMEX grid.

The surge current generator is a power supply which charges a capacitor to 10,000 volts and a hydrogen thyatron and series current limiting resistor. The firing of the hydrogen thyatron causes the capacitor to discharge through the

---

\*Some of the tests performed with the 0.0005 in. material were repeated with ORCON utilizing a 0.003 in. Kapton base film. See Section 4.3.2 for these tests.

series resistor ( $100\Omega$ ) and the VDA film/conducting epoxy/aluminum ground strap. The total charge flow is determined by the capacitance and the charging voltage. For the capacitors used of  $3.6 \times 10^{-9}$ ,  $10.0 \times 10^{-9}$  and  $100 \times 10^{-9}$  F and the charging voltage of 10,000 volts, it follows that total charge flows for the various tests were  $\sim 36$ , 100, and 1000  $\mu\text{c}$ . The characteristic durations of these current surges were  $\sim 0.36$ , 1.0, and 10.0  $\mu\text{sec}$ .

Two types of resistance measurements were made. The first of these is a steady-state measurement from the input clamp to the output clamp on the surge current generator, made after each current-burst. Only very low sensing voltages are used in these measurements. The second resistance measurement is a "dynamic" measurement, and is made during the time of the high current passage through the VDA/ground strap combination. Significant differences may exist between these two measurements, particularly at the high burst number level where the removal of VDA near the ground strap bond has taken place.

### 3.2 Steady State Resistance

Ohmmeter type measurements were carried out on six ground straps. The results of these resistance measurements are given in Figures 1 through 6 as a function of the number of current bursts applied and for the three levels of capacitance in the high voltage storage capacitor.

Figures 1 and 2 illustrate results for a 3600 pF capacitor, charged to 10,000 volts and with a series resistance of  $100\Omega$  (leading to a peak surge current of 100 A). The shape of the  $R(n)$  curve is similar to those obtained previously. For a large number of bursts, the steady state, post-burst, resistance remains approximately constant. Above some burst number, however, increases in resistance are comparatively rapid. In previous tests of ground straps,<sup>1</sup> these rapid increases in resistance were attributed to the removal of the last remaining portions of the VDA film leading into the conducting epoxy bond.

While removal of VDA occurs for the present samples (as well as for previous ones), there are two major differences between the behavior observed here for the added NOMEX grid and the previous samples where the grid has been absent. The first major difference is that the number of bursts required to reach the "knee" of the  $R(n)$  curve is now considerably larger than for the previous ground straps. For example, (see Figure 7, Hoffmaster et al<sup>1</sup>), the knee of  $R(n)$  curve for  $3.6 \times 10^{-9}$  F,  $100\Omega$ , and  $10^4$  volts was observed at  $\sim 300$  bursts for the ground straps used there, while in the present case, over 1000 bursts were required to reach the rapid rising portions of  $R$  versus  $n$ .

A second major difference between present and previous results is that, for the present (NOMEX aided) ground strap, visible surface arcs did not occur, even

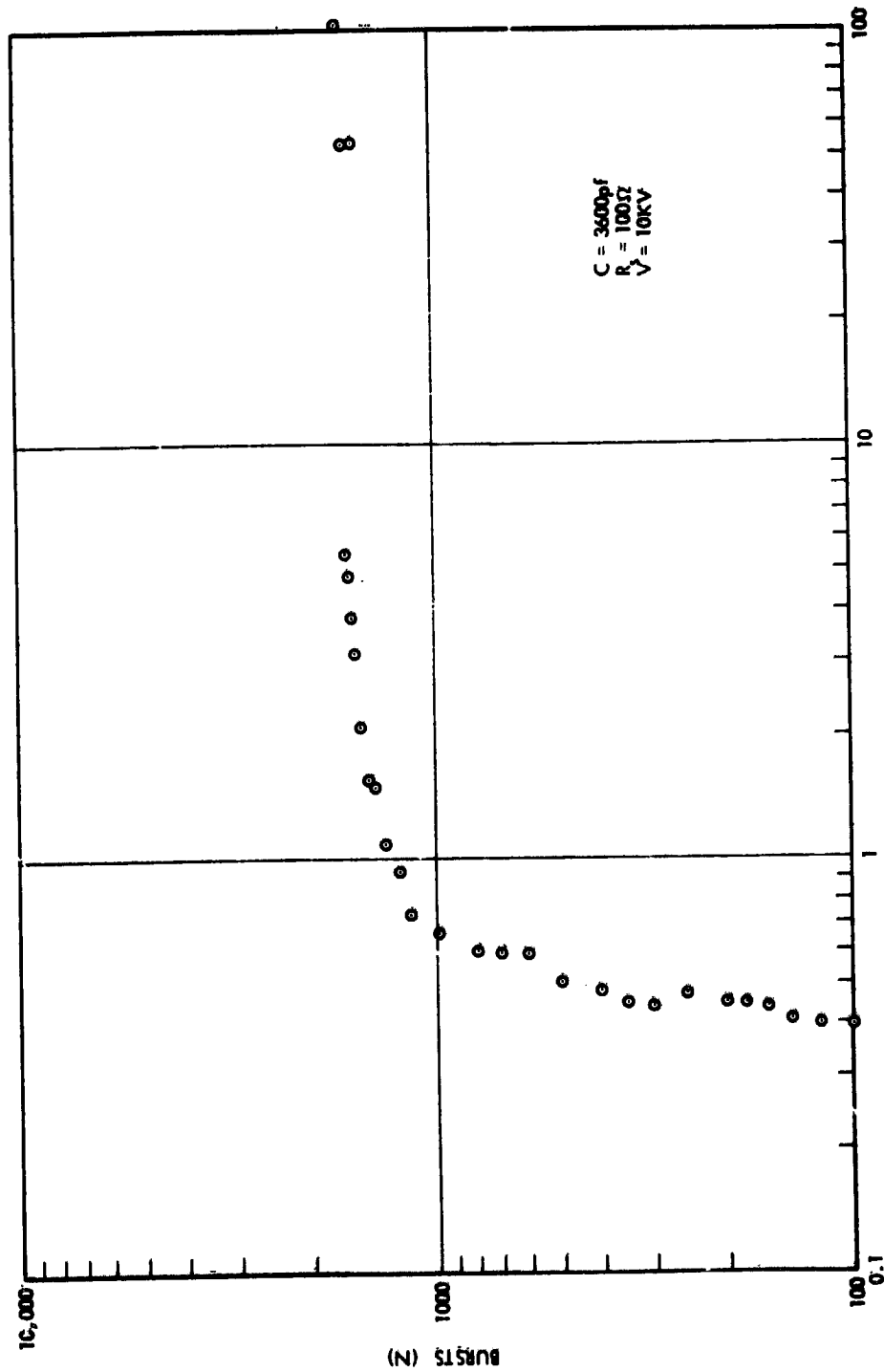


Figure 1. Resistance of VDA/NOMEX/groundstrap Sample 1 as a Function of the Number of Current Bursts. Initial surge current = 100 A and total charge throughput = 36  $\mu\text{c}$

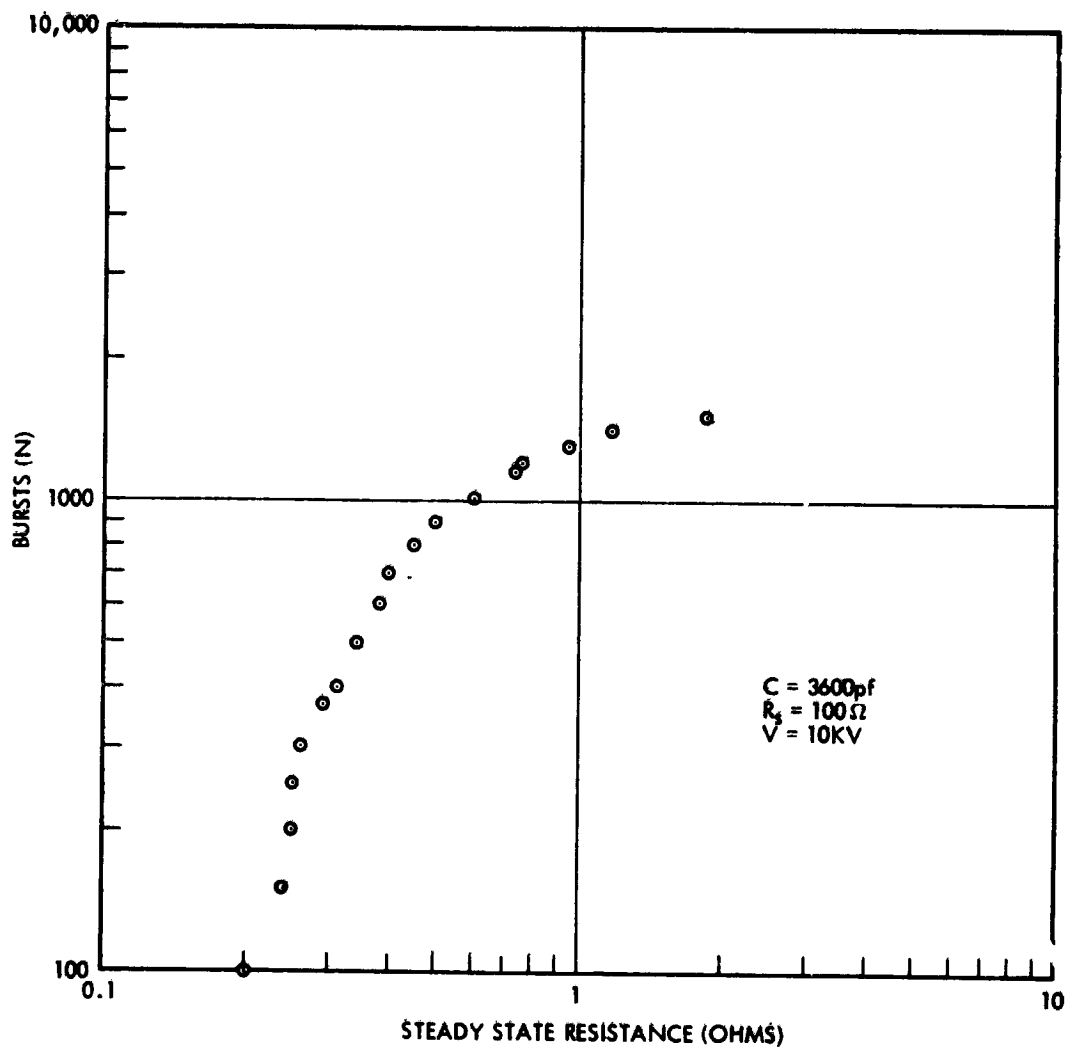


Figure 2. Resistance of VDA/NOMEX/Groundstrap Sample 2 as a Function of the Number of Current Bursts. Initial surge current = 100 A and total charge throughput = 36  $\mu\text{c}$ .

after the VDA film had been removed from the region of the bond. It is apparent that the presence of the NOMEX grid provides alternative conduction paths and that the conduction of this new construction does not result in the metal-to-metal arcs across dielectric surfaces observed earlier. This is a significant improvement in performance and indicates a large reduction in surface discharge current noise, should conduction be required and if the VDA film near the bond has been removed by previous current bursts. Section 3.3 will consider these dynamic current conduction processes further.

Figures 3 and 4 illustrate the steady state resistance as a function of the number of bursts for a larger capacitor than above. The increase in C from  $3.6 \times 10^{-9}$  to  $10 \times 10^{-9}$  F results in a loss of ground strap life. VDA film removal now occurs at  $\sim 300$  bursts. When the capacitance is increased to  $100 \times 10^{-9}$  F, the film removal occurs after  $\sim 20$  bursts. These results are given in Figure 5. Visible surface arcs were not observed for these higher capacitance discharges, following

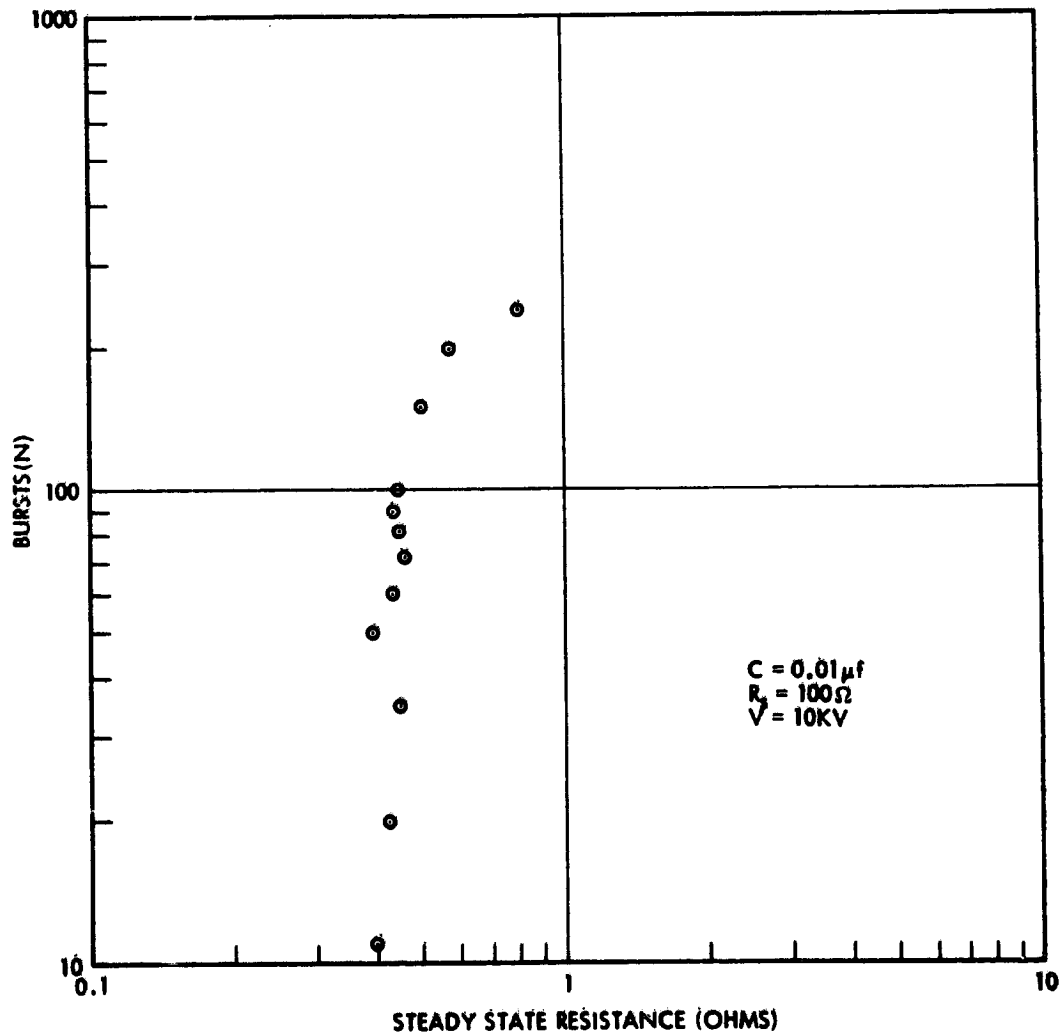


Figure 3. Resistance of VDA/NOMEX/Groundstrap Sample 3 as a Function of the Number of Current Bursts. Initial surge current = 100 A and total charge throughput = 100  $\mu c$

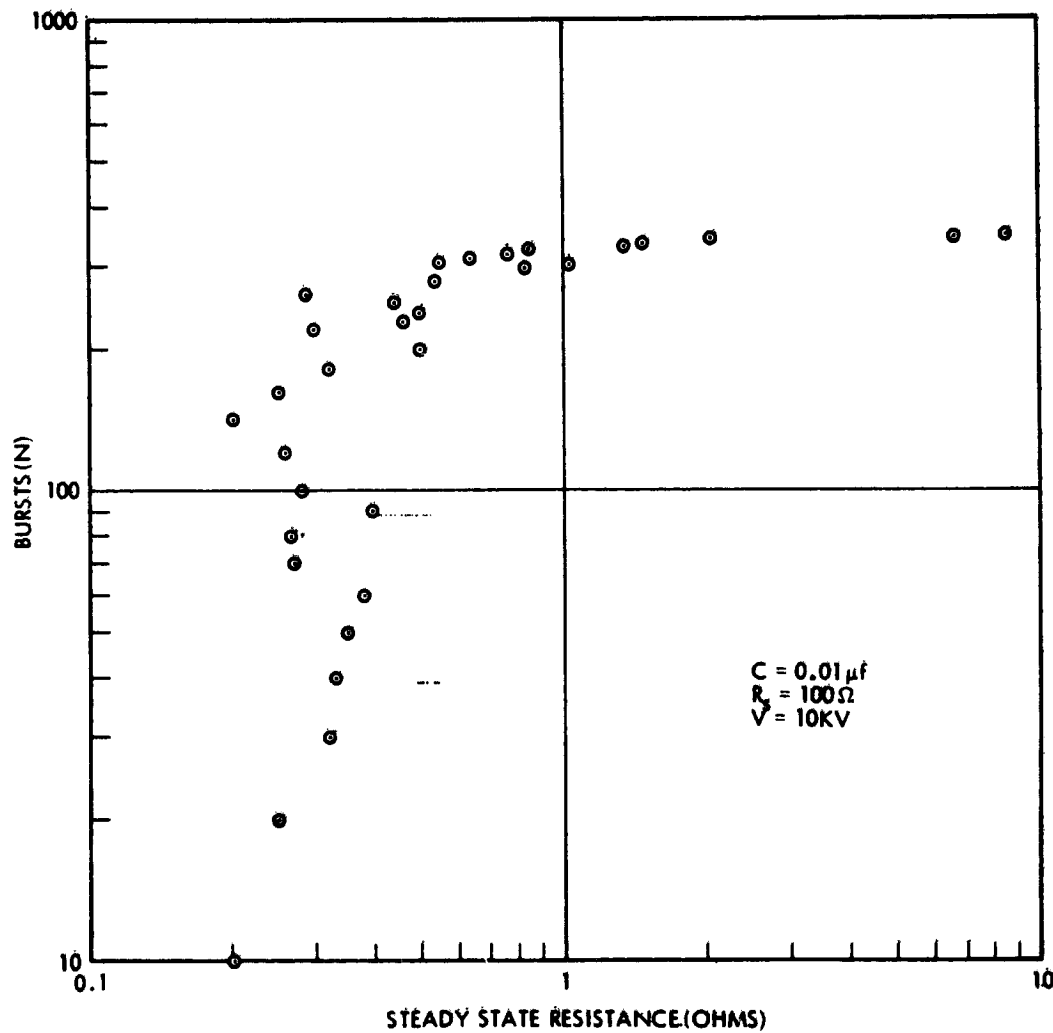


Figure 4. Resistance of VDA/NOMEX/Groundstrap Sample 4 as a Function of the Number of Current Bursts. Initial surge current = 100 A and total charge throughput = 100  $\mu c$

loss of VDA and the increase in the steady state resistance. The loss of allowable burst number before VDA removal with increasing capacitance is expected to occur and had been observed previously in the ground strap experiments of Hoffmaster et al<sup>1</sup> (see, for example, Figure 9, of Hoffmaster<sup>1</sup>). The most significant feature, however, for this newer configuration is a conduction ability after VDA removal and without surface breakdown.

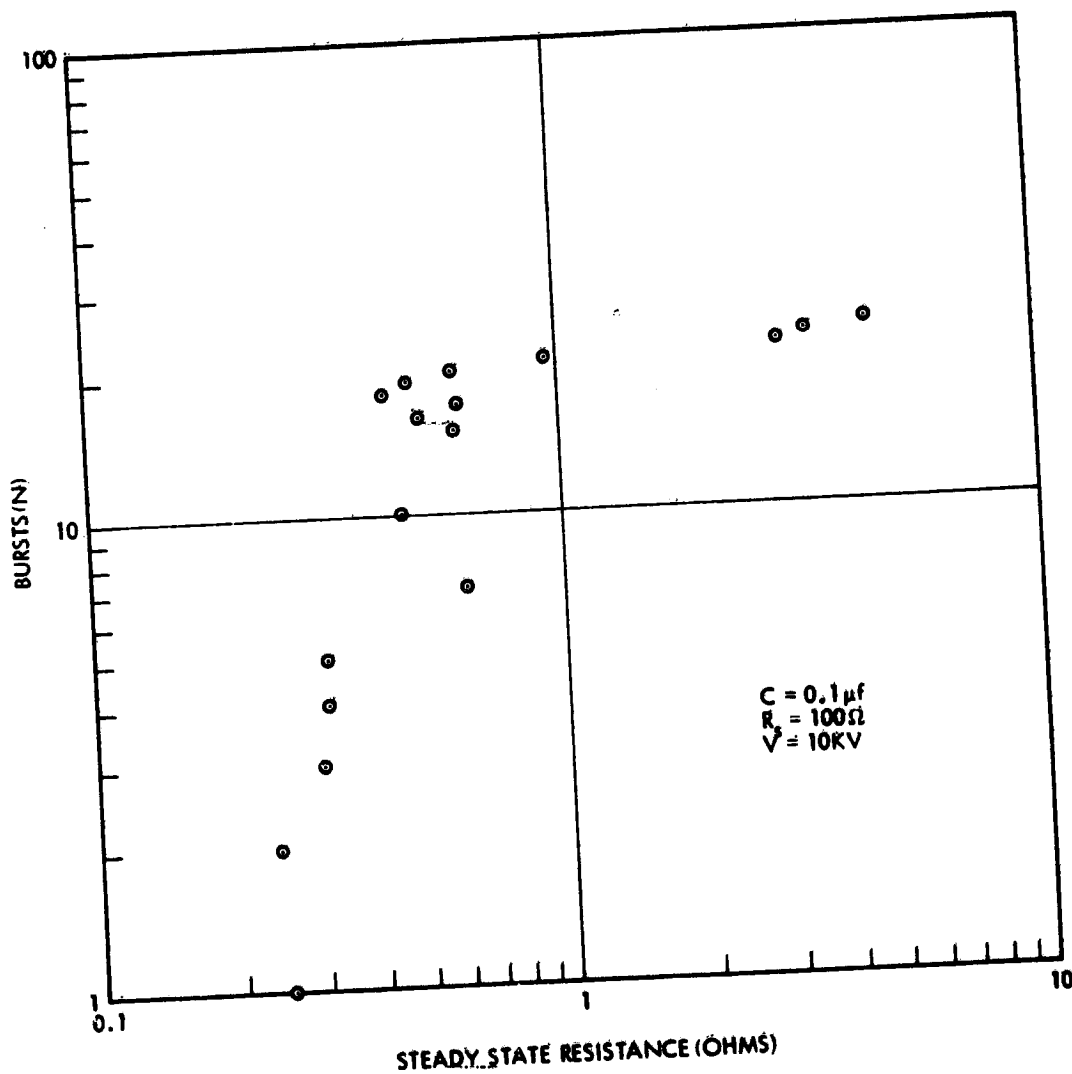


Figure 5. Resistance of VDA/NOMEX/Groundstrap Sample 5 as a Function of the Number of Current Bursts. Initial surge current = 100 A and total charge throughput = 1000  $\mu c$

### 3.3 Dynamic Resistance

The dynamic resistance measurements are obtained by measured current flow in the circuit and the accompanying clamp-to-clamp voltage during the current burst. This dynamic resistance will not be equal to the steady state resistance, in general, and, also of importance, will not remain at the same value during the current burst. To illustrate the differences between steady state and dynamic

resistances, this section will contain measurements of both, although principal emphasis will be on resistance during the current burst.

For these measurements, a fresh sample, (Sample No. 6), was examined for both steady state and dynamic values as a function of burst number and as a function of time during the current burst. Figures 6 - 9 have the results of these measurements. In Figure 6, the conventional, steady state, resistance is given. For a capacitance of 10,000 pF,  $10^4$  volts, and 100  $\Omega$  in series resistance, this sample withstood in excess of 400 bursts before exhibiting a deterioration of the VDA film. Excess of 900 bursts were required to reach high level steady state resistance.

The dynamic resistance was measured at three time periods, 0.33  $\mu$ sec, 0.94  $\mu$ sec, and 2.5  $\mu$ sec after the initiation of the current burst (Figures 7 - 9). Two effects are apparent. The first of these is a diminution of dynamic resistance for later periods in the burst conduction, and is evidence in a change in the surface material properties. The second effect is that dynamic resistance proceeds to values significantly less than the post burst steady state resistance.

The exact nature of the surface change taking place during the burst has not been determined. There is no visible surface arc. There is, nevertheless, some surface (or perhaps NOMEX) alteration which provides an increasingly effective conduction path for current, for increased flow duration, and which acts, after the VDA removal, as an effective, alternate, conduction path.

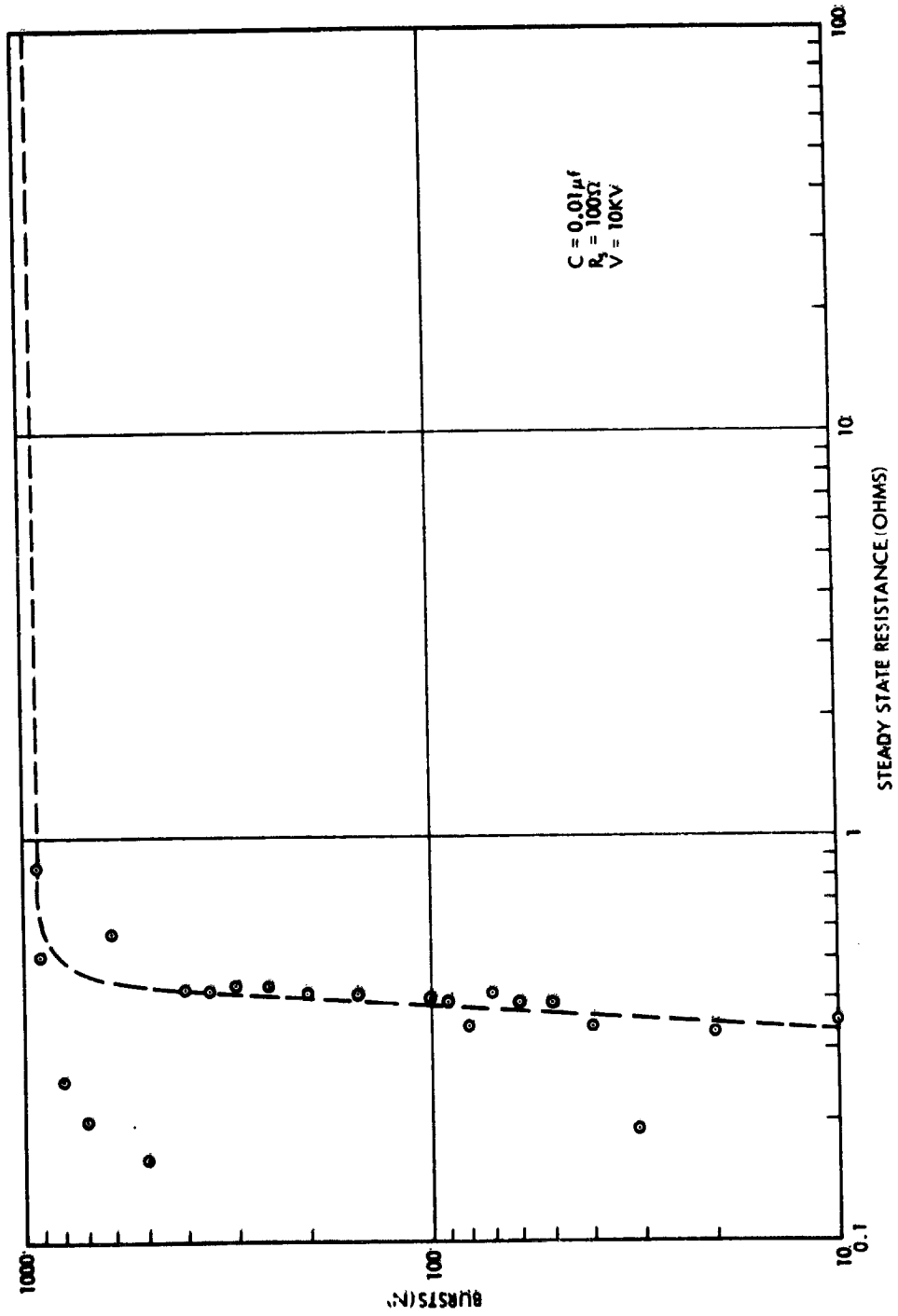


Figure 6. Resistance of VDA/NOMEX/Groundstrap Sample 6 as a Function of the Number of Current Bursts. Initial surge current = 100 A and total charge throughput = 100  $\mu c$

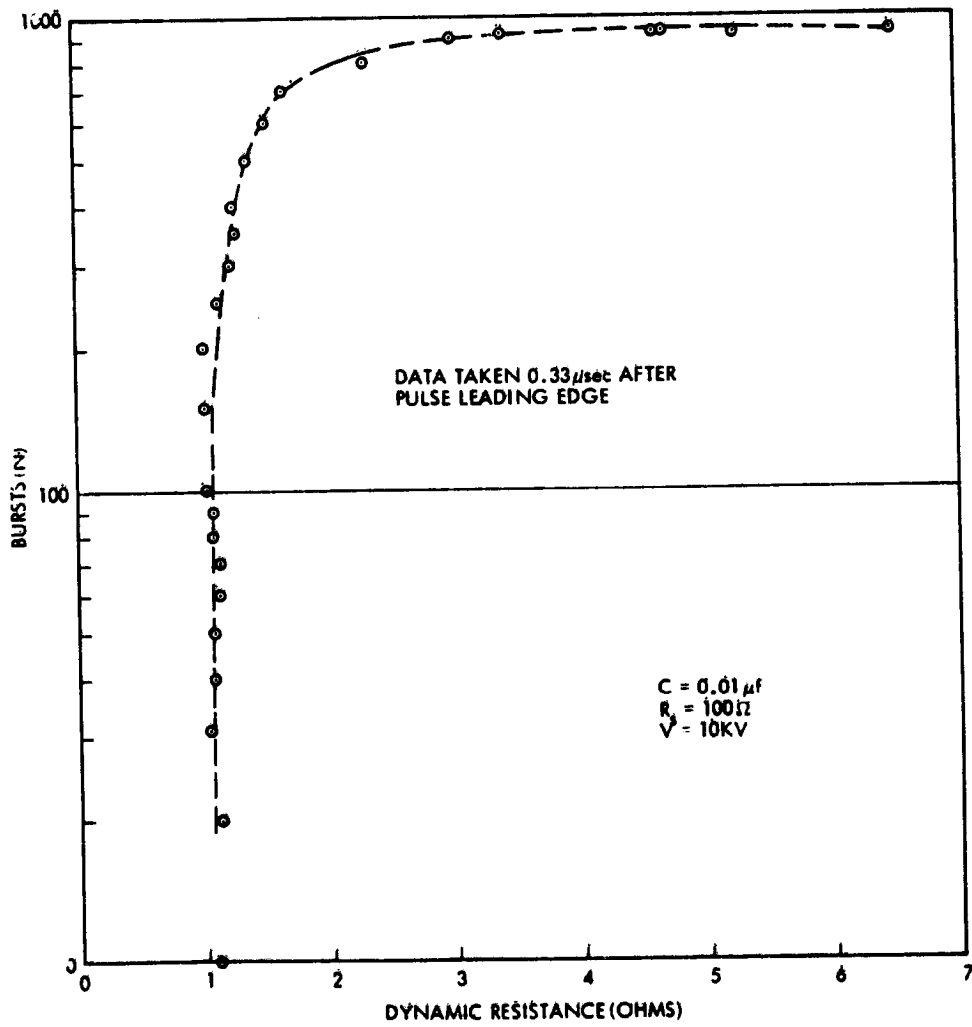


Figure 7. Dynamic Resistance of VDA/NOMEX/Groundstrap Sample 6 as a Function of the Number of Current Bursts at 0.33  $\mu$ sec after Current Surge Initiation

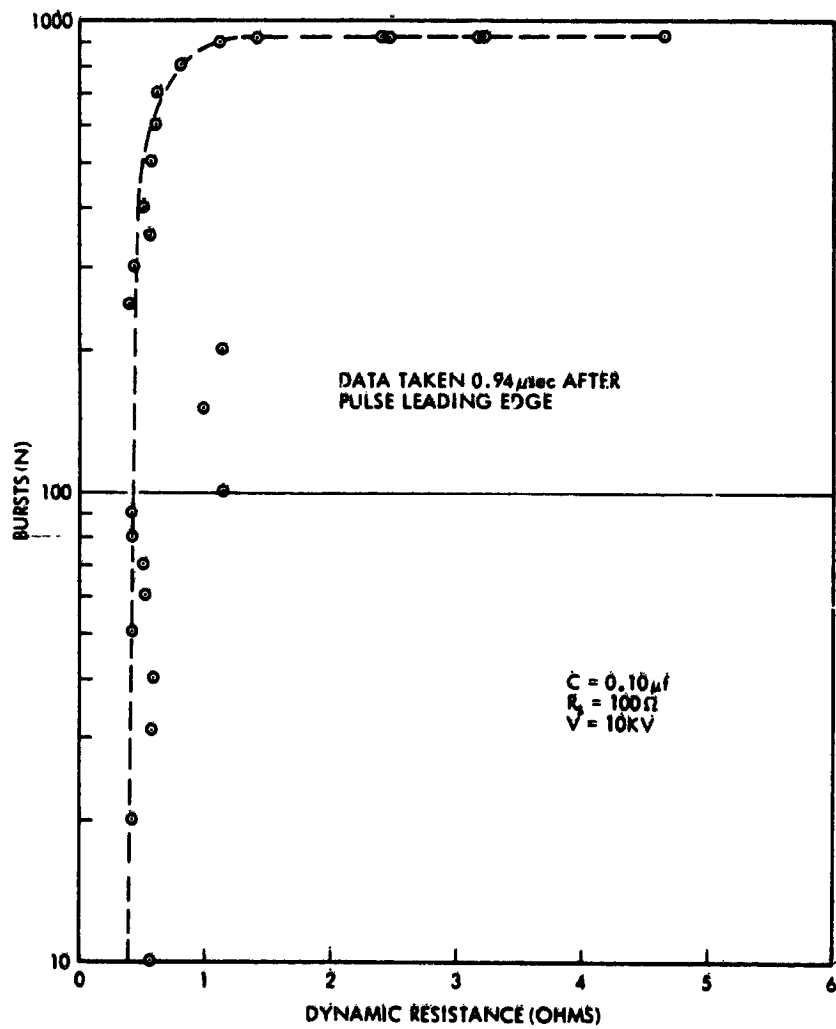


Figure 8. Dynamic Resistance of VDA/NOMEX/Groundstrap Sample 6 as a Function of the Number of Current Bursts at 0.94  $\mu$ sec after Current Surge Initiation

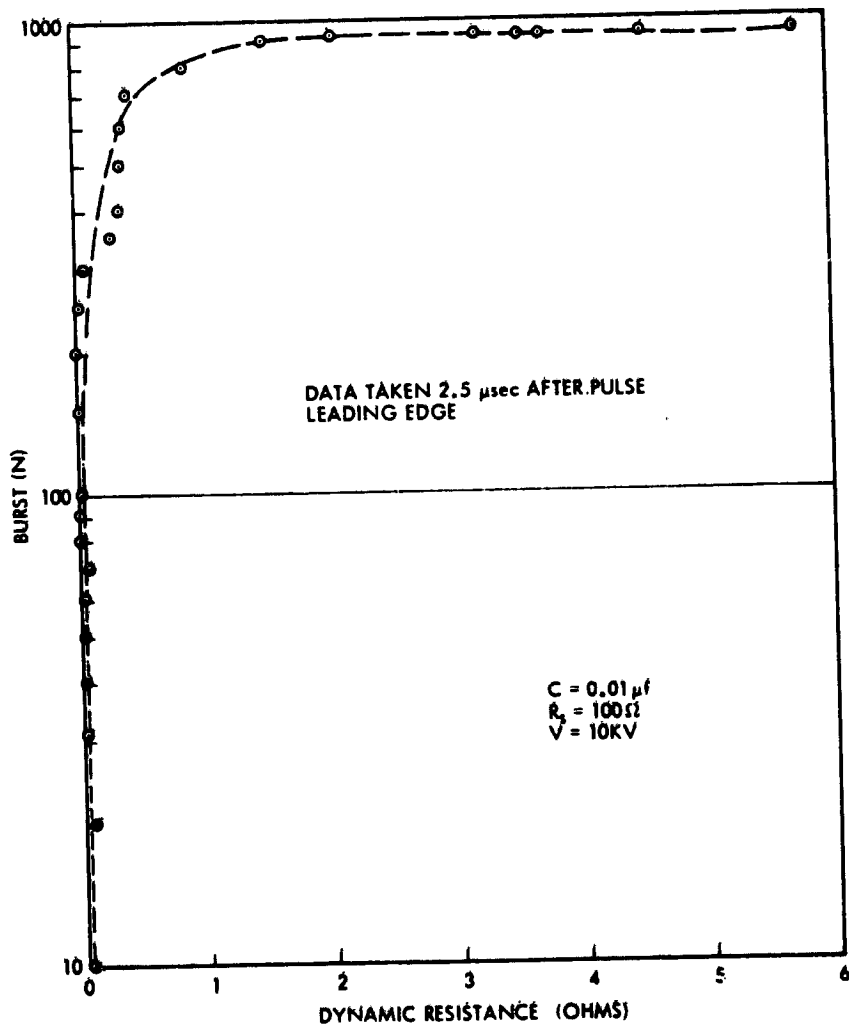


Figure 9. Dynamic Resistance of VDA/NOMEX/Groundstrap Sample 6 as a Function of the Number of Current Bursts at 2.5  $\mu$ sec after Current Surge Initiation

## 4. ELECTRON SWARM TUNNEL TESTS

### 4.1 General Considerations

The results of the current surge tests indicated that the presence of the NOMEX grid on the rear face aids in conduction of these large current bursts. In the process of grid attachment, however, it appeared as a possibility that the NOMEX grid could cause a field intensification for electron conduction through the bulk of the Kapton film which could (possibly) result in dielectric-to-metal arcs from the Kapton interior to the rear face VDA for severe charge-up on the Kapton surface. The Electron Swarm Tunnel (EST) tests were initiated to explore this second, and important, charge conduction process.

The EST used for these tests is the 2 ft × 4 ft facility described earlier in Hoffmaster and Sellen.<sup>1</sup> In this chamber, a monoenergetic electron beam streams along the chamber axis and deposits on the exterior face of the dielectric film, thus simulating the electron deposition process during magnetic substorms in space. In the 2 ft × 4 ft EST, both electron flux and electron energy are variable. Although light sources are present in this facility, there was no deliberate application of light during the electron deposition, and, thus, no deliberate appeal to photoconductive transport of deposited electrons through the foil. In the deposition tests to be discussed here, electron acceleration energy varied from 2 to 6 kV and deposition flux from 10 nA/cm<sup>2</sup> to 20 nA/cm<sup>2</sup>.

### 4.2 Sample Configuration

Figure 10 illustrates the sample configuration used in the EST tests. The measured drainage current is at the rear face VDA film for forward face electron deposition. The added ring on the front surface (with overlying insulating films) acts as a guard ring to prevent surface drainage current entrance into the rear face VDA film. The resulting measurements are, thus, of bulk conduction currents in the Kapton as a result of the deposition of energetic electrons on the front surface of the film.

### 4.3 Electron Drainage Current Measurements

#### 4.3.1 DRAINAGE THROUGH KAPTON AT 0.0005 IN. THICKNESS

Figure 11 illustrates the drainage current density (in nanoamperes per square centimeter) as a function of the acceleration voltage of the deposited electrons and for varying levels of electron flux in the deposition. The order in which the exposures have been made is significant.

The initial deposition condition was a 2 keV electron flow at 10 nA/cm<sup>2</sup>, leading to a rear face drainage current of ~0.05 nA/cm<sup>2</sup>. This drainage current is

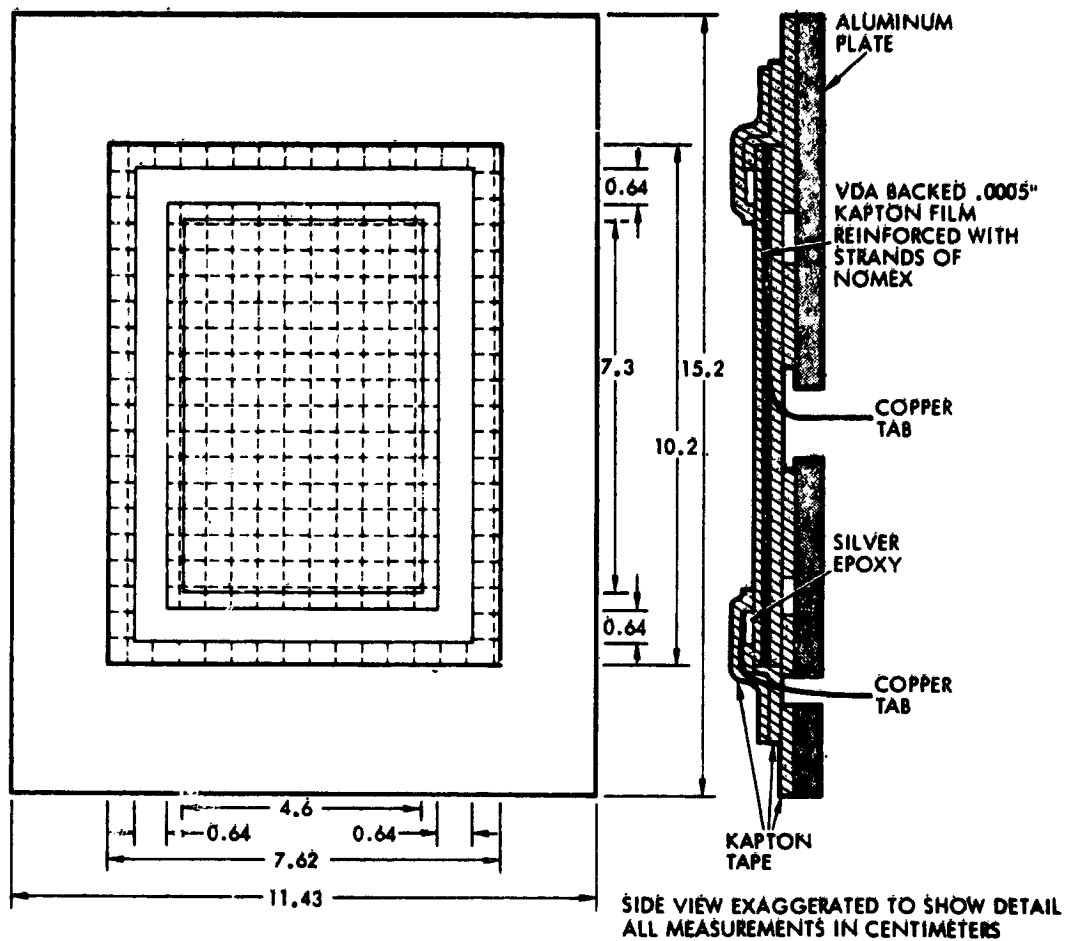


Figure 10. Kapton/VDA/NOMEX Thermal Control Material Sample Configuration for Electron Swarm Tunnel Tests

considerably larger than that observed for 0.002 in. ( $5 \times 10^{-3}$  cm) Kapton foil, measured earlier. Larger drainage is expected, of course, because of the reduced thickness ( $1.27 \times 10^{-3}$  cm) of the foil.

Increases in beam energy to 4 keV caused drainage current density to increase to  $\sim 0.5$  nA/cm<sup>2</sup>. This rapid increase in conduction current density as beam energy increased is typical, and is attributed to field enhanced conductivity in the material. A continued increase in electron acceleration energy to 6 keV, caused an increase in conduction current to 1.5 nA/cm<sup>2</sup>. Since the incident flux at this point was only 10 nA/cm<sup>2</sup>, and since secondary electron emission causes a rerelease, back to space, of significant amounts of electrons, the observed

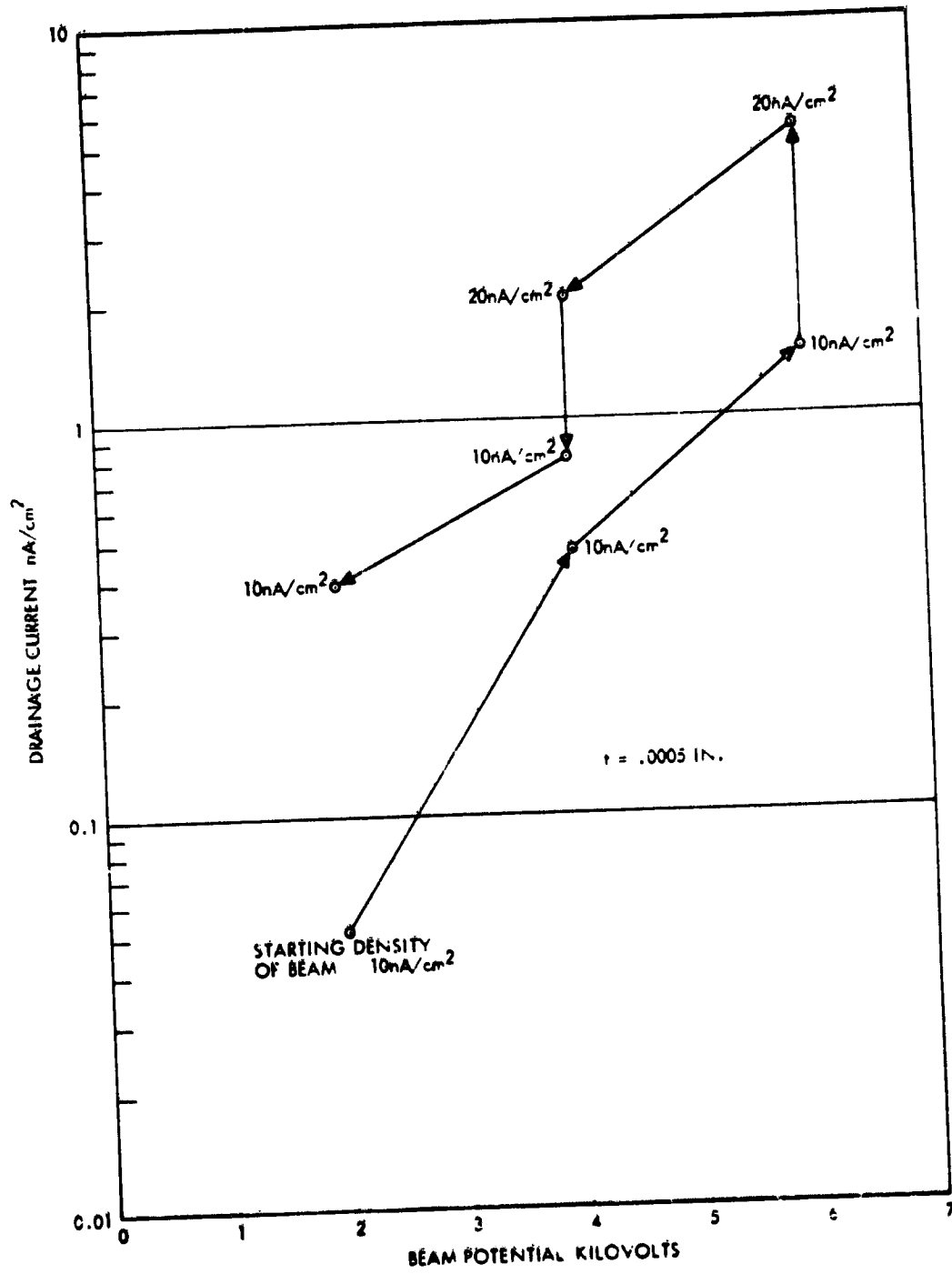


Figure 11. Electron Drainage Current Density as a Function of Electron Beam Acceleration Voltage for Deposition Flux Densities of 10 nA/cm<sup>2</sup> and 20 nA/cm<sup>2</sup> on JRCO Utilizing 0.0005 in. Kapton Base Film

conduction could be limited by incident flux rather than by material resistivity. To test this possibility, the deposition flux was increased from 10 nA/cm<sup>2</sup> to 20 nA/cm<sup>2</sup> and conduction current density increased from 1.5 to 5.4 nA/cm<sup>2</sup> thus confirming notions of conduction limited to incident deposition.

These extraordinary drainage levels (in excess of substorm depositions) usually lead to material alteration. To examine the possibility of permanent alteration, the deposition conditions were then moved to (4 keV, 20 nA/cm<sup>2</sup>) to (4 keV, 10 nA/cm<sup>2</sup>) and, finally, to (2 keV, 10 nA/cm<sup>2</sup>). The evidence clearly demonstrates that a permanent alteration of the material has occurred as a result of the high level drainage at the upper end point of the acceleration voltages applied.

The drainage current measurements also examined the conduction current trace for evidence of material electrical breakdown. Although occasional alterations of drainage current were observed, there were no major interruptions. At the conclusion of the drainage current tests, the sample was removed from the test chamber and subjected to visual and microscopic examination. There was no evidence of electrical breakdown. This is not to conclude that optical properties (absorptivity, emissivity) of the Kapton film have remained unaltered by the high electric stress electron drainage conduction. Measurement of optical properties should be carried out both before and after the electron deposition to determine if film alteration has occurred.

#### 4.3.2 DRAINAGE THROUGH KAPTON AT 0.003 IN. THICKNESS

Section 1 has noted that the ultimate selection of spacecraft surface materials will involve many different features of the materials. Mechanical strength of the base film is amongst those features. At the conclusion of the tests with the 0.0005 in. Kapton film sample described in the sections above, and concurrent with the availability for test of a material similar to the first sample (NOMEX grid and VDA features unchanged) but with 0.003 in. thick Kapton as the base film, it was considered of interest to repeat the current conduction tests. The surge current conduction behavior would not appear likely to be dependent upon the base film thickness, because these surge currents are within the VDA film and the NOMEX fibers. There was no apparent reason, thus, for a repetition of the surge current conduction for the ORCON film utilizing the thicker Kapton as the base film. The bulk conduction of electrons through the film in the EST tests, on the other hand, could be expected to be thickness dependent, and these electron deposition experiments were repeated with the new, thicker film, samples.

The 0.003 in. Kapton film ORCON sample construction was the same as that illustrated in Figure 10, except that the Kapton film, as previously noted, is now 0.003 in. thick, and the lateral dimensions of the sample whose drainage is under examination are 7.1 × 7.1 cm (rather than the 4.6 × 7.3 dimensions used in the 0.0005 in. base film case).

The second ORCON sample was placed in the EST and the beam energy varied from 4 to 10 keV at current densities of 10 nA/cm<sup>2</sup> and 20 nA/cm<sup>2</sup>. Figure 12 illustrates the measured conduction current in this sample with the thicker Kapton film. Several features of the results shown there differ considerably from the drainage current results shown in Figure 11 for the thinner Kapton. The major difference between the two films is that the drainage current density is greatly reduced for the thicker film, compared to the drainage of the 0.0005 in. sample. Under a conventional approach to this electron conduction it might be expected that drainage currents would be reduced by a factor of 6, because the film thickness increases by a factor of 6 (0.0005 in. to 0.0003 in.) and because film resistance in conventional conduction should be proportional to film thickness. It should be noted, however, that the conduction is reduced by ratios much larger than the thickness ratio. At 4 keV, 10 nA/cm<sup>2</sup> conditions the drainage current densities are ~0.5 nA/cm<sup>2</sup> for the thin material and 0.009 nA/cm<sup>2</sup> for the thicker material. At 6 keV, 10 nA/cm<sup>2</sup> conditions, the respective drainage current densities are 1.5 nA/cm<sup>2</sup> and 0.025 nA/cm<sup>2</sup>. The ratio of the drainage current densities at 4 keV is 55 and at 6 keV is 60, which in both instances is very much larger than the thickness ratio of 6.

The marked drop in electron drainage as material thickness  $t$  increases, appears to be the result of field dependent bulk resistivity. It has been previously noted in these drainage experiments that bulk resistivity is clearly nonconstant for electric stress values above some critical upper bound. The field point at which conduction increases rapidly is considered to be near  $10^5$  V/cm. For the thinner film this condition is attained for ~125 volts from one face of the film to the other. For the thicker film,  $\Delta V \sim 10^3$  volts, before the  $10^5$  V/cm point is attained. For  $E > 10^5$  V/cm, the bulk resistivity appears to decline as  $\exp\{-K\sqrt{E}\}$ , possibly as the result of Foble-Frenkel effect. Irrespective of the exact cause of the extra conduction, however, it should be emphasized that the thinner film has a much larger electric stress as a result of e-beam deposition than for the thicker film, and, hence, will conduct substantially larger drainage currents.

A second major difference between the behavior of the two sample thicknesses is in the permanent material alteration observed for the thinner film as a result of the e-beam exposure, while the thicker Kapton sample returns to the same drainage level when the e-beam deposition conditions are returned to earlier voltage and flux levels (the order of exposure for the thicker film was 4 keV, 10 nA/cm<sup>2</sup>; 6 keV, 10 nA/cm<sup>2</sup>; 8 keV, 10 nA/cm<sup>2</sup>; 10 keV, 10 nA/cm<sup>2</sup>; 10 keV/20 nA/cm<sup>2</sup>; 8 keV, 20 nA/cm<sup>2</sup>; 6 keV, 20 nA/cm<sup>2</sup>; and 6 keV, 10 nA/cm<sup>2</sup>). The "closure" experiment at 6 keV, 10 nA/cm<sup>2</sup> revealed no permanent material change for the thicker sample, while the thinner sample exhibited almost one order of magnitude

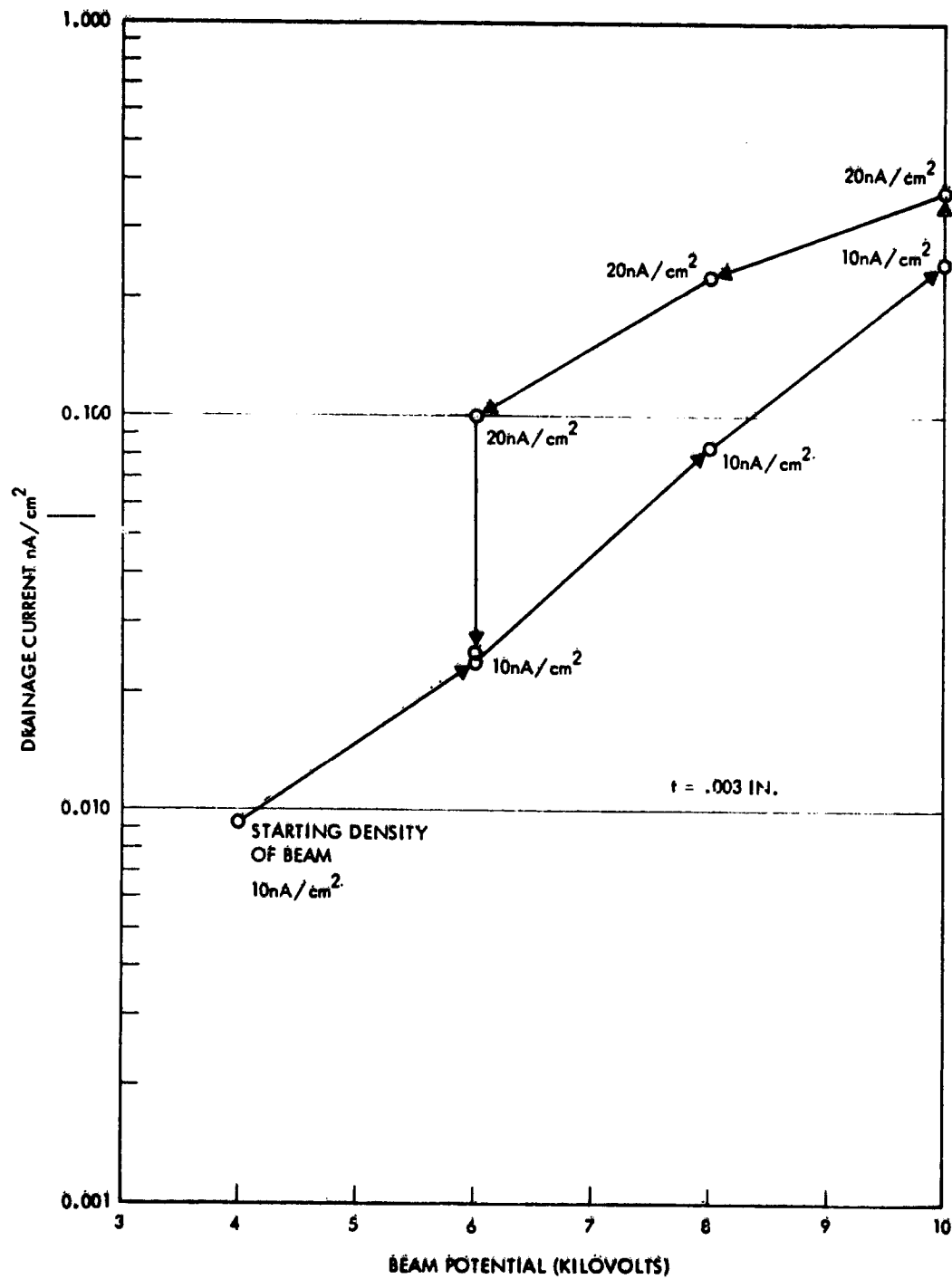


Figure 12. Electron Drainage Current Density as a Function of Electron Beam Acceleration Voltage for Deposition Flux Densities of 10 nA/cm<sup>2</sup> and 20 nA/cm<sup>2</sup> on ORCON Utilizing 0.003 in. Kapton Base Film

change from its two 2 keV, 10 nA/cm<sup>2</sup> exposures, and a factor of approximately 2 at the 4 keV, 10 nA/cm<sup>2</sup> conditions (see Figure 11).

From the results given in Figures 11 and 12 it is apparent that the thinner material has much higher drainage currents than the thicker material, and that permanent alteration has taken place in the thinner material. These results are encouraging from the standpoint of the use of the 0.003 in. Kapton. A remaining question is the possible occurrence of dielectric-to-metal arcs in the thicker material. To monitor the possible occurrence of such breakdowns in the film, the drainage currents were continuously displayed on chart recorders. There was no evidence of material breakdown in the recorded drainage current traces. Following the e-beam tests, the sample was removed from the test chamber and visually examined for pinhole breakthroughs. There was no visible evidence that any such breakthroughs had occurred. Measurements of  $\alpha$  and  $\epsilon$  were not carried out and should be included in future e-beam deposition tests. From the present evidence it would appear that permanent alteration in the material did not occur, either in observed drainage currents or in visible punch-throughs.

## 5. SUMMARY AND RECOMMENDATIONS

The response of the rear face VDA film/NOMEX/ground strap configuration to surge currents has been examined and found to be superior to that of earlier VDA/ground straps. More bursts are allowed before ground strap resistance begins its sharp rise, and, even after the removal of the VDA, conduction occurs (presumably through the NOMEX) without surface breakdowns.

The forward face Kapton layer of the 0.0005 in. ORCON material was exposed to an EST beam ranging from 2 to 6 keV and with fluxes of 10 nA/cm<sup>2</sup> and 20 nA/cm<sup>2</sup>. Drainage currents were large and increased with continued exposure to the electron deposition, indicating a material change. There was no evidence, however, of dielectric to metal arcs. There were no measurements of surface absorptivity or emissivity, so there is no way of determining at present if these quantities altered as a result of the electron deposition. These measurements should be carried out. The forward face Kapton layer of a 0.003 in. ORCON material was also exposed to an EST beam. For this material the beam energy ranged from 4 to 10 keV. The observed drainage currents were greatly reduced compared to the thinner Kapton film. There was no evidence of permanent film alteration in the bulk conduction as a result of the e-beam deposition, and examination of the drainage current traces and visual examination of the sample failed to reveal any evidence of dielectric to metal arcs.

The behavior of this material was generally superior to that of previous film/bonding/ground strap configurations in the surge current tests. In the electron drainage measurements of bulk conduction, the 0.003 in. Kapton sample was considerably superior in performance to that of the 0.0005 in. thickness sample. From the results of these measurements the use of the NOMEX grid backing is indicated as desirable and the thickness of Kapton should be the 0.003 in. case rather than the 0.0005 in. material.

## References

1. Hoffmaster, D. K., Komatsu, G. K., Roy, N. L., and Sellen, J. M., Jr. (1974) Surge Current Conduction in Vacuum Deposited Aluminum Films and Bonded Aluminum Ground Straps, TRW 4351.3.74-34.
2. Hoffmaster, D. K., and Sellen, J. M., Jr. (1974) Electron Swarm Tunnel Measurements of Kapton Bulk Resistivity at High Electric Stress Levels, TRW 4351.3.74-59.



(4) Beam characteristics depend on accelerating voltage — it was found that with simple lens arrangements, changing beam energy also changed other beam parameters.

(5) Complex electrostatic lenses required — progressively more complex lenses were needed to achieve desired beam properties.

(6) Light from filament — in photoconductivity experiments, the light from the filament can alter material behavior. Accordingly, it was decided that an alternate electron source should be devised.

## 2. MULTIPACTOR BREAKDOWN

Past experience with rf voltage-breakdown mechanisms in low-pressure systems indicated that a process was available with the promise of generating an electron beam without the disadvantages of thermionic cathode systems. As indicated in Figure 1, when an rf signal is applied to a pair of parallel plate electrodes and the ambient pressure is reduced monotonically, one finds that the voltage required to produce breakdown decreases until a minimum is reached (at a pressure of  $\approx 50$  microns Hg in the Figure) and then increases again (along the dashed line in the Figure).<sup>1</sup> If the electrode spacing is correct, however, one finds that the breakdown voltage becomes independent of pressure and follows the solid curve at low pressures.<sup>2,3</sup> In this case, a new type of breakdown called "multipactor" occurs.

The mechanism of multipactor discharge is illustrated in Figure 2. If rf frequency and spacing are correct, an initial electron occurring near the lower electrode will be accelerated across the gap, strike the upper electrode, and generate one or more secondary electrons just as the field changes polarity. The secondary electrons, in turn, are accelerated across the gap and generate additional secondaries when they strike the lower electrode. In this way, the number of electrons in the breakdown cascades until various loss mechanisms come into play and limit further growth in the number of electrons participating in the breakdown.

Thus, the multipactor breakdown may be thought of as a sheet of electrons oscillating between a pair of electrodes in synchronism with the applied rf field. It should be noted that there is no requirement for the presence of gas molecules to sustain the breakdown. In fact, if there are air molecules present, they will ultimately be struck by an electron and ionized. These ionized gas molecules are responsible for the slight glow visible in the breakdown. The multipactor proceeds very well, however, even in hard vacuums.

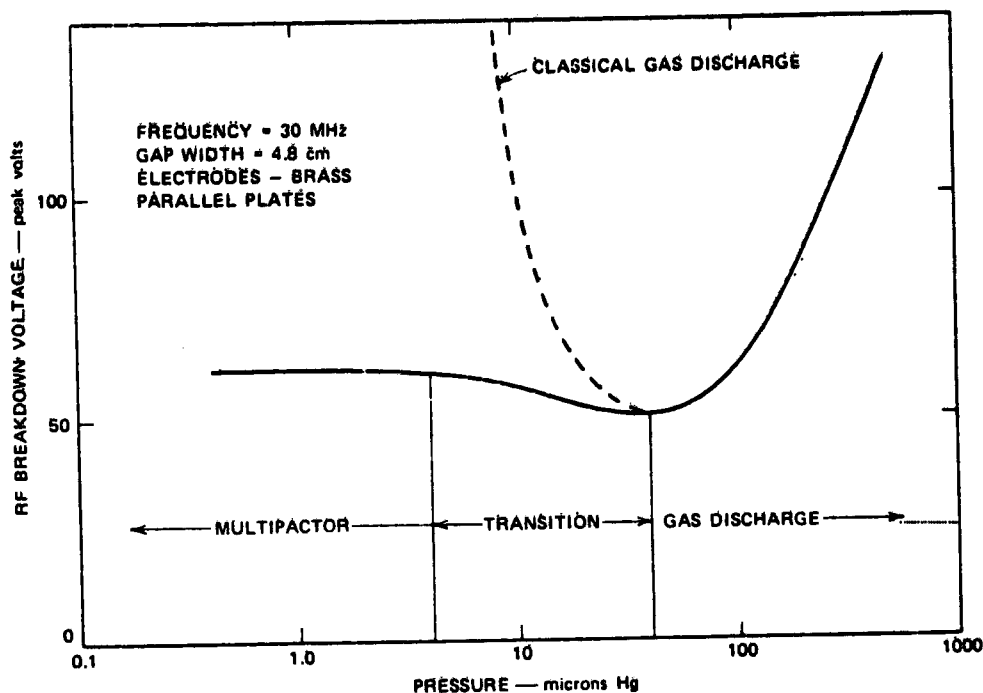


Figure 1. Variation of RF Breakdown Voltage With Pressure

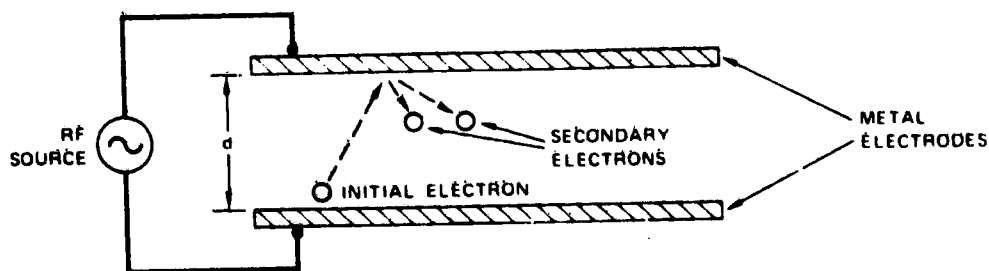


Figure 2. Illustrating Multipactor Discharge

Although the multipactor breakdown is a resonance phenomenon, the resonance is very broad as is evident from Figure 3 which shows the regimes over which multipactor breakdown can occur. For example, frequency can be varied over a 2 to 1 range, and applied voltage can be varied by a factor of 3 without extinguishing the breakdown. The numbers ( $n$ ) indicate the various modes possible ( $n$  corresponds to the number of half cycles required for an electron to cross the gap).

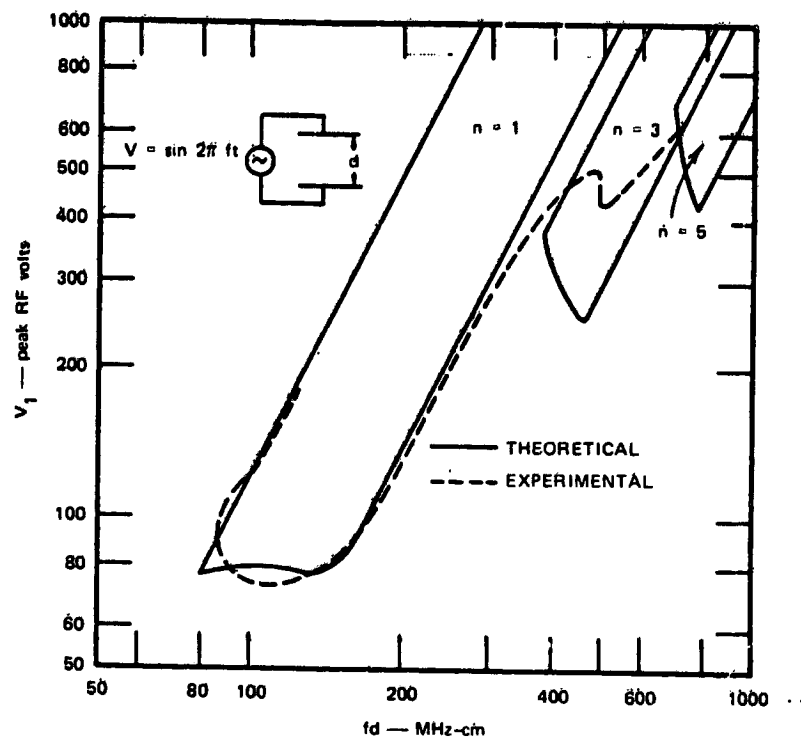


Figure 3. Multipactor Breakdown Voltage as a Function of Frequency and GAP Width for Parallel-Plane Electrodes

### 3. MULTIPACTOR ELECTRON SOURCE

As was indicated earlier, the number of electrons participating in the breakdown increases until loss mechanisms become important. These include diffusion of electrons from between the gaps as the result of Coulomb forces, deviation from synchronism of some of the electrons, etc. Past experience in trying to avoid multipactor indicated that considerable additional loss can be tolerated without extinguishing the discharge. This in turn indicated that it should be possible to deliberately extract a sizable electron current from the discharge.

The first approach at devising a scheme for electron extraction is shown in Figure 4. Holes were simply drilled in one of the electrodes to permit part of the electron sheet to pass through the electrode once per rf cycle. It was found that this scheme worked remarkably well. It was possible to drill a sufficient number of holes in the plate that at a distance of 12 to 18 in. from the multipactor source, there was no pattern evident in the beam when it illuminated a phosphor target.

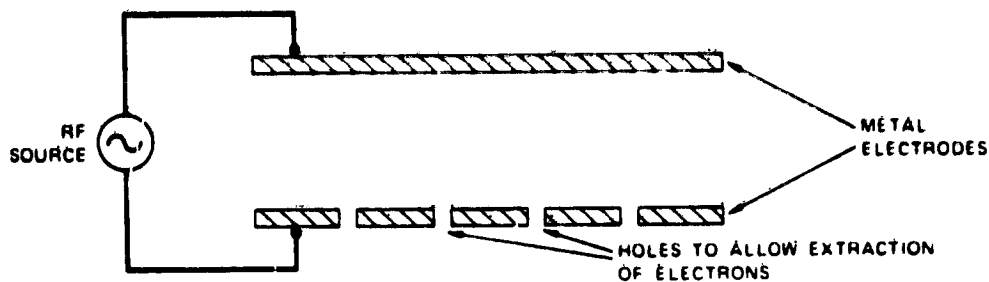


Figure 4. Multipactor Discharge Electrode Modified to Permit Extraction of Electrons

As the result of this initial success, and because an electron source was badly needed for a series of experiments that were getting under way, there was no further experimentation to devise alternate schemes for electron extraction.

The setup presently in use for the study of insulator photoconductivity is shown in Figure 5. A control grid (consisting of a second metal sheet drilled with the same hole pattern as the lower multipactor electrode plate) was added to the source to permit simple control of beam current. For these experiments, the accelerating voltage is applied between the gun and the target. By simply adding a grounded grid above the target, it is possible to obtain the same beam current while maintaining a region of zero field above the target. Radio frequency power requirements to feed the source are modest (under 10 W). Ceramic capacitors are used in series with the coaxial cable from the rf source to provide isolation for the 0-20 kV accelerating voltage used with the system.

The multipactor source currently in use provides a beam 8 in. in diameter at the source, and somewhat larger at the target. In the limited experimentation carried out on the source so far, electron beam current densities of up to  $5 \mu\text{A}/\text{cm}^2$  have been achieved. It is not clear that this represents the highest current achievable with this source. It is also likely that the present source design does not represent the optimum scheme for generating maximum current, however, the presently attainable beam current density is almost 3 orders of magnitude higher than typical substorm currents.

A larger beam can be achieved by using larger diameter plates in making the source. An advantage of this approach over trying to spread the beam via lenses is that, with the present setup, beam size is virtually entirely independent of accelerating voltage.

The characteristics of the multipactor source can be summarized as follows:

- (1) Contamination resistant
- (2) Physically simple

- (3) Produces large diameter beam directly
- (4) Beam characteristics independent of accelerating voltage
- (5) Stability good
- (6) No light output

Its operation, in the year since it was first assembled, has been highly satisfactory, and it is recommended as an electron source for systems that must operate under conditions where normal good vacuum practice regarding long term cleanliness must be ignored.

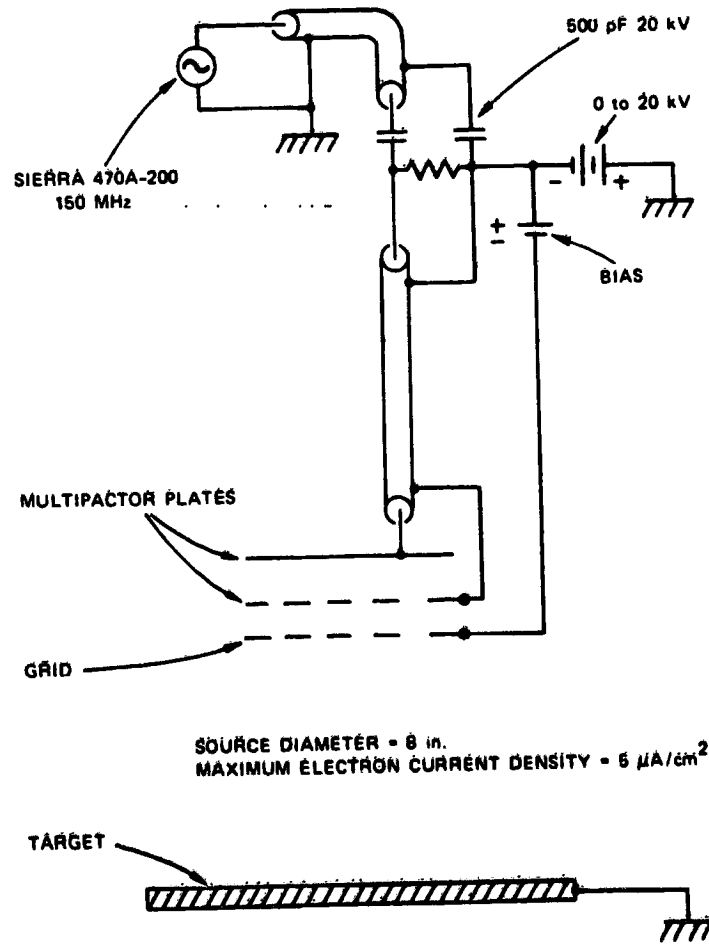


Figure 5. Schematic of Multipactor Electron Source

## References

1. Chown, J. B., Scharfman, W. E., and Morita, T. (1959) Voltage breakdown characteristics of microwave antennas, Proc. IRE 47(No. 8):1331-1337.
2. Chown, J. B., Nanavicz, J. E., and Vance, E. F. (1970) VHF Breakdown on a Nike-Cajun Rocket, JPL Technical Memorandum 33-447.
3. August, G., and Chown, J. B. (1970) Reduction of Gas Breakdown Thresholds in the Ionosphere Due to Multipacting, JPL Technical Memorandum 33-447.

**SESSION IV  
MATERIALS DEVELOPMENT**

**PRECEDING PAGE BLANK NOT FILMED**

**Contents**

1. Introduction	560
2. Background	560
3. Materials Development Program	562
4. Materials Characterization	565
5. Conclusions	566
References	566

**1. Conductive Spacecraft Materials Development Program**

William L. Lehn  
 Air Force Materials Laboratory  
 Wright-Patterson Air Force Base, Ohio

**Abstract**

A jointly planned U. S. Air Force-NASA program has been established to investigate the spacecraft charging phenomenon. The objectives of this program are to provide design criteria, techniques, materials, and test methods to ensure control of absolute and differential charging of spacecraft surfaces. The materials development task of the investigation is the responsibility of and is being directed by the Air Force Materials Laboratory (AFML).

The control of absolute and differential charging of spacecraft cannot be effected without the development of new and improved or modified materials or techniques that will provide electrical continuity over the surface of the spacecraft. The materials' photoemission, secondary emission, thermooptical, physical, and electrical properties in the space vacuum environment both in the presence and absence of electrical stress and ultraviolet, electron, and particulate radiation, are important to the achievement of charge control. The materials must be stable or have predictable response to exposure to the space environment for long periods of time. The materials of interest include conductive polymers, paints, transparent films and coatings as well as fabric coating interweaves. The program initiated by the AFML and related efforts to develop these new or modified materials will be discussed.

## 1. INTRODUCTION

A jointly planned U. S. Air Force-NASA interagency interdependency cooperative research and technology program<sup>1</sup> has been established to investigate the synchronous orbit spacecraft charging phenomena. The objectives of this program are to provide design criteria, techniques, test methods, analytical models, environmental data, and materials to ensure the control of absolute and differential charging of spacecraft surfaces for the reduction/elimination of arcing/discharging. The investigation has been divided into a number of concurrent tasks or topics represented by the program topics of the Air Force/NASA Spacecraft Charging Technology Conference; Geosynchronous Environment, Spacecraft Charge Modeling, Materials Characterization, Materials Development, and Design and Test. Responsibility and direction of these tasks have been assigned to various Air Force and NASA laboratories and centers. The materials development task of the investigation is the responsibility of and is being directed by the AFML.

## 2. BACKGROUND

The exterior surfaces of a synchronous orbit satellite, present a variety of dissimilar material surfaces ranging from polished metals to organic and inorganic dielectrics to the ambient and disturbed, magnetic storm, environment. A satellite immersed in the synchronous environment will come into electrical equilibrium, developing surface charges of the proper sign and magnitude to reduce the net current between satellite and the environment to zero. A satellite with parts in the sun and parts in the shade can be expected to charge differentially due to the photoemission effects. During periods of eclipse or in the case of three-axis stabilized satellites with sun oriented solar arrays, some surfaces of the spacecraft are never exposed to sunlight. Without the photoemission of electrons to discharge the satellite surfaces, extremely high negative potentials can then appear. The capacitance and resistance between the various parts, as well as the dynamic characteristics of the ambient flux and satellite spin rate, will determine the charging/discharging rates. If adjacent parts or areas of a satellite are charged to be multikilovolt differential, then the electrical stress may be great enough to cause breakdown of arcing between the parts. The resultant arcing/discharging may then give rise to electromagnetic interference generated anomalous behavior or even catastrophic failure in the satellite electronics and related subsystems and/or degradation of the thermal control properties of the surfaces. The latter results in a rise in satellite component temperatures. Since the lifetime requirements of geosynchronous satellites are increasing from the present

three to five to seven to ten years, it is necessary to prevent this degradation to ensure satellite lifetime and performance.

Various active and passive techniques have been proposed for the control of the surface potential of a satellite in synchronous orbit in order to reduce or eliminate the charging problems. These range from the use of ion or electron thrusters as on ATS-5 and -6<sup>2,3</sup> and active control of the Jupiter Orbiter probes<sup>4</sup> to the use of electron emitting probes.<sup>5,6</sup> The use of selected materials with high secondary electron emissions have been proposed to help avoid high negative equilibrium potentials.<sup>7</sup> Simple models have been developed for estimating the surface potential of satellites with insulating coatings.<sup>8</sup> However, in all of these cases, strong potential gradients will inevitably exist and the simple models and achievement of an isopotential surface will be achieved only if the entire exterior surface of the satellite is conductive. Therefore, in order to achieve control of the absolute or differential charging of a satellite, the entire exterior surface must be made electrically conductive.

Examination of current and future generation geosynchronous satellites reveals the presence of a relatively small number of exterior materials: transparent dielectric solar cell covers for large surface solar arrays, the backside of the array may be a bare or painted organic, dielectric or metallic material; areas of multilayer thermal insulation, (MLI) blankets, with outer metallized polymeric dielectric layers for the ends, sides, and/or back of much the spacecraft body; flexible, metallized polymeric films or inorganic, fused silica, series emittance coatings or optical solar reflectors (OSR's) for high heat rejection surfaces. Other painted or metallized polymeric dielectric tapes or films are used as shrouds and antenna covers or to wrap booms and other structures. A minimum area of painted or bare metallic surfaces make up the remainder of the exterior thermal control surface. With the exception of the bare metallic surfaces none of these materials are electrically conductive.

In the case of most operational satellites, the control of differential charging below the arc/discharge threshold will prevent the anomalous and catastrophic behavior previously observed, while on scientific technology satellites the absolute control of surface potential is often necessary in order to accurately define the satellite sheath and plasma environment. The effect of spacecraft surface potential on contamination; that is, the attraction of ionized outgassing organic species, is another consideration and is the subject of a later paper, (Air Force Materials Laboratory ML 12) Spacecraft Charging/Contamination Experiment on SCATHA.<sup>9</sup> The SCATHA SC1, Spacecraft Surface Potential Monitor (SSPM) Experiment<sup>10</sup> will evaluate the surface potential of a variety of selected satellite thermal control materials exposed to the synchronous space environment.

The Air Force SCATHA Satellite<sup>11</sup> scheduled for launch in mid 1978 will study the spacecraft charging phenomena and measure the substorm generated

environmental parameters. The engineering experiments on SCATHA will measure the materials response to environmental charging and the effects of charging on materials contamination. The data obtained will be used to substantiate and correlate with laboratory in situ simulation measurements and to guide materials development. However, these data will not be available in a time frame to effect the material selection for a number of operational Air Force satellites or the immediate material development efforts.

The time required for the development, evaluation and flight qualification of a new spacecraft thermal control material acceptable to the spacecraft thermal designers and engineers is estimated to be from three to five or more years. In particular, this is true, for any material expected to perform for seven to ten years or more in the space environment.

### 3. MATERIALS DEVELOPMENT PROGRAM

Based upon the above background it is obvious that the control of absolute and differential charging of spacecraft cannot be effected without the development of new and improved or modified materials or techniques which will provide electrical continuity over the surface of the spacecraft. A coordinated Air Force/NASA program was initiated by the AFML to develop these new or modified materials. The materials of interest include conductive polymers, paints, transparent films and coatings as well as fabric interweaves. The program roadmap is indicated in Figure 1. In order to meet the near term satellite conductive materials requirement the approach has been to develop materials modifications and techniques which can be applied to current state-of-the-art thermal control materials which can be integrated directly into the current and near term generation of satellites without a long three to five years or more period necessary to space qualify new materials. At the same time promising approaches for the development of new and novel materials will be identified for later research and development.

#### 3.1 Conductive Fabric Coatings

The concept of silica fabric type thermal control coatings was developed under AF sponsorship. These materials are extremely space stable, contamination free materials and are candidates for any thermal control applications requiring coatings with low solar absorptance to emittance ratios such as white paints, as the outer layers of multi layer blankets or on the back of solar array panels

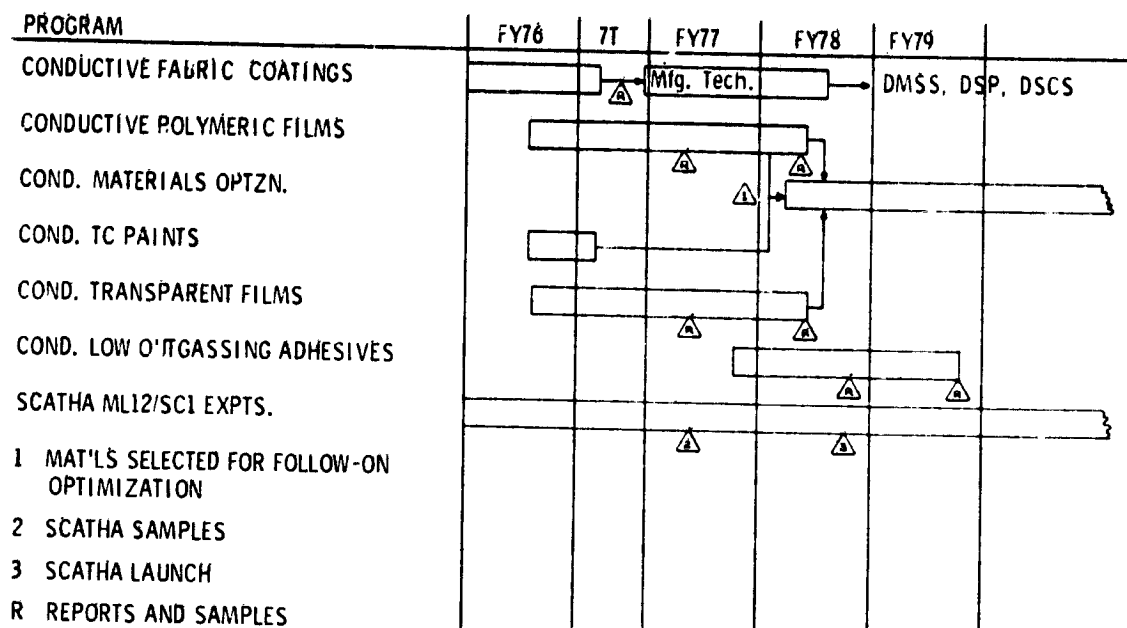


Figure 1. Combined AFSC/NASA Conductive Spacecraft Materials Development Roadmap

A contractual program to develop conductive interweaves of metallic aluminum, stainless steel, or other conductive filaments such as carbon, and space stable, silica fabric type thermal control coatings was initiated. Alternate approaches include the use of sewn in conductive yarns or conductively coated silica yarns. As reported elsewhere in this meeting<sup>12, 13</sup> it has been found since this interweave program was initiated that the basic silica fabric when applied as the outer layer of a thermal blanket does not arc/discharge. The conductive interweaves will ensure a minimum distance from any area of the coating to a stable ground conductor limiting the area or total charge available for discharge. The conductor will have adequate capacity to conduct any discharge to ground without conductor loss by heating or sputtering such as might occur with thin vacuum deposited conductors.

A program to develop the manufacturing technology to prepare an optimized fabric in the proper weight and physically desirable widths for satellite use including cleaning, handling, shipping, and other techniques has just recently been initiated. The materials developed have been proposed for use in a number of current and future satellite thermal control applications.

### 3.2 Conductive Polymeric Films

The development of techniques and modifications which will reduce or prevent the accumulation of a spacecraft charge on the surfaces of FEP Teflon or Kapton used in thermal blankets and tapes and films is being pursued under contract at General Electric. Approaches include materials modifications and conductive metallic or oxide grids and coatings prepared by vacuum deposition or photo resistant techniques as well as the development of stable grounding techniques. Details will be discussed in a later paper.<sup>14</sup>

### 3.3 Conductive Thermal Control Paints

Potential routes for the development of stable white paint type thermal control coatings have been investigated under a contractual program at ITRI and will be reported on in a later paper.<sup>15</sup> Approaches included the investigation of conductive and nonconductive polymeric organic (quaternary ammonium polymers, polyvinyl-carbazole) and inorganic (alkaline silicate) binders applied separately or in conjunction with conductive pigments, fiber or filaments.

The development of conductive, space stable, (five to ten years) white thermal control coating pigments is a very challenging technical problem. The techniques used to impart conductivity such as doping or non-stoichiometry being contrary to the factors necessary to impart long term space stability.

Conductive inorganic based thermal control paints have been developed in-house at NASA in support of the ISEE program.<sup>16</sup> Recent laboratory investigations<sup>12</sup> under simulated synchronous orbit, substorm conditions indicate that the thermal control paints charge but do not arc/discharge. The conductivity of the paints tend to increase with surface potential bleeding the charge imposed by the electron flux to ground. The conductive paints do not charge conducting the charge to ground. Conductive black thermal control coatings are available.

### 3.4 Conductive Transparent Films

Research and development of low cost conductive transparent coatings for application to both organic and inorganic series emittance coatings or optical solar reflectors (OSR's) and solar cell covers is being conducted under a contractual program at General Electric. Approaches include the deposition or formation of transparent and metallic conductive grids and transparent inorganic coatings by vacuum, electrochemical and mechanical techniques. The affect of the coatings or grids on the thermo-optical properties, energy conversion, and long term stability of the state-of-the-art materials will be evaluated. The development and use of conductive glasses for the covers are also being evaluated. Grounding techniques will be developed.

Conductively coated solar cell covers and OSR's are commercially available, but the prices are prohibitive if one envisions a large solar array of many tens of thousands of solar cells.

### 3.5 Materials Optimization

Materials will be selected for further development and optimization based upon the results of the initial programs. Samples of the most promising materials will be evaluated as potential samples for inclusion in the SCATHA and other space flight experiments.

### 3.6 Conductive Low Outgassing Adhesives

A program for the development of conductive, low outgassing/low contamination adhesives will be initiated late in the current fiscal year. The use of conductive adhesives to apply metallized inorganic and organic OSR's has been shown to reduce the contamination released from the adhesive layer as well as the loss of the vapor deposited metallized mirror layers due to arcing and thereby enhances the long term optical performance of these materials. Similar enhancement of long term optical properties due to reduced contamination is expected.

## 4. MATERIALS CHARACTERIZATION

The engineering properties beyond the initial screening evaluations of the materials developed under the above programs will be evaluated in the synchronous space environmental simulation facilities developed by the NASA/Lewis Research Center as a part of the cooperative AF/NASA program. The material's photoemission, secondary emission, thermo-optical, physical and electrical properties in the vacuum environment both in the presence and absence of electrical stress and ultraviolet, electron, and particulate radiation are important to the achievement of charge control. A literature search<sup>17</sup> on the dielectric properties and electron interaction phenomena related to spacecraft charging has been conducted by personnel of the Rome Air Development Center (formerly assigned to Air Force Cambridge Research Laboratory). The continuing role of this research group in the measurement of the classical electrical, thermal, and optical properties, as well as the basic physical structure of the materials developed is not clear.

Studies of the photoconductivity effects of selected spacecraft materials are being pursued by Nanevich and coworkers at Stanford Research Institute under a NASA sponsored program.<sup>18, 19</sup>

## 5. CONCLUSIONS

A coordinated, joint U.S. Air Force-NASA program for the development of conductive spacecraft materials has been initiated. This program is part of a total coordinated, interdependent program to investigate the spacecraft charging phenomena and to provide design criteria, techniques, materials, and test methods to ensure the control of absolute and differential charging of spacecraft surfaces.

## References

1. Lovell, R. R., Stevens, N. J., Schober, W., Pike, C. P., and Lehn, W. L. (1975) Spacecraft Charging Investigation: A Joint Research and Technology Program Spring Annual Meeting, American Geophysical Union, Washington, D. C.
2. Purvis, C. K., Barlett, R. L., and DeForest, S. E. (1976) Active control of spacecraft charging on ATS-5 and ATS-6, paper I-5, in this publication.
3. Goldstein, R. (1976) Active control of potential of the geosynchronous satellite ATS-6, paper I-6, in this publication.
4. Beattie, J. R., and Goldstein, R. (1976) Active spacecraft potential control system selection for the Jupiter orbiter probe mission, paper I-9, in this publication.
5. Gonfaloné, A., Grard, R. J. L., and Pederson, A. (1975) Control of the spacecraft surface potential in magnetospheric plasma using electron emitting probes, Paper SM127F presented at spring annual meeting, American Geophysical Union, Washington, D. C.
6. Grard, R. J. L. (1975) Spacecraft potential control and plasma diagnostic using electron field emission probes, Space Science Instrumentation 1:363-376.
7. Knott, K. (1972) Equilibrium potential of a magnetospheric satellite in an eclipse situation, Planet. Space Sci. 20:1137-1146.
8. Koenemann, B., and Schroeder, H. (1974) Influence of capacitor effects on the surface potential of satellites with partially insulating surfaces in the solar wind, Planet. Space Sci. 22:321-331.
9. Hall, D. F. (1976) Spacecraft charging/contamination experiment on SCATHA, paper IV-9, in this publication.
10. McPherson, D. A., and Schober, W. R. (1975) Spacecraft charging at high altitudes: the SCATHA satellite program, paper presented at AIAA 13th Aerospace Sciences meeting, Pasadena, California.
11. Shane, D. F., and Stevens, J. R. (1976) Space test program spaceflight P78-2 (SCATHA) keynote address in this publication.
12. Stevens, N. J., Berkopce, F. D., Staskus, J., and Blech, R. A. (1976) Testing of typical spacecraft materials in a simulated substorm environment, paper III-2, in this publication.
13. Bélanger, F. J., and Lagles, A. E. (1976) Secondary emission conductivity of high purity silica ( $\text{SiO}_2$ ) fabric, paper IV-6, in this publication.

## References

14. Amore, L., Eagles, A. E., and Okress, E. (1976) Development and testing of spacecraft polymer materials for electrostatic discharge control, paper IV-5, in this publication.
15. Gilligan, J. (1976) Electrically conductive paints for satellites, paper IV-3, in this publication.
16. Shai, C. M. (1976) Development of conductive thermal control paints, paper IV-4, in this publication.
17. Wall, J. A., Burke, E. A., Frederickson, A. R., and Garth, J. C. (1976) Results of a literature search on dielectric properties and electron interaction phenomena related to spacecraft charging, paper IV-2, in this publication.
18. Adamo, R. C., and Nanevich, J. E. (1976) Photoconductivity effect in high-voltage space insulating materials, paper IV-7, in this publication.
19. Adamo, R. C., and Nanevich, J. E. (1976) Oscillations in insulator leakage current under steady state conditions of synchronous orbit plasma and photo-illumination, paper IV-11, in this publication.

Contents --

1. Introduction	569
2. Conductivity	572
3. Estimation of Electric Field Developed During Electron Irradiation of an Insulator	581
4. Secondary Emission	583
5. Backscatter	585
6. Electron Range and Rate of Energy Loss	586
7. Dielectric Breakdown	587
8. Conclusion	587
Bibliography	589

## 2. Results of Literature Search on Dielectric Properties and Electron Interaction Phenomena Related to Spacecraft Charging

J.A. Wall, E.A. Burke, and A.R. Frederickson  
Deputy for Electronic Technology (RADC)  
Solid State Sciences Division  
Hanscom AFB, Massachusetts

### 1. INTRODUCTION

#### 1.1 Background

It has been known for over two decades that electron irradiation of insulators can produce an accumulation of charge sufficient to cause dielectric breakdown. The first published description of this effect appears to be due to Gross<sup>1</sup> who investigated dielectric breakdown produced by 2 MeV electrons in Plexiglass. This and subsequent publications on electron induced breakdown by Gross and others (see bibliography) contained only qualitative or semi-quantitative descriptions of the phenomenon. Also, electrons with energies greater than 1 MeV were generally used to induce breakdown. Consequently, when the possibility that the problem of spacecraft charging could be due to a similar effect was considered, that is, that space-plasma electrons incident on the dielectric materials used on the exterior of satellites could cause charge buildup and subsequent dielectric breakdown,

1. Gross, B. (1958) Irradiation effects in Plexiglass, J. Polymer Sci. 27:135.

a literature search was begun to determine how much information was currently available on the interaction of electrons with energies comparable to those encountered in space. In addition, the search was to cover information that might be useful in obtaining a more quantitative description of electron induced breakdown.

The literature search was originally intended to form the basis of an experimental program with the objective of determining the required material properties and electron interaction parameters needed for modeling charge buildup and breakdown in insulators. However, it was found that a number of publications had appeared in recent years in which electrons with energies in the 1 to 50 keV range had been used to investigate insulator properties such as conductivity and charge storage. As the search continued it was found that much of the data needed appeared to be available in the literature, but it was scattered among reports related to various interests ranging from fundamental properties of insulators to engineering applications such as electrophotography and electrets. Also, results obtained for specific properties and parameters varied widely among different authors. It was therefore decided that the literature search should be continued in depth in order to evaluate and correlate the available data prior to initiating an experimental program.

Only a brief overview of the results of the literature search can be given here. A partial list of the references covered is included in a bibliography at the end of the paper to enable the reader to obtain more complete coverage of particular areas of interest. Although inorganic insulators were also considered in the search, we limit coverage in this paper to the organics, primarily Kapton and Teflon, for the sake of brevity.

## 1.2 Factors Covered in Literature Search

Figure 1 illustrates the electron interactions related to charge buildup in insulators. Energetic electrons incident on the insulator penetrate the surface of the material. Some of the electrons undergo elastic (Coulombic) collisions with the constituent atoms and are "backscattered" out of the material. The remaining electrons interact inelastically with the orbital electrons of the atoms generating electron-hole pairs by ionization as they lose energy and eventually slow to thermal energy near the end of their maximum range in the material. (Interactions such as significant x-ray production, atomic displacements, etc., are neglected here.) Some of the electrons produced by ionization escape from the surface of the material as secondary electrons and these, along with the backscattered electrons, reduce the net excess charge that enters the material from the initial incident electron flux. The remaining electron-hole pairs and the thermalized incident electrons act as current-carriers, producing a region of enhanced (radiation induced) conductivity in that portion of the insulator included in the range of the incident electrons. The

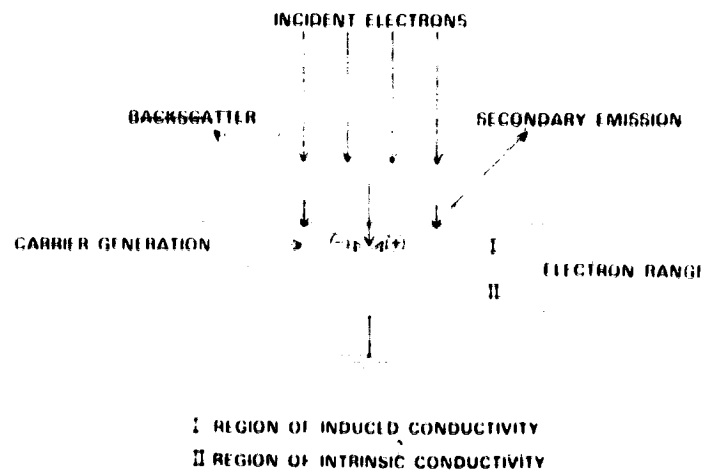


Figure 1. Electron Interactions Related to Charge Buildup in Insulators

time integral of the net electron current penetrating the insulator is the charge accumulated by the insulator. This charge can drift under the influence of its own field, or image forces, toward an electrode attached to the material. If it cannot drift and be removed from the insulator at a sufficient rate, charge buildup can occur producing an electric field strong enough to cause dielectric breakdown. In the configuration shown in Figure 1 for example, the charge would have to drift through the region of intrinsic conductivity to be removed from the insulator. The intrinsic conductivity of most good insulators, such as Kapton and Teflon, is much too low to permit a sufficient rate of drift to prevent charge buildup. In some materials, however, it may be possible to take advantage of the region of radiation induced conductivity by applying an electrode to the surface of electron incidence to remove the excess charge.

From the above brief description of the processes involved in electron-induced charge buildup in insulators it can be seen that the factors that needed to be covered in the literature search were:

- (1) Conductivity (including thermal, high-field, and radiation effects),
- (2) Secondary electron emission,
- (3) Electron range and rate of energy loss.

In addition to these, dielectric breakdown processes were also covered in the search.

## 2. CONDUCTIVITY

### 2.1 Parameters Needed to Characterize Conductivity in Insulators

The energy band model, used to describe conduction processes in crystalline solids such as semiconductors, has generally been adapted to apply to amorphous materials such as organic (and most inorganic) insulators. Consequently, the expression for the conductivity of an insulator is given as

$$\sigma = e(n_+ \mu_+ + n_- \mu_-) \quad (1)$$

where  $\sigma$  is the conductivity,  $e$  the electron charge,  $n_{\pm}$  the concentration of holes (+) or electrons (-) in the conduction band and  $\mu_{\pm}$  the corresponding mobility. (Here we neglect the possibility of current transport by hydrogen nuclei considered by some authors as charge carriers in organic materials.) Because organic insulators contain a high concentration of trapping centers distributed in energy between the valence and conduction bands, the mobilities in Eq. (1) cannot be interpreted as simply as they can, for example, for semiconductors. For the insulators, conduction is usually described as a "trap-hopping" process in which the carriers move from one trapping center to another, remaining for a finite time at each center. Values of mobility are therefore usually given as time-averages, called the trap-modulated mobility. The value of the trap-modulated mobility is a function of the number of available traps, that is, it depends on the number of trapping centers that are occupied. Consequently, it is a function of the number of excess carriers injected into the insulator as well as temperature, electric field, and time.

In addition to the charge carrier mobilities, values of the following parameters are needed to model conductivity in insulators:

- (1)  $n$ : The concentration of potentially available charge carriers, that is, trapped plus mobile charges. This includes intrinsic carriers as well as those injected from external sources.
- (2)  $W_x$ : The activation energy of parameter  $x$  for

$$x = x_0 \exp(-W_x/kT) \quad (2)$$

where  $k$  is Boltzmann's constant,  $T$  the absolute temperature and  $x$  is a parameter such as the concentration of carriers in the conduction band, mobility, or a combination of parameters such as conductivity. It is not

---

Some authors give values of mobility for carrier transport between traps and these can be several orders of magnitude greater than the trap-modulated mobilities. In using these values of mobility Eq. (1) must be modified to include trapping parameters.

always clear from a given paper to which factor the author intended the activation energy to apply, but its value is frequently reported since most of the parameters related to conductivity show the exponential form of Eq. (2) over a range of temperatures.

(3)  $N_t$ : The concentration of trapping centers.

(4)  $E_t$ : The energy, or depth, of trapping centers. This along with  $N_t$  (as a function of  $E_t$ ) gives the trap distribution in an insulator. Frequently, however, a "single trapping level" model is used which assumes that all traps are concentrated at a single level. In this case the value of  $E_t$  reported is actually a weighted average over  $N_t$ .

(5)  $\tau$ : Carrier lifetime between traps. This parameter may also appear in the literature as the time spent by a carrier in traps. It is not always clear which meaning a particular author has given to  $\tau$ . Another form of this parameter is the recombination coefficient, designated by various symbols, that measures the fraction of carriers that remain free per unit time.

(6)  $\eta$ : The number of carrier pairs generated per incident electron (or photon). This parameter is related to radiation induced conductivity. Another quantity frequently used instead is the energy that must be dissipated in the material by an electron or photon to produce a single carrier pair.

Although there are other parameters used in modeling conductivity, some of which are alternates for—or combinations of—the above, those listed are the most frequently encountered in the analysis of conduction processes in insulators. It should be noted that the symbols used in the literature for various parameters are by no means uniform. Those used here are probably the most commonly encountered.

## 2.2 Methods Used to Measure Conductivity Parameters

The method used to measure a particular conductivity parameter can significantly affect the value obtained. This is due, at least partly, to the fact that the technique used to measure the parameter may affect the insulator in a way that cannot be accounted for in the model used to interpret the results of the measurement. When taking the value of a parameter for insulator conductivity from the literature, therefore, it is important to be aware of the method used to measure it in order to evaluate its validity for the application intended.

Figure 2 shows schematically four methods used to determine conductivity parameters for organic insulators. Part (a) of the Figure shows the "classic" method used to measure conductivity. Electrodes are pressed, painted, or evaporated onto two opposite surfaces of the sample. A potential,  $V$ , is applied to the electrodes and the current,  $I$ , through the insulator is measured by meter  $M$ . The

0-17

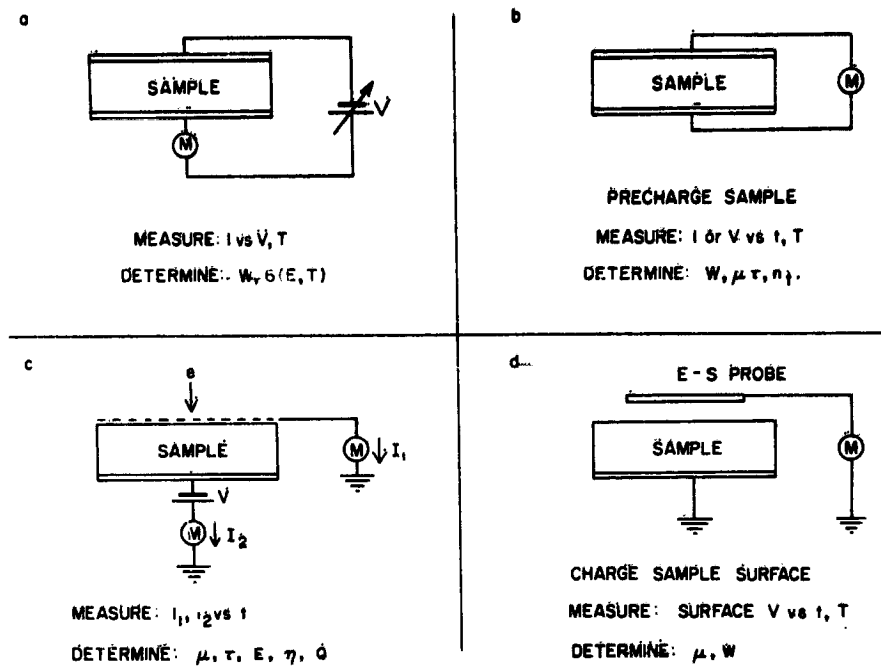


Figure 2. Methods Used for Measuring Conductivity Parameters in Insulating Materials

conductivity can then be calculated from the ratio of  $I$  to  $V$  and the dimensions of the sample. By varying the applied potential and the temperature, the conductivity as a function of electric field ( $E$ ) and temperature ( $T$ ) can be obtained. From this data an activation energy,  $W$ , for conductivity can be derived. The problem with this method is that the electrodes can have a significant affect on the results obtained. Lilly and McDowell<sup>2</sup> used this method to measure the conductivity in Mylar and Teflon. They found that their results did not agree with theories of current injection from the electrodes which must be accounted for in measurements of this type.

The procedure illustrated in part (b) of Figure 2 reduces some of the electrode effects by using the electrodes as charge collectors instead of sources of current carriers during the measurement. The sample is precharged either before or after application of the electrodes by exposure to an electron beam, a corona discharge or application of a potential. The charging source is removed and a meter attached to the electrodes to measure either the potential between the electrodes or the current (charge) released by the insulator as a function of time and temperature. The resultant data can then be used to determine parameters such as activation

2. Lilly, A. C., Jr., and McDowell, J. R. (1968) High-field conduction in films of Mylar and Teflon, J. Appl. Phys. 39:141.

energy, the product of mobility and carrier lifetime, and the number of initially trapped carriers ( $n_t$ ). Perlman and Unger<sup>3</sup> used this method with electron-charged samples to measure trap densities in Teflon.

Part (c) of Figure 2 shows a method that has recently been used fairly extensively because of its versatility and reliability. An electron beam with insufficient energy to fully penetrate the sample is used to supply charge to the insulator. The electrode on the surface of electron incidence is thin enough to be transparent to the electrons. The applied potential,  $V$ , is usually low enough (it may be zero) to minimize carrier injection from the electrodes. Observation of the currents  $I_1$ , which originates from the region of radiation induced conductivity (see Figure 1), and  $I_2$ , which is the net sample current including that in the non-irradiated region, as functions of time, yields values for the mobility, carrier lifetime, the average electric field ( $E$ ) in the insulator, the number of carrier pairs produced per incident electron and the stored charge. Details of this method have been analyzed by Gross, Sessler, and West.<sup>4</sup>

The method illustrated in part (d) of Figure 2 reduces electrode and other extraneous effects to a minimum. The sample has a grounded electrode on one surface only. A charge is deposited on the surface of the sample and the surface potential measured as a function of time with a non-contacting electrostatic probe (E-S). The surface potential decreases in time as the charge drifts through the insulator under the influence of its own field and image forces due to the presence of the grounded electrode. The resultant data can be used to calculate the intrinsic mobility of the charge carriers deposited on the sample. The activation energy for the mobility can be obtained by repeating the measurement at different temperatures. This procedure was introduced by Davies<sup>5</sup> to investigate static charge decay in polyethylene and glass. It was further developed by Batra et al<sup>6</sup> for the analysis of materials used in electro-photography. It has recently been applied to other insulating materials because it is perhaps the best method currently available that can give an unambiguous measure of carrier mobility in very low-conductivity materials.

### 2.3 Carrier Mobilities in Teflon

Although many of the parameters used in modeling conductivity have been measured for a variety of insulators it is not possible to consider all of them here.

3. Perlman, M. M., and Unger, S. (1972) TSC study of traps in electron-irradiated Teflon and Polyethylene, J. Phys. D 5:2115.
4. Gross, B., Sessler, G. M., and West, J. E. (1974) Charge dynamics for electron irradiated polymer-foil electrets, J. Appl. Phys. 45:2841.
5. Davies, D.K. (1967) 1967 Static Electrification Conference Institute of Physics and the Physical Society, London, p. 29.
6. Batra, L. P., Keiji Kanazawa, K., and Seki, H. (1970) Discharge characteristics of photoconducting insulators: J. Appl. Phys. 41:3416.

even for one material. This is because of the diversity of values of some of the parameters reported for a given material as well as the fact that all authors do not present the values they obtain in the same way. For example, carrier lifetime, as indicated in Section 2.1, can be reported with different (but equivalent) physical meanings and its value may be reported as a single value or as the coefficient of an exponential function associated with an activation energy. The purpose of this section is to illustrate this diversity of values and show that one should not simply accept a value for a given parameter from the literature without first evaluating its source. To do this, we have chosen the values of mobility for charge carriers found in the literature for Teflon as an example. Table 1 shows some of the mobility values found.

Table 1. Values of Carrier Mobility in Teflon

Mobility ( $\text{cm}^2/\text{V}\cdot\text{sec}$ )	Comments
$2 \times 10^{-12}$	Hole from 0.7 eV trap
$7.6 \times 10^{-14}$	Hole from 1 eV trap
$7.4 \times 10^{-22}$	Electron from 1.8 eV trap
$1.3 \times 10^{-9}$	Electron Charged sample
$\leq 4 \times 10^{-10}$ $\sim 5 \times 10^{-17}$	Electron induced conductivity Room temperature, non-irradiated
$5 \times 10^{-4}$ $5 \times 10^{-5}$	Hole, pulsed electrons Electron, pulsed electrons

The first three mobility values are from a recent paper by Sessler and West.<sup>7</sup> They used the open-circuit method shown in part (d) of Figure 2, precharging the sample by application of a voltage to the open surface of the sample before starting the measurement. The temperature was raised from about 20 to 200°C during the surface potential measurements. This gave mobility as a function of temperature from which the activation energies (shown in Table 1 as trap levels in eV) of mobility were derived. The values of mobility shown in Table 1 were derived from a plot of mobility vs temperature given in the paper and were extrapolated to room temperature (300°K) for comparison with the other values shown. It is clear from these results that holes are the predominant charge carrier in Teflon.

7. Sessler, G.M., and West, J.E. (1976) Trap-modulated mobility of electrons and holes in Teflon FEP, J. Appl. Phys. 47:3480.

The fourth value of mobility shown is from a paper published a few months earlier by Gross, Sessler, and West.<sup>8</sup> The sample was electron irradiated as in method (c) of Figure 2, raising the temperature from room temperature to 750°C. It is not clear from the paper at what temperature the value of mobility reported applies. The authors attribute the higher value of mobility (they reference unpublished work of Sessler and West, which is probably our Reference 7 that had not yet been published) to a greater concentration of electrons obtained by irradiation instead of voltage-charging the sample. Although the sign of the carriers was not determined, they were assumed to be holes injected by image forces from the electrode adjacent to the non-irradiated region of the Teflon, and assume the higher value of mobility was obtained because more traps were filled in the sample.

The next two values of mobility in Table 1 were also determined by Gross, Sessler, and West<sup>4</sup> using method (c) of Figure 2, but without changing the sample temperature. Approximate values for some parameters were used to calculate the mobility from the data, thus the "less than or equals" sign before the value given. The estimated mobility in the non-irradiated region of the sample was derived from charge-decay estimates and the authors state that the value obtained is probably too low.

The last two values of mobility in Table 1 were obtained by Hayashi et al.<sup>9</sup> using pulsed electrons in a modified version of method (c) of Figure 2. In the model used to interpret their data, they assumed that both electrons and holes could act as charge carriers. This may account for the much higher values of mobility they report.

From the example given, it can be seen that in selecting a parameter for modeling conductivity in an insulator, one must be very careful to evaluate not only the method used to obtain it but also the authors' interpretation of the data. Lacking a better basis on which to judge the parameter values available, it is probably best to select a value that has been measured by a method most closely resembling the application one has in mind for the data.

#### 2.4 Temperature Dependence of Conductivity

The temperature dependence of conductivity for most insulators usually follows the exponential form

$$\sigma = A \exp(-W/kT) \quad (3)$$

8. Gross, B., Sessler, G. M., and West, J. E. (1976) TSC studies of carrier trapping in electron- and  $\gamma$ -irradiated Teflon, J. Appl. Phys. 47:968.
9. Hayashi, K., Yashino, K., and Inuishi, Y. (1973) Mobility measurements in polymers using pulsed electron beams. 1973 Conference on Electrical Insulation and Dielectric Phenomena (National Academy of Sciences, 1974), pp 424-430.

near and above room temperature. Here, A and W are empirical constants. As in Eq. (2) of Section 2.1, W is the activation energy of conductivity. Starting at lower temperatures (for example, near 80°K) different values of W are found as the temperature is raised, corresponding to the emptying of different trap levels. (Actually this occurs above room temperature also, but is not usually observed except in very carefully controlled experiments.)

The temperature dependence of conductivity is usually measured by the method shown in part (a) of Figure 2. As mentioned in the discussion of that method (Section 2.2) the electrodes applied to the sample can influence the results obtained. The material used for the electrodes, the nature of the contact (ohmic, blocking, etc.) made with the insulator, and effects such as Schottky emission (essentially the thermionic emission of carriers from the electrodes into the insulator) must be considered in the measurement. Because of difficulties in evaluating the electrode effects, theoretical values of A and W are not usually in good agreement with experiment.

The values obtained for A and W also depend on the sample thickness and the potential used in the measurements because the conductivity of most insulators is a function of the electric field applied. For example, with an applied field of approximately  $5 \times 10^4$  V/cm, Amborski<sup>10</sup> found the activation energy for Kapton to be about 1 eV. Hanscomb and Calderwood<sup>11</sup> measured the current passed by samples of Kapton as a function of both applied field and temperature. They extrapolated their data to zero applied field and found the activation energy to be 1.55 eV. (No comparison can be made between the values of A for these two papers because of insufficient data.)

## 2.5 Electric Field Dependence of Conductivity

The conductivity of insulators as a function of applied electric field has been measured by a number of authors, many of whom developed theories to explain their data. Adamec and Calderwood<sup>12</sup> developed the following relationship for the relative conductivity of insulators as a function of applied field:

$$\sigma/\sigma_0 = \frac{2 + \cosh(\beta F^2/2kT)}{3} \quad (4)$$

where

10. Amborski, L. E. (1963) H-film—a new high temperature dielectric, Ind. and Eng. Chem. -Prod. R and D 2:189.
11. Hanscomb, J. R., and Calderwood, J. H. (1973) Thermally assisted tunnelling in polyimide film under steady-state and transient conditions, J. Phys. D 6:1093.
12. Adamec, V., and Calderwood, J. H. (1975) Electrical conduction in dielectrics at high fields, J. Phys. D 8:551.

$$\beta = (e^3 / \pi \kappa \epsilon_0)^{1/2} = 1.216 \times 10^{-23} \kappa^{-1/2}$$

$\kappa$  = dielectric constant of the insulator,  
 $e$  = electron charge,  
 $\epsilon_0$  = permittivity of vacuum,  
 $F$  = applied field in V/m,  
 $\sigma_0$  = insulator conductivity at zero applied field.

They compared this expression with theories developed by six other authors to show that it gave the best fit to data for Kapton, Mylar, Polyethylene, and other insulators.

Figure 3 is a plot of the relative conductivity of Kapton vs applied field calculated from Eq. (4) compared with measurements from Reference 12. As can be seen from the plot, agreement between theory and experiment is very good. Similarly good agreement was obtained for the other insulators for which comparisons were made.

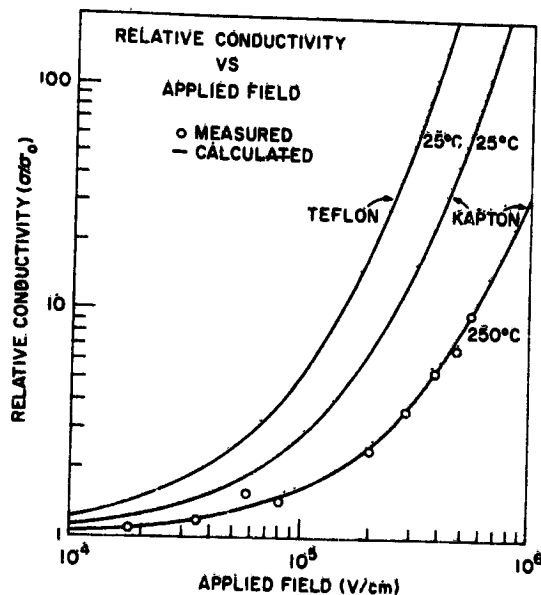


Figure 3. Dependence of the Conductivity of Kapton and Teflon on Electric Field. Kapton data taken from Reference 12. Solid curves calculated from Eq. (4)

Because of the low conductivity of Kapton at room temperature, the data shown in Figure 3 was taken at 250°C. For comparison, we used Eq. (4) to calculate the field dependence of conductivity for Kapton at 25°C. The results are also plotted in Figure 3 along with the results of a similar calculation for Teflon.

## 2.6 Radiation Induced Conductivity

The generally accepted expression for the increase in conductivity induced in an insulator by energetic radiation is

$$\sigma - \sigma_0 = K D^\Delta \quad (5)$$

where

- $\sigma_0$  = the intrinsic conductivity,
- $\sigma$  = conductivity during irradiation,
- $D$  = dose rate,
- $K, \Delta$  = constants.

Although in principle the constants  $K$  and  $\Delta$  can be predicted theoretically, empirical values are invariably used. Theory predicts that  $K$  and  $\Delta$  should be independent of the type and energy of the radiation (that is, electrons, gamma- or x-rays), but the empirical values reported differ among various authors by too great a range to confirm this. The reasons for the differences are not clear, but as with other measurements on insulators, particularly polymers, it could involve electrode effects, thermal effects, etc., as well as changes in material properties caused by radiation damage during the measurements. However, the constant  $K$  is the more significant of the two because  $\Delta$  is the most frequently found to be within 10 percent of unity. Errors in  $\Delta$  therefore have relatively little effect on the magnitude of the induced conductivity calculated from Eq. (5).

To illustrate the differences that can occur in the value of  $K$ , Table 2 shows the range of  $K$  found in the literature for some of the polymers.

Table 2. Range of Values of  $K$  in Units of  $\text{sec}/\Omega\text{-cm-rad}$ .

Material	$K_{\text{max}}$	$K_{\text{min}}$
Kapton	$6 \times 10^{-18}$	$1.2 \times 10^{-19}$
Teflon	$1 \times 10^{-16}$	$2 \times 10^{-18}$
Mylar	$2.1 \times 10^{-19}$	$1.8 \times 10^{-19}$
Polyethylene	$4.5 \times 10^{-18}$	$3 \times 10^{-19}$
Polystyrene	$1 \times 10^{-16}$	$2 \times 10^{-18}$

As with other parameters associated with insulators, it is probably best to select a value of  $K$  from the literature that was determined under conditions most

closely related to the application intended for the data. For upper and lower limit calculations, the appropriate maximum or minimum value should be used.

### 3. ESTIMATION OF ELECTRIC FIELD DEVELOPED DURING ELECTRON IRRADIATION OF AN INSULATOR

Analysis of charge transport in electron-irradiated polymers in some recent papers has suggested the following application of radiation induced conductivity data. While measuring electron induced conductivity in polyethylene terephthalate, Beckley et al.<sup>13</sup> experienced difficulties with frequent electrical breakdowns of their samples. They used an analysis based on work by Nunes de Oliveira and Gross<sup>14</sup> to show that the breakdowns could be caused by fields built up by differential charging of the insulator during irradiation. Beckley and his coworkers based their calculations on a somewhat more obscure form of the original relationships developed by Nunes de Oliveira and Gross. We use the expressions from the paper by the latter authors to illustrate the procedure for Kapton and Teflon.

Referring to Figure 1, assume that a grounded electrode is located on the surface of electron incidence of the insulator as well as on the opposite surface. After correcting for secondary emission and backscatter, take the net current entering the insulator to be  $I_0$ . Assuming no current flows in the non-irradiated region of the insulator (region II of Figure 1), at equilibrium the field in the irradiated region (region I of Figure 1) will be

$$F_1 = I_0 / \sigma_i \quad (6)$$

where  $\sigma_i$  is the radiation induced conductivity, since the current entering the region must equal the current leaving (by Kirchoff's law). (Note that we have ignored the direction of the current flow, and therefore the field, which would have no relation to the occurrence of breakdown.) The dose rate in rad/sec in region I is

$$\dot{D} = (dE/dx) \times 10^{11} I_0 \quad (7)$$

where  $dE/dx$  is the rate of energy loss of the electrons in MeV-cm<sup>2</sup>/g and  $I_0$  is in amperes. Combining Eq. (5) for the radiation induced conductivity (neglecting  $\sigma_0$  and taking  $\Delta = 1$ ) with Eqs. (6) and (7) gives

$$F_1 = 1 / (dE/dx) \times 10^{11} K \quad (8)$$

13. Beckley, L. M., Lewis, T. J., and Taylor, D. M. (1976) Electron-beam-induced conduction in polyethylene terephthalate films, J. Phys. D 9:1355.
14. Nunes de Oliveira, L., and Gross, B. (1975) Space-charge-limited currents in electron irradiated dielectrics, J. Appl. Phys. 46:3132.

Since the potential across the sample is zero

$$F_1 R = F_2 (D - R) \quad (9)$$

where  $R$  is the electron range and  $D$  the sample thickness. The field in the non-irradiated region,  $F_2$ , is therefore

$$F_2 = F_1 R / (D - R) . \quad (10)$$

Figure 4 shows plots of  $F_1$  and  $F_2$  vs electron energy for a range of thicknesses of Kapton and Teflon. The values of  $K$  used to calculate the plots were taken from Weingart.<sup>15</sup> These  $K$  values are relatively low so that an upper limit estimate of the field is obtained (for Kapton,  $K = 1.2 \times 10^{-19}$  sec/ $\Omega$ -cm-rad and for Teflon  $K = 3.1 \times 10^{-18}$  sec/ $\Omega$ -cm-rad). As can be seen from the plots, breakdown is most likely to occur at the surface of electron incidence. The field in Kapton approaches the breakdown range of the order of  $10^6$  V/cm much more rapidly than the field in Teflon. However, Teflon has a lower dielectric strength than Kapton and Gross et al.<sup>16</sup> have shown that breakdown may occur in electron irradiated Teflon at least a factor of 2 below the published dielectric strength. If there is a significant current flow in the non-irradiated region of the insulator due, for example, to field enhanced conductivity which has been neglected here, the fields calculated from Eqs. (8) and (10) would be reduced by the factor  $(1 - I/I_0)$ , where  $I$  is the current in the non-irradiated region.

These calculations should be understood to give only rough estimates of the fields built up in insulators during electron irradiation since several factors that could affect the results have been neglected. For example, charge drift during the transient period before equilibrium is reached has been ignored, as well as possible radiation effects, image forces at the electrodes, the previously mentioned field enhanced conduction, etc. However, the procedure is a simple way of evaluating materials regarding their relative tendency to break down during electron irradiation and shows that making both surfaces of an insulator conducting will not necessarily prevent breakdown.

15. Weingart, R. C., Barlett, R. H., Lee, R. S., and Hofer, W. (1972) X-ray induced photoconductivity in dielectric films, IEEE Trans. Nuc. Sci. NS-19(No. 6):15.
16. Gross, B., Sessler, G. M., and West, J. E. (1973) Conduction and breakdown in polymer foils charged by electron irradiation. 1973 Conference on Electrical Insulation and Dielectric Phenomena (National Academy of Sciences, 1974), p. 485.

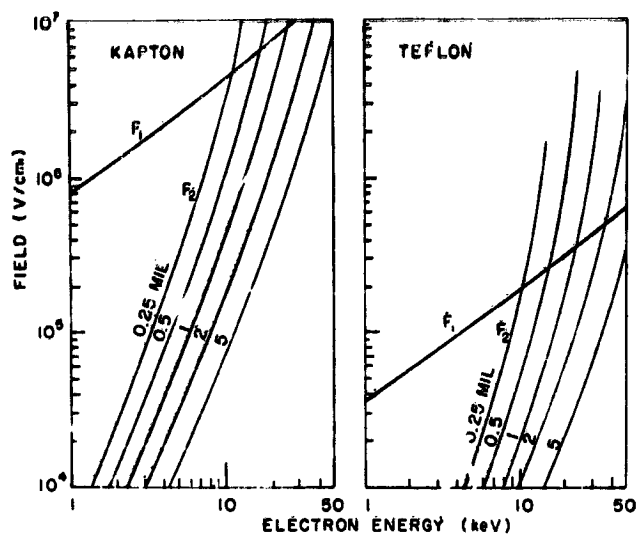


Figure 4. Estimated Equilibrium Electric Fields in Kapton and Teflon Resulting From Electron Irradiation. Grounded conductive coatings on both surfaces of sheets of the materials with thicknesses indicated.  $F_1$  is the field in the region between the surface of electron incidence and the electron range.  $F_2$  is the field in the non-irradiated region which is assumed to be non-conducting. The curves for  $F_2$  in Teflon terminate near the energy at which the electron range exceeds the insulator thickness

#### 4. SECONDARY EMISSION

Because of its practical applications, secondary emission has long been a subject of investigation. As a result, a considerable volume of data exists covering many materials including organic and inorganic insulators. Although not all incident electron energies of interest have been covered for all materials, sound theoretical and semi-empirical relationships have been developed that can be used to extend the available data. An example of such a relationship is the "universal secondary emission curve". It is given by

$$\frac{\delta}{\delta_m} = \frac{g_n(x_m E/E_m)}{g_n(x_m)} \quad (11)$$

where

$$g_n(x) = [1 - \exp(-x^n)] / x^{n-1}$$

$\delta$  = secondary emission coefficient,

$\delta_m$  = maximum value of  $\delta$ ,

$E$  = incident electron energy,

$E_m$  = value of  $E$  at which  $\delta_m$  occurs,

$x_m$  = value of  $x$  for which  $g_n$  has a maximum.

For a given material,  $x_m$  and  $n$  must be determined numerically to fit the available data. Most measured values of the secondary emission coefficient can be fit to the universal curve. In fact, if data is found that cannot be fit to the curve, there were probably errors made during measurement of the coefficient.

Figure 5 shows secondary emission data for Teflon taken from Matskevich<sup>17</sup> fitted to the universal curve. The data was taken from a plot in the paper and deviations of some of the points from the curve are probably due as much to reading the plot as to experimental error.

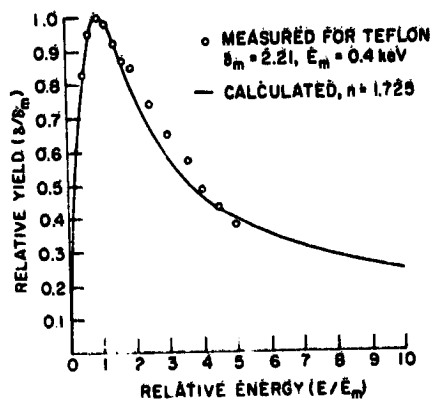


Figure 5. Universal Secondary Emission Curve for Teflon Fitted to Data Taken From Reference 17

For electron energies above about 0.5 keV, the following empirical relationship holds well:

$$\delta = KE^{-m} \quad (12)$$

where  $K$  and  $m$  are constants. For most organics  $m$  is found to be about 0.725 and  $K$  depends on the specific material. Figure 6 shows Cair's data<sup>18</sup> for Kapton and the Matskevich data for Teflon fitted to Eq. (12).

17. Matskevich, T. L. (1959) Secondary electron emission of some polymers, Fiz. Tverd. Tela., Akad. Nauk, SSSR 1:277, (in Russian).
18. Cair, S. (1974) Electron backscattering and secondary electron yield measurements from dielectric materials, Proc. IEEE Ann. Conf. on Nuc. and Space Rad. Effects, p. 177.

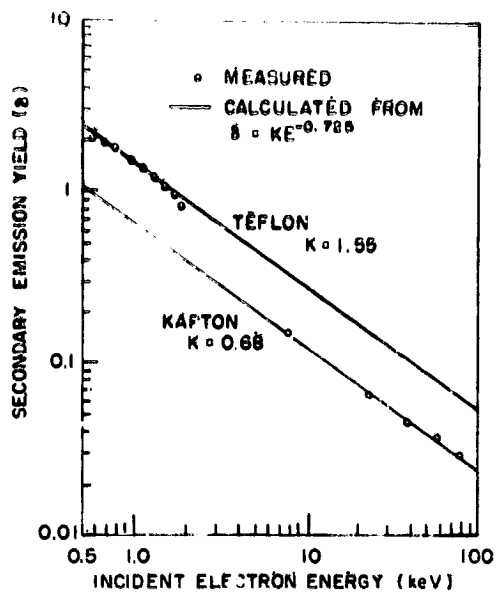


Figure 6. Plot of Empirical Relationship [Eq. (12)] Between Secondary Emission Yield and Incident Electron Energy for Teflon and Kapton. Measured values taken from References 17 and 18

The angular dependence of secondary emission follows the semi-empirical relation

$$\delta_{\theta} = \delta_0 \exp c (1 - \cos \theta) \quad (13)$$

where

$\theta$  = angle of incidence of electrons with respect to the surface normal,

$\delta_0$  = secondary emission coefficient at normal incidence,

$\delta_{\theta}$  = secondary emission coefficient for electrons incident at angle  $\theta$ .

The constant  $c$  is determined empirically. For most polymers we have found  $c \sim 2$ .

## 5. BACKSCATTER

Since information on backscatter is needed for most secondary emission measurements, data on backscatter is about as extensive as for secondary emission. Theoretical and empirical relationships have also been developed for the calculation of backscatter coefficients.

For most of the available data, the following empirical relationship holds:

$$\beta = AE^{-m} \quad (14)$$

where  $\beta$  is the backscatter coefficient, E the incident electron energy and A and m are constants. For the polymers, we have found that A = 0.1 and m = 0.2 fit most of the available data fairly well.

The backscatter coefficient,  $\beta_\theta$ , for electrons incident at angle  $\theta$  to the surface normal was found by Darlington<sup>19</sup> to be given for metals by

$$\beta_\theta = B(\beta_0/B)^{\cos \theta} \quad (16)$$

where  $\beta_0$  is the coefficient at normal incidence and B a constant. This expression also fits the polymer data taking B = 1.

## 6. ELECTRON RANGE AND RATE OF ENERGY LOSS

There have been numerous measurements of electron range and rate of energy loss for electrons with energies above 10 keV. Many empirical relationships for the calculation of range have been published and reliable theory has been developed for calculating both range and rate of energy loss above this energy. Computer generated tabulations, such as that by Berger and Seltzer,<sup>20</sup> based on the theory are available. For electron energies below 10 keV, however, there have been relatively few measurements and theoretical procedures have not been fully developed and tested.

Ashley et al are investigating electron range and energy loss for energies below 10 keV under a contract with RADC/ETS (formerly AFCRL/LQ). A report<sup>21</sup> on this work containing a tabulation of range and rate of energy loss in aluminum and aluminum oxide for electrons with energies down to 1 eV is available. The work is being continued to cover other materials including polymers.

19. Darlington, E. H. (1975) Backscattering of 10-100 keV electrons from thick targets, J. Phys. D **8**:85.
20. Studies in Penetration of Charged Particles in Matter, National Academy of Sciences-National Research Council, Washington, D. C., Publication 1133, 1964.
21. Ashley, J. C., Tung, C. J., Anderson, V. E., and Ritchie, R. H. (1975) Inverse Mean Free Path Stopping Power, CSDA Range and Straggling in Aluminum and Aluminum Oxide for Electrons of Energy  $\leq$  10 keV, AFCRL-TR-75-0583.

## 7. DIELECTRIC BREAKDOWN

Although many experimental and theoretical studies of dielectric breakdown have been performed, it is difficult to obtain a consistent view of the phenomenon from the literature. Repeated measurements of the dielectric strength of a given insulating material, performed by the same laboratory using a single procedure, can give results differing by an order of magnitude or more. This variability is probably due to minute structural differences (such as thickness variations, internal gas pockets, variations in microcrystalline structure, etc.) between samples. Differences in ambient conditions and measuring techniques also have significant effects on the results obtained.

The lack of consistent data on dielectric breakdown has made progress in the development of theories that can be used to explain and analyze the breakdown process very difficult. Some progress has been made in developing a theory for dielectric breakdown in thin films of inorganic insulators such as silicon dioxide, but very little has been accomplished in explaining breakdown in polymers. Structural changes, both microscopic and macroscopic, that occur in polymers under electric stress make analysis of the breakdown process very complex. Much more work is needed in this area.

## 8. CONCLUSION

A considerable amount of information related to electron interactions and material properties involved in charge buildup in insulators is available in the literature. Although all of the parameters needed in this area for analysis of the spacecraft charging problem may not be available in the open literature, much progress has been made in this direction. Perhaps the most significant finding is that, after some evolutionary errors, techniques have been developed for the measurement of those parameters that may be needed but for which data is not already available. Theoretical procedures for the analysis of the charge buildup process have progressed along with the measurement techniques and, although some refinements may still be needed, they are much more reliable than those available a few years ago. These developments have resulted from a renewed interest in the conduction and charge storage properties of polymers and other amorphous insulators. Most of the available information on these factors have been generated during the past ten years. In fact, about 60 percent of the relevant material found in the search was published during the past four years. If this trend continues, much of the information needed to evaluate insulating materials for use on spacecraft may soon appear in the literature.

There are areas where the literature did not indicate adequate progress. As pointed out earlier, much more work is needed on the dielectric breakdown processes in polymers. Relatively little work has been done on the effects of ambient conditions on parameters such as carrier mobility, trapping cross-sections, etc., and the changes in material properties related to charge storage that could occur, particularly in polymers, during prolonged exposure to high vacuum, cryogenic temperatures, low energy electrons and other environmental factors that may be encountered in space.

Although the open literature contains a very good base of information, only data taken on specific satellite insulating materials under controlled conditions and with particle spectra similar to the space environment can properly test the value of this information in relation to the problem of spacecraft charging.

## Bibliography

Following is a partial list of references covered during the literature search. Some of the references given in the text are also repeated here for the sake of completeness. An attempt has been made to select books and review articles where possible to minimize the number of references. Many of the references contain a variety of information and in that sense their classification into categories is somewhat arbitrary.

### ELECTRON INDUCED CHARGE BUILDUP AND BREAKDOWN

- Evdokimov, O. B., and Gusel'nikov, V. N. (1975) Phenomenological model for the buildup of space charge in dielectrics irradiated with fast electrons, High Energy Chemistry 8(No. 5):359.
- Furuta, J., Hiraoka, E., and Okamoto, S. (1966) Discharge figures in dielectrics by electron irradiation, J. Appl. Phys. 37:1873.
- Gross, B. (1958) Irradiation effects in Plexiglass, J. Polymer Sci. 27:135.
- Gross, B., Dow, J., and Nablo, S. (1973) Charge buildup in electron-irradiated dielectrics, J. Appl. Phys. 44:2459.
- Gross, B., and Nablo, S. (1967) High potentials in electron irradiated dielectrics, J. Appl. Phys. 38:2272.

### CONDUCTIVITY

- Kryszewski, M., and Szymanski, A. (1970) Space charge limited currents in polymers, Macromolecular Reviews 4:245.
- Lampert, M., and Mark, P. (1970) Current Injection in Solids, Academic Press, New York.
- Rambaum, E., and Lendel, J., Eds. (1967) Electrical conduction properties of polymers, J. Polym. Sci. C (No. 17).
- Seanor, D. A. (1972) Electrical properties of polymers, chapter 17, in Polymer Science V2, A. D. Jenkins, Ed., North Holland Publishing Co.
- Scher, H., and Montroll, E. W. (1975) Anomalous transit-time dispersion in amorphous solids, Phys. Rev. B12:2455.

### MEASUREMENT OF CONDUCTIVITY PARAMETERS AND RELATED ANALYSES

- Batra, L. P., Keiji Kanazawa, K., and Seki, H. (1970) Discharge characteristics of photoconducting insulators, J. Appl. Phys. 41:3416.
- Batra, L. P., and Seki, H. (1970) Photocurrents due to pulse illumination in the presence of trapping, J. Appl. Phys. 41:3409.
- Beckley, L. M., Lewis, T. J., and Taylor, D. M. (1976) Electron-beam induced conduction in polyethylene terephthalate films, J. Phys. D 9:1355.
- Creswell, R. A., and Perlman, M. M. (1970) Thermal currents in corona-charged Mylar, J. Appl. Phys. 41:2385.
- Das Gupta, D. K., and Jöyner, K. (1976) On the nature of absorption currents in polyethylene terephthalate (PET) J. Phys. D 9:829.

## Bibliography

- Davies, D.K. (1972) Carrier transport in polythene, J. Phys. D 5:162.
- Gross, B., and Nunes de Oliveira, L. (1974) Transport of excess charge in electron irradiated dielectrics, J. Appl. Phys. 45:4724.
- Gross, B., Sessler, G.M., and West, J.E. (1976) Trap-modulated mobility of electrons and holes in Teflon FEP, J. Appl. Phys. 47:3480.
- Gross, B., Sessler, G.M., and West, J.E. (1976) TSC studies of carrier trapping in electron- and  $\gamma$ -irradiated Teflon, J. Appl. Phys. 47:968.
- Gross, B., Sessler, G.M., and West, J.E. (1974) Charge dynamics for electron-irradiated polymer-foil electrets, J. Appl. Phys. 45:2841.
- Hayashi, K., Yashino, K., and Inushi, Y. (1973) Mobility measurements in polymers using pulsed electron beams. 1973 Conference on Electrical Insulation and Dielectric Phenomena (National Academy of Sciences, 1974), pp. 424-430.
- Lilly, A.C., Jr., and McDowell, J.R. (1968) High-field conduction in films of Mylar and Teflon, J. Appl. Phys. 39:141.
- Martin, E.H., and Hirsch, J. (1972) Electron induced conduction in plastics I. Determination of carrier mobility, J. Appl. Phys. 43:1001.
- Montieth, L.K. (1966) Trapping and thermal release of irradiation electrons from polyethylene terephthalate films, J. Appl. Phys. 37:2633.
- Montieth, L.K., and Hauser, J.R. (1967) Space-charge effects in insulators resulting from electron irradiation, J. Appl. Phys. 38:5355.
- Moreno, R.A., and Gross, B. (1976) Measurement of potential buildup and decay, surface charge density, and charging currents of corona-charged polymer foil electrets, J. Appl. Phys. 47:3397.
- Nunes de Oliveira, L., and Gross, B. (1975) Space-charge-limited currents in electron irradiated dielectrics, J. Appl. Phys. 46:3132.
- Sessler, G.M., and West, J.E. (1976) Trap modulated mobility of electrons and holes in Teflon FEP, J. Appl. Phys. 47:3480.
- Sonnóstiné, T.J., and Perlman, M.M. (1975) Transient injection currents in insulators with pre-existing space charge, Phys. Rev. B12:4434.
- Wintle, T.J. (1975) Transient charging currents in insulators. Solid-state Electronics 18:1039.
- Wintle, T.J. (1972) Surface-charge decay in insulators with nonconstant mobility and with deep trapping, J. Appl. Phys. 43:2927.
- Wintle, T.J. (1971) Decay of excess charge in dielectrics with shorted electrodes, J. Appl. Phys. 42:4724.

### TEMPERATURE DEPENDENCE OF CONDUCTIVITY

- Amborski, L.E. (1963) H-film—a new high temperature dielectric, Ind. and Eng. Chem. -Prod. R and D 2:189.
- Hanscomb, J.R., and Calderwood, J.H. (1973) Thermally assisted tunnelling in polyimide film under steady-state and transient conditions, J. Phys. D 6:1093.

### ELECTRIC FIELD DEPENDENCE OF CONDUCTIVITY

- Adamec, V., and Calderwood, J.H. (1975) Electrical conduction in dielectrics at high fields, J. Phys. D 8:551.

## Bibliography

Arnett, P. C. (1975) Transient conduction in insulators at high fields, J. Appl. Phys. 46:5236.

Pai, D. (1975) Electric-field-enhanced conductivity in solids, J. Appl. Phys. 46:5122.

### RADIATION INDUCED CONDUCTIVITY

Ahrens, T. J., and Wooten, F. (1976) Electrical conductivity in insulators by pulsed radiation. IEEE Trans. Nuc. Sci. NS-23(No. 3):1268.

Frankevich, E. L., and Yakolev, B. S. (1974) Radiation-induced conductivity in organic solids, Int. J. for Radiation Phys. and Chem. 6:281.

Weingart, R. C., Barlett, R. H., Lee, R. S., and Hofer, W. (1972) X-ray induced photoconductivity in dielectric films. IEEE Trans. Nuc. Sci. NS-19(No. 6):15.

### SECONDARY EMISSION

Dekker, A. J. (1958) Secondary electron emission, Solid State Phys. 6:251.

Gair, S. (1974) Electron backscattering and secondary electron yield measurements from dielectric materials, Proc. IEEE Conf. Ann. Conf. on Nuc. and Space Rad. Effects, July 1974, p. 177.

Märkhov, A. F. (1976) An empirical relation for the secondary electron emission of solids, Sov. Phys. Solid State 17:1589.

Matškevich, T. L. (1959) Secondary electron emission of some polymers, Fiz. Tverd. Tela., Akad. Nauk, SSSR 1:277. (in Russian).

### BACKSCATTER

Darlington, E. H. (1975) Backscattering of 10-100 keV electrons from thick targets, J. Phys. D 8:85.

Darlington, E. H., and Corlett, V. E. (1972) Backscattering of 0.5-10 keV electrons from solid targets, J. Phys. D 5:1969.

### ELECTRON RANGE AND RATE OF ENERGY LOSS

Studies in the Penetration of Charged Particles in Matter, National Academy of Sciences-National Research Council, Washington, D. C., Publication 1133 (1964).

Ashley, J. C., Tung, C. J., Anderson, V. E., and Ritchie, R. H. (1975) Inverse Mean Free Path, Stopping Power, CSDA Range, and Straggling in Aluminum and Aluminum Oxide for Electrons of Energy  $\leq 10$  keV, AFCRL-TR-75-0583.

### DIELECTRIC BREAKDOWN

O'Dwyer, J. J. (1973) The Theory of Electrical Conduction and Breakdown in Solid Dielectrics, Clarendon Press, Oxford.

## Contents

1. Introduction	593
2. Technical Discussions	595
3. Space Simulation Tests and Results	604
4. Conclusions	609
Acknowledgments	611
References	611

### 3. Electrically Conductive Paints for Satellites

J.E. Gilligan  
ITT Research Institute  
Technology Center  
Chicago, Illinois

R.E. Wolf and C. Ray  
DeSoto, Inc.  
Des Plaines, Illinois

#### Abstract.....

A program was conducted to develop and test electrically conductive paint coatings for spacecraft. A wide variety of organic and inorganic coatings were formulated using conductive binders, conductive pigments, and similar approaches. Z-93, ITTRI's standard specification inorganic thermal control coating, exhibits good electrical properties ( $\sim 10^9$  ohms) and, of course, is a very space-stable coating system. Several coatings based on a conductive pigment (antimony-doped tin oxide) in silicone and silicate binders offer considerable promise. Paint systems using commercially available conductive polymers also appear to be of interest, but will require substantial development. Evaluations were made based on electrical conductivity, paint physical properties, and the stability of spectral reflectance in space environmental testing.

#### 1. INTRODUCTION

In traversing those regions of space where energetic charged particle fluxes exist, a spacecraft may acquire a very large electrical potential.<sup>1,3</sup> Because the

instantaneous incident flux will vary (with time) in magnitude, energy, and composition, the environment is a dynamic one; the resulting charge buildup also varies with time.

Space Charge Accumulation (SCA) represents a serious threat to spacecraft performance; at high electrical potentials it poses the threat of electrical discharge with resultant material damage and an rf burst. At low potentials, in certain applications, SCA interferes with measurements of the electrical environment. On some spacecraft even very small differences in potential from one point to another can seriously degrade the sensitivity of instrumentation to incident charged particle fluxes. The greater the potential, the greater is the disparity in the measurement. The SCA problem then is either the moderate one of reducing SCA to levels at which electrical discharge is highly improbable or the more difficult one of developing serviceable materials with sufficiently high electrical conductivity to eliminate high electrical potentials.

The underlying problem in this program is that the "standard" requirements placed on low  $\sigma/\epsilon$  systems are not compatible with the concurrent requirement for high electrical conductivity. Solar absorptance, in fact, generally parallels electrical resistivity. Nonetheless, because all external surfaces of a spacecraft have a thermal control function, the essence of the SCA problem is to achieve high electrical conductivity in surface materials without seriously compromising thermal radiative properties and performance.

In this program we have investigated several approaches to the SCA problem—all from a materials standpoint. The objective may be stated rather simply: to identify surface materials with high electrical conductivity and acceptable optical and physical properties. Although quantitative criteria and objectives were not specified, the general requirements of satisfactory surface coatings are shown in Table 1.

Table 1. Desirable Properties of High Electrical Conductivity Thermal Control Coatings

Property	Desirable Value
Solar Absorptance, $\alpha_s$	< 0.4
Thermal Emissance, $\epsilon$	> 0.8
Electrical Conductivity	$\sim 10^9$ ohms
Optical Stability, $\Delta\alpha_s$	< 0.1/5-10 years
Outgassing/Contamination	< $10^{-5}$ gm/cm <sup>2</sup> -year

## 2. TECHNICAL DISCUSSIONS

### 2.1 Statement of the Problem.

The successful development of a conductive paint system for spacecraft applications requires that the resistivity of the dielectric materials which comprise them be reduced. The scope of the program includes all pigmented coatings and surface materials, except those applied by adhesives or by similar techniques. To increase the conductivity of a paint coating, the usual approach is to use a highly conductive pigment, for example, carbon black. This latter approach, however, would lead to a paint with very high  $\sigma_g/\epsilon$ .

The incorporation of metal pigments in paints to decrease electrical resistivity has been largely unsuccessful, because pigments remain in the dispersed phase. Thus, the incorporation of metal, semiconductive, or highly conducting pigments in resins will almost inevitably encounter the problem of wetting. In "successful" paint binders, the pigment particles will be 100 percent wetted and thus become physically and electrically isolated by the binder.

The very nature of a paint—a dispersed pigment or pigments (discontinuous phase) in a binder (continuous phase) suggests that the binder be made conductive. The overall problem, therefore, is to produce a paint coating whose binder is electrically conductive or whose pigment has such a character that it can, via stringing, flocculation, hydrogen-binding, etc., effectively form a continuous filament.

The problem, apart from any environmental stability or other practical considerations, is that increased electrical conductivity in organic materials is generally accompanied by increased optical absorption (decreased transparency). In simple but fundamental terms, electrical conductivity arises from the motion of electrons in the conduction band. Transparency, the absence of absorption, arises from the very low probability of transitions to the conduction bands. The further apart are the valence and conduction bands, the less the probability of an electron reaching the latter, and accordingly both the electrical conductivity and optical absorption will be low. Conversely, the closer these bands, the more likely that the material will be colored, possibly even black, and also that it will have high electrical conductivity. In short, the fundamental properties giving rise to high transparency in a dielectric material are the same ones which underlie its high resistivity. One should not conclude that transparency and conductivity are mutually exclusive, but rather that some compromises may be necessary.

### 2.2 General Approaches

A great number of conductive materials are available, many commercially, some in limited experimental quantities, and still others only by synthesis. The

general approach involved a search for these materials—resins, pigments, fibers, etc.—preliminary determination of their properties and availability, and a series of experimental studies to evaluate their feasibility. Conductive polymers, both organic and inorganic, received primary attention.

The enhancement of conductivity in IITRI's specification thermal control coatings, S-13G/LO and Z-93, production and evaluation of conductive pigments, fibers, and the synthesis and evaluation of conductive polymers were important elements in the program.

The program took three general directions: Conductive Organic Polymers, Conductive Inorganic Binders, and Conductive Pigments. In each approach, attempts were made to obtain commercially available materials or, if the preparative route was simple and direct, to synthesize them.

### 2.3 Conductive Organic Polymers

Many potential materials were identified but most of the materials were rejected because they are highly colored or black, carbon-pigmented materials, aerosol antistats, or similar materials which are not in a useful form. Five quaternary ammonium chloride polymers and poly(vinyl carbazole), PVK, were investigated as binders which possess conductive or photoconductive properties. The five cationic polymers were: DeSoto C-112, the diquaternary salt of  $\alpha, \alpha'$ -dichloro-oxylyene and N,N,N',N'-tetramethylethylene diamine; DeSoto C-112, the methyl chloride quaternary salt of poly(4-vinyl pyridine); DeSoto C-113, the trimethylamine quaternary salt of poly(epichlorohydrin); Dow ECR-34, the trimethylamine quaternary salt of poly(4-vinyl benzyl chloride); Merck 261, the methyl chloride quaternary salt of poly(diallyl n.ethyl amine).

The conductive polymers chosen for evaluation in this program were originally developed as conductive treatments for paper in the electrophotographic copy industry. These polymers are used to increase the conductivity of the paper base stock and to dissipate the corona induced surface charge in the light imaging process.<sup>4,5</sup> PVK, a photoconductive polymer, has also been utilized to dissipate charge under light imaging conditions in the electrophotographic process. PVK is of interest because of its conductive properties when illuminated with photons from an ultraviolet light source (~360 nm). PVK has a conductivity of  $10^{-13} \text{ ohm}^{-1} \text{ cm}^{-1}$  when exposed to an ultraviolet light source and a dark conductivity of  $5 \times 10^{-16} \text{ ohm}^{-1} \text{ cm}^{-1}$ . The addition of dopants and formation of charge transfer complexes with PVK has been shown to shift the absorption spectrum into the visible region, resulting in increased conductivity in the same region ( $\sim 10^{-13} \text{ ohm}^{-1} \text{ cm}^{-1}$  at 550 nm).<sup>7,8</sup>

### 2.3.1 FILM STUDIES

Film studies on Dow ECR-34 indicated that films applied at relatively low humidities developed hairline cracks upon drying. Conditioning of the films during drying at 50 percent relative humidity provided initial films for surface and volume resistivity measurements.

Films of Dow ECR-34 (as received), cast from solution, developed craters and showed inhomogeneous coverage of the aluminum substrate (Alclad 2024 T3, hot alkaline cleaned). The source of this behavior was attributed to the high surface tension of the aqueous solution of the Dow ECR-34,  $\sim 57$  dynes/cm<sup>2</sup>.

In the preparation of Merck 261 films, it was observed that drying these films at 50 percent relative humidity resulted in tacky films. This material shows film-forming properties similar to those of the Dow ECR-34. The surface tension was determined to be 72-74 dynes/cm<sup>2</sup>. Triton X-100, a nonionic surfactant was added to improve film formation characteristics prior to making electrical measurements.

Films of PVK, with and without film forming aids, with various levels of crystal violet (CV) dye added ( $2.5 \times 10^{-7}$  to  $2.5 \times 10^{-5}$  mole per gram PVK) were prepared. The presence of film forming aids is necessary for the CV to completely dissolve in the present system.

A solvent system compatible with both the PVK and 2,4,7 trinitro-9-fluorenone (TNF) was found. Films of the 1:1 (mole) complex of PVK and TNF were cast.

### 2.4 Electrical Measurements

Surface and volume resistivity measurements were made or attempted on all of the coating candidates. In general, IITRI accomplished the measurements on the inorganic materials while DeSoto, Inc. made measurements on the organic system. DeSoto made all of the charge acceptance measurements.

The resistivity-measuring equipment used by IITRI consists of a Hewlett-Packard Model 4329A High Resistance Meter used in conjunction with an HP Model 16008A resistivity cell.

At DeSoto, Inc., electrical property measurements were made with a Keithley 615 Digital Electrometer and 246 High Voltage Supply coupled with a 6105 Resistivity Adapter. These three components permit the measurement of the volume and surface resistivities of materials in accordance with ASTM D257-66 "Standard Method of Test for Electrical Resistance of Insulating Materials." The determination of the surface and volume resistivity in this method assumes the validity of Ohm's law for the materials tested.

#### 2.4.1 CONDUCTIVE ORGANIC POLYMERS

Surface resistivity measurements were made at 5 percent relative humidity on the various polymer films prepared for this program. The results of these

measurements are summarized in Table 2. For the conductive polymers tested the surface resistivities fall into a rather narrow range ( $\sim 10^{11}$  ohms). Polyvinyl carbazole (PVK) and modified films of PVK exhibited resistivities approximately one or two orders of magnitude higher than the conductive polymers.

Table 2. Surface Resistivities of Polymer Films 25°C at 5% Relative Humidity

Material	$\rho_s$ (ohms)
DeSoto C-111	$2.4 \times 10^{11}$
DeSoto C-111 <sup>a</sup>	$2.4-2.6 \times 10^{11}$
DeSoto C-112	$1.6 \times 10^{11}$
DeSoto C-113 <sup>b</sup>	$1.7 \times 10^{11}$
Dow ECR - 34 <sup>c</sup>	$1.3-3.8 \times 10^{11}$
Merck 261 <sup>d</sup>	$1.8-2.4 \times 10^{11}$
PVK	$2.2 \times 10^{13}$
PVK with filming aids	$2 \times 10^{11}$
PVK + DV <sup>e</sup> + filming aids	$2 \times 10^{12} - 2 \times 10^{13}$
PVK + CV <sup>e</sup>	$2.2 \times 10^{11} - 1.3 \times 10^{14}$
PVK + TNF <sup>f</sup>	$9 \times 10^{11} - 9 \times 10^{12}$

- a. Triton X-100 (Rohm & Haas), a nonionic surfactant, was added at 0.002g/g C-112 polymer.
- b. Amaizo 745 D (American Maize Products Co.); used at 0.25g/g polymer.
- c. Triton X-100 was added at 0.013g/g polymer.
- d. Triton X-100 was added at 0.003g/g polymer.
- e. Concentration of crystal violet (CV) in PVK ranged from  $2.5 \times 10^{-7}$  to  $2.5 \times 10^{-5}$  mole/g PVK.
- f. A 1 to 1 molar complex of trinitrofluorenone (TNF) and PVK.

The surface resistivity values obtained for the quaternary ammonium polymers are consistent with known effects of relative humidity on resistivity. The surface resistivity increases with a decrease in relative humidity.<sup>4, 9, 10</sup> A comparison of the surface resistivities at differing humidities is shown in Table 3.

Several attempts were made to measure the volume resistivity of the thin polymer films on aluminum. With the impressed voltage at 500 V, the power supply became overloaded and no measurements could be recorded. Attempts were made to determine the volume resistivity at lower voltages but these efforts were also

hampered by frequent overloading. In the film thickness range studied, the films were sufficiently conductive to bleed the impressed charge to ground under the experimental conditions.

Table 3. Surface Resistivity of Quaternary Ammonium Polymers at Various Relative Humidities

Polymer	Concentration (lb/3000 ft <sup>2</sup> )	Surface Resistivity $\rho_s$ , ohm (% R. H.)		
		46%	13%	5%
DeSoto C-111	1.25	$3.8 \times 10^8$	$5.2 \times 10^9$	$2.5 \times 10^{11}$
DeSoto C-112	0.8	$2.5 \times 10^7$	$3.4 \times 10^9$	$1.6 \times 10^{11}$
DeSoto C-113	1.5	$1.9 \times 10^{7a}$	$1.9 \times 10^{9b}$	$1.7 \times 10^{11}$
Dow ECR-34	0.9	$5.0 \times 10^7$	$7.3 \times 10^8$	$2.6 \times 10^{11}$
Merck 261	1.3	$3.7 \times 10^7$	$4.2 \times 10^9$	$2.1 \times 10^{11}$
a. 50% Relative Humidity.		b. 17% Relative Humidity.		

#### 2.4.2 INORGANIC BINDERS

The inorganic binders evaluated are soluble alkali silicates. Potassium, lithium, and sodium silicates were obtained from commercial suppliers for evaluation. They are listed in Table 4.

Table 4. Alkali Metal Silicates

Trade Name	Supplier	Weight Ratio $M_2O:SiO_2$
<b><u>SODIUM SILICATES:</u></b>		
S 35	Philadelphia Quartz	1:3.75
N	Philadelphia Quartz	1:3.22
K	Philadelphia Quartz	1:2.90
RU	Philadelphia Quartz	1:2.40
B-W	Philadelphia Quartz	1:1.60
<b><u>POTASSIUM SILICATES:</u></b>		
KASIL No. 1	Philadelphia Quartz	1:2.50
KASIL No. 6	Philadelphia Quartz	1:2.10
<b><u>LITHIUM SILICATES:</u></b>		
LITHSIL-4	Lithcoa	1:9.41
LITHSIL-6	Lithcoa	1:11.7
LITHSIL-5	Lithcoa	1:6.53

A broad range of silicates with varying alkali-to-silicate ratios are shown. As reported in the literature,<sup>11</sup> increasing electrical conductivity may be expected with increasing alkali content.

Considerable difficulty was experienced in making measurements with repeatable results. A temperature-humidity conditioning procedure and close observance of measurement procedures were necessary. Table 5 presents electrical measurement data for a series of inorganic paints under ambient humidity conditions. In view of the uncertainty in the measurement accuracy, the expected trend is not evident, and it appears that only a slight advantage might occur in the use of sodium silicate rather than potassium or lithium silicate-binders.

Table 5. Summary of Electrical Measurements for Conductive Inorganic Coatings

Binder	Surface Resistivity (ohm)	
	ZnO Pigmented	Zn <sub>2</sub> TiO <sub>4</sub> Pigmented
<u>Na<sub>2</sub>O·SiO<sub>2</sub></u>		
PQ S-35	7.7×10 <sup>8</sup>	1.7×10 <sup>9</sup>
PQ B-W	8.5×10 <sup>8</sup>	---
<u>Li<sub>2</sub>O·SiO<sub>2</sub></u>		
Lithsil No. 4	2.4×10 <sup>9</sup>	3.6×10 <sup>9</sup>
Lithsil No. 6	1.2×10 <sup>9</sup>	3.8×10 <sup>9</sup>
<u>K<sub>2</sub>O·SiO<sub>2</sub></u>		
Kasil No. 1	---	2.4×10 <sup>9</sup>

All of these coatings exhibit good adhesion, good whiteness and no indication of cracking, and thus can be considered for further evaluation (and improvement) as low  $\alpha_g/\epsilon$  coatings. The "standard" inorganic coatings exhibit low and rather consistent resistivity values.

#### 2.4.3 CHARGE ACCEPTANCE MEASUREMENTS

The surface charge acceptance measurements were made according to procedures common to the electrophotographic industry in the evaluation of photoconductive paper.<sup>4</sup> A high voltage corona (3-5 kV) is used to induce a charge on the surface of the films. Experimentally, the voltage induced in a probe is measured, not the charge density. It can be shown, however, that a simple relationship exists between the voltage on an infinite plane at distance r, and the charge density,  $\sigma$

$$v = \frac{q}{r}.$$

(1)

The charge density is directly proportional to the voltage at a fixed distance.

The probe used in the work reported here was calibrated by using the Keithley 246 High Voltage Power Supply as a source of constant voltage. In general, the charging of films with a corona wand provides a saturation voltage, that is, the maximum voltage capable of being accepted by a given polymer film. After charging is discontinued, the voltage impressed upon the film gradually decays to ground potential. The rate at which the charge dissipates depends on the electrical characteristics of the material and the external conditions. For electrical insulators the decay rate may be infinitesimally slow. For photoconductors, such as PVK, light illumination greatly increases the decay rate and for conductive polymer films often no charge buildup is observable. Surface charge measurements are recorded for a variety of materials in Table 6 using a negative corona at 5 percent relative humidity.

Table 6. Surface Charge Acceptance Measurements of Clear and Pigmented Coatings

Material	Corona Current - Time	Probe Reading (volts)
DeSoto C111	0.1mA, 30 sec	0
Dow ECR-34	0.1mA, 30 sec	0
	0.2mA, 30 sec	0
Merck 261	0.2mA, 30 sec	0
PVK	0.1mA, 30 sec	-35
PVK + CV	0.1mA, 30 sec	-30
PVK + TNF	0.1mA, 30 sec	0
	0.1mA, 60 sec	0
	0.1mA, 60 sec	-200
S-13G/LO (8.5 mil) <sup>a</sup>	0.1mA, 30 sec	-29
	0.1mA, 60 sec	-48
	0.1mA, 60 sec	-200
RTV-602 (1.5-3.5 mil) <sup>a</sup>	0.1mA, 60 sec	-422
Z-93 (3.4 mil) <sup>a</sup>	0.1mA, 60 sec	0

a. Materials supplied by IIT Research Institute.

At the request of the Air Force Materials Laboratory, samples of aluminized FEP Teflon (2 mil), aluminized Kapton (1 mil), and Astroquartz fabric (style 581, heat treated 3 hours at 800°C) were evaluated for surface charge acceptance in the same manner as the conductive polymers and thermal control materials. The data for these materials are presented in Table 7. A static charge may have been developed during the handling of the samples in the dry box. The voltages developed

in the Teflon FEP and Kapton materials were lower than expected. These same materials were tested in the 6105 Resistivity Adaptor at + 500 V in the volume resistivity mode. For the Teflon FEP the effective resistance was  $\sim 1.7 \times 10^{11}$  ohm; and for Kapton,  $\sim 1.2 \times 10^{12}$  ohm. The Astroquartz material registered an effective resistance of  $\sim 5 \times 10^{13}$  ohm.

Table 7. Surface Charge Measurements of Plastic Materials

Material	Current - Time	Probe Reading (volts)
Teflon FEP (2 mil), polymer side	0.1mA, 30 sec	-80
	0.1mA, 60 sec	-94
	0 <sup>a</sup>	-97
Teflon FEP (2 mil), metal side	0.1mA, 30 sec	-130
	0.1mA, 60 sec	+73
	0.2mA, 60 sec	+68
	0 <sup>a</sup>	+73
Kapton (1 mil), metal side	0.1mA, 30 sec	-102
	0.1mA, 60 sec	-52
	0.2mA, 60 sec	+2
	0 <sup>a</sup>	+43
Kapton (1 mil), polymer side	0.1mA, 30 sec	-57
	0.1mA, 60 sec	-50
	0.2mA, 30 sec	-45
	0 <sup>a</sup>	-70
Astroquartz	0.1mA, 30 sec	-312
	0.1mA, 60 sec	-506
	0 <sup>a</sup>	+435

a. Readings obtained before exposure to corona current; charge induced by handling material.

During the course of measuring the surface charge of the various polymer systems, the power supply voltage exhibited some variation between 3-5 kV. Accordingly, the data in Tables 6 and 7 should be viewed as qualitative in nature.

#### 2.5 Conductive Paint Systems - Coatings Evaluation

A large number of clear and pigmented films of both the organic and inorganic polymers were prepared for evaluation as films and coatings. Many, if not most, of the organic formulations were found to be unsuitable. DeSoto polymers C-112 and C-113, for example, are too low in molecular weight to be good film formers and remain liquid. Some films would adhere to aluminum substrates only if

pigmented; others, only without pigmentation. Adhesion is a major problem for many of these coatings; another is compatibility with solvents (aqueous and organic). Since RTV 602/LO is a space-qualified paint binder, we attempted to modify it electrically by "doping" it with DeSoto and commercial polymers. These attempts were completely unsuccessful because of immiscibility.

The intent of these laboratory efforts was to determine which candidate materials, or combinations of them, would be most useful as practical conductive coatings. Table 8 presents surface resistivity data pertaining to some of the more useful coatings. These coatings are grouped in several categories. The first, of course, contains ITRI's two specification coating systems, S-13G/LO and Z-93. The second group illustrates the difficulty, mentioned earlier, in overcoming the wetting problem, even with highly conductive pigments. The third group is composed of a specially developed conductive pigment (a  $\text{SnO}_2\text{:Sb}$  pigment developed under AF Contract No. F33615-72-C-1657), in silicone and silicate binders. The next group is made up of zinc oxide and zinc orthotitanate pigmented silicate coatings; in this case, the pigments are space-qualified and the silicate binders are experimental. The final group shows the only two employing conductive polymers that have some potential for use as practical low  $\alpha_g/\epsilon$  thermal control coatings.

As can be seen in the first group, the ZnO pigmented silicate, Z-93, possesses relatively good conductivity, but the ZnO-pigmented silicone, S-13G/LO does not. The metal pigmented silicones further illustrate the "wetting" problem.

The conductivity of the antimony-doped tin oxide ( $\text{SnO}_2\text{Sb}$ ) pigment is very good. It should be noted, however, that the conductivity of coatings containing this pigment depends sensitively on pigment volume concentration (PVC). Especially of interest is the very large change in conductivity in RTV602 coatings with only a doubling of the PVC. This contrasts sharply with the observations above that RTV602 cannot be made conductive by pigmenting it with conductive pigments.

Table 8. Summary of Electrical Measurements

Materials Description	Surface Resistivity (ohms)
<u>Conventional Coatings</u>	
S-13G/LO	$1.5 \times 10^{13}$
Z-93	$4.5 \times 10^8$
<u>Leaving Metal-Pigmented Silicones</u>	
Al. Powder/RTV602	$3.2 \times 10^{12}$
ZN Powder/RTV602	$1.6 \times 10^{13}$
Cu Powder/RTV602	$4.8 \times 10^{14}$

Table 8. Summary of Electrical Measurements (Cont)

Materials Description	Surface Resistivity (ohms)
<u>Antimony-doped Tin Oxide Coatings</u>	
SnO <sub>2</sub> :Sb/RTV602 (low PVC)	2.8 × 10 <sup>13</sup>
SnO <sub>2</sub> :Sb/RTV602 (high PVC)	1.2 × 10 <sup>9</sup>
SnO <sub>2</sub> :Sb/PS-7 (low PVC)	1.2 × 10 <sup>8</sup>
SnO <sub>2</sub> :Sb/PS-7 (high PVC)	2.1 × 10 <sup>7</sup>
<u>Inorganic Coatings</u>	
ZnO*/Na <sub>2</sub> SiO <sub>3</sub> (S-35)	7.7 × 10 <sup>8</sup>
ZnO*/Na <sub>2</sub> SiO <sub>3</sub> (B-W)	8.5 × 10 <sup>8</sup>
ZnO*/Li <sub>2</sub> SiO <sub>3</sub> (Lithosil 4)	2.3 × 10 <sup>9</sup>
ZnO*/Li <sub>2</sub> SiO <sub>3</sub> (Lithosil 6)	1.2 × 10 <sup>9</sup>
Zn <sub>2</sub> TiO <sub>4</sub> 7K <sub>2</sub> SiO <sub>3</sub> (Kasil 1)	2.4 × 10 <sup>9</sup>
Zn <sub>2</sub> TiO <sub>4</sub> /Li <sub>2</sub> SiO <sub>3</sub> (Lithosil 4)	3.6 × 10 <sup>9</sup>
Zn <sub>2</sub> TiO <sub>4</sub> /Li <sub>2</sub> SiO <sub>3</sub> (Lithosil 6)	3.8 × 10 <sup>9</sup>
Zn <sub>2</sub> TiO <sub>4</sub> /Na <sub>2</sub> SiO <sub>3</sub> (S-35)	1.7 × 10 <sup>9</sup>
<u>Conductive Organic Coatings</u>	
S-13G Pigment/Merck No. 261	3.4 × 10 <sup>6</sup>
S-13G Pigment/Dow ECR-34	2.2 × 10 <sup>6</sup>

\*Calcined ZnO

### 3. SPACE SIMULATION TESTS AND RESULTS

The determination of which coatings would be evaluated for ultraviolet radiation stability was made on the basis of many evaluations, including electrical properties, optical properties, appearance, integrity, coating and film-forming properties, and adhesion. Three tests were conducted in the Combined Radiation Effects Facility (CREF). The first contained a series of primarily organic-based coatings; the second, inorganic coatings; and the third, the coatings which performed best in the first two.

In all of these tests the reflectance spectra of all samples were measured in-situ before and after irradiation. The spectra were recorded in the range 325 to 2600 nm. The ultraviolet radiation source employed is a Hanovia 5000W Mercury-Xenon burner, which illuminates the samples at an equivalent solar UV intensity of 4X. The spectral data at specific wavelengths is shown in Tables 9, 10, and 11.

### 3.1 CREF Test No. 19 - Results

Table 9 lists the sample materials and the in situ before-and-after-test reflectance values at selected wavelengths. Standard S-13G and Z-93 coatings were included in this test for reference. Total UV exposure was 256 ESH. Reflectance spectra for the Dow and Merck clear films were recorded in the wavelength interval 250 to 2600 nm. These two samples, however, disintegrated in establishing vacuum conditions.

Table 9. CREF Test No. 19 - Test Results

Sample Description (Pigment/Binder)	Exposure (ESH)	Reflectance Values (%)			
		R <sub>400</sub>	R <sub>600</sub>	R <sub>800</sub>	R <sub>1000</sub>
MERCK No. 261*	Disintegrated in vacuum before irradiation				
PVK-Crystal Violet*	0 256	11 11	11 30	11 30	58 53
PVK-Trinitrofluorenon*	0 256	10.5 10.5	10.5 10.5	51 51	62.5 62.5
PVK*	0 256	54 23	61 54	58.5 57.0	68 67
DOW ECR-34*	Disintegrated in vacuum before irradiation				
S-13G Pigment/DOW ECR-34	0 256	76 62	90 86	88.5 87.0	88 86.5
S-13G Pigment/DeSoto C-111	0 256	63 52	70.0 66	56 53	44 41
AFML** Pigment/RTV 602	0 256	63 52	71.5 67	61 56	48 46
AFML** Pigment/PS-7	0 256	73 69	81.5 76.5	76 73	66.5 65
S-13G Pigment/MERCK	0 256	74 73	87 86	87 85.5	87 85.5
S13G	0 256	79 77	92.5 91.0	92.5 91	91 90
Z-93	0 256	83.5 82	95 94	95.5 94	95 94.5

\*Transparent, unpigmented films.

\*\*AFML Pigment is electrically conductive antimony-doped tin oxide (SNO<sub>2</sub>:Sb) supplied by AFML.

It is obvious from the table that most of the coatings tested are highly unstable. The degradation of Z-93 and of S-13G/LO, particularly the unusual character of the spectral changes, suggest substantial contamination. The photo-decomposition of the Dow and DeSoto polymers is strongly suspected. Apart from the specifica-

tion coatings, i.e. coating of S-13G pigment in Merck No. 261 shows good initial properties and reasonable UV-stability. Even though relatively stable, the doped PVK films exhibit unacceptable absorption. The behavior of the undoped PVK film contrasts slightly with that observed in another program where highly purified PVK was used. In this study the PVK contained a film-former additive. Consequently, the observed degradation may be due to impurities - and possible to contamination from other samples.

### 3.2 CREF Test No. 20

This test is similar to the previous one except that it contained only inorganic samples. Z-93, in this test also, was included for reference purposes. As expected, the inorganic coatings sustain comparatively minor degradation. Furthermore, the spectral changes in Z-93 are not quite characteristic, suggesting that some of the contamination from the previous irradiation test remained in the CREF, apparently, to increase the damage.

The samples in CREF Test No. 20 were exposed under vacuum ( $P < 2 \times 10^{-7}$  Torr) to a total of 204 ESH of simulated solar ultraviolet radiation.

Table 10. CREF Test No. 20 - Results

Sample Description (Pigment/Binder)	Exposure (ESH)	Reflectance Values (%)			
		R <sub>400</sub>	R <sub>600</sub>	R <sub>800</sub>	R <sub>1000</sub>
ZnO/S-35	0	68	90	89	88.5
	204	75	88.5	87	87
ZnO/Lithosil 6	0	73	91	90	89
	204	68	87	87	87
ZnO/Kasil 1	0	79	91	91	90
	204	78	90	91	90
ZnO/Lithosil 4	0	72	90	88.5	87.5
	204	70	88.5	88.5	87.5
Z-93	0	71	92	92.5	92
	204	71	90	92	92
ZnO/W-W Silicate	0	66	88	89	88
	204	66	88	88	87
ZOT/Kasil 1	0	80	84	83.5	82
	204	77	83	84.5	84
ZOT/(S-35)	0	80	88	87	86.5
	204	77	87	89	88
ZOT/OS-7	0	81	87	86.5	75
	204	78	85.5	88.0	87
ZOT/Lithosil 4	0	73	88.5	83	77.5
	205	80	87	84	78.5
ZOT/B-W Silicate	0	82	88	88	87.5
	204	78	86	90	90
ZOT/Lithosil 6	0	84	90	90	90
	204	80	88	92	91.5

The abbreviations in Table 10 are described as follows:

ZnO	Calcined SP-500 Zinc Oxide (New Jersey Zinc)
ZOT	Zinc Orthotitanate. IITRI Batch No. LH-101 precalcined at 600°C/2 hr, calcined at 900°C/2 hr
S-35	Sodium Silicate, Philadelphia Quartz Co. No. S-35
B-W	Sodium Silicate, Philadelphia Quartz Co. No. B-W
Kasil-1	Potassium Silicate, Philadelphia Quartz Co. Kasil No. 1
Lithosil-4	Lithium Silicate, LITHCOA, Inc., Lithosil No. 4
Lithosil-6	Lithium Silicate, LITHCOA, Inc., Lithosil No. 6
PS-7	Potassium Silicate, Sylvania Elec. Co., No. PS-7
DOW	Dow Chemical Co. Electroconductive Resin ECR-34
MERCK	Merck Chemical Co. Electroconductive Resin No. 261
S-13G Pig	Potassium Silicate Encapsulated SP-500 ZnO- the pigment used in S-13/LO thermal control coating

### 3.3 CREF Test No. 21

Those samples which exhibited the best initial properties and UV stability in the two previous tests were selected for testing in CREF Test No. 21. They are listed in Tables 11 and 12 along with pre- and post-test reflectance data at selected wavelengths.

Table 11. CREF Test No. 21 - Results

Sample Description (Pigment/Binder)	Exposure (ESH)	Reflectance Values (%)			
		R <sub>400</sub>	R <sub>600</sub>	R <sub>800</sub>	R <sub>1000</sub>
S-13G PIG/MERCK	0	79	81	91	92
	180	76	88	88	88
	558	77	89	89	90.5
	1032	79	90.5	90.5	91.5
S-13G PIG/DOW	0	74	89	89.5	88.5
	180	65	84.5	86	85
	558	67	88	89.5	88.5
	1032	61	83.5	90	89
ZnO/Lithosil 6	0	70	91	92	91
	180	69	86	88	87
	558	73	91	92	91
	1032	73	91	93	91.5
ZOT/Kasil 1	0	80	86	87	85
	180	75	81	82.5	81.5
	558	78	84.0	84.5	84.5
	1032	78	84.5	87	85
ZOT/S-35	0	81	88	89.5	88.5
	180	78	87.5	88	88
	558	77	87.5	88	87
	1032	77	87.5	89.5	88.5

Table 11. CREF Test No. 21 - Results (Cont)

Sample Description (Pigment/Binder)	Exposure (ESH)	Reflectance Values (%)			
		R <sub>400</sub>	R <sub>600</sub>	R <sub>800</sub>	R <sub>1000</sub>
ZOT/Lithosil 6	0	85	90.5	92	91.5
	180	82	88	81	90.5
	558	81	86.5	89	88.5
	1032	80.5	88	92	91.5
ZnO/B-W	0	71	89	91	
	180	71	89	91	
	558	71	89	90.5	
	1032	71	89	92	
ZOT/Lithosil 4	0	84	89	89.5	89.5
	180	81	87	89	88.5
	558	81	87	89	98.5
	1032	81	87	89.5	89.5

In this test the samples were exposed in vacuo ( $P < 2 \times 10^{-7}$  Torr) to a total of 1032 ESH at a nominal intensity of four (4) equivalent suns. Reflectance spectra in the wavelength range from 325 to 2600 nm were taken after nominal exposures of 180, 550, and 1000 ESH. After a careful review of these spectra it was concluded that the anomalous behavior of the 180 ESH data is due to contamination. The remainder of the data follow the trends we expect. It is quite possible that the contamination resulted from the photodecomposition of the S-13G/DOW ECR-34 coating.

Table 12. CREF Test No. 21 - Results

Sample Description (Pigment/Binder)	Exposure (ESH)	Reflectance Values (%)			
		R <sub>400</sub>	R <sub>600</sub>	R <sub>800</sub>	R <sub>1000</sub>
ZnO/S-35	0	67	92	94	93
	180	70	92	89.5	87.5
	558	67	91	93.0	92
	1032	67	91	94	93
ZnO/Lithosil 4	0	68	89	90	88
	180	71	89	89	88.9
	558	71	89	89	88.5
	1032	71	89	90	88
ZnO/Kasil 1	0	79	92	93.5	93
	180	79	92	93	92
	558	79	92	93	92
	1032	79	92	93.5	93

The subsequent data (at 500 and 1000 ESH) reflect a stabilization of the organic coatings.

The relatively good properties and performance exhibited by S-13G Pigment/Merck 261 in CREF Test No. 19 is repeated in this test. The S-13G Pigment/Dow ECR-34 coating performed similarly. In general, all of the coatings in Test No. 21 possess acceptable initial properties and reasonable stability.

#### 3.4 Remarks on Environmental Test Results

The coatings tested all have conductivity values considerably higher than that of S-13G/LO. Most also have reasonable low  $\alpha_g$  values. While we can be reasonably assured of the optical stability of these coatings, their electrical property stability remains in doubt. We have not calculated  $\alpha_g$  for these materials because most are highly developmental. The tests consequently were designed to provide comparative information rather than absolute values. It is important to stress that we have measured only optical properties in-situ, not electrical properties. We do not know whether the latter arise from intrinsic photoconductive or extrinsic processes, or combinations of them. In overview, the coating tests and the environmental stability tests have served to identify several promising pigment/binder systems.

#### 4. CONCLUSIONS

The objectives of this program were to evaluate materials approaches to solving the spacecraft SCA problem—basically, to assess various approaches toward the development of space-stable, electrically conductive, low  $\alpha_g/\epsilon$  spacecraft thermal control coatings. Emphasis was placed on conductive paint binders, primarily because, in classical paint coatings, the binder is the continuous (homogeneous) phase and the pigment is the dispersed phase.

From an overall point of view, the inorganic silicate coatings offer the greatest potential toward solving the SCA problem. Z-93 in particular, a NASA specification coating system, holds the greatest promise for an immediate, yet practical ("off-the-shelf") solution. Within 1 to 2 years, we could expect that a superior inorganic coating could be developed. Historically, however, the use of inorganic coatings for spacecraft temperature control has been limited, — primarily because of the belief that such coatings are difficult to apply and to keep clean.

The reluctance to accept inorganic coatings makes it imperative that organic coatings for anti-SCA use be developed. Because of our experience with the binder wetting problem, we believe that there are only two basic approaches. The first is the modification of specification (that is, flight qualified) coatings; the second, the

development of new coatings. The modification approach could involve, in increasing order of potential benefit, simple additives, structural changes to the polymeric binder, copolymerization, chemical complexing, and conductive pigments. We have assigned this order because we have not been able to find any electrically conductive additive compatible with RTV602 and because a conductive pigment (at high PVC) in RTV602 has markedly improved conductivity (compared to RTV602). The difficulties associated with obtaining effective structural changes either by complexing or copolymerization or otherwise are judged to be intermediate.

The development of new anti-SCA coatings represents a monumental task because of all the other principal requirements that space-stable low  $\sigma_g/\epsilon$  coatings must meet. Here too there are two basic approaches. The first is through the modification of current electrically conductive polymers; the second, through the development of new polymers.

Of considerable importance in all of the above conclusions and observations are the criteria for evaluating acceptable properties and performance of anti-SCA coatings. We are concerned that the lack of any correlations of electrical conductivity with anti-SCA performance detracts seriously from the relevance of most measurements of electrical properties. It may not even be proper to claim that materials with low surface or bulk resistivity are better anti-SCA materials than those with high values, unless, for instance, the resistivity vs applied electrical stress characteristics are known and accounted for.

In summary, the results of this program indicate that inorganic coatings are viable materials for both immediate and near term practical anti-SCA materials. Organic coatings will require substantial investments in time and funds. The necessity to meet conventional requirements for space-stable low  $\sigma_g/\epsilon$  materials assures a long developmental period.

## Acknowledgments

The authors wish to thank T. Yamauchi (IITRI) and Marge Miller (DeSoto) for assistance in the experimental work of the program.

## References

1. Rosen, A. (1975) Large discharges and arcs on Spacecraft, AIAA J. (Am. Inst. Aeronaut. Astronaut.) June:36-44. See also Rosen, A. (1975) Spacecraft charging: environment-induced anomalies. Paper No. 75-91 presented at AIAA 13th Aerospace Sciences meeting, Pasadena, California.
2. Inouye, G. T. (1975) Spacecraft charging model. Paper No. 75-255 presented at AIAA 13th Aerospace Sciences meeting, Pasadena, California.
3. Meulenberg, A., Jr. Evidence for a New Discharge Mechanism for Dielectrics in a Plasma (to be published).
4. Dolinski, R. J., and Deau, W. R. (1971) Chem. Tech. May:304-309.
5. Schaper, R. J., Seese, K. A., Sinkovitz, G. D., and Slagel, R. C. (1971) TAPPI, Reprography Conference Collection of papers, p. 75.
6. Hoegl, H. (1956) J. Phys. Chem. 69:755.
7. Kriz, K. (1972) Photographic Science and Engineering 18:58.
8. Goodings, E. P. (1976) Conductivity and super conductivity in polymers, Chem. Soc. Rev. (London) 5(1):95-123.
9. Dow Chemical Co., Dow ECR 34 Electroconductive Resin, Bulletin 191-40-70.
10. Merck and Co., Inc. Merck Chemical Division, Bulletin PA 20441072.
11. Kingery, W. D. (1960) Introduction to Ceramics, Wiley and Sons, Inc., N. Y.

N 78-10-103

**Contents**

1. Introduction	614
2. Formulation of Coatings	614
3. Qualification of Electrically Conductive Coatings	618
4. Conclusion	619
Acknowledgments	620
References	620

**4. Formulation of Electrically Conductive Thermal-Control Coatings**

Michael C. Shel  
Space Environment and Simulation Branch  
Engineering Services Division  
NASA/Goddard Space Flight Center  
Greenbelt, Maryland

**Abstract**

Formulation of electrically conductive, thermal-control coatings was undertaken for use on the International Sun Earth Explorer (ISEE) spacecraft. The primary effort was aimed at formulation of a coating with bulk resistivity less than  $1 \times 10^5$  ohm-m<sup>2</sup> and optical absorptance and normal emittance of approximately 0.55 and 0.90, respectively. The required stability in space called for bulk resistivity less than  $1 \times 10^5$  ohm-m<sup>2</sup>, absorptance less than 0.67 and normal emittance of 0.90 after exposure to approximately  $4 \times 10^{16}$  proton/cm<sup>2</sup> of solar wind particles and 5300 equivalent sun hours. These exposures represent two years of the ISEE orbit.

Unsuccessful formulation efforts as well as the successful use of oxide pigments fired at 1175°C are described. Problems attributed to reactivity of specific coating vehicles exposed to high humidity are discussed.

Measurement and testing methods, including resulting data are mentioned, but the emphasis, in this report, is placed on coating formulation and application techniques. Methods of varying, as desired, optical properties are also described as well as formulations of white, low-absorptance coatings.

**CONFIDENTIAL**

## 1. INTRODUCTION ----

The Engineering Applications Branch at the Goddard Space Flight Center was given the task of developing a coating for the International Sun Earth Explorer (ISEE) spacecraft that not only had to meet the specifications of the thermal design engineers, but in addition, the thermal control coating had to be electrically conductive. Electrical conductivity was necessary to prevent charge buildup on the exterior of the spacecraft which would interfere with the detection of low-energy level plasma waves and thermal electrons. Specifically, we were confronted with the task of developing a coating which would have the following properties:

- (1) Solar absorptance of 0.55,
- (2) Thermal emittance of 0.90,
- (3) Area-resistance of less than  $1 \times 10^5$  ohm-m<sup>2</sup>,
- (4) Environmental lifetime of two years in the solar wind environment, with less than 0.07 change in optical absorptance value.

## 2. FORMULATION OF COATINGS

During the early stages of developing the conductive coatings, numerous formulations were tried with varying degrees of negative results. The basic laboratory efforts were more of trial-and-error processes. After many false starts, including the obvious attempt of adding metals such as gold and chromium to standard binders, a formulation with fired pigment oxides was made. The optical and electrical resistivity characteristics were most promising. Thereafter, all attention was directed to coating formulations based upon both sodium and potassium silicate binders containing fired oxide pigments added in such proportions as to optimize the absorptance and conductance (area-resistance product).

### 2.1 Sodium Silicates (See Table 1)

#### 2.1.1 MATERIALS

Sp500 zinc oxide was obtained from New Jersey Zinc Co.; the aluminum oxide (Type C) from Union Carbide; and sodium silicate (Star) from Philadelphia Quartz Co.

#### 2.1.2 PREPARATION OF PIGMENTS

The required amounts of pigment oxides (by weight) are added to distilled water and slowly stirred for five hours. This slurry is initially heated for 48 hr at 90°C and then for an additional 72 hr at 110°C. The pigments are fired at 1175°C for 15 min in 50-g batches. In the final preparation stage, the pigments are ground and sieved to select the desired particle sizes. The desired optical properties, absorptance and emittance, are determined by the relative amounts added to

the binder. For example, NS43E which has an  $\bar{\alpha}$  of 0.57 to 0.60 and  $\rho_d$  of  $2 \times 10^3$  ohm-cm<sup>2</sup>, contains a pigment mixture of fired 98 percent ZnO, 1 percent Co<sub>3</sub>O<sub>4</sub> and 1 percent Al<sub>2</sub>O<sub>3</sub> which is then combined with an equal amount of a pigment composed of fired 99 percent ZnO and 1 percent Al<sub>2</sub>O<sub>3</sub>.

Table 1. Formulation of Electrically Conductive, Thermal-Control Coatings with Sodium and Fired Oxides

GSFC CODE #	PIGMENT - %			VEHICLE-BINDER			PIGMENT CONCENTRATION	WATER	
	Al <sub>2</sub> O <sub>3</sub>	ZnO	Co <sub>3</sub> O <sub>4</sub>	WT-RATIO SiO <sub>2</sub> /Na <sub>2</sub> O	% Na <sub>2</sub> O	% SiO <sub>2</sub>			WEIGHT-RATIO BINDER: PIGMENT
NS 43G	1	99		2.50	10.6	26.5	25:75	5%	
NS 53B	1	98.75	0.25	2.50	10.6	26.5	25:75	5%	
NS 43E	A		B		WT-RATIO SiO <sub>2</sub> /Na <sub>2</sub> O	% Na <sub>2</sub> O	% SiO <sub>2</sub>	WEIGHT-RATIO BINDER: PIGMENT	5%
	Al <sub>2</sub> O <sub>3</sub>	ZnO	Co <sub>3</sub> O <sub>4</sub>	Al <sub>2</sub> O <sub>3</sub>					
	1	98	1	1	99	2.50	10.6	26.5	
	WEIGHT-RATIO								
	A	B							
	50%	50%							

### 2.1.3. FORMULATION AND APPLICATION

The conductive pigments are added to the silicate solution (Star) in a binder-pigment ratio of 25:75 by weight and thinned with distilled or deionized water not exceeding 5 percent of the total of pigment plus binder. The mixture is stirred with a teflon-coated magnet in a 250 ml beaker for approximately 2 hrs, allowed to set for 10 to 12 hr and finally stirred for 2 hrs before application. The coating is then sprayed with compressed, dry nitrogen on the suitably prepared surface. The coating is applied with slow, overlapping strokes with a spray gun held about 6 in. from the surface. The first layer should be allowed to dry for several minutes before the second coat is applied. Caution must be used in applying all coats to avoid dry spray which is caused by applying the coating too fast or having a spray which is too thin.

### 2.1.4 OPTICAL AND ELECTRICAL PROPERTIES

A Beckman DK-2A with a Gier-Dunkle reflectance attachment is used to make absolute reflectance measurements in air before and after testing of all samples

to determine their absorptance. Shown in Figure 1 are three representative samples formulated with the sodium silicate binder. The absorption effects of the fired green oxides are due to the cobalt oxide.

Normal total emittance measurements are also made at room temperature with a DB-100 Portable Emittance Meter.

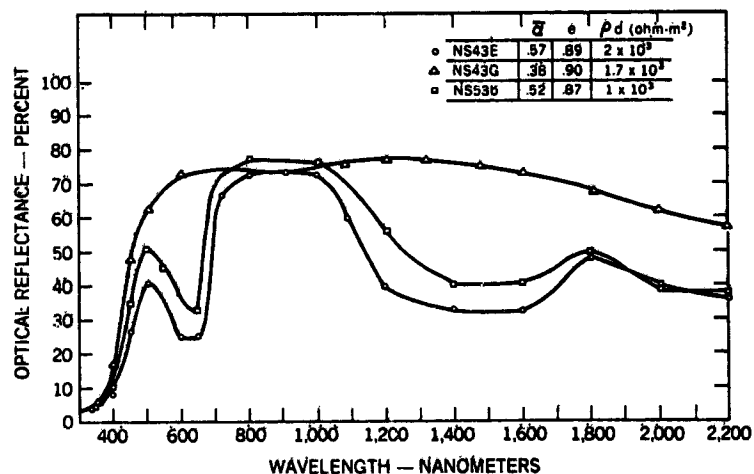


Figure 1. Optical Reflectance of Electrically Conductive, Thermal-Control Coatings Formulated with Sodium Silicate Binder

## 2.2 Potassium Silicate

### 2.2.1 FORMULATION OF PIGMENTS AND BINDER

The formulation of the potassium silicate coatings is basically the same as that of the sodium silicates. Referring to Table 2, potassium silicate PS-7 purchased from Sylvania is used as the binder for coatings NS43C and NS55F. The fired-oxide pigments are prepared as previously described for the sodium silicate coatings.

### 2.2.2 OPTICAL AND ELECTRICAL PROPERTIES

The reflectance of two distinctly different types of electrically conductive coatings are shown in Figure 2. NS43C has excellent reflectance properties and is sufficiently conductive  $1 \times 10^5$  ohm-m<sup>2</sup> to fall within the specifications of the ISEE Program.

Table 2. Formulation of Electrically Conductive, Thermal-Control Coatings with Potassium Silicate and Fired Oxides

GSFC CODE #	PIGMENT - %			VEHICLE-BINDER			PIGMENT CONCENTRATION	WATER	
	Al <sub>2</sub> O <sub>3</sub>	ZnO	Co <sub>3</sub> O <sub>4</sub>	WT-RATIO	%	%			
NS43C	1	99		CCI*/K <sub>2</sub> SiO <sub>3</sub>	K <sub>2</sub> O	SiO <sub>2</sub>	WEIGHT-RATIO BINDER: PIGMENT 25: 75	5%	
				1:1	11.3	23.7			
ADD 1 PART OF ABOVE FORMULATION TO TWO PARTS GSFC-MS74									
NS 55F	A		B		WT-RATIO	% K <sub>2</sub> O	% SiO <sub>2</sub>	WEIGHT-RATIO BINDER: PIGMENT 25: 75	5%
	Al <sub>2</sub> O <sub>3</sub>	ZnO	Co <sub>3</sub> O <sub>4</sub>	Al <sub>2</sub> O <sub>3</sub>					
	1	98	1	1	99	1:3.31	11.3	23.7	
	WEIGHT-RATIO								
	A		B						
	50%		50%						

\*GSFC FORMULATION COMPOSED OF LITHIUM AND POTASSIUM SILICATES.

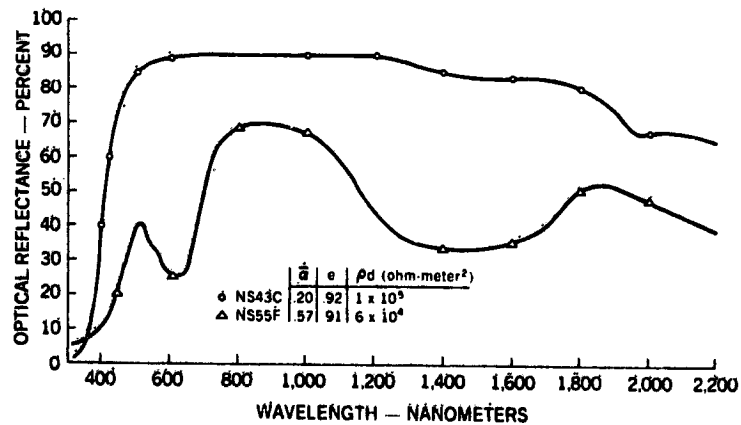


Figure 2. Optical Reflectance of Electrically Conductive, Thermal-Control Coatings Formulated with Potassium Silicate Binder

### 3. QUALIFICATION OF ELECTRICALLY CONDUCTIVE COATINGS

#### 3.1 Electrical Resistivity Measurements

A separate phase of the coatings development program and one which we found just as challenging, has been the measurement of the conductivity (area-resistivity). Our previous experience in the optical measurement and space environment simulation has been extensive so no difficulties were encountered. However, the measurement of the area resistance has proven to be more than we bargained for. Problems with reproducibility, coating stability, experimental measurement techniques, to name a few, made it necessary to separate this qualification from our coatings formulation efforts. All area-resistance data is the work of Walter Viehmann who will present in a later paper the details of his contactless resistivity measurements.

#### 3.2 Environmental Test Data

##### 3.2.1 UV DEGRADATION

One of the most promising features of this family of fired-oxide coatings is their capability to withstand extremely high levels of UV radiation. Samples from each formulation after exposure to 1000 hr in a high vacuum environment showed virtually no change in optical surface reflectance. The source in this screening test set-up is a low pressure mercury lamp which has more than 45 percent of the output energy below 400 nm.

##### 3.2.2 SOLAR WIND

The principal source of possible damage to the coatings on the exterior spacecraft surfaces is their bombardment by high fluence levels of low-energy protons contained in the solar wind and solar flares. The relatively constant stream of low-energy protons continuously emitted from the sun has a flux of approximately  $2.5 \times 10^8$  p/cm<sup>2</sup>/sec and an average energy of 1 keV with a maximum of the order of 50 keV. The ISEE spacecraft is expected to encounter roughly  $2 \times 10^{16}$  p/cm<sup>2</sup> low-energy protons during a two-year period. As a consequence, the GSFC Solar Wind Test Facility was used to determine the degradation rates of the conductive coatings. Shown in Figure 3 are the optical degradation of coatings which have been selected for use on the spacecraft. The coatings were exposed to 5 keV protons to a fluence of  $4 \times 10^{16}$  p/cm<sup>2</sup> and simultaneously irradiated with UV energy. Previous test data taken in other UV degradation test facilities have shown these samples to be highly UV tolerant. Therefore, the changes in the optical properties of these coatings have been attributed mainly to the effects of the low-energy protons. After exposure to an equivalent two-year orbital lifetime the electrical and optical properties are well within the ISEE specifications.

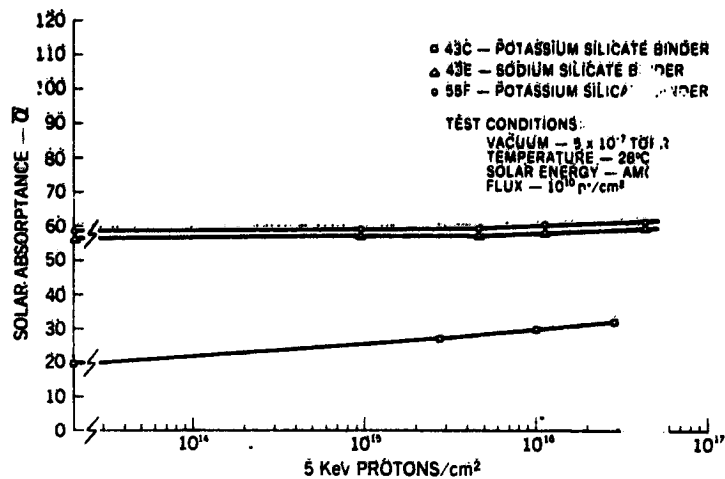


Figure 3. Degradation of Coatings Exposed to UV and Low-Energy Protons

### 3.3.3 THERMAL-VACUUM CYCLING

The conductive coatings have been thermal cycled from  $-150^{\circ}$  to  $+150^{\circ}\text{C}$  for a total of 66 cycles of 90-min duration. No damage was visible on any of the samples and all of them passed a "scotch tape" adhesion test.

## 4. CONCLUSION

The electrically conductive coatings formulated with potassium and sodium silicate binders and fired-oxide pigments have met all specifications required by the ISEE Program. A summary of their optical and electrical properties are outlined in Table 3. As we have previously reported, these coatings are now flight qualified after having passed all phases of the environmental testing which included UV, low-energy proton (solar wind), and thermal-vacuum cycling. They are now being applied to portions of the spacecraft.

**Table 3. Summary of Environmental Test Data of Electrically Conductive, Thermal-Control Coatings**

	AREA RESISTANCE $\rho_d$ (ohm-m <sup>2</sup> )	ABSORPTANCE $\alpha$	EMITTANCE $\epsilon$
NS 43G	$1.7 \times 10^3$	.38	.90
NS 53B	$1 \times 10^3$	.52	.87
NS 43E	$2 \times 10^3$ ohm-m <sup>2</sup>	.57	.89
NS 43C	$1 \times 10^5$ ohm-m <sup>2</sup>	.20	.82
NS 55F	$6 \times 10^4$ ohm-m <sup>2</sup>	.57	.91

### Acknowledgments

Formulation and development of the coatings has been the responsibility of Charles Shai. Qualification and environmental tests were performed by Danny Lester, James Mullins, Lawrence Bromery, Frank Paczkowski, and John Henninger under the supervision of Jule Hirschfield. Resistivity measurements were made by Walter Viehmann. The entire program was supported by ISEE Project. R. Hoffman and J. Triolo of the Thermal Systems Branch have provided continual input during the qualification stages. Joseph Colony of the Materials Branch provided technical consultation support.

### References

1. Bentlage, H., Spanier, H., and Wilkens, W. Changes in Electrical Cross-Resistance of Conductive Coatings Due to Contamination by Outgassing of Silicon Rubber Material Silastic 35.
2. Electrically Conductive Coating Materials. General Electric Report, Air Force Materials Laboratory, TR-73-207 Parts I and II.
3. Philadelphia Quartz Bulletin 17-1.

## Contents

1. Introduction	622
2. Materials Testing	623
3. Approaches to the Problem	626
4. Baseline Data: Results of Screening Tests	634
5. Static Charge Testing	635
6. Conclusions	653
Acknowledgments	654
References	654

## 5. Materials and Techniques for Spacecraft\* Static Charge Control

L.J. Amore and A.E. Eagles  
General Electric Company  
Space Division  
Valley Forge, Pennsylvania

### Abstract

An overview of the design, development, fabrication, and testing of transparent conductive coatings and conductive lattices deposited or formed on high resistivity spacecraft dielectric materials to obtain control static charge buildup on spacecraft external surfaces is presented.

Fabrication techniques for the deposition of indium/tin oxide coatings and copper grid networks on Kapton and FEP Teflon films and special frit coatings for OSR and solar cell cover glasses are discussed. The techniques include sputtering, photoetching, silkscreening, and mechanical processes.

A facility designed and built to simulate the electron plasma at geosynchronous altitudes is described along with test procedures. The results of material characterizations as well as electron irradiation aging effects in this facility for spacecraft polymers treated to control static charge are presented. The data presents results for electron beam energies up to 30 kV and electron current densities of  $30 \text{ nA/cm}^2$ . Parameters measured include secondary emission, surface leakage, and through the sample currents as a function of primary beam energy and voltage.

\*This work was supported by the Air Force Materials Laboratory under Contracts F33615-76-C-5075 and F33615-76-C-5258.

## 1. INTRODUCTION

The primary means for maintaining reasonable operating temperatures within a spacecraft is by discretely adjusting the amount of energy absorbed from the sun and the amount that is radiated at the infrared wavelength corresponding to the local surface temperature. This technique is known as passive temperature control and is highly dependent on the reflective and emissive properties of the materials located on the external surfaces. Surface temperatures and subsequently the overall spacecraft equilibrium temperature can be adjusted using active or semiactive techniques such as louvers that are opened and closed to effectively change the reflective and emissive properties in the louver area. Heat pipes have been used to move internally generated heat to the surface where it can be radiated efficiently to space.

To achieve passive thermal control, dielectric insulating materials must necessarily be used, because only these materials have the combination of inherent high solar reflectance and high emittance required for acceptable thermal balance. This class of materials includes back surface aluminum and silver coated FEP Teflon films, high purity silica glass thermal control materials, and Kapton and Mylar films used in multilayer insulation blankets.

In geosynchronous orbit these dielectric materials are directly exposed to bombardment by the indigenous electron plasma. As electrical insulators they support charge buildup until dielectric breakthrough or arcing to areas or components of lower potential occurs. The results of these incidents include degradation of material, thermo-optical, and mechanical properties and disruption of components operating at radio frequencies by the electromagnetic noise generated by an arc.

The purpose of this study is to develop materials and techniques to control static charge buildup on conventional spacecraft coatings and materials for use during geosynchronous orbit satellite missions. This study represents the progress made during the first six months of a planned 24-month program. The results are preliminary, but significant progress has been made to indicate that transparent conducting oxide overlay coatings and conducting grids or screens placed over dielectric surfaces offer potential solutions to the problem.

The materials investigated thus far in the study include:

- (1) Aluminized FEP Teflon films used extensively as a high emittance, solar reflecting second surface mirror thermal control coating.
- (2) Back surface aluminized Kapton film used as a top layer for multilayer insulation blankets.
- (3) Optical Solar Reflecting (OSR) tiles which perform similar to the FEP film coating described above, but consisting of an 8 mil thick slice of 7940 Silica glass with a back surface coating of silver, then Inconel, to produce a second surface mirror, and

- (4) Glasses, such as Corning 7940 and microsheet used to cover silicon solar cells.

## 2. MATERIALS TESTING

### 2.1 Philosophy and Approach to Static Charge Control Testing

In a materials development program fundamental material parameters are of major importance, because as materials are developed and observed in a simulated space environment it is necessary to identify those characteristics responsible for the observed behavior. With this in mind a facility was developed which could both observe behavior in a simulated environment and then perform the fundamental measurements associated with surface phenomena. If we can identify the location and motion of all charged particles within a closed system we will be well on the way to identifying and defining the processes taking place on and within the material being studied.

In meeting this objective it is necessary to know the flux, energy distribution, and spatial distribution of the flood gun beam so all charges arriving at the surface under test are known. It is required to have a secondary charged-particle collector to identify and quantize all charges leaving the surface and means of measuring the current diffusing through the surface to the substrate upon which the sample has been mounted. Lastly, a capability is needed to measure that charge which is residing on the surface itself.

Another important consideration is in simulating the high pumping speed within the closed system that an exposed surface in deep space would see. Here pumping speed is more important than ultimate pressure as a material under particle bombardment will evolve gas resulting in a high pressure very close to the surface. At localized pressures around  $10^{-3}$  Torr or higher, discharge phenomena not common to a deep space environment will occur and could result in improper conclusions during experimental work. These problems are alleviated only through a system with very high pumping speed in pressure regions greater than  $10^{-4}$  Torr. Vacion and vacion triode pumps cannot pump efficiently at pressures greater than  $10^{-4}$  Torr to  $10^{-1}$  Torr. Augmented diffusion pumps on the other hand have their peak pumping speed between  $10^{-4}$  and  $10^{-2}$  Torr. By placing a booster in the foreline of a 500-1/sec diffusion pump, its speed can be increased up to 2500 1/sec in the critical region between  $10^{-4}$  and  $10^{-6}$  Torr.

### 2.2 Electrostatic Discharge (ESD) Test Facility

Using the criteria established in the previous section a system was designed and built at GE. The system is shown schematically in Figure 1 and in the photographs

of Figure 2. The chamber is large enough to provide adequate pumping volume and room to work inside through large access ports when placing and adjusting samples for evaluation.

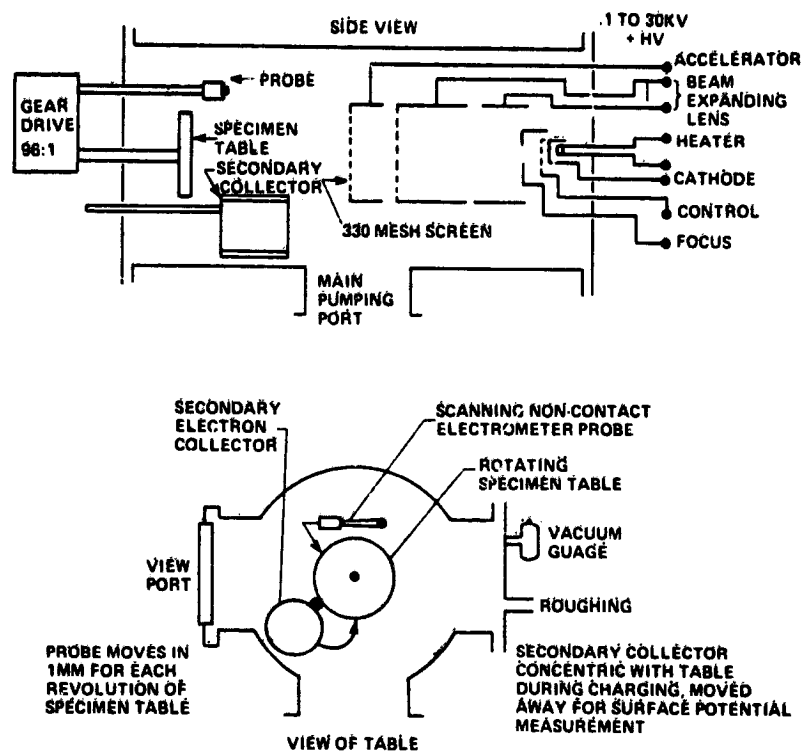
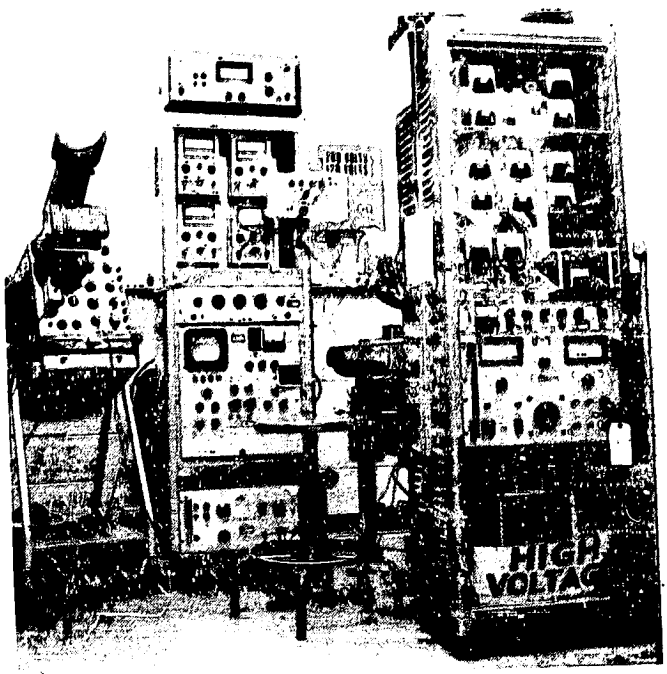


Figure 1. Functional Diagram of ESD Test Facility

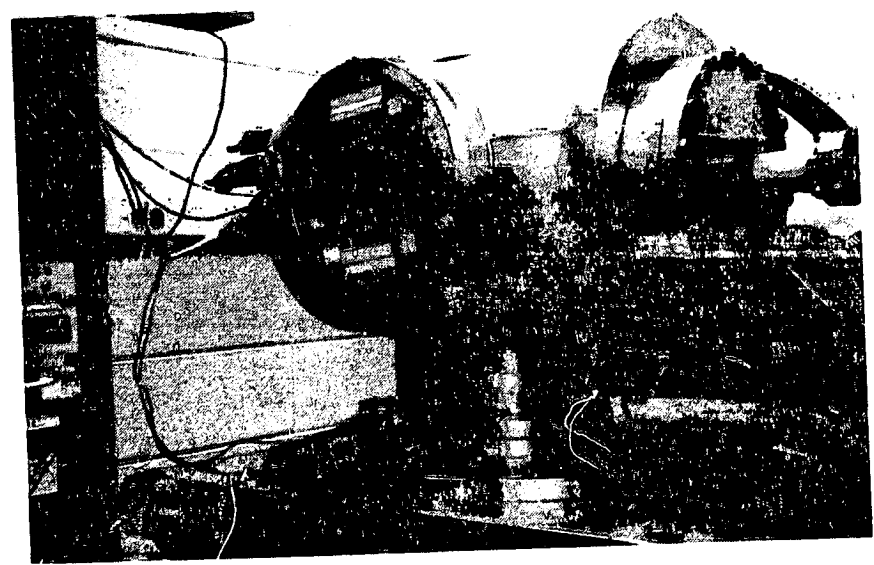
At the heart of the facility is the electron flood gun which is used to simulate the space environment with respect to charged particle bombardment. It should be noted that this facility does not make provisions for ion and proton bombardment; however, Knott<sup>1</sup> and others have shown that these do not significantly affect spacecraft charging, since they have a lower probability of striking the spacecraft. The electron flood gun was designed to simulate the electron environment measured at ATS-5 as modified by more recent data from ATS-6. The design of the gun includes an electrostatic, three-element lens to assure uniform beam expansion in the restricted space of the chamber, control grids which can be modulated to simulate the measured electron energy distribution, and a wide range of adjustment in flux density.

The specimen diagnostic assembly is mechanically the most complicated sub-assembly but it has great versatility for the measurement of fundamental properties.

ORIGINAL PAGE IS  
OF POOR QUALITY



a. Associated Diagnostic Equipment



b. Close-up of Vacuum Chamber

Figure 2. ESD Facility

It consists of an electrically isolated rotating table for holding specimens up to a 5-in. diameter. By measuring the current flowing through the table the diffusion current through the specimen may be monitored. A non-contact surface potential probe is mounted on a movable arm which is connected through a gear box to the rotating table. The gear ratio is such that for every rotation of the table the probe arm is advanced in millimeter steps allowing the probe to track the surface of the sample much like a tone arm tracks a record on a phonograph. This motion is driven by a dc reversible electric motor which is also coupled to a resistance commutator for driving one axis of an X-Y recorder. A Monroe model 144 probe is used that has high resolution and is relatively independent of probe-to-surface distance. The electronics incorporates a phase-lock loop amplifier for the reduction of spurious/pick-up, and noise. During the bombardment phase of the tests this probe can be swung completely out of the way so no part of it will shadow the sample during charging.

A secondary electron collector ring is also part of the assembly which is swung in place around the sample during the charging phase and it is used to monitor charged particles leaving the surface of the sample. By pulsing the flood gun beam it can also measure the secondary emission ratio of the specimen under test. With slight modification this electrode may also be used to monitor surface erosion products during charging similar to the experiments performed by Nanewicz<sup>2</sup> of Stanford Research Institute.

### 3. APPROACHES TO THE PROBLEM

#### 3.1 Transparent Oxides

The most commonly used transparent conductive coatings are combinations of indium and tin oxides (ITO) or indium oxide, doped with fluorine or antimony. These coatings were first developed for heating canopies of aircraft, transparent back conductors for liquid crystal displays.

The techniques for depositing these materials onto varied geometries has mushroomed over the past four years, varying from vacuum vapor deposition, chemical vapor deposition, dc sputtering, RF diode sputtering, and magnetron sputtering techniques.

The one primary objective in depositing transparent conductors of metallic oxides is to closely control the doping cations or oxygen vacancies. Over oxidation causes the film to be highly electrically resistive. Under oxidation causes the film to be highly metallic or brown; the proper balance of oxygen pressure during evaporation results in a coating that is transparent and conductive.

The electrical conductivity of sputtered ITO films decrease as the partial pressure of oxygen rises beyond  $1 \times 10^{-5}$  as can be seen in Figure 3. This data was taken from measurements using RF diode sputtered films of ITO on microsheet substrates. Recent results using magnetron sputtering where the glass surface is cool during deposition have also supported the ITO coatings dependence on partial pressure of oxygen.

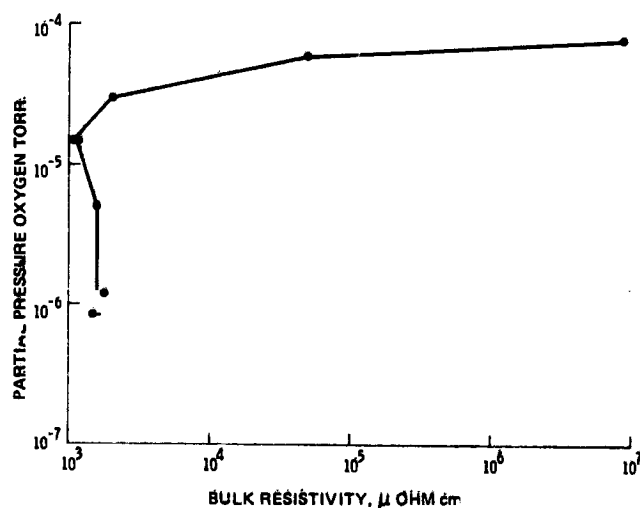


Figure 3. Resistivity of Sputtered Indium Oxide/Tin Oxide Films

ITO and indium films were prepared on Kapton and FEP by conventional vapor deposition from a crucible source, dc coaxial sputtering and magnetron sputtering. All techniques have been successful for ESD applications and Table 1 shows the base variations in surface resistivities obtained from three different techniques.

Based on measurements to date, 250 Å of ITO have measurable but no catastrophic effect on  $\alpha/\epsilon$  characteristics of films. Tables 2 and 3 give electrical and optical data for ITO films deposited by sputtering techniques on FEP and Kapton thin film substrates.

Other conductive variations of semiconductor coatings are currently being considered such as cadmium stannate and also variations of aluminum oxide and oxides of chrome.

Table 1. Surface Resistivities of 100 Å Films Deposited by Various Techniques

	Coaxial	Magnetron	In <sub>2</sub> O <sub>3</sub> Filament
Kapton	100 K	7.9 K	5 × 10 <sup>7</sup>
FEP	200 K	7.9 K	5 × 10 <sup>7</sup>
Microsheet Coverglass	90 K	7.9 K	5 × 10 <sup>7</sup>

Table 2. Electrical and Optical Characteristics 90% In<sub>2</sub>O<sub>3</sub> / 10% (ITO) Coated FEP

FEP Thickness	Resistance kΩ/□	ITO Thickness, Å	(Visible) Transmission
0.002	76 - 318	250 ± 50	0.91
0.002	115 - 352	250 ± 40	0.90
0.005	183 - 450	250 ± 50	0.87
0.002	5.16 - 21.3	500 ± 50	0.80
0.002	9.2 - 35.3	500 ± 50	0.81
0.002	27 - 48.1	500 ± 50	0.81
0.005	8.1 - 52.3	500 ± 50	0.80
0.005	46 - 86	900 ± 50	0.77
0.005		Uncoated	0.94
0.002		Uncoated	0.95

Table 3. Electrical and Optical Characteristics 90% In<sub>2</sub>O<sub>3</sub> / 10% SnO<sub>2</sub> (ITO) Coated Kapton (2 mil)

ITO Thickness, Å	Resistivity kΩ/□	(Visible) Transmission
900	0.45 - 0.75	56.6
900	0.45 - 0.75	53.1
500	3 - 7	59.4
500	3 - 7	58.7
250	80 - 150	59.9
250	80 - 150	59.9
Uncoated	10 <sup>10</sup>	60.0

3.1.1 PRELIMINARY SCANNING ELECTRON MICROSCOPE (SEM)  
ANALYSIS OF KAPTAN AND ITO COATED KAPTAN

Surface characteristics of Kapton and ITO coated Kapton were observed with an electron microscope at 10,000X (see Figures 4, 5, and 6). Figure 4 reveals a uniform Kapton surface with no evidence of imperfections. Figure 6 reveals a surface that underwent severe flexing (180° bend) with subsequent micro-fracturing of the film. This defect did not affect the conductivity of the film under electron beam bombardment as will be described later.



Figure 4. Uncoated Kapton Surface (at 10,000X)



Figure 6. Microcracks in 500 Å ITO Coating on Kapton After Severe Flexing (180° Bend) (at 10,000X)



Figure 5. Kapton Coated with 500 Å of ITO (at 10,000X)

### 3.2 Conductive Grids

Conductive lattices were prepared by various techniques on Kapton, Teflon, and Mylar. A summary of the work follows.

#### 3.2.1 PHOTOETCHING

General Electric's standard microcircuit photoetching techniques were used to form grid patterns on copper coated Kapton substrates. In our first trial a 1/2-in. pattern was successfully obtained having a line pattern 0.015 in. wide and 1000 Å thick. The techniques allow processing of line patterns as thin as 0.001 in. and thicknesses in the 100 to 200 Å range. The copper lattice on Kapton film shown in Figure 7 was prepared by the following process:

- (1) Art work is generated to produce the desired grid pattern,
- (2) The art work is photo-reduced to the desired dimensions and a negative is produced,
- (3) An appropriate thickness of copper is vapor deposited on the dielectric film,
- (4) Photo-resist is deposited on the copper coating,
- (5) The negative is placed over the photo-resist and is illuminated with ultra-violet radiation,
- (6) The UV exposed pattern is placed in a developing solution and then baked at 120°F,
- (7) The developed pattern is rinsed in aqueous solution to remove the developed photo-resist leaving the desired pattern which is then:
  - (a) flushed with alcohol and dried,
  - (b) etched in chromic acid,
  - (c) rinsed with water, and
  - (d) rinsed with MEK or trichloroethylene.

#### 3.2.2 PYRALUX FOIL

Grids on Kapton films of thicknesses greater than 0.003 in. up to 0.015 in. can be photoetched from DuPont's Pyralux, thin foil copper clad Kapton. This material is formed using a process whereby the surface of the Kapton undergoes an activation process which permits laminating the Kapton surface with copper and results in a well adhering laminate. These clads are reported to be used where fine lines and spacings are required. Etched edges are sharper than those resulting from thin film etching, thus minimizing field emission problems resulting from feathered edges, under electron bombardment.

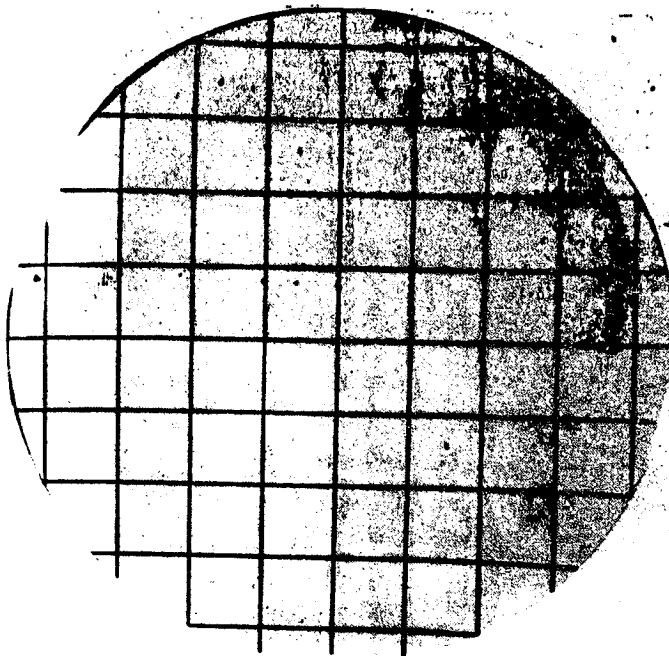


Figure 7. Photoetched Copper Lattice on Kapton ..

### 3.2.3 MESH IMBEDMENT

The challenge to laminate fine wire mesh into FEP has been a most difficult one. Initial samples appeared to have all the proper mechanical characteristics except aluminum wire bond disrupted during flexure testing. Current tests indicate that meshes of zinc, nickel, or silver attain a superior FEP to metal bond.

Mesh material laminated into FEP thus far have yielded bond strengths only up to 2 lb/inch.

### 3.2.4 SILK SCREENING TECHNIQUES

Silk screening masks with pitch varying from  $3/8$  to  $3/4$  in. have been fabricated. A silver epoxy screening material, No. 11095, manufactured by Electroscience Laboratories, Pennsauken, New Jersey, appears to be very promising. The process for silk screening is not anticipated to present a problem. It offers potential as a conductive surface for ground strap connections, for mechanical interconnects and as a solderable surface.

### 3.3 OSR and Solar Cell Cover Glass Modification

Four coatings were investigated for glass modification. One was aluminogermanoborate glass modified with oxides of zinc, lead, and lithium. Another

was a lithium borosilicate modified with oxides of lanthanum, tantalum, zinc, and cerium. The other two were commercially available aqueous potassium silicates. The coatings were applied to Pyrex glass coupons about 0.75 in. x 0.76 in. x 0.010 inch. Transmittance data were obtained on all of the specimens. Surface resistivity data were obtained for all specimens except the lithium borosilicate coating.

The aluminogermanoborate and lithium borosilicate glasses were developed several years ago under AFML Contract F3316-71-C-1656. The former was designated GE-5973-8; the latter is GE-1TL. Both were selected for the current program because of their very good transmission and resistance to beta irradiation. Very fine particles ( $\sim 10 \mu$ ) of each glass were suspended in isopropyl alcohol and the slurry was gently poured onto a coupon of the Pyrex glass described previously.

After sufficient time for a sedimented layer to form, the excess slurry is siphoned off, the coated Pyrex coupon is dried and then fired at  $550^\circ\text{C}$  for times which vary with the composition. Usually, a time between 5 and 10 min is sufficient to bond the glass particles to each other and to the pyrex coupon. Subsequent examination revealed no stresses on the coated Pyrex compared to an uncoated Pyrex coupon.

\*Kasil No. 1 and \*Kasil No. 6, the aqueous potassium silicates, are proprietary, trademark registered products of the Philadelphia Quartz Company. The No. 1 material has a  $\text{K}_2\text{O}/\text{SiO}_2$  ratio of 1:2.5; the No. 6 material has a  $\text{K}_2\text{O}/\text{SiO}_2$  ratio of 1:2.1. Both silicates are commercially available as liquids which can be applied as thin coatings by spraying, brushing or dipping.

Kasil No. 1 and Kasil No. 6, as received from the manufacturer, were applied to the Pyrex coupons. In addition, Kasil No. 1 was modified with 0.5 percent  $\text{CeO}_2$  and applied to Pyrex coupons. In all cases, the silicate coatings were dried at  $100^\circ\text{C}$  for two hours.

The transmittance of uncoated Pyrex and each of the uncoated specimens is shown in Figure 8. Examination of this data reveals that in the wavelength region of 0.3 to about  $1.7 \mu$  there is very little difference in transmission between the uncoated Pyrex and the silicate-coated Pyrex specimens. In the same range of wavelengths, the aluminogermanoborate coated Pyrex specimens exhibit slightly less transmission than the control specimen. The lithium borosilicate coated Pyrex transmission is identical to that of the uncoated control sample throughout the measurement spectrum, except for a slight absorption (due probably to the OH radical) at about  $3.6 \mu$ . The difference in transmission for the two 5973-8 coated specimens is due to the difference in thickness of the coatings. One (No. 2 specimen) is 0.4 mil thick; the other (No. 3 specimen) is 0.6 mil thick which represent a 50 percent increase in coating thickness. Electrical resistivity data shown in Table 4 indicates that this property is significantly reduced by all of the coatings with the aqueous silicate coatings having the greatest effect.

\*Kasil is a trademark of Philadelphia Quartz Co.

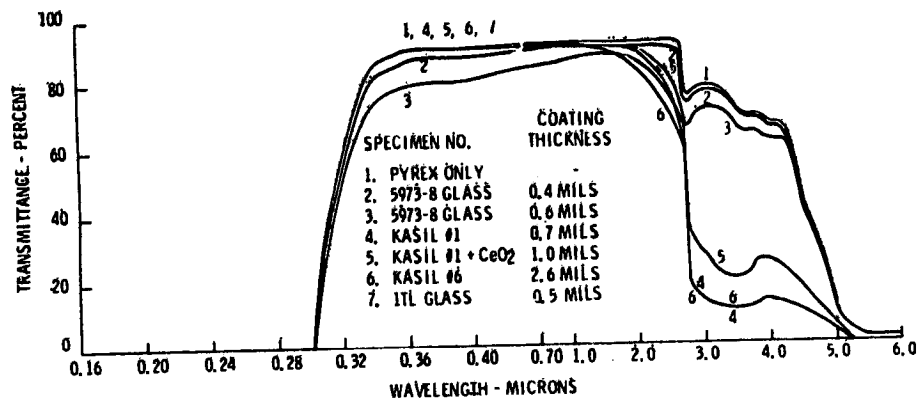


Figure 8. Transmittance of Coated and Uncoated 10-mil Pyrex Coupons

Table 4. Electrical Resistivity of Frit Coated Glasses

Speciman No.	Coating	Coating Thickness (Mils)	Electrical Resistivity ( $\Omega/\square$ )
1	None	None	$10^9$
2	5973-8 Glass	0.4	$6.0 \times 10^8$
3	5973-8 Glass	0.6	$4.0 \times 10^8$
4	Kasil No. 1	0.7	$3.2 \times 10^6$
5	Kasil No. 1 CeO <sub>2</sub>	1.0	$8.0 \times 10^6$
6	Kasil No. 6	2.6	$6.0 \times 10^6$
7	ITL Glass	0.5	$5.0 \times 10^8$

#### 4. BASELINE DATA: RESULTS OF SCREENING TESTS

The initial phase of this program was concerned with establishing the performance level of some typical spacecraft materials. The simulated space tests were conducted in the facility described previously. These tests established the onset of discharging for the four materials listed in Table 5 at a current density of  $30 \text{ nA/cm}^2$ . The point of discharge was determined visually in a darkened room. The qualitative data collected is typified in the photograph of Figure 9, which shows arcing along the edges of the  $1 \times 1$  in. tiles in the OSR mosaic.

Table 5. Summary of Static Charging Screening Tests at 30 nA/cm<sup>2</sup>

Material	Onset of Discharging, kV
Kapton, 2 mil - back surface aluminized	12 - 15
FEP Teflon, 5 mil - back surface silvered	20
Optical Solar Reflecting (OSR) coating mosaic	12
Solar Array Composite, 0211 microsheet over 2 x 2 cm cells	12

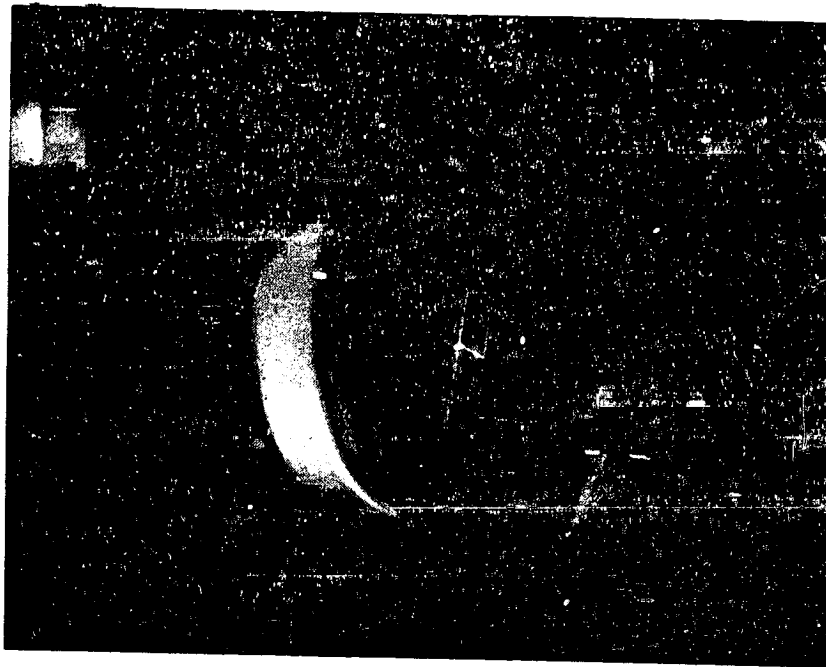


Figure 9. Arcing on an OSR Mosaic Under 15 kV - 30 nA/cm<sup>2</sup> Electron Bombardment

## 5. STATIC CHARGE TESTING

### 5.1 Introduction -

Polymer materials were subjected to electron beam bombardment in the facility described previously. Results of the simulated environmental testing, which is performed in a vacuum of less than 10<sup>-6</sup> Torr, are given in Table 5. Parameters normally measured during electron bombardment include: Primary beam current (I<sub>P</sub>), surface leakage current (I<sub>R</sub>), and backplate leakage (through the sample) current (I<sub>L</sub>). The primary beam current as measured is the sum of the other currents, that is,

$$I_P = I_S + I_R + I_L$$

Table 6. Summary of Static Charging Tests

Sample No.	Substrate	Back Surface Coating	Front Surface Coating	Observations	Conclusions
23 and 24	0.003" Mylar	None	None	Very large discharging occurring at 25 KV, 30 nA/cm <sup>2</sup> followed by quiescence lasting five minutes during which electro-luminescence prevailed	Unsatisfactory for static charge control.
26	0.005" FEP Teflon	None	250Å <sup>2</sup> of 10 mole % SnO <sub>2</sub> in In <sub>2</sub> O <sub>3</sub> .	No discharges observed or recorded. Electro-luminescence observed through 25 KV, 30 nA/cm <sup>2</sup> .	Suitable for static charge control to at least 25 KV and 30 nA/cm <sup>2</sup> .
27	0.002" Kapton	None	250Å <sup>2</sup> of 10 mole % SnO <sub>2</sub> in In <sub>2</sub> O <sub>3</sub> .	No discharges observed or recorded. Electro-luminescence observed through 25 KV, 30 nA/cm <sup>2</sup> .	Suitable for static charge control to at least 25 KV and 30 nA/cm <sup>2</sup> .
28	0.002" FEP Teflon	None	Photoetched copper grid with 1/2 in. pitch. Copper filaments 0.015 in. wide x 3000Å <sup>2</sup> thick.	At 15 KV, 30 nA/cm <sup>2</sup> clusters of electrical discharges occurred at a rate of 20 second within a 1 - in. diameter near center of sample. Other discharges occurred over entire 6 in. diameter surface randomly. Discharge amplitude to 200 nA.	Unsatisfactory performance. Probably due to poor bond between copper and FEP.
30	0.005" FEP Teflon	1000Å <sup>2</sup> Vapor Deposited Aluminum	Same as Sample 28	Same performance as noted for Sample No. 28 except microscopic examination revealed some copper grid filaments to be broken.	Unsatisfactory performance. More intimate contact is needed between copper grid and FEP.
31	0.003" Kapton	None	Photoetched copper grid with 1/2 in. pitch. Copper filaments 0.015 in. wide x 0.003 in. thick copper applied to Kapton with DuPont Pyralux.	No discharges observed visually or by scope monitoring through (25 KV, 30 nA/cm <sup>2</sup> ). Some electro-luminescence observed.	Suitable for ESD control to at least 25 KV and 30 nA/cm <sup>2</sup> .
32	0.001" Kapton	None	Silver Frit silk screened 1/2" pitch. Conductor .015" wide Frit material is Electrosence No. 11095.	No discharges observed visually or by scope monitoring (25 KV, 30 nA/cm <sup>2</sup> )	Suitable for ESD control subject to mechanical and irradiation testing.

## 5.2 Mylar

As shown in Figure 10 for 3 mil thick Mylar there is no indication of any charging below 2 kV. Above 2 kV the drop in  $I_S/I_P$  indicates that the secondary emission coefficient is less than one causing a net buildup in negative charge. With the increase in surface charge the surface leakage current ratio  $I_R/I_P$  increases. For beam accelerations above 12 kV charge penetration is sufficient in combination with the space charge fields of trapped charges in the dielectric to cause conductivity. This conductivity is referred to as electron bombardment induced conductivity. Discharging and electroluminescence results from this tendency of the dielectric to hold a space charge. Throughout the 2 to 25 kV range the dominant electron loss from Mylar is by secondary electron emission.

Figures 11 through 14 are photo micrographs of a Mylar surface after 25 min of electron bombardment at 30 kV, 30 nA/cm<sup>2</sup>. Damage is manifested as tracking and treeing. Table 7 summarizes the data for Figures 11 to 14.

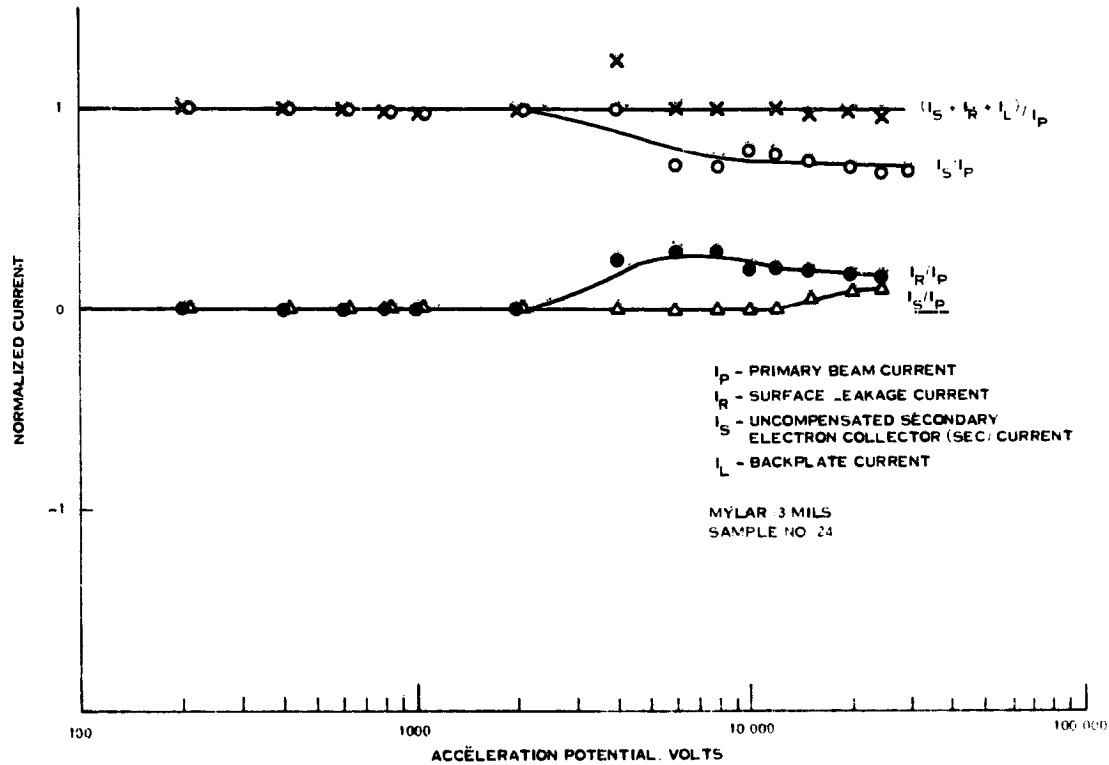


Figure 10. Charging Characteristics of Mylar Film (3 mils) at 30 nA/cm<sup>2</sup>

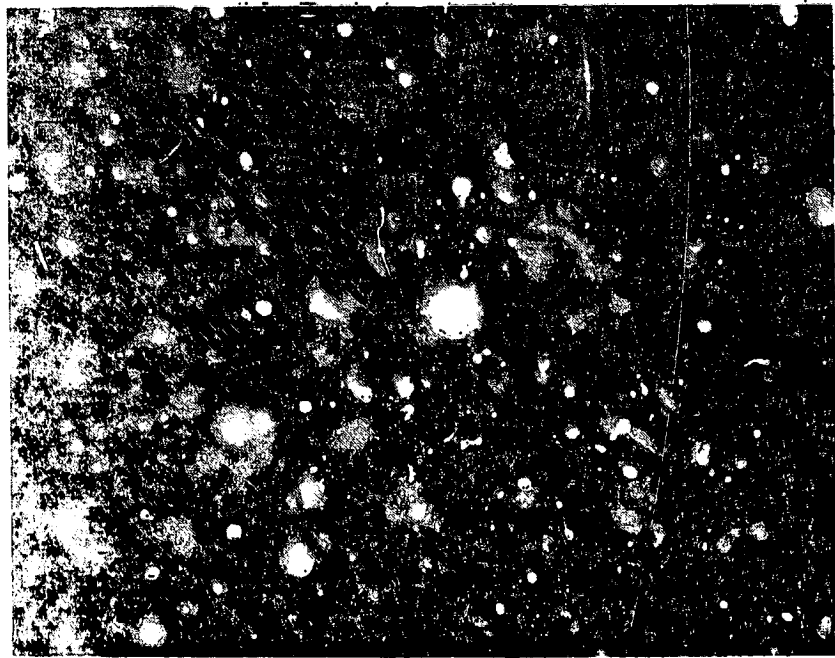


Figure 11. As Received Mylar (200X)  
Dark Field Illumination

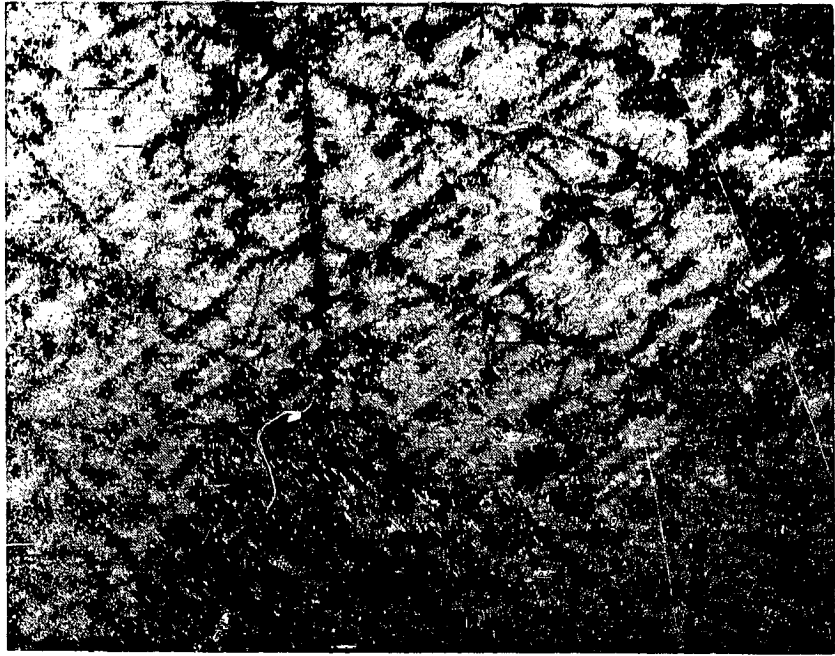


Figure 12. Electron Bombarded Mylar (100X)  
Plain Polarized



Figure 14. Electron Bombarded Mylar (400X)  
Plain Polarized

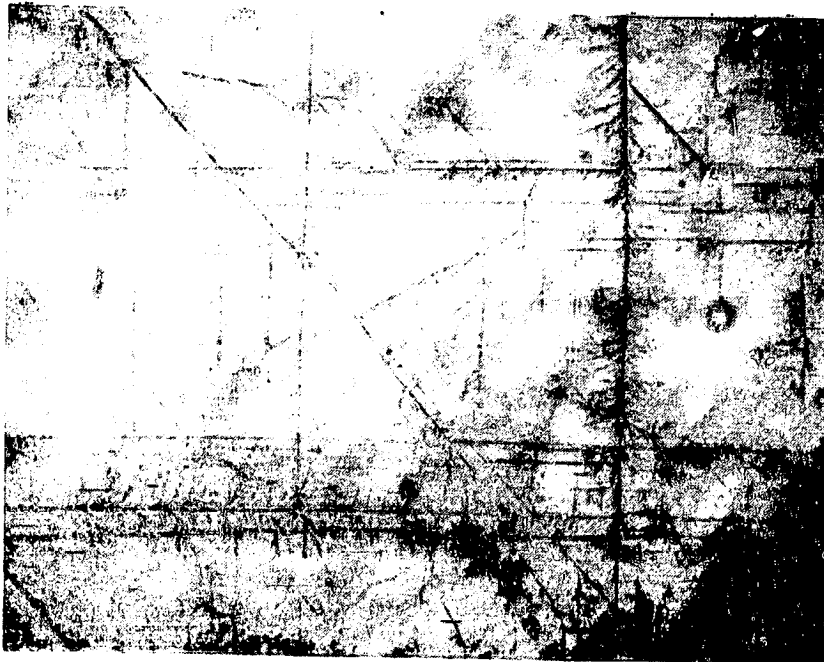


Figure 13. Electron Bombarded Mylar (200X)  
Plain Polarized

Table 7. Data Summary for Figures 11 Through 14

	Sample No. 1	Sample No. 2A/B	Sample No. 3	Sample No. 4
Material	Mylar	Mylar	Mylar	Mylar
Thickness	0.003 in.	0.003 in.	0.003 in.	0.003 in.
Exposure	Room Illumination	Electron Beam	Electron Beam	Electron Beam
Voltage	---	30 keV	30 keV	30 keV
Current	---	30 nA/cm <sup>2</sup>	30 nA/cm <sup>2</sup>	30 nA/cm <sup>2</sup>
Magnification	200X	100X	300X	~400X
Inclusions	~0.0001 in.	Present	Present	Present
Microscope Illumination	Dark Field	Plain Polarized	Plain Polarized	Plain Polarized
Aluminum back (not bonded)	None	Yes	Yes	Yes
Side Viewed	---	Electron Bombarded	Electron Bombarded	Electron Bombarded

No visual evidence of electric discharges could be seen (at 50X magnification) on the Mylar. However, at higher magnification brick pattern-treeing is evident, as illustrated by the photographs.

Brick pattern treeing, caused by electron beam irradiation etching, increases the surface energy of the Mylar by breaking bonds at and within a few microns of the surface. With respect to the treeing pattern, internal or frozen-in stresses may result from molecular orientation or from thermal stresses attributable to rapid cooling of the polymer. The intensity of the crazing increases with exposure time to electrons.

Apparently, large (micron size) structures of 500 to 1000 Å diameter spheres develop in the dielectric during the fabrication process, and lie in rows along the stretch direction of the polymer fibers. They represent the distribution of highly organized strain, due to fabrication stresses. The spheres, spatially ordered over a long period, are composed of highly ordered molecular groups (and crystallites) which may move as rheological identities. The tree patterns which develop over the strain pattern are due to surface electric discharges at the patterns. Correlation of physical properties (for example, % elongation, tenacity, tear, modulus) with structural size of brick pattern is apparently indicated, especially in the brick size of 1 to 100 μ. Strain distribution is an important parameter with respect to physical properties.

Laminar structure may also arise in stretched polymers due possibly to anisotropic heat transfer during fabrication by anisotropic structure introduced into

the polymer. The regularity displayed by these structures indicates that the applied stress has been fairly uniform. In essence then, the parallel stretch direction lines and brick structure (unlike a grid structure, since the perpendicular lines, originating from parallel lines, do not generally cross adjacent parallel lines) are etched into one-way stretched polymer films. The number of lines are dependent upon the polymer history. In contrast, the two-way stretched polymer film etchings reveal lamellate composition, each layer having brick wall-like structure. Micron size bricks are apparently composed of spheres or groups of molecules of about 700 Å, aligned to a moderate extent. The electric discharge trees traverse paths of least resistance along the various higher energy strain trajectories of the brick pattern and to a lesser degree over the surfaces of the polymer. Some die lines also appear on the Mylar film along which the electric discharges traversed.

Mylar is not a commonly used external spacecraft material because of its sensitivity to the radiation components of the natural space environment which cause catastrophic degradation in its physical properties. The results of this investigation show that it is not suitable for use in a high electron flux environment, particularly when exposed directly to electron bombardment. However, its use in multi-layer insulation (MLI/blankets) is acceptable where protected by a cover layer of a protective material such as Kapton or Teflon or any other material which will shield it from direct exposure.

### 5.3 $\text{In}_2\text{O}_3/\text{SnO}_2$ (ITO) Coating

Figures 15, 16, and 17 show the effects of the ITO semiconductor coating on the current/voltage characteristics of polymeric films. For both Kapton and Teflon substrates the secondary emission coefficient is greater than 1 for accelerating potentials below 4 kV. The aluminized backing shows no effect on the characteristic curves. The similarity between the curves for both Kapton and Teflon indicate the dominant effect of the semiconductor film with little effect on the crossover point between  $I_R$  and  $I_S$  for the two dielectrics. The rise in surface leakage current indicates low charge buildup on the surface of the dielectrics.

Micrographs of ITO (250 Å) coated FEP Teflon after electron beam irradiation are shown in Figure 18b indicating "electron-etched" cracking and crazing. These craze-cracks (due to large applied anisotropic stress or tensile force) run along parallel direction of stretch lines to which the material was subject (that is, longitudinal drawing or pulling and radial blowing), as is evidence by the micrograph of the unexposed spacecraft material (Figure 18a) and less evident outside the electron beam irradiation area (Figure 18c). The stretch lines correspond to the direction of molecular orientation, preferentially, since the polymer under the coating has less strength perpendicular to the direction of orientation. Crystallization occurs along these oriented molecules.

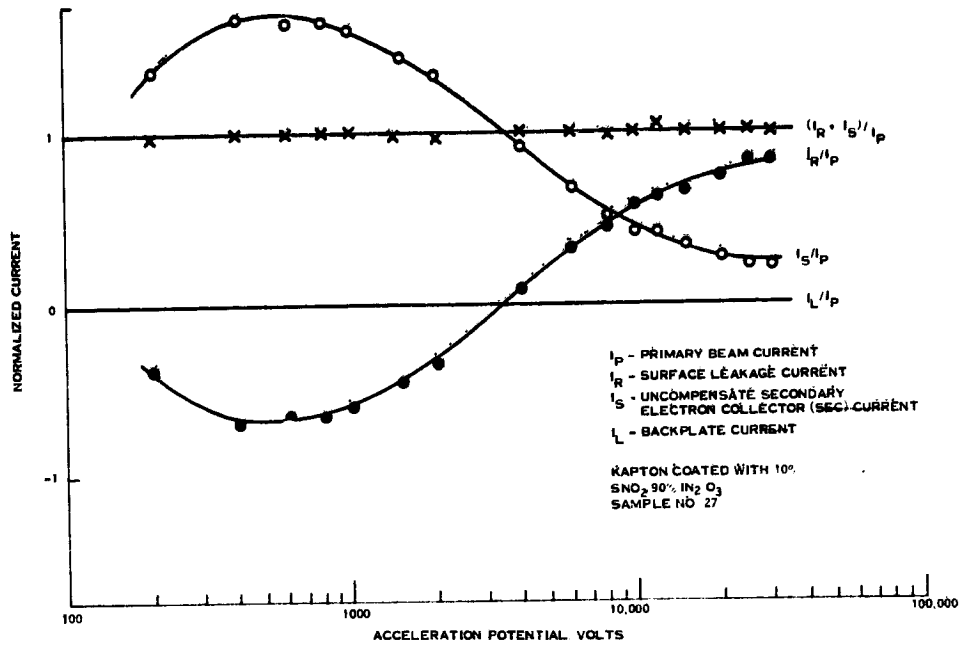


Figure 15. Charging Characteristics for ITO Coated Kapton Film at  $30 \text{ nA/cm}^2$

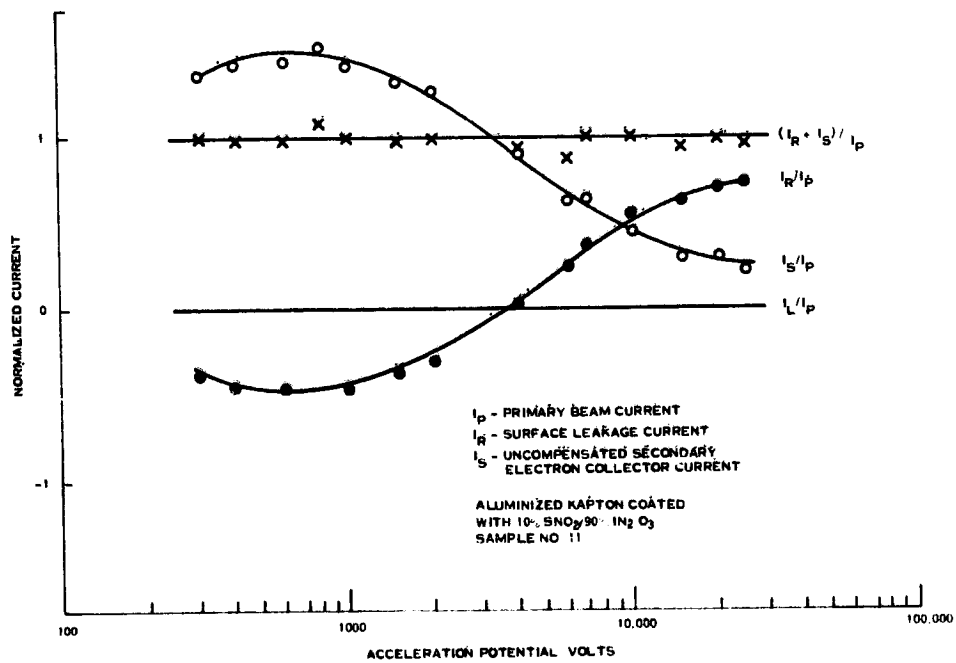


Figure 16. Charging Characteristics for ITO Coated Aluminized Kapton Film at  $30 \text{ nA/cm}^2$

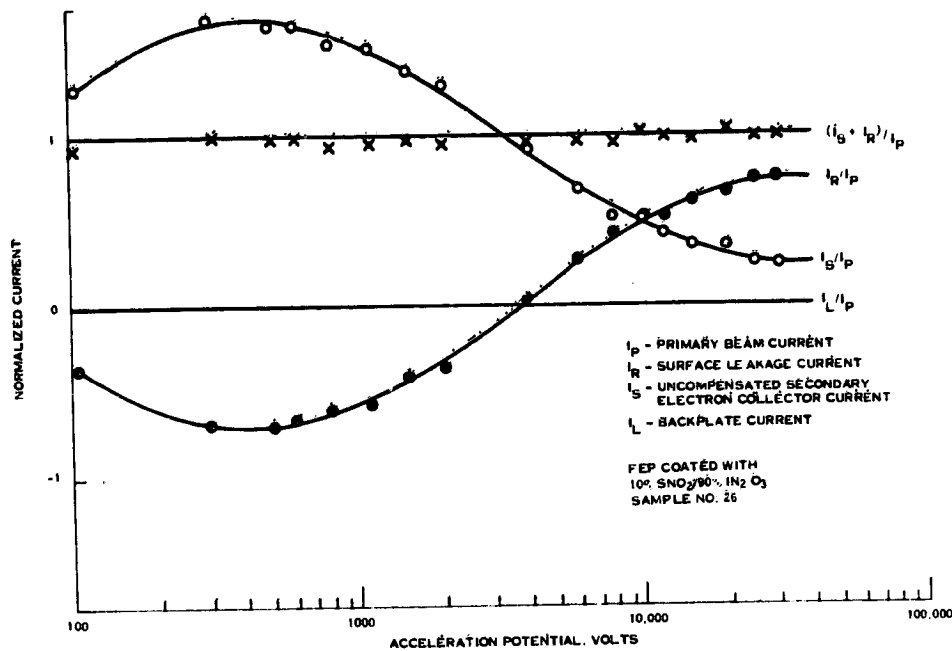


Figure 17. Charging Characteristics for ITO Coated FEP Film at  $30 \text{ nA/cm}^2$

Within these imperfections and voids intrapped gas is ionized by electron beam charging. Local temperatures rise, chemical reactions occur and stress is created, as in the case of chemical or vapor etching.

Intensity of crazing rises with exposure time to the electron irradiation. Crazing of polymers apparently is related to domain structure of the polymer (that is, definite homogenous regions surrounded by others of like kind with boundaries between them). More craze lines form whenever the stretching occurred without lateral restraint than if the stretching occurred with lateral restraint for the same stretching ratio.

In essence, crack-crazing in polymers is associated with large micron size regular structures, which in general occur in anisotropically stretched (or uniform applied stressed) films. This structure is inherent in the film during the fabrication therefore a distribution of strain is produced by fabrication stress.

ORIGINAL PAGE IS  
OF POOR QUALITY

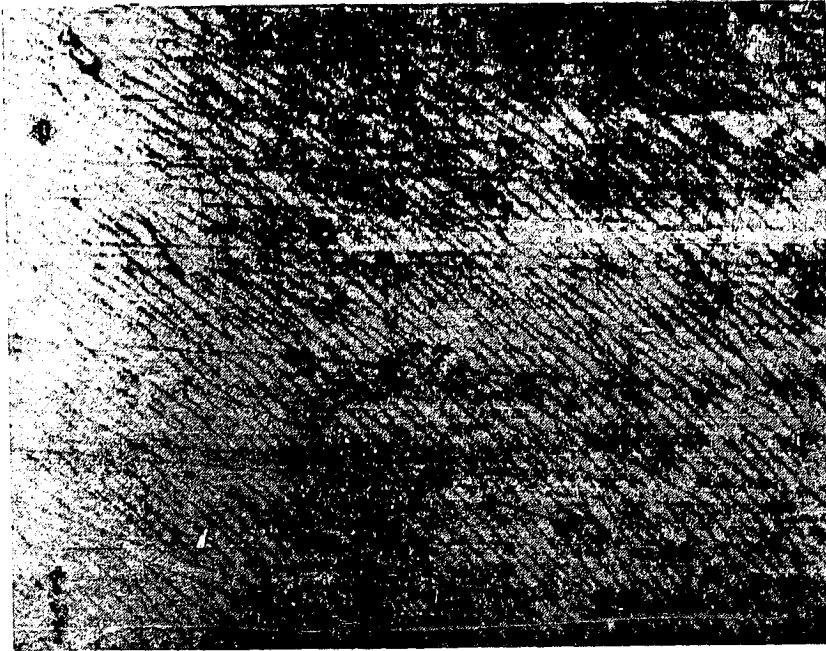


Figure 18b. FEP/ITO After Electron Irradiation at the Central Region of the Electron Beam. Electron etched craze lines appear on the FEP-Teflon surface, together with fabrication die lines, under the transparent semi-conductor (200X)



Figure 18a. Transparent Semi-Conductor of 250 Å Tin and Indium Oxide (10 percent mole SnO: 90 percent mole In<sub>2</sub>O<sub>3</sub>) on 2-mil FEP-Teflon Before Electron Irradiation. Typical die lines appear on the FEP-Teflon surface, under the transparent semi-conductor

ORIGINAL PAGE IS  
OF POOR QUALITY

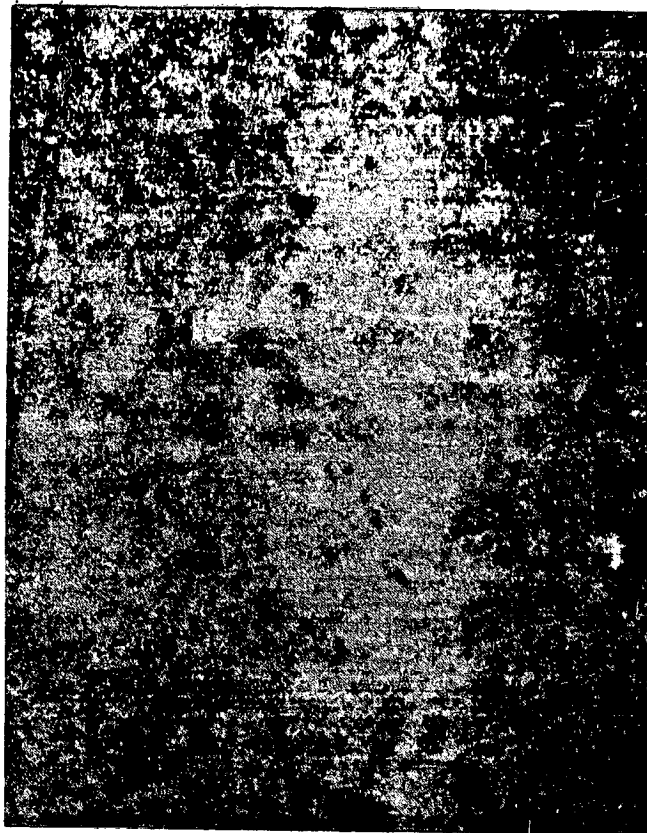


Figure 18c. FEP/ITO After Electron Irradiation  
Near the Edge of the Sample Outside the Primary  
Beam Projection Area

The micron size structure of "spheres" (500 to 1000 Å) denotes distribution of strain, due to fabrication stress. These "spheres" are highly ordered molecular groups and they move as rheological groups. The internal stresses may result from molecular orientation or from thermal stresses due to rapid cooling of the polymer. In the case of single way stretch in fairly evenly spaced long parallel lines of uniform width (for example, to  $7\mu$ ) etched into the surface along the stretch path, the density of the lines (for example, number of lines per unit length) is apparently proportional to the stretch ratio, whereas the line width is proportional to the inverse of this stretch ratio.

#### 5.4 Copper Grids

Figures 19 to 23 represent the characteristic curves for Teflon and Kapton substrates of various thickness with copper grids applied by a photoetching process. All of these curves show the same general behavior between 1 kV and 10 kV. As in the Mylar substrate the low value of  $I_R/I_P$  indicates a net charge buildup on the surface. Above 10 kV the penetration depth and charge buildup results in an increase in the electron bombardment conductivity. An anomolous behavior was observed in the 5-mil sample of Teflon, plain and aluminized, with the copper grid below 1 kV when the secondary current indicated a current ratio greater than 1 (Figure 20).

Comparison of the voltage-current characteristics of 2-mil Teflon (Figure 19) with 5-mil material (Figure 23) shows that the resistance of FEP increases with increased thickness. The relatively rapid rise of backplate leakage (through the sample) current,  $I_L$ , beyond 10 kV and the associated surface-currents,  $I_R$ , indicates the presence of micropores in the 2-mil thick film, some of which reach the backplate, as indicated by Malter avalanche emissions from these sites. This accounts for point emission distribution over the electron irradiated surface as a consequence of the associated spreading potential.

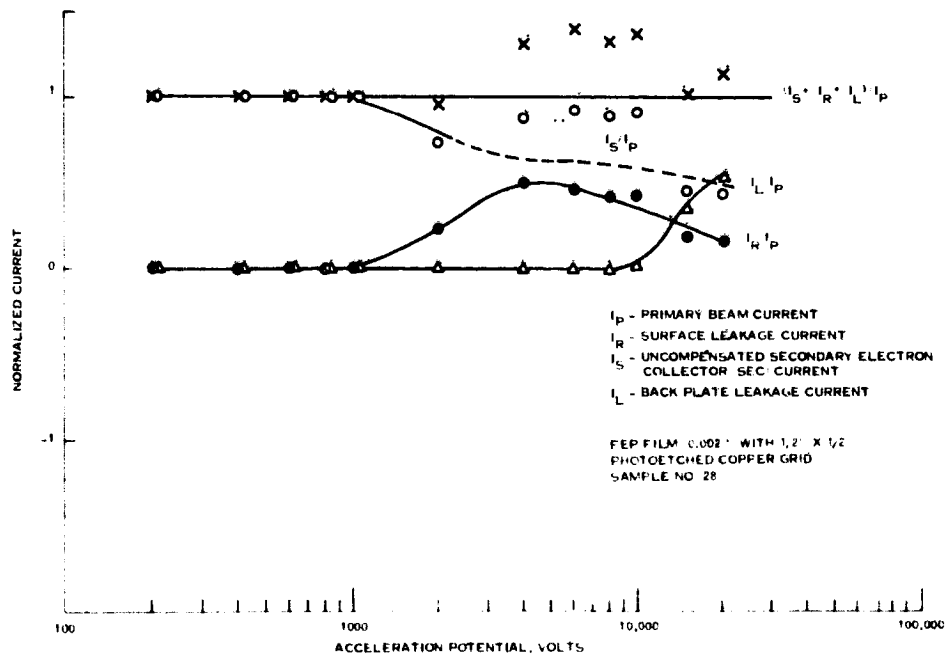


Figure 19. Charging Characteristics for 2-mil FEP With Photoetched Copper Grid at  $30 \text{ nA/cm}^2$

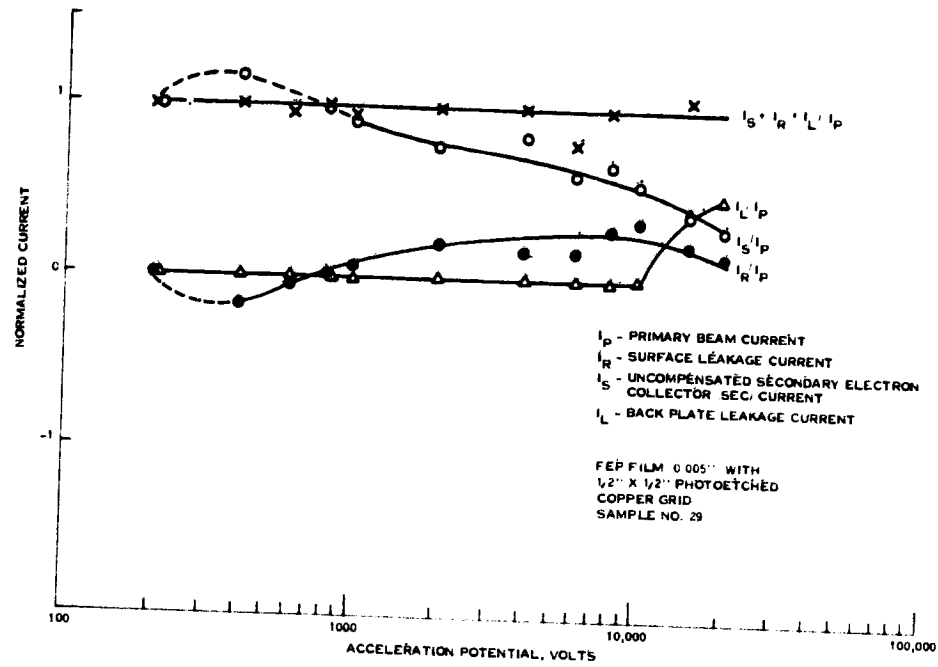


Figure 20. Charging Characteristics for 5-mil FEP With Photoetched Copper Grid at 30 nA/cm<sup>2</sup>

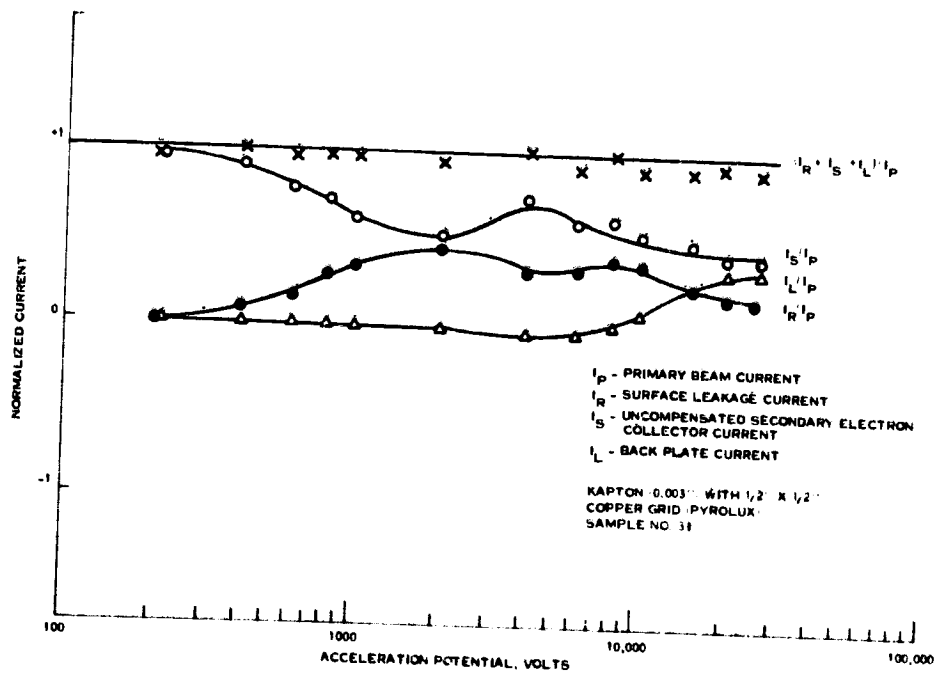


Figure 21. Charging Characteristics of Kapton Film (3-mil) With Photoetched (Pyralux) Copper Grid at 30 nA/cm<sup>2</sup>

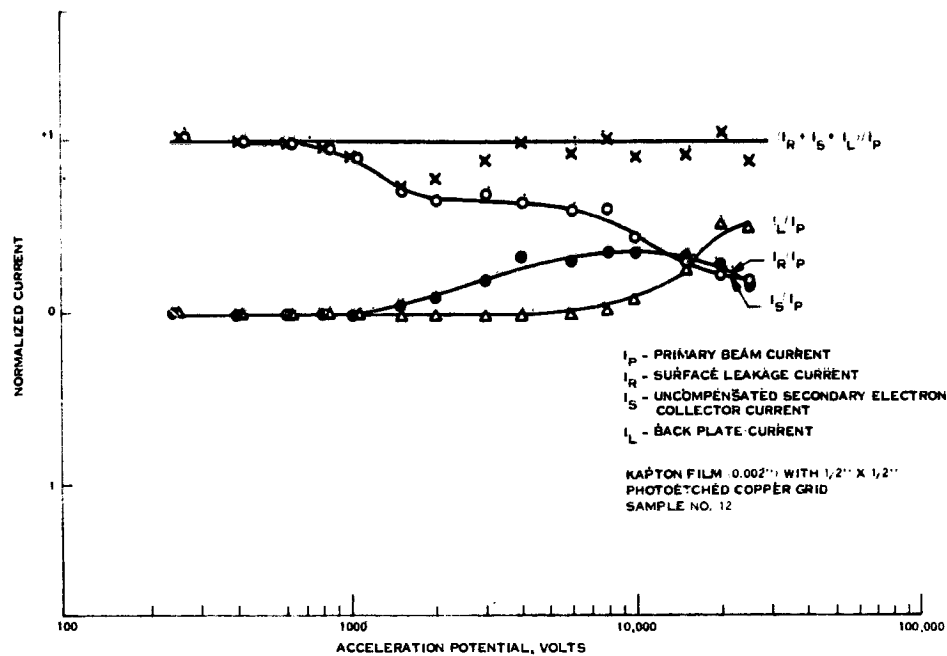


Figure 22. Charging Characteristics for Kapton Film (2-mil) With Photoetched Copper Grid at  $30 \text{ nA/cm}^2$

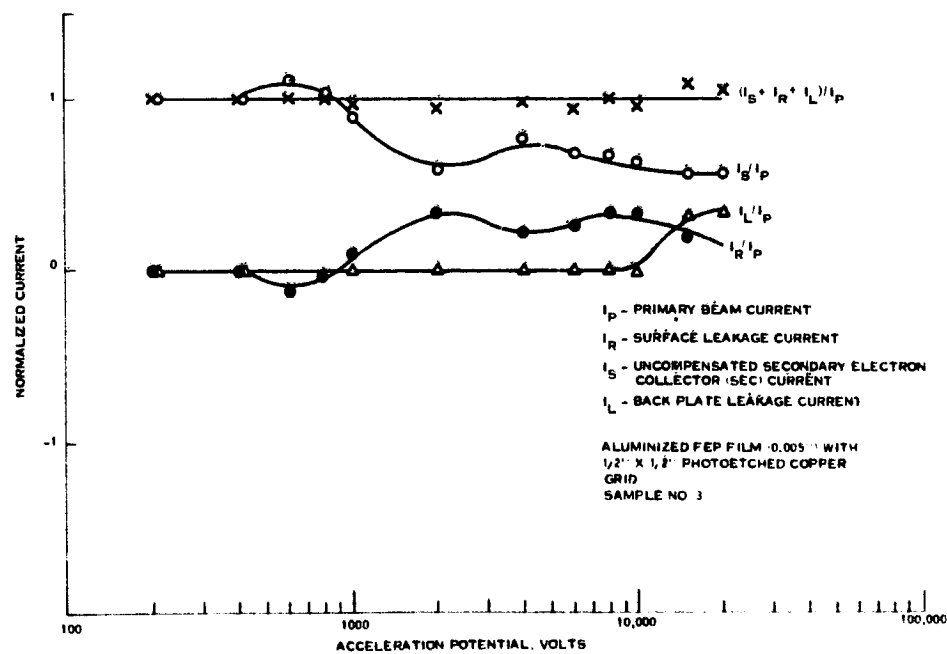


Figure 23. Charging Characteristics for Aluminized FEP Film (5-mil) With Photoetched Copper Grid at  $30 \text{ nA/cm}^2$

Aside from the foregoing Malter avalanche emission, discharge breakdown in micropores of occluded gas in the Teflon can result in cavity ionization and thermal breakdown prior to intrinsic breakdown. This would account for some observed intermittent sparking observed. The moderate decreasing surface leakage current,  $I_R$ , beyond their respective peaks for both the 2- and 5-mil materials indicates that the residual gas surface discharge threshold for the reduced charge (that is, ratio of surface charge to dielectric constant) as a function of dielectric resistivity has not been attained for the thicker film within the applied primary electron beam energy of 10 to  $\geq 20$  kV; whereas, it apparently did occur for the 2-mil material beginning about 15 kV. Examining the 2-mil Teflon at 10X magnification revealed that for the region displaying copious sparking, evidence of gaps in the copper grid occurred (Figure 24). Some filaments had as many as six very small gaps (order of a tenth of a millimeter) in one filament within the grid patch (that is, 12 in.). Some grid filaments had gaps on the order of millimeters wide, with no evidence of prior bonding in those gaps.

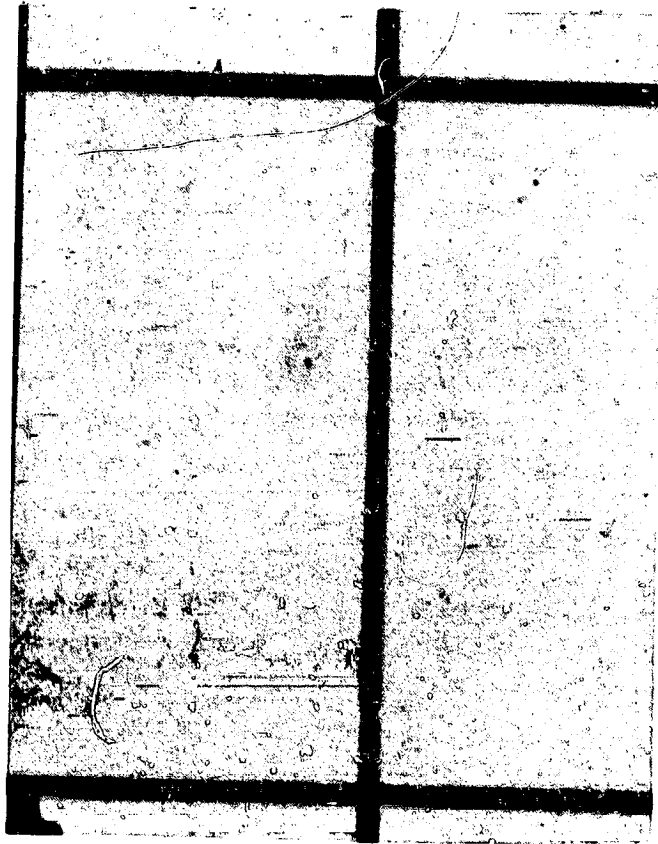


Figure 24. FEP Teflon (2-mil) Showing Discontinuities (As a Result of Electron Bombardment) in the Photoetched Copper Grid Along Extrusion Lines in the Polymer

The unsatisfactory performance of this particular copper gridded Teflon is attributed to the numerous and small gaps in too many filaments of the grid. Uniformity of bonding is suspect, since no evidence of bonding occurs in the larger (several millimeters) wide gaps. The copper filaments themselves have clean distinct edges, with no raggedness, and of uniform, constant width. By electrically\* increasing the surface energy of the Teflon, substantially improved bonding and absence of filament gaps is anticipated. Therefore, copper grid bond Teflon warrants improved processing and re-test.

Throughout the range of primary electron beam voltage,  $V_P$ , (> 200 to > 20 kV), the dominant electron loss from 5-mil FEP is by secondary electron emission as indicated by its  $I_S$ .

The surface leakage current,  $I_R$ , is relatively dominant, with respect to the backplate leakage current,  $I_L$ , from 850 V to 10 kV, whereas beyond this voltage (~ 12.5 kV) the backplate leakage current,  $I_L$ , assumes relative dominance over the surface leakage current,  $I_R$ .

The backplate leakage current,  $I_L$ , is relatively negligible, from about 200 V to about 10 kV and then rises abruptly approaching 15 kV. Near 30 kV, meters indicated electric discharging to be occurring at relatively frequent intervals (that is, 1 per 20 sec). However, actual electric discharging could not be seen on the sample in spite of several small (that is,  $\ll 1/10$  mm) and a few substantially larger (that is, several mm) gaps in the copper grid filaments which were found during the post test microscopic examination.

#### 5.5 Silk Screen Grid on Kapton

A net charge buildup is observed (see Figure 25) for accelerating potentials above 1 kV for 1-mil Kapton with a silk screen silver grid. Above 4 kV the surface leakage shows a decrease along with a faster decline in the secondary electron emission. Above 10 kV the predominant charge movement is by EBC indicating significant penetration into the dielectric substrate and large charge buildup on the surface.

The superior performance of the silk screened Kapton is evident from its voltage-current characteristics with respect to the substantial secondary electron emission (SEE) yield and backplate leakage current. In contrast, the surface leakage

\*E-C bond breaking by electron irradiation or displacing sufficient F's by O's via microwave discharge, the surface energy of Teflon can be increased from  $102^\circ \pm 4^\circ$  (natural) to  $65^\circ \pm 8^\circ$  contact angle with a water vapor microwave discharge. The surface free energy,  $E_{SG}$ , of the dielectric relative to vacuum is related to the equilibrium contact angle,  $\theta$ , by proportion:  $E_{SG} \approx [1(1 + \cos \theta) + \pi_e]2$ . The maximum reversible work of adhesion,  $W_a$ , of the two solid surfaces,  $S_1, S_2$ , in contact, is related to the contact angle,  $\theta$ , by the proportion:  $W_a \approx (1 + \cos \theta)$ , emphasizing only the contact angle among other intentionally undefined and omitted variables, for the interim.

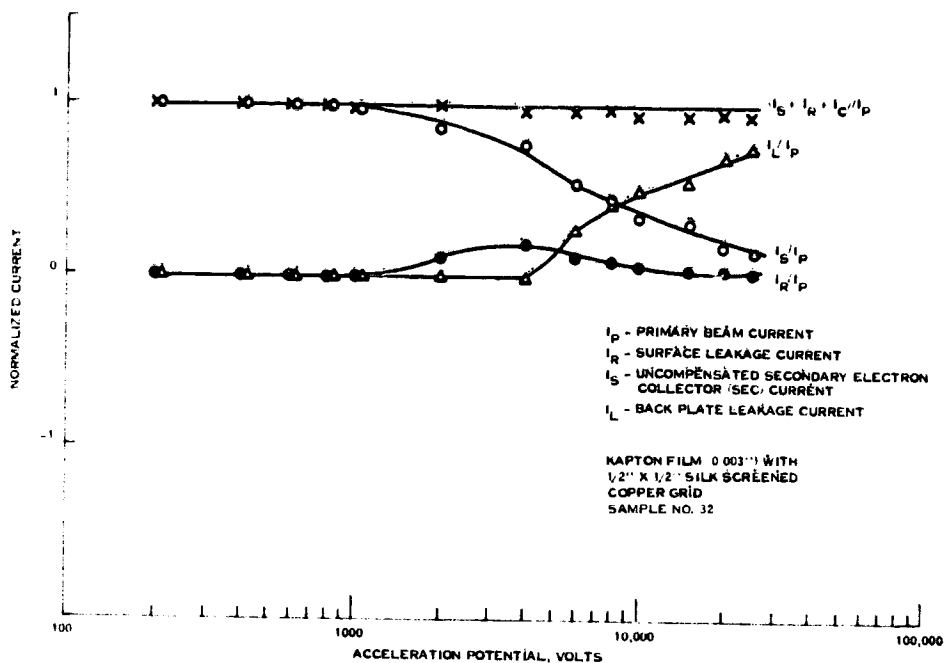


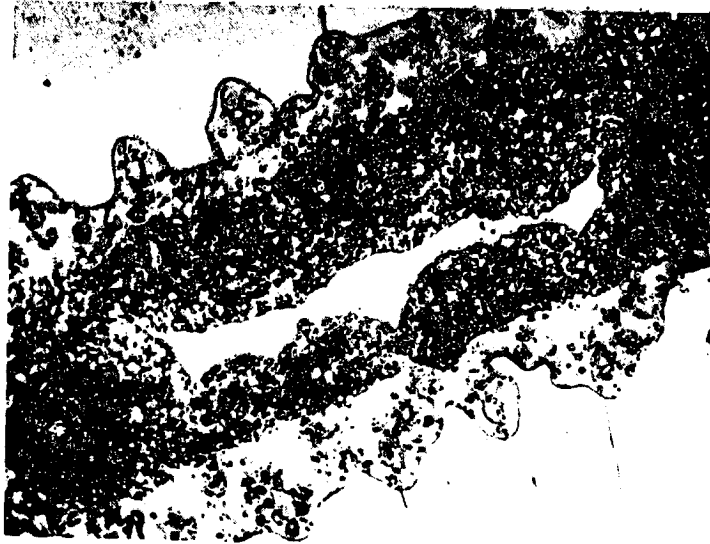
Figure 25. Charging Characteristics for Kapton Film (3-mil) With Silkscreened Copper Grid

current,  $I_R$ , although initially large, subsequently decreases rapidly, due to the rapid rise in backplate leakage current beyond 4 kV primary electron beam energy. Up to the latter voltage, the dominant electron current loss from this material is due to SEE current,  $I_S$ ; and to a minor degree, surface leakage current,  $I_R$ , while the backplate current,  $I_L$  remained negligible. However, beyond a primary electron beam energy of 4 kV, the dominance of backplate leakage current,  $I_L$ , rapidly asserts itself. While the SEE current,  $I_S$ , relatively rapidly decreases, the backplate leakage current,  $I_L$ , becomes substantially dominant beyond 8 kV with respect to the SEE current,  $I_S$ , and surface leakage current,  $I_R$ .

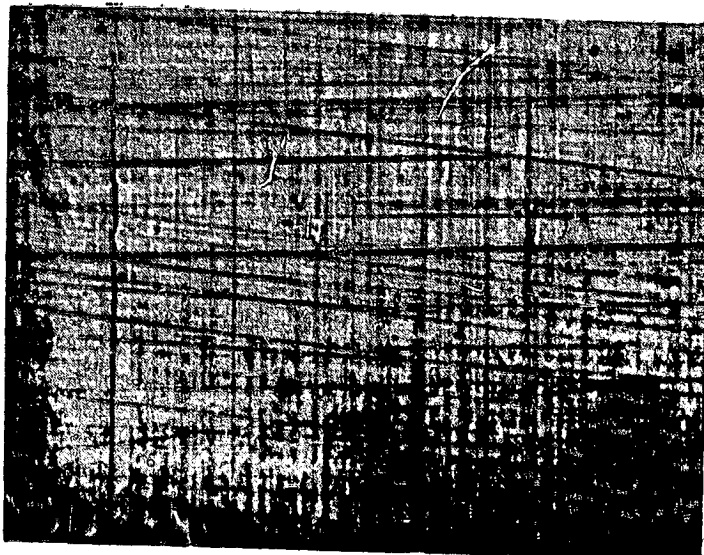
Examination of the silver-grid bonded Kapton (at 10X magnification) reveals that the filaments of the grid are of fairly uniform width and deposition. They are uniformly well bonded to the Kapton. However, there are some regions of silver scarcity in that localized portions of some filaments have extremely thin (~ 1/10 width of filament) silver bridges connecting them, defects which must be remedied to obtain optimum performance. The surface of the silver filaments are relatively rough, though apparently this disadvantage does not cause localized discharges. Die marks are evident on the central regions of the Kapton windows of the grid (due

**ORIGINAL PAGE IS  
OF POOR QUALITY**

to processing. However, electron irradiation etching of the Kapton (bond breaking) is not obvious at 100X and 400X magnification (Figure 26). That is, no parallel single- nor double-way stretch (stress) patterns, nor brick-stress pattern is evident. This is apparently attributed to the charge dissipative ability of the grid in conjunction with significant electron bombardment induced conductivity in the Kapton, between the grid filaments, as well as the substantially lower resistance of the thin (1-mil) Kapton.



a. (100 X) Grid Filament



b. (400 X) Kapton

Figure 26. Kapton Film (1-mil) With Silk Screened Silver Grid After Electron Bombardment

There were no measureable discharges for this material during electron bombardment through 25 kV and is apparently a satisfactory prospect for spacecraft thermal blanket application.

## 6. CONCLUSIONS

Mixtures of indium and tin oxides (90/10) reduce the surface resistivity of polymeric films sufficiently to control static charge buildup in simulated environmental tests. In this study a film thickness of only 250 Å was sufficient to attain a resistance in the  $10^6$  ohm-cm range without significantly reducing the visible transparency of FEP Teflon. No discharging occurred under electron bombardment to 25 kV with an associated current density as high as  $30 \text{ nA/cm}^2$ . The additional data needed to qualify this material for spacecraft use is that which will show reasonable stability in the space environment and resistance to damage by flexing the coated film.

On the first condition it is hypothesized that only slight discoloration of the ITO will occur under space UV and electron irradiation because of the thinness of the coating required ( $\leq 250 \text{ Å}$ ) to obtain the conductivity to spread out the charge arising from solar substorms. This hypothesis is based on data taken on ITO coated OSR's produced by OCLI and Lincoln Laboratory in the GE Combined Effects Chamber in 1975 for the AFML Sponsored Thermal Control Coating Development Program.<sup>3</sup> A  $\Delta\alpha_S$  of 0.01 was related to ITO coating during a EUVS exposure. The reason for the slight effect of the degrading ITO on the performance of the solar reflecting mirror is that the extinction coefficient is not only a function of the amount of light that is absorbed in the ITO, but also its thickness. A long term exposure to UV and low energy (few eV) particles (electrons and protons) which are deposited primarily in the conductive coating and FEP or disruption of the FEP surface during coating deposition will thereby reduce performance of the polymer under irradiation. These effects should be minimal using Magnetron equipment to deposit coatings because of the very low temperature rise which occurs during the deposition process.

Cracking or crazing of ITO films during flexing of the polymer substrate may or may not affect static charge control performance. Preliminary data indicates that this will not be a problem. Microcracks in an ITO coated Kapton film were observed (under a microscope) after vigorous flexing of the film. However, the sample showed no discharges, and in fact, performed as well as an unflexed specimen to 30 kV,  $30 \text{ nA/cm}^2$ .

Once these potential problem areas have been cleared, ITO can conveniently be deposited in quantities large enough for spacecraft systems using conventional roll-coating equipment.

Our preliminary evaluations indicate that conductive grids formed by photo-etching copper or silk-screening silver filled paint on Kapton to be effective in controlling discharging to 25 kV and 30 nA/cm<sup>2</sup>. A square 1/2-in. grid pattern was used based on an analysis recently completed for AFML.<sup>4</sup> Optimization of the grid pitch can be done empirically. However, this item does not appear to be critical from a passive temperature control point of view because Kapton is not used for control of critical surfaces and in using 0.015-in. wide filaments only 6 percent of the Kapton surface is covered by the grid.

Very poor performance was obtained from FEP Teflon with copper grids because of poor bonding of the grid to the polymeric film. A remedy to this situation is not apparent, because bonding can only be improved by etching the FEP surface and this has proven to significantly disrupt the UV stability of the FEP. Alternatively, heat sealing a wire grid into the Teflon surface is another approach, but it too is expected to affect the stability of the FEP film in radiation environments. This is a cause for concern because back surface metallized FEP is used for passive temperature control of critical surfaces where even minor changes in solar absorptance produce unwanted temperature increases.

## Acknowledgments

We gratefully acknowledge the contributions made by consultant Dr. E. Okress for his assistance in designing the ESD test facility and in interpreting test data.

## References

1. Knott, K. (1972) The equilibrium potential of a magnetospheric satellite in an ellipse situation, Planet. Space Sci., 2:1137-1146.
2. Nanewicz, J. E., et al (1976) Spacecraft charging studies of voltage breakdown processes on spacecraft thermal control mirrors, Program in Astronautics and Aeronautics, Vol. 47.
3. Eagles, A. E. (1975) Exploratory Development of Thermal Control Coatings, Technical Management Report for Contract F33615-74-C-5087.
4. Eagles, A. E. (1976) Conductive Coatings for Satellites, AFML-TR-76-233.

## Contents

1. Introduction	655
2. Review of the Secondary Emission Process	657
3. Secondary Emission Conductivity	658
4. Charge Density Amplification	660
5. Secondary Emission Conductivity in Silica Fabric	661
6. Electrostatic Discharge Induced Radio Frequency Interference	664
7. Conclusions	667
Acknowledgment	668
References	668

## 6. Secondary Emission Conductivity of High Purity Silica Fabric \*

V.J. Belanger  
and  
A.E. Eagles  
General Electric Company  
Space Division  
Valley Forge, Pennsylvania

### Abstract

High purity silica fabrics have been proposed for use as a material to control the effects of electrostatic charging of satellites at synchronous altitudes. These materials have exhibited very quiet behavior when placed in simulated charging environments as opposed to other dielectrics used for passive thermal control which exhibit varying degrees of electrical arcing. Secondary emission conductivity is proposed as a mechanism for this superior behavior.

Design of experiments to measure this phenomena and data taken in GE research facilities on silica fabrics are discussed as they relate to electrostatic discharge (ESD) control on geosynchronous orbit spacecraft. Studies include the apparent change in resistivity of the material as a function of the electron beam energy, flux intensity, and the effect of varying electric fields impressed across the material under test.

### 1. INTRODUCTION

While the temperature of a satellite can be adjusted through the use of active and semiactive devices such as louvers and heat pipes, the thermal designer relies

\*This work was supported by the Air Force Materials Laboratory under Contract No. F33615-C-75-5267.

heavily on passive techniques. Here the amount of heat into a spacecraft by incident solar illumination and the amount radiated or reradiated at infrared wavelengths is adjusted by selecting external materials and coatings with appropriate reflectances, absorptances, and emittances. Because this passive temperature control subsystem comprises the entire outer shell of a satellite, it must bear directly the brunt of the indigenous space environment. At geosynchronous altitudes this includes the electron plasma which can produce static charge buildup with the attendant problems of electrical arcing and discharging.

The most critical elements in a spacecraft passive temperature control subsystem are the white, high emittance coatings used not only to reflect a major portion of incident solar energy, but also to dissipate internally generated heat. Historically, white paints employing zinc or titanium oxides have been used. However, these have been shown to degrade rapidly by discoloration under solar ultraviolet illumination. The degradation is manifested by a decrease in the amount of incident solar energy that is reflected, which results in increased surface and subsequent equilibrium temperature because the energy which is not reflected is absorbed by the coating.

Solar reflecting coatings derived from fabrics produced from high purity silica ( $\text{SiO}_2$ ) yarn such as those available under the J. P. Stevens Company's Astroquartz trademark have been shown to be extremely stable to the damaging radiation components of space.<sup>1</sup> The high radiation stability which is typical of high purity  $\text{SiO}_2$  is derived from the fabric by merely removing the sizing or finish placed on the yarn to facilitate weaving by baking in air at temperatures in the 800 to 1000°C range. The solar reflectance of the processed fabric is in excess of 0.82 while its hemispherical emittance is 0.82 at 0°C. A total loss in reflectance of only 0.03 is experienced after long term exposure to solar ultraviolet radiation.

To obtain high solar reflecting, high emittance characteristics, only dielectric materials can be used. These of course will support static charge buildup at geosynchronous orbit. Electrically conducting materials in many instances exhibit high reflectances to solar energy, but without exception have low thermal emittances which violate the requirements for solar reflecting coating applications.

At the onset of this study it was planned to investigate modifications of the strictly dielectric characteristics of silica fabric by interweaving occasional conductive yarns, such as aluminum or stainless steel, within the material. These would provide paths for the drainage of static charge as it develops in geosynchronous orbit missions. Conductor spacings were to be close enough to effect reduction of large surface gradients.

Although the experimental plan called for fabrication of silica/metal yarn interweaves, baseline data collected initially for silica fabric itself showed that the fabric did not support charge buildup under electron beam bombardment at

energies to at least 30 keV with associated current densities in excess of 30 nA/cm<sup>2</sup>. This seemed to be anomalous in view of the high resistivity of silica which is in excess of 10<sup>17</sup> ohm/m at ambient conditions. This study, then, was undertaken to explain the unusual behavior exhibited by silica fabric under bombardment by highly energetic electron beams designed to simulate conditions found at geosynchronous altitudes.

## 2. REVIEW OF THE SECONDARY EMISSION PROCESS

Behavior of silica fabrics in a simulated plasma charging environment indicated that the secondary electron emission (SEE) process would be the overriding consideration in the absence of photoelectric effect due to solar illumination. Solar illumination, of course, will not play an important role in neutralizing static charge buildup during that time a geosynchronous spacecraft is in umbra which has been shown to be the most probable time for anomalous events.<sup>2</sup> Knott<sup>3</sup> has also shown the importance of SEE in the equilibrium process for non-illuminated spacecraft.

Experimental data on the secondary emission of materials yield the characteristically shaped curve in Figure 1 which is common to most substances. This curve relates the secondary emission ratio ( $\delta$ ) to the energy of the bombarding primaries ( $E_p$ ). For most metals and graphite,  $\delta$  does not exceed 1; however, a slight oxide layer on a metal can produce a much higher value for  $\delta$ .

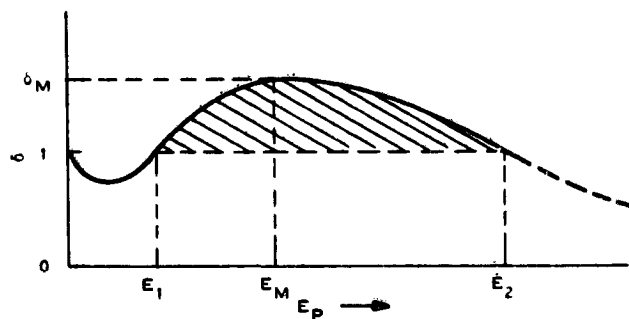


Figure 1. Characteristic Secondary Emission Curve for Most Materials

The primary features of interest in this characteristic are:  $E_1$ , the first crossover,  $E_2$ , the second crossover,  $E_M$ , the primary energy of maximum  $\delta$ ,  $\delta_M$ , the maximum secondary emission ratio, and the cross-hatched area where the secondary emission ratio is greater than 1. A simplified explanation for the

shape of the curve would be that the secondary emission ratio increases with increasing primary energy. However, these secondaries are generated along the path of the primary electron as it penetrates into the crystal lattice of the material and the secondaries must then diffuse to the surface where they can be emitted as a free secondary electron. Associated with this diffusion is a diffusion probability that is a decreasing function of path length. At the point  $E_M$  in the characteristic,  $\delta(E_p)$  becomes dominated by the decreasing diffusion probability and, hence, passes through a maximum. This, of course, has been more rigorously treated by many authors. The Sternglass approximation discussed by Dekker<sup>4</sup> is most frequently cited. His approximation for this function is semi-empirical and considers electron shell structure of materials as related to atomic number. This approximation has been shown to correlate well with experimental data when corrected for back-scattered electrons.

The major shortcoming of the Sternglass approximation is that it does not consider non-normal incidence primaries. Again, Dekker,<sup>4</sup> in interpreting efforts by Bruning, has shown that  $\delta(E_p)$  is a strong function of the primary incidence angle with an approximate  $1/\cos \theta$  dependence. This dependence has the effect of both increasing  $\delta_M$  and shifting  $E_2$  towards the higher energy primaries thus increasing the cross-hatched area shown in Figure 1. From this and consideration of the surface geometry in silica fabric, which has the following characteristic numbers for normal incidence primaries

$$\begin{aligned} \delta_{\max} &= 2.1 \text{ to } 2.9 \\ E_{\max} &= 400 \text{ to } 440 \text{ eV} \\ E_1 &= 30 \text{ to } 50 \text{ eV} \\ E_2 &= 2.3 \text{ keV} \end{aligned}$$

it can be concluded that secondary emission conductivity can effectively reduce differential charging in the electron bombardment environment found at geosynchronous orbit.

### 3. SECONDARY EMISSION CONDUCTIVITY

Secondary Emission Conductivity (SEC) is a well known process used primarily in image processing vacuum tubes such as the SEC Vidicon TV camera tube. SEC targets used in these tubes are somewhat different than silica fabric; however, they have in common an inorganic dielectric matrix mixed with continuous voids of free space. Generally speaking, inorganic dielectrics have secondary emission ratios greater than 1. Silica, for example, runs from 2 to 3 for normal incidence primaries. This ratio can go much higher for non-normal and grazing incidence. As will be shown later, this increase in the peak secondary emission ratio ( $\delta_M$ ) and the

shift of the second cross-over towards higher energy primaries for non-normal incidence primaries contributes to the enhancement of SEC in silica fabrics. Both of these shifts may be viewed as an increase in that area of the secondary emission curve which lies above the  $\delta = 1$  line. Figure 2 illustrates the SEC process as related to a quartz fiber yarn fabric.

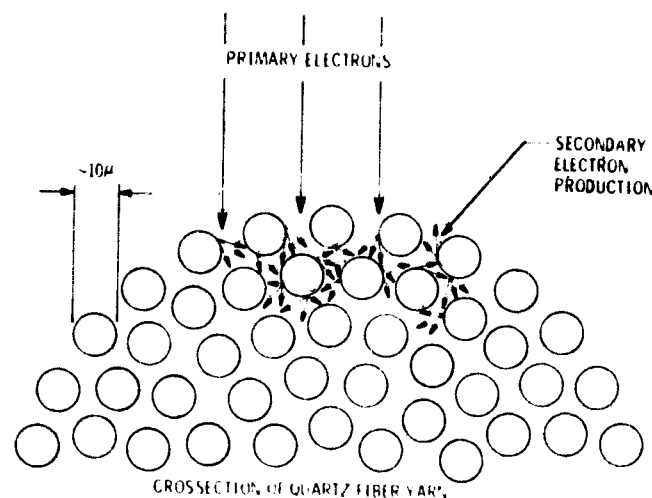


Figure 2. The SEC Process as Related to a Quartz Fiber Yarn Fabric

Because secondary electrons generated have energies less than 10 eV and therefore have a longer mean life time as compared to primaries given the same mean free path, the SEC process, (Figure 2), continues until free electrons exist in all the inter-fiber voids. This mean free path is, of course, a mechanical property of the dielectric matrix and is therefore the same for both secondaries and primaries.

A typical silica fabric contains 10- $\mu$  diameter filaments. Approximately 250 filaments are contained in a yarn strand and 16 strands or more are used to produce a weaving yarn. There are nominally 60 weaving yarns per lineal inch of fabric so each contains almost a quarter of a million filaments. From this, it is evident that there is an extremely large surface to volume ratio associated with silica fabric which is an essential criteria for SEC effect. Secondary electron emission being primarily a surface effect is the contributing factor responsible for this surface to a volume ratio dependence.

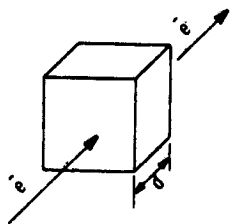
Secondaries may then be thought of as a cloud of free charges within the dielectric matrix and in the presence of an electric field will migrate through the matrix

in the direction of that field much in the same manner as charge carriers move through a conductor. If the field is caused by a differential charge residing on the dielectric, conductivity will continue until the differential charge is neutralized and the E field dissipated.

The SEC effect should not be confused with electron bombardment induced conductivity (EBIC), a somewhat related phenomena exhibited in dielectric solids, since the EBIC effect is not a surface process as is SEC. Both processes require electron bombardment and an external electric field to cause the generated secondaries to drift producing a conduction current through the material. In the EBIC process the internal secondaries drift in the conduction band of the solid, while in the SEC process secondaries are "emitted" and move under the influence of the field through the vacuum space in the pores of a low density dielectric.<sup>5</sup>

#### 4. CHARGE DENSITY AMPLIFICATION

Several questions may arise from the discussion so far. What is the population density of the free electrons in the fabric? And since the fabric behaves like a conductor in a charge bombardment environment, will it attenuate the propagation of electromagnetic radiation? These questions are related since electromagnetic wave propagation is affected by the presence of a plasma medium. Subsequently it will be shown that the free electron density in the fabric is low enough to have negligible effect on wave propagation at communications frequencies. This will be a non-rigorous analysis of the free electron population/concentration within the fabric.



The three controlling factors of this phenomena are, as discussed in previous sections: the fixed mean free path independent of velocity; the low velocity of secondary electrons; and the high secondary emission ratio of the fused silica enhanced by non-normal incidence of the primary beam.

Consider a finite volume in space of cubic dimensions (d) subject to an electron flux.

The average charge density ( $\sigma$ ) inside this volume will be proportional to the time (t) that an electron is within its boundaries. Since

$$t = \frac{d}{v_e},$$

and since

$$\sigma \propto t,$$

the charge density is inversely proportional to the electron velocity. If an electron were to slow down from  $V_p$  to  $V_s$ , there would be a resultant increase in charge density ( $\Delta\sigma$ ) which would be proportional to the velocity ratio

$$\Delta\sigma = \frac{V_p}{V_s}$$

The velocity of an electron is proportional to the square root of its energy and by convention the velocity of an electron is usually referred to by its energy, therefore

$$\Delta\sigma = \sqrt{\frac{E_p}{E_s}}$$

The charge density can also be increased by increasing the electron flux which essentially occurs with the secondary emission process concurrently with a velocity reduction so in effect if there is secondary emission within this finite volume, the charge density increase is approximated by

$$\Delta\sigma = \delta \sqrt{\frac{E_p}{E_s}}$$

where ( $\delta$ ) is the secondary emission ratio.

Considering a primary electron energy of 10 keV, the fact that secondary electrons are within the 10 eV order of magnitude and an approximate secondary emission ratio of 10 within the silica fabric,

$$\Delta\sigma = 10 \sqrt{\frac{10^4}{10}} \approx 320$$

it appears that the free charge density within the fabric will be approximately 320 times the charge density in the primary electron environment.

Traditional metal conductors which could be modeled as solid plasma have free charge concentrations many orders of magnitude greater than that estimated for the fabric. For the purpose of electromagnetic radiation shielding, therefore, the fabric will not behave as a conductor and further calculation using theories developed for wave propagation in plasma would show the charge concentration levels here to be of little consequence in attenuating electromagnetic radiation.

## 5. SECONDARY EMISSION CONDUCTIVITY IN SILICA FABRIC

Tests were performed to measure SEC for several silica fabrics. Results of these tests explain the superior behavior of this material when subjected to a plasma environment.

Silica fabrics were subjected to bombardment by an electron beam with a known electric field imposed across the cross-section of the fabric. This was accomplished by mounting a fabric sample on a conductive backplate. The sample was held in place by a wire screen (~90 percent transmission) in intimate contact with the fabric. A potential was placed between the screen and the backplate and the current flow monitored while varying the potential across the fabric. Resistance of the fabric was calculated from the  $V/I$  characteristics as a function of beam energy and density. Figure 3 shows this test configuration schematically.

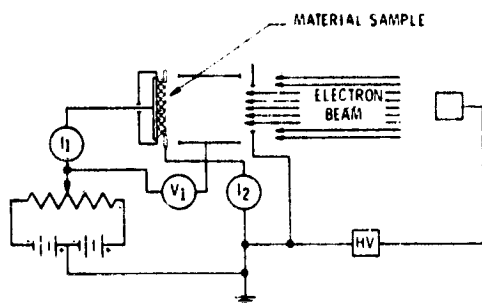


Figure 3. Schematic of Secondary Emission Conductivity Test

Voltage ( $V_1$ ) was varied and the current ( $I_1$ ) was measured. These were used to calculate the resistances of the silica fabrics which are shown in Figure 4 for J. P. Stevens Style 581 and Figure 5 for Style 570 Astroquartz Fabrics.\* As shown in these figures both fabrics exhibit a constant resistance out to 50 to 75 V across the fabric with the Style 581 having the lower resistance of the two. The resistance, however, is much lower than the dc resistance of the fabric due to the presence of the bombarding beam. This resistance then decreases as the voltage across the fabric is increased until it reaches another plateau above 120 to 150 V. This plateau results from depletion of the free charge carriers within the cloth as the bombarding beam can no longer sustain the requirement for charge carriers in the fabric. This saturation results from the fact that the experiment is forcing a potential across the cloth; whereas, in an actual space environment, the potential will disappear as the charges are depleted. This is further evidenced by the lower resistance characteristics which develop as the current density of the beam is increased.

Though it was more difficult to measure and control the bombarding beam when its energy was reduced below 3 keV, it appears that lower energy bombardment would further enhance the conductivity of the fabric. This is substantiated by the fact that above the  $\delta = 1$  line, the area under the secondary emission curve increases as integration is extended towards the lower energy primary electrons.

\* Style 581 is an 11-mil thick fabric which weighs 8 oz/yd<sup>2</sup>, while Style 570 is 27 mils thick with a weight of 19 oz/yd<sup>2</sup>.

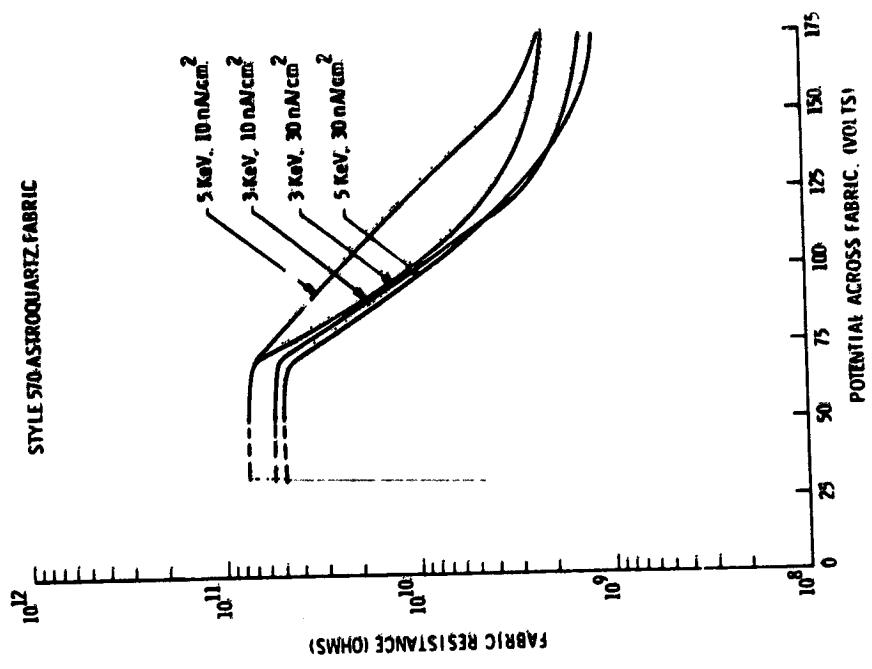


Figure 5. Resistivity of Style 570 Astroquartz Under Electron Bombardment

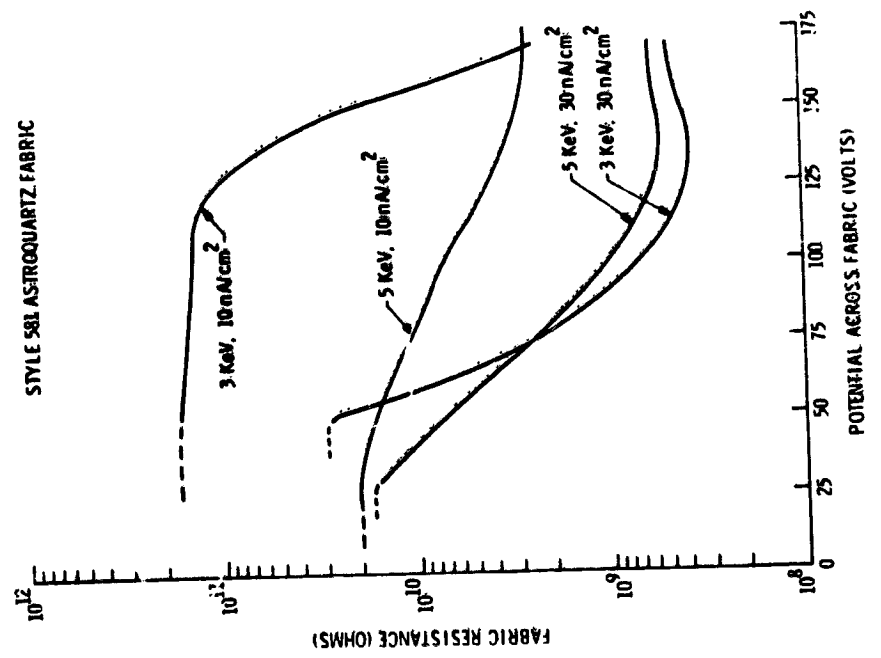


Figure 4. Resistivity of Style 581 Astroquartz Under Electron Bombardment

As the beam energy is increased above 5 keV, the resistance of the fabric tends to increase because the incident electrons generate secondaries deeper within the material where they are unavailable to act as charge carriers near the first surface (wire screen side). In this case the test tends to be pessimistic because at geosynchronous altitude there are always 3 to 5 keV electrons present to generate secondaries near the surface.

In reviewing the results of this experiment it would appear that in an actual environment, where this is a continuous distribution of electron energies, the fabric can be expected to support no more than a 200 V gradient. In fact from conversations with Walter Viehman<sup>6</sup> of NASA Goddard, measurements were conducted in his laboratory which indicated that a 100 V gradient would probably be the maximum encountered. This is in contrast to the kilovolt order static potentials measured at GE and NASA-LeRC in other experiments using monoenergetic electron beams with energies greater than 5 keV.

#### 6. ELECTROSTATIC DISCHARGE INDUCED RADIO FREQUENCY INTERFERENCE

In considering the process by which deposited charge is redistributed within silica fabric, the possibility of micro-discharge was considered. These could conceivably produce electro-magnetic radiation causing radio frequency interference (RFI) to electronic subsystems. In an effort to study these effects an experiment was conducted to measure radiation in proximity to materials in an electron bombardment environment.

Material samples were placed in an evacuated Bell-jar mounted on a grounded metal plate. A Brad-Thompson Industries electron gun was employed as the electron beam source. A thin film of gold (200 Å) was deposited on the inside surface of the Bell-jar. This film is used to prevent a charge buildup on the inside glass surface and possible RFI from spurious discharges. This conductive film was so thin that it produced little attenuation of the electrostatic discharge (ESD) propagated field (3 dB loss at 100 kHz and 0.0 dB loss at 1 MHz). All tests were performed in a shielded room which effectively prevented externally produced fields from interfering with the measurements and of the ESD propagated fields. The set-up is shown schematically in Figure 6.

Samples were bombarded by a high energy monoenergetic electron beam at a current density of  $5 \text{ nA/cm}^2$  which is greater than that normally experienced during geomagnetic substorms. The beam voltage was varied from 5 to 25 kV. Field strength data were measured at 30 cm from the interference source and is expressed in units of dB relative to an arbitrary level. Calibrated, tuned antennas were used to measure the ESD produced fields. The spectral density at UHF, X- and S-band

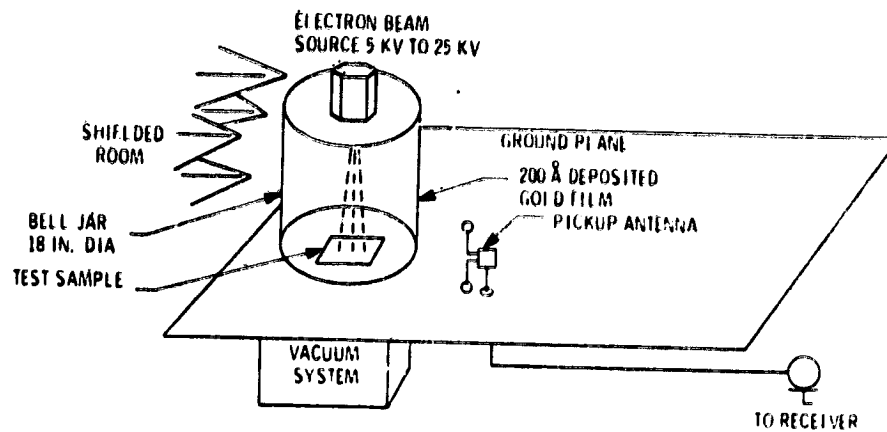


Figure 6. Experimental Test Set-up for ESD Induced RFI Spectrum Measurements

were of primary concern. The antennas were sufficiently directive to reduce the influence of the propagated fields produced by the electron gun source itself. This can be explained as follows. The potential difference between the electron gun and the samples changes simultaneously with the electrostatic discharge and the change in this potential difference produces a propagating field. A directive antenna effectively reduces this source of spurious fields. The results of the ESD induced RFI field measurements are shown in Figure 7.

The materials evaluated in this experiment were:

- (1) A conventional multilayer insulation blanket consisting of 15 layers of 1/2 mil aluminized Mylar with an outer (top) layer of 2 mil thick single sided aluminized Kapton placed with the uncoated side facing out. All metallic film surfaces were connected to a common ground point with a ground strap.
- (2) A multilayer insulation blanket identical to that described in (1) above but with an outer layer of J. P. Stevens, Style 503 Astroquartz fabric (8 mils thick - weighing 3.5 oz/yd<sup>2</sup>) which had been baked at 800°C for two hours to remove sizing.
- (3) A 6-in. aluminum disc with 2 x 2 cm glass covered silicon solar cells bonded to the disc with Eccobond 57C conductive adhesive. This solar array composite was grounded via a strap attached to the back of the aluminum plate.
- (4) Optical Solar Reflector (OSR) tiles bonded to a 6-in. diameter aluminum plate with Eccobond 57C conductive adhesive. A ground strap was connected to the back face of the aluminum disc of this OSR composite.

(5) Two layers of J. P. Stevens, Style 581 Astroquartz Fabric (each 8 mils thick and weighing 8 oz/yd<sup>2</sup> per layer) baked at 800°C for three hours to remove sizing. Both layers were tied to a common ground point with a ground strap.

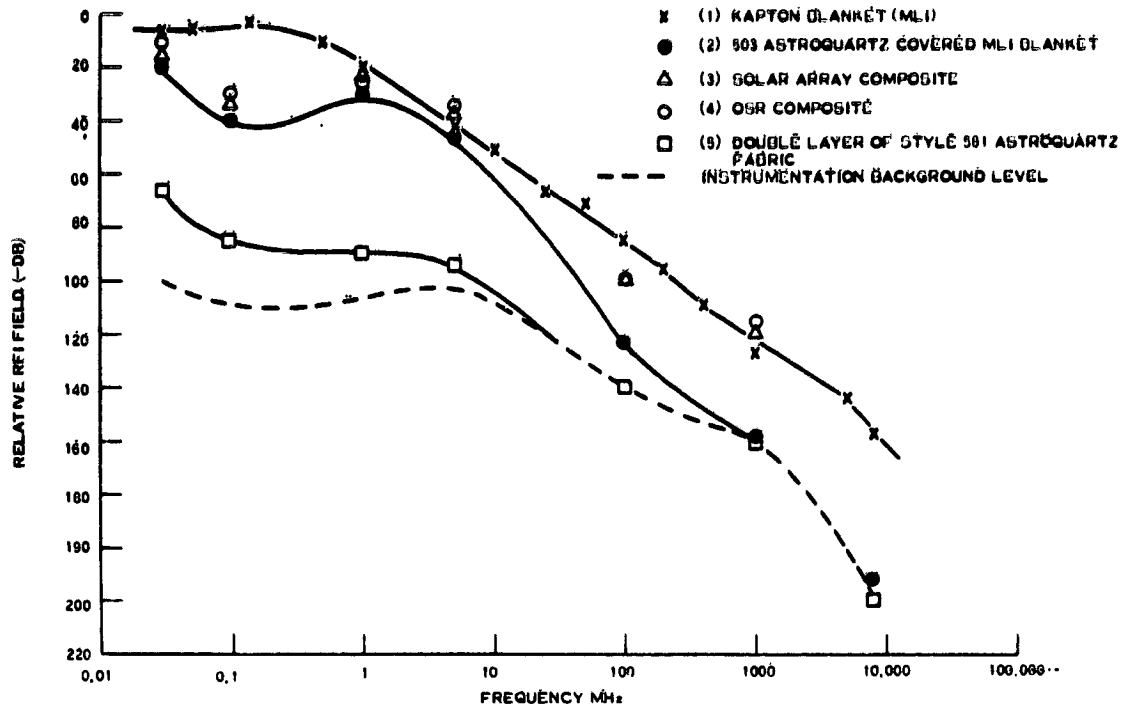


Figure 7. Electric Field Strength Spectral Distribution for Some Spacecraft Materials Under 15 kV - 5 nA/cm<sup>2</sup> Electron Bombardment

Results obtained from this series of ESD induced RFI tests, indicate that the multilayer insulation blanket with the Kapton outer covering, OSR plates, and solar cell arrays produce substantial RFI field strengths in the frequency range 100 to 10,000 MHz. Astroquartz 503 and 581 (especially) produced significantly little or no RFI field strengths in the 100 to 10,000 MHz frequency range. It should also be noted that about 1000 MHz where most spacecraft communication is done, the RFI generated by the silica fabric samples were within experiment noise.

## 7. CONCLUSIONS

Silica fabric exhibits rather unique behavior as a dielectric spacecraft thermal control coating. It has been shown that it will not sustain a differential charge in excess of 100 V while in a simulated electron plasma charging environment. This is contrary to the behavior of other dielectrics tested under similar conditions. Secondary emission conductivity has been established as the process responsible for this desirable characteristic. Essentially, the primary beam is transmitted through the material after reducing its velocity to under 100 eV, where it can be harmlessly conducted and uniformly distributed to the spacecraft structure. Through active means such as electron guns or plasma engines the structure potential can be controlled with respect to the plasma if mission requirements dictate.

As the bombardment intensity increases the resistivity of the material correspondingly decreases to maintain a fixed differential potential, thus the material acts as a passive control device in a changing environment employing a process much like dc conductivity. Other dielectrics redistribute charge by electrical arcing and hence can produce significant RFI which can disrupt a variety of spacecraft subsystems. Though the fabric behaves like a conductor during bombardment, the charge carrier density in the material is sufficiently low so that it does not interfere with propagation of electromagnetic radiation. This means the material can be used even over antennas and feed horns.

So far, testing of this material has been done with monoenergetic electron beams. In the actual environment, the charged, bombarding particles will be distributed over a broad range of energies from a few eV to possibly 50 keV; however, the major portion of the population will be below 10 keV. With the low energy component always present secondary emission will be greater and the fabric behavior can be expected to be much improved as compared to the results reported here. Monoenergetic bombardment is the most conservative test that can be done on materials which depend on high secondary emission for desirable behavior unless the bombarding energy is held within their most efficient emission range.

High purity silica fabrics should be considered as a prime candidate for thermal control application on geosynchronous satellites. The properties discussed here show what can be expected of the material, and with utilization design, its benefits can be maximized for each spacecraft application.

## Acknowledgments

We gratefully acknowledge the contributions made by Mr. G. Condón of the General Electric Company in conducting the RFI measurement experiments.

## References

1. Eagles, A. E., et al Fabric Coatings: A New Technique for Spacecraft Passive Temperature Control AIAA paper no. 75-868, AIAA 10th Thermophysics Conference, Denver, Colorado, May 1975.
2. McPherson, D. A., Kaufman, D. P., Schober, Capt. W. Spacecraft Charging at High Altitudes, the SCATHA Program, AIAA 13th Aerospace Sciences Meeting, Pasadena, California, 20-22 January 1975.
3. Knott, K. The equilibrium potential of a magnetospheric satellite in an eclipse situation, Planet. Space Sci., 20:1137-46.
4. Dekker, A. J. (1958) Secondary electron emission, Solid State Physics, Vol. 6, Academic Press.
5. Kazan, B., and Knoll, M. (1968) Electronic Image Storage, Academic Press.
6. Private Communication.

#### Contents

1. Introduction	669
2. Some Test Results	670
3. Conclusions	686
References	686

## 7. Conductivity Effects in High-Voltage Spacecraft Insulating Materials

Richard C. Adamo and Joseph E. Nanevitz  
Electromagnetic Sciences Laboratory  
Stanford Research Institute

and

Norman Grier  
Lewis Research Center, NASA

### 1. INTRODUCTION

A series of laboratory measurements has been performed to explore the effects of various external parameters on the conductivity properties of several typical and potential spacecraft insulating materials in a simulated space environment.

The materials tested include Kapton, Teflon, quartz, and polyvinylidene fluoride. The parameters varied in these tests include sample thickness, temperature, applied voltage, illumination intensity and wavelength, and electron beam energy and current density. Tests were performed both with conventional optically transparent gold front-surface electrodes and with the front surfaces of the test samples exposed directly to an electron beam. All tests were conducted in a vacuum chamber at a pressure of approximately  $10^{-8}$  torr.

During the course of this program,<sup>1,2</sup> a rather large number of tests were performed and many tests were repeated several times to verify unexpected results.

It is not the intent of this paper to present a detailed compilation of the results of these tests but to summarize some of the more interesting general properties of the materials tested.

Many of these properties should be of specific interest to those involved in the modeling of spacecraft charging effects, in laboratory simulation testing of spacecraft materials, and in the design of future spacecraft.

## 2. SOME TEST RESULTS

The test setup shown schematically in Figure 1 was used to obtain the results shown in Figures 2 through 11.

Test samples were prepared by sputtering 200 Å thick gold center and guard electrodes on the front surfaces and somewhat thicker gold ground electrodes on the back surfaces.

The area of the center electrode is approximately 7 cm<sup>2</sup>. Although total measured bulk currents are shown in the figures, the effective bulk resistivities ( $\rho_{\text{bulk}}$ ) can be calculated, since

$$\rho_{\text{bulk}} = \frac{7(10^{-4})}{Id} \text{ (ohm-m)} \quad (1)$$

where  $V$  is the applied voltage,  $I$  is the measured current, and  $d$  is the sample thickness in meters.

Sample temperatures were controlled by heating or cooling the large aluminum block on which the samples were mounted.

For some tests, a xenon light source was used to illuminate the samples through a quartz window in the vacuum chamber. Provisions were included for attenuating the light using neutral density filters and for selecting a particular portion of the optical spectrum using a series of bandpass filters.

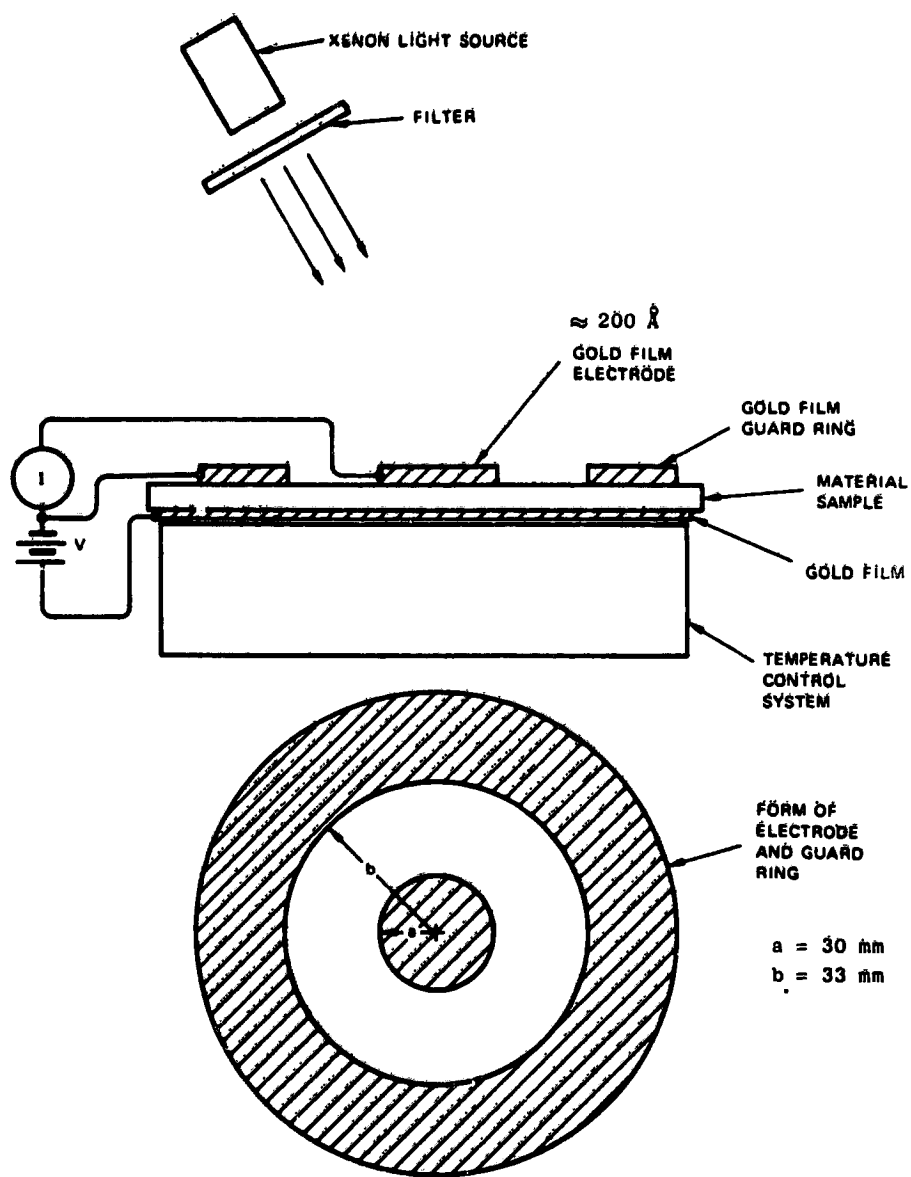


Figure 1. Setup for Front-Surface Electrode Tests

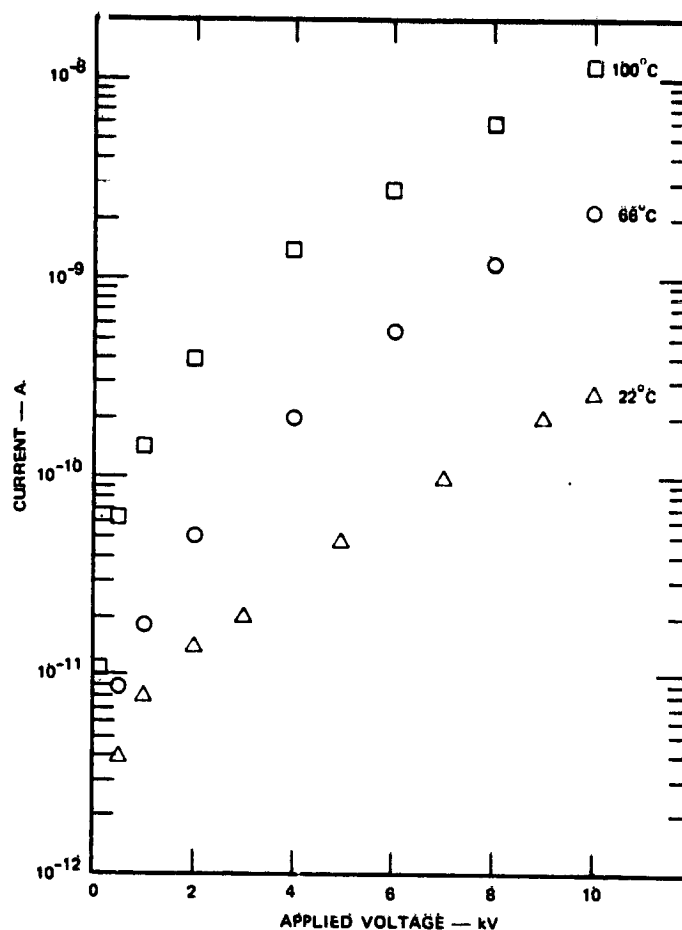


Figure 2. Dark-Bulk Current in Kapton V (5 mil) at Various Temperatures

Figure 2 shows an example of variations in conductivity with changes in sample temperature. The sample material in this case was Kapton V.

It should be noted that several types of Kapton are available. Kapton H (which was also tested) has been widely used in spacecraft thermal blankets. Kapton V is reported to have similar general properties but to allow less shrinkage at elevated temperatures.

It can be seen from Figure 2 that the dark bulk conductivity of Kapton V increases considerably with increasing temperature.

The values of current shown in Figure 2 were each measured 1 min after the corresponding voltages were applied.

In these particular tests, the initial displacement currents appeared to have become negligible and the conduction currents were relatively stable after 60 sec-

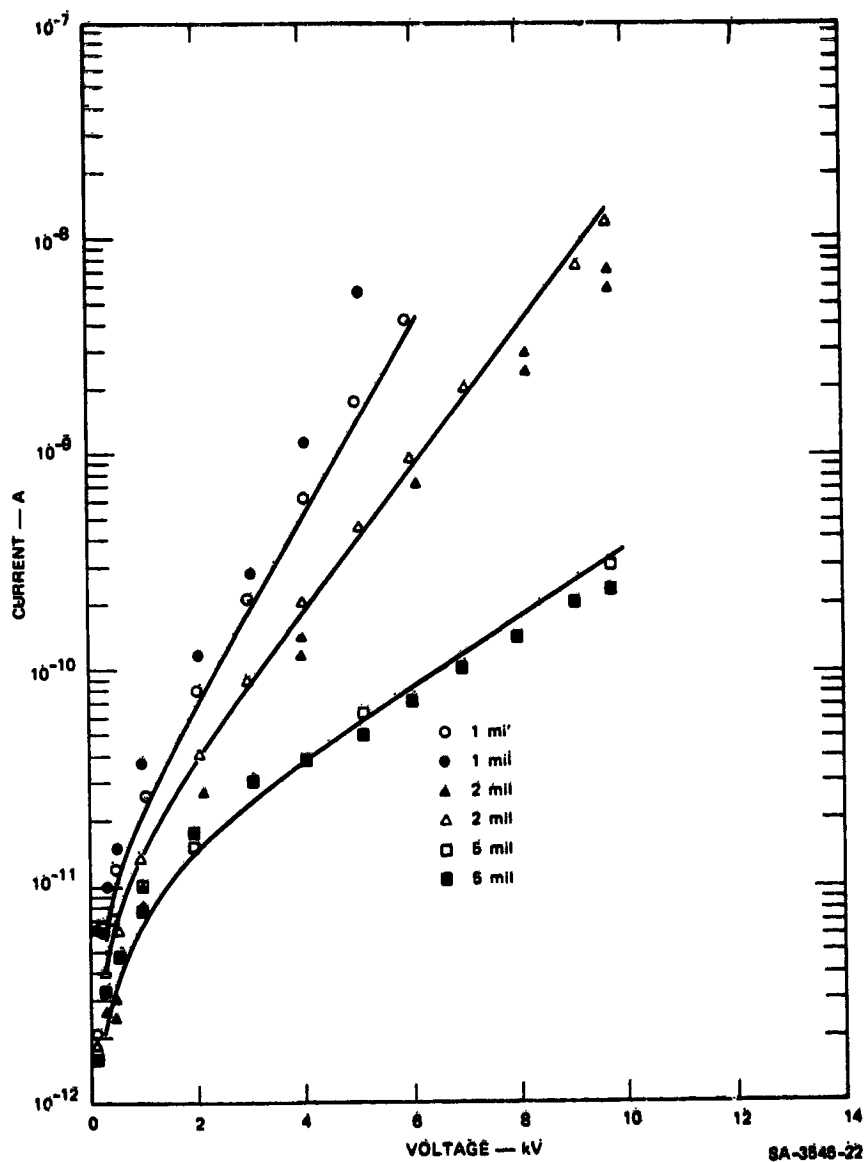


Figure 3. Dark-Bulk Current in Various Thicknesses of Kapton H at 22°C

onds. This was not true in all tests, however, and in many cases, the measured currents in various materials under certain conditions continued to change considerably for periods of several hours.

Figure 3 illustrates the effect of material thickness on effective bulk conductivity of Kapton H. It can be seen, for example, that with an applied voltage of 10 kV, reducing the material thickness by a factor of 2.5 produces an increase in current of two orders of magnitude. This corresponds to a 40X increase in effective bulk conductivity.

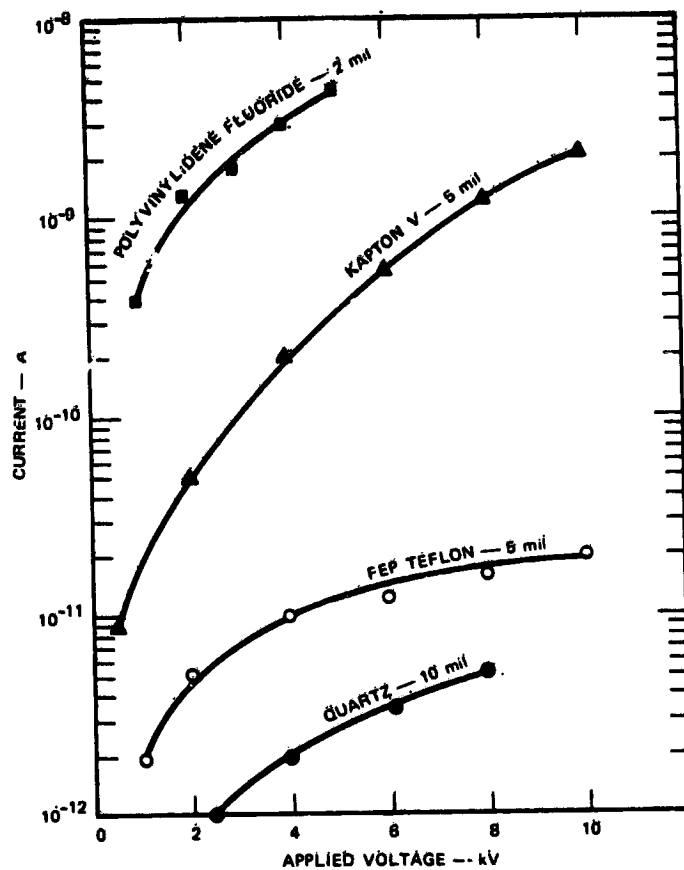


Figure 4. Dark-Bulk Currents in Various Materials at 66°C

Figure 4 shows the dark bulk currents measured in various materials of different thicknesses. Due to the nonlinear effect illustrated in Figure 3, it is not possible to use a simple linear correction to eliminate material thickness as a parameter in the Figure 4 data. In general, however, it has been observed that in the dark, FEP Teflon and quartz are better insulators than Kapton and polyvinylidene fluoride by approximately two orders of magnitude.

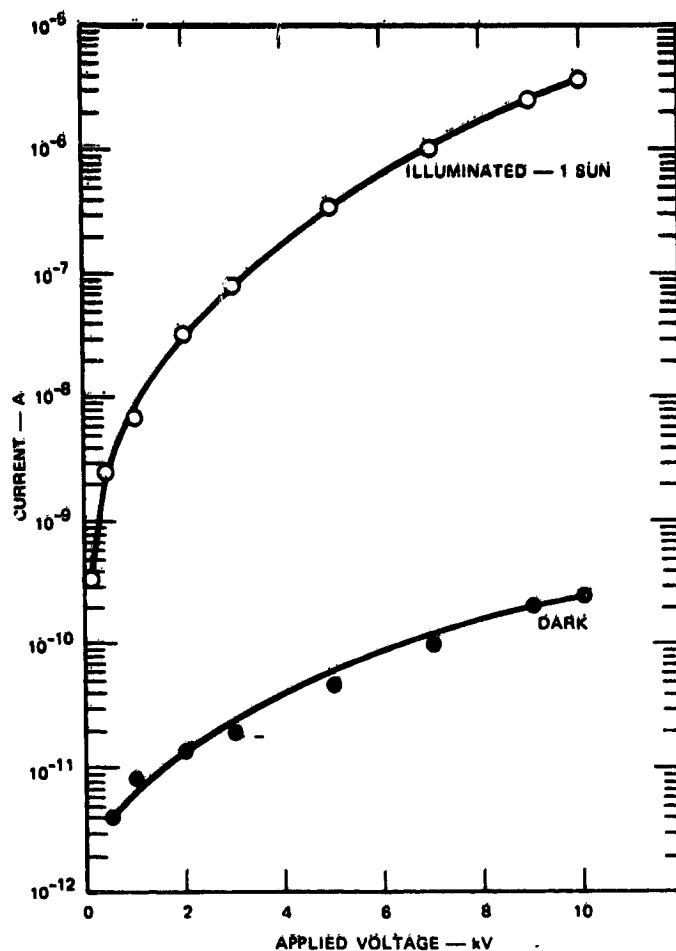


Figure 5. Bulk Current in Kapton V (5 mil) at 22°C

Figure 5 illustrates the short-term effect of illumination on the bulk conductivity of Kapton V. The xenon lamp, in this case, was used to produce a power density of 1 solar constant ( $\approx 1.4 \text{ kW/m}^2$ ) at the sample surface. With an applied voltage of 10 kV, the measured bulk current with illumination is more than four orders of magnitude higher than the dark bulk current.

Similar but less pronounced effects were observed in FEP Teflon and in quartz as shown in Figures 6 and 7.

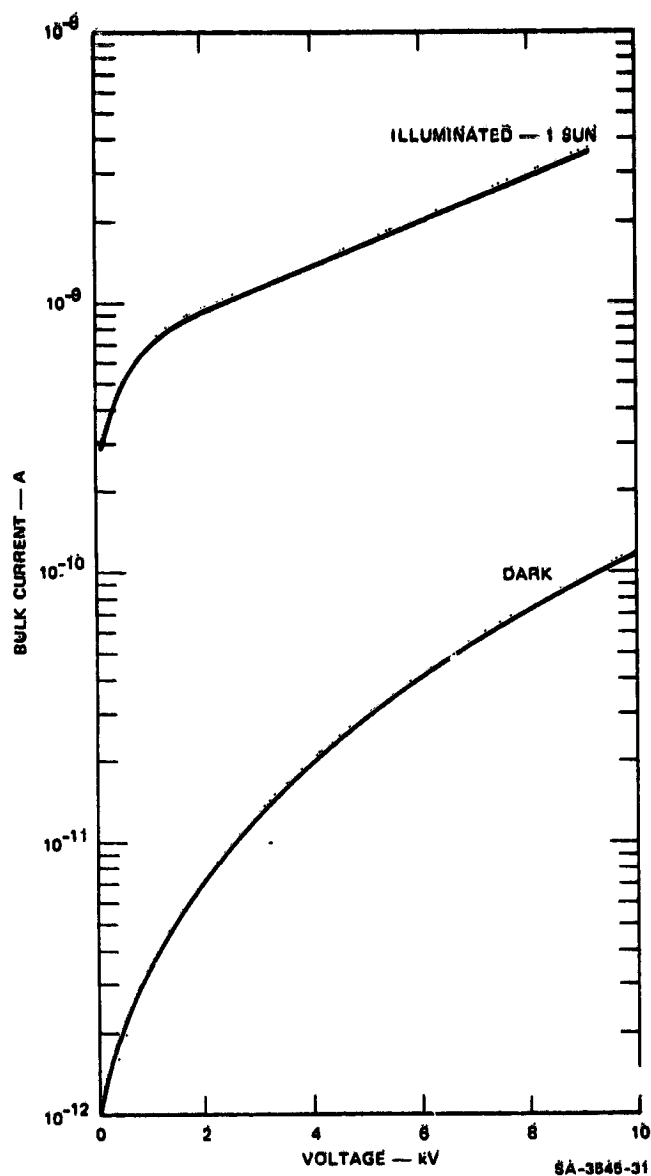


Figure 6. Bulk Current in FEP Teflon (5 mil) at 100°C

The data in Figure 6 were obtained at 100°C. The effect of illumination was reduced at lower temperatures. Even at 100°C, the relative increase in conductivity in FEP Teflon was two orders of magnitude less than that observed in Kapton V at 22°C.

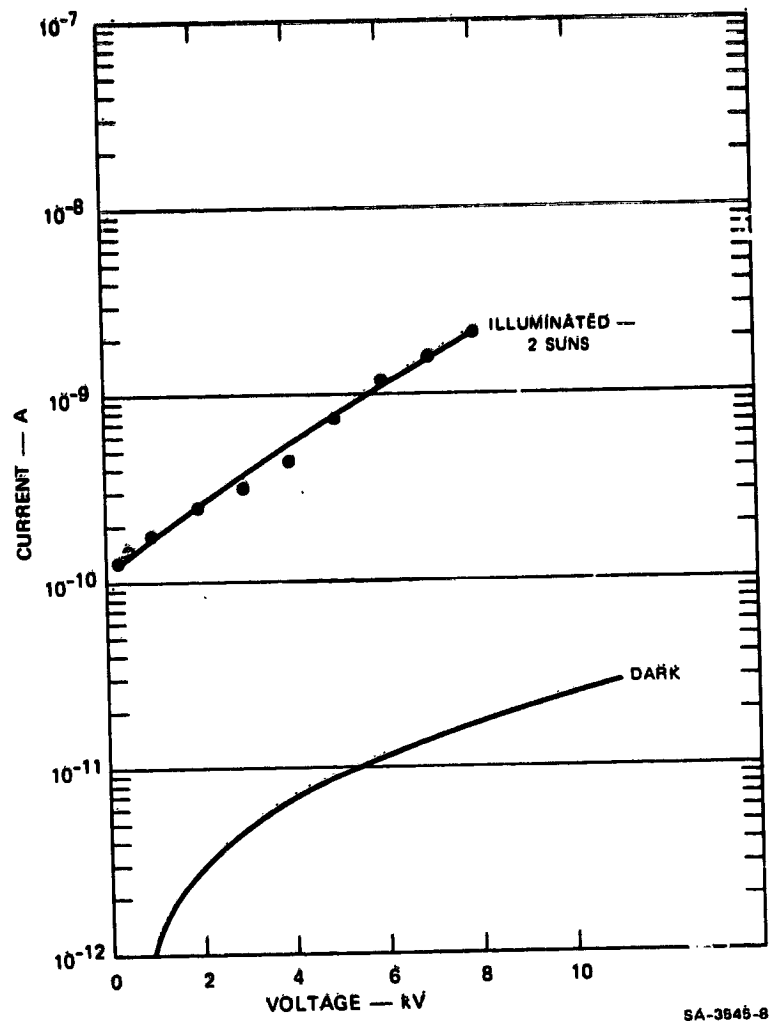


Figure 7. Bulk Current in Quartz (10 mil) at 100°C

The data in Figure 7 were obtained at 100°C with an incident energy density equivalent to two solar constants. It can be seen that the effect of illumination on the conductivity of quartz is also significantly lower than that observed in Kapton V.

The data in Figures 5, 6, and 7 were all obtained within 5 min of the time that the samples were initially exposed to illumination.

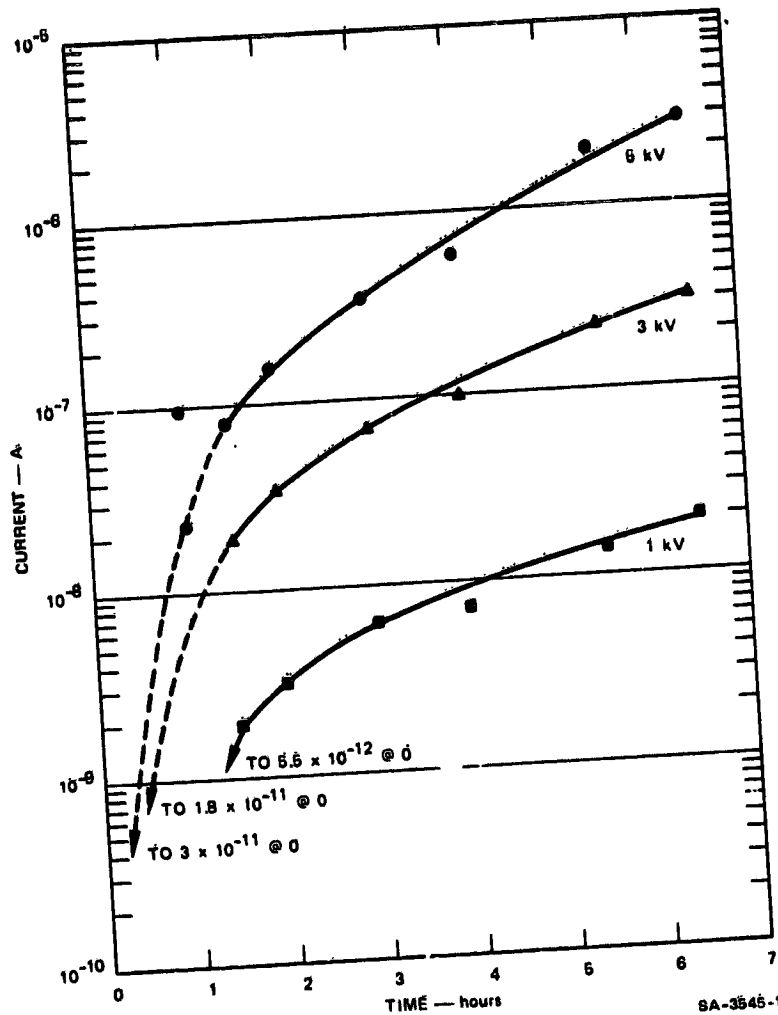


Figure 8. Dark-Bulk Current in Kapton H (5 mil) at 22°C Shortly After Various Periods of 1 Sun Illumination

An additional series of tests was performed in which Kapton H samples were illuminated for longer periods and the dark bulk currents were measured with various applied voltages within minutes after the lamp was turned off. The results of these tests are shown in Figure 8. It can be seen that the dark bulk current measured shortly after 6.5 hr of illumination is as much as five orders of magnitude higher than the dark bulk current before illumination.

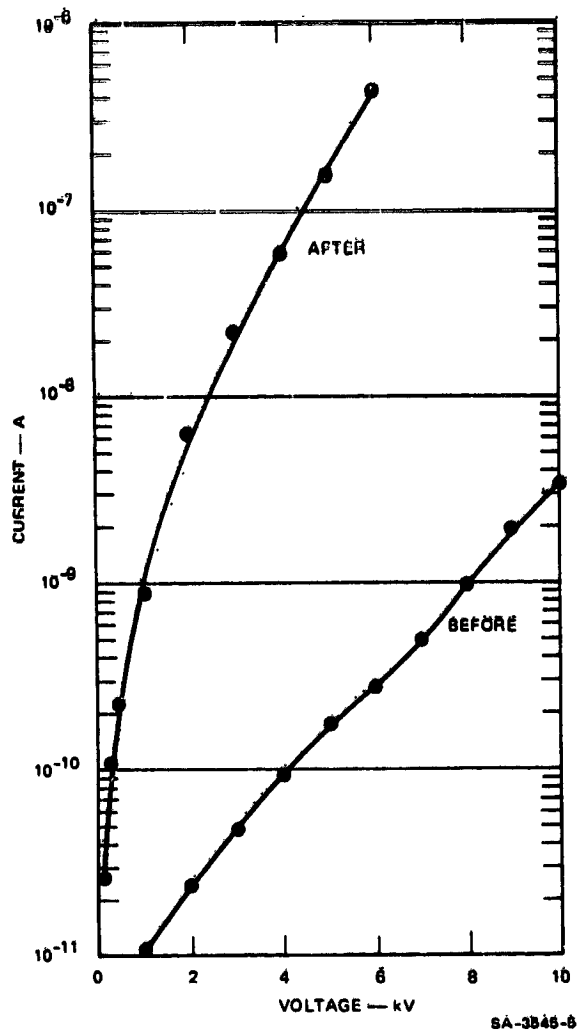


Figure 9. Dark-Bulk Current in Kapton H (5 mil) at 100°C Before and 65 Hours After 6.5 Hours of 1 Sun Illumination

Figure 9 illustrates that the dark bulk conductivity after 6.5 hr of illumination remains three orders of magnitude higher even 65 hr after the lamp is turned off.

This long-term phenomenon may have an important effect on the charging properties of Kapton H materials on synchronous orbit satellites, particularly during eclipse periods.

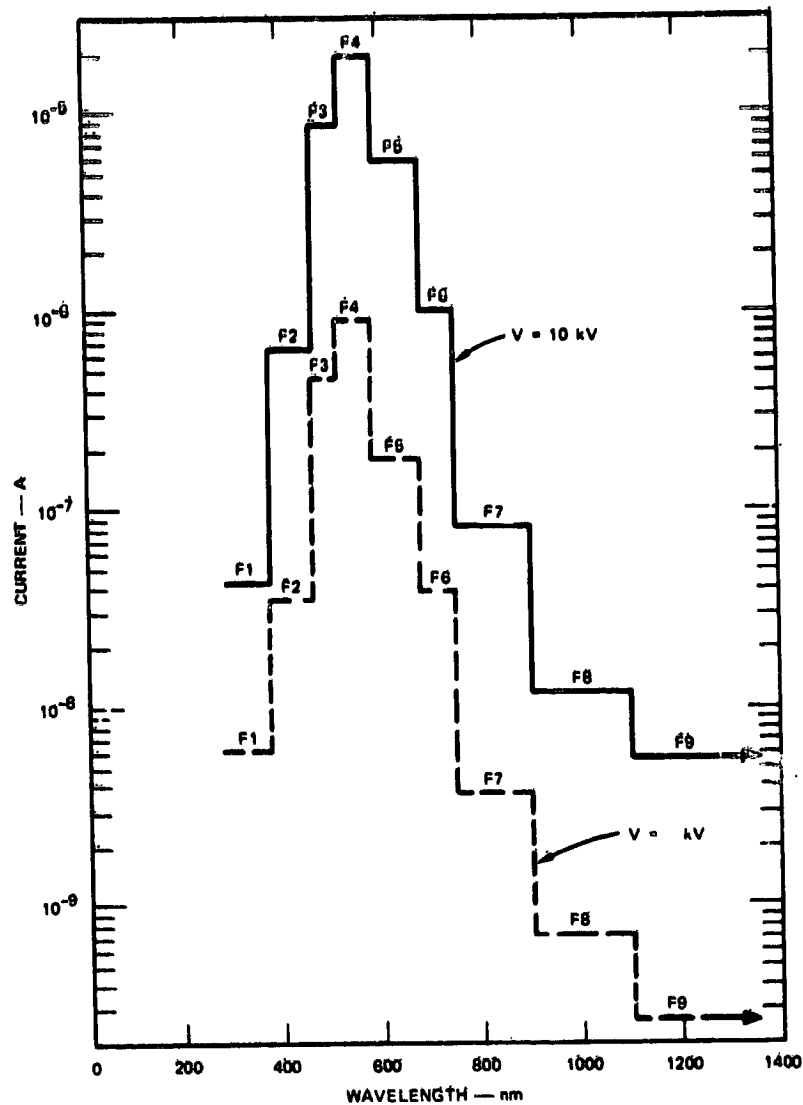


Figure 10. Normalized Bulk Photocurrents in Kapton V (5 mil) at 22°C

In order to determine the optical wavelengths at which the conductivity of the sample materials is most enhanced, tests were performed with various bandpass filters inserted between the xenon lamp and the samples. Since the actual power density at the test sample location varies with bandpass filter transmission properties and available lamp power within the passband, the raw results of these tests have been normalized. The bulk currents shown in Figures 10 and 11 represent

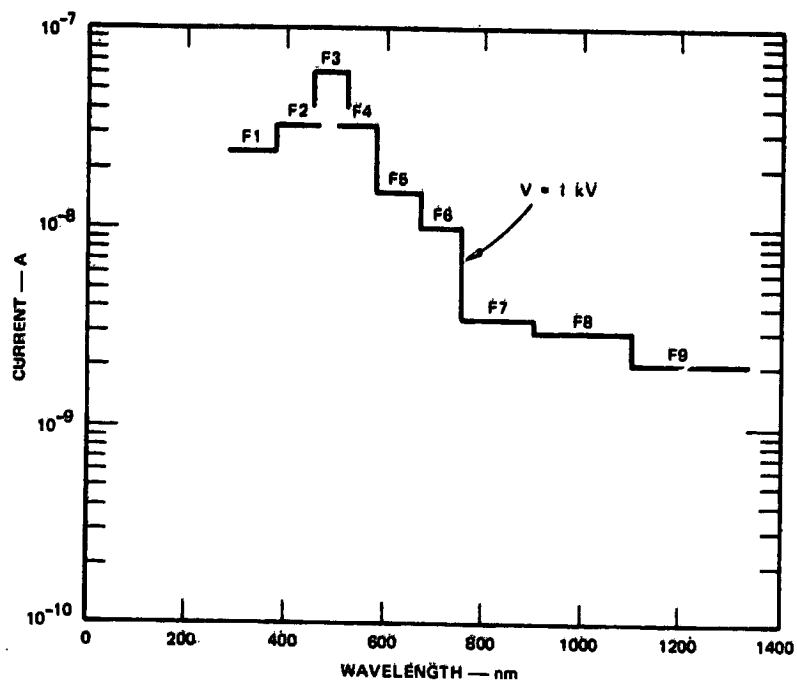


Figure 11. Normalized Bulk Photocurrent in Polyvinylidene Fluoride (2 mil) at 22°C

the measured currents normalized for an incident power density of  $1.4 \text{ kW/m}^2$  concentrated within the filter passband.

It can be seen that the peak bulk normalized current occurs in the 500 to 580 nm passband for Kapton V and in the 450 to 524 nm passband for polyvinylidene fluoride. For both of these materials, these wavelengths correspond to regions of transition from high optical density to low optical density.

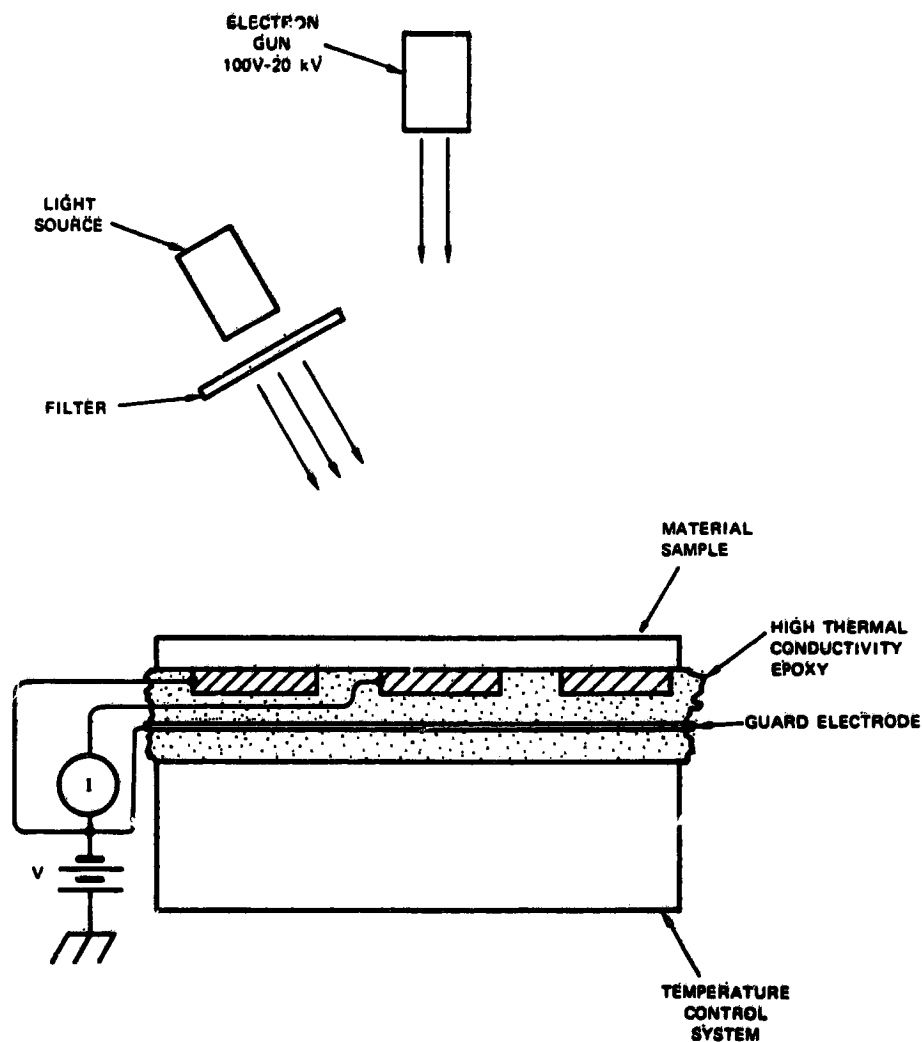


Figure 12. Setup for Electron-Beam Tests

The test configuration used for tests in which the front-surfaces of samples were exposed directly to an electron-beam is shown in Figure 12.

During the performance of electron-beam tests on Kapton-V, it was found that with a constant incident electron-beam density, the magnitude of the bulk current obtained at a specific electron-beam energy depends on the beam energies used for preceding test points.

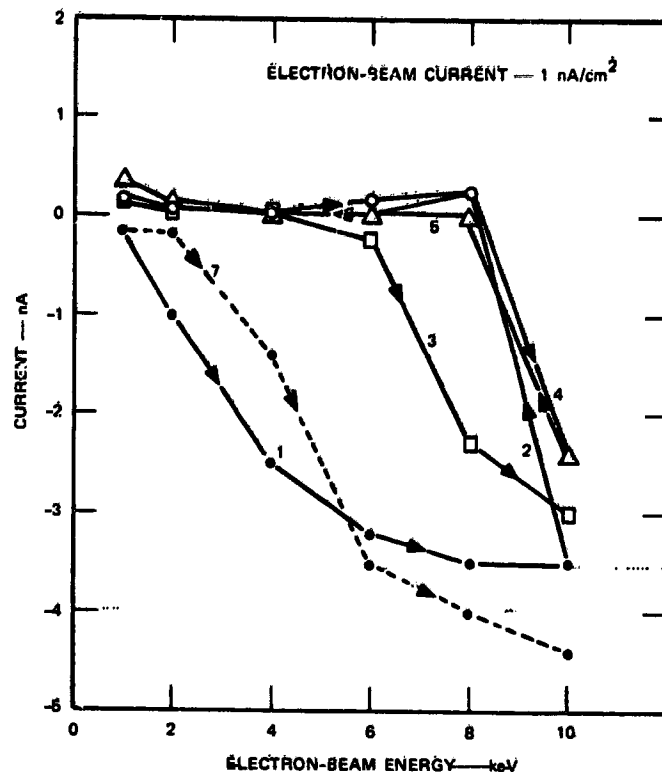


Figure 13. Dark-Bulk Current vs Beam Energy in Kapton V (5 mil) at 22°C

An example of this "hysteresis" effect is shown in Figure 13. It should be noted that the left-hand current scale on this figure is not logarithmic but linear.

The initial measured currents obtained by stepping the incident electron-beam energy up from 1 keV to 10 keV, while maintaining the incident beam current constant at  $1 \text{ nA/cm}^2$ , are connected by the line labeled 1. Each of these currents was measured after the incident beam had remained at the indicated energy for 60 seconds.

The line labeled 2 shows the currents obtained as the beam energy was stepped down from 10 keV. It can be seen that curves 1 and 2 are quite different. Additional tests indicate that after stepping through the entire energy range several times in the dark, the results become similar in either direction (as shown in curves 4 and 5) and the "hysteresis" effect is no longer evident.

However, after the completion of Test 5, the electron-beam was turned off for 60 sec while the sample was exposed to 1 sun of illumination. The lamp was then turned off and the dark electron-beam test was repeated yielding the results shown by curve 7.

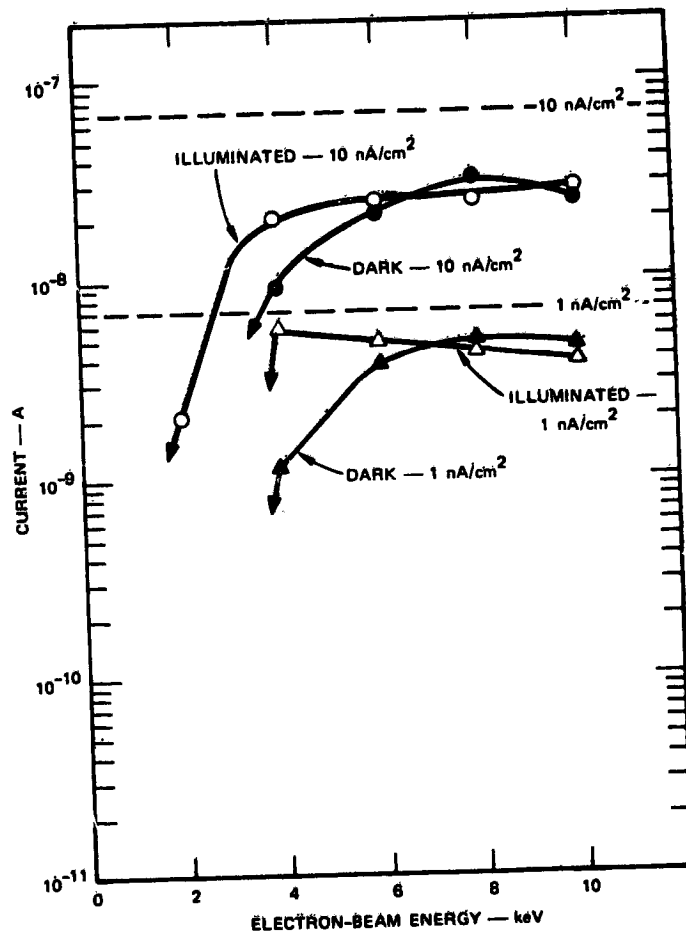


Figure 14. Bulk Currents in Polyvinylidene Fluoride (2 mil) at 22°C

The results of this and other tests indicate that short periods of illumination tend to "erase" the sample and return it to near its original state.

The results shown in Figure 13 were obtained with Kapton V. Similar effects were observed using polyvinylidene fluoride samples.

In additional tests it was found that this hysteresis effect does not occur if the samples are illuminated throughout the test sequence.

Preliminary results of both dark and illuminated electron-beam tests on polyvinylidene fluoride and Kapton 7 are shown in Figures 14 and 15.

Figure 14 indicates that for polyvinylidene fluoride, at incident beam energies above approximately 6 keV, the bulk current is limited by the available incident beam current density. This is true both with and without illumination.

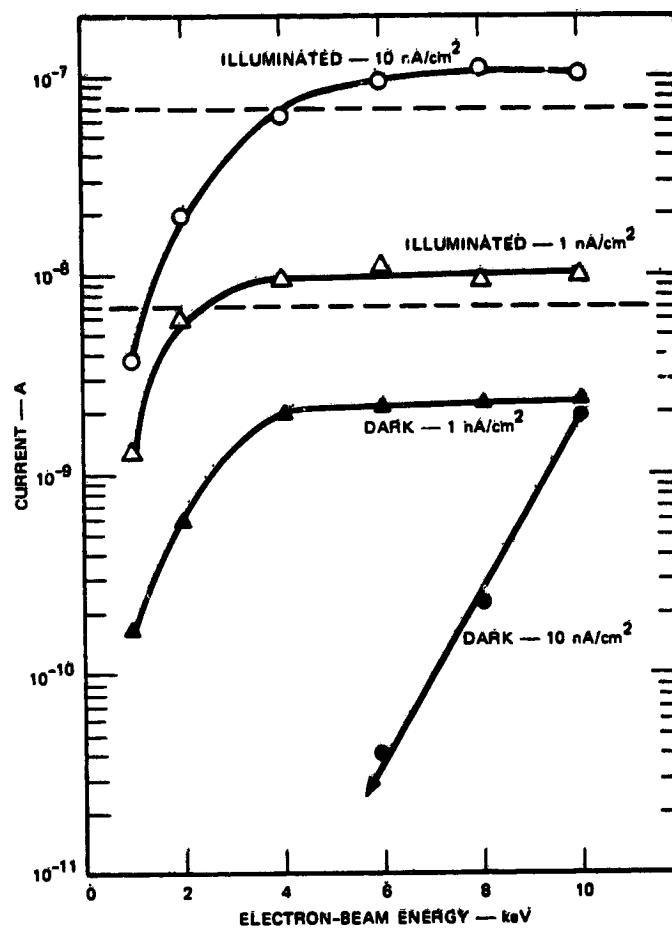


Figure 15. Bulk Currents in Kapton V (5 mil) at 22°C

With Kapton V, however, the bulk current increases significantly under illumination as is shown in Figure 15.

The reasons for reduced dark bulk currents with increased incident current density, particularly at lower beam energies observed in Kapton V, have not yet been explored.

### 3. CONCLUSIONS

The data presented illustrate some of the complexities in electrical characteristics exhibited by typical spacecraft materials as a result of interactions with various conditions of their environment.

Increased concern with spacecraft charging phenomena and their effects has recently resulted in increased efforts to provide more complete models of the space environment and its interaction with spacecraft. There is, however, at present, a critical lack of theoretical and experimental information on material properties for use in these efforts as well as in the design of future spacecraft and in the development of new spacecraft materials.

In particular, efforts should be made to provide a better understanding of both the short-term and long-term effects of the space environment on material properties and of the effects of material properties on spacecraft charging phenomena.

### References

1. Coffey, H. T., Nanevich, J. E., and Adamo, R. C. (1975) Photoconductivity of High-Voltage Space Insulating Materials, Project 3545, Final Report, Contract NAS3-18912, Stanford Research Institute.
2. Adamo, R. C., and Nanevich, J. E. (1977 - in preparation) Photoconductivity and Light Aging of Kapton and Polyvinylidene Fluoride, Project 4904, Final Report, Contract NAS3-20080, Stanford Research Institute.

## Contents

1. Introduction	687
2. Measurement Setup and Procedure	689
3. Coatings	691
4. Results and Analysis	692
5. Conclusions	697
Acknowledgments	697
References	698

## 8. Investigation of Conductive Thermal Control Coatings by a Contactless Method in Vacua

W. Viehmann, C.M. Shai, and E.L. Sanford  
Goddard Space Flight Center, NASA  
Greenbelt, Maryland

### Abstract

A technique for determining the conductance per unit area of thermal control coatings for "electrostatically clean" spacecraft is described. In order to simulate orbital conditions more closely, current-density-voltage ( $j$ - $V$ ) curves are obtained by a contactless method in which the paint on an aluminum substrate is the anode of a vacuum diode configuration with a tungsten filament cathode. Conductances per unit area which satisfy the International Sun Earth Explorer (ISEE) requirement of  $j/V \geq 10^{-9}$  A/V  $\text{cm}^2$  have been observed on black paints containing carbon and in "white" and green paints filled with zinc oxide which has been "fired" in order to induce defect conductivity. Because of surface effects and the non-homogeneous nature of paints, large discrepancies are found between measurements with the contactless method and measurements employing metallic contacts, particularly at low current densities. Therefore, measurements with metallic contacts are considered to be of questionable value in deciding the suitability of coatings for electrostatic charge control.

### 1. INTRODUCTION

In order to minimize interference of spacecraft charging with low energy plasma and electric field measurements on the ISEE missions, potential differences

between dark and illuminated sections of the spacecraft surface are to be kept to less than 1 volt. Under net current densities ( $j$ ) of about  $10^{-9}$  A cm<sup>-2</sup> resulting from photoelectrons and plasma electrons in ISEE orbits, conductance per unit area of  $\Sigma/A = j/V \geq 10^{-9}$  A cm<sup>-2</sup> V<sup>-1</sup> are therefore required of thermal control coatings over metal surfaces. In terms of material parameters, this requirement can be expressed as

$$\frac{V}{j} = R \cdot A = \rho \cdot d \leq 10^9 \Omega \text{cm}^2 \quad (1)$$

where  $\rho$  is the specific resistivity in  $\Omega$  cm and  $d$  the thickness of the coating in cm. For their product the term "area resistance" seems to be appropriate, since it is also the product of a resistance,  $R$ , and the area,  $A$ , over which it is measured.

Thermal control paints are typically  $5 \cdot 10^{-3}$  to  $10^{-2}$  cm thick, and resistivities of  $< 10^{11}$   $\Omega$  cm are therefore required. Inorganic paints, particularly those based on zinc oxide and alkali silicates, were considered as promising candidates with "semiconducting" zinc oxide as pigment. Their preparation, optical properties, and environmental stability are described in a previous paper.<sup>1</sup>

By expressing the resistivity requirement in the form of Eq. (1), one tacitly assumes that—at constant temperature— $\rho$  is a true material parameter, independent of voltage, that is, the conduction mechanism is ohmic in nature. In wide gap semiconductors and insulators, however, ohmic conduction is the exception, rather than the rule, because it occurs only if the concentration of (thermally generated) free, or conduction, electrons far exceeds that of injected (space charge) electrons. Since the concentration of thermal electrons in insulators is small and injected and trapped charge densities are strongly field dependent, conduction in thin films of insulators or semiconductors is strongly voltage dependent with the ohmic (linear) portion of the  $j$ - $V$  curve occurring at low voltages, where it is easily obscured by contact effects, that is, by interface potentials at the semiconductor-contact interface. Recognizing that conductivity is both voltage and electrode dependent, we prefer to express the "conductivity specification" as a conductance-per-unit-area requirement in the form

$$j > 10^{-9} \text{ A cm}^{-2} \text{ V}^{-1} \text{ for } V \leq 1 \text{ Volt} \quad (2)$$

with the added stipulation that such conductance be measured under conditions closely simulating those of the actual application, that is, with a "free"—or contactless—surface in an electron plasma. Such a contactless technique has been described by Bentlage et al,<sup>2</sup> and applied to determine the changes in conductance resulting from surface contamination of conductive coatings. We have adapted this method to the measurement of thermal control paints and other spacecraft coatings in the course of developing conductive paints for the ISEE program.

## 2. MEASUREMENT SETUP AND PROCEDURE

The test setup as schematically shown in Figure 1 is a vacuum diode configuration consisting of a tungsten filament cathode and 2 symmetrically arranged anodes. Both anodes are 2.5 cm diameter aluminum discs, one of which is covered on one side with the coating to be measured and the other serves as reference diode. They are mounted in a copper block, which can be heated and cooled by means of copper coils through which liquid  $N_2$  or hot air is passed. Electrical insulation of the anodes against the copper block is provided by a Teflon mount and an effective anode surface of  $1 \text{ cm}^2$  area is defined by an aperture in the form of a copper ring preceding the anode. This aperture is directly attached to the copper block, which is at ground (cathode) potential.

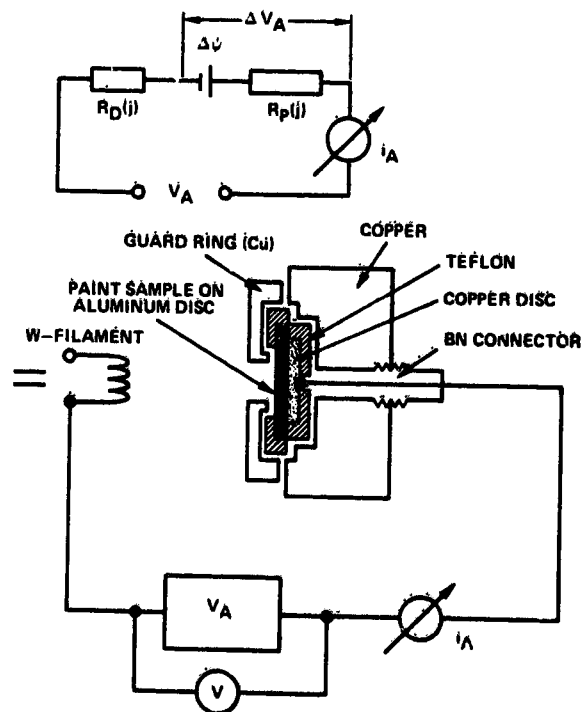


Figure 1. Schematic of Test Setup for the Contactless Measurement of Paint Resistances (Lower Part), and its Equivalent Electrical Circuit (Upper Part). The reference anode, arranged symmetrically to the filament, is not shown

Filament power is supplied by a current regulated dc power supply<sup>(a)</sup> and anode voltage by either a bipolar<sup>(b)</sup> or positive regulated power supply.<sup>(c)</sup> Anode voltage and current are measured by means of a high impedance ( $> 2 \cdot 10^{10} \Omega$ ) digital voltmeter<sup>(d)</sup> and digital picoamp-meter,<sup>(e)</sup> respectively. All electrical connections are made by means of shielded cables, permitting current measurements above a noise current of approximately  $2 \cdot 10^{-11}$  amperes.

The equivalent circuit of the measurement setup can be represented by a resistance,  $R_p$ , in series with the internal resistance of the diode and an EMF,  $\Delta\psi$ , equal to the work function difference between the paint and its substrate (aluminum). Accordingly, the conductance per unit area of the paint is determined from the difference in slope of the j-V curves of the reference diode, and of the (painted) measurement diode of equal area, A, as illustrated in Figure 2. For a given current density, j, the anode voltage  $V_A$  across the measurement diode is higher by  $\Delta V_A = jR_p \cdot A + \Delta\psi$  than that across the reference diode. For  $j \rightarrow 0$ , this difference becomes equal to  $\Delta\psi$  and the conductance per unit area of the paint can be determined as

$$\left(\frac{\Sigma}{A}\right)_{\text{paint}} = \frac{j}{\Delta V_A - \Delta\psi} \quad (\text{A cm}^{-2} \text{V}^{-1}) \quad (3)$$

The conductance of the reference diode at current densities of  $10^{-9} \text{ A cm}^{-2} < j < 10^{-7}$  is of the order of  $5 \cdot 10^{-6} \text{ A cm}^{-2} \text{V}^{-1}$ , which determines the upper limit of conductance values that can be reliably measured as approximately  $10^{-7} \text{ A cm}^{-2} \text{V}^{-1}$ . The lower limit is set by the noise current and a maximum anode voltage of  $\sim 200 \text{ V}$  as  $\sim 10^{-13} \text{ A cm}^{-2} \text{V}^{-1}$ .

(a) Kepco Model Ck8 - 5 MHS

(b) Kepco Model BOP 72,  $-70 \text{ V} < V_A < +70 \text{ V}$

(c) Kepco Model HB 4 AM, for  $0 < V_A < 300 \text{ V}$

(d) Multimeter H. P. 34

(e) Keithly Model 440

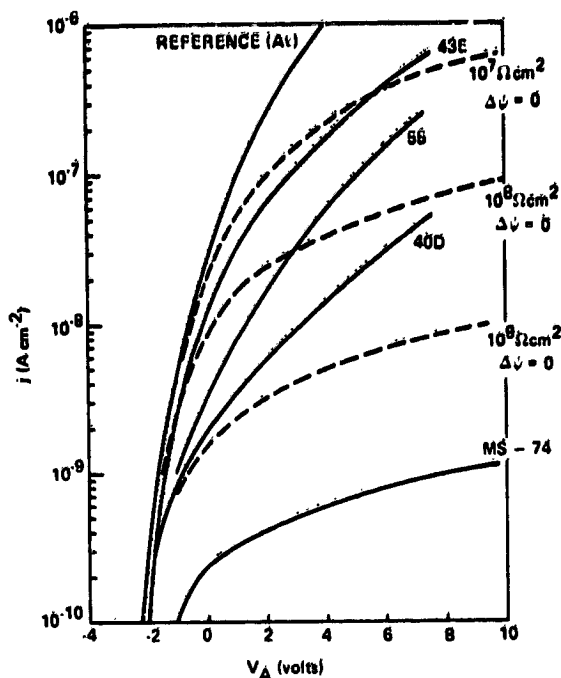


Figure 2. Typical Current-density vs Voltage Curves for the Reference Anode (Aluminum) and Anodes Painted with Various Zinc Oxide-Silicate Paints (Solid Curves). Calculated curves for "ohmic" coatings having area resistances of  $10^7 \Omega \text{ cm}^2$ ,  $10^8 \Omega \text{ cm}^2$  and  $10^9 \Omega \text{ cm}^2$  and the same work function as the reference anode (Al) are shown for comparison. Real paints are characterized by a change in work function ( $\Delta\psi$ ) and a voltage-dependent conductance per unit area

### 3. COATINGS

The inorganic coatings investigated here are modifications of a previously developed stable, white paint, designated as MS-74. This flight-proven coating is formulated with calcined zinc oxide pigment of the type SP-500 (New Jersey Zinc) and potassium silicate as vehicle. By substituting "conductive" zinc oxide for SP-500, electrically conductive coatings can be prepared. Commercially available conductive oxides as well as "fired" SP-500 have been investigated with potassium silicate, sodium silicate, and a mixture of lithium and potassium silicate as binders. The "firing" process consists of heating the SP-500 to  $1150^\circ\text{C}$  for 15 min in air. The process employed for the commercial oxides HC 016 and HC 238 are proprietary to the manufacturer. The lattice defects introduced by these processes result in donor, acceptor, and trapping centers that not only govern the charge transport but also act as color centers and therefore affect the optical properties as well. Considerable effort was, therefore, expanded to arrive at coatings which meet both the conductance requirement of  $j/V > 10^{-9} \text{ A cm}^{-2} \text{ V}^{-1}$  and solar absorptance requirement of  $\alpha_S \lesssim 0.3$  of the "white" areas of the ISEE spacecraft. For the main body of the satellite, thermal design called for a green paint of  $\alpha_S \sim 0.6$ , which has been achieved by adding  $\sim 2$  percent of cobalt oxide to the zinc oxide before firing. For black surfaces, a commercial, carbon filled polyurethane paint (Chemglaze H322) with  $\alpha_S = 0.96$  and  $\epsilon_n = 0.86$  was recommended. We include measurements of this

paint because it exhibits the most marked difference between contactless conductance values and conductance measured with metallic (Ag-paint) contacts.

#### 4. RESULTS AND ANALYSIS

##### 4.1 Contactless Measurements.

Typical conductance vs voltage curves are shown in Figure 3. At low voltages current density increases linearly with voltage (Ohm's Law) which can be expressed as

$$j = n_0 e \mu_0 \frac{V}{d} \quad (4)$$

where  $n_0$  is the equilibrium carrier density,  $e$  the electronic charge,  $\mu_0$  the mobility and  $d$  the thickness of the sample. With paint thicknesses of approximately  $10^{-2}$  cm., conductivities,  $\sigma = n_0 e \mu_0$ , range from  $\sim 10^{-12}$  ( $\Omega \text{cm}$ ) $^{-1}$  for calcined SP-500 in K-silicate to  $\sim 10^{-9}$  ( $\Omega \text{cm}$ ) $^{-1}$  for fired SP-500 in the Na-silicate; HC-016 yields conductivities comparable to those of fired SP-500, whereas HC 238 is only marginally higher than (unfired) SP-500. The vehicle-or binder-also affects the conductance per unit area; Na-silicate based coatings are more conductive than K-silicate coatings and mixed Li-K-silicate paints give intermediate values.

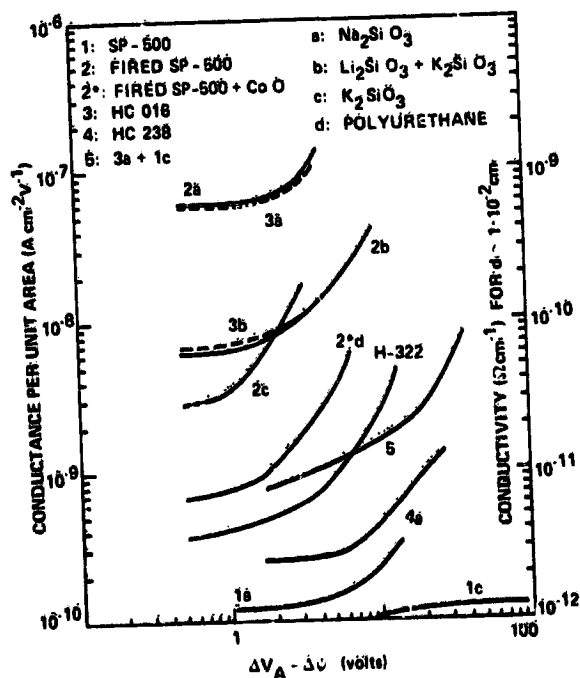


Figure 3. Conductance Per Unit Area as a Function of Voltage for Various Zinc-Oxide/Silicate Combinations and for Carbon (Chemglaze H-322) and Conductive-Zinc Oxide in Polyurethane

When the voltage is increased, current density increases quadratically with voltage (Child's Law), or the conductance increases linearly with voltage. This characteristic is typical of Space Charge Limited Conductance (SCLC), that is, of charge transport governed by the interaction of injected (space) charge with trapping centers of the material, whose energy levels lie between the steady state Fermi level and the conduction band. According to the theory of SCLC, summarized in Figure 4, the relationship between current density,  $j$ , and voltage,  $V$ , is given by

$$j = \frac{9\mu\theta\epsilon\epsilon_0}{8d^3} \cdot V^2 \quad (5)$$

where  $\mu\theta$  is an effective mobility,  $\epsilon$  the dielectric constant and  $d$  the thickness of the material. The trapping factor,  $\theta$ , is the ratio of free space charge,  $\rho_f$ , (in the conduction band) and the trapped space charge  $\rho_t$ , under equilibrium conditions and is given by

$$\theta = \frac{\rho_f}{\rho_t} = \frac{N_C}{N_T} \exp - \frac{E_C - E_T}{kT} \quad (6)$$

where  $N_C$  is the density of states in the conduction band and  $N_T$  the density of electron traps at an energy  $E_T$  below the conduction band, situated at energy  $E_C$ .

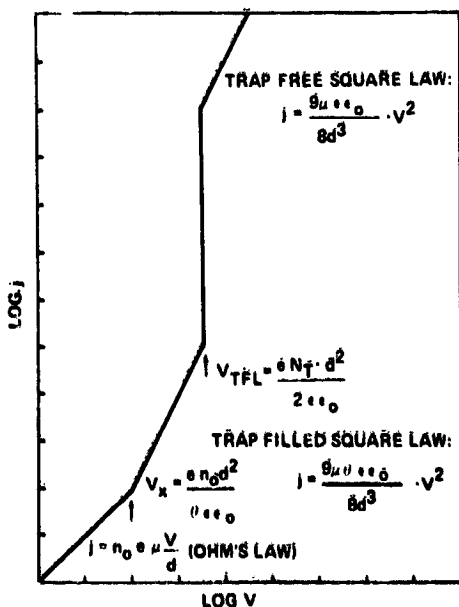


Figure 4. Space Charge Limited  $j$ - $V$  Characteristic for an Insulator Containing Shallow Traps

#### 4.2 Temperature Dependence

It is apparent from Eqs. (5) and (6) that the temperature dependence of the effective mobility, or of the conductivity, will give the position of the trap level in the band gap. For our standard paint MS-74 (SP-500 in K-silicate), the temperature dependence is plotted in Figure 5, \* from which the energy of the trap level is obtained as  $(E_C - E_T) \approx 0.75 \pm 0.05$  eV in good agreement with published values for high-resistivity, Li-doped ZnO.<sup>3</sup> It is important to note here that conductivity variations from sample to sample of the same batch are of the order of a factor 3 to 5, and to point out that measurements on a different batch showed the same temperature dependence and variation within the batch, but conductivity was about 10 times higher overall. We attribute these variations to the heat treatment inherent in the measurement procedure, in which the samples are heated to  $\sim 200^\circ\text{C}$  for various lengths of time and measured while cooling. Room temperature conductivities of MS-74 which has never been heated are about 100 times higher than those shown in Figure 5. After heating to  $300^\circ\text{C}$  for 30 min, a decrease in conductivity by a factor of 10 to 20 was noted. Preliminary experiments on fired SP-500 in Na-silicate did not reveal any dependence on heat treatment, but further work is required to establish the mechanism responsible for this effect.

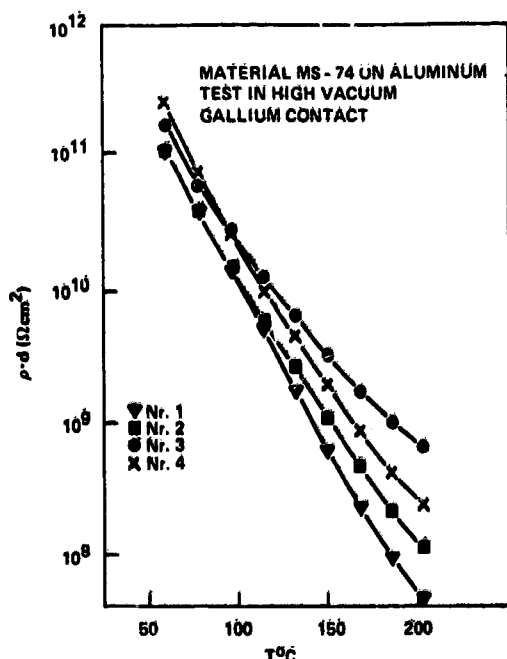


Figure 5. Temperature Dependence of the Area Resistance of MS-74 Paint (SP-500 in Potassium-Silicate)

\*These data in Figure 5 were obtained at DFVLR, Braunschweig, Germany, with liquid gallium contacts.

### 4.3 Trade-off Between Solar Absorptance and Conductance

As was alluded to earlier, the "firing" process which results in increased electrical conductivity of zinc oxide, also induces color centers. In the case of SP-500, the oxide turns yellow and solar absorptance increases from 0.2 to 0.4. The conductive commercial oxide HC 016 also has an  $\alpha_S$  of  $\sim 0.4$ . In attempts to produce whiter paints while staying within the ISEE conductance specification, we investigated mixtures of the highly conductive formulation (3, a = HC 016 in Na-silicate) and our standard white paint MS-74 (1, c = SP-500 in K-silicate). The results are summarized in Figure 6 from which it is apparent that paints having conductance-per-unit-area of  $\geq 10^{-9}$  A cm $^{-2}$  V $^{-1}$  and solar absorptances of  $< 0.3$  cannot be obtained by this approach. Whether a better trade-off can be achieved by variations of the temperature, time, and atmosphere of the zinc oxide firing process remains to be investigated.

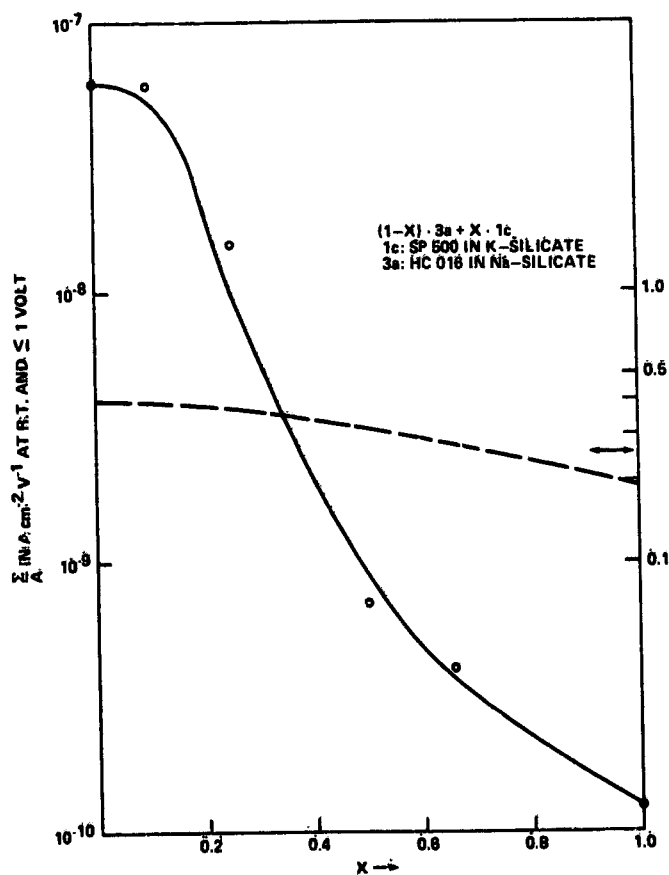


Figure 6. Solar Absorptance ( $\alpha_S$ ) and Conductance Per Unit Area as a Function of the Mixing Ratio for Mixtures of a Conductive Paint (3, a = HC 016 ZnO in Na-Silicate), and a White, Non-Conductive Paint MS-74 (1, c = SP-500 ZnO in K-Silicate)

#### 4.4 Comparison of Contact and Contactless Measurements

In general, conductance obtained with silver paint contacts show the same strong voltage dependence, but are higher by up to several decades than those obtained by the contactless method and they are higher in air than in vacuum. The differences between the two methods in vacuum is most pronounced for paint formulations in which the conductivities of pigment and binder are orders of magnitude apart, as illustrated in Figure 7 for carbon and conductive zinc oxide in polyurethane. The commercial black paint Chemglaze H-322 (5 weight % carbon) appears about  $10^5$  times more conductive with metal electrodes than with the

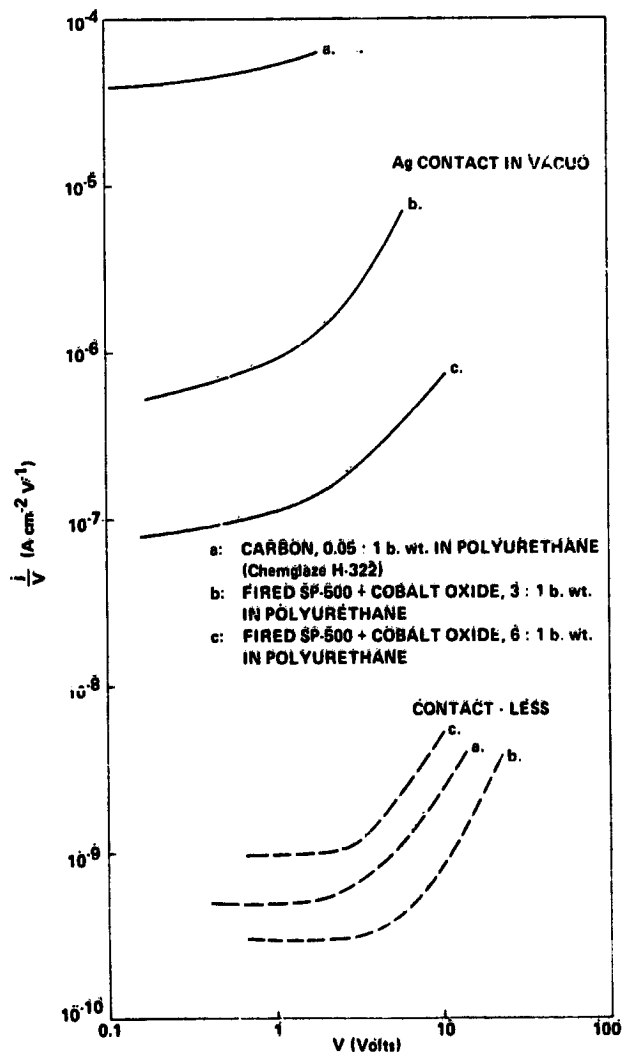


Figure 7. Comparison of Conductance Values of Carbon/Polyurethane and Zinc-Oxide/Polyurethane Paints Obtained by Measurements with Ag-Paint Contacts (Solid Lines) and by Contactless Measurements (Broken Lines)

electron plasma as surface contact. In the case of the more heavily loaded zinc oxide/polyurethane paint, the difference is about a factor of  $10^3$  which, at least in part, is due to the lower conductivity of zinc oxide as compared to carbon. The different results obtained by the two contacting techniques can perhaps be qualitatively understood as being due to the heterogeneous nature of paints on a microscopic scale. As a dispersion of a "conductive" phase (the pigment) in a "non-conductive" dielectric (the binder), the paint surface, consisting of conductive islands in a non-conductive matrix charges to a highly non-uniform surface potential, with insulating areas essentially at cathode potential and conductive areas at anode potential, respectively. The effective potential, which governs the anode current, is a complex function of absolute and relative island geometry, that is, of particle size and concentration of the pigment. With a metallic contact, on the other hand, the surface becomes an equipotential surface. The resistive areas are "shorted out" and the measured conductance is the sum of the conductances of all conductive paths through the sample, and therefore mainly a characteristic of the conductive component alone, rather than of the paint as a whole.

## 5. CONCLUSIONS

Thermal control paints which meet the ISEE conductance specification of  $j/V \geq 10^{-9} \text{ A cm}^{-2} \text{ V}^{-1}$  at  $V = 1 \text{ volt}$  and  $T \sim 300 \text{ K}$  have been formulated with semiconducting zinc oxide pigment and alkali silicate binders. As in semiconductors, their charge transport properties are strong functions of voltage and temperature and depend on both pigment and binder. Because of surface effects and the heterogeneous nature of paints, order-of-magnitude discrepancies are found between conductance values measured with metallic contacts and those obtained with a contactless method employing a thermal electron plasma in vacuum. In the evaluation of surface coatings for electrostatic charge control on spacecraft, careful definition of measurement parameters and of appropriate measurement techniques are therefore essential.

## Acknowledgments

The authors thank Mr. Walter Wilkens and co-workers of DFVLR-Braunschweig/Germany for the data presented in Figure 5 and for valuable personal communications and discussions.

## References

1. Shai, M. C. (1976) Formulation of electrically conductive thermal control coatings, Paper No. IV-4 in this publication.
2. Bentlage, H., Spanier, H. P., and Wilkens, W. (1975) Internal Report IB 152-75/04, Deutsche Forschungs und Versuchsanstalt fuer Luft und Raumfahrt e. V. (DFVLR).
3. Seitz, M. A., and Whitmore, D. H. (1968) Electronic drift mobilities and space charge limited current in lithium doped zinc oxide, J. Phys. Chem. Solids 29:1033-1049.

## 9. Spacecraft Charging/Contamination Experiment on SCATHA

David F. Hall  
The Aerospace Corporation  
El Segundo, California

### Abstract

The ML12 experiment to be flown on Air Force Space Vehicle P78-2, SCATHA (Spacecraft Charging at High Altitudes), is designed to determine if spacecraft charging contributes significantly to the rate of contamination arriving at exterior spacecraft surfaces, and some of the characteristics and effects of the contamination collected. The contamination transport mode under investigation involves the ionization within the vehicle plasma sheath of molecules outgassed or released by the vehicle and their subsequent electrostatic reattraction to the vehicle.

Two sensor types will be flown. One type is a combination retarding potential analyzer (RPA) and temperature controlled quartz crystal microbalance (TQCM). With it, distinction can be made between charged and uncharged arriving molecules, and information can be obtained concerning the temperature dependence of contamination adsorption and desorption rates. The other sensor type exposes samples of different spacecraft surface materials to arriving contamination and continuously measures the solar absorptance ( $\alpha_s$ ) of these materials. Changes in  $\alpha_s$  of space-stable samples will be entirely ascribed to contamination effects whereas changes in other samples will result from a combination of contamination, photochemical, and radiation effects. Upon ground command, some samples will go through a heating sequence designed to roughly determine the temperature at which contamination is desorbed.

In addition to describing the goals and techniques of ML12 in more detail, the expected performance of the sensors and the need for coordination with other experiments on SCATHA will be discussed.

## Contents

1. Introduction	702
2. Radiation Environment	703
3. Dose Calculations	705
4. Extended Duration Missions	708
5. SCATHA High-energy Spectrometer	710
Acknowledgments	712
References	713

## 10. The Effects of the Geosynchronous Energetic Particle Radiation Environment on Spacecraft Charging Phenomena

J.B. Reagan, W.L. Imhof, and E.E. Gaines  
Lockheed Palo Alto Research Laboratory  
Palo Alto, California

### Abstract

The energetic electron environment at the geosynchronous orbit is very intense, dynamic, penetrating, and responsible for a variety of adverse charging effects on spacecraft components. The most serious of these is the degradation and failure of widely used complementary-metal-oxide-semiconductor (CMOS) electronic components as a result of internal charge-buildup induced by the energetic electrons. Efforts to accurately determine the expected lifetime of these components in this orbit have been hampered by the lack of detailed knowledge of the electron spectrum and intensity, particularly of the more penetrating energies  $> 1.5$  MeV. Large uncertainties therefore exist in current radiation models for this region as a result of these deficiencies. This problem is illustrated through the calculation of the dose received by a CMOS device from the energetic electrons and associated bremsstrahlung as a function of aluminum shielding thickness using the NASA AE-6 and the Aerospace measured electron environments. Two computational codes which have been found to be in good agreement were used to perform the calculations. For a given shielding thickness the dose received with the two radiation environments differ by as much as a factor of seven with a corresponding variation in lifetime of the CMOS. The important role of bremsstrahlung to the problem at the larger shielding thicknesses is evident from the results. These discrepancies, which adversely impact spacecraft shielding designs, will be resolved on the SCATHA mission since the High-Energy Particle Spectrometer experiment (SC-3) will provide fine resolution measurements of the electron fluxes, energy spectra, and pitch-angle distribution over the energy range 100 keV to 4 MeV and the integral flux between 4 to 10 MeV. Protons from 1 MeV to 100 MeV and alpha particles from 6 MeV to 60 MeV will also be measured. The differential and accumulated dose received as a function of shielding thickness will be determined in real time throughout the mission from the measured quantities and the calculational codes.

160  
THIS INFORMATION IS UNCLASSIFIED

## 1. INTRODUCTION

A satellite in the geosynchronous orbit is subjected to an intense, continuous, highly dynamic, and very penetrating radiation environment. The energetic electron population ( $> 100$  keV) exhibits large variations in intensity and spectral shape associated with geomagnetic storms and substorms. In addition, the particle population exhibits diurnal and longitudinal variations that are significant. At the time of solar particle events, high-energy protons, electrons, and alpha particles of solar origin also have ready, efficient, access to the geosynchronous orbit. This complex radiation environment, which is difficult to model, is responsible for a variety of adverse charging effects on spacecraft components. The most serious of these problems, just identified in recent years, is the degradation and ultimate failure of complementary-metal-oxide-semiconductor (CMOS) electronic components due to internal-charge-buildup induced by the ionizing radiation in the gate oxide and at the semiconductor-insulator interface of the devices. This process occurs at radiation dose levels approximately two to three orders of magnitude below the level where bulk radiation damage occurs in typical semiconductor devices. The overwhelming attractiveness of CMOS devices including their low power consumption and large-scale-integrated circuit capabilities has resulted in increased usage of these devices for satellite applications, including long-lived geosynchronous satellite orbit applications, despite these problems.

Contending with the charge-buildup problem requires that three distinct areas be investigated: (1) the sensitivity of CMOS, PMOS, and other components to ionizing radiation must be determined as a function of radiation particle type and energy, component part type, manufacturing process, and application; (2) the radiation environment to which the devices will be exposed in orbit must be established; and (3) based on the environment and the mission lifetime desired, the added shielding to maintain the radiation dose below the damaging levels must be determined.

Radiation sensitivity tests on a variety of components are underway in several laboratories employing principally radioactive gamma-ray emitting sources and electron accelerators. Both of these sources only approximate the actual complex electron spectrum encountered in geosynchronous orbit but the accuracy of the technique is felt to be better than our present knowledge of the environment itself.

The principal models of the electron radiation environment in the geosynchronous orbit are provided by NASA and are referred to as the AE-4<sup>1</sup> and the AE-6 models.<sup>2</sup> Both models are thought to have accuracies of only a factor of two to three. Recently, energetic electron measurements made on the ATS-6 synchronous satellite by the Aerospace group<sup>3</sup> suggest that the actual electron flux is higher and the spectrum more energetic than the NASA model predicts. The consequences of

the adoption of the latter environment are significant to spacecraft designers in that greater shielding is required to maintain the CMOS devices below the damage level. Increased shielding means increased weight which always has an adverse effect on spacecraft design. The principal reasons for the inaccuracies and discrepancies in the model environments are the limited measurements available over long time periods, extended energy ranges and with sufficient spectral resolution. Until this situation improves, the spacecraft designer will be unable to optimize his shielding treatment and must design conservatively.

In this paper an experiment will be described that will be flown aboard the SCATHA satellite in near-synchronous orbit in 1979. A prime goal of the experiment, identified as SC-3, will be to define the energetic particle radiation environment in considerable detail and to determine the actual dose received in this orbit by devices such as CMOS behind various shielding thickness. The experiment will be operated continuously for at least a year and the differential and accumulated radiation dose will be determined in near-real time. The dose will be determined from the measured differential spectrum of electrons, protons, and alpha particles in conjunction with particle transport calculations that establish the surface dose behind different thicknesses of aluminum shielding.

Until the above measurements are available, determination of the dose acquired in the geosynchronous orbit and the required shielding of CMOS devices will have to be made with the available environmental models. Extensive dose calculations have been performed at Lockheed and are described in this paper using both the NASA and Aerospace electron environments and employing two different transport codes to develop confidence in the technique. The calculations have included the dose acquired from the bremsstrahlung generated by the electrons in the shielding. Solar flare proton doses as a function of shielding thickness have also been determined for an extended mission satellite operating over the solar maximum period.

## 2. RADIATION ENVIRONMENT

The dose in the synchronous orbit comes principally from the outer radiation belt electrons. Figure 1 shows the integral flux of these electrons as a function of energy obtained from the latest NASA AE-6 model<sup>2</sup> and from the Aerospace measurements.<sup>3</sup> The AE-6 model fluxes are mean values applicable in the 1980 time period for a magnetic L-shell of 6.6, representative of the synchronous orbit. It should be noted that no substantial differences exist between the AE-6 and the earlier AE-4 models in this region of space. As mentioned earlier, the NASA model is believed to be accurate to within  $\pm 2$  to  $\pm 3$ . The Aerospace values are based on a few hundred days of data obtained in 1975-76 with an instrument on the

ATS-6 satellite and confirmed by earlier data obtained on the ATS-1 synchronous satellite.

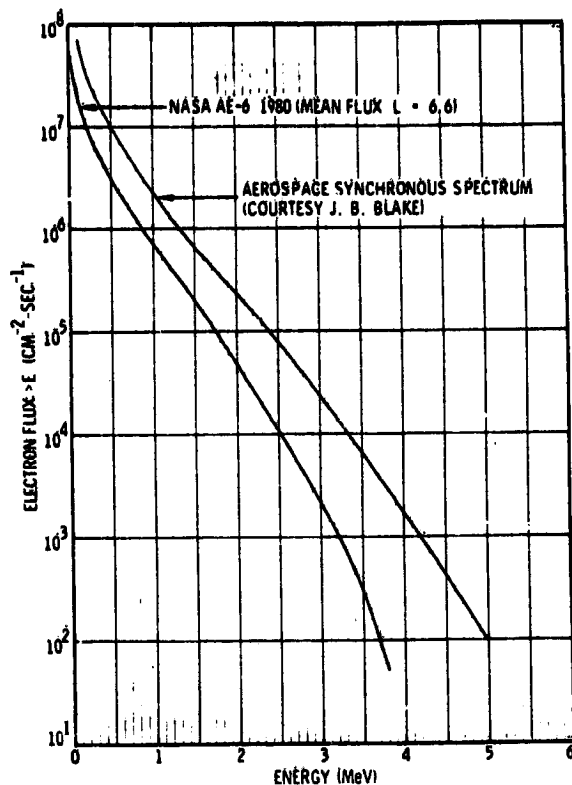


Figure 1. Integral Electron Fluxes in the Geosynchronous Orbit as a Function of Energy. The mean values of the AE-6 model in the 1980 time period at L = 6.6 are shown along with the mean values obtained from the Aerospace measurements

The most significant differences in the two environments exist at the higher energies > 1.5 MeV. At 1 MeV energy the Aerospace flux values are  $\times 3$  higher than the mean AE-6 values, but the upper limit of the latter model would be consistent with the former values. Above this energy the differences become progressively larger with the Aerospace fluxes being a factor of 5 and 12 higher than the AE-6 values at energies of 2 and 3 MeV, respectively. These differences are due to a softer electron spectrum used in the AE-6 model, that is, the flux decreases more rapidly with increasing energy.

Because of the quasi-random nature of the occurrences, fluences, and spectra of solar particle events, solar proton fluxes must be treated statistically. For a synchronous satellite mission operating for four years in the 1978 to 1982 time period encompassing the next maximum in solar activity, the solar proton fluences were derived from the model generated by King.<sup>4</sup> This model is based heavily on

the data obtained during the last solar cycle-20 which is assumed to be typical of the upcoming cycle-21. It should be noted that approximately 85 percent of the fluence experienced in cycle-20 was acquired during the single large event of August 1972.

### 3. DOSE CALCULATIONS

The electron spectra shown in Figure 1 have been used as input to two independent computer programs that calculate dose. The first program called AURORA was originally developed at Lockheed to treat the energy deposited in the atmosphere by precipitating electrons.<sup>5</sup> The program was adapted for this purpose by substituting plane-parallel sheets of aluminum as the absorbing media in place of the atmospheric constituents. The program utilizes finite difference techniques to numerically solve the Fokker-Planck steady-state equation for electrons diffusing through the medium. The derivation of the diffusion equation is rigorous and takes into account changes in the electron distribution function as a function of time, pitch angle, energy, and the radial distance from the axis of the electron beam. The diffusion coefficients used to describe the pitch-angle scattering in the diffusion equation are valid down to electron energies of ~ 1 keV. The treatment is relativistic and therefore valid at all higher electron energies. The AURORA code does not, however, include the surface dose at the CMOS chip due to the production of bremsstrahlung in the slabs by the input electrons.

In Figure 2 the surface dose accumulated per year in the synchronous orbit at the surface of a CMOS chip sandwiched between two infinite plane aluminum shields of equal thickness is shown for both the AE-6 and the Aerospace electron fluences as inputs. The 0.010-in. nickel cover on the CMOS elements provides a measure of shielding and this has been included in the calculations. The shielding thickness shown in Figure 2 is the additional shielding required around the component.

The second set of electron dose calculations were kindly performed by the Air Force Weapons Laboratory (AFWL)<sup>6</sup> using their Monte Carlo technique. This program includes the secondary dose due to bremsstrahlung. Comparison in Figure 2 of the AFWL and AURORA code outputs for the Aerospace flux profiles reveals essential agreement for shielding thicknesses up to 0.15 inch. For greater shielding the bremsstrahlung dose included in the AFWL code begins to dominate. This illustrates the impracticality of utilizing large thicknesses of low-density material to shield "soft" devices in this environment. If a soft component requires greater than ~0.2 in. ( $1.39 \text{ g/cm}^2$ ) of aluminum shielding to survive the mission duration then additional consideration must be given to using high-density shielding such as lead, tungsten, copper, etc., inside the aluminum to attenuate the bremsstrahlung

dose. This latter effort is much more difficult and weight-demanding than shielding the direct electrons and is not addressed further in this paper.

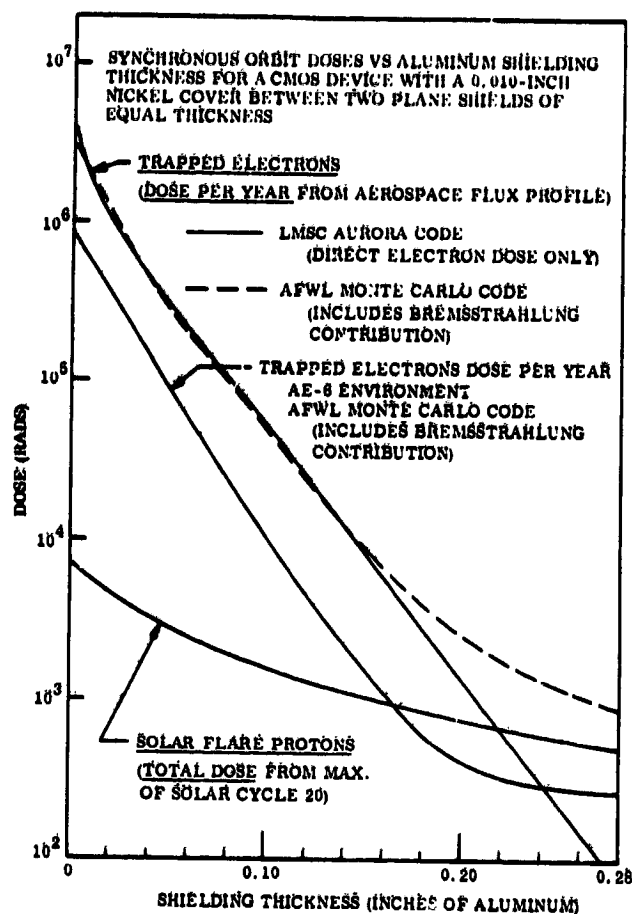


Figure 2. The Dose Acquired in Synchronous Orbit From Trapped Electrons and Solar Protons as a Function of Shielding Thickness. The annual electron dose has been calculated for the Aerospace Environment utilizing two independent computer codes described in the text. The annual dose due to the AE-6 electron environment and the associated bremsstrahlung has been calculated with the AFWL code

The impact of the two electron environments can also be easily seen in Figure 2. For a shielding thickness of 0.10 in., a thickness that typically surrounds a CMOS chip encased in an electronics box within a spacecraft skin, the CMOS chip

would receive a yearly dose of 10,000 rads in the AE-6 environment but a dose of 70,000 rads in the Aerospace environment. An equivalent way of expressing this impact is that a CMOS device behind 0.1-in. aluminum that has a damage level at 10,000 rads would function for one year in the environment represented by the AE-6 model but only 51 days in the Aerospace environment. The impact on mission lifetime is obviously very significant and at present the spacecraft designer must shield conservatively.

The most probable dose received in a mission near the solar maximum period from solar protons is also shown in Figure 2. The total fluence experienced in cycle-20 as a function of proton energy was obtained from King<sup>4</sup> and was assumed to be typical of the maximum fluences to be encountered in cycle-21. A proton energy deposition computer program called PROTON<sup>7</sup> developed at Lockheed was used to determine the dose behind plane-parallel slabs of aluminum shielding. To determine the total dose received by a CMOS device behind a given shield thickness, the contribution from the solar protons must be added to the contribution from the trapped electrons.

The relationship between the dose level shown in Figure 2 to the damage levels of CMOS, PMOS, and most bipolar junction transistors is illustrated in Figure 3. The annual dose due to electrons and bremsstrahlung in both the AE-6 and Aerospace environments is shown out to shielding thicknesses of 0.7 inch. The relatively constant bremsstrahlung dose of between 250 to 800 rads per year (AE-6 vs Aerospace models) accumulated behind thick shields is quite evident and along with the solar proton dose becomes the limiting factor on the radiation softness of a device that can be tolerated in a long duration synchronous orbit mission.

Currently available soft CMOS and PMOS devices exhibit serious degradation at levels between 4000 to 16,000 rads due to the charge-buildup problem. Reliable utilization of these devices in even a one-year mission would require aluminum shielding of approximately 0.2-in. thickness. Hardened CMOS devices, now becoming available, have degradation levels in excess of 150,000 rads. A nominal shielding thickness of 0.08 in. aluminum will protect a hard CMOS device for a minimum of one-year operation in the synchronous orbit. Many linear integrated circuits have exhibited damage levels as low as 20,000 rads and correspondingly greater shielding is required with these devices. As mentioned earlier, knowledge of the radiation sensitivity of the electronic components to be used in an application is essential to long-lived, reliable operation. Unfortunately, the radiation sensitivity of currently available devices having identical part types can vary greatly from supplier to supplier depending upon the manufacturing process used and can even vary significantly from wafer to wafer within the same manufacturing process. Extreme caution is the watchword.

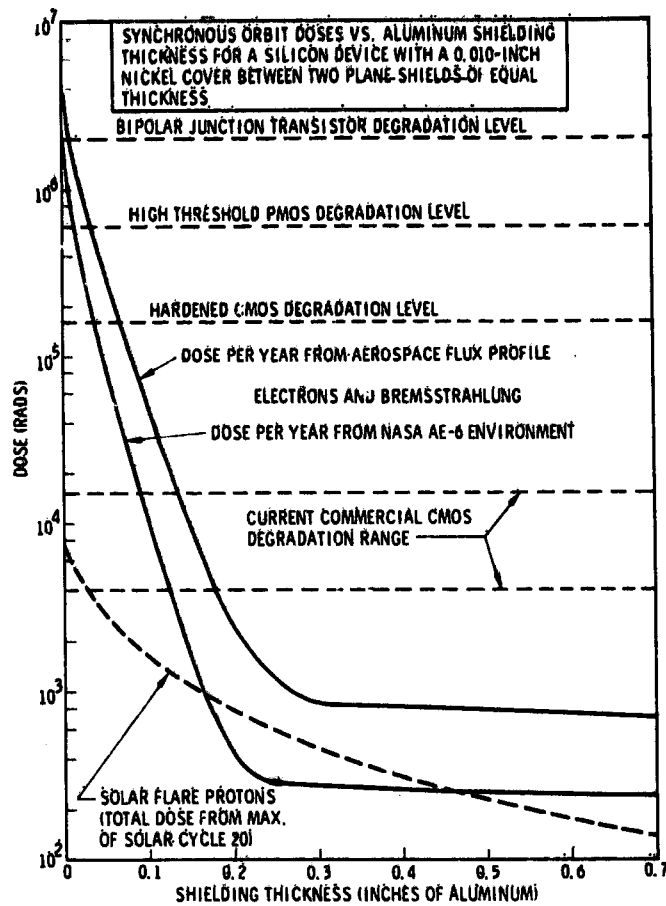


**Figure 3. Relationship Between the Annual Dose vs Shielding Levels Acquired in the Synchronous Orbit From Electrons and the Associated Bremsstrahlung and the Damage Levels of Typical Electronic Devices. The solar flare proton dose is that likely to be acquired on a long-duration mission operating during the solar maximum period 1978-1982**

#### **4. EXTENDED DURATION MISSIONS**

Most synchronous satellite missions are designed to operate for more than one year in orbit. To illustrate the impact of the radiation environment on these extended missions the total dose accumulated as a function of shielding thickness has been tabulated in Table 1 for a four-year mission operating in the solar maximum period 1978 to 1982.

Assuming that a typical payload containing CMOS or equivalent components would be shielded with a minimum of 0.1 in. of aluminum, Table 1 shows that the

chip would receive a total dose over the 4-year period of 43,600 rads or 193,600 rads depending on whether the AE-6 or the Aerospace environment, respectively, is used. Hard CMOS with this shielding would survive in the AE-6 environment but could be marginal in the Aerospace environment. Most linear integrated circuits would require 0.2 in. of shielding to survive the Aerospace environment for four years, but less than 0.15 in. if the NASA environment is more representative.

Table 1. Total Dose (rads-Si) vs Aluminum Shielding for 4-Year Synchronous-Orbit Mission 1978 to 1982

Aluminum Shielding Thickness* (in.)	Electron Plus Bremsstrahlung Dose		Solar Protons	Total Mission Dose	
	AE-6	Aerospace		AE-6	Aerospace
0.050	340,000	1,200,000	2,800	342,800	1,202,800
0.075	116,000	460,000	2,050	118,050	462,050
0.100	42,000	192,000	1,600	43,600	193,600
0.150	6,200	37,200	1,050	7,250	38,250
0.200	1,720	9,600	760	2,480	10,360
0.250	1,140	4,720	580	1,720	5,300
0.500	1,000	3,200	230	1,230	3,430
0.700	960	2,800	140	1,100	2,940

\*CMOS chip with 0.010-in. Ni cover behind two plane aluminum shields of equal thickness.

Finally, since soft CMOS and PMOS devices can experience problems at dose levels as low as 4000 rads, shielding of these devices for a 4-year mission should conservatively consist of an outer layer of aluminum approximately 0.25-in. thick with an inner layer of lead or equivalent foil (0.02 to 0.05 in.) to further reduce the bremsstrahlung contribution. Other sandwich combinations of aluminum and high-density metals can be used effectively but caution must be exercised. High density materials are more weight-effective in reducing the transmission of the incident electrons since a higher fraction of the electrons backscatter out of a high-density shield. However, the bremsstrahlung production in a high-density shield is greater than in a low-density shield of the same electron shielding effectiveness by a factor of approximately the ratio of the atomic numbers. Hence, the bremsstrahlung production is 7.5 times higher in a lead shield than in an aluminum shield of the same electron stopping power. A good compromise in shielding soft devices is to stop most of the incident electrons in a low-Z material such as aluminum and

to follow this, if necessary, with a high-Z material to attenuate the bremsstrahlung photons generated in the outer shield.

##### 5. SCATHA HIGH-ENERGY SPECTROMETER

The SCATHA satellite, which will be launched in 1979 into a near-synchronous orbit, will carry a high-energy particle spectrometer, referred to as the SC-3 experiment. One of the prime objectives of the experiment is to define the energetic radiation environment in this orbit in considerable detail and to determine in near-real time the dose acquired by the payloads and spacecraft equipment. To accomplish this, the spectrometer will be operated continuously and the measured differential spectra of electrons and protons will be used as inputs to the dose calculation codes described in this paper.

The spectrometer is very similar in design to one described in an earlier paper<sup>8</sup> that has been successfully flown in space four times on two low-altitude missions. The spectrometer consists of a stacked array of surface-barrier silicon detectors surrounded by an active plastic scintillator. Passive shielding consisting of an outer layer of aluminum and an inner layer of tungsten surrounds the entire assembly to shield against electrons with energy  $< 4$  MeV and against the associated bremsstrahlung. The stacked silicon detectors are arranged with a thin (200- $\mu$ ) detector in front to measure the rate of energy loss by the incoming electrons, protons, and alpha particles. Since these three particle types have significantly different characteristics in passing through matter, the energy loss in the thin detector can be used to uniquely identify the particle type under analysis. Behind the thin  $dx/dx$  detector is an array of five detectors that are used to stop and to measure the incident energy of the particle under analysis. By arranging several different combinations of coincidence and anticoincidence between the two detector systems, different particle types over a wide energy range can be analyzed in a time-multiplexed manner. The active plastic scintillator is always used in anticoincidence with pulses in the main detectors and thus only particles entering through the narrow collimation system are analyzed.

The collimator is designed to have a 3-deg field-of-view and because the satellite is spinning, pitch-angle distributions of the particles will be obtained with this angular accuracy. The spectrometer will have the broad energy coverage listed in Table 2. Electrons from 100 to 4100 keV will be measured with 12-channel differential energy resolution. The channels can be programmed in flight to cover the entire energy range or a limited energy range with high-energy resolution. The flux of electrons between 3500 to 10,000 keV will be measured in a differential channel. Solar protons from 1 to 100 MeV will also be measured with 12-channel

energy resolution in several different modes of operation selectable by command. Thus, all the particle types and energy ranges of concern to the radiation dose problem will be measured in this single instrument.

Table 2. SC-3 High-Energy Particle Experiment on SCATHA Mission Characteristics

Particle Type	Energy Range	Resolution	Comments
Electrons	100 to 4100 keV >3500 keV	12-channel integral	Channel widths programmable from 15 keV to 100 keV
Protons	1 to 100 MeV	12-channel	Multiple energy modes required to cover energy range
Alphas	6 to 60 MeV	12-channel	

The capabilities of the SC-3 experiment to resolve the fundamental difference between the NASA and the Aerospace environment is illustrated in Figure 4. As mentioned earlier, the AE-6 model exhibits a much steeper fall-off of the higher energy electrons than the Aerospace measurements indicate. In the former case this results principally from a lack of experimental data above ~2 MeV in energy. As shown, the SC-3 experiment will define in great detail the shape of the electron spectrum out to 4.1 MeV through the several operating modes available in the instrument.

In the future the spacecraft designers will have a better definition of the energetic radiation environment as input to his shielding analysis. Until that data becomes available, however, he must design component shielding in a conservative manner using the more severe and adverse environment suggested by the Aerospace measurements.

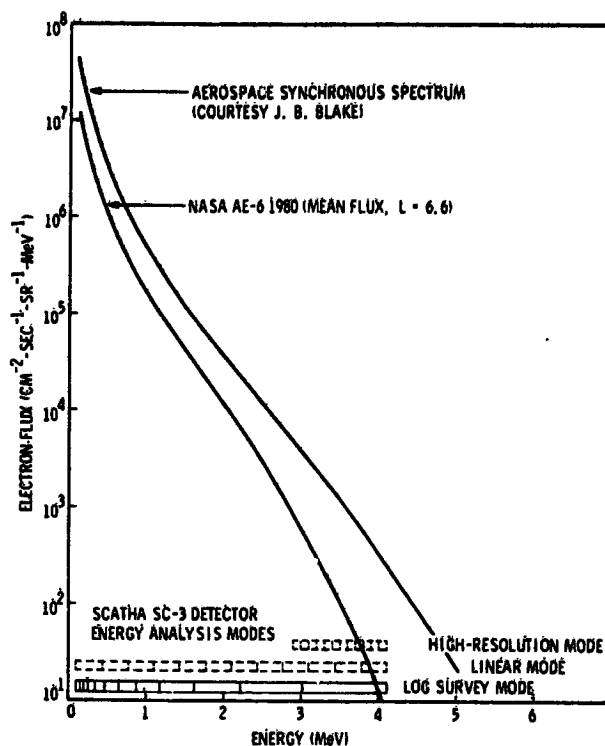


Figure 4. Illustration of the Various Energy Analyses that the SC-3 Experiment on SCATHA Will Provide on the Synchronous Orbit Electron Environment

## Acknowledgments

The SC-3 experiment for the SCATHA mission is being developed under Contract N00014-76-C-0444 with the Office of Naval Research. The support of Dr. Henry Mullaney of ONR is greatly appreciated. The authors would like to thank Drs. J. B. Blake and G. A. Paulikas of the Aerospace Corporation for many valuable technical discussions and for the early use of their ATS-6 synchronous satellite data. The SCATHA mission is a joint satellite program between NASA, the Office of Naval Research and the U.S. Air Force. The real-time dose determination capability will be provided by the USAF Space Test Program. The support of Lt. Col. D. F. Shane, SCATHA Project Officer, in this matter is acknowledged and appreciated. This work was partially supported under the Lockheed Independent Research Program.

## References

1. Singley, G. W., and Vette, J. I. (1972) The AE-4 Model of the Outer Radiation Zone Electron Environment, National Space Science Data Center Report NSSDC 72-06, NASA/Goddard Space Flight Center, Greenbelt, Maryland.
2. Teague, M. J., Chan, K. W., and Vette, J. I. (1976) AE-8: A Model Environment of Trapped Electrons for Solar Maximum, National Space Science Center and World Data Center-A Report NSSDC/WDC-A-R&S 76-04, NASA/Goddard Space Flight Center, Greenbelt, Maryland.
3. Blake, J. B., and Vampola, A. L. (1977) The outer zone energy electron environment: Hazards to CMOS. Paper presented at the 15th AIAA Aerospace Sciences Meeting, 24-26 January 1977, Los Angeles, California.
4. King, J. H. (1973) Solar Proton Fluences as Observed During 1966-1972 and as Predicted for 1977-1983 Space Missions, NASA Report X-601-73-324.
5. Walt, M., and Chappell, C. R. (1968) Penetration of particles into the atmosphere, in Atmospheric Emissions, B. M. McCormac and A. Omholt, Van Nostrand Reinhold Co., N. Y., p. 245.
6. Hollars, Capt. D. (1976) Air Force Weapons Laboratory, Kirtland Air Force Base, New Mexico, Private communication.
7. Francis, W. E., and Bradbury, J. N. (1975) PROTON - A Code for Generating Ionization Production Rates in the Atmosphere Due to Solar Protons and Alpha Particles, Lockheed Report No. D409467.
8. Reagan, J. B., Bakke, J. C., Kilner, J. R., Matthews, J. D. and Imhof, W. L. (1972) A high-resolution, multiple particle spectrometer for the measurement of solar particle events, IEEE Trans. on Nucl. Sci. NS-19:554.

PRECEDING PAGE BLANK NOT FILMED

## 11. Oscillations in Insulator Leakage Current Under Steady Conditions of Synchronous Orbit Plasma and Photoillumination.

R.C. Adamo and J.E. Nenevitz  
Stanford Research Institute  
Stanford, California

### Abstract

In connection with the study of photoconductivity of insulating materials under conditions representative of spacecraft environment, it was found that oscillations (up to 30 percent of the maximum current) can occur in the leakage current through the sample when the sample is simultaneously exposed to an incident electron flux and an optical illumination of roughly one sun. For example with an incident current density of  $10^{-9}$  A/cm<sup>2</sup> of 4 keV electrons and an illumination of one sun, the frequency of oscillation of leakage current was 0.3 Hz. Decreasing the current density to  $0.2 \times 10^{-9}$  A/cm<sup>2</sup> reduced the frequency to 0.06 Hz. The effect of changing incident electron energy does not appear to be as pronounced as changing current density. With a 0.005 in. -thick sample of Kapton V, oscillations were not observed at energies below 2 kV, were maximum at about 4 kV, and their amplitude decreased with increasing energy above 4 kV.

This instability is of interest because it indicates that the measured parameters of an insulator under constant conditions of plasma and solar illumination may be far from constant, and may strongly affect the instantaneous differential potentials and therefore the occurrence of electrical discharges between adjacent areas on a space vehicle.

**SESSION V**  
**DESIGN AND TEST**

**PRECEDING PAGE BLANK NOT FILMED**

## 1. System Aspects of Spacecraft Charging

S.P. Bower  
The Aerospace Corporation  
El Segundo, Calif.

Satellites come in a variety of sizes and configurations including spinning satellites and three-axis stabilized satellites. All of these characteristics have a significant effect on spacecraft charging considerations. There are, however, certain fundamentals which can be considered which indicate the nature and extent of the problem.

The global positioning system satellite will serve to illustrate certain characteristics. Each of the two solar panels has the potential for charging and discharging on the front surface which consists of 12 mils of cover glass over the solar cells. The body of the spacecraft has a variety of surfaces. Some areas consist of multiple layer thermal blankets which are typically about 2 mils of dielectric such as Kapton on the outer surface with a layer of vacuum deposited aluminum or silver on the back surface. Another portion of the body has panels of second surface mirrors which are approximately 2 mils of cover glass backed by a thin layer of aluminum or silver. Each of these surfaces becomes a capacitor when electrons are deposited on or near the front dielectric surface.

As others have indicated, under certain conditions these surfaces will charge to the breakdown voltage and then punch through the dielectric and/or discharge around the periphery. The principle effect is to induce spurious signals in the cables between electronic boxes with the possibility of upsetting the electronics or

burning them out. With the exception of two possible cases, our problems have been with upset rather than burnout. These problems range all the way from the nuisance of having to reset the satellite from the ground to cases where the satellite was almost lost before necessary diagnosis and recommand could be accomplished. The three obvious ways of eliminating this problem are to

- (1) eliminate the charging/discharging,
- (2) prevent signal coupling into cables by RF shielding of cables and/or satellite housing, and
- (3) design electronics which are immune to upset.

Although technology developments may result in materials which eliminate the charge/discharge problem, these are not currently available and we must use other techniques at this time. Utilizing rf shielding may result in a greater weight increase than is practical or necessary. The preference at this time is to design immunity into the electronics. In general, there is no particular weight increase and in the case of military satellites, which are hardened for nuclear effects, the same design fixes may protect the satellite from x-ray ionization, SGEMP, EMP and spacecraft charging.

Such fixes can be based on pulse amplitude or pulse duration. For a variety of reasons, it is preferable to design fixes based on pulse duration. Fortunately, the pulse duration of these effects is similar.

In addition to designing protection into the satellite, it is desirable to conduct tests to verify the fixes. There is a wide range of testing possibilities ranging from testing an entire satellite in a vacuum chamber while subjecting it to a plasma all the way down to moving a Tesla-coil along the spacecraft cables and monitoring for upset.

The first possibility has the disadvantage of relatively high cost and schedule impact on the program. The second possibility is the most convenient and has the smallest impact. However, it is difficult to achieve realistic simulations from the standpoint of signal amplitude and coupling characteristics.

Our current thinking is in terms of testing an entire operating satellite in an ambient environment while subjecting it to simulated discharges and monitoring the satellite operation with the test equipment.

In an actual case, the discharge will be distributed over some portion of a surface and result in both a radiated field which can couple into electric cables and also a current which flows through the structure and grounding paths of the satellite. This latter current also can couple into cables which are near grounding paths such as structural members. Due to difficulties in obtaining a discharge over a large area, our current thinking is in terms of using a point source discharge and grounding to the nearest ground point in an effort to simulate both radiated and conducting conditions. It is further anticipated that the discharge

would be located at various points near the center and periphery of capacitive surfaces.

The principle problem in connection with this testing is knowing how large a surface will discharge. Tests conducted by NASA-Lewis on thermal blankets, solar arrays, and second surface mirrors indicate that areas up to at least 1 sq. ft may discharge at one time with a pulse duration of approximately 400 nsec. Tests have not been made with larger areas. We have satellites with solar arrays greater than 100 sq. ft in area and with thermal blankets greater than 100 sq. ft. If one considers the capacitance of such surfaces, the breakdown voltage (which is typically around 8000), assumes that the pulse width remains no greater than 400 nsec and that the entire surface discharges, the result is a peak pulse of a approximately 100,000 A. It goes without saying that suggesting such a test to a program office on a multimillion dollar satellite will not result in immediate approval. It is also true that there are reasons to believe that we have not been getting discharges of total capacitor surfaces in current satellites or we would have had much more trouble with burning out electronics. Our interim thinking in this area is to assume discharge of areas no greater than 10 sq. ft and to also assume that if the area increases from 1 sq. ft to 10 sq. ft, the pulse duration increases proportionately. Therefore, a typical test would result in pulses of 1000 A with a 400 nsec to 4  $\mu$ sec duration and a breakdown voltage of approximately 8000.

**Contents**

1. Background	723
2. Test Satellite Instrumentation	724
3. Orbital Data	727
4. Scatha Transient Pulse Monitor	731
References	734

## 2. Transient Response Measurements on a Satellite System

J.E. Nanevics and R.C. Adams  
Electromagnetic Sciences Laboratory  
Stanford Research Institute

### 1. BACKGROUND

In 1974, a set of instruments designed to detect the occurrence of electrical breakdowns was flown on a synchronous-orbit satellite.<sup>1</sup> The measurements make an interesting complement to those reported earlier at this conference by Bob Lovell of NASA LeRC. The LeRC sensors were installed on cables inside the vehicle.<sup>2</sup> Accordingly, they respond to signals coupled into the satellite wiring system. The SRI sensors were located on the exterior of the vehicle and detected the rf noise pulses associated with surface breakdowns.

The results of the earlier SRI program are being used to design and develop a set of instrumentation suitable for inclusion as a general piggy-back package for the detection of the onset of satellite charging and breakdowns on synchronous orbit satellites. This system will be flown as the Transient Pulse Monitor (TPM) system on the SCATHA spacecraft.

SEEK BY AUTOMATIC SEARCH

## 2. TEST SATELLITE INSTRUMENTATION

The instrumentation flown on the test satellite was capable of detecting the onset of geomagnetically disturbed conditions and of detecting and counting electrical breakdowns.<sup>1</sup> The system, shown in Figure 1, used a sensor plate mounted on the outside surface of the vehicle as both an electric dipole antenna to pick up noise pulses and as a Langmuir ion probe. Since the probe electrode was biased -5.6 volts with respect to the vehicle frame, it normally collected positive ions and repelled photoelectrons. Under disturbed conditions the ion probe system measures the difference between the photoelectron current from the surface of the detector plate and the plasma electron current incident on the plate. Thus, substorms are indicated by a depressed probe current. Since the dc amplifier used with the ion probe system was unipolar, times when the current is reversed are indicated by a zero ion probe current reading.

Noise pulses induced in the sensor plate antenna are coupled through capacitor C to the preamplifier-counter electronics. Sensitivity tests of the pulse counting system were conducted using the set up shown in Figure 2. A thermal-control panel was placed inside a glass bell jar and illuminated with an electron beam to generate discharges from the mirror cells comprising the surface of the panel. The sensor electrode and electronics system flown on the flight vehicle were used to detect the noise pulses generated. Provisions were made to place the sensor at various distances from the edge of the thermal control. The results of these tests indicated that the pulse counter would reliably detect breakdowns within roughly a meter of the sensor plate.

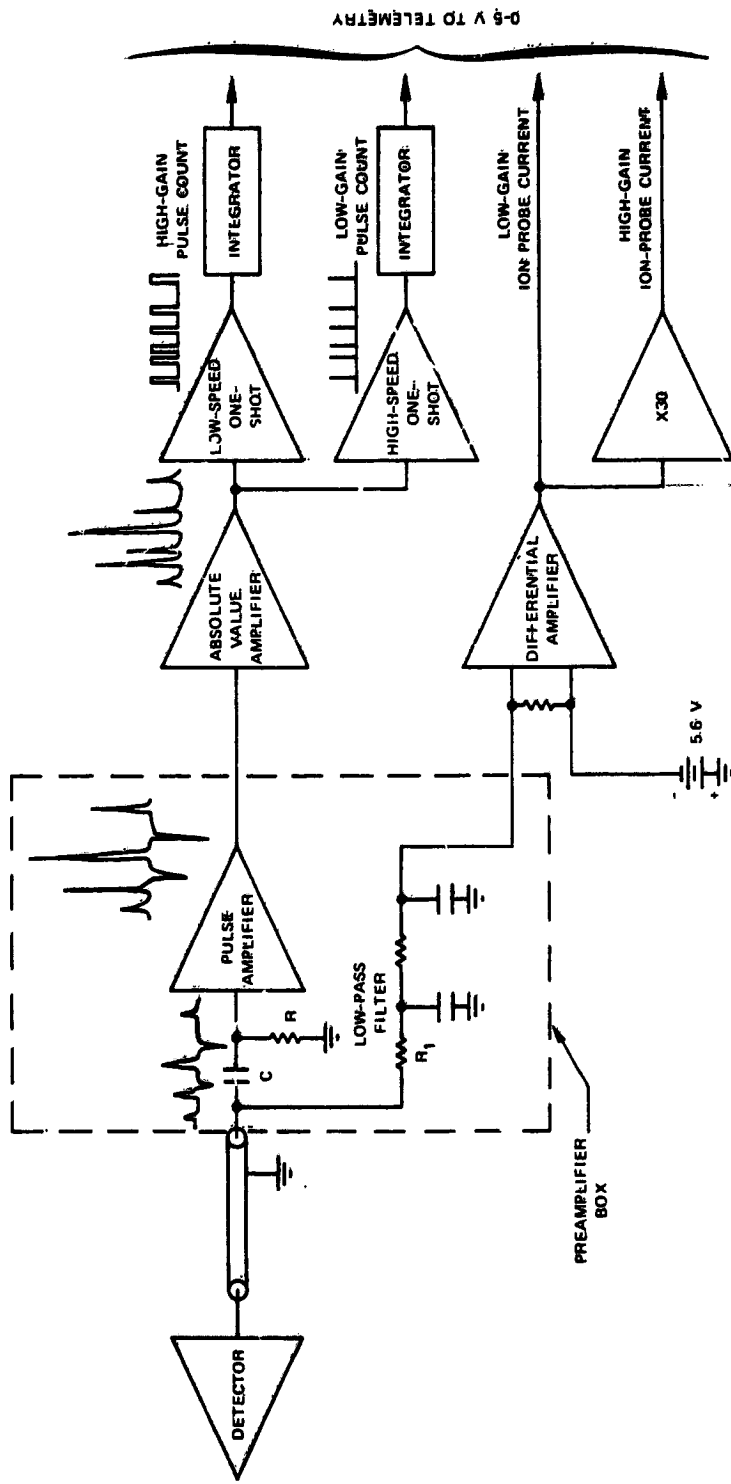
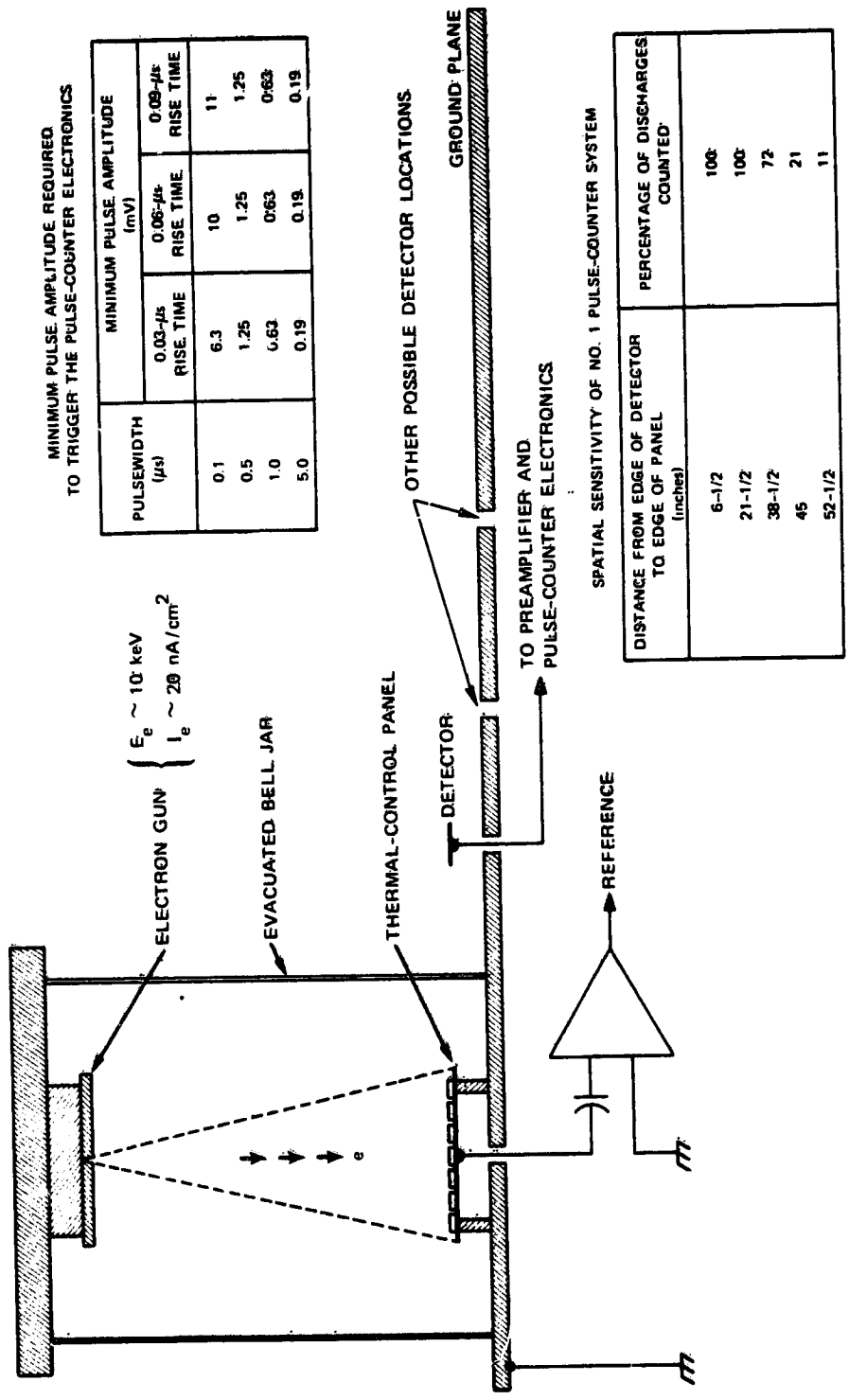


Figure 1. Block Diagram of Ion-Probe/Pulse-Counter System



MINIMUM PULSE AMPLITUDE REQUIRED TO TRIGGER THE PULSE-COUNTER ELECTRONICS

PULSEWIDTH ( $\mu$ s)	MINIMUM PULSE AMPLITUDE (mV)		
	0.03- $\mu$ s RISE TIME	0.06- $\mu$ s RISE TIME	0.09- $\mu$ s RISE TIME
0.1	6.3	10	11
0.5	1.25	1.25	1.25
1.0	0.63	0.63	0.63
5.0	0.19	0.19	0.19

$$\left\{ \begin{array}{l} E_e \sim 10 \text{ keV} \\ I_e \sim 20 \text{ nA/cm}^2 \end{array} \right.$$

SPATIAL SENSITIVITY OF NO. 1 PULSE-COUNTER SYSTEM

DISTANCE FROM EDGE OF DETECTOR TO EDGE OF PANEL (inches)	PERCENTAGE OF DISCHARGES COUNTED
6-1/2	100
21-1/2	100
38-1/2	72
45	21
52-1/2	11

SA-2011-24R

Figure 2. Experimental Setup for Pulse-Counter Sensitivity Test

### 3. ORBITAL DATA-

Figures 3 and 4 show data recorded during both undisturbed and disturbed geomagnetic field conditions for one complete satellite orbit. At synchronous altitudes, each orbit is 24 hr long, sampling all local times equally. Data from the ion-current probe are plotted as a function of local time (LT) in the upper panel of Figures 3 and 4. These data were selected at points in the satellite rotation at which the total probe current was a maximum (this corresponds to the orientation at which the detector plate is most nearly perpendicular to the sun direction resulting the maximum photoemission current). The geomagnetic field conditions were determined by examination of  $A_p$  and  $K_p$  shown at the top of Figures 3 and 4. Figure 3 shows data typically recorded during undisturbed geomagnetic field conditions. It shows the diurnal variation occurs because of the dependence of photoelectron current on the angle between the sun direction and the detector plate. At local evening and local morning the sun is normally incident to the detector plate, and the peak photoelectron current-density has a maximum of about  $80 \mu A / m^2$ . At local midnight the sun is obliquely incident to the detector plate, and the peak photoelectric current has a minimum of about  $30 \mu A / m^2$ . Near local noon the body of the spacecraft shadows the detector, and the photoelectron current is reduced nearly to zero, as shown from 10.7 - 13.3 hours LT in Figure 3. These data represent the usual diurnal variation of peak photoelectron current, and no depressions of the probe current indicating the injection of energetic electrons are observed.

The pulse-counter data are shown in the lower panels of Figures 3 and 4. The data plotted are the number of discharges per minute that are detected by the pulse counter. The number of counts were collected and averaged over a 10-min period. For the quiet geomagnetic period shown in Figure 3, few discharges are detected by the instrument except from local evening to local midnight during which rates averaging slightly less than 1/min are observed. Count rates typically near 30/hr are observed on almost every orbit from local evening to local midnight.

Figure 4 illustrates data recorded during an orbit on 31 January 1974 for which a moderate geomagnetic field disturbance was indicated by the magnetic indices. The injection of energetic electrons at synchronous altitude was detected by depressions of the total probe current caused by increases in the plasma-electron current during the injection event.

Two examples of data recorded during satellite eclipse are shown in Figures 5 and 6. Figure 5 shows the ion-current probe and pulse counter data recorded during undisturbed geomagnetic conditions. During satellite eclipse the probe current from the detector plate drops to nearly zero because solar ultraviolet radiation is not present to cause photoemission from the detector plate.

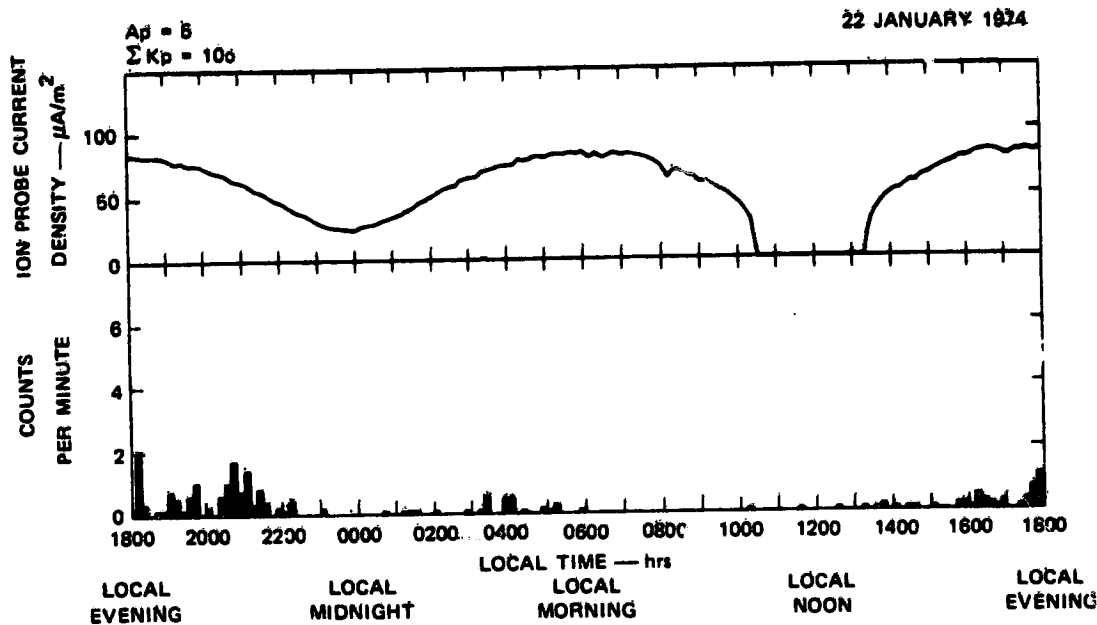


Figure 3. Static-Charge Experiment Data From an Orbit for which No Substorm Activity was Observed. (The ion-current probe data shows the usual diurnal variation. Few electrical discharges are observed except on the interval from local evening to local midnight.)

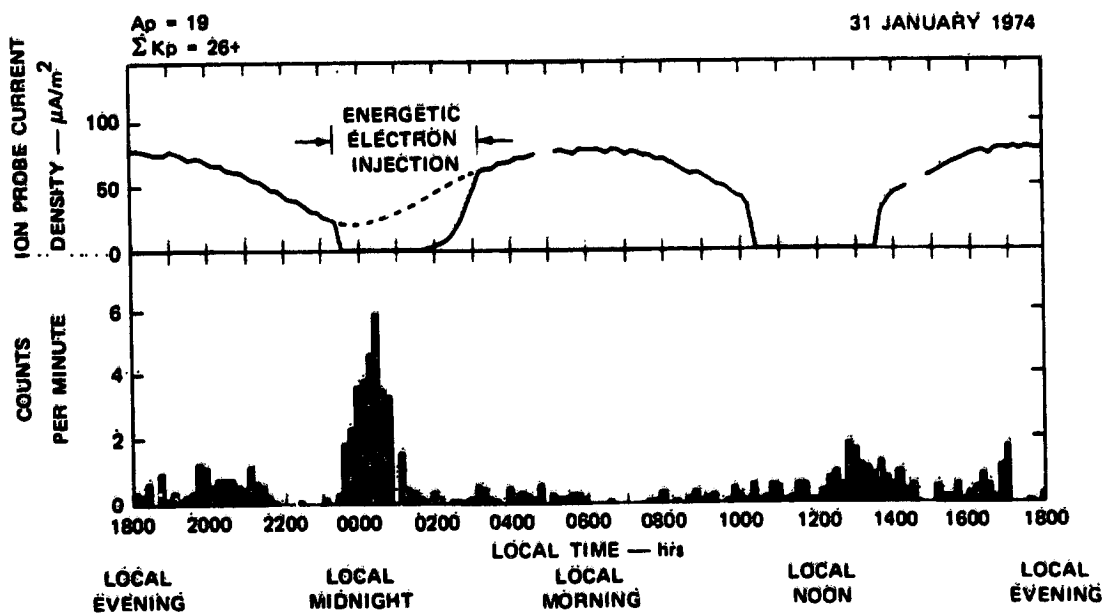


Figure 4. Static-Charge Experiment Data From an Orbit for which Substorm Activity was Observed. (Depressions of the ion-probe current near local midnight are caused by the injection of energetic electrons to synchronous altitudes. Discharge rates as high as six per minute are measured by the pulse counter during the electron injection event.)

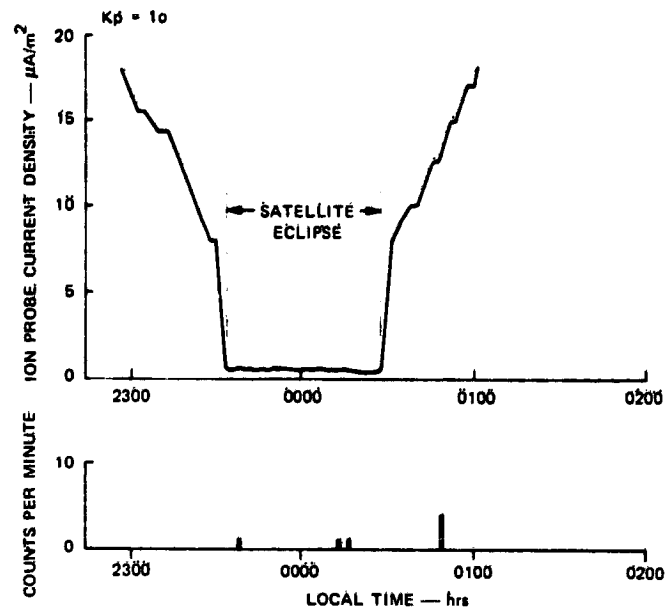


Figure 5. Static-Charge Experiment Data Recorded During Undisturbed Geomagnetic Field Conditions Through Satellite Eclipse. (The probe current drops to nearly zero when the photoelectric current is cut off by the earth's shadow. Only a few discharges are observed during this pass.)

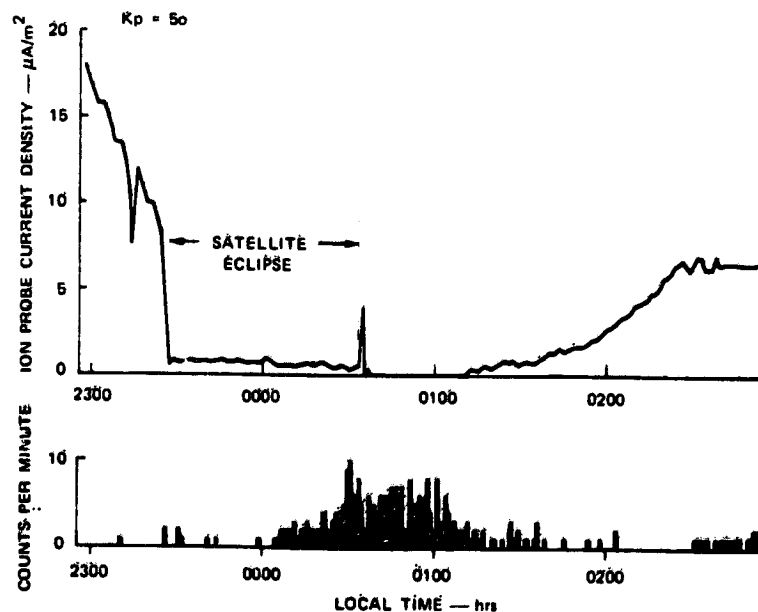


Figure 6. Static-Charge Experiment Data Recorded During Disturbed Geomagnetic Field Conditions Through Satellite Eclipse. (An energetic electron injection event and discharge rates as high as ten per minute are observed during this pass. The discharges are associated with the injection event (note depressed ion probe current) rather than with satellite eclipse.)

Smooth changes in the total probe current on either side of satellite eclipse are caused by changes in the satellite orientation (see Figure 3 and the related discussion of the diurnal variation in total probe current). Only a few pulse counts are observed by the pulse counter during this pass. (The pulse counter data are accumulated and averaged over a 2 min period for the data shown in Figures 5 and 6.)

Figure 6 shows an example of data recorded during a magnetospheric substorm near satellite eclipse. A depression of the ion probe current indicating the injection of energetic electrons is observed just after the satellite emerges from eclipse (compare these data with those shown in Figure 5). Discharge rates as high as 10/min are observed in association with this substorm electron-injection event.

The data in Figure 6 show that the discharges are associated with the injection of the energetic electrons near local midnight, and not with satellite eclipse. The beginning of the plasma-injection event shown in Figure 6 cannot be determined from the ion-current probe data because the satellite is in eclipse. It is possible that the discharge rates may have been enhanced during satellite eclipse; however the generating mechanism of the discharge is clearly the energetic plasma injection during the magnetospheric substorm.

These four examples of discharges observed by the static charge experiment are typical of the several conditions under which synchronous orbiting satellites must function. They show that electrical discharges are observed during substorms at rates near 10/min on the satellite's external surface. These discharges occur when energetic electrons are injected to synchronous altitudes near local midnight. These discharges are probably caused by the charging of dielectric surfaces to large negative potentials during the electron injection events.

Other discharges are observed near local evening and at other points in orbit at which discharges were not expected to occur. These discharges have lower rates (1/2 min); however, they occur on essentially all satellite orbits from local evening to local midnight. The generation of these discharges is not well understood at the time of this writing.

Several types of engineering orbital anomalies have occurred on this satellite that have been supposed to be related to electrical discharges. These anomalies consist of a type of anomalous detector response and an uncommanded reset of a satellite command circuit. These anomalies have occurred on several other satellites in addition to the satellite on which this experiment was flown. An examination of the values of ground-based geomagnetic indices at the times of occurrence of the anomalies strongly suggests that they are related to intense substorm activity. Thus, it was suggested that such anomalies were generated by interference from the electromagnetic radiation of electrical discharges.

During the period of operation of this experiment, several occurrences of both types of these anomalies were reported. For the anomalous detector response, a total of 35 occurrences were reported. For 31 of these cases a discharge was observed by the experiment coincidently with the anomalous detector response. These anomalous responses were reported on several different days, and the probability that the coincidences occurred by chance is essentially zero. There were a total of 6 of the uncommanded circuit resets, and 5 of these resets occurred coincidently with detection of discharges by the experiment. Thus, data from this experiment has confirmed the hypothesis that these types of orbital engineering anomalies are caused by interference from these electrical discharges.

#### 4. SCATHA TRANSIENT PULSE MONITOR

Based on the experience gained in the satellite tests, a low-level program of planning and instrument development was initiated at SRI. The objective was the development of a set of compact, lightweight instruments to detect the occurrence of an electron injection event, to measure electric field E and current density J at the vehicle surface, and to detect, count, and characterize the pulse waveforms from electrical breakdowns on the satellite surface. A design goal was to develop simple instruments suitable for use on a piggy-back basis on a large number of satellites.

The pulse detection and characterization system will be repackaged and flown on the SCATHA satellite as a TPM. Although the TPM system can be used to measure pulses either on the outside or inside of the satellite, the SCATHA TPM system will be used entirely with internal sensors since the electromagnetic signature of the breakdown pulse on the exterior of the vehicle will be characterized by the SC1-2 experiment.

The purpose of the TPM system will be to acquire amplitude and pulse characteristics of transients coupled into vehicle power and signal lines when the spacecraft experiences arc discharges. Requirements imposed on the TPM system are as follows:

- (1) Measure peak pulse amplitude both + and - separately.
- (2) Determine number of transients absolute (+ and -).
- (3) Measure total energy both + and - separately.
- (4) Accomplish these measurements within the following constraints:
  - (a) 60 dB dynamic range on amplifiers.
  - (b) Select either a single pulse and/or multiple pulses.
  - (c) Frequency response  $> 50$  MHz.

These measurement capabilities are illustrated graphically in Figure 7.

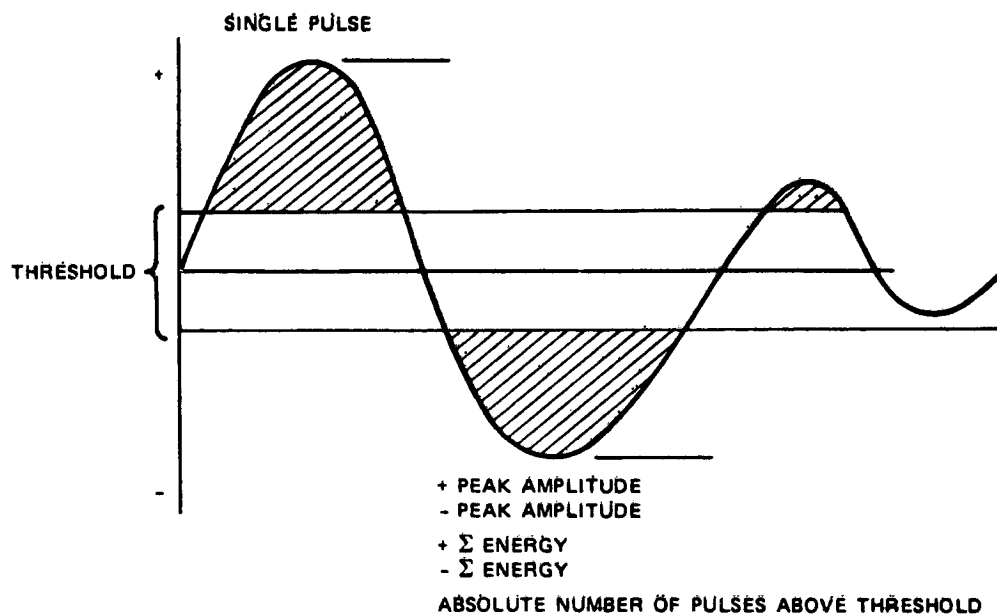


Figure 7. Data Derived From Transient-Pulse Monitor

The functional deployment of the TPM system will be as follows:

- (1) Four (4) separate channels capable of yielding the complete data stipulated under requirements for each channel.
- (2) Locations within the spacecraft will be:
  - (a) Cable bundle antenna (low impedance).
  - (b) Cable bundle antenna (high impedance).
  - (c) Current probe on primary power reference ground.
  - (d) Current probe on solar array power input.

A functional block diagram of the TPM is shown in Figure 8. The ultimate form of the system stemmed from the requirement that it be able to provide information about the induced noise pulses even though the parameters of interest might vary over a considerable range. Wide dynamic ranges were achieved in several ways. First, logarithmic amplifier/detectors were used in the pulse-peak measuring system. The pulse-integral measuring system has provisions for adjusting threshold in orbit to avoid the possibility of data being inadvertently contaminated by system noise. Since it is not clear what the prof of breakdowns on SCA THA will be, provisions are included to command the pulse-peak and pulse-integral measuring systems to operate with a 1 sec measuring window or to operate for only 100  $\mu$ sec after the first pulse occurring in a telemetry window.

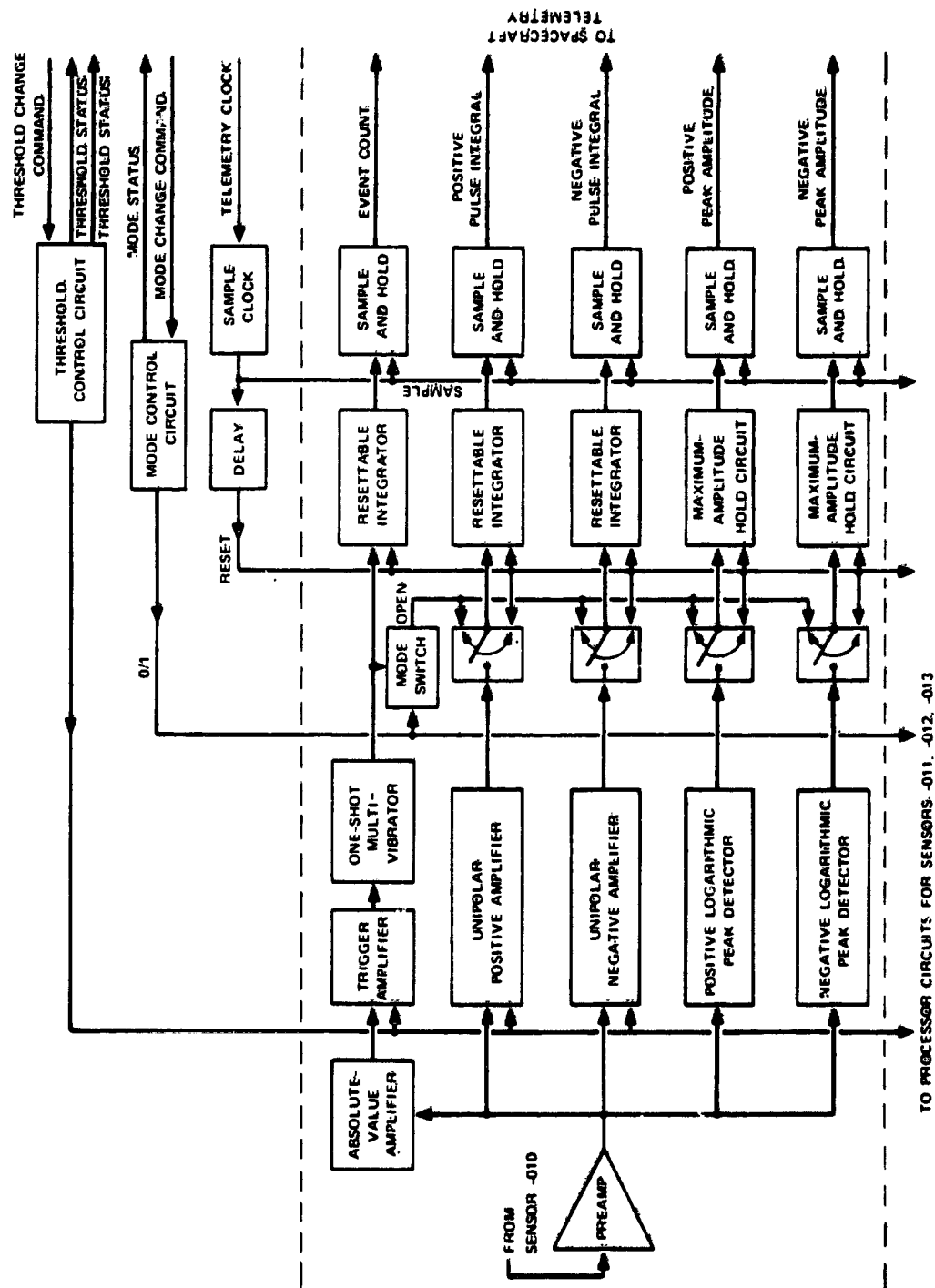


Figure 8. Transient-Pulse Monitor System Functional Block Diagram

The sample-and-hold circuit for each output channel is arranged so that data obtained during one telemetry window are transferred to the sample-and-hold where they are stored for one telemetry period during which time all of the output channels are interrogated by the telemetry system. Thus, all of the data read during a particular window were generated during the same single telemetry period.

The pulse-peak detectors indicate the peak amplitude observed during the commanded window. (If several pulses occur, the highest will be measured.) The pulse-integral system indicates the integral over the entire window of that signal above the commanded threshold level. The event-counter indicates the number of pulses occurring during a 1 sec period regardless of which mode is commanded for the pulse-peak and pulse-integral systems.

Packaging of the system is such as to minimize size and weight in order that it can be used as a piggy-back installation with minimum weight, volume, and power impact.

## References

1. Nanevich, J. E., Adamo, R. C., and Scharfman, W. E. (1974) Satellite-Life-time Monitoring, Final Report Project 2611, Contract FO4701-71-C-0130, Stanford Research Institute, Menlo Park, Calif.
2. Stevens, N. J., Lovell, R. R., and Klinect, V. W. (1976) Preliminary Report on the CTS Transient Event Counter Performance Through the 1976 Spring Eclipse Season, NASA Technical Memorandum NASA TM X-73487, Lewis Research Center, Cleveland, Ohio.

**Contents**

1. Introduction	735
2. Derivation of the Specification	737
3. Discussion	742
4. Concluding Remarks	743
References	743

### 3. Provisional Specification for Satellite Time in a Geomagnetic Environment

N. John Stevens, Robert R. Lovell, and Carolyn K. Purvis  
National Aeronautics and Space Administration  
Lewis Research Center  
Cleveland, Ohio

#### Abstract

Satellites in geosynchronous orbit have been experiencing operational anomalies. These anomalies are believed to be due to the environment charging the spacecraft surfaces to a point where discharges occur. In designing future satellites for long term operation at geosynchronous altitude, it is important that designers have a specification that will give the total time per year, the particle flux density and particle energies that their satellites can be expected to encounter in these sub-storm environmental conditions. The limited data currently available on the environmental conditions has been used to generate the provisional specification given in this report.

#### 1. INTRODUCTION

Satellites in geosynchronous orbit have been exhibiting anomalous behavior, particularly during the local dusk to dawn portion of their orbit.<sup>1</sup> It is now believed that these anomalies are due to the noise generated by the discharges from the differential electrostatic charging of the various spacecraft surfaces to kilovolt

potentials by the environment. The electromagnetic energy released from such discharges can trigger sensitive electronic logic systems, resulting in the anomalous spacecraft behavior. In addition, the discharges can damage thermal control surfaces, resulting in higher than anticipated temperatures in the spacecraft system. The charging of these surfaces can also result in their enhanced contamination.

Data from the ATS-5 and ATS-6 satellites have shown that clouds of kilovolt electrons can occur at geosynchronous altitude in the local midnight to dawn quadrant.<sup>2</sup> The occurrence of such particle clouds has been correlated with geomagnetic substorm activity.<sup>3,4</sup> Furthermore, they persist for periods of several hours. These kilovolt electrons impinging on the spacecraft can cause the spacecraft surfaces to charge to kilovolt potentials. ATS-5 and ATS-6 observations indicate charging of the spacecraft grounds to greater than 10 kV negative in the eclipse phases of their mission and to a few hundred volts negative in sunlight in the presence of these kilovolt particles. If the spacecraft grounds can be charged in this manner, then it must be assumed that insulator surfaces can also be charged to kilovolt levels. The shaded insulator surfaces can be charged to these levels even when the spacecraft grounds are maintained at the few hundred volt level, resulting in differential charging of the various satellite surfaces.

The spacecraft charging phenomenon is currently under investigation at several ground facilities.<sup>5-9</sup> It has been shown in these investigations that insulating surfaces can be charged by beams of kilovolt electrons and that the subsequent discharges do produce conducted and radiated electromagnetic interference. In addition, it has been shown that the discharges can damage the insulator surfaces. The number of discharges which must be absorbed by electrical systems as well as the degree of damage to surfaces has been shown to be proportional to the average particle energy and to the incoming flux of particles. From an engineering standpoint it is important to know the anticipated discharge rate for multiyear missions so that this factor can be considered in the specifications for the electronic circuit design and for the thermal design. Therefore, it is desirable to develop a specification defining the time per year that a synchronous satellite could expect to spend in a substorm environment, the relative proportions of time spent in severe, moderate and mild substorms, and the particle energies and currents characteristic of these substorms. With such a specification in hand, it would be possible to conduct tests to determine the performance of surface materials for a proposed mission. In this report, the available data on the substorm environment are used to generate a provisional specification for use in designing satellite systems.

## 2. DERIVATION OF THE SPECIFICATION

The information on the geomagnetic substorm environment at synchronous altitude is based on data from the ATS-5 and ATS-6 Auroral Particles Experiments. Considerable data exists on particle flux as a function of energy both in quiet times and in substorms; however, data on substorm particle energy and current flux variations over the local dusk to dawn quadrants is scarce. This latter type of data is necessary in order to derive a specification for the time history of particle energy and flux per year of mission life.

The available data include: a survey of the substorm environment for a three month period of 1970;<sup>10</sup> time histories of two substorms obtained as a result of this survey; and data on the level of charging of ATS-6 spacecraft grounds during the fall 1974 eclipse season.<sup>11</sup> These data are shown in Table 1 and Figures 1 - 3 respectively, and form the basis for the present specification for the substorm environment.

Table 1. Summary of ATS-5 Measurements of Charged Particle Environment..

<p>PLOT OF 2 JAN 1970 SUBSTORM</p> <p><u>Electrons</u></p> <p>Currents up to 0.85 mA/cm<sup>2</sup> for ≈ 30 min Average Current 0.5 mA/cm<sup>2</sup> for &gt; 8 hr Peak Temperature of 12-13 kV for ≈ 45 min Average Temperature of ~6 kV for ≈ 8 hr</p> <p><u>Protons</u></p> <p>Currents up to 13 pA/cm<sup>2</sup> Average Current 7 pA/cm<sup>2</sup> Peak Temperatures of 16-20 kV for ≈ 30 min Average Temperature of ~12 kV</p> <p>OTHER SUBSTORMS</p> <p><u>Electrons</u></p> <p>Currents observed up to 2 nA/cm<sup>2</sup>, Typical 0.1 to 0.2 Possible: 8 nA/cm<sup>2</sup> Maximum (Noisy Data) for 5-10 min Temperatures up to 20-30 keV Typical Temperature 2-6 keV</p>
---

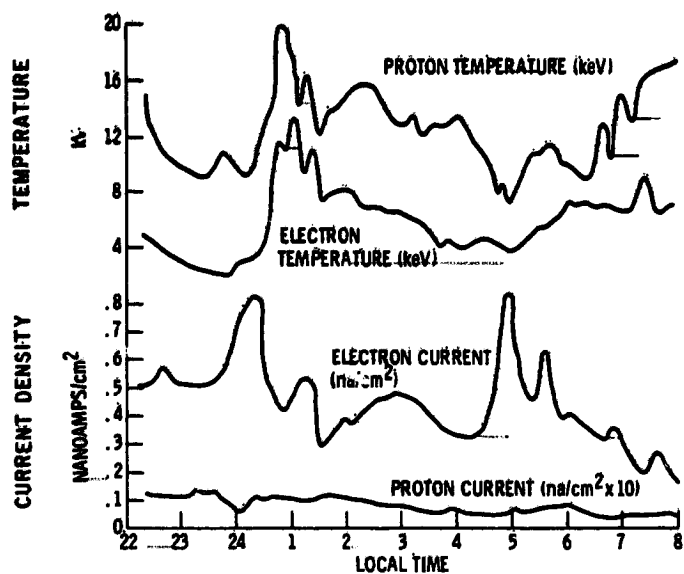


Figure 1. Environmental Conditions From 2 January 1970 Substorm

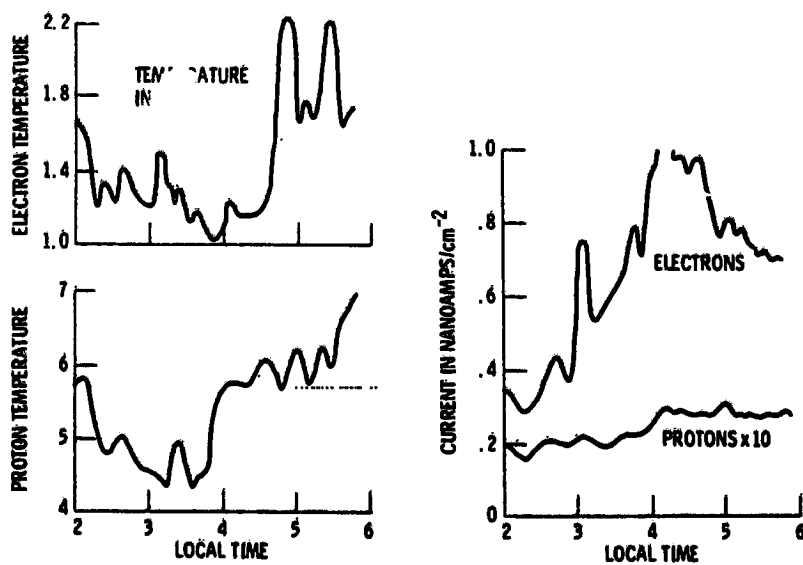


Figure 2. Temperature and Current Profiles for 27 March 1970 Substorm (Rosen<sup>4</sup>)

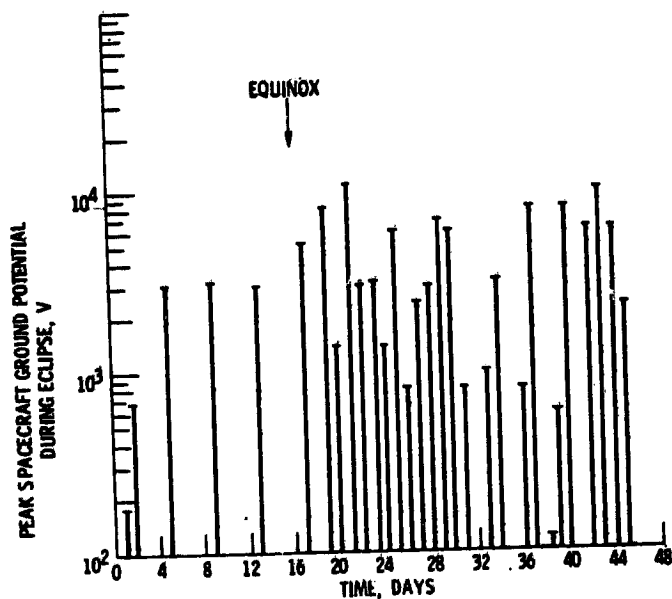


Figure 3. ATS-6 Spacecraft Charging Data. Fall eclipse period, 1974 (Bartlett<sup>10</sup>)

A study of Table 1 and Figures 1 - 3 mentioned above indicates a number of factors which must be considered in developing the specification. First, particle energies are not constant over the substorm period; they fluctuate throughout. Second, there is a large variation in substorm intensity; the average particle energies are higher in some substorms than in others. This is shown by the variation in the level of charging of the spacecraft grounds in Figure 3. Third, the electron current density is low when the average electron energy is high, and conversely (Figures 1 and 2). Finally, the relationship between proton and electron average energies and current densities is reasonably linear. For the purposes of this specification, it is assumed that the average proton energy is twice the average electron energy, and that the proton current density is about 1/50 of the electron current density. These assumptions are based on Figures 1 and 2.

The temporal specification deduced from these limited data and the considerations noted above is shown in Figure 4. A more detailed discussion of the derivation of the specification is given in the following paragraphs.

## 2.1 Total Hr/Year in Substorm

It is necessary to specify particle energy and current density as functions of time in a substorm environment per year of mission life. The first task is

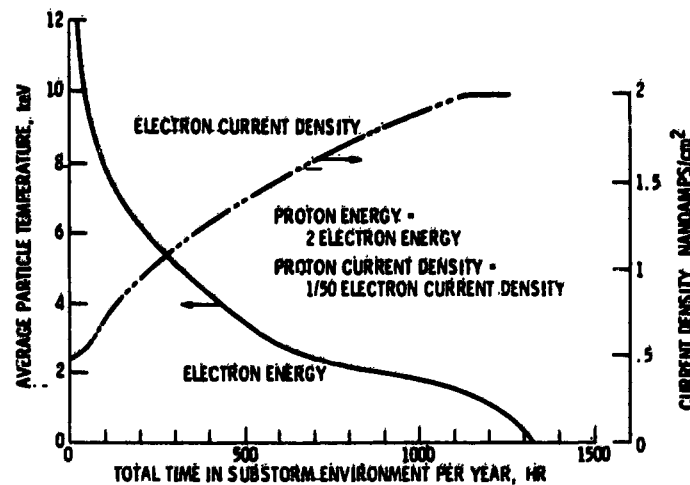


Figure 4. Provisional Specification for Satellite Time in a Geomagnetic Substorm Environment

therefore to determine the average number of hours/year that a synchronous spacecraft will spend in a substorm environment.

According to a simplified evaluation of the occurrence of substorms,<sup>4</sup> substorm activity occupies about 30 percent of the time during any given year. For purposes of this specification, it is assumed that a satellite can find itself in a changing environment during the local dusk to dawn portion of its orbit. Based on these assumptions, a satellite can be in a substorm environment for a total of 1314 hr/year. This number is denoted by  $H_s$  (hours per year in substorm).

## 2.2 Particle Energy

Two further factors are required to obtain a specification for particle energy as a function of time. First, it is necessary to determine a "time variation factor" indicating the fraction of time in any one substorm that the particles can be at or above various energy levels. This factor depends on the particle energy of interest and is herein denoted by  $f_t(E)$ . The second required factor is a "substorm intensity factor" indicating the proportions of severe, moderate, and mild substorms expected to occur in a year. This factor is also related to the energy level of interest (via the ATS-6 ground potential data) and is herein denoted by  $f_s(E)$ .

In order to determine  $f_t(E)$ , it is necessary to characterize the variation of particle energies during a substorm. For this purpose, the 2 January 1970 substorm (Figure 1) is taken as the model of a severe substorm in terms of energy fluctuations. Data from this substorm are used to define the fractions of the total

substorm time (10 hr) during which the average energy of the charged particle population attained or exceeded specified values. The model for the moderate substorm is assumed to be the same as the severe but with the average energy scale cut in half. The mild substorm model is assumed to be the same as the moderate substorm model but with the energy scale again halved.

The "substorm intensity factor"  $f_s(E)$  is obtained from the measurements of the ATS-6 spacecraft ground potential during the 1974 eclipse period (Figure 3). It is assumed that when the ATS-6 spacecraft ground had been biased to a voltage level of between -6 kV and -12 kV, the satellite had encountered a severe substorm. When the ATS-6 ground had been biased to values between -3 kV and -6 kV, it is assumed that the satellite encountered a moderate substorm. An encounter with a mild substorm is assumed to have occurred when the ATS-6 ground had been biased to values between 0 and -3 kV. The intensity factor is determined by the ratio of the number of days that the spacecraft ground voltage reached these voltage ranges to the total number of days that the satellite experienced a substorm during this eclipse period. Therefore, the intensity factor takes on 3 values: 0.33 for severe substorms (10 days out of 30), 0.27 for moderate substorms (8 days out of 30), and 0.4 for a mild substorm (12 days out of 30). It is assumed that this ratio remains constant throughout the year.

The specification for the average electron energy as a function of time (Figure 4) is then obtained by determining  $H(E)$ , that is, hr/year in a substorm environment of average electron energy  $\geq E$ , from the

$$H(E) = H_s \{ [f_t(E)f_s(E)]_{\text{severe}} + [f_t(E)f_s(E)]_{\text{mod}} + [f_t(E)f_s(E)]_{\text{mild}} \}$$

Values of these terms for selected average energies are given in Table 2.

Table 2. Factors Used in Deriving Specification

Electron Temp. (KeV)	Category of Storm						H(E) (hours)
	Severe		Moderate		Mild		
	$f_t(E)$	$f_s(E)$	$f_t(E)$	$f_s(E)$	$f_t(E)$	$f_s(E)$	
12	0.025	0.33	-----	-----	---	---	11
10	.1	↓	-----	-----	---	---	43
8	.2		-----	-----	---	---	87
6	.5		0.025	0.27	---	---	226
4	.8		.2		---	---	418
2	1.0		.6		0.2	0.4	823

The specification for ion energy versus time in the substorm environment is simply that the average ion energy is approximately twice the average electron energy as was discussed above. It is recognized that categorizing the substorms in the manner outlined above is arbitrary. As more information on the substorm environment becomes available, the assumptions which have been used can be improved.

### 2.3 Particle Current Density

The specification for the electron current density in Figure 4 is again based on data from the 2 January 1970 substorm as the model substorm. These data indicate that the current density is  $0.5 \text{ nA/cm}^2$  at the high average electron energies, and that as the average electron energy decreases, the current density increases monotonically to  $2 \text{ nA/cm}^2$  in approximate inverse proportion to the average energy. The current density specification is devised based on this information plus the previously derived energy specification. Again, the ion specification is simply stated based on the earlier observation that the ion current density is about  $1/50$  of the electron current density.

### 2.4 Field Aligned Fluxes

It should be noted that throughout the development of this specification, isotropy of the environment has been assumed. Recent data indicate that field aligned fluxes are in fact present,<sup>12</sup> and that particle fluxes aligned with the magnetic field lines are considerably larger at certain energy levels than the fluxes at large pitch angles. No attempt has been made to incorporate such anisotropies into the present specification.

## 3. DISCUSSION

The specification presented in Figure 4 shows that for a large fraction of time, the satellite will encounter only mild substorms. Computations of surface behavior of the normal spacecraft materials in this environment show that the resulting surface potential in such substorms is not high enough to cause discharges. This may explain the apparent randomness of the observed spacecraft anomalies, which do not always occur when substorms are detected at a ground station.

The specification can be used in conjunction with a ground test program to determine the behavior of an insulator surface proposed for a satellite. By simulating the substorm parameters, the test surface can be subjected to the specification profile to determine the surface charging characteristics for a given mission life. The discharge threshold will also be determined along with the material

degradation and transients associated with the discharges. This information can then be used in designing the satellite systems to accommodate the surface behavior. Hence, the specification is used as an engineering tool to aid in system designs.

#### 4. CONCLUDING REMARKS

The specification presented herein is based on a very limited amount of data, and many assumptions. No margins or variances have been included in this specification simply because the data are insufficient to allow reasonable calculations of such parameters. For these reasons, the present specification has been denoted as a provisional specification; it is expected that refinements will be made as more data become available.

Despite the preliminary nature of this specification, it is felt that it provides a useful engineering tool which can be used to provide a guideline for ground test procedures to estimate the effects of substorm activity on a spacecraft during a specified mission life.

#### References

1. McPherson, D. A., Cauffman, D. P., and Schober, W. (1975) Spacecraft Charging at High Altitudes - The Scatha Satellite Program, AIAA Paper 75-92.
2. DeForest, S. E., and McIlwain, C. E. (1971) Plasma clouds in the magnetosphere, J. Geophys. Res. 76 (No. 16):3587-3611.
3. DeForest, S. E. (1972) Spacecraft charging at synchronous orbit, J. Geophys. Res. 77 (No. 4):651-659.
4. Rosen, A. Spacecraft Charging: Environment Induced Anomalies, AIAA Paper 75-91.
5. Stevens, N. J., Lovell, R. R., and Gore, V. (1975) Spacecraft charging investigation for the CTS project, Presented at the Conf. on Spacecraft Charging by Magnetospheric Plasmas, Amer. Geophys. Union, Annual Spring Meeting, Washington, D. C. (also NASA TM X-71755).
6. Sellen, J. M., Jr. Spacecraft materials response to geosynchronous substorm conditions, Presented at the Conf. on Spacecraft Charging by Magnetospheric Plasmas, Amer. Geophys. Union, Annual Spring Meeting, Washington, D. C.
7. Adams, R. C., and Nanevicz, J. E. (1975) Spacecraft charging studies of voltage breakdown processes on spacecraft thermal control mirrors, Presented at the Conf. on Spacecraft Charging by Magnetospheric Plasmas, Amer. Geophys. Union, Annual Spring Meeting, Washington, D. C.

8. Balmain, K. G., Orszag, M., and Kremer, P. (1975) Surface discharges on spacecraft dielectrics in a scanning electron microscope, Presented at the Conf. on Spacecraft Charging by Magnetospheric Plasmas, Amer. Geophys. Union, Annual Spring Meeting, Washington, D. C.
9. Fogdall, L. B. et al (1975) Combined environmental effects on polymers, Proc. of 8th Conf. on Solar Simulation, NASA SP-379, pp. 259-260.
10. Inouye, G. T. (1975) Spacecraft Charging Model, AIAA Paper 75-225.
11. Bartlett, R. O., DeForest, S. E., and Goldstein, R. (1975) Spacecraft Charging Control Demonstration at Geosynchronous Altitude, AIAA Paper 75-359.
12. McIlwain, C. E. (1975) Auroral electron beams near the magnetic equator, Presented at the Nobel Symp., Kiruna, Sweden.

**Contents**

1. Background	745
2. Description of Environmental Monitors	746
3. Discussion	749
4. Concluding Remarks	750
References	750

**4. Development of Environmental Charging Effect Monitors for Operational Satellites**

N. John Stevens, John C. Stuman, and Frank D. Berkopac  
National Aeronautics and Space Administration  
Lewis Research Center  
Cleveland, Ohio

**Abstract**

An instrumentation package to monitor the effects of the environmental charging of spacecraft surfaces on the systems of operational spacecraft is being developed at the Lewis Research Center of NASA. This package is to perform two functions: first, the local charged particle flux and the particle characteristic energy will be monitored; and second, transients in the spacecraft electrical harness will be counted as a function of amplitude, and time. This package is considered to be a monitor of the spacecraft system. It will be used to determine the duration and effect of any environmental charging of the spacecraft surfaces. Thus, it will be possible to determine the relationship between the occurrence of the anomalies and the charging phenomenon. Design details and design goals of this package are presented.

**1. BACKGROUND**

Spacecraft charging occurs when spacecraft surfaces react to the charged particles of the geomagnetic substorm environment and charge to negative potentials relative to the space plasma. Such charging occurs predominately when the spacecraft is in the midnight-to-down portion of its orbit. Spacecraft surfaces in

sunlight can charge from several tens of volts negative to several kilovolts negative. Spacecraft surfaces in the shade can charge to several tens of kilovolts negative. The actual surface potentials depend upon the substorm intensity. Spacecraft surface potentials of this order have been deduced from scientific measurements made by instruments aboard geosynchronous spacecraft. <sup>1, 2, 3</sup>

The occurrence of anomalies on geosynchronous spacecraft is consistent with charging of spacecraft surfaces in the midnight-to-down quadrant of the orbit. Direct relationship of the occurrence of spacecraft system anomalies, primarily changes in the state of electronic logic, and the charging of spacecraft surfaces has been inferred from operations aboard geosynchronous spacecraft. <sup>4</sup> There is scant one-to-one correlation of spacecraft anomalies with the local environment in which the spacecraft finds itself.

Spacecraft surfaces are covered with a variety of materials and can be variously shaped. Differential charging of these surfaces, then, can result <sup>4, 5</sup> which can lead to electrical breakdown or discharges. These discharges can couple into spacecraft harnessing and may cause interference with electronic circuits. <sup>6</sup>

To date, spacecraft that have experienced anomalies have not had sensors to detect geomagnetic substorm conditions. In addition, there are indications that differences in spacecraft configurations, specifically those differences between spin-stabilized spacecraft and three-axis-stabilized spacecraft, result in different reaction of the spacecraft to its immediate environment. <sup>7, 8</sup>

To address the spacecraft charging phenomena more data is needed. Data is needed from many missions. Simultaneous information about the spacecraft internal housekeeping environment and the local geomagnetic substorm environment is required. This can be accomplished with simple instrumentation that is usable on the greatest number of spacecraft. It will then be possible to correlate transient events with environmental conditions. Such instrumentation is being developed at the Lewis Research Center. Design details and some design goals of this instrumentation follow.

## 2. DESCRIPTION OF ENVIRONMENTAL MONITORS

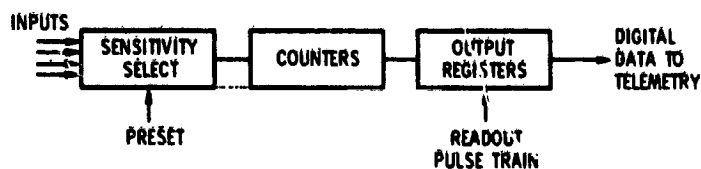
### 2.1 Design Philosophy

To correlate spacecraft discharge-induced transient events with environmental conditions it is considered sufficient to count transient events induced in the spacecraft housekeeping harness, to make a measurement of the characteristic energy of the incident charged particles, and to measure the average current density of the incident charged particles. These are reasonable engineering

measurements to make. The environmental monitors are analogous to a spacecraft system power monitor, a diagnostic device. The information obtained with these monitors can be used to supplement data obtained from scientific instruments.

## 2.2 Transient Event Counter

The monitor to be used to sense discharge-induced transients in the harnesses of spacecraft is a transient event counter. This is a growth version of the Transient Event Counter (TEC) presently returning data from the Communications Technology Satellite (CTS). Its characteristics are given in Figure 1. Four sensors are assembled with the spacecraft harness. These sensors are coaxial cables with one end unterminated and stripped for a length of 30 to 60 cm. Each sensor signal is amplitude discriminated to one of three levels set during the final stage of TEC assembly. Only transients over the preset signal strength, measured at the input to the discrimination circuitry, are counted. The counting circuitry incorporates a 10- $\mu$ sec delay after a discharge pulse is counted to avoid counting of line ringing as discrete transient events. The counting circuitry incorporates a ring counter to eliminate transients induced by noise in the spacecraft-to-ground communication link. The four continuous sensor measurements are output to telemetry on separate digital channels. The TEC physical characteristics are summarized in Figure 1 and reflect both design goals and what has been achieved to date. The TEC should be located within the satellite interior because of the rf shielding the electrically grounded spacecraft structure and thermal insulation provides.



### CHARACTERISTICS

4 SENSORS

AMPLITUDE DISCRIMINATION, 3 LEVELS, PRESET

PHYSICAL: APPROX 1½ W, 0.5 KG, 100 CM<sup>2</sup> FOOTPRINT

OUTPUT: 4 DIGITAL TELEMETRY CHANNELS

LOCATION: SATELLITE INTERIOR

Figure 1. Summary Description of the Transient Event Counter

### 2.3 Characteristic Energy Sensor

The characteristic energy sensor, described in Figure 2, consists of an electrically floating metal plate coupled to a voltage sensor. The voltage sensor is a capacitively-coupled electrostatic voltmeter that operates on a null-balance principle whereby the potential of the voltmeter sensor is brought to the potential of the metal plate by a power supply. This design provides a very accurate local voltage measurement and minimizes large voltage gradients at the measurement location. The sensing range, +50 V to -20 kV, is based on present knowledge of the environment.<sup>9</sup> The frequency response bandwidth, dc to 5 Hz, is based on characteristic charging times that have been observed in testing.<sup>10</sup> The physical characteristics shown in Figure 2 reflect both design goals and what has been achieved to date. The output is analog but analog-to-digital conversion can be performed, with the attendant increases in power and weight. It is necessary to locate this sensor on the satellite exterior, preferably not in the sun.

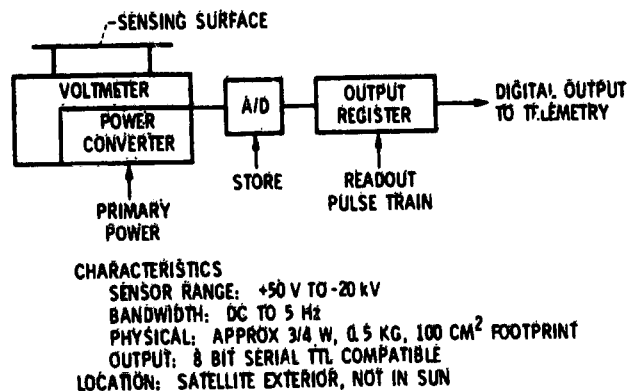


Figure 2. Summary Description of the Characteristic Energy Sensor

### 2.4 Current Density Sensor

The current density sensor is described in Figure 3. It consists of a plain metal current collecting plate and current measurement circuitry. Current measurement is by means of an electrometer. The sensor range, 0.01 to 5 nA/cm<sup>2</sup>, is based on present knowledge of the environment.<sup>9</sup> The frequency response bandwidth is dc to 1 Hz. The physical characteristics given in Figure 3 are a combination of goals and what has been achieved to date. The output is analog; conversion to digital output can be performed, with the attendant weight and power increases.

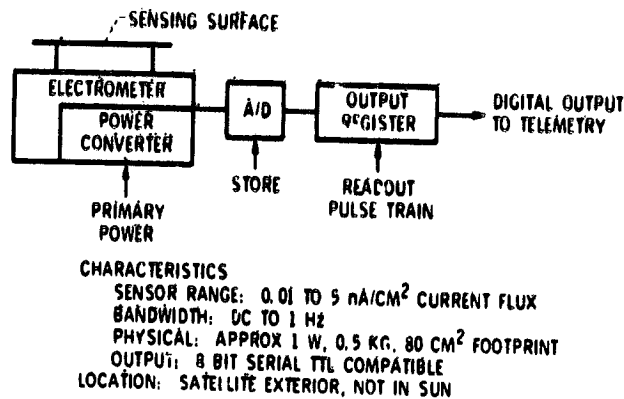


Figure 3. Summary Description of the Current Density Sensor

Sensor location is required to be on the spacecraft exterior, preferably not in the sun.

### 3. DISCUSSION

Utilization of the spacecraft charging monitors, briefly described herein, on the greatest possible number of operational spacecraft will serve to broaden the base of engineering data on the spacecraft charging phenomenon. Their use will also enable a heretofore unobtained one-to-one correlation of transient events with environmental activity.

The spacecraft charging monitors can serve as a warning system. The occurrence of a substorm electron injection into the local environment can be sensed within some fraction of a minute. The response of the dielectric surfaces of a spacecraft to the charging environment would be on the order of minutes.<sup>10</sup> Thus, the differential charging that can lead to breakdown could be dealt with by means of some active charge control or action could be taken to put the spacecraft in a fail-safe or standby mode of operation until the danger had passed.

The spacecraft charging monitors can serve as a diagnostic tool. Any anomalous behavior can be isolated as charging-induced or the result of other causes. The real-time capabilities the monitors can provide in this regard should be particularly beneficial to operational spacecraft.

#### 4. CONCLUDING REMARKS

The Lewis Research Center is developing a package of engineering instruments to serve as spacecraft charging monitors. They sense the local spacecraft environment (the characteristic energy and flux of charged particles) and transients induced into spacecraft harnessing (as a result of breakdowns resulting from differential charging). The monitors are simple and conservatively designed. Their use can serve to warn of adverse changes in the local spacecraft environment. The data they can return will broaden the data base upon which spacecraft system design and test criteria specifications rest.

It is in the interest of all those involved in the use of operational spacecraft to integrate spacecraft charging monitors into their spacecraft systems. The state of knowledge of the spacecraft charging phenomenon is such that the warning and diagnostic functions that they would perform would serve to insure a successful mission.

#### References

1. DeForest, S. E. (1972) Spacecraft charging at synchronous orbit, J. Geophys. Res. 77:651-659.
2. Bartlett, R. O., DeForest, S. E., and Goldstein, R. (1975) Spacecraft Charging Control Demonstration at Geosynchronous Altitude, AIAA Paper 75-359.
3. DeForest, S. E. (1973) Electrostatic Potentials Developed by ATS-5, Photon and Particle Interactions with Surfaces in Space, R. J. L. Garad, Editor, D. Reidel Publ. Co., Boston, pp. 263-276.
4. Fredricks, R. W., and Scarf, F. L. (1973) Observations of Spacecraft Charging Effects in Energetic Plasma Regions, in Photon and Particle Interactions with Surfaces in Space, R. J. L. Garad, Editor, D. Reidel Publ. Co., Boston, pp. 277-308.
5. Whipple, E. C., Jr. (1975) Observation of Spacecraft Generated Electrostatic Fields in the Vicinity of the ATS-6 Satellite, AAS Paper 75-220.
6. Cauffman, D. P., and Shaw, R. P. (1975) Transient Currents Generated by Electrical Discharges, in Space Science Instrumentation, D. Reidel Publ. Co., Boston, pp. 125-137.
7. Stevens, N. J., Lovell, R. R., and Klinect, V. W. (1976) Preliminary Report on the CTS Transient Event Counter Performance through the 1976 Spring Eclipse Season, NASA TM X-73487.
8. Nanevicz, J. E. (1976) Transient response measurement on an Air Force satellite system, Paper presented at the USAF/NASA Spacecraft Charging Technology Conference, U. S. Air Force Academy, Colorado.

9. Stevens, N.J., Lovell, R.R., and Purvis, C.K. (1976) Provisional Specification for Satellite Time in a Geomagnetic Substorm Environment, NASA TM X-73446.
10. Stevens, N. John et al (1976) Testing of typical spacecraft materials in a simulated substorm environment, Paper presented at the USAF/NASA Spacecraft Charging Technology Conference, U. S. Air Force Academy, Colorado.

**Contents**

1. Electrostatic Charging Designs	753
2. Design Evaluation	755
3. Space Vehicle Verification Testing	761
Appendix A	763
Appendix B	765

**5. Viking and STP P78-2 Electrostatic Charging Designs and Testing**

R. O. Lewis, Jr.  
Lakewood, Colo.

**Abstract**

Both the Viking and the P78-2 (SCATHA) vehicles must withstand arcing. This paper presents the design provisions of both vehicles and a mathematical analysis of the effect of arcing on typical interface circuits. Results of verification testing of the analysis are presented as well as vehicle testing for tolerance to arcing.

**1. ELECTROSTATIC CHARGING DESIGNS**

**1.1 Viking Electrostatic Charging Design**

The Viking lander was designed to survive entry into the Martian atmosphere and landing on Martian soil. Entry deceleration was controlled by aeroshell ablation, followed by parachute deployment and controlled engine flight to the surface. During entry there was a possibility of flight through carbon dioxide clouds, dust devils, and encounter with unknown particles. All of these, as well as engine and parachute charging, could cause arcing on the external surfaces of the vehicle.

**NEW INFORMATION**

Viking was designed to operate with corona and survive any arcing that might occur. Prevention of corona and arcing was not considered practical. The design included the following provisions:

- (1) The vehicle body was an rf enclosure bonded together by joints having a resistance of less than 10 m $\Omega$ .
- (2) All external conductive pieces were bonded to the vehicle structure.
- (3) All wiring external to the vehicle body was shielded with the shield grounded at both ends.
- (4) The bioshield had a 4-in. grid of conductive paint to minimize charge buildup.
- (5) The bioshield cap was supported so that the material could not drape down onto vehicle components.
- (6) The antennas were of a dc short design (exposed metal on the antennas and feeds had a direct dc path to ground).
- (7) Antennas were designed to operate without corona at critical pressure, with twice the expected rf power. Foaming and/or configuration of the ends of the elements provided acceptable designs.
- (8) Separation connectors had deeply recessed female contacts that remained with the lander. These connectors could operate in a hot plasma without arcing.
- (9) Command and control interfaces were 50 ohm differential circuits (Harris) driven from a current source (high impedance).
- (10) Interfaces with components having voltages over 300 V were provided with corona protection circuitry, where a failure could allow high voltage leakage or corona through the wiring to other components. Fail-short zener diodes provided the protection.
- (11) Potting, pressurization, foaming, and vacuum deposited covering of circuit boards were used to allow all landed components to operate at critical pressure.
- (12) Communication and radar receiver frequencies, bandwidths, and lock circuits were designed to tolerate signal inputs from corona.

One of the design features that increased the probability of corona and arcing was that the external surface of the lander had to be covered with a rubbery non-conductive substance to protect the vehicle from windblown dust. A tape of the rubbery material was wrapped over all external cable bundles and other parts were painted with the rubbery coating. The coatings were good insulators and would certainly produce corona when exposed to 200 mph wind-blown dust at 5 torr pressure as well as the entry environment.

## 1.2 STP P78-2 Electrostatic Charging Design

The P78-2 vehicle is being designed to measure plasma parameters at and near synchronous earth orbits. It will be subject to energetic particle charging and subsequent arcing. The design approach is to shield all wiring internal to the lower half of the vehicle (which is to be an rf shielded region) and to double shield all wire external to the shielded region. The single shielding is done by using a braided shielded and jacketed wire. The wire will be the same type used on Viking, which is insulated with 3 mils of Kapton. The second shield will be a bundle shield, achieved by wrapping the bundle with aluminum foil tape that has a conductive adhesive. The outside of the foil will not be insulated or coated in any way, and will be grounded at each cable clamp. Braided shielding will be substituted for the foil wrap where flexibility is important.

The power subsystem is being designed to accept high voltage transients from the solar array without transferring them to the power bus.

The shielding and power subsystem transient suppression are the only design features of P78-2 for protection from arcing. The question, then, is whether these designs represent adequate protection to pass the required testing necessary to verify an interference margin.

## 2. DESIGN EVALUATION

The design evaluation depends on how large a signal can be coupled into a circuit from an arc discharge. This evaluation will treat only the circuit types and configurations used for Viking and P78-2. Other circuits and configurations will necessarily provide different answers. The method shown here is a general solution, but care must be taken in applying the results. The solution should be exercised completely before a final answer is obtained. That is, the effect of each assumption should be evaluated by varying the value of the assumed parameter over its maximum possible range and observing the variation in the answer. After a few times through the solution in this manner, one feels the effect of variations and begins to understand the relationships between the physical parameters and what is happening in the coupling process.

### 2.1 Defining the Source

First, consider the source characteristics. The arc voltage has been estimated to be between 10 and 25 kV and the arc current to be between 10 and 1000 A. This would then suggest that the source could be characterized as a 10- to 25-kV voltage source with a source impedance of 2.5 to 1000 ohms. This source must

be simulated during electromagnetic compatibility (EMC) testing to determine the susceptibility of the vehicle and external components. MIL-STD-1541 has an electrostatic sensitivity test that consists of a 10-kV arc containing 2.5 nJ. Laboratory tests with a 3.5-mJ, 10-kV source in air at Denver altitude has shown the source impedance to be approximately 370 ohms and the pulse to have a rise time of 3 nsec and an average duration of 7 nsec. The arc was formed by gradually increasing the voltage of the source until arcing occurred at a 60 Hz repetition rate.

With a test arc established that is fairly representative of a space arc, let us analyze its effect upon a circuit. Assume that there is an arc to the center of a 5-ft shielded circuit. Since the rise time of the arc is less than the transmission time down the shield and back, the shield acts like a long transmission line with  $Z_0$  impedance. The voltage on the shield is then a strong function of the shield configuration with respect to the ground plane.  $Z_0$  can vary from approximately 11 to 181 ohms, this being one half of the characteristic impedance of the transmission line (because there are effectively two in parallel at the point of the arc discharge, see Appendix A). Eleven ohms represents a kapton-covered shield adjacent to the ground plane or adjacent to other shields in a bundle, and 181 ohms represents a shield 10 in. above the ground plane. The above values are based upon a twisted shielded pair wire insulated with 3 mils of kapton. If the design restricts single shields to being next to structure, then the calculated voltage on the shield, due to a 10 kV arc would be 289 volts. The calculations are shown in Appendix A. The measured voltage on the shield was 256 volts. This represents approximately half the error of the measuring system (2 dB).

## 2.2 Electric Field Coupling

The task of determining how much of the voltage on the exterior surface of the shield is coupled to the internal circuit wires requires the circuit model shown in Figure 1 and its transient solution.

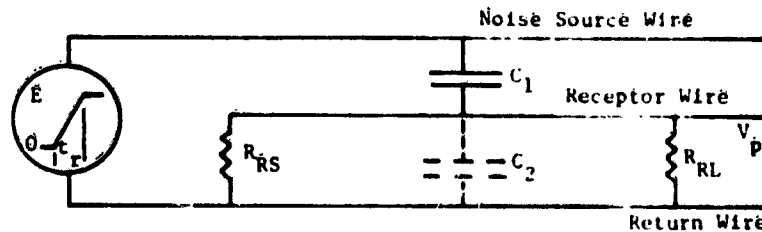


Figure 1. Electric Coupling Model

$C_1$  then represents the capacity between the outside of the shield and the internal circuit wire, and  $C_2$  represents the capacity between the internal circuit wire and the internal return wire. The transient solution to this circuit is

$$V_p = \frac{E}{t_r} R_T C_1 \left[ 1 - \exp \left( - \frac{t}{R_T(C_1 + C_2)} \right) \right] \quad (1)$$

and

$$V_{pmax} = \frac{E C_1}{C_1 + C_2} \quad (2)$$

where  $R_T =$  parallel resistance of  $R_{RS}$  and  $R_{RL}$ . The maximum value of  $V_p$  occurs when  $t = t_r$ . The complete definition of parameters appears in Appendix B.

Applying the solution to the circuits of Figures 2 and 3, yields the following results for Tables 1 and 2:

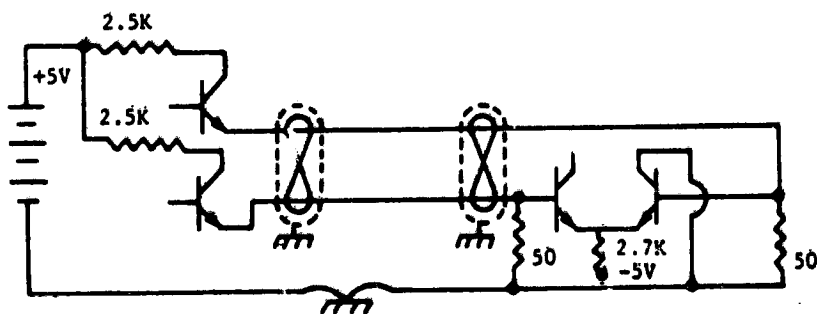


Figure 2. Viking Interface Circuit

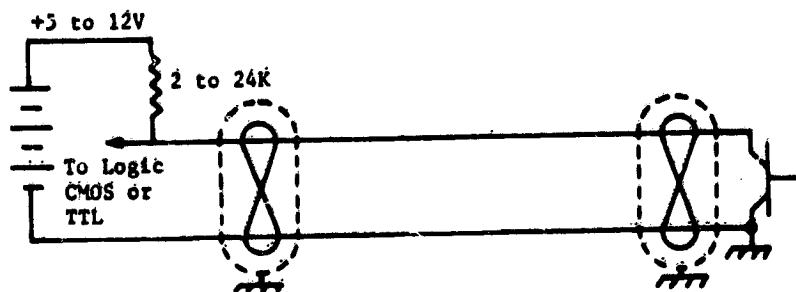


Figure 3. P78-2 Interface Circuit

Table 1. Viking Design

$t_r$	(e factor)	$V_p$
$1 \times 10^{-9}$	$4.5 \times 10^{-2}$	13.49
$3 \times 10^{-9}$	$1.3 \times 10^{-1}$	12.89
$10 \times 10^{-9}$	0.368	11.07
$100 \times 10^{-9}$	0.99	2.98
$1 \times 10^{-6}$	1.0	0.301
$10 \times 10^{-6}$	1.0	0.03

$C_1 = 20.8 \times 10^{-12} \text{ F}$   
 $C_2 = 415 \times 10^{-12} \text{ F}$   
 $R_T = 50 \text{ ohms}$

Table 2. P78-2 Design (Preliminary)

$t_r$	(e factor)	$V_p$
$1 \times 10^{-9}$	$1.1 \times 10^{-4}$	13.79
$3 \times 10^{-9}$	$3.4 \times 10^{-3}$	13.79
$10 \times 10^{-9}$	$1.1 \times 10^{-3}$	13.79
$100 \times 10^{-9}$	$1.1 \times 10^{-2}$	13.72
$1 \times 10^{-6}$	$1.1 \times 10^{-1}$	13.04
$10 \times 10^{-6}$	0.6801	8.23

$C_1 = 20.8 \times 10^{-12} \text{ F}$   
 $C_2 = 415 \times 10^{-12} \text{ F}$   
 $R_T = 20,134 \text{ ohms}$

These data show that the electric field coupling differs only as to rise time of the interference pulse. The P78-2 design is susceptible to longer rise time pulses than the Viking design. Since the arc rise time is very short, the response to the arc is quite similar. The measured coupling to the Viking circuit was 12.4 volts and to the P78-2 circuit was 12.0 volts.

The value of  $C_1$  is obtained by multiplying the capacity between the wire and the internal surface of the shield (415 pF) by the lack of coverage of the shield (95 percent coverage and therefore 0.05 lack of coverage) or by actual measurement. The measured value was 18 pF while the calculated value was 20.8 pF.

### 2.3 Inductive Coupling

The previous analysis has defined the capacitive coupling to the circuits. The inductive coupling must also be determined. This task required the following circuit (Figure 4) model and its transient solution:

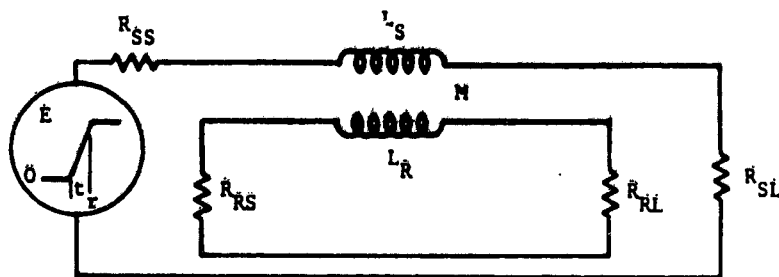


Figure 4. Inductive Coupling

$L_S$  is the inductance in the source circuit,  $L_R$  is the inductance in the receptor circuit, and  $M$  is the mutual inductance between circuits. A more complete definition of parameters and the complete transient solution appear in Appendix B.

The simplified transient solution to this circuit is as follows:

$$V_p = \frac{E M R_{RL}}{t_r R_S R_R} \left[ 1 - \exp \left( - \frac{t R_S R_R}{L_S (R_S + R_R)} \right) \right] \quad (3)$$

and

$$V_{pmax} = \frac{E M R_{RL}}{L_S (R_S + R_R)} \quad (4)$$

where  $R_S = R_{SS} + R_{SL}$  and  $R_R = R_{RS} + R_{RL}$ . Applying the solutions to the interface circuits of Figures 2 and 3, yields the following results for Tables 3 and 4:

Table 3. Viking Design

$t_r$	(e factor)	$V_p$
$1 \times 10^{-9}$	$4.7 \times 10^{-2}$	0.28
$3 \times 10^{-9}$	$1.3 \times 10^{-1}$	0.26
$10 \times 10^{-9}$	$3.8 \times 10^{-1}$	0.22
$100 \times 10^{-9}$	0.99	0.06
$1 \times 10^{-6}$	1.0	0.006
$10 \times 10^{-6}$	1.0	0.0006

$M = 1.2 \times 10^{-8} \text{ H}$      $L_S = 0.23 \times 10^{-6} \text{ H}$   
 $R_{RL} = 50\Omega$      $R_R = 2550\Omega$      $R_S = 11\Omega$

Table 4. P78-2 Design (Preliminary)

$t_r$	(e factor)	$V_p$
$1 \times 10^{-9}$	$4.7 \times 10^{-2}$	13.9
$3 \times 10^{-9}$	$1.3 \times 10^{-1}$	13.3
$10 \times 10^{-9}$	$3.8 \times 10^{-1}$	11.3
$100 \times 10^{-9}$	0.99	3.0
$1 \times 10^{-6}$	1.0	0.3
$10 \times 10^{-6}$	1.0	0.03
$100 \times 10^{-6}$	1.0	0.003

$M = 1.2 \times 10^{-8} \text{ H}$      $L_S = 0.23 \times 10^{-9} \text{ H}$   
 $R_{RL} = 4,700\Omega$      $R_R = 4,750\Omega$      $R_S = 11\Omega$

These data show that the inductive coupling in the Viking design is unimportant. This is because the loop resistance in the receptor circuit (2550 ohms) is 51 times the resistance across the digital receiving circuit (50 ohms). Conversely, the P78-2 design has practically all the resistance (24,000 ohms) across the digital input, when the transistor is conducting.

#### 2.1 P78-2 Design Modification

The P78-2 preliminary design shows that voltages greater than the noise rejection capability of normal digital circuitry (1 volt) can occur when there is an arc discharge to the circuit shield. The design must, therefore, be modified to reduce the voltage to below 1 volt, which is the digital noise rejection capability. Adding a second braided shield was considered, but since it would only reduce the coupled voltage slightly, it was rejected. The reduction is only slight, since the shield voltage increases from 256 V to a measured 730 V, because of the increase of  $Z_0$  between the two configurations and the second shield only provides a shielding increase of 20 dB. The configuration included having the overshield 0.37-in. above the ground plane.

A solid overshield will reduce the coupled voltage better than a braided shield and, therefore, will be used in the final space vehicle design. The aluminum foil overwrap was tested on the typical circuits with the following results as shown in Table 5.

Table 5. Viking and P78-2 Design

<u>Viking Design</u>	
Electric coupling	0.45 V peak
Total coupling	0.35 V peak
<u>P78-2 Final Design</u>	
Electric coupling	3.5 V peak
Total coupling	4.0 V peak

### 3. SPACE VEHICLE VERIFICATION TESTING

#### 3.1 Viking Testing

The Viking Lander was tested in an environment which simulated corona interference. The vehicle operated properly without degradation during this test. A capacitor discharge test was performed to simulate arcing that could occur during parachute deployment by charging a 0.05  $\mu$ F capacitor to 2000 V and discharging it

through the vehicle structure to the parachute attach point and the foot pads, respectively. This test at first caused the ground equipment to malfunction. After the ground equipment was reconfigured to be less susceptible, the vehicle passed the test.

### 3.2 P78-2 Planned Testing

The P78-2 vehicle will be tested by arcing directly to the vehicle at several selected points where arcing can possibly be expected. The arc source will be a 10 kV, 2.5-mJ source and the vehicle must operate without degradation of performance.

## Appendix A

### Calculation of the Voltage on a Shield Due to an Arc Discharge to the Shield

Consider the following configuration, Figure A1:

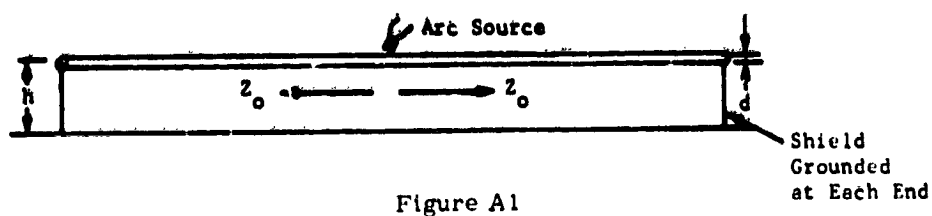


Figure A1

$$Z_0 = 138 \log_{10} \frac{4h}{d} = 138 \log_{10} 4 \frac{10 \text{ in.}}{0.096 \text{ in.}} = 361.53 \text{ ohms} \quad (A1)$$

Impedance at arc point is then

$$\frac{361.53}{2} = 180.77 \text{ ohms} \quad (A2)$$

Voltage on shield = arc current  $\times$  180.77. If shield wire is in a bundle of shielded wires (see Figure A2 and equations A3-A4)

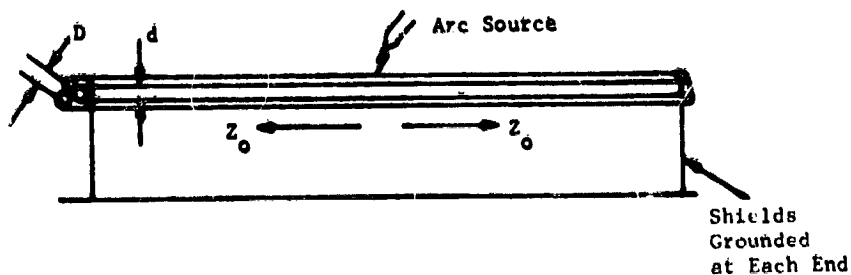


Figure A2

then

$$Z_o = \frac{120}{2\sqrt{\epsilon_r}} \cosh^{-1} \frac{D}{d} = \frac{120}{2\sqrt{3.5}} \cosh^{-1} \frac{0.10}{0.094} \quad (A3)$$

$$Z_o = 32.07 \times 0.345 = 11.06 \text{ ohms} \quad (A4)$$

6-9

## Appendix B

### Method for Calculating Electromagnetic Interference Coupled into a Circuit From an Adjacent Circuit (Time Domain Method)

#### 1. ELECTRIC FIELD COUPLING

The electric field interference is capacitively coupled from an interference source wire into the receptor circuit. The model circuit (see Figure B1) to be used for this coupling is as follows:

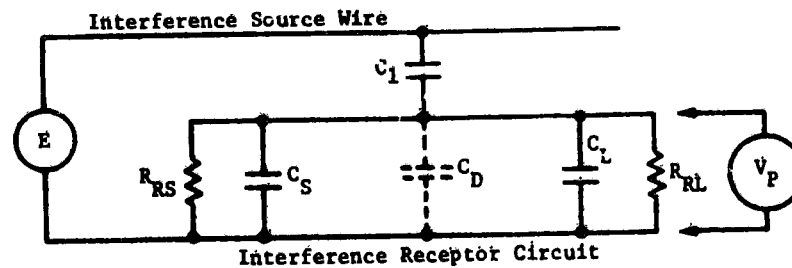


Figure B1

where:

- $E$  = interference source voltage, in volts.
- $C_1$  = maximum coupling capacity between source and receptor circuit, in farads.
- $R_{RS}$  = maximum source resistance of signal in receptor circuit, in ohms.
- $C_S$  = maximum capacity of signal source circuit in the receptor circuit, in farads.
- $C_D$  = maximum distributed capacity in the receptor circuit, in farads.
- $C_L$  = maximum capacity of load circuit in receptor circuit, in farads.
- $R_{RL}$  = maximum load resistance in receptor circuit, in ohms.
- $V_P$  = peak noise voltage induced in the receptor circuit, in volts.

$$R_T = \frac{R_{RS} \times R_{RL}}{R_{RS} + R_{RL}} \quad (B1)$$

$$C_2 = C_s + C_D + C_L \quad (B2)$$

Assuming that  $t_r$  is the minimum rise time or fall time of the interference source voltage  $E$ , in seconds, the solution to the model circuit equations is as follows (see Equation B2):

$$V_P = \frac{E}{t_r} R_T C_1 \left[ 1 - \exp \left( -\frac{t_r}{R_T(C_1 + C_2)} \right) \right] \quad (B3)$$

$$V_{P\text{MAX}} = E \frac{C_1}{C_1 + C_2} \quad (B4)$$

where rise-time of  $E$  is very short.

The area of the interference pulse in the receptor circuit is  $ER_T C_1$ :

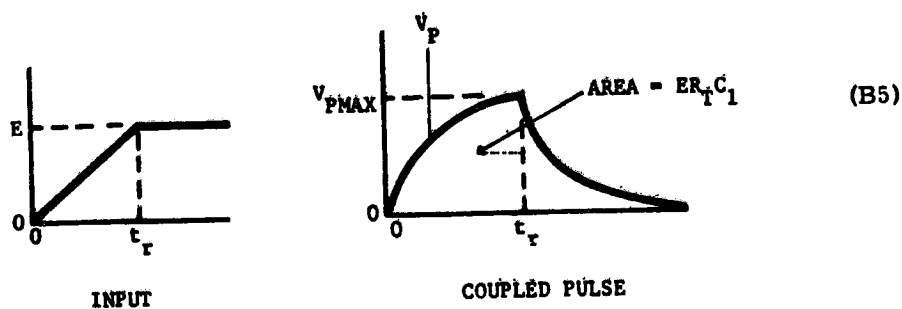


Figure B2

The coupling capacity and the distributed capacity for unshielded wires can be calculated with the following formulas (see Figure B3):

$$C = \frac{12.051 \times 10^{-12}}{\log_{10} \left[ \frac{2S}{d} \cdot \frac{1}{\sqrt{1 + \left(\frac{S}{2h}\right)^2}} \right]} \text{ farads} \quad (B6)$$

where:

- C = capacity between wires of a "go and return" circuit, in farads.
- l = maximum length of wire, in meters.
- S = separation between wires (in same units as d and h).
- d<sub>1</sub> = minimum diameter of the wire including insulation (in same units as S, d, and h). If unshielded wires are in the same bundle, then S = d<sub>1</sub>.
- d = maximum diameter of the wire conductor (in the same units as S and h).
- h = minimum average height above the ground plane (in the same units as d, and S).

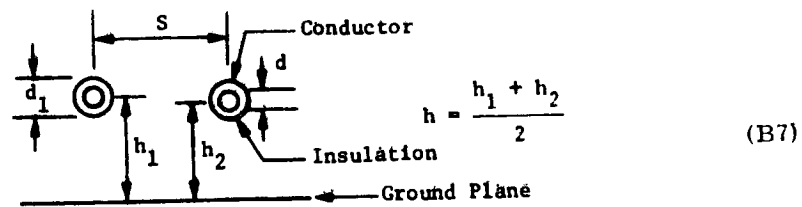


Figure B3

The capacity from a wire to the ground plane is as follows (see Figure B4):

$$C = \frac{24.12 l \times 10^{-12}}{\log_{10} \left( \frac{4h}{d} \right)} \text{ farads} \quad (B8)$$

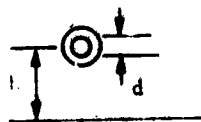


Figure B4

Capacities for shielded wires can be calculated as follows:

$$C = \frac{24.1 \epsilon_r l}{\log_{10} \frac{D}{d}} \text{ picofarads} \quad (B9)$$

where:

$C$  = capacity between inner conductor and inside of shield, in picofarads.

$\epsilon_r$  = relative dielectric constant of the inner wire jacket (relative to air = 1.0).

$l$  = length of the coax, in meters.

$D$  = maximum inside diameter of the shield (in the same units as  $d$ ).

$d$  = minimum outside diameter of the inner conductor (in the same units as  $D$ ).

Capacity between the inner conductor and the outside of the shield is the capacity calculated above times the lack of shielding coverage (that is,  $C \times 0.05$  for a shield coverage of 95 percent).

The capacity between two wires, with a shield between the wires, is the capacity between the wires without the shield times the lack of shielding coverage for the shield. If there are two shields between the wires, the capacity is reduced by the product of the lack of shield coverage (that is,  $0.05 \times 0.05 \times C$ ).

Note that twisted shielded pair wire should be measured. The formulas do not provide accurate answers where insulation is very thin. Viking wire measured 415 pF for 5 ft (capacity between one wire and the shield with other wire terminated in 5k ohm to ground).

## 2. MAGNETIC FIELD COUPLING

The magnetic field interference is magnetically coupled from an interference source circuit into a receptor circuit. The model to be used for this coupling is as follows (see Figure B5):

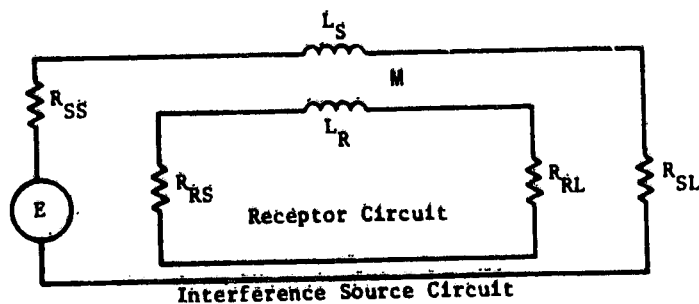


Figure B5

where:

E voltage versus time is as follows (see Figure B6):

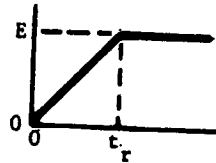
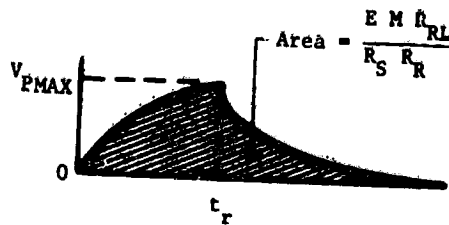


Figure B6

and  $V_p$  is as follows (see Figure B7):



(B10)

Figure B7

Assuming that  $t_r$  is the minimum rise-time or falltime of the interference source voltage E, in seconds, the solution to the model circuit (see Figure B8) is shown in Eqs. (B12)-(B17), and with simplification is as follows:

$$V_P = \frac{E M R_{RL}}{t_r R_S R_R} \left[ 1 - \exp \left( - \frac{t_r R_R R_S}{L_S (R_R + R_S)} \right) \right] \quad (B11)$$

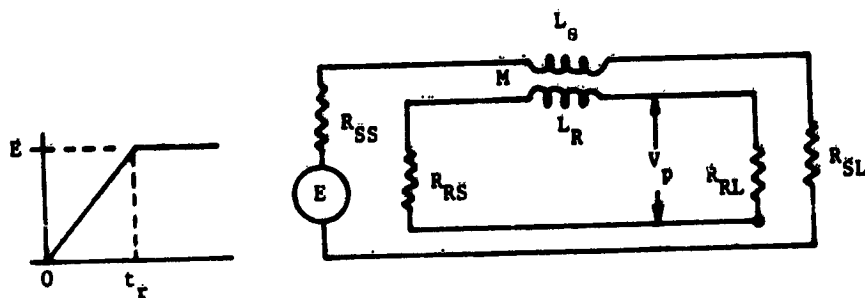


Figure B8. Magnetic Field Coupling Circuit

$$V_P = \frac{E M R_{RL}}{t_r R_S R_R} \left[ 1 + \frac{e^{-\frac{2 R_S R_R t}{Q}}}{\frac{4 R_S R_R (L_S^2 - M^2)}{Q^2} - 1} + \frac{e^{-\frac{Q t}{-2(L_S^2 - M^2)}}}{\frac{Q^2}{4 R_S R_R (L_S^2 - M^2)} - 1} \right] \quad (B12)$$

where

$$Q = L_S(R_S + R_R) \pm \sqrt{L_S^2(R_S + R_R)^2 - 4(L_S^2 - M^2) R_S R_R} \quad (B13)$$

$$R_{SS} + R_{SL} = R_S \quad (B14)$$

$$R_{RS} + R_{RL} = R_R \quad (B15)$$

$$V_P = V_{MAX} \text{ when } t = t_r \quad (B16)$$

$$V_{P_{MAX}} = \frac{E M R_{RL}}{L_S(R_R + R_S)} \text{ if rise-time of } E \text{ is very short.} \quad (B17)$$

Retardation is not considered.

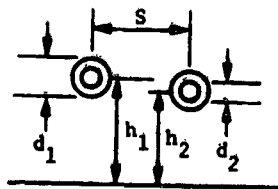
where:

- E = interference source voltage, in volts.
- R<sub>SS</sub> = minimum interference source circuit resistance, in ohms.
- R<sub>SL</sub> = minimum interference source circuit load resistance, in ohms.

- $R_S = R_{SS} + R_{SL}$   
 $R_{RS}$  = maximum source resistance of signal in receptor circuit, in ohms.  
 $R_{RL}$  = maximum load resistance in receptor circuit, in ohms.  
 $R_R = R_{RS} + R_{RL}$   
 $L_S$  = maximum inductance of the interference source circuit, in henries.  
 $L_R$  = maximum inductance of the interference receptor circuit, in henries.  
 $M$  = maximum possible mutual inductance between the interference source circuit, in henries.  
 $V_{P_{MAX}}$  = maximum peak noise voltage induced in the receptor circuit load due to E, volts, with a very rapid rise in E.

L in a go and return circuit (see Figure B9) can be computed as follows:

$$L = 0.921 \times 10^{-6} \times l \times \log_{10} \left[ \frac{2S}{d_2} \frac{1}{\sqrt{1 + \left(\frac{S}{2h}\right)^2}} \right] \text{ henries} \quad (\text{B18})$$



$$h = \frac{h_1 + h_2}{2} \quad (\text{B19})$$

Figure B9

where:

- $L$  = inductance of a go and return circuit above a ground plane, in henries.  
 $l$  = maximum length of cable, in meters.  
 $S$  = maximum average separation between wire centers in the cable bundle (in the same units as  $d_2$  and  $h$ ).  $s = d_1$  if twisted.  
 $d_2$  = minimum diameter of the wire conductor (in the same units as  $S$  and  $h$ ).  
 $h$  = minimum average height above the ground plane (in the same units as  $S$  and  $d_2$ ).

The inductance of a single ended circuit (see Figure B10) (ground plane return) is as follows:

$$L = 0.460 \times 1 \times 10^{-6} \times \log_{10} \frac{4h}{d_2} \text{ henries} \quad (\text{B20})$$

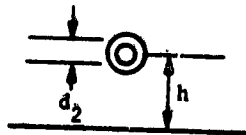


Figure B10.

M in a normal digital cable bundle, where all circuits use a common return wire, is as follows:

$$M = L_S - L_L \quad (\text{B21})$$

where  $L_L$  = leakage inductance between the source circuit and the receptor circuit.  
Then:

$$M = L_S - \frac{1 \times 10^{-6}}{2} \ln \frac{2d_1}{d_2} \quad (\text{B22})$$

where  $d_1$  = minimum diameter of the wire including insulation (in the same units as  $d_2$ ) and  $d_2$  = minimum diameter of wire conductor (in same units as  $d_1$ ).

$$\ln = \log_e \quad (\text{B23})$$

**Contents**

1. Introduction	774
2. Spacecraft Wiring and Grounding	776
3. Electrical Protection Against EMI Generated by Discharge	779
4. The Deployable Solar Arrays	781
5. Spacecraft Level EMI Testing With a Spark Source	783
6. Anomalies	784
7. Conclusions and Recommendations	786
Acknowledgments	787
References	787

**6. Design, Construction and Testing of the  
Communications Technology Satellite  
Protection Against Spacecraft Charging**

**J. Victor Gore**  
**Communications Research Centre**  
**Department of Communications**  
**Shirley Bay, Station H**  
**Ottawa, Ontario**

**Abstract**

This paper discusses in detail the measures taken on the Communications Technology Satellite (CTS or Hermès) which provide protection against the effects of spacecraft charging. These measures include: a comprehensive grounding philosophy and implementation; provision of command and data line transmitters and receivers for transient noise immunity; and a fairly restrictive EMI specification.

Ground tests were made on materials at the Lewis Research Center (LeRC). The impact of these tests on the CTS spacecraft is described.

Hermès, launched on 17 January 1976 on a 2914 Delta vehicle, has successfully completed 10 months of operations. Anomalies observed are being assessed in relation to spacecraft charging, but no definite correlations have yet been established.

The paper ends with a list of conclusions with regard to the CTS experience and list of recommendations for future spacecraft.

## 1. INTRODUCTION

The Communications Technology Satellite is an experimental communications satellite, operating in geosynchronous orbit. CTS was a joint project of the Communications Research Centre, Ottawa, Canada and NASA Lewis Research Center, Cleveland, Ohio. Major components were provided by the European Space Agency.

The purpose of CTS was to demonstrate the technological and social possibilities of a high power (230 W) SHF transponder on the spacecraft used in conjunction with small low cost earth terminals. The high power demanded a three-axis stabilized configuration, large deployable sun tracking solar arrays, and thermal requirements wherein almost the entire external surface of the spacecraft was dielectric. CTS probably had more static charge accumulating area than any previous spacecraft in synchronous orbit. Figure 1 is a photograph of the flight model with the deployable arrays extended. Each deployable array blanket is 21.4 ft by 4.2 ft. The substrate is a Kapton-fiberglass laminate. The solar cells are covered by nonconducting coverglasses. On the body of the spacecraft, the dielectric areas are:

- (1) Solar cell coverglasses and fiberglass substrates cover the east and west panels.
- (2) Thermal blankets cover almost the entire forward and aft panels.
- (3) Kapton shields, not installed in this photograph, provide thermal protection for the SHF antennas.
- (4) Second surface mirrors, thermal blankets, and paints cover the north and south panels.
- (5) A thermal radiator fin extending forward from the south panel is part of a variable conductance heat pipe system that provides cooling for the SHF Transmitter Experiment Package (TEP). Both sides of the fin are covered with silvered Teflon.

The largest conducting external surfaces are the separation ring, the apogee motor nozzle, and the Bistern boom behind the deployable arrays.

For thermal and EMI reasons there are very few holes into the interior volumes. Venting was provided by a few screened apertures, loose flaps on thermal blankets that closed after ascent stage, and a thin annulus around the TEP collector. Electron penetration into the interior was thereby minimized.

The CTS project was started in 1970, and by 1974, when we fully recognized the danger presented by spacecraft charging, the engineering model tests were in progress and the flight model spacecraft and subsystems were being built. Major changes to hardware would have had an enormous impact on the project. Also,

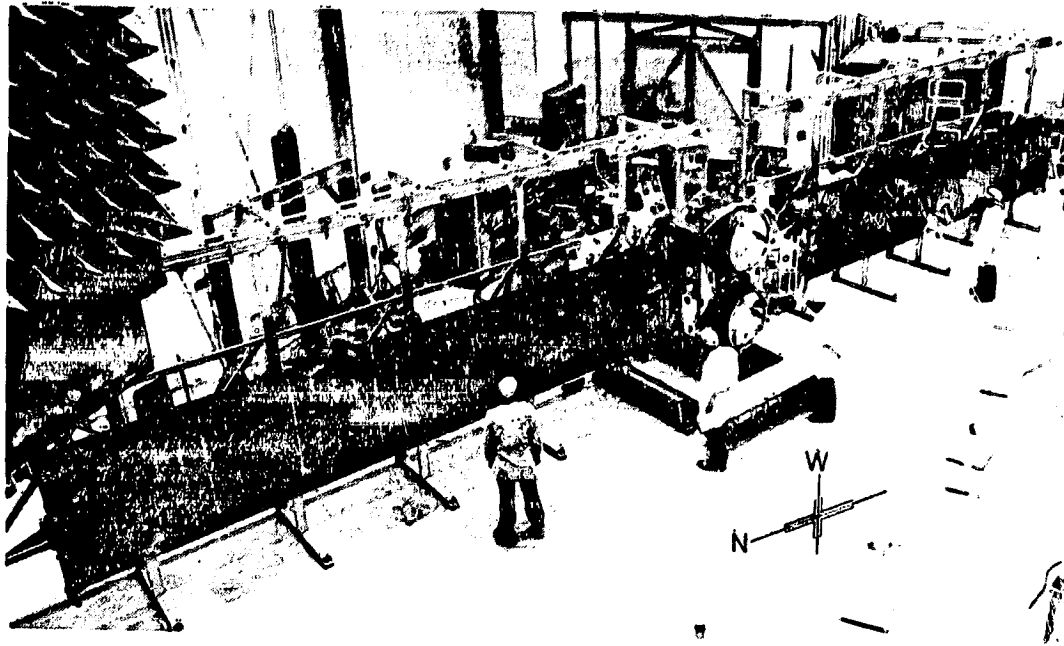


Figure 1. The Communications Technology Satellite (CTS) in the Integration Area. The deployable solar arrays extend from the north and south panels

the weight requirements were very tight. Therefore, changes were considered only if they were relatively minor and if the consequences of not making them would present a significant threat to the mission. Fortunately, during the initial design phase certain precautionary measures had been enforced that minimized the modifications necessary to provide protection against spacecraft charging effects. These measures included: stringent grounding to meet the Launch Safety Requirements as detailed in range safety manual AFETRM 127-1; stringent electrical interface design standards to ensure electrical compatibility and noise immunity; and design and test EMI requirements based on MIL-STD-461.

In late 1974, an investigation was started in Lewis Research Center, with the cooperation of CRC, to perform quickly the following tasks:

- (1) Evaluate the magnitude of the danger.
- (2) Obtain the electrical signature of discharges that would occur on external surfaces.
- (3) Prepare a test specification for spacecraft level EMI testing using a spark source. This source was to have an electrical signature consistent with the results of the second task.

John Stevens set up an electron swarm chamber<sup>1</sup> and ran a very rapid and prolific test program.

Primarily as a result of this work:

- (1) The grounding of thermal blankets was improved.
- (2) Teflon second surface mirrors were removed and reinstalled using conductive adhesive.
- (3) A review was made to ensure electrical connections were made between all metallic parts and surfaces to the greatest possible extent. Some improvements were made.
- (4) The EMI specification and interface protection circuits were reviewed.
- (5) A cautious EMI test using a spark source was done on the flight spacecraft.

(6) A Transient Event Counter (TEC)<sup>2</sup> was included on the spacecraft to detect high speed noise bursts on three cable harness bundles. No changes were made to subsystem components to provide extra EMI protection nor was any extra shielding added to the wiring harness.

Up to 10 months after launch we have had two major faults that could have been initiated by charge accumulation or a discharge as described in Section 6. Also, there have been several trips in a Traveling Wave Tube Assembly (TWTA) that are probably caused by noise bursts on an internal command line. No spurious commands have been experienced and the telemetry has proven to be effectively free of noise.

The remainder of this paper describes in more detail the grounding methods and the EMI protection that were used. Two special tests, one on the command belt antenna and receiver, and the second on a sample of solar array, made in the LeRC facility are briefly described. The paper ends with a list of recommendations.

## 2. SPACECRAFT WIRING AND GROUNDING

The CTS spacecraft uses a common electrical plane ground configuration as opposed to a single point ground scheme. For the TEP only, special ground wires are provided. The spacecraft structure primarily the north, south, forward and aft decks provide the ground return paths.

The primary power, secondary power, telemetry and commands were carried on wires grouped into four separate wire harnesses. The only spacecraft wiring that was shielded were 5 volt power lines to logic circuits, data lines between attitude control sensors and the attitude control electronics, and the reaction control system wiring.

The only changes to the flight spacecraft to provide protection against charging were made to improve the reliability of the grounding of thermal blankets and second surface mirrors, and some small metal parts.

## 2.1 Grounding of Individual Mounted Units

For all individually mounted units (IMU), except the TEP, the ground returns for power, telemetry, and commands are through the spacecraft structure. The primary ground connections for the IMUs are through their mounting surfaces. The requirements for IMU grounds were for less than  $2.5 \text{ m}\Omega$  between the IMU and the mounting deck, and for less than  $25 \text{ m}\Omega$  between any two IMUs. Secondary ground returns were provided by wires from connectors to a nearby ground lug on a mounting deck.

For the TEP separate ground wires were run from the TEP unit to the telemetry encoder, command decoder, and to the main power ground on the north deck. This arrangement kept the interface between the TEP and the spacecraft as simple as possible, and it also isolated the large current drawn by the TEP from the ground plane used by the rest of the spacecraft.

For the telemetry channels that required extra noise immunity for higher accuracy, wires were run from the ground on the telemetry encoder to differential circuits in the IMU. These wires are used for voltage reference only and do not carry return currents.

## 2.2 Grounding of Thermal Blankets

All thermal blankets are provided with grounding connections. Blankets with an area of less than one square foot have one ground connection, and blankets of larger area have two or more grounds.

Figure 2 shows three ground configurations, types I, V and IX. With type I and V the metallized layers, without the interlayer scrim cloth, are extended in a tab, a strip of aluminum foil 0.001 in. thick and 0.5 in. wide is woven between the layers, and the tab is then riveted with washers top and bottom. With type I a solder lug is included, and with type V the aluminum foil is extended for attachment to a deck ground. The aluminum foil provides a positive ground connection to each layer and it also provides contact over a reasonably large area. Other types from I to VIII are variations of either I or V. The type IX is a less secure ground. The aluminum foil is wrapped around the outer layers only and contact to inner layers is made by occasional contact to the rivet. No ground of type IX were used on the flight model of CTS.

## 2.3 Grounding of Second Surface Mirrors (SSMs) and Silvered Teflon-Electron Swarm Tests at LeRC

In the LeRC experiments, it was found that quartz SSMs produced relatively few and weak discharges. The quartz mirrors on the north and south panels were bonded with a nonconductive adhesive and were not changed. However, silvered teflon produced very frequent intense discharges and so the teflon SSMs on the

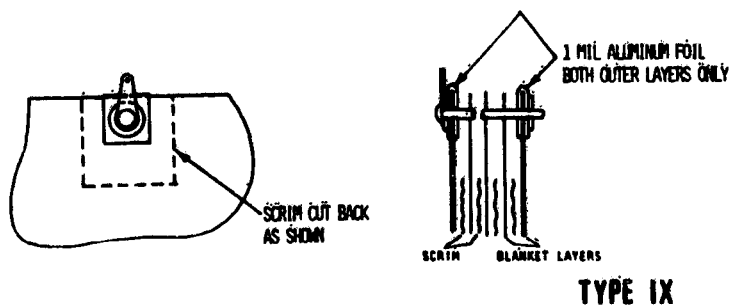
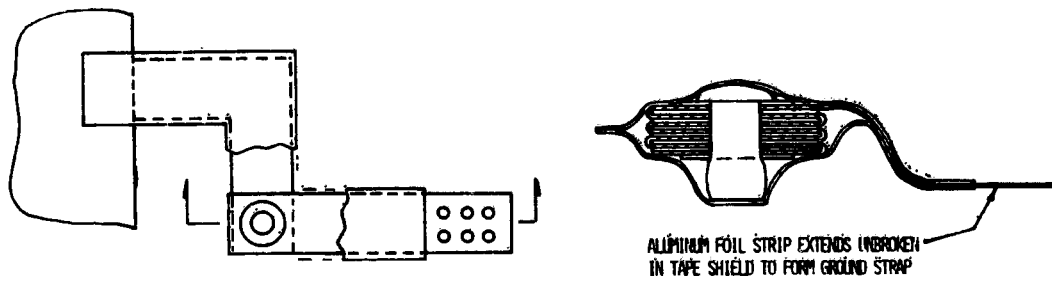
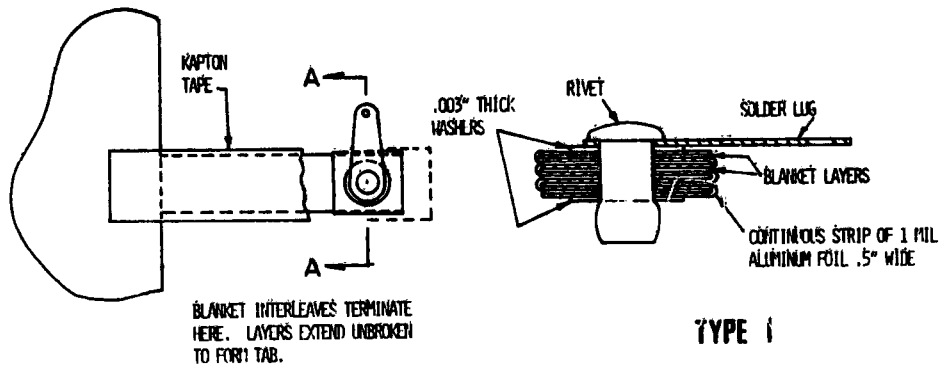


Figure 2. Standard Configurations for Thermal Blanket Grounds

north and south decks were removed and reinstalled using a conductive adhesive. The discharges on silvered teflon bonded with nonconductive adhesive not only produced electrical noise but also a considerable quantity of the silver was eroded. This indicated that during the electron irradiation the silver layer was being charged, by leakage or possibly by micro-discharges from the surface. It also meant that metal to metal arcs were occurring. In a simulated 2 year mission, test on a sample representative of the TEP radiation fin about 12 percent of the silver was eroded. This erosion would have decreased the thermal radiation from the fin by increasing the average absorptivity and by decreasing the heat conducted from the fin substrate into the teflon. The erosion could probably have been tolerated, without increasing TEP component temperatures above acceptable limits. However we felt that the EMI generated by metal to metal arcs was likely to be much greater than the discharges off the surface of the teflon. The teflon was therefore removed from most of the fin area and rebonded with a conductive adhesive.

### 3. ELECTRICAL PROTECTION AGAINST EMI GENERATED BY DISCHARGE

#### 3.1. General EMI Specifications

No special measures were taken to protect units against the EMI that could be generated by discharges. However, the existing specified limits for susceptibility to conducted interference on power lines extended from 30 Hz to 40 MHz. In the range where EMI from discharges is expected, 150 kHz to 400 MHz, the limit was the 1 percent of the supply voltage or 1 volt RMS whichever was greater. Also units had to tolerate on any power rail, without malfunction, a spike of twice the nominal supply voltage or 50 volts whichever was less. The spike rise time was less than one  $\mu$ sec and the duration was 10  $\mu$ sec.

#### 3.2 Command and Data Line Interface Circuits

Command and data line transmitters and receivers were used to provide immunity from noise and fast transients on command and data lines. The characteristics of these interface circuits are listed in Table 1. Figure 3 shows typical applications for these circuits. The interface circuits were purchased to a single set of specifications and furnished to contractors as GFE items. Although not all contractors used the GFE circuits, generally alternate circuits provided similar interface characteristics.

In the spacecraft level testing with the spark source (see Section 5), the typical noise burst generated by the spark was a few volts high and about 200 nsec long. The interface circuits would protect adequately against this.

**Table 1. Characteristics of the Command and Data Line Transmitters and Receivers**

	COMMAND LINE TRANSMITTER	DATA LINE TRANSMITTER	COMMAND LINE TRANSMITTERS IN THE DECODER
"0" LEVEL	.25V @ -20 $\mu$ A	.25V @ -20 $\mu$ A	0 to .1V
"1" LEVEL	3.8V @ 10 mA	3.8V @ 10 mA	3.8V @ 10 mA
FALL TIME	100 $\mu$ S	1 $\mu$ S	50 $\mu$ S
RISE TIME	100 $\mu$ S	1 $\mu$ S	50 $\mu$ S
DELAY TIME "0" TO 3.2V	100 $\mu$ S	("0" TO 2.0V) 50 $\mu$ S	
DELAY TIME "1" TO .75V	100 $\mu$ S	("1" TO .6V) 50 $\mu$ S	
	COMMAND LINE RECEIVERS	DATA LINE RECEIVERS	
"0" LEVEL	.75V @ -3 $\mu$ A	.75V @ -3 $\mu$ A	
"1" LEVEL	3.2V @ 2.5 mA	3.2V @ 2.5 mA	
DELAY TIME "0" TO 2V	100 $\mu$ S	20 $\mu$ S	
DELAY TIME "1" TO .5V	100 $\mu$ S	20 $\mu$ S	
TRANSIENT REJECTION	5 VOLT PULSE 5 $\mu$ S	5 VOLT PULSE 1 $\mu$ S	
NOISE REJECTION	5V RMS @ 10 MHz	5V RMS @ 10 MHz	

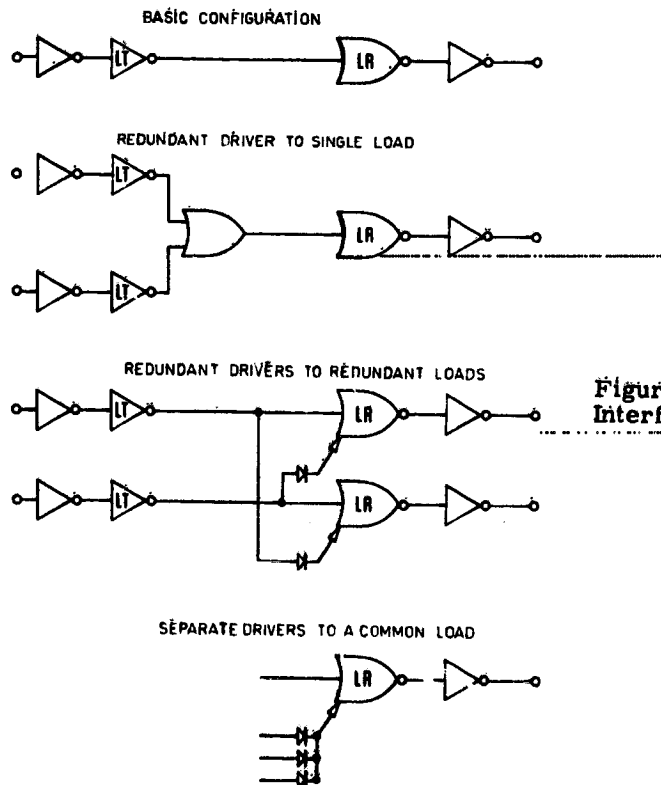


**Figure 3. Typical Applications for Interface Circuits**

### 3.3 Telemetry Interface Requirements

The requirements for analog voltages, flags and digital words that are input to the telemetry encoder are listed in Table 2. The types of input protection in the encoder are also listed. The telemetered data has proven to be effectively free of noise. Generally, analog channels show much less than one bit of noise.

### 3.4 Special Tests on the Command Receiver at NASA Lewis Research Center<sup>3</sup>

The telemetry/command belt antenna is a pattern of metal patches and feed lines on a fiberglass-tylon substrate. The substrate is backed with aluminum sheet. The belt antenna is completely exposed to the external particles and we were concerned about possible interference to commands or ranging, and possible damage to the thin feed lines.

Two short tests were set up in the LeRC electron swarm chamber. First, a short section of belt antenna was placed in the tank facing the electron beam. The command output from the antenna was connected into the engineering model filters and command receiver. The receiver ranging and command outputs were monitored. With a 20 keV beam discharges did occur though not visibly on the belt. The largest arcs produced a short duration 2 sec, 800 mV pulse on the receiver ranging output. No disturbance was apparent on the command output. The pulse on the ranging mode was judged to be of no consequence. For the second test, the belt antenna was placed in the tank with the metal ground plane facing the electron beam and the forward side facing a 6 in. x 8 in. sample of silvered teflon. The teflon produced frequent high amplitude arcing. No effects were observed on the receiver ranging or command outputs. After the test the belt was carefully examined; no damage was apparent on the feed lines.

## 4. THE DEPLOYABLE SOLAR ARRAYS

The large light weight deployable solar arrays are unique to synchronous orbit spacecraft. The array substrate is 0.001 in. thick kapton laminated with a fiberglass/polyester layer. The solar cells are carefully bonded to the substrate so as to leave the gaps between the cells free of opaque adhesive. The substrate is about 30 percent transparent to sunlight, the glass fibers will scatter some light into the areas behind the solar cells. Therefore there will be a certain amount of photoelectron emission from the rear surface, and the substrate conductivity may be increased by photoconduction effects. The arrays are nevertheless the largest area of external shadowed dielectric on the spacecraft and consequently are possibly sources of frequent discharges.

Table 2. Interface Requirements for Telemetry

<b>ANALOG SIGNALS</b>	
NOMINAL RANGE	0V TO 5.0V
FULL SCALE	0V TO 5.1V
ONE BIT	20 mV
SOURCE IMPEDANCE	<5 K $\Omega$
LOAD IMPEDANCE DURING SAMPLING	1.0 M $\Omega$
ENCODER INPUT PROTECTION BEFORE ANALOG SWITCHES	4.7 K $\Omega$ RESISTOR TO DIODE CLAMPS TO +5.6V AND TO GROUND
FILTER AFTER THE ANALOG SWITCHES-TIME CONSTANT	10 $\mu$ S
<b>FLAGS</b>	
FLAG	4.0V TO 5.5V
ZERO	0V TO .7V
DECISION THRESHOLD	2V
RISE TIME	1 $\mu$ S TO 10 $\mu$ S
SOURCE IMPEDANCE	<5 K $\Omega$
ENCODER INPUT PROTECTION	75 K RESISTOR TO DIODE CLAMPS TO +5.6V AND TO GROUND
<b>DIGITAL WORDS</b>	
WORD "1"	4.0V TO 8.0V
ZERO	0V TO .25V
RISE TIME	1 $\mu$ S TO 10 $\mu$ S
SOURCE IMPEDANCE - "1"	<1.5 K
"0"	<2.5 K
ENCODER INPUT PROTECTION	

Tests were made on a small section of array in the LeRC chamber, with electrons incident on the rear side of the array. In a dark chamber, weak discharges occurred with visible points of arcing, primarily in the vicinity of interconnects between the cells. Measurements of the electrical output of the cells before and after the test showed that no deterioration resulted from the discharges. No changes to the arrays were considered because the flight units were completed at this time and only a catastrophic failure would have forced any modifications.

Flight data has shown no unusual electrical degradation of the arrays.

Launch ESTEC has made further tests on an array sample,<sup>4</sup> with both a dark chamber and with a light source illuminating only the solar cell side of the sample. They have observed discharges with an illuminated sample at temperatures  $-10^{\circ}\text{C}$ . Except for transit through eclipse and immediately after the eclipse, the lowest temperature of the flight arrays is  $40^{\circ}\text{C}$ . This test would indicate that there are possibly no discharges off the arrays in sunlight, again except for a few minutes after eclipse exit.

##### 5. SPACECRAFT LEVEL EMI TESTING WITH A SPARK SOURCE

Based on measurements in their experiments, the LeRC group made a spark source for the spacecraft level EMI test. The source discharged a 500 pF capacitor, charged to 10 kV across a spark gap. The discharge was underdamped with a ringing frequency of 25 MHz. The spark repetition rate was about 5 pulses per second.

A series of tests were made on the flight spacecraft. These tests were cautious because we were using the flight spacecraft with no previous test experience. Also we were very uncertain as to the magnitude of the surface potentials, and discharge current's that would be experienced in space. A report by Shkarofsky and Tam<sup>5</sup> indicated that the rear surface of the deployable array blanket could charge to 4.4 kV and that the corresponding energy density would be  $0.27 \text{ mJ/cm}^2$ . The 2.5 mJ in the sparker would therefore correspond to discharging 100 square centimeters of blanket. The same report indicated that the TEP radiator fin could charge to 23 kV and the 2.5 mJ would correspond to a discharge of only 10 square centimeters. It was felt that these figures, and the test results from LeRC represented "worst case" situations; however, they were sufficiently alarming to justify the spacecraft level test.

For the test, the deployable arrays were deployed as shown in Figure 1.

### 5.1 Deployable Array Tests

The purpose of this test was to simulate the occurrence of arcs on the rear surface of the deployable array blanket. The procedure was for the spark source to be held about 1 m from the rear surface of the blanket and to be moved slowly towards the blanket. During the arcing, the telemetry output connection on an accelerometer mounted on the tip of the array was monitored with a high speed oscilloscope. Each spark generated a noise burst. For reasons of caution the approach towards the array was stopped when the noise burst exceeded 6 volts peak to peak. This was done at three vertical positions, first opposite the instrumentation wiring on the array centerline, second opposite the areas containing solar cells, and third opposite the power wiring along the edge of the blanket. At the centerline positions the closest approach was about 30 cm, at the power wiring the closest approach was about 3 cm (as close as the cover on the spark source allowed). During the test telemetry channels associated with instrumentation on the arrays was monitored on strip charts. After the tests a computer search of all the spacecraft channels was made. During all the sparking no telemetry data was observed that could have been attributed to the arcing.

### 5.2 TEP Radiator Fin Test

For this test the spark source was held close to the radiator fin, on both sides, but at some distance from sensor wiring. Selected telemetry channels associated with the TEP, particularly those temperature sensors mounted on the fin were monitored on strip charts. No change in output was observed.

### 5.3 Thermal Blanket Tests

In this test the spark source was held near thermal blankets on the forward deck, but for reasons of caution, not near to sensors. The computer search showed no unusual telemetry data.

Obviously a more comprehensive set of tests would have been desirable but only with previous test experience on nonflight hardware.

## 6. ANOMALIES

The power subsystem is divided into two independent sections: housekeeping and experiments as shown in Figure 4. The housekeeping section has three power sources, the body mounted solar array, the deployable array and batteries. All sources are connected to the unregulated bus with isolating diodes. The experiment section obtains power from the deployable arrays only. The voltage sensor on the experiment unregulated bus is on the array side of the over/under voltage switch.

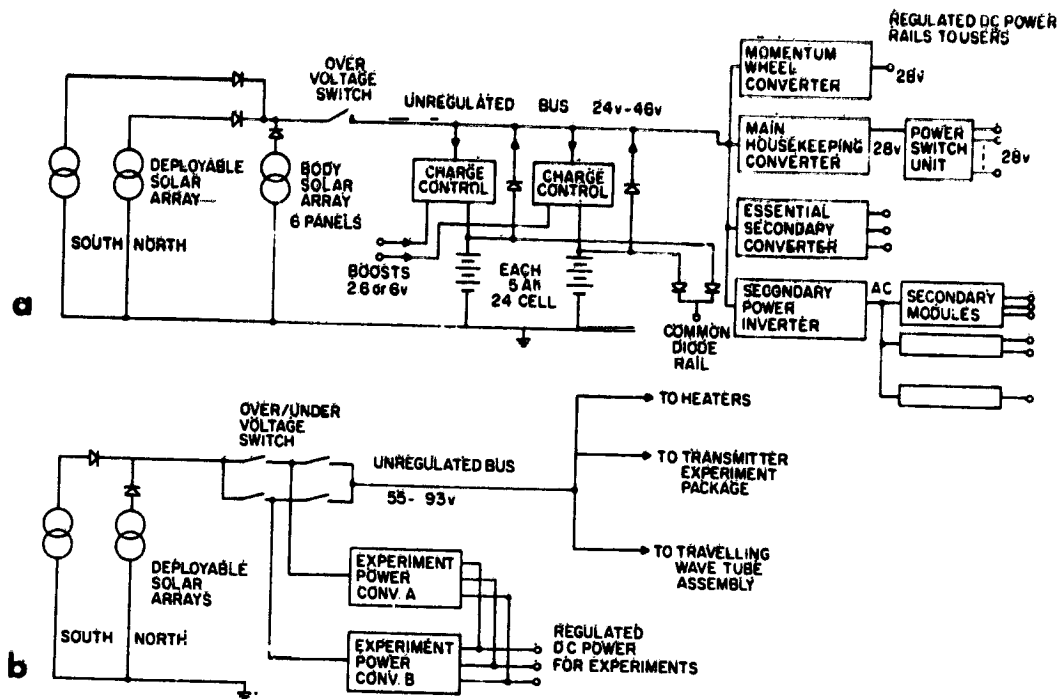


Figure 4. Power Subsystem. (a) Housekeeping section, and (b) experiment section

On 8 June 1976 at 06:43 GMT (22:59 spacecraft time) a short circuit occurred on the experiment unregulated power bus. Immediately the short occurred, the over/under voltage switch disconnected all spacecraft loads from the arrays. The short continued 24 sec then cleared itself. The most probable location for the short circuit was on a board containing the power isolating diodes. This board is mounted on the inboard pallet on the deployable solar arrays, and is completely exposed to the external environment. During the 24 sec the voltage on the experiment bus varied erratically between 19 and 42 volts, behaviour typical of an arc. Also the TEC recorded many noise bursts on the array power and instrumentation lines during the 1st, 18th, 21st, 22nd and 25th sec. These bursts were probably generated by the short circuit. The TEC had not recorded any transients in the 2 hr proceeding the fault. A moderate substorm had been observed a few hours earlier. A micrometeorite hit, charge accumulation or a small discharge resulting from charge accumulation on the diode board could have initiated the short circuit. The fault has not reoccurred.

On 28 September 1976 the housekeeping Secondary Power Inverter and all associated submodules tripped off. Unfortunately, this inverter supplied power to

the telemetry encoders so we immediately lost data. The Inverter was turned on some hours later and it has functioned normally since. A very large transient on the power bus could have caused this fault. The TEC had not registered counts in the previous hour and the magnetosphere was quiet. This anomaly is still under consideration.

Since launch there have been about 20 unexplained trip-offs on the power converter (EPC) associated with a 20 W TWTA. The EPC can get its turn off command on an internal command line. The EPC does not use a command line receiver on this line and it is known that a noise burst will result in a trip. None of the trips occurred coincident with TEC counts or with other spacecraft commanding. However, it is possible that discharges could be introducing fast noise bursts and causing the trips.

## 7. CONCLUSIONS AND RECOMMENDATIONS

During the first 8 months of flight operations on CTS, we have experienced:

- (1) No anomalies commands (except the 20 W TWTA trips).
- (2) Effectively noise free telemetry.
- (3) Two major anomalies that could possibly have been caused by charge accumulation or discharges.

(4) Several trips on the 20 W TWTA power converter where a command line transmitter receiver was not used.

(5) No unusual degradation on the electrical performance of the flexible arrays.

From a spacecraft charging point of view, the important design features on CTS are:

(1) A unified ground plane configuration was used, thus saving the weight of return wiring.

(2) Command line and data line transmitters and receivers were used to achieve immunity from fast transients.

(3) All layers of the thermal blankets and all metal parts were grounded.

(4) Teflon second surface mirrors were bonded using conductive adhesives.

(5) Few wires were shielded, therefore the wiring harness was as light as possible.

(6) Very little weight was added for protection against charging.

(7) A simple transient event counter was flown.

Based on the CTS experience, I would make the following recommendations:

(1) Use command and data line interface circuits which provide protection against short, high level transients.

(2) Bond second surface mirrors including quartz ones with conductive adhesives.

(3) Ground all layers of all thermal blankets using a ground configuration of Type I or better.

(4) Ground all metal parts.

(5) Carry out a spacecraft level test on the engineering model, using a very fast spark source, to establish the electrical signature of transients on power, command, and telemetry lines. These data should then be used to specify EMI protection on flight model units. A comprehensive test should be made on the flight spacecraft.

(6) EMI specifications should include limits on emission and susceptibility on telemetry and command lines.

(7) Transient sensors should be carried. These sensors should be of more comprehensive and sophisticated design than the CTS TEC.

## Acknowledgments

I would like to thank the people in NASA Lewis Research Center, System Engineering Branch, Spacecraft Technology Division under R. R. Lovell for their participation and support on the CTS charging investigation. I would also like to thank the CRC, Spacecraft Operations Group for their assistance in preparation of this paper.

## References

1. Stevens, N.J., Lovell, R.R., and Gore, J.V. (1976) Spacecraft charging investigation for the CTS project, spacecraft charging by magnetospheric plasmas, A. Rosen, Editor, AIAA Progress in Astronautics and Aeronautics, 47.
2. Stevens, N.J., Lovell, R.F., and Klinec, V.W. (1976) Preliminary Report on the CTS Transient Event Counter Performance through the 1976 Spring Eclipse Season, NASA Technical Memorandum NASA TMX-73487.
3. Effects of Spacecraft Charging on the TT&C Receiving System (1975) CTS Project Test Report TR15-03-1.
4. Bogus, K.P. (1976) Investigation of a CTS solar Cell Test Patch under Simulated Geomagnetic Substorm Charging Conditions, ESTEC Internal Working Paper TEC/DB/lml/0469.

5. Shkarofsky, I. P., and Tam, S. Y. K. (1975) Investigation of the Charging of External Surfaces on CTS Synchronous Orbit and Consequent Phenomena, RCA Report No. FXC 84-1, Lab. Report No. PSP-114, MNL D-75-TR-007.

Contents

1. Introduction	789
2. A Comparison of the ESD, DEMP, and SGEMP Environment and Spacecraft Performance Concerns	790
3. A Comparison of ESD, DEMP, and Semp Electromagnetic Signal Characteristics	793
4. Comparison of EMI Levels for Shielded and Unshielded Cases	795
5. Other System Design Techniques for Reduction of EMI from ESD, DEMP, and SGEMP	798
6. Conclusions	802

7. Common Approach to Solving SGEMP, DEMP, and ESD Survivability

D. Ling  
 General Electric Company  
 Valley Forge Space Center  
 Philadelphia, Pa.

Abstract

System Generated Electromagnetic Pulse (SGEMP) and Dispersed Electromagnetic Pulse (DEMP) are nuclear generated spacecraft environments. Electrostatic discharge (ESD) is a natural spacecraft environment resulting from differential charging in magnetic substorms. All three phenomena, though differing in origin, result in the same problem to the spacecraft and that is Electromagnetic Interference (EMI). A common design approach utilizing a spacecraft structural Faraday Cage is presented which helps solve the EMI problem. Also, other system design techniques are discussed which minimize the magnitude of these environments through control of materials and electrical grounding configuration.

1. INTRODUCTION

The common design approach of the Abstract is applicable to any high altitude spacecraft in an elliptical or synchronous orbit whose altitude subjects it to the spacecraft charging environment and also has a nuclear survivability requirement.

The nature of the ESD, DEMP, and SGEMP environments and the EMI concern is discussed as follows.

## 2. A COMPARISON OF THE ESD, DEMP, AND SGEMP ENVIRONMENT AND SPACECRAFT PERFORMANCE CONCERNS

### 2.1 ESD (Electrostatic Discharge)

Electrostatic charging of synchronous spacecraft results from a natural radiation of charged particles collecting on the spacecraft surfaces. Electrostatic discharge occurs when the differential charging of the spacecraft surface materials exceed their dielectric breakdown strength. The resulting system effects of the discharge are electromagnetic interferences such as circuit upset and burnout. ESD occurs in a five-step process. First, a magnetic substorm results in an injection of charged particles, ions and electrons, into the dusk-to-dawn sectors of local time and roughly from 4 to 8 earth radii. Magnetospheric effects cause preferential eastward drift of electrons into the midnight-to-dawn quadrant while ions drift westward. Appreciable electrons have been observed (A TS-5) at 5-30 keV.

The second step is the encounter of the spacecraft surfaces with the hot, negative plasma. If a surface is self shadowed or in eclipse, it will charge to approximately a potential equivalent to the most probable energy of the electron energy distribution, less a potential drop corresponding to secondary electron emission from the surface. If the surface is in sunlight, photoelectric emission will prevent it from charging to a negative potential and in fact the surface may go a few volts positive. It is apparent that different surfaces, due to different exposure to sunlight (and hence photoelectric discharge) and different secondary electron emission and photoemissive properties, will charge to different potentials. Thus step 2 results in differential voltages of several thousand volts appearing at different sites on the spacecraft's exposed surfaces.

The third step is electrostatic discharge whenever the differential potential exceeds the dielectric breakdown of the material.

The fourth step is the electric or magnetic field coupling from the discharge arc into spacecraft harnesses or the irradiation of antenna assemblies associated with the arc (see Figure 1).

The fifth step is the induction of a transient pulse into the circuit with sufficient magnitude to activate the circuit or burnout some of its components, or communication and telemetry interference.

Other possible effects than circuit upset or burnout is direct damage to thermal control surfaces resulting from the arc, discharge, and contamination to surfaces.

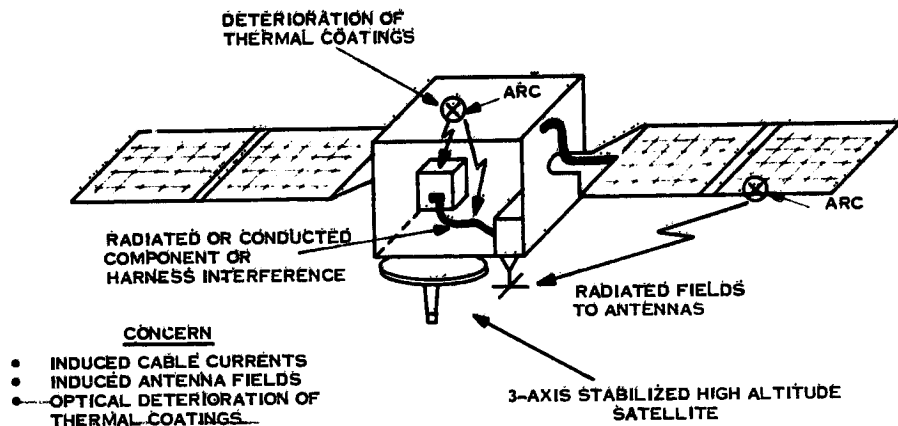


Figure 1. Arcing Induced Satellite Environment Due to S/C Charging

## 2.2 DEMP (Dispersed Electromagnetic Pulse)

A nuclear weapon detonated in or near the atmosphere generates a copious stream of Compton-electrons. Part of the latter constitutes a time-changing, nonradial current which in turn produces propagating electromagnetic fields. At the spacecraft, the latter have propagated through the ionosphere which acts as a high-pass filter and thus only frequencies above a certain cutoff are observed. Also, frequencies that do propagate to the spacecraft are dispersed and arrive at different times. Impingement of the DEMP on the spacecraft structure and antennas induces structural currents which in turn couple electromagnetic fields into harnesses and communications receiver front ends. This results in EMI and RFI similar to spacecraft arcing (ESD). (See Figure 2).

## 2.3 SGEMP (System Generated Electromagnetic Pulse)

SGEMP, strictly speaking, is not an external environment but rather a secondary environment produced primarily by the interaction of x-rays with the surfaces and harnesses of the spacecraft. SGEMP can be classified as (1) direct and (2) indirect. The direct refers to coupling of X-rays directly into cables and electronic components. The indirect SGEMP is generated by a two-step process in which first x-rays impinge on surface materials and release secondary electrons through Compton and photoelectric processes. The secondary electrons constitute an accelerated charge and hence generate propagating electric and magnetic fields. The latter couple into cables and circuits according to the particular coupling coefficients that apply to the wavelength of the fields and the geometry of the cables and circuits. Again, transient upset and burnout of the electronics result (See Figure 3).

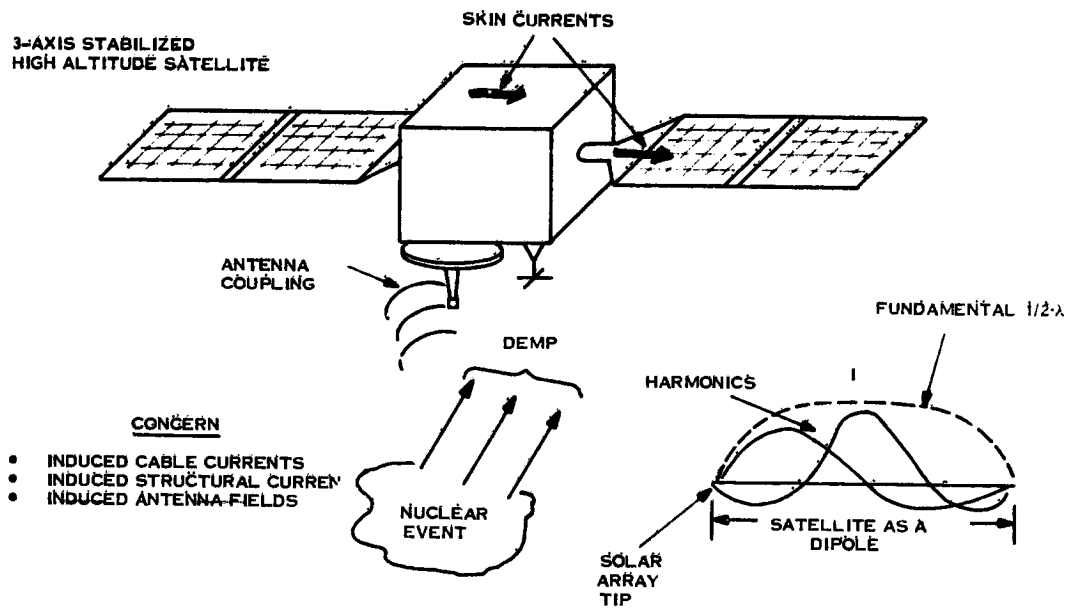


Figure 2. DEMP Induced Satellite Environment (Dispersed Electromagnetic Pulse)

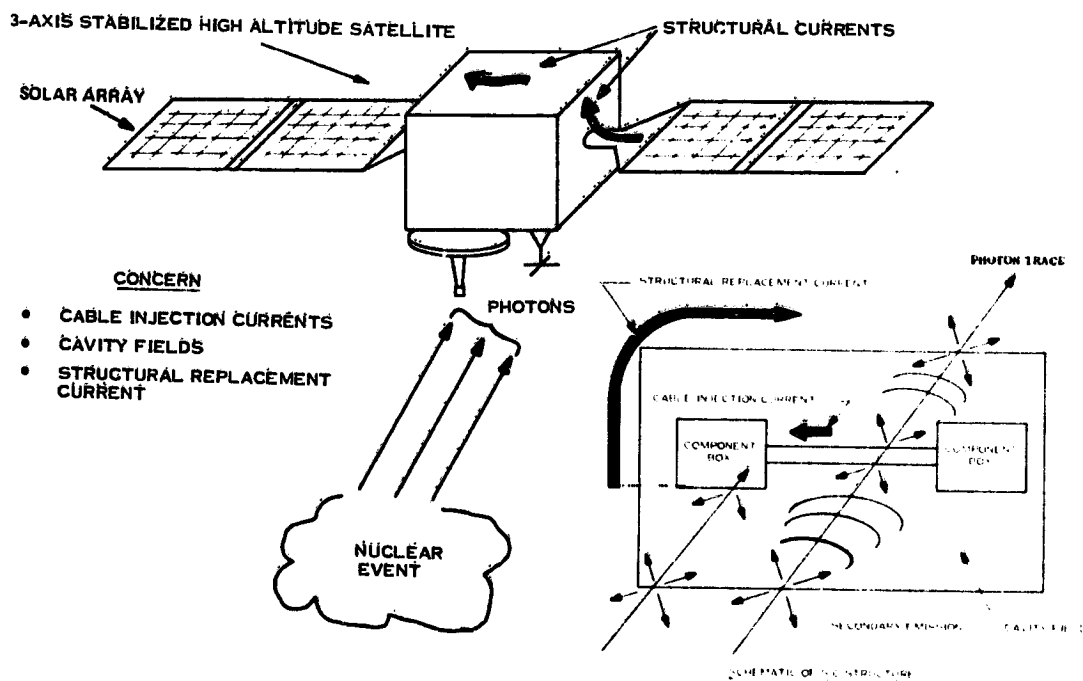


Figure 3. SGEMP Induced Satellite Environment (System Generated EMP)

### 3. A COMPARISON OF ESD, DEMP, AND SEMP ELECTROMAGNETIC SIGNAL CHARACTERISTICS

Figure 4 illustrates the commonality of the electromagnetic signal characteristics in both the time and frequency domains. \* From Figure 4 it can be seen that the fast rise in all three cases produces significant energy in the frequency spectrum out to ~100 MHz and then rolls off at 40 dB/decade. The similarity in the spectrum makes it possible and desirable to find a common design technique which addresses all three phenomena at one time. The common design technique proposed is to design the spacecraft structure such that it encloses the electronics and harnessing in the form of a Faraday cage. Figure 5 illustrates the classical presentation of how the Faraday cage works as an EMI shield. Figure 6 illustrates the comparison between the theoretical shielding effectiveness of an ideal Faraday cage and also what is achievable in practice. Shielding effectiveness in an actual spacecraft is limited by physical construction of the structure which necessitates bonding, riveting, and bolting of structural subassemblies, thus producing metal-

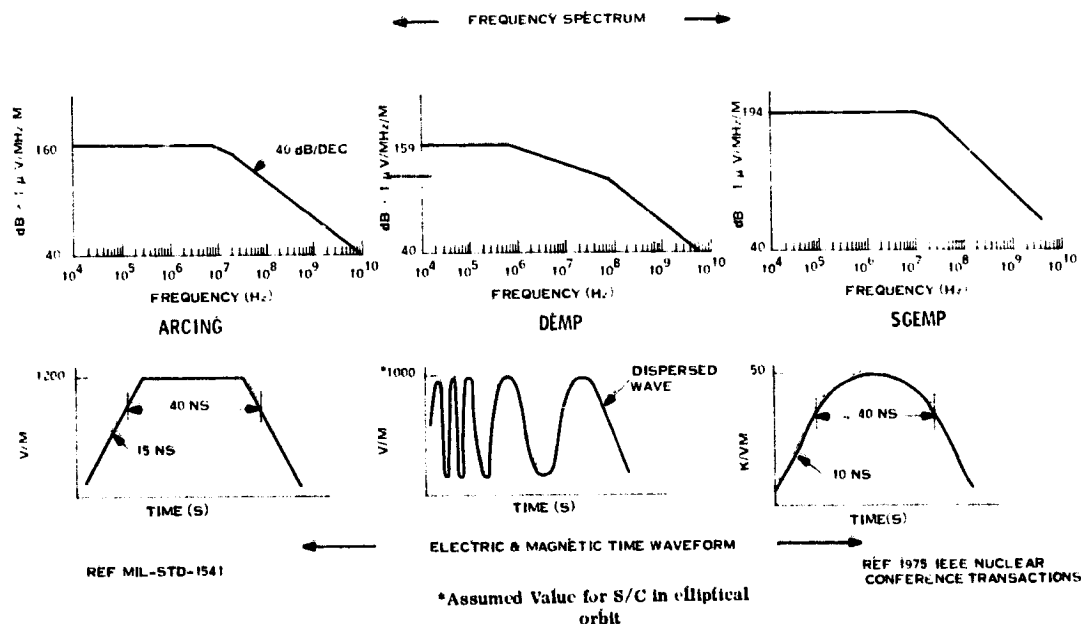


Figure 4. Environment Electromagnetic Signal Characteristics

\*The signal characteristics of the photon flux and DEMP and the response levels of the satellite cables and structure have been obtained or derived from the 1974, 1975 and 1976 IEEE Annual Conference Transactions on Nuclear and Space Radiation Effects.

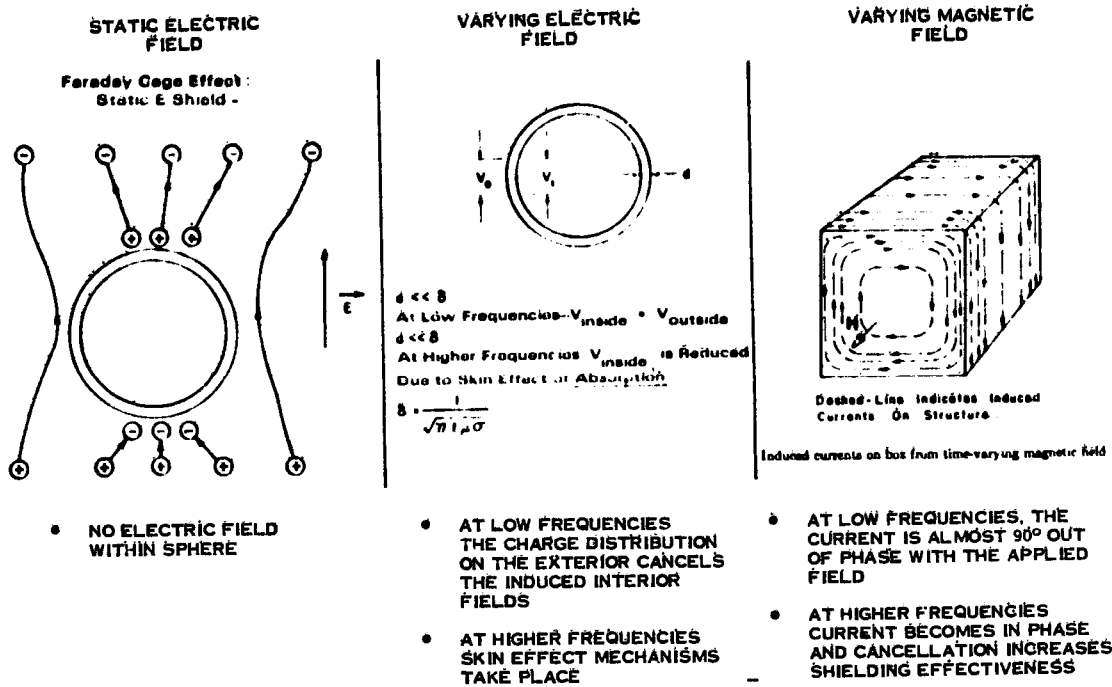


Figure 5. Faraday Cage Shielding Effects

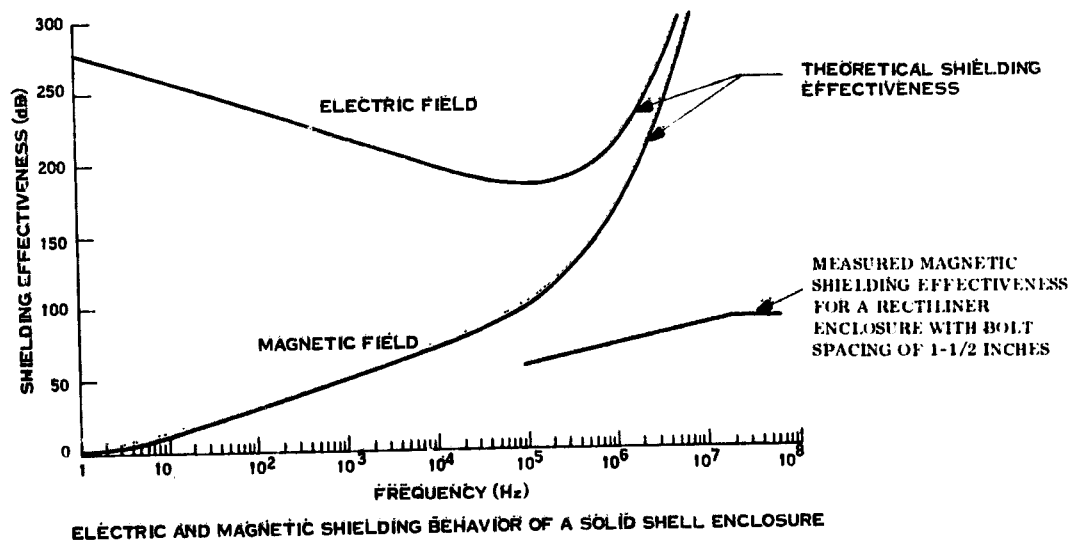


Figure 6. Faraday Cage Shielding Effectiveness

to-metal seams allowing electromagnetic leakage. Rivet spacing, number of harness penetrations, access parts, etc., all influence the levels of shielding effectiveness. Fortunately, in terms of spacecraft weight considerations, the use of metal foils conductively bonded between structural elements makes nearly as an effective shielding as does a solid sheet metal enclosure. The actual magnetic shielding effectiveness of a bolted enclosure (1-1/2 in. bolt spacing) is shown in Figure 6. A 30 to 50 dB magnetic shielding effectiveness is achievable.

#### 4. COMPARISON OF EMI LEVELS FOR SHIELDED AND UNSHIELDED CASES

Figures 7 - 9 illustrate in principle how the Faraday shielding attenuates the interfering signal characteristics of Figure 4. It can be seen from the last items in Figures 7 and 8 that the resultant magnitude of the interfering signal both in the ESD and DEMP cases is reduced below circuit component burnout damage levels. The magnitude of the attenuated signal may, however, still be sufficient to cause interference (~0.5 volts). With particularly sensitive digital logic circuits or mission critical functions pulse width discrimination should also be considered as a candidate for inclusion in the EMC design.

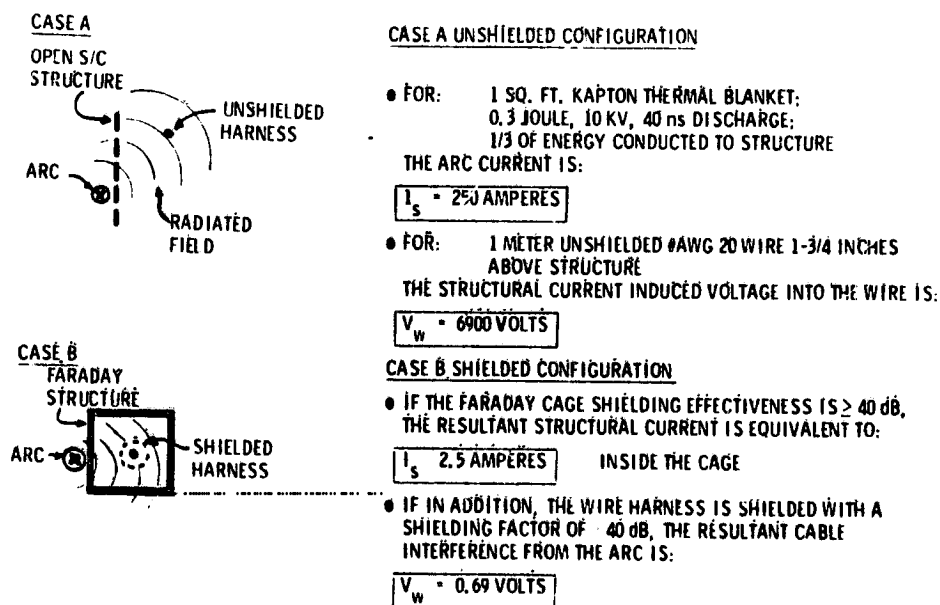


Figure 7. Shielding for Electrostatic Discharge

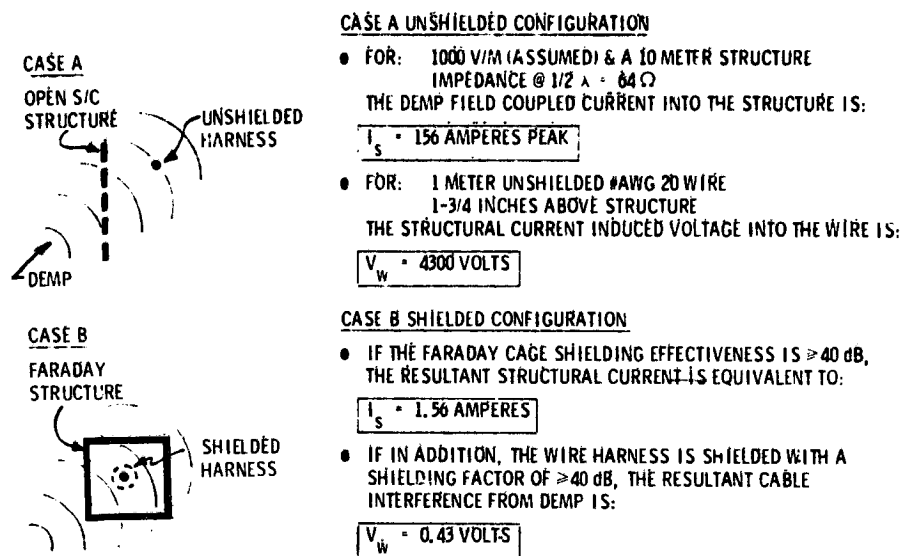


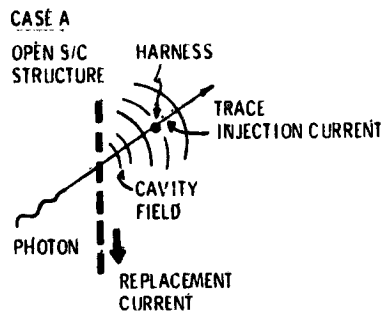
Figure 8. Shielding for DEMP

Figure 9 (the SGEMP shielding case) is a more complex case in that the interfering cable currents are obtained by three different modes:

- (1) Coupling to the cable from structural replacement currents.
- (2) Coupling to the cable by cavity fields.
- (3) Direct current injection by x-ray impingement.

Harness and Faraday cage shielding are both effective at suppressing EMI from the structural replacement currents ( $I_{C2}$ ). Harness shielding, only, is effective at suppressing cavity field induced currents ( $I_{C1}$ ). Neither harness shielding or Faraday cage shielding are effective suppressing EMI from direct cable x-ray current injection ( $I_{C3}$ ).

In this latter case, cable current injection must be minimized through the use of low atomic number materials, dielectric shielding, bundling of cable wires, etc. The EMI protection for this particular problem must be addressed by using circuit terminating devices which will limit the inrush current below burnout levels or voltage clamp the input below damage or upset levels.



**CASE A UNSHIELDED CASE**

- IF PEAK FIELD INTENSITY FROM SGEMP IS 1 TO 50 AMPERES/METER PLAK STRUCTURAL CURRENT FOR A 2 METER STRUCTURE IS:

$$I_s = 2 \text{ TO } 100 \text{ AMPERES PEAK}$$

- IF CAPACITANCE OF WIRE 1-3/4 INCHES OFF OF STRUCTURE =  $2 \times 10^{-11}$  F/M AND PULSE RISE TIME OF 50 KV/M FIELD = 15 ns, THEN THE INDUCED CURRENT INTO THE WIRE FROM CAVITY FIELDS IS:

$$I_{c1} = 60 \text{ AMPS PEAK}$$

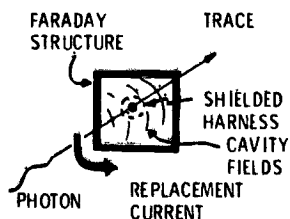
- IF THE STRUCTURAL REPLACEMENT CURRENT IS 100 AMPERES/METER AND THE METER CABLE IS 2 INCHES AWAY

$$I_{c2} = 0.66 \text{ AMPERES/METER}$$

- IF THE CABLE TEST DATA PRESENTED AT THE 1976 IEEE NUCLEAR & SPACE RADIATION CONFERENCE BY CLEMENT, WULLER & CHIVINGTON IS SCALED UP TO LEVELS BELOW WHERE THERMAL MECHANICAL SHOCK BECOMES THE OVERRIDING CONSIDERATION, THEN THE INJECTION CABLE CURRENT IS:

$$I_{c3} = 1.4 \text{ AMPERES/METER}$$

**CASE B**



**CASE B SHIELDED CONFIGURATION**

- CABLE CURRENT DUE TO CAVITY FIELDS =  $I_{c1}$  - 40 dB CABLE SHIELDING EFFECTIVENESS

$$I_{c1} = 0.60 \text{ AMPERES PEAK}$$

- CABLE CURRENT DUE TO STRUCTURAL REPLACEMENT CURRENT AFTER SHIELDING =

$$I_{c2} = 0.66 \times 10^{-4} \text{ AMPERES/METER}$$

(UNSHIELDED) (FARADAY SHIELD) CABLE SHIELD

$$I_{c2} = 0.66 \times 10^{-4} \text{ AMPERES/METER}$$

- CABLE CURRENT DUE TO CABLE INJECTION (AFTER SHIELDING & INCLUDING DIELECTRIC LINING)

$$I_{c3} = 1.4 \text{ AMPERES/METER}$$

Figure 9. Shielding for SGEMP

## 5. OTHER SYSTEM DESIGN TECHNIQUES FOR REDUCTION OF EMI FROM ESD, DEMP AND SGEMP

### 5.1 ESD EMI Reduction Techniques

The spacecraft discharge phenomenon can be controlled by reducing the differential potential buildup between various outer surface thermal blankets and coatings and the metallic spacecraft structure. This goal is achievable through the use of conductive paints and thermal blanket materials such as astroquartz cloth which has low surface resistance when bombarded by electrons.

In addition, possible discharges between the various inner metallic layers of thermal blanket materials and the resulting degradation of the thermal properties of the blanket can be eliminated by connecting all blanket metallic layers and grounding the composite blanket to the metallic structure. All structural members can also be electrically interconnected to share a common ground potential for prevention of differential structural voltages. All apertures such as the earth coverage antennas can be covered with dielectric/thermal materials (astroquartz cloth) which exhibit high levels of surface and throughput leakage, thereby preventing large charge buildup. In those cases where discharges may not be eliminated, such as on the glass sections of the solar arrays, then the line-of-sight to communications antennas should be eliminated to prevent RFI. Table 1 lists spacecraft design guidelines for preventing arcing.

### 5.2 DEMP and SGEMP EMI Reduction Techniques

Principal areas of concern from nuclear effects are system transient upsets and permanent degradation of parts and materials. Prevention of damage to piece parts and materials is accomplished through hardened circuit design, nuclear and electromagnetic shielding, and the use of hard materials. All materials, including critical external thermal control materials, must be carefully selected to prevent any significant x-ray induced thermal-mechanical effects and to adequately withstand the natural radiation environments.

The system transient upset and recovery requirements are met by functionally configuring each subsystem to minimize the impact at the component and circuit level. The system is allowed to respond as much as possible without causing undesirable system effects and to functionally recover within the desired time period. This is achieved by ensuring fast circuit recovery through proper piece-part selection and circuit design, preventing the generation and execution of false commands, logic upset, and the use of hardened data storage where required.

Table 2 itemizes design controls for minimizing EMI from SGEMP and DEMP.

**Table 1. Spacecraft Design Guidelines for Preventing Arcing**

1. The graphite epoxy used for structural members is textured to be conductive and presents minimum discontinuity in structural ground connections.
2. All epoxy and other nonmetallic structural bonding adhesives are conductive and present minimum discontinuity in structural ground.
3. Solar array panels are grounded to each other with grounding jumpers.
4. Solar array panels are grounded to the spacecraft structure through special slip rings, providing a one milliohm path.
5. All antennas and support structures are grounded to the main structure.
6. All electrical components and subsystems are grounded.
7. Spacecraft thermal blanket materials and coatings have been selected which have high surface leakage and bulk leakage.
8. All external cable harnesses are shielded and the shield is connected to structural ground at both ends.
9. All apertures, including RF antenna apertures, are covered with high surface leakage silica cloth composites.
10. All waveguide elements are electrically connected with spot weld connections and grounded to the main frame.
11. The support members of all antennas will be connected to the spacecraft structure with conductive epoxy such that each support joint represents approximately a one ohm connection to structure.
12. All deposited thin film conductors (in thermal blankets or otherwise) shall have a ground strap of sufficient area to carry the transient current loads expected (a 2 joule rating is self-applied).
13. Electrical resistance from any point on vacuum-deposited conductive films (in thermal blankets or otherwise) to spacecraft structural ground shall not exceed 10 ohms.
14. Electrical resistance from any point on a thermally isolated substructure to spacecraft structural ground with required grounds in place shall not exceed .01 ohms.
15. There shall be at least one grounding point on each electrically continuous substructure.

Table 1. Spacecraft Design Guidelines for Preventing Arcing (Cont'd)

16. The electrical resistance of each ground strap bond between the strap bond and the structure shall not exceed .03 ohms.
17. Thermal blanket conducting straps to ground shall be electrically equivalent to a copper conductor of wire of AWG #22.
18. Each structural ground strap shall be electrically equivalent to a copper conductor of wire of AWG #14.
19. Redundant logic is employed in command and other sensitive logic and receiver circuitry.
20. The solar array consists of a honeycomb aluminum base structure with the following layers of materials: coverglass, solar cells, and mica-ply substrate and graphite epoxy. All lateral strips or rows of cells are bonded together by a ground wire at each end of the solar panel, such that the resistance between any two rows of cells does not exceed 5 milliohms.
21. The solar cell string is electrically connected to spacecraft structural ground at the shunt regulator and via natural capacitive paths.
22. All outer solar panels are connected to the inner solar panels by ground wires.
23. Thermal windows on north panel (N.P.) and south panel (S.P.) are covered with second surface mirrors consisting of OSR glass with silver coating on one side. The OSR glass is attached to the panel surfaces with conductive epoxy.
24. Component enclosures and chassis are designed to provide an RF attenuation of 50 dB to radiated fields produced by ESD.
25. All internal and external cables are shielded on a cable bundle basis.
26. Cable shields will be multipoint grounded to the spacecraft structure by low impedance connections.
27. Mounting hardware used to bolt or fasten components to the spacecraft structure shall also serve as ground bonding paths.
28. Nonconductive finishes such as anodized surfaces or painted surfaces will not be used on any of the grounding interfaces.

Table 2. Design Controls for Minimizing EMI from SGEMP & DEMP

DESIGN IMPLEMENTATION	SYSTEM RESPONSE
<b>System Level</b>	
1. All electronics in Faraday Cage > 40 dB attenuation	1. Reduces external SGEMP/DEMP field coupling to internal harness
2. Controlled structure and penetration impedances < 10 milliohms	2. Controls skin current and the placement current flow minimizes internal coupling
3. Low Z surface materials	3. Minimizes secondary electron emission, reduces external fields and structural replacement currents
<b>Subsystem Level</b>	
1. Internal cavities coated to control secondary emission	1. Minimizes IEMP fields and replacement currents
2. Optimum grounding (Single and Multipoint)	2. Reduces replacement current coupling effects
3. Harness and box RF shielded to > 40 dB	3. Reduces cavity field coupling effects
4. Harness design for minimum direct X-ray response	
a. Multiconductor bundle cables instead of flexible coax	4. a. Minimizes weight and SGEMP response
b. Aluminum RF shield plus inside dielectric liner over cable bundles	b. Reduced direct X-ray response
c. Controlled cable routing to avoid replacement current funnel points	c. Minimizes replacement current coupling
d. Multipoint shield grounds	d. Minimizes current coupling transient response
<b>Box Level</b>	
1. All interface and buried circuits protected with terminal protection circuits as required	1. Prevents circuit burnout
2. Circuits designed for maximum practical burnout threshold	2. Minimizes need for terminal protection
3. All boxes RF tight to > 40 dB	3. Minimizes cavity field coupling response

ORIGINAL PAGE IS  
OF POOR QUALITY

## 6. CONCLUSIONS

EMI from ESD, DEMP, and SGEMP has similar time and frequency domain signal characteristics. Thus, a common design approach to prevent EMI can be implemented through the use of a spacecraft structure configured as a Faraday cage shield. Harness shielding, integral structural grounding, and materials control are also common design features for the minimization of the ESD, DEMP, and SGEMP interference. Figure 10 and Table 3 illustrate the integrated design approach.

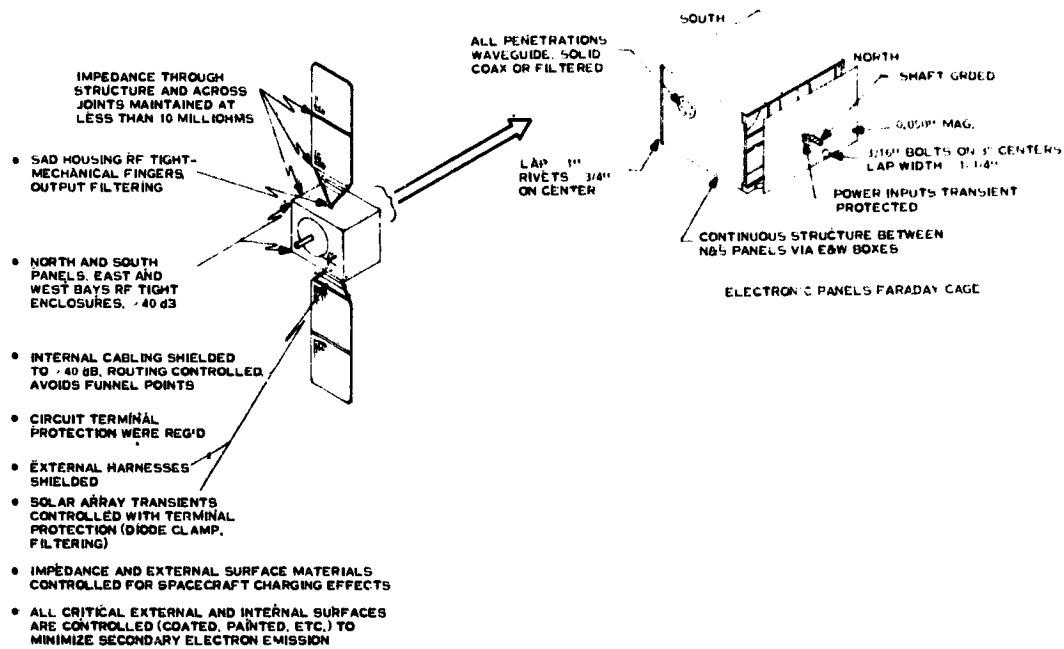


Figure 10. Structural and Materials Implementation of Common Design Approach to SGEMP, DEMP, and ESD Survivability

Table 3. Integrated Survivability/EMC/Spacecraft Charging Design Approach

ENVIRONMENT			
COMMON DESIGN FEATURE	SGEMP/DEMP PREVENTION & PROTECTION	S/C CHARGING PREVENTION & PROTECTION	EMC BETWEEN SUBSYSTEMS
Structure configured to form a Faraday Cage EMI/RFI shield	Electronics and harness protected from EMP field SGEMP induced structural currents quickly damped	Electronics and harness protected from arcing EMI products	Electronics and harness protected from RFI from transmit antennas
All antennas, solar arrays, structure and electrical components share common low impedance ground	Differential circulating current magnitude minimized	Differential structural voltages eliminated	Shielding effectiveness optimized
All component boxes RF tight	Protects component from cavity fields	Protects components from arcing EMI products	Protected from conducted and radiated S/S interference
All harnesses aluminum shielded	Protects component from cavity fields	Protects components from arcing EMI products	Protected from conducted and radiated S/S interference
All harnesses bundled configured by signal type	Minimizes direct SGEMP current effects	---	Protected from mutual signal interference
Multipoint grounding system	Best grounding configuration for high frequency transients	Best grounding configuration for high frequency transients	Best grounding configuration for RFI protection
All harness entries in and out of structure RF tight	Prevents DEMP fields from being coupled to electronics	Prevents EMP fields from being coupled to electronics	Prevents RF fields from being coupled to electronics
Materials configuration	Low "Z" materials minimizes secondary electron emission effects <ul style="list-style-type: none"> <li>• Aluminum/magnesium structure</li> <li>• Silica cloth thermal blankets</li> <li>• OSR</li> <li>• Chemglaze</li> </ul>	Silica cloth prevents charging and provides thermal control	---

## Contents

1. ESD - A New EMI Environment	805
2. ARC Source	808
3. ESD Testing	810
4. Summary	813

## 8. Plasma Charging Testing of Communication Satellites

F. Rosen  
General Electric Company  
Valley Space Center  
Philadelphia, Pa.

### Abstract

This paper discusses ESD as a radiated electromagnetic environment and compares the ESD environment to "standard" EMI test environment. An arc generator used to assess the sensitivity of typical spacecraft electronics is described.

The results of radiated susceptibility tests conducted on breadboard circuits and a satellite electrical model of a communication satellite are discussed.

#### 1. ESD - A NEW EMI ENVIRONMENT

EMC requirements for communication satellites built at GE Space Division specify the test requirements of MIL-STD-461 and the test levels of MIL-STD-462 tailored to the specific mission. The radiated susceptibility tests typically specified are RS02 and RS03.

RS02 (see Figure 1) is a low frequency magnetic susceptibility test. A wire is wrapped around the harness of the unit under test and the voltage spike in Figure 1 is impressed on a 10 ohm resistor.

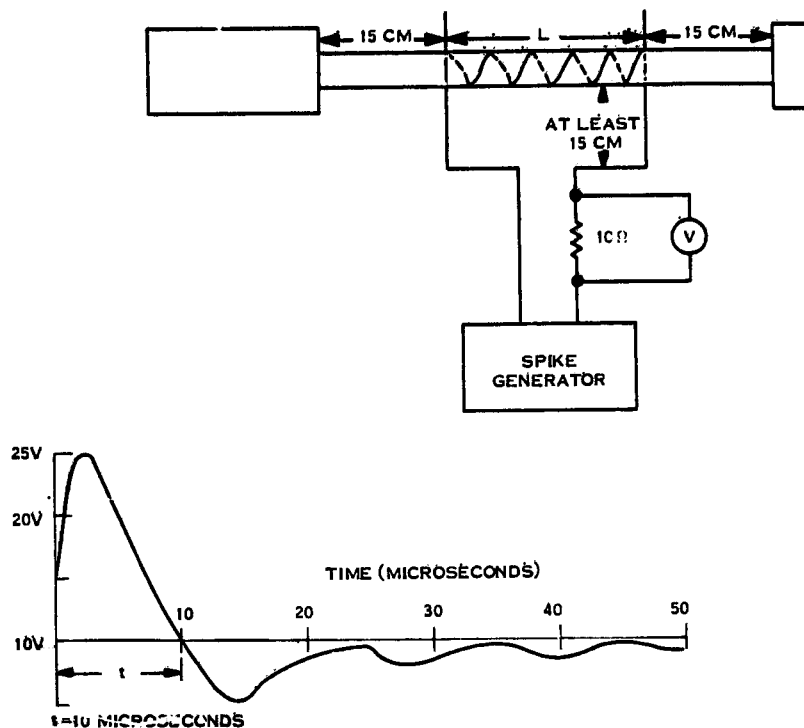


Figure 1. RS02

RS03 is a wideband electric field sensitivity test. The test is performed with a series of antennas and oscillators to cover the spectrum shown in Figure 2. The test oscillator is swept so that only one frequency at a time is applied to the test sample. The peaks in the spectrum correspond to the frequencies of on board transmitters.

Recognition of the plasma charging phenomena and the accompanying arc discharge results in a different EMI phenomena - high level radiation with frequency components extending from the low kilohertz to the gigahertz region.

Figure 3 illustrates the spectrum of a trapezoidal pulse with a 15-nsec rise time, a 40-nsec pulse width, and a peak amplitude of 1200 V/M. A significant difference between the curves of Figure 2 and Figure 3 is that the frequencies in Figure 3 are radiated simultaneously, while those of Figure 2 are radiated discretely.

This environment had not been previously tested at GE Space Division. A test program was instituted to assess the arc vulnerability of typical circuitry designed to tailored 462 levels and standard EMC practices, that is:

- (1) Minimize circuit bandwidth.
- (2) Use twisted pair wiring and differential techniques for low level signals.
- (3) All boxes well bonded to structure.

The objectives of the test were:

- (1) To determine if the arc was destructive to spacecraft circuitry.
- (2) To establish upset levels of digital interface circuits.
- (3) To establish response thresholds of analog circuits.
- (4) To determine if "latch-up" modes were excited when IC inputs were pulled above and below the supply voltages.

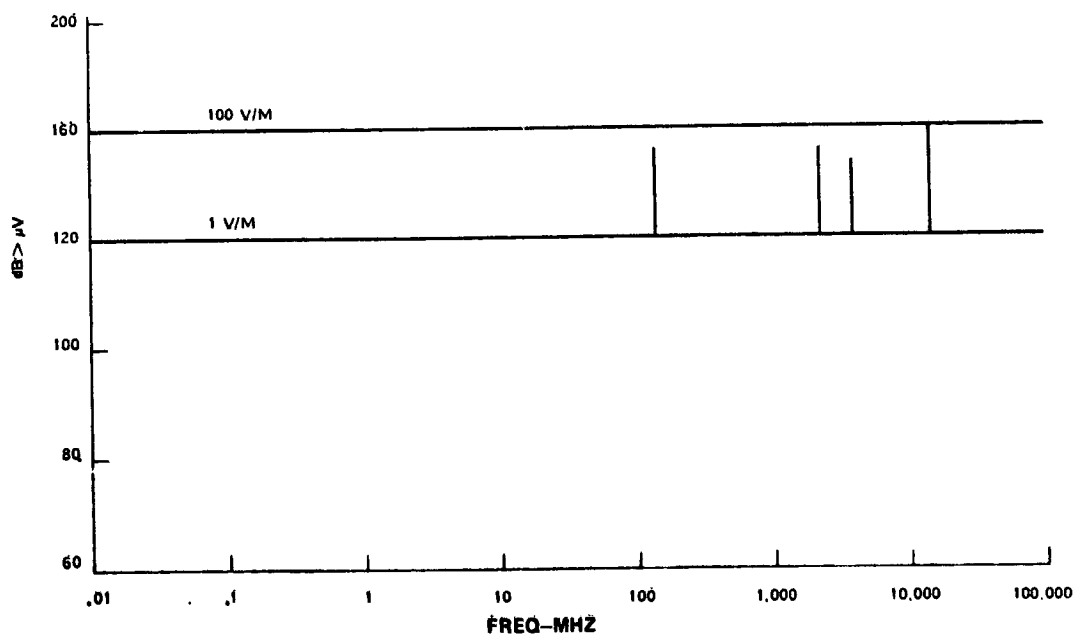


Figure 2. Typical RS03 Limits

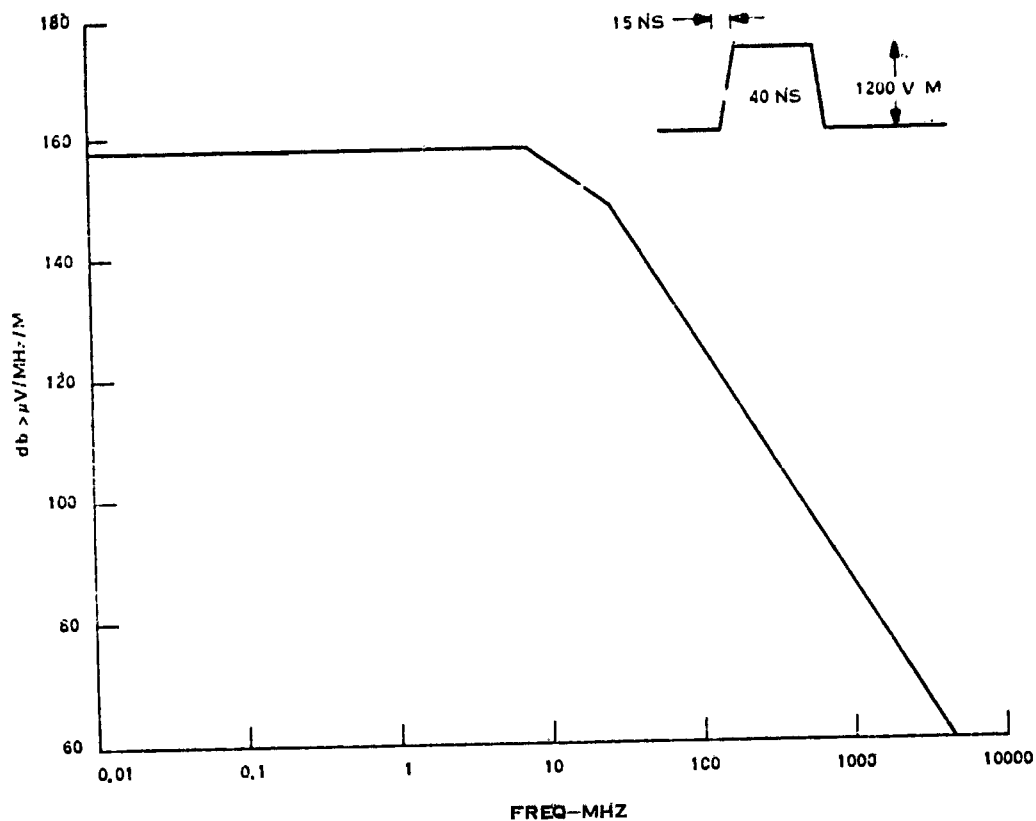


Figure 3. ARC Spectrum

## 2. ARC SOURCE

Since the plasma charging environment is not well defined, specification of a suitable arc source required engineering judgement. The arc source fabricated was based on a NASA approach and was similar to an arc source used during CTS testing. A block diagram of the arc generator is shown in Figure 4. A high voltage power supply charged the capacitor C through resistor R1. When the capacitor voltage reached the tube breakdown voltage, the capacitor discharged through R2 and the tube. The tube, capacitor, and resistors were easily changed so the breakdown voltage and arc energy were easily varied. A picture of the arc generator is shown in Figure 5.

ORIGINAL PAGE  
OF POOR QUALITY

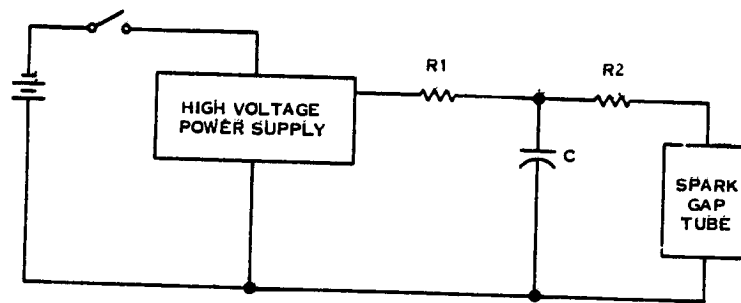


Figure 4. Block Diagram - ARC Generator

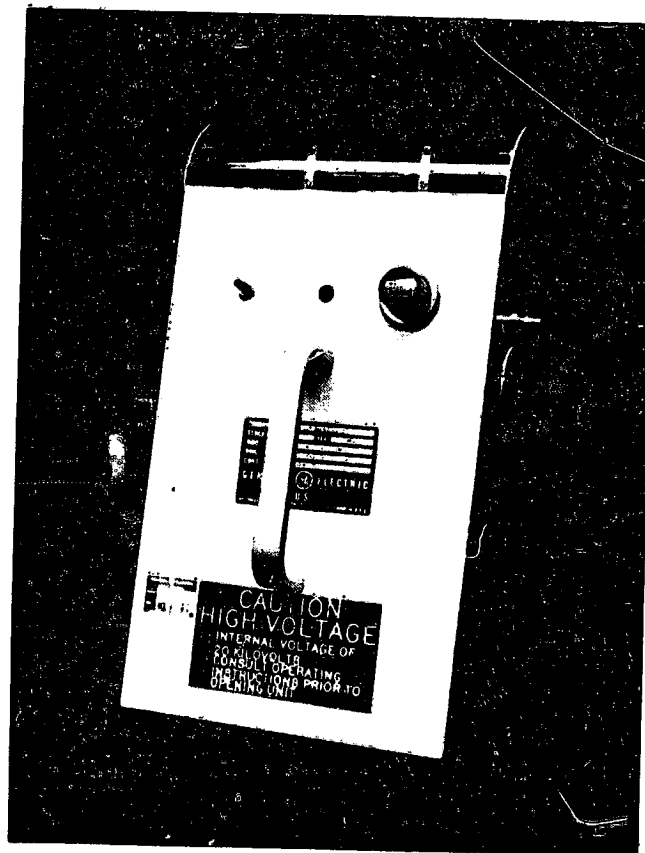


Figure 5. ARC Generator

### 3. ESD TESTING

#### 3.1 Circuit Testing

The testing proceeded in two phases. In the initial phase, breadboards of typical spacecraft circuits judged to be most sensitive to ESD were fabricated. The circuit test setup was as shown in Figure 6. The test circuits were located outside of the screen room and the arc generator was inside the screen room. The test procedure was to move the arc generator progressively closer to the test harness and to observe circuit performance. This test approach assumed the component boxes were well sealed and the harness was unshielded. The wires in the screen room were routed 5 cm above the ground plane and were radiated by the arc generator at distances of 30 cm to 2 cm. Test levels for the breadboard testing were set at 10 kV and 36 mJ.

The first circuit tested was the analog telemetry conditioning circuit shown in Figure 7. The 100 ohm resistor simulates a temperature sensor and the 1 M $\Omega$  resistor simulates a telemetry encoder input resistance. The encoder is vulnerable because of the high resistance single-ended interface. In operation, a low bandwidth sample and hold circuit is usually incorporated in the encoder to minimize high frequency pickup. The voltage induced at various test points was photographed as the arc generator was moved from 30 cm to 2 cm. Only one wire was in the screen room at a time. The induced voltage was an exponentially damped sine wave lasting approximately 400 nsec. The chart in Figure 7 indicates the maximum peak-to-peak voltage induced when AD was in the screen room. Similar irradiating of the 100 ohm resistor resulted in 110 volts peak-to-peak at 2 cm at the bridge input. In all cases there was no damage and no circuit latch up. The high voltages induced in the 1 M $\Omega$  resistor indicated that damage to a telemetry encoder was possible.

The next circuit tested was a digital interface shown in Figure 8. The twisted pair interconnecting harness was radiated at distances from 30 cm to 2 cm. The induced voltage again was 20 MHz with a 400 nsec duration. The maximum peak-to-peak voltage is shown in the chart on Figure 8. At distances to 7 cm there was no circuit malfunction. At 2 cm the circuit malfunctioned. Considering the + input of the LM 139 receiver, the negative excursion of the ringing was clamped by the diode across the 100k resistor; however, the positive excursion of the ringing pulled the + input above the supply voltage and excited a parasitic mode. The receiver was upset for 400  $\mu$ sec. The receiver was not damaged and subsequently functioned normally. Wrapping the harness with 3 mil copper foil reduced the ringing amplitude at G to 45 volts and eliminated the spurious response.

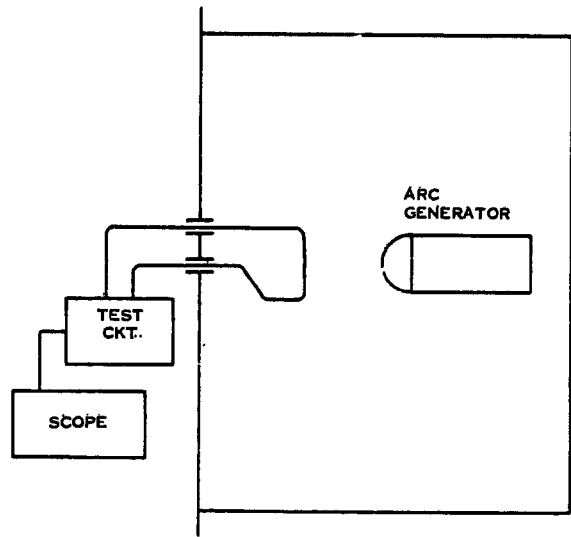


Figure 6. Circuit Test Setup

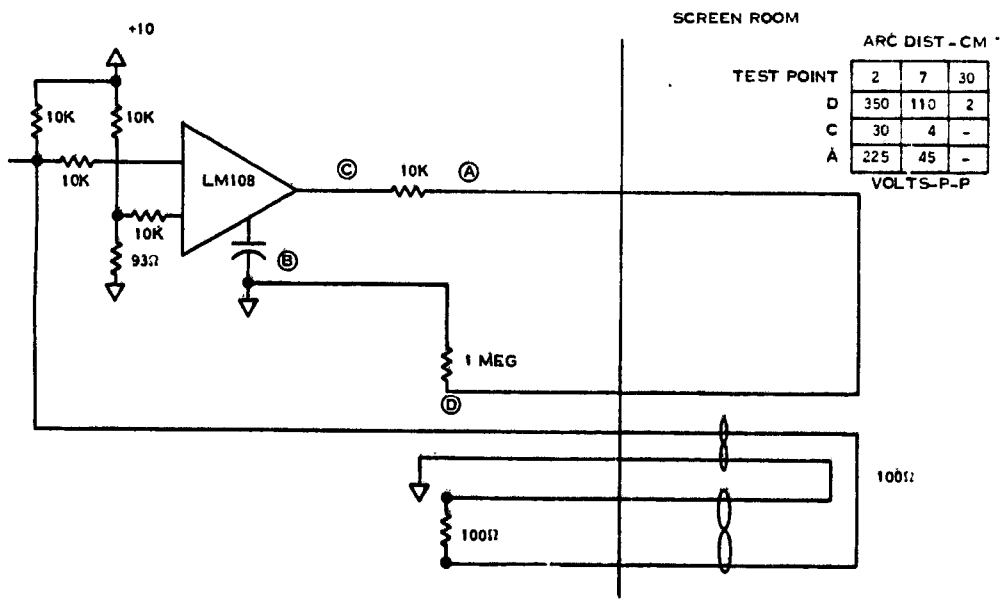


Figure 7. Analog TLM Conditioner CKT

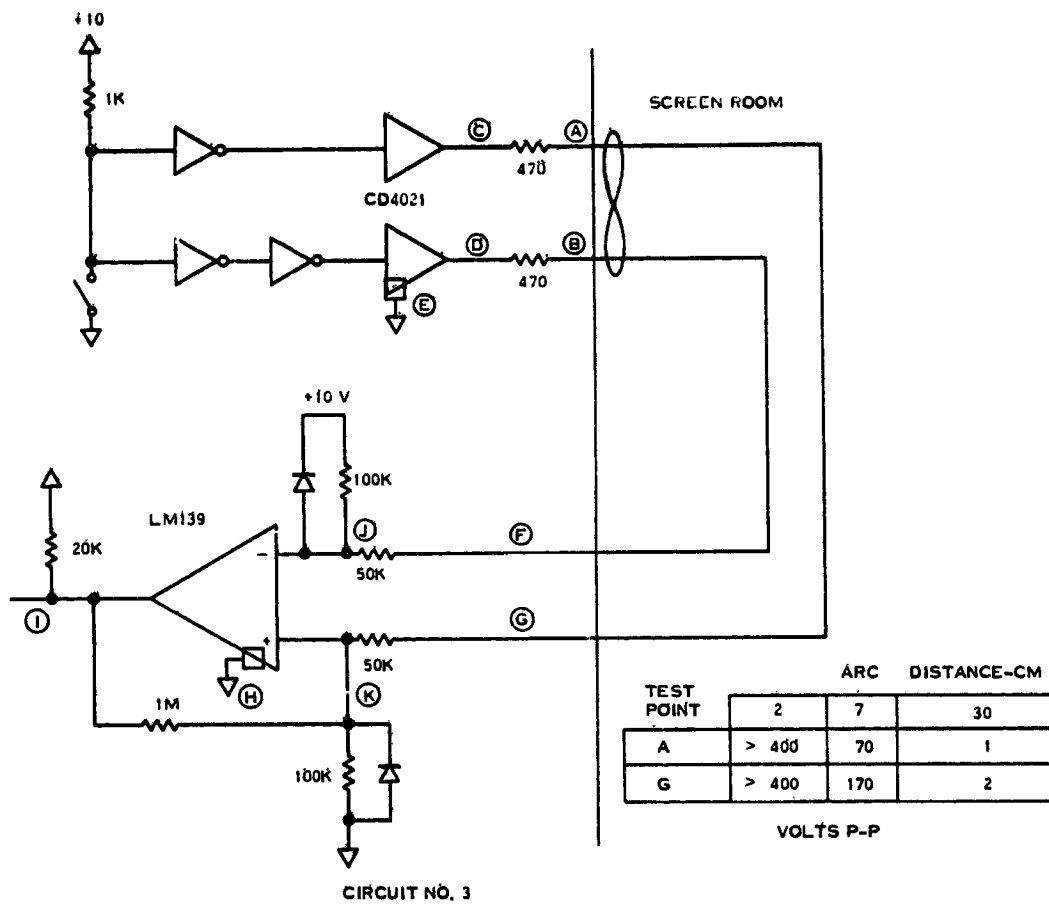


Figure 8. Digital Interface CKT

### 3.2 Satellite Electrical Model Testing

After completion of the breadboard tests, a test was conducted on a satellite electrical model of a communication satellite currently under development. Figure 9 is a diagram of a typical satellite electrical model. These models are built with engineering model components. The harness is flight-like, but is unshielded. A heavy sheet of aluminum foil is mounted on the underside of the table and all boxes are electrically bonded to the ground plane. Performance of the satellite electrical model is monitored via a telemetry link to a test ground station. The test procedure was to radiate all harness segments, box interface connectors, and box surfaces at distances from 30 cm to 2 cm. The arc source was set at 13 kV and 455 mJ.

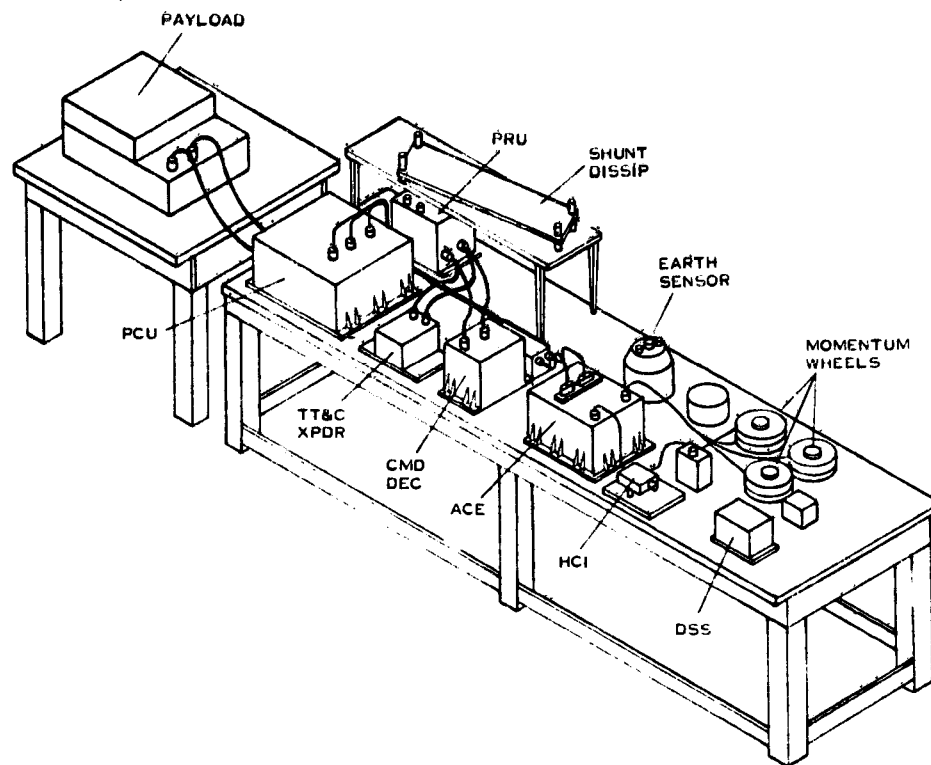


Figure 9. Typical Satellite Electrical Model

When the arc source was more than 7 cm from the hardware, there was no noticeable effect on system performance. At 2 cm the telemetry encoder lost frame sync. There was no upset of the serial digital interface circuit. This was attributed to the shielding effect of other wires in the harness bundle. Transient anomalies were recorded on two telemetry readings. The command system was unaffected at 2 cm arc distance. The PIN diodes in the transponder experienced a transient gain change, but quickly returned to normal operation.

#### 4. SUMMARY.

At arc distances greater than 7 cm, there was no effect on circuit or electrical satellite model performance. At 2 cm, upsets but no damage was experienced. The testing was severe; however, there is no assurance that we over-tested. Clearly, the efforts to understand and characterize the charging phenomena must continue so that meaningful test levels can be established.

## Contents

1. Introduction	815
2. System Design Features	816
3. Test Development Considerations	818
4. Skin/Structural Current Estimates	820
5. Coupling Approaches	822
6. Summary	827
References	828

## 9. Qualification Model Spacecraft Tests for DEMP, SGEMP, and ESD Effects

E. Paul Chivington and Peter J. Madle  
TRW Defense and Space Systems Group  
Redondo Beach, Calif.

Peter H. Stadler  
Space and Missile Systems Organization  
Los Angeles Air Force Station, Calif.

### 1. INTRODUCTION

This paper describes the development of a satellite design demonstration test program. The test is planned in lieu of a dispersed electromagnetic pulse (DEMP) test at the ARES facility. The test approach is comprehensive in that it includes the effects from electrostatic discharge (ESD), system generated electromagnetic pulse (SGEMP), as well as DEMP. The comprehensive test concept is based on the similarity of the satellite's responses to the several environments.

The original FLTSATCOM hardness demonstration approach was to test the qualification model spacecraft in the ARES facility to a simulated DEMP environment. The revised test concept focuses on inducing the predicted effects from several environments, rather than exposing the system to a simulation of only one of the environments.

The approach has some risks because one must not only predict the environment but also the effect of the environment. However, the alternate approach,

simulating the environment, also has risks. The compromises which are made in the construction of simulators lead at best to an approximation of the desired environment. Thus, not only are simulators themselves approximations, but the cost associated with a sequence of tests at several different simulators will be large. It was decided to assess system survivability by using a sequence of effect simulations from the several predicted electromagnetic environments.

The degree to which test objectives can be satisfied by an alternative test approach was fundamental in the test selection process. The purpose of these tests is to demonstrate proper operation while the system is subjected to the predicted effects of the environments. This "simple" objective was motivated by the fact that a complex sequence of subsystem responses and interactions constitutes "system operation." As long as the objective is satisfied, some liberties with the environmental simulation itself may be justified. This is particularly valid if environmental interactions lend themselves to first order coupling analysis involving some operationally passive subset of the total system (Faraday cage structure).

## 2. SYSTEM DESIGN FEATURES

Figure 1 depicts the major FLTSATCOM communication customers. FLTSATCOM is being built by TRW under SAMSO contract, with the Navy acting as the funding and executive agency. Both the Navy and the Air Force will enjoy the benefits from FLTSATCOM capabilities. The Navy high priority FLTBROAD-CAST mode consists of a single (redundant) channel providing communication from command facilities to the fleet at large. Similarly, the Air Force is assured a critical communication link with its strategic forces. Both services are furnished an additional number of routine communication channels, the relay channels. Finally, FLTSATCOM provides a wideband channel intended for presidential communications.

FLTSATCOM's construction features, characteristic of a three-axis stabilized spacecraft, are shown in Figure 2. Both receive and transmit antennas, as well as the solar panels, deploy after separation from the ATLAS-CENTAUR launch vehicle. Thermal control of the vehicle is provided by second surface mirrors, paints, and multilayered aluminized mylar and kapton blankets. Significant for the following discussion is the fact that the vehicle itself is constructed as a leaky Faraday cage. The lower, or equipment bay, internally separated from the upper,

ORIGINAL PAGE IS  
OF POOR QUALITY

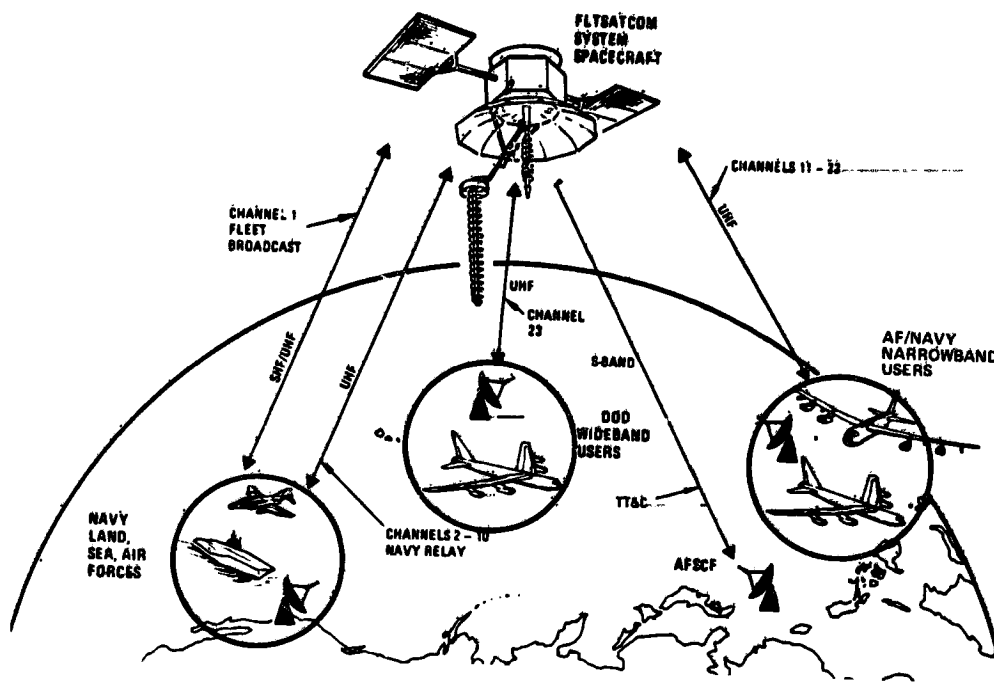


Figure 1. FLTSATCOM Communications Customers

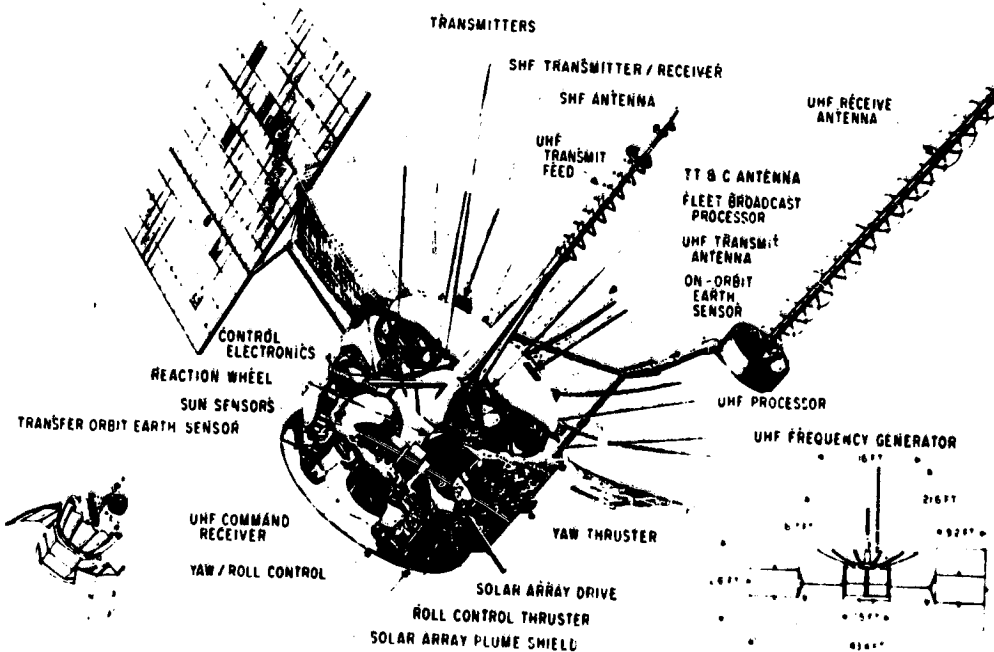


Figure 2. FLTSATCOM Design Features

or payload bay by a shelf, consists of honeycomb panels and a titanium lined rocket motor acting as close-out for electromagnetic signals. The payload bay, housing the transmitters and receivers, is formed by the separating shelf, similar honeycomb sidepanels and the UHF antenna center dish (connected via four braided groundstraps to the panels). Primary areas of concern from a spacecraft charging point consist of the solar panel surfaces and the dielectric surfaces of the thermal blankets and mirrors covering the sides. Major points of entry for electromagnetic energy are the solar boom penetration points and the thermal blanket covered area between the spacecraft body and the large UHF antenna.

### 3. TEST DEVELOPMENT CONSIDERATIONS

Figure 3 illustrates the significant electromagnetic environments. Electrostatic discharge results from the build up of electrons on the surface of dielectrics such as the thermal blankets. When the electric field builds up to the material's breakdown strength, an arc occurs through or at an edge or corner of the thermal blanket. In response to a DEMP, structural currents are excited by the incident electromagnetic wave. In addition, when the spacecraft antennas are tuned to

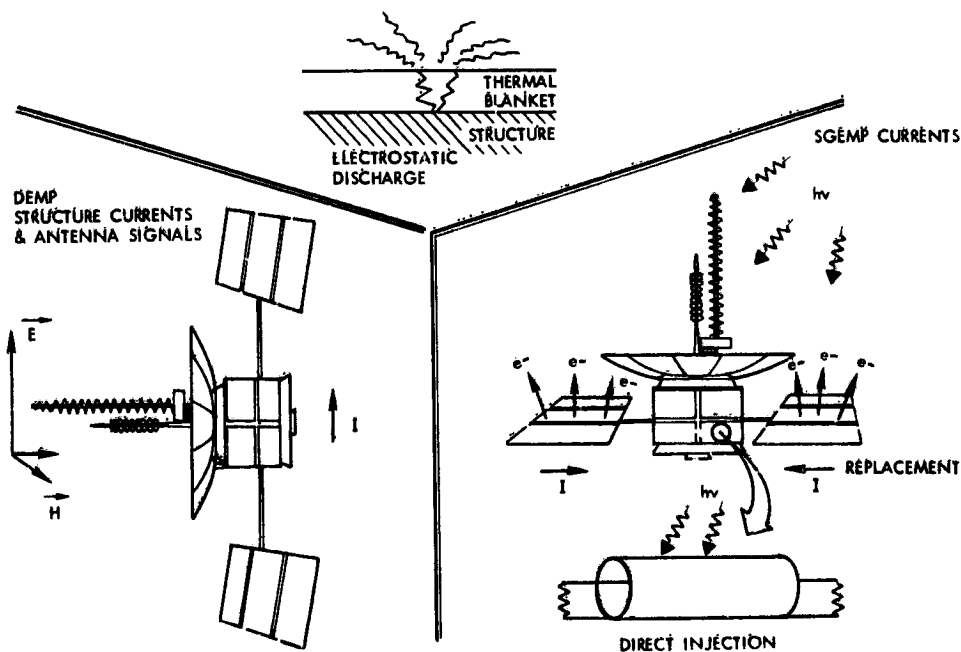


Figure 3. Spacecraft Electromagnetic Environments

frequencies present in the DEMP spectrum, currents are coupled directly into the communications electronics. There are at least three modes of SGEMP response: external replacement currents, direct injection currents on cables, and internal cavity fields. Figure 3 shows the external replacement currents caused by the redistribution of electrons on the spacecraft. Incident photons liberate electrons causing a charge imbalance which must be equilibrated. Direct injection currents result from the interaction of photons with cables. These latter currents will dominate in a well rf shielded system.

For the different environments, key common parameters used to develop a comprehensive test are summarized in Table 1. Note in particular the fact that no requirement to design for the spacecraft charging/discharging environment had been placed on the contractor. Note also that the environment now generally accepted to result in the smallest coupled currents was a design requirement, and the only environment against which the design was to be tested. Peak currents estimated to flow on external surfaces are summarized for each environment. The cable core current from direct photon deposition (cable injection) is listed separately. Also given are the test facilities which were considered. The confidence statements express not only the degree to which coupling estimates were considered valid, but say something about the difficulties anticipated in conducting each test (measured both by the effort required to develop the test technique, and by the degree of design stress evoked by each test).

Table 1. Summary of Phenomenology and Program Considerations

Environment	Requirement	Primary Response/Levels	Test Beds	Confidence
DEMP	Design/Verification	Field Coupled Skin Currents 10 A/Long	ARES Skin Injection	Good
SGEMP	Design	Skin Currents 200 A/Short  Direct Injection 10 A/Short	Photon Source (Low)  Cable Injection	Good
S/C Charging	None	Skin Currents 50-1000 A/Med	Arc Discharge Skin Injection	Fair

If the contention that the FLTSATCOM design affords significant shielding from externally induced environmental effects is valid, it remains only to demonstrate design adequacy to the relatively large photon direct injection currents. Tests exposing cables to a low energy photon source have demonstrated that our estimates of this effect are good to a factor of probably two. Since the effects from these environments will result in transients on cables, it is efficient to couple transients directly to the system via the cable harness of the operating qualification model spacecraft. Whether it is necessary to couple currents to the entire harness simultaneously, or whether a systematic investigation of all interconnections, or even a sample of those, is adequate, depends a great deal on the functional autonomy of the boxes linked by the cables and the similarity of the circuits used throughout the system.

It is necessary to verify the assumption that the vehicle does provide good shielding. This is best done by inducing skin or structure currents and verifying that the cable response is as low as predicted, or at least lower than what will be used during the cable harness direct injection tests.

#### 4. SKIN/STRUCTURAL CURRENT ESTIMATES

Two aspects of the electromagnetic environments have been studied in order to describe the spacecraft's response. The first aspect, particle kinematics, permits the description of a driving function for each environment. The second aspect, lumped element modeling, incorporates the drivers into an equivalent electrical circuit for the spacecraft.

Lumped element electrical circuits of the spacecraft have been created for the various environments. These consist of resistors, capacitors, inductors and sources, and have varied widely in complexity. A model of the spacecraft for SGEMP response is shown in Figure 4. The spacecraft has a capacitance to infinity for each of the selected nodes. The nodes are connected by inductances to a number of nodes since phase delay effects will be important. Space charge limited current drivers from the solar panel are connected in parallel with the capacitance to infinity to represent the loss of electrons.

Using the models described above, estimates have been obtained for the DEMP, SGEMP, and ESD surges. Various groups have computed the response and because of differences in modeling assumptions the results vary somewhat. The composite results are plotted in Figure 5.<sup>1</sup> The high frequency characteristic exhibited by the SGEMP reflects the short rise time of the x-ray pulse, and the low frequency content is due to the unipolar time history of the pulse. The DEMP has a low frequency cutoff due to ionospheric absorption of the low frequencies.

ESD surges are generally thought to be somewhat slower than SGEMP transients and may have a dc component.

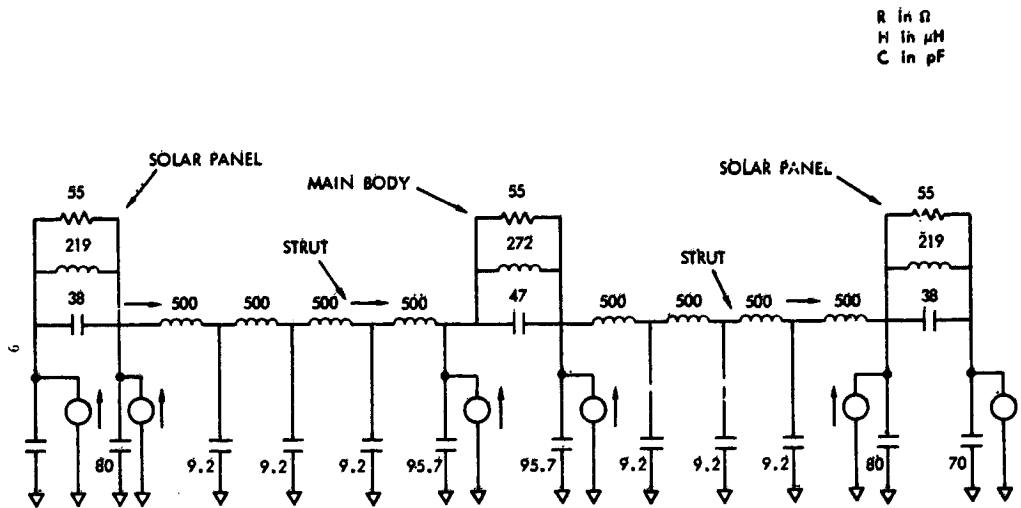


Figure 4. FLTSATCOM Model Used for SGEMP Excitation

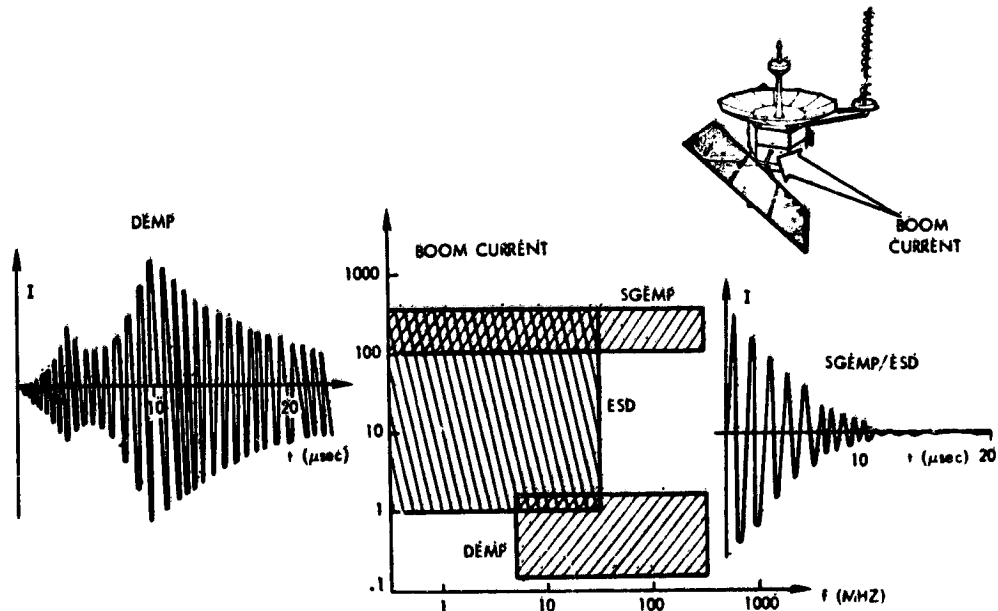


Figure 5. Electromagnetic Environment Characteristics

## 5. COUPLING APPROACHES

Two test techniques are being developed to simulate the SGEMP and ESD coupled skin currents. A parallel effort is investigating simulation of direct injection into cables. The technique for driving SGEMP replacement currents was suggested by Mangan, et al.<sup>2</sup> There are two virtues of the technique. One, the technique requires no direct electrical connection to the spacecraft. Two, the technique produces surface current responses that agree favorably with SGEMP predictions. In the technique, plates are used to capacitively couple currents to the spacecraft structure. The spacecraft is dielectrically isolated from ground by use of a wooden support structure. Figure 6 shows the skin injection test setup. The functional performance of the spacecraft will be monitored through the telemetry and communications links. This diagnostic approach maintains the dielectric isolation from ground. Additional response data will be collected on external boom and internal spacecraft cable currents. These measurements will be made with a microwave data link which uses dielectric waveguide to couple the modulated X band carrier.

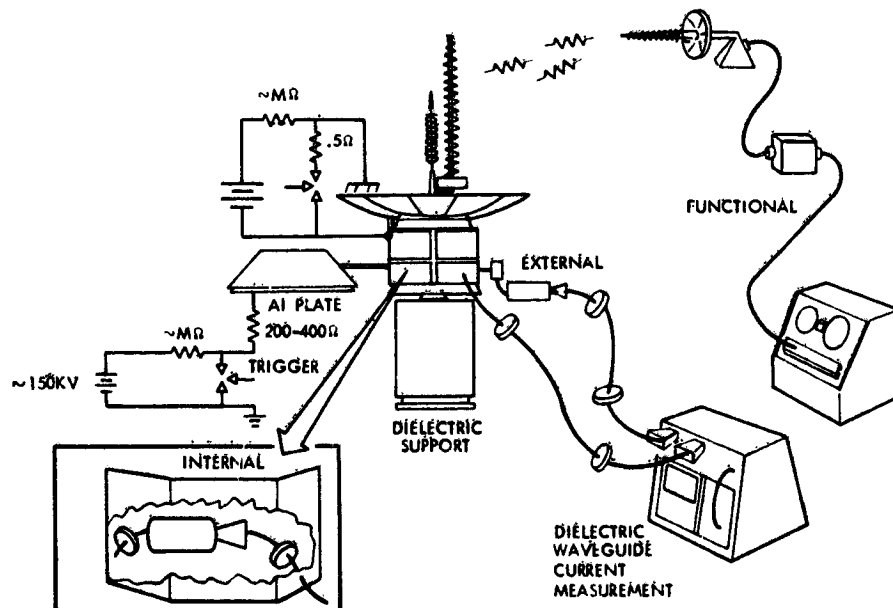


Figure 6. Skin Injection Tests (SGEMP/ESD)

A simplified electrical circuit of the replacement current drive technique is given in Figure 7. Either one or two drive plates can be used depending on the mode to be simulated. The capacitance between the drive plate(s) is charged to approximately 60 kV. A triggered spark gap is used to discharge the capacitor through the 200 $\Omega$  resistor to ground. Upon discharge, a boom current will flow and depending on whether one or two drive plates are used, the spacecraft symmetric or antisymmetric mode will be stimulated.<sup>3</sup>

The test setup pictured on Figure 6 will also be used for the arc discharge simulation. Spacecraft isolation is required and will be afforded by a wooden support, the radiating telemetry and communications links, and the dielectric waveguide coupled microwave transmitters to measure currents. The major difference between the two tests is the method of simulating the environment. The arc discharge driver provides more localized coupling. The simulation will be used to induce discharge currents at a number of different locations around the spacecraft while harness bundle currents and functional performance are monitored. A sheet of copper foil will be placed over the dielectric material to simulate the layer of electrons which would be collected in the space environment. The copper foil will be charged to a voltage near the predicted breakdown level with respect to spacecraft structure. The discharge will be created by a triggered spark gap at representative arc location. An equivalent circuit for the arc discharge simulation is shown in Figure 8. Figure 9 is a waveform obtained on a prototype of the pulser to be used during the FLTSATCOM tests. The waveform characteristics are controlled by the area of the copper foil (capacitance), lead inductance, and the discharge resistance.

The third type of test which will be performed during the FLTSATCOM test program will simulate SGEMP direct injection currents. These tests differ from the replacement current and arc discharge tests in that dielectric isolation is not required. Currents will be injected directly onto the spacecraft signal lines inside the cable shields simulating the SGEMP direct injection mode wherein the shielding does not provide any protection. This will be the severest test of spacecraft hardness to upset and permanent damage since, based on predictions and test data, the injection levels will be on the order of amperes.<sup>4</sup> The coupling method into spacecraft signal lines is shown in Figure 10.

ORIGINAL PAGE IS  
OF POOR QUALITY

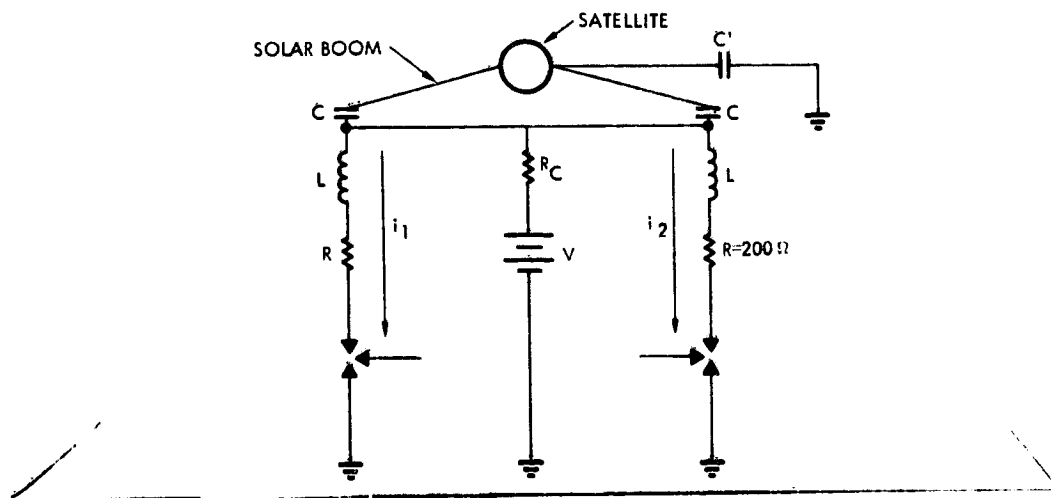
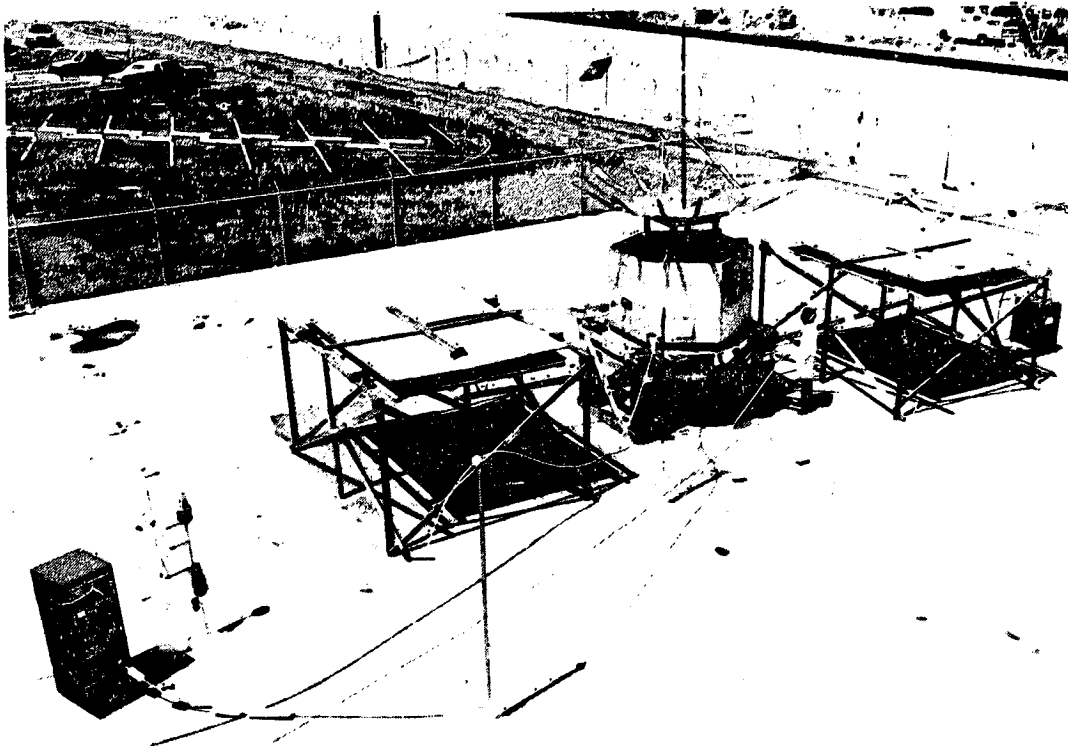
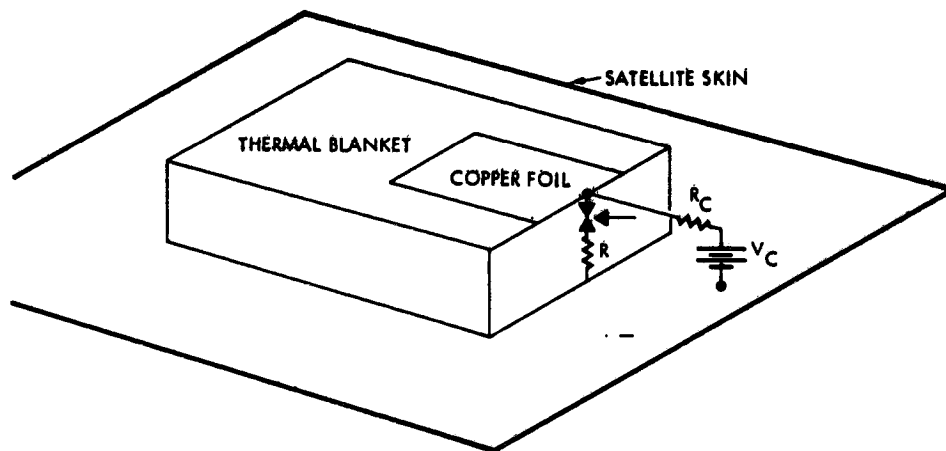
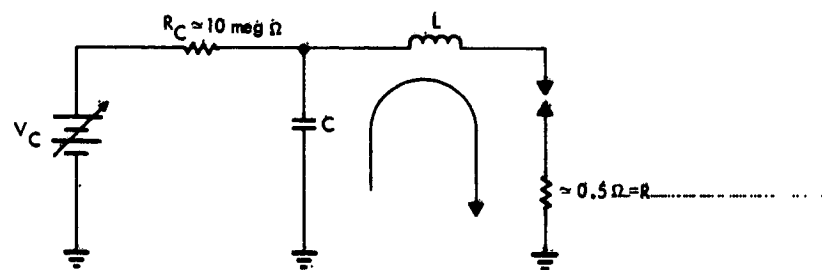


Figure 7. SGEMP Replacement Current Test Setup (with Spacecraft Mockup) and Equivalent Circuit Showing Drive Technique



ARC DISCHARGE PULSER PLACEMENT



EQUIVALENT CIRCUIT

- $V_C$  = CHARGE VOLTAGE
- $R_C$  = CHARGE RESISTOR
- $C$  = CAPACITOR FORMED BY COPPER FOIL & VDA
- $L$  = GAP & STRAY INDUCTANCE
- $R$  = LOAD RESISTOR

Figure 8. Equivalent Circuit for ARC Discharge Technique

ORIGINAL PAGE IS  
OF POOR QUALITY

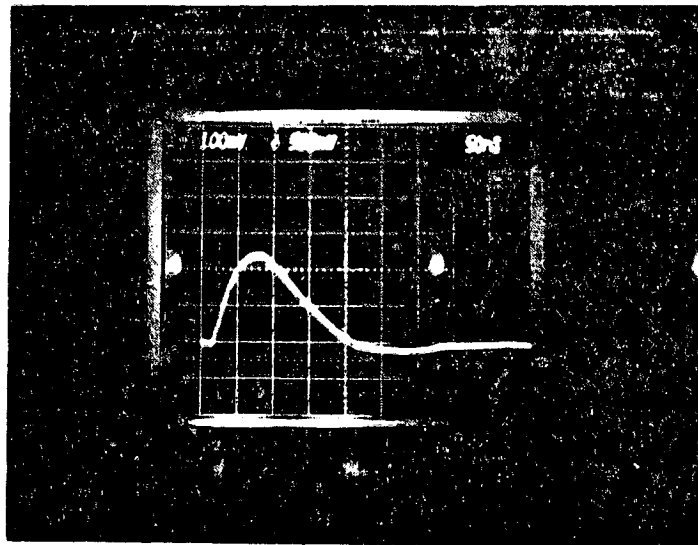
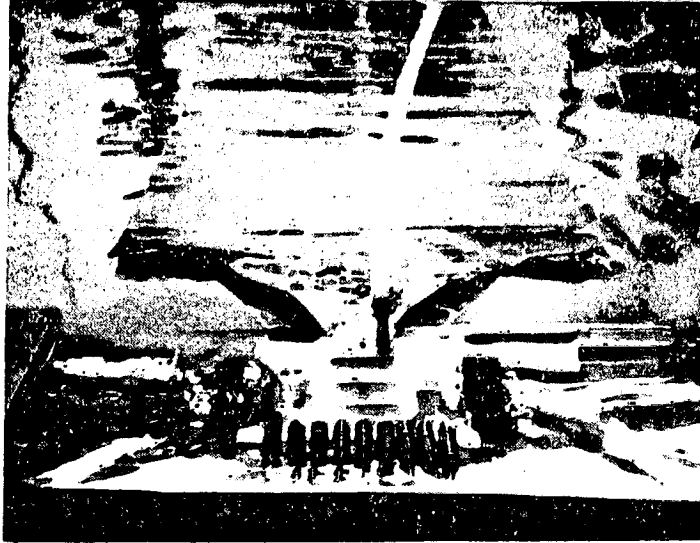


Figure 9. Prototype ARC Discharge Pulsar and Wave-  
form Obtained. Charge voltage -5 kV, discharge  
résistance -0.5 $\Omega$ , copper foil - 1 m  $\times$  0.3 m, thermal  
blanket -0.008 cm thick

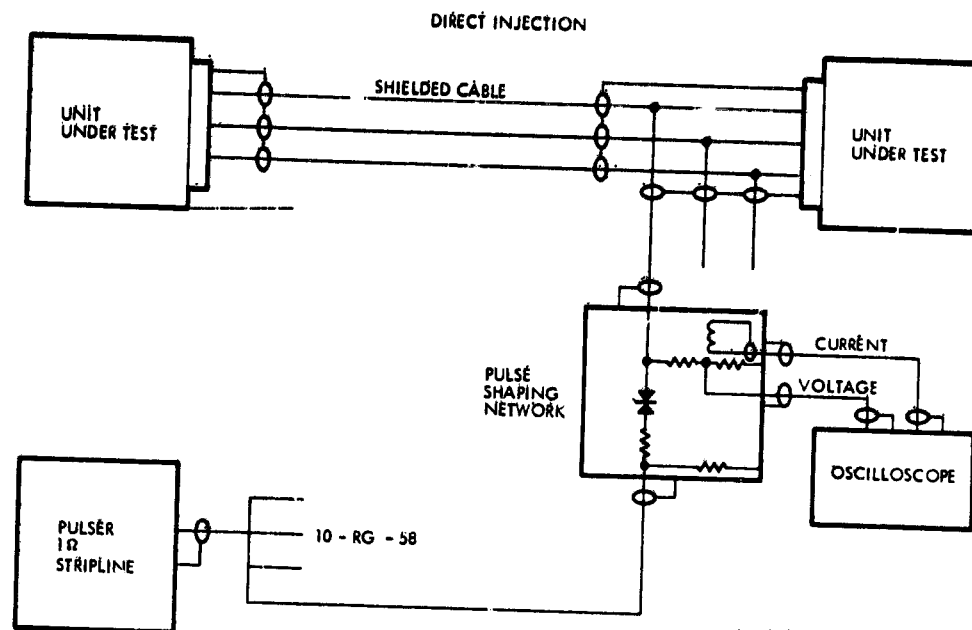


Figure 10. Direct Injection Coupling Technique

## 6. SUMMARY

We have described a test program which will serve to evaluate a spacecraft design hardened to DEMP, SGEMP, and ESD effects. One of the elements of the program is the injection of skin currents onto the qualification model spacecraft. The other element is the direct injection of currents into the cable harness. Although direct injection currents are expected to be the dominant coupling mechanism, this assumption will be confirmed by measuring harness currents during the skin injection tests simulating external DEMP, SGEMP, and ESD effects. The tests have two significant characteristics. First, the spacecraft will be live and operating so that performance anomalies will be detected at the systems level. Second, the effects of the photon and electron environments will be induced, no attempt will be made to recreate the environment itself.

## References

1. Webb, R. M. (1976) Minutes of FLTSATCOM Spacecraft Charging Meeting, 4733.76-45, TRW Defense and Space Systems Group.
2. Mangan, D. L., and Perala, R. A. (1975) Satellite SGEMP Surface Current Simulation Techniques, AMRC-R-50, Mission Research Corp.
3. Sheppard, T. J. (1976) Electromagnetic Excitation by Capacitively Coupled Current Injection, 27228-3003-RU-00, TRW Defense and Space Systems Group.
4. Fitzwilson, R. L., et al (1975) Radiation induced currents in shielded multi-conductor and semirigid cables, IEEE, Trans. on Nuclear Science 21(No. 6): 276-283.

**Contents**

1. Introduction	829
2. Description of the Various Types of Anomalies	831
3. Correlation With Ground Based Geomagnetic Activity Indices	832
4. Seasonal and Local Time Correlations	837
5. Correlation With the Day of the Week	841
6. Long Term and Progressive Effects	843
7. Summary and Conclusions	846
Acknowledgments	847
References	847
Appendix A	849

## 10. Spacecraft Charging Anomalies on the DSCS II, Launch 2 Satellites

George T. Inouye  
TRW Defense and Space Systems Group  
Redondo Beach, Calif.

### Abstract

Six different types of anomalous events have occurred on two DSCS II satellites. The total number of events, over 100, and the long operational period, nearly 3 years, permits some statistical analyses to be performed. Correlation of occurrences of particular types of anomalies with equinoxes and seasons of the year are consistent with a spacecraft charging model. On the other hand, an interesting correlation of occurrences with days of the week has been found. Finally, a long term diminution in the frequency of occurrence of events has been observed, and is discussed in terms of environmental activity, material degradations and the need for more data.

#### 1. INTRODUCTION

The DSCS II Launch 2 satellites, 9433 and 9434, were launched on 13 December 1973 and nearly 3 years of operational data are now available for these two geosynchronous orbit spacecraft. Figure 1 shows the longitudes of the two satellites from initial orbit insertion to final operating positions, one over the Atlantic and the other over the Pacific Ocean. Also shown are the occurrences of the anomalous events during the first few months. Over the 33 month period since launch, over

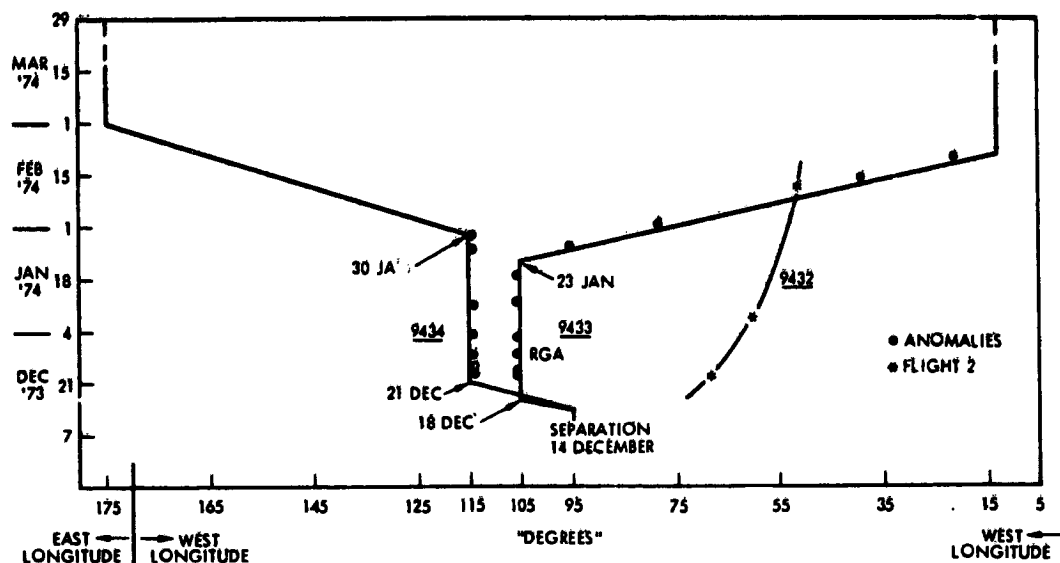


Figure 1. 9433/9434 Orbital Position

100 anomalous events have been observed. These events, rather than being of a single type, have been manifested in six different types of anomalies occurring in different locations on the spacecraft as well as in affecting different operating circuits at these locations.

The conclusions to be drawn from the results to be presented in this paper are that much further work, both in the Laboratory and in orbit, needs to be performed in the areas of spacecraft design and immunity verification testing. Studies that should be implemented run the gamut of materials' characterizations to analysis and test of specific spacecraft configurations. Finally, simplified in-flight monitoring of charging/discharging in the housekeeping telemetry of all geosynchronous satellites would serve as an invaluable diagnostic in the eventuality that anomalous events do occur. Our experience on the DSCS satellites has been that a great deal of effort was required to identify the sources, of anomalous behavior, whether internal or due to the ambient environment.<sup>1-7</sup> In the final analysis, in spite of concentrated "detective work," some of the conclusions that the environment was the most likely causative source were arrived at by an elimination process rather than by a more direct approach because of the lack of diagnostic data.

## 2. DESCRIPTION OF THE VARIOUS TYPES OF ANOMALIES

The first type of anomalous behavior, the anomalous firing of the reset generator assembly (RGA upsets), was evidenced on the Launch 1 pair of satellites. Analysis of these events by Fredricks and Scarf<sup>8</sup> led to the first realization that these events were related to the hot plasma environment of the geosynchronous orbit rather than to any internal malfunction within the spacecraft itself. Once identified, these anomalies were eliminated on the Launch 2 payloads by appropriate redesign except for a single recurrence which can be accounted for by the galactic cosmic ray environment. Figure 2 is an exploded cut-away view of the spacecraft. On top is the despun section containing the communications antenna array and most of the associated electrical hardware. "Despinning" permits the antennas to be continuously pointed towards the earth while the main spinning portion provides attitude stability. The spin axis is oriented to be parallel to the earth's polar rotational axis. The cylindrical outer shell of the spinning section is covered in with solar cells in eight sections or panels. On the spinning platform are located the supportive electrical hardware such as the power conditioning, housekeeping telemetry, and attitude control subsystems. The RGA associated circuitry is also located on the spinning platform.

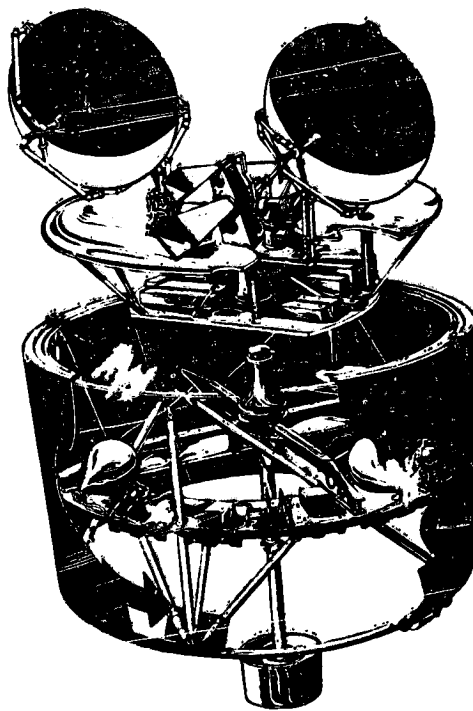


Figure 2. DSCS II Configuration

With the despun platform in place, the only access paths for ambient plasma and sunlight into the spinning platform cavity are the annular opening on top between the spinning and despun sections, eight slits between solar array panels, and portholes used for sensors and for attitude control thrusters in four of the solar array panels. The pressure transducer which failed during the first equinox season on Flight 4 (9434) is also located on the spinning platform as is the hardware associated with the spin type anomalies ("S"). The "S" events are also equinox related. All of the remaining types of anomalies, the anomalous activation of the Tunnel Diode Amplifier Logic, power converter switching and gimbal reset (the "T," "C" and Gimbal anomalies) are associated with circuits contained in an electronic unit located on the upper despun platform.

All of the anomalous behavior observed, aside from that of the pressure transducer, were the result of the upsetting of the state of bistable logic circuits, flip-flops, which could be caused by arc discharges in the near vicinity of the relevant electrical hardware. The ability of simulated arc discharges to cause all of the observed varieties of logic upsets has been demonstrated on a prototype (qualification model) spacecraft. It has been demonstrated that it is the coupling of arc discharges to the lines entering the various electronic boxes via the connector which causes the logic circuit upsets rather than any electromagnetic signals entering through the walls of the boxes. In the case of the pressure transducer, it was determined that nearby arc discharges could cause its failure in the manner observed in orbit. The failure mode is one in which the sensor does not recover, and therefore occurs only as a one-time event.

Of all of the various types of anomalies, the "S" were the potentially most serious, having to do with the spacecraft spin or despun rate control. After the fourth S-event, false command countermeasures were instituted. Thus, the problem was solved operationally, but at the same time the solution eliminated the possibility of obtaining additional data of the type discussed here.

### 3. CORRELATION WITH GROUND BASED GEOMAGNETIC ACTIVITY INDICES

The geomagnetic activity indices, the daily A-Index from Anchorage, Alaska and Fredericksburg, Virginia are the most easily accessible measure of disturbances in the geomagnetic field. The relationship between geomagnetic substorms, the resulting hot plasma environment at synchronous orbit altitudes, and ground-based measurements is a subject of current research. Figures 3-5 are plots of these A-indices over the 33 month period from launch to the present. The occurrence of anomalous events are shown at the top of these figures with a 24 hr vertical scale of local time. The type of anomaly and spacecraft, 9433 or 9434, are

ORIGINAL PAGE IS  
OF POOR QUALITY

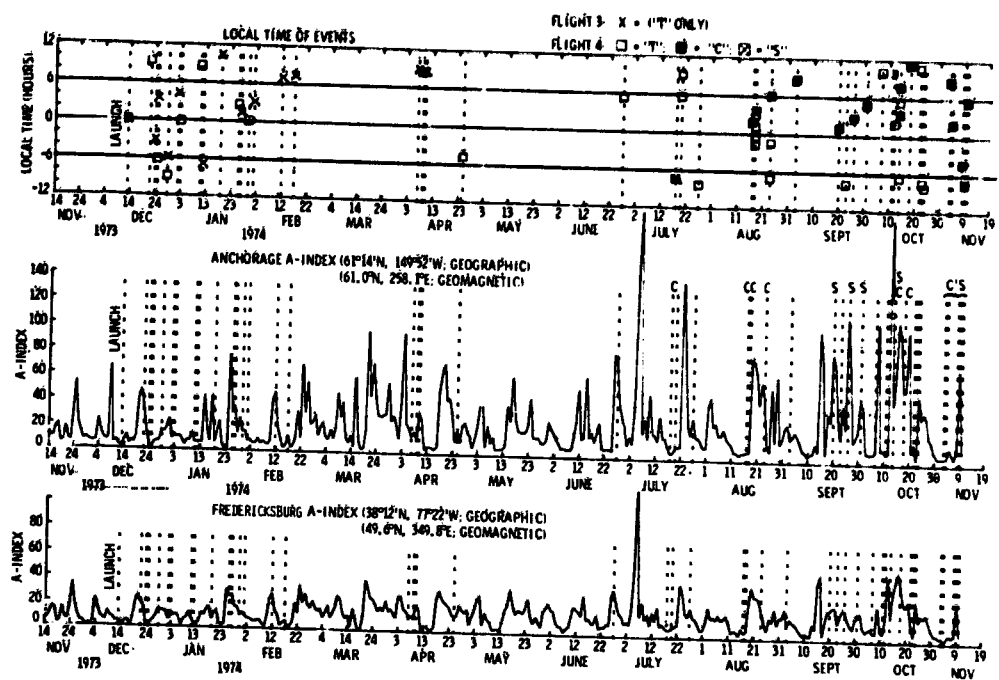


Figure 3. Timing of Events on Flights 3 and 4 and the Daily A-Indices From Fredericksburg and Anchorage for 1974

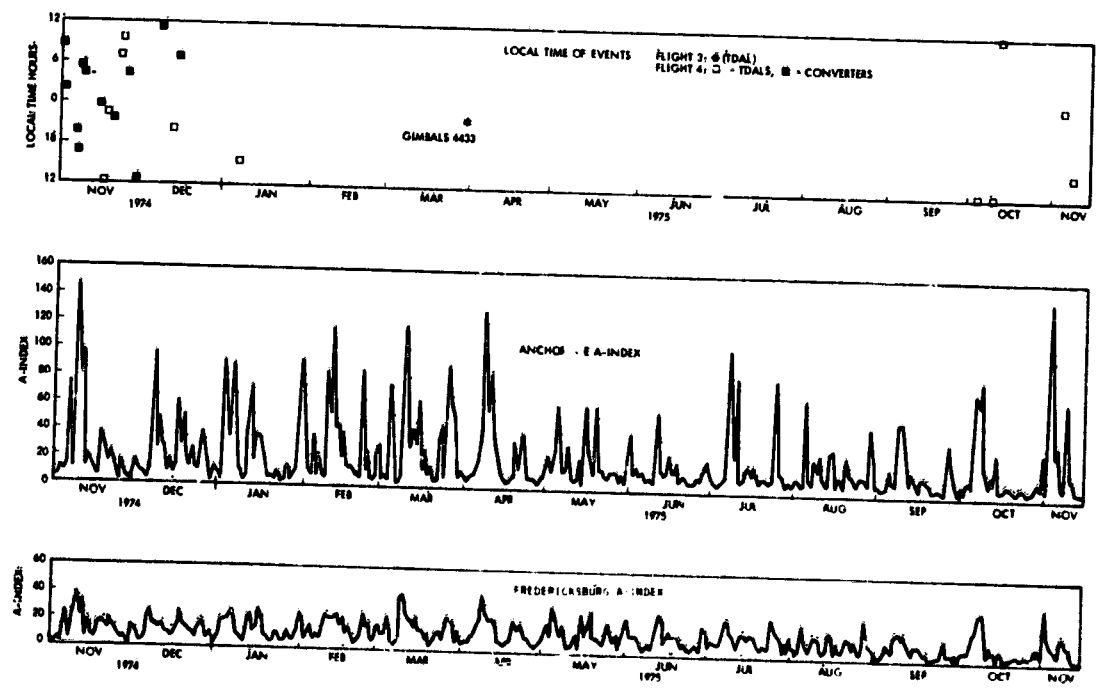


Figure 4. Timing of Events on Flights 3 and 4 and the Daily A-Indices From Fredericksburg and Anchorage for 1975

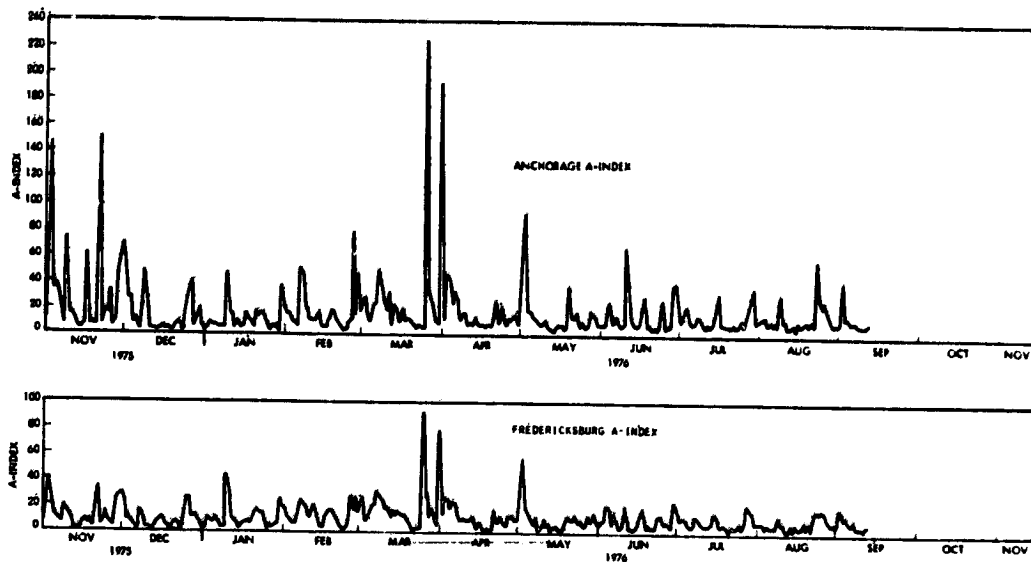


Figure 5. Timing of Events on Flights 3 and 4 and the Daily A-Indices From Fredericksburg and Anchorage for 1976

identified. All of the events are listed with greater detail in tabular form in Appendix A. The following features are most prominent in Figures 3-5:

- (1) There is no obvious correlation of event occurrences with the A-Indices.
- (2) The rate at which anomalies occur decreases with time.
- (3) There are no obvious preferred local times of occurrence.

The first feature, which is the subject of this section, will be discussed now and the other points will be discussed in following sections.

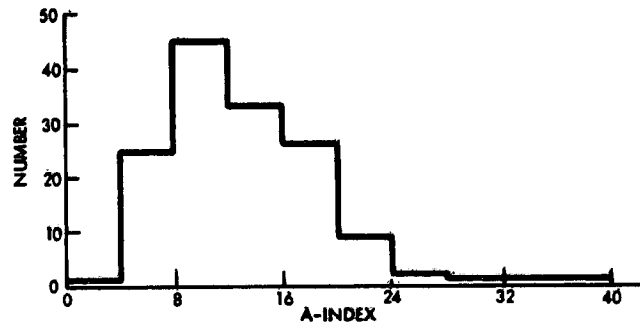
The Fredericksburg A-Index generally shows a lesser variability as well as smaller magnitudes as compared to the Anchorage index. We may surmise that if the latter station, which is more closely related to the geosynchronous orbit, had been located exactly at the "footprint" of the geomagnetic field line passing through one of the satellite positions, a much better correlation with the occurrence of anomalies would have been obtained. It should be noted, however, that the ground position of the footprint associated with a particular geosynchronous longitude is subject to large seasonal and geomagnetic storm induced variations because the geosynchronous altitude is close to the magnetospheric boundary. Geomagnetic substorms, with which the presence of hot plasma and the dearth of cold plasma is associated, are generally short-lived (approximately 0.1-1.0 hr), and are localized in longitude as well as in latitude or altitude. Being located at a lower latitude, the Fredericksburg station's A-Index should be expected to give a better

indication of geomagnetic activity over all longitudes. It is for this reason that this index is used in the following statistical analyses.

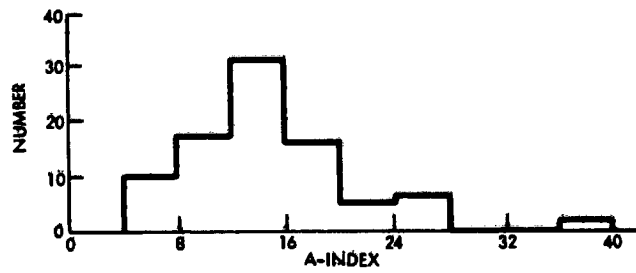
Figure 6(a) shows the number of times that each value of A-Index at Fredericksburg occurred during the 33 month period. Each consecutive 7 day period was averaged to give a single data point, and the A-Index resolution was limited to multiples of four. Figure 6(b) shows the number of anomalies, which occurred in each A-Index group. Figure 6(c) is a histogram of Figure 6(b) divided by Figure 6(a) for each A-group, giving a corrected anomaly distribution which would be obtained if the A-Indices had been equally probable rather than as in Figure 6(a). Figure 6(c) shows a generally increasing trend in which the number of anomalies increased with the A-Index. The bars in Figure 6(c) have been broken down to show the individual contributions of the "T," "C" and "S" type anomalies. The figure does not show any dramatic threshold effect except for the "S" anomalies. The fact that a significant number of events occurred at low A-Index values (4 to 8) is a convincing argument for not pursuing the correlation further in such a crude manner.

Inspection of Figure 3 for the "S" anomalies which occurred in 1974 show that all four of these events did occur on A-Index peaks. Why they occurred on only one spacecraft and only in the fall equinox is not clear. This question of why events occurring on one spacecraft are not correlated with those on the other is unanswered. One possibility is the existence of configurational differences in the sense of spacecraft charging, (grounding of thermal blankets, thickness of vacuum deposited aluminum) of two spacecraft which are ostensibly identical. The other possibility is that there is a statistical variation in geosynchronous orbit environments. Figure 7 shows the geomagnetic latitude variation with geographic longitude. Spacecraft 9434 is at  $-5^{\circ}$  South and 9433 is at  $+6.5^{\circ}$  North. The two spacecraft are located at slightly different L, B points. Lyons et al,<sup>9</sup> for example, show that energetic particle populations and their pitch angle distributions are expected to vary greatly with magnetic L, B values.

a) DISTRIBUTION OF DAILY A-INDEX OCCURRENCES



b) DISTRIBUTION OF ANOMALIES VS A-INDEX



c) (a) DIVIDED BY (b)

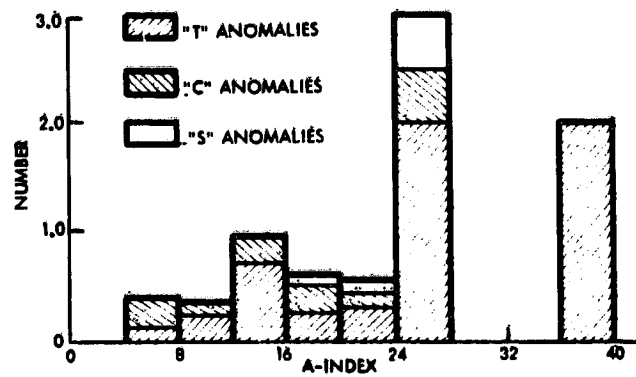


Figure 6. Distributions of Anomalies Versus Fredericksburg A-Index (7-day Averages)

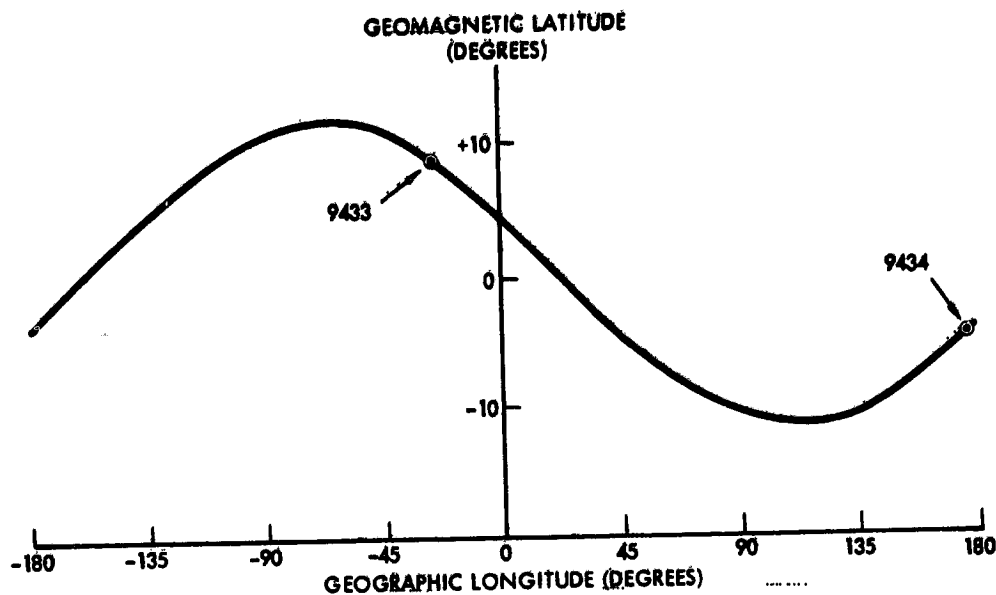


Figure 7. Geosynchronous Orbit Magnetic Latitude Versus Geographic Longitude

#### 1. SEASONAL AND LOCAL TIME CORRELATIONS

As mentioned previously, "S" anomalies have been internally countermanded so that they cannot occur since the fall of 1974. Both the "S" anomalies during the fall equinox and the pressure transducer failure on spacecraft 9434 during the spring equinox of 1974 are consistent with the author's<sup>10</sup> charging model prediction of a large negative spacecraft ground potential during the equinox when the metallic surface area of the spacecraft exposed to sunlight is at a minimum as shown in Figure 8(a). From Figure 3 for 1974 it may be seen that a 49 day period from February 17 to April 7 had no "T" anomalies. During the 1974 fall equinox season a similar period of 39 days lasted from August 24 to October 2 except for a single event on September 23. "C" type anomalies did not begin until July 20 and stopped occurring on December 15, 1974. This type of anomaly has been shown to be more nearly attributable to internal causes than any of the others.<sup>5</sup> Here also, however, a 41 day period from September 3 to October 14 is void of these anomalies. Of the total of nine anomalies occurring during 1975, the two "Gimbal" anomalies occurred on March 12 and 14, and a "T" anomaly on March 31. These three events would tend to invalidate the equinox arguments from the charging model analysis, although the total number of events is much smaller than for the first year. During 1976 not a single anomaly has been observed so far.

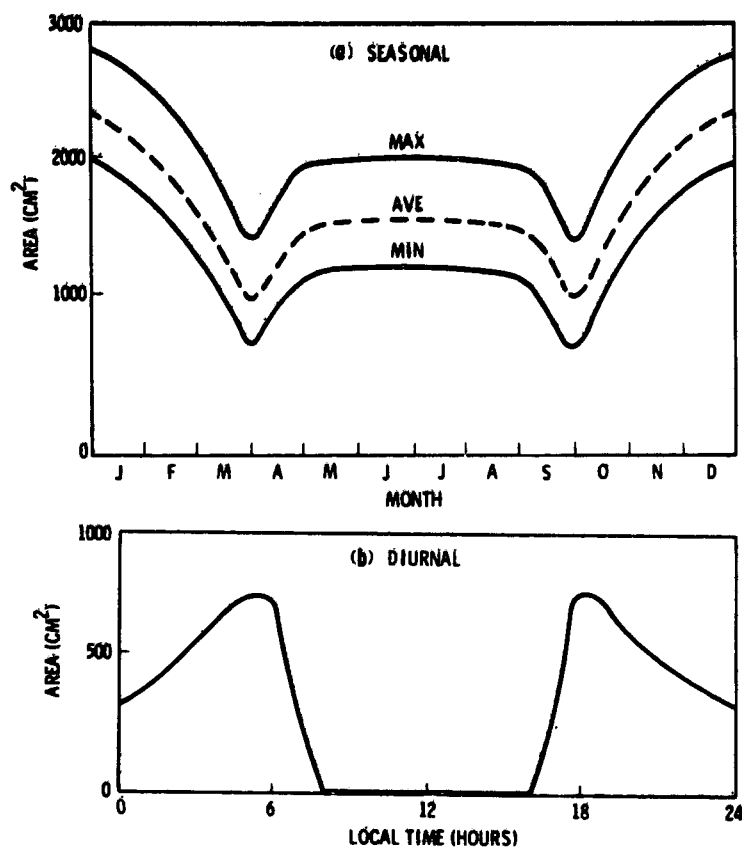


Figure 8. Seasonal and Diurnal Variation of Metallic Surface Areas Exposed to Sunlight

The comparison of the timing of anomalous events with local time may be examined in Figure 9. The results published by Fredricks and Scarf<sup>b</sup> on the analysis of anomalous events on the Launch 1 DSCS satellites showed an excellent correlation (19 out of 23 events) with geomagnetic substorms. In particular the occurrence of anomalies during the midnight/dawn sector of local time was very convincing evidence of an environmental origin. "C" anomalies occurring within an hour of any initial event have been eliminated in the statistics. This accounts for the fewer number of events plotted in Figure 10 than are listed in the Appendix. The four "S" anomalies, as in their A-Index correlation with expected behavior, seem to meet the test of occurring during the midnight/dawn local time sector. The "T" and "C" anomaly distributions do not meet this test although the midnight/dawn sector seems to be somewhat more favored, particularly with the "C" anomalies. The most prominent features of the "T" anomaly distribution are a

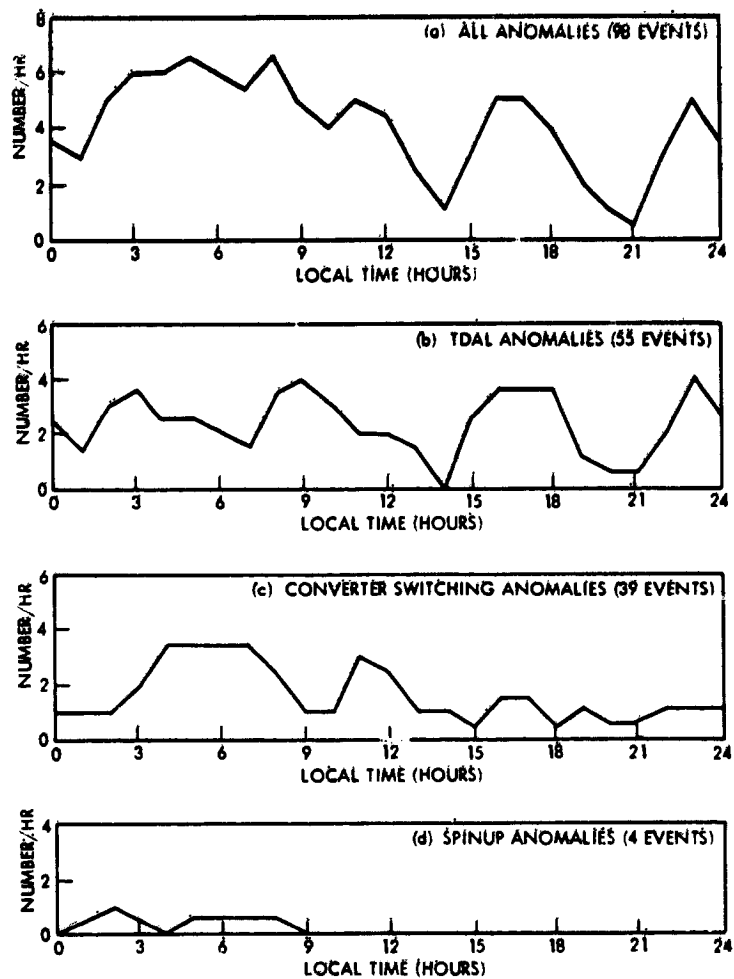


Figure 9. Distribution of Anomalous Events on DSCS in Local Time

fairly deep minimum near local noon and slightly enhanced peaks or "wings" a few hours before and after the dip. Figure 8(b) which shows the diurnal variation of the spacecraft metallic surface area exposed to sunlight also has these features. The minimum around local noon occurs when the despun antenna array is pointed away from the sun, and the dawn and dusk maxima occur when the sunlight impinges broadside on the six waveguide struts in front of the two large dish antennas. At local midnight the sunlight hits the waveguides directly on the narrower of its two-cross-sectional dimensions. The maximum/minimum lines on Figure 8(a) for the seasonal variation represent the excursions due to the diurnal variation. The latter is a significant fraction of the former, especially during the equinoxes.

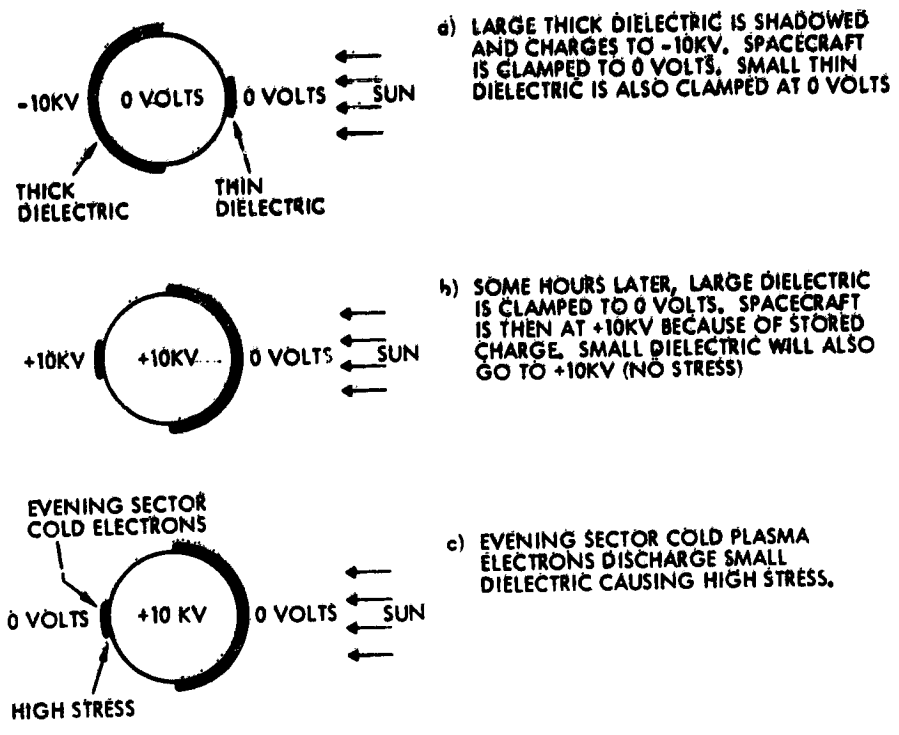


Figure 10. Hypothetical Mechanism for Generation of Afternoon/Evening Time Sector Arc Discharges

The "T" and "C" anomaly distributions suggest that a combination of environmental and spacecraft configuration/orientational factors are at work. The occurrence of afternoon to evening events requires further discussion since the environment in these sectors is not conducive to spacecraft charging. In the paper on spacecraft charging models, it was pointed out that much of the outer dielectric surface materials were very good insulators and that leakage time constants could be in the order of several days. With this charge storage mechanism, it is possible to conceive of configurations in which sunlight applied to a dielectric surface in the late afternoon could cause an increased stress and resulting arc discharge at that time. It is also possible for an enhanced cold plasma environment such as the afternoon/evening detached plasma sector and plasmopause bulge described by Chappell et al<sup>11</sup> to selectively reduce the potential of a surface and to therefore cause it to arc. Figure 10 shows diagrammatically how the delayed arc discharges could occur.

## 5. CORRELATION WITH THE DAY OF THE WEEK

Figure 11 shows the distribution of the days of occurrence of anomalous events according to the day of the week. Separate distributions for the individual types as well as for all of them together are shown. The latter shows a peak on Saturday and Sunday which is about three times the midnight minimum. Individually, the "T" and "C" anomalies also show a weekend peak, but the midweek dips are more nearly a half of the weekend peak, and the transitions from day-to-day are not as smooth as for the composite graph. The "S" anomalies of which there were only four, are about as evenly distributed as they could be. On obtaining this surprising result, the distribution of Fredericksburg and Anchorage A-Indices over the entire period was computed. The results shown in Figure 12 have a maximum variability of 7 percent about the mean. A Friday or Saturday peak in activity is evident but the ratio of maximum to minimum is far less than for the anomalies.

Discussions with F. L. Scarf resulted in one possible explanation. He suggested that a reduced loading of the Canadian power system on weekends might be contributing to the selective depletion of the energetic particle population at geosynchronous altitudes. Helliwell et al<sup>12</sup> have described magnetospheric ELF waves which are induced by the Canadian power system. They point out that VLF radiated powers of less than 10 W could cause noticeable magnetospheric signals and that harmonics of the 1000 MW load of the Alcan aluminum refineries should radiate considerably more power. Fraser-Smith<sup>13</sup> has analyzed many years of geomagnetic data and has concluded that an approximately 7 percent enhancement exists in the  $A_p$  index on weekends, "which may reasonably be associated with the fact that power consumption is lower (by 30 percent) on weekends." An alternative possibility that has been discussed with the spacecraft operational engineer is the possibility of increased (or decreased) payload usage on weekends resulting in thermal power dissipation effects. The differential usage as well as thermal effects are stated to not having been noticeably dependent on the day of the week, although they have not been looked at in detail with the weekend effect in mind.

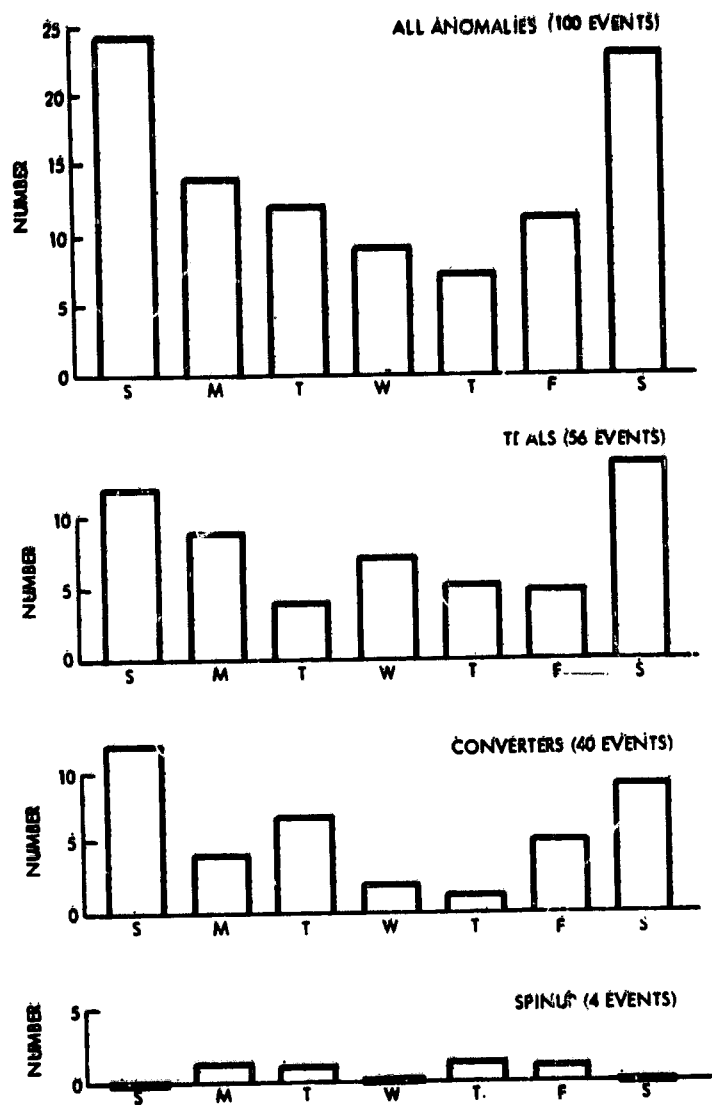


Figure 11. Distribution of Anomalous Events on DSCS Flights 3/4 With Day of the Week

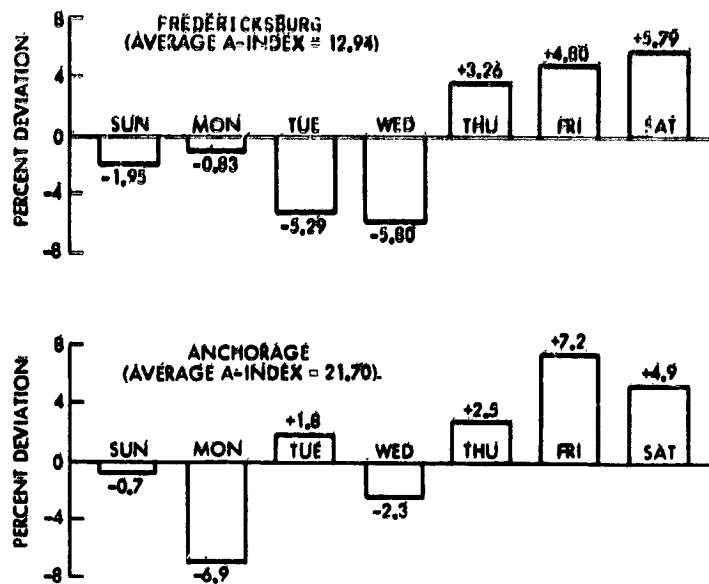


Figure 12. Percent Deviation From Average A-Indices, November 1973-September 1976

#### 6. LONG TERM AND PROGRESSIVE EFFECTS

The most prominent feature of Figures 3-5 is that the frequency of occurrence of anomalies has been decreasing drastically with time. Figure 13 shows the Fredericksburg A-Index smoothed and on a more compressed time scale covering the entire 33 month period since launch. The trend seems to be consistent with the sunspot cycle in that 1974 was in a decreasing phase, and 1976 is near the sunspot minimum. In this sense, the decrease in the number of anomalies might be correlated to the decrease in geomagnetic activity. Reference to Figure 6(c), however, shows that the amount of decrease in average A-Index, coupled with the fact that actual day-to-day variability is much greater than any longer term average, does not account for the decrease in the number of anomalies.

Results of laboratory experiments, of which Figure 14 from Hoffmaster, Inouye and Sellén<sup>14</sup> is an example, show that there are many long term and progressive effects which could account for decreasing rate of anomaly occurrences. Figure 14 shows the hysteretic effect of high energy particle bombardment in reducing bulk conductivity. Another feature observed in laboratory tests is the burnoff of thin films of vacuum deposited aluminum on thermal blankets and second surface mirrors with each arc discharge. It is possible for the increased spark gap length to gradually increase the arc breakdown threshold or for the carbonized

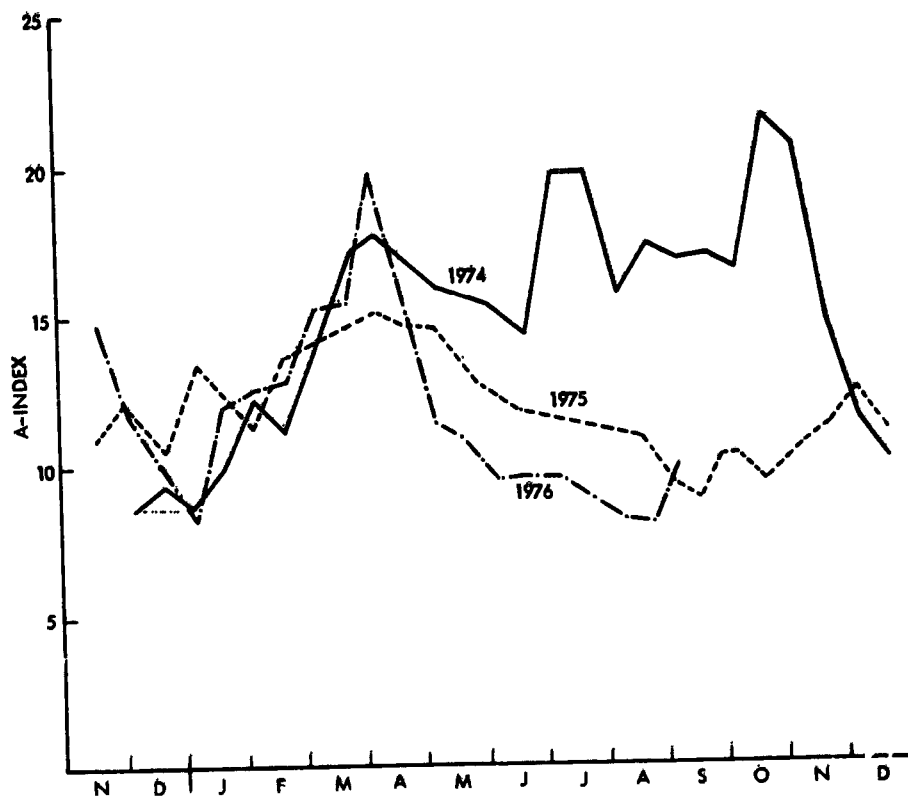


Figure 13. Fredericksburg A-Index Smoothed to Show Yearly Changes

material to decrease the threshold for succeeding discharges. From the view-point of an electrical circuit designer, thin film conductors are extremely poor devices because they are difficult to connect to and are electrically unstable in terms of point-to-point resistance from handling and crinkling. Thermal and ultraviolet irradiation degradation effects on breakdown threshold have not been investigated. Many other long term effects on material and surface characteristics such as photoemission and secondary emission need to be studied. Our view is that these long term and progressive degradation effects are the cause of the long term decrease in the occurrence of anomalous events.

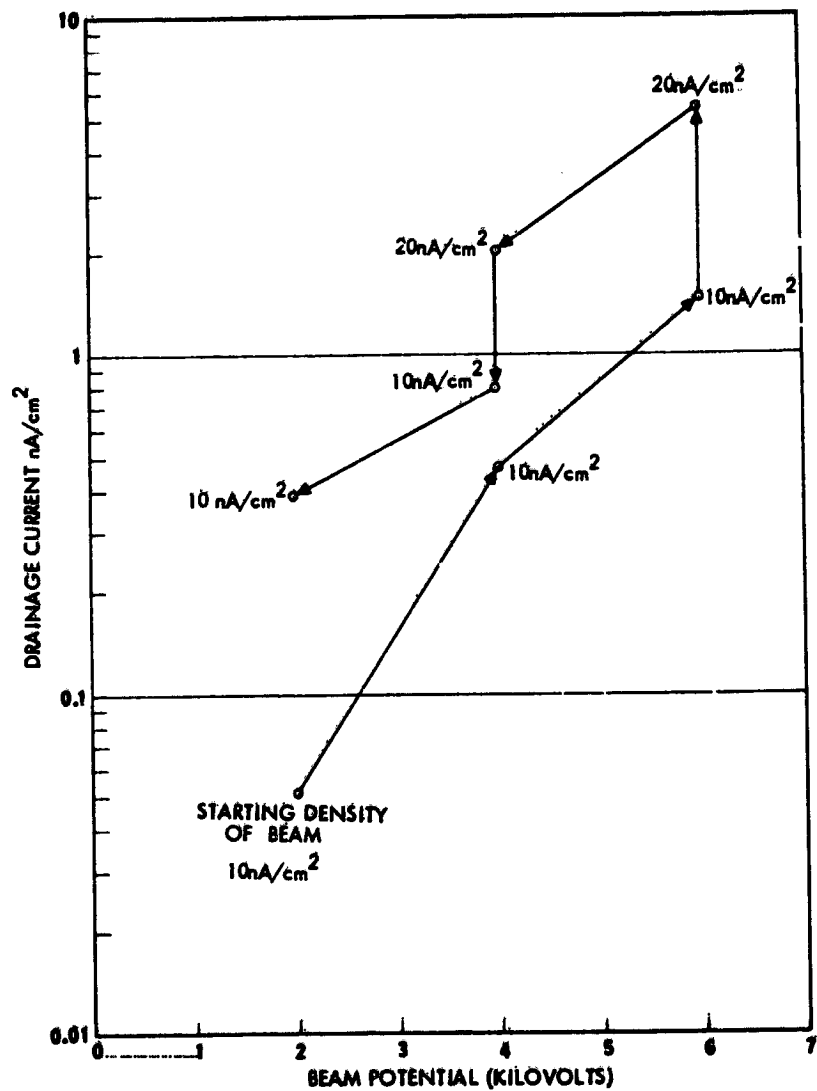


Figure 14. Electron Drainage Current Density as a Function of Electron Beam Acceleration Voltage for Deposition Flux Densities of  $10 \text{ nA/cm}^2$  and  $20 \text{ nA/cm}^2$

## 7. SUMMARY AND CONCLUSIONS

The anomalous events occurring on the DSCS II Launch 2 satellites have been studied with a view towards understanding their causes and initiating countermeasures to eliminate them on future spacecraft. The work presented here underscores the studies of many areas which must be implemented towards achievement of enough information to be able to design spacecraft which are able to withstand the geosynchronous orbit environment.

A basic problem addressed here is whether and how these anomalies are related to the environment. The correlation of the "S" type anomalies with the environment seems quite clear from the A-Index, the local time of occurrence and the equinox season of occurrence. The A-Index correlation of the other types of anomalies was shown to be dubious. Consistency was shown for the other types of anomalies with analytical model predictions of seasonal dependence and location on the spacecraft. The local time distribution of "T" and "C" type anomalies while not meeting the midnight/dawn criterion are, statistically speaking, not inconsistent with an environmental forcing function. The question of why events do not occur in any correlated fashion on two ostensibly identical satellites as close as  $10^{\circ}$  or as far apart as  $180^{\circ}$  in longitude has been discussed. Both environmental and/or uncontrolled spacecraft differences are possible sources of the observations. Capacitive energy storage in the outer dielectric surfaces makes it possible to postulate means whereby arc discharges could occur outside the midnight/dawn local time sector. The peak on weekends of the distribution of events on a day-of-the-week basis is a surprising result which may or may not be related to the environment. Finally, the long term decrease in the frequency of occurrence of anomalous events does not seem to be directly related to the environment but rather to on-board progressive and long term degradation effects. In addition to the need for much further work, the conclusion is inescapable that in-flight spacecraft charging/discharging monitors would be an invaluable adjunct to the housekeeping telemetry system of every geosynchronous satellite.

## Acknowledgments

This work presented here was performed at TRW under Air Force Contract No. FO 4701-69-C-0091. The author acknowledges the many informative and helpful discussions with members of the Space Sciences Department under A. Rosen, E.W. Greenstadt, N.L. Sanders, and F.L. Scarf; J. Durschinger and R. Alborn of the DSCS II Project Office for spacecraft details and operations and Mrs. B. Benefield for typing, assembling and correcting the manuscript.

## References

1. Rosen, A., Fredricks, R.W., Inouye, G.T., Sanders, N.L., Scarf, F.L., Greenstadt, E.W., Vogl, J.L., and Sellen, J.M. Jr. (1972) Final Report RGA Analysis: Findings Regarding Correlation of Satellite Anomalies With Magnetospheric Substorms, and Laboratory Test Results, TRW Defense and Space Systems 09670-7020-R0-00.
2. Final Report TDAL Gain State Analysis (1973) TRW Defense and Space Systems 09670-7040-RU-00.
3. Final Technical Report Program 777 Anomaly Investigation for Satellites 9433 and 9434 (1974) (3 volumes) TRW Defense and Space Systems 09670 RFP 050-01.
4. Final Report, Performance Anomaly Flight 9431 (1973) TRW Defense and Space Systems 24512-AR-006-01.
5. Final Technical Report Program 777 Anomaly Investigation for Satellite 9434 Converters (1975) July-October 1975, TRW Defense and Space Systems 26722-AR-008-01.
6. Rosen, A. (1976) Spacecraft charging: environment induced anomalies, J. Spacecraft and Rockets 13:129-136.
7. Inouye, G.T. (1976) Spacecraft potentials in a substorm environment, in Spacecraft Charging by Magnetospheric Plasmas, Alan Rosen, Editor, Vol. 47 Progress in Astronautics and Aeronautics, MIT Press, pp. 103-120.
8. Fredricks, R.W., and Scarf, F.L. (1973) Observations of spacecraft charging effects in energetic plasma regions, in Photon and Particle Interactions with Surfaces in Space, R.J.L. Grard, Editor, D. Reidel Pub. Co., Dordrecht-Holland, pp. 277-308.
9. Lyons, L.R., Thorne, R.M., and Kennel, C.F. (1972) Pitch angle diffusion of radiation belt electrons within the plasmasphere, J. Geophys. Res. 77:3455-3474.
10. Inouye, G.T. (1975) Spacecraft charging model, J. Spacecraft and Rockets 22:613-620.
11. Chappell, C.R., Harris, K.K., and Sharp, G.W. (1971) The dayside of the plasmasphere, J. Geophys. Res. 76:7632-7647.

12. Hellwell, R. A., Katsufakis, J. P., Bell, T. F., and Raghuram, R. (1975) VLF line radiation in the earth's magnetosphere and its association with power system radiation, J. Geophys. Res. 80:4249-4258.
13. Fraser-Smith, A. (1976) to be published.
14. Hoffmaster, D. K., Inouye, G. T., and Sellen, J. M. Jr. (1976) Surge current and electron swarm tunnel tests of thermal blanket and ground strap materials, TRW Defense & Space Systems 76.4351.1-103, also Presented at USAF/NASA Spacecraft Charging Technology Conference.

## Appendix A

### DSCS-II S/C 9433 and 9434 Anomalous Events

Event No.	S/C Event No.	Type No.	Date	Day No.	Day	GMT	Local Time	Comments
Launch	-----	----	12-13-73	1	THU	----	-----	Launch
1	9434-1	T-1	12-22-73	10	SAT	1653	09.21	Both S/C at initial positions 12-21-73
2	9433-1	T-2	12-24-73	12	MON	0348	20.80	-
3	9434-2	T-3	12-25-73	13	TUE	0121	17.68	-
4	9433-2	T-4	12-25-73	13	TUE	----	03.42	0900-1150 GMT
5	9433-3	AGA	12-29-73	17	SAT	0108	18.13	Only AGA event
6	9434-3	T-5	12-29-73	17	SUN	2224	15.08	-
7	9433-4	T-6	1-2-74	21	WED	1114	04.23	-
8	9434-4	T-7	1-3-74	22	THU	0731	23.85	-
9	9434-5	T-8	1-11-74	30	FRI	1621	08.68	-
10	9433-5	T-9	1-12-74	31	SAT	0008	17.13	-
11	9433-6	T-10	1-19-74	38	SAT	1726	10.43	S/C 9433 starts moving 1-23-74
12	9434-6	T-11	1-26-74	45	SAT	1023	02.71	-
13	9433-7	T-12	1-27-74	46	SUN	0705	01.41	-
14	9434-7	T-13	1-30-74	49	WED	0745	00.08	S/C 9434 starts moving 1-30-74
15	9433-8	T-14	2-1-74	51	FRI	0757	03.10	-
16	9433-9	T-15	2-12-74	62	TUE	0958	06.95	-
17	9433-10	T-16	2-17-74	67	SUN	0936	07.41	Both S/C at final positions 3-1-74
18	9433-11	T-17	4-7-74	116	SUN	--	08.97	0710-1230 GMT
19	9433-12	T-18	4-9-74	118	TUE	--	08.75	0700-1215 GMT
20	9433-13	T-19	4-10-74	119	WED	--	08.58	0644-1210 GMT
21	9434-8	T-20	4-25-74	134	THU	--	19.19	1716-2251 GMT
22	9434-9	T-21	6-27-74	197	THU	--	05.38	1420-2105 GMT

ORIGINAL PAGE IS  
OF POOR QUALITY

Event No.	S/C Event No.	Type No.	Date	Day No.	Day	GMT	Local Time	Comments
23	9434-10	C-1	7-18-74	218	THU	0505	16.75	First Converter Anomaly
24	9434-11	T-22	7-20-74	220	SAT	1800	05.67	-
25	9434-12	T-23	7-20-74	220	SAT	2130	09.17	-
26	9434-13	T-24	7-27-74	227	SAT	0305	15.75	-
27	9434-14	C-2	8-17-74	248	SAT	1418	01.97	-
28	9434-15	C-3	8-17-74	248	SAT	1819	05.98	-
29	9434-16	C-4	8-17-74	248	SAT	1819	05.98	1819.3 GMT
30	9434-17	C-5	8-17-74	248	SAT	1832	06.20	-
31	9434-18	C-6	8-17-74	248	SAT	1859	06.65	-
32	9434-19	T-25	8-18-74	249	SUN	1040	22.33	-
33	9434-20	T-26	8-18-74	249	SUN	1139	23.32	-
34	9434-21	T-27	8-18-74	249	SUN	1139	23.32	1139.4 GMT
35	9434-22	T-28	8-18-74	249	SUN	1325	01.08	-
36	9434-23	T-29	8-18-74	249	SUN	1515	02.92	-
37	9434-24	C-7	8-18-74	249	SUN	1600	03.67	-
38	9434-25	C-8	8-18-74	249	SUN	1640	04.33	-
39	9434-26	C-9	8-18-74	249	SUN	1644	04.40	-
40	9434-27	T-30	8-24-74	255	SAT	--	17.03	0225-0840 GMT
41	9434-28	T-31	8-24-74	255	SAT	--	22.62	0820-1344 GMT
42	9434-29	C-10	8-24-74	255	SAT	1830	06.17	-
43	9434-30	C-11	9-3-74	265	TUE	2106	08.77	-
44	9434-31	C-12	9-3-74	265	TUE	2256	10.60	-
45	9434-32	S-1	9-20-74	282	FRI	1330	01.17	First Spinup Anomaly
46	9434-33	T-32	9-23-74	285	MON	0440	16.33	-
47	9434-34	S-2	9-26-74	288	THU	1512	02.87	-
48	9434-35	S-3	10-1-74	293	TUE	1721	05.02	-
49	9434-36	T-33	10-2-74	294	WED	1706	04.77	-

Event No.	S/C Event No.	Type No.	Date	Day No.	Day	GMT	Local Time	Comments
50	9434-37	T-34	10-7-74	299	MON	2230	10.17	-
51	9434-38	T-35	10-11-74	303	FRI	2225	10.08	-
52	9434-39	T-36	10-12-74	304	SAT	1420	02.00	-
53	9434-40	T-37	10-14-74	306	MON	0539	17.32	-
54	9434-41	C-13	10-14-74	306	MON	1550	03.49	-
55	9434-42	C-14	10-14-74	306	MON	1557	03.62	-
56	9434-43	T-38	10-14-74	306	MON	1741	05.35	-
57	9434-44	S-4	10-14-74	306	MON	2013	07.88	Last Spinup Anomaly
58	9434-45	C-15	10-18-74	310	FRI	2359	11.35	-
59	9434-46	C-16	10-19-74	311	SAT	0008	11.80	-
60	9434-47	C-17	10-22-74	314	TUE	2310	10.83	-
61	9434-48	C-18	10-22-74	314	TUE	2330	11.17	-
62	9434-49	T-39	10-23-74	315	WED	0543	16.72	-
63	9434-50	T-40	10-24-74	316	THU	0415	15.92	-
64	9434-51	C-19	11-3-74	326	SUN	2114	08.90	-
65	9434-52	C-20	11-4-74	327	MON	1140	23.33	-
66	9434-53	C-21	11-4-74	327	MON	1508	02.08	Switched $\approx$ 57 times
67	9434-54	C-22	11-8-74	331	FRI	0810	19.83	-
68	9434-55	C-23	11-8-74	331	FRI	1015	22.17	-
69	9434-56	C-24	11-9-74	332	SAT	0510	16.83	-
70	9434-57	C-25	11-9-74	332	SAT	0655	18.58	-
71	9434-58	C-26	11-10-74	333	SUN	1756	05.60	-
72	9434-59	C-27	11-10-74	333	SUN	2005	07.75	-
73	9434-60	T-41	11-16-74	339	SAT	1219	23.98	-
74	9434-61	C-28	11-17-74	340	SUN	1645	04.42	-
75	9434-62	C-29	11-17-74	340	SUN	1927	07.12	-
76	9434-63	T-42	11-18-74	341	MON	0025	12.08	-

Event No.	S/C Event No.	Type No.	Date	Day No.	Day	GMT	Local Time	Comments
77	9434-64	T-43	11-20-74	343	WED	1030	22.19	-
78	9434-65	C-30	11-22-74	345	FRI	1003	21.72	-
79	9434-66	C-31	11-22-74	345	FRI	1240	00.33	-
80	9434-67	T-44	11-24-74	347	SUN	1935	07.25	-
81	9434-68	T-45	11-25-74	348	MON	2201	09.68	-
82	9434-69	C-32	11-27-74	350	WED	1701	04.68	-
83	9434-70	C-33	11-27-74	350	WED	1943	07.38	-
84	9434-71	C-34	12-1-74	354	SUN	0052	12.67	-
85	9434-72	C-35	12-1-74	354	SUN	0512	16.87	-
86	9434-73	C-36	12-10-74	363	TUE	0008	11.80	-
87	9434-74	C-37	12-10-74	363	TUE	0125	13.08	-
88	9434-75	C-38	12-10-74	363	TUE	0305	14.75	-
89	9434-76	T-46	12-14-74	367	SAT	0652	18.53	-
90	9434-77	C-39	12-15-74	368	SUN	1909	06.82	-
91	9434-78	C-40	12-15-74	368	SUN	NA	NA	Switched 6 times. Last converter anomaly.
92	9434-79	T-47	1-6-75	390	MON	0355	15.58	-
93	9434-80	Gimbal-1	3-12-75	455	WED	NA	NA	Gimbal anomaly only
94	9434-81	Gimbal-2	3-14-75	457	FRI	1459	02.65	Gimbal anomaly only
95	9433-14	T-48	3-31-75	474	MON	1021	22.02	S/C 9433 anomaly
96	9434-82	T-49	10-5-75	662	SUN	0055	12.58	-
97	9434-83	T-50	10-10-75	667	FRI	0035	12.25	-
98	9434-84	T-51	10-12-75	669	SUN	0013	11.88	-
99	9434-85	T-52	11-6-75	694	THU	1527	03.12	-
100	9434-86	T-53	11-9-75	697	SUN	0357	15.62	Last anomaly as of 8-23-76

Contents

1. Introduction	853
2. Investigations of Anomalous Telemetry Data	854
3. Anomalies Attributed to Electromagnetic Interference	854
4. Correlation of Anomalies With Environmental Effects	856
5. Susceptibility of SKYNET 2B to Environmentally Induced Anomalies	859
6. Conclusions	861
References	862

## 11. Space Environmental Effects on the SKYNET 2B Spacecraft

A. Robbins and C.D. Short  
Royal Aircraft Establishment  
Farnborough, England

### Abstract

This paper refers to environmentally induced electrical anomalies which are known to occur on geosynchronous spacecraft, and in particular to those which have occurred on the SKYNET 2B communications spacecraft. Details are given of the investigation made into anomalous telemetry data received from SKYNET 2B during its first 23 months of operation. The frequency and timing of these anomalous events appear to differ from those described in earlier reports of such phenomena. Attempts are made to correlate the anomalous telemetry data with data describing the spacecraft environment. Some details are given of the spacecraft configuration and comments made on its susceptibility to anomalies of this type.

### 1. INTRODUCTION

The SKYNET System forms part of the United Kingdom (UK) Defence Communications Network. The most recent spacecraft, SKYNET 2B<sup>1</sup> was launched from the American Eastern Test Range on 23 November 1974 into geosynchronous orbit

and was stationed at longitude approximately 49° East. The spacecraft is controlled and monitored continuously by the Royal Air Force from its Telemetry and Command Station (TCS) located at Oakhanger, England. Throughout the period of orbital operations, although satisfactory communications have been maintained, a considerable number of anomalous telemetry events have been recorded and investigated. This report refers to those events that have been attributed to electromagnetic interference (EMI) caused by electrical discharges within the spacecraft, which have been deduced as having been environmentally induced.<sup>2, 3, 4</sup> Anomalies of this type are caused by EMI generated by electrical discharges within the spacecraft. Electrical discharges can result from the differential charging of spacecraft surface materials to high voltages after exposure to the local plasma environment at geosynchronous altitude. Spacecraft charging is frequently associated with magnetic substorm activity when energetic plasma is dispersed after the interaction of the solar wind with the magnetosphere.<sup>5, 6, 7</sup>

## 2. INVESTIGATIONS OF ANOMALOUS TELEMETRY DATA

The SKYNET 2B telemetry data, transmitted continuously from the spacecraft are received by TCS, recorded on tape and also automatically checked by a computer in real time to ensure that individual telemetered parameters remain within prescribed limits. All deviations from nominal values, omissions or mistimed data are scrutinised and in each case standard anomaly investigation procedures are observed, involving the detailed assessment of every new type of anomaly by a special committee of advisers. Anomalies are classed either as discrete or repetitive, those in the latter category recurring at various times throughout the year. Certain of the discrete anomalies observed to date indicated individual malfunctions within the spacecraft, and in each of these cases a detailed failure mode analysis was carried out, and where necessary, redundant spacecraft systems were switched in by command. In all such cases, contingency action was successfully employed and satisfactory communications operations were maintained.

It is not proposed in this paper to refer further to operational aspects of SKYNET 2B, but rather to consider in more detail the investigations which led to the conclusion that most of the repetitive anomalous telemetry events were caused by the effects of the space environment on the spacecraft.

## 3. ANOMALIES ATTRIBUTED TO ELECTROMAGNETIC INTERFERENCE

During the first 3 months of orbital operations, a small number of discrete anomalies had been observed on the SKYNET 2B spacecraft. During March/April

1975, repetitive anomalies occurred with increasing frequency and far outnumbered the discrete anomalies. A special investigation of these anomalies was made which concluded that most, but not all, of the repetitive type of anomalous events occurred within the spacecraft. These anomalies were generally of short duration and gave no immediate indication of permanent component failure. The most likely explanation was the introduction of EMI, from unknown sources within the spacecraft, into the logic timing circuits of the Telemetry and Command Subsystem. It was apparent by this time that the characteristics of these particular anomalies were very similar to the environmentally-induced anomalies experienced by other geosynchronous spacecraft. 8, 9, 10, 11, 12

Although it is now known that most geosynchronous spacecraft have experienced anomalous behaviour that could be due to spacecraft charging phenomena, few have been fitted with the necessary instrumentation for monitoring the extent of electromagnetic noise generated by electrical discharges during orbital operations. 13 and SKYNET 2B has no special instrumentation for this purpose. For this reason it was decided to continue to maintain careful records of all SKYNET 2B anomalous telemetry events, and from those diagnosed as being caused by EMI, to isolate those anomalies that could only have been caused by phenomena occurring within the spacecraft. Anomalous telemetry data could of course arise from a variety of sources including the effects of electromagnetic interference at any point in the overall communication system, that is, the spacecraft, the radio frequency transmission link, the receivers, and the data reduction equipment at the ground station. It was necessary to discard anomalies from the analysis unless additional evidence showed that they originated in the spacecraft and hence might have originally been induced by the geosynchronous environment. In order to maintain a high confidence level when attributing an anomaly to electrical discharges within the spacecraft, numerous checks were carried out to eliminate the ground-based receiving and data processing equipment as a possible source. Fortunately the SKYNET 2B system utilizes two separate transmission links operating in different frequency bands, with separate ground stations, and with parts of the standard telemetry format duplicated in each link. This means that anomalies occurring simultaneously on both transmissions can be considered as originating within the spacecraft to a high level of confidence.

Figure 1 shows the distribution since launch of repetitive anomalous telemetry events attributed to EMI generated within the spacecraft (a total of approximately 300). These anomalies represent approximately 20 percent of the total number that were considered to be the result of electromagnetic interference somewhere in the overall system. It is probable that a large proportion of the remaining 80 percent could also have originated within the spacecraft; however, this cannot be rigorously proved. The anomalies shown in Figure 1 are unevenly distributed

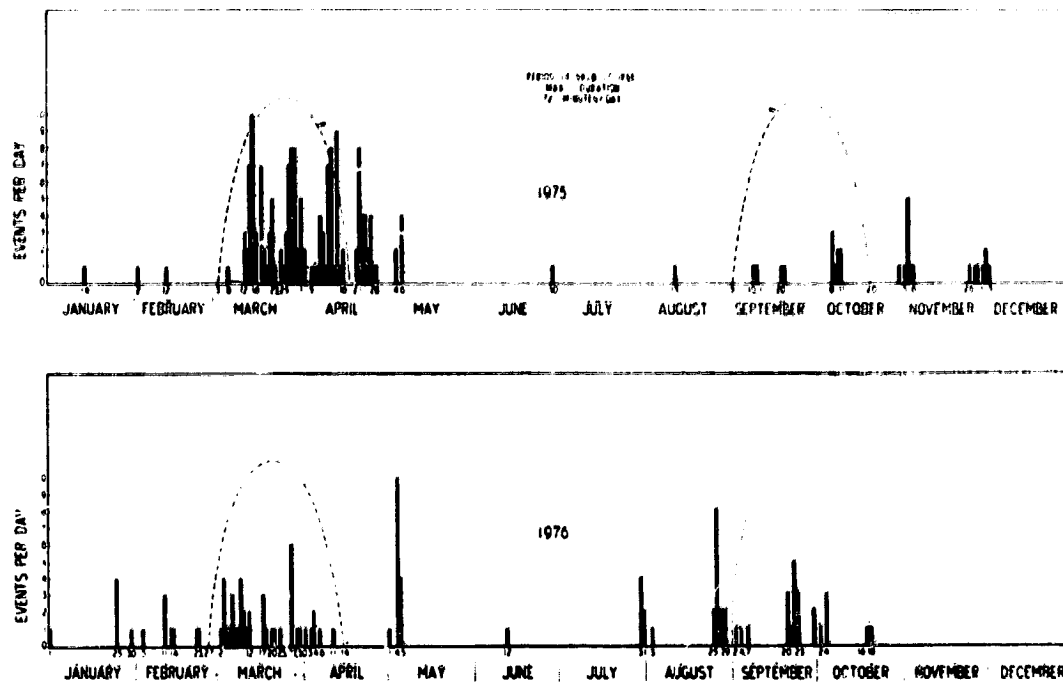


Figure 1. SKYNET 2B Anomalies in Flight Telemetry Data Attributed to Electromagnetic Interference Within the Spacecraft

with time of year, fewer occurring in Summer and Winter months than Spring or Autumn. The largest number of anomalies occurred in 1975 after the commencement of the Spring eclipse season, when the spacecraft is eclipsed by the Earth once per daily orbit. Anomalies during 1976 have followed a similar pattern to 1975 but are fewer in number.

#### 1. CORRELATION OF ANOMALIES WITH ENVIRONMENTAL EFFECTS

Environmentally-induced anomalies, as the name implies, result from the interaction between a spacecraft and its environment. Important factors contributing to this interaction are: first, the daily impact of the solar wind on the magnetosphere and the resulting composition and variations in energy state of the geosynchronous environment in the vicinity of the spacecraft; second, the operational conditions of the spacecraft, for example, its velocity, position, solar illuminance, the spacecraft-sun angle, attitude, eclipse or shadowing effects etc; and third, the spacecraft type and configuration.

In the case of SKYNET 2B attempts were made to correlate the repetitive anomalies of Figure 1 with environmental data such as: time of day, sun-spot or magnetic activity, operational conditions, degree of solar illumination, eclipse periods, etc. <sup>14, 15</sup> Figure 2 indicates the distribution throughout the day of anomalies attributed to environmentally-induced effects within the spacecraft. The relatively even daily local-time distribution of anomalies is significant, because it differs from distributions reported from other geosynchronous satellite projects, which indicated that anomalies tended to occur with greater frequency in the local midnight to dawn sector. Such distributions are consistent with the theory that spacecraft, after passage through the antisolar tail of the magnetosphere, become charged to very high potentials as they encounter high energy electrons which are injected into this sector of geosynchronous orbits during local magnetic substorm activity. Furthermore, it was assumed that anomalies due to this cause would be unlikely to occur in significant numbers outside this time sector. <sup>2, 16</sup> There is now, however, little doubt that a significant number of environmentally-induced

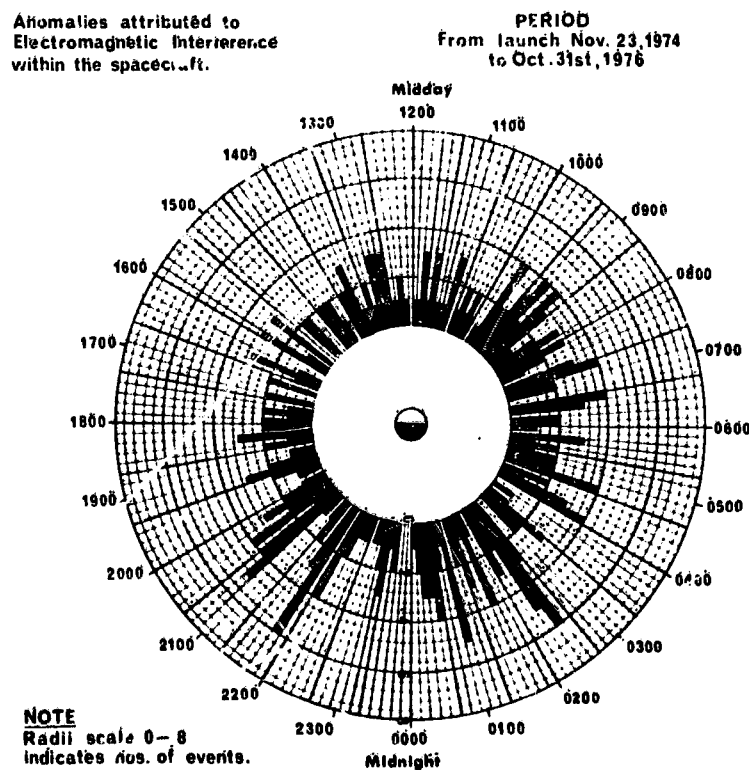


Figure 2. SKYNET 2B Anomalies in Telemetered Data Local Time Dependence

2-10

anomalies do in fact occur outside the local morning sector. The precise mechanisms to explain the occurrence of such anomalies are not yet understood. One possibility suggested in the case of the US DSCS II Communications satellite anomaly investigations, is the subsequent interaction of a spacecraft, charged during the midnight to dawn sector, with detached regions of cold (low energy) plasma causing partial discharge and differential voltage breakdown.<sup>17</sup>

In order to account for the very large numbers of anomalous events recorded on SKYNET 2B, it seems more likely that different types of discharge which have a lower threshold or do not require very high breakdown potentials may be responsible. Alternative mechanisms that have been reported are so called 'Malter' discharges or Bilayer 'scintillation' types of discharge.<sup>18, 19</sup>

A very significant factor concerning the SKYNET 2B data is that, by recording and analysing relatively minor occurrences throughout each day, a relatively large statistical sample of anomalies has been obtained. A check was made of the length of time during which the ground receiving station or the computer monitoring were out of commission. It was concluded that on average this was less than 10 percent of the total time and, therefore, did not significantly affect the time distribution of recorded anomalies.

There was no obvious correlation between the anomalies and daily values of sunspot number (Zurich relative sunspot number RZ). However, this would be unlikely in view of the variable time delay of between 20 and 100 hr before any significant effects are experienced at geosynchronous altitude following surface activity on the sun.

Figure 3 shows the geomagnetic activity index  $A_p$  plotted to the same time-scale as the anomalies. There is evidence of correlation between some of the higher peaks of magnetic activity and the frequency of anomalous events. Correlation was also sought between the anomalies and the 3-hourly magnetic K indices from selected high-latitude observatories North of the spacecraft, with similar results.

It is apparent from the overall distribution of anomalies through the year, that factors other than geomagnetic activity must also be significant. There was, for example, a very noticeable increase in anomalous events during the 1975 Spring spacecraft eclipse season, which seemed to suggest that each daily eclipse increased the likelihood of differential spacecraft charging and hence of subsequent discharge events. Although other eclipse seasons also show an increase in the number of anomalies there is, nevertheless, a small but significant number outside the eclipse seasons. One possible explanation is that changes in sun angle with respect to the spacecraft and the detailed spacecraft configuration are also relevant factors.

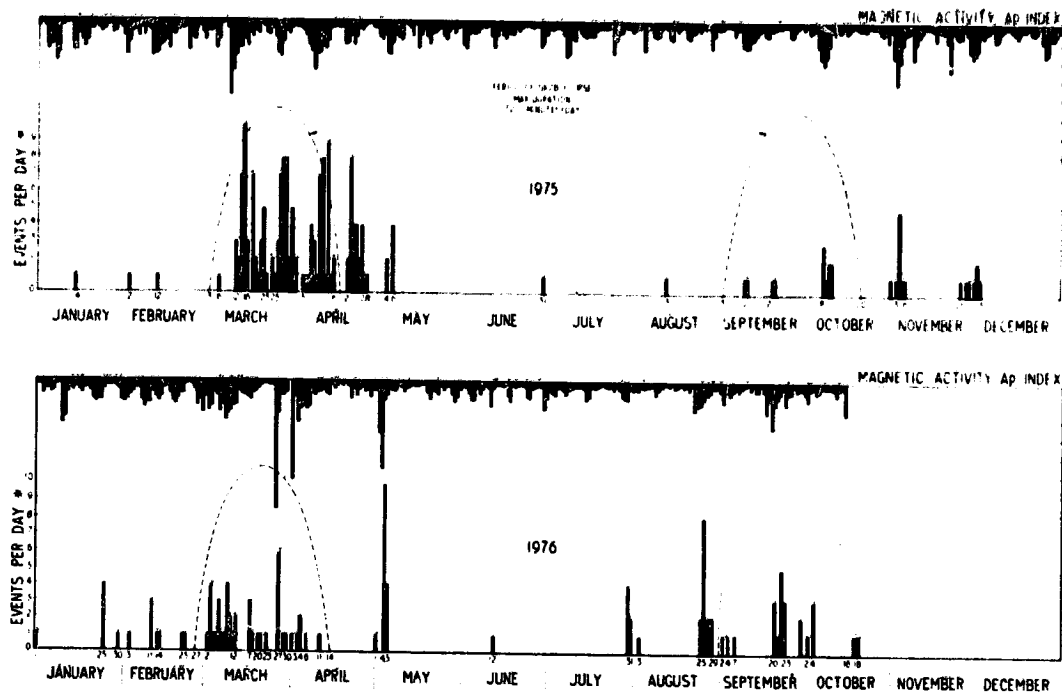


Figure 3. SKYNET 2B Anomalies in Flight Telemetry Data (Attributed to Electromagnetic Interference Within the Spacecraft)

##### 5. SUSCEPTIBILITY OF SKYNET 2B TO ENVIRONMENTALLY INDUCED ANOMALIES

The susceptibility of a geosynchronous spacecraft to environmentally induced anomalies is very dependent upon its precise geometric configuration and detailed mechanical and electrical properties.<sup>20, 21, 22</sup> The accumulation of charge and spacecraft floating potential will depend upon the type of surface materials exposed to the energetic plasma environment, and the different secondary electron emission and photoemissive properties of individual conductors and dielectrics. An important factor is the extent to which such surfaces are illuminated by the Sun or shadowed. Furthermore, apertures and projections in the spacecraft configuration can become significant when related to the spacecraft Sun angle and its attitude. Other important factors include the voltage breakdown characteristics of individual surfaces and the susceptibility of the various spacecraft subsystems to EMI.

Figure 4 shows the basic SKYNET 2B configuration. The spacecraft uses spin stabilization with a nominal 90 rpm spin rate. The sides of the spacecraft, apart from the thrusters and sensors, are almost completely covered with solar

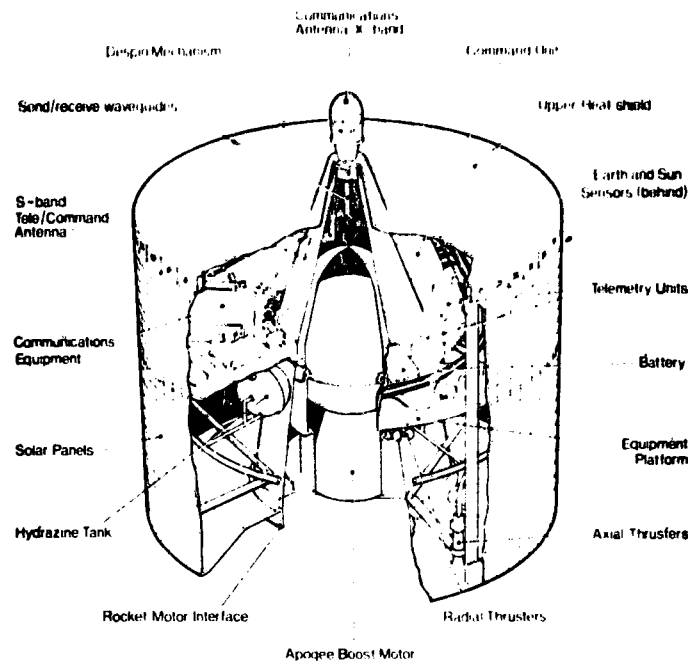


Figure 4. SKYNET 2B Satellite

cells mounted on fiberglass substrates. The solar cells having fused silica cover slips should be relatively immune from large discharges. The forward and aft end shields, however, seem more likely to be susceptible to spacecraft charging effects.

Figure 5 shows the variations in sun angle relative to the spacecraft equator with time of year for SKYNET 2B. During the Winter months the forward shield is in shadow and the aft shield illuminated, these conditions being reversed during the Summer months. The spacecraft is eclipsed for a maximum period of approximately 70 min each day during March and September when the Sun angle is normal to the sides of the spacecraft. There are a number of small apertures in the sides of the spacecraft and the possibility of solar illumination reaching isolated conductive or dielectric surfaces inside the spacecraft cannot be discounted.

SKYNET 2B successfully completed a prelaunch test program including standard EMC test procedures involving the injection of interfering pulses into selected power lines etc; however, no special tests were made that would simulate the effects of electrical discharges in the vicinity of the spacecraft. There was no obvious source of arcing within the spacecraft subsystems and no evidence of self-generated interference during prelaunch tests.

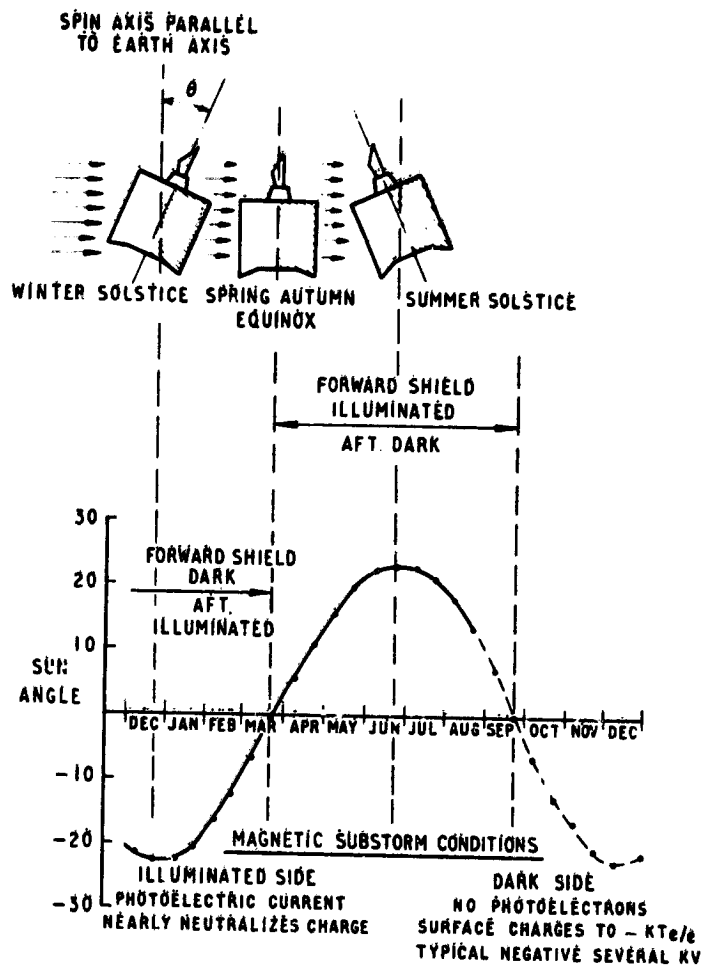


Figure 5. Seasonal Variation of Sun Angle With Respect to Satellite Equator

It seems likely that the SKYNET 2B Telemetry Subsystem would be more susceptible than other subsystems to external interference because of the relatively large number of switching devices that it contains.

## 6. CONCLUSIONS

The main conclusions reached from the investigations of SKYNET 2B anomalous telemetry data are as follows:

(1) The majority of the repetitive types of SKYNET 2B telemetry anomalies can be attributed to environmentally-induced spacecraft charging effects for the following reasons:

- (a) The most likely source of these anomalies is the presence of short bursts of electromagnetic interference in the vicinity of the spacecraft. (Anomalies due to EMI from other sources having been eliminated by careful scrutiny of the data.)
- (b) There was no other more conventional source of EMI within the spacecraft and there was no previous evidence of such interference during prelaunch ground test programmes.
- (c) The occurrence of the anomalies is accentuated over the Eclipse seasons and, therefore, may be associated with photoemissive effects and changes in spacecraft Sun angle (see Figure 5).
- (d) There is some degree of correlation of the anomalies with geomagnetic activity.

(2) Important features of the SKYNET 2B data compared with those of other spacecraft are:

- (a) The very large numbers recorded due to continuous monitoring, and
- (b) The relatively even daily distribution with local spacecraft time.

(3) The most important unanswered questions concern the precise nature of the environmental phenomena and their interaction with the spacecraft. The charge/discharge mechanisms which would produce a large number of anomalous events with a relatively even daily distribution such as observed on SKYNET 2B and additionally have the observed seasonal distribution, also require further study.

## References

1. Lovell, W. M. (1972) Design of the Skynet II Communications Satellite, Journal of Science and Technology 39(No. 1).
2. Rosen, A. (1976) Spacecraft charging - Environment induced anomalies, AIAA Paper 75-91, Journal of Spacecraft.
3. Robbins, A. (1975) Environment-Induced Anomalies in the Performance of Geosynchronous Spacecraft, RAE Technical Memorandum Space 227.
4. Gard, R. (1975) Effect of the ambient medium upon the electric properties of the spacecraft surface and environment, Conference on Lighting and Static Electricity, Culham Laboratory.
5. Martin, A. (1973) Spacecraft Plasma Interactions, City University, London, Dept. of Aeronautics Report, Aero 73/1.

6. Akasofu, S.I. (1975) The roles of the N-S component of the interplanetary magnetic field on large scale auroral dynamics observed by the DMSP satellite, Planetary Space Science 23:1349-1354.
7. Kane, R. P. (1976) Geomagnetic field variations, Space Science Reviews 18(No. 4).
8. Rosen, A. (1975) Large discharges and arcs on spacecraft, Astronautics and Aeronautics.
9. Wadham, P. N. (1976) Communications satellite outages due to the environment, SMPTE Journal 85.
10. Symphonie I victime de mystérieux parasites, Air et Cosmos, p. 41.
11. Rosen, A. et al (1972) RGA Analysis: Findings Regarding Correlation of Satellite Anomalies with Magnetospheric Substorms and Laboratory Test Results, TRW Report 98670-7020-R0-00.
12. Fredericks, R. N., and Kendall, D. (1973) Geomagnetic Substorm Charging Effects on DSCS - Phase II, TRW Report No. 09 670-7032-RU-00.
13. McPherson, D., Cauffman, D. and Schober, W. (1975) Spacecraft Charging at High Altitudes - The Scatha Satellite Programme, AIAA Paper 75-92.
14. Pike, C. P. (1975) A correlation study relating spacecraft anomalies to environmental data, AGU Conference.
15. King, J. (1971) Handbook of Correlative Data, NSSDC 71-05.
16. Fredericks, R. and Scarf, F. (1973) Observations of Spacecraft Charging Effects in Energetic Plasma Regions, Photon and Particle Interactions with Surfaces in Space, D. Reidel Publisher, Holland, p. 277-308.
17. Lejeune, W. R. (1974) Final Technical Report, Programme 777 Anomaly Investigation for Satellites 9433 and 9434, TRW 9670 REP 050-01, Vol II, Appendix A.
18. Nanevich, J., and Adamo, R. (1975) Malter discharges as a possible mechanism responsible for noise pulses observed on synchronous orbit satellites, AGU Paper SA71.
19. Meulenberg, A. (1976) Electrical discharges on spacecraft at synchronous altitude, Com Sat Technical Review 6(No. 1).
20. Inouye, G. (1975) Spacecraft Charging Model, AIAA Paper 75-255.
21. Keiser, B. (1975) ATS-6 Spacecraft surface treatment for the control of electrical discharges, IEEE Trans. on EMC EMC17(No. 4).
22. Cauffman, D. (1973) Recommendations concerning spacecraft charging in the magnetosphere, Aerospace Corporation Report TR 0074 (9260-U9)-5.

12-30-63

**Contents**

1. History	865
2. Spacecraft Characteristics	866
3. Spacecraft Charging Approach	868
4. Spacecraft Design Techniques	869
5. Structural	869
6. Thermal	870
7. Electronic	870
8. Conclusions	870
References	871
Bibliography	871

**12. RCA Satcom 3-Axis Spacecraft Experience  
at Geosynchronous Altitude**

Joseph Napoli  
RCA American Communications, Inc.  
Piscataway, N.J.

Joseph Seliga  
RCA Astro-Electronics  
Princeton, N.J.

**Abstract**

The RCA Satcom space segment presently consists of two three-axis stabilized communication satellites which have been in orbit at geosynchronous altitudes for 11 and 8 months respectively. Both satellites have experienced two eclipse seasons since the beginning of operations. Neither spacecraft has exhibited any anomalous behavior that can be attributed to the effects of spacecraft charging. A brief discussion of the history, spacecraft characteristics and design techniques is presented.

**1. HISTORY**

The RCA Satcom communication satellites are owned and operated by RCA American Communications, Inc. Under a fixed-price contract RCA Astro-Electronics Division developed and delivered the first flight spacecraft within

**PRECEDING PAGE BLANK NOT FILMED**

**865 UNUSUALLY BLANK**

24 months. On 12 December 1975 the F-1 satellite was launched and on 15 December 1975, the apogee motor placed the satellite in its synchronous orbit. The spacecraft achieved synchronous altitude at 137° W. long. and then was commanded to drift at a 1.25° per day to its position at 119° W. long. During this drift period and the time at station through commencement of commercial service on 28 February 1976, the payload support subsystems and transponder payload had successfully undergone extensive preoperational calibration and testing.

On 26 March 1976, the second spacecraft was launched and also placed at 119° W. long. After verifying satisfactory performance of all payload support subsystems and that the antenna coverage patterns and the radiated power met the requirements for CONUS and Alaska, traffic was switched from F-1 to commence F-2 service on 2 June 1976. The F-1 was commanded to drift at a 0.3° per day on June 11 to a newly assigned location at 135.8° W. as an in-orbit spare. Since the first week of August 1976, the satellites have been maintained at 135.8° W. and 119° W. for F-1 and F-2 respectively.

Before, during, and after these maneuvers all subsystems are monitored via telemetry on a continuous basis by either or both RCA Satcom Telemetry, Tracking and Control facilities located on the East and West coasts.

## 2. SPACECRAFT CHARACTERISTICS

The orbital configuration of the spacecraft is shown in Figure 1. It features a three-axis stabilization system, with a fixed nondeploying antenna platform pointing to earth, and efficient power collection via sun-oriented, flat-panel solar arrays. Housekeeping and communications equipments are mounted on North and South-facing equipment panels which are always oriented to cold space, thereby affording efficient thermal control. Earth pointing is accomplished via a bias momentum-type control system which provides pitch control via a momentum wheel and magnetic torquing for yaw and roll control. The spacecraft is maintained on station via a blowdown monopropellant hydrazine reaction control system. Capability is provided for East/West and North/South drift corrections for 8 years, and for station relocation as required.

The antenna assembly directs all 24 channels to Alaska, as well as to the lower 48 states. Hawaii can be serviced with up to 12 channels by separate offset-spot beams.

Frequency reuse in the 4/6 GHz bands is employed in order to establish 24 independent 34 MHz bandwidth channels within the allocated 500 MHz frequency band.

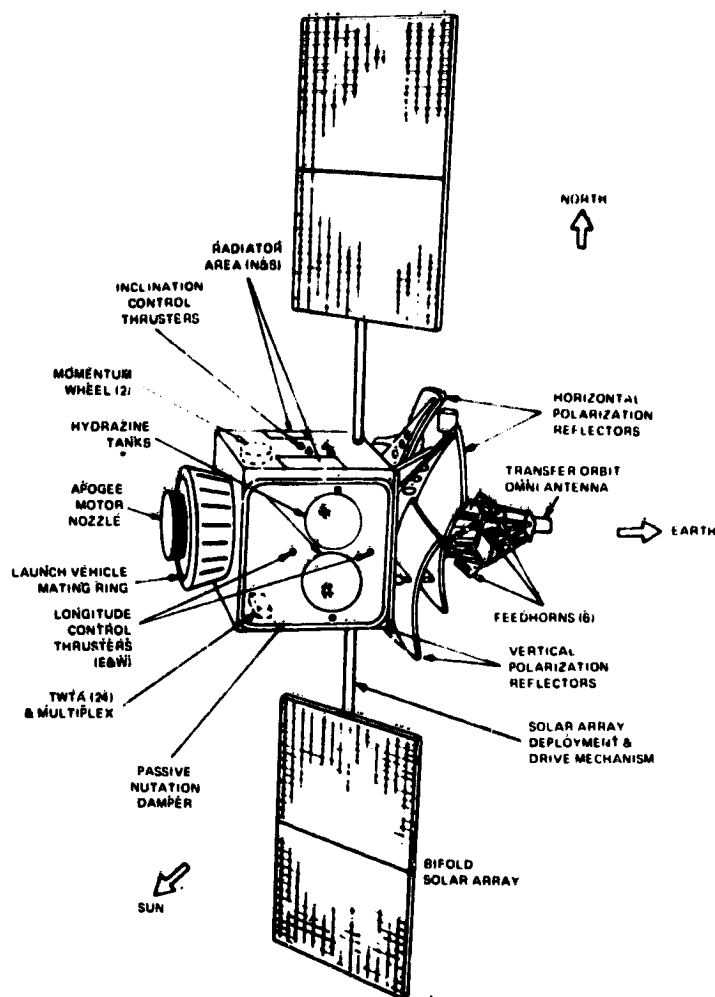


Figure 1. Orbital Configuration of the Spacecraft

The channels are spaced on 20 MHz centers, but are transmitted via alternately horizontal and vertical polarizations in order to isolate adjacent channels. A summary of the spacecraft performance features is given in Table 1.

Four of the unique RCA Satcom developments which have been instrumental in achieving a 24-channel service within the weight and volume capacity of the Delta 3914 launch vehicle are listed below. These developments are the keys to providing an economical high-capacity spacecraft compatible with low-cost Thor Delta launches.

Table 1. RCA Satcom Performance Features

Element	
Communications	
24 34-MHz channels to Conus and Alaska	Minimum EIRP 32 dBW
12 34-MHz channels to Hawaii	Minimum EIRP 26 dBW
Cross polarization isolation	Receive 33 dB Transmit 33 dB
Frequency bands	Receive 5925 to 6425 MHz Transmit 3700 to 4200 MHz
Power	550 W at end of 8 years full eclipse capability
Attitude	Pointing: $\pm 0.19^\circ$ E/W, $\pm 0.21^\circ$ N/S Stationkeeping: $\pm 0.26^\circ$ E/W, N/S Offset Pointing: $0^\circ$ to $\pm 5^\circ$
Telemetry	128 channels for operational and diagnostic information
Reliability	R = 0.5 at 17 channels for 8 years Full subsystem redundancy

(1) The lightweight composite construction of the fixed antenna and feed assembly, which maintains accurate antenna beam alignment and requires no mechanical deployment.

(2) Microwave filters of lightweight graphite fibre epoxy composite (GFEC), which provides sufficient weight saving to make the spacecraft compatible with the Delta launch vehicle.

(3) The three-axis stabilization system, which provides the maximum power-to-weight ratio for spacecraft that could operate in the specified payload-power regime.

(4) High-efficiency, direct-energy-transfer power system developed for RCA Satcom and utilizing one-third of the equivalent solar cells of dual spin spacecraft minimizes the weight of the electrical power generation and regulation subsystem, while maximizing efficiency.

### 3. SPACECRAFT CHARGING APPROACH

RCA Astro-Electronics Division performed an in-depth study on the possibility of adverse effects on spacecraft operation at geosynchronous altitudes because of

spacecraft charging as a result of the paper by Fredericks and Kendall.<sup>1</sup> Our understanding of the problem was furthered by discussions with Mr. R. W. Ellison of the Martin Marietta Company, Dr. D. A. McPherson of the Aerospace Corporation, and Dr. A. Rosen and Dr. G. T. Inouye of the TRW Systems Group.

The RCA Satcom spacecraft design was reexamined in light of the design practices recommended in the literature of minimize the possibilities of discharges and their effects.<sup>1,2</sup> The three areas that were given highest priorities were the structural design, thermal blankets and electronic interface circuitry, bearing in mind that any design changes made to the spacecraft had to be in consonance with the weight constraints posed by the launch of the 24 channel spacecraft on a Delta 3914. Testing was considered but not planned because of the inability to identify valid criteria of acceptability.

#### 4. SPACECRAFT DESIGN TECHNIQUES

The principal design features incorporated into the RCA Satcom spacecraft to minimize its vulnerability to the effects of spacecraft charges are as follows:

- (1) The entire spacecraft is a closed body except for the apertures required for the horizon sensor, the solar array drive, and the apogee motor.
- (2) Every section of the thermal blanket is grounded in two places.
- (3) The outerlayer of the thermal blanket is kapton
- (4) The mechanical structure, including the wrappers of all boxes, has electrical continuity.
- (5) The harness wiring contains shielded twisted pairs, coaxial and triaxial cables for selected interfaces and is functionally grouped into separate bundles.
- (6) The electronic interface circuits were designed to have high noise immunity.

#### 5. STRUCTURAL

The almost complete closure of the spacecraft minimized the possibilities of internal differential charging. All units on the spacecraft have their cases grounded to the structure via electrically conductive mounting surfaces. In addition, special mounting inserts that cut and wedge into the honeycomb to provide good electrical continuity were used for all unit mountings. All structural members were designed so that electrical continuity between all sections of the spacecraft and all unit wrappers was obtained. The solar array panels were designed so that each structural section was connected together and grounded to the main spacecraft structure via the slip rings of the solar array drive.

## 6. THERMAL

Kapton was selected as the outer layer of the multilayer thermal blanket because of the improvement of its conductivity when stressed and illuminated by sunlight. In addition, each aluminized layer of the multilayer thermal blanket was grounded in two places to the main spacecraft structure. The harness from the solar array to the spacecraft is covered along the booms and in the hinge areas. The use of conductively coated solar cell cover glass or second surface mirrors was considered but rejected because of the weight penalty and its unknown radiation effects.

## 7. ELECTRONIC

The RCA Satcom spacecraft was initially designed with good EMC practices foremost in mind, with attention given to wire selection and routing in the internal harnessing. The spacecraft harness is grouped and bundled by function: power and power returns, signal lines and returns, and telemetry lines and returns. A single point ground system has been used throughout the spacecraft, with the exception of communications equipment.

COSMOS devices were selected for the command interface circuitry because of their high noise immunity and relatively low useful bandwidths. Shielded twisted pairs and coaxial cables were used to further reduce noise sensitivity for selected interfaces. Triaxial cables were used for clock frequencies above 100 KHz.

## 8. CONCLUSIONS

The performance characteristics for the communications payload and support subsystems have been analyzed and is continually being monitored for evidence of anomalous behavior. Gain changes, equipment switching or other unexplained causes as experienced by other satellites at geosynchronous altitude have not been observed to date. Consequently, no changes to the design of the RCA Satcom series of spacecraft is envisioned at this time.

## References

1. Fredericks, R. W., and Kendall, D. E. (1973) Geomagnetic substorm charging effects on defense satellite system phase II, Paper Presented at the Air Force Weapons Laboratory's Command, Control and Communications Assessment Program Review, Kirtland AFB, N. M.
2. Rosen, A. (1975) Spacecraft charging: Environment induced anomalies, Paper Presented at AIAA 13th Aerospace Sciences Meeting, Pasadena, Calif.

## Bibliography

- McPherson, D. A., Cauffman, D. P., and Schober, Capt. W. (1975) Spacecraft charging at high altitudes - The SCA THA satellite program, Paper Presented at the AIAA 13th Aerospace Sciences Meeting, Pasadena, Calif.
- Inouye, G. T. (1975) Spacecraft charging model, Paper Presented at the AIAA 13th Aerospace Sciences Meeting, Pasadena, Calif.
- Cauffman, D. P. (1973) Recommendations Concerning Spacecraft Charging in the Magnetosphere, Air Force Report No. SAMSO-TR-73-348.

PANEL DISCUSSION

873

872  
1  
873  
873

PRECEDING PAGE BLANK NOT FILMED

## Panel Discussion

Panel Chairman: A. Rosen - TRW  
Panel Members:  
E. C. Whipple, Jr. - University of California San Diego  
S. E. DeForest - University of California San Diego  
S. P. Bower - Aerospace Corp.  
R. R. Lovell - NASA Lewis Research Center  
N. J. Stevens - NASA Lewis Research Center  
M. L. Minges - Air Force Materials Lab.  
W. L. Lehn - Air Force Materials Lab.  
M. H. Bunn - SAMSO  
J. M. Sellen, Jr. - TRW  
C. P. Pike - Air Force Geophysics Lab.

### THEME

In view of the data generated on spacecraft charging, how should program and project managers proceed with the design of synchronous spacecraft and verify their design?

### TOPICS

#### Spacecraft Design and Fabrication

What analysis tools, standardized design criteria and requirements, standardized environmental specifications are required?

### Spacecraft Testing

What, if any, specific tests should be instituted to assure the integrity of the design and immunity from environmental effects?

### Housekeeping Monitors

When should an operational system carry housekeeping monitors and what kind?

### Laboratory and Space Data--

What additional material and environmental data is required for spacecraft design development?

### Panel Member

### Discussion

A. Rosen

The theme of this discussion is that in view of the data generated at this conference, and prior to this conference, how should program managers and project managers proceed with the design of synchronous spacecraft and verify their design? Progress in this field has been significant: in the area of spacecraft design and fabrication, in the area of spacecraft testing, in the area of housekeeping monitors, in the area of laboratory data, and in the area of space data. But are we really doing enough? Are there gaps in our coverage? We have been exposed to conflicting bits of data at this conference. How should we proceed in the future? The first person to reply to our theme questions is Sherman DeForest who is going to talk about the environment.

S. DeForest

Okay, I have approximately five minutes, I guess. I have three points that I think are rather important. One is that just at this meeting, I got my first look at data we took this Spring with the ATS-6 neutralizer. In other words, we are still getting new data and scratching our heads. The data base is incomplete. GEOS going up with our European colleagues, and SCATHA going up; I think that will really help. The main point is that the data base is incomplete. The second thing is that even with the data base that we have, two days ago I had put out my ideas of what an acceptable model or environmental specification should be. I

have been trying to talk to everyone I could out here to get some feedback on what they thought. The readings I am getting, loud and clear, is that there are a lot of engineers who do not want a good model, rather they need some numbers right now. So on the tape here I am going down on record as saying I will switch my efforts for the present time to getting out a short term, better grade interim model which will be relatively simple, of limited use, but will have some numbers to work to. I think this is one message I have gotten back from you people. The third point is one that I feel was missed, and it has to do with the theme here; that is, future directions on where to go. There is only one paper which really mentions it and that is the spacecraft have changed state. I am going to make a weather analogy. We know how to build houses that would survive tornados or earthquakes. It is not cost effective to build these kind of houses. You can't put all military bases under Cheyenne mountain. I think the same thing should be true of spacecraft. We need a prediction capability, and I don't think anyone here has considered that. I deliberately avoided that, myself, to hear what other people thought. But I think we should get some ideas toward using the advances that we have in magnetospheric dynamics, our understanding of it, to set up a method of predicting. I think with the state-of-the-art, right now, if we want to do it, we could get twenty minute warnings, without too much trouble. If you had this sort of system on line, then you could have your spacecraft send up a command to it and say a storm is coming, shut yourself down. This might be a lot cheaper in the long run than having the spacecraft itself sense that something is happening. You might want to do that for a military spacecraft but for communications spacecraft, I think it might be too expensive. So one thing that I would like to see in the future, in going along with the theme, is the idea to set up a predictive or line capability and then designing spacecraft that might be able to change their state and in some way be more hard, for short periods.

A. Rosen

The next speaker is Elden Whipple on Modeling.

E. Whipple

Okay, I just have three points too. I have been very encouraged by the results that have been presented here, at this conference, on the modeling. I am talking here about modeling the sheath, modeling the currents from the environment to the spacecraft that cause a charging problem. I think that we really are making progress, and there is a three-dimensional program in the works and more than one group is involved in this kind of effort. I think in the next year we shall start seeing some real good results, in this area. I realized one thing in talking to people, the Systems Science and Software, Inc. effort is taking a first crack by neglecting space charge, and I think that is a very good approach. It may be a very realistic approximation. The Debye lengths are very big out in this area. It may be that when we understand the problem, that we can neglect space charge completely. And this could be a help in our modeling of the currents. It will make it much easier for engineers and people involved in designing spacecraft. So I think that possibility is really very encouraging and we should certainly look at that approximation first and see how good it is. I think eventually we ought to be able to get analytic or algebraic expressions for the currents. Now Lee Parker and I were able to do this some years ago. We were worried about a two-electrode system and we were able to approximate our computer calculations. After we had done the computer calculations, we saw a way of approximating them such that we could get algebraic expressions for the charging currents. It is a lot easier if you have something like that to work with, to calculate what the charges are eventually going to be. I think that should be kept in mind. The computer, the exact calculations, have to be done to give us a bench mark. But once you have them you ought to be able to find out where to make your approximations, so you get tractable expressions that anybody can work with to do their design with. Finally, I would like to emphasize . . . . No, one more point connected with the modeling. Nobody has started working yet on a specific three-dimensional model for the SCATHA spacecraft. Now I think that is being talked about, but I

haven't heard it talked about publicly and I would like to go on the record as saying that should be started. It is not going to be an easy thing, I don't think. It should be started soon, so that when SCATHA does go up, we have a working model we can go to and start using to compare the data. Okay, my final point is to emphasize again what I said in my talk, the usefulness of lab work. Again, I think this is an area that has been relatively neglected. There was more here at the conference than I anticipated, and especially the work that is going on at Lewis Research Center is very encouraging. That way they are able to generate fluxes of energetic particles in their vacuum systems and see the effect on materials. But I think we should go beyond just looking at the effects on specific materials and put together a composite miniature spacecraft that truly represents real spacecraft configuration, materials; and see what happens. We need to have some kind of a model to use to predict what will happen and go in and see what does happen and begin to get some confidence in the calculations.

A. Rosen

M. Sellen

Mike Sellen on Laboratory Research and Simulation.

I would like to address three points and one of these is the question of similitude. This gets to be fairly fascinating when once you get into laboratory experiments and try to duplicate space. It would be a healthy viewpoint to say similitude yes, but always in moderation. There has been one experience in combined environmental test facilities which I think is consistent; that is, that they continue to insist on more and more similitude, the usefulness of the facilities tends to go down. You can always ask if the cosmic rays should be there or whether the extremely hard EUVL should be there or a variety of things. On the other hand, it is rather clear that there are certain openers as far as this testing goes, and the spacecraft is going to operate in vacuum and it is going to operate with some kind of electron environment and some kind of photons. I think it gets to be a hard and fast rule that basically is where the test results will come. You simply will not test spacecraft in ambient air under any circumstances unless that is the

medium you intend to fly it in. The second thing is to try and talk about what I think might be the overall purpose of a great deal of the lab research, and I say that there is one outstanding thing that comes out of it that gives you a sense of perspective. If there is a single physical parameter that has a greater variation than conductivity, I am not sure right off what it is. It goes from  $10^{18}$  ohms centimeters down to microhm centimeters. It has a variation of  $10^{24}$  in it from one material to another and particularly when you get into weakly conducting materials, it is just a function of just about anything you can think of, particularly in what we will call weak field conduction, less than  $10^5$  volts per centimeter. And so one thing that can come out of it is the possible perception that you are dealing with a 12 parameter problem that includes all of the history, including that of the manufacturer on the night that he made the sample you are looking at. And if that is the case, then maybe one thing that the laboratory experiments will try to do is not to try and solve the whole problem, it may simply have too many parameters in there, but it will tend to direct the effort off into what I'll say is just reducing the problem. We will talk about that in this third point. The other possibility of using the laboratory again for perspective is that I am sure there is going to be an increased analytic effort and already the computers are, I guess, going to be brought to bear. I think the laboratory will serve as a very necessary antedote to this. I always discovered even when I am doing it myself, that there is a subtle narcotic effect toward having the computer begin to run things out and, about once a day, have an experiment keep some of the perspective because the initial assumptions of the computer program are forgotten I think within a few hours. And these are very sparingly based most of the time. The third point that I would like to discuss is the use of the laboratory to reduce the problem. I think the majority of the program offices would rather see a quick solution to a small problem than an elegant solution and a prolonged solution to a very complicated one, and there are all these questions about using these methods to either bring the man to the mountain and vice versa and the only

question is whether you can use the laboratory to keep this thing from being a mountain. Most of the charge up problems, the gross ones, I think the ones that could do damage to spacecraft will go away if you make the material conductive. We will always be troubled with problems of the scientific spacecraft. The major thing is to use the laboratory to very rapidly simplify the problem that one is looking at, because most of the applications here, I think, would really rather get on to many other things that spacecraft have on their agenda. Thank you.

A. Rosen

J. Stevens

John Stevens on Laboratory Spacecraft Investigations.

I would like to talk about three different items as well. What can project managers do to help their design? You've heard a couple of papers today talking about the use of sparkers and looking into the harness response. I think this type of test should be amplified; it should be done early in the design phases and get away from using the flight spacecraft which imposes severe limitations. You can couple a sparker into a typical spacecraft engineering model (or something similar) and look at what goes into the harnesses. I believe this will improve the transient specifications. Another point is that actual spacecraft response to the environment is needed. For that you have to scale. You can't simply go from small sample responses to a full size spacecraft. I believe you are going to have to get into testing complicated, large spacecraft models in a simulated environment. Combine this with Elden's comment on developing a model to predict your performance. Then, you might be able to handle how to design the whole system without having anomalies. The last point is that operational satellites, hopefully, will be carrying monitors in one form or another. We need space data. We need something to tell what is going on in the spacecraft in response to the environment. With these things together, hopefully, you can build yourself a spacecraft that would survive, without anomalies, in the space environment in which it must operate.

A. Rosen

Bill Lehn on Material Research.

W. Lehn

As you have heard in the presentations in the Materials Development Session, materials research and development is underway and new and modified materials are being developed under these programs for consideration and application by the spacecraft community in the design and construction of spacecraft. There is available right now the new fabric thermal control coating type material which you have heard discussed. I feel that the application of this material offers an excellent opportunity to alleviate, at least in part, the problems of designing around some of the major spacecraft arcing problems resulting from dielectric multilayer blankets and solar array substrates. The other materials being developed, the modified polymers, and others are a little longer range before successful application will be realized. So, at least for the immediate future, the designers are going to have to use the materials that are currently available and design, build and test the various spacecraft systems with these materials. Hopefully, the other materials solutions to reduced surface potentials in addition to reduced arcing will be forthcoming. These materials solutions, though, will require the combined coordinated technical efforts and inputs of not only the engineering simulation and characterization group but all of the results of the classical or materials properties group being inputted to the materials program. Hopefully, by this combination of efforts, materials solutions will be forthcoming. Some of these are longer range but will lead to useful materials. Reducing the overall surface potential of a spacecraft to low values, is not a short term but rather a longer range problem. It is not quite as simple as modeling as some of the other problem areas.

A. Rosen

Stu Bower on Spacecraft Testing

S. Bower

Both John Stevens and Mike Sellon have made some comments on the subject. I guess a little dissension is a good thing at a meeting like this, so I think I'll furnish a little. I agree with you on testing by small discharges along cables combined with analysis to evaluate what your needs are and how to use this as a design tool in the early stages

of the satellite design. On the other hand, I back off a little from Mike's thought where he wants to test in the ambient environment. Perhaps testing a full satellite in a vacuum chamber with a plasma source is a highly desirable thing from a research standpoint and to determine how this corresponds to what you can do with less expensive, less time consuming test such as simulated discharges. I sort of feel in the long run that it may not be necessary to use such an elaborate test on all spacecraft as a validation test. You can learn from this and ultimately we should be able to apply this knowledge and cut the test down to something less expensive and less time consuming. Regarding the thought that you can never get an adequate test unless you test in the actual environment, I would like to make mention of the fact that this is very rarely done in any kind of system, aerospace or otherwise. You depend on simulation test, for example, in survivability of a satellite. We do not test them in underground tests nor do we test them in space. We do this entirely with simulation. It takes a certain amount of research and thought before you are satisfied that you have an adequate way of doing this and you usually incorporate some safety factor to give you confidence. Just one more comment along this line. Earlier this morning, one of the RCA people was talking to me and pointing out that they have two synchronous satellites up; one has been up for almost a year and the other has been up for a number of months. These satellites were designed with no provisions for spacecraft charging. Nothing was done about that. They simply designed them, on what they thought were good design practices for those satellites. They have no evidence of any upset from spacecraft charging in their electronics at this point in time, and the evidence of discharges occurring in the solar arrays, coming down through the boom, are very minimal. Those that they have had, amount to just a few amperes, perhaps 5 amperes, which is certainly very small discharges coming down through there. The principal reason I bring this up is I guess that I want to make sure that we don't go for an overkill here. Maybe they just plain lucked out on this thing. But in questioning them a little bit, they had a

three-axis stabilized satellite with the spacecraft body a fairly good Faraday cage, and I suspect also their signal lines normally were coax cables. They were getting rf protection from two sources. And the point is, if you can without any effort and research and all the other fine things, design spacecraft that will operate in this environment without discharges, I think we will have to be a little practical about it. Along this same line, of course, ATS 6 is relatively free of anomalies of this source. Granted, they went to some rather extensive steps for rf shielding.

A. Rosen

I am glad that someone came up with something that represents some degree of controversy, especially here in the area of overkilling the problem. We have on the panel, members who are a little bit closer to the management of spacecraft systems. I want to ask these members of the panel to comment and also ask questions of other panel members. The question, as I see it is what is the correct response to the point that Stu Bower raised. How do we achieve any degree of standardization so that we can address the problem in a sensible way. I would like the persons who are closer to management to comment on this. Do we need committees? Should the managers themselves participate in the program. To open this thing up, I will ask Bob Lovell, Maury Bunn, Charlie Pike, and Meryl Mitges to comment on these points. Let's start with Maury Bunn.

M. Bunn

Having just come out of a program office, I think it is quite important that we include the managers of program systems. I spent two years on the DSCS program trying to get them to fly monitors and I was not successful. I think if they had been at this symposium, it might have been easier to convince them that these things do exist and we have got to design the systems to withstand or be insensitive, or not to respond to these effects. I guess I would like to say that we should definitely include the management from the Program Offices, the Air Force, in particular and I would assume that in the civilian COMSAT community, it would hold also.

C. Pike

Along the line of what Maury has just said, I have actually been working with Maury for a number of years in this area. In general, there certainly is a great reluctance to fly monitors and the prevailing philosophy has been the quick fix. Ultimately what will result from our work and I feel what we really turn into the operational community has to be something rather boiled down. If our results are in a very complex fashion, by the time they get into the working community, our results could be lost. Unless our results are in a very handy form, we really would have missed a lot of our goal. So along the line of quick fixes, recommendations should be to the point, but of course based on a lot of good engineering and scientific research.

A. Rosen

Bob Lovell for comments. Do you have any questions?

R. Lovell

I guess I am answering the question or commenting on the question on how do we coordinate our activities. Is that right? Okay. I don't know how many of you know about the joint programs that the Air Force and NASA have. There is a piece of paper out that was published in the open literature. This basically describes what several of us here worked on and together it is what we call a road map. It lays out our plan of attack on this problem. Part of the road map calls for a sort of a Steering Group. Again some of the same people or most of us here are on that Steering Group. It was described at the AGU meeting last June 18 and its title "Spacecraft Charging Investigations. A Joint Research and Technology Program." It's a piece of paper like that.

A. Rosen

By the way I ought to mention that it's also published in AIAA as Progress in Astronautics and Aeronautics Series Publication, Vol. 47 "Spacecraft Charging by Magnetospheric Plasmas."

R. Lovell

My point is that we are trying to coordinate this with everyone. The users, the people who need this information, and so we have a Steering Group. The Steering Group has set up working groups. These working groups are identified. I guess we are the only ones who know their names right now; but basically they are the people you have heard talk

and they fit into the five elements that we have broken up the problem into. The definition of the environment, is chaired by Lt. Hank Garrett. Modeling which is cochaired by Al Rubin, and Carolyn Purvis. And so on. So we have these groups of people. What I encourage you to do is get better acquainted with the working groups. Now we have asked them to go out and consult, not only with the Air Force and NASA people, but the university people and industry that is working on this problem and making the contributions and also the European communities. I would encourage you to contact them. If you have some thoughts and if you think that this effort is not going the way it should be or should receive different emphasis, contact those people, because we are looking to them to give us planning direction and we are trying to get the resources and try to make sure this whole thing keeps going. We on the Steering Group all keep talking to each other, but we are really looking toward the working groups. So I guess my answer is that we are trying to coordinate it that way and maybe now I have told you that the groups exists, you can contact them and get your inputs in.

A. Rosen

M. Mingos

Merrill Mingos on Materials Development.

From the material development view, I am both encouraged and discouraged by what I have heard the last three days. Encouraged in the sense that we are learning a lot of new things about materials, but like the planetary probe work, for each question we answer in the process of testing we raise two new questions. This situation develops from what Mike Sellén was saying about the multiplicity of parameters that must be at least considered if not actually introduced in experimentally evaluating and characterizing the Materials for spacecraft use. Thus, I would ask the question of either the people who develop the materials and run the tests on them, the characterization tests, or the spacecraft designers: "Can we come up with an agreed upon list of parameters and evaluations that we ought to be conducting on materials to assure dependable system design?" Can we standardize on the tests that we should be performing so that they will be reasonably complete in

a physical principal sense, but not get into overkill in terms of time and resources required? Another issue relates to the level of materials development funding, because I feel we are somewhat out on a limb in developing electrically conductive materials for spacecraft systems. The funding is very marginal in my view relative to the risk associated with the developments. I think that conductive paints is one typical example. I don't feel in the near term that we are going to get a conductive satellite paint that has anywhere near the desirable thermal control characteristics that we would like. We can always find a conductive black paint or a green one but you pay for that in terms of the heat load you put into the satellite because these are not optimized in thermal control terms for example. In our Air Force interagency deliberations with NASA over the past number of years, the net result is that NASA is looking toward the Air Force to put most of the funds into materials development. Well, we have responded positively, but it is a modest sum, overall. Further, in assessing what is going on in Europe it is my opinion that there is very little materials development work there, although we are looking more closely. So again, I feel that we have only a modest amount of funding considering the magnitude of the problem, and I hope that this funding in materials development isn't swamped by the complexities of the testing data that is required.

A. Rosen

I would like to open the discussion so that panel members could ask other panel members questions first before opening it up to the audience. Charlie Pike had a question that was directed to Eldon Whipple.

C. Pike

In your comments with regard to requirements for a model for SCATHA, to what level of geometrical detail do you feel we should go into to accurately model the spacecraft configuration. What level of mathematical detail is required, in your opinion, for this modeling.

E. Whipple

Well, I haven't really thought about that. I guess my intuitive feeling is that, as you know, SCATHA is a very complicated satellite. It has lots of booms, a very long antenna for measuring electric fields, several shorter

booms for measuring sheath and spacecraft related electric fields, and a magnetometer boom. I think that we should have something that is realistic enough, that the rough surface features are represented. It should have booms in some crude sense, the antenna, the magnetometer boom and it should also simulate the surface, the gross surface properties. You know where there are insulators and should represent with an insulating model and, where it is conducting, with a conducting model. Not in the centimeter scale perhaps, but certainly on the ten centimeter scale.

A. Rosen

I have a question appropriate to this topic. During this conference we heard models described that ran the whole gamut from simple circuits, lumped circuits, to very elegant three-dimensional, dynamical computer codes that simulate the trajectories of particles coming in. Are the simple models at all valuable? They are much easier to operate at this time and very easy to discuss and analyze and know what you are getting. Are they worthless? What is your feeling about simple models at this time?

E. Whipple

Well, I think simple models are very valuable. They serve to illustrate the basic physical processes that are going on. They serve to eliminate processes that are not there and help you to get at the right ones and in the work that I have done in the past where I have had to worry about low energy particle measurements, it has always surprised me how well a very crude model can describe the data. For example, I showed a slide in my talk where I had electron current as a function of voltage. Well, I used the Debye potential to model the potential distribution around the sphere. We know that is not an accurate solution, but it fit the data extremely well. And looking back on it after we did it, I think we can explain why. But certainly the very simple representations, I think, can be very useful and surprisingly good in those cases.

M. Bunn

Elden, in considering the SCATHA vehicle, in particular, to get a first order effect approximation, let's say, what effects do you think we could assume away? I see that we have to run the simple models to try to get to the internal

response of the system. And I also think that we have to do some extensive in depth modeling so that the experimenters will know what is going on in that sheath region. The problem is that it is going to happen in reverse. If you have the all-up modeling to show you which were 2nd and 3rd order effects, then you could go into the simple modeling and do it right. Is there a way of coming up with the 2nd or 3rd order effect without the all-up modeling so that the simple modeling can be conducted now when you need it? And then have the all-up sheath modeling, what you call 3-D modeling, continue in the future.

E. Whipple

I am not sure I understand completely what you are asking, but I think what I have in mind is, first of all, when SCATHA goes up, Joe Fennel for example, is going to have his booms out there to measure the sheath fields. Well, I think the zero order thing we need is the geometry. That sort of determines the gross features of the electric field pattern. Now we need the geometry and we would need the surface properties. I think that kind of a 3-D model, you know have 3-dimensions with real geometry but neglect space charge and don't worry about effects of photoemission on the sheath or even effects of the plasma, the environmental plasma, on the sheath. I think that will probably give a pretty good representation of gross electric field configuration. Now, we are not, I don't think, even at that point yet. We may be close to it because if you neglect space charge it reduces to just solving Poisson's problem for complicated geometry and that shouldn't be too hard to do. And the next step would be to put in the particles and merely see where they go, to track them from their source through the system and then back out again or to wherever they go. And that will give you a feeling for the look angles for the instruments. You know, what are they seeing when they look into a certain direction. And that is the first question that experimenters will start asking; when they see particles, they want to know what it is that they are seeing. Are they photoelectrons, are they environmental electrons, where have they been accelerated? And that kind of question you should be able to answer with this kind

of a simple, simple in the sense that it is not self consistent, but complicated in the sense that it really represents the geometry. But we know how to solve that sort of problem. Does that answer your question?

M. Bunn

Yes. I have just been trying to get a handle on how we go about this whole modeling technique, and the way that I see it is probably about what you described where we take a relatively simple model to find out how the vehicle is going to respond, as soon as possible. Some ground tests should then be performed in order to understand it more when it gets into orbit and to verify this model, and then to continue in the more complicated modeling for the experimenters.

E. Whipple

Yes, I guess one thing that I should add here. My viewpoint, I think, probably represents pretty much those of the experimenters where we are more interested in the science of what is going on around the vehicle and not to first order in anomalies in the spacecraft. Although if something happens, we are going to be very interested. But the kind of modeling that I described may not suffice for getting at when discharges would occur. So that may not be sufficient for what you want eventually, but I think that is what the experimenters want to analyze their data.

A. Rosen

I'll recognize Bob Lovell at this point. Did you want to ask a question?

R. Lovell

I would just like to say something and get everyone's response here. When we ask a question about how much is enough in anyone of these areas, whether it is modeling, materials development or whatever, I would like to think of the spacecraft charging problem in terms of how it manifested itself. There are four levels that I see. The first thing that we see is EMI. And that is an immediate problem and I think one that is on the top of the pile. That is the first thing that we have to handle. The next is material degradation. You might recall from some of the talks that some of the material does get destroyed and for some mission we would see some thermal problems and I think that is the next level. The third level is what I would call contamination. After you solve the other two, you might

be worried about what comes back to the satellite and fouls up your optical surfaces or that sort of thing. Finally, the science. The people who want to do science missions may require very sophisticated models and precise control. When we are working on this problem, that is the priority that I perceive and I hope we have agreed on the priority here. I would like some feedback on it. We have to start at the top of that and go down. Now when we introduced the SCATHA in our program, which is a big investment and a necessary step, that may require that you get very sophisticated to get everything out of SCATHA that you need so that you can come back around and have those answers.

E. Whipple ..... It bothers me a little that you put science at the bottom of those four levels. I think maybe that your point is that spacecraft has to survive before we can do the science, and that is fair enough.

R. Lovell I think that our customers out there in the world are mostly operational people these days, and they're the ones having the problems.

S. Bower One might put it a different way and I think we must be a little bit careful. Among the contractors and the people who design these things, there is a heck of a lot more manpower there than there is here. That is, a lot more concentrated manpower who are closer to the problem. They are going to come up with some fairly clever solutions once they see what the basic situation is. They'll come up with some rather simple fixes for some of these things that won't require a lot of science and we'll come along later with a lot of science and by the time we do, there will be fixes that people will be using in general. Along the same line I would like to make the comment that regardless of what any group such as this does in coming out with specifications or requirements, the individual program offices will make the decisions. We will not dictate to them. Their life is totally one of making decisions and tradeoffs. The first question that they're going to ask on any of this stuff is what does it weigh, what is the cost, and what is the scheduling impact? The next question they are going to ask is what are my alternatives, and they are going to

insist on alternatives. The next question is going to be what if I don't do anything, what do I lose? And on the basis of that they may tell us to drop dead, they are not going to do anything. In fact, this has happened in the past. I hate to be so brutal and so practical, but this is the way programs run.

C. Pike

I want to amplify a little bit on my initial comment in regards to what is ultimately turned over to the program offices and the contractor community. The result should be in a simple and boiled down form; but not at the expense of some very fine scientific research which is something that we really don't want to lose sight of. The problem is, from a physics and engineering point-of-view, extremely complex. The community that is working this problem must keep in their mind that the ultimate product must be something in a useful form. It's a comment I made earlier and I make again.

A. Rosen

I would like to put in perspective some of the comments that have been made. We are operating on a variety of levels and I feel with Elden that science should not be at the bottom of the pile. On the other hand, in many cases we are talking about spacecraft that have objectives that are non-scientific, yet we are looking to these spacecraft to carry environmental monitors, to do scientific analysis. There is no question that a lot of work has to be done in the scientific areas; however, programs with non-scientific objectives are not interested in the science per se. They are interested in design fixes accomplished in the simplest possible way with the least expenditure of money. The thing that we can do as scientists is come up with methods of doing these things economically, and efficiently. From their point of view, our greatest service would be to find methods of giving them the necessary assurance of the integrity of their design and have them do nothing. I would like to open this discussion up to the floor.

A. Vampola

Obviously, the purpose of this conference is to design or come up with some sort of specification to design spacecraft to. The modeling, the materials development, all these

things are means to an end as far as the spacecraft community is concerned, although the scientific community may consider it an end in itself. We have been given some data by Dr. Gore which shows that paying attention to details of signal conditioning on a spacecraft which is otherwise quite dirty from a charging point of view can, in fact, alleviate most of the problems and I would like to ask Stu Bower what is his opinion after seeing all the material presented the last three days. What is the possibility of sitting down right now and writing a specification that would have a high probability of producing a spacecraft that would not go bump in the night?

S. Bower

I think there is a pretty good probability with one exception, which I mentioned this morning when I was talking; namely, the concern that I have for how large an area will discharge at once. Although there are some reasons for believing that it is not going to be the whole surface, there is no rigorous proof available obviously. This causes some concern. We have a handle on about how large an area; if we had a better handle on the size of the pulse, I think the probability is pretty good and it is based on two things. We can basically identify the characteristics of the discharges that take place and where they would take place. Secondly, the contractors who are designing the satellite have access, in general, to the kinds of information generated from the work that NASA Lewis has done and the design handbook which they are working on. So they have a clue and a starting point and then beyond that it is based on the fact that the designers themselves are fairly sharp people who know their systems, and given the basic circumstance are quite capable of designing around these problems. They have been doing it for years.

E. Whipple

May I ask a question? I guess this should be addressed to Bob Lovell or John Stevens. This represents a discussion in that hall, I think yesterday, commenting on the fact that it appears, for example, in ATS 5 and 6; as far as we know, we have had no anomalies. And I think the NASA spacecraft have not experienced as many anomalies in this environment as some of the other ones, and I know that

Bob and John began to look into that. I think ... well let them speak for themselves. I am just interested if they have any comments as to why that might be so.

R. Lovell

Let me just say something and let John finish it up. About a year and one-half ago, John, Stu Bower and myself, travelled around to industry and we asked some questions. How do you build your satellite? And we picked out selectively some companies that we knew who had satellites up that were not having problems and some that did. We did not, systematically, put that information together and follow through on it. We are delinquent in that. That is, it is our intent to rectify that, to do that and get that information out. I think, in terms of conclusions, at that time, the ones I remember are the same things I heard today. If you pay attention to grounding and shielding, and you do a good job, whatever that really means, then you are not going to have trouble. I am not sure that we see that. The biggest doubt in my mind is associated with CTS. When we were working on CTS, we concluded that if we did all those good things it would be heavy like a brick house. CTS was a very light weight, relatively open spacecraft. I don't know what Vic Gore has to say about it, I think he said a couple of anomalies, but I really don't think we have spacecraft charging anomalies on CTS.

J. Stevens

As a result of the tour that we took through the aerospace industry, it became evident to us, that the satellites that were experiencing anomalies were the ones that used computer level logic and stored commands. Those satellites that are building in the possible source of anomalies, because the satellite is configured such that any upset would start a whole series of commands. The NASA satellites, the ATS 5 and 6 and the SMS satellites were basically controlled from the ground. There was really very little that could get them into trouble. The SMS used latching relays. The ATS 6 depressed the logic levels so that it took something like a 15 volt spike to get the logic to change state. This is in addition, of course, to SMS and ATS 6's Faraday cage, and the shielded wire. Stu Bower's comment at the time was that operational satellites didn't have

large weight margins and you probably couldn't do everything that was done for the NASA satellites. Exactly how much was really required we were never able to figure out.

4. Bower

In regard to your reference to my remark. We could not afford the weight of rf shielding which was done on ATS 6. Now of course that was done because the body of the satellite, all the electronics, sit right in the main antenna beam and the concern was with the upsets from the main antenna beam. The fixes that are handled by logic design essentially add no weight to the program as I mentioned this morning. We did go back and redesign a satellite which is a very undesirable thing to do. We want to do it in first place.

A. Rosen

Ray Goldstein had a question. Do you still have it? It was answered. Okay.

M. Sellen

One sort of thing when I'm sitting around where anomalies are being discussed is the sort of frustrating feeling you have with very little amount of data on what actually goes on in the spacecraft. You have a few terminals that give you numbers and at that stage you finally can define whether you have an anomaly or not just on the basis of the information you get off of that. And if keeping the bird on the air and having it do its appointed thing, which is transmitting messages or something like that, it is the primary function of the mission, then you can very well say, hey we might already be there. The only other thing, of course, is saying that we don't really know what is happening on the surface of the spacecraft except those things that happen at the time you have the circuits on. And if you look into the science, you can say, was your science anomalous? Well if you happen to know what the ambient particles in space were at that moment, and know that your instruments were turning out a different result, then yes you have got an anomaly. But there is no way of knowing directly in that circumstance whether it was anomalous or not. You have only the data from your terminals. And I think this forms one of the bases. I would like to come back to something we talked about later. This is one of the places where you get perspective. And a laboratory allows you to have some

command over the parameters that you are imposing on this thing. And if the thing, with its limited diagnostics that exist on the spacecraft or a model of a spacecraft, doesn't tell you the right things, then you know you have got an anomaly. And most of the time you just simply don't have that capability. It is very easy to take a small model of the spacecraft and put it in and have a sensor give you the same answer for 15 different conditions, but it gives only one kind of reading, and you can twist it around all over the place. And that is valuable in terms of what we really know about what's happening on the spacecraft. We know a very limited amount. My experience is true in the other way. I think half the loading you charge to particle data is wrong and the other half is questionable. What is very difficult for some poor devil who has spent five years on the instrument, you know, is to say that. It shows up in the JGR.

J. Laframboise

I have three comments to make. First of all I think that the entire situation that we have been discussing this week is a classic result of neglecting basic science. I think that is something that ought to be obvious to everyone who is here, but I think there are still a lot of people who don't like to hear that kind of thing. About ten years ago, it became very difficult for people to talk anybody into hanging particle and field experiments on satellites. And I think the total cost of what has happened may very well be greater than the money that was saved at the time. That is my first comment. My second comment is in regard to numerical models. As the proposer of either the only two-dimensional numerical model that has been discussed, or one of the only two (I am not sure whether Lee Parker would refer to his model as "two-dimensional"), I want to talk about the importance of two-dimensional models. There have been a lot of one-dimensional models and there is a very impressive three-dimensional model that has been described. A two-dimensional model is the simplest model that you can think of, which is going to give you the basic feature of this problem, and that is the asymmetry between sunlit and shaded areas. One-dimensional models can't do it, and three-dimensional models are more elaborate than

you need, to do that. So I think that two-dimensional models will turn out to be extremely important in getting at a lot of the basic physics that is involved in this problem. Finally, I would like to make an analogy to a situation in aircraft design. Now, when someone rolls a new airplane out of the hangar, you already know it is going to fly, furthermore you know exactly how it is going to fly. You probably have got a simulator built and trained pilots already. That's because there are computer codes for simulating the performance of that airplane at all levels of complexity. There are many, they overlap. There are some simple ones that illustrate basic phenomena and there are some complicated ones that give you three significant digits or more. I think that ten or twenty years from now, hopefully that will be the situation in the design of synchronous spacecraft. There will be codes available that will give you that kind of confidence.

A. Rosen

Lee, do you want to comment?

L. Parker

Well, the model that I showed has an R-Z geometry. It could be called 2-1/2-dimensional if you add up all the velocity and configurational dimensions, or 2-dimensional if you plotted in R-Z space.

S. DeForest

I would like to comment just a little bit on the very first sentence you made. I don't think that basic physics has been neglected. Gee, I knew these things were charged up in 1967. The people at Lockheed and I wrote a letter to the ATS project office and we quoted things all the way back to 1924 which showed that they would charge up. And they do charge up. We have the author up here, Rejean Grard, who sponsored a similar symposium, I think back in 1971, who printed a book, this one very nice book. The stuff has been around for a long time. I don't think it's neglected basic physics. I think it's neglected anthropology. That kind of problem.

J. Laframboise

Okay, but I think you'll probably agree that in cases where anomalies occur, there are hardly any cases where there is instrumentation on the same spacecraft to see what the environment was.

M. Sellen

I think everyone is a friend to the computer and there is no doubt but what it's going, you know, to increase productivity and do a variety of things. What I think might be important to keep in mind though about the computer designed airplane as well as the computer designed spacecraft, that as far as ... if we look into aviation history there are those occasional brushes with reality and I can think of three, but I am sure there are more: which was the retrofit of the Electra wing, the landing speed and angle of attack of 727 and the DC-10 baggage door. All of which, I am sure, you know, were not picked up in the computer. I think we are going to find quite a bit more as we go through there. Clearly, people will make use of analysis. What I was trying to argue for was some kind of check on open loop analysis. It, literally, gets fascinated with, you know, the complexity and brilliance of its codes and sort of goes open loop without an experiment.

A. Rosen

Pete Stadler, you want to make a comment and possibly show some charts?

P. Stadler

Let me ask a question in the light of the previous comments, and hopefully not to produce any emotionalism. Let us put on the communication satellite program manager's hat and ask what can be gained by knowing the environment, what advantage is there to him in putting sensors on the spacecraft? How can we motivate program managers to add sensors?

J. Laframboise

Do you want me to answer that?

A. Rosen

No, anybody in the room?

J. Laframboise

I guess it is a matter of what one thinks is going to save money. And I have a feeling that knowing what is going on, is the best way to save money in the long run.

P. Stadler

Look, I know that something upset-inducing was going on.

J. Laframboise

Yes, but you don't know what the environment was. And if a problem occurred and you don't know what the environment was, then it is very difficult to design a spacecraft in the future that isn't going to have that problem.

P. Stadler

Let's reduce it to something reasonable. The kind of sensors that I'm talking about are those which you can possibly convince somebody to fly on an operational communications spacecraft. Are you talking about a sensor of 5 volts in a space of less than half a cubic foot? What can you really tell about the environment with those small sensors?

J. Laframboise

Well, obviously there are going to be different kinds of spacecraft with more or less elaborate sensors.

S. DeForest

Can I address this, just a minute? Let's assume that your spacecraft doesn't exist in a vacuum. Let's assume that you have got this little thing that you've put on there, a noise sensor, maybe a simple Faraday cup, and then suppose you have a continuing program of monitoring the environment. Then I would say, you've got it. If you've just got your simple, you know, half a kilogram, 10 bits per second something or other and don't know anything else about the environment, maybe you're trying to correlate with a ground base station or something. Then, I agree, you're going to get very little information. Eternal vigilance is the price of liberty. That is what we have got to have. We've got to know what is going on up there. I am saying the million and one-half dollar type plasma analyzer, you don't need on everything. Okay? But you should have one somewhere. Doing something. And maybe cheaper. I don't know. But you should have something up there all the time. And if you have very, very simple noise monitors, plasma type things, on the vehicle itself, which is being effected. And then I think we can apply physics. SCATHA and GEOS both have good instruments.

R. Lovell

I would give you the answer to that question. If you put a simple sensor on, like the ones that were discussed here today, and if you are project manager, then I would tell you the reason you should put it on if you don't care at all about helping the science community is that when you have an anomaly on your spacecraft, you'll save yourself some money in your failure review activities. A very serious point because we have seen it. Dr. Gore mentioned it, maybe you didn't catch it today. Whenever there is a

problem on CTS, the very first place they go is the transient effect counter and say "What Happened?" So, it'll save you money and it's useful to help explain to your boss why something fouled up.

- A. Rosen I would like to support this.
- E. Smith Is it worth half a million dollars?
- R. Lovell No, I don't think it is worth a half-a-million dollars. What question am I answering?
- E. Smith ..... How much money are we going to save against the cost of the machine?
- R. Lovell Well, the instrument is simple, which I thought his question was. He is shaking his head, yes, and you're saying no. ...
- E. Smith When you have to make changes to an existing system, including the changes in software, telemetry, all the other stuff, it is about a \$200K change on a military system, before you start. Now you add \$5K instrument on top of it. It costs you \$205K. Now how are you going to save money?
- J. Napoli I would like to answer that question. I think I can answer that question by trying to explain the commercial environment for satellites. I guess there are about ten commercial satellites in the geosynchronous altitude and these companies plan to be there. These missions were all seven to eight years. If you could put a means of detecting or trying to correlate an anomalous onboard catastrophic failure, okay, against something that is induced by the environment or something else that is related to the spacecraft charging, which causes the catastrophic failure which gives you only a three year bird; you have lost six years, or you have lost four years of revenue, at two million dollars a channel, twenty-four channels. That is a lot of money. Versus a 205 thousand dollar saving. This is from a commercial standpoint.
- Audience The real answer you need to give and what you care about in these operational systems is the fact that you have a bird up there operating, and if you convince people that by putting on a sensor, you are going to be able to solve these problems faster, so that you have longer life satellites,

they will fly those sensors. Just to get data, they won't fly them.

J. Napoli

Well, I think that is another problem. I think a problem here, too, is if you look at these commercial programs there is a budget, a very competitive atmosphere, and if you look at the people in the business, COMSAT, Western Union, RCA, the Canadians, well I guess the Canadians really don't have much competition, but their type programs, two year programs, these are heavy incentives on the contractor to deliver in two years. We don't have this luxury of running all these test programs we would like to see and then again if you do go up and you are maybe lucky, like RCA is, in not having anomalies at all, try to go back and convince management to fly on the third, on F-3 and F-4, fly a monitor on there. It is a difficult thing to do at this point.

E. Whipple

It seems to me that we are putting the cart before the horse a little bit. We have been talking about flying sensors to find out why we have anomalies. And really what we want to do is be able to avoid anomalies in the first place. Now, if you have a sensor that just tells you that you had anomalies, and maybe correlates it with something in the environment, that is fine for analyzing what has happened, but maybe your spacecraft is dead by then. Now, hopefully by flying some of these environmental sensors we can find something out in the environment that is a precursor for what causes the problem. Sherman DeForest has shown that these injection events correlate with a high charging states of the spacecraft. I think it is very likely that these injection events that happen in the magnetosphere are pre-figured or pre-shadowed by some kind of electromagnetic wave. And if we could identify such a thing and use that as a warning signal, that would really be valuable. Then we could shut down the satellite, wait until the event is over, and then go back up again.

C. Pike

I would like to amplify on that and say that if indeed there is a signature - I see a representative from the Air Weather Service here, Capt. Halcrow - if there is a firm operational requirement for monitoring, and if there is, indeed, an

environmental signals which one could realistically monitor, then that is something that really falls within the Air Weather Service's purview of responsibility.

M. Bunn

I think I would like to offer another answer to Ed Smith's question as to how you justify that \$205K. On the DSCS program during a 2 year period, we spent about \$200K just studying anomalies that we were experiencing. And that doesn't account for the cost of the fixes after we decided what we were going to fix.

A. Rosen

Capt. Bunn, with due respect, I want to say that the amount that was spent was well in excess of \$200K.

M. Bunn

Thank you. That just reinforces my ...

A. Rosen

It does? Because the amount that was actually spent involves a team of over fifty people who traced various aspects of the anomalies. I would guess that in terms of the four or five anomalies studies that I was able to observe, the amount spent was much closer to two to eight million dollars. The amount that was spent in our group alone, and that is just the analysis group, to study the environment to try to pin down the phenomena and try to get Sherman DeForest and anybody else involved in this, was well in excess of \$200K.

M. Bunn

I guess I would still like to see monitors on those birds right now and I have been trying, but it is difficult, as Pete knows.

P. Stadler

Wouldn't it be appropriate for this group to consolidate these arguments and try to present, as one of the results of this conference, a recommendation, with substantiating arguments, that we should fly sensors on each military satellite and/or commercial satellite. Wouldn't that be helpful at this time?

R. Lovell

I think that is a good idea and I think we should take it as an action item for the Steering Group. I think that is a good idea.

J. Napoli

I go along with that idea.

R. Lovell

We will do that.

A. Rosen

A. Muelenberg

You have my encouragement also.

The concept is that millions of dollars are being programmed insuring a couple of spacecraft from failure. It seems ridiculous not to put a couple hundred thousand dollars into on board monitoring, which has practically the same probability of failure these days. The other thing is that looking at some of the massive data, you can see the onslaught of these substorms in time to warn people to get on the stick, something is going to happen. Is it going to happen or is it not, even if you have ten minute warning. If you know what to look for, you can prepare for it most of the time. You can take care of it. It is simple insurance.

Audience . . .

It is a bit of a change in topic but earlier on the first day we talked about active control, electron emitters on ATS 5, 6 and there will be some on SCATHA. . . How do the program people feel about putting active control on their satellite?

M. Bunn

I guess from my standpoint I really can't answer that question, until we find out what happens on the SCATHA bird with the active controls on that.

A. Rosen

Bob, would you like to try that also from the NASA point of view?

R. Lovell

Well, NASA's satellites are more in the science category. I think there is not any doubt that there is a desire to reduce the potential to very low levels and that will probably take an active control device. I am not sure what kind that will be. In our program that I talked about earlier, we had laid out a fairly clear path to get there where the development of passive (mainly materials) and active control devices (things like shinning light bulbs, squirting out electrons and whatever) will be investigated. It is down stream because you need the kind of work that the modelers and the environmental people are doing before you can begin to really evaluate.

M. Bunn

Let me add something here. If you can't get the operational systems to put a \$200K monitor on, you're not going to get them to put on an active electron gun or whatever. I think it has to be flown experimentally which is being done on SCATHA, although probably not all the possible active devices, but it will give us a handle.

C. Pike

I would like to add that the Air Force Geophysics Lab is putting the electron and ion beam system on the SCATHA satellite, and the objective of the experiment is technique development for vehicle charge control and to come up with, essentially, how to do it in effective fashion. Our program will be complimented with the ATS 5 and 6 results.

M. Mingos

I would like to present an analogy with active thermal control. From the Air Force point of view, one of the principal design objectives is long life satellites, in the range from five to ten years. If you can provide an active spacecraft charge control system with no moving parts, if it doesn't weigh much, and if you can assure a high level of reliability for the five to ten year period, then you would get a responsive audience. If you can't demonstrate that, then I think operational acceptance of any active system would be difficult to achieve.

A. Rosen

Ray Goldstein, would you like to comment on this question?

R. Goldstein

I think I would have to distinguish between two kinds of spacecraft. The service type communication satellite is basically up there, runs, and is passive. The other type is the one that NASA is primarily involved in, the science type of satellite. My feeling is that it is possible with passive methods, that is, materials, circuitry and whatnot, to have a spacecraft in a charging environment without any upset. That was previously mentioned, for example, for ATS 6. Bob Lovell and John Stevens talked about the differences between those spacecraft which don't and other spacecraft which do see anomalies. There is a difference in the philosophy of how you build a spacecraft. So I think it is possible to build a spacecraft at least with a protective point-of-view, so that even exposed to the charging environment it will survive. The cost trade-off between putting in fifty pounds of shielding versus twenty pounds for an active control device must be done. But from the point-of-view of a scientific satellite, there is no question that in order to get good low energy data you need some sort of active as well as inactive type of control. I agree with Mike Sellon that most of the low energy particle data are questionable. The case of Pioneer 10 and 11, which was briefly mentioned the other day, is a good example.

M. Sellen

There is one other thing that you might want to emphasize here, and that is that it was you know, a nice piece of fortune that one had a spacecraft that was geosynchronous and that could go into eclipse and come out and that had a particle counter on it and could suddenly watch the spectra shift up and down by about ten kilovolts, and had enough passes at that sort of thing to clearly identify the effect. And yet, you know, a Jovian encounter is a Jovian encounter and there isn't the possibility of doing something repeatedly there. And so specifically, if you try now to divide the interests along here into those spacecraft that have very limited encounters with an environment, it may be a better thing to put all kinds of insurance on there and then include the active device. For that simple reason, you have such a limited time and you have such an unknown environment in which you are going to have to operate anyway. I don't think anyone really has an idea what the Jovian situation can be in certain passes.

Audience

I would like to address this question to Sherman. With a predictive on-line capability, don't you feel that the Space Environment Lab at NOAA could be a starting point for that? Say the GOES data.

S. DeForest -

It is a starting point. But as I said before we have a lot of sales problems. Don Williams has been working for years, as you know I'm sure, to get plasma instruments on board. There are no plasma instruments on board GOES. The lowest energy on any of those is a solid state detector which catches the upper end of the injections. They are very useful spacecraft; particularly useful are the magnetometers on board which I have studied with Joe Barfield, beautiful data, but it would be worth much more, if there were even a simple plasma device on board. At the present time, I don't think there are any plans for any plasma devices on any of the NOAA spacecraft. That thing is a proper function and should be pursued.

Audience

Why?

I think because nobody has asked for them to do it.

S. DeForest

No, no. Don has been trying for years to get on; at least that's what he tells me and the people who work for him . . . I've got to believe that. Is there anyone from NOAA here that you know of to defend yourself, I'll withdraw that.

M. Bunn .

Sherman.

Could I interject a quick question? How do you feel about the correlation between ground based magnetometer data and activity at geosynchronous for example?

S. DeForest

Okay, that is a very good question. Actually, I had slides set aside earlier in this area, in case someone asked. In terms of injection, when there is injection of particles at geosynchronous altitude, there is a one to one, never fail, substorm on the ground. The classical definitions of an auroral substorm, the southern most arc brightens, the whole thing. There are features on the ground, particularly along towards dawn in the "dangerous region," called the patchy aurora, rayed structures, and stuff like this. There is no analog in the plasma for those features. Okay. Contrarily, there are things that happen in the equatorial zones that are not mirrored on the ground. For gross things there is a one to one correlation and if you count the detailed effect, it is not there. Now let's look at something else. Now when there is injection, there are currents flowing between the spacecraft and the ground. The currents change the magnetic field. You are on the ground looking up, and you have an accuracy of where you can locate an arc, you miss by half a degree, you're pretty close but you have got a half of a degree error. That translates into over 1 earth radius. You're going to miss by 1 earth radius in the equatorial zone. In addition to that, you have got these currents in between. So you don't know how to map, even if you had it absolutely accurate on the ground, you don't know how to map. I think you know this, but I spent a lot of time doing this, trying to correlate between ground base and equatorial measurements. I think the answer is that we can improve our ground based measurements. DMSP pictures are very very useful. I don't think we will even get detailed one to one correlation.

J. Laframbois

I would like to make another comment on instrumentation. I think clearly the ideal situation is a few elaborate instruments and a lot of little ones, preferably standardized. If you think again of aircraft, you see that aircraft all carry crash recorders. If you had that arrangement with a few elaborate instruments and a lot of simple ones, the elaborate ones could calibrate the simple ones. Furthermore, think of a situation if you had the same instrument on a lot of synchronous spacecraft at different longitudes. If a substorm comes along it is going to hit one before the others, you'll have a little time to react, and you can do something with the others if you have that kind of arrangement.

C. Pike

I want to add a comment on the very localized nature of the disturbances which are seen on the ground as mapped down from synchronous altitudes. And that is that one needs a very dense chain of magnetometers in the auroral region to accurately identify that there is, indeed, a disturbance going on. And there are chains of magnetometers along magnetic meridians and the Air Weather Service has data from one of these chains in real time. The unambiguous identification of these injection events is a very difficult thing to infer from magnetometer data.

R. Lovell

I would like to ask Sherman if he would care to give us a ten year weather forecast? Are there storms ahead?

S. DeForest

Well, if you have been following the literature, there is a thing known as the Maunder minimum. I expect that is what you might be referring to. For a very long time, essentially for a lifetime of active astronomers, there were no sunspots and there were no ... there was no aurora and there were no disturbances and if we had been around at the time of Galileo, none of these anomalies would occur. Is that going to happen again? This is current research. It did not come on immediately. It sort of petered out for a period of time, but I think the answer is yes, we will have another solar cycle and yes we will have more substorms and according to one book that I read in "1533" we are going to have lots of sunspots. And

there will be a big earthquake in California. As Charlie points out, we are having these anomalies right now, and this is solar minimum. Around 1983 it will get worse.

Audience

I am somewhat concerned about this question of prediction. I am prepared to grant you that you can predict these injections. But what are you going to do about it? Because no commercial operator is going to turn his spacecraft off, unless he really believes he is going to lose it. I think in the last three days we have heard enough evidence, he really isn't likely to lose it. He may have interference, he may have bumped telemetry, but he is going to be on the air. These are commercial contracts and you can't afford to turn the darn things off. That is what you're being paid for. Continuity of service.

A. Rosen

A very good point. The other point is that monitors don't prevent anomalies, they merely record them and I think the predictive capability is not one that the operational projects, spacecraft project managers want to have. There is only one area where they may want to have some predictive capability, and that is in planning their launches and possibly finding a place to store satellites at synchronous altitudes. Would you like to comment on that also?

J. Napoli

I don't quite follow that last remark about planning their launches?

A. Rosen

Yes, there is a question as to whether there is a longitudinal position at which the environment is less adverse than at other longitudes. Now, the thing that you want to do when you use operational spacecraft is that you don't want any down time at all. So one of the schemes that has been proposed is to have a passive satellite that is ready to go on the air momentarily and take its position in order to not have any discontinuity in service. And the question is, where do you store it while it is passive, in what region? Possibly there is research that could be done in this area.

J. Napoli

From a commercial standpoint that is a very difficult thing to try and accomplish because if you look at the spectrum there, between 90 and 135 degrees, it is like the Long Island Expressway during the rush hour. And you want to have

immediate continuity or restoration of service. You would have to be at just about the same location or within a degree, and in many cases and if your intent is fixed antennas on a spacecraft, which most of the commercial satellites are. I don't know if that is applicable to the commercial spacecraft which are dominating the equatorial plane right now.

R. Lovell

I would like to address your point a little bit. I think it would be reasonable to project that spacecraft communications, or operational spacecraft, maybe in the next ten years, will carry an operational station keeping device, like an electrical thruster, an ion engine. And would you not be willing, if you had a warning, to turn that thing on, if it also turns out to be effective as a neutralizer. So I think there is a great merit in having this warning capability.

Audience

I think there is merit in having the warning, even after the fact, because if something happens, then you are suddenly faced with something has gone wrong and what is it, and you look and you say gee, I had a warning five minutes ago that this was going to happen, it does point you in the direction you have to look.

A. Rosen

It is getting very close to adjournment. There are a couple of items that I wanted to cover. One of them was a request by Pete Stadler and Paul Chivington to address the question of testing. In this area, there has been many approaches, procedures, and methods that have been used and Paul Chivington wants to say a few words. Afterwards, I also wanted Réjean Grard, to comment on what the Europeans are doing in material research and spacecraft charging. So we will start with Paul Chivington.

P. Stadler

Editor's Note: The reader is referred to the paper by Chivington and Stadler.

A. Rosen

We will take one question on Pete Stadler's comments.

E. Smith

We did current injection by discharging capacitors over the various parts of a qual model satellite that was left over from a program that was launched otherwise. We got quite a surprise. It was not radiated EMI that was causing our upsets. It was coupling in structural terms, for example. I just thought I would pass that on to you.

- P. Stadler Well, we will certainly be looking for that very thing here. One of the prime things . . . .
- A. Rosen A procedural note: we have to terminate the formal part of this panel discussion. All of you can stay and continue on. We will be here to answer questions and make comments. I wanted Dr. Grard to make the final comment and after that I think most of us will be available and we can continue. The formal parts are over, but before we terminate, Dr. Grard.
- R. Grard I feel that we are really shying away from the straight approach to spacecraft testing. We are presently trying to stimulate anomalous spacecraft behavior with Tesla coils and spark generators. It would indeed be much more realistic and efficient to place the spacecraft in a vacuum chamber and to subject it to electron bombardment. I cannot see where the difficulties are. . . . .
- R. Lovell This is something that we at NASA think is a good idea. But it is an expensive proposition. For the commercial users, I don't think they can afford it.
- R. Grard Today it is customary to submit spacecraft to vibrations and to expose them to simulated solar and vacuum environments before launch. I believe that testing their susceptibility to surface charging will become in the future a routine procedure which all spacecraft will undergo. We do not have to design new vacuum chambers; we only need an electron gun and a battery of ultraviolet lamps.
- R. Lovell It is not the expense of the chamber. Expense of handling a piece of flight hardware, the associated ground support equipment, staff. It is just expensive.
- A. Rosen I am sorry. I will have to make a closing comment. There is a joint NASA/Air Force committee in existence right now and they are open to suggestions and comments from anybody in the audience and anybody interested in this field.
- M. Bunn Bob Lovell and myself are contact points on that Steering Committee.
- A. Rosen I would like to thank this whole group and state formally that the panel discussion is closed.